**Mineral deposit research
for a high-tech world**

Proceedings

VOLUME 4

12th Biennial SGA Meeting

12–15 AUGUST 2013, UPPSALA, SWEDEN

Mineral deposit research for a high-tech world

Proceedings

Volume 4

Edited by
Erik Jonsson et al.

The 12th Biennial Meeting was organised by the Geological Survey of Sweden with assistance from Uppsala University, Stockholm University, the Geological surveys of Finland and Norway, Luleå University of Technology and the Swedish Museum of Natural History.

A digital version of these volumes is available from the SGA website at www.e-sga.org

Cover photograph: View of the Aitik open pit copper mine in the very north of Sweden. Mining operations started in 1968 and the current mining depth is 430 m. The open pit is c. 3 km long and 1.1 km wide. The production in 2012 was 34,3 million tonnes of ore containing 67 100 tonnes of copper, 51 700 tonnes of silver and 1,9 tonnes of gold. Photo: Olof Martinsson, Luleå University of Technology.

VOLUME 4

High-tech elements – deposits and processes **1679**

S 3.11:
Metallogeny of the Urals

Convenor:
Richard Herrington

Endogenous metallogeny of the Urals

Nikolay S. Bortnikov & Ilya V. Vikentyev
IGEM, Russian Academy of Sciences, Moscow, Russia

Abstract. Major chromite, magnetite, copper-pyritic and gold deposits of the Urals are reviewed in the frame of historical metallogeny. Variations of chemical composition of ores are consistent with magmatic evolution: from sodium tholeite basalts through sodium rhyolite-basalt bimodal and to potassic granitoids. Most deposits are subduction-related and bear metals of ensimatic (mantle-derived) profile (Fe, Ti, V, Cr, Cu, Zn, Co, Ni, Au and PGE).

Keywords. Endogenous deposit, subduction, ore mineralization, copper-zinc massive sulfide, gold

Introduction

The Uralian orogen is one of the largest single ore belts in the world and contains 15 Bt iron ore, 350 Mt chromites, 2.5 Bt non-ferrous metal ore (70 Mt of Cu+Zn) and 2300 t gold reserves in endogenous ore deposits. Many deposits were discovered (Fe, Cu-Zn, Au and Cr) in the end of 20th century. Many of them became the new types for the Urals: deposits of copper, gold and some others. The tectonic setting of the deposits, timing and geodynamics of the region as well as geochemical and petrography features of host rocks are still subject to discussion (Brown et al 2011, Herrington et al 2005, Puchkov 2013).

1 Regional setting

Several zones are distinguished within the Urals (Fig. 1): Preuralian foredeep, West Uralian, Central Uralian, Tagil–Magnitogorsk (Tagil and Magnitogorsk zones), East Uralian and Transuralian zones (Koroteev et al 1997, Puchkov 2013). Most of the endogenous ore deposits are found in the Tagil-Magnitogorsk zone, located to the east of the Main Uralian fault.

The Tagil zone (T. trough) is filled with Ordovician-Silurian volcanics. Volcanic-plutonic complexes of calc-alkaline, K-Na-rich rocks (D_{2-3}) occurred in its axial part. *The Magnitogorsk zone* (M. trough) is composed of volcanics of Middle Devonian to Middle Carboniferous. Upper Devonian to Early Carboniferous sedimentary rocks occurred along its axial zone. The *East-Uralian zone* and *Transuralian zone* (including Kustanai trough) are located to the east of the Tagil and Magnitogorsk troughs. They are composed of irregularly metamorphosed Paleozoic volcanic and sedimentary rocks. Blocks of Pre-Cambrian rocks and large granitic massifs of Late Paleozoic are widespread over the East-Uralian zone.

2 Tectonic-magmatic evolution and ore mineralization

The evolution of the Urals during the Paleozoic was correspond to a 'Wilson Cycle', which included ocean floor spreading, subduction, formation of island-arcs and collision of the latter with adjacent continents (Puchkov

2013). The Tagil and the Magnitogorsk zones have demonstrably similar geodynamic environments: evolution of volcanism from ophiolitic (tholeitic) series to Na-bimodal basalt-rhyolite (calc-alcali) and subalcaline basalt-trakhite (shoshonite) series suggests deeper levels of partial melting in mantle with time (Fershtater 2013). The location of the youngest fragment of Tagil arc (Turyinsk zone) along the extension of the Magnitogorsk arc suggests that the Magnitogorsk subduction zone was partly inherited from the Tagil zone (Puchkov 2013).

Mineralization of the **continental-rifting stage** (PR – Є) is mainly distributed within the Central Urals zone. Small chromite (Saranov), ilmenite-titanomagnetite (Kusin), barite-lead SEDEX (Saurey), some rare-metal (Ta, Nb, Zr, REE) and superlarge siderite (Bakal, ~1,100 Ma) deposits were formed during this stage (Koroteev et al 1997, Puchkov 2010).

The spreading environment occurred during the Ordovician within the Tagil and Magnitogorsk zones (Puchkov, 2010). The relics of **crust of oceanic type** contain small Co-Ni occurrences and giant chromite deposits but both of them relate to subduction processes. Few small Co-Ni serpentinite-hosted sulfide deposits were formed in a forearc setting (Herrington et al 2005, Nimis et al., 2010), occurring in blocks within Main Uralian fault zone. Pyrrhotite is the dominant ore mineral, demonstrating elevated concentrations of Co, Ni, and As.

There are a series of world-class deposits of podiform chromite in the southeastern part of the **Kempirsai Massif** (West Kazakhstan, Urals). They occur within an obducted fragment of ophiolite sequence. Massive chromite ores are confined to the upper part of the dunite-harzburgite bodies. Chromitites are surrounded by dunite envelopes with transitional boundaries to harzburgite. The ore bodies have lenticular shapes, and in some places chromitites cut the host dunites. Deposits usually comprise single lenses of chromitite ranging up to 1800 m in length and from 5 to 150 m in widths. They are usually of 100 m, rarely up to 230 in thickness. Chromitites containing 50 to 60 wt % Cr_2O_3 are dominant and they are enriched in the refractory platinoids (Os, Ir, and Ru) (Mechler et al 1999). Large blocks of the ophiolite originally formed during seafloor spreading (during Middle Ordovician) were involved in subduction (under the Magnitogorsk arc) in Late Ordovician - Early Devonian (Puchkov 2010). The final formation of large podiform chromitites was resulted from a multi-stage process involving interaction of hydrous, second-stage high-Mg melts and mantle fluids, in the supra-subduction setting (Mechler et al 1999).

3 Volcanic arc regime

Island-arc volcanic rocks in the Tagil zone were formed

during Late Ordovician–Early Devonian, while the Magnitogorsk and Kustanai troughs developed during the Late Emsian–Givetian. Deposits of copper-zinc massive sulfides, titanomagnetite as well as skarn-magnetite, porphyry copper, and small gold-polymetallic deposits all originated in similar island-arc environment.

The **Kachkanar type** titanomagnetite deposits are related to the zoned dunite-clinopyroxene-gabbro bodies, which form of a chain of massifs in the Tagil zone (Fig. 1). The central parts of these massifs are composed of dunites, which are replaced by clinopyroxenites and then by olivine gabbro toward the periphery. These complexes are assumed to be diapir fragments of the melanocratic basement protruded into the Earth crust. They were cut later by gabbro-norites with formation (along their contacts) the reaction of ferroclinopyroxenites with a schlieren-disseminated titanomagnetite mineralization (Koroteev et al 1997, Puchkov 2013). Fe-Ti-V (+PGE) ore of the Kachkanar massif are superlarge iron accumulation (6.9 billion t of Fe reserves). Late-magmatic Cu-Fe-Ti-V-P (+PGE, Au) mineralization (exemplified as the large Volkovsk deposit) is hosted in olivine gabbro (Fig. 1).

Volcanic-hosted massive sulphide (VMS) deposits were mostly related to sodic rhyolite-basalt complexes corresponding to primitive arc stages of Early Silurian (Tagil zone) and Middle Devonian (Magnitogorsk zone) (Prokin, Buslaev 1999, Herrington et al 2005). *Dombarovsk* type (close analogue of Cyprus type) deposits occur within basaltic pillow lava and are small (up to 20 million tons) and rather rare (Mauk, Letnee, Osenee, Zimnee, Levoberezn). They are hosted by tholeitic basalts, occurring in the basal parts of the volcanic sequences of the Tagil and Magnitogorsk troughs (Herrington et al 2005, Nimis et al 2010). Ore bodies are lens-like or lenticular, lying conformably to the host rocks and consisting mainly of pyrite and chalcopyrite with minor sphalerite and pyrrhotite. The ores contain 0.02–0.1 wt% Co, 0.1–0.3 ppm Au and 4–8 ppm Te.

World-class deposits with 3-10 Mt of (Cu+Zn) reserves are located within the Magnitogorsk zone (Fig. 1). They can be classified as *Uralian* (Cu-Zn-pyritic) type (Prokin, Buslaev 1999) and contain ores with Cu≥Zn (Gaisk, Jubileinoye, Safyanovsk etc.), or Zn>Cu (Uchaly, Uzelginsk, Degtyarsk, Podolsk, Sibai etc.). Deposits of this type were generated within intra-arc basins in submarine paleovolcanic belts and relate to depressions filled by products of large stratovolcanoes (Seravkin 2013). Nine large deposits contain more than 65% of the bulk initial base metal reserves of the Urals. Eight of them contain >100 t Au and >1000 t Ag. Large ore bodies (usually lenses) and their groups are hosted by locally altered (sericite-quartz and sericite-chlorite-quartz) felsic rocks.

A few small gold-enriched massive sulfide deposits are classified as *Baimak* type (the total ore tonnage of individual bodies usually is of 1 to 3.5 million tons). They occur in andesite-dacite-granite complexes. Ores (mainly stringer-disseminated) are enriched Cu, Zn, Pb, Ba, Au

Figure 1. Structural zones of the Uralides and position of ore deposits (according to Puchkov 2010, modified).
Ore deposits: 1 Novogodnee-Monto, Pervopavlovsk, 2 Chudnoe, 3 Vorontsovsk, 4 Berezovsk, 5 Bereznyakovsk, 6 Kochkar, 7 Svetlinsk, 8 Varvarinsk, 9 Ray-Iz, 10 Saureysk, 11 Amursk, 12 Uchaly, Novo-Uchaly, 13 Uzelginsk, 14 Molodezn, 15 Aleksandrinsk, 16 Sibai, 17 Bakr-Tau, Balta-Tau, Uvarjazh, Tash-Tau, 18 Maysk, 19 Jubileinoye, 20 Podolsk, 21 Oktabrsk, 22 Gaisk, 23 Blava, Komsomolsk, Yaman-Kasy, 24 Dzhusinsk, 25 Barsytchiy Log, 26 Letnee, Osenee, Levoberezn, 27 Vesenee, 28 Priorsk, 29 50-let Oktjabrja, 30 Kundidzi, 31 Degtyarsk, 32 Safyanovsk, 33 San-Donato, 34 Krasnogvardeysk, 35 Levikha, 36 Kachkanar, 37 Galkinsk, 38 Valentorsk, 39 Auerbakh, 40 Volkovsk, 41 Bakal, 42 Gumeshevsk, 43 – Tominsk, Kalinovsk, 44 Tarutinsk, 45 Mikheevsk, 46 Magnitogorsk, 47 Sokolovsk, Sarbaysk, Kocharsk, 48 Benkala, 49 Kempirsai group, 50 Jubileynoe (Au)
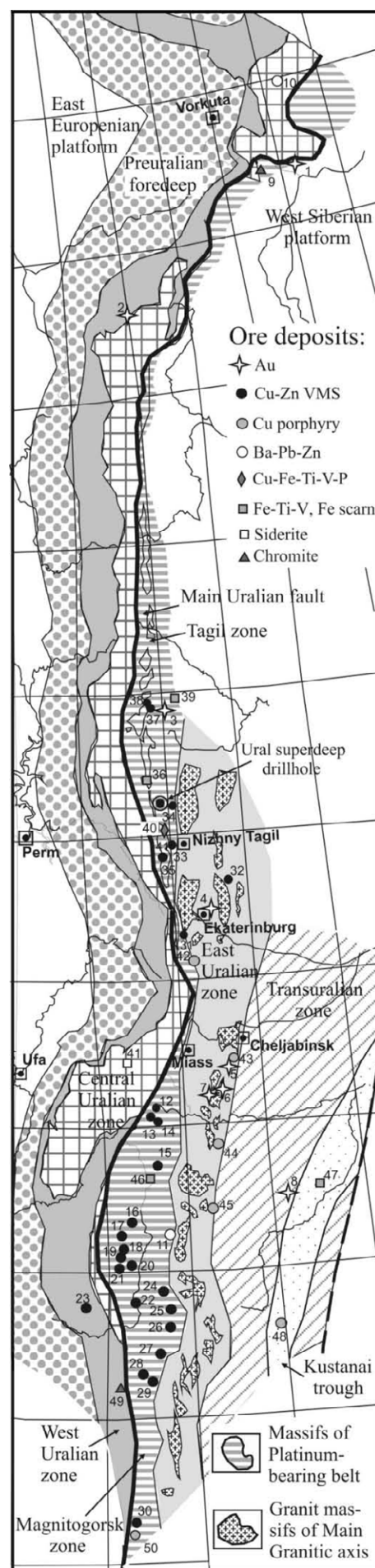
and Ag. In this respect, they have been considered to be transitive between VMS and porphyry-copper-gold deposits. The predominance of the stockwork ores over the massive ores can be explained by subsurface (in shallow water) environment of ore formation and by paragenetic links between the ores and the subvolcanic felsic rocks. Some sulfide lenses were deposited in intercupola and intervolcanic depressions, whereas the major ore mass formed as stockwork in the fractured subvolcanic rhyodacites. These deposits are close analogues of Kuroko-type deposits (Prokin, Buslaev 1999, Herrington et al 2005).

The **porphyry-copper/gold deposits** are confined to the hypabyssal gabbro-diorite and diorite-plagiogranite intrusives, which appear to be comagmatic to the volcanic-arc sodium andesite-basalt association (lavas, tutts and tuffites) (Puchkov 2010, Grabezhev 2012). They conform to diorite model of porphyry copper systems (island arc geochemical type). Porphyry-copper deposits are composed of a stringer-disseminated pyrite-chalcopyrite ores with low copper content (0.2-0.4 wt.%). They originated mainly in Early Silurian (425-429 Ma – Tominsk, Bereznyakovsk) and in Early-Middle Devonian (Jubileinoe, Novogodnee-Monto, Petropavlovskoe) (Fig. 1).

The ore bodies of the **Bereznyakovsk** gold field occur in Lower Silurian dacite-andesite tuff, limestone, subvolcanic dacite and andesite bodies (Grabezhev 2012). The disseminated and stringer-disseminated orebodies are accompanied by quartz-sericite hydrothermal alteration. Three ore stages were identified (Plotinskaya et al 2009): pyrite (380-320°C), polymetallic (with enargite, fahlore-telluride, and gold-telluride substages; 300-170°C, P=0.4-0.2 kbar)**,** and galena-sphalerite (220-185°C) ones. The fluids were of moderate salinity 4–9 wt.% NaCl equiv.

The **Novogodnee ore field** contains the Petropavlovsk gold-porphyry deposit and Novogodnee-Monto gold-skarn-porphyry deposit (Puchkov 2010, Soloviev et al 2012). Gold mineralization is related to gabbro-diorite-tonalite complex. Ore bodies are conformable to contacts of the porphyry bodies. The calcareous skarn mineralization was overprinted by a gold-magnetite-sulfide mineral assemblage accompanied by a solution acidity increase and a temperature decrease from 600 to 350°C. Finally, the gold-sulfide-quartz stockwork and veins were formed between 270 to 130°C and ~1 km depths from chloride solutions with salinity of 20 to 10 wt.% NaCl equiv. The ore-bearing fluid displayed a δ^{18}O range from 0 to +6‰, that may correspond to a mixing of primary magmatic and meteoric waters. The source of fluid constituents is believed to be a mantle-related magmatic chamber (^{87}Sr/^{86}Sr = 0.704±0.002; δ^{34}S$_{pyrite}$ = 0±1‰) (Soloviev et al 2012).

4 Arc-continent collision and active continental margin regimes

During the Late Devonian-Early Carboniferous conditions evolved to a dominantly active continental margin (Koroteev et al 1997, Sazonov et al 2001). During the last decade, it is considerd as an arc-continent collision regime (Brown et al. 2006, Puchkov 2010). An eastward

subduction of the oceanic and island-arc complexes below the Tagil and Magnitogorsk zones (comprising a few microcontinents) occurred. The andesitic complexes (typical for the continental margins) with a widely varied compositions of magmatic rocks from andesite-basalts to dacite and rhyolite, and from gabbro-diorites to syenites and granites are assumed to be formed above the subduction zones (Grabezhev 2012, Puchkov 2013, Fershtater 2013). These complexes made up the volcano-plutonic belts, and were superimposed on the deformed and slightly metamorphosed island-arc structures, fragments of continental crust which host a series of skarn-magnetite, skarn-copper-magnetite, and copper-molybdenum-porphyry deposits as well as gold deposits.

The skarn-magnetite deposits (and related copper- and gold-bearing deposits) are distributed over the eastern parts of the Tagil and Magnitogorsk zones. The deposits constitute several groups near the volcano-plutonic centers (Magnitogorsk, Tagil-Kushvin, Auerbakh). The volcano-plutonic complexes containing economic skarn-magnetite ores were found to be higher in iron content in the intrusive rocks and lower iron content in the comagmatic volcanics. The copper-skarn deposits are located in the eastern zone of the Auerbakh-Tur'in ore district where the pyrite-chalcopyrite mineralization is superimposed on the skarn-magnetite ores. The intrusive rocks are more basic and sodium-enriched when compared to those of the western zone of the ore district (where only skarn-magnetite deposits without economic copper mineralization are found). The giant iron-skarn deposits of Kustanai trough are preresumed to be formed in regime of superimposed (epicontinental) volcanic-plutonic belt (close to the ensialitic volcanic arc) in rift zones close to the continental margin in a supra-subduction setting (Herrington et al 2005, Grabezhev 2012).

The newly-discovered **Vorontsovsk deposit** is similar to the deposits of the "Carlin" type (Sazonov et al 2001). The geological section of the deposit consists of two suites: limestone and overlying volcanic-sedimentary: interlaying sandstone and siltstone (are dominant), andesite lavas and tuffs. Mixed breccias with limestone clasts are present at the contact zone between these suites. The stringer-disseminated ores mainly occur within the breccia horizon. The main ore minerals are pyrite and arsenopyrite (together 3-8 vol.%); chalcopyrite, sphalerite, pyrrhotite, gold (1-70 μm), realgar, orpiment, and cinnabar also occur. The ore bodies are of an irregular or lense-like shape. They are confined to the intersections of variously oriented faults, where the host rocks are altered into argillizites. The K-Ar age of sericite and, supposedly, of the gold mineralization was established as Carboniferous (299 ± 8 Ma, Sazonov et al 2001).

Copper-molybdenum-porphyry mineralization occur within the areas where the superimposed volcano-plutonic belts are located on the rifted subcontinental crust and they are predominantly of andesite composition comprising volcanic and subvolcanic rocks. The porphyry deposits are confined to small subvolcanic and hypabyssal massifs of diorites, quartz diorites, and plagiogranites. The ore-bearing intrusive massifs are characterized by a multiphase development, intra-

chamber differentiation, and the presence of explosive breccias (Grabezhev 2012). The ore bodies are isometric stockworks or linear zones. Mo, Au, Ag, Co, Re, and Se occur in ores.

5 Collision-related mineralization

The most intensive processes of continent–continent (Laurussia–Kazakhstania and then Laurussia–Siberia) collisions, accompanied by the formation of large granitoid massifs, took place in the Late Paleozoic (Puchkov 2013). The known *orogenic gold deposits* (Kochkar, Berezovsk etc.) are related to granitoids of the tonalite-granodiorite composition. Genetic models for the gold-sulphide-quartz deposits were elaborated by V.Sazonov with coauthors (Koroteev et al 1997, Sazonov et al 2001 etc), who argued for a major magmatic input during ore formation. This idea is supported by petrology and geochemical data (Fershtater 2013).

The *Berezovsk orogenic gold-quartz deposit* mined since 1748, is the major gold producer in the Urals. Its production and proved reserves are estimated to be 350 t of gold. The numerous ore veins occur within granitiods dykes and in their host rocks The Berezovsk deposit is considered to be a typical intrusive-related mesothermal vein gold deposit (Sazonov et al 2001, Bortnikov 2006). Geologic evidences, particularly the spatial and temporal association between gold quartz veins and Shartashsk granite complex suggest that intrusive massif could generate the mineralising fluids. Isotopic data support the hypothesis of magmatic source for fluid and metals to form the Berezovsk deposit. The variations of isotope compositions of ore-forming fluids indicate the fluid immiscibility and the incorporation of components from the country rocks.

The recently discovered *Svetlin gold-telluride deposit* is located in schists near granite-gneiss complexes, controlled by deep faults and associated with the gabbro-diabase dikes. Ore bodies have irregular, or lens-like forms. Host rocks are extensively altered mostly terrigenous sediments (with alteration comprising chlorite, albite, biotite). The age of the alteration is Carboniferous (300-320 Ma). Ore zones contain 5-10 vol.%, rarely up to 50-60 vol.% of sulfides comprising quartz veins and disseminated mineralization. The stringer-disseminated ore bodies are composed of pyrite, pyrrhotite, chalcopyrite, gold, calaverite, silvanite, hessite, petzite, and other minerals (Bortnikov 2006, Sazonov et al 2001). There are lensoid veinlets and veins (thicknesses are up to 10-15 cm; length is a few meters, sometimes 30-50 m). The vertical range of ore mineralization is demonstrably more than 1500 m. The presence of Cr and Ni in the geochemical haloes of the ores, as well as presence of argentopentlandite, troilite, mercuric gold, various tellurides, and native metals (iron, zinc) suggests that the ore-bearing fluids were reducing, and of a crustal-mantle origin (Bortnikov 2006, Sazonov et al., 2001).

Conclusions

1. The character of the ore mineralization of the Urals has been ruled by the geodynamic environments of its formation. Being closely related with oceanic and island arc magmatic complexes of mantle nature ore deposits mainly contain Fe, Ti, V, Cr, PGE, Cu, Zn, Ni, Co, Au with lower significance of Pb, Ag, Bi, Sn, W, Mo, REE, Ta, Nb.

2. The ensimatic (mantle-derived) nature of subduction-related magmatism (O_3-C_1) corresponds to predominance of ore deposits of the mafic profile: orthomagmatic chromite (Kempirsaip group), titanimagnetite (Kachkanar type) and arc-related copper-zinc massive sulfide deposits (Ural type) occur in large and superlarge ore accumulation.

3. The gold deposits originated in various geodynamic environments, but the largest arose duing the collision regime in connection with granite-tonalite pluton formation.

References

Bortnikov NS (2006) Geochemistry and origin of the ore-forming fluids in hydrothermal-magmatic systems in tectonically active zones. Geol Ore Deposits 48(1):1–22

Brown D, Spadea P, Puchkov V et al (2006) Arc-continent collision in the Southern Urals. Earth Sci Rev 79:261–287

Brown D, Herrington RJ, Alvarez-Marron J (2011) Processes of arc-continent collision in the Uralides. In: Brown D, Ryan P (eds) Arc-Continent Collision: The Making of an Orogen. Springer Frontiers in Earth Science Series, pp 311–340

Fershtater GB (2013) The main features of the Uralian Paleozoic magmatism and the epioceanic nature of the orogen. Miner Petrol 107(1):39–52

Grabezhev AI (2012) Rhenium-bearing Uralian porphyry-copper systems: geological position, isotope-petrogeochemical and spatial-timing lateral zoning. Lithosphere 4:190–207

Herrington R, Zaykov VV, Maslennikov VV et al (2005) Mineral deposits of the Urals and links to geodynamic evolution. In: Hedenquist JW, Thompson JFH, Goldfarb RJ, Richards JR (eds) Econ Geology 100th Anniv Vol, pp 1069–1095

Koroteev V A, Boorder H, Necheukhin V M, Sazonov VN (1997) Geodynamic setting of the mineral deposits of the Urals. Tectonophys 278:291–300

Melcher F, Grum W, Thalhammer TV, Thalhammer OAR (1999) The giant chromite deposits at Kempirsai, Urals: Constraints from trace element (PGE, REE) and isotope data. Miner Deposita 34:250–272

Nimis P, Omenetto P, Buschmann B et al (2010) Geochemistry of igneous rocks associated with ultramafic–mafic-hosted Cu (Co, Ni, Au) VMS deposits from the Main Uralian Fault (Southern Urals, Russia). Contrib Mineral Petrology 100(3):201–214

Plotinskaya OYu, Groznova EO, Kovalenker VA et al (2009) Mineralogy and formation conditions of ores in the Bereznyakovskoe ore field, the Southern Urals, Russia. Geol Ore Deposits 51 (5):371–397

Prokin VA, Buslaev FP (1999) Massive copper-zinc sulfide deposits in the Urals. Ore Geol Rev 14:1–69

Puchkov VN (2010) Geology of Urals and Cis-Urals (actual problems of stratigraphy, tectonics, geodynamics and metallogeny). Ufa, DesignPoligraphService, 280 p (in Russian)

Puchkov VN (2013) Structural stages and evolution of the Urals. Miner Petrol 107(1):3–37

Sazonov VN, van Herk AH, de Boorder H (2001) Spatial and Temporal Distribution of Gold Deposits in the Urals. Econ Geol 96(4):685–703

Seravkin IB (2013) Correlation of compositions of ore and host rocks in volcanogenic massive sulfide deposits (on the samples of South Urals). Geol Ore Deposits 55(3):68–83

Soloviev SG, Kryazhev SG, Dvurechenskaya SS (2012) Geology, mineralization, stable isotope geochemistry, and fluid inclusion characteristics of the Novogodnee-Monto oxidized Au-(Cu) skarn and porphyry deposit, Polar Ural, Russia. Miner Deposita 47:1–25

Mineral and chemical peculiarities of vent chimneys from the Yubileynoye VMS deposit at the Early Devonian basalt-boninite basement of west Magnitogorsk Arc, the Southern Urals, Russia

Valeriy V. Maslennikov, Nuriya R. Ayupova, Svetlana P. Maslennikova & Alexander S. Tseluyko
Institute of Mineralogy, Ural Branch, RAS, South Ural University, Miass, Russia

Ross R. Large, Leonid V. Danyushevsky
CODES ARC (Centre of Excellence in Ore Deposits), University of Tasmania, Private Bag 79, Hobart, Tasmania 7001

Alla Yu. Lein, Yuriy A. Bogdanov
Institute of Oceanology, RAS, Moscow, Russia

Abstract. The Yubileynoye Cu-Zn VMS deposit is located in the fore-arc boninite-basaltic basement of the Devonian West Magnitogorsk incipient arc. Ore body is reconstructed as strongly degraded sulfide mound with apron of sulfide breccia, turbidites and ferruginous shales. The sulfide breccia consists of colloform pyrite crusts and talc-, calcite- or quartz-rich chalcopyrite-pyrite-sphalerite chimney fragments. Tellurium-bearing minerals are generally scarce in a chimney material from mafic-hosted VMS deposits. However, Yubileynoye deposit yields abundant telluride minerals including altaite (PbTe), calaverite ($AuTe_2$), petzite ($AuAg_3Te_2$), hessite (Ag_2Te), coloradoite (HgTe), tellurobismuthite (Bi_2Te_3), rucklidgeite ($PbBi_2Te_4$) and cervelleite ($Ag_{4-x}TeS$). The LA-ICP-MS study has shown systematic trace element distribution patterns across chimneys governed by the strong temperature gradient. Chalcopyrite in the central conduits is relatively high in Se, Te and Sn, but is low in other elements. Sphalerite in the conduits and the outer chimney wall contains elevated Sb, As, Pb, Mo. The high concentrations of most trace elements (Ni, Bi, Te, Au, Ag, Pb, Mn, Tl W, V, and As) are characteristic for colloform and crystalline pyrite. The model of hydrothermal fluid interactions with host rocks, seawater and SO_2 is suggested to explain the concentration of the tellurides.

Keywords. boninitic basalt, massive sulfide deposit, Southern Urals, chimneys, tellurides, trace elements in sulfides, and LA-ICP-MS

1 Introduction

The Urals VMS deposits yield very well-preserved vent chimneys broadly comparable with modern black smokers by mineral zonation (Herrington et al., 1998; Maslennikov et al., 2009, 2013). However, the chimneys compared against each other and to modern black smokers display mineral and chemical diversity. This phenomenon can be explained by the results of accessory mineral and trace element microprobe analyses resolving variation in physicochemical conditions of forming processes in different geological settings.

The mineralogical study was carried out with a scanning electron microscope (REMMA–2M SEM) equipped with energy dispersive X–ray (EDAX) and Microprobe JCXA JEOL 733 at the Institute of Mineralogy, RAS. The quantitative LA-ICP-MS analysis was performed to identify a wide range of major and trace elements at the CODES, University of Tasmania [Danyushevsky et al., 2011].

2 Geological Setting

The Yubileynoye VMS deposit is situated in the Buribai VMS-bearing district at the West Magnitogorsk zone interpreted as a fore-arc region of incipient oceanic island arc (Herrington et al., 2005). The deposit is located within the intra-arc rift complicated by caldera of axial volcano (Seravkin, 2010). The host rocks are related to basalt-boninite basement of bimodal mafic Baimak-Buribai succession (Spadea et al., 1998). The main ore bodies are underlined by the altered basaltic pillow lavas and their breccias impregnated with chalcopyrite and pyrite dissemination and stockwork veins. In the hanging wall, the ore bodies are consequently covered by basaltic hyaloclastites, rhyolite, dacite lavas and andesitic basalts. Upper dacite unit encloses several small polymetallic massive sulfide bodies.

The ore lens may be reconstructed as a strongly destroyed sulfide mound. In the lower part of the mound core, massive compact pyrite and disseminated chalcopyrite are dominant minerals. The chimneys have been found in adjacent sulfide breccias (Maslennikov et al., 2013). Rare minerals such as marcasite, pyrrhotite, arsenopyrite, galena, tennantite, magnetite, bornite, hematite, electrum and native gold were detected at the deposit (Bolotin, Buslaev, 1988). In the previous research, despite the high grade of Te (up to 200 ppm), rare hessite was found in sphalerite, only (Maslennikov et al., 2013).

The ore of the deposit contains 1.5 % Cu, 1 % Zn, and 44 % S. Total ore resources are estimated at over 106 Mt. Despite the location in mafic unit, the Yubileynoye VMS deposit was identified as a Cu-rich (Cu>Zn) Uralian subtype "U1" (Seravkin, 2010).

3 Vent Chimneys

3.1 Mineral Zonation

The vent chimney fragments are 2-12 cm in diameter and 5–25 cm in length (Fig. 1). The chimneys are subdivided into pyrite-chalcopyrite, chalcopyrite-pyrite-sphalerite, sphalerite-pyrite and pyrite mineral varieties. The textural and mineral zonations of the chalcopyrite-rich chimneys are broadly comparable with modern black smokers. Outer walls of the chimneys (zone A) are incrusted with colloform and euhedral pyrite. The conduits (zones B and C) are consequently infilled with chalcopyrite, pyrite, sphalerite, quartz or talc and calcite. Sphalerite pyrite chimneys are probably related to modern white smokers, while pyrite varieties are similar to "clean" smokers or diffusers.
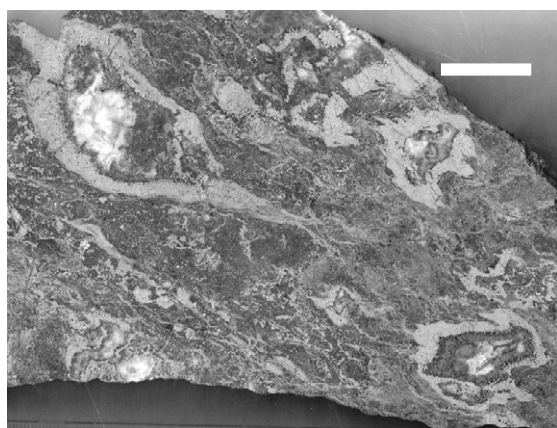
Figure 1. Sulfide breccia with chalcopyrite-sphalerite-quartz chimney fragments. Ore body 2. The scale bar is 3 cm.

3.2 Rare Mineral Assemblages

Chalcopyrite-pyrite chimneys are commonly depleted in rare minerals. Fragments of chalcopyrite-sphalerite-pyrite chimneys contain arsenopyrite, relic pyrrhotite, altaite (PbTe), calaverite (AuTe$_2$), petzite (AuAg$_3$Te$_2$), stutzite (Ag$_{1.88}$Te), hessite (Ag$_2$Te), and coloradoite (HgTe). Tellurobismuthite (Bi$_2$Te$_3$) and its Pb- and Ag-rich intermediate solid solution (xAg$_2$Te·yPbTe·zBi$_2$Te$_3$) including rucklidgeite (PbBi$_2$Te$_4$) are common in the chalcopyrite-rich chimneys. Native gold in association with tellurides and galena occur in chalcopyrite crustification, while electrum is widespread in sphalerite in association with galena, chalcopyrite, and rare tennantite.

Seafloor hydrothermal and postdepositional telluride assemblages have been distinguished in the clastic sulfides. Primary tellurides are preserved in seafloor altered sulfide turbidites, chloritic and calcareous ferruginous shales. In these rocks, some tellurides display epigenetic signatures especially in the pseudomorphous chalcopyrite and euhedral pyrite formed after Te-rich colloform pyrite. Neogenic tennantite, Se-rich galena, clausthalite (PbSe), hessite and cervelleite (Ag$_{4-x}$TeS) in association with native gold are common in altered sulfide turbidites and their products of seafloor oxidation. Sulfide breccia replaced by bornite contains neogenic renierite.

3.3 Chemical Zonation

Three chimney fragments for fifty-sixty individual LA-ICP-MS analyses were taken across all subzones of the chalcopyrite-pyrite-sphalerite-talc chimneys and some results are displayed in Fig. 2.

Zone A. In the outermost subzone A1, colloform pyrite is characterized by elevated contents of Mn (646–1348 ppm), Ni (up to 60 ppm), Pb (0.5–3 wt.%), Au (2–36 ppm), Ag (66–352 ppm), Sb (902–1322 ppm), V (up to 20 ppm), Tl (3–100 ppm), and As (up to 0.15 wt.%). In subzones A2 and A3, marcasite and massive pyrite exhibit consistently lower trace element levels, except for As (up to 1.3 wt.%) and Tl (up to 305 ppm).

Zone B. Chalcopyrite is enriched in Se (up to 265 ppm), Sn (up to 49 ppm), Te (up to 186 ppm), and Mo (up to 27 ppm), but is depleted in other trace elements predominant in pyrite from the zone A. Sn, Se and slightly Ag exhibit a gradual increase toward the inner part of zone B. High Au, Ag, and Sb contents occur in sphalerite, only (see Fig. 2).

Zone C. Subhedral pyrite and sphalerite are characterized by considerable enrichment in most trace elements relatively to the zone B. Pyrite crystals are characterized by high Au, Ag, Pb, and Te contents. In sphalerite, Mo contents are elevated (up to 23–35 ppm). Variable values of As, Sb, Pb, and Tl are likely to be caused by micro-inclusions of tetrahedrite-tennantite and galena within both pyrite and sphalerite.
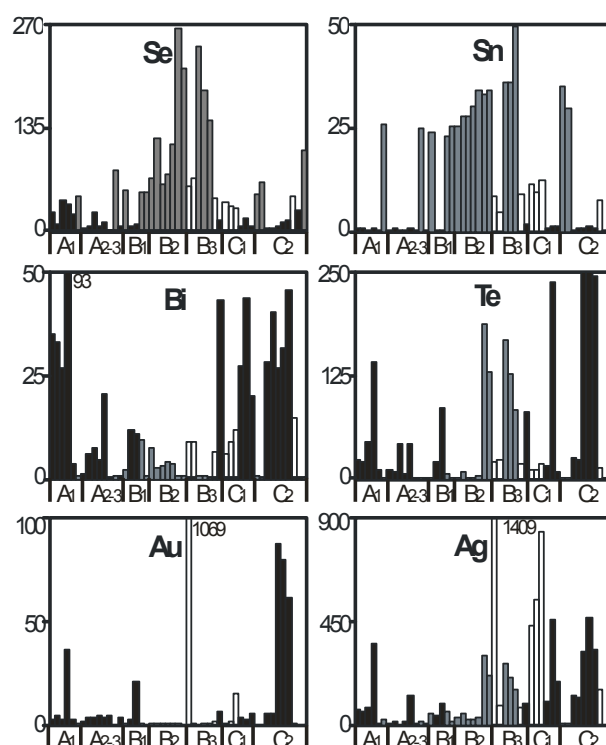
Figure 2. Distribution of trace elements (ppm). Filling: black – pyrite, grey – chalcopyrite, white – sphalerite. A$_1$….– zones.

3.4 Chemical Peculiarities of Sulfides

Chalcopyrite. Drusy chalcopyrite takes intermediate place in the range between modern black smokers from

MOR and diffusers from anywhere by contents of Se, Sn, Bi, Te and Mo (Table 1). In modern black smokers, these elements are concentrated at mid to high temperature under highly reducing conditions (Halbach et al., 2003). However, the barite-rich black smokers from mature vent site formed above hot spots (Menez Gwen, Lucky Strike, Axial Seamount) display much lower contents of Bi, Sn and Te with elevated Se (Fig. 3).

Chalcopyrite of chimneys from the Yubileynoye deposit is depleted in Co relative to chalcopyrite of modern black smokers (see Table 1).

Table 1 Trace elements in chalcopyrite of chimneys from the Yubileynoye VMS deposit and mafic-hosted modern vent sites*

Name	n		Co	Ni	Se	Mo	Ag
YB	30	av	0,005	0,09	119	5,1	69
		δ	0,008	0,24	65	18,8	78
MOR1	179	av	366	4,01	1710	48	56
		δ	844	6,94	1017	208	80
MOR2	17	av	0,22	0,37	13	0,1	315
		δ	0,32	0,76	5	0,1	159
HS	59	av	19,7	0,29	1306	42	76
		δ	34,3	0,53	964	135	100
BA	33	av	2,11	0,42	16	0,2	95
		δ	2,81	1,65	10	0,5	86
			Sn	Te	Au	Pb	Bi
YB	30	av	25	26	0,44	86	1,3
		δ	8	53	0,38	341	2,3
MOR1	179	av	15	76	0,07	12	7,2
		δ	24	66	0,10	36	17,8
MOR2	17	av	318	0,03	0,09	1	0,004
		δ	322	0,04	0,10	2	0,005
HS	59	av	5	0,7	0,12	26	0,03
		δ	5	1,3	0,35	70	0,11
BA	33	av	36	0,2	0,06	2	0,01
		δ	26	0,2	0,08	7	0,01

*Yb – Yubileynoye VMS deposit; MOR1 – black smokers from Mid Ocean Ridge vent sites (Broken Spur, Snake Pit, EPR 9°50′N); MOR2 – sphalerite-rich chimneys and diffusers from Mid Ocean Ridges (Snake Pit and EPR 9° 50′ N); HS – black smokers from vent sites located above hot spots (Lucky Strike, Menez Gwen, Axial Seamount); BA – sphalerite-rich chimneys and diffusers from back arc vent sites (North Manus, North Lau, Central Lau); δ- standard deviation; av – average;
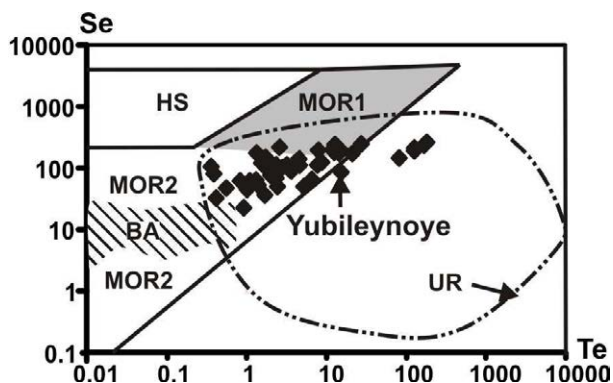
Figure 3. The diagram plots transitional position of chalcopyrite of chimneys from the Yubileynoye deposit

between black smokers and sphalerite-rich chimneys and diffusers.
MOR1 – black smokers from Mid Ocean Ridge vent sites (Broken Spur, Snake Pit, EPR 9°50′N); MOR2 – sphalerite-rich chimneys and diffusers from Mid Ocean Ridge (Snake Pit and EPR 9° 50′ N); HS – black smokers from vent sites located above hot spots (Lucky Strike, Menez Gwen, Axial Seamount); BA – sphalerite-rich chimneys and diffusers from back arc vent sites (North Manus, North Lau, Central Lau); UR – chimneys of Uralian type from the VMS deposits (Yaman-Kasy, Uzelga, Molodezhnoye)

Sphalerite. Most sphalerite in the chimneys from the Yubileynoye deposit and modern vent sites is characterized by similar high concentrations of Ag, Pb, As, and Sb due to inclusions of galena and tennantite. Concentrations of Fe and Cu vary widely consistent with the presence of chalcopyrite emulsion ("chalcopyrite disease"). Higher Fe/Cu ratios at low Cu contents indicate that Fe also substitutes for Zn in sphalerite of chimneys from the Yubileynoye deposit and modern vent sites. In addition to Fe, other elements such as Co, Sn, Cd, Mn, readily substitute for sphalerite because their ion radiuses are similar to Zn. The contents of Fe, Sn and Co in sphalerite from the Yubileynoye deposit are much lower than in MOR1-type black smokers but higher than in BA-type diffusers. Sphalerite has low Se and Te contents compared to chalcopyrite. The contents of these elements are similar in sphalerite from MOR-1-type and Yubileynoye chimneys. Sphalerite in chimneys from the Yubileynoye deposit is enriched in Au due to abundant inclusions of electrum (Table 2).

Table 2 Trace elements in sphalerite of chimneys from The Yubileynoye VMS deposits and mafic-hosted modern vent sites*

Name	n		Fe	Co	Sn	Se	Cd
Yb	19	av	18948	0,005	5	28	2772
		δ	8659	0,01	4	20	185
MOR1	116	av	81120	330	29	111	2504
		δ	41942	741	84	185	1810
MOR2	25	av	71107	0,06	80	3	**4625**
		δ	39042	0,12	46	2	2174
HS	37	av	42263	28	3	272	2520
		δ	33667	41	9	527	1909
BA	39	av	25440	1,46	11	5	3837
		δ	37421	2,98	22	5	2120
			Cu	Te	Ba	Au	Bi
Yb	19	av	13042	13,4	0,1	**67**	4,52
		δ	11708	10,9	0,2	**243**	4,48
MOR1	116	av	9326	4,8	1,8	1,2	14,4
		δ	16688	12,8	10,5	6,3	47,8
MOR2	25	av	9079	0,15	0,2	2,8	7,08
		δ	9386	0,33	0,3	3,2	15,3
HS	37	av	8045	0,20	13	0,8	0,02
		δ	6258	0,27	64	1,0	0,04
BA	39	av	2705	0,05	0,3	0,3	0,01
		δ	2999	0,08	0,7	0,5	0,01

*Captures are under Table 1.

Pyrite. Colloform pyrite in the chimneys from the

Yubileynoye deposit is enriched in (ppm): W 2.9, Bi 17.2, Au 7.3, Te 69, Se 48 and Ni 25, and is depleted in Co 0.1. In conduits of chimneys from the Yubileynoye deposit, subhedral pyrite and marcasite are strongly enriched in Au (up to 88 ppm), Ag (up to 564 ppm), Mn (up to 2400 ppm). Tl (up to 272 ppm), As (up to 1.1 wt. %), Bi (45 ppm), and Te (up to 680 ppm) due to inclusions of tellurides, native gold and galena. Galena contains 137 ppm Te, 1560 ppm Se, and 564 ppm Ag.

4. Discussion and Conclusions

Tellurium-bearing minerals are generally scarce in a chimney material from mafic and bimodal felsic hosted VMS deposits, but are abundant in chimneys from the Ural VMS deposits located in Silurian and Devonian bimodal mafic sequences (Maslennikov et al., 2013). The Yubileynoye deposit is the first ancient mafic-hosted VMS deposit, where abundant tellurides have been found in the chimneys. This deposit occupies the first position in the range from mafic to bimodal mafic- and bimodal felsic-hosted deposit types of the Urals: Yubileynoye → Yaman-Kasy → Molodezhnoye → Uzelga → Valentorskoye → Oktyabrskoye → Alexandrinskoye → Tash-Tau → Jusa. In this range, decreasing amounts of colloform and pseudomorphic pyrite after pyrrhotite, tellurides and sulfoarsenides in chimneys are coupled with increasing sphalerite, galena and tennantite-tetrahedrite, quartz or barite in chimneys. This trend represents a transition from low- to high-sulfur conditions and these changes are consistent with the progression in VMS compositions. Nevertheless, the lack of tellurides in another mafic class of VMS deposits is still poorly understood and should be explained.

Despite the high grades of Te in chalcopyrite of modern black smokers, they contain no plentiful telluride assemblages. The flat LA-ICP-MS trends of pulses suggest that Te^{2-} as well as Se^{2-} can substitute for S^{2-} in chalcopyrite. Despite the differences in ion radiuses, the substitutionst is, probably, partly possible in high-temperature and high-reducing conditions. Simple mixture of hydrothermal fluid with seawater results in H_2Te oxidation to Te° and $HTeO_3^-$ The moderate oxidation leads to decrease of H_2Te contents in fluids and Te^{2-} in chalcopyrite, while high contents of Se^{2-} can be preserved as herein observed for HS-type chimneys. Next stage is almost complete oxidation of H_2Te and H_2Se to $HTeO_3^-$ and $HSeO_3^-$. This leads to low Se and Te in chalcopyrite in MOR2- and BA-types of chimneys and diffusers. The $HTeO_3^-$ can be reduced to Te° due to interaction with SO_2. High $?Te_2$ can lead to telluride precipitation (Afifi et al., 1988). The magmatic contribution is suggested for occurrence of tellurides in chimneys from the Brothers Submarine volcano, Kermadec arc (Berkenbosch et al., 2012). On the other hand, in fore-arc setting, subducted sediments may be considered as an additional source of Te (Cook et al., 2009). Contribution of the host rocks as a source to trace elements can be testified by high Ni/Co ratios in sulfides that are consistent with the ratios attributed for boninitic basalts (Spadea et al., 1998). This hypothesis is worth of further research.

References

Afifi AM, Kelly WC, Essene EJ (1988) Phase relations among tellurides, sulfides, and oxides: II. Application to telluride-bearing ore deposits. Econ Geol 83:395–404

Berkenbosch HA, de Ronde C EJ, Gemmel JB, McNeill AW, and Goemann K. Mineralogy and Formation of Black Smoker Chimneys from Brothers Submarine Volcano, Kermadec Arc (2012) Econ Geol 107:1613–1633

Bolotin YuA, Buslaev FP (1988) Yubileynoye deposit. In: Massive sulphide deposits of Urals: geological structure. Sverdlovsk Urals Branch of RAS, pp 85–94 (in Russian)

Cook NJ, Ciobanu CL, Spry PG, Voudouris P and the participants of IGCP-486 (2009) Understanding gold-(silver)-telluride-(selenide) deposits. Episodes 32:249–263

Danyushevsky LV, Robinson R, Gilbert S,Norman M, Large R, McGoldrick P, Shelley JMG (2011) Routine quantitative multi-element analysis of sulfide minerals by laser ablation ICP-MS: standard development and consideration of matrix effects. Geochim Explor Environm Anal 11:51–60

Halbach PE, Tunnicliffe V, Hein JR (2003) Energy and mass transfer in marine hydrothermal systems. 89th Dahlem Workshop, Berlin, October 14-19, p 365.

Herrington R J, Maslennikov VV, Spiro B, Zaykov VV, Little CTS (1998) Ancient vent chimney structures in the Silurian massive sulfide s of the Urals. In: Mills RA, Harrison K (eds) Modern ocean floor processes and the geological record. Geol Soc Lond 148:241–257

Herrington R, Zaykov V, Maslennikov V., Brown D, Puchkov V (2005b) Mineral deposits of the Urals and links to geodynamic evolution. Econ Geol One Hundredth Anniversary Volume: 1069–1095.

Maslennikov VV, Maslennikova SP, Large RR, Danyushevsky LV (2009) Study of trace element zonation in vent chimneys from the Silurian Yaman-Kasy VHMS (the Southern Urals, Russia) using laser ablation inductively coupled plasma mass spectrometry (LA-ICP MS). Econ Geol 104:1111–1141

Maslennikov, V.V., Maslennikova, S.P., Large R.R., Danyushevsky, L.V., Herrington, R.J., Stanley, C.J. (2013) Tellurium-bearing minerals in zoned sulfide chimneys from Cu-Zn massive sulfide deposits of the Urals, Russia. Mineralogy and Petrology, Special Issue: Ore deposits of the Urals 107 (1): 67–99.

Seravkin IB (2010) The metallogeny of the Southern Urals and the Central Kazakhstan. Gilem, Ufa: 281 p (in Russian)

Spadea P, Kabanova LYa, Scarrow J (1998) Petrology, geochemistry, and geodinamic significance of Mid-Devonian Boninitic rocks frm the Baimak-Buribai area (Magnitogorsk zone, Southern Urals) Ofiolit, 23 (1): 17–36.

Porphyry deposits of the Urals

Olga Yu. Plotinskaya[a], Anatoly I. Grabezhev[b]
[a] Institute of Geology of Ore Deposits, Petrography, Mineralogy, and Geochemistry Russian Academy of Sciences (IGEM RAS), Staromonetny per. 35, Moscow 119017, Russia
[b] Institute of Geology and Geochemistry UB RAS, Pochtovy per. 7, Ekaterinburg 620151, Russia

Abstract. Most of porphyry deposits are located in the South and Middle segments of the Urals. They are confined to three main N-S trending volcanic belts, i.e. the Tagyl−Magnitogorsk (Salavat, Yubileynoe, Voznesenskoe etc.), East-Uralian (Birgilda-Tomino ore cluster, Mikheevskoe etc) and Valerianovka (Benkala, Batala, etc.) megazones. Usually they are genetically linked with subduction-related calc-alkaline low K intrusions.

Keywords. Urals, copper, molybdenium, porphyry, gold, epithermal, subduction related

1 Introduction

The Urals region is known mostly for its chromite, PGE, VHMS and Au orogenic (mesothermal) deposits (Herrington et al., 2005 and references therein). However it also hosts numerous porphyry and porphyry related deposits and occurrences (including epithermal and skarn types): over 30 porphyry deposits and occurrences have been found during the last 30-40 years In the Middle and South Urals and some of them are currently under exploration. This paper is aimed to give a short overview of porphyry deposits of the Urals and to describe several key examples in details.

2 Distribution of porphyry mineralization

In the Cis-Polar and Polar Urals porphyry deposits are rare – only the Lekyn-Talbey Cu porphyry deposit (Polar Urals) and the Yanoslor Mo porphyry occurrence (Cis-Polar Urals) along with a few poorly studied prospects and occurrences are known. Most of porphyry deposits and occurrences of the South and Middle Urals are confined to three main N-S trending volcanic belts, i.e. the Tagyl−Magnitogorsk, East-Uralian and Valerianovka megazones (Fig.1).

The westernmost Tagyl−Magnitogorsk megazone consists mostly of a series of Silurian to late Devonian oceanic island arcs, which host Au-Cu and Cu porphyry deposits. They are associated with diorite, quartz-diorite, and locally gabbro-diorite porphyries, e.g. the Early Devonian Gumevskoe Cu-Au skarn-porphyry deposit in the Tagyl (Middle Urals) segment, the Devonian Salavat and Late Devonian Voznesenskoe Cu porphyry deposits in the Magnitogorsk segment, and the Late Devonian – Early Carboniferous Yubileinoe Au porphyry in the Mugodzhary sector.

The East Uralian volcanic megazone comprises fragments of volcanic arcs of Late Devonian to Early Carboniferous age intruded by syn- and post-collisional Carboniferous to Permian granitic rocks.

(Zonenshain et al., 1984). Cu and Mo-Cu porphyry deposits are mostly related to diorite and quartz diorites. These are: the Carboniferous Mikheevskoe (Mo)-Cu deposit and the Late Devonian to Early Carboniferous Birgilda-Tomino ore cluster, and less known Takhtalym and Zeleny Dol Cu porphyry occurrences, Tarutino scarn-porphyry occurrence, etc.
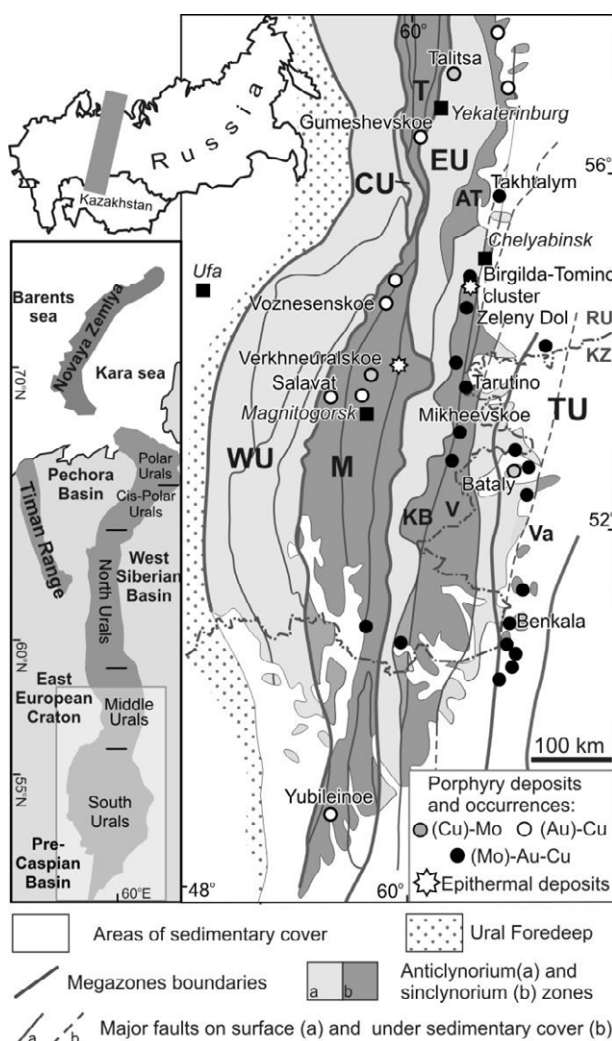
Figure 1. Simplified tectonic scheme of the Middle and South Urals, and locations of porphyry and epithermal deposits and occurrences, modified after (Mineral deposits…, 2007; Plotinskaya et al., 2013). Geotectonic belts: WU – West Uralian; CU – Central Uralian; T – Tagyl; M – Magnitogorsk; EU – East Uralian (volcanic zones: AT– Alapaevsk-Techa, KB– Kosobrodka-Bredy, V– Varna; TU – Trans Uralian (Va – Valerianovka volcanic zone).

Most porphyry Cu deposits of the Urals are related to intrusions of calc alkaline K-Na and sometimes Na series and are similar to porphyry deposits of the

"diorite type" as described by Hollister (1975). Cu-Mo and Mo porphyry deposits are rare are associated with sub-alkaline intrusions and do not exhibit any well defined patterns in their distribution. The best known deposit of this type is Talitsa in the Middle Urals described below and also the Verkhneuralskoe occurrence in the Magnitogorsk megazone and Batala occurrence in the Valerianovka magazone.

There is a general evolutionary trend of porphyry-bearing magmatism in the Urals (Fig. 2) from Na to K-Na series in space (from west to east) and from Na via K-Na to K series in time (from Devonian to Carboniferous) noted by Grabezhev and Borovikov (1993). Both trends correlate with a decrease in the Cu/Mo ratio and increase in Mo/Re ratio in ores (Grabezhev, 2013).
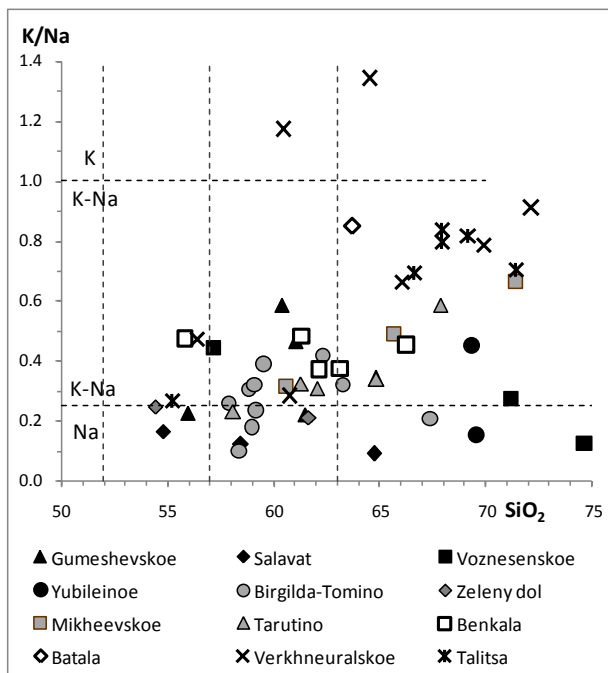
Figure 2. SiO_2 via K/Na diagram for intrusions associated with Cu porphyry mineralization from the Magnitogorsk megazone (black symbols), East Uralian megazone (grey symbols) and Valerianovka megazone (white symbols); intrusions associated with Mo porphyry mineralization are shown by crosses.

3 Key porphyry and porphyry related deposits

3.1 The Birgilda-Tomino ore cluster

Birgilda-Tomino ore cluster is situated in the East Uralian volcanic megazone. It covers a north-trending corridor 20-25 km wide and 40 km long. The Ordovician aphyric basaltic lavas and tuffs are a bottom of the visible section and host Tomino, Kalinovka, and Birgil'da porphyry copper deposits with total inferred recourses of about 2.8 Mt Cu. They are overlain by the Middle Ordovician–Lower Silurian marble hosting the Biksizak skarn-related carbonate replacement Zn deposit (inferred recourses 1.7 Mt Zn) and the Lower to Upper

Silurian limestone the Upper Devonian–Lower Carboniferous andesitic–dacitic volcanosedimentary rocks host the Michurino Au-Ag sub-epithermal ocurrence and Bereznyakovskoe Au-Ag-Te epithermal field (inferred recourses 36 t Au). The block structure of the studied territory led to the spatial combination of porphyry and epithermal deposits in a relatively small area (Lehmann et al., 1999; Grabezhev et al., 2000). The deposits are related to quartz diorite and andesite porphyry intrusions of the K-Na calc-alkaline series (the Birgil'da–Tomino igneous complex), associated to a subduction-related volcanic arc. Ore mineralogy, alteration types, fluid inclusion data and mineral geothermometry show that the Birgilda-Tomino ore cluster represents a porphyry-epithermal continuum, with a vertical extent of about 2-3 km, controlled by temperature decreases and fS2 and fTe2 increase from deeper to shallow levels (Plotinskaya et al., 2013 and references therein).

3.2 The Mikheevskoe deposit

The Mikheevskoe Cu(Mo) porphyry deposit occurs in the eastern margin of the East Uralian volcanic megazone near its board with the Trans Uralian megazone. The deposit is hosted by Late Devonian to Early Carboniferous sandstones, tuffstones, basaltic andesites, etc overlain by Early Carboniferous basaltic lavas, tuffs, sandstones. Intrusions are represented by Carboniferous quartz diorite stocks and numerous diorite and granodiorite porphyry dykes (Shargorodsky et al., 2005). Mineralization (0.53 % Cu, 0.0076% Mo, 0.23 ppm Au, Cu/Mo=70) is hosted by volcanic-sedimentary rocks rather then by dykes (Shargorodsky et al., 2005). Alteration and mineralization establish complicated zoning which can be generalized as follows (from central to margins): (i) minor actinolite alteration with magnetite; (ii) pervasive biotite with quartz ± biotite ± bornite + chalcopyrite veinlets and dissemination; (iii) more abundant phyllic alteration with quartz ± molybdenite±chalcopyrite veinlets and dissemination; most wide-spread propylitic alteration with pyrite-chalcopyrite veinlets and stringers.

3.3 The Talitsa deposit

The Talitsa Mo porphyry deposit is located in the western margin of the East Uralian megazone in the Middle Urals within a sub-alkaline intrusion of about 4 km2 hosted by Devonian ultrabasic rocks and rhyolite-basalt volcanics. The Talitsa intrusion consists of granodiorite to quartz monzonites and minor monzodiorites cross-cut by granodiorite to quartz monzonite and granite porphyry stocks and dykes. The youngest phase is represented by presumably post-ore granosienite aplites (Azovskova, Grabezhev, 2008). Zones of potassic alteration (mainly K-feldspar) are confined to porphyry stocks and dykes. Phyllic (sericite and quartz-sericite) alteration is developed throughout the central zone of the Talitsa intrusion while propylitic alteration is typical for its margins. Mineralization (0.04-0.34% Mo, 0.09-0.47% Cu, 0.1-0.4 ppm Au, Cu/Mo=0.5 to 3) occurs as dissemination and stockworks zones and

forms several generation of veinlets. These are: (i) quartz + pyrite + molybdenite, (ii) quartz + K-feldspar + molybdenite, (iii) quartz + molybdenite + chalcopyrite ± pyrite ± fahlore ± galena ± sphalerite, and (iv) rare quartz-pyrite veinlets with electrum and tellurides (Azovskova, Grabezhev, 2008).

4 Summary

The Urals exhibits a large spectrum of porphyry style mineralization: Cu, Au, and Mo porphyry deposits are known. In addition there are porphyry related deposits, i.e. skarn or Au-Ag epithermal, etc. Most of porphyry deposits are confined to Palaeozoic volcanic arcs and are genetically linked with subduction-related calc-alkaline low K intrusions. General evolution of porphyry-bearing magmatizm from Na to K-Na series in space (from west to east) and from Na via K-Na to K series in time (from Devonian to Carboniferous) correlates with a decrease in the Cu/Mo ratio and increase in Mo/Re ratio in ores.

Acknowledgements

References

Azovskova OB, Grabezhev AI (2008) The Talitsa porphyry copper-molybdenum deposit, the first object of a subalkaline porphyry system in the Central Urals. Dokl Earth Sci 418(1):99−102.

Grabezhev AI (2013) Rhenium in Porphyry Copper Deposits of the Urals. Geol Ore Deposits 55:13−26.

Grabezhev AI, Borovikov YN (1993) Porphyry copper deposits of the Urals. Resour Geol (15):275−84.

Grabezhev AI, Sazonov VN, Murzin VV, Moloshag VP, Sotnikov VI, Kuznetsov NS (2000) The Bereznyakovsk Gold Deposit (South Urals, Russia). Geol Ore Deposits 42:33−46.

Herrington RJ, Zaykov VV, Maslennikov VV, Brown D, Puchkov VN (2005) Mineral deposits of the Urals and links to geodynamic evolution. Econ Geol 100:1069−1095.

Hollister VF (1975) An appraisal of the nature of some porphyry copper deposits. Minerals Science and Engineering 7:225−233.

Lehmann BJ, Heinhorst J, Hein U, Neumann M, Weisser JD, Fedosejev VV. (1999) The Bereznjakovskoe gold trend, southern Urals, Russia. Miner Deposita 34:241−249.

Mineral Deposits of the Urals, 1M Scale Map and Database, Short Description (Explanatory Notes) (2007) Petrov O. et al. (eds). CERCAMS, NHM, London

Plotinskaya OY, Grabezhev AI, Groznova EO, Seltmann R, Lehmann B (2013) The Late Paleozoic porphyry-epithermal spectrum of the Birgilda−Tomino ore cluster in the South Urals, Russia. J Asian Earth Sci. doi:10.1016/j.jseaes.2013.01.015

Seltmann R, Porter TM (2005) The Porphyry Cu-Au/Mo Deposits of Central Eurasia: 1. Tectonic, Geologic & Metallogenic Setting and Significant Deposits. In: Porter TM (ed) Super Porphyry Copper & Gold Deposits: A Global Perspective. v. 2. PGC Publishing, Adelaide, pp 467-512.

Shargorodsky BM, Novikov IM, Aksenov SA (2005) The Mikheevskoe copper porphyry deposit in the South Urals.

Otechestvennaya Geologia (2):57−61. [in Russian].

Zonenshain LP, Korinevsky VG, Kazmin VG, Pechersky DM, Khain VV, Matveenkov VV (1984) Plate tectonic model of the South Urals development. Tectonophysics 109:95−135.

Timing of hydrothermal activity and source of metals in Urals – implications for tectonic setting

Svetlana Tessalina
John de Laeter Centre for Isotopic Research, Curtin University, Australia

Valery V. Maslennikov, Victor Zaykov
Institute of Mineralogy of Russian Academy of Sciences, Miass, Russia

Richard Herrington, Baruch Spiro
Natural History Museum, London, United Kingdom

Jean-Jacques Orgeval
Bureau de Recherche Géologiques et Minières, Orléans, France

Abstract. Formation of the Southern Urals Volcanogenic Massive Sulphide (VMS) deposits is considered to be related with the intra-oceanic stage of the Magnitogorsk island arc development (Herrington et al. 2011) in Silurian - Middle Devonian time (444–385 Ma). Here we present direct dating results of sulphide mineralisation from Yaman-Kasy and Kul-Yurt-Tau VMS deposits using Re-Os isotope systematics showing similar ages of 362±9 Ma and 363±1 Ma. These ages coincide with the previous Re-Os dating of Alexandrinka and Dergamish VMS deposits. This Late Devonian age slightly post-dates the 'Magnitogorsk arc – Laurussia continent' collision event (Brown et al. 2011). Contribution from subducted Proterozoic continent and/or sediments is supported by the Pb isotopic studies of 14 Urals VMS deposits. Low radiogenic 'old' lead signatures decrease from the fore-arc to the arc setting, and becomes almost nil in the back-arc setting. This pattern confirms metals endowment from subducted continent/sediments near the subduction front. These young repetitive Re-Os model ages together with lead isotopes data may suggest that the closure of Re-Os radiogenic 'clock' for Southern Urals VMS deposits has happened no later than the Late Devonian time (~360 Ma), slightly after the 'Magnitogorsk island arc – Laurussia continent' collision event.

Keywords. Volcanogenic Massive Sulphide deposit, Urals, Re-Os systematics, Pb isotopes

1 The tectonic setting and sampling

In the Southern Urals, the intra-oceanic subduction has triggered the volcanism leading to the Magnitogorsk island arc development starting from the Early Devonian time (~400 Ma ago). The timing of collision of this volcanic arc with adjacent Laurussia continent was established at 380 – 372 Ma based on Ar-Ar, U-Pb and Sm-Nd dating of high-pressure metamorphic rocks and sediments belonging to the continental margin (Beane and Connelly 2000). The formation of Southern Urals Volcanogenic Massive Sulphide deposits was restricted to the intra-oceanic stage (Herrington et al. 2011), with the youngest age of 385 Ma, based on biostratigraphic studies of ore-hosting volcanic and sedimentary rocks (Artyuszkova and Maslov 2008).
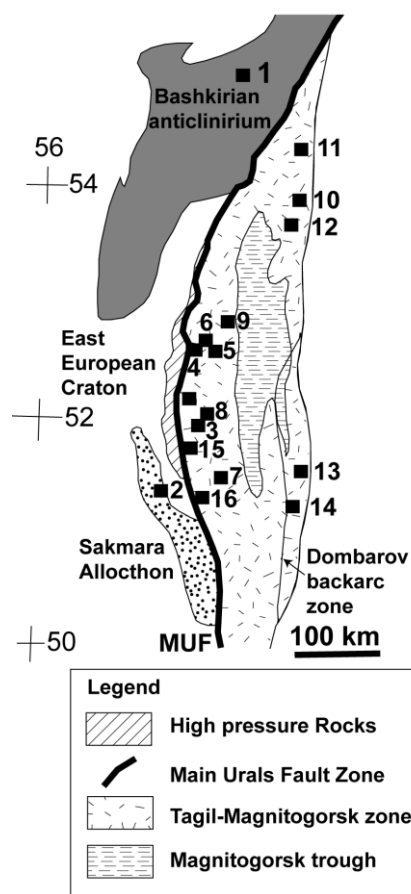
Figure 1. Simplified geological map of the Southern Urals showing main regions of arc volcanic sequences and location of studied VMS deposits. The following subdivisions are shown: (1) Main Urals Fault (MUF) suture zone with relics of ophiolite in a tectonic melange containing blocks with ages ranging from Ordovician up to Late Devonian; (2) Magnitogorsk island arc zone, consisting of volcanics and sediments of Devonian age. An intermediate "intra-arc" basin, filled by Late Devonian-Lower Carboniferous volcanics and sediments, divides the Magnitogorsk structure into the West and East-Magnitogorsk zones; (3) Sakmara allochthon, whose origin is not clear. Massive sulphide deposits: 1 – Bakal, 2 – Yaman-Kasy, 3 – Oktyabrskoe, 4 – Bakr-Tau, 5 – Balta-Tau, 6 – Tash-Tau, 7 – Gay, 8 – Podolskoe, 9 – Sibay, 10 – Molodezhnoe, 11 – Uchaly, 12 – Alexandrinka and Babarik, 13 – Djusa, 14 – Barsuchi Log, 15 – Dergamish.

In this study, sulphide samples were collected from two VMS deposits occurring in distinct geodynamic settings. The studied Yaman-Kasy deposit (Maslennikov et al. 2009) is restricted to the Sakmara allochton and is hosted by an early Silurian volcano-sedimentary bimodal sequence. The mound-like Yaman-Kasy orebody consists of massive and clastic ore facies, with preserved fragments of sulphide chimneys and vent fauna. This is one of the best preserved Palaeozoic sulphide mound-like VMS deposits, analogous to the modern black-smoker VMS deposits. The hydrothermal chimney fragments were collected, including 4 pyrite-marcasite samples from the outer wall, 2 chalcopyrite samples from the inner wall, and 1 pyrite-marcasite-sphalerite sample from the chimney core.

The studied Kul-Yurt-Tau deposit is situated within West-Magnitogorsk island arc (Fig. 1) and restricted to the middle part of Baimak-Buribai formation. This mound-like ore body occurs on the flank of a rhyolite-dacite dome within the volcanoclastic horizon. The felsic volcanic host rocks at the top and flanks of ore body are transformed into sericite-pyrophyllite-quartz metasomatic rocks. The studied molybdenite samples form 0.1-2 mm thick coat-like aggregates in association with pyrophillite within these metasomatic rocks.

For Pb isotopic studies, we collected various types of galena samples from 14 VMS deposits across the Urals paleo-island arc system (Fig. 1), covering the range from fore-arc, arc and back-arc settings. Most galena samples were obtained from massive ores and footwall stockwork zones of the deposits.

2 The Results

2.1 Re-Os Systematics

The Rhenium-Osmium isotope systematics is used for accurate isotopic dating and fingerprinting the source of metals. Both the parent (^{187}Re) and daughter (^{187}Os) are chalcophile and siderophile in character, leading to their enrichment in sulphide minerals relative to silicates. This is a unique combination of chemical and isotopic features which allows the direct dating of sulphide mineralisation. The common sulphide mineral molybdenite is particularly useful in this regard, because it often contains high concentrations of Re, but virtually excludes Os during crystallisation. Thus, no correction is required for the presence of initial Os.

The plot of the isotope data for the Yaman-Kasy ores on the Re-Os isochron diagram (Fig. 2) defines a best-fit line with the age of 361.7 ± 9.0 Ma (MSWD = 3.4), which is much younger than the biostratigraphic Silurian age (*ca.* 443–419 Ma) of ore hosting rocks. In addition to that, the isotope data of the molybdenite samples from the Kul-Yurt-Tau deposit gave a model age of 363.4 ± 1.1 Ma (Late Devonian) which is similar to the preceding dating of the Yaman-Kasy deposit, and it is ~40 Ma younger than the biostratigraphic Early Devonian age (*ca.* 400 Ma) of host rocks of the Kul-Yurt-Tau deposit (Artyuszkova and Maslov 2008).
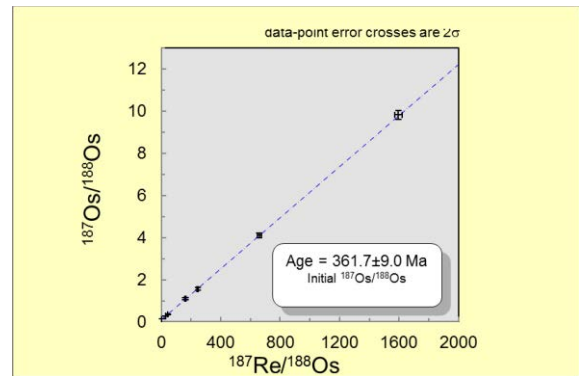
Figure 2. Re-Os isochron diagram for Yaman-Kasy deposit.

2.2 Source of metals defined by Pb-Pb isotope systematics

Galena is virtually free of U and records the initial composition of lead at the time of ore formation. For this reason, the lead isotopic composition in galena is an ideal indicator for the sources of lead and other metals.

The lead isotope data from 14 VMS deposits (Fig. 1) display a systematic increase in lead isotopic ratios across the Urals paleo-island arc zone, from fore-arc with the least radiogenic lead compositions to back-arc with the most radiogenic lead (Fig. 3). The latter shows Pb model ages close to the age of the arc volcanics (~400 Ma). The less radiogenic lead from fore-arc settings is indicative of a source older than the volcanics and implies a contribution of lead from older subducted material. The Pb isotopic composition of subducted Proterozoic rocks may be inferred from the analysis of lead occurrences from the Proterozoic rocks of Bashkirian anticlinorium (Bakal deposit). According to Fig. 3, the contribution of lead from these Proterozoic rocks can account for the composition of less radiogenic lead from VHMS deposits in fore-arc settings.
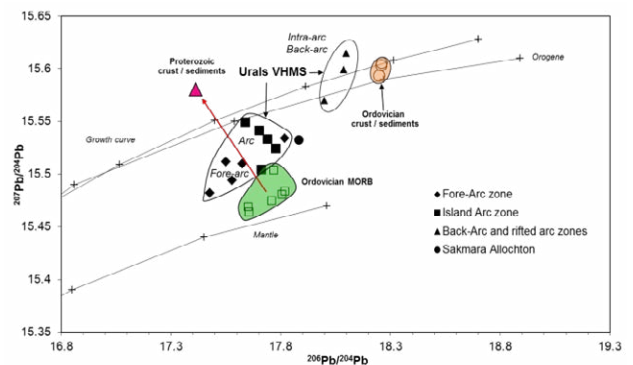
Figure 3. ^{206}Pb/^{204}Pb vs. ^{207}Pb/^{204}Pb diagram showing average composition of studied VHMS deposits. Ordovician Mantle field was delineated using Ordovician MORB hosted VHMS deposits from the Caledonides of Norway (Bjørlykke et al. 1993). The Ordovician sediments field corresponds to the galena from the Ordovician sediments-hosted Saureyskoe Zn-Pb deposit, Polar Urals. The lead isotope composition of Precambrian sediments (*ca.* 1.3 Ga) from Bakal stratiform Pb-Zn deposit (Bashkirian anticlinorium) is shown.

3   Timing of VMS formation

Previously published Re-Os isotope data for two other Urals VMS deposits, namely Alexandrinka (Tessalina et al. 2008) and Dergamish (Gannoun et al. 2003), defines similar Late Devonian ages of 355±15 Ma and 366±2 Ma, respectively, post-dating the presumed biostratigraphic age of ore hosting volcanics.

The K-Ar ages for sericites from 8 Urals VMS deposits (Buslaev and Kaleganov 1992) show the range from 390 to 301 Ma, with an average value of 348±27 Ma. The K-Ar ages in sericites often show a range spanning the whole life of a hydrothermal system. This range includes the age of the end of the hydrothermal activity, which can be few Ma younger than the age of the ore formation itself (Hu et al. 2012). The average K-Ar age is consistent with the Sm-Nd and Rb-Sr ages of 347±12 Ma for the Berezovskoe Au deposit formation from the Middle Urals (Baksheev and Beliatsky 2011), marking the end of intense hydrothermal activity.

The repetitive Late Devonian Re-Os model ages for sulphides for four studied Urals VMS deposits are younger than their respective host rocks and overlaying sediments based on biostratigraphy (Artyuszkova and Maslov 2008). Even though the additional chronological constraints for host volcanic rocks and sediments are needed to better constrain the geochronology of the Urals VMS deposits, the Re-Os model age would need to be much older to explain the formation of the Silurian Yaman-Kasy deposit, with perfectly preserved initial seafloor hydrothermal facies such as chimneys and fauna. However, this Late Devonian age may correspond to the later hydrothermal overprint for the Devonian Kul-Yurt-Tau deposit. In what follows, we examine several possible mechanisms for the Re-Os system re-setting.

Re-setting of the Re-Os isotopic system could occur under the following circumstances: (A) metamorphic overprint; (B) incomplete homogenisation of two or more components with different initial Os ratios during ore deposition; (C) open behaviour of hydrothermal system. These possibilities are examined in detail:

(A) In the history of the Urals development, the Late Devonian (385-359 Ma) corresponds to the 'Arc-Continent' collision, which was associated with exhumation of high-pressure metamorphic complexes (Beane and Connelly 2000). However, the good state of preservation of initial ore textures for the studied deposit Yaman-Kasy (colloform structures, relics of hydrothermal chimneys and fauna) does not favour the metamorphic overprint.

(B) The formation of VHMS deposits is due to the mixture of at least two components represented by seawater and hydrothermal fluid, which may have different isotopic composition at the time of ore formation, with osmium in the hydrothermal fluid coming mostly from the leaching of host volcanic and sedimentary rocks. Mixture of hydrothermal fluid with seawater during ore formation could produce mixed isotopic characteristics at the time of ore formation, which subsequently evolved to yield linear data arrays of questionable age significance. However, the similarity of model ages for the four deposits makes this possibility very unlikely.
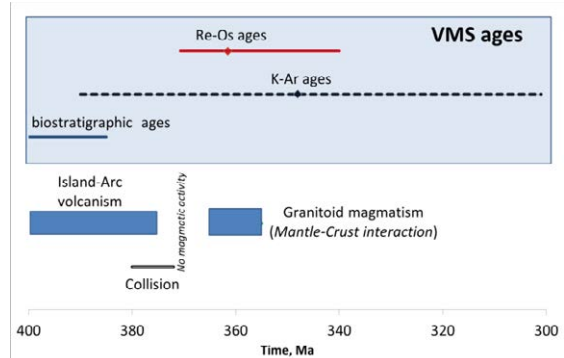
Figure 4. Summary of available dating for Urals VMS using Re-Os and K-Ar systems (see references in the text), along with contemporaneous magmatic (Fershtater et al. 2007) and tectonic events (Beane and Connelly 2000).

(C) Open behaviour of the ore system is the most plausible scenario to explain the younger age of studied deposits. In this case, the gain of Re is the most possible explanation for the younger ages, which is estimated to be between 10 and 20%. The gain of Re could be related with interaction between sulphide ore and seawater, the latter having the Re/Os ratio of ~820. However we can argue that the closure of Re-Os systems for four studied Urals VMS deposits has happened no later than ~360 Ma.

4   Implication for tectonic setting

The evidence of continental crust/metals recycling from Proterozoic Laurussia craton into the mantle comes from the presence of zircons of crustal origin in subduction-related dunite-clinopyroxenite-gabbro massif of the Middle Urals (Bea et al. 2001). These zircon ages of 370-350 Ma correspond to the beginning of Arc-Continent collision in the Southern Urals. Moreover, the presence of zircons of crustal origin in subduction-related mafic-ultramafic complexes suggest contribution of melt directly from melting of subducted crust/sediments of Laurussia craton, which entrained restitic zircons.

The Pb isotope data in galena from 14 Urals VMS deposits suggests that the contribution of fluids from subducted continental crust/sediments progressively diminish with increasing distance from the subduction front, becoming almost nil in some of the mature arc and back-arc settings.

This dataset is rather consistent with ensialic origin of the Northern part of the Uralian island arc structure, inferred from geophysical data of the basement (continental crust) and geochemistry of volcanics (Yazeva and Bochkarev 1996; Smirnov et al. 2008).

In the Southern Urals, this stage of island arc development has been identified as hydrous suprasubduction melting during the mantle-crustal interaction (Fershtater et al. 2007) with large-scale granitoid magmatism. These intrusions provide necessary heat to promote the hydrothermal circulation along the existing tectonic faults.

Viewed on a larger scale, the Devonian episode of

volcanic and hydrothermal activity corresponds to the beginning of the Pangea supercontinent assembly by amalgamation of Laurussia, Siberia and China-Korea continental blocks. At that time, numerous microcontinents and volcanic arcs divided by basins of different character were present.

The fundamental plate boundary re-arrangements in Late Devonian, on a planetary scale, appear to be marked by intense magmatism under tectonic activation. This is manifested in island arc volcanism paired with episodic continental rifting, as well as hydrothermal activity on rifted or faulted outer continental margins, comprising large clusters of VHMS deposits in Spain, Portugal (Iberian Pyrite Belt province), Rudny Altai (Siberia), and the North American margin (Alaska). These deposits formed in local extensional volcanic basins within an overall contractional geodynamic environment during or after termination of convergence by accretion of an island arc or crustal block (Huston et al. 2010) throughout the Devonian until Early Carboniferous time.

5   Conclusions

Thus, these two radiogenic datasets (Re-Os and Pb-Pb), together with previous K-Ar dating, point out that the hydrothermal circulation was still active at the final stage of the island arc development after the collision initiation with an adjacent continent. The Re-Os model ages of hydrothermal system 'closure' correspond to the granitoid magmatism, initiated after the 'Arc-Continent' collision.
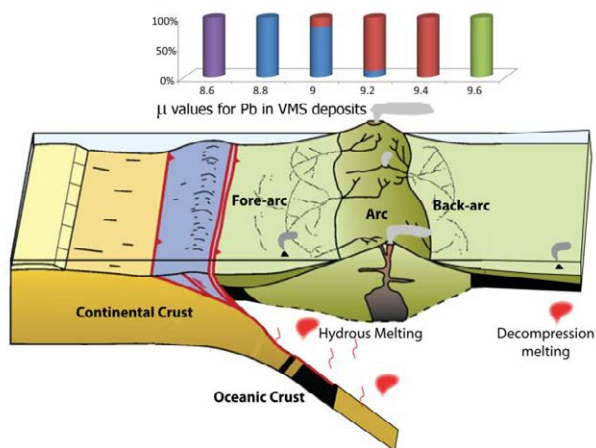
Figure 5. Schematic model for arc-continent collision in Southern Urals (modified after Brown and Spadea 1999). Entering of Proterozoic rocks into subduction zone caused high-pressure metamorphism accompanied by release of fluid. This fluid provoked hydrous melting in overlying mantle wedge. The lead isotopic composition of Proterozoic rocks is characterised by low μ-value of 8.8. In fore-arc setting, the μ-value of VMS deposits is close to that of Proterozoic rocks. Farther to the mature arc setting, the μ-value progressively increases, with maximum value of ~9.4. In back arc setting, the anhydrous decompressional melting of oceanic crust prevails, with highest μ-values corresponding to that of Ordovician crust (Fig. 3).

References

Artyuszkova OV and Maslov VA (2008) Detailed correlation of the Devonian deposits in the South Urals and some aspects of their formation. Bulletin of Geosciences 83(4), Czech Geol Survey, Prague

Baksheev IA and Beliatsky BV (2011) Sm-Nd and Rb-Sr isotopic systems of sheelite from Beresovskoe Au-bearing deposit (Middle Urals), Lithosphere 4: 110-118

Bea F et al. (2001) Recycling of continental crust into the mantle as revealed by Kytlymdunite zircons, Ural Mts, Russia. Terra Nova 13, 407-412

Beane RJ and Connelly JN (2000) $^{40}Ar/^{39}Ar$, U-Pb, and Sm-Nd constraints on the timing of metamorphic events in the Maksyutov Complex, southern Ural Mountains. Journal of Geol. Society, London, 157, 811-822

Bjørlykke A, Vokes F M, Birkeland A, Thorpe RI (1993) Lead isotope systematics of strata-bound sulfide deposits in the Caledonides of Norway. Econ Geol 88: 397-417

Brown D, Herrington RJ, Alvarez-Marron J (2011) Processes of Arc-Continent Collision in the Uralides In: Brown D and Ryan PD (eds) Arc-Continent collision, Springer-Verlag, Berlin Heidelberg, pp 311-340

Buslaev FP and Kaleganov BA (1992) The age of sulfide-ore formation according to the K/Ar method. In: Prokin VA and Buslaev FP (eds) Copper-sulfide deposits of the Urals: Conditions of formation. Russian Academy of Science, Ural Branch. Ekaterinburg, pp 186-199 (in Russian)

Fershtater GB, Krasnobaev AA, Bea F, Montero P, Borodina NS (2007) Geodynamic settings and history of the Paleozoic intrusive magmatism of the Central and Southern Urals: Results of Zircon Dating. Geotectonics 41, 465-486

Gannoun A et al. (2003) Re–Os isotopic constraints on the genesis and evolution of the Dergamish and Ivanovka Cu (Co, Au) massive sulphide deposits, south Urals, Russia. Chem. Geol.196, 193-207

Herrington RJ and Brown D (2011) The generation and preservation of mineral deposits in arc-continent collision environment. In: Brown D and Ryan PD (eds) Arc-Continent collision, Springer-Verlag, Berlin Heidelberg, pp 145-162

Hu R-Z, Wei W-F, Bi X-W, Peng J-T, Qi Y-Q, Wu L-Y, Chen Y-W (2012) Molybdenite Re-Os and muscovite 40Ar/ 39Ar dating of the Xihuashan tungsten deposit, central Nanling district, South China. Lithos 150: 111-118

Huston DL, Pehrsson S, Eglington BM, Zaw K. (2010) The Geology and Metallogeny of Volcanic-Hosted Massive Sulfide Deposits: Variations through Geologic Time and with Tectonic Setting. Econ Geol 105: 571-591

Maslennikov VV, Maslennikova SP, Large RR, Danyushevsky LV (2009) Study of Trace Element Zonation in Vent Chimneys from the Silurian Yaman-Kasy Volcanic-Hosted Massive Sulfide Deposit (Southern Urals, Russia) Using Laser Ablation-Inductively Coupled Plasma Mass Spectrometry (LA-ICPMS) Econ Geol 104: 1111–1141

Smirnov VN, Fadeicheva IF and Ivanov KS (2008) Geochemistry of Volcanic Rocks in the Tagil Zone of the Urals as an Indicator of Geodynamic Environments of Their Formation. Doklady Earth Sciences, 423 (8): 1278–1281

Tessalina SG et al. (2008) Osmium isotope distribution within the Palaeozoic Alexandrinka seafloor hydrothermal system in the Southern Urals, Russia. Ore Geol Rev 33: 70-80

Yazeva RG and Bochkarev VV (1996) Silurian island arc of the Urals: structure, evolution and geodynamics. Geophysics 29 (6): 478-489

Disseminated gold-sulfide mineralization of Verkhneniyajuskoe-2 deposit (the Manitanyrd Ridge, the Polar Urals)

Ustjugova Ksenia
Suktyvkar State University, zelenika@list.ru

Abstract. The Verkhneniyajuskoe-2 deposit is located in Upper Riphean metavolcanic rocks and is confined to a distinct structural corridor (shear zone). Two types of mineralization are known in the deposit: massive and disseminated (veinlet disseminated). Disseminated sulfide mineralization is generally represented by pyrite and arsenopyrite with accessory chalcopyrite, sphalerite, galena and tetrahedrite. Both massive and disseminated ores show two mineralization stages: an early stage of high-temperature gold-pyrite-arsenopyrite assemblage and a later, lower-temperature stage of electrum-chalcopyrite-sphalerite-galena-tetrahedrite. A simpler assemblage is found in the disseminated sulfides but this also contains gold.

Keywords. The Polar Urals, the Manitanyrd Ridge, Verkhneniyajuskoe-2 deposit, gold-sulfide-quarz mineralization.

The Verkhneniyajuskoe-2 gold deposit is located in central part of the Manitanyrd Ridge in the Polar Urals.

It was discovered in the 1960s. Recently research to re-estimate the resources of the deposit and those in the Niyajusko-Niyahoisky ore cluster were completed.

The aim of this research was to define the composition and forming conditions of the disseminated (veinlet-disseminated) sulphide mineralization and its enclosing at the Verkhneniyajuskoe-2 deposit.

Structurally, the Manitanyrd Ridge is a brachyanticline related to the Central Urals structural zone (Fig. 1). Its core is composed of volcanic and volcano-sedimentary rocks of the Bedamelskaya series ($R_{3-4}bd$), sandstones, shales and silt stones of the Enganepeyskaya suite (R_4-V_1en), overlain by terrigenous strata of the Manitanyrdskaya series (Є_3-O_1mt). North-east trending faults are important. Mafic intrusive bodies, the main foliation and fracturing zones, gold deposits and occurrences are all associated with this structure. All the rocks in the region are metamorphosed to greenschist facies.
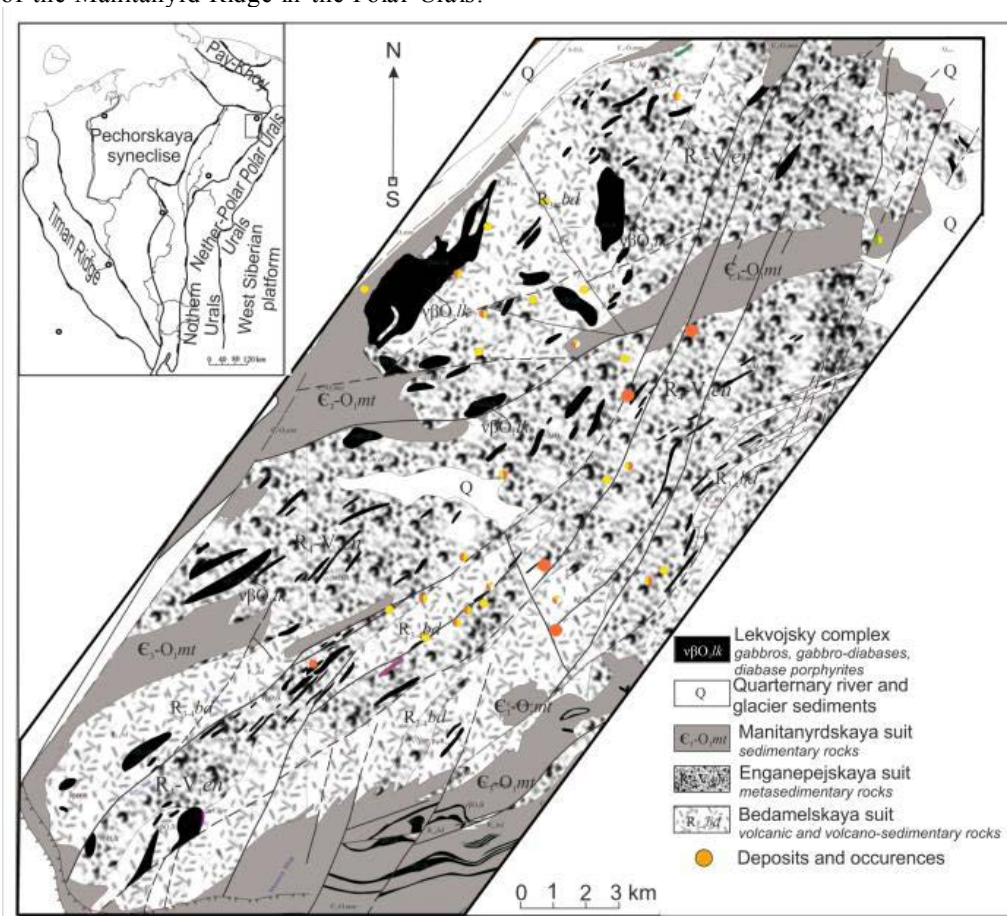
Fig.1. Geological structure and location of the Manitanyrd Ridge and location of major gold deposits and occurrences.

The ore bodies of Verhneniyayuskoe-2 deposit occur in the mafic, intermediate, rarely acid metavolcanic and volcano-sedimentary rocks of the Bedamelskaya series and are located in the before-mentioned fault zone. The latter is marked by the development of mylonites and rare boudinaged quartz veins. Disseminated (veinlet-disseminated) sulfide mineralization is confined to this zone.

For our research we studied quartz-vein and disseminated sulfide mineralization in the fault zone. Electron-microprobe studies (SEM JSM-6400 EMF «Link», IG Komi SC UB RAS, an analyst V.N. Filippov) showed that the main ore minerals are pyrite and arsenopyrite (Fig. 2). Submicron inclusion accessories of chalcopyrite, sphalerite, galena, tetrahedrite and gold are determined.
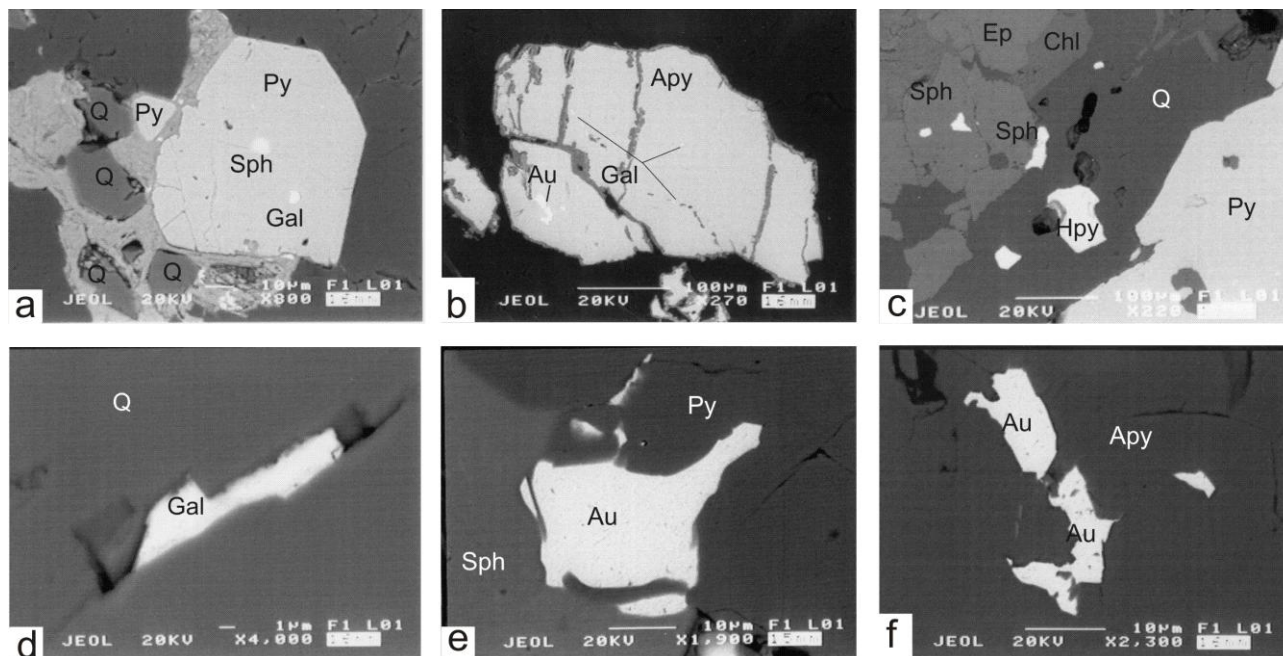
Fig.2. Micro association of disseminated and quartz veins sulphide mineralization (Py - pyrite, Apy - arsenopyrite, Hpy - chalcopyrite, Sph - sphalerite, Gal - galena, Au - gold, Ep - epidote, Chl - chlorite, Q - quartz).

Pyrite is the main ore mineral in quartz veins. It occurs in the form of subhedral and isometric individuals and their accretions. The predominant grain size is 7-10 microns, but some crystals reach 100 microns. Pyrite is barren of any impurity elements, its composition is calculated to be $Fe_{1.04}S_2$. Sphalerite, chalcopyrite, galena, tetrahedrite, gold, garnet and quartz are found in pyrite in the form of micro inclusions. *Arsenopyrite* is the main mineral of veinlet-disseminated ore type and is absent from quartz veins. It forms euhedral and subhedral grains, ranging in size from 10 to 500 microns. The generalized formula is calculated to $Fe_{1.01-1.11}As_{0.94-1.03}S_{0.97-1,06}$. Arsenopyrite contains micro-inclusions of galena and gold. Its grains are cut by cracks, in which develops scorodite. *Chalcopyrite* forms fine disseminations in the host rocks and micro-inclusions in pyrite from quartz veins. It is characterized by irregular and highly elongated shape, filling cracks and voids. The grain size varies from 1 to 70 microns. The generalized formula is calculated to $Cu_{0.88-0.98}Fe_{0.97-1.01}S_2$. *Sphalerite* is noted as scattered disseminations in the host rocks, inclusions in pyrite and chalcopyrite, accretions with pyrite in quartz veins. Most often the mineral has an irregular shape due to shape of voids, sometimes it is confined to cracks. The grain size ranges from 2 to 50 microns. In sphalerite impurities of Fe (5,02-11,29 wt.%), and in a single case of Cd (0.29 wt.%) are noted. The generalized formula is calculated to $Zn_{0.8-0.94}Fe_{0.08-0.12}S$. *Galena* occurs as finely dispersed disseminations in the host rocks and in the form of micro-inclusions in pyrite in quartz veins. Galena forms grains of angular and irregular form that have size of 0.5-10 microns and contains impurities of Fe and Ag. The generalized formula is calculated to $Pb_{0.99-1.03}S$. Tetrahedrite was observed in the form of micron-sized grains, filling cracks in pyrite. The generalized calculated formula: $(Cu_{8.2}Fe_{1.9}Zn_{0.8}Ag_{0.1}) Sb_{3.6}S_{13}$.

Gold forms submicron inclusions of irregular shape, confined to cracks and voids in pyrite in quartz veins and arsenopyrite in disseminated ores. Its size is 0.1-0.5 micron, rarely reaching 12 microns. In quartz vein gold is noted at the edges of pyrite next to sphalerite. The purity of gold in pyrite is 706-751 ‰, including micro-inclusions of electrum 478-577 ‰. In arsenopyrite gold inclusions have a higher tenor of 872-902 ‰. In gold from pyrite are diagnosed such impurity elements as Ag (23-29 wt.%) and Hg (0.9-1.8 wt.%), in arsenopyrite only Ag (9.8-13.7 wt.%). For gold and electrum phases in contact with sphalerite, an electrum-sphalerite geothermometer [3] was used to determine the temperature of their formation. For gold temperature was estimated to be 454-501°C, for electrum 331-384°C. By using the arsenopyrite geothermometer [1] the temperature of formation of arsenopyrite is estimated at 410-490°C.

The ore association, both disseminated (veinlet-disseminated) and quartz-vein mineralization, is clearly epigenetic, hydrothermal. Its mineral and chemical

composition is similar to that of massive ore deposits [2], but has a smaller diversity of sulfide phases. In the quartz vein main ore mineral is pyrite containing micro-inclusions of galena, sphalerite, chalcopyrite, tetrahedrite, and gold. The main mineral of disseminated (vein-disseminated) ore is arsenopyrite, minor - pyrite and sphalerite, forming separate grains of micron size. Arsenopyrite contains micro-inclusions of sphalerite and gold.

Arsenopyrite and more high-grade gold from the disseminated ores show similar temperatures of formation and correspond to the early mineralization stage for the deposit. Electrum formed at lower temperatures is associated with chalcopyrite, sphalerite, galena, and tetrahedrite, filling voids in main sulfides, and probably formed during the later stages of mineralization.

References

1. Kretschmar U., Scott S.D. Phase relations involving arsenopyrite in the system Fe-As-S and their application / / Canadian Mineralogist. 1976. V.14. Number 3. P.364-386.
2. Kuznetsov S.K., Mayorova T.P., Sokerina N.V. Filippov V.N. Gold mineralization on the Verhneniyayuskoe field in the Polar Urals. / / RMO Letters. 2011. CXXXX. Number 4. P.58-71.
3. Molosag V.P. The use of minerals to assess physical and chemical conditions of sulfide ores formation in the Urals / / Lithosphere. 2009. Number 2. P. 28-40.

Volcanic-hosted massive sulfide deposits of the Urals, Russia: evidence for a magmatic contribution of metals and fluid

Ilya V. Vikentyev
IGEM, Russian Academy of Sciences, Moscow, Russia

Vladimir A. Simonov
IGM, Siberian Branch of Russian Academy of Sciences, Novosibirsk, Russia

Anastassia Y. Borisova
GET-OMP, Toulouse, France; Geological Department, MSU, Moscow, Russia

Valentina S.Karpukhina & Vladimir B.Naumov
GEOKHI, Russian Academy of Sciences, Moscow, Russia

Abstract. The formation of volcanic-hosted massive sulfide (VMS) deposits of Urals is related to shallow chambers of acidic magma. Melt inclusions of felsic rocks (rhyolite-basalt bimodal complex) correspond to tholeiitic series compositions. For the Uzelginsk ore field LA-ICP-MS analyses of inclusions of magmatic fluid and melt in quartz phenocrysts reveal high concentrations of metals (Cu, Zn, Au etc.). Magmatic vapour was enriched with Cu, Se and Au relative to coexisting melt.

Keywords. VMS deposit, melt inclusion, fluid, magmatic vapour, LA-ICP-MS analysis

1 Introduction

All economic VMS deposits are located at a range of lithostratigraphic levels corresponding to two major and a few local stages of Lower Silurian and Middle Devonian arc-related volcanism (Prokin and Buslaev 1999, Herrington et al. 2005, Maslennikov et al. 2012). Genetic relationships between the VMS deposits of the Urals and acid volcanism are still under debate (e.g. Chernyshev et al. 2008, Seravkin 2013, Simonov et al. 2010).

In spite of acceptance of a definite role of shallow magma chambers in ore formation, the source of components of the hydrothermal fluid is still not clear. Authors have studied melt inclusions (MIs) and vapour (fluid) inclusions in quartz phenocrysts in samples of dacite, rhyodacite and rhyolite of flanks of VMS (Zn>Cu) deposits of the Southern Urals.

Our investigations of felsic volcanic rocks of the Uzelginsk ore field performed using high-precision local method of laser-ablation mass-spectrometry (LA-ICP-MS) show a high saturation of magmatic fluid and melt by metals (Cu, Zn, Au, etc.). This contributes direct evidence towards the relationship between the magmatic processes in the evolving arc sequences of the Urals and the origin of massive sulfide deposits they contain. Thus, it has been obtained the direct data on the ore potential of volcanic complexes of primitive island arcs, with which sulfide deposits of the Urals are spatially associated.

2 Geodynamical setting

The discovery of numerous VMS deposits in the Urals in the third quarter of the past century has confirmed this region as a leading VMS ore belt with large reserves of Cu, Zn and associated gold, comparable to those in the
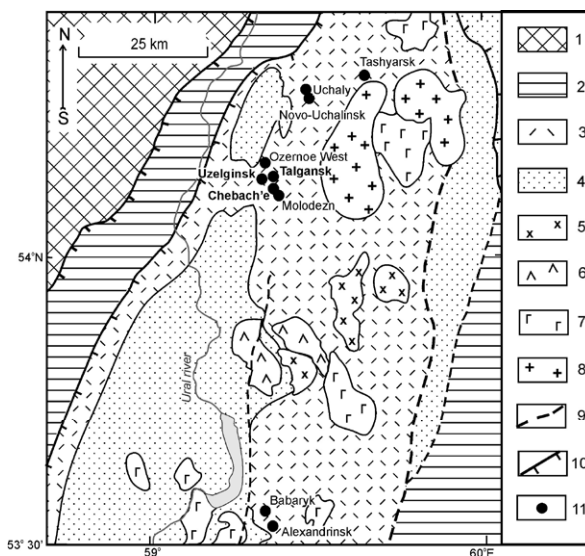
Figure 1. Scheme of Uchaly region (South Urals). 1- Central Ural uplift; 2- ophiolites O–S$_1$; (3,4)- island arc basalt–rhyolite D$_2$ (3) and andesite–basalt, basalt–trachyte complexes D$_3$–C$_1$, some limestone C$_1$t (4); 5- granodiorite, plagiogranite (D$_2$–D$_3$fr); 6,7- gabbro–granite series D$_3$fm–C$_1$t$_1$ (6) and C$_1$ (7); 8- granite P$_1$; 9- fault; 10- overthrust; 11- VMS deposit.

Iberian Pyritic Belt. Major ore deposits are located in the Magnitogorsk zone, comprising ensimatic arc-related complexes of Ordovician to early Carboniferous age (Herrington et al. 2005, Seravkin 2013, Vikentyev 2006). Most VMS bodies are hosted by slightly metamorphosed Devonian felsic rocks. The **Uzelginsk ore field** is one of the largest in the Urals (Fig. 1). Ore-bearing structures are weakly deformed and the deposits are considered to typical Ural type massive sulphide deposits (Baranov et al. 1988, Copper ... 1992, Prokin and Buslaev 1999, Vikentyev 2004). Volcanic rocks at the flanks of the Uzelginsk, Talgansk and Chebach'e deposits (Fig. 1) were studied. Silurian **Yaman-Kasy** deposit (Mednogorsk region) is not metamorphosed (see Herrington et al. 2005, Simonov et al. 2006, Maslennikov 2009).

3 Microanalytical methods

Homogenized MIs were analyzed for major elements and F, Cl by electron microprobe and REE, H$_2$O were ana-
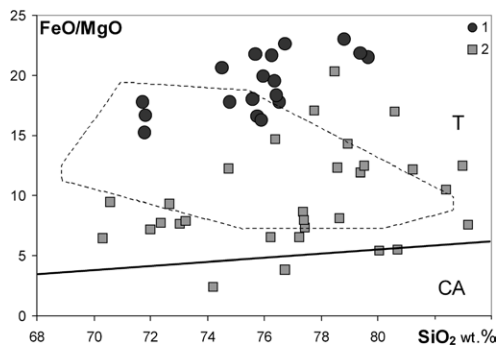
Figure 2. FeO/MgO-SiO$_2$ diagram of MIs in quartz from VMS deposits of South Urals. 1 - Yaman-Kasy deposit (Simonov et al. 2006); 2 – Uzelginsk field (Naumov et al. 1999). Dashed line counters the fields of quartz-hosted melt inclusions from Yubileinoe VMS deposit (Rudny Altai) (Simonov et al. 2010). T - tholeiitic series, CA - calc-alkaline series.

lyzed using secondary ion microprobe (SIMS) (Naumov et al. 1999, Simonov et al. 2006). Fluid magmatic inclusions in quartz have been studied using thermometric method (Karpukhina et al. 2009) and the trace and some major elements were analysed in MIs and fluid inclusions using near-infrared femtosecond laser-ablation inductively-coupled-plasma quadrupole mass spectrometry at the GET in Toulouse with use of the standardization method and ablation cell (Borisova et al. 2010, 2012). The international reference glasses NIST-SRM-612 or NIST 610 were used for external calibration, whereas ^{23}Na was used as an internal standard.

4 Melt inclusion study

There are two main types of MIs in volcanics of Uzelginsk field: the most usual devitrified inclusions, and rarely found glasses, some of them contain globules of magnetite and also sulphides, represented by pyrrhotite, pentlandite, chalcopyrite and bornite, defined by electron microprobe (Naumov et al. 1999). Re-equilibration experiments showed melting of glasses occurred at 600-720°C, homogenization at 850-1130°C, while for devitrified inclusions – occurred at 750-820°C and 950-1210°C, respectively. The concentrations of volatiles in the MIs are (in wt%) are H$_2$O up to 4.7, Cl up to 0.28, F up to 0.42 contents; the average content of sulfur is 0.025 wt%. Glass of MIs is significantly enriched with metals (ppm): Cu 1100, Zn 1400, Ag 40, Au 1.3 (Fig. 5).

The study of acidic magmatic melts by SIMS on the Yaman-Kasy deposit demonstrated their essentially lower metal potential: 30-74 ppm (Simonov et al. 2006); in addition, they are characterized by low F concentrations (<0.01-0.05 wt % in comparison with 0.01–0.42 wt % in melts of the Uzelginsk ore field).

5 High density fluid inclusions in quartz phenocrysts

Micro-Raman investigation (the Raman microprobe of a Labram type: Dilor, G2R, Nancy with a Notch filter and with a CCD detector cooled at -30°C) demonstrated only a presence of H$_2$O in fluid inclusions.
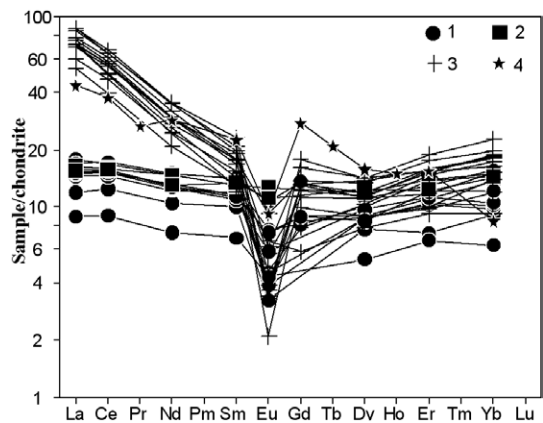
Figure 3. REE patterns of MIs in quartz from VMS deposits of South Ural: 1- Yaman-Kasy deposit (Simonov et al. 2006); 2- Uzelginsk field (Naumov et al. 1999); 3- Yubileinoe deposit (Rudny Altai) (Simonov et al. 2010); 4- rhyolite of Kuril-Kamchatka arc (Kuzmin 1985). Normalized to chondrite C1 after (Boynton 1984).

LA–ICP–MS spectra for magmatic vapour inclusions in quartz phenocrysts (Fig. 5) demonstrate the intensities of isotopes of major and minor elements. The first peak of ^{63}Cu, ^{66}Zn, and many minor elements in association with major components (^{23}Na, ^{39}K) reflects ablation of the fluid inclusion. The peaks of ^{107}Ag and ^{197}Au associate with ^{23}Na, which provides evidence for their presence in the fluid. Magmatic fluid contains high concentrations (ppm) of B (40-2000), Cu (300-3700), Zn (80-3400), Pb (14-1000), Ba (20-2200), Sn (4-1600), Au (4-8) and Ag (4-11).
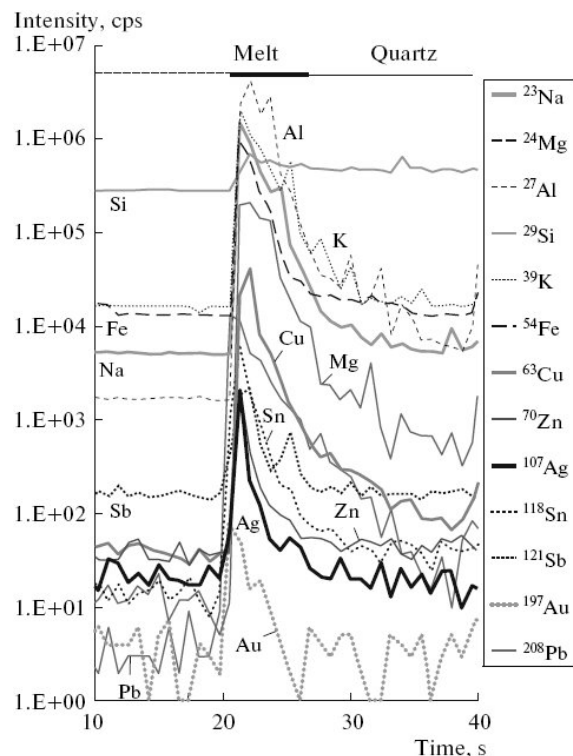
Figure 4. Results of ablation of the melt inclusion (50 µm) in the quartz phenocrystal. Peaks of Al, K, Na, Fe, Mg, Cu, Sn, Zn, Pb, Ag, and Au within the range of 21–25 s correspond to ablation of the melt inclusion. Sample U-294. Here and in Fig. 5, the dashed horizontal line illustrates that laser is switched off.
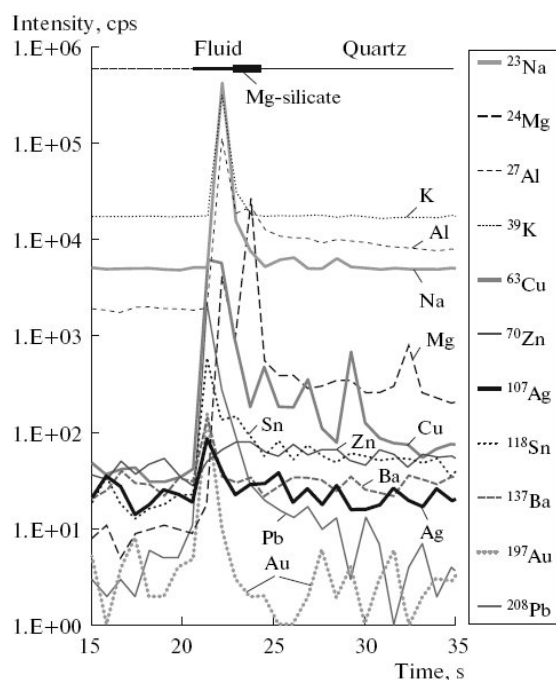
Figure 5. Typical ablation signal for magmatic vapor inclusion (~40 μm, sample U-294) in quartz. Growing peaks ^{23}Na, ^{63}Cu, ^{66}Zn, ^{107}Ag, and ^{197}Au demonstrate the start of inclusion ablation. The ^{24}Mg peak corresponds to the inclusion of silicate and does not influent for the quality of inclusion analysis.
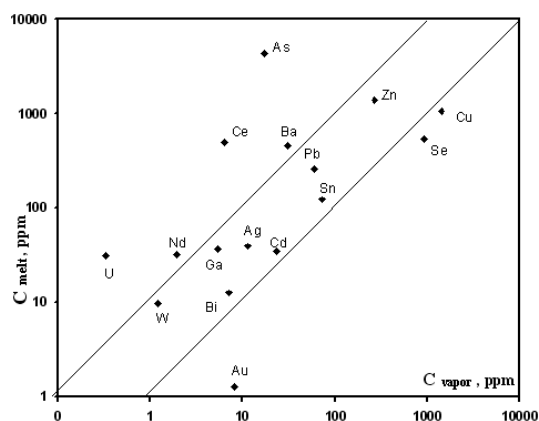
Figure 6. Concentrations of metals in coexisting magmatic fluid (C_{vapor}) and the melt (C_{melt}), according to the data of laser ablation of melt and fluid inclusions in quartz (sample U-294).

Analysis of the data on the fluid/melt distribution (Fig. 6) demonstrated that fluid (vapor) coexisting with the melt was enriched in Cu, Se, and Au in relation to the melt to the highest degree.

6 Discussion

It is suggested that metals of sulfide-forming solutions were entirely leached from underlying volcanic rocks (e.g., Copper ... 1992, Grichuk 2012, Seravkin 2013); however, estimations by V.Prokin and V.Rudnitskii (Copper ... 1992) demonstrated that the contents of these metals were not sufficient for the formation of large Cu-Zn deposits. Alternative ideas on the deep magmatic nature of metals (Marakushev et al. 2011) were proposed prior to our study. Many geologists support the

magmatogenic hypothesis of sulfide ore formation (e.g. Yang and Scott 2006, Zaw et al. 2007).

Ore-forming fluids in the deposits of the Urals studied by fluid inclusions in hydrothermal quartz, sphalerite, barite, and calcite have salinities in most cases 2–3 times as high as mineralization of seawater (up to 23 wt % eq. NaCl) (Baranov et al. 1988, Vikentyev 2004).

At the same time, the SIMS method demonstrated the high copper concentrations in acid melts of sulfide deposits of Southern Siberia: Yubileinoe (Rudnyi Altai, Russia) and Kyzyl-Tashtyg (Tyva, Russia), 25–4070 and 410–3230 ppm, respectively, at low Pb concentrations (5–15 and 0.7– 1.5 ppm, respectively) (Simonov et al. 2010). Unfortunately, the data on other ore-forming metals for felsic melts with related sulfide deposits are absent in published papers. All the other numerous papers, in which the concentrations of metals in melt inclusions in quartz phenocrysts are discussed, deal with the investigation of copper porphyry ore-forming systems. The copper concentrations in silicate melts of these magmatogenic deposits (the upper limits for different deposits are from 450 to 7000 ppm Cu) are similar to those in VMS deposits (e.g., Simonov et al. 2010 and refs. therein).

Most researchers agree with VMS origin from hydrothermally circulated seawater transformed during interaction with the host volcanic rocks. However, the isotope data (Sr, H, O, C) provide evidences for a mixed (Baranov et al. 1988, Vikentyev 2004) or a predominantly deep (Amplieva et al. 2008, Bobokhov et al. 1989) nature of hydrothermal fluid. ^{87}Sr/^{88}Sr ratio for carbonates (0.7048-0.7063) corresponding to a primary $(^{87}$Sr/^{88}Sr$)_o$ was found to be close or exceed those for acid volcanites of the Uzelginsk ore field (0.7041-0.7064, Bobokhov et al. 1989). A very narrow range of $(^{87}$Sr/^{88}Sr$)_o$ = 0.70597-0.70625 indicates a negligible involvement of seawater and high input of magmatic water characteristic for ores and host rocks of the lower ore level; the smallest ratios occur in carbonates of latest quartz-carbonate veins in diabase dykes. Isotope compositions of O and C of carbonates (δ^{18}O= +13 to +26.5‰, δ^{13}C= –28 to +1‰ for massive ores and δ^{18}O= +9 to +27‰, δ^{13}C= –20 to –1‰ for altered igneous rocks) confirm the evidence for a marked addition of magma-derived components (Fig.7). Data from limestones samples, from the unit overlying the ore bodies of the upper ore level, demonstrate that hydrothermal endogenous input occurred during their formation: the footwall of the limestone layer has δ^{18}O= +26‰ and samples from further up have δ^{18}O= +27.5 to +28.5‰, approaching the field of isotope composition of marine carbonates (Fig.7).

The major role of the mantle component (DMM-A and EM I) is evident from lead isotope ratios (by high-precision MC-ICP-MS method) of galena in sulphide ores of the Urals (Chernyshev et al. 2008).

Yaman-Kasy deposit with mean gold content 3.3 g/t is close to those considered auriferous (>3.46 g/t, Mercier-Langevin et al. 2011). Four from 10 deposits of Uchaly region (see Fig.1) are anomalous in terms of gold content; their total gold reserves ranges 632 t. They associate with transitional from tholeiitic to calc-alkaline felsic volcanic rocks. Trace element signatures (Au-Ag-As-Sb-Se-Te-Hg) suggest a direct magmatic input in ore systems (e.g. Mercier-Langevin et al. 2011).
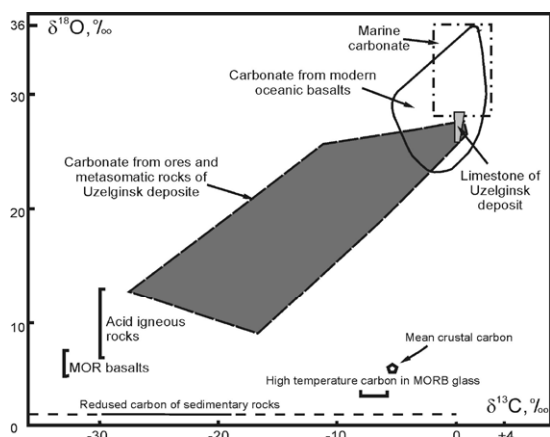
Figure 7. O-C isotope compositions in carbonates of ores and host rocks. Isotope reservoirs after (Faure, Mensing 2005).

Partition coefficients between coexisting vapor and melt ($K_d^{v/m}$) according to LA-ICP-MS analyses (sample U-294) range 1.36 for copper and 6.38 for gold. Comparable ratios were reproduced in experiments in magmatic-hydrothermal systems at 800°C and 100 MPa (Frank et al. 2011). They demonstrate that copper and gold partitioned strongly into the magmatic volatile phase(s) (i.e., vapor or brine) relative to a silicate melt, $K_d^{v/m}$ ranging from 2.1 (±0.7) to 18 (±5) for copper and 7(±3) to 1.6(±1.6) x 10^2 for gold.

7 Conclusions

The new data from the Uzelginsk VMS field provides the first direct data on the composition of magmatic fluid contained in felsic melt (up to 4.7 wt % H_2O). It is shown that the magmatic vapour was enriched in Cl and metals (Na, Cu, Zn, Fe, Au, and Ag), providing direct evidence for a major magmatic contribution to the formation of VMS deposits with only minor inputs from seawater.

Acknowledgments

References

Amplieva EE, Vikentyev IV, Karpukhina VS, Bortnikov NS (2008) The role of magmatogene fluid in the formation of the Talgan copper–zinc–pyritic deposit, Southern Urals. Doklady Earth Sci 423A (9):1427–1430

Baranov EN, Schteinberg AD, Karpukhina VS (1988) A genetic model and exploration criteria for buried massive sulfide deposits of the Verkhneuralsky area, southern Urals, USSR. Proc. 7th IAGOD Symp, pp 449–460

Bobokhov AS, Gorozhanin VM, Kuzmin SA (1989) Strontium Isotope Data for Acid Volcanic Rocks of the Magnitogorsk Megasynclinorium of the Southern Urals. Ufa [in Russian]

Borisova AY, Freydier R, Polve M et al. (2010) Multi-elemental analysis of ATHO-G rhyolitic glass (MPIDING reference material) by femtosecond and nanosecond LA-ICP-MS: evidence for significant heterogeneity of B,V, Zn, Mo, Sn, Sb, Cs, W, Pt and Pb at mm-scale. Geostand Geoanal Res 34:245-255

Borisova AY, Thomas R, Salvi S et al. (2012) Tin and associated metal and metaloid geochemistry by femtosecond LA-ICP-MS microanalysis in pegmatite-leucogranite melt and fluid inclusions: New evidence for melt-melt-fluid immiscibility. Mineral Mag 76(1):91-113

Boynton WV (1984) Geochemistry of the rare earth elements: meteorite studies. In: Henderson P (ed) Rare earth element geochemistry. Elsevier, pp 63–114

Chernyshev IV, Vikentyev IV, Chugaev AV et al. (2008) Sources of material for massive sulfide deposits in the urals: evidence from the high-precision MCP-ICP-MS isotope analysis of the galena-hosted Pb. Doklady Earth Sci 418(1):178–183

Copper Sulfide Deposits of the Urals. Conditions of the Formation (1992) Ivanov SN, Prokin VA (eds) Yekaterinburg [in Russian]

Faure G, Mensing TM (2005) Isotopes: principles and applications. Hoboken, N.J.: Wiley

Frank MR, Simon AC, Pettke T, Candela PA, Piccoli PM (2011) Gold and copper partitioning in magmatic-hydrothermal systems at 800°C and 100 MPa. Geochim Cosmochim Acta 75:2470–2482

Grichuk DV (2012) Thermodynamic model of ore-forming processes in a submarine island-arc hydrothermal system. Geochem Intern. 50(13):1069–1100

Herrington RJ, Maslennikov VV, Zaykov VV et al. (2005) Classification of VMS deposits: Lessons from the South Uralides. Ore Geol Rev 27:203–237

Karpukhina VS, Naumov VB, Vikentyev I, Salazkin AN (2009) Melt and high-density fluid inclusions of magmatic water in phenocrysts of quartz from acidic volcanic rocks of the Verkhneuralsk ore district, South Urals. Doklady Earth Sci 426(4):580–583

Kuzmin MI (1985) Geochemistry of magmatic rocks of Phanerozoic mobile belts. Novosibirsk: Nauka [in Russian]

Marakushev AA, Paneyakh NA, Zotov IA (2011) Petrogenetic types of massive sulfide and polymetalic deposits. Lithosphere 3:84–103

Maslennikov VV, Maslennikova SP, Large RR, Danyushevsky LV (2009) Study of trace element zonation in vent chimneys from the Silurian Yaman-Kasy VHMS (the Southern Urals, Russia) using laser ablation inductively coupled plasma mass spectrometry (LA-ICPMS). Econ Geol 104 (8):1111–1141

Maslennikov VV, Ayupova NR, Herrington RJ et al. (2012) Ferruginous and manganiferous haloes around massive sulphide deposits of the Urals. Ore Geol Rev 47:5–41

Mercier-Langevin P, Dubé B, Bécu V, Hannington MD (2011) The gold content of volcanogenic massive sulfide deposits. Mineral Deposita 46(5):509–539

Naumov VB, Karpukhina VS, Baranov EN, Kononkova NN (1999) Composition of melts of felsic volcanites of the Verkhneuralsky area (Southern Urals) on data of melt inclusion studies in quartz. Geochem Intern 4:289–301

Prokin VA, Buslaev FP (1999) Massive copper-zinc sulfide deposits in the Urals. Ore Geol Rev 14:1–69

Seravkin IB (2013) Correlation of compositions of ore and host rocks in volcanogenic massive sulfide deposits (on the samples of South Urals). Geol Ore Deposits 55(3):68–83

Simonov VA, Kovyazin SV, Terenya EO et al. (2006) Physicochemical parameters of magmatic and hydrothermal processes at the Yaman-Kasy massive sulfide deposit, the Southern Urals. Geol Ore Deposits 48(5):369–383

Simonov VA, Gaskov IV, Kovyazin SV (2010) Physico-chemical parameters from melt inclusions for the formation of the massive sulfide deposits in the Altai-Sayan region, Central Asia. Austral J Earth Sci 57:737–754

Vikentyev IV (2004) Conditions of the Formation and Metamorphism of Sulfide Ores. Moscow [in Russian]

Vikentyev IV (2006) Precious metal and telluride mineralogy of large volcanic-hosted massive sulfide deposits in the Urals. Mineral Petrol 87: 305−326

Yang K, Scott SD (2006) Magmatic fluids as a source of metals in seafloor hydrothermal systems. In: Back-arc spreading systems: geological, biological, chemical, and physical interactions. Geophys. Monogr. Series 166:163–184

Zaw K, Peters SG, Cromie P et al. (2007) Nature, diversity of deposit types and metallogenetic relations of South China. Ore Geol Rev 31:3–27

S 3.12:
Skarn deposits – 138 years after Törnebohm

Convenors:
Nils Jansson & Zhaoshan Chang

A brief history of skarn

Lawrence D. Meinert

U. S. Geological Survey, 12201 Sunrise Valley Drive, MS 913, Reston, VA 20192 USA, Lmeinert@usgs.gov

Abstract. Skarns have been mined for millennia, and studied for centuries. Much of that history was centered in Sweden and then spread to the rest of the world with the development of new deposits, techniques, and equipment. Skarns are defined by their mineralogy and classified by their economic metal content. They can occur in almost any rock type and form from a variety of metamorphic, metasomatic, and hydrothermal processes. There are correlations between skarn type, petrology of associated intrusions, and tectonic setting. The understanding of skarn deposits has evolved from field-based studies in the early 20th Century, through theoretical and experimental studies in the mid 20th Century, to a modern state that combines field, petrologic, mineralogic, and geochemical studies in the latter part of the 20th Century and continuing to the present.

Keywords. Sweden, Skarn, History

1 Sweden and Skarns

It is fully appropriate that a symposium entitled "Skarn deposits – 138 years after Törnebohm" should be held in Uppsala, Sweden. Sweden has a long history of mining of skarn deposits, exceeded perhaps only by the Banat region of Romania (Nicolescu 1996). The skarns of Sweden are the type locality for many mineral species such as bastnäsite, bergslagite, cerite, dannemorite, lanthanite, linnaeite, and törnebohmite (Geijer 1921); the word "skarn" itself is of Swedish origin, with several interesting meanings in both old and modern Swedish.

The first published use of the term "skarn" is by the Swedish geologist Alfred Elis Törnebohm (1875), hence the title of this symposium. In addition, Uppsala is the home of the Geological Survey of Sweden, an institution for which Törnebohm was five times elected as chairman (1880, 1886, 1891, 1894, and 1899), thus further cementing strong links between Sweden and skarn history.

Skarn deposits are one of the more abundant ore types in the earth's crust and form in rocks of almost all ages. Skarn is a relatively simple rock type defined by a mineralogy usually dominated by calc-silicate minerals such as garnet and pyroxene. Although the majority of skarns are found in lithologies containing at least some limestone, they can form in almost any rock type during regional or contact metamorphism and from a variety of metasomatic processes involving fluids of magmatic, metamorphic, meteoric, and/or marine origin. Although most are found adjacent to plutons, they also can occur along faults and major shear zones, in shallow geothermal systems, on the sea floor, and at lower crustal depths in deeply buried metamorphic terranes. Thus, neither a pluton nor limestone is necessarily required to form skarn. Most skarn deposits are zoned, and the general pattern is proximal garnet, distal pyroxene, and minerals like wollastonite, vesuvianite, or massive sulfides and/or oxides near the marble front. Recognition of distal alteration features such as bleaching, fluid escape structures, and isotopic halos can be critically important in exploration. Because most economic skarn deposits are related to magmatism, details of igneous petrogenesis and tectonic setting form a framework for exploration and classification.

For the seven major skarn types (Fe, Au, Cu, Zn, W, Mo, and Sn) a general correlation exists among igneous major and trace element composition and skarn type (Meinert 1995). Plutons associated with Fe and Au skarns contain significantly more MgO and less K_2O or SiO_2, Au and Sn skarn plutons are more reduced, and Cu, Zn, and Mo skarn plutons are more oxidized than average skarn plutons. In terms of geochemical evolution, there is a fairly linear array from relatively primitive calcic Fe skarn plutons through Au, Cu, Zn, to W, Mo, to relatively evolved Sn skarn plutons. Calcic Fe skarn plutons are metaluminous, high in compatible elements such as Ni, V, and Sc, and have Rb/Sr <1. Relative to Fe skarn plutons, Cu skarn plutons have higher Si, K, Ba, Sr, La, and Fe^{3+}/Fe^{2+}, and contain significantly less Mg, Sc, Ni, Cr, and V. Au skarn plutons are similar to Fe skarn plutons in their metaluminous nature and their Si, Mg, Cr, and Sc contents and are similar to Cu skarn plutons in their Ni, V, and Y content. In general, plutons associated with Sn, Mo, and W skarns have a much stronger crustal signature than do plutons associated with other skarn types.

2 The History of Skarn Research

As detailed by Burt (1982), early research on skarns focused on European deposits, largely by European scientists such as in the classic studies by von Cotta (1864) and Goldschmidt (1911), with a few exceptions such as by Fukuchi (1907) in Japan. This trend shifted in the first half of the 20th Century as the American West was settled and major skarn deposits were developed, with seminal studies done by Lindgren (1902, 1905, 1924), Weed (1903), Barrell (1907), Umpleby (1913, 1916), Knopf (1918), and Schmitt (1939). Many of these studies were by scientists of the U.S. Geological Survey utilizing the results of detailed surface and underground mapping.

In the middle part of the 20th Century Russian scientists such as Korzhinsky (1946, 1955, 1970), Zharikov (1959, 1970), and Smirnov (many early studies but the first accessible work in English was in 1976), came to the fore with breakthroughs in the understanding of metasomatism and zonation. This advance was followed by experimental and theoretical studies of calc-

silicate equilibria, such as in Greenwood (1967) and Kerrick (1974) that allowed significant progress on understanding the petrologic development of skarn deposits.

All of the preceeding work came together in what could be termed the beginning of the modern skarn era when a thorough understanding of mineralogy and geochemistry was married with careful field work in studies like Theodore and Blake (1975, 1978), Burt (1977), Atkinson and Einaudi (1978), Einaudi (1982a,b), and Newberry (1982). Much of this work was synthesized for the first time in the 75th Anniversary Volume of Economic Geology (Einaudi et al. 1981).

This period was followed by the discovery and production of large skarn deposits such as Antamina and Las Bambas in Peru, El Toqui in Chile, Ok Tedi in Papua New Guinea, multiple skarns of the Ertsberg district in Irian Jaya, skarns and related porphyries of the Cadia District in Australia, and large numbers of big skarn deposits in China, which still have not been well studied. A few of these world class deposits have received modern study, e.g., Meinert et al. (1997), but most await further understanding.

Other skarn studies documented the close association of igneous intrusions with different types of skarn deposits (Meinert 1993, 1995). This in turn led to better understanding of petrogenesis, tectonic setting, and the magmatic-hydrothermal transition.

The latter half of the 20th Century was marked by continued analytical advances in the development of equipment and analytical techniques such as the electron microprobe (e.g., Shimazaki 1975 1980; Nakano 1978 1998; Ochiai 1987; Ray 1997), fluid inclusion (Meinert 1987; Meinert et al. 1997), and isotope geochemistry (Taylor and O'Neil 1977; Shimazaki 1988; Shimazaki and Kusakoabe 1990; Bowman 1998). This trend continued into the 21st century with the advent of LA-ICPMS technology used to analyse mineral and fluid compositions that previously were beyond detection (e.g., Baker and Lang 2003; Meinert et al. 2003; Baker et al. 2004). Many of these advances were summarised in the 100th Anniversary Volume of Economic Geology (Meinert et al. 2005).

3 The Future of Skarn Research

The present symposium represents the future of skarn studies and it is appropriate that some of them (e.g. Jansson et al. 2013) are returning to the type localities in Sweden where the term skarn was first defined. There is still much to be learned about skarns and the world awaits what will be revealed by future studies.

References

Atkinson WW Jr, Einaudi MT (1978) Skarn formation and mineralization in the contact aureole at Carr Fork, Bingham, Utah. Econ Geol 73:1326–1365

Baker T,Lang JR (2003) Reconciling fluid inclusions, fluid processes and fluid source in skarns: an example from the Bismark skarn deposit, Mexico. Mineral Deposita, 38:474–495

Baker T, van Achterberg E, Ryan CG, Lang JR (2004) Composition and evolution of ore fluids in a magmatic-hydrothermal skarn deposit. Geology 32:117–120

Barrell J (1907) Geology of the Marysville mining district, Montana. US Geol Survey Prof Paper 57, 178 pp

Bowman JR (1998) Stable-isotope systematics of skarns. Miner Assoc Canada Short Course Ser 126:99–145

Burt DM (1977) Mineralogy and petrology of skarn deposits. Rendiconti della Soc Italiana Mineral Petrol 33:859–873

Burt DM (1982) Skarn deposits—historical bibliography through 1970. Econ Geol 77:755–763

Einaudi MT (1982a) Descriptions of skarn associated with porphyry copper plutons, southwestern North America. In Titley SR (ed) Advances in geology of the porphyry copper deposits, southwestern North America. Tucson, Univ Arizona Press, pp 139–184

Einaudi MT (1982b) General features and origin of skarns associated with porphyry copper plutons, southwestern North America. In Titley SR (ed) Advances in geology of the porphyry copper deposits, southwestern North America. Tucson, Univ Arizona Press, pp 185–210

Einaudi MT, Meinert LD, Newberry RJ (1981) Skarn deposits. In Skinner BJ (ed) Econ Geol 75th Ann Vol, 1905-1980. Econ Geol Publ Company, Lancaster, Penn, USA, pp 317–391

Fukuchi N (1907) Mineral parageneses in the contact-metamorphic ore-deposits, found in Japan. In Wada T (ed) Beiträge zur Mineralogie von Japan 3:75–109

Geijer P (1921) The cerium minerals of Bastnäs at Riddarhyttan. Sveriges Geol Undersök C304, 11–24

Goldschmidt VM (1911) Die kontakmetamorphose im Kristianiagebiet. Oslo Videnskaplige Skrifter, I, Mat-Natur K1(1), 483 pp

Greenwood JH (1967) Wollastonite: stability in H2O-CO2 mixtures and occurrence in a contact metamorphic aureole near Salmo, British Columbia. Am Mineral, 52:1669–1680

Jansson NF, Erismann F, Lundstam E, Allen RL (2013) Evolution of the Paleoproterozoic volcanic-limestone-hydrothermal sediment succession and Zn-Pb-Ag and iron oxide deposits at Stollberg, Bergslagen region, Sweden. Econ Geol 108:309–335

Kerrick DM (1974) Review of metamorphic mixed-volatile (H$_2$O-CO$_2$) equilibria. Am Mineral 59:729–762

Knopf A (1918) Geology and ore deposits of the Yerington district, Nevada. US Geol Survey Prof Paper 114, 68 pp

Korzhinsky DS (1946) Metasomatic zoning in wallrock alteration and veins. Soc Russe Mineral Mem 75:321–332

Korzhinsky DS (1955) Outline of metasomatic processes: main problems in the science on magmatogenic ore deposits. Moscow, Academic Science Publishing pp 334–456

Korzhinsky DS (1970) Theory of metasomatic zoning. Oxford, Clarendon Press, 162 pp

Lindgren W (1902) The character and genesis of certain contact deposits. Am Inst Mining Engr Trans 31:226–244

Lindgren W (1905) The copper deposits of the Clifton-Morenci district, Arizona. US Geol Survey Prof Paper 48, 875 pp

Lindgren W (1924) Contact metamorphism at Bingham, Utah. Geol Soc Am Bull 35:507–534

Meinert, LD (1987) Skarn zonation and fluid evolution in the Groundhog Mine, Central Mining District, New Mexico. Econ Geol, 82:523-545

Meinert, LD (1993) Igneous petrogenesis and skarn deposits. in (RV Kirkham, WD Sinclair, RI Thorpe, & JM Duke, eds). Geol. Assoc. Can. Special Paper, 40:569-583

Meinert, LD (1995) Compositional variation of igneous rocks associated with skarn deposits - Chemical evidence for a genetic connection between petrogenesis and mineralization. in Thompson, JFH, ed, Magmas, fluids, and ore deposits, Min. Assoc. Can. Short Course Series, 23:401-418

Meinert LD, Dipple GM, Nicolescu S (2005) World skarn deposits. In Hedenquist JW, Thompson JFH, Goldfarb RJ, Richards JP (eds) Econ Geol 100th Ann Vol, 1905-2005. Soc Econ Geol Inc, Littleton, Colo, USA, Includes supplementary appendices on CD-ROM (filename: Meinert):299–336

Meinert LD, Hedenquist JW, Satoh H, and Matsuhisa Y (2003) Formation of Anhydrous and Hydrous Skarn in Cu-Au Ore Deposits by Magmatic Fluids. Econ Geol, 98:147-156

Meinert LD, Hefton KK, Mayes D, and Tasiran I (1997) Geology, zonation, and fluid evolution of the Big Gossan Cu-Au skarn deposit, Ertsberg district, Irian Jaya. Econ Geol, 92:509-526

Nakano T (1978) The zoned skarn developed in diorite porphyry in the Shinyama area, Kamaishi mine, Japan. Min Geol 28:99–109

Nakano T (1998) Pyroxene geochemistry as an indicator for skarn metallogenesis in Japan. Miner Assoc Canada Short Course Ser 126:147–168

Newberry RJ (1982) Tungsten-bearing skarns of the Sierra Nevada. I. The Pine Creek mine, California. Econ Geol 77:823–844

Nicolescu S (1996) The Ocna de Fier-Dognecea skarn deposit (Banat, Romania)—4000 years of human endeavour. Szeged, Acta Mineralogica-Petrographica, 37, Supplementum, p 84

Ochiai K (1987) A reaction model relating skarn zones and ore formation at the Nippo copper ore deposit, Kamaishi mine, northeastern Japan. Econ Geol 82:1001–1018

Ray GE (1997) Skarns in British Columbia. B.C. Ministry Employ Invest Bull 101, 200 pp

Schmitt H (1939) The Pewabic mine. Geol Soc Am Bull 50:777–818

Shimazaki H (1975) The ratios of Cu/Zn-Pb of pyrometasomatic deposits in Japan and their genetic implications. Econ Geol 70:717–724

Shimazaki H (1980) Characteristics of skarn deposits and related acid magmatism in Japan. Econ Geol 75:173–183

Shimazaki H (1988) Oxygen, carbon and sulfur isotope study of skarn deposits in Japan. In Zachrisson, E (ed) Proceed 7th Quad IAGOD Symp. Stuttgart, E. Schweizerbart'sche Verlagsbuchhandlung, pp 375–381

Shimazaki H, Kusakoabe M (1990) Oxygen isotope study of the Kamioka Zn-Pb skarn deposits, central Japan. Min Deposita 25:221–229

Smirnov VI (1976) Skarn deposits. In Geology of mineral deposits. Moscow, MIR Publications, pp 156–188

Taylor BE, O'Neil JR (1977) Stable isotope studies of metasomatic Ca-Fe-Al-Si skarns and associated metamorphic and igneous rocks, Osgood Mountains, Nevada. Contr Mineral Petrol 63:1–49

Theodore TG, Blake DW (1975) Geology and geochemistry of the Copper Canyon porphyry copper deposit and surrounding area, Lander County, Nevada. US Geol Survey Prof Paper 798-B, 86 pp

Theodore TG, Blake, DW (1978) Geology and geochemistry of the West orebody and associated skarns, Copper Canyon porphyry copper deposits, Lander County, Nevada (with a section on electron microprobe analyses of andradite and diopside by NG Banks). US Geol Survey Prof Paper 798-C, 85 pp

Törnebohm AE (1875) Geognostisk beskrifning ofver Persbergets Grufvefält. Sveriges Geol Undersök, Stockholm, P.A. Norstedt and Sons, 21 pp

Umpleby JB (1913) Geology and ore deposits of Lemhi County, Idaho. US Geol Survey Bull 528, 182 pp

Umpleby JB (1916) The occurrence of ore on the limestone side of garnet zones. Univ California Dept Geology Bull, 10:25–37

von Cotta B (1864) Erzlagerstätten im Banat und in Serbien. Vienna, Ed. W. Braunmüller, 105 pp

Weed WH (1903) Ore-deposits near igneous contacts. Am Inst Mining Eng Trans 33:715–746

Zharikov VA (1959) Geology and metasomatic processes at the skarn base metal deposits of the western Karamazar. Trans Inst Mineral Geochem Ore Deposits, Russian Acad Sci, Moscow (IGEM AN SSSR), 14

Zharikov VA (1970) Skarns. Intern Geol Rev 12:541–559, 619–647, 760–775

Geological characteristics and genesis of the Caijiaying Zn-Au deposit, China

Zhaoshan Chang* Noel C. White
EGRU (Economic Geology Research Centre), School of Earth and Environmental Sciences, James Cook University, Townsville, Queensland 4814, Australia *Zhaoshan.chang@jcu.edu.au
CODES ARC Centre of Excellence in Ore Deposits, University of Tasmania, Hobart, Tasmania 7001, Australia, and Ore Deposit and Exploration Centre, Hefei University of Technology, Hefei, China

Rupert W.A. Crowe, Warren Woodhouse, Glenn Whalan & Nigel Wilson
CSA Global Pty Ltd, PO Box 141, West Perth, Western Australia 6872, Australia

Abstract. The Caijiaying Zn-Au deposit is mainly hosted in Proterozoic high-grade metamorphic rocks with marble lenses, with minor ores in Jurassic volcanic cover rocks. It contains skarn ores, breccia ores, banded/folded ores, and locally epithermal features along a major fault, suggesting different origins such as metamorphic, skarn and epithermal. We have found that the breccia ores and the banded/folded ores are part of the skarn system, and the epithermal features may have formed in a later event. Gold is related to Bi minerals and may have been collected and transported by Bi melts. The location of orebodies is controlled by marble.

Keywords: Caijiaying, Zn-Au, skarn

1 Introduction

The Caijiaying mine is located at 115°14'55'' - 115°18'00'' E and 41°24'50'' - 41°26'35'' N in Hebei Province, China, and is about 250 km NW of Beijing (Fig. 1). There are five identified mineralized zones, among them the Zone III was most intensively explored and is currently being mined (Fig. 2). The current resource of Zone III is 32 Mt @ 4.5 % Zn, 0.25% Pb, 0.74 g/t Au, and 25 g/t Ag (Griffin Mining Limited, 2011 Annual Report). Recently more exploration was carried out in Zone II, which resulted in a resource of 20 million tonnes grading 3.2% Zn, 0.73% Pb, 0.26 g/t Au and 25 g/t Ag (Griffin Mining Limited, 2011 Annual Report). Ongoing exploration in Zone III, II, and other zones is still expanding the resource.

The Caijiaying deposit is unusual in containing significant amounts of both zinc and gold. The geology is baffling and intriguing, with features suggesting different origins such as metamorphic, skarn and epithermal. In this study we document the geological characteristics, interpret the genesis, and look for indicators and vectors that can enhance exploration efficiency and success rate.

2 Deposit geology

The Caijiaying mine is in the North China Craton of the Sino-Korea domain, close to the northern margin of the craton, within the Neimeng (Inner Mongolia) Axis (Fig. 1; Wang and Mo, 1995). The stratigraphy at Caijiaying consists of Early Proterozoic high-grade metamorphic rocks, including granulite, gneiss, migmatite and amphibolite, with marble lenses and disseminated graphite, overlaid by Late Jurassic volcaniclastic rocks, andesitic-basaltic lavas and rhyolitic to trachytic ignimbrite. All the rocks are cut by rhyolite porphyry dykes, some pre-mineralisation and some syn-mineralisation, and minor diorite porphyry dykes (Fig. 2). The rhyolite porphyry dykes have porphyritic textures and glassy, flow-banded margins that contain spherulites, indicating shallow depth. The metamorphic rocks are folded, with the fold axis trending NNW in the southern part and NNE in the northern part where it is similar to the strike of the Zone III orebodies. There are regional NE faults to the N and S of Caijiaying, with the southern one named F45. A set of NNE faults is parallel to the orebodies in Zone III, as revealed by magnetic survey. There are also E-W faults.

Both the Proterozoic silicate metamorphic rocks and the Jurassic volcanic rocks have sericite and chlorite alteration. The sericite ranges from illite to interlayed illite/smectite (I/S), with the illite crystallinity (IC) determined by Short Wavelength Infra-Red (SWIR) spectral techniques ranging from 0.5 to 3.9, dominantly below 2.1. Marble in small lenses or at the margin of large lenses has been altered to Fe-rich pyroxene containing 77-93 mol% hedenbergite. The retrograde alteration of the skarn is strong and occurred in several stages. Earlier retrograde alteration is composed of ilvaite and amphibole (actinolite–ferroactinolite). Some specular hematite was present and may have formed during this stage; the specular hematite was subsequently altered to magnetite with the crystal shapes preserved, forming mushketovite. Later there was strong overprint and open-space filling of quartz, chlorite, and siderite, plus sphalerite, pyrite, marcasite, minor galena, arsenopyrite, chalcopyrite, and even later dolomite, calcite, pyrrhotite, bismuthinite, native Bi, Pb-Bi sulfosalts, and electrum.

In addition to skarn-style ores there are more abundant breccia-style ores. The clasts have various degrees of rounding, with the larger ones typically more angular and the smaller ones more rounded. The clasts are composed of various types of metamorphic wall rocks and pyroxene skarns. All the clasts have intensive illite-I/S, carbonate, and/or chlorite alteration. The cement is mainly composed of quartz, carbonate, and chlorite, plus sulfides, sulfosalts and electrum. The alteration-mineralization assemblage of breccia ores is identical to the late stage retrograde skarn assemblage,
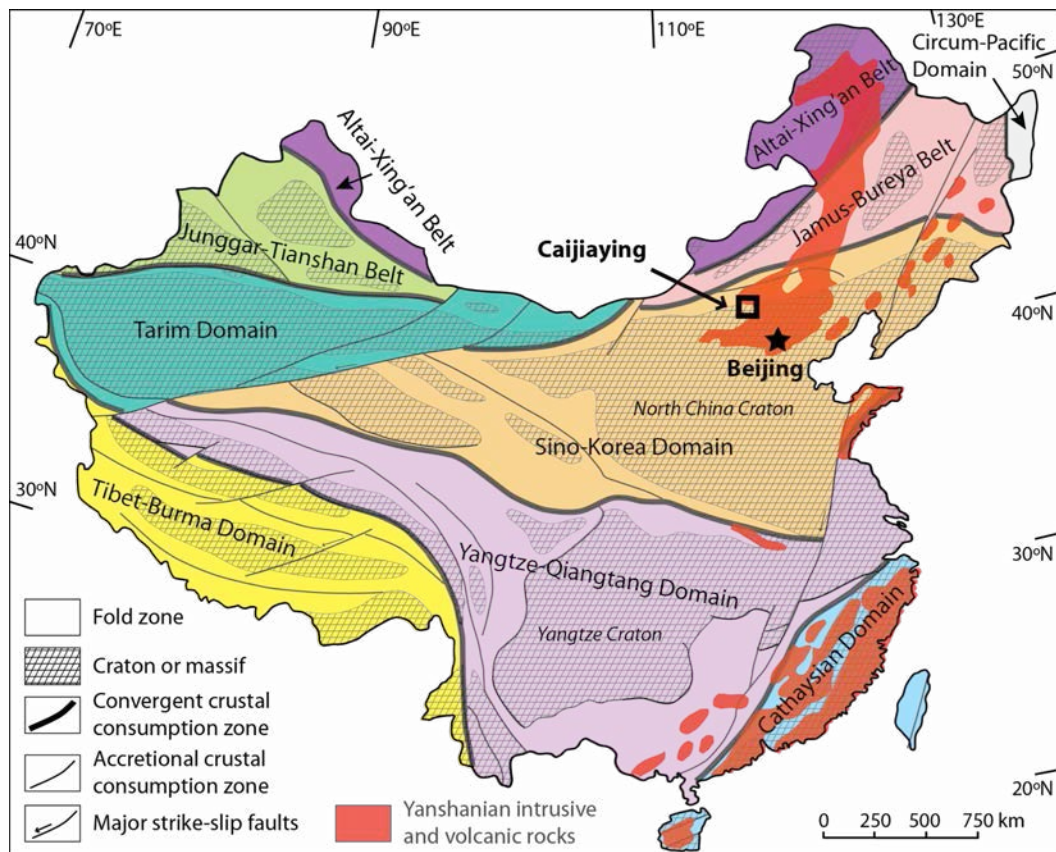
Figure 1. Tectonic map of China, showing the tectonic setting of the Caijiaying deposit (simplified after Wang and Mo, 1995). Excluding the Yanshanian magmatic rocks, the figure shows the tectonic framework by 210 Ma. There are 9 domains consisting of cores of Precambrian cratons and fold belts surrounding them. The domains are separated by crust-consuming convergent zones. After 210 Ma, Yanshanian (210-90 Ma) intrusive and volcanic rocks formed in a gigantic NE belt in eastern China, caused by the subduction of the Pacific plate under the Eurasian plate.

indicating that the breccia ores are part of the skarn system.

Minor ores have banded and folded textures. The mineralized bands are typically composed of quartz-carbonate-sulfides-sulfosalts-electrum. The textures seemingly indicate a pre-deformation timing for the mineralization. However, cathodoluminescence (CL) imaging indicates that the quartz accompanying sphalerite in such ores has regular growth bands, in contrast to the CL-featureless quartz in metamorphic rocks in the adjacent un-mineralised bands, indicating the banded/folding textures formed later than metamorphism and were probably caused by selective replacement; the mineralised bands are interpreted to have been calcareous before alteration.

There are abundant epithermal features (White and Hedenquist, 1990; Hedenquist et al., 2000; Simmons et al., 2005) within and along the F45 fault at the surface, including lattice textures and chalcedony+quartz+minor fluorite veins and breccias with orthoclase alteration in wall rocks. No mineralisation has been found in rocks with such epithermal features yet. The features N of F45 indicate greater depth than S of F45. Close to F45 there is botryoidal quartz-carbonate, an epithermal product, cementing sphalerite ores.

The Caijiaying orebodies are mostly hosted in the metamorphic basement, with little mineralisation locally found in the volcanic cover rocks.

Gold ores are indistinguishable from Zn ores except for the Au content, which indicates that the Au

mineralisation and the Zn mineralisation may have occurred in the same event and by the same fluids but at different stages. The Au occurs mostly as electrum but also as solid solutions in the lattice of pyrite, marcasite, and arsenopyrite based on LA-ICP-MS analyses; the latter type may account for only small portions of the Au resources. Electrum has a strong spatial association with Pb-Bi sulfosalt minerals, native Bi and bismuthinite. Electrum and the Bi-bearing minerals occur within or at the grain boundaries of all the hydrothermal minerals including amphibole, ilvaite, hematite, magnetite, quartz, sphalerite, siderite, pyrite, marcasite, arsenopyrite, calcite, chlorite, except for the earliest mineral, pyroxene. Electrum grains are typically small, <20 μm but locally up to ~440 μm. Bismuth minerals, with or without electrum, are typically <50 μm but locally up to ~500 μm. Bismuth mineral and/or electrum patches typically have straight edges and are moulded by the surrounding grains of other minerals, as well as by clasts in breccias, but electrum within Bi minerals typically has rounded shapes. Rarely, some Bi-bearing minerals and/or electrum±pyrrhotite also occur as veins cutting sphalerite along cleavages or cutting arsenopyrite, or occur in calcite veins cutting sphalerite. Electrum grains tend to occur in clusters, with many grains occurring in small patches. Within a patch many electrum grains, locally as sub-micron "clouds", may occur inside mineral grains or on the boundaries of any mineral, regardless of their timing. Gold resources are higher below 1300 m elevation. The electrum grains and
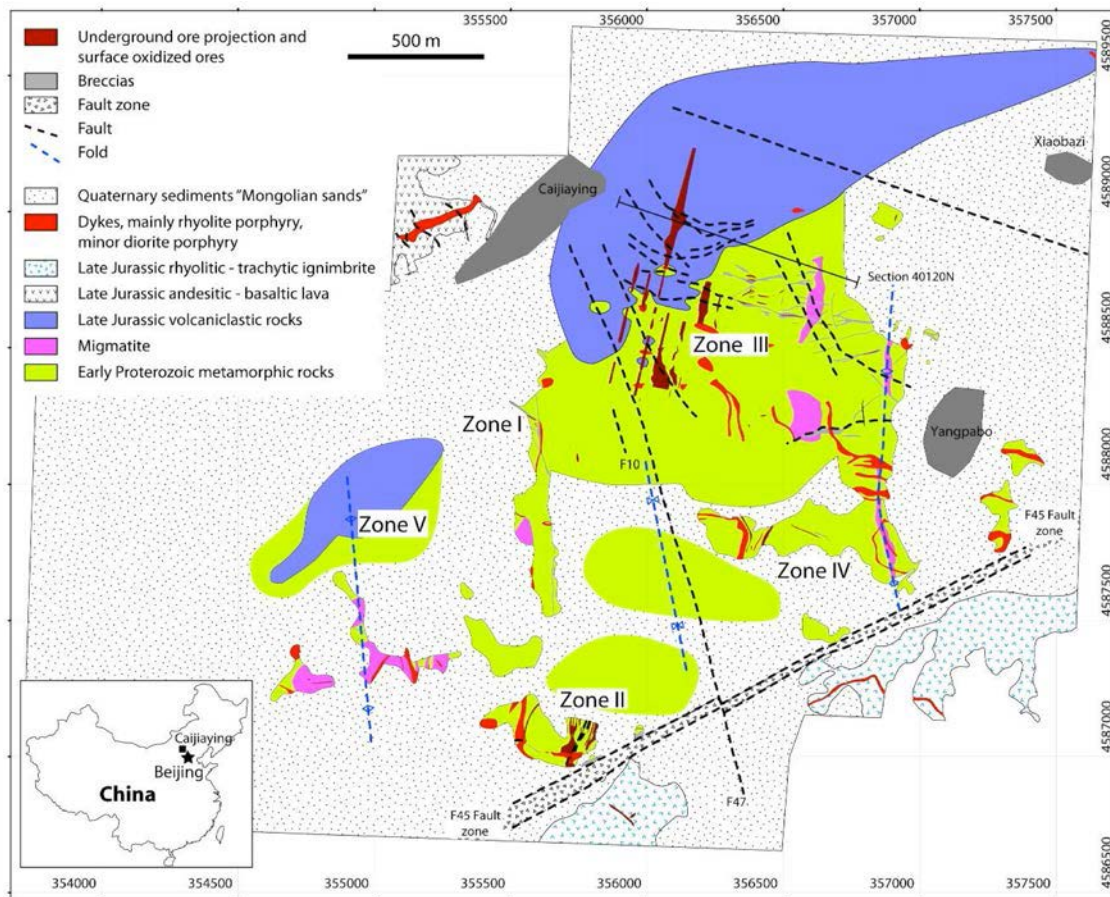
Figure 2. Bed rock geology of the Caijiaying deposit. This map incorporates the Griffin (2005) map and information from all the drill holes penetrating the Quaternary sediments available in 2007. The map grid is UTM_WGS84.

patches consisting of Bi-mineral and electrum also seem to increase in size with depth.

Systematic zoning occurs around the orebodies. The Caijiaying deposit is surrounded by an illite halo ~ 3 x 2 km in size. Within the halo pyrite occurs hundreds of meters away from orebodies. Siderite starts to appear ~200 m from the orebodies, and the intensity increases towards ore. A few tens of meters from the orebodies, the white mica Al-OH absorption peak in SWIR spectra shifts to lower wavelength position (≤2198nm). A similar trend has been reported in several deposits (e.g., Chang and Yang, 2012, and references therein). The illite crystallinity decreases to ~ 0.8-1.1, indicating a lower temperature overprint. The chlorite Fe-OH absorption peak shifts to higher wavelengths (≥ 2254nm), indicating higher Fe content (e.g., Thompson et al, 2009). Pyroxene in Zone III contains up to 12 mol% of johannsenite (Jo). Towards the south the Jo content decreases to mostly <5 mol%.

3 Fluid inclusions

Primary fluid inclusions in pyroxene have liquid-dominant L+V phases. They homogenize to liquid at 328-378°C, with the mode ranging from 360-380°C. The salinities range from 22-23 wt% NaCleq, calculated using the equation of Bodnar (1993). Primary fluid inclusions in quartz intergrown with sphalerite in the cement of breccia ores have vapour bubbles in aqueous liquids. The homogenization temperatures (Th) range

from 171-263°C, with the mode at 200-220°C. The salinities range from 0.4 to7.8 wt% NaCleq, mostly in the 4-6 wt% NaCleq range. The quartz also contains secondary L+V fluid inclusions with Th ranging from 139 to197°C. The salinities range from 3.8 to 5.5 wt% NaCleq, similar to the primary ones. Primary fluid inclusions were also found in epithermal quartz cementing clasts of fine-grained quartz on the surface to the north of F45. They are all liquid-dominant L+V ones, with Th from 176 to 257°C, mostly in the 180-200°C range. The temperatures are only slightly lower than the quartz intergrown with sphalerite, but the salinity, 0-1.2 wt%, is significantly lower.

Secondary fluid inclusions in sphalerite occur in arrays cutting the compositional growth bands. There are coexisting liquid-dominant fluids inclusions and vapour-dominant ones in the arrays, indicating the fluids were boiling when trapped. The liquid-dominant fluid inclusions have Th 139-182°C, mostly in the 140-160°C range. The salinity has a larger range compared to fluid inclusions in coexisting quartz, 5-18 wt% NaCleq, and falls into two groups, 5-6 wt% NaCleq and 17-18 wt% NaCleq. The sphalerite must have formed before the secondary fluid inclusions, therefore > ~190°C.

4 Summary, discussion, and conclusions

Formation of the deposit started with pyroxene replacing marble and calcareous rocks, caused by saline fluids (22-23 wt% NaCleq) at 360-380°C. At the same

time high crystallinity sericite replaced silicate rocks. Pyroxene was then replaced by amphibole and ilvaite, followed by hematite, magnetite, then quartz-sphalerite at 200-220°C (4-6 wt% NaCleq), then siderite-chlorite-pyrite-marcasite-arsenopyrite-galena, and finally calcite-chlorite-electrum - native Bi - bismuthinite- Pb-Bi sulfosalt. The breccias may have been caused by the dissolution of marble lenses and subsequent collapse. In breccia ores only the later retrograde assemblage after hematite was developed. The mineralisation assemblage in banded/folded ores have not been recrystallized or deformed, which indicates that they formed after metamorphism and deformation. The assemblage is also identical to the late retrograde alteration assemblage of the skarns, similar to the breccia ores. In summary, the breccia ores and the banded/folding ores are all part of the skarn system.

The quartz in the epithermal breccia on the surface N of and close to F45 formed at ~180-200°C, slightly lower than quartz accompanying sphalerite but from dilute fluids with ~0-1.2 wt% NaCleq salinity, indicating that the fluids may be different from the Zn mineralising fluids. Close to F45 epithermal botryoidal quartz-carbonate cements sphalerite ores, indicating that the epithermal features may be later than the skarns.

The Caijiaying skarn is similar to many distal skarns (Meinert et al., 2005, and references therein), with low formation temperatures, some Mn in pyroxene, and a high pyroxene/garnet ratio; indeed, no garnet has been found in Caijiaying. It is different from many other skarns (Chang and Meinert, 2004, 2008; Meinert et al., 2005) in that the host is mostly silicate rocks; marble lenses are small in volume. Consequently the amount of prograde skarn minerals is relatively small. The same fluids forming prograde skarns altered the silicates wall rocks and caused extensive illite alteration.

The whole system is Fe-rich, indicated by the abundance of Fe-rich pyroxene, amphibole, ilvaite, chlorite, and siderite. Marble cannot provide the required amount of Fe and the metamorphic silicate rocks are also unlikely to be able to supply so much Fe. It is speculated that the Fe may have been supplied by the mineralizing fluids.

The skarn is in general reduced, with the presence of pyrrhotite and Fe mostly occurring as Fe^{2+} in most minerals, although some oxidizing conditions may have locally occurred at the early retrograde stage as indicated by the presence of minor specular hematite. The fluids continued to become more reducing afterwards with the formation of magnetite, then sulfides. The overall reducing conditions may be related to the graphite in the metamorphic wall rocks.

The mineralisation dominantly occurs in the Proterozoic metamorphic rocks, with very little in the overlying volcanic rocks. This is probably related to the marble. Zinc is typically transported as Zn-Cl⁻ complexes. Deposition of sphalerite will cause an increase in acidity of the fluids. Marble can buffer the acidity and facilitate the Zn precipitation. It is more difficult for silicate volcanic rocks to buffer acidity, which suppresses Zn deposition.

Gold at Caijiaying has a close association with Bi minerals, indicating the possibility of Au being collected and transported by Bi melt at some stage. Similar mechanism has been proposed in other Au skarns (e.g., Meinert et al., 2005; Kim et al., 2012). Pure Bi has a meting temperature of only 271°C and the eutectic temperature of the Bi-Bi₂S₃ join is 265°C (van Hook, 1960). Molten Bi is able to incorporate as much as 37 mol% Au (Okamoto and Massalski, 1983). The droplets of the Au-Bi-rich melts and/or particles of electrum and Bi minerals could have been carried up by attaching to vapour bubbles in later boiling fluids, suggested by fluid inclusions in calcite and secondary fluid inclusions in sphalerite. This explains the clustered occurrence of electrum, the delicate moulding textures, the curved boundaries between electrum and Bi-rich minerals, and the metal association.

Pyroxene in Zone III contains lower Mn towards the south, indicating the causative intrusion may be located to the S of Zone III (Meinert, 1997).

Acknowledgements

References

Chang, Z., and Meinert, L.D., 2004, The magmatic-hydrothermal transition - evidence from quartz phenocryst textures and endoskarn abundance in Cu-Zn skarns at the Empire mine, Idaho, USA: Chemical Geology, v.210, p.149-171.

Chang, Z., and Meinert, L.D., 2008, The Empire Cu-Zn Mine, Idaho, USA: Exploration implications of unusual skarn features related to high fluorine activity: Economic Geology, v. 103, p. 909-938.

Chang, Z., and Yang, Z., 2012, Evaluation of inter-instrument variations among Short Wavelength Infra-Red (SWIR) devices: Economic Geology, v. 107, p. 1479-1488.

Hedenquist, J.W., Arribas, A., and Gonzalez-Urien, E., 2000, Exploration for epithermal gold deposits: Reviews in Economic Geology, v. 13, p. 245–277.

Kim, E-J., Park, M-E., and White, N.C., Skarn gold mineralisation at the Geodo Mine, South Korea: Economic Geology, v. 107, p. 537-551.

Meinert, L.D., 1997, Application of skarn deposit zonation models to mineral exploration: Exploration and Mining Geology, v. 6, p. 185-208.

Meinert, L.D., Dipple, G.M., and Nicolescu, S., 2005, World skarn deposits: Economic Geology 100th Anniversary Volume, p. 299-336.

Okamoto, H., Massalski, T.B., 1983, Au–Bi (gold–bismuth): In: Massalski, T.B., et al. (eds) Binary alloy phase diagrams, vol 1: Ac–Au to Fe–Rh. Ohio, ASM International, Materials Park, Ohio, p. 238–240.

Simmons, S.F., White, N.C., and John, D.A., 2005, Geological characteristics of epithermal precious and base metal deposits: Economic Geology 100th Anniversary Volume, p. 485-522.

Thompson, A., Scott, K., Huntington, J., and Yang, K., 2009, Mapping mineralogy with reflectance spectroscopy: Examples from volcanogenic massive sulfide deposits: Reviews in Economic Geology, v. 16, p. 25-40.

van Hook, H.J., 1960, The ternary system Ag₂S-Bi₂S₃-PbS: Economic Geology, v. 55, p. 759-788.

White, N.C., and Hedenquist, J.W., 1990, Epithermal environments and styles of mineralization: Variations and their causes, and guidelines for exploration: Journal of Geochemical Exploration, v. 36, p. 445–474.

Sulfide distribution and its relation to different types of skarn alteration at the Tapuli deposit, northern Sweden

Nikola Denisová
Luleå University of Technology

Åsa Allan
Northland Resources AB

Olof Martinsson
Luleå University of Technology

Abstract. The Tapuli deposit is a skarn iron ore located in the Pajala municipality in Northern Sweden. It is situated at the margin of the Karelian craton, at the stratigraphic contact between Karelian and Svecofennian rocks. The ore forms stratabound lenses concordant with the metasedimentary sequences and dips 45 – 60 degrees towards NW. Footwall rocks are dolomitic marbles, phyllites and graphitic phyllites; the hanging wall comprises phyllites and quartzites. Mafic dykes and sills crosscut the stratigraphic succession. Magnetite is the only ore mineral. The skarn minerals are serpentine, diopside, tremolite and actinolite. The skarn altered rocks show a zonation with serpentine skarn closest to or as part of the ore, thereafter, tremolite-diopside skarn and, finally, actinolite skarn closest to the phyllites and quartzites in the hanging wall. Sulfides occur in minor amounts, but their content generally increases with proximity to the footwall rocks. The dolomitic marble was the precursor of the serpentine and tremolite-diopside skarn. Immobile element data suggests that mafic dykes and sills were the precursors of the actinolite skarn. Possible controls of the sulfide distribution are the presence of sulfide-bearing source rocks (dolomitic marble, graphitic phyllite) and remobilization of sulfides during the intrusion of mafic dykes.

Keywords. Iron ore, magnetite, skarn, alteration, sulfides.

1 Introduction

The Tapuli skarn iron ore is located in the Pajala municipality (Fig. 1), 3 km north of the Kaunisvaara village. The deposit has been developed into a mine by Northland Resources AB and production started in November 2012. The calculated ore reserve for Tapuli is 94.5 Mt of iron ore at 26.31 % Fe (Baker et al. 2011). The deposit was discovered by magnetic measurements in 1918 by V. Tanner. The Tapuli deposit occurs along the stratigraphic contact between Karelian (2.44 – 2.0 Ga) and Svecofennian (1.96 – 1.75 Ga) rocks. There are other skarn deposits in the same stratigraphic position along the strike of one of the faults of the Pajala Shear Zone, from N to S: Palotieva, Tapuli, Stora, Östra and Södra Sahavaara. Tapuli has the lowest sulfur content of all of these deposits (0.18 wt. % S, compared to 0.5 – 2.5 wt. % S for the other deposits; Lindroos, 1974). The sulfide minerals at Tapuli are unevenly distributed and the control on the sulfide distribution is unknown. The aim of this study is to gain insight into the processes that

formed and controlled the distribution of the sulfides in the Tapuli deposit.
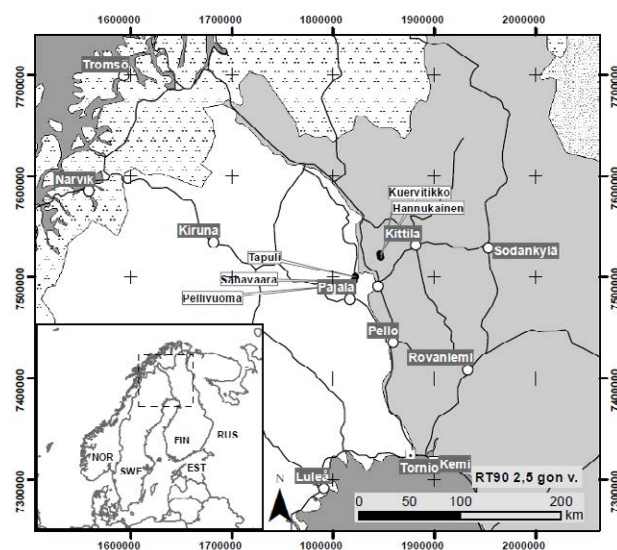
Figure 1. Location of the Tapuli deposit.

2 Methods

Based on drill core logging, 92 hand samples were collected, of which 28 samples were prepared and sent to Vancouver Petrographics for preparation of polished thin sections. Twenty-four polished thin sections, provided by Northland Resources AB from previous studies of the deposit, were also used in this study. Polished thin sections were studied using a Nikon Eclipse E600 polarization microscope.

Another five samples were prepared and sent to ALS Chemex in Öjebyn, Sweden for whole rock geochemistry analysis using ICP-MS, ICP-AES, Leco and WST-SEQ instruments.

3 Regional Geology

3.1 The bedrock of Northern Norrbotten

The bedrock of Northern Norrbotten is heterogeneous and comprises rocks of various age, ranging from Archean supracrustal rocks (2.7 Ga), intrusions and supracrustal rocks of Karelian age (2.44 – 2.0 Ga) that indicate a changing rift setting, to rocks of the

Svecofennian orogeny (1.96 – 1.75 Ga; Bergman et al, 2001). Karelian rocks of the Greenstone Group consist of metabasalts, graphitic metaargillites, crystalline carbonate rocks and ultramafic rocks. These rocks are comfortably overlain by Svecofennian supracrustal rocks (Bergman et al. 2001). The area has undergone several phases of ductile and brittle deformation (Bergman et al. 2001).

The Pajala area is located on the margin of the Karelian craton adjacent to the westernmost fault of the Pajala Shear Zone (PSZ; Baker et al. 2011). The PSZ is a zone of ductile deformation at least 10 km wide and 150 km long crossing the border into Finland (Bergman et al. 2001).

3.2 Iron deposits in Northern Norrbotten

Northern Norrbotten hosts various types of Fe deposits, including apatite iron ores (e.g. the Kirunavaara and Malmberget deposits), skarn-rich iron formations (e.g. the Tapuli and Sahavaara deposits), IOCG deposits (e.g. the Tjårrojåkka deposit) and banded iron formations. The skarn-rich deposits are stratabound in character and are associated with tuffites, black schists and dolomites. Some deposits grade laterally into banded iron formations (e.g. deposits in the Pajala and Masugnsbyn areas; Bergman et al. 2001).

The main ore mineral in the skarn deposits is magnetite. The skarn minerals are most commonly serpentine, diopside and tremolite. Iron sulfides (pyrrhotite and pyrite) occur disseminated and in veinlets (Bergman et al. 2001). Copper is sometimes slightly enriched in the skarn deposits and occurs as chalcopyrite (Bergman et al. 2001).

4 The Tapuli deposit

4.1 Geology

The Tapuli deposit is situated on the NW limb of a major NE trending anticline on the westernmost part of the PSZ (Baker et al. 2011).

The rocks in the stratigraphic footwall of the mineralization are dolomitic marble, phyllite and graphitic phyllite, while the hanging wall comprises phyllite and quartzite (Fig. 2; Baker et al. 2011). Mafic dykes and sills that cross-cut the sequence, are commonly intensely altered and are only a few meters thick, although some can be as thick as 15 meters (Lindroos, 1972).

The ore occurs as a set of stratabound lenses that are concordant with the metasedimentary sequences and dip between 45 and 60 degrees, mainly towards the NW and WNW. The deposit has been drilled to a depth of 300 meters and remains open down dip (Baker et al. 2011).

Phyllite and graphitic phyllite are the stratigraphically lowermost members of the footwall sequence. The phyllite is thinly bedded, consisting of biotite, quartz, muscovite and feldspars, with occasional amphibole and scapolite grains (Lindroos, 1974). The graphitic phyllite usually overlies the phyllite and the boundaries are commonly gradual. The graphitic phyllite has high sulfide content. Sulfides occur both as disseminated fine grains, and as larger grains together with quartz and amphibole. The main sulfides are pyrrhotite and pyrite with minor chalcopyrite. The sulfur content of the graphitic phyllite varies between 2 and 6 wt. % S (Lindroos, 1972).

A dolomitic marble unit, in places more than 100 meters thick, occurs immediately below the ore-hosting skarn layers. The contact between the skarn and the marble is gradual. The dolomitic marble locally contains bands of skarn, most commonly disseminated serpentine grains. Occasionally, up to 4 meters thick, irregular bands of magnetite mineralization occur. Up to 2.5 meters wide massive sulfide veins (mainly pyrite and pyrrhotite) occur sporadically. The dolomite contains sulfide veinlets and fine-grained disseminated sulfides, mainly pyrrhotite and pyrite, only rarely chalcopyrite. The contact between the skarn and the hanging wall phyllites is also gradual, usually over a few meters.

The mafic dykes and sills are commonly pervasively altered, usually to actinolite, biotite, chlorite or scapolite. The contacts with surrounding rocks are commonly sharp. In the metasedimentary rocks, the rock surrounding the dykes is albitized.
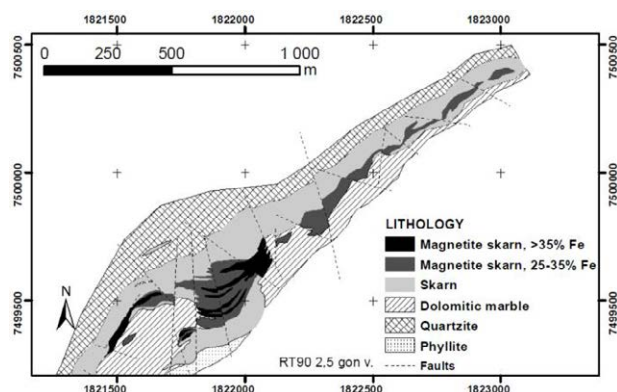
Figure 2. Geology of the Tapuli deposit.

4.2 Skarn zonation

The skarn altered rocks show a zonation with serpentine skarn closest to or as part of the ore, thereafter, tremolite-diopside skarn and, finally, actinolite skarn closest to the phyllites and quartzites in the hanging wall. The main gangue minerals are serpentine, clinopyroxene (diopside), actinolite and tremolite. Minor gangue minerals are biotite, chlorite and calcite. Calcite occurs as thin veins and veinlets.

Serpentine skarn ranges from yellow green to black in color and contains, apart from magnetite, veinlets of talc and chrysotile, as well as patches of chlorite and biotite.

The pale green clinopyroxene skarn contains variable amounts of tremolite (Lindroos, 1972). The clinopyroxene skarn ranges in grain size from very fine to very coarse and contains locally bands and blebs of actinolite, chlorite or serpentine.

The actinolite skarn is dark green, fine- to coarse-grained, and locally contains bands of diopside-tremolite skarn, chlorite, biotite or serpentine.

The mineralized lenses comprise skarn with variable

amount of magnetite.

Although, the different skarn types show a general zonation, they overlap in areas where banded skarn occurs or where there is a transition from one skarn type to another.

4.3 Ore description

The only ore mineral is magnetite and it occurs in irregular bands or veins of varying thickness in the skarn or as ore breccia. The grain size varies from 0.1 to 1 mm (Lindroos, 1972). According to Lindroos (1972), recrystallized sections are much coarser. The phosphorous content is low, on average 0.07 wt. % P (Lindroos, 1971). The ore is divided into two types based on sulfur content (Baker et al. 2011): low sulfur ore (< 0.5 wt. % S) and high sulfur ore (> 0.5 wt. % S). The high S ore occurs in the deeper parts of the stratigraphy, closer to the footwall contact. The average sulfur content of the deposit is 0.18 wt. % S (Lindroos, 1972). The main sulfides are pyrite and pyrrhotite, with minor chalcopyrite, occurring in thin veins and veinlets, commonly with calcite or as disseminated grains within the skarn and ore.

5 Sulfide distribution

The sulfides are unevenly distributed in the deposit but are most abundant in the southern part of the deposit and closer to the footwall contact. Most sulfides occur in veins and veinlets, commonly with calcite. In the serpentine skarn, sulfides occur in serpentine-calcite-talc veins and veinlets, or as disseminations. Sulfides also occur disseminated within the different skarn types. Closer to the hanging wall, pyrite in association with medium-grained magnetite and epidote occurs in carbonate veins. The sulfide content is higher in proximity to the graphitic phyllite.

In thin section, sulfides are observed to postdate most silicates, carbonates, and angular, fractured magnetite grains, and commonly infill the fractures in the grains, or the spaces in between them (Fig 3 and Fig 4). In some polished thin sections, the sulfides are intergrown with euhedral grains of actinolite (Fig 5).

The earliest sulfide is most commonly chalcopyrite, but it occurs only in minor quantities. Other Cu minerals (e.g. digenite) occur rarely with chalcopyrite. Both pyrite and pyrrhotite are abundant, as large grains or as infill. Pyrite occurs abundantly, either early with chalcopyrite (Fig. 3), or after pyrrhotite formation in euhedral crystals. Pyrrhotite is the most abundant sulfide and often the paragenetically youngest.
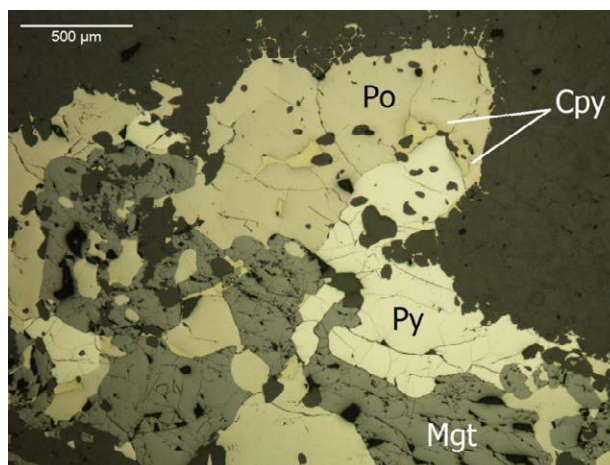
Figure 3. Sulfides and magnetite in reflected light (Cpy – chalcopyrite, Mgt – magnetite, Po – pyrrhotite, Py – pyrite).
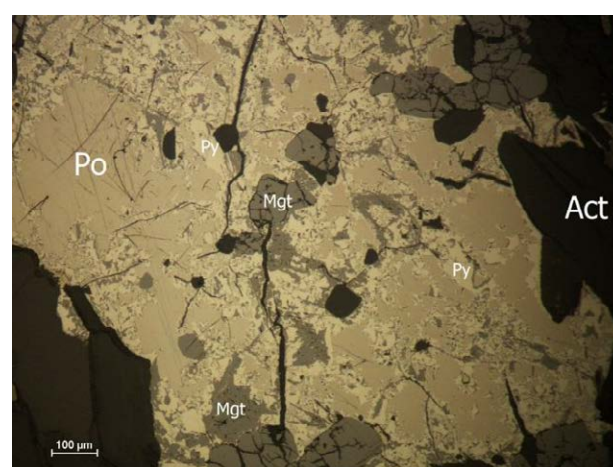
Figure 4. Sulfide veinlet in actinolite-tremolite skarn, reflected light (Act – actinolite, Mgt – magnetite, Po – pyrrhotite, Py – pyrite).
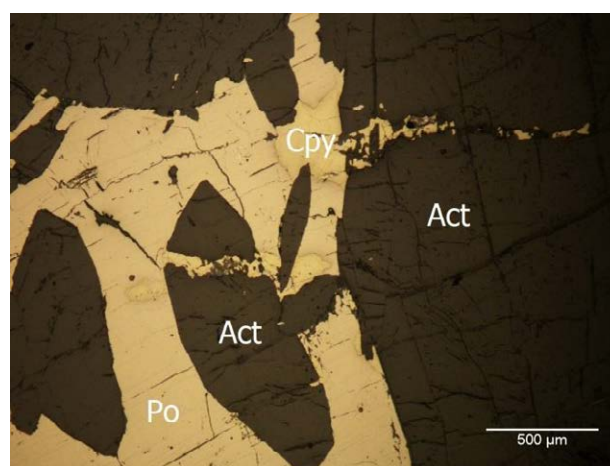
Figure 5. Pyrrhotite (Po) intergrown with actinolite (Act) crystals, younger chalcopyrite (Cpy), reflected light.

6 Skarn precursors

Dolomitic marble is considered to be the precursor of the serpentine, diopside, tremolite skarns and the mineralization (Baker et al. 2011). In drill core, dark

green actinolite skarn commonly shows sharp contacts towards other skarn types and is more fine-grained and homogeneous than the surrounding skarn types. The dark green actinolite skarn forms up to 10 meters thick layers, but the average thickness is between 2 and 3 meters. It mostly occurs close to the contact to the hanging wall rocks, but also deeper in the stratigraphy. Possibly, the precursors of the dark green actinolite skarn were mafic dykes or sills that intruded the dolomite, rather than the dolomite itself. The chemical analysis of two samples of actinolite skarn with these characteristics support this (Table 1). When comparing the immobile elements ratios, the values of the dark green actinolite skarn resemble much more the values of the altered mafic dyke than the values of serpentine-magnetite skarn, which formed by alteration of dolomite.

Table 1 Representative whole-rock lithogeochemistry of different skarn types from the Tapuli deposit

Sample no.	07003 -S1	07003 -S2	07006 -S2	08MET 26-S7	08MET 26-S8
SiO_2 (%)	45	45.1	49.9	19.1	23
Al_2O_3 (%)	9.92	9.83	16.6	0.9	0.46
Fe_2O_3 (%)	9.75	8.72	5.8	45.6	37.8
CaO (%)	12.95	16.65	4.96	0.21	0.19
MgO (%)	16.4	16	7.67	23.2	28
Na_2O (%)	2.16	2.24	2.4	0.05	0.02
K_2O (%)	1.1	0.4	5.86	0.22	0.14
Cr_2O_3 (%)	0.03	0.03	0.01	<0.01	<0.01
TiO_2 (%)	0.66	0.67	1.41	0.2	0.07
MnO (%)	0.08	0.06	0.06	0.09	0.07
P_2O_5 (%)	0.16	0.18	1.36	0.15	0.13
S (%)	0.02	<0.01	0.24	0.06	0.14
Ba (ppm)	104	71.6	>10000	54.8	31.3
Ce (ppm)	37.8	39	425	5.2	5.1
Nb (ppm)	6.7	7.4	12.9	0.2	0.2
Sr (ppm)	58.5	42.9	1365	4.3	3.8
Th (ppm)	2.16	2.79	10.55	0.38	0.41
Y (ppm)	24	25.7	26	0.5	<0.5
Zr (ppm)	150	159	335	9	5
$(10000*Zr)$ $/TiO_2$	227.27	237.31	237.59	45.00	71.43
$(10000*Zr)$ $/Al_2O_3$	15.12	16.17	20.18	10.00	10.87
Al_2O_3/TiO_2	15.03	14.67	11.77	4.50	6.57

Samples 07003-S1 and S2 are actinolite skarn with varying amounts of diopside, 07006-S2 is a mafic dyke, 08MET26-S7 and S8 are magnetite-serpentine skarn.

7 Controls of sulfide deposition

The sulfides often show a close spatial correlation with dark green actinolite skarn-altered mafic dykes and generally occur in veins or veinlets together with calcite, or disseminated within the actinolite skarn. The veinlets, with or without calcite, crosscut the skarn-altered mafic dykes. The mafic dykes could have acted as a source of

heat for local fluid circulation, remobilizing pre-existing sulfides. Another possibility is that the mafic dykes and faults acted as channel-ways for later fluids, which were not associated with the main ore-forming event, altering the mafic dykes and depositing sulfides.

8 Conclusions

There are at least two possible controls of the sulfide distribution at Tapuli, possibly interacting together: the proximity to sulfide-bearing footwall rocks (dolomitic marble and graphitic phyllite) and the presence of mafic dykes. At Tapuli, the sulfur content is highest close to the footwall dolomite and graphitic phyllite. These lithologies could possibly have acted as a source for sulfur during later deformation or remobilization events, as most of the sulfides seem to have formed after skarn alteration and the main ore-forming event. Mafic dykes could have contributed as a heat source for local remobilization. Another possibility is that the mafic dykes functioned as channel-ways for later fluids that are not associated with the main magnetite-forming event. These fluids could have altered the mafic dykes to actinolite skarn and transported the remobilized sulfur.

Acknowledgments

References

Baker H, Pattison D, Reardon C (2011) Technical review of the Kaunisvaara iron project, Sweden. June 2011. Cardiff: SRK Consulting (UK) Ltd., 178 p.

Bergman S, Kübler, L & Martinsson O (2001) Description of regional geological and geophysical maps of northern Norrbotten county (east of the Caledonian orogen). SGU, Ba 56, 110 p.

Lindroos H, Nylund B, Johansson K (1972) Tapuli and Palotieva iron ore occurrence. SGU, unpublished report, series C, Avhandlingar och uppsatser, 695, Årsbok / SGU, 68:2, 18 p.

Lindroos H (1974) The stratigraphy of the Kaunisvaara iron ore district, Northern Sweden. Stockholm: SGU, 71 p.

Smältarmossen – a 1.89 Ga contact metasomatic iron skarn deposit in the cradle of skarn, Bergslagen, Sweden

Nils F Jansson
Boliden Mines, Exploration Department, 936 81 Boliden, Sweden.

Rodney L Allen
Division of Geosciences and Environmental Engineering, Luleå University of Technology, 971 87 Luleå, Sweden
Boliden Mines, Exploration Department, 776 98 Garpenberg, Sweden

Abstract. The Bergslagen region in southern Sweden hosts thousands of iron oxide deposits, including banded iron formations, apatite iron ores and enigmatic magnetite deposits hosted by former limestone and associated with skarn. The latter class of deposits include the type-locality of skarn (Persberg), as first defined by Alfred Elis Törnebohm in 1875. During the last 100 years, these deposits have been regarded either as contact metasomatic iron skarn deposits, metamorphosed and/or metasomatized calcareous iron formations, or metamorphosed carbonate replacement deposits. The general view has largely shifted in favour of the second alternative. Smältarmossen belongs to the same class of Fe oxide deposits in Bergslagen as Persberg; the class known as Mn-poor Fe oxide deposits in marble/skarn. Approximately 3.7 Mt of massive magnetite was mined from a c. 50 m calcic skarn zone at the contact between meta-rhyolite and stratigraphically overlying marble. A metamorphosed dacite porphyry intrusion in the footwall has numerous apophyses that extend into the mineralized zone. A detailed study of geological setting, alteration textures, mineralogy and lithogeochemistry indicate that magnetite formed by replacement of limestone whereas the skarns replaced dacite and rhyolite. The evidence is most compatible with a syn-volcanic, contact metasomatic origin for the deposit, and its associated skarn.

Keywords. Bergslagen, Smältarmossen, Garpenberg, Skarn, Magnetite

1 Introduction

The Bergslagen region of the southern Fennoscandian shield hosts the type-locality of skarn, as first published scientifically by Törnebohm (1875). Despite this, skarn-hosted base metal and iron oxide deposits in Bergslagen are somewhat unusual when compared with 'normal' skarn deposits in the modern sense of the word (e.g. Meinert et al. 2005). Among other things, the deposits occur in supracrustal successions that were multiply deformed, medium-grade metamorphosed and intruded during the 1.9-1.8 Ga Svecokarelian orogeny (Stephens et al. 2009), and the deposits themselves record significant superimposed ductile deformation and regional metamorphism (e.g. Allen et al. 2003, Jansson 2011). The host rocks were originally dominantly submarine felsic volcanic rocks with subordinate limestone interbeds, formed in a continental back-arc environment at c. 1.90-1.89 Ga (Allen et al. 1996). Important to the skarn discussion is the fact that this

environment was also favourable for the formation of stratiform iron oxide and sulphide deposits, showing evidence in favour of a syngenetic-exhalative origin (e.g. Allen et al. 1996 and references therein). Examples include banded iron formations (e.g. Stråssa), Mn-Fe oxide deposits (e.g. Långban) and massive Zn-Pb-Ag-(Cu) sulphide deposits with similarities to SEDEX, BHT and VHMS-type deposits (e.g. Zinkgruvan).

Historically, the discussion on skarn genesis in Bergslagen has largely focused on whether the deposits are contact metasomatic, or if skarn minerals formed during Svecokarelian metamorphism and/or alteration of syngenetic-exhalative deposits. Indeed, skarn minerals such as garnet, clinopyroxene, amphibole and locally vesuvianite commonly form distinct interbeds or occur as gangue minerals in many interpreted syngenetic-exhalative deposits (e.g. Geijer and Magnusson 1944, Hedström et al. 1989, Jansson and Allen 2011b). In these cases, it seems logical that skarn minerals formed during metamorphism and/or metasomatism of seafloor deposits, i.e. at interfaces between chemically distinct lithologies or laminae in laminated facies. However, many of the several thousand iron oxide and sulphide deposits in Bergslagen, including some of the most economically significant, conform poorly to such a model. The 100 Mt Garpenberg Zn-Pb-Ag-(Cu-Au) deposits (Fig. 1), for example, formed by replacement of a limestone horizon, which hosted no prior syngenetic-exhalative deposits (Allen et al. 2003). Mineralization at Garpenberg is furthermore intimately associated with skarn minerals, and can be linked at least temporally to a significant, dominantly dacitic intrusive event, directly following a large caldera-forming volcanic eruption (Allen et al. 2003).

Similarly, many Fe oxide deposits lack evidence of a syngenetic-exhalative origin when put under scrutiny. One such deposit is the 3.7 Mt Smältarmossen iron deposit (mined 1873-1979), which is hosted by the same stratigraphic interval that hosts the Garpenberg sulphide deposits (Fig. 1). This contribution summarizes the characteristics of this deposit, and discusses its implication for the origin of Fe oxide deposits in Bergslagen.

2 Methodology

The Smältarmossen mine is inaccessible and very few

outcrops occur at the surface. Very detailed mine plans were however produced during its operation. By studying these and combining them with geological, mineralogical and lithogeochemical data obtained from new drill core logging and sampling, geological cross-sections and plans of the deposit have been produced (e.g. Fig. 2).

Analysis of major and certain trace elements in 65 samples were performed by Acme Laboratories Ltd. in Canada by inductively coupled plasma (ICP)-emission spectroscopy after lithium borate fusion and nitric acid digestion. Rare earth elements (REE) and refractory trace elements were analyzed by ICP-mass spectrometry following similar sample preparation procedures. Total carbon and sulfur were determined by Leco Furnace.

Wavelength dispersive X-ray spectroscopy electron microprobe analyses were carried out with a Jeol JXA8200 Superprobe at the University of Copenhagen, Denmark, at operating conditions of 15–20 kV acceleration voltage and 10–15 nA beam current. Measured peaks were calibrated against natural and synthetic standards.
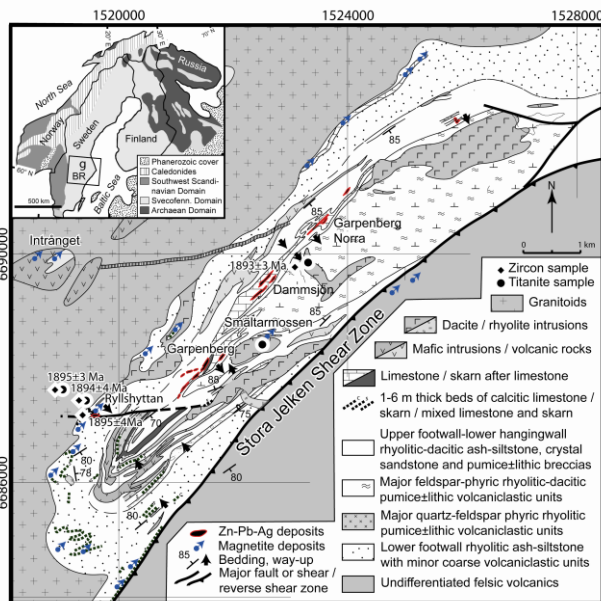
Figure 1. Regional geological map of the Garpenberg area, from Jansson and Allen (2011c). Outlined names denote mines and ore fields. Radiometric ages (U-Pb zircon) are from Jansson and Allen (2011a). Grid is Swedish National Grid RT90. Inset shows position of Bergslagen ('BR') and Garpenberg ('g'in the Fennoscandian shield).

3 Results

3.1 Geological setting

Smältarmossen occurs on the SE limb of the doubly plunging Garpenberg syncline, which is bordered to the SE by a large reverse shear zone (Fig. 1). Both structures have been correlated with regional F_2 folds as defined in Stephens et al. (2009), since they deformed an earlier, bedding-parallel S_1 foliation. The marble host, which also hosts the Garpenberg sulphide deposits, is a pure calcitic marble devoid of mineralization distal from the

mineral deposits. Allen et al. (2003) interpreted it as a metamorphosed microbial stromatolitic limestone.

The mined magnetite at Smältarmossen occurred as tabular, E-W striking bodies with steep but variable dips ranging from N to S. They were hosted by a c. 50 m zone of calcic skarn, at the boundary between rhyolitic metavolcanic rocks (original stratigraphic footwall) and calcite marble. Locally, the rhyolitic rocks have been completely pushed aside by a metamorphosed feldspar-porphyritc dacite intrusion, whose marginal phase is a complex network of porphyry apophyses that extend into the ore zone and chaotically enclose skarn, metavolcanic rock and massive magnetite (Fig. 2). The porphyry locally displays gradational contacts towards skarn and is, as will be shown below, itself altered to skarn. The upper boundary between the calcic skarn zone and calcite marble is knife-sharp. The deposit records similar tectonic fabrics as other rock bodies in the Garpenberg area, and is consequently inferred to predate regional metamorphism.

3.2 Alteration

Most skarns at Smältarmossen lack textural evidence of their alteration precursors. However, Jansson and Allen (2013) showed that the skarns have similar ratios between the immobile elements Zr, Al_2O_3 and TiO_2 as the local felsic rocks, including the dacite porphyry. It was concluded that most if not all skarns formed by replacement of rhyolitic volcanic rocks and the dacite porphyry. This is furthermore suggested by observations of endoskarns of epidote-calcic clinoamphibole and garnet-clinopyroxene that mimic the feldspar-porphyritic texture of the dacite porphyry, as well as the generally high content of aluminous skarn minerals such as epidote (Fe/Fe+Al = 0.26-0.32) and grossularitic garnet in the skarn zone. A gradation from skarn-poor rhyolite, to skarn-veined rhyolite, to massive skarn with relict volcanic textures is furthermore observed from the footwall to the ore zone. In contrast, massive magnetite has similar low immobile element contents as the limestone. Consequently, most magnetite is interpreted as formed by replacement of roof pendants of limestone.

Besides skarn alteration, Smältarmossen meta-rhyolite and meta-dacite display anomalously high Na vs. K content, interpreted as resulting from Na alteration by fluids which were heated in the thermal aureole of the dacite porphyry. Skarn veins cross-cut the Na-altered rocks.

Compared to other skarns in the Garpenberg area, Smältarmossen skarns are anomalously rich in LREE and anomalously poor in Mn. The former most likely reflect the presence of allanite, which is relatively common in the Smältarmossen skarns.

3.3 Skarn zonation

The Smältarmossen skarns show mineralogical zonation from garnet- and epidote-dominated skarns in the stratigraphically lower part of the deposit, to clinopyroxene–andradite skarns after rhyolite and dacite
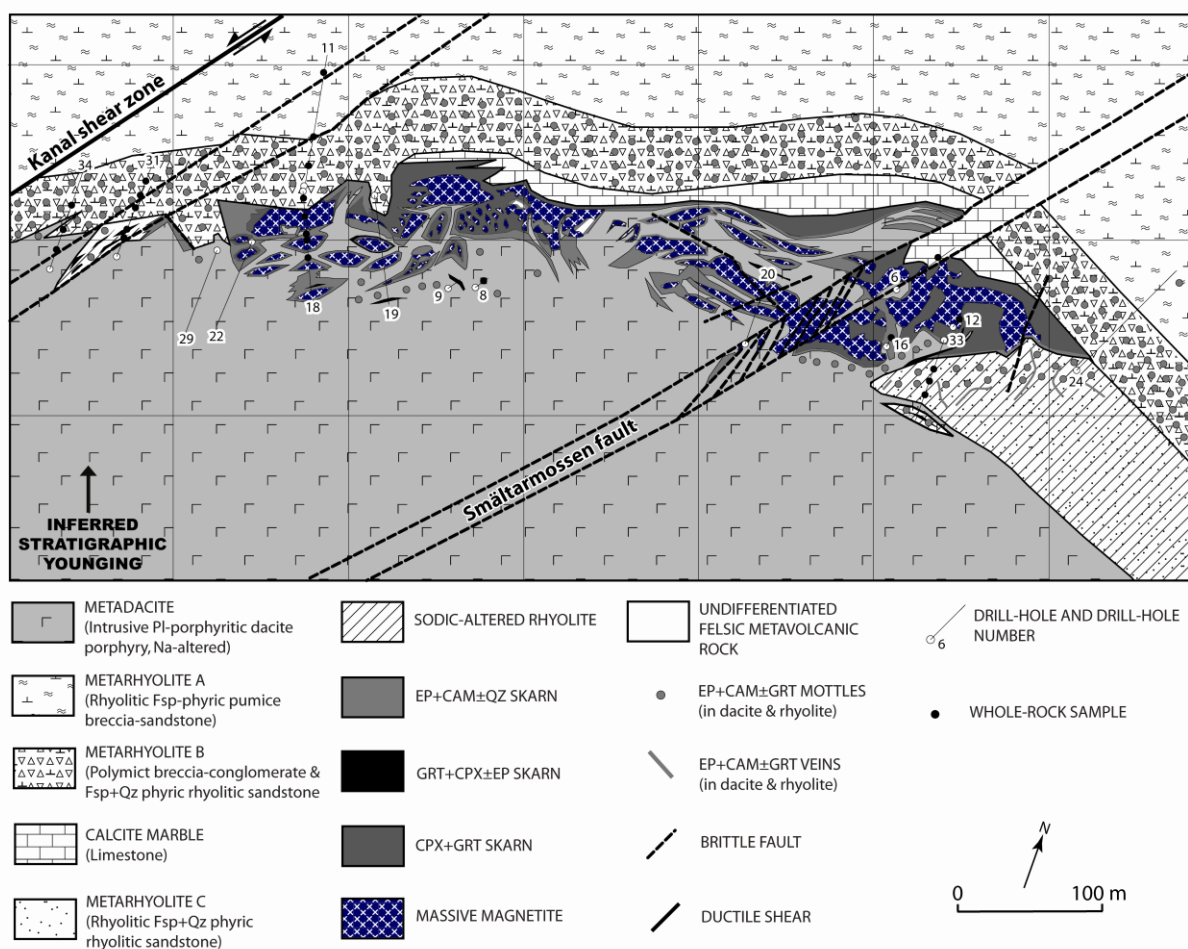
Figure 2. Map of the 223 m level of the Smältarmossen mine, based on old mine plans, new core logging and internal Boliden Mineral data. Abbreviations: CAM: calcic clinoamphibole, EP: epidote, FSP: feldspar, GRT: garnet, PL: plagioclase, QZ: quartz. Grid is local mine grid. Modified after Jansson and Allen (2013)

alternating with massive magnetite ore after limestone in the upper part of the deposit. There is moreover a subtle increase in andradite versus grossular ratio and an increase in johannsenite component in pyroxene towards the skarn front.

In terms of temporal zonation, skarn garnet records complex growth histories as evidenced by oscillatory zoning between andraditic and grossularitic garnet as well as textural evidence for cementing of older garnet euhedra by vug-lining garnet (Fig. 3). Earlier coarser (c. 1-2 mm) garnet-clinopyroxene skarns are furthermore commonly recrystallized to finer-grained, compositionally similar granoblastic polygonal skarns. The skarns are commonly affected by retrograde alteration to calcite, epidote and clinozoisite-rich assemblages.

Except for retrograde skarn veins cross-cutting magnetite, prograde skarn assemblages have not been observed to overgrow or overprint magnetite.

4 Discussion

Jansson (2011) demonstrated that the Smältarmossen dacite porphyry is chemically identical to, and likely co-magmatic with a microgranodiorite which forms the marginal phase of the early Svekokarelian granitoid complex NW of the Garpenberg area (Fig. 1). This intrusion and its surroundings also record strong Na alteration. The granodiorite was dated at 1894±4 Ma by SIMS U-Pb zircon by Jansson and Allen (2011a). The Smältarmossen dacite porphyry is interpreted as formed from the same magma, yet at a higher crustal level, and consequently to be of similar age.

As with most mineral deposits in Bergslagen, the strong Svekokarelian overprint presents a major obstacle to ore genesis inquiries. We do however find that the reconstructed geometry of the porphyry, host rocks, and mineralization combined with evidence from lithogeochemistry, petrography and mineral chemistry are most consistent with formation of magnetite and skarn by replacement of limestone and rhyolite–dacite, respectively, in the marginal zone of the dacite porphyry. The pervasive replacement of dacite porphyry by skarn furthermore suggests that the porphyry cannot have intruded after hydrothermal alteration related to the formation of the magnetite deposit. Consequently, the magnetite deposit is interpreted as essentially syn-porphyry in timing. We furthermore interpret the setting, timing, mineralogical zoning and alteration textures as fully compatible with a contact metasomatic skarn model for magnetite and skarn genesis.
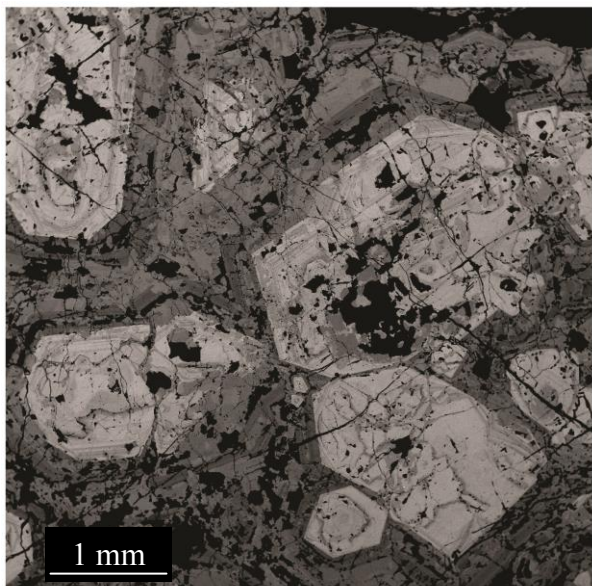
Figure 3. Back-scatter electron (BSE) image of massive garnet skarn from Smältarmossen, showing euhedral-subhedral andradite with oscillatory zoned rims and cores of anhedral andradite (BSE bright, c. Adr_{97-99}, minor skiagite, almandine and spessartine). The andradite crystals are cemented by oscillatory zoned garnet, dominated by grossularitic andradite (BSE dark, c. $Adr_{60-80}Grs_{20-40}$, minor almandine).

5   Conclusions

The setting of Smältarmossen, the pervasive replacement of igneous rocks by skarn, a high Fe oxide/skarn ratio in the ore zone, the deposit-scale skarn zonation and sharp skarn front, mesoscale textural relationships (i.e., garnet+epidote veins cross-cutting albitized rocks), microscale relationships (e.g., oscillatory zoned garnets), as well as lack of textural evidence of skarn minerals replacing or overgrowing magnetite are easiest to reconcile with a contact metasomatic mode of skarn formation, involving fluid-infiltration-induced growth of skarn minerals. The skarns and massive magnetite are interpreted as the products of the interaction of a single, Fe-rich hydrothermal fluid with two chemically contrasting lithologies in the thermal aureole of the dacite porphyry.

The results of this study suggest that contact metasomatic Fe skarn deposits formed at around 1.89 Ga are present in Bergslagen. It is likely that some other skarn-hosted Fe oxide deposits in Bergslagen formed by similar processes. However, the lack of detailed geological data from many skarn/limestone hosted Fe oxide deposits coupled with earlier mentioned evidence for a syngenetic-exhalative origin at some, precludes the possibility to make broad, unambiguous generalizations regarding the regional significance of contact metasomatic Fe oxide ore genesis.

Future work is recommended to focus on establishing criteria for distinction between metamorphosed, metasomatized/altered and contact metamorphic Fe oxide deposits, that can be used with data from the e.g. the database of the Geological Survey of Sweden to reclassify Fe oxide deposits in Bergslagen. Only then can the true significance of contact metasomatic Fe oxide ore genesis in the home of skarns be fully understood.

References

Allen RL, Lundström I, Ripa M, Simeonov A, Christofferson H (1996) Facies analysis of a 1.9Ga, continental margin, back-arc, felsic caldera province with diverse Zn–Pb–Ag–(Cu–Au) sulfide and Fe oxide deposits, Bergslagen Region, Sweden. Econ Geol 91:979-1008

Allen RL, Bull S, RipaM, Jonsson R (2003) Regional stratigraphy, basin evolution, and the setting of stratabound Zn–Pb–Cu–Ag–Au deposits in Bergslagen, Sweden. Final report for SGU-FoU project 03-1203/99, jointly funded by SGU and Boliden Mineral AB

Geijer P, Simeonov A, Malmström L (1989) The Zinkgruvan ore deposit, south-central Sweden: A Proterozoic, proximal Zn-Pb-Ag deposit in distal volcanic facies. Economic Geology 84:1235-1261

Jansson NF (2011) The origin of iron ores in Bergslagen, Sweden, and their relationships with polymetallic sulphide ores. Doctoral thesis, Luleå University of Technology, ISSN: 1402-1544, 73 p

Jansson NF, Allen RL (2011a) Timing of volcanism, hydrothermal alteration and ore formation at Garpenberg, Bergslagen, Sweden. GFF 133:3-18

Jansson NF, Allen RL (2011b) The origin of skarn beds, Ryllshyttan Zn–Pb–Ag+magnetite deposit, Bergslagen, Sweden. Miner Petrol 103:49-78

Jansson NF, Allen RL (2011c) SIMS U-PB zircon age constraints on the ages of syn-volcanic iron oxide and Zn-Pb-Cu-(Ag-Au) deposits, Bergslagen, Sweden. In: Proceedings of the 11th SGA meeting, Antofagasta, September 2011.

Jansson NF, Allen RL (2013) Timing and setting of skarn and iron oxide formation at the Smältarmossen calcic iron skarn deposit, Bergslagen, Sweden. Mineral Deposita 48:313-339

Meinert LD, Dipple, GM, Nicolescu S (2005) World skarn deposits. In: Hedenquist JW, Thompson JFH, Goldfarb RJ, Richards JP (eds) Economic geology 100th Anniversary volume 1905–2005:299-336

Stephens MB, Ripa M, Lundström I, Persson L, Bergman T, Ahl M, Wahlgren CH, Persson PH, Wickström L (2009) Synthesis of the bedrock geology in the Bergslagen region, Fennoscandian Shield, south-central Sweden. Sver Geol Unders Ba 58:1-259

Törnebohm AE (1875) Geognostisk beskrifning öfver Persbergets Grufvefält. Sver Geol Unders C 14:1-21

Archean gold skarns in iron formation, Southern Cross greenstone belt, Yilgarn Craton, Western Australia: midcrustal granite-related replacement deposits

Andreas G. Mueller
Consultant, 12a Belgrave Street, Maylands W.A. 6051, Australia. E-mail: andreasm@iinet.net.au

Abstract. The Bounty (41 t Au), Nevoria (12 t Au) and Southern Star (2.2 t Au) deposits in the 3.05-2.95 Ga amphibolite-facies Southern Cross greenstone belt, Yilgarn Craton, Western Australia, are stratabound to quartz-grunerite iron formation (BIF). The pyrrhotite-rich ore (5-8 g/t) is characterized by a hedenbergite-actinolite and almandine-hornblende ± quartz gangue classified as "skarn" in the sense of Törnebohm (1875). Amphibolite intercalated with BIF is replaced in contact zones by diopside-hornblende-biotite, cummingtonite-plagioclase-biotite, and biotite-cordierite-quartz skarn, the latter two containing minor almandine and gedrite. Grossular-diopside ± prehnite ± scheelite veins are part of the proximal skarn at Nevoria, where the TIMS garnet age (2635.7±1.2 Ma) of the ore and the SHRIMP zircon age (2634±4 Ma) of the granite below agree within error. In combination with Au-Bi enrichment in the roof pegmatite, the U-Pb ages identify the granite as the source of the skarn-forming fluid. In the distal Copperhead deposit (29 t Au), actinolite-carbonate ± pyrrhotite ore replaces BIF and forms thick veins in adjacent hornblende-biotite skarn and talc-chlorite schist. Granite porphyry sills are altered to quartz + chlorite + cordierite. The mineral assemblages indicate that the gold skarns formed at 550-600°C fluid temperature in a mid-crustal environment of 330-400°C ambient temperature.

Keywords. Archean, gold, skarn, gedrite, cordierite

1 Introduction

The Southern Cross greenstone belt is located in the continental foreland of the Eastern Goldfields Province (EGP), the youngest orogenic terrane of the Yilgarn Craton, Western Australia (Fig. 1). Despite its small area, the Southern Cross Belt records a production of 344 t Au (>11 Moz; 1887-2011) derived from about thirty individual deposits (0.5-62 t Au). Most of these (98.5%) are characterized by calc silicate-biotite alteration while the remaining ones are gold-quartz veins. Granite-pegmatite dikes are exposed in two thirds of the mines. The classification of the deposits as intrusion-related "skarns" (Mueller 1991; 1997) contrasts with their interpretation as "hypozonal orogenic deposits" formed at >12 km depth during folding in the Eastern Goldfields Province and the ascent of metamorphic fluids in crustal-scale shear zones (Groves et al. 1998; Goldfarb et al. 2005).

We describe gold-bearing calc-silicate and quartz-cordierite alteration associated with the Bounty (41 t Au), Copperhead (29 t Au), Nevoria (12 t Au), and Southern Star (2.2 t Au) deposits, all stratabound to

reduced silicate-facies iron formation. At Nevoria, concordant U-Pb ages constrain the time of skarn formation relative to amphibolite-facies metamorphism and relative to local granite emplacement. Geochemical data constrain the nature of Mg-Al metasomatism.
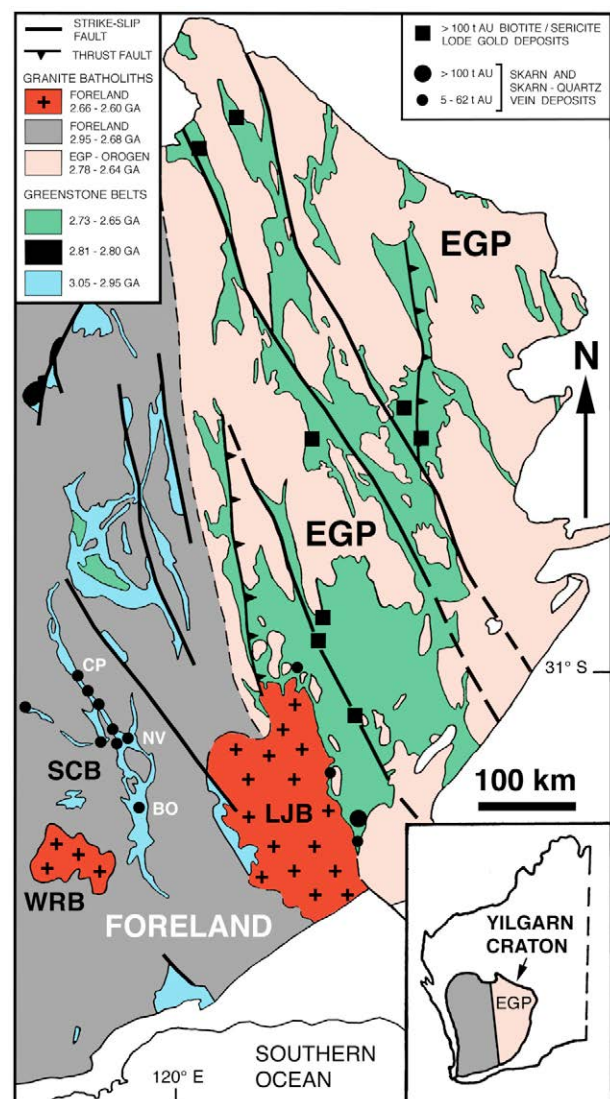
Figure 1. More than 30 gold skarn deposits including Nevoria (NV), Bounty (BO) and Copperhead (CP) have been mined in the Southern Cross greenstone belt (SCB) in the foreland of the Eastern Goldfields Province (EGP), Yilgarn Craton. They are related to magnetite-series granite plutons clustering north to northwest of the Wave Rock (WRB) and Lake Johnston (LJB) batholiths. Skarn deposits also occur at the eastern margin of the LJB but are subordinate to mesothermal lode gold deposits in the EGP. Note the inset map of Western Australia.

2 Terminology

The term "skarn" was introduced by Törnebohm (1875) to describe the garnet-pyroxene-amphibole gangue of magnetite ore replacing felsic volcanic rocks in the Persberg district, Bergslagen, Sweden. He also applied the term to parts of the Falun deposit, where calc silicate and quartz-cordierite-anthophyllite rocks constitute the gangue of Cu-Au and Zn-Pb sulfide ore (Törnebohm 1893). Geijer (1917) interpreted Falun as a replacement deposit formed in a deep batholithic setting but could not quantify the PTt-conditions given the limited analytical capabilities at his time. Modern skarn nomenclature, still in accordance with Törnebohm's descriptive approach, is summarized in Einaudi and Burt (1982): "The feature that sets skarn deposits apart from other types of mineral deposits is the gangue, a … mixture of Ca-Mg-Fe-Al silicates formed by metasomatic processes at high temperature and termed skarn."

3 Regional geology

The Archean Yilgarn Craton is deeply eroded to the batholith level, and granites underlie about 75% of the present surface. The Southern Cross greenstone belt is part of the Youanmi Terrane in the central part of the craton (Cassidy et al. 2006), which is characterized by supracrustal belts composed of 3.05-2.95 Ga mafic-ultramafic volcanic rocks. The terrane constitutes the continental foreland of the Eastern Goldfields Province (Fig. 1), a north-trending orogen defined by a 2.73-2.65 Ga volcano-sedimentary succession folded and metamorphosed at 2.65 Ga (Groves et al. 1998).

The Southern Cross Belt consists of a lower unit of tholeiitic basalts separated by beds of banded iron formation (BIF) from an upper unit of komatiites, high-Mg basalts and gabbro sills, which is in turn overlain by greywacke. Quartz porphyry sills in the iron formation have SHRIMP zircon ages of 2934±7 Ma to 2912±5 Ma. The BIF marker beds and the greywacke outline deformed isoclinal folds draped around the margins of composite granite gneiss domes dated at 2775±10 to 2691±7 Ma (SHRIMP zircon). Amphibolite-facies broad-aureole metamorphism in the belt took place during the emplacement of the batholith border phases at 2775-2724 Ma (Mueller and McNaughton 2000). Mineral assemblages indicate peak PT-conditions of 400±100 MPa and 600-650°C.

Both the orthogneiss domes and the greenstones are intruded by 2665±7 to 2631±3 Ma old (SHRIMP zircon) magnetite-series granite plutons, which cluster north to northwest of the Wave Rock and Lake Johnston batholiths (Fig. 1) and display a close spatial relationship to the gold deposits in the belt (Mueller et al. 2004).

4 Host rocks and structural control

The BIF marker horizon comprises 1-20 m thick beds of mesobanded quartz-grunerite ± magnetite iron formation characterized by high FeO (30 wt%) but low Al_2O_3 (0.3-0.7%) and TiO_2 (<0.05%) contents. The iron formation is intercalated with amphibolite (meta-basalt and meta-gabbro), ultramafic amphibole-chlorite rock (meta-komatiite) and, locally, graphitic quartz-biotite schist. Ore skarn averaging 5-8 g/t Au is stratabound to the lithologic contacts and extends 1-4 m into the iron formation leaving the centre of thick beds barren. Pinch-and-swell and crosscutting veins indicate minor tectonic movement during mineralization. At Nevoria, the orebodies form a 1 km long array of tabular shoots on the limb of an anticline striking east. The skarn terminates at 200-250 m depth at a granite-pegmatite pluton and is intrusion-proximal. At Bounty, the main contact orebody strikes north, is up to 750 m long, and extends to 950 m vertical depth. The Copperhead deposit, located 150 m southwest of the Ghooli Dome batholith but distal from late granite-pegmatite intrusions, consists of two isoclinal BIF synforms plunging 40-45° northwest. The southern synform, enclosed in ductile talc-chlorite schist, has the shape of a sheath fold and comprises ore skarn in BIF. The northern synform contains a thick actinolite-dolomite infill vein (5 g/t Au) mined 930 m down plunge.

5 Ore skarn in BIF

The ore skarn selectively replaces grunerite ± magnetite mesobands (Fig 2), and forms crosscutting masses and veins. At Nevoria, Bounty and Southern Star, four skarn types are distinguished in decreasing order of abundance: (1) actinolite-hedenbergite, (2) almandine-hornblende, (3) quartz-rich skarn of types 1 and 2, and (4) massive pyrrhotite ore. Accessory scheelite and chalcopyrite are common but base metal grades are low (<0.05 wt%). Native gold (10-26 mol% Ag) occurs enclosed in almandine, hedenbergite, actinolite and quartz, and in contact with pyrrhotite. Retrograde stilpnomelane and chlorite are minor (1%).

Actinolite-hedenbergite skarn, the main type in the three deposits, consists of ferro-actinolite and lesser ferro-hornblende intergrown with 10-15% pyrrhotite and with 1-15% hedenbergite. Disseminated grains of loellingite-arsenopyrite are present in parts of the orebodies. This skarn is weakly enriched in aluminium.

Almandine-hornblende bands are zoned from cores of almandine, intergrown with minor cummingtonite, biotite, tourmaline, and 5% pyrrhotite, to narrow margins of ferro-hornblende. The almandine contains inclusions of ilmenite, titanomagnetite, allanite, and zircon. Gold skarn of this type is enriched in elements commonly considered immobile during metasomatism including Ti, Al, Nb, Th, Zr, and the REE.

Lenses and veins of quartz-rich actinolite-hedenbergite and almandine-hornblende skarn, most located close to the contacts with amphibolite or meta-komatiite, are enriched in gold (30-120 g/t) and in bismuth due to the association of pyrrhotite, native gold, bismuth tellurides and tellurosulfides, and Au-Bi alloy.

Massive pyrrhotite occurs at Bounty in contact zones up to 3 m thick and 130 m long. Gold grade is high (25 g/t) where the pyrrhotite matrix (70 vol%) contains

aggregates of early-stage hedenbergite and calcite, and low (1 g/t) where it contains late-stage biotite and clinozoisite (Weedon and Stallman 1995). Euhedral actinolite is disseminated throughout, and fragments of BIF and quartz occur locally.
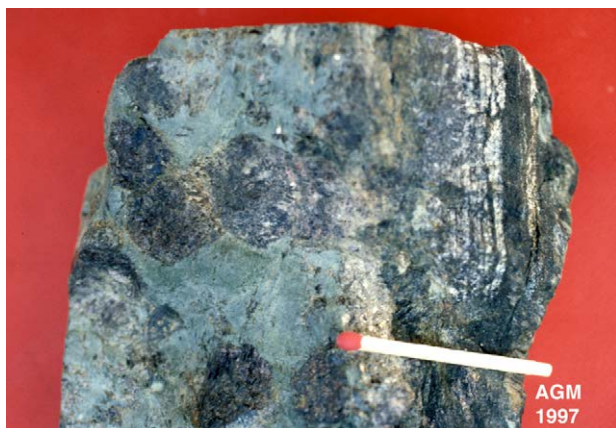
Figure 2. Contact between actinolite-pyrrhotite skarn and white quartz mesobands in BIF (at matchstick = 4 cm) and almandine-phlogopite-chlorite schist replacing meta-komatiite. The almandine porphyroblasts enclose Ti-magnetite, pyrrhotite and gold, and are not rotated relative to the chlorite fabric. Nevoria Main shaft 3 level.

At Copperhead, net-textured ore in BIF (7-10 g/t) consists of pyrrhotite-rich hornblende-actinolite-calcite and tremolite-siderite skarns. The dolomite infill vein (5 g/t Au; ≤0.02 wt% TiO_2) adjacent to BIF contains contorted actinolite bands (20 vol%), zoned quartz-actinolite veins, and disseminated pyrrhotite and galena. Mg, Ca and CO_2 are strongly, and Si, Fe and Al are moderately enriched (Mueller and McNaughton 2000).

6 Skarn in amphibolite / metakomatiite

Wall-rock alteration in the volcanic rocks is mostly sub-economic (≤ 1 g/t Au) but may extend 150-200 m into the hanging wall and footwall of the BIF-horizon comprising distal biotite bands in amphibolite and serpentine-magnetite aggregates in amphibole-chlorite rock. At Nevoria, Bounty and Southern Star, there is a 15 m thick zone of replacement skarn in amphibolite along the footwall contact of the main mineralized BIF. Skarn is also developed at other lithologic contacts but is thinner (0.1-2.5 m) and discontinuous. Disseminated pyrite and pyrrhotite (1-2%), and rare scheelite are widespread. The skarn zones are characterized by pervasive potassium, and by local magnesium and aluminium enrichment (Mueller 1997).

The main contact zones enclose lenses of remnant amphibolite, and consist of bands differing in mineralogy on a centimetre to decimetre scale. Skarn types include, in decreasing order of abundance: (1) diopside-hornblende-biotite, (2) biotite-cummingtonite-anorthite, (3) calcite-chlorite-humite, and (4) quartz-biotite-cordierite. The first skarn type is zoned from inner diopside + calcite + microcline to intermediate

hornblende + pargasite to outer biotite + chlorite + clinozoisite ± prehnite. Magnesian skarn (<5 vol%) forms up to 10 cm thick inner zones in some diopside bands. It consists of calcite + Mg-chlorite, variably serpentinized minerals of the humite group, and disseminated magnetite and pyrrhotite.

The other common skarn type varies in biotite and cummingtonite content, grades into grey cummingtonite-plagioclase rock, and contains 5% almandine and/or gedrite porphyroblasts. The plagioclase is calcic, commonly anorthite in composition, and retrograded to zoisite + sericite in aggregates imparting a spotted texture. At Nevoria, this skarn type encloses lenses of quartz-biotite-cordierite rock containing minor gedrite, almandine, tourmaline, and magnetite.

In ultramafic amphibole-chlorite rock, most contact zones are thin (<0.5 m) and consist of chlorite-phlogopite ± hornblende schist marked by almandine porphyroblasts (Fig 2) or by diopside-calcite-actinolite aggregates. Magnetite and pyrrhotite (2-5%), and gersdorffite and niccolite (0.1%) are disseminated.

In the proximal Nevoria deposit, the contact skarns are associated with spaced replacement veins, 1-15 cm thick, of more oxidized grandite-diopside skarn. These veins overprint the metamorphic amphibole lineation in the host amphibolite or meta-komatiite. The grossular-andradite core contains minor quartz, calcite, alkali feldspar, Mo-scheelite, and late epidote and prehnite.

In the distal Copperhead deposit, garnet and pyroxene are absent. Amphibolite is altered to hornblende-biotite-clinozoisite skarn, and meta-komatiite to talc-chlorite schist and talc-ankerite-magnetite rock. Granite porphyry sills are replaced by andalusite- and sillimanite bearing quartz-cordierite rock containing antithetic amounts of chlorite + muscovite and phlogopite.

7 Conditions and time of skarn formation

Mineral reaction and Fe-Mg exchange thermometry constrain the peak temperature of the skarn-forming fluid to 550±50°C at Copperhead (Mueller and McNaughton 2000), 560±50°C at Bounty (Weedon and Stallman 1995), and to 590±50°C at Nevoria. Pressure estimates based on skarn assemblages from Nevoria and three other gold deposits, scattered along strike of the Southern Cross Belt, are 300-400 MPa corresponding to a burial depth of 11-14 km. Assuming a geothermal gradient of 30°C/km, the ambient temperature at that depth is estimated at 330-400°C consistent with the maximum thermal stability (400±20°C) of prehnite (Mueller et al. 2004). The ambient terrane temperature sets the minimum the gold-bearing fluid could cool to. Aqueous and aqueous-carbonic fluid inclusions in skarn from Nevoria homogenize to liquid at 190-380°C (T_h not corrected for pressure), and have low to moderate salinities (0.1-9.9 wt% $NaCl_{equiv}$). First-melting temperatures as low as -45°C indicate the presence of $CaCl_2$ and $MgCl_2$ (Fan et al. 2000).

Allanite inclusions in almandine from Nevoria, the only deposit precisely dated, provide a concordant TIMS

U-Pb age of 2635.7±1.2 Ma for skarn formation. Consistent biotite Rb-Sr and Ar-Ar ages from the Nevoria granite and two other localities in the Southern Cross Belt indicate that the terrane did not cool below 300°C until ca. 2560 Ma implying persistent deep burial (10 km) and slow uplift (Mueller et al. 2004).

8 Skarn-related granite and pegmatite

Pegmatite dikes are absent at Copperhead, sparse at Southern Star and Bounty but abundant at Nevoria, where they form a screen above the 500m-thick pluton terminating the skarn at 200-250 m depth. The pluton is zoned upward from muscovite- and sillimanite-bearing biotite granite to a 100m-thick intermediate zone of interlayered two-mica granite and pegmatite overlain by an 80m-thick roof zone of muscovite pegmatite. The roof pegmatite contains accessory Mn-almandine, biotite, fluorite, and trace corundum and molybdenite.

Bulk whole-rock geochemistry reveals element (and fluid) mobility from the deep granite to the roof pegmatite. Relative to the granite, the pegmatite is depleted in Ca, K, Th, Zr and the REE, and enriched in Al, Au, Bi, Cu, Nb and W. All of these elements are at least locally enriched in the exoskarn above. These metasomatic patterns, in particular with regard to least-mobile elements (Al, Nb, Th, Zr, REE), and the SHRIMP zircon U-Pb age of 2634±4 Ma (Qiu et al. 1999), identify the granite pluton as the fluid source of the Nevoria gold deposit. Remnant igneous magnetite + ilmenite and a high differentiation index (CIPW normative q+or+ab = 92-93) indicate that this pluton represents a fractionated member of the post-orogenic granite suite emplaced into the foreland of the Eastern Goldfields Province (Mueller et al. 2004).

9 Conclusions

(1) The BIF-hosted gold deposits in the 3.05-2.95 Ga Southern Cross greenstone belt postdate amphibolite-facies metamorphism in the aureoles of 2.78-2.72 Ga granite batholiths by at least 90 million years, (2) the deposits show a close relationship in space and time to pegmatite-granite complexes, fractionated plutons of a magnetite-series suite emplaced at 2.66-2.63 Ga, (3) based on gangue mineralogy, they classify as "skarns" in the descriptive sense of Törnebohm (1875), (4) in feldspar-rich precursor amphibolite and quartz porphyry, stratabound skarn is associated with quartz-cordierite-biotite ± gedrite ± almandine or quartz-cordierite-chlorite-muscovite ± phlogopite rock, the product of granite-related Mg-Al metasomatism, (5) the ore skarns formed by replacement at high fluid temperature (550-600°C) at 11-14 km depth in a mid-crustal environment of 330-400° ambient temperature, (6) the Southern Cross gold deposits are located in the continental foreland of the Eastern Goldfields Province, are unrelated to deformation within this orogen, are not controlled by crustal-scale shear zones, and cannot be classified as "hypozonal orogenic" as in Goldfarb et al. (2005).

References

Cassidy KF, Champion DC, Krapez B, Barley ME, Brown SJA, Blewett RS, Groenewald PB, Tyler IM (2006) A revised geological framework for the Yilgarn Craton, Western Australia. Geological Survey of Western Australia, Record 2006/8, 8 pp

Einaudi MT, Burt DM (1982) Introduction – terminology, classification, and composition of skarn deposits. Economic Geology 77: 745-754

Fan HR, Groves DI, Mikucki EJ, McNaughton NJ (2000) Contrasting fluid types at the Nevoria gold deposit in the Southern Cross greenstone belt, Western Australia: Implications of auriferous fluids depositing ores within Archean banded iron-formations. Economic Geology 95: 1527-1536

Geijer P (1917) Falutraktens berggrund och malmfyndigheter. Sveriges Geologiska Undersökning, Norstedt and Sons, Stockholm, 316 pp

Goldfarb RJ, Baker T, Dubé B, Groves DI, Hart CJR, Gosselin P (2005) Distribution, character and genesis of gold deposits in metamorphic terranes. Economic Geology 100th Anniversary Volume, pp 407-450

Groves DI, Goldfarb RJ, Gebre-Mariam M, Hagemann SG, Robert F (1998) Orogenic gold deposits: A proposed classification in the context of their crustal distribution and relationship to other deposit types. Ore Geology Reviews 13: 7-27

Mueller AG (1991) The Savage Lode magnesian skarn in the Marvel Loch gold-silver mine, Southern Cross greenstone belt, Western Australia: Part I. Structural setting, petrography and geochemistry. Canadian Journal of Earth Sciences 28: 659-685

Mueller AG (1997) The Nevoria gold skarn deposit in Archean iron-formation, Southern Cross greenstone belt, Western Australia: I. Tectonic setting, petrography, and classification. Economic Geology 92: 181-209

Mueller AG, McNaughton NJ (2000) U-Pb ages constraining batholith emplacement, contact metamorphism, and the formation of gold and W-Mo skarns in the Southern Cross area, Yilgarn craton, Western Australia. Economic Geology 95: 1231-1257

Mueller AG, Nemchin AA, Frei R (2004) The Nevoria gold skarn deposit, Southern Cross greenstone belt, Western Australia: II. Pressure-temperature-time path and relationship to postorogenic granites. Economic Geology 99: 453-478

Qiu YM, McNaughton NJ, Groves DI, Dalstra HJ (1999) Ages of internal granitoids in the Southern Cross region, Yilgarn Craton, Western Australia, and their crustal evolution and tectonic implications. Australian Journal of Earth Sciences 46: 971-981

Törnebohm AE (1875) Geognostik beskrifning ofver Persbergets Grufvefällt. Sveriges Geologiska Undersökning, Norstedt and Sons, Stockholm, 21 pp

Törnebohm AE (1893) Om Falu grufvas geologi. Geologiska Föreningens i Stockholm Förhandlingar 15: 609-690

Weedon P, Stallman M (1995) Bounty gold mine. In: Schwebel PJ (ed) Southern Cross greenstone belt, geology and gold mines. Geoconferences Inc., Nedlands, Western Australia, p 113-117

The Gränsgruvan Zn-Pb-Ag deposit, an outsider in the Stollberg ore field, Bergslagen, Sweden

Hein Raat, Nils F Jansson, Erik Lundstam
Boliden Mines, Exploration Department, Garpenberg, Sweden

Abstract
The Stollberg ore field is located in the Bergslagen region of the Fennoscandian shield. The field comprises a 5 km long steeply east-dipping belt of Mn-rich, magnetite and Zn-Pb-Ag sulfide deposits hosted by marble, skarn and hydrothermally altered meta-volcanic rocks. The deposits have been mined continuously from medieval times until 1982. The Gränsgruvan Zn-Pb-Ag deposit is located 2 km west of the historic Stollberg workings and is interpreted to be stratigraphically equivalent. The old Stollberg mines are situated on the eastern limb of a regional syncline, whereas Gränsgruvan is located on the western limb. Formation of the ore deposits directly followed a major rhyolitic, volcanic eruption and formation of a submarine caldera. The earliest mineralization comprised exhalative Fe oxides concurrent with limestone formation. Post-caldera subsidence and burial induced a shift in style of mineralization, whereby the limestone became a trap to replacement-type magnetite and Zn-Pb-Ag sulfide mineralization. The Gränsgruvan deposit differs from the other deposits in not being hosted by marble or skarn; it is hosted by a strongly silicified and hydrothermally brecciated rhyolite, interpreted as the stratigraphic footwall of the main limestone. The mineralization is stratabound and occurs in stringers and subordinate semi-massive sulfide lenses.

Keywords. Zn-Pb-Ag mineralization, Gränsgruvan, Stollberg, Bergslagen.

1 Introduction

The Gränsgruvan deposit is located in the western part of the Bergslagen region, southern Sweden. It was discovered in 1939 using a ground magnetic survey. The deposit was mined intermittently during 1943-1978. Boliden Mineral AB bought the mine in 1972 and produced 0.26 Mt with 4.8 % Zn, 2.1 % Pb and 29 g/t Ag, down to 225 m depth (Raat and Åberg 2012). In this contribution, Gränsgruvan is regarded as part of the Stollberg ore field, due to its similar stratigraphic position (Jansson et al. 2013). The Stollberg deposits comprised combined Mn-rich iron-oxide deposits and stratabound, carbonate replacement Zn-Pb-Ag-(Cu-Au) sulfide deposits. In total 6.65 Mt ore was mined from medieval times until 1982 (Jansson et al. 2013).

Recent research and exploration have focused on the stratigraphy and structure of the Stollberg ore field (Jansson et al., 2013). However, the geology of the Gränsgruvan deposit has never been described in detail. This contribution provides an updated geological map of the Stollberg area and a detailed geological cross section of Gränsgruvan. Based on the results, it is concluded that the Gränsgruvan deposit differs from other deposits in the field in terms of alteration and setting. These variations and their significance for exploration in the area are discussed.

2 Geological Background

Over 6 000 mineral deposits and prospects are known in Bergslagen. Most are hosted by marble units within ca. 1.91-1.89 Ga, dominantly rhyolitic, metavolcanic inliers that are enclosed by syn-volcanic to early Svecokarelian, granitoid intrusions. The precursors to the metavolcanic rocks formed in a subaqueous, back-arc basin on continental crust (Allen et al. 1996). The supracrustal succession, early intrusions, and mineral deposits were deformed and metamorphosed under mainly amphibolite facies conditions during the Svecokarelian orogeny at c. 1.9-1.8 Ga (Stephens et al. 2009).

Most deposits in the Stollberg ore field occur along the N-S striking eastern limb of an upright to steeply east-dipping, steeply S-plunging syncline (Fig 1). The Gränsgruvan deposit however, occurs on the western limb. The core of the syncline comprises meta-sediments (Fig. 1; Ripa 1994), which are separated from the ore horizon by c. 800 m of massive to banded rhyolitic meta-volcanic rocks (Ripa 1988). These hanging-wall rocks are generally not strongly altered but locally contain abundant patchy, calc-silicate aggregates and local zones of elevated cordierite, muscovite and quartz, interpreted as regional metamorphosed syn-volcanic alteration zones. Proximal to the ore horizon on the eastern limb, gradation into biotite+quartz-rocks with abundant porphyroblasts (locally more than 50 vol.%) of garnet, gahnite, cordierite, andalusite, sillimanite and amphibole is observed. These grade further eastward into marble and skarn, which is the main host to mineralization. Similar porphyroblastic rocks occur east of the ore horizon in the stratigraphic footwall and grade into less-porphyroblastic, quartzose biotite schists. These grade further eastward into gedrite-porphyroblastic albite+quartz±garnet rocks (Fig. 1). The porphyroblastic rocks constitute a metamorphosed, syn-volcanic, zoned hydrothermal alteration envelope that is mainly in the stratigraphic footwall of the Stollberg deposits, but extend irregularly up into the stratigraphic hanging-wall (Ripa 1988, 1994). The garnet+ biotite-rich rocks formed by metamorphism of chlorite+sericite-rich alteration zones, whereas the gedrite+albite-rich rocks formed from chlorite+albite-altered zones (Ripa 1988). The skarns in the Stollberg ore host have been interpreted as metamorphosed mixtures of altered rhyolite, limestone, and hydrothermal sediments (Jansson et al. 2013).

The sulfide mineralizations in the old Stollberg mines were dominated by sphalerite, pyrrhotit, arsenopyrite and lesser chalcopyrite and pyrite. They grade irregularly into semi-massive and locally massive sulfide bodies, which are considerably richer in galena. Average grades in the mined deposits ranged between 0.5-5 wt.% Zn, 0.5-15.6 wt.% Pb and 5-320 g/t Ag.
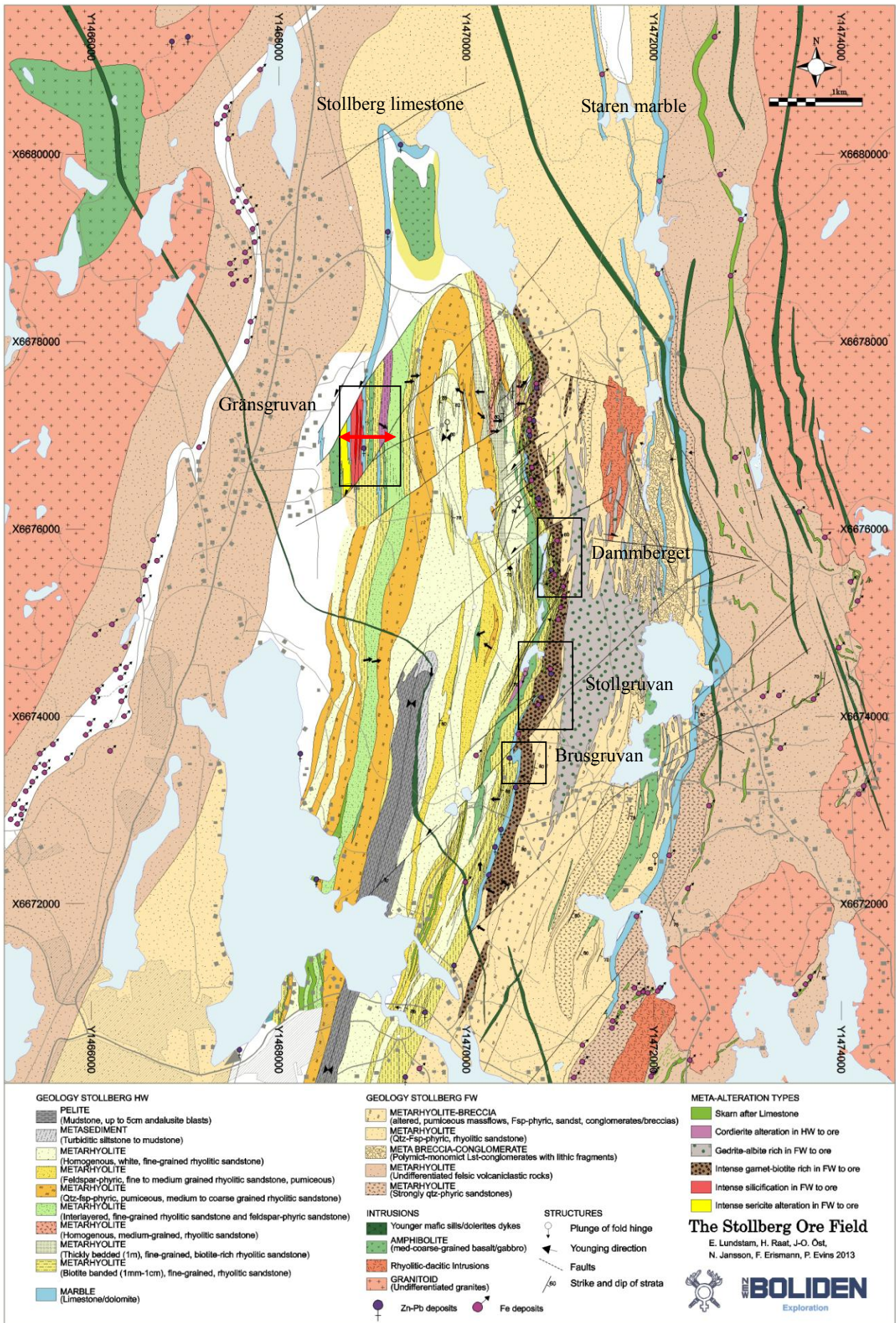
Figure 1. Geological map of the Stollberg ore field (Lundstam et al. 2013) showing Fig. 2 cross-section line. Modified after Jansson et al. (2013). Interpreted pre-metamorphic protoliths are given in brackets. Grid: Swedish National Grid RT90.
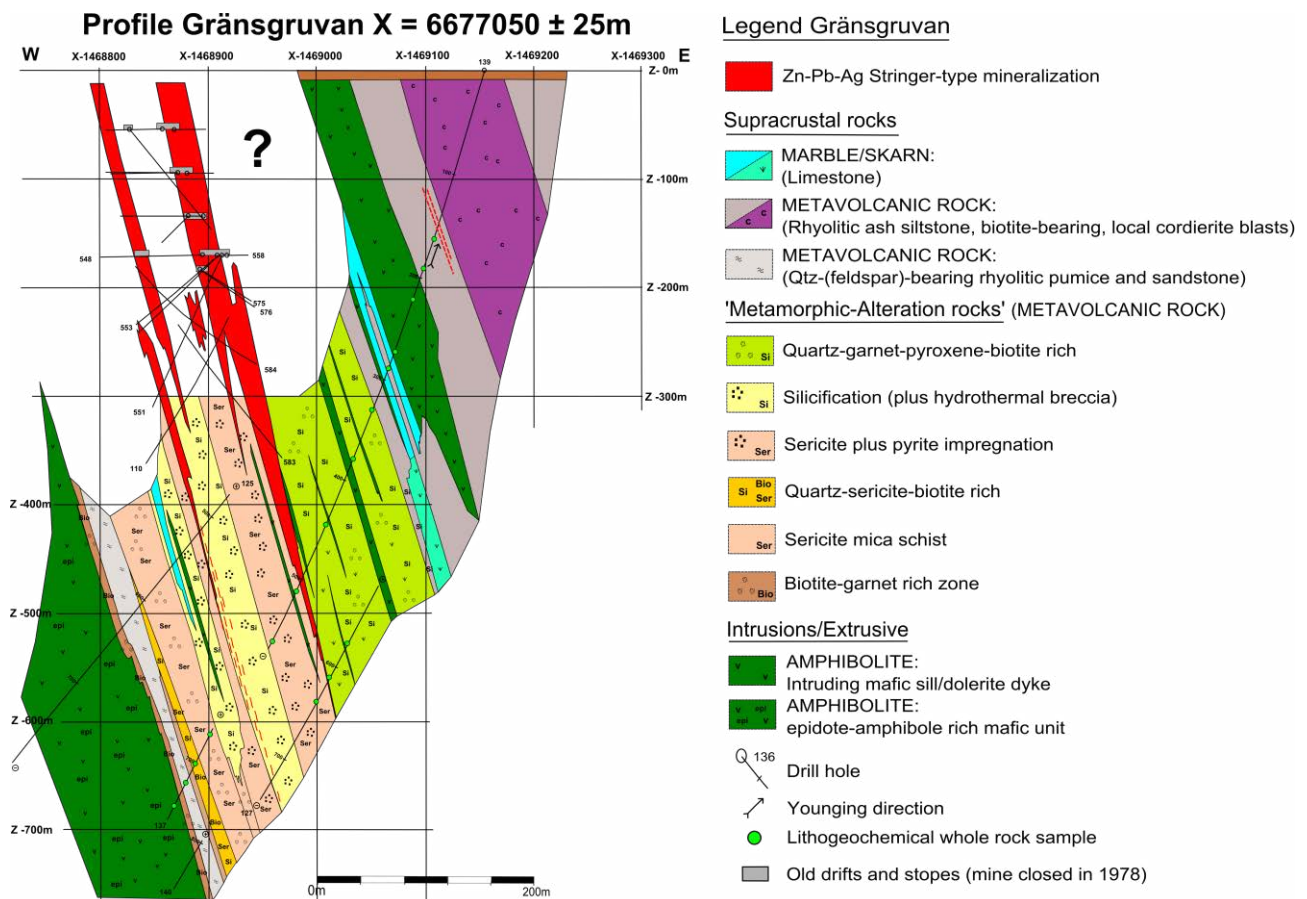
Figure 2. Geological cross section of the Gränsgruvan deposit. Grid: Swedish National Grid RT90, with z = 0 m at surface.

The Zn/(Zn+Pb) ratio ranged between 0.17-0.89, yet it was below 0.68 for most deposits (Jansson et al. 2013). Magnetite mineralization (10-40 wt.% Fe) occurred as massive to semi-massive limestone replacement, in skarns (knebelite, almandine-spessartine, serpentine, grunerite, actinolite etc.) and as banded magnetite-garnet-amphibole rocks. The latter is interpreted as metamorphosed exhalite facies. The skarns associated with the ores have been interpreted as metamorphosed mixtures of altered rhyolite, limestone and mineralization (Jansson et al. 2013).

Besides the meta-volcanic rocks, a number of metamorphosed felsic and mafic syn-volcanic intrusions are present (Fig. 1).

3 Stratigraphic Evolution

Jansson et al. (2013) conducted sedimentary and volcanic facies analysis on rock-types in the Stollberg area and proposed a model for the geological evolution, prior to metamorphism and deformation. The succession from the Staren limestone (ca. 1 km stratigraphically below/ east of the Stollberg ore horizon) to the Stollberg limestone was shown to originally have comprised a c. 600-m-thick shallowing-upwards sedimentary sequence in which normal graded subaqueous mass flow deposits pass upwards to polymict limestone-volcanic breccia-conglomerates. This succession is overlain by ca. 500 m of juvenile rhyolitic pumice breccia. The latter was interpreted as a major pyroclastic deposit. The entire succession was interpreted to reflect basin instability, erosion, subsidence and fan-delta sedimentation,

culminating in a major, caldera-forming volcanic eruption. The Stollberg limestone and Fe-rich exhalites were shown to be conformable above the rhyolitic pumice breccia, which most likely constitute a caldera-fill deposit. Consequently, an intra-caldera setting was proposed for the ore field. The Stollberg limestone is overlain by planar-stratified, rhyolitic ash-siltstones and subordinate sedimentary breccias deposited below wave base from turbidity currents and suspension.

Jansson et al. (2013) inferred that the hydrothermal-exhalative Mn-rich Fe oxide mineralization formed at a post-caldera stage, during waning volcanism, broadly coeval with limestone formation. The replacement style magnetite and Zn-Pb-Ag sulfide deposit formed slightly later, after burial of the hydrothermal system by sediments of the stratigraphic hanging-wall. At this stage, the Stollberg limestone interacted with hotter and more sulfur-rich hydrothermal fluids below the seafloor, producing stratabound replacement bodies.

4 Gränsgruvan geology

At Gränsgruvan, fining upwards sequences indicate stratigraphic younging towards the east (Fig. 2). Fine-grained, laminated, biotite-bearing, metamorphosed, felsic ash-siltstones with local cordierite blasts, represent the top of the local stratigraphic succession (Björklund, 2011). An up to 30 m thick marble-skarn unit, which locally grades into massive diopside-hedenbergite skarn occurs stratigraphically below. The marble-skarn unit is correlated with the Stollberg ore host on the eastern limb. Sulfide mineralization is absent, yet magnetite

porphyroblasts are locally observed. Over 200 m of metamorphosed alteration rocks are observed stratigraphically below the marble-skarn unit (Fig. 2). Björklund (2011) suggested a rhyolitic protolith based on lithogeochemical analysis. The upper 100 m of this unit contain quartz-garnet-pyroxene-biotite-rich rocks with local cross-cutting pyroxene-rich veins. These grade downwards into a hydrothermally brecciated zone, dominated by pervasive silicification, which is host to the sphalerite, galena and pyrite stringer-type mineralization of the Gränsgruvan deposit. The silicified and brecciated rocks grade stratigraphically downwards into a schistose sericite-altered zone with local pyrite impregnation. The alteration intensity decreases downwards in the stratigraphy and a transition into less altered, quartz crystal-bearing rhyolitic sandstones is observed. A meter-size, strong biotite-garnet rich zone comprise the contact with an epidote-amphibole-rich mafic unit. Younger, medium- to coarse-grained amphibole-biotite-rich mafic sills with sharp contacts occur in various parts of the stratigraphy (Raat and Åberg, 2012).

5 Discussion

The Gränsgruvan deposit differs from the other Stollberg deposits in several aspects including: 1) absence of marble/skarn hosted mineralization, 2) higher Zn/(Zn+Pb) ratio (0.72) despite comparable grades, 3) near absence of magnetite, pyrrhotite and arsenopyrite, 4) very high pyrite vs. pyrrhotite ratio, 5) predominance of intensely silicified and sericite-pyrite altered rocks in the footwall, 6) absence of a known, deeper, underlying zone of Na-Fe-Mg-enriched rhyolites with gedrite porphyroblasts.

The Gränsgruvan deposit has similarities in alteration and mineralization style to the footwall mineralization of the marble-skarn hosted Garpenberg stratabound Zn-Pb-Ag-(Cu-Au) deposit (>100 Mt @ 5.2 % Zn, 2.1 % Pb and 130 g/t Ag), 60 km east of Gränsgruvan. Footwall mineralization at Garpenberg mainly comprises pyrite-sphalerite-chalcopyrite-veinlets, cross-cutting intensely silicified and phyllosilicate-altered felsic volcanic rocks (Allen et al., 2003). By analogy, this implies that the mineralization at Gränsgruvan may largely constitute footwall stringer-type mineralization, and that potential for finding mineralization in the overlying marble-skarn unit exists (Fig. 2).

As for the relationship to the deposits on the eastern limb, the higher pyrite vs. pyrrhotite ratio, the paucity of Mn-rich iron oxide mineralization, the higher Zn ratio and the higher proportion of stringer-type mineralization in intensely altered volcanic rocks may imply that Gränsgruvan occupies a more proximal setting relative to a hydrothermal upflow zone. However, Ripa (1988) and Jansson et al. (2013) also showed that a relict hydrothermal upflow zone is present below the old Stollberg mines on the eastern limb (Fig. 1). Possibly, this indicates the presence of multiple hydrothermal centers in the Stollberg area at the time of mineralization.

The genesis of the skarns at Gränsgruvan is uncertain. Skarns may either have formed at the time of mineralization or later, during the Svecokarelian orogeny and related amphibolite facies regional metamorphism (cf. Jansson et al. 2013).

6 Summary and Conclusions

The Stollberg deposits formed at a time of basin subsidence combined with evolution of a rhyolitic caldera in a subaqueous felsic volcanic complex. The Fe oxide and Zn-Pb-Ag sulfide deposits on the eastern limb are interpreted as metamorphosed, syn-volcanic mineralization, comprising both Fe-rich exhalites (metamorphosed to magnetite-garnet-amphibole rocks) and overprinting carbonate-replacement type, combined magnetite and Zn-Pb-Ag sulfide mineralization. The Gränsgruvan deposit, on the western limb, differs in being hosted by strongly silicified and hydrothermally brecciated rocks, which can be correlated within the stratigraphic footwall sequence on the eastern limb. Consideration of stratigraphic setting, metal ratios, alteration style and analogy with the large Garpenberg deposit implies that Gränsgruvan may represent a more proximal mineralization type compared to the other deposits. By inference, this implies a potential for finding high-grade, carbonate-replacement type marble/skarn-hosted Zn-Pb-Ag mineralization, similar to Garpenberg, in parts of the structurally and stratigraphically overlying limestone.

References

Allen RL, Bull S, Ripa M, Jonsson R (2003) Regional stratigraphy, basin evolution, and the setting of stratabound Zn-Pb-Cu-Ag-Au deposits in Bergslagen, Sweden: Final report for SGU-FoU project 03-1203/99, 80 p

Allen RL, Lundström I, Ripa M, Simeonov A, Christofferson H (1996) Facies analysis of a 1.9 Ga, continental margin, back-arc, felsic caldera province with diverse Zn-Pb-Ag-(Cu-Au) sulfide and Fe oxide deposits, Bergslagen region, Sweden: Econ Geol 91: 979-1008

Björklund E, (2011) Mineralogy and Lithogeochemical Signature of a Stratigraphic Profile through the Gränsgruvan Zn-mineralization, Bergslagen, Sweden: M.Sc thesis, Uppsala University, ISSN 1650-6553, 37 p

Jansson N, Erismann F, Lundstam E, Allen RL (2013) Evolution of the Paleoproterozoic volcanic-limestone-hydrothermal sediment succession and Zn-Pb-Ag and iron oxide deposits at Stollberg, Bergslagen region, Sweden: Econ Geol 108: 309-335

Lundstam E, Raat H, Öst J-O, Jansson N, Erismann F, Evins P (2013) Geological map of the Stollberg Ore Field. Unpublished map, Boliden Mineral

Raat H, Åberg L (2012) Geology, grade and tonnage estimate of the Gränsgruvan Zn-Pb-Ag deposit, Bergslagen Central Sweden: Internal Report, Boliden Mineral, 2012-21

Ripa M, (1988) Geochemistry of wall-rock alteration and of mixed volcanic-exhalative facies at the Proterozoic Stollberg Fe-Pb-Zn-Mn(-Ag)-deposit, Bergslagen, Sweden: Geologie en Mijnbouw 67: 443-457

Ripa M (1994) The mineral chemistry of hydrothermally altered and metamorphosed wall-rocks at the Stollberg Fe-Pb-Zn-Mn(-Ag) deposit, Bergslagen, Sweden: Mineral Deposita 29: 180-188

Stephens MB, Ripa M, Lundström I, Persson L, Bergman T, Ahl M, Wahlgren C-H, Persson P-O, Wickström L (2009) Synthesis of the bedrock geology in the Bergslagen region, Fennoscandian Shield, south-central Sweden: Geological Survey of Sweden Ba58, 259 p

Geology and genesis of granites and polymetallic skarn ores at Pitkäranta, Ladoga Karelia, Russia

Mira M. Valkama, Krister Leon Sundblad
Department of Geography and Geology, FIN-20014 University of Turku, Finland

Kyril I. Lokhov
SPb state university, St-Petersburg, Russia

Nigel J. Cook
Centre for Tectonics, Resources and Exploration, School of Earth and Environmental Sciences, University of Adelaide, Adelaide S.A. 5005, Australia

Abstract. The Pitkäranta ores are located northeast of Lake Ladoga in the southeastern part of the Fennoscandian Shield. They are hosted by Lower Proterozoic metamorphosed supracrustal rocks, < 1 km from the 1.54 Ga Salmi rapakivi batholith. The Pitkäranta ores constitute a classical skarn type, formed when granite-related hydrothermal fluids reacted with marble.

Combined U-Pb and Lu-Hf studies of zircons in small granite stocks, stockscheider pegmatites and stratiform pegmatites, outside the main Salmi Batholith, indicate severely disturbed U-Pb systems in these ore-related granites and pegmatites, which are considered to be caused by the ore-forming hydrothermal activity. Based on metal contents and ore mineral parageneses, several ore types have been identified. These types are not restricted to individual mines or mining districts but considered to reflect zoning within each ore body, which in turn reflect variations in the depositional conditions for the individual metals and respective mineral. The elevated contents of Cu, Zn, Pb, Ag, In, Sn, W, Mo and Be in the Pitkäranta ores, together with matching Pb isotope signatures between ore galena and potassium feldspar in the Salmi Batholith, confirm a rapakivi-related origin for the ores.

Keywords. pitkäranta, skarn, ore, granite, petrology, geochemistry

1 Introduction

Pitkäranta is an historic mining area along the northeastern shore of Ladoga, where Fe, Cu, Zn, Pb, Sn and Ag were exploited from more than 50 mines and prospects from 1810 to 1904. Numerous mineralogical publications already existed when Alfred Elis Törnebohm visited this mining district as a private consultant in autumn 1889. One result of his visit was that his skarn concept, developed for ores in Bergslagen (Sweden) in 1875, now came in use for ore systems outside Sweden; other results were the first geological map and the first genetic ideas on Pitkäranta that Törnebohm published in 1891. This pioneering work was soon followed by other classical studies, e.g Trüstedt (1904; 1907; 1908), Vernadsky (1911) and Erämetsä (1938). Other important studies include Palmunen (1939), Eskola (1949; 1951) and Khazov (1973). Most authors have chosen a skarn model suggesting that hydrothermal fluids emanated from the Salmi Batholith and reacted with the marble horizons. Very few geochemical and ore petrological studies have,

however, been made on Pitkäranta, none making use of multi-element analytical and modern microscope techniques.

The material used in this study was collected from outcrops and active quarries as well as from the dumps in the historic mine area in 2008, 2010 and 2011.

2 Geological background

The Pitkäranta region forms part of the Svecofennian and Archaean Domains in the southeastern part of the Fennoscandian Shield. The bedrock of the area (Fig. 1) is dominated by Palaeoproterozoic supracrustal rocks, which, together with gneissic Archaean dome structures, constitute an allochthonous terrane complex that amalgamated to the Archaean continent during the Svecokarelian orogeny at 1.9-1.8 Ga. The gneissic domes are surrounded by Early Proterozoic (Jatulian) amphibolite and marbles, which are overlain by Kalevian quartzites and mica schists.

All metamorphic rocks were cut by the 1.53-1.55 Ga Salmi Batholith, an A-type rapakivi granite complex (Neymark et al. 1994, Amelin et al. 1997). Several small (<1 km) granite stocks and stratiform pegmatitoids occur in the Proterozoic supracrustal sequence, immediately southwest of the Salmi Batholith at the same stratigraphic level as the ore-bearing skarns.

No orogenic episode post-dates the emplacement of the Salmi Batholith but deposition of adjacent sandstones and the emplacement of dolerites at 1452 Ma (Lubnina 2009) is recognized.

The polymetallic skarn ores of Pitkäranta constitute a 20 km long zone of hydrothermal products in the marble horizons. In addition, hydrothermal alteration and fluorite veins are also common in the small granite stocks immediately west of the Salmi Batholith.

The area is commonly divided into the Old Mining Area (within Pitkäranta town), the mining areas of Herberz, Vinberg, Hopunvaara and Lupikko as well as several smaller mines and prospects, like Kelivaara, Heposelkä and Uuksu.

The ores in the Pitkäranta district occur in the lower and upper carbonate layers of the Jatulian succession and are typical skarn ores. The main skarn minerals are diopside, garnet and epidote in association with fluorite and scheelite. Eskola (1951) divided the deposits into two groups; ores in the lower and upper carbonate
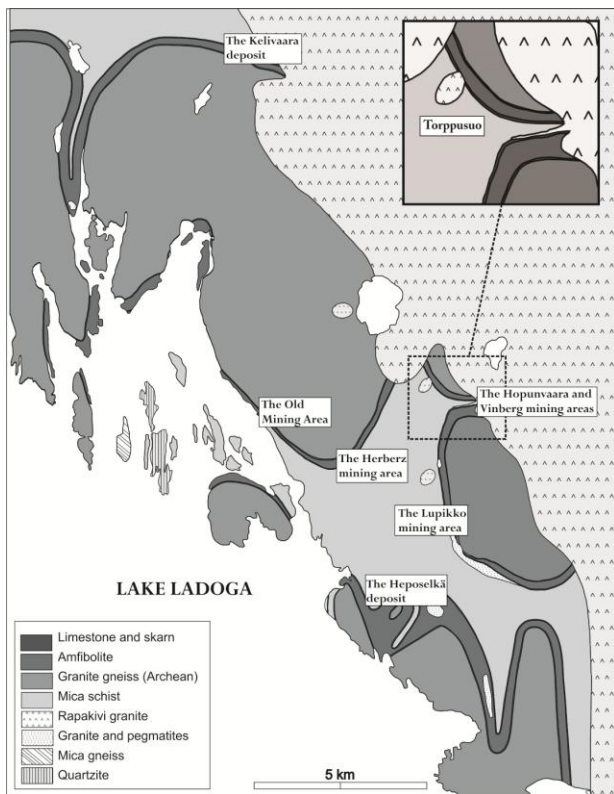
Figure 1. Geological map of the Pitkäranta region. Modified from Trüstedt (1907).

horizon respectively. The genesis and age of the ores have been discussed by numerous scientists. Törnebohm (1891), Trüstedt (1907), Eskola (1951), Khazov (1973) and many others have concluded a close relation between the Fe-, Cu-, Zn-, Pb-, Ag- and Sn- ores, skarn minerals and the emplacement of the rapakivi granites of the Salmi Batholith. This was supported by the lead isotopic work carried out by Larin et al. (1990) and Sundblad (1991) as well as the Sm-Nd age determination of the skarn minerals, which resulted in an age of 1491 ± 42 Ma (Amelin et al. 1991). Eskola (1951), Trüstedt (1907) and Palmunen (1939) also recognized that small scale deposition of molybdenite and pyrrhotite took place in conjunction with the intrusion of the Late Svecofennian (post-Ladogian) granites and pegmatites, when also the limestone was metasomatized into skarn. Such a two-stage formation of the Pitkäranta ores (minor Late Svecofennian Mo-mineralization and significant rapakivi-related Fe-Cu-Pb-Ag-Sn minor mineralization) was confirmed by the Re-Os data presented by Stein et al. (1996).

The ore and skarn minerals of Pitkäranta are rather well documented but the distribution of major and trace elements in the ore is less studied, except for the indium distribution (Vernadsky 1911; Erämetsä 1938) indicating up to 1 wt.% In in sphalerite and up to 0.5 wt.% in chalcopyrite. In addition to the common In-rich sphalerite, Valkama (2009) discovered roquesite in a sample from Hopunvaara with unusually high In/Zn ratio.

3 Results and Discussion

3.1 The granites and the pegmatites

Based on SIMS U-Pb investigations of zircons in the stratiform pegmatoid at Hopunvaara, age estimates were obtained, which group into 250-300, 950-1100 and 2756 Ma, as well as a concordant cluster with the age 1706±13 Ma. The zircons from the stratiform pegmatoid at Torppusuo constitute a concordant cluster with an upper intercept age estimate at 1482 ±14 Ma, while two zircon grains yielded a lower intercept age at 1025 ±16 Ma, both ages considered to reflect real events. Another grain gave an apparent age of 1200 Ma, but this grain is very discordant.

Two samples of the Lupikko granite stock were collected two meters under a stockscheider pegmatite. In the first sample, the zircons yielded concordant clusters at 255, 575-600 and 1620-1640 Ma and discordant clusters with ages in the range 980-1200 Ma. In the second sample, the zircons display two concordant clusters at 1710 ±16 and 1448 ±16 Ma respectively, thus very different from the first sample.

The above-mentioned age estimates are dramatically different from available geochronological data on the Salmi Batholith. In order to obtain an understanding of the scattered U-Pb age distribution in the investigated zircons, isotopic Hf-Nd systematics by LA-ICP-MS Lu-Hf in zircons and whole-rock TIMS Sm-Nd were applied. The main result of these investigations is that none of the investigated zircons can be considered as truly magmatic. Instead, most data plot outside the terrestrial array field (TA) for magmatic zircons of Vervoort & Blichert-Toft (1999), indicating significant metasomatic disturbance.

Another interesting result is that most of the zircons contain some excess radiogenic hafnium (above the TA field); with some calculated εHf(T) values of > 20, resulting in very young (and even negative!) hafnium model ages. Such an effect could originate from intense fluid-rock interaction and alteration due to Hf extraction from host rock minerals with high Lu/Hf ratios (Goltsin et al. 2010, Valley et al. 2010). In order to be able to transport high strength field elements (HSFE) as Zr and Hf, some water-halogen (Cl, F) fluids are necessary (Korzhinskaya & Ivanov 1988). Because fluorite is common, both as veins in the ore-forming granite stocks and in the skarn assemblage, adequate conditions for HSFE transport by the ore fluids are indicated, which is confirmed by the presence of excess radiogenic hafnium in zircons.

Zircons with unrealistically low U-Pb ages are considered metasomatic, while the zircons with too high ages are considered metasomatically altered, because they contain radiogenic Hf and plot above the TA field. The robust behavior of the U-Pb system in zircons under such conditions is thus strongly questioned. From one hand, the presence of abundant fluorine in the ore-forming fluid could dramatically change the U/Pb ratios in the zircons due to the high U mobility under such conditions, hence age estimates by the U-Pb isotopic system do not fit realistic geological scenarios, and are considered as an analytical artefact.

3.2 The Ores

The Old Mining Area. Approximately 880000 tons of ore were mined in the Old Mining Area from 1810 to 1904 for Fe, Cu and Sn as well as Ag (the latter from 1882). The mining area is divided into six groups; Schwartz, Meyer, Omeljanoff, Usko-Toivo-Rakkaus, Pervoi and Ristaus-Kelinoja. The ore types are usually quite Sn-rich (up to 27.5 wt.%) but show significant variations with respect to the Zn, Cu and Fe contents.

The ore in the Meyer mine represents the Cu-rich upper part of the mineralization while the lower part of the mineralization is more Fe rich. Positive correlations exist between several element pairs; Cu-Ag, Cd-Zn, Cu-Au, Zn-Bi, Fe-Li and Cd-S. Cassiterite, chalcopyrite and magnetite are the dominant ore minerals with accessory sphalerite and pyrite. Bornite, digenite, chalcocite and covellite are common in the Cu-rich parts of the ore.

The ore types in the Omeljanoff mine group show distinct variations with respect to Sn, Zn, Fe and Cu and a moderately high W content (up to 443 ppm). The Omeljanoff III mine was the most Sn-rich mine in Pitkäranta while the Omeljanoff IV mine mainly produced Cu. Positive correlations are noted for Cu-Ag, Cd-Zn, Cu-Zn, Mn-Sn, In-Bi and negative correlations for Cu-Fe and Sn-Cd. The dominant ore minerals are cassiterite with minor amounts of sphalerite and chalcopyrite.

The ore in the Usko-Toivo-Rakkaus mines contains up to 27 wt.% Zn, 3.5 wt.% Cu and 0.9 wt.% Sn and was mainly exploited for copper and zinc. 0.4 ppm Au has locally been noted but gold has never been exploited commercially. Positive correlations between Cu-Ag, Cu-Au, Zn-Cd and negative correlations between Fe-Li, Fe-Pb and Mn-Cd are noted. The dominant ore minerals in the Usko-Toivo-Rakkaus mines are sphalerite, chalcopyrite and pyrite with accessory cassiterite, pyrrhotite, magnetite and various Bi-minerals.

Hopunvaara. Mineralization in Hopunvaara became known already in 1814 and has been exploited for a number of commodities, including limestone and metals, but on a very small scale (in total 34 tons). It consists of two ore groups; Beck-Koskelo in the lower carbonate horizon and Pellinen-Klara in the upper carbonate horizon.

The Hopunvaara mines are magnetite-rich, but show locally high contents of Sn, Fe and Zn. Cu-rich ore is only found in the upper carbonate horizon. This ore also has high contents of Ag and As. Each mine has a characteristic trace element signature; Klara I/II is In-rich (up to 105 ppm), Klara III is rich in Mn, Be, In (up to 36.9 ppm) and locally Ga, the Arsenic shaft is very In-rich (up to 600 ppm) and Bi and locally W. A correlation between Zn and Cd is seen in all upper horizon mines. In Klara I/II, positive correlations for the element pairs Cu-As, Cu-Bi, In-Cd, Sn-Fe, Zn-In and In-Mn exist, while the only clear correlations for Klara II are between Cu-In, Mn-Sn, Mn-Zn and Sn-W. Magnetite and sphalerite dominate over accessory hematite, galena, chalcopyrite, arsenopyrite and cassiterite.

Vinberg. The Vinberg mining area can be divided into two parts (south; shaft 1 and north; shafts 2 and 3). The ore in shaft 3 contains up to 19.5 wt.% Fe, up to 400 ppm Sn, moderately high Li contents (up to 172 ppm) but very low As contents. Magnetite is the major ore mineral with accessory chalcopyrite, pyrite and sphalerite.

Herberz. The Herberz mining area was exploited for magnetite ore 1896 to 1904. It can be divided into two groups: Pikku Herberz and Iso Herberz, both in the upper dolomite carbonate. Magnetite ore occurs as a 1.5—2 m thick compact zone with a banded structure and occasionally (together with sulphides) in veins in the carbonate rock.

The Herberz ore has up to 44.70 wt.% Fe, 31.4 wt.% Zn, 400 ppm Sn, 148 ppm In and 2280 ppm As with a positive correlation between Cu-In, Fe-Mn, Fe-Sn and In-S. The ore is dominated by magnetite or sphalerite with accessory cassiterite, arsenopyrite, löllingite, galena and pyrite.

Lupikko. Small amounts (147000 tons) of ore were exploited from the Lupikko mining area for a few years (until 1904). Magnetite ore was the main commodity but the locally high Cu and Zn contents were also exploited economically. It is divided into a western and an eastern part, of which the western part was revealed by a strong magnetic anomaly. In the eastern part, a meter-thick magnetite-sphalerite ore with small amounts of chalcopyrite and pyrrhotite was mined. The western part of the Lupikko mining area includes the shafts 1, 1a, 3 and 4 as well as several smaller prospecting pits. Palmunen (1939) reported the ore in the western part as Fe-rich and Sn-rich sometimes even with tin lump ore in Lupikko 1 mine.

Samples investigated from Lupikko are all rich in Cu (up to 10.6 wt.%), Zn (up to 24.5 wt.%), Sn (up to 0.09 wt.%) and In (up to 109 ppm) locally also with high Ag contents (up to 166 ppm). Dominating ore minerals are cubanite and sphalerite as well as accessory pyrrhotite, chalcopyrite, löllingite and magnetite. Positive correlations exist for Cu-Fe, Cu-Sn and Ag-Cu and a negative correlation for Cu-Mn.

Kelivaara. The Kelivaara deposit is located 15 km north of the Old Mining area of Pitkäranta, where magnetite ore was indicated by geophysics (Trüstedt 1904). In the 1970's, Soviet geologists renamed this target "Kitilä" when the presence of ore was verified by drilling. The ore was test mined for Sn, Zn, Cu and Fe but the low metal prices did not allow proper exploitation (Khazov 1973, Smirnov 1977). Wolfram, In, Cd, Ag and Bi have also been recorded locally.

The Kelivaara ore represents at least two different ore types; one extremely Fe-rich (up to 52.80 wt.%) and another more Cu-rich (up to 6.86 wt.%) with up to 0.5 ppm Au and 132 ppm Ag). Positive correlations exist for Cu-Ag, Cu-In and Zn-In. Tin is moderately high (c. 0.1-0.2 wt.%) in most Kelivaara samples. A very high U content (212 ppm) was recorded in one sample. The dominating ore minerals are magnetite and sphalerite (with accessory chalcopyrite, pyrite and cassiterite) in the Fe-rich type and chalcopyrite and pyrite (with accessory sphalerite, galena, cassiterite and various Ag-minerals) in the Cu-rich type.

Heposelkä. The Heposelkä deposit is located south of Pitkäranta town and was for a short period mined for low-grade copper. The abundant fluorite made the ore

particular attractive for the smelter at Pitkäranta (Trüstedt 1907). Samples investigated in this study all have low contents of Cu, Fe, Zn, In and moderately high Sn contents (up to 570 ppm). Small amounts of pyrite, chalcopyrite and black sphalerite have been recognized together with minor amounts of chalcocite, covellite, digenite, cassiterite and sphalerite.

4 Conclusions

Although the true age of the stratiform pegmatoids and granite stocks are assumed to be similar as the main Salmi Batholith, U-Pb data fail to confirm this. Based on Lu-Hf isotope data it is suggested that the U-Pb balance in the zircons was intensely disturbed by the ore-forming fluids.

Several different ore types are found in a number of individual ore deposits from Kelivaara in the north, through the Old Mining field of Pitkäranta to the mining areas of Herberz, Hopunvaara, Lupikko and Heposelkä in the south. Although the mines and prospects exist in two separated carbonate horizons in the Pitkäranta-Kelivaara-Heposelkä district, none of these ore types are restricted to an individual mine or mining district. On the contrary, two or several ore types typically occur in one and the same mine, with gradational borders between each population, most probably reflecting zoning within each mine (ore deposit). The zoning most probably reflect variations in the depositional conditions for the individual metals and respective mineral. The fugacity of S and O_2 as well as temperature in hydrothermal fluids probably fluctuated during the deposition. The Cu-rich ore types formed during the stage of high sulphidation (high fS and T) while the Fe-rich ore types formed during a low sulphidation stage (low fS, T and higher fO_2). The presence of elevated contents of typical granite-related elements (e.g. Sn, W, Mo and Be) in each of these populations, makes a granite-related origin for these ores highly likely, which is in agreement with e.g. Trüstedt (1904), Palmunen (1939), Sundblad (1991).

The Pitkäranta deposits are potential objects for further investigations. Deeper knowledge of the ore types and ore parageneses, by means of ore petrology and fluid inclusion studies is needed so that the zoning patterns in each deposit and their precipitation conditions can be understood. A modern technical-economical resource evaluation of the Pitkäranta ores is also needed.

Acknowledgments

References

Amelin Y, Beljaev A, Larin A, Neymark L and Stepanov K. (1991) Salmi batholith and Pitkäranta ore field in Soviet Karelia. Rapakivi granites and related rocks symposium, IGCP Project 315, University of Helsinki.

Amelin YV, Larin AM & Tucker RD (1997) Chronology of multi-phase emplacement of the Salmi rapakivi granite-anorthosite complex, Baltic Shield: implications for magmatic evolution. Contib Mineral Petrol 127: 353-368.

Erämetsä O (1938) Über die Verbreitung des Indiums in Finnischen Mineralen und über seine Trennung von anderen Metallen, Ann Acad Scie Fenn A 154. Helsinki.

Eskola P (1949) The problem of mantle gneiss domes. Quarterly J Geol Soc 104: 461-476.

Eskola P (1951) Around Pitkäranta. Ann Acad Scie Fenn A Geol Geogr 27. Helsinki.

Goltsin NA, Lokhov KI, Kapitonov IN, et al. (2010) Polystage alteration of high carbon rocks from Ludikovi of the Onega depression. Reg Geol Metal 41:66-79.

Khazov RA (1973) Geological features of tin-mineralization in the Northern Ladoga district. Proc Acad Sci Karel filial 15. Petrozavodsk.

Korzhinskaya VS and Ivanov IP (1988) Experimental study of incongruent solubility of zircon in the system ZrO_2-SiO_2-H_2O-HCl at T=400-600°C and P=1 kbar. Doklady Acad Nauk USSR 299:4, pp. 970-973.

Larin AM, Neymark LA, Gorochovskij BM and Ovchinnikova GV (1990) Link between complex skarn ores of Pitkäranta region and Salmi rapakivi granites: Pb isotope evidence. Geological series 5, Akad Nauk, SSSR, Moscow, pp. 47-57

Lubnina NV (2009) East-European craton from Neoarcean to Paleozoic by paleomagnetic data. PhD thesis, Moscow.

Neymark LA, Amelin YV, Larin AM (1994). Pb-Nd-Sr isotopic and geochemical constraints on the origin of the 1.54-1.56 Ga Salmi rapakivi granite-anorthosite batholith (Karelia, Russia). Mineral Petrol 50:173-193.

Palmunen MK (1939) Pitkäranta: vv. 1934-1938 suoritettujen vuoriteknillisten tutkimusten valossa. Geologinen toimikunta. Geoteknillisiä julkaisuja 44.

Smirnov VI (ed.) (1977) Ore deposit of the USSR, volume III. Pitman Publishing, London, pp. 243-246.

Stein HJ, Markey RJ, Morgan JW, Sundblad K and Larin A (1996) Re-Os dating of molybdenites from Pitkäranta, Russia reveals two temporally district periods of ore formation: A rapakivi granite mask on late svecofennian Mo-W ores. International IGCP Project 315, Abstract volume, University of Helsinki, pp. 68-70.

Sundblad K (1991) Lead isotopic evidence for the orgin of 1.8-1.4 Ga ores and granitoids in the southeastern part of the Fennoscandian shield. Precambr Res 51:265-281.

Törnebohm AE (1891): Om Pitkäranta malmfält och dess omgifningar. Geol Fören Förh 13: 313-334.

Trüstedt O (1904) Om Keliwaara nyupptäckta malmfält vid Ladoga. Teknikern 374: 252-253.

Trüstedt O (1907) Bulletin de la commision géologique de Finlande no 19. Die Erzlagerstätten von Pitkäranta am Ladoga-See. Frenckellska tryckeri-aktiebolaget, Helsingfors.

Trüstedt O (1908) Geologiska Kommissionen i Finland Geotekniska Meddelander no 2. Bidrag till Pitkäranta malmfälts historik. Helsingfors tidnings och tryckeri-aktiebolagets tryckeri.

Valkama M (2009) An ore petrological and geochemical study of the polymetallic skarn ores at Pitkäranta, Ladoga, Karelia, Russia. MSc thesis. University of Turku.

Valley PM, Fischer CM, Hanchar JM (2010) Hafnium isotopes in zircon: A tracer of fluid-rock interaction during magnetite-apatite ("Kiruna – type") mineralization. Chem Geol 275:208-220.

Vernadsky V (1910) Notes on the distribution of chemical elements in the Earth's crust. Bulletin de l'Académie Impériale des Sciences de St.-Pétersbourg, pp. 1129-1144.

Vervoort JD & Blichert-Toft J (1999) Evolution of depleted mantle: Hf evidence from juvenile rocks through time. Geochim Cosmochim Ac 63:533–556.

The Nihe iron deposit, Anhui Province, eastern China: skarn, IOCG or porphyritic iron deposit?

Lejun Zhang
School of Resources and Environmental Engineering, Hefei University of Technology, Hefei 230009, China
Centre of Excellence in Ore Deposit (CODES), University of Tasmania, Hobart 7005, Australia
e-mail: Lejun.Zhang@utas.edu.au

Taofa Zhou
School of Resources and Environmental Engineering, Hefei University of Technology, Hefei 230009, China

David R Cooke
Center of Excellence in Ore Deposit (CODES), University of Tasmania, Hobart 7005, Australia

Yu Fan
School of Resources and Environmental Engineering, Hefei University of Technology, Hefei 230009, China

Zhaoshan Chang
Centre of Excellence in Ore Deposit (CODES) University of Tasmania, Hobart 7005, Australia
Economic Geology Research Unit (EGRU), School of Earth and Environmental Sciences, James Cook University, Townsville, Queensland 4811, Australia

Huayong Chen
Key Laboratory of Mineralogy and Metallogeny, Guangzhou Institute of Geochemistry, Chinese Academy of Sciences, Guangzhou 510640, China

Abstract. The Nihe iron deposit is a newly discovered large scale iron oxide deposit in the central part of the Middle and Lower Yangtze River region in eastern China. This study presents the latest discoveries from field and laboratory works dealing with the iron deposit. The hydrothermal alteration and mineralization have recently been subdivided into six stages and each stage is described in detail. Moreover, petrological, geochemical, geochronological (U-Pb dating and Ar-Ar dating) results are also reported. Our results show that the age of the magmatic and mineralization corresponds to the Early Cretaceous. Mineral chemistry (EPMA and LA-ICPMS) show fluids became more oxidized towards the late hydrothermal stage, and the trace elements in the magnetite are similar with selected skarn and IOCG deposits.

Keywords. Nihe iron deposit, Alteration, Mineralization, Geochronology, Mineral chemistry

1 Introduction

The Middle and Lower Yangtze River area, Eastern China, extends from Wuhan (Hubei province) to western Zhenjiang (Jiangsu province) and represents a major polymetallic mineral belt that includes more than 200 economic mineral deposits (Chang et al., 1991; Tang et al., 1998; Pan and Dong 1999). World-class iron ore deposits occur in the Lu-Zong and Ning-Wu ore clusters, which are continental fault-bounded volcanic-sedimentary basins. Iron oxide deposits tend to occur within diorite porphyry and in the contact zone between subvolcanic intrusions and volcanic or sedimentary rocks (Fig. 1). They are also hosted in volcanic rocks or in intercalated sedimentary beds. Previous studies have

termed these ore systems either "porphyrite iron deposits" (Ningwu Research Group, 1977; Mao et al., 2006, 2010) or skarn deposits (Pirajno, 2009). The typical alteration mineral assemblage comprises magnetite–apatite–actinolite (± pyroxene), similar to the Kiruna class of iron deposits (Frietsch, 1978; Hilderband, 1986). Some researchers have therefore suggested that these deposits can be classified as an end-member of the iron-oxide copper-gold (IOCG) deposit class (Mao et al., 2006, 2008). This study documents the geology, geochemistry, geochronology and isotope systematics of the Nihe iron deposit and proposes a new genetic model and classification of this type of iron oxide mineralisation.
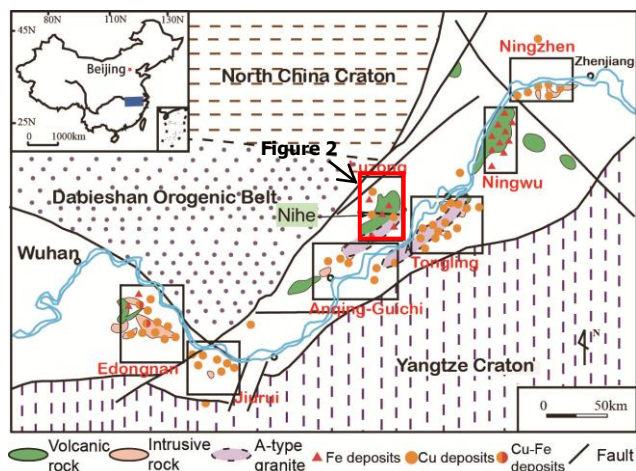
Figure 1. Geological map of the Middle and Lower Yangtze River area, Eastern China

2 Regional and deposit geology

The Luzong volcanic basin is located in the central part of the Middle and Lower Yangtze River area and contains numerous Cu-Au-Fe deposits. The sedimentary sequences in the Lu-Zong volcanic basin mainly belong to the Triassic, Jurassic, Cretaceous and Quaternary periods (Fig. 2). The overlying volcanic rocks are divided into four groups (from oldest to youngest): the Longmenyuan Formation (mainly hornblende trachyandesite, tuff and sandstone), the Zhuanqiao Formation (mainly trachyandesite, tuff and sandstone), the Shuangmiao Formation (mainly andesite, tuff and siltstone) and the Fushan Formation (mainly trachyandesite, tuff and ignimbrite). A number of Cretaceous syenite, monzonite and quartz diorite intrusions have intruded the sedimentary and volcanic rocks.

The Nihe Iron deposit is part of the Nihe mining district in the northwest of Luzong volcanic basin. Bedrocks comprise two volcanic units, the Zhuanqiao and Shuangmiao Formations. Intrusive rocks include diorite porphyry, syenite and monzonite. At Nihe, diorite porphyry and adjacent volcanic rocks are intensely and pervasively altered adjacent to massive magnetite orebodies that are hosted by both the intrusions and the volcano-sedimentary stratigraphy. Where least altered diorite porphyry preserves remnants of primary plagioclase and minor ortho-pyroxene phenocrysts, with a Fe-Ti oxide phase in the groundmass.
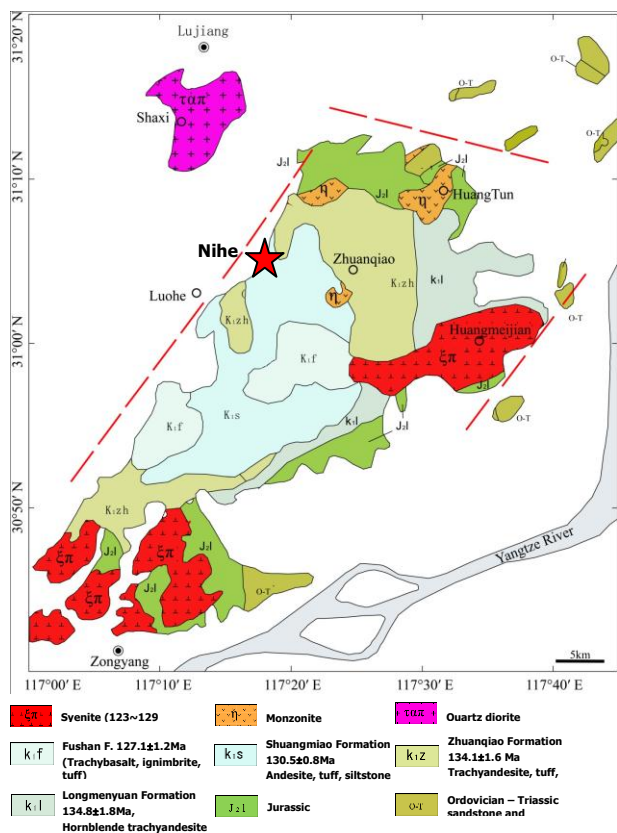
3 Alteration and mineralization

The diorite porphyry and the volcanic rocks surrounding the magnetite bodies are intensely and pervasively altered. There is little diorite porphyry that has not experienced some form of hydrothermal alteration. Weakly altered diorite porphyry preserves the original mineralogy, which consists of phenocrysts of plagioclase and minor orthopyroxene with a Fe-Ti oxide phase in matrix. We have divided hydrothermal alteration at Nihe into six stages. These are (from early to late) (1) an early alkali feldspar alteration stage, (2) prograde skarn, (3) retrograde skarn, (4) silicic alteration and sulphide alteration stage, (5) late vein stage and (6) supergene stage. Magnetite mineralization occurred during both the prograde and retrograde skarn stages, whereas sulfide mineralization formed during the siliceous and sulfide alteration stage.

The magnetite ore bodies occur in the diorite porphyry intrusion and at the contact between the diorite porphyry and trachyandesite of the Zhuanqiao Formation. Pyrite ore bodies are mainly hosted in volcanic rocks of the Zhuanqiao formation. The main iron ore types include massive, disseminated and vein type, locally with breccia textures. The iron ore bodies mostly comprise magnetite with coexisting pyroxene, garnet and anhydrite.

4 Geochronology

By using LA-ICP-MS zircon dating, we determined the ages of the magmatic rocks in the Nihe district. The results are summarised in Fig. 3, which shows that the magmatic activity in this area spanned from 134 Ma until 129 Ma, and most of the intrusions and dykes are associated with Zhuanqiao Formation volcanic rocks, and only the syenite porphyry is associated with the Shuangmiao Formation volcanic rocks.

We constrained the age of the mineralization by dating phlogopite, which co-existing with magnetite. The phlogopite $^{40}Ar/^{39}Ar$ dating gives an age of 131.2± 0.9 Ma, which is similar to the age of diorite porphyry.

Figure 2. Geological map of the Luzong volcanic basin, ages from Zhou et al. (2008)
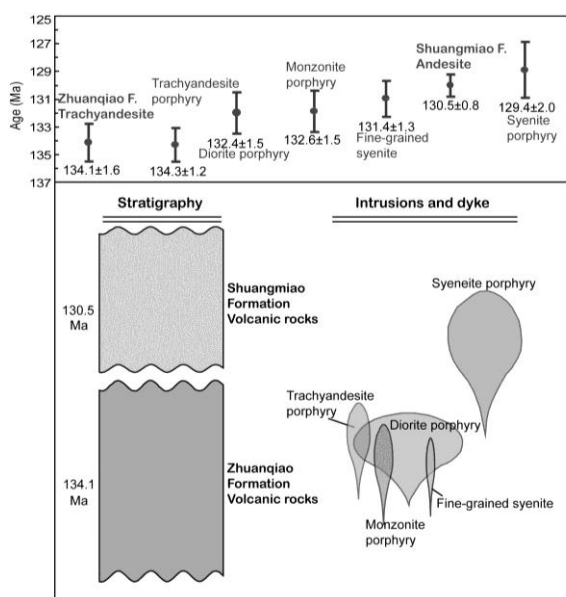
Figure 3. LA-ICP-MS zircon age determinations and schematic diagram depicting relative and absolute age constraints for the intrusions dated. The age of the Zhuanqiao Formation trachyandesite and Shuangmiao Formation andesite are from Zhou et al., 2008.

5 Conclusions

Several hydrothermal alteration stages have been investigated, the overlapping relationship indicate a complex history of fluid activity related to the formation of the Nihe iron deposit. The magmatic activity in the Nihe district spanned from 134 Ma until 129 Ma. The phlogopite $^{40}Ar/^{39}Ar$ dating result is 131.2± 0.9 Ma, which is similar to the age of diorite porphyry, and represent the age of magnetite mineralization. Based on the above geological and geochemical studies, The Nihe iron deposit is concluded to be a magnetite skarn deposit.

Acknowledgements

References

Chang YF, Liu XP, Wu YC, et al (1991) The Copper-Iron Belt of the Lower and Middle Reaches of the Changjiang River(in Chinese with English abstract). Beijing: Geol. Pub. House pp 1-56

Mao JW, Wang YT, Lehmann B (2006) Molybdenite Re–Os and albite 40Ar/39Ar dating of Cu–Au–Mo and magnetite porphyry systems in the Yangtze River valley and metallogenic implications. Ore Geology Reviews 29, 307-324

Mao JW, Yu JJ, Yuan SD, et al (2008) Iron oxide–copper–gold deposits: characteristics, present research situation and ore prospecting. Mineral Deposits 27, 267-278 (in Chinese with English abstract)

Mao JW, Xie GQ, Pirajno F, et al (2010) Late Jurassic–Early Cretaceous granitoid magmatism in Eastern Qinling, centraleastern China: SHRIMP zircon U–Pb ages and tectonic implications. Australian Journal of Earth Science 57, 51-78

Ningwu Project Group (1978) The porphyrite iron deposit of Ningwu. Beijing: Geological Publishing House, 1-320P（in Chinese）

Pan YM, Dong P (1999) The Lower Changjiang(Yangzi/Yangtze River) metallogenic belt, east central China: intrusion and wall rock-hosted Cu-Fe-Au, Mo, Zn, Pb, Ag deposits. Ore Geology Reviews 15(1): 177-242

Pirajno, F., Ernst, R.E., Borisenko, A.S., Fedoseev, G., Naumov, A.E., 2009. Intraplate magmatism in Central Asia and China and associated metallogeny. Ore Geology Reviews 35, 114-136

Tang YC, Wu YC, Chu GZ, et al (1998) Geology of Copper-Gold Polymetallic Deposits in the Along-Changjiang Area of Anhui Province (in Chinese with English abstract). Beijing:Geol. Pub. House pp 60-85

Zhou TF, Fan Y, Yuan F, Lu SM, Shang SG, David RC, Sebastien M, Zhao GC (2008) Geochronology of the volcanic rocks in the Lu-Zong (Lujiang-Zongyang) basin and its significance. Science in China (Serice D-Earth Sciences) 51(10): 1470-1482

Singoyi B, Danyushevsky L, Davidson GJ, Large R, Khin Zaw (2006) Determination of trace elements in magnetites from hydrothermal deposits using the LA ICP MS technique in: Abstracts of Oral and Poster Presentations from the SEG2006 Conference, Keystone, USA pp367-368

S 3.13:
Uranium and thorium deposits

Convenors:
Michel Cuney & Peter Sorjonen-Ward

The giant Alum Shale polymetallic deposits of Jämtland, Sweden – a major potential low cost supplier of uranium for the future

Robert Beeson
Aura Energy Ltd, 19-23 Prospect Street, Box Hill, Victoria 3128, Australia

Abstract.

The Alum Shale of Jämtland is host to extremely large deposits of uranium and vanadium. A widespread unit through northern Europe, the Alum Shale has been a historic source of alum, oil and uranium. The Alum Shale is essentially a black schist, comprising fine grained quartz, white mica, organic carbon and pyrite, with frequent quartz-calcite veining. In Jämtland the Alum Shale occurs at or close to the base of the Caledonoid thrust sheets overlying the Baltic Shield. Structural thickening has resulted in thicknesses up to 250 metres. Total mineral resources in the district are approximately 5 billion tonnes, at a grade of approximately 160ppm U_3O_8, plus important co-products vanadium, nickel, molybdenum and zinc. Previously considered uneconomic, bacterial leach technologies have demonstrated that metals in the shales can be extracted at low cost. Leach extractions of up to 85% of the uranium, and 66% of the nickel indicate the suitability of the Shale to this technology. A scoping study has suggested that a notional 30Mtpa operation would produce approximately 8 Mlbs of U_3O_8 per annum, plus other metals. Such a project has a Net Present Value of $1.85 billion, and operating costs, after co-product credits, of less than $30/lb.

Keywords. uranium, vanadium, carbonaceous, Alum Shale, bacterial leach

1 Introduction

The Alum Shale Formation is a thin, generally 10-60m, shale unit of Upper Cambrian and Lower Ordovician age, overlying the stable Baltic Shield. The Alum Shale has a broad lateral extent, from the Maritime Provinces of Canada to Estonia.

The unit is carbonaceous, generally containing 10-15% organic carbon in central Sweden. At low metamorphic grades the Alum Shale is an oil shale, and was a source of oil in Sweden during the Second World War. This carbon is anthracitic in maturation level in Jämtland.

These shales have high concentrations of certain metals, notably uranium, vanadium, molybdenum, nickel and zinc. Uranium was previously produced at Ranstad in southern Sweden and Estonia.

2 The Alum Shale in Jämtland

Exploration for uranium in the 1970s located several tens of square kilometres with the development of relatively thick Alum Shale in Jämtland. Typical thicknesses of the Alum Shale where this is not deformed are from a few metres to 60 metres. However, tectonic repetitions of the Shale in Jämtland have produced thicknesses of the Shale of in excess of 250m. This thickening, combined with the relatively thin cover of overlying Ordovician limestone, offers the possibility of low cost mining. .
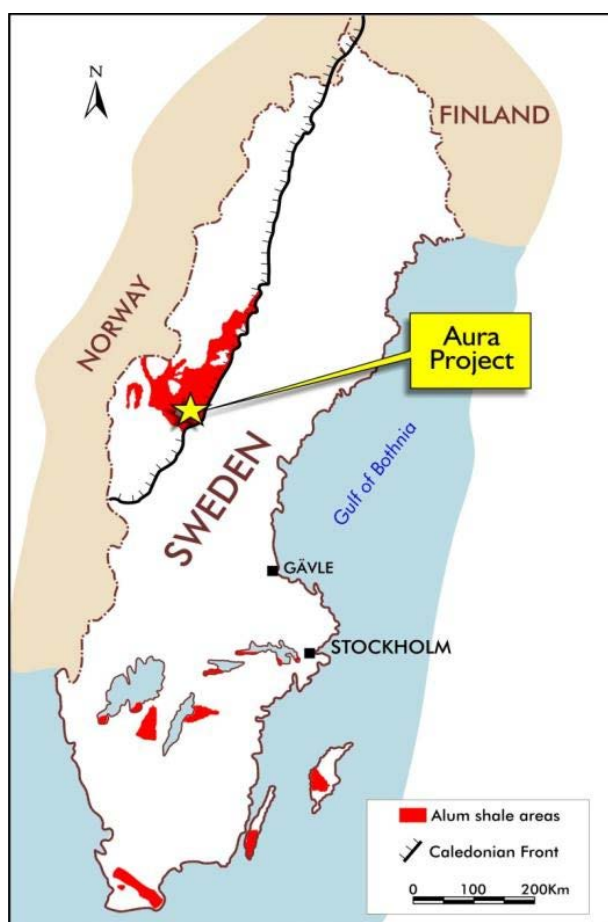
Figure 1. Location of Häggån Project within the Swedish Alum Shale belt, Jämtland, Central Sweden

The Jämtland Alum Shales occur in the lower nappes of the Caledonian allochthon. The shales are more penetratively deformed than in other areas of Sweden, and have been subject to temperatures of 200-300C (Andersson, A., Dahlman, B, Gee, D.G., and Snall, S, 1985).

The Alum Shale is underlain by sandstones and siltstones, locally carbonaceous, of Middle Cambrian age. It is generally overlain by an Ordovician limestone.

3   The mineralogy of the Alum Shale

The Alum Shale in Jämtland is a fine-grained, carbonaceous schist. The groundmass comprises quartz, feldspar, white micas and carbon.

The schist contains two forms of pyrite, one pre-deformation, and the second post-deformation. In addition the schist contains variable amounts of quartz-calcite veining.
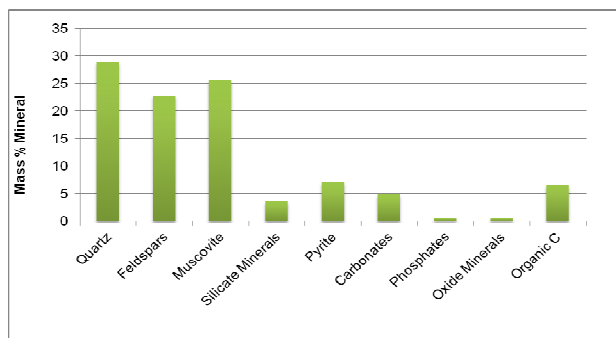
Figure 2 - Modal mineralogy of Häggån sample determined by QEMSCAN PMA analysis.

Limestone bands of centimetres to metres thickness occur within the schist.

The uranium, molybdenum and vanadium have been shown to be concentrated in the organic/mica matrix. Nickel and zinc are preferentially concentrated within the pyrite grains.

3   Uranium resources in the Häggån Project

A total resource has been estimated for the deposit reported in accordance with the JORC Code and Guidelines, using the method of ordinary block kriging to estimate grade and tonnage.

U_3O_8 (100ppm Cutoff)	Tonnes (Bt)	U_3O_8 (ppm)
Inferred	**2.35**	**155**

Table 1: Inferred Resources for the Häggån Project (Bt = billion tonnes)

The average grade of other metals present in the resource are: molybdenum 207ppm, vanadium 1,519ppm, nickel 316ppm, and zinc 431ppm.

These polymetallic resources are exceptionally large, and the uranium resource constitutes the second largest undeveloped resource anywhere in the world. In addition the Project hosts one of the largest vanadium resources.

4   Low-cost bacterial leach technology

Black schists are typically considered to be challenging metallurgically. As with the Alum Shale resources can be very large, but grades can be modest. Hence the Alum Shale has been previously considered a potential high cost source of uranium.

The primary issue has been the high cost associated with acid addition to extract the uranium. Recently the pyrite

has been recognised as a possible source of acid within the ore itself. Re-examination of the geochemical data showed that on average the material should be net acid generating, providing an excellent basis to pursue this option.

Generation of sulphuric acid requires a means of oxidation of the pyrite. Bacterial leaching to catalyse the oxidation of pyrite was demonstrated to be the most effective process for generating this acid.

Bacterial heap leaching is widely applied in the copper industry, particularly in Chile. The process is also well suited to uranium leaching as the oxidation of pyrite produces ferric iron, which acts as the oxidant in the uranium dissolution reaction. Precipitation of ferric iron to ferrous sulphate produces the sulphuric acid required for the uranium leaching reaction. In the presence of appropriate bacteria the process is autocatalytic, allowing for sustained leaching.

Method	Extraction			
	U (%)	Ni (%)	Mo (%)	V (%)
Column	85%	66%	22%	0.7%

Table 2 - Summary of bacterial column leach results

The results suggest that excellent uranium recovery can be achieved by bacterial heap leaching. These extractions can be obtained at coarse crush sizes up to 25mm. This result demonstrated the potential to utilise a coarse-crushed low-cost bacterial heap leach operation for the Häggån material. Importantly the acid consumption was drastically reduced, while the recovery was maintained.

5   Conclusions

The Jämtland County of Sweden has now been demonstrated to contain some of the world's largest deposits of uranium, vanadium and other metals. Exploration over the past seven years has defined these resources, and emerging technologies have identified a means of extracting the metals economically.

A Scoping Study completed for the Häggån Project has estimated that bacterial heap leaching can transform a previously uneconomic deposit into an economically attractive project.

The key outputs of the Scoping Study include a Net present Value, at a 10% discount rate, of US$1.85B, and a rate of return of 49%.

Importantly the Project would have an operating cost of less than US$30/lb U_3O_8 when nickel and molybdenum are treated as by-products. Annual production from such a project would place it among the world's largest uranium producers.

Acknowledgements

References

Andersson, A, Dahlman, B, Gee, D.G., and Snäll, S, 1985,
"The Scandinavian Alum Shales: Sveriges Geologiska
Undersoekning, Serie Ca: Avhandlingar och Uppsatser I A4,
NR 56, 50p.

The paragenesis and chemistry of alteration minerals within the basement rocks associated with the P2 fault and the McArthur River uranium deposit, Athabasca Basin

E.E. Adlakha*; K. Hattori
Department of Earth Science, University of Ottawa, Ottawa, Ontario, Canada, K1N 6N5
*eadla028@uottawa.ca

E.G. Potter
Geological Survey of Canada, Booth Street Complex, Ottawa, Ontario

Abstract. The main ore body (Zone 2) of the McArthur River deposit, Athabasca Basin, is almost completely hosted in the basement rocks immediately below the Athabasca sandstones, and is spatially associated with the P2 reverse fault. The Paleoproterozoic basement rocks have undergone upper-amphibolite facies metamorphism, retrograde metamorphism, paleo-weathering, diagenetic effects from the overlying sandstones and multiple episodes of hydrothermal alteration. Peak metamorphism produced garnet-biotite-cordierite assemblages in paragneiss and metapelite, plus quartzite. Three distinct horizons occur below the unconformity: i) a lowermost Green Zone formed through retrogression then paleo-weathering and is characterized by the chloritization of ferromagnesian minerals and illitization of K-feldspar, ii) an overlying Red Zone of pervasive hematite and kaolinite alteration due to paleo-weathering, and iii) a Bleached Zone that formed along the unconformity from K-bearing, diagenetic, basinal fluids that crystallized coarse-grain illite and altered kaolinite to dickite. Multiple stages of hydrothermal activity overprinted earlier alteration minerals, particularly along the P2 Fault and proximal to the ore body. Two generations of tourmaline occur along the P2 Fault Zone: an earlier, coarse-grained dravite, and later, fine-grained magnesiofoitite. A second chlorite-forming event, a third illite-forming event, and a second hematitization-rutilization event have also occurred along the P2 fault within the basement.

Keywords. Uranium, Athabasca Basin, McArthur River, Alteration, Fault

1 Introduction & Background

The basement rocks below the eastern Athabasca Basin are part of the Wollaston Group and host the McArthur River deposit (Fig. 1), the largest known high-grade uranium deposit. The Wollaston Group consists of pelite, semi-pelite, arkose, calc-silicate and quartzite that was were subsequently metamorphosed during the Tran-Hudson orogeny (ca. 1.8-1.9 Ga; Lewry and Sibbald 1980) under upper amphibolite facies conditions. Granitic pegmatite lenses intrude the metasediments and likely formed from local partial melting after peak metamorphism. Substantial erosion during exhumation of the basement rocks developed a paleo-weathering profile before the deposition and subsequent diagenesis of the Athabasca Group sandstones (beginning at ca. 1.73 Ga; Kyser et al. 2000). The Athabasca Group sandstones consist of a succession of fluvial to marine quartz-dominated sediments, currently preserved at a maximum thickness of 1500 m in the centre of the basin. Above the McArthur River deposit, the preserved thickness of the sandstones is approximately 500 m. Immediately above the deposit, the sandstone has been intensively silicified.

The Zone 2 ore body (primary mineralization at 1521 ± 8 Ma; McGill et al. 1993) is the main deposit at McArthur River and is almost entirely hosted within the basement rocks immediately below the unconformity. The ore body is structurally controlled by two faults: the P2 reverse fault and the Vertical Quartzite fault. The P2 reverse fault is one of the most prominent structures within the Athabasca Basin is responsible for thrusting the basement rocks above the overlying sandstones by as much as 80 m (McGill et al. 1993). The structure, trending 045°/45°SE, is predominantly hosted within graphitic pelite in the basement but is also expressed as a series of splays in the overlying sandstones due to the later reactivations of the fault. Hydrothermal alteration has been documented to be structurally controlled along the P2 Fault, as it occurs along the shear zone, splay faults, and fractures (Jefferson et al. 2007). The Vertical Quartzite (VQ) fault is a steeply dipping structure between the footwall quartzite and cordierite-bearing pelite. The rocks adjacent to the P2 and below the ore body show evidence of extensive fluid/rock interaction as they are highly brecciated and altered. Therefore, the P2 Fault may have served as a fluid pathway for uraniferous fluids to permeate the basement rocks and precipitate the ore.

2 Sampling & Methods

Field work was conducted in August, 2012, and consisted of the sampling of drill-core along the P2 structure and within the McArthur River underground mine (Fig. 1). Two background holes (non-mineralized and not intersecting the P2 Fault: MC-344 and -385) and four drill-holes along the P2 Fault were sampled: two are non-mineralized and cross-cut the P2 Fault (MC-361/2), and two are sub-economic holes that cross-cut the P2 (MC-370, -349). Twelve drill-holes were sampled from the McArthur River mine site: two from Zone 1, nine from Zone 2 (the main ore body), and one from Zone 3. Thin section petrography using transmitted and reflective light microscopy was used to identify minerals and to
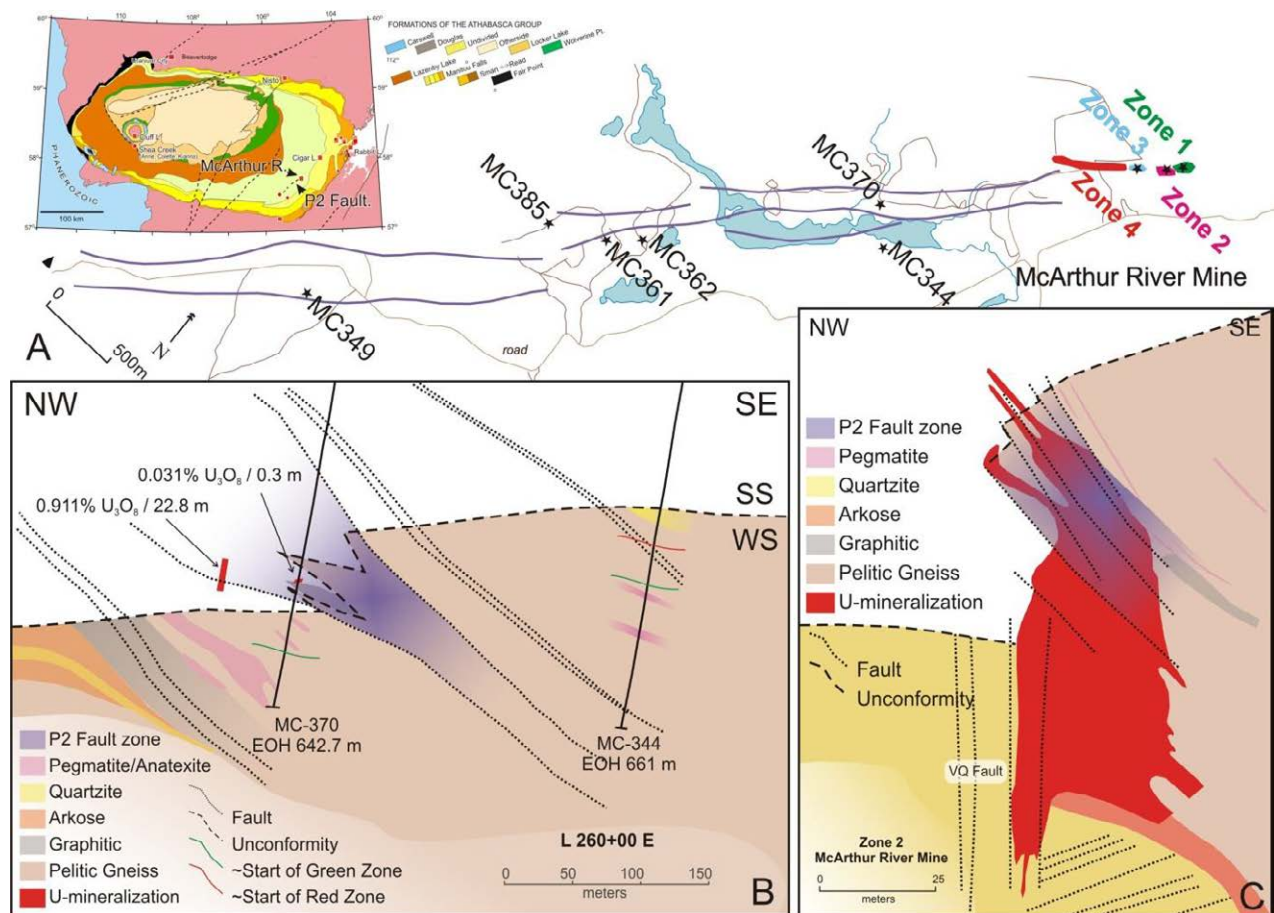
Figure 1. A) A plan-view map showing the P2 Fault surface expression, respective sample drill collars, and the McArthur River mine site. A regional map (adapted from Jefferson et al., 2007) of the Athabasca Basin is in the upper left corner and shows high-grade uranium deposits and major structural features including the P2 reverse fault (highlighted in white). **B)** Cross-sections (NW-SE) of exploration line 260E showing sampled drill holes MC-370 & MC-344 and **C)** the Zone 2 ore-body from McArthur River Mine. The P2 Fault Zone is highlighted in both sections.

characterize textural relationships in polished thin sections. Qualitative identification of alteration minerals was carried out by Terraspec short-wave infrared spectroscopy (SWIR) on drill-core samples and electron dispersive spectroscopy (EDS) using a JEOL 6610LV scanning electron microscope (SEM) at the University of Ottawa on carbon-coated polished thin sections. Textural relationships between alteration phases were determined through back-scattered electron (BSE) imaging. Quantitative analysis of biotite, garnet, illite, chlorite, and tourmaline for major and minor element constituents (SiO_2, TiO_2, Al_2O_3, FeO, MnO, ZnO, MgO, CaO, Na_2O, K_2O, Cl, BaO, F and SrO) were measured using a JEOL 8230 electron-probe microanalyzer (EMPA) at the University of Ottawa. EMPA data for magnesiofoitite is presented in Table 1.

3 Results

3.1 Alteration preceding the uranium mineralization

In order to understand the alteration associated with the P2 fault and the McArthur River ore body, detailed work focused on two drill-cores approximately 150 – 200 m away from the P2 Fault (and any apparent mineralization) to characterize regional alteration.

Below the unconformity (200-300 m) the rocks show

a laterally extensive alteration profile consisting of overprinting zones: a lower Green Zone, a middle Red Zone, and a Bleached Zone that occurs along the unconformity. Relatively unaltered metapelite is found well below the unconformity and contains pink garnet, fresh to slightly chloritized biotite, chloritized cordierite, slightly illitized K-feldspar, and quartz (Fig. 2A). BSE-images of cordierite show evidence of illitization at grain boundaries and fractures (Fig. 2C). The least-altered rocks gradationally transition into the overlying Green Zone that records chloritization due to retrogression, which was enhanced during paleo weathering and hydrothermal activity. The Green Zone is dominated by two generations of chlorite: i) Al-chlorite (sudoite) that completely replaces garnet and cordierite, and ii) Fe-chlorite that occurs as coarse (300 μm) radial aggregates and that replaces biotite. The feldspar in the Green Zone is completely replaced by fine-grain illite. There is also evidence for the addition of K within chloritized garnets as illite occurs as discrete fine-grained aggregates within the altered grains (Fig. 2B). The Green Zone is overprinted by the Red Zone that developed during the weathering of the basement rocks. Hematite and kaolinite are abundant within the Red Zone and alter Fe-bearing minerals and illite, respectively (Fig. 2D). The presence of kaolinite and hematite alteration is consistent with alteration that would result from a low temperature, oxidizing, and surficial fluid. The Bleached Zone occurs

Table 1: Chemical composition of dravite and magnesiofoitite within rocks along the P2 Fault. Atom proportions are O = 24.5

drill-hole	MO227 (mineralized)	MC3559 (mineralized)		MC362 (barren)	MC361 (barren)	MC349 (sub-ec)
sample (depth)	146 (Zone 2 u/g)	201 (Zone 1 u/g)		122 (637.9 m)	109 (587.6 m)	99 (~578 m)
host rock	*pelite*	*graphitic pelite*		*bleached SS*	*pegmatite*	*brecciated pelite*
	magnesiofoitite	magnesiofoitite	dravite	magnesiofoitite	dravite	dravite
	x̄ 1σ	x̄ 1σ	x̄ 1σ	x̄ 1σ	x̄ 1σ	x̄ 1σ
wt%						
SiO2	35.03 1.22	35.68 3.31	35.35 0.31	34.37 0.29	35.34 0.09	35.52 0.26
TiO2	<0.02	<0.02	1.06 0.15	<0.02	1.36 0.08	1.29 0.08
Al2O3	34.85 0.88	34.06 1.25	32.06 0.15	33.29 0.91	31.75 0.15	31.83 0.19
FeO (T)	1.45 0.33	0.20 0.02	3.56 0.02	2.10 0.20	4.77 0.02	4.68 0.18
MnO	<0.02	<0.02	0.01 0.01	<0.02	0.03 0.01	0.02 0.02
ZnO	<0.02	<0.02	0.01 0.01	<0.02	0.00 0.01	0.01 0.02
MgO	7.26 0.20	8.11 0.80	8.34 0.06	6.96 0.04	7.63 0.04	7.68 0.06
CaO	0.11 0.04	0.02 0.01	1.27 0.25	0.05 0.01	1.01 0.05	1.36 0.12
Na2O	0.73 0.21	0.59 0.04	1.71 0.11	0.83 0.07	2.05 0.04	1.73 0.07
K2O	0.02 0.02	<0.02	0.07 0.01	<0.02	0.07 0.01	0.07 0.01
Cl	<0.02	<0.02	<0.02	<0.02	<0.02	<0.02
BaO	0.02 0.02	<0.02	0.01 0.01	<0.02	0.02 0.02	0.01 0.01
F	0.04 0.02	0.14 0.22	0.42 0.03	0.18 0.09	0.22 0.08	0.57 0.08
SrO	<0.02	<0.02	0.00 0.01	0.03 0.04	0.01 0.01	0.02 0.02
Total	79.51 1.51	78.79 5.22	83.70 0.22	77.77 0.93	84.15 0.13	84.56 0.13
F/Cl	12	80	134	24	246	557
apfu						
T: Si	5.81	5.92	5.75	5.87	5.76	5.77
Al	0.19	0.08	0.25	0.13	0.24	0.23
ΣT	6.00	6.00	6.00	6.00	6.00	6.00
Z: Al	6.00	6.00	5.90	6.00	5.85	5.86
Fe			0.10		0.15	0.14
Y: Al	0.64	0.60		0.56		
Fe	0.20	0.03	0.39	0.30	0.50	0.49
Ti			0.13		0.17	0.16
Mg	1.80	2.00	2.02	1.77	1.85	1.86
Ca			0.22		0.18	0.24
□	0.40	0.36	0.24	0.36	0.31	0.26
ΣY	3.03	3.00	3.00	2.99	3.00	3.00
X: Na	0.23	0.19	0.54	0.28	0.65	0.55
K	0.01	0.01	0.01	0.01	0.01	0.02
□	0.76	0.80	0.44	0.71	0.34	0.44
ΣX	1.00	1.00	1.00	1.00	1.00	1.00
B: B*	3.00	3.00	3.00	3.00	3.00	3.00
O: OH*	3.98	3.93	3.79	3.90	3.89	3.71
F	0.02	0.07	0.21	0.10	0.11	0.29
ΣO	4.00	4.00	4.00	4.00	4.00	4.00

□ = vacancy; u/g = underground collared hole; * determined by stoichiometry;   FeO (T) = total Fe

above and below the unconformity as fine grained white-yellow clay alteration that overprints the Red Zone in drill-core. Samples from the Bleached Zone (Fig. 2F) show that alteration is dominated by fine-grained dickite and two generations of illite: early, fine-grained illite and late, coarse-grained illite. Coarse-grained illite also persists to the Red Zone along the P2 Fault. SWIR spectral analyses of the Red and Bleached Zone suggest a mixture of illite-kaolinite and illite-dickite, respectively. The presence of dickite in the Bleached Zone indicates that the fluid responsible for its formation was higher temperature than the fluid that produced the kaolinite in the Red Zone. Therefore, the Bleached Zone was probably formed by a higher temperature, K-bearing, diagenetic, basinal fluid that reacted with the basement rocks and propagated along the P2 during the lithification of the Athabasca sandstones.

3.2 Alteration associated with the P2 fault

Two generations of Mg-tourmaline occur consistently along the P2 Fault (within 50 m) and are absent from the aforementioned regional alteration profile: early dravite and later magnesiofoitite (alkali-deficient dravite). Euhedral-subhedral, coarse-grained (up to 0.5 mm), dravite $[(\square_{0.4}Na_{0.6})(\square_{0.2}Mg_{1.9}Fe_{0.5}Ca_{0.2}Ti_{0.2})(Al_{5.9}Fe_{0.1})(Si_{5.7}Al_{0.3}O_{18})(BO_3)_3(OH_{3.8}F_{0.2})]$ forms wide (1-2 cm) veins (Fig. 3A) or isolated grains, and radial aggregates of fine-grained (<0.2 mm) magnesiofoitite $[(\square_{0.75}K_{0.08}Na_{0.17})(\square_{0.23}Ca_{0.02}Fe_{0.04}Mg_{2.10}Al_{0.61})Al_6(Al_{0.22}Si_{5.78}O_{18})(BO_3)_3(F_{0.02}OH_{3.98})]$ occur as thin veinlets (< 2 mm), as overgrowths on earlier dravite (Fig. 3C) or disseminated within fine-grained illite (Fig. 3F). Both species of tourmaline show high atomic ratios of F/Cl. Discrete alteration events also occur along fractures and as veinlets along the P2 Fault Zone: i) late chlorite and illite assemblage occurs as veins and cross-cut tourmaline alteration (Fig. 3F) adjacent to the Zone 2 orebody (H493), and ii) a second oxidation event (hematite + rutile) restricted to fractures within the P2 zone overprints tourmaline (Fig. 3D) proximal to sub-economic mineralization (MC349).

4 Summary
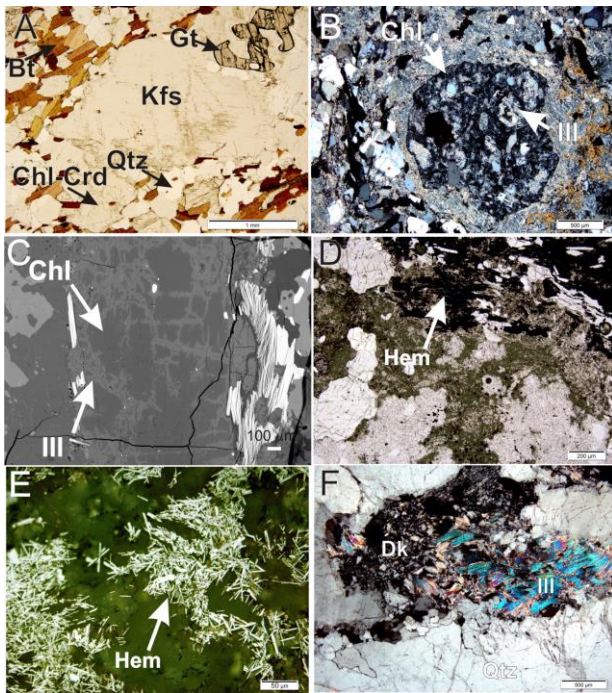
Figure 2. Microphotographs showing representative mineralogy of the alteration profile observed within the basement rocks. **A)** Unaltered biotite (Bt) and garnet (Gt), slightly illitized K-feldspar (Kfs), chloritized cordierite (Chl-Crd) and quartz within metapelite (MC344, 651.5 m). **B)** Chloritized and illitized garnet, and **C)** chloritized cordierite (BSE image) showing illitization along fractures from a metapelite (MC344, 525.9 m) of the Green Zone. **D&E)** Hematite overprinting metapelite in the Red Zone (MC385, 678.8 m). **F)** Coarse-grain illite and dickite overprint fine-grain illite within basal quartzite (MC344, 499.4 m).

Figure 3. Microphotographs that show alteration phases along the P2 Fault and the host rocks the ore body. **A)** An early dravite (Dv) vein (see Table 1 for chemical analysis) along the P2 in Zone 1 (H3559, 20.5 m). **B&C)** Two generations of tourmaline: early coarse grain dravite and later fine-grain aggregates of magnesiofoitite (Mgf) that occur as veinlets and overgrowths (MC349, 575 m). **D&E)** Rutilization of early dravite along grain boundaries and fractures (BSE-image) and hematite overprinting quartz in metapelite along the P2 Fault (MC349, 578 m). **F)** A chlorite/illite veinlet that crosscuts magnesiofoitite alteration within a chlorite breccia along the P2 fault proximal to the Zone 2 ore-body (H347, 45 m).

The alteration along the P2 fault cross-cuts the chlorite and illite alteration of the Green Zone that formed by retrogression and paleo-weathering fluids, the hematite and kaolinite alteration of the Red Zone that formed from paleo-weathering of the basement regolith, and the dickite and illite alteration of the Bleached Zone that formed from a diagenetic K-bearing fluid. Two generations of tourmaline occurs along the entire length of the P2 and their major chemistry is consistent regardless of their position relative to mineralization. A late chlorite and illite event overprints the tourmaline formation proximal to the Zone 2 ore body, and a hematite + rutile oxidation event overprints the tourmaline proximal to sub-economic mineralization farther along the P2. Intense alteration is concentrated within the P2 structure adjacent to the McArthur River deposit, confirming that the P2 fault was a conduit for an uraniferous hydrothermal fluid. Further investigation into the chemistry and paragenesis of alteration associated with mineralization is in progress to elucidate the reactions during the uranium mineralization event.

References

Jefferson CW, Thomas DJ, Gandhi SS, Ramaekers P, Delaney G, Brisbin D, Cutts C, Quirt D, Portella P, Olson RA (2007c) Unconformity-associated uranium deposits of the Athabasca Basin, Saskatchewan and Alberta. Mineral Deposits of Canada: A Synthesis of Major Deposit Types, District Metallogeny, the Evolution of Geological Provinces, and Exploration Methods. Geological Association of Canada, Mineral Deposits Division, Special Publication No 5:273-305

Kyser K, Hiatt E, Renac C, Durocher K, Holk G, Deckart K (2000) Diagenetic fluids in Paleo- and Meso-Proterozoic sedimentary basins and their implications for long protracted fluid histories. Mineralogical Association of Canada Short Course 28:225–262

Lewry JF, Sibbald TII (1980) Thermotectonic evolution of the Churchill province in northern Saskatchewan. Tectonophysics 68:45–82

MacDonald C (1980) Mineralogy and geochemistry of a Precambrian regolith in the Athabasca Basin. Dissertation. University of Saskatchewan

McGill B, Marlatt J, Matthews R, Sopuck V, Homeniuk L, Hubregtse J (1993) The P2 North uranium deposit Saskatchewan, Canada. Exploration Mining Geology 2(4):321

Fraser Lakes Zone B uranium-thorium-REE deposit, Saskatchewan, Canada: 3D GOCAD modeling to initiate a NI 43-101 inferred resource estimate

Irvine R. Annesley* & Christine L. McKenchnie, Allan Armitage
University of Saskatchewan, Saskatoon, Canada, ira953@mail.usask.ca, (* presenting author), cla598@mail.usask.ca

Julie Mercadier
Formerly of G2R, Nancy-Universite, CNRS, CREGU, Nancy, France, julien.mercadier@yahoo.fr

Alan Sexton
GeoVector Management Inc., Nepean, Canada, aarmitage@geovector.com, asexton@geovector.com

Terrance S. Bogdan
Formerly of JNR Resources Inc., Saskatoon, SK, S7K 0G6, terranceb@jnrresources.net

Abstract. The Fraser Lakes Zone B uranium-thorium-rare earth element (U-Th-REE) mineralization is associated with a series of ca. 1800 Ma sub-parallel granitic biotite-quartz-feldspar pegmatite dykes intruded into the tectonic decollement between the Paleoproterozoic Wollaston Group pelitic (+/-graphitic) gneisses and the underlying Archean granitoid orthogneisses. A 3D GOCAD model of the U-Th-REE mineralization indicates there is between 7,146,652 and 17,866,629 lbs U (i.e. between 3,248 and 8,121 metric tons U) in the mineralized granitic pegmatite, with abundant Th and REES. A preliminary NI 43-101 inferred resource estimate yielded 6,960,681 lbs of U_3O_8 (i.e. 3,164 metric tons) within 10,354,926 tonnes at an average grade of 0.030% U_3O_8, with a high Th content (i.e. using the COG of 0.01% U_3O_8) of 5,339,219 lbs of ThO_2 (i.e. 2,427 metric tons) at an average grade of 0.023% ThO_2, and high quantities of rare earth element oxides (REO), specifically La_2O_3, Ce_2O_3, Yb_2O_3, and Y_2O_3. Both models are consistent, showing high amounts of U, Th, and REE, and provide evidence for Rossing-type mineralization at Fraser Lakes Zone B, as both potential economic ore and potential source rock for the U/C-type uranium deposits of the Athabasca Basin.

Keywords. magmatic uranium-thorium, Fraser Lakes Zone B, U-Th-REE deposit, GOCAD modeling, inferred resource estimate

1 Introduction

The world's highest grade uranium deposits are the unconformity-type (U/C-type) deposits of the Athabasca Basin of northern Saskatchewan, which occur mainly at the interface between the basin and its underlying crystalline basement complex (Annesley et al. 2005, Jefferson et al. 2007, Kyser and Cuney 2009, and references therein).

The genetic model(s) for this deposit type is (are) overall well established (cf. Jefferson et al. 2007, Cuney 2009, Kyser and Cuney 2009, Boiron et al. 2010, and references therein). However, several outstanding questions remain, including their uranium source. This paper presents 3D GOCAD modeling results from the Fraser Lakes Zone B uranium-thorium-rare earth elements (U-Th-REE) deposit, which yields evidence

for this magmatic deposit being both potential economic ore (i.e. Rossing-type, Cuney and Kyser 2009) and potential source rock for the U/C-type deposits of the Athabasca Basin (Cuney 2009).

2 Regional Geological Setting

Fraser Lakes Zone B is located ~20-25 km southeast of the Athabasca Basin within the eastern Wollaston Domain of northern Saskatchewan, Canada (Fig. 1).
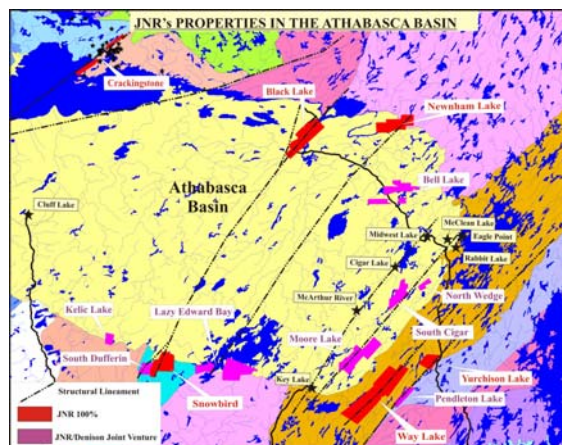
Figure 1. Geological setting, unconformity-type uranium occurrences, and former (until 2013) JNR properties of the Athabasca Basin region in northern Saskatchewan, Canada. Heavy dashed lines are selected major reactivated fault zones.

3 Fraser Lakes U-Th-REE Deposit

The Fraser Lakes area, part of the Way Lake uranium project, is underlain by Archean and Paleoproterozoic rocks of the eastern Wollaston Domain (Fig. 1 and 2). Fraser Lakes Zone B occurs immediately west of Fraser Lakes, and is located within a highly tectonized contact between Archean granitoids and the overlying basal Wollaston Group pelitic metasediments (Fig. 2). The tectonized contact/shear zone is folded around Archean granitic domes, and is thickest within the NE-plunging antiformal noses (Figs. 2 and 3). There are multiple
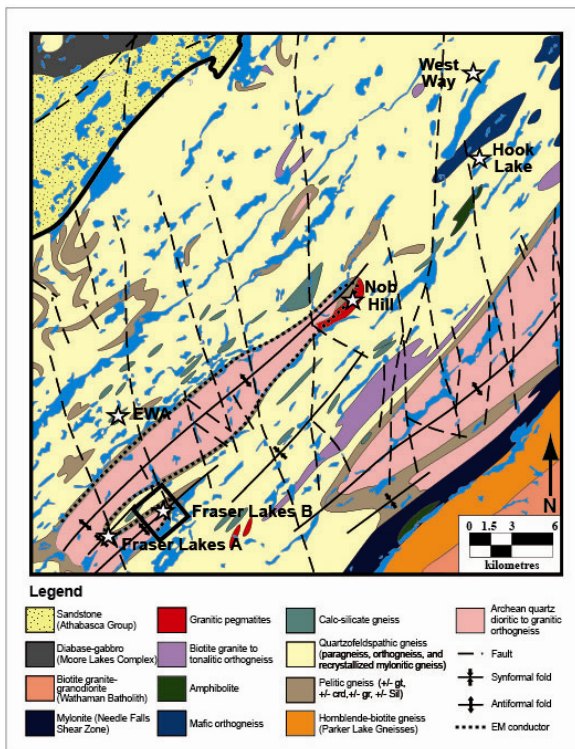
Figure 2. Regional geological map of the Fraser Lakes and surrounding area, modified from Ray (1980).
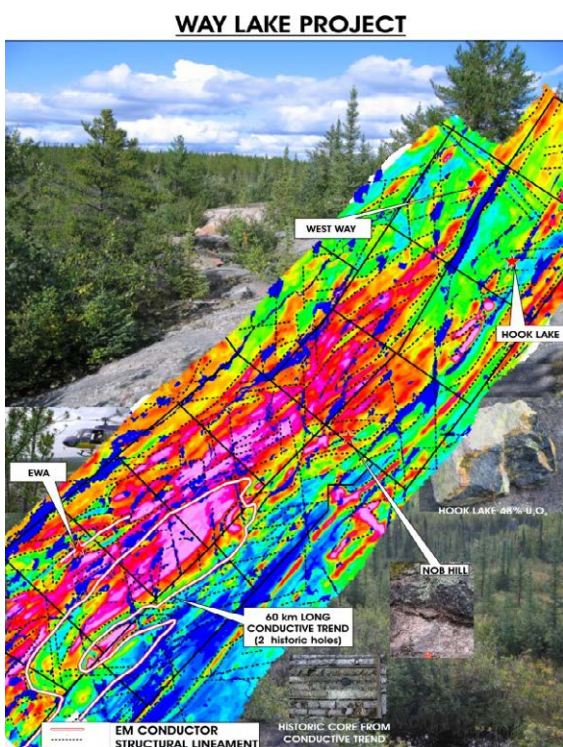
Figure 3. Regional aeromagnetic map of the Fraser Lakes and surrounding area, with superimposed EM conductor and structural lineaments.

generations of granitic pegmatites; the mineralized pegmatites are usually syntectonic and older, and the non-mineralized pegmatites are typically late-tectonic

and younger. U-Pb age dating of magmatic uraninite returned ages of 1850-1780 Ma for the mineralized granitic pegmatites (Annesley et al. 2010, McKechnie et al. 2012, Mercadier et al. 2013). The U-Th-REE mineralized granitic pegmatites at Zone B occur in a NE-plunging antiformal fold nose cut by an E-W dextral ductile-brittle cross-structure and younger NNW-trending and NNE-trending brittle faults. The mineralized pegmatites have been further sub-divided (McKechnie et al. 2012, 2013) into two groups based on their U, Th, and REE contents and relative position within the fold nose. The Group A intrusives are U-rich, syn- to late-tectonic pegmatites that intrude the NW limb of the fold. The Group B intrusives are the syn- to late-tectonic, Th-REE-rich pegmatites that intrude the central part of the fold nose.

4 Fraser Lakes GOCAD model

4.1 Available data

The Fraser Lakes area offers fair to good outcrop exposures of the various Archean and Paleoproterozoic lithological units, including the mineralized granitic pegmatites and leucogranites of Hudsonian age. No Athabasca sandstones are present in the immediate area. Most of the geological structures are known from outcrops, drilling, and/or airborne geophysics (Fig. 3, for details refer to Annesley et al. 2009, 2010, McKechnie et al. 2012, 2013).

Locally, the only available data are DDH data, which provide accurate local information on the distribution, nature, and importance of the various lithological units and geological structures. The DDH data in conjunction with outcrop exposures provides essential constraints on the lateral continuity of lithological units very locally. However for most of Zone B, it is necessary to integrate locally both the hard but local data (such as outcrop and DDH information), with more interpretive data (like geological cross-sections). Four main types of data were used to build the 3D model of Fraser Lakes Zone B:

- A set of about 25 logs of DDHs provided by JNR Resources Inc. The drilling was done along several sub-parallel, NW-SE-oriented drill hole fences. The distribution is relatively dense in the NE part of the studied area, allowing for accurate characterization of geological structures. To the SW, the drilling is more widely spaced, with up to 250m between drill holes along very widely spaced fences. The drill holes provide geological (e.g. descriptive logs of the different units), petrological (e.g. mineral and alteration assemblages), and downhole logging data (e.g. whole-rock geochemistry and radiometrics). Geochemical data are available along mineralized sections for all the drill holes.
- Outcrop data from historical geological mapping and prospecting programs, followed up by JNRs recent mapping and prospecting programs.
- Airborne geophysical surveys (i.e. aeromagnetics, VTEM, radiometrics) tracing conductive geophysical anomalies linked to graphitic gneisses in the basement, and associated faults. This type of data is very interesting as ore deposits are generally

associated with these two markers. It also provides information about the general trend of the folds and faults. Using this data, four types of ductile shear zones to brittle faults were recognized based on their orientation and type of motion. These structures are considered to be Palaeoproterozoic in age, with some likely reactivated during and after the Mesoproterozoic era.

- Eight interpreted roughly sub-parallel, vertical cross-sections, constructed from a detailed logging and mapping of lithological units and structures along the drill cores.

4.2 3D Model Construction

Construction of a 3D model in an exploration or mining environment typically includes data such as 3D drill core information, lithological and structural information, geochemical data, and interpretive cross-sections. The data are generally more or less regularly spaced, are incomplete in 3D space, and hence do not have the same level of uncertainty. 3D modeling represents a first-order tool for integrating different kinds of data and insuring consistency between the data and the resulting models. In this study, the geometrical modeling was performed using the GOCAD 3D modeler (c.f. Mira Geoscience web site, 2013).

4.3 GOCAD results and calculations

A first-order 3D model of the Fraser Lakes Zone B was built, including lithological contacts, a consistent fault network, and the envelopes of the mineralized granitic pegmatite bodies at/near the highly deformed Archean-Paleoproterozoic contact (Fig. 4). The mineralized bodies (based on a cutoff of 0.01% or 100 ppm) generally appear as stacked sheets around a moderately NE-plunging antiformal fold nose. Their thicknesses vary from centimeters to 10s of meters to a maximum of about 15 m, with an average value of 5 m. The mineralized bodies are more concentrated in the fold nose area, providing evidence for a structural control on the emplacement of the granitic pegmatites by both folding and the Archean-Paleoproterozoic contact. A late brittle conjugate fault network offsets the mineralized pegmatite bodies.
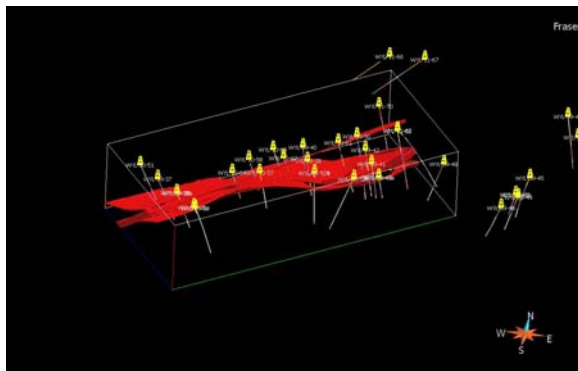
Figure 4. 3D GOCAD voxet of Fraser Lakes Zone B showing location of DDHs used in the model.

The GOCAD voxet includes the surface relief. The ground surface is 525 m to 495 m above sea level (asl) and the voxet top is at 588 m asl; thus the voxet has an air component. The overburden thickness varies from 0 to 40 meters. The bottom of the voxet is 260 m asl. The voxet is 1300 m long by 630 m wide by 328 m deep, and contains 171,532,100 cubic meters of crystalline basement; circa 200 m thick. The basement includes Hudsonian granitic pegmatite (12,031,400,000 cubic meters), Archean orthogneiss (83,637,000 cubic meters with 2-5 ppm U), and Wollaston Group metasediments (75,863,700 cubic meters with 3-8 ppm U). The mineralized granitic pegmatite (>100 ppm U) is 7 vol. % of the 171,532,100 cubic meters of crystalline basement.

For the granitic pegmatite, we have 12,031,400 cubic meters (times average density of 2.7 = 32,484,780,000 kg). Using the 32,484,780,000 kg, we can make the following calculations:

- x 250 ppm U (0.025%) or multiplying by 0.00025 = 8,121,195 kg uranium = 17,866,629 lbs uranium = 8,121 metric tons of uranium.
- x 100 ppm U (0.01%) or multiplying by 0.0001 = 3,248,478 kg uranium = 7,146,652 lbs uranium = 3,248 metric tons of uranium

These calculations indicate there is between 7,146,652 and 17,866,629 lbs uranium (or 3,248 to 8,121 metric tons U) in the mineralized granitic pegmatite. Additionally, this rock volume contains abundant Th and REES.

5 Fraser Lakes NI 43-101 Inferred Resource Estimate

On the basis of the 3D GOCAD model, GeoVector Management Inc. was contracted by JNR in 2012 to complete an initial resource estimate for the Fraser Lakes B Zone, using GEMCOM (Fig. 5), and prepare a technical report on the estimate in compliance with the requirements of NI 43-101 (Armitage and Sexton 2012). Using a base case cut-off grade (COG) of 0.01% U_3O_8, the Fraser Lakes B Zone deposit is currently estimated to contain an inferred resource of 6,960,681 lbs of U_3O_8 in 10,354,926 tonnes, at an average grade of 0.030% U_3O_8. There are also significant quantities of rare earth element oxides (REO), specifically La_2O_3, Ce_2O_3, Yb_2O_3, and Y_2O_3. The inferred resource also contains a high Th content. Using the COG of 0.01% U_3O_8, there is 5,339,219 lbs of ThO_2 at an average grade of 0.023% ThO_2 (Armitage and Sexton 2012).
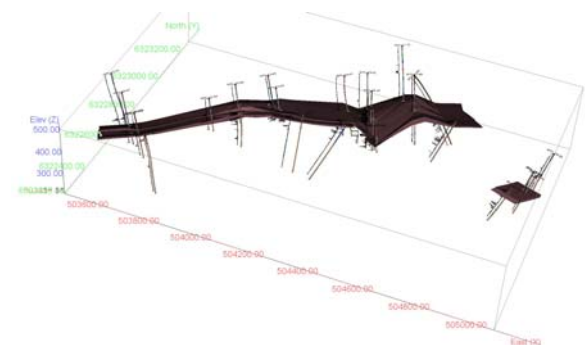
Figure 5. 3D GEMCOM model showing the main zone of

Group A U-Th mineralized granitic pegmatites and a much smaller zone of Group B Th-REE mineralized granitic pegmatites.

6 Summary and Conclusions

The construction of the 3D model was based mainly on DDH data and interpretive cross-sections. Obviously, the lack of accurate data at depth may induce a wide range of interpretations. In addition, the irregular distribution of the drill holes might have biased the data for both lithological contacts and ductile-brittle structural elements. However, the interpretive cross-sections constitute a consistent synthesis of available data.

Both models (Figs. 4 and 5) show that there are significant amounts of U, Th, and REE at Fraser Lakes Zone B, and provide evidence for this Rossing-type magmatic deposit being both potential economic ore (i.e. Hudsonian mineralization) and potential source rock for the Mesoproterozoic U/C-type uranium deposits of the Athabasca Basin.

Acknowledgements

References

Annesley, I.R., Madore, C., Portella, P. (2005) Geology and thermotectonic evolution of the western margin of the Trans-Hudson Orogen: evidence from the eastern sub-Athabasca basement, Saskatchewan. Can. J. Earth Sci. 42: 573-597.

Annesley, I. R., Cutforth, C., Billard, D., Kusmirski, R. T., Wasyliuk, K., Bogdan, T., Sweet, K., Ludwig, C. (2009) Fraser Lakes Zones A and B, Way Lake Project, Saskatchewan: Geological, geophysical, and geochemical characteristics of basement-hosted mineralization. Proceedings of the 24th International Applied Geochemistry Symposium (IAGS), Fredericton, NB. Conference Abstract Volume 1: 409–414.

Annesley, I.R., Austman, C.L., Creighton, S., Mercadier, J., Ansdell, K.M., Gittings, F., Bogdan, T.S., Billard, D. (2010) Fraser Lakes U-Th-REE mineralization, southeastern Athabasca basement: composition and U-Th-Pb chemical/isotopic ages with consequences for U protore and U/C-type mineralization. *in* Open House 2010 Abstract Volume: Saskatchewan Geological Survey, p. 8.

Armitage, A. and Sexton, A. (2012) RESOURCE ESTIMATE ON THE WAY LAKE URANIUM PROJECT, FRASER LAKES ZONE B: Located in the Wollaston Group, east of the Atahabasca basin, northern Saskatchewan. SEDAR Technical Report: 57p.

Boiron, M.C., Cathelineau, M., Richard, A. (2010) Fluid flows and metal deposition near basement ∕cover unconformity: lessons and analogies from Pb–Zn–F–Ba systems for the understanding of Proterozoic U deposits. Geofluids 10: 270–292.

Cuney, M. (2009) The extreme diversity of uranium deposits. Mineral. Deposita 44: 3-9.

Cuney, M. and Kyser, T.K. (2009) Deposits related to partial melting. *In* Recent and Not-So-Recent Developments in Uranium Deposits and Implications for Exploration (M. Cuney & T.K. Kyser, eds.). Mineral. Assoc. Can., Short Course 39: 79-95.

Jefferson, C.W., Thomas, D.J., Gandhi, S.S., Ramaekers, P.,

Delaney, G., Brisban, D., Cutts, C., Portella, P., and Olson, R.A. (2007) Unconformity associated uranium deposits of the Athabasca Basin, Saskatchewan and Alberta. In Mineral Resources of Canada: A synthesis of Major Deposit-types, District Metallogeny, the Evolution of Geological Provinces, and Exploration Methods, W.D. Goodfellow (ed); Mineral Deposits Division of the Geological Association of Canada, p. 273-306.

Kyser, T.K. and Cuney, M. (2009) Unconformity-related uranium deposits. *In* Recent and Not-So-Recent Developments in Uranium Deposits and Implications for Exploration (M. Cuney & T.K. Kyser, eds.). Mineral. Assoc. Can., Short Course 39: 161–219.

McKechnie, C.L., Annesley, I.R., Ansdell, K.M. (2012) Radioactive abyssal granitic pegmatites and leucogranites in the Wollaston Domain, northern Saskatchewan, Canada: mineral compositions and conditions of emplacement in the Fraser Lakes area. Can. Mineral. 50: 1637-1667.

McKechnie, C.L., Annesley, I.R., Ansdell, K.M. (2013) Geological setting, petrology and geochemistry of granitic pegmatites hosting the Fraser Lakes Zone B U–Th–REE mineralization, Wollaston Domain, northern Saskatchewan, Canada. Explor. Mining. Geol. 21: 1-26.

Mercadier, J., Annesley, I.R., McKechnie, C.L., Bogdan, T.S., Creighton, S. (2013) Magmatic and metamorphic uraninite mineralization in the western margin of the Trans-Hudson Orogen (Saskatchewan, Canada): major protores for unconformity-related uranium deposits. Econ. Geol. 108: (in press).

Ray, G.E. (1980) Geology of the Parker Lake-Nelson Lake vicinity. Saskatchewan Geological Survey, Report No. 190: 40 p.

Unconformity-related U deposits: recent advances from fluid inclusions and their host minerals

Antonin Richard
Geological Survey of Finland (GTK), P.O. Box 96, 02151 Espoo, Finland

Michel Cathelineau, Marie-Christine Boiron, Michel Cuney, Julien Mercadier, Christophe Rozsypal, Jean Cauzid
GéoRessources, Université de Lorraine, CNRS, CREGU, B.P. 70-239, Vandoeuvre-lès-Nancy, France

David A. Banks
School of Earth and Environment, University of Leeds, Woodhouse Lane, Leeds, LS2 9JT, UK

Philippe Boulvais
Geoscience UMR 6118, CNRS – Université de Rennes 1 Campus de Beaulieu, 35042 Rennes Cedex, France

Mark A. Kendrick
The School of Earth Sciences, The University of Melbourne, Vic. 3010, Australia

Thomas Pettke
Institute for Geological Sciences, University of Bern, Baltzerstrasse 1+3, CH-3012 Bern, Switzerland

Abstract. The Paleoproterozoic Athabasca Basin (Canada) hosts numerous world class unconformity-related uranium deposits. Many aspects of their genesis remain debated. The objective here is to review recent fluid inclusion and stable isotope studies that have contributed to a better understanding of: (1) the origin and P-T-X conditions of the mineralizing fluids; (2) the conditions for transport of metals and in particular uranium; (3) the relationships between fluid chemistry and alteration features (fluid-rock interaction) and (4) some aspects of uranium deposition. As a whole, the Athabasca system was dominated by basinal brines of evaporated-seawater origin. The brines have percolated through reactivated basement structures, leached metals in basement rocks, and caused intensive Mg-B alteration. Furthermore, the brines were anomalously acidic and have transported the uranium at the highest concentration so far reported for crustal fluids. This feature alone could simply explain the spectacular alteration and also the tremendous grades and tonnages of the Athabasca uranium deposits.

Keywords. Unconformity, Uranium, Brines, Fluid Inclusions, Host minerals, Athabasca Basin

1 Geology and fluid inclusion sampling

The Athabasca Basin unconformably overlies an Archean to Paleoproterozoic basement separated into two provinces (the Rae Province in the west and the Hearne Province in the east) by the northeast-trending Snowbird tectonic zone (Fig. 1). These two provinces consist of Archean gneisses, Paleoproterozoic metapelites and mafic to felsic intrusions. They were affected, respectively, by the ~2.0 to ~1.9 Ga Thelon-Talston and the ~1.9 to ~1.8 Ga Trans-Hudson orogenies (Annesley et al. 2005).

The sedimentary sequence of the Athabasca Basin was deposited starting from ~1.75 Ga (Ramaekers et al. 2007). From the base to the top, the Athabasca Group is composed of fluvial to marginal marine quartz-rich sandstones, marine sandstones, phosphatic siltstones, phosphatic mudstones, fluviatile sandstones, shales and finally stromatolitic carbonates. The current maximum thickness of the sedimentary cover is ~1.5 km and could have originally been as much as ~5 km, based on P-T estimations from fluid inclusions (Pagel, 1980; Derome et al. 2005).

The U deposits are generally located near the basement/cover interface, and structurally controlled by sub-vertical faults rooted in graphite-rich basement metapelites. The earliest UO_2 ores in the Athabasca Basin have been dated to between 1.6 and 1.4 Ga and successive late episodes of mineralization, and/or recrystallisation occurred until ~0.7 Ga (Alexandre et al. 2012). Remobilization of primary UO_2 by meteoric fluids likely occurred around 400 Ma and subsequently, until recent times (Mercadier et al., 2011a).

The main alteration features associated with the U-ores include successively: (1) partial to complete replacement of the original basement minerals (K-feldspar, biotite, plagioclase, hornblende) by an illite + sudoite (Mg-chlorite) ± dravite (Mg-tourmaline) assemblage (also referred to as "bleaching") as well as the precipitation of illite and sudoite in sandstones; (2) quartz dissolution in basement rocks as well as in the sandstones and (3) precipitation of dravite + quartz + UO_2 + dolomite + bitumen in quartz dissolution voids and in veins and breccias (Derome et al., 2005; Mercadier, 2010). Alteration surrounding the U deposits is associated with rare earth element mobilization and redistribution among aluminium phosphate-sulphate minerals and uraninite (Mercadier et al., 2011b).

Sandstone silicification, and quartz and dolomite veins are spatially and temporally associated with the main alteration minerals and U mineralization (Fig. 1). Hence, they are likely to host fluid inclusions that are relicts of the mineralizing fluids. The veins crosscut various lithologies such as basement gneisses and pegmatoids as well as basin sandstones. Veins were sampled in relatively fresh to extensively altered and mineralized rocks.

2 P-T-X characteristics of brines

Two phase (liquid-vapour) or three phase (liquid-vapour-halite) fluid inclusions (5 to 25 µm in size) are typically observed in both quartz and dolomite and secondary fluid inclusion planes in basement quartz (Kotzer and Kyser, 1995; Derome et al. 2005; Mercadier et al. 2010; Richard et al. submitted to Ore Geol Rev). The volumetric proportion of the vapour phase is ~10% (Fig. 1).

Microthermometry and reconstruction of fluid inclusions compositions in the H_2O-NaCl-$CaCl_2$-system shows that the fluid inclusion salinity is comprised between 25 and 35 wt% equivalent NaCl. Fluid inclusion LA-ICP-MS compositions display a continuum between a NaCl-rich end-member (Cl>Na>Ca≈Mg>K) and a $CaCl_2$-rich end-member (Cl>Ca≈Mg>Na>K). The $CaCl_2$-rich brine has the highest salinity and shows evidence for NaCl-saturation at the time of trapping. The majority of homogenization temperature of fluid inclusions is comprised between 100 and 150°C for the NaCl-rich brine, and 80 and 140°C for the $CaCl_2$-rich brine end-members (Derome et al. 2005; Richard et al. 2010; Richard et al. submitted to Ore Geol Rev).

The continuum of microthermometric and LA-ICP-MS compositional data between the NaCl-rich brine and the $CaCl_2$-rich brine end-members suggest that the two brines have mixed in all deposits at the time of U deposition. P-T reconstructions suggest that mixing was non-isothermal (NaCl-rich brine: 180 ± 30°C and 800 ± 400 bars; $CaCl_2$-rich brine: 120 ± 30°C and 600 ± 300 bars) and occurred under fluctuating pressure conditions (hydrostatic to supra-hydrostatic).

3 Brine flow in crystalline basement

Detailed analysis of oriented secondary fluid inclusion planes within magmatic and metamorphic quartz in basement rocks reveals that the NaCl-rich and $CaCl_2$-rich brines have penetrated extensively into the basement not only through faults and major pathways (as shown by quartz and dolomite veins) but also by way of dense networks of microfractures which favoured the percolation of fluids at least hundred metres below the unconformity (Mercadier et al. 2010).

Microfracture networks, which opened during the basinal brine stage (ca. 1600–1400 Ma) are interpreted as sets of mode I cracks corresponding to a specific stage of deformation and occur as fluid inclusion planes after healing. The stress field at that stage (σ1=N130–150°E, subvertical) partly reopened the earlier microcrack networks (σ1=N80–110°E and N130–150°E, subvertical) inherited from late retrograde metamorphic stage of the Trans-Hudson Orogeny (ca. 1795–1720 Ma).

This demonstrates the existence of a similar stress field direction acting before and after the basin formation. Moreover, the brine circulations in the basement acted throughout a wider volume than the clay-rich alteration halo surrounding the U-ores, generally considered as the main envelope of fluid percolation outside the fault systems. The data on the chemistry of the fluids and on the geometry of their migration at various scales emphasise the fundamental role of the basement in the chemical evolution of highly saline brines, as for many other Proterozoic to recent U and base metal basin-hosted systems (Boiron et al. 2010)
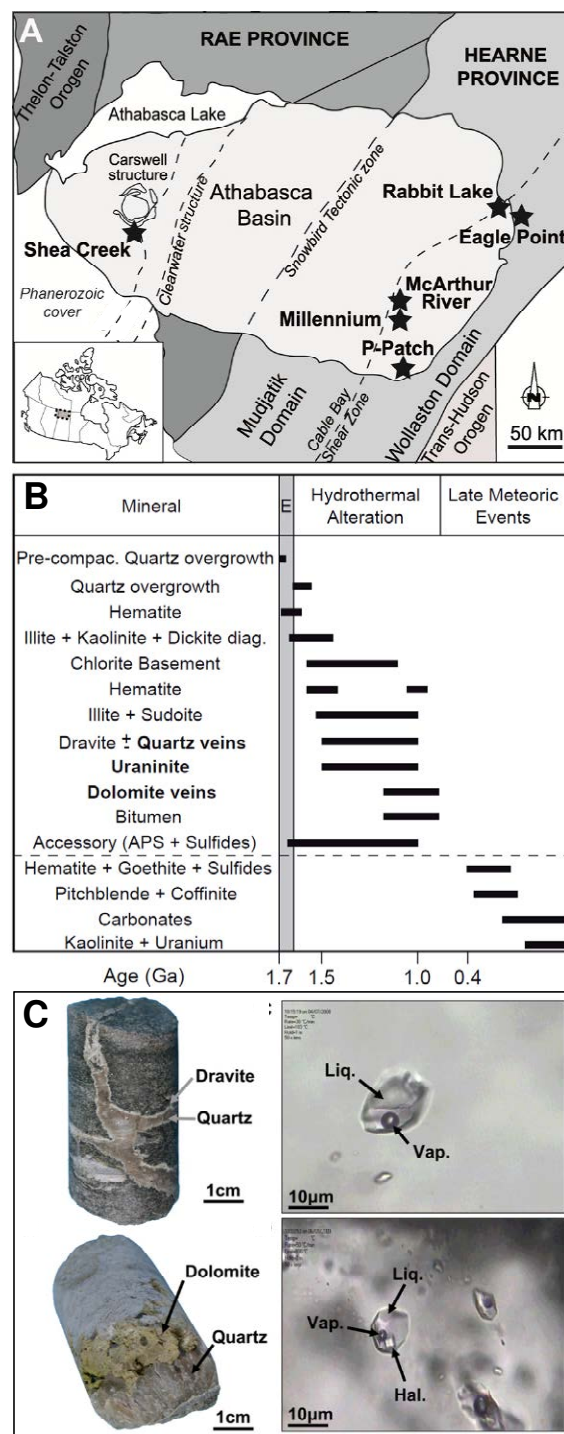
Figure 1. (A) Simplified geological map of the Athabasca Basin and Basement, Canada. Stars indicate the studied deposits. (B) Simplified mineral successions (E: early diagenetic, hydrothermal and late meteoric) for unconformity-related U deposits in the Athabasca Basin (modified from Mercadier et al. (2012) and references therein). APS: aluminium phosphate-sulphate (C) Example of quartz and carbonate veins, hosting fluid inclusions studied in this work (Richard et al. 2011).

4 Origin of brines

Noble gas, crush-leach, stable chlorine isotope and LA-ICP-MS analyses of fluid inclusions show that the brines have molar Br/Cl ratios from 5×10^{-3} to 10×10^{-3}, and I/Cl ratios from 2×10^{-6} to 12×10^{-6}, and $\delta^{37}Cl$ values of -0.6 and 0‰ (Richard et al. 2011; Leisen et al. 2012; Richard et al. submitted to Precambrian Res). These compositions are consistent with the fluids deriving the bulk of their salinity by sub-aerial evaporation of seawater, beyond the point of halite saturation.

The chloride has an unambiguous, dominantly marine origin and has required large-scale seawater evaporation and minor evaporite deposition. Although direct evidence for evaporative environments in the Athabasca Basin is lacking due to the erosion of ~80% of the sedimentary pile, halogens have behaved conservatively at the basin scale and throughout basin history.

Stable boron isotope compositions of dravite (Mg-tourmaline) ($\delta^{11}B$ = 19.6‰ to 36.5‰) associated with quartz and dolomite veins indicate that most of the boron has a marine origin, consistent with halogen data. Because evaporated-seawater is typically Mg-rich, it is proposed that the Mg enrichment in altered rocks (Mg-tourmaline, Mg-chlorite) is due to the input of Mg-rich evaporated-seawater brines (Mercadier et al. 2012).

5 Fluid-rock interaction

$\delta^{18}O$ values of quartz veins ($\delta^{18}O$ = 11‰ to 18‰) and previously published $\delta^{18}O$ values of the dominant alteration minerals (illite, chlorite and tourmaline), show that quartz and alteration minerals were isotopically equilibrated with the same fluid at ~180°C (Richard et al. 2013a).

The $\delta^{13}C$ values of trace amounts of CO_2 dissolved in dolomite-hosted fluid inclusions ($\delta^{13}C$ = -30.1‰ to -3.8‰) and the $\delta^{13}C$ values of dolomite ($\delta^{13}C$ = -23.5‰ to -3.5‰) indicate that CO_2 originates from brine-graphite interaction in the basement. The calculated $\delta^{18}O$ values of the mineralizing brines ($\delta^{18}O$ = -1‰ to 8‰) have shifted considerably from those acquired during evaporation of seawater, as has the δD value as measured directly on fluid inclusions (δD = -150‰ to -50‰). The positive $\delta^{18}O$ shift is explained by protracted fluid-rock interaction within the basin and basement rocks. The negative δD shift is attributed to incomplete mixing between the brines and low δD water. This low δD water is likely to have been produced during the abiogenic synthesis of bitumen by Fisher-Tropsch-like reactions involving CO_2 derived from brine-graphite interaction, and radiolytic H_2. (Richard et al. 2013a).

Several scenarios are proposed to account for the chemical conversion of evaporated seawater into a NaCl-rich and a CaCl$_2$-rich brine. It appears that a combination dolomitization, mixing with halite-dissolution brine and albitization accounts for the observed composition of the NaCl-rich brine. The CaCl$_2$-rich brine possibly acquired its Ca-dominated composition by extensive albitization although petrographic evidence to support this is lacking. This suggests that the two brines have had distinct flow paths and fluid-rock interaction histories in the Athabasca Basin and Basement (Richard et al. 2013a; Richard et al. submitted to Ore Geol Rev).

The majority of samples contain fluid inclusions with age-corrected $^{40}Ar/^{36}Ar$ of between the modern atmospheric value of ~300 and 450. These values are typical of upper crustal sedimentary formation waters. $^{40}Ar_E$ concentrations are between 0.03 and 0.8 $\mu g.g^{-1}$ ($^{40}Ar_E$ denotes crustally-derived excess ^{40}Ar). Fluid inclusion non-radiogenic $^{84}Kr/^{36}Ar$ and $^{129}Xe/^{36}Ar$ ratios are intermediate to between air and air-saturated brines. The fluids contain 1.9 to 62 ppb ^{36}Ar which is up to twenty times the ^{36}Ar concentration of air-saturated seawater. The noble gas data are interpreted to reflect acquisition of atmospheric ^{36}Ar, ^{84}Kr and ^{129}Xe from sedimentary rocks. The lack of a strong enrichment in radiogenic ^{40}Ar and preservation of low $^{40}Ar/^{36}Ar$ ratios suggests that interaction of the brines with basement rocks occurred at high water-rock ratios or low temperatures (<200ºC) (Richard et al. Submitted to Precambrian Res).

6 U and metal transport

LA-ICP-MS analysis of fluid inclusions shows that the two brines have high content: up to 600 $\mu g.g^{-1}$ U, 3000 $\mu g.g^{-1}$ Mn, 4000 $\mu g.g^{-1}$ Zn, 6000 $\mu g.g^{-1}$ Cu and 8000 $\mu g.g^{-1}$ Pb. The CaCl$_2$-rich brine carries ~ one order of magnitude more metals than the NaCl-rich brine (Richard. et al 2010; 2012; Richard et al. submitted to Ore Geol Rev).

Fluid inclusions from two quartz samples of the McArthur River and Rabbit Lake deposits were analysed by synchrotron X-ray fluorescence (SXRF) and X-ray absorption near-edge spectroscopy (XANES). SXRF results show that fluid inclusions contain appreciable amounts of Br, Fe, Sr, transition metals (Mn, Ni, Cu, Zn), Pb, U and rare earth elements (REE) (La, Ce). XANES on 4 McArthur River sample fluid inclusions at room temperature and at 150°C (homogenized fluid inclusion) as well as in solid and liquid U(IV) and U(VI) standards, respectively, shows that the uranium has remained in the form of U(VI) from the time of trapping to the present in the fluid inclusion (Richard et al. 2013b).

The metal (Cu, Pb, Zn, Mn, Fe) concentrations are comparable to the highest recorded in present-day sedimentary formation waters and in fluid inclusions from basin-hosted base metal ore deposits for which a basement metal source has been frequently proposed. Trends between Cu, Pb, Zn, Mn, Fe and U concentrations in fluid inclusions suggest that the metals were leached from a proximal source, basement rocks being the most likely candidate (Richard et al. 2012; Richard et al. submitted to Ore Geol Rev).

The solubility of U(VI) was measured experimentally as a function of NaCl content and pH in mixtures that are analogous to ore-forming brines at 155°C. To account for the high uranium content observed in the fluid inclusions, the brines must have been unexpectedly acidic, with a pH between 2.5 and 4.5. Although the origin of acidity in the studied brines remains to be better

understood, it seems that pH is a key factor contributing to the highly efficient transport of uranium in the Athabasca system (Richard et al. 2012).

7 UO$_2$ deposition

UO$_2$ deposition requires reduction of U(VI) to U(IV) and is one of the least understood processes in these deposits. Fluid inclusion data do not allow us to determine precipitation mechanism here but put at least some constraints on plausible vs implausible hypotheses. Raman spectrometry shows that trace amounts of potentially reducing gases (e.g. CH$_4$, H$_2$) are present (Derome et al 2003a). Mg-rich alteration has long been regarded as originating from a basement-derived reducing fluid, but from the present studies is now considered as originating from evaporated seawater-derived brines (Mercadier et al. 2012). The low I/Cl ratios do not favour fluid interaction with organic matter, or hydrocarbons, as a reductant (Richard et al. Submitted to Precambrian Res).

8 Conclusion and perspectives

Detailed characterization of fluid inclusions in the Athabasca basin has allowed us to better understand many genetic aspects of their genesis. Mechanisms for quartz dissolution and UO$_2$ deposition remain enigmatic. More comparative work on Australian unconformity-related U deposits (Derome et al. 2003b; 2007) and other Proterozoic to recent U and base metal basin-hosted systems (Boiron et al. 2010) would be helpful to better understand large-scale brine circulation at basement-cover interfaces and metal transport.

Acknowledgements

References

Alexandre P, Kyser K, Jiricka D, Witt G (2012) Formation and evolution of the Centennial unconformity-related uranium deposit in the South-Central Athabasca Basin, Canada. Econ Geol 107:385-400.

Annesley IR, Madore C, Portella P (2005) Geology and thermotectonic evolution of the western margin of the Trans-Hudson Orogen: Evidence from the eastern sub-Athabasca basement, Saskatchewan. Can J Earth Sci 42:573-597.

Boiron MC, Cathelineau M, Richard A (2010) Fluid flows and metal deposition near basement/cover unconformity: lessons and analogies from Pb–Zn–F–Ba systems for the understanding of Proterozoic U deposits. Geofluids 10:270-292.

Derome D, Cathelineau M, Lhomme T, Cuney M (2003a) Fluid inclusion evidence of the differential migration of H$_2$ and O$_2$ in the McArthur River unconformity-type uranium deposit (Saskatchewan, Canada). Possible role on post-ore modifications of the host rocks. J Geochem Explor 78-79:525-530.

Derome D, Cuney M, Cathelineau M, Fabre C, Dubessy J, Bruneton P. Hubert A (2003b) A detailed fluid inclusion study in silicified breccias from the Kombolgie sandstones (Northern Territory, Australia): Inferences for the genesis of middle-Proterozoic unconformity-type uranium deposits. J Geochem Explor 80:259-275.

Derome D, Cathelineau M, Cuney M, Fabre C, Lhomme T, Banks DA (2005) Mixing of sodic and calcic brines and uranium deposition at the McArthur River, Saskatchewan, Canada. A Raman and laser-induced breakdown spectroscopic study of fluid inclusions. Econ Geol 100:1529-1545.

Derome D, Cathelineau M, Fabre C, Boiron MC, Banks D, Lhomme T, Cuney M (2007) Paleo-fluid composition determined from individual fluid inclusions by Raman and LIBS: Application to mid-proterozoic evaporitic Na-Ca brines (Alligator Rivers Uranium Field, northern territories Australia). Chem Geol 237: 240-254.

Kotzer TG, Kyser TK (1995) Petrogenesis of the Proterozoic Athabasca Basin, Northern Saskatchewan, Canada, and its relation to diagenesis, hydrothemal uranium mineralization and paleohydrogeology. Chem Geol 120:45-89.

Leisen M, Boiron MC, Richard A, Dubessy J (2012) Determination of Cl and Br concentrations in individual fluid inclusions by combining microthermometry and LA-ICPMS analysis: Implications for the origin of salinity in crustal fluids. Chem Geol 330-331:197-206.

Mercadier J, Richard A, Boiron MC, Cathelineau M, Cuney M (2010) Brine migration in the basement rocks of the Athabasca Basin through microfracture networks (P-Patch U deposit, Canada). Lithos 115:121-136.

Mercadier J, Cuney M, Cathelineau M, Lacorde M (2011a) U redox fronts and kaolinisation in basement-hosted unconformity-related U ores of the Athabasca Basin (Canada): late U remobilisation by meteoric fluids. Miner Deposita 46:105-135.

Mercadier, J., Cuney, M., Lach, P., Boiron, M.C., Bonhoure, J., Richard, A., Leisen, M., Kister, P., 2011b. Origin of uranium deposits revealed by their rare earth element signature. Terra Nova 23:264-269.

Mercadier, J., Richard, A., Cathelineau, M., 2012. Boron and magnesium-rich marine brines at the origin of giant unconformity-related uranium deposits: δ^{11}B evidence from Mg-tourmalines. Geology 40:231-234.

Mercadier J, Annesley IR, McKechnie CL, Bogdan TS, Creighton S, (2013) Magmatic and metamorphic uraninite mineralization in the western margin of the Trans-Hudson Orogen (Saskatchewan, Canada): a uranium source for unconformity-related uranium deposits? Econ Geol, in press.

Pagel M, Poty B, Sheppard SMF (1980) Contribution to some Saskatchewan uranium deposits mainly from fluid inclusion and isotopic data. In: IAEA (ed) International Uranium Symposium on the Pine Creek Geosyncline, Vienna, pp 639-654.

Ramaekers P, Jefferson CW, Yeo GM, Collier B, Long DG, Catuneanu O, Bernier S, Kupsch B, Post R, Drever G, McHardy S, Jircka D, Cutts C, Wheatley K, 2007. Revised geological map and stratigraphy of the Athabasca Group, Saskatchewan and Alberta. Bull Geol Surv Can 588:155-191.

Richard A, Pettke T, Cathelineau M, Boiron MC, Mercadier J, Cuney M, Derome D (2010) Brine-rock interaction in the Athabasca basement (McArthur River U deposit, Canada): consequences for fluid chemistry and uranium uptake. Terra Nova 22:303-308.

Richard A, Banks DA, Mercadier J, Boiron MC, Cuney M, Cathelineau M (2011) An evaporated seawater origin for the ore-forming brines in unconformity-related uranium deposits (Athabasca Basin, Canada): Cl/Br and δ^{37}Cl study of fluid inclusions. Geochim Cosmochim Ac 75:2792-2810.

Richard A, Rozsypal C, Mercadier J, Banks DA, Cuney M, Boiron MC, Cathelineau M (2012) Giant uranium deposits formed from exceptionally uranium-rich acidic brines. Nat Geosci 5: 142-146.

Richard A, Boulvais P, Mercadier J, Boiron MC, Cathelineau M, Cuney M (2013a) From evaporated seawater to uranium-mineralizing brines: Isotopic and trace element study of quartz-dolomite veins in the Athabasca system. Geochim Cosmochim Ac, in press.

Richard A, Cauzid J, Cathelineau M, Boiron MC, Mercadier J, Cuney M (2013b) Synchrotron-XRF and XANES investigation of uranium speciation and element distribution in fluid inclusions from unconformity-related uranium deposits. Geofluids, in press.

Richard A, Cathelineau M, Boiron MC, Mercadier J, Banks DA, Cuney M, Metal-rich brines in the Athabasca Basin and Basement, Canada: New P-T-X constraints from fluid inclusions, origin of solutes and consequences for unconformity-related U deposits. Submitted to Ore Geol Rev.

Richard A, Kendrick MA, Cathelineau M, The origin of mineralising brines in Proterozoic unconformity-related U deposits: New insights from noble gases (Ar, Kr, Xe) and halogens (Cl, Br, I) in fluid inclusions. Submitted to Precambrian Res.

The Bayinwula roll front-type uranium deposit, Erlian Basin, NE China.

Christophe Bonnetti[1], Michel Cuney[1], Fabrice Malartre[1], Raymond Michels[1], Sylvain Bourlange[1], Xiaodong Liu[2], Yunbiao Peng[3], Jianxing Yang[3]
[1]Université de Lorraine, GEORESSOURCES-CNRS-CREGU, F54506 Vandoeuvre-les-Nancy, France
christophe.bonnetti@univ-lorraine.fr
[2]East China Institute of technology, Fuzhou, China, liuof99@163.com
[3]Geological Team No.208, BOG, CNNC, Baotou, China, 208y@bog.com.cn

Abstract. The Bayinwula roll front-type uranium deposit is one of the uranium deposits discovered in the Mesozoic Erlian Basin, located in NE China. Uranium mineralization is hosted in a confined sandstone reservoir of the Aptian – Albian Saihan Formation belonging to the lower Cretaceous Bayanhua Group. The permeable sandstone layers hosting uranium mineralization formed by amalgamation of braided channels deposited in a fluvial environment. Sandstone is primary reduced, light to dark grey in colour, and is rich in detrital organic matter (S_{tot}: 0.01 – 1.5 %wt; C_{org}: 0.01 – 25 %wt). Organic matter fragments are inherited of land plants as they belong to type III or type IV (HI<100; OI: 30 – 120). No secondary reduction by migrated reduced fluids of sandstone units was identified. Uranium background concentrations in reduced sandstone are elevated and range from 10 to 50 ppm U. Secondary oxidation is considered responsible for both the remobilization of part of the uranium disseminated within sandstone, as the oxidized zone often shows uranium contents lower than 10 ppm U, as well as the initiation of a redox front where the uranium mineralization of the roll front-type Bayinwula deposit was precipitated.

Keywords. Erlian Basin, Saihan Formation, sandstone-hosted, roll front-type uranium deposits.

1 Introduction

Central Asia represents one of the largest uraniferous provinces in the world, with deposits located in the Transbaikal region, Kazakhstan, Uzbekistan, Mongolia and northern China. In comparison with other world class provinces (Canada, Australia and Africa), which are associated with Archaean to Paleoproterozoic basements, the present study area provides an opportunity to investigate genetic conditions of uranium deposits generated within a very young uraniferous province. All of the deposits discovered in this region are of sandstone-hosted tabular or roll-front type (Dahlkamp, 2009) which currently represents one of the most economic uranium resources with respect to using ISR mining processes.

The Erlian Basin in NE China (Fig. 1) is an intracontinental basin (1000 km long x 50-200 km wide) formed during the Mesozoic continental extension of eastern Asia and filled by fluvial-lacustrine sedimentary units (Charles, 2010; Dou and Chang, 2003; Lin et al. 2001). The main stage of deposition in the Erlian Basin occurred from late Jurassic to the end of the early Cretaceous, during the rifting stage (Lin et al. 2001; Meng et al. 2003). The Basin developed in three main tectonic stages separated by two major unconformities

(Lin et al. 2001; Graham et al. 2001; Dou et al. 1998; Wei et al. 2005; Sha, 2007): (i) The pre-rift stage, mainly
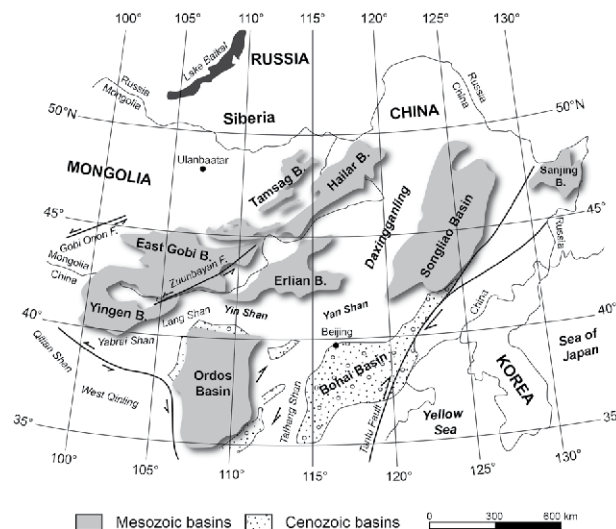
Figure 1, Tectonic map showing the distribution of the sedimentary basins in northern China (modified after Meng, 2003). B= Basin; F= Fault.

characterized by late Jurassic/early Cretaceous volcanic rocks of the Qinganling Group (156.0 – 142.6 Ma; (Graham et al. 2001; Cheng and Cheng 1997; Wuang, 1985). (ii) The syn-rift stage, represented by early Cretaceous stratigraphic units belonging to the Bayanhua Group (Dou et al. 1998; Sha, 2007; Gou et al. 1986) and deposited during the development of half-grabens: the Arshan Formation is dominated by fluvial deposits, and the Tengge'er Formation by lacustrine sediments. (iii) The post-rift stage began at the end of early Cretaceous (Lin et al. 2001), during Aptian time, where thermal subsidence replaced tectonic subsidence (Charles, 2010; Meng et al. 2003; Wei et al. 2005). At that time, the Erlian Basin experienced relative uplift resulting from NW-SE compression caused by the subduction of the Pacific plate towards the Eurasian continent (Wei et al. 2005). The NE trending basement faults became activated in sinistral strike-slip mode. Early Cretaceous Saihan Formation and late Cretaceous Erlian Formation were both deposited during this post-rift stage (Lin et al. 2001; Meng et al. 2003), in a predominantly fluvial-shallow lacustrine environment.

Several sandstone-hosted uranium deposits have been discovered in the Erlian Basin, including the Saihangaobi deposit, located in the eastern part of the Wulanchabu sub-Basin and the Bayinwula deposit in the western part of the Manite sub-Basin (Nie et al. 2007).

These deposits are both hosted by the early Cretaceous Saihan Formation, deposited during Aptian – Albian age (Nie et al. 2007; Fan et al. 2008), as determined from paleomagnetic and palynological data. The Bayinwula sandstone-hosted deposit occurs in the upper member of the Saihan Formation, within the Tabei Sag at about 20 km to the North of Sunite city. This part of the Manite sub-Basin is flanked to both north and south by both biotite and two-mica granites and acidic volcanic rocks which could represent primary uranium source-rocks. The Bayinwula deposit consists of three sinuous NW-trending ore bodies, defining a mineralized zone of about 7,5 km long by 500 m wide. The average grade of this deposit is 100 – 300 ppm U. Only a minor proportion of the mineralization reaches 500 – 1000 ppm U.

2 Material and methods

In order to characterize sedimentological setting and genetic conditions leading to the formation of the Bayinwula uranium deposit, a total of 6 drill holes were logged and sampled including 3 stratigraphic drill holes and 3 drill holes located along a NW-SE oriented section crosscutting the main ore body, from the oxidized zone to the reduced zone. The aim of this study was first to identify the sedimentary facies of the depositional environments of the Saihan Formation. Then, a multidisciplinary study including petrographical and mineralogical observations, organic matter characterization, geochemical and geochronological analyses of the ore zone will enable determination of the geological processes involved in the genesis of this uranium deposit.

3 Results

3.1 Facies architecture of the Saihan Formation

The observations made on the stratigraphic drill holes show that the sediments of the upper member of the Saihan Formation represent both braided channel dominated fluvial depositional environments and overbank dominated depositional environments. The boundary between the lower and upper members of the Saihan Formation is marked by coal seams occurring at the top of the lower member. Sedimentary facies formed in braided channels correspond to a lithofacies combination of gravel and very coarse to fine-grained sand showing fining-upward trends. Gravels are more or less stratified, sometimes pebbly and correspond to minor channel fills. They occur as 10 cm – 1 m thick layers located at the bottom of channels. These sediments are clast-supported and detritus is mainly composed of lithoclasts, sub-angular to sub-rounded quartz and feldspar grains. Sandstones are poorly sorted and very coarse to fine-grained, clast-supported and composed of sub-angular to sub-rounded quartz and feldspar grains. Sandstone units comprise 10 cm – 5 m thick layers displaying either trough or planar crossbeds. Channel sands can also show ripple crosslamination in the case of a lower flow regime. Overbank sedimentary

facies are represented by a lithofacies combination of floodplain fines and crevasse splays. Floodplain fines correspond to deposits of overbank sheet flows, floodplain ponds and swamps. They form sheet-like layers that can extend laterally for several km, with thicknesses of tens of meters (Miall, 2010). Floodplain fines are mainly composed of very fine-grained sand, silt and mud often occurring with poorly sorted floating gravels or coarse quartz grains. Crevasse splays occur as lenses from 10 cm – 5 m thick probably extending laterally for several kilometers (Miall, 2010), and correspond to delta-like progradation from a crevasse channel into the floodplain. Deposits are characterized by massive layers of sand, silt and mud frequently associated with floating gravels and coarse quartz grains.

3.2 Typology of organic matter

Sedimentary facies of the overbank and channels both contain a large amount of organic matter (S_{tot}: 0.01 – 1.5 %wt; C_{org}: 0.01 – 25 %wt) and pyrite. Permeable sandstone layers of the Saihan Formation are primary reduced as they show a light to dark grey colour and are rich in detrital organic matter fragments such as phytoclasts and coal debris. The finest fragments can be found either disseminated or accumulated in sand. Coarser elements can highlight crossbeds and have mainly accumulated at the bottom of channels. Pyrolysis (rock-eval analyses) on organic matter-rich samples from both stratigraphic drill holes and from drill cores located in the reduced zone of the ore body show that organic matter belongs to type III or type IV (HI<100; OI: 30 – 120). Therefore this kind of organic matter is derived from land plants. No secondary reduction by migration of reduced fluids through sandstone units was identified.

3.3 Roll front-type uranium mineralization

Three drill holes were selected for the study regarding their position along a profile oriented NW-SE crosscutting the ore body of the Bayinwula deposit, from the oxidized to the reduced zone (Fig. 2). The mineralized interval is located between 100 m and 160 m depth and the reservoir thickness hosting the ore body is about 10 to 20 m. This permeable sandstone layer likely represents an amalgamation of channels and is interbedded with discontinous siltstone to mudstone sheets. Relatively continuous sheets of floodplain fines occur at the bottom and at the top of the reservoir hosting uranium mineralization. Therefore they represent good non-permeable to semi-permeable aquitards for groundwater flow. Two drill holes display yellow to orange oxidation affecting the sandstone layer hosting the mineralization whereas one downdip drill hole is reduced and pervasively mineralized. Therefore this secondary oxidation due to groundwater flow through permeable sandstone layers contributed to the formation of a redox front and thus led to ore deposition in the Bayinwula deposit. As illustrated in Figure 2, the arcuate shape of the Bayinwula deposit is typical of roll front-
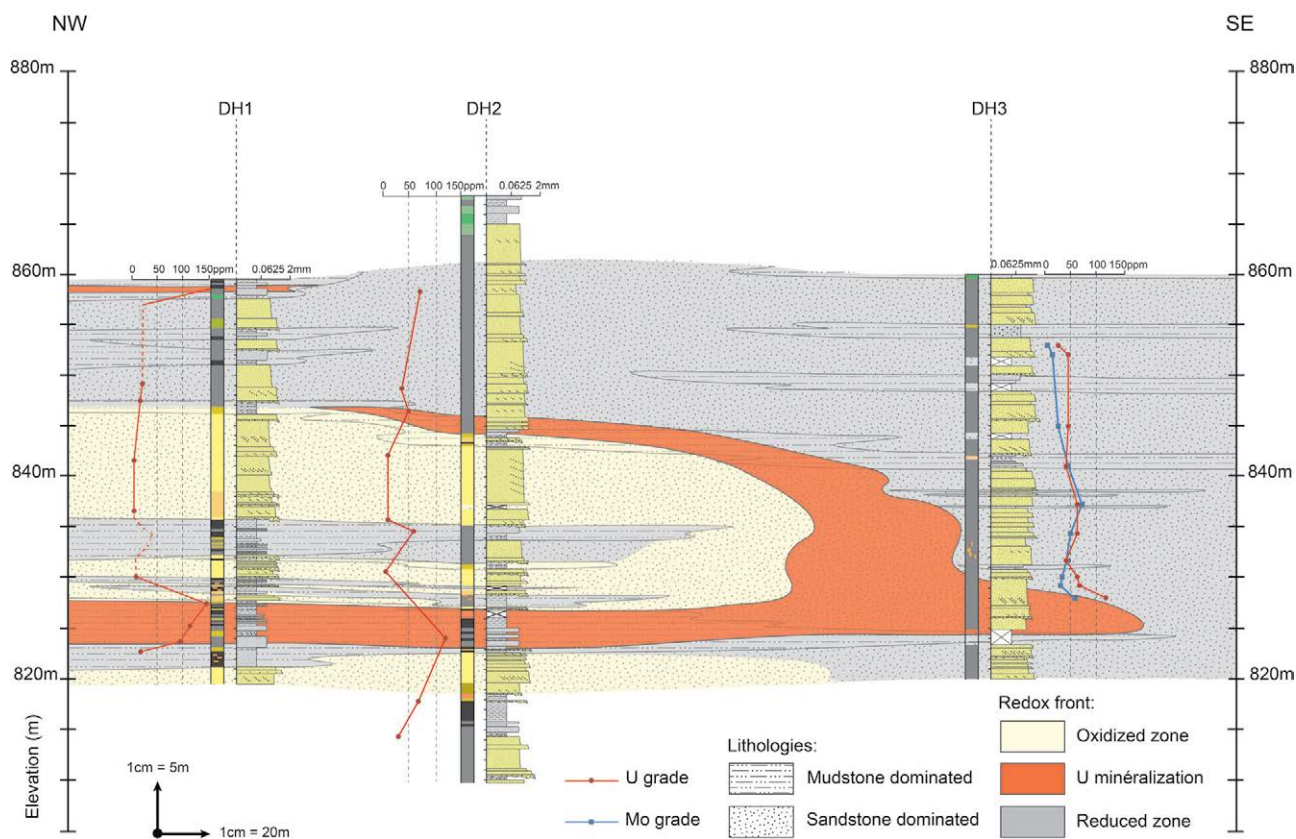
Figure 2, Drill hole cross-section of the Bayinwula Deposit, Manite sub-Basin. This section is oriented NW-SE. Two drill holes are located in the oxidized zone (DH1 and DH2); one drill hole is located in the reduced zone (DH3). U = uranium; Mo = molybdenum.

type uranium mineralization. Indeed according to geochemical data, the two oxidized drill holes have mineralization located at the contact between a sheet of floodplain fine interbeds and sandstone. The major part of uranium mineralization occurs between drill holes at the redox front. DH3 located just after the redox front, in the reduced zone, crosscuts the distal down-dip part of the tongue of the roll corresponding to the main ore body. Uranium mineralization observed in the section is low grade, ranging from 100 to 150 ppm. Uranium background concentration in reduced sandstone is elevated (10-50 ppm U) whereas the background in oxidized sandstone is just a few ppm U (< 10). This indicates that a significant uranium preconcentration was present in the reduced sandstone. Then part of the initial uranium content of these sandstones was leached and remobilized by oxidizing fluids flowing through the reservoir to finally be deposited at the redox front. In DH3 uranium grade is much higher than molybdenum grade (up to 117 ppm U; 54 ppm Mo) at the bottom of the reservoir. As maximum molybdenum concentration more likely appears at the distal down-dip edge of the ore zone, it is proposed that the ore body extends several tens of meters to the SW of the profile.

4 Conclusions

The Erlian Basin is an intermontane basin (like that in Wyoming) with no evidence of marine transgression with near shore environments (as for example in Texas). This basin appears to have good potential for the occurrence of uranium roll front-type deposits.

This type of deposit has been in fact discovered in the eastern part of the Wulanchabu sub-Basin (e.g. Saihangaobi deposit) and in the western part of the Manite sub-Basin (e.g. Bayinwula deposit). The depositional environments of the Saihan Formation hosting the Bayinwula deposit are dominated by braided channel fluvial facies rich in detrital organic matter. Development and accumulation of channels led to the formation of permeable sandstone layers. Where these sandstone layers are interbedded with relatively continuous floodplain fine sheets, they can facilitate the flow of oxidizing fluids through permeable sands without too much uranium dispersion. Therefore primary reduced sandstone layers containing abundant detrital organic matter fragments and pyrite will be progressively oxidized. Secondary oxidation is the cause of both the remobilization of part of the uranium disseminated within sandstones and the initiation of a redox front where the uranium mineralization of the Bayinwula deposit was precipitated. No evidence of secondary reduction by fluids migrated from deeper oil reservoir has been found.

Acknowledgements

References

Charles N (2010) Mécanismes de l'extension continentale au Mésozoïque en Asie de l'Est. PhD thesis, University of Orleans, France.

Cheng Y and Cheng W (1997) Mesozoic volcanic in western Liaoning Province and adjacent areas in China: chronology, geochemistry and tectonic background. Beijing, Earthquake Publishing House, p. 279.

Dahlkamp FJ (2009) Uranium Deposits of the world: Asia. Springer Ed., p. 29-35; 65-71.

Dou L and Chang L (2003) Fault linkage patterns and their control on the formation of the petroleum systems of the Erlian Basin, eastern China. Marine and Petroleum Geology 20, p.1213-1224.

Dou L, Zhu Y, Yang T, Xu S, Ping X (1998) Origins of heavy oils in the Erlian Basin\ NE China. Elsevier, Marine and Petroleum Geology 15, p. 658_670.

Fan X, Nie F, Chen Y, Wang W (2008) Discussion on age and paleo geographical environment of ore bearing strata for sandstone-type uranium deposits in Bayanwula area, Erlian Basin. Uranium Geology, Vol. 24-3, p.151-154. (in Chinese, English abstract).

Gou YX, Wang ZZ, Yang JD, et al. (1986) Cretaceous Ostracoda from Eren Basin of Nei Mongol along with sedimentary environments. In: Nanjing Institute of Geology and Palaeontology, Academia Sinica, the First Exploration Company, North China Oil Field, Ministry of Oil Industry (Eds.), Cenozoic-Mesozoic Palaeontology and Stratigraphy of East China. Series 2. Cretaceous Ostracod and Sporo-Pollen Fossils of Eren Basin. Anhui Science and Technology Publishing House, Hefei, 104 pp. (in Chinese, English abstract).

Graham SA, Hendrix MS, Johnson CL, Badamgarav D, Badarch G, Amory J, Porte M, Barsbold R, Webb LE, Hacker BR (2001) Sedimentary record and tectonic implications of Mesozoic rifting in southern Mongolia. Geological Society of America, Bulletin 113, 1560-1579.

Lin C, Eriksson K, Sitian L, Yongxian W, Jianye R, and Yanmei Z (2001) Sequence architecture, depositional systems, and controls on development of lacustrine basin fills in part of the Erlian basin, northeast China. AAPG Bulletin, v.85, NO. 11, p. 2017-2043.

Meng QR, Hu JM, Jin JQ, Zhang Y, Xu DF (2003) Tectonics of the late Mesozoic wide extensional basin system in the China-Mongolia border region. Basin Research 15, 397–415.

Miall AD (2010). Facies Models 4, Alluvial deposits, Edited by James NP and Dalrymple RW, Queen's University, Kingston, Canada, p.105-138.

Nie F, Chen A, Hu Q, Shen K, Qin M, Li M, Jiang M (2007) Discussion on the early Cretaceous sandstone-type uranium deposits, Erlian Basin, Inner Mongolia. Journal of Stratigraphy, Vol. 31-3, p.272-279. (in Chinese, English abstract).

Sha J (2007) Cretaceous stratigraphy of northeast China: non-marine and marine correlation. Cretaceous Research, 28, 146-170.

Wei S, Qin M, Li Y, He Z, Chen A, Shen K (2005) Late Mesozoic-Cenozoic tectono-sedimentary evolution and sandstone-hosted uranium mineralization of the Erlian basin. Mineral Deposit Research: Meeting the Global Challenge, 8th Biennial SGA Meeting Beijing, metallogeny and exploration, Chapter 3-27, p. 320-322.

Wuang X (1985) The Jurassic strata in China. Beijing, Geological Publishing House, p. 235.

The oldest uraninite of the world from the Mpuluzi and Heerenveen granites/pegmatites (Barberton area, South Africa): a possible source for the Dominion Reef quartz pebble conglomerate uranium mineralisation

Simon Carrouée, Jean-François Moyen
Université Jean Monnet, Laboratoire de Transferts Lithosphériques, Saint-Etienne, France

Michel Cuney
Université de Nancy, UMR G2R 7566 CNRS-CREGU, Nancy, France

Abstract. The detritical uraninite crystals from the Archaean quartz pebble deposits in South Africa must originate from felsic magmatic rocks. As Archaean TTGs are too poorly enriched in incompatible elements to permit uraninite crystallization, the 3105 Ma potassium-rich magmatic series around the Barberton Greenstone Belt have been investigated.

The Heerenveen and Mpuluzi batholiths represent such incompatible elements enriched magmatic suites. They are composed by different facies belonging to several magmatic phases: early sheeted leucogranites were followed by the intrusion of a large core of porphyritic granite, then by the intrusion of diverse facies in the marginal shear zones of both batholiths.

Although the average uranium content of both batholiths is low, late phases emplaced in shear zones are significantly richer. However, many of the intrusions show U/Th ratios similar to those of the bulk of the intrusions. Only the late leucogranite, its associated pegmatitic dykes in the Heerenveen batholith, and the late pegmatite in the Mpuluzi batholith, show Th/U ratios lower than one and uranium concentrations compatible with uraninite crystallization. The oldest uraninite crystals recorded on Earth have been found in a uranium-rich sample (about 290 ppm) in a pegmatite dyke from the margin of the Mpuluzi batholith.

Keywords. Uraninite, Archaean, batholith, pegmatite

1 – Archaen uraninite placers and uranium rich granites in South Africa

The oldest economic uranium deposits on Earth are the quartz pebble conglomerates (QPC) containing uraninite from the Dominion Group (3086 ± 3 Ma to 3074 ± 6 Ma) and the Witawatersrand Supergroup (2970 to 2780 Ma), within the Kaapvaal craton in South Africa (Duhamel, 2010). Before 2.2 Ga, because of the low level of oxygen in the atmosphere, tetravalent uranium was not oxidized, which means that uraninite crystals eroded from uranium-rich granitic rocks could be transported as detrital grains and concentrated in placers.

Because of its large radius and high valency, uranium is a very incompatible element and thus tends to concentrate in residual melts during partial melting and fractional crystallization, attaining the highest concentrations in the most felsic magmatic rocks (Cuney, 2010). During the Archaean, the continental crust predominantly consisted of basalts and magmatic rocks belonging to the TTG suite (trondjhemite, tonalite, granodiorite). TTG are enriched in sodium but weakly enriched in incompatible elements such as potassium, thorium and uranium. Uranium concentrations in TTG generally not exceed a few ppm, dominantly incorporated in refractory accessory minerals, and do not permit the crystallisation of uranium-rich minerals such as uraninite.

However, to explain the presence of detrital uraninite in the QPC deposits, some magmatic rocks sufficiently enriched in uranium to crystallize uraninite must have existed. In the Barberton area, north-east of South Africa, the Paleoarchaean TTG suite is intruded by the 3.1 Ga GMS suite (granodiorite, monzogranite, syenogranite). The GMS suite consists of rocks enriched in potassium (in contrast to the sodium enrichment in the rocks of the TTG suite). Uranium and thorium concentrations are also higher in the GMS than in the TTG and some may be sufficiently enriched in uranium to crystallize uraninite.

The aim of the study was find within the GMS suite of the Barberton area, the granites which are the most enriched in radioactive elements and then to study the distribution of the radioactive elements and to characterize the uranium bearing minerals.

2 – Barberton area granites

2.1 – The GMS suite batholiths

The Barberton area forms the nucleus of the Kaapvaal craton. The mid-Archaean (3600 – 3100 Ma) Barberton Greenstone Belt is surrounded by several gneissic plutons belonging to the TTG suite (3500 – 3200 Ma). The TTG plutons are intruded by the 3107 – 3074 Ma GMS suite, which consists of four batholiths: the Nelspruit batholith to the North, the Pigg's Peak to the South-East, the Mpuluzi to the South, and the Heerenveen to the South-West. The GMS batholiths form voluminous laccoliths covering a large area. The Boesmanskop and Kees Zyn Dooms syenites form elongated small bodies emplaced at about the same age as the larger batholiths.

2.2 – The Heerenveen batholith

Located to the southwest of the Barberton Greenstone Belt, the Heerenveen batholith is the smallest of the

GMS batholiths. It is separated from the Mpuluzi batholith by a valley and may belong to the same

intrusive complex. It is composed of 8 different facies belonging to 4 main phases
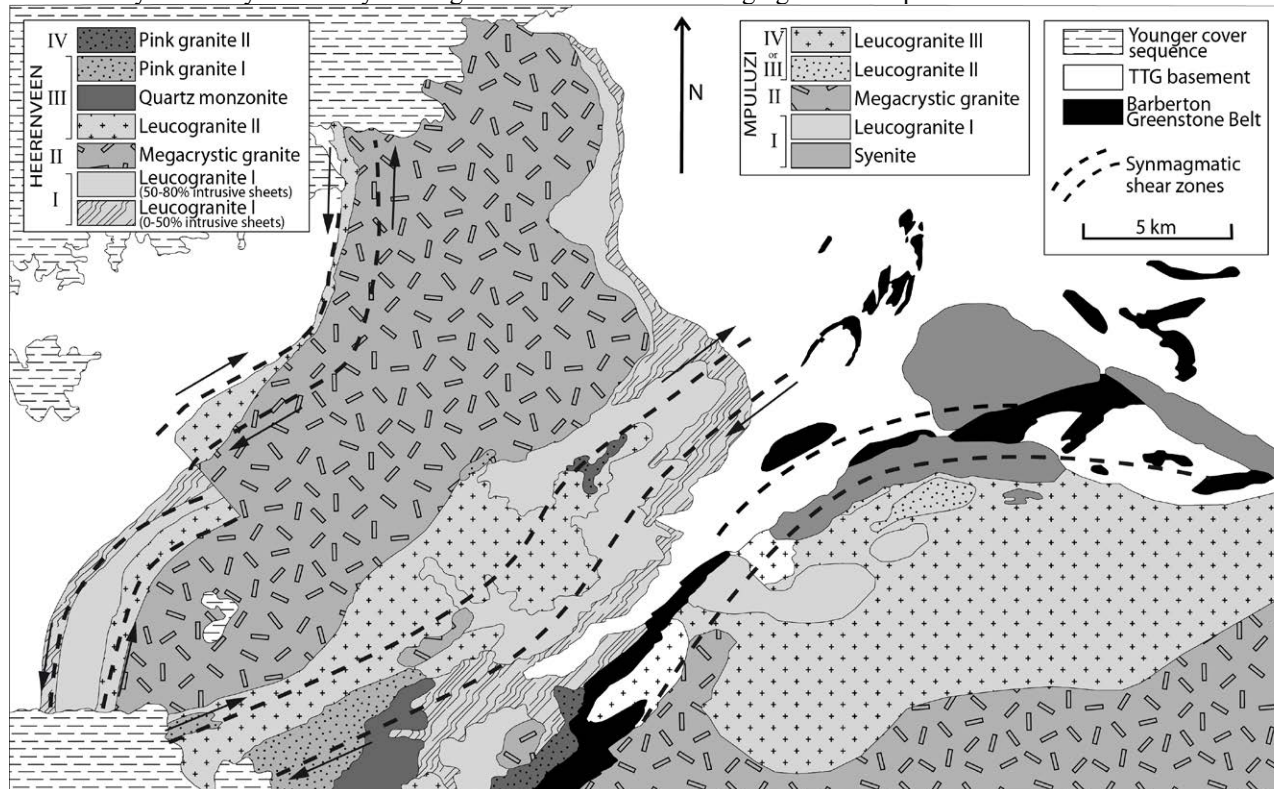
Figure 1. Geological map of the Heerenveen batholith (on the left) and the margin of the Mpuluzi batholith (on the right), after Westraat *et al.,* 2005 and Belcher & Kisters 2006. The map shows the different facies and their four phases of emplacement. The whole Heerenveen batholith and the northwest trending shear zone along the margin of the Mpuluzi batholith have been investigated.

of emplacement : a first sheet-like leucogranite was emplaced in the gneissic basement and was followed by the intrusion of an homogeneous, weakly deformed, large body of porphyritic granite (the main phase in the Heerenveen and Mpuluzi batholiths). Then a series of smaller, strongly deformed bodies (a second phase of leucogranite, a quartz-monzonite and a first phase of pink granite) were injected into shear zones developed at the margin of the batholith. The final and fourth phase consists of the post-tectonic intrusion of a second phase of pink granite devoid of any deformation (Belcher & Kisters, 2006; Clemens et al., 2010) (figure 1).

2.3 – The Mpuluzi batholith

The Mpuluzi and Heerenveen batholiths are separated by the Mkhomazane valley. The porphyritic granite represents the main intrusion in both batholiths. However, the Mpuluzi batholith covers a very large area, and only its north-western margin, adjacent to the Heerenveen batholith, was considered in this study. The different intrusions emplaced within the marginal zone are associated with a shear zone, similar to the one occurring at the south-eastern margin of the Heerenveen batholith on the other side of the valley.

The different magmatic units in the Mpuluzi margin are: a syenogranite similar to those of the Boesmanskop pluton, intruded by sheets of the first

phase of leucogranite and associated aplites/pegmatites. These two units were injected by multiple granodiorite intrusions (mainly coarse granodiorite and a few sheets of fine-grained granodiorite), followed by the second phase of medium- to coarse-grained leucogranite to the east of the Eagle High outcrop, and finally by sub-horizontal aplitic/pegmatitic dykes (Figure 1).

3 – Selected material and analytical techniques

During a first field visit 80 samples representing the different rock types have been collected over the Mpuluzi and the Heerenveen GMS batholiths. Whole rock analyses have revealed that the highest uranium concentrations are located in the shear-zones of the two batholiths. During a second field visit a portable gamma-ray spectrometer was used to make systematic grid measurements of the distribution of U, Th and K at different scales throughout the Heerenveen batholith and on some selected outcrops, and to assist in selecting samples with the highest uranium concentrations. Selected whole rock samples were analyzed by ICP-OES for the major elements and ICP-MS for 43 trace elements. The petrography of the samples have been studied on polished thin sections and autoradiographies have been made on three uranium-rich samples : one from the Heerenveen

batholith (second leucogranite, about 60 ppm U), one from the Mpuluzi margin (late pegmatite, about 290 ppm U) and one from the Boesmanskop pluton (a pegmatite too, about 210 ppm). These samples have been studied with a scanning electron microscope to characterize the uranium bearing minerals.
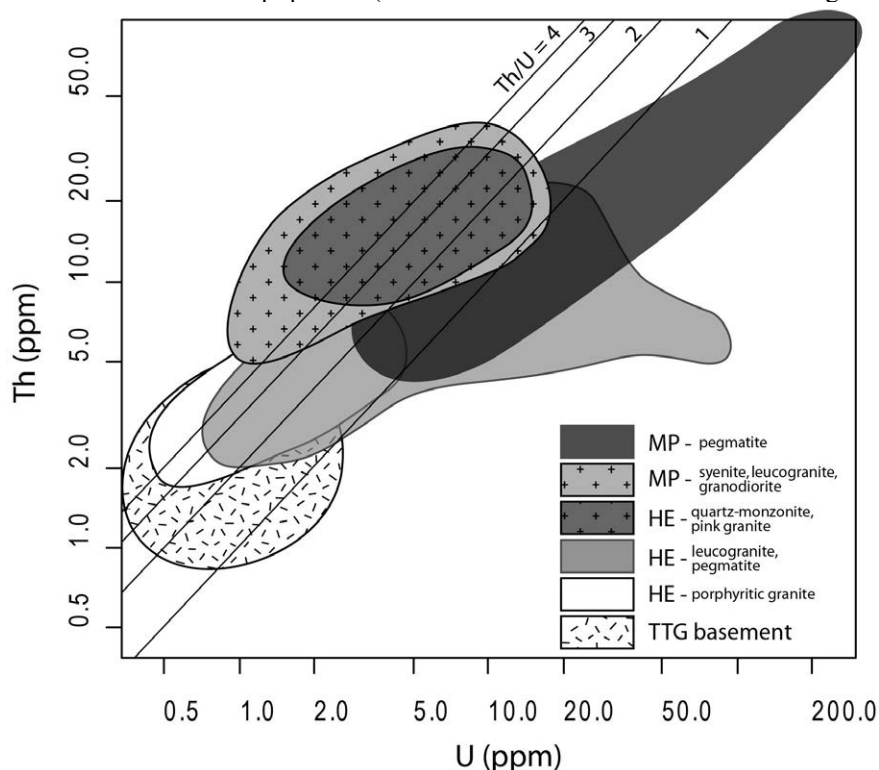
Figure 2. Th vs. U (ppm) diagram showing the geochemical variations between the different facies. White zone, porphyritic granite from the Heerenveen batholith ; light grey zone, leucogranite and pegmatite from Heerenveen ; dark grey zone with crosses, quartz-monzonite and pink granites from Heerenveen ; light grey zone with crosses, syenite, leucogranites and granodiorite from the Mpuluzi batholith ; and dark grey zone, pegmatite from Mpuluzi.

4 – Results: multi-scale uranium and thorium distribution

4.1 – Regional scale distribution

Sample analyses and spectrometric data show that average uranium concentrations in the two batholiths vary from 3 to 6 ppm. Such uranium concentrations are too low to permit uraninite crystallisation. The composition of later phases of the Heerenveen batholith injected in the shear zone, such as the pink granites and the quartz-monzonite both uranium and thorium are enriched, maintaining the primitive Th/U ratio of about 3-4, are also incompatible with the crystallization of uraninite. In the Heerenveen batholith, the only samples having Th/U ratios lower than one, permitting the crystallization of uraninite, have been found in the second leucogranite phase and associated pegmatite dykes with uranium values up to 60 ppm (figure 2).

At the margin of the Mpuluzi batholith, average uranium and thorium concentrations are higher than average U and Th concentrations in the Heerenveen batholith, but are comparable to the concentrations measured in the different facies associated with the shear zones, especially those of the pink granites and the quartz-monzonite. The different facies in the Mpuluzi shear zone show exactly the same U and Th concentration ranges and Th/U ratios (about 3 to 4),

except for the late aplite/pegmatite dykes. In those dykes, uranium concentrations are often higher than in the other facies, and Th/U ratios are much lower (often below 1), as was measured in the same unit in the shear zone of the Heerenveen batholith (Figure 2).

4.2 – Outcrop scale distribution

In the Heerenveen batholith, the intrusions of the second leucogranite took place within or close to the shear zones and at least some of them were intruded while shear zones were active, since some of the leucogranite sheets are strongly deformed with fine to elongated grains, whereas others are coarse-grained and only weakly deformed. The leucogranite sheets are intruded by a great number of pegmatite dykes commonly showing evidences of mixing with the enclosing leucogranite.

This second leucogranite is not always enriched in uranium: some metre-scale "hot spots" can be surrounded by large areas with much lower uranium concentration. The main uranium enrichment seems to be associated with the pegmatite dykes. In some outcrops, the highest uranium concentrations seem to be associated with the strongly deformed leucogranite, mixed with elongated pegmatite dykes. In other outcrops, where both the leucogranite and the pegmatite are less deformed, uranium hot spots are associated with the sub-vertical pegmatite dykes, and

with brittle fracture zones within the leucogranite.

In the Mpuluzi shear zone, uranium hot spots are clearly associated with the late pegmatite dykes, as in the Heerenveen batholith. But unlike the late pegmatite from the Heerenveen shear zones, the pegmatite dykes intrude all the magmatic units with sharp contacts, with no evidence of mixing as observed in the Heerenveen shear zone.
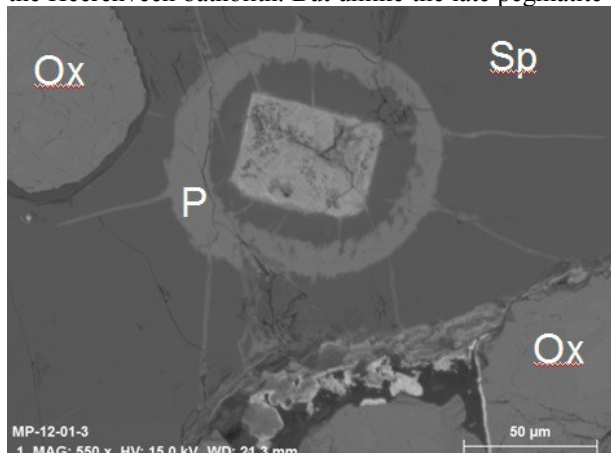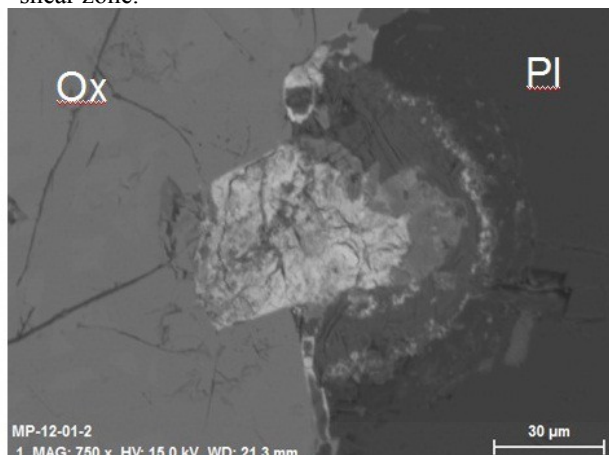
Figure 3. Two SEM images in backscattered electron mode of two altered uraninite crystals. Ox, iron oxide ; P, unidentified phosphate ; Sp, sphene ; Pl, plagioclase.

4.3 – Sample and microscopic scale uranium distribution

At the sample scale, autoradiographies of samples richest in uranium reveal a great number of radioactive spots disseminated in the granitic/pegmatitic material and also the presence of fractures filled with secondary redistributed radioactive material.

In the samples with high Th/U ratios, uranium is mainly associated with thorium and/or REE bearing accessory minerals such as uranothorite, monazite and xenotime. Only small grain (about 10 μm) containing 60% U_2O_3 associated with iron and titanium has been found in a sample from the Mpuluzi shear zone.

Monazite crystals are often strongly altered and replaced by apatite containing small uranothorite crystals, REE being reincorporated in newly formed allanite. Uranium liberated from the altered monazites is incorporated in the uranothorite crystals, but a part of the uranium could have been released into the alteration fluids. Uranium is also found at the margin of altered titanium-iron minerals such as ilmenite (up to 5% U_2O_3 in the altered margins and less than 1% into the non-altered core of the crystals).

Primary magmatic uraninite crystals have been found in the samples that are most enriched in uranium (from a late pegmatite dyke from the Mpuluzi shear zone) (Figure 3). Those uraninite grains are about 40 to 100 μm across. They have been strongly altered by the supergene fluids, with a residual thorium-rich core (though sometimes containing more uranium than thorium), surrounded by the typical destruction rim developed at the expense of the host minerals (mostly feldspars).

5 – Conclusion

The magmatic fractionation processes in the GMS batholiths were able to generate pegmatites sufficiently enriched in uranium and relatively depleted in thorium to permit the crystallisation of magmatic uraninite. The age and the size of the uraninite crystals (the oldest recorded on the Earth) from the pegmatite of the Mpuluzi shear zone wall correspond to those of the Dominion Reef quartz pebble conglomerates and such pegmatites represent a possible source of uraninite for these QPC. Deeper drilling would be necessary to obtain fresh uraninite crystals.

A geochemical study is now being undertaken to specify the different magmatic series and their source(s), in order to better understand the mechanisms of uranium and thorium enrichment during a period in Earth history when magmatic rocks rich in incompatible elements were very rare.

References

Belcher R. W. & Kisters A. F. M. (2006). Progressive adjustments of ascent and emplacement controls during incremental construction of the 3.1 Ga Heerenveen batholith, South Africa. *Journal of Structural Geology* **28**, 1406-1421.

Clemens J. D., Belcher R. W. & Kisters A. F. M. (2010). The Heerenveen batholith, Barberton Mountain Land, South Africa: Mesoarchaean, potassic, felsic magmas formed by melting of an ancient subduction complex. *Journal of Petrology* **51**, 1099-1120.

Cuney M. (2010). Evolution of uranium fractionation processes through time: driving the secular variation of uranium deposit types. *Economic Geology* **105**, 553-559.

Duhamel I. (2010). Caractérisation des sources d'uranium à l'Archéen. Mécanisme de genèse des gisements d'uranium les plus anciens (3,0 à 2,2 Ga) et des préconcentrations uranifère paléoprotérozoïques. *Thèse Géosciences. Vandoeuvre lès Nancy, Université Pointcarré – Faculté de sciences.*

Westraat J. D., Kisters A. F. M., Poujol M. & Stevens G. (2005). Transcurrent shearing, granite sheeting and the incremental construction of the tabular 3.1 Ga Mpuluzi batholith, Barberton granite–greenstone terrane, South Africa. *Journal of the Geological Society* **162**, 373-388.

The synmetamorphic uranium deposits in high-grade Neoproterozoic rocks in the Lufilian belt, Domes region, Zambia

Aurélien Eglinger[1], Alexandre Tarantola[1], Olivier Vanderhaeghe[1], Anne-Sylvie André-Mayer[1], Clément Ferraina[1], Michel Cuney[1], Mike Richards[2], Marc Brouand[3]

[1] UMR GeoRessources, CNRS-CREGU, Université de Lorraine, Nancy, France
[2] Barrick exploration, Lumwana, Zambia
[3] AREVA, BU Mines, Paris, France

Abstract: The Pan-African Lufilian belt, in the Democratic Republic of Congo and Zambia, is known for its world-class copper and cobalt deposits. In addition, the Lufilian belt hosts several uranium occurrences localized within deformed siliciclastic rocks of the basal Neoproterozoic Katanga Supergroup. The western part of the Domes region, in the internal zone of the orogenic belt, is characterized by metamorphism reaching upper amphibolite grade. Several uranium occurrences are described from this area, along the contact between sheared metasediments of the Lower Roan Group and the gneissic-migmatitic basement. The host rocks are kyanite micaschists and ore minerals are represented by uraninite and brannerite associated with rutile, molybdenite and graphite. New U-Pb isotopic ages on uraninite at ca. 530 Ma were obtained using *in-situ* SIMS analyses. Conventional rutile and graphite thermometers yielded a temperature for uranium oxide crystallization at ca. 600-630 ℃. Fluid inclusion study indicates two potential uranium-bearing fluid events, described as syn- to late-orogenic. These fluids, with $H_2O-N_2-H_2-CaCl_2$-NaCl and $H_2O-CO_2-CO-CaCl_2$-NaCl compositions, are characterized by a high salinity (respectively, 31-40 wt% $CaCl_2$, 13-27 wt% NaCl and > 35 wt% $NaCl_{eq}$) and a high homogenization temperature (> 350 ℃). These metamorphic fluid circulation events are associated with pervasive Ca and Na-Ca (scapolitization) alterations coring the gneissic-migmatitic domes. We propose that uranium was leached from U-rich minerals by metamorphic brines during this hydrothermal event and deposited within the kyanite micaschist outcropping around the gneissic-migmatitic domes.

Keywords: Lufilian belt; uranium oxide; fluid inclusions; syn- to late-orogenic; *P-T-t* path; uranium source

Introduction

The Lufilian belt formed during the Pan-African orogeny as a result of collision between the Congo and Kalahari cratons contributing to the formation of the Gondwana supercontinent (Unrug, 1983). This orogenic belt hosts (i) world-class Cu-Co deposits within deformed Neoproterozoic Katanga metasedimentary rocks and (ii) uranium occurrences with isotopic U-Pb ages of ca. 650 Ma and ca. 530 Ma (Decrée et al., 2011; Fig. 1). The first uranium event, at ca. 650 Ma, is due to late diagenetic to hydrothermal processes preceding the Pan-African orogeny (Eglinger et al., in press). This mineralizing event is considered as a Neoproterozoic equivalent to the world-class Canadian and Australian unconformity related U deposits, thus representing the youngest known deposits of this type (Eglinger et al., in press). The second uranium mineralization event, at ca. 530 Ma, appears to be synchronous with the Pan-African orogeny, associated with hydrothermal-metamorphic processes

(Cosi et al., 1992; Decrée et al., 2011; Eglinger et al., in press). In this paper, we document and discuss the *P-T-t* path of U mineralizations and their host rocks in the western part of the Domes region in Zambia. We also characterize the ore fluids and discuss the potential source of uranium within the context of a global metallogenic system.

1 Geological setting of the Lufilian belt
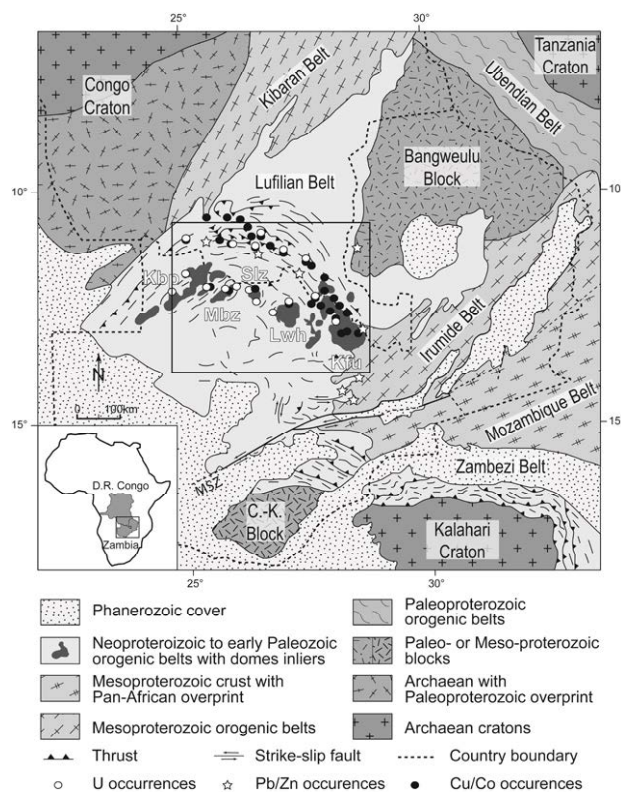
Figure 1. Geological map of the Lufilian belt and Cu-Co-U occurrences (modified after De Waele et al., 2008). Abbreviations: Kbp = Kabompo dome; Mbz = Mwombezhi dome; Slz = Solwezi dome; Lwh = Luiswishi dome; Kfu = Kafue anticline; MSZ = Mwembezhi shear zone. (Black rectangle: study area enlarged in Figure 2).

The Lufilian belt is subdivided into four lithotectonic units, from the external (north) to internal (south) zones: External fold-and-thrust belt, Domes region, Synclinorial belt and Katanga high (De Swardt and Drysdall, 1964). The metamorphic grade increases from prehnite-pumpellyite in the External fold-and-thrust belt to upper Amphibolite facies in the Domes region. The Domes region is characterized by complexly folded metasediments of the Katanga Supergroup overlying a gneissic and migmatitic unit interpreted as representing

the basement of the Katanga Supergroup and exposed in the core of dome-shaped structures (Mendelsohn, 1961; De Swardt and Drysdall, 1964; Cosi et al., 1992; Porada and Berhorst, 2000). Within the Domes region, the metamorphic grade increases from east to west, from upper Greenschist to upper Amphibolite facies. Uranium mineralization occurs mainly in the metamorphosed equivalent of the Lower Roan Group, which crops out for 600 km along the contact between a metasedimentary cover and the gneissic-migmatitic basement (Meneghel, 1981). Uranium occurrences are distributed over about 300 km from west to east and include Lolwa, Kawanga, Malundwe, Mitukuluku, Musoshi and Nkana showings (Menegel, 1981; Cosi et al., 1992). In this paper, we focus on the western part of the Domes region (Fig. 1).

2 Uranium mineralization in the Domes region (internal zone of the Lufilian belt)

In the western part of the Domes region, the uranium deposits are mostly located within shear zones marking the contact between isoclinally folded metasedimentary rocks of the Lower Roan Group, at the base of the Katanga Supergroup, and the gneissic-migmatitic basement, for example at the Lolwa, Kawanga (Kabompo dome) and Mitukuluku (Solwezi dome) deposits (Meneghel, 1981; Cosi et al., 1992). Alternatively, uranium mineralization is also found within a sheared tectonic slice of gneissic-migmatitic basement intercalated between the Lower Roan metasedimentary sequences, as in the case of the Malundwe deposit (Mwombezhi dome; Bernau, 2007; Fig. 2).
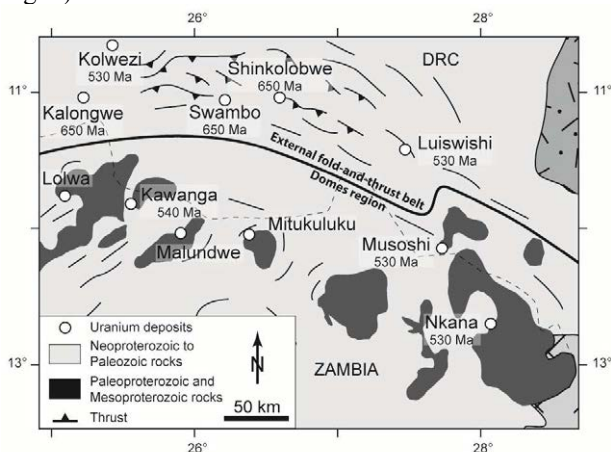
Figure 2. Location of the main uranium occurrences with age data (Cathelineau et al., 1990; Decrée et al. 2011). Dashed black line : international boundary between the Dem. Rep. of Congo and Zambia; thick black line: limit between the Ext. fold-and-thrust belt and the Domes region.

Uranium mineralization is hosted in quartz-rich micaschists affected upper Amphibolite grade metamorphism characterized by porphyroblasts of kyanite associated with phlogopite, white mica, Mg-chlorite and talc (Meneghel, 1981; Cosi et al., 1992). The protolith of the Lower Roan metasediments is derived from an evaporitic sequence (Selley et al, 2005). The gneissic-migmatitic domes are characterized by orthogneiss, paragneiss, migmatite and peraluminous granite. Ore mineralogy is characterized by uraninite

[UO_2] and brannerite [(U, Ca)(Ti, Fe)$_2$O$_6$], with associated minerals such as rutile, iron oxide, copper sulphides, apatite, monazite, zircon and scapolite. The highest grade/thickness intersection has been sampled in drill holes at the Mitukuluku showing, with 1.4 wt.% U_3O_8 over a thickness of 9 m (Arthurs, 1974). In the Kawanga showing, discontinuous uranium mineralization has been intersected by drilling over several with U_3O_8 content as high as of up to 1 wt% (Meneghel, 1981).

3 Results

3.1 Uraninite dating from the sheared micaschist

Three new *in-situ* U-Pb isotopic ages were obtained for uraninites from the western part of the Domes region and more precisely from the Kawanga (Kabompo Dome), Malundwe (Mwombezhi dome) and Mitukuluku (Solwezi Dome) deposits. Twelve uraninite grains were selected from thin section and analyzed on a SIMS CAMECA IMS1270 at the CRPG (Nancy, France). U-Pb isotopic data for uraninites from Kawanga, Malundwe and Mitukuluku deposits plotted in concordia diagrams gives discordia with upper intercepts at 517±13 Ma, 538±9 Ma and 531±7 Ma, respectively.

3.2 Thermobarometry study of the mineralization and host rocks

In order to determine at which temperature uranium oxides crystallized, we used conventional thermometry such as the substitution of zirconium within rutile (Watson et al., 2006; Tomkins et al., 2007) and the degree of organisation of carbonaceous material (Beyssac et al., 2002). In the Malundwe deposit (Mwombezhi dome), uraninite grains, scattered within the foliation defined by phlogopite and kyanite crystals, are cogenetic with rutile and molybdenite. Zirconium content within rutile grains was obtained by LA-ICPMS, at GeoRessources laboratory (Nancy, France), using a NIST 610 SRM certified glass as external standard (Lach et al., 2013). Zirconium in the rutile grain substitutes for titanium. Nine analyses were made on different grains, core and/or rim, and yielded a Zr average of 181 ppm with a standard deviation (1σ) of 10 ppm. Using the equations of Watson et al. (2006) and of Tomkins et al. (2007), a temperature of 603±4 °C is calculated for rutile crystallization. In addition, in the Malundwe deposit, uranium oxide is cogenetically associated with carbonaceous material. During increasing metamorphism, organic matter is progressively transformed into graphite. The degree of organisation of carbonaceous material (CM) is directly controlled by the metamorphic grade (Beyssac et al., 2002). Following the methodology of Beyssac et al. (2002), we characterized the degree of organization of CM by Raman spectroscopy and obtained an average temperature of 626±50 °C. The same temperature range is obtained with Zr-in-rutile thermometry. These *in-situ* temperatures obtained on minerals, intimately associated with uranium oxides, are in good agreement with *P-T* conditions obtained on whole rocks. Using the bulk chemistry of kyanite-bearing micaschist samples from the Lower

Roan Group, a *P-T* pseudosection was modelled by Perpel_X software in the KFMASH (K$_2$O, FeO, MgO, Al$_2$O$_3$, SiO$_2$, H$_2$O) system (Connolly, 2005). The equilibrium assemblage for this rock is: quartz-kyanite-phlogopite±chlorite. This paragenesis reflects the metamorphic peak and is constrained by a trivariant field with a temperature ranging from 590 to 670 °C at a pressure ranging from 6 to 14 kbar.

3.3 Fluid inclusion study

In order to examine the *PVTX* properties of the fluid(s) responsible for the uranium mineralization described in the Domes region, a fluid inclusion study was performed on a representative sample from Lolwa deposit (Kabompo dome). This study focused on a smoky quartz vein, transposed within kyanite micaschist (Lower Roan Group), and intimately associated with uranium oxides. Uranium is present under the form of brannerite with the following calculated structural formula: (U$_{0.6}$Ca$_{0.2}$)(Ti$_{0.9}$Fe$_{0.1}$)$_2$O$_6$. The different fluid inclusion populations were mapped carefully and analyzed by microthermometry and Raman spectroscopy.

Petrographic and microthermometric data of fluid inclusions indicate the presence of several fluid events, underlining the complexity of the hydrothermal system in the Domes region. On the basis of the relative chronology of the fluid inclusion planes, of the shape and the phases present at room temperature, four populations are distinguished.

The first population is characterized by multiphase (liquid+vapor+halite+solids) aqueous inclusions. The vapor phase is composed of N$_2$ and H$_2$. The inclusions contain hematite, calcite and other unidentified minerals. The eutectic temperature indicates that the fluid is composed by H$_2$O-CaCl$_2$-NaCl system. Salinity of this fluid is calculated from the antarticite and halite dissolution temperature and is in the range 31-40 wt% CaCl$_2$ and 13-27 wt% NaCl. This fluid circulated during high-temperature grain boundary migration and chessboard subgrain recrystallization of quartz grains.

The second population of inclusion is triphasic (liquid+vapor+halite). It is a CO$_2$-CO bearing aqueous dominated fluid with a homogenization temperature higher than 350 °C. The eutectic temperatures characterize a H$_2$O-NaCl-CaCl$_2$ system. The halite dissolution temperature range corresponds to salinities higher than 35 wt% NaCl$_{eq}$. This population could represent the fluid which circulated through the quartz vein during ductile deformation.

The third population is characterized by two fluid inclusion types observed within the same planes with (i) carbonic dominated inclusions in the CO$_2$±CO-H$_2$O system and (ii) aqueous inclusions with the presence of halite characterized by H$_2$O-CO$_2$-CO-NaCl-CaCl$_2$ system. The halite dissolution temperature range corresponds to a salinity higher than 33 wt% NaCl$_{eq}$. These inclusions are interpreted as the result of an unmixing of the fluid of the second population at about 250-300 °C at the ductile/brittle transition.

Finally, the ultimate population is an only-aqueous fluid. This post-deformation population is the latest fluid which circulates through the quartz. This fluid has a lower salinity ~ 15 wt% NaCl$_{eq}$ and is characterized by homogenization temperature close to 100 °C.

3.4 Petrography of the accessory minerals of the gneissic-migmatitic domes (Solwezi and Mwombezhi domes)

Mineralogy of accessory minerals from the gneissic and migmatitic rocks outcropping within the Solwezi and Mwombzehi domes is characterized by the presence of monazite, allanite, zircon, apatite, (Th-REE)-silicate, urano-thorite and a REE carbonate. Monazite grains display a corona texture with allanite and epidote rims. Allanite crystals are strongly altered and filled with newly-formed (Th-REE)-silicate, REE carbonate and apatite. The monazite => allanite reaction reflects an alteration associated with circulation of a fluid rich in Ca. Scapolite is present in different lithologies of the domes (Mwombezhi and Solwezi domes) and varies in composition between three end-members: Ca$_4$(Si, Al)$_{12}$O$_{24}$(CO$_3$ or SO$_4$) and Na$_4$(Al, Si)$_{12}$O$_{24}$Cl, méionite or sylvialite and marialite, respectively.

4 Discussion

New U-Pb ages at ca. 530 Ma, presented in this abstract for the Solwezi, Kabompo and Mwombezhi domes, complement the previously published ages by Cathelineau et al., (1990) and Decrée et al., (2011). This age at ca. 530 Ma on uraninite is known in the External fold-and-thrust belt from Kolwezi, Luiswishi and Kamoto deposits but also in the eastern part of the Domes region from Nkana and Musoshi deposits (Decrée et al., 2011). This age is in good agreement with that of peak Lufilian metamorphism, dated at ca. 530 Ma on monazite from the Domes region (John et al., 2004). The metamorphic peak of the host rocks is constrained between 590 and 640 °C at a pressure around 10±4 kbars. The same temperature is also obtained by *in-situ* thermometry on minerals (rutile and graphite), associated with the uranium oxides, temperature ranging from 599 °C (minimum estimate on rutile) to 676 °C (maximum estimate on graphite).

The fluid inclusion study revealed two potential uranium-bearing fluids. This interpretation is based on the fact that these fluids present a metastable composition with the presence of oxidizing and reducing phases (hematite-H$_2$ for the first one and CO$_2$-CO-H$_2$O for the second one). This atypical composition is interpreted to reflect radiolysis in presence of uranium complexes in the fluid inclusions (Dubessy et al. 1988). It is proposed that the first U-bearing fluid, characterized by (i) a complex composition H$_2$O-N$_2$-H$_2$-CaCl$_2$-NaCl, (ii) a high salinity (31-40 wt% CaCl$_2$; 13-27 wt% NaCl) and (iii) heterogeneous homogenization temperature (but mainly higher than 350 °C), represents a metamorphic fluid produced by dehydration, dissolution of evaporites and reactions involving destabilization of NH$_4$-bearing minerals. This fluid was trapped during the temperature peak of the Pan-African metamorphism in crustal thickening context at ca. 530 Ma, clearly within ductile deformation domain. The second U-bearing fluid, characterized by (i) a complex composition H$_2$O-CO$_2$-CO-NaCl-CaCl$_2$, (ii) a high salinity (> 35 wt% NaCl$_{eq}$)

and (iii) a homogenization temperature higher than 350 °C, represents a metamorphic fluid produced by decarbonation and dehydration reactions. We suggest that CO_2-rich fluid circulated during the thermal relaxation of the orogenic belt and was trapped within the ductile to brittle-ductile deformation domains.

All these U-bearing fluid circulations provided a vector for the pervasive Ca- (monazite => allanite + apatite) and/or Na-Ca (scapolitization) alteration described in the gneissic-migmatitic rocks coring the domes. The alteration of monazite and allanite might liberate uranium in solution during hydrothermal events. A mass balance calculation, based on reaction monazite => allanite + apatite, has been calculated from migmatite bulk chemistry and electron microprobe analyses of the minerals. Assuming that all cerium (Ce) content of the whole rocks (119.3 ppm) resides in monazite (23.7 wt.% Ce), the average amount of monazite in the whole rock is 501 ppm. The average Th and U contents in monazite being respectively 0.80 and 0.05 %, the Th and U amounts contained in monazite in the whole rock are respectively 4.0 and 0.3 ppm. Comparison of the average Th/U ratio in monazite (14.9) and in allanite (29.4) allows calculating that about 50 % of uranium from monazite was leached during its alteration. Accordingly, 1 km^3 of granite containing 501 ppm of monazite with 0.05 % of U is capable of liberating (under conditions of maximum extraction efficiency): 0.501 x 0.50 = 0.250 ppm of U, corresponding to 650 $t.km^{-3}$ of U during hydrothermal alteration of monazite. The same mass balance-sheet for allanite alteration to (Th, REE) silicate gives similar results. About 60 to 70 % of U is leached from the allanite. For a Ce content of gneissic rocks (in the dome) at 50 ppm, the hydrothermal alteration of allanite can potentially liberate 500-600 $t.km^{-3}$ of U.

Conclusion

Uranium deposits dated at ca. 530 Ma in the western part of the Domes region in Zambia are typical high grade U mineralizations characterized by brannerite and uraninite. They crystallized during the *T* peak of regional metamorphism, between 600 and 640 °C, during the Pan-African orogeny. Uranium (re-)mobilization was facilitated by metamorphic fluids, with an oxidized saline character, expelled during the metamorphism of evaporitic Neoproterozoic metasediments. The localization of mineralization was controlled by major tectonic structures: schistosity, shear zones and fault/thrust zones and subsequent uranium oxide precipitation was spatially associated with the presence of organic matter (graphite) and sulphide rich (copper sulphides) units, which may have acted as redox interfaces. Circulation of these metamorphic fluids allowed leaching of U-bearing minerals such as monazite, allanite and uranothorite…

Acknowledgements

References

Arthurs, J.W., 1974. The geology of the Solwezi area (Explanation of degree sheets 1226 No. 36), Zambia Geological Survey.

Bernau, R., 2007. The geology and geochemistry of the Lumwana basement hosted Cu-Co-(U) deposits, Zambia (PhD dissertation).

Beyssac, O., Goffé, B., Chopin, C., Rouzand, N., 2002. Raman spectra of carbonaceous material in metasediments: a new geothermometer. J. Metamorphic Geol. 20, 859-871.

Cathelineau, M., Boiron, M.C., Holliger, P., Poty, B., 1990. Metallogenesis of the French part of the Variscan orogen. Time-space relationships between U, Au and Sn-W ore deposition and geodynamic events — mineralogical and U-Pb data. Tectonophysics 177, 59–79.

Connolly, J.A.D., 2005. Computation of phase equilibria by linear programming: a tool for geodynamic modeling and its application to subduction zone decarbonation. Earth and Planetary Sciences Letters. 236, 524-541.

Cosi, M., De Bonis, A., Gosso, G., Hunziker, J., Martinotti, G., Moratto, S., Robert, J.P., Ruhlman, F., 1992. Late proterozoic thrust tectonics, high-pressure metamorphism and uranium mineralization in the Domes Area, Lufilian Arc, Northwestern Zambia. Precambrian Research 58, 215–240.

Decrée, S., Deloule, É., De Putter, T., Dewaele, S., Mees, F., Yans, J., Marignac, C., 2011. SIMS U–Pb dating of uranium mineralization in the Katanga Copperbelt: Constraints for the geodynamic context. Ore Geology Reviews 40, 81–89.

De Swardt, A.M.J., Drysdall, A.R., 1964. Precambrian geology and structure in central Northern Rhodesia.

De Waele, B., Johnson, S.P., Pisarevsky, S.A., 2008. Palaeoproterozoic to Neoproterozoic growth and evolution of the eastern Congo Craton: Its role in the Rodinia puzzle. Precambrian Research 160, 127–141.

El Desouky, H.A., Muchez, P., Cailteux, J., 2009. Two Cu–Co sulfide phases and contrasting fluid systems in the Katanga Copperbelt, Democratic Republic of Congo. Ore Geology Reviews 36, 315–332.

Dubessy, J., Pagel, M., Beny, J.-M., Christensen, H., Hickel, B., Kosztolanyi, C., Poty, B., 1988. Radiolysis evidenced by H_2-O_2 and H_2-bearing fluid inclusions in three uranium deposits. Geochimica and Cosmochimica Acta. 52, 1155-1167.

Eglinger, A., André-Mayer, A.-S., Vanderhaeghe, O., Mercadier, J., Cuney, M., Decrée, S., Feybesse, J.-L., Milesi, J.-P., in press. Geochemical signatures of uranium oxides in the Lufilian belt: from unconformity-related to syn-metamorphic uranium deposits during the Panafrican orogenic cycle. Ore Geology Reviews.

John, T., Schenk, V., Mezger, K., Tembo, F., 2004. Timing and PT evolution of whiteschist metamorphism in the Lufilian Arc- Zambezi Belt orogen (Zambia): Implications for the assembly of Gondwana. The Journal of geology 112, 71–90.

Lach, P., Mercadier, J., Dubessy, J., Boiron, M.-C., Cuney, M., 2012. In-situ quantitative measurement of rare earth elements in uranium oxides by Laser Ablation-ICPMS. Geostandard and Geoanalytical Research.

Mendelsohn, F., 1961a. The Geology of the Northern Rhodesian Copperbelt . (Ed.) Macdonald, London, 523 pp.

Meneghel, L., 1981. The occurrence of uranium in the Katanga: System of northwestern Zambia. Economic Geology 76, 56–68.

Porada, H., Berhorst, V., 2000. Towards a new understanding of the Neoproterozoic-early palæozoic Lufilian and northern Zambezi belts in Zambia and the Democratic Republic of Congo. Journal of African Earth Sciences 30, 727–771.

Selley, D., Broughton, D., Scott, R.J., Hitzman, M., Bull, S.W., Large, R.R., McGoldrick, P.J., Croaker, M., Pollington, N., 2005. A New Look at the Geology of the Zambian Copperbelt. Society of Econ. Geologists, Inc. 100th anniversary volume, 965–1000.

Tomkins, H.S., Powell, R., Ellis, D.J., 2007. The pressure dependence of the zirconium-in-rutile thermometer. J. Metam. Geol. 25, 703-713.

Unrug, R., 1983. The Lufilian Arc: a microplate in the Pan-African collision zone of the Congo and the Kalahari cratons. Precambrian Research 21, 181–196.

Watson, E.B., Wark, D.A., Thomas, J.B., 2006. Crystallization thermometers for zircon and rutile. Contrib. Mineral. Petrol. 150, 413-433.

Uraninite chemistry as provenance tool

H. E. Frimmel, S. Schedel, M. Depiné, M. Kern
Institute of Geography and Geology, University of Würzburg, Am Hubland, D-97074 Würzburg, Germany

H. Brätz
GeoZentrum Nordbayern, University of Erlangen-Nürnberg, Schlossgarten 5a, D-91054 Erlangen, Germany

Abstract. Systematic analyses of trace element concentrations in genetically different uraninite grains from a variety of localities revealed that trace, including rare earth element patterns in this mineral can be used to constrain its provenance. Furthermore, our new results obtained for the Witwatersrand uraninite confirm a placer origin and a derivation of the detrital uraninite grains from a high-temperature, presumably granitic source.

Keywords. Uraninite chemistry, LA-ICPMS, provenance

1 Introduction

Uraninite is the principle uranium ore and thus the most important raw material for fuelling nuclear reactors. It occurs in a huge variety of genetically different deposits, ranging from magmatic, metamorphic, various hydrothermal to sedimentary deposits. Thus the question arises as to the possibility of fingerprinting the source of a given uranium oxide. With modern LA-ICPMS technology and suitable standards, it is now possible to routinely analyze uranium oxide grains not only for their major components but also for their trace, including rare earth element (REE) chemistry.

With the aid of LA-ICPMS element mapping, Frimmel et al. (2009) could show that uraninite grains from the auriferous Mesoarchaen Witwatersrand conglomerates are marked not only by hugely variable and on average high Th contents (as observed already previously by EMPA, e.g. Grandstaff 1981) but also contain significant amounts of trace elements, such as W, Bi, Y, and REE. In a recent study Mercadier et al. (2011) presented evidence of uraninite from genetically different deposit types being distinguishable based on REE distribution patterns, thus providing a useful reference against which samples from other (unknown) localities can be compared.

In this study we extend the available data base to magmatic/pegmatitic uraninite deposits (Ekomedion, Cameroon; Spessart, Germany), a high-temperature hydrothermal example (Mary Kathleen, Australia), a range of epi- to mesothermal vein-type deposits in the Hercynian Belt of Central and Eastern Europe, the presumably syngenetic Shinkolobwe deposits (DRC) and the Witwatersrand reefs. We analyzed uraninite grains from these deposits not only for their REE concentrations but also for Th, Si, Al, Fe, Mn, Ca, Mg, P, Ti, V, Cr, Co, Ni, Pb, Zn, As, Y, Zr, Nb, Mo, Ag, Ta, W, Au, and Bi.

2 Results

Our results illustrate that higher formation temperatures facilitate the incorporation of a great number of elements into the uraninite structure, notably Th, Zr, Mo, Bi, Y and the REE, whereas epithermal uranium oxides that formed at lower temperatures are typically devoid of these elements. Granitic-pegmatitic uraninite has the highest REE contents and flat chondrite-normalized REE patterns with no or variable negative Eu-anomaly that is inherited from early plagioclase fractionation in the melt.

Hydrothermal uraninite is characterized by an enrichment in light REE, with $(\sum LREE/\sum HREE)_N$ between 10 and 100, which supports the conclusion drawn by Mercadier et al. (2011) that the REE patterns of hydrothermal uraninite mimic those of the host rock and that no major fractionation occurs during source leaching, REE fractionation and uraninite crystallization, with monazite being the most important REE source. At the Mary Kathleen deposit (Queensland) uraninite is associated with large amounts of allanite and its REE patterns again mimic that of the strongly LREE-enriched allanite. While the REE patterns help in distinguishing between magmatic and hydrothermal uraninite and in constraining a likely REE source, other trace elements can aid in further provenance studies. For example, hydrothermal uraninite from vein-type deposits in the Hercynian basement of Central/Eastern Europe (Erzgebirge, Sudeten) is extremely enriched in As (≤ 23000 ppm) and W (≤ 6250 ppm), whereas hydrothermal uraninite from other parts of the world has only a few to a few tens of ppm As and W. Similarly, uraninite from the Erzgebirge is strongly enriched in Bi (≤ 15000 ppm) and V (≤ 7600 ppm) in contrast to that from other areas. In most localities Mo contents in uraninite are on the order of maximal a few tens of ppm, but in uraninite that is associated with molybdenite in Pan-African S-type granite of Cameroon, it can reach more than 1000 ppm. That uraninite is also enriched in Nb, Y and Zr by two orders of magnitude.

Our results obtained for the Witwatersrand Reefs confirm a placer origin for the uraninite there and a magmatogenic provenance thereof. The chemistry of commonly rounded to sub-rounded uraninite is highly variable from grain to grain but generally marked by elevated Th, Fe, W, Co, Bi, Mo, Nb, Ta, Y, REE, P, As, Zn, and Ag contents and unusually high Au concentrations. Especially the high Th contents and the chondrite-normalized REE patterns are incompatible with post-sedimentary hydrothermal genetic models for the U-mineralization and point to derivation of the detrital uraninite from a high-temperature,

magmatogenic, presumably granitic to pegmatitic source (Fig. 1). The elevated Au concentrations (of as much as 67 ppm) in some uraninite grains are unique to the Witwatersrand (Fig. 2) and hint at a granitic hinterland that was enriched in both U and Au, thus presenting a potential source domain for some of the detrital gold in the Witwatersrand conglomerates. Although the correlation between element concentrations amongst all the Witwatersrand samples is poor, there can be a good correlation amongst some elements, e.g. Au/Ag (Fig. 3), within samples from the same reef. Uraninite grains from different reefs of from the same reef but from different goldfields can vary systematically by orders of magnitude with respect to a number of trace elements, such as Bi and P – a further feature that is difficult to reconcile with an epigenetic, hydrothermal model for the Witwatersrand ore bodies.
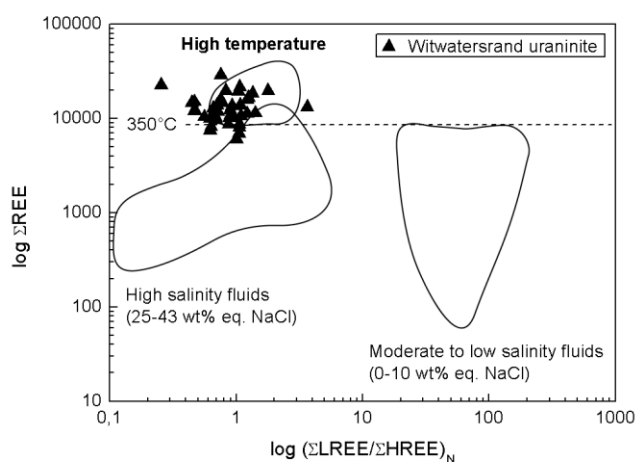
Figure 1. Total rare earth element contents versus rare earth fractionation in uraninite grains from the Witwatersrand relative to data fields outlined by Mercadier et al. (2011) for different uraninite deposit types.

3 Conclusions

The substitution of a range of different elements in uraninite, as found in this study, can be explained by their similar ionic radii compared to U^{4+} in eight-fold coordination. This applies particularly to Th^{4+} (ionic radius of 1.05 compared to 1.00 Å for U^{4+}), the REE^{3+} (1.16 – 0.977 Å), and Y^{3+} (1.019 Å; Shannon 1976). The incorporation of these elements into the uraninite structure is mainly a function of temperature and element availability. The highly different solubility of U in its different oxidation states facilitates U-mobilization by low-temperature hydrothermal fluids, provided they are oxidizing. In contrast, Th is far less mobile in hydrothermal environments due to the low solubility of Th^{4+}, the only oxidation state of this element. Consequently, it can be expected that high-temperature, magmatic uraninite is capable of incorporating significantly larger amounts of Th than low-temperature, hydrothermal uraninite.

The highly different physical conditions of U ore formation and different availabilities of other elements at the various localities led to uraninite displaying a wide range of compositions, depending on locality. Thus the trace element distribution in uraninite can be used as a provenance tool, be it for reconstructing the source of hydrothermal ore fluids or detrital uraninite grains (as in the case of the Witwatersrand), or for fingerprinting the provenance of uraninite on the black market.
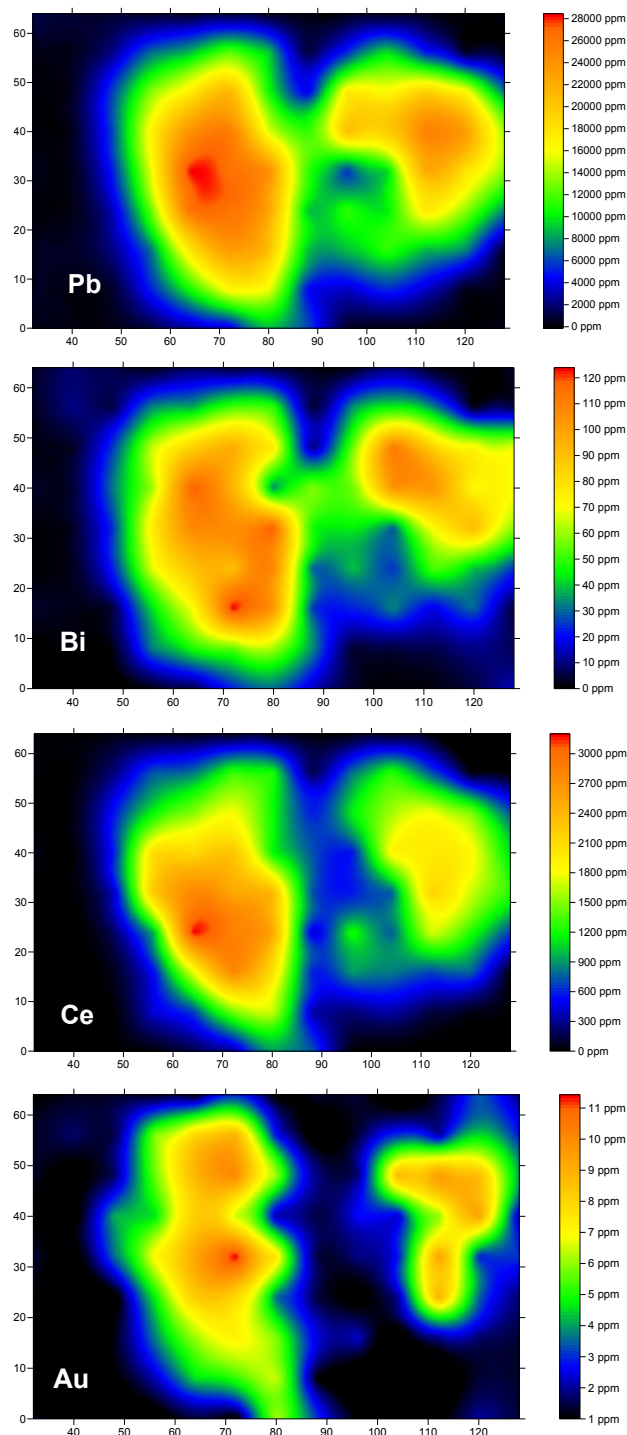
Figure 2. LA-ICPMS element (Pb Ce, Bi, Au) concentration maps of two fragments of a broken-up uraninite grain that is embedded in pyrobitumen from the B-Reef (Free State Geduld mine). Note that the Au distribution follows closely that of (radiogenic) Pb and thus the outline of uraninite (partly from Frimmel et al. 2009); length of x-axis approx.. 100 μm.

References

Frimmel HE, Emsbo P, Koenig AE (2009) The source of Witwatersrand Gold: Evidence from uraninite chemistry In: Williams PJ, et, al. (eds) Smart Science for Exploration and Mining, Proc 10th Biennial SGA Meeting, 17-20 August 2009. Townsville, pp 353-355.

Grandstaff DE (1981) Microprobe analyses of uranium and thorium in uraninite from the Witwatersrand, South Africa, and Blind River, Ontario, Canada In: Armstrong FC (ed) Genesis of uranium- and gold-bearing Precambrian quartz-pebble conglomerates. U. S. Geological Survey, Reston, pp J1-J5.

Mercadier J, Cuney M, Lach P, Boiron M-C, Bonhoure J, Richard A, Leisen M, Kister P (2011) Origin of uranium deposits revealed by their rare earth element signature. Terra Nova 23:264-269.

Shannon RD (1976) Revised effective ionic radii and systematic studies of interatomic distances in halides and chalcogenides. Acta Crystallographica, Series A 32:751-767.
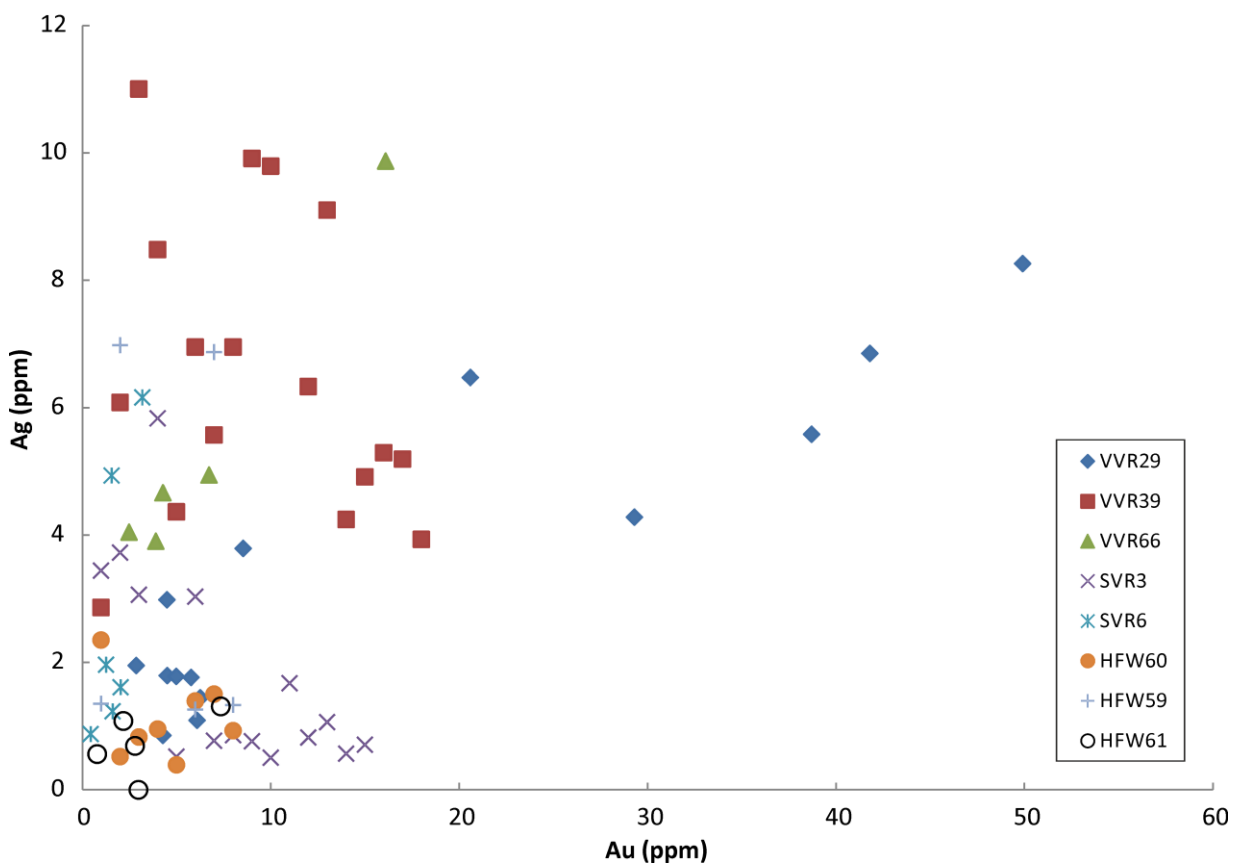
Figure 3. Correlation diagram of Ag versus Au contents in uraninite grains from different samples of the Vaal Reef at Vaal Reefs Mine (VVR29, VVR39, VVR66), the Vaal Reef at Stillfontein Mine (SVR3, SVR6), the Vaal Reef at President Steyn Mine (HFW60), the Carbon Leader Reef at West Driefontein Mine (HFW59), the Saaiplaas Reef at Saaiplaas Mine (HFW61), and the Steyn Reef at President Steyn Mine (HFW106).

Uranium mineralization in the Retortillo–Santidad Area (Salamanca, Spain): role of late alteration

F. Javier Huertas
Instituto Andaluz de Ciencias de la Tierra (Universidad de Granada-CSIC), Avda. de las Palmeras 4, 18100 Armilla, Granada, Spain.

Fernando Gervilla
Departamento de Mineralogía y Petrología and Instituto Andaluz de Ciencias de la Tierra (Universidad de Granada-CSIC), Facultad de Ciencias, Avda. Fuentenueva, s/n 18071 Granada, Spain.

Craig Gwatkin
Berkeley Minera España S.A., carretera SA-451, Km 30, 37216 Retortillo, Salamanca, Spain.

Abstract. The Retortillo-Santidad uranium deposit is hosted by Ordovician black slates of the Iberian zone, located near the Bañobarez granite intrusion (Salamanca province, NW Spain). It consists of three main ore assemblages: i) cofffinite-pitchblende-pyrite-calcite filling veins/breccias, 2) cofffinite-pitchblende fine-grained aggregates disseminated in altered zones, and 3) autunite filling cross-cutting veins. Whereas the first assemblage could be considered as primary, the distribution of the other two assemblages correlate with the alteration zoning of the host black shales and most probably formed by late remobilization of the primary ore by continuous downward percolating of meteoric solutions.

Keywords: Uranium deposit, pitchblende, coffinite, autunite, black slates, uranium remobilization,

1 Introduction

Uranium was exploited in the Salamanca province in NW Spain mainly in Mina Fe mine from 1974 to 2000. This mine, as well as some other deposits (Mina Esperanza, Mina Caridad, Alameda, Palacios, Sageras...), is hosted by Precambrian slates (with variable organic matter/graphite content) of the Esquisto-Grauváquico Formation, in the Centro Iberian Zone of the Iberian Massif (Arribas, 1970, 1985; Both et al. 1994; Martín-Izard et al. 2002). All these uranium deposits occur in close connection with late Hercynian granite intrusions but its genetic link with such granites has not been proven. In contrast, Arribas (1985) consider that the host black slates should constitute the primary source of uranium, which was remobilized by hydrothermal solutions during the Alpine Orogeny (Martín-Izard et al. 2002).

The Santidad uranium deposit has been recently discovered in the Salamanca province by Berkeley Minera España S.A. (formerly Minera de Rio Alagón S.A.). It is located in the Retortillo-Santidad area, extending NW from the Retortillo village (Figure 1). In contrast to the other uranium deposits of the Salamanca province, the Retortillo-Santidad uranium deposit is hosted by Ordovician black slates. Its primary origin is still unclear but mineralogical and textural evidences suggest a genetic evolution characterized by a complex alteration process associated with downward percolation of probably meteoric water. Percolating solutions should be able to remobilize the primary uranium ore and reconcentrate uranium minerals in nearby areas.

2 Geology

The Retortillo-Santidad uranium deposit is hosted by Ordovician gray/black slates which occupy the core of a NW-SE-trending synform, above a thick quartzite formation (the Armorican Quartzite; Figure 1). This Ordovician sequence is intruded by a coarse grained, muscovite-poor and biotite-rich granite (the Bañobarez granite) of late Variscan age. The granite itself and the associated black slates are intruded by variably thick (from several centimetres to tens of centimetres) pegmatite, aplite and quartz veins. The slates are locally tourmalinized.

The black slates have a relatively homogeneous composition made up of muscovite, quartz, biotite and andalusite, with cordierite in unaltered zones and secondary kaolinite, chlorite and minor smectite in altered zones. The samples frequently show variably defined banding, consisting of alternating quartz-rich and mica-rich bands. The thickness of bands varies from 0.1 millimetres to few centimeters. Most slates contain quartz-sulfide(±carbonate) veins of variable thickness (from tens to hundreds of micrometers), mostly oriented parallel to the foliation-banding of the rock. Sulfides mainly consist of pyrite and/or pyrrhotite with minor amounts of marcasite. Pyrite and pyrrhotite also occurs disseminated in the rock and pyrite forms narrow veins (< 10 μm thick) parallel to the foliation.

3 Alteration zoning

Alteration is relatively heterogeneous but tends to increase to the surface. Shallow samples (<15m) are characterized by the abundance of Fe hydroxides, the absence of sulfides, the strong alteration of cordierite (rarely andalusite) to pinnite and the alteration of mica and chlorite to kaolinite and/or smectite. Below this zone, slates exhibit moderate alteration consisting of partial replacement of biotite by chlorite, muscovite and chlorite by kaolinite, cordierite by pinnite, and andalusite by smectite. Textural relations and the distribution of chlorite and kaolinite suggest that chlorite formed earlier by replacement of biotite and both minerals (together
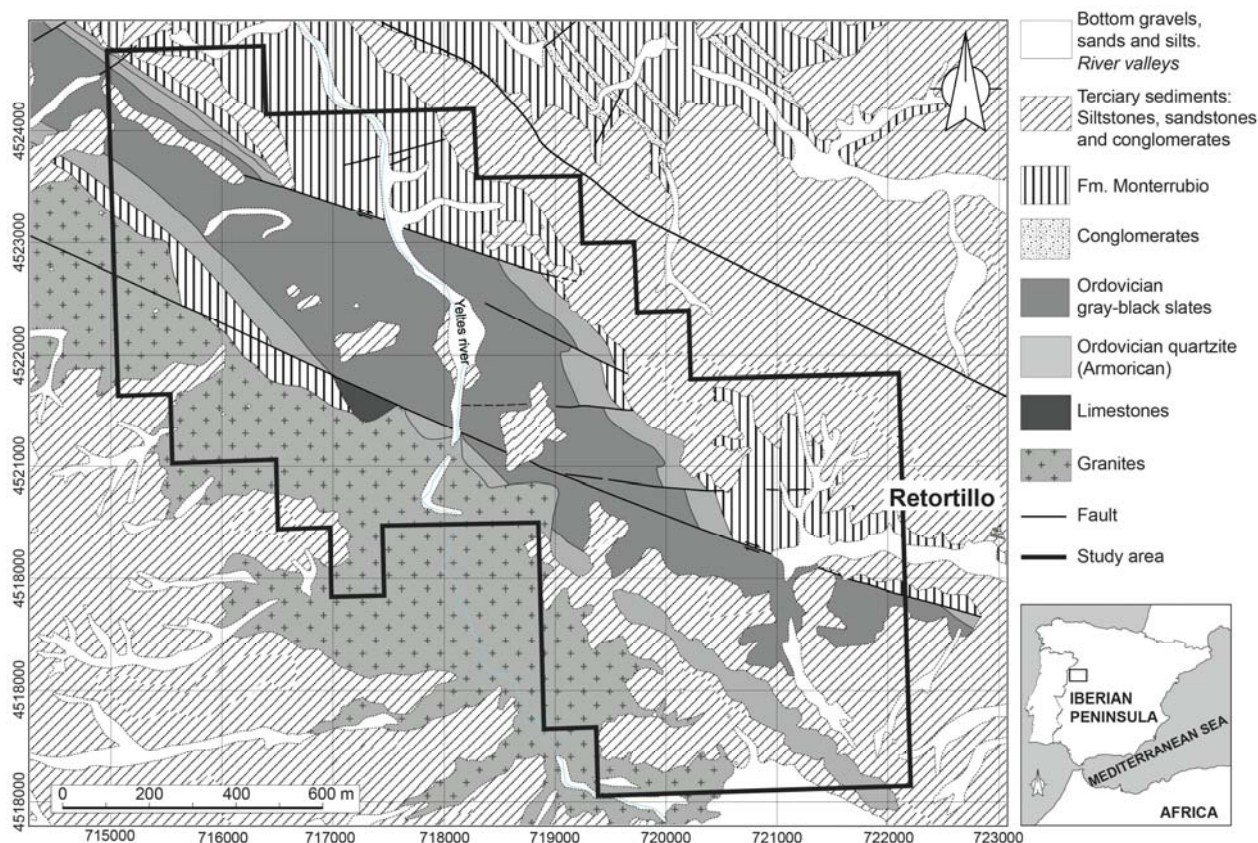
Figure 1. Geological map of the Retortillo-Santidad area.

with some muscovite) were later replaced by kaolinite, especially in the shallow samples. Pyrite, together with some marcasite, is the most abundant sulfide in this zone. The frequent occurrence of pyrrhotite as irregular, partly corroded inclusions in pyrite and marcasite suggest that these disulfides form by replacement of pre-existing pyrrhotite. In fact, pyrrhotite occurs in deep, mostly unaltered samples (it is the only Fe sulfide) whereas pyrite and marcasite are the most abundant sulfides in moderately altered samples. Deep, unaltered samples always contain cordierite. Graphite (no organic matter is preserved) is unevenly distributed among the different, variably altered zones.

The deepness reached by alteration varies from drill core to drill core, ranging between RTO-10 (slates become almost unaltered at 40 m deep) and RTO-18 (slates become slightly altered at 115 m deep).

4 Uranium mineralization

The uranium mineralization does not show regular spatial distribution but concentrates along a NW-SE-trending body within the Ordovician gray/black slates in the core of the Retortillo-Santidad synform. The spatial distribution of uranium mineralization shows several maxima, especially in the Retortillo area. In one of these maxima, drill core RTD-105 cut a strongly mineralized zone consisting of pitchblende and coffinite veins/breccias cross-cutting the foliation/banding of the partly tourmalinized host slate. These veins/breccias show a complex sequence of crystallization. The main

vein shows a nearly symmetrical crustification texture consisting of irregular bands of calcite, calcite+pitchblende-coffinite+pyrite, calcite+pyrite and pyrite+coffinite+smectites from the walls to the centre of the vein (Figure 2A). The walls of the mineralized veins are also impregnated by pyrite+coffinite+pitchblende (here coffinite becomes more abundant than pitchblende). Massive pitchblende-coffinite aggregates include idiomorphic crystals of calcite, portions of fractured tourmaline and altered crystals of biotite. These aggregates are usually dusted with abundant rounded aggregates of pyrite and, at lesser extent, marcasite of very small size (1-30 μm across). In another sample from the same mineralized vein/breccia, coffinite and pitchblende occur attached to the walls of a late open fracture too, often growing perpendicular to such walls. The silicate hosts of these open veins are deeply impregnated with coffinite, which coats pyrite grains and becomes intergrown with smectites. Coffinite and pitchblende occur associated with pyrite-marcasite and calcite showing a crystallization sequence made up of pyrite-marcasite, pyrite-marcasite+pitchblende, pitch-blende+coffinite+calcite+pyrite-marcasite and calcite from the walls to the centre of the vein. In this mineralized zone, no relationships have been found between the occurrence of uranium minerals and the presence of graphite.

Apart from this local, vein/breccia-type mineralization, the occurrence of uranium ore is quite heterogeneous. As a whole, it can be stated that uranium ore neither occurs in the shallow, strongly altered (weathered) portions of the cores nor in the deep (variable from 40 to 115 m

deep) unaltered zones. The most important uranium mineralization is located in the intermediate, moderately
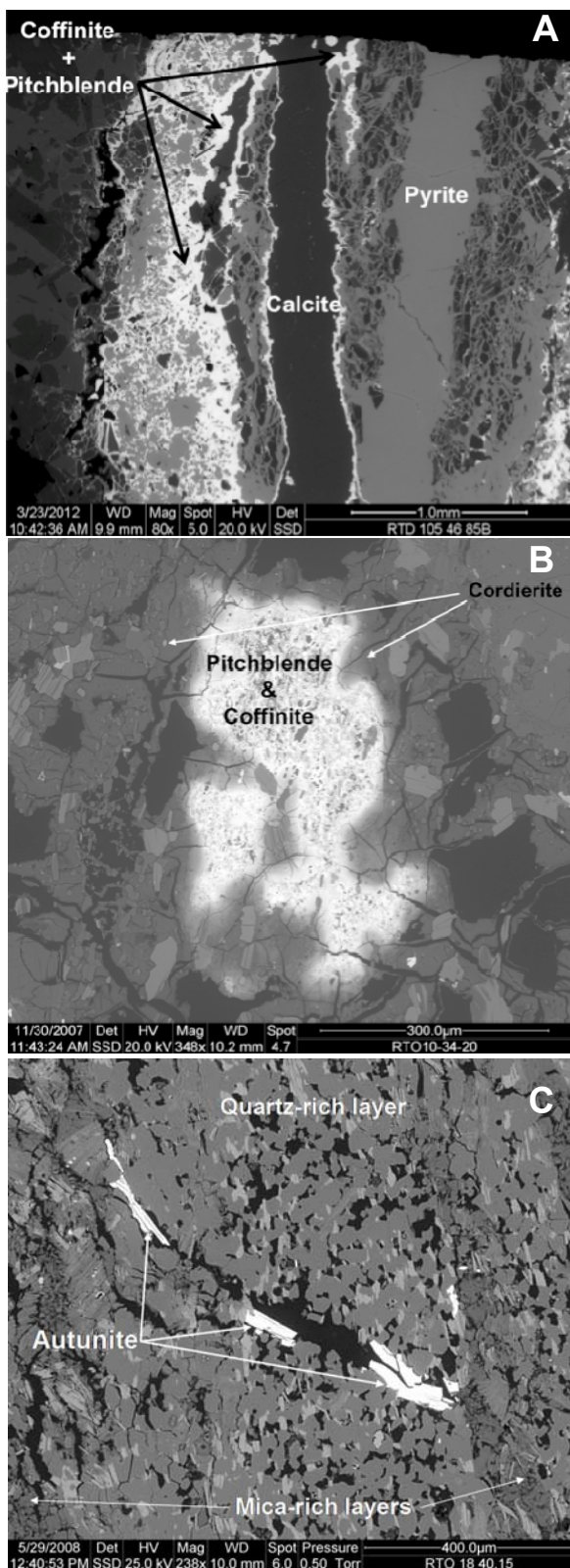
Figure 2. A: primary coffinite-pitchblende-pyrite-calcite veins; B: disseminated, patchy aggregates of coffinite with minor pitchblende; C: autunite crystals in cross-cutting veins.

altered zone of the cores showing an irregular zonal distribution: i) towards the upper part of this zone, just below the strongly altered zone (except in RTO-18 where it represent the whole mineralized zone), the

mineralization consists of uranium phosphates (autunite with minor hydrogen autunite) filling open fractures; ii) below this zone it is mainly made up of disseminated pitchblende and coffinite occurring in a varied set of textural positions: a) along grain boundaries, fractures and pores of pyrite aggregates (where uranium minerals occur associated with pyrite, they tend to coat pyrite grains); b) associated with partly dissolved biotite (mainly coffinite); it is frequent to observe coffinite aggregates arranged along the inner walls of dissolution holes in biotite; c) associated with partly altered plagioclase (mainly coffinite); d) associated with pinnite aggregates (kaolinite) after cordierite; e) intimately associated with smectite and/or pyrite filling fractures and grain boundaries of andalusite (some fractures also contain gypsum); f) along grain boundaries and fractures of rutile and apatite (mainly pitchblende). These assemblages have a very heterogeneous distribution even within a single thin section.

5 Discussion

The results of this study have revealed that the Ordovician gray/black slates hosting the uranium mineralization are variably altered from the surface downwards. Shallow samples are characterized by strong alteration of cordierite to fine grained kaolinite (pinnite), the alteration of biotite to chlorite, kaolinite and/or smectite, the partial replacement of muscovite by kaolinite and the alteration of Fe sulfides to Fe hydroxides. In contrast, deep samples tend to preserve the primary, metamorphic assemblage, including minor amounts of pyrrhotite. The latter tends to be replaced by pyrite as the alteration progress.

Textural relations suggest that chlorite and kaolinite+smectite form in two different alteration events. Whereas the formation of chlorite seems to be related with the intrusion of cross-cutting, carbonate veins, kaolinite (frequently together with smectite) forms later by replacement of muscovite, biotite and chlorite.

The uranium mineralization assemblage mainly consists of pitchblende, coffinite and/or autunite, with minor amounts of meta-autunite and hydrogen autunite. Nevertheless these minerals are not homogeneously distributed but concentrate in three main ore assemblages: i) pitchblende-coffinite ores filling cross-cutting veins/breccias; ii) autunite ores filling veins, and iii) pitchblende-coffinite ores associated with secondary kaolinite and smectite.

The pitchblende-coffinite veins/breccias show hydrothermal features similar to those described by Arribas (1985), Both et al. (1994), Martín-Izard et al. (2002) and Gervilla (unpublished data) in the Mina Fe and the Alameda, Palacios and Sageras prospects but are very rare in the Retortillo-Santidad area. In contrast, the most important mineralization is represented by the autunite veins and the disseminated pitchblende-coffinite-kaolinite-smectite ores. Both types of ores are always associated with the moderately altered zone but arranged in an irregular zonal distribution: autunite ores

tend to occur towards the upper part of the alteration zone, just below the strongly altered (weathered) zone and the pitchblende-coffinite-kaolinite-smectite ores tend to occur at the lower part of such zone.

The spatial distribution of uranium ores suggests that the mineralized veins/breccias are remnants of the primary uranium mineralization. They should form during late-Variscan or Alpine times (geological and geochronological data are somewhat contradictory; Both et al. 1994; Gómez-Barreiro and Martínez-Catalán, unpublished data) associated with a low-temperature hydrothermal event. The source of uranium is not well constrained either. Although Arribas (1985) and Martín-Izard et al. (2002) consider that uranium come from the host organic matter-rich slates, the hypothesis of a granite-related source cannot be ruled out.

The main pitchblende-coffinite-kaolinite-smectite ores as well as the autunite ores should form during a second, late alteration event. This event could be associated with downward percolation of meteoric water through sub-vertical foliation planes and fractures, as well as through porous, quartz-rich bands of the slates. These percolating solutions should be saturated in atmospheric oxygen which promoted the alteration of Fe sulfides to Fe hydroxides, supplying SO_4^{2-} and H^+ ion to the solutions, thus contributing to increase their acidity. This gave rise to an acid-oxidizing front migrating downwards that contributed to remobilize the primary uranium ores, re-distributing this metal in the nearby areas of the primary, mineralized veins/breccias. The acid-oxidizing solutions transported uranium, probably in the form of $UO_2SO_4^0$. As these solutions percolated downward through the slates they became reduced and partly neutralized, causing the reduction of uranyl sulfate complexes and the precipitation of pitchblende and coffinite, depending on the local silica activity. The decomposition of the uranyl-sulfate complexes took place by reaction of the percolating solutions with the host (the role of graphite seems to be secondary) contributing to supply the additional sulfur necessary to transform pyrrhotite into pyrite (it´s worth to note the frequent association of uranium minerals with pyrite) and to precipitate gypsum in some mineralized zones. The following equations could explain the described process:

$$9FeS + UO_2SO_4^0 + 8H^+ \rightarrow$$
Pyrrhotite

$$\rightarrow 5FeS_2 + UO_2 + 4Fe^{2+} + 4H_2O$$
Pyrite Pitchblende

and

$$9FeS + SiO_2 + UO_2SO_4^0 + 8H^+ \rightarrow$$
Pyrrhotite

$$\rightarrow 5FeS_2 + USiO_4 + 4Fe^{2+} + 4H_2O$$
Pyrite Coffinite
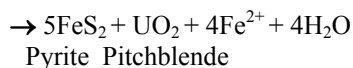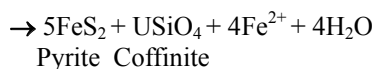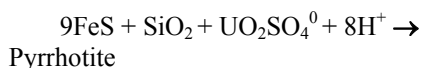
Under slightly more acid conditions, reduction of uranyl sulfate complexes could also be associated with the alteration of cordierite to kaolinite:

$$9FeS + UO_2SO_4^0 + (Fe,Mg)Al_4Si_5O_{18} + 12H^+ \rightarrow$$
Pyrrhotite   Cordierite

$$\rightarrow 5FeS_2 + 2Al_2Si_2O_5(OH)_4 + USiO_4 + 5Fe^{2+} + Mg^{2+} + 2H_2O$$
Pyrite   Kaolinite   Coffinite
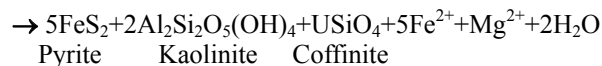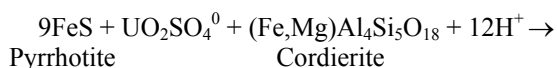
The downward percolating solutions tended to become neutralized and impoverished in uranium with depth. As a consequence deep slates tended to remain unaltered (with their primary cordierite-biotite-pyrrhotite assemblage) and barren.

It is not clear if the formation of autunite ores filling veins formed earlier or later than the pitchblende-coffinite-kaolinite-smectite mineralization. Nevertheless, textural relations show frequent replacement textures of pitchblende and coffinite by autunite suggesting that during a late stage of the alteration of the primary ores, the solutions became rich in phosphorus contributing to the replacement of uranium oxides and silicates by phosphates. These solutions could be able to remobilize some uranium as $UO_2(HPO_4)_2^{2-}$ (Romberger, 1984); then pitchblende and coffinite were either replaced by autunite or removed, being uranium re-deposited in the form of autunite. With the progress of alteration new highly acid solutions promoted partial replacement of autunite by hydrogen autunite and, finally, removilization of uranium phosphates, forming Fe hydroxides.

Acknowledgements

References

Arribas, A. (1970). Las pizarras uraníferas de la provincia de Salamanca. Estudia Geológica Salmantinesca, 7-45.

Arribas, A. (1985). Origen, transporte y deposición del uranio en los yacimientos en pirzarras de la provincia de Salamanca. *Estudios geológicos*, 41, 301-321.

Both, R., Arribas, A. and Saint-André, B. (1994). The origin of breccia-hosted uranium deposits in carbonaceous metasediments of the Iberian Peninsula: U-Pb geochronology and stable isotope studies of the Fé deposit, Salamanda province, Spain. *Economic Geology*, 89, 584-601.

Martín-Izard, A., Arribas, A., Arias, D., Ruiz, J. and Fernández, F.J. (2002). The Fe deposit, west-central Spain: Tectonic hydrothermal uranium mineralization associated with transpressional faulting of Alpine age. *The Canadian Mineralogist*, 40, 1505-1520.

Romberger, S.B. (1984). Transport and deposition of uranium in hydrothermal systems at temperatures up to 300ºC: Geologic implications. In *Uranium Geochemistry, Mineralogy, Geology, Exploration and Resources,* B. De Vivo, et al. Eds. Institute of Mining and Metallurgy (London). P. 12-17.

Paleoproterozoic U-mineralization in the Archean Pudasjärvi Complex, northern Fennoscandian Shield

Laura S. Lauri
Geological Survey of Finland, P.O. Box 77, FI-96101 Rovaniemi, Finland

Irmeli Mänttäri
Geological Survey of Finland, P.O. Box 96, FI-02151 Espoo, Finland

Abstract. Uraninite ages were measured from three samples representing different rock types present in the Asentolamminoja radioactive boulder field in southern Lapland. The boulder field is part of an uraniferous zone cross-cutting the Archean Pudasjärvi complex. The uraninites have Paleoproterozoic ages between ~2.0 Ga and 1.76 Ga, representing both original mineralization event and remobilization during a thermal event associated with voluminous granite magmatism in the area.

Keywords: uranium, age determination, uraninite, TIMS, Finland

1 Introduction

The northern part of the Archean Pudasjärvi complex in Finland (Fig. 1) hosts several uranium mineralizations that are characterized by abundant U-minerals in association with biotite, apatite, and sulphides. Mineralizations occur within deformation zones that brecciate Archean host rocks. Hydrothermal alteration (silicification, carbonate alteration and albitization) is associated with U-mineralization. The Kuohunki U-occurrence was discovered and has been drilled to some extent in the 1970's, whereas the Asentolamminoja U-boulder field was found in 2007. The known uranium occurrences lie along a 25 km-long trend extending from the Kuohunki occurrence at the Archean craton margin in the north, through the Asentolamminoja boulder field to the Isokangas area in the south, where several uranium-bearing outcrops were found (Fig. 1).
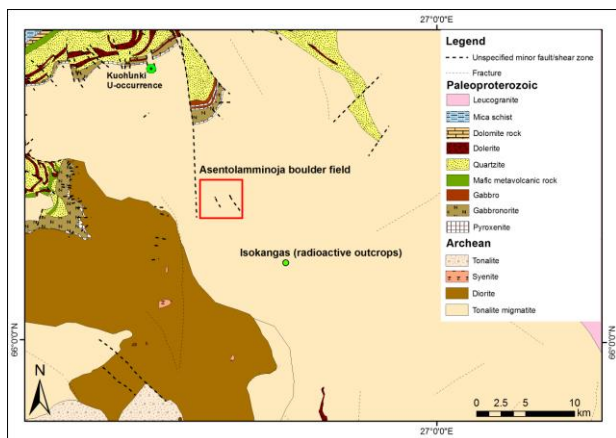
Figure 1. Geologic map of the Asentolamminoja area (DigiKP bedrock database, ©GTK). The Kuohunki U-occurrence is marked with a hexagon. The Asentolamminoja boulder field is within the square.

The Asentolamminoja boulder field (Fig. 1) consists of thousands of radioactive boulders in a 3 km by 3 km area within the glacial till that covers the bedrock. The boulders are found in the upper part of the till bed and at the surface. No outcrops are known within the boulder field. Most of the boulders are at least 50 cm in diameter and angular. The local glacial cover is part of a ribbed moraine field, where the transport distance of the boulders is interpreted to be only of the order of 50-500 m (Sarala, 2005). Thus the Asentolamminoja boulders were most probably derived from the local bedrock.

2 Sample descriptions

Three radioactive boulder samples representing different stages of alteration were studied. The biotite-rich sample A1937 is most altered of the three (Fig. 2). Due to intense alteration the original rock type of the sample is hard to constrain. The sample mostly consists of biotite, quartz and altered (weathered?) feldspar. It also contains apatite and secondary U minerals. Biotite in sample A1937 is U-bearing and abundant metamict monazite is also present. The heavy mineral fraction separated from the sample contains lustrous, black minerals that were interpreted to be uraninite. BSE images and EDS analyses of uranium minerals in sample A1937 show both U-rich and U-poor domains within single grains, U content varying from <1 wt.% to 70 wt.%.
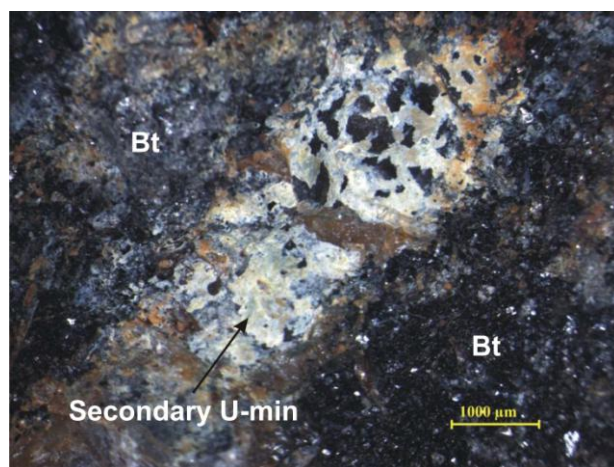
Figure 2. Sample A1937. Black minerals are mostly biotite with uraninite inclusions. Lighter coloured minerals are secondary U minerals.

The second sample A1938 consists of radioactive biotite-bearing granitoid that shows silicification and carbonate

alteration. Originally the rock may have been tonalitic gneiss. The carbonate alteration seems to cross-cut the rock in irregular veinlets (Fig. 3). The sample contained both U-minerals and carbon-bearing spherules that were thought to be thucholites. However, the carbon spherules did not contain any uranium. Some U-rich grains in sample A1938 contained no Pb.
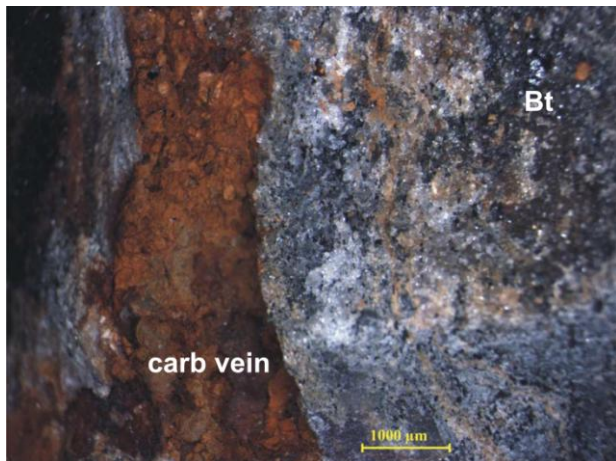
Figure 3. Sample A1938, radioactive biotite granitoid. The original gneiss texture is vaguely seen around a carbonate veinlet that contains radioactive minerals. Biotite in upper right corner most probably represents biotite alteration similar to sample A1937.

The least altered sample A1939 is relatively fresh, red granite (Fig. 4) where a small amount of rather unaltered uraninites occur in brittle fractures.
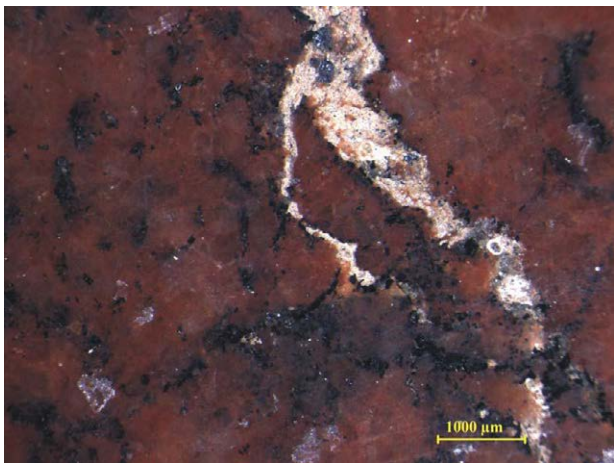
Figure 4. Sample A1939, radioactive granite.

3 Age determinations

Uraninites from the Asentolamminoja mineralization show $^{207}Pb/^{206}Pb$ ages between 1.75 Ga and 1.98 Ga (Fig. 5; Table 1). Two fractions were analysed from sample A1937. One fraction was leached for 15 minutes in 10% HF in ultrasound bath; this fraction gave a $^{207}Pb/^{206}Pb$ age of ~1.81 Ga. The other fraction was abraded prior to analysis; this fraction gave a minimum age of 1.76 Ga for sample A1937. Although the data is discordant, the fractions fall on a reference line that intercepts the Concordia curve at 1.81 Ga, which is conformable with uraninite and thucholite ages from western Lapland (Mänttäri, 1995).

Five fractions were analysed from sample A1938. Two fractions comprise graphite spheres that were thought to be thucholite. The U content of graphite spheres was very low; however, $^{207}Pb/^{206}Pb$ age acquired for the B fraction was 1.76 Ga. The C fraction consists of black, dull grains with low U content. The age result is discordant and the $^{207}Pb/^{206}Pb$ age gives the fraction a minimum age of ~1.9 Ga. Fractions D and E comprised black, dull (D) and lustrous (E) grains, which were leached with HF in ultrasound bath prior to analysis. Both fractions gave inversely discordant age results that suggest a minimum age of 1.97 Ga.

Uraninite from the Kuohunki mineralization has an unpublished age of 2.1 Ga. The older, ~2.0 Ga ages fall close to a Discordia line defined by the two heaviest fractions from sample A1938.
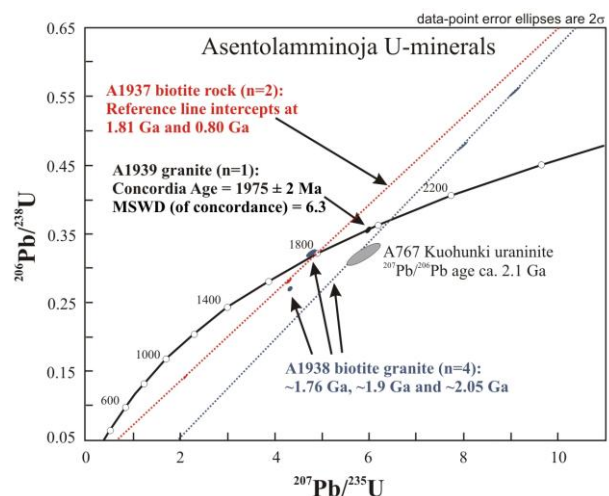
Figure 5. Concordia diagram of uraninite ages from the Asentolamminoja and Kuohunki occurrences, southeastern Lapland, Finland.

4 Discussion and conclusions

Uraninite ages between 1.80-1.76 Ga are common throughout Lapland and coincide with a period of abundant granitic magmatism in central Lapland (Mänttäri 1995). At Asentolamminoja, the younger uraninite ages reflect most probably remobilization of uranium. We interpret the older ~2.0 Ga ages as being closer to the original mineralization event. The reason for the reverse discordance observed in the D and E fractions in sample A1938 is not clear, but their $^{207}Pb/^{206}Pb$ ages seem to fall close to the original mineralization event.

The mineralization type of the Asentolamminoja occurrence is difficult to ascertain due to lack of outcrop. Based on the appearance of the radioactive boulders found in the area the dominant mineralization type seems to consist of cross-cutting fractures that are rich in biotite, uraninite, molybdenite and apatite. Similar mineralization type was found in diamond drillings in the Kuohunki area (see Fig. 1). Based on old drill core descriptions from Kuohunki and the radioactive boulders investigated in this study the uranium mineralization

Table 1. U-Pb isotopic data for the Asentolamminoja and Kuohunki samples.

Sample information / Analyzed mineral and fraction	Sample mg	U % or ppm	Pb % or ppm	$^{206}Pb/^{204}Pb$ measured	$^{208}Pb/^{206}Pb$ radiogenic	ISOTOPIC RATIOS[1]						Rho[2]	APPARENT AGES/Ma±2σ		
						$^{206}Pb/^{238}U$	±2σ%	$^{207}Pb/^{235}U$	±2σ%	$^{207}Pb/^{206}Pb$	±2σ%		$^{206}Pb/^{238}U$	$^{207}Pb/^{235}U$	$^{207}Pb/^{206}Pb$
A1937 Biotite rock															
A) mixed uraninite: 10% HF leached, black fragments with metallic lustre	0.36	11.2 %	3.1 %	68513	0.05	0.2811	0.60	4.278	0.60	0.1104	0.05	0.99	1597	1689	1806±1
B) mixed uraninite, abraded 20 min, black fragments with metallic lustre	0.20	19.5 %	2.7 %	169867	0.03	0.1399	0.40	2.072	0.40	0.1074	0.06	0.99	844	1140	1756±1
A1938 Biotite granite															
A) fracture carbon balls: fresh, black fragments	0.44	4.6 ppm	2.4 ppm	135	0.02										1753±17
B) fracture carbon balls: fresh, black fragments, 10% HF leach	0.50	7.2 ppm	2.7 ppm	258	0.01	0.3219	0.90	4.763	1.20	0.1073	0.64	0.82	1799	1778	1755±12
C) U-bearing? turbid, 10%HF leach	0.21	1371 ppm	375 ppm	2105	0.03	0.2704	0.40	4.296	0.40	0.1152	0.1	0.96	1543	1693	1883±2
D) uraninite?: black, dull, pitted fragments. 10% HF leach	0.26	14.50 %	6.90 %	44070	0.03	0.4783	0.92	7.977	0.92	0.1210	0.07	0.99	2520	2229	1970±2
E) uraninite?: black, solid fragments, 10%HF leach	0.24	9.90 %	5.47 %	50050	0.03	0.5576	0.77	9.092	0.77	0.1183	0.07	0.99	2857	2347	1930±2
A1939 Granite															
A) mixed uraninite: black, pitted, turbid fragments, 10% HF leach	0.49	6.4 %	2.3 %	30427	0.03	0.3565	0.45	5.962	0.45	0.1213	0.6	0.99	1966	1970	1975±1
A767 Kuohunki uraninite[3]	2.59	39.7 %	12.9 %	18911	0.04	0.3214	4.01	5.813	4.84	0.1312	3.30	0.80	1796	1948	2113±59

[1] Isotopic ratios corrected for fractionation, blank (30 or 50 pg) and age-related common lead (Stacey and Kramers, 1975; $^{206}Pb/^{204}Pb$±0.2, $^{207}Pb/^{204}Pb$±0.1, $^{208}Pb/^{204}Pb$±0.2). [2] Rho: Error correlation between $^{206}Pb/^{238}U$ and $^{207}Pb/^{235}U$ ratios. All errors are 2σ. [3] Analyzed by Matti Vaasjoki.
Analytical methods: The decomposition of minerals and extraction of U and Pb for multigrain ID-TIMS isotopic age determinations follows mainly the procedure described by Krogh (1973, 1982). However, better concordance were tried to achieve by leaching the mineral fraction with 10%HF. After repeated washing steps with uc. H_2O, the U-minerals were dissolved in HNO_3 in Savillex teflon beakers on a hot plate. $^{235}U/^{208}Pb$ spiked and unspiked isotopic ratios were measured using a VG Sectio 54 thermal ionization multicollector mass spectrometer. According to repeated measurements of Pb standard SRM981, the measured lead isotopic ratios were corrected for 0.12-0.10±0.05% /a.m.u. fractionation. Pb/U ratios were calculated using the PbDat program (Ludwig, 1991). Plotting of the isotopic data and age calculations were performed using the Isoplot/Ex3 program (Ludwig, 2003). Age errors are calculated at 2σ and decay constant errors ignored. Data-point error ellipses in Fig. 5 are 2σ.

may be assigned either to hydrothermal or metamorphic type. Reports of pegmatite-related uranium mineralization in the Kuohunki drill cores suggest that at least some of the uranium may originally have been granite-related; however, the majority of the radioactive boulders in the Asentolamminoja boulder field seem to represent other mineralization types associated with alteration like silicification, carbonate alteration and biotitization. Small phosphorite-type uranium occurrences are known in the Paleoproterozoic supracrustal Peräpohja belt on the northern side of the Kuohunki occurrence, but they are clearly different from the Kuohunki and Asentolamminoja mineralizations.

Mafic magmatism of ~2.0 Ga age is widespread in Lapland and indications of ~1.97-1.98 Ga bimodal magmatism have also been found in northern Finland (Hanski et al., 2005). Based on our data we conclude that the Asentolamminoja and Kuohunki U-mineralizations were generated ~2.0 Ga ago by hydrothermal activity associated with a tectonomagmatic event that affected the ~2.7 Ga host rocks and were further remobilized at ~1.80-1.76 Ga, due to another hydrothermal event connected with the intrusion of the different phases belonging to the central Lapland granite complex.

Acknowledgements

References

Hanski, E., Huhma, H., Perttunen, V. 2005: SIMS U-Pb, Sm-Nd isotope and geochemical study of an arkosite-amphibolite suite, Peräpohja Schist Belt: evidence for ca. 1.98 Ga A-type felsic magmatism in northern Finland. Bull. Geol. Soc. Finland 77, 5-29.

Krogh, T.E. 1973: A low-contamination method for hydrothermal decomposition of zircon and extraction of U and Pb for isotopic age determinations. Geochim. Cosmochim. Acta 37, 485–494.

Krogh, T.E., 1982: Improved accuracy of U-Pb zircon ages by the creation of more concordant systems using air abrasion technique. Geochim. Cosmochim. Acta 46, 637–649.

Ludwig, K.R. 1991: PbDat 1.21 for MS-dos: A computer program for IBM-PC Compatibles for processing raw Pb-U-Th isotope data. Version 1.07.

Ludwig, K.R. 2003: Isoplot/Ex 3. A geochronological toolkit for Microsoft Excel. Berkeley Geochronological Center. Spec. Publ. No. 4.

Mänttäri, I. 1995: Lead isotope characteristics of epigenetic gold mineralization in Palaeoproterozoic Lapland greenstone belt, northern Finland. Geol. Surv. Finland, Bull. 381.

Sarala, P. 2005: Glacial morphology and dynamics with till geochemical exploration in the ribbed moraine area of Peräpohjola, Finnish Lapland. Geol. Surv. Finland, Espoo, 17 p.

Stacey, J.S., Kramers, J.D. 1975: Approximation of terrestrial lead isotope evolution by a two-stage model. Earth Planet. Sci. Lett. 26, 207–221.

Uranium behaviour during metamorphism of black shales: evidence from the Talvivaara Ni-Zn-Cu-Co deposit (Finland)

Andreï Lecomte, Michel Cathelineau
GeoRessources, Université de Lorraine, CNRS, CREGU, Boulevard des Aiguillettes B.P. 239 F-54506 Vandoeuvre lès Nancy, France

Etienne Deloule
CRPG, CNRS, 15 rue Notre-Dame-des-Pauvres 54500 Vandoeuvre lès Nancy, France

Marc Brouand
AREVA, 1 place Jean Millier F-92084 Paris La Défense Cedex, France

Kirsti Loukola-Ruskeeniemi, Esa Pohjolainen
Geological Survey of Finland, P.O. Box 96, FI-02151 Espoo, Finland

Hannu Lahtinen
Talvivaara Exploration Ltd., Talvivaarantie 66, FI-88120 Tuhkakyla, Finland

Abstract. The Talvivaara Ni-Zn-Cu-Co deposit is located in the central part of the Fennoscandian Shield and is hosted by Palaeoproterozoic metamorphosed black shales. In spite of the very low grade of the U mineralization (10 to 30 ppm), the homogeneous distribution of U in rocks and the nearly complete leachability of the U-bearing phases in a bio-heapleaching process are two extremely favorable criteria for uranium beneficiation. In these black metasediments, uranium occurs as uraninite rimmed by carbonaceous matter. Concentrations of rare earth elements (REE) and dating of theses crystals indicate synmetamorphic crystallization during Svecofennian orogeny, under maximum P-T metamorphic conditions. Taking into account a probable syngenetic preconcentration of uranium, together with base metals, several possible mechanisms may explain this association between uraninite and bitumen nodules: (a) a mineralization from migrated hydrocarbons (with uranium as organo-metallic complexes or nano-uraninite particles dispersed in oil), followed by the co-precipitation of uraninite and heavy hydrocarbons ; or (b) a late post-metamorphic polymerization of bitumen through radiolytic polymerization of hydrocarbons at the contact of uraninite.

Keywords. Uranium, Bitumen nodules, Metamorphism, Sulphide ore deposit, Talvivaara, Finland

1 Introduction

Black shales are fine-grained sedimentary rocks which have elevated metal contents compared to ordinary shales, especially Ni, Mo, Co, Cu, Zn, U, V, As, Se, Ag, Au and PGE (Vine & Tourtelot, 1970; Holland, 1979; Wignall, 1994). In these sedimentary rocks rich in organic carbon, uranium is thought to be dispersed and related to an early sedimentary preconcentration although its distribution in such low-grade rocks is generally unknown. Moreover, metamorphism of metalliferous black shales to black schists may remobilize and recrystallize primary uranium mineralization.

The Talvivaara deposit is a low-grade Ni-Zn-Cu-Co hosted by graphite-rich metasedimentary rocks. Uranium concentrations are low, ranging from 3 to 30 ppm. The deposit is being exploited with open pit mining and bio-heapleaching technology by the Talvivaara Mining Company Plc. The total mineral resources, as defined by the JORC code, are 2053 Mt in 2012 with 0.22% of Ni, 0.13% of Cu 0.02% of Co and 0.50% of Zn. Despite of the very low grade of uranium in the ore, the Talvivaara plant could produce up to 350 tons of U as a by-product leached during the bio-heapleaching process.

The work presented here focuses on the particular uranium petrography and on possible mechanisms of uranium concentration in C-rich metasedimentary rocks.

2 Geological setting

The Talvivaara deposit is located in the central part of the Fennoscandian Shield, within the Palaeoproterozoic Kainuu Schist Belt (Fig. 1). A thick metasedimentary sequence encloses black schists hosting the Ni-Zn-Cu-Co mineralization. This sequence is composed of three main stages (Loukola-Ruskeeniemi & Lahtinen, 2012; Eilu et al., 2012): (i) cratonic and epicratonic quartzites-arkosites of Sumi-Sariola and Jatuli stage (2.5-2.1 Ga); (ii) rift-associated wackes-pelites of Lower Kaleva stage (2.1-1.95 Ga) including Talvivaara black sediments; (iii) deep-water turbidites-pelites of Upper Kaleva stage (1.95-1.90 Ga).

Talvivaara black shales are deep-water sediments deposited after the break-up of the Archean Karelian continent. The sedimentation of these strata occurred during the last time of rifting. After this phase of extension, convergence initiated and a complex arc system developed, with several subduction zones, magmatic island arcs, foreland and back-arc basins (Nironen, 1997). This period of convergence ended with
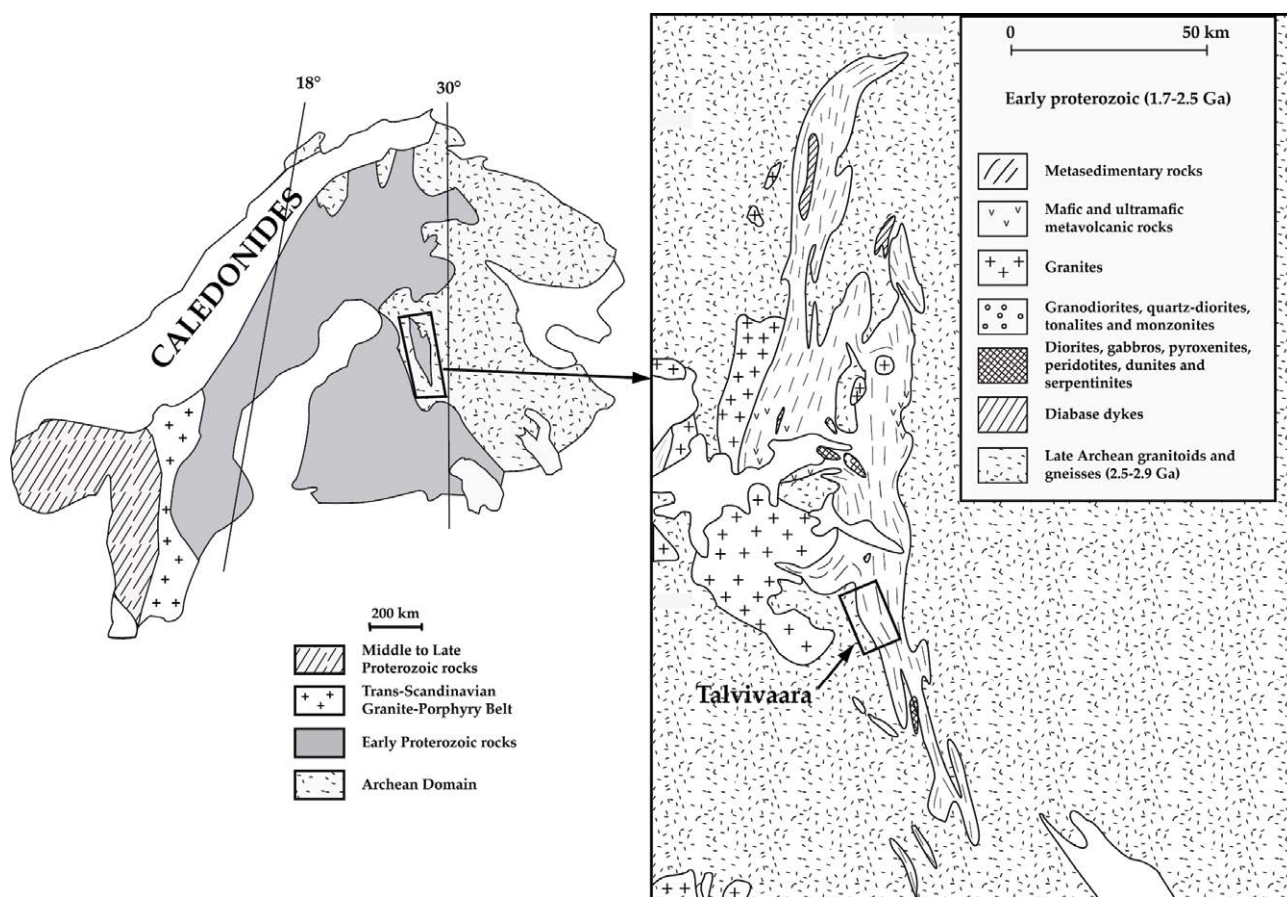
Figure 1. Geological map of the Fennoscandian Shield with details on the Kainuu Schist Belt (adapted from Loukola-Ruskeeniemi & Heino, 1996)

multiple collisions and accretion, associated with the Svecofennian orogeny (e.g. Korja et al., 2006; Lahtinen et al., 2008).

In particular, the Kainuu Schist Belt corresponds to imbricated thrust sheets emplaced over the Karelian craton during this orogenic phase. Progressive oblique accretion of the Svecofennian island arc complex brought about regional scale refolding, thrusting, and shear zone development (Koistinen, 1981; Lahtinen, 1994; Kärki & Laajoki, 1995; Sorjonen-Ward, 1997).

3 Mineralization

Talvivaara black schists can be divided into 3 groups: Ni-rich black schists (Ni $\geq$ 0.1%), Mn-rich black schists (Mn $\geq$ 0.8%) and Ni-Mn-poor black schist (Ni $\leq$ 0.1% and Mn $\leq$ 0.8%). In these black metasediments, main mineral constituents are quartz, micas, graphite and sulphides. Common accessory minerals include rutile, apatite, zircon, feldspar and garnet, whereas uraninite, thucholite, tourmaline and monazite are rarer (Loukola-Ruskeeniemi & Lahtinen, 2012). Ni-Zn-Cu-Co bearing minerals in Talvivaara black schists are sulphides, mainly pyrite and pyrrhotite (Loukola-Ruskeeniemi & Heino, 1996). Other sulphides include chalcopyrite, sphalerite, and pentlandite. Cobalt is hosted mainly by pyrite, Ni by pyrrhotite and pentlandite exsolutions, Cu by chalcopyrite and Zn by sphalerite.

Uranium mineralization is mainly represented by anhedral uraninite crystals, often included/associated with bitumen nodules or rims and minor pyrites (Fig. 2). In rare cases, uraninites are not associated with carbonaceous matter and are generally highly-altered. No particular zonation has been observed in uraninites. However, most crystals show secondary alteration features, with cracks and gulfs along the crystal edges filled with a complex assemblage of uranium silicates (coffinite) and micro-scale pyrites.

Numerous chemical analyses on these uraninite crystals allowed us to select some unaltered areas for chemical U-Pb-Th dating and SIMS U-Pb dating. These results lead to an age of around 1.87 Ga, which corresponds to the peak of metamorphism during the Svecofennian orogeny. Rare Earth Elements concentrations, measured with LA-ICP-MS, also correspond to those of synmetamorphic uraninites (Mercadier et al., 2011).

4 Discussion and conclusions

4.1 Uranium preconcentration in black shales

Talvivaara black sedimentary rocks are organic-rich and were originally deposited on the seafloor in deep anoxic conditions (Loukola-Ruskeeniemi & Heino, 1996). Considering the uniform distribution of metal concentrations and the uniformly high Ni/Cu and Ni/Zn ratios, primary concentrations of uranium at Talvivaara
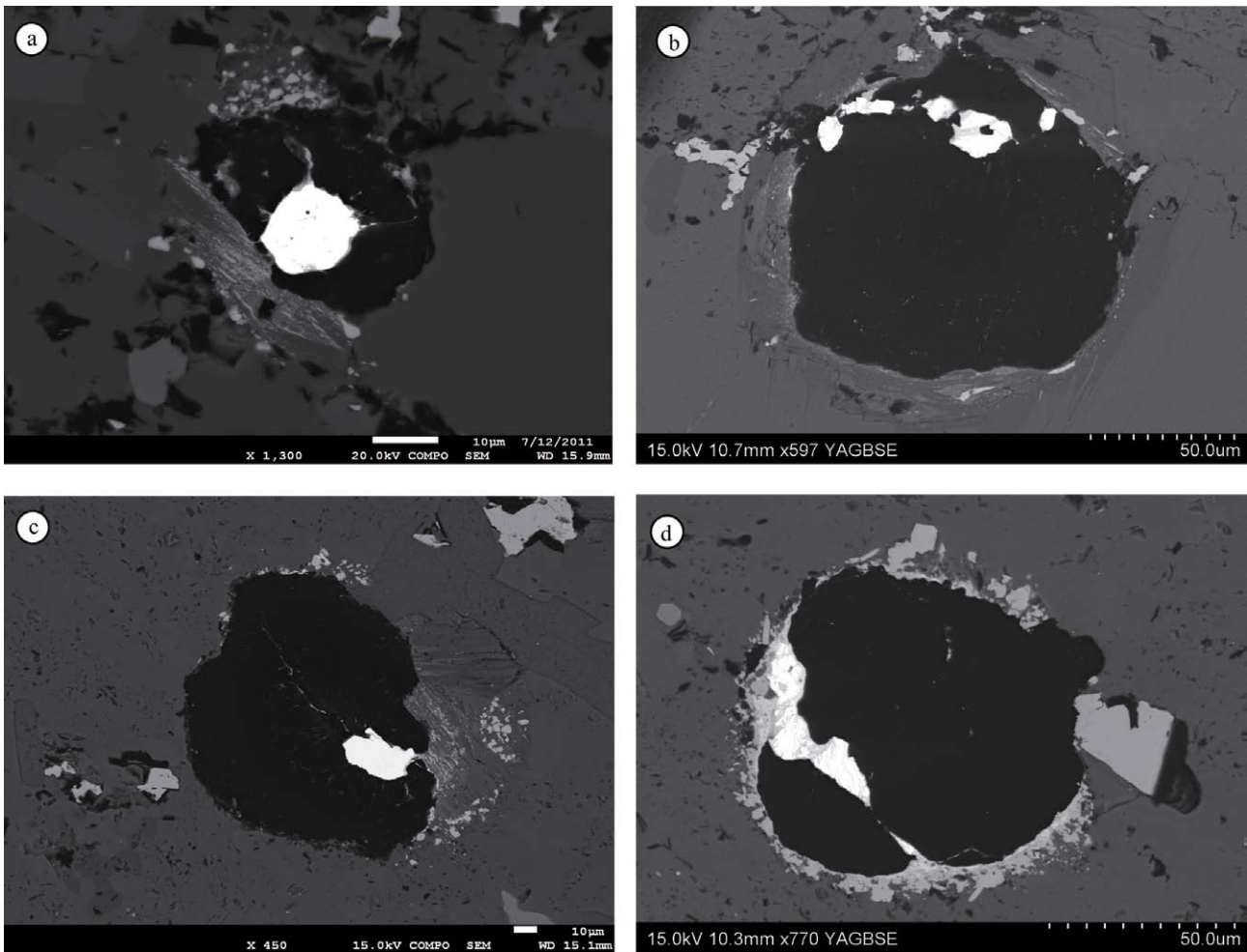
Figure 2. Uraninites (white) associated with carbonaceous matter (black). Secondary alteration in uraninites is visible with darker fractures (BSE). Nodules are often surrounded by pyrites (light grey)

can result from the precipitation in a well-mixed large oceanic reservoir. Moreover, in the metasedimentary sequence, Ni-rich black schists are surrounded by Mn-rich black schists, which may be interpreted as the result of a boundary between oxic/suboxic and anoxic/euxinic waters (Eilu et al., 2012, Loukola-Ruskeeniemi & Lahtinen, 2012). Taking into account the above observations, it is possible to infer that the primary U mineralization was, like base metals, at least in part syngenetic. In that case, uranium, which is soluble in oxic seawater as a uranyl tricarbonate complex $UO_2(CO_3)_3^{4-}$, may be diffused from the water column into the anoxic-euxinic sediments and precipitated mainly as uraninite through adsorption and reduction processes (e.g. Klinkhammer & Palmer, 1991; Crusius et al., 1996; Morford et al., 2001; Chaillou et al., 2002; McManus et al., 2005). The existence of a microbially-mediated reduction of uranium cannot be excluded as sulfate-reducing or iron-reducing bacteria are able to precipitate nanometer-size uraninites (e.g. Lovley et al., 1991, 1993; Lovley & Philips, 1992).

4.2 Uranium recrystallization during metamorphism

Uraninite dating and geochemical features indicate unambiguously that uraninites crystallized under metamorphic conditions, i.e. probably those of the maximum metamorphic P-T conditions, associated with Svecofennian orogeny. Taking into account a probable syngenetic preconcentration, together with other metals, uranium has been redistributed during metamorphism, from a dispersed concentration to well-developed uraninite crystals.

The particular occurrence of these uraninites associated with carbonaceous nodules and rims constitute an interesting example of an association between a synmetamorphic UO_2, precipitated through a dissolution-precipitation process from a disseminated U pre-concentration and carbonaceous matter derived from the maturation of kerogen in the black shale.

The formation of these uraniferous bitumen nodules may be explained by two distinct scenarios: (a) the migration of a U-enriched oil (with organo-metallic complexes or nano- to micro-UO_2), which leads to the co-precipitation of a growing central uraninite and heavy hydrocarbons; (b) a late post-metamorphic radiolytic polymerization of gaseous hydrocarbons in contact with uranium, as proposed by Landais et al. (1993) to explain bitumen formation in Athabasca uranium deposits.

Acknowledgements

We are grateful to Talvivaara Mining Company for welcoming us on the field, providing us the samples used in this study, and for technical and scientific assistance.

References

Chaillou G, Anschutz P, Lavaux G, Schäfer J, Blanc G (2002) The distribution of Mo, U, and Cd in relation to major redox species in muddy sediments of the Bay of Biscay. Marine Chemistry 80: 41-59.

Crusius J, Calvert S, Pedersen T, Sage D (1996) Rhenium and molybdenum enrichments in sediments as indicators of oxic, suboxic and sulfidic conditions of deposition. Earth and Planetary Science Letters 145: 65-78.

Eilu P, Ahtola T, Äikäs O, Halkoaho T, Heikura P, Hulkki H, Iljina M, Juopperi H, Karinen T, Kärkkäinen N, Konnunaho A, Kontinen A, Kontoniemi O, Korkiakoski E, Korsakova M, Kuivasaari T, Kyläkoski M, Makkonen H, Niiranen T, Nikander J, Nykänen V, Perdahl J-A, Pohjolainen E, Räsänen J, Sorjonen-Ward P, Tiainen M, Tontti M, Torppa A, Västi K (2012) Metallogenic areas in Finland Mineral deposits and metallogeny of Fennoscandia. Geological Survey of Finland, pp 207-342.

Gaál G, Gorbatschev R (1987) An outline of the Precambrian evolution of the Baltic Shield. Precambrian Research 35: 15-52.

Holland HD (1979) Metals in black shales; a reassessment. Economic Geology 74: 1676-1680.

Kärki A, Laajoki K (1995) An interlinked system of folds and ductile shear zones-late stage Svecokarelian deformation in the central Fennoscandian Shield, Finland. Journal of Structural Geology 17: 1233-1247.

Klinkhammer GP, Palmer MR (1991) Uranium in the oceans: Where it goes and why. Geochimica et Cosmochimica Acta 55: 1799-1806.

Koistinen TJ (1981) Structural Evolution of an Early Proterozoic Strata-bound Cu-Co-Zn Deposit, Outokumpu, Finland. Transactions of the Royal Society of Edinburgh, Earth Science 72: 115–158.

Korja A, Lahtinen R, Nironen M (2006) The Svecofennian orogen: a collage of microcontinents and island arcs. Geological Society, London, Memoirs 32: 561-578.

Lahtinen R (1994) Crustal evolution of the Svecofennian and Karelian domains during 2.1-1.79 Ga, with special emphasis on the geochemistry and origin of 1.93-1.91 Ga gneissic tonalites and associated supracrustal rocks in the Rautalampi area, central Finland. Geologian tutkimuskeskus.

Lahtinen R, Garde AA, Melezhik VA (2008) Paleoproterozoic evolution of Fennoscandia and Greenland. Episodes 31: 20-28.

Landais P, Dubessy J, Dereppe J-M, Philp RP (1993) Characterization of graphite alteration and bitumen genesis in the Cigar Lake deposit (Saskatchewan, Canada). Canadian Journal of Earth Sciences 30: 743-753.

Loukola-Ruskeeniemi K, Heino T (1996) Geochemistry and genesis of the black shale-hosted Ni-cu-Zn deposit at Talvivaara, Finland. Economic Geology 91: 80-110.

Loukola-Ruskeeniemi K, Lahtinen H (2012) Multiphase evolution in the black shale –hosted Ni-Cu-Zn-Co deposit at Talvivaara, Finland. Ore Geology Reviews (in Press).

Lovley DR, Phillips EJP (1992) Reduction of uranium by Desulfovibrio desulfuricans. Applied and Environmental Microbiology 58: 850-856.

Lovley DR, Phillips EJP, Gorby YA, Landa ER (1991) Microbial reduction of uranium. Nature 350: 413-416.

Lovley DR, Roden EE, Phillips EJP, Woodward JC (1993) Enzymatic iron and uranium reduction by sulfate-reducing bacteria. Marine Geology 113: 41-53.

McManus J, Berelson WM, Klinkhammer GP, Hammond DE, Holm C (2005) Authigenic uranium: Relationship to oxygen penetration depth and organic carbon rain. Geochimica et Cosmochimica Acta 69: 95-108.

Mercadier J, Cuney M, Lach P, Boiron MC, Bonhoure J, Richard A, Leisen M, Kister P (2011) Origin of uranium deposits revealed by their rare earth element signature. Terra Nova 23: 264-269.

Morford JL, Russell AD, Emerson S (2001) Trace metal evidence for changes in the redox environment associated with the transition from terrigenous clay to diatomaceous sediment, Saanich Inlet, BC. Marine Geology 174: 355-369.

Nironen M (1997) The Svecofennian Orogen: a tectonic model. Precambrian Research 86: 21-44.

Sorjonen-Ward P (1997) An overview of the geological and tectonic evolution of eastern Finland. In: Ruskeeniemi K, Sorjonen-Ward P (eds) Ore deposits in eastern Finland (4th biennial SGA Meeting, August 11–13, 1997, Turku, Finland, Excursion Guidebook A4). Geological Survey of Finland.

Vine JD, Tourtelot EB (1970) Geochemistry of black shale deposits; a summary report. Economic Geology 65: 253-272.

Wignall PB (1994) Black shales. Clarendon Press-Oxford University Press, Oxford-New York.

The geology and the ages of Baiyanghe Be-U deposit in Xinjiang province, northwest China

Xiaofeng Li, Wei Mao
State Key laboratory Ore Deposit Geochemistry, Institute of Geochemistry, Chinese Academy of Sciences, Guiyang 550002, China

Guo Wang, Mou Wang, Yanlong Li, Manchuan Ren
216 Team, CNNC, Urumqi 830011, China

Rong Xiao
Hunan Institute of Geological Survey, Changsha 410116, China

Zuohai Feng, Feng Yang
Guilin University of Technology, Guilin 541004, China

Abstract. The Baiyanghe U-Be deposit is a large Be deposit related to Yangzhuang granite porphyry in the Northwestern margin of Junggar basin. The orebodies are mainly hosted in the contact zone between the granite and the Permian tuffaceous sandstone. The muscovite Ar-Ar age indicates that the U-Be mineralization occurred at 302.99±1.58 Ma. The data show the Be-U mineralization might occur in late Carboniferous. The Baiyanghe Be-U deposit formed in an extensional setting.

Keywords. U-Be deposit, Bertrandite, Pitchblende, Ar-Ar age, Fluorite.

1 Introduction

The Baiyanghe U-Be deposit is located to the Northwestern margin of the Junggar plate within late Palaeozoic Xiemisitan-Kulankazi island arc (Wang et al., 1997; Tang et al., 1998; Dong et al., 2010). It is a uranium and beryllium deposits discovered in the western Xuemisitan volcanic rock belt. There are three types of ore in the deposit, namely: a single uranium type, a single beryllium type and uranium and beryllium co-exist type (Xiao et al, 2011; Wang et al, 2012; Xiu et al., 2011). The uranium occurred was first discovered by No.519 Team from CNNC in 1956. The high Be concentration samples were found by Xinjiang Geological Bureau in 1975, and was regards as the topaz rhyolitic type Be-U deposit. The further exploration was conducted by No.216 team from CNNC from 2006-2010. The uranium reserves amounts to middle scale and the beryllium reserves amounts to huge scale. It has the largest Be resources in Asia (Ma, 2010). Up to know little is known about the features of the deposit, the age of the U-Be mineralization. The paper presents the geology of the Be-U mineralization, the muscovite Ar-Ar age that associated with the purple fluorite, and discusses the genesis of the U-Be mineralization.

2 The Geology of Baiyanghe U-Be deposit

2.1 Geological Setting

Baiyanghe U-Be deposit is located at the northwestern margin of the Xuemisitan volcanic belts. The belt mainly consists of early Palaeozoic island arc volcanic-sedimentary rocks and ophiolite in addition to late Palaeozoic marine and/or continental volcanic-sedimentary rocks. Ancient Central Asian plate was cleavaged in the Mesoproterozoic, forming the Paleo-Asian Ocean and a large number of micro-plates within it. The Kazakhstan plate collided with the Siberian plate from the Devonian. During early Carboniferous Paleo-Asian Ocean closed. Due to the delamination of the oceanic slab and underplating of mantle magma, alkaline granite intruded and acidic volcanic erupted. The area was uplifted at the end of the Carboniferous, and the continental rhyolite and large scale magmas occurred along the collision belt (Wang et al., 1997; Tang et al., 1998; Dong et al., 2010).

2.2 The Geology of the Deposit

Baiyanghe U-Be deposit is related to the late Carboniferous Yangzhuang granite porphyry. The exposed strata in the ore field are the Upper Devonian Tarbaghatai group, the Late Carboniferous Heishantou group, and the Permian Jiawu group. Early Permian granite porphyries intruded and interspersed with NW-, NS-trending diabase dikes. The Yangzhuang granite porphyry occurred as near EW-trending along the Chagantaolegai-Bayinbulake deep faults. The orebodies occur along the contact zone between granite porphyry and wall rocks and nearby. Ore bodies occurred along the fractures within the contact zone (Fig. 1). The uranium and beryllium of the Baiyanghe deposit are mainly occurred as minerals. The original uranium minerals are pitchblende and niobium uranium mineral. The secondary mineral of uranium is uranophane. The beryllium mineral is bertrandite. The hydrothermal alteration minerals are composed of hematite, fluorite, quartz, chlorite, muscovite (Wang et al.,

2012). Quartz and fluorite are mainly associated with Be mineralization, and the purple fluorite,

The muscovite sample was collected from the muscovite-fluorite veins with Be-U mineralization.
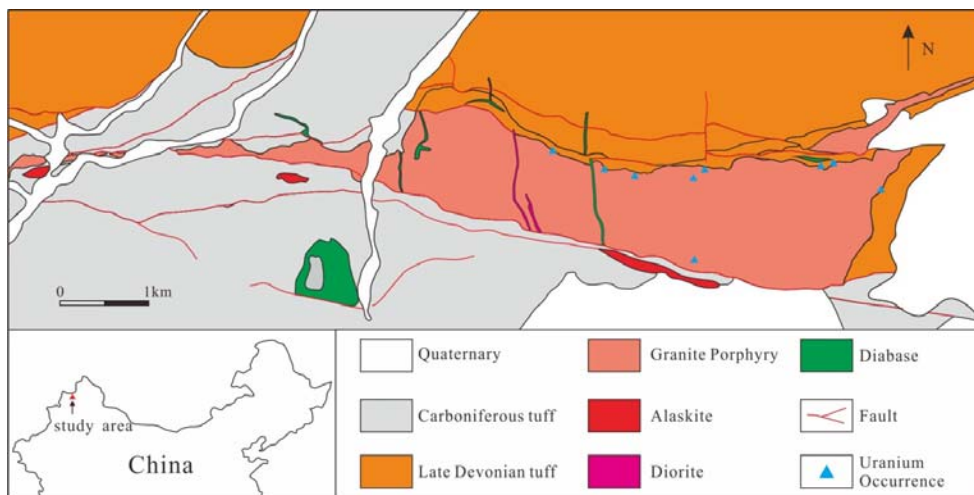
Figure.1 The geological map of Baiyanghe Be-U deposit, Xinjiang, Northwest China

muscovite and hematite are mainly associated with U mineralization (Fig. 2). Four stages of fluorite were identified, early fluorite is generally poorly developed, dark purple and has a mottled texture, This stage fluorite mostly contain uranium minerals. The second stage fluorite is highly zoned with alternating zones of clear and purple fluorite. The second stage fluorite occurs in miarolitic cavities and veins and is associated with euhedral quartz and minor sericite. The third stage fluorite is generally colourless and occurs in veins with

The muscovite was purified using a magnetic separator and then cleaned in an ultrasonic ethanol bath. The purity of these mineral grains is >99%. Samples were irradiated for 51 h in the nuclear reactor at the Chinese Institute of Atomic Energy in Beijing. $^{40}Ar/^{36}Ar$ stepwise heating analysis was performed at the Institute of Geology, Chinese Academy of Geological Science using an MM-1200B Mass Spectrometer. Measured isotopic ratios were corrected for mass discrimination, atmospheric Ar component, blanks and irradiation-
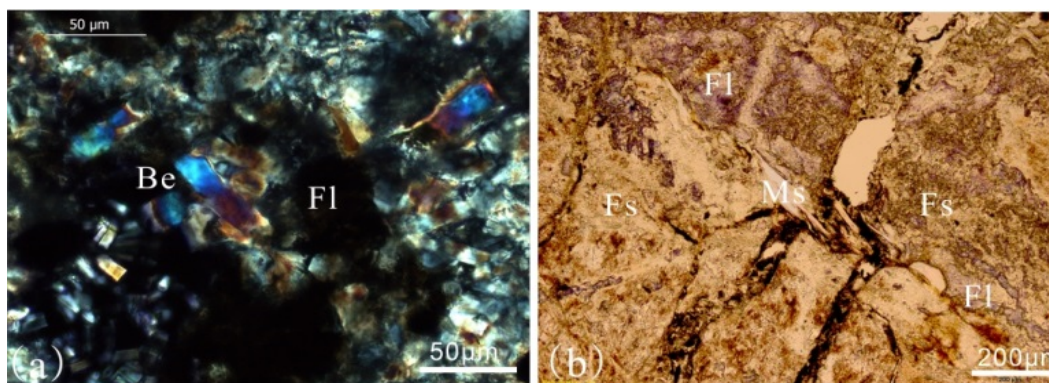
Figure. 2 (a) The mineral bertrandite (Be) is associated with purple fluorite (Fl) in ore samples; (b) The muscovite (Ms) occurred as veinlet with fluorite (Fl) hydrothermal alteration in uranium ore samples

euhedral quartz. The third stage fluorite veins contain the majority of the Be mineralization in the form of bertrandite, sulfides and oxide minerals, chlorite and tourmaline. The latest stage of fluorite occurs in voids within the second stage and the third stage fluorite veins and is generally zoned with blue and purple zones. These stages of mineralization are cut by late carbonate veins and stained by hematite (Mao et al., 2013).

3 Ar-Ar Age of Muscovite

3.1 Samples and the analytical methods

induced mass interference. The decay constant used is δ = 5.543×10^{-10} /year (Steiger & Jäger, 1977). All ^{37}Ar were corrected for radiogenic decay (half-life 35.1 days). Uncertainty in each apparent age is given at 2σ. The monitor used in this work is an internal standard: Fangshan biotite (ZBH-25) for which the age is 132.7 Ma and potassium content is 7.6% (J=0.005617). Detailed analysis techniques are described in Chen et al. (2002).

3.2 Results

The ages and 2σ uncertainties are plotted against the cumulative released ^{39}Ar fraction to establish

the age spectra (Fig. 3). The argon isotope ratios are presented on isotope correlation plots using the program ISOPLOT of Ludwig (2001). The ^{40}Ar-^{39}Ar data incorporates the apparent age spectra and the atmospheric argon and Ca:K ratios from each heating. The biotite from sample BH-1 has a plateau age of 302.99±1.58Ma, calculated from steps 3-15, representing 98.7% of the total argon release (Fig. 3a). The isochron age of 300.8±2.9Ma (MSWD = 3.4, initial ^{40}Ar/^{36}Ar =305) is concordant with the plateau age (Fig. 3b).

4 The age of Be-U Mineralization and Its Implication for metalliogenesis

Little is known for precious Be-U mineralization in the Baiyanghe deposit because no suitable minerals for age dating were available. Ma (2010) dated the pitchblende U-Pb ages, and got dispersed data of 224±3.1Ma-237.8±3.3Ma, 197.8± 2.8, 97.8±1.4 Ma and 30.0±0.4 Ma. The muscovite sample we collected in the muscovite-fluorite veins. The fluorite occurred as dark purple, and associated with uranium mineralization. The age of muscovite might representative the age of the U-Be mineralization.

The Yangzhuang granite porphyry was dated at 293±15 Ma using whole rock Rb-Sr method (Ma 2010). The granite was dated at 285.2±2.0Ma by zircon LA-ICP-MS U-Pb (Li et al., unpublished data). These data show the Yangzhuang granite porphyry emplaced after the Paleo-Asian Ocean closure under an extensional tectonic setting.
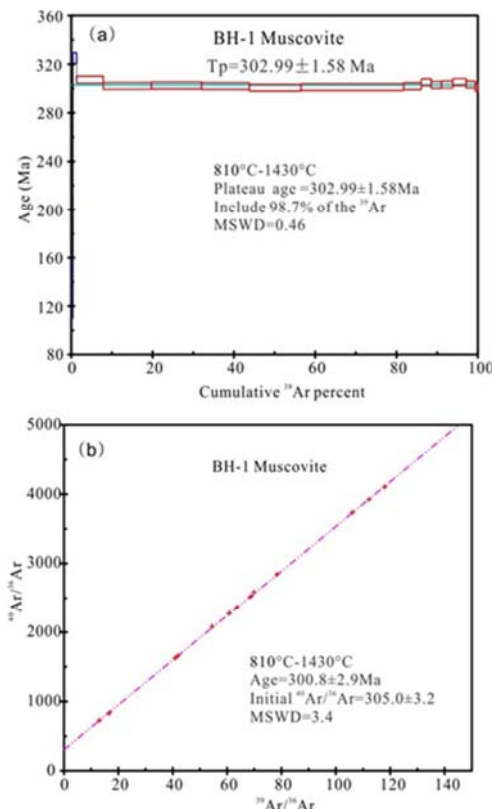
Figure 3. (a) ^{40}Ar/^{39}Ar plateau age and (b) isochron age of muscovite from sample BH-1.

5 Conclusion

Baiyanghe Be-U deposit is related to the late Carboniferous Yangzhuang granite porphyry. The uranium-bearing mineral is pitchblende and niobium uranium. The secondary mineral of uranium is uranophane. The beryllium mineral is bertrandite. The typical alteration is characteristic of different colour fluorite. The Ar-Ar age of muscovite was dated at 302.99±1.58Ma, which show the Be-U mineralization might occur in late Carboniferous. The Baiyanghe Be-U deposit formed in an extensional setting.

Acknowledgements

References

Chen W, Zhang Y, Zhang YQ, Jin GS, Wang QL (2006) Late Cenozoic episodic uplifting in southeastern part of the Tibetan plateau - evidence from Ar-Ar thermochronology. Acta Petrologica Sinica, 22(4): 867-872

Ludwig K R (2001) User's manual for Isoplot/Ex.Version 2.47. A geochronological tool for Microsoft Excel. Berkeley Geochronology Center, Berkeley, 43p

Mao W, Li XF (2013) The study of fluid inclusions at Baiyanghe U-Be deposit, Xinjiang, SW China. Mineral deposit (in Press)

Steiger RH and Jager E (1977) Subcommission on geochronology: convention on the use of decay constants in geo- and cosmochronology. Earth Planet. Sci. Lett., 36:359-362.The references are in 8.5pt Times New Roman. See instructions for authors and the specimen abstract for formatting requirements.

Wang M, Li XF, Wang G, Li YL, Shi ZL, Lu KZ (2012) The characteristics of Baiyanghai U-Be deposit, Xinjiang, NW China. Mineral exploration, 34-40

Xiu XQ, Fan HH, Ma HF, Yi LS (2011) Hydrothermal alteration and its geochemical characteristics at Baiyanghe U-Be deposit, Xinjiang, NW China. Uranium Geology, 215-220

Zhang Y, Chen W, Chen KL, Liu XY (2006) Study on the Ar-Ar age spectrum of diagenetic I/S and the mechanism of ^{39}Ar recoil loss_Examples from the clay minerals of P-T boundary in Changxing, Zhejiang Province. Geological Review, 52(4):556-561.

Dong LH, Feng J, Liu DQ, Tang YL, Qu X, Wang KZ, Yang ZF. 2001. Research for classification of metallogenic unit of Xinjiang. Xinjiang Geology, 28(1):1-15

Tang HS, Wang ZY (1998) Late palaeozoic plate-tectonics and its relationship with copper deposits in northern Junggar, Xinjiang. Mineral Resources and Geology, 64(12):91-95

Wang ZY, Tang HS (1997) Major types, ore controlling conditions and ore prospecting perspective of copper deposits in northern Junggar, Xinjiang. Mineral Resources and Geology, 61(11):319-324

Isan U and Th mobility and related ore mineralisation

Matt McGloin, Andrew Tomkins, Roberto Weinberg
School of Geosciences, Monash University, Melbourne, Victoria, 3800, Australia

Abstract. Isan Orogeny deformation and magmatism in the Mount Isa Inlier produced abundant saline metamorphic and magmatic fluids, in which U is highly mobile, but Th is typically immobile. Various metasomatic U mineralisation styles are found at Mount Isa, often with unusual mineral associations including Zr-enrichment and complex refractory ore minerals. There is no evidence for unconformity-style mineralisation with common saline fluids unsuitable metal carriers. Unlike the adjacent McArthur Basin, Mount Isa is a fluorine-rich province. Compared to sediments, Isan granites are excellent reservoirs for not only F, but U, Th and rare metals within refractory minerals. We demonstrate that F^- plays a key role in mobilising these elements from granites. The large variety of element associations and mineral paragenesis is controlled by F^-, CO_2 and fO_2 fluid content. We argue that F^--rich fluids can both break-down U-rich minerals like zircon, and transport immobile Th or Zr whilst CO_2 content in these fluids limits Th mobility. Fluid chemistry controls U and Th mobility and ore association with Cu or Zr. We classify the different mineralisation styles by element association and argue that U-Th exploration models be governed by F, Th, Cu and Zr content of granites and ore deposits.

Keywords: uranium, thorium, fluorine, ore-forming fluids, granites

1 Introduction

The Proterozoic Mount Isa Inlier hosts numerous diverse uranium mineralisation styles during the Isan Orogeny (1600 to 1490Ma), associated with metamorphic and magmatic fluids generated from abundant mafic and felsic magmatism, deformation and metamorphism. Isan uranium mineralisation styles are distinct from unconformity-style processes and include metasomatic, metamorphosed skarn-associated, and carbonate vein and pod-related styles, with uranium also enriched in some IOCG deposits. In contrast, there is limited pegmatite and skarn-related thorium mineralisation. Regional genetic models for U and Th deposits remain unclear. We classify the different U and Th mineralisation styles based on element associations in mineralised ores, sources and relative Th and U mobility in ore-forming fluids, evaluating pertinent spatial, temporal and geochemical characteristics.

2 Mount Isa U mineralisation styles

(1) Mary Kathleen U-REE mine typifies over forty skarn-hosted metamorphosed style uraninite-allanite prospects in the Eastern Succession. Uranium is hosted within metamorphosed and folded diorite and metasediments of the Corella Formation (Maas et al. 1987). The Elaine Dorothy deposit appears to be a Cu-rich end member of this U-REE mineralisation style. (2) The Western Fold Belt of Mount Isa hosts ~100 occurrences of metasomatic U mineralisation, exemplified by the Valhalla uranium-rare metal deposit.

Various refractory uranium minerals including brannerite and uranium-zirconium silicates are associated with significant rare metal (Zr, Y, REE and Nb) enrichment (Gregory et al. 2005). Albite, calcite, riebeckite, dolomite and apatite are associated with uranium, hosted in local brecciated shear zones of interbedded metavolcanics and metasediments and occasional underlying basement units. Emancipation, near Mica Creek, is one of several uraninite-allanite prospects hosted in amphibolite schist.

(3) Numerous carbonate veins and pods in the Eastern Succession host U-Ti mineralisation associated with ilmenite (Di Florio, 2008). Lawrence et al. (1957) also identified davidite-ilmenite mineralisation near Cloncurry. U-enriched carbonate veins cross-cut shear hosted ore in the Anderson's Lode metasomatic uranium deposit, near Mount Isa. (4) Elevated U content can be found in several IOCG deposits of the Eastern Succession, including Ernest Henry, Monakoff and E1. Ernest Henry ore breccia has modest U (50ppm) and high F content (1.45%) (Mark et al. 2006). Both Monakoff and E1 have higher U and F content and U-REE mineralisation is associated with late stage fluorite, barite and calcite (Williams, 2013).

3 Mount Isa Th mineralisation styles

(1) Skarn-associated, metamorphosed U-REE Mary Kathleen and Elaine Dorothy deposits in the Eastern Succession contain elevated Th content in Th-rich allanite (Maas et al. 1987). (2) REE-Th pegmatite mineralisation hosted in an amphibolite-grade granite shear zone was discovered 20km south of Mt Isa during 2012 fieldwork. The zoned pegmatite has a barren quartz-muscovite core with distal tourmaline. Several small, deformed zones of REE-Th mineralisation are contained in brown to colourless mica-quartz-hematite on the eastern margin of the pegmatite. The mineralisation has significant total REE (1.78%) including 0.53% HREE, 1.14% Y and 0.12% Th. Nearby unaltered granite has high U and Th content, and adjacent Th-rich quartz breccias appear to be metasomatised-granite, suggesting formation post-granite intrusion. (3) High Th content in monazite and allanite is associated with subeconomic tin mineralisation in the Queen Elizabeth Pluton (QEP) near Mica Creek, within pegmatite veins and muscovitic microgranite dykes on ~1km² margin of biotite-hornblende granite (Towsey and Patterson, 1984).

4 U and Th mineralisation geochemistry

Key geochemical observations for U and Th mineralisation (Table 1 and Figure 1) include; (a) high Cu/U ratios indicating Cu-U association for IOCG+U and Cu-rich skarn-style mineralisation, with no significant Cu in metasomatic uranium deposits; (b)

U/Th mineralisation style	Cu	Th	U	Th/U	Zr	F (%)	ΣREE	ΣHREE
Metasomatic reduced (Valhalla)	5	85	2.28%	4×10^{-3}	3440	0.65	545	90
Metasomatic reduced (A Lode)	8	184	0.33%	5.4×10^{-2}	894	0.76	253	155
Metasomatic oxidised (Emancipation)	-	124	0.84%	1.5×10^{-2}	705	0.02	419	132
Skarn-related U-REE (M Kathleen)	34	0.29%	0.52%	0.56	20	0.13	156753	28
Skarn-related Cu-U-REE (E Dorothy)	0.5%	42	29	1.45	-	-	>4200	2
HREE-Th pegmatite (S of Mica Creek)	-	0.126%	254	4.96	183	0.12	17780	4489
U-Ti carbonate (Six Kangaroos and A Spot)	34	2	1.84%	1.1×10^{-4}	4	-	218	31
IOCG+U (Monakoff)	>1%	1	277	4×10^{-3}	6	7.48	3664	2

Table 1. Geochemical data for Mt Isa Inlier U and Th mineralisation styles and deposits/prospects. Data in ppm unless stated Sources from this study, Maas'87, Williams'13, Chinalco Yunnan Copper Ltd Report '10, QLD Dept of Mines, Lawrence'57.

high fluorine content in all U and Th mineralisation except for Emancipation amphibolite-hosted uranium and carbonate hosted-U-Ti mineralisation; (c) Very high Zr content in metasomatic uranium mineralisation and high Zr in Th-pegmatites (d) Low Th/U ratios, particularly for metasomatic and IOCG+U deposits, except for skarn-hosted and Th-pegmatite mineralisation.

7   U, Th, Cu and Zr fluid mobility

U and Th ore-forming fluids were hot and mostly very saline, except for presumably CO_2-rich U-Ti carbonate-related fluids. Skarn related-ores formed from saline, volatile-rich magmatic fluids and later metasomatic fluids (Oliver et al. 1993). U-REE in IOCG mineralisation associated with barite, fluorite and calcite, formed by mixing of oxidised F^-- and SO_4^{2-}-rich magmatic fluids with reduced saline fluids at 235 to >400°C (Davidson et al. 2012; Williams, 2013). Limited data on metasomatic ore-forming fluids is available, but Valhalla calcite and riebeckite formed from oxidised, F-rich fluids at 340-380°C (Polito et al. 2009). Although chloride-rich, saline fluids were very effective in mobilising uranium in other Proterozoic terrains (Richard et al. 2011) such fluids cannot explain the low Th/U ratios and high Cu and Zr content of different Isan U and Th mineralisation.

Experiments by Keppler and Wyllie (1991) demonstrate that both U and Cu are easily partitioned into fluids by chloride so that IOCG+U mineralisation should have higher Cu/U ratios, representing high Cu-U fluid content. In contrast, Isan metasomatic uranium is Cu-poor (Hitzman and Valenta, 2005) with brannerite-riebeckite mineralisation containing ferrous iron, implying relatively reduced ore-forming fluids compared to relatively oxidised magnetite-hematite-uraninite in IOCG+U deposits. If these uranium-forming fluids had higher fO_2, greater Cu mobility would be expected, especially considering the abundant Cu-Au mineralisation in the Mount Isa Inlier. Therefore, relatively reduced fluids preclude Cu-Au mineralisation, with higher fO_2 in IOCG forming fluids having some control on Cu-Au content of IOCG+U systems. Skarn-style mineralisation appears to show a continuum between Cu-rich and Cu-poor U-REE mineralisation that may also be related to different fO_2 of magmatic and metasomatic fluids. Fluid fO_2 cannot be the sole control on U and Th mobility at Mount Isa however because reduced fluids do not commonly favour U transport. Nor do they explain high Zr content and low Th/U ratios.

High F content in mineralisation is thus very significant. Keppler and Wyllie (1991) demonstrate that at 2 kbar and 750°C, U is mobilised by both HCl- and HF-rich fluids, based on fluid-melt partitioning. U can therefore be transported in relatively reduced fluids providing they are F-rich. Th also requires F-rich fluids for effective mobility, explaining the association of high Th and F content in late-stage fractionation of Isan Th-pegmatites. Fluoride is also a powerful transporter of highly immobile zirconium in hydrothermal fluids (Migdisov et al. 2011), but is ineffective at partitioning Cu-Au into fluids (Keppler and Wyllie, 1991) and in combination with relatively low fO_2, further prohibits significant Cu-Au association with metasomatic uranium deposits. Fluoride can effectively dissolve and re-precipitate zircon (Valero et al., 1998). Zr- rich metasomatic U deposits and Th-rich pegmatites at Mount Isa can therefore be explained by the presence of fluoride-rich fluids in ore-formation.

U and Th commonly occur together in high temperature igneous rocks (producing high Th/U ratios) but Th is not easily partitioned into hydrothermal fluids, indicated by relative lower Th/U ratios in pegmatites and hydrothermal veins. High Th/U ratios in Isan Th-rich pegmatites are formed by relative Th immobility compared to U in pegmatite melts and exsolved hydrothermal fluids. The very low Th/U ratios in both Isan IOCG+U and metasomatic uranium mineralisation are not typical of hydrothermal fluids, suggesting a further control on relative U and Th mobility in these fluids. The high F content of these mineralisation styles is problematic because F^- effectively mobilises both U and Th, supporting Th mobility. Although high fO_2 fluids would favour U mobility over Th, the very low Th/U ore ratios make this process alone an unlikely control.

High carbonate and apatite mineral content in metasomatic uranium mineralisation implies ore-forming fluids were CO_2- and PO_4^{3-}-rich. In the presence of carbonate, Th^{4+} has limited stability in fluids. Keppler and Wyllie (1991) demonstrate that adding CO_2 to F-rich fluids, permits CO_2 complexing with U, but importantly, not with Th, whilst still permitting Zr complexing with F^-. This mechanism may explain low Th/U ratios in metasomatic deposits if fluorocarbonic-rich fluids were involved. It may also explain high Th content in skarn-related Mary Kathleen U-REE mineralisation. Metasomatised carbonate-rich sediments would probably limit Th mobility for intrusion-related magmatic fluids.

5   Temporal and spatial relationships to U and Th mineralisation

Different U and Th mineralisation are hosted in a great variety of Paleoproterozoic host rocks, even amongst occurrences of the same mineralisation style. Although compositional and structural differences between

U AND TH MINERALISATION AT MOUNT ISA; FOR MINERALISATION > 50ppm U or Th
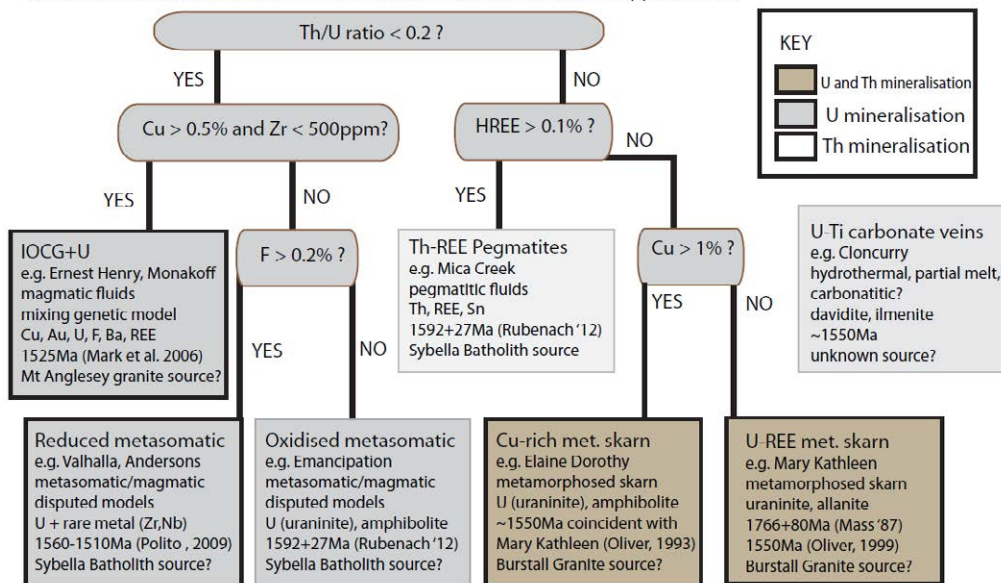
Figure 1.
Flow- chart for Mount Isa U and Th mineralisation styles, categorised by various Th/U ratios, Cu, Zr, HREE and F content. Note the outlying U-Ti carbonate veins mineralisation style with a lack of data and unknown origins. Boxes with bold outlines indicate currently economic U or Th mineralisation styles.

adjacent rock units may preferentially localise fluid flow and influence gangue minerals precipitated (e.g. calc-silicate alteration of sedimentary carbonates in skarns), the variety of host rocks imply that specific host rocks do not control the location of mineralisation.

All known U and Th mineralisation (Figure 1) is spatially associated with granites, and coincides with the Isan Orogeny (1600 to 1490Ma). IOCG+U deposits are coeval with Isan Orogeny magmatism, but metasomatic-, modified skarn- and pegmatite-related mineralisation occur at least 100Ma after granite emplacement, although early skarn U-REE mineralisation was magmatic-derived. Little evidence for modification of carbonate U-Ti mineralisation during regional deformation suggests a syn-Isan age. The temporal and spatial associations of U and Th mineralisation to granites suggest a key influence on their formation.

6 U and Th mineralisation sources

Only limited and deposit-specific discussion for sources of U and Th in the Mount Isa Inlier exist. For skarn-related and IOCG mineralisation, magmatism coincides with the timing of at least initial mineralisation. Regional metamorphogenic fluids (Oliver and Wall, 1987) were abundant at Mary Kathleen but sources for U and Th remain unclear. Early U-REE skarn enrichment (1766±80Ma) was probably magmatically derived, coeval with the intrusion of the Burstall Granite (~1750-1730Ma) some 200Ma before main stage U-REE mineralisation (Maas et al. 1987). The vast majority of IOCG+U mineralisation is thought associated with magmatic fluids of the Williams-Naraku Batholith between 1545 to 1490Ma (Mark et al. 2006). Magmatic fluids were probably not influential in the formation of

metasomatic uranium, U-Ti carbonate veins and Th-pegmatites mineralisation, with no known coeval granite magmatism in the Sybella and Burstall granites. Polito et al. (2009) suggested Valhalla uranium was sediment-derived, as no evidence existed for local magmatic activity after emplacement of the Sybella Batholith (~1670±9Ma, zircon U/Pb SHRIMP age). This leaves a problematic ≥100Ma hiatus between granite magmatism and the formation of spatially-associated U and Th mineralisation. This problem could be resolved by a Sybella Batholith source for metasomatic uranium suggested by Wyborn and Lister (1985) to have formed through metamorphism.

Whether Isan granites were magmatic or crystalline during U and Th ore formation, these granites represent excellent source rocks for mineralisation as the largest regional reservoirs for U and Th. The Sybella Batholith (Kitty Plains Microgranite (KPM) and QEP), Burstall and Mount Anglesay granites (Table 2) are highly fractionated, oxidised and F-rich, with high U, Th, REE and Zr content, hosted in refractory minerals like zircon, particularly in the QEP phase. The Mount Anglesay Granite is less fractionated and Cu-rich by comparison.

Evidence for KPM shear zone metasomatism by regional fluids coeval with the Isan Orogeny provides a suitable source mechanism for some local U and Th mineralisation. Metamorphosed zircon from these shear zones have U/Pb SHRIMP ages of 1589±29Ma and high Th/U ratios, as well as having lost F and U compared to unaltered KPM (McGloin et al. 2012). This relative U mobility over Th, suggests infiltrative fluids govern the very low metasomatic ore Th/U ratios.

Pegmatite mineralisation also has relevance to Isan Orogeny-related metasomatism. Granite margins of the QEP are recrystallised with elevated accessory apatite,

Granite Phase	Cu	Th	U	Th/U	Zr	F (%)	ΣREE	ΣHREE
KPM (metasomatic reduced – Valhalla)	4.3	40	13	3.1	247	0.09	271	15
KPM sheared (as above)	3.1	42	7	6	257	<0.01	210	9
QEP (metasomatic oxidised – Emancipation) (HREE-Th pegmatites)	-	43	20	2.15	881	0.277	1338	75
Burstall Granite (skarn-, Mary Kathleen)	37	66	12	5.5	178	0.01	221	22
Mount Anglesay Granite (Monakoff))	10	54	5	10.8	20	0.09	502	10

Table 2. Geochemical data for selected Mt Isa F-rich granites; KPM= Kitty Plains Microgranite, QEP= Queen Elizabeth Pluton with related mineralisation in parentheses. Data in ppm unless stated. Sources: this study, Mark '06, Maas'87, Qld Dept. of Mines

fluorite, allanite, titanite and F-rich annite content in mafic foliations. Where nearby leucocratic granite shows depletion in these minerals, Brooks (1960) suggested Th remobilisation into nearby pegmatites. At Mica Creek, a new monazite U/Pb 1592±27Ma pegmatite age suggests pegmatite genesis is not coeval with granite emplacement, but related to peak metamorphism (M. Rubenach, 2013, pers. comm.) This implies that amphibolite-grade metamorphism was suitable to partially melt granite and country rocks, whereas in the KPM to the north, lower grade, greenschist hydrothermal metasomatism prevailed. If correct, this explains both the spatial relationship and apparent temporal disparity between some granites and U-Th mineralisation. Such a process would have produced coeval formation of different ore-forming fluids, under varying metamorphic conditions, in different parts of the Mount Isa Inlier.

In both the QEP, and the same sheared KPM phases demonstrating metasomatic U and F loss, rare primary igneous carbonates have been observed that have not previously been found at Mount Isa. Within KPM shear zones, calcite and REE fluoro-carbonates are however absent compared to unaltered granite. It is therefore reasonable to suggest F^- and CO_2-rich fluids, suitable for mobilising U, but not Th, were influential during this metasomatism.

The KPM underwent lower greenschist grade metamorphism, however higher amphibolite grade metamorphism in the QEP produced partial melting and pegmatites. These partial melts have implications for regional genetic models on U-Ti carbonate mineralisation with unknown origins. Flöess et al. (2012) show evidence for partial melting of calcite with REE partitioning into the melt, at the Adamello contact aureole, Italy, driven by contact metamorphism at 650°C. This is consistent with experimental melting in the $CaCO_3$-H_2O system at 625°C akin to wet melting of silicates. Isan amphibolite-grade partial melting of carbonate-bearing granites produced pegmatite fluids and silicate melts, but may have also produced crustal-derived CO_2-rich fluids or carbonatites.

8   Conclusions

The Mount Isa Inlier is a fluorine-rich province that underwent extensive Isan Orogeny deformation and magmatism. U and Th exploration models should be governed by ore-deposit chemistry (F, Th, Cu and Zr content) and the influence of granite source rocks, because abundant regional saline fluids made U highly mobile in a range of magmatic and hydrothermal fluids, producing unusual element associations and complex refractory minerals in a variety of mineralisation styles, including IOCG+U, metamorphosed skarn-hosted, carbonate-hosted and metasomatic uranium deposits. In contrast, Th is relatively immobile with only granites and pegmatites hosting Th-mineralisation. Both crystalline and magmatic regional granites, temporally and spatially associated to mineralisation, are excellent reservoirs for F, a key influence on the chemistry of saline regional fluids. These granites also have high U, Th and rare metal content hosted in refractory minerals. F^-, CO_2 content and fO_2 of ore-forming fluids are fundamental controls on whether U and/or Th mineralisation is associated with Cu or Zr. Whilst Cl^- can mobilise both Cu and U, only fluoride can effectively control transport of typically immobile Th^{4+} or Zr^{4+} in fluids, though fluorocarbonic fluids are ineffective at mobilising Th^{4+}. These concepts challenge ideas of common saline fluids and sediment-derived sources involved in U and Th ore formation at Mount Isa. There remains no evidence for unconformity-style uranium mineralisation, as observed in the McArthur Basin, north of the Mount Isa Inlier.

References

Brooks JH (1960) The U deposits of northwestern Queensland: Publications of the Geol Survey, Queensland 197: 50 pp.

Davidson GJ, Davis BK, Garner A (2002) Structural and geochemical constraints on the emplacement of the Monakoff IOCG deposit, Mt Isa Inlier, 2: 49–76.

Di Florio V (2008) The Mobility of Ti in Hydrothermal Systems within the Mary Kathleen Fold Belt in the Mt Isa Inlier, NW QLD, Australia., Monash University, Australia.

Floess D, Baumgartner L, Muentener O, Ulianov A, Vonlanthen P (2012) Partial melting of carbonates in the Adamello contact Aureole. Abstract. 34th International Geological Congress.

Gregory MJ, Wilde AR, Jones PA (2005) Uranium deposits of the Mt Isa region and their relationships to deformation, metamorphism and Cu deposition. Econ Geol 100:537-546.

Hitzman MW, Valenta RK (2005) Uranium in Iron Oxide-Copper Gold (IOCG) Systems, Econ Geol, 100:1657-1661.

Keppler H, Wyllie PJN (1991) Partitioning of Cu, Sn, Mo, W, U, and Th between melt and aqueous fluid for haplogranite-H_2O-HCl haplogranite-H_2O-HF. Contrib Min Petrol 109: 139-150.

Lawrence LJ, See GT, McBride F, Hofer H (1957) Davidites from the Mt Isa-Cloncurry District, Qld. Econ Geol 52:140-148.

Mark G, Oliver NHS, Williams PJ (2006) Mineralogical and chemical evolution of the Ernest Henry IOCG system, Cloncurry district, NW Qld, Australia, Min Dep 40: 769-801.

Maas R, McCulloch M T, Campbell I H, Page RW (1987) Sm-Nd isotope systematics in U-REE mineralization at the Mary Kathleen U mine, Queensland. Econ Geol: 82, 1805-1826.

Migdisov AA, Williams-Jones AE, Van Hinsberg V, Salvi, S (2011) An experimental study of the solubility of baddeleyite (ZrO2) in fluoride-bearing solutions at elevated temperature. Geochem Cosmo 75: 7426-7434.

McGloin M, Tomkins AG, Weinberg R (2012) Shear zones in fF-rich granites as a source for U-REE deposits. SEG 2012 Conference Publication. Lima, Peru.

Oliver N, Wall V (1987) Metamorphic plumbing system in Proterozoic calc-silicates, Qld Australia. Geology 15: 793-796.

Oliver NHS, Cartwright I, Wall VJ, Golding SD (1993) Stable isotope signature of km-scale fracture-dominated metamorphic pathways, Mary Kathleen, Australia J. Met Geol 11:705-720.

Polito PA, Kyser TK, Stanley C (2009) The Proterozoic, albitite-hosted, Valhalla U deposit, Australia: Min Dep 44:11-40.

Richard A, Rozsypal C, Mercadier J, Banks DA, Cuney M, Boiron MC, Cathelineau M (2011) Giant uranium deposits formed in exceptionally U-rich acidic brines. Nature Geosci 5:142-146.

Towsey CAJ, Patterson, DJ (1984) Tin exploration at Mount Isa – a case history. Journal of Geochemical Exploration, 22: 71-82.

Valero R, Durand B, Guth JL, Chopin T (1998) Mechanism of hydrothermal Synthesis of zircon in a fluoride medium. Journ. Sol-Gel Sci Tech, 13:119-124.

Williams MR (2013) Mineralogical and Fluid Characteristics of the Monakoff Style IOCG mineralisation, Cloncurry, QLD, Australia. MGeol thesis, University of Leicester, UK.

Wyborn LA, Lister GS (1985) Alteration styles in the western Mt Isa Inlier and their significance for Cu and U mineralisation. 14th BMR Symposium, 33: 39-40.

Petrography and geochemistry of the pelitic schist in the Dufferin Lake Zone, south central Athabasca Basin, Saskatchewan, Canada

Marjolaine Pascal*, Kevin Ansdell & Irvine R. Annesley
University of Saskatchewan, Saskatoon, Canada, mjp313@mail.usask.ca, (presenting author),
kevin.ansdell@usask.ca, ira953@mail.usask.ca*

Aaron Brown, Tom Kotzer & Gary Witt
*Cameco Corporation, Saskatoon, Canada, aaron_brown@cameco.com,Tom_Kotzer@cameco.com,
gary_witt@cameco.com*

Dan Jiricka
D.E Jiricka Enterprises, djiricka@sasktel.net

Abstract. Unconformity-type uranium deposit are considered to be the result of mixing between oxidized basinal brines and basement derived reduced fluids, and/or reduced basement rocks. The role of graphite and/or its breakdown products is also suggested to be responsible for the formation of the uranium mineralization.
Variably graphitic pelitic schist from the Dufferin Lake Zone, south central Athabasca Basin (Saskatchewan, Canada) have been studied petrographically and geochemically to determine the different types of carbonaceous matter and graphite and to compare with altered pelitic schist just below the unconformity which appears to have lost or partially lost graphite. The aim is to constrain the processes that may have led to graphite loss, and to determine whether graphite may have played a role in the formation of uranium mineralization.

Keywords. Athabasca Basin, graphite, carbonaceous matter, pelitic schist

1 Introduction

The unconformity-type deposits located in the Athabasca Basin of northern Saskatchewan include the world's highest grade uranium deposits. Most of these deposits are located at the interface between the sedimentary basin and the Archean to Paleoproterozoic basement. In addition, the deposits are usually situated close to faults that intersect the unconformity and that are associated with graphitic schist in the basement.

These deposits are generally considered to be the result of mixing between oxidized basinal brines and basement-derived reduced fluids (Hoeve and Sibbald 1978, Hoeve and Quirt 1987), and/or by the interaction of basinal brines with reduced basement lithologies (Hoeve and Quirt 1984, Kominou and Sverjensky 1996, Fayek and Kyser 1997).

Although these uranium deposits have been the focus of numerous studies over the years, one of the questions that remain unanswered is whether graphite, semi-graphite and/or carbonaceous matter in the basement rocks has any direct role in the formation of mineralization. In addition, graphite and its breakdown products are also considered to be indicative of basement structures, and thus exploration for uranium deposits is focused often on electromagnetic conductors and their associated alteration systems. This study is part

of a project designed to examine the processes that may have led to the consumption of graphite in the basement rocks underlying uranium mineralization in the Dufferin Lake Zone, south-central Athabasca Basin.

2 Geology and Lithological Units at Dufferin Lake Zone

The Dufferin Lake Zone (DLZ) is located in the south central Athabasca Basin, in northern Saskatchewan (Canada) (Fig. 1), and is associated with the Virgin River shear zone (VRSZ), which forms the boundary between the Virgin River Domain and the Taltson magmatic zone. In the DLZ area, the Virgin River Domain is dominated by felsic gneisses, although there are quartzite, pelitic and variably graphitic metasedimentary rocks, and deformed granitoids and pegmatites which have been metamorphosed to upper greenschist to lower amphibolite grade (Gilboy 1985).
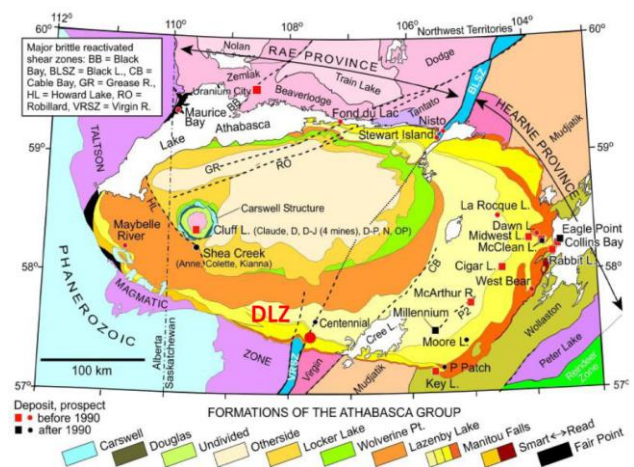
Figure 1. Geological setting and unconformity-type uranium occurrences of the Athabasca Basin region of Saskatchewan/Alberta, Canada. Canada (modified after Jefferson et al. 2007). Heavy dashed lines are selected major reactivated fault zones.

In this area, the post-Athabasca Dufferin Lake thrust fault is the dominant structural element, and is considered to be a product of brittle reactivation of the Virgin River Shear Zone.

Uranium mineralization in the DLZ is hosted mainly in the Manitou Falls sandstones (Fig. 2), and is associated with bleaching and clay alteration. The basement rock directly underlying the DLZ is composed primarily of variably graphitic (and sometimes sulphidic) pelitic schist (Fig. 2).

Visible graphite is not apparent directly below the unconformity (U/C). A variably bleached zone, a few metres thick, is underlain by a strong hematitic and chloritic alteration (Red/Green zone - RGZ) similar to the paleoweathering profile described by MacDonald (1980, 1985). The transition from this paleoweathering profile to fresh rock occurs gradually with depth, and metamorphic textures and structures observed in the basement are preserved in the RGZ. The strong foliation and shear zones are oriented at 10° to 30° to core axis, albeit contorted and microfolded, which means that the variably graphitic pelitic schists extend into the RGZ. This suggests that some process must have removed the graphite from these rocks. The bleached zone is thickest in the vicinity of the larger shear zones (Fig. 2). The lower part of the RGZ is more chlorite-rich than the upper part, which is more hematite-rich. The lower part has thus preserved more reducing conditions and graphite may thus be preserved in this part of the RGZ.
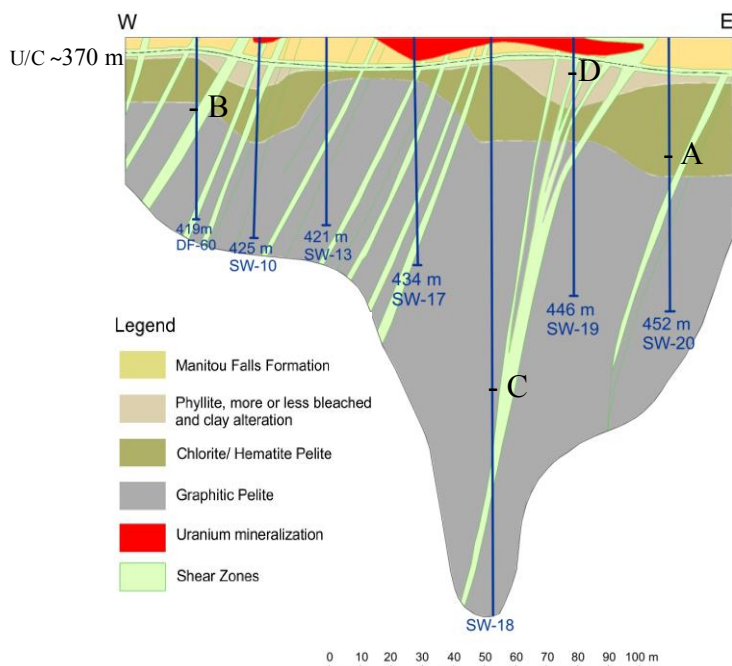
Figure 2. Geological cross section from the Dufferin Lake Zone, illustrating the presence of graphite-depleted and graphite-rich zones, as well as the different rock units.

3 Petrography

The carbon classification and terminology of this investigation follows that of Kwiecińska and Petersen (2004). The pelitic schists exhibit hetereogeneous and complex textures and types of graphite (Gr), semi-graphite (HGr) (Annesley et al. 2001, Kwiecińska and Petersen 2004, McCready and Annesley 2006) and carbonaceous matter (CM). The rocks are porphyroblastic to granoblastic, and variably mylonitic.

The alteration assemblage in the RGZ consists of clay minerals, chlorite and hematite (Fig. 3), with no macroscopic graphite. However, although not observed as yet, microscopic graphite may be present in the lower part of the RGZ.
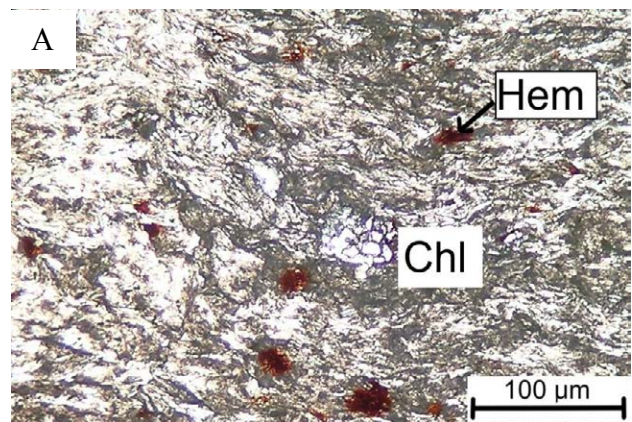
Figure 3. Sample SW20-397.5, characteristic appearance of the RGZ with chlorite (Chl) and hematite (Hem) (PPL Transmitted light).
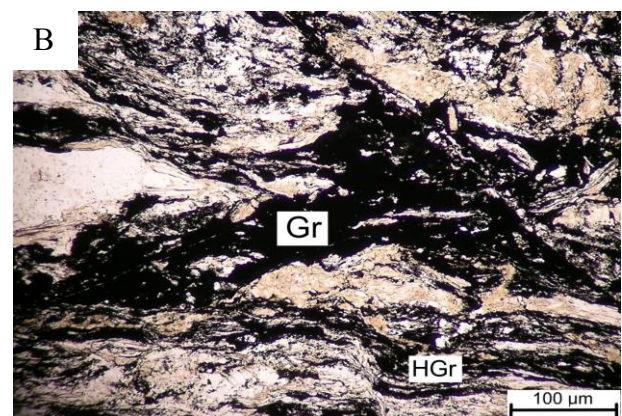
Figure 4. High temperature retrograde graphite (Gr) and semi-graphite (HGr) within a high C content pelitic schist (PPL Transmitted light) (DF60-384.2).
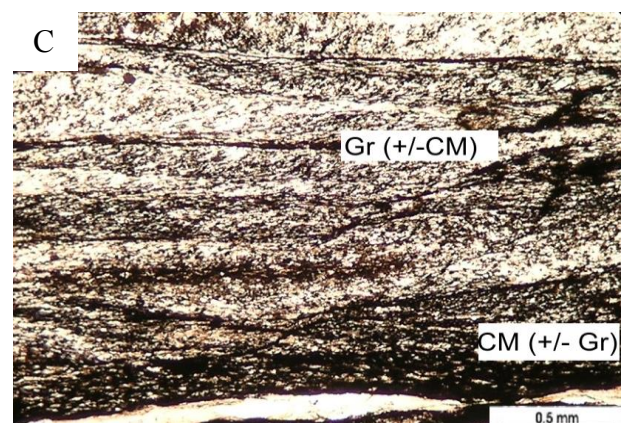
Figure 5. Gr and CM in a medium C content pelitic schist (PPL Transmitted light) (SW18-495.0).

The samples display a strong ductile deformation fabric comprising mainly quartz, chlorite and muscovite. The porphyroblasts when present, are garnet and staurolite. Pyrite occurs as disseminated grains or in

veins. The mylonitic fabric shows C-S structure and the porphyroblasts are rotated.

Two types of graphite, highly crystalline graphite and semi-graphite (or hydrothermal graphite), and CM (Fig. 4, Fig. 5), can be identified using reflected light microscopy, as the reflectivity is correlated with the degree of crystallinity. Graphite (as well semi-graphite and CM) is concentrated along the foliation and within shear zones and along younger fault zones.

4 Geochemistry

Major and trace element geochemical analyses of 45 pelitic schist samples were obtained from the Saskatchewan Research Council Geoanalytical Laboratories (Saskatoon, Canada) using lithium metaborate fusion followed by ICP-OES and ICP-MS analyses. Carbon and sulfur analyses were obtained using a LECO induction furnace.

The pelitic schists have a C content that varies between 0.08 and 5.37 wt%, and is correlated with the amount of graphite in the sample. The samples also exhibit a correlation between total carbon and total sulphur (McCready et al. 2004), whereas the samples from the bleached zone and RGZ have low C and S (Fig. 6). The samples from the bleached zone are enriched in TiO_2, Al_2O_3, Na_2O and K_2O, whereas there are no distinct differences in major elements between the RGZ and the fresh basement rocks. The Na enrichment may result from the possible growth of fine-grained albite within the clay mineral assemblage. Some of the pelitic schists are weakly mineralized (U up to 187 ppm) with hydrothermal uraninite along fractures, while the samples with high B content (from 30 ppm to 13.100 ppm) from the bleached zone have high dravite content (Fig. 7).
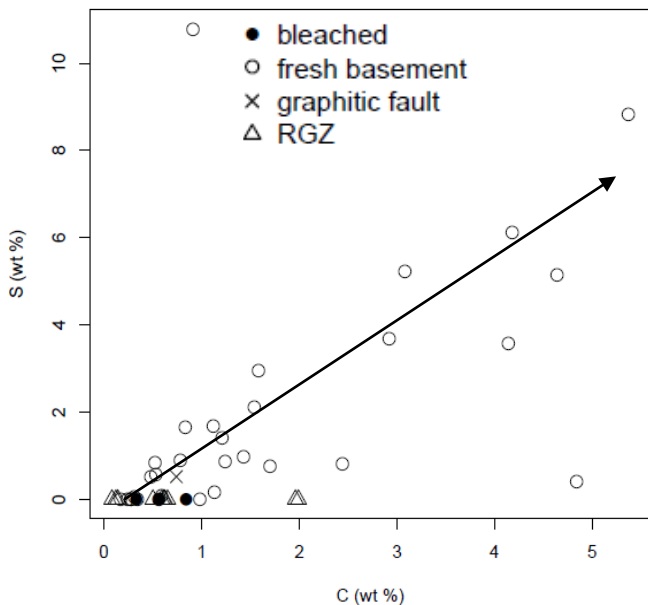
Figure 6. Total sulfur versus total carbon plot for pelitic schist.

The samples show LREE enrichment with (La/Yb)N varying from 1.2 to 36.9 (Fig. 8). The highest concentrations of the HREE are observed in one sample

from the RGZ which may be related to the presence of xenotime.
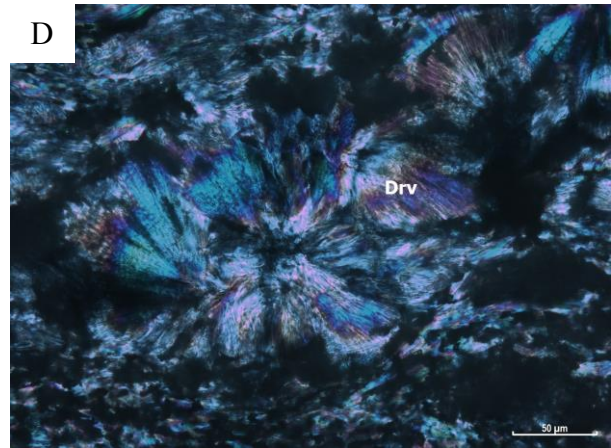
Figure 7. Dravite (Drv) responsible of high boron content in the bleached zone (SW19-369.5).
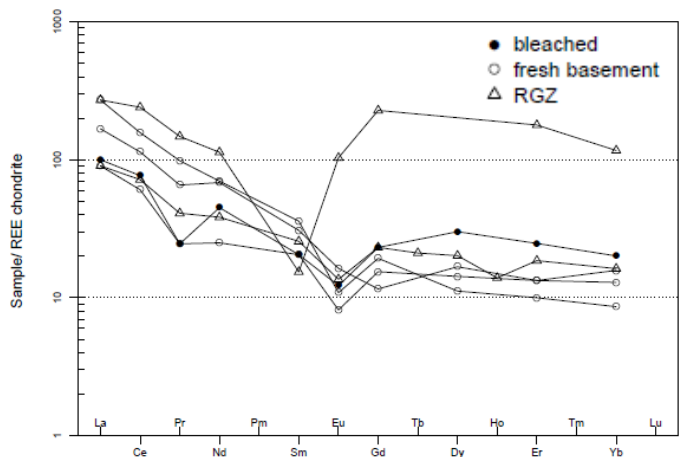
Figure 8. Representative chondrite-normalized REE patterns, using the values of Boynton (1984).

5 Conclusions

The pelitic schists are variably graphitic, and contain different structural habits of graphite, semi-graphite, and carbonaceous matter. The depletion of graphite has been confirmed macroscopically with the absence of visible graphite in the rocks in the bleached and the RGZ, and from geochemical analysis. The geochemical composition of the pelitic schist and RGZ is similar, although the latter contains the highest HREE concentrations and is variably depleted in C and S. The bleached zone represents the most highly altered rocks with increases in Al, Ti, Na, K, and B.

Acknowledgements

McKechnie for field support, and Blaine Novakovski for thin sections. Michel Cuney is thanked for comments on a draft.

References

Annesley I.R., Madore C., Cutler J., 2001. Synchrotron X-Ray analysis of graphtic pelitic gneisses in the vicinity of unconformity-type uranium mineralization. In summary of Investigations 2001, v. 2, Saskatchewan Geological Survey, Sask. Energy Mines, Misc. Rep. 2001-4.2, p.132-140.

Boynton, W.. 1984. Geochemistry of the rare earth elements: meteorite studies. In: Henderson, P. (ed), Rare Earth Element Geochemistry, Elsevier, 63Ð114.

Gilboy, C.F., 1985. Basement geology, part of the Cree Lake (south) area: Saskatchewan Energy and Mines, Report 203, 47p.

Hoeve, J. and Sibbald, T., 1978. On the Genesis of Rabbit Lake and Other Unconformity-type Uranium Deposits in Northern Saskatchewan, Canada; Econ., Geol., v. 73, p. 1450-1473.

Hoeve, J., and Quirt, D., 1984. Mineralization and host rock alteration in relation to clay mineral diagenesis and evolution of the middle Proterozoic Athabasca basin, northern Saskatchewan, Canada. Saskatchewan Research Council Technical Report 187, 187 p.

Hoeve, J., and Quirt, D. 1987. A stationary redox front as a critical factor in the formation of high grade, unconformity-type uranium ores in the Athabasca basin, Saskatchewan, Canada. Bulletin Minéralogie, v. 110, p. 151–171.

Jefferson, C.W., Thomas, D.J., Gandhi, S.S., Ramaekers, P., Delaney, G., Brisban, D., Cutts, C., Portella, P., and Olson, R.A., 2007. Unconformity associated uranium deposits of the Athabasca Basin, Saskatchewan and Alberta, In Mineral Resources of Canada: A synthesis of Major Deposit-types, District Metallogeny, the Evolution of Geological Provinces, and Exploration Methods, W.D. Goodfellow (ed); Mineral Deposits Division of the Geological Association of Canada, p. 273-306.

Kwiecińska, B., and Petersen H.I., 2004. Graphite, semi-graphite, natural coke, and natural char classification—ICCP system Original Research Article International Journal of Coal Geology, Volume 57, p. 99-116.

Komninou A., Sverjensky D.A., 1996. Geochemical modeling of the Formation of an Unconformity-Type uranium Deposit. Economic Geology Vol. 91, 1996, pp. 590-606

Macdonald, C., 1980. Mineralogy and geochemistry of a Precambrian regolith in the Athabasca Basin; M.Sc. Thesis: University of Saskatchewan, 151 p.

Macdonald, C., 1985. Mineralogy and geochemistry of the sub-Athabasca regolith near Wollaston Lake; in T.I.I. Sibbald and W. Petruk , eds.,Geology of Uranium Deposits, Proceedings of the CIM-SEG Uranium Symposium, September 1981: The Canadian Institute of Mining and Metallurgy, Special Volume 32., p. 155-158.

McCready A. J., Stumpfl E. F., Lally J. H., Ahmad M., and Gee R. D., 2004. Polymetallic Mineralization at the Browns Deposit, Rum Jungle Mineral Field, Northern Territory, Australia; Economic Geology, March 2004, v. 99, p. 257-277.

McCready A. J., and Annesley, I.R., 2006. Deciphering EM target conductor responses in the Atahabasca Basin with Raman and synchrotron spectroscopy: applications and benefit to uranium exploration. in Proceedings and abstract Volume, Saskatoon CIM Section 2006 meeting, abstract and poster.

Characterization of a redox front by infrared spectroscopy: a new application to a roll-front uranium deposit in Mongolia

Tony Pons[1,2], Maurice Pagel[1]
[1]Université Paris Sud, UMR 8148 IDES, Bât 504, 91405 Orsay, France

Régis Roy[2], Jean Reyx[2]
[2]AREVA Mines, 1place Jean Millier, 92084 Paris La Défense, France

Abstract. This study concerns the use of an infrared field spectrometer to determine mineralogical variations associated with roll-front uranium deposits. The essential process in the formation of this ore deposit type is the variations of redox condition. This study focuses on the use of iron minerals as pathfinders for uranium deposits. An infrared field spectrometer (TerraSpec®) was used to read spectra between 350 and 2500 nm in order to characterise the mineralogical composition of collected samples. The determination of minerals should be used to estimate the proximity to a uranium deposit. The Visible-Near-Infra-Red (i.e. VNIR, between 350 and 1300 nm) spectrum corresponds to iron oxyhydroxides (e.g. hematite and/or goethite). A novel spectral parameter was developed:

$$\text{OxFe index} = \frac{R_{770} + R_{1060}}{R_{870}}.$$

Goethite is found close to the ore body whereas hematite is present updip of the roll-front. Furthermore, total iron content is highest in the hematite zone. The Short Wave Infra-Red (i.e. SWIR, between 1300 and 2500 nm) spectrum is largely dominated by the spectral signature of montmorillonite, and to a lesser extent by kaolinite and/or chlorite.

Keywords: roll-front, field infrared spectroscopy, redox, hematite, goethite

1 Introduction

The main process generally involved in the formation of U(IV) deposits is a redox process. Within the host rocks, uranium is transported as uranyl ligands by oxygen-rich ground waters flowing through permeable sand bodies bounded above and below by les permeable strata. In fact, the solubility of uranium is linked to the redox conditions in its surroundings. Under oxidizing conditions, uranium is hexavalent and soluble. Upon reducing conditions, uranium became reduced to the tetravalent state and precipitated as uraninite or pitchblende. As a result, uranium deposits are located at redox fronts. The best examples of roll-front deposits are those studied in the 1970s by Harshman (1974); Harsham and Adams (1981) and Goldhaber and Reynolds (1977). Roll-front deposits are a perfect illustration of the process by which uranium is concentrated by a redox process. Uranium is leached from a source of uranium (granitic or volcanic rock), and is then transported by meteoric waters. As the oxygen-rich waters flow in a chemically reduced environment, there is a development of an interface, or redox boundary, that separates reduced from oxidized rocks.

In practice, geologists use the colour of sediments to locate uranium deposits. Reduced sediments are often grey or black in colour while oxidised sediments are whitish, yellow or red. The change in the colour of sediments is mainly due to changes in iron valence states. Iron-bearing minerals under reduced conditions are iron sulphides (e.g. pyrite, marcasite), while iron-bearing minerals under oxidized conditions are iron oxyhydroxides (e.g. hematite, goethite).

Colour changes can be observed around the oxidised zone, as it has been reported by Reynolds and Goldhaber, 1978. These colour variations are interpreted as being already written above mineralogical changes in the nature of iron oxyhydroxides, from limonite to hematite (Reynolds and Goldhaber, 1978). A novel characterisation of minerals along the oxidized-reduced front is required in order to gain a better understanding of the zonation and to increase exploration efficiency for uranium deposits hosted in sandstone.

In this study, we propose to focus on iron-bearing minerals in a roll-front deposit located in the Eastern Gobi region of Mongolia using infrared field spectrometry. The goal of this work is to measure the spectral signature using a field infrared spectrometer (TerraSpec®) in order to characterize iron-bearing minerals in samples and to define specific spectral parameters to differentiate minerals of the reduced zone from those present in the oxidized zone and, if possible, to determine the proximity of uranium deposits.

2 Geological setting

The study area is located in the Sainshand basin, a NE-SW sub-basin of the Eastern Gobi basin. The Sainshand basin is 20 km wide and 100 km long. It is bordered either by Palaeozoic sediments or igneous rocks. Uranium deposit occurs in fluvio-lacustrine sediments of the Upper Cretaceous units, locally knows as the Sainshand formation (K2SS) (Prost, 2004).

3 Materials and methods

3.1 Sampling

245 samples were obtained from a suite of cores drilled along a line (Figure 1), from oxidized to the reduced units. Figure 1 shows the locations of the 12 sampled

boreholes with the redox distribution in the background. This map was established by interpreting the redox state of samples by their colour (yellow to red for oxidised samples and grey for reduced samples). The most highly oxidised samples were found in borehole n°12 while the most reduced in borehole n°8. The other boreholes are close to the redox interface. A denser sampling was performed at the redox front (boreholes n°9, 10, 11 and 12), and principally along a cross-section (boreholes n°1 to 8) oriented NE-SW composed by 8 boreholes spaced every 200 m (Figure 2). This cross-section shows the 8 boreholes sampled with the redox interpreted using the colours of samples. This section was established using the resistivity log to place the clay and sand formations. Uranium mineralisation was interpreted using gamma probe measurements.
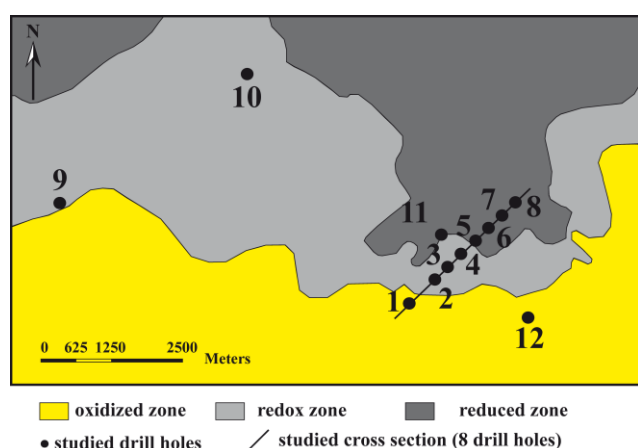
Figure 1. Location of drill holes sampled for this study in the redox area (Eastern Gobi bassin, Mongolia).
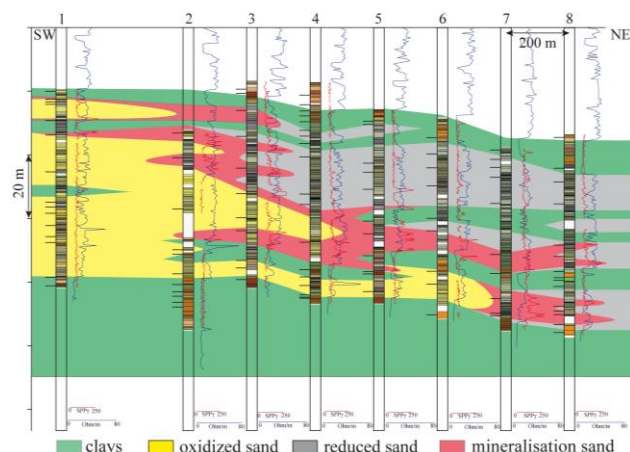
Figure 2. Geological cross-section established using both resistivity (in blue line) and radiometric log data (in red line) and sample colour based on the Munsell colour chart (drillhole centre). Collated samples depths are shown by black lines.

3.2 Methods

Infrared spectrometry allows characterizing rock-forming minerals; in particular iron oxyhydroxides and phyllosilicates (Hunt et al, 1971; Hunt et al, 1973). Infrared spectra were acquired using an ASD TerraSpec® spectrometer. This spectral device measures the radiation reflected by minerals in the wavelength range between 350 and 2500 nm. The spectral resolution (resampled to 1 nm) is 3 nm between 350 and 1000 nm, 6 nm between

1000 and 1800 nm and 7 nm between 1800 and 2500 nm. Collated spectra were then interpreted using TSG Core software (The Spectral Geologist) and the USGS spectral library (Clark et al, 2007).
Total iron content for whole rock were obtained by chemistry, ICP-OES at the SARM laboratory, CRPG (Nancy, France).

4 Results

4.1 Mineralogical characterization

Minerals identified in spectra correspond to iron oxyhydroxides and phyllosilicates (Figure 3).
Iron oxyhydroxides produce characteristic absorption features between 350 and 1050 nm (Hunt et al, 1971; Hunt and Ashley, 1979; Morris et al, 1985; Sherman and Waite, 1985; Cudahy and Ramanaidou, 1992, 1997). These absorptions are due to electronic processes involving octahedral Fe^{3+} bound to oxygen for hematite, or oxygen and the hydroxyl group for goethite. Two simple electronic transitions can be observed here: $^4T_1 \leftarrow ^6A_1$ to 870 – 1030 nm and $^4T_2 \leftarrow ^6A_1$ to 650 – 710 nm. There is also an absorption due to a charge transfer process at 480 – 550 nm (Sherman and Waite, 1985). Differences between hematite and goethite spectra can be observed in Figure 3. Hematite spectrum is characterized by three absorption features centred at 541, 670 and 880 nm, while goethite spectrum display, three absorption bands centred at 490, 670 and 942 nm. These spectra cannot be mistaken with other iron oxyhydroxide because the main features of the spectrum are primarily determined by the valence state of the ion, and by its coordination number and site symmetry. For example, maghemite has characteristic bands at 780, 925 and 1150 nm and lepidocrocite has a characteristic band around 1450 nm.
Furthermore, zoning is observed for iron oxyhydroxides: goethite is closer to the deposit whereas hematite is present updip of the front.
Montmorillonite is present in all spectra. This mineral display three absorption features at 1414, 1909 and 2208 nm (Figure 3). The two first bands are produced by both OH and H_2O molecules contained in the montmorillonite while the latter is due to the Al-OH group (Hunt et al., 1973).
Kaolinite was identified in some samples. Its presence is highlighted by a first absorption feature near 2167 nm and a second band at 2208 nm, also common to montmorillonite (Figure 3).
Chlorite is characterized in spectra of some samples by multiple absorption features in both the VNIR and SWIR (Figure 3). The three absorption bands in the VNIR (715, 920 and 1100 nm) are caused by transfer of electronic energy levels of anions Fe^{2+} and Fe^{3+} in octahedral position: 715 nm: the transition of $(Fe^{3+})^{VI}$: $^6A_{1g} \rightarrow ^4T_{2g}$; 920 nm: the transition of $(Fe^{3+})^{VI}$: $^6A_{1g} \rightarrow ^4T_{1g}$; 1050 nm: the transition of $(Fe^{2+})^{VI}$: $^5T_{2g} \rightarrow ^5Eg$ (White and Keester, 1966). In the SWIR, the diagnostic bands of this mineral occur at 2250 and 2348 nm. The absorptions are caused by the vibration of both Fe-OH and Mg-OH groups respectively (Hunt et al., 1970).
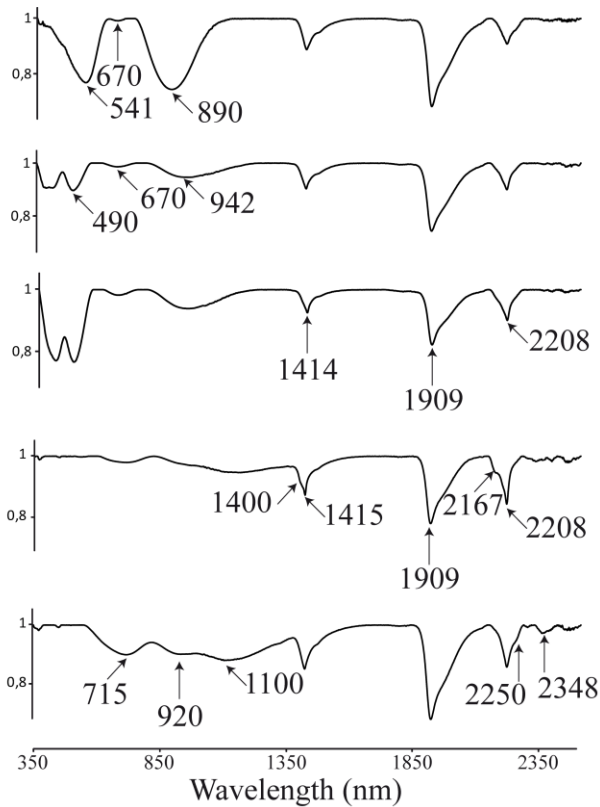
Figure 3. Hull quotient spectra of endmember samples characterized from top to bottom by hematite, goethite, montmorillonite, kaolinite and chlorite. Note that all samples contain montmorillonite. The spectra are offset for clarity.

4.2 Redox spectral parameter definition

A novel spectral parameter sensitive to oxidation has been established to highlight the limit of both oxidized and reduced zones:

$$OxFe\ index = \frac{R_{770} + R_{1060}}{R_{870}}$$

where: R_{770} and R_{1060} are the reflectance values at 770 and 1060 nm (i.e. 870 nm feature shoulders); R_{870} the reflectance at 870 nm (i.e. for the maximum absorption). Note: values were taken on hull quotient spectra. This spectral parameter allows focusing on a specific iron oxyhydroxide absorption feature, of hematite (absorption band centred at 890 nm) and goethite (absorption band centred at 935 nm). Figure 4 A shows the *OxFe index* histogram coloured using the Munsell colour chart extracted from spectra using TSG Core. A threshold at *OxFe index* ≈ 2 is defined to split oxidized from reduced samples. Values lower than 2 correspond to reduced samples while values higher than 2 correspond to oxidized samples. Note that *OxFe index* values are highly correlated with samples colour.

Endmember spectra of both reduced and oxidized sample are shown in Figures 4 B and C. Hull quotient spectra shows three absorption features in the VNIR (diagnostic of chlorite) for the reduced sample while oxidized sample spectra show three absorptions characteristic of iron oxy-hydroxides.
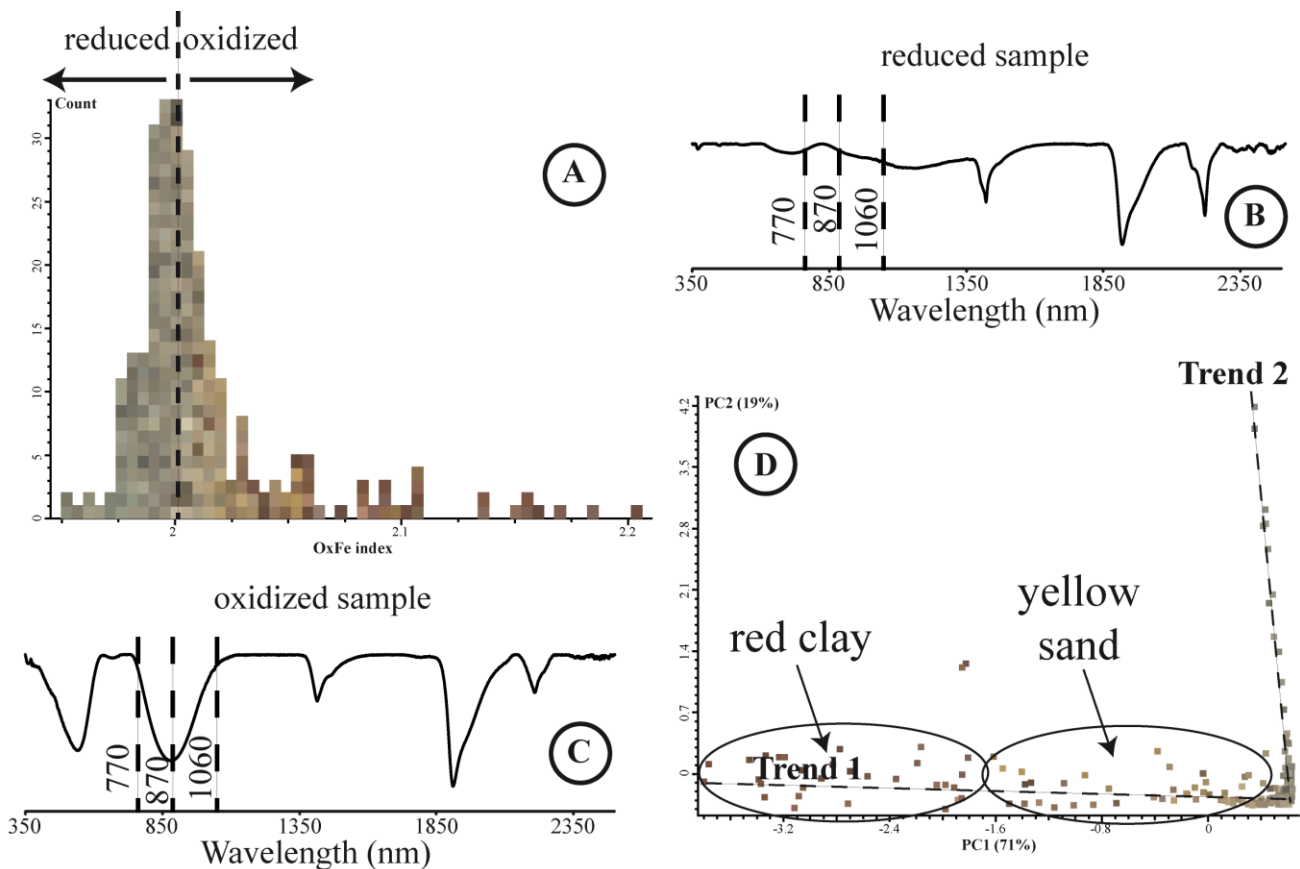
Figure 4. A: *OxFe index* histogram. Samples were coloured using the Munsell colour chart extracted form TSG Core. B: Reduced sample spectrum. C: Oxidized sample spectrum. D: Principal Component (PC) scatter plot (x: PC1 and y: PC2); Oxidized samples: trend 1; Reduced samples: trend 2.

The above result is confirmed by a principal component analysis (PCA) performed on the VNIR range. Figure 4 D shows the scatterplot of the first two principal components (PC1 and PC2) sensitive to the redox state of the samples. Oxidized samples are aligned along a straight horizontal line (trend 1) while the reduced samples are aligned along a straight vertical line (trend 2).

4.3 Iron distribution

The average total iron in reduced samples is around 1 % Fe_2O_3 while in oxidized samples is close to 2 % Fe_2O_3. The samples farthest updip from the front present values ranging up to 7 % Fe_2O_3.

5 Conclusions

The study of a roll-front uranium deposit in the Sainshand basin using field infrared spectrometry identified phyllosilicates and iron oxyhydroxides. Minerals characterized in the VNIR correspond to iron oxyhydroxides (e.g. hematite and/or goethite). Spectra are mainly dominated by absorption features of montmorillonite and, to a lesser extent of kaolinite and/or chlorite in the SWIR.

The mineralogical data provided by infrared spectrometry for this roll-front show that it is composed of four different zones:
- a reduced zone, without iron oxyhydroxides
- an oxidised zone, with goethite
- an oxidised zone, with the presence of goethite and hematite
- an oxidised zone, with the presence of hematite

The main mineralogical changes in the roll-front are associated with the presence of iron oxyhydroxides, goethite (in contact with the uranium deposit) and hematite further updip.

The mineralogical zoning of both hematite and goethite is correlated with the total iron content in samples. Iron content is higher in the hematite zone.

These zonings will require further mineralogical studies of samples in order to better characterize the relationship between hematite and goethite.

The definition of a novel spectral parameter allows highlighting the presence of iron oxyhydroxides in spectra. This parameter is sensitive to the oxidation state and can assist the user to orientate the direction in which the roll-front will be found during exploration.

References

Adler HH (1974) Concepts of uranium-ore formation in reducing environments in sandstones and other sediments. Formation of uranium ore deposits. IAEA Conference, Athens, Greece, pp:141-167

Clark RN, Swayze GA, Wise R, Livo E, Hoefen T, Kokaly R, Sutley SJ (2007) USGS digital spectral library splib06a: U.S. Geological Survay, Digital data series 231

Cornell RM, Schwertmann U (2003) The iron oxides, Structure, Properties, Reactions, Occurrences and Uses. 664pp.

Cudahy T, Ramanaidou ER (1992) Relationships between spectral properties and ferric oxides, CSIRO/AMIRA Project P243: Wembley, Australia, CSIRO Division of Exploration Geoscience Report 244R, 68 p

Cudahy T, Ramanaidou ER (1997) Measurement of the hematite:goethite ratio using field visible and near-infrared reflectance spectrometry in channel iron deposits, Western Australia: Australian Journal of Earth Sciences 44:411−420

Fischer RP (1950) Uranium-bearing sandstone deposits of the Colorado plateau. Economic geology, V45:1-11.

Goldhaber MB, Reynolds LR (1977) Geochemical and mineralogical studies of a south Texas roll front uranium deposit. US Departement of the interior, geological survey, open file report 77-821, 38p.

Goldhaber MB, Reynolds RL, Rye RO (1978) Origin of a South Texas roll-type uranium deposit—2. Sulfide petrology and sulfur isotope studies. Econ Geol 73:1690–1705

Granger HC, WarrenCG (1969) Unstable sulfur compounds and the origin of roll-type deposits. Econ Geol 64:160

Harshman EN (1974) Distribution of elements in some-type uranium deposits, in formation of uranium ore deposits. IAEA, Proc., Vienna, p.169-183.

Harshman EN, Adams SS (1981) Geology and recognition criteria for roll-type uranium deposits in continental sandstones. US-DOE, GJBX-1 (81), 185p.

Hunt GR, Ashley RP (1979) Spectra of altered rocks in the visible and near-infrared. Econ Geol 74:1613−1629

Hunt GR, Salisbury JW (1970) Visible and near-infrared spectra of minerals and rocks: I. Silicate minerals. Modern Geology 1:283-300

Hunt GR, Salisbury JW, Lenhoff (1971) Visible and near infrared spectra of minerals and rocks: III. Oxides and hydroxides. Modern Geology 2:195-205

Hunt GR, Salisbury JW, Lenhoff (1973) Visible and near infrared spectra of minerals and rocks: VI. Additional silicates. Modern Geology 4:85-106

Morris RV, Lauer HV, Lawson CA, Gibson EK, Nace GA, Stewart C (1985) Spectral and other physicochemcial properties of submicron powders of hematite (alpha-Fe2O3), maghemite (gamma-Fe2O3), magnetite (Fe3O4), goethite (alpha-FeOOH) and lepidocrocite (gamma-FeOOH). Journal of Geophysical Research-Solid Earth and Planets 90:3126−3144

Prost GL (2004) Tectonics and hydrocarbon system of the East Gobi basin, Mongolia. AAPG Bulletin, V. 80:483-513.

Reynolds RL, Goldhaber MB (1978) Origin of south Texas roll-type uranium deposit: I. Alteration of iron-titanium oxide mineral. Economic geology, V73:1677-1689.

Shawe DR, Granger HC (1965) Uranium ore rolls-an analysis. Economic geology 60:240-250

Sherman DM, Waite TD (1985) Electronic spectra of Fe^{3+} oxides and oxide hydroxides in the near IR to near UV. Am Mineral, V70:1262-1269.

White WB, Keester KL (1966) Optical absorption spectra of iron in the rock-forming silicates. The American mineralogist 51:774-791.

Alteration and uranium mineralization in the Kiggavik–Andrew lake structural trend, Nunavut, Canada

Thomas Riegler[1,2]*, Dave Quirt[3] & Daniel Beaufort[1]
[1]ERM
[2]University of Poitiers, IC2MP / HydrASA
[3]AREVA Resources Canada
*thomas.riegler@univ-poitiers.fr

Abstract

Basement hosted uranium mineralization have been recognized along the SE erosional contact of the Paleoproterozoic Thelon Basin, Nunavut, Canada during the mid 70's airborne radiometric surveys lead by Urangeslshalft Canada (UG) (Fuchs and Hilger 1989). Now known as the Kiggavik project and actively explored by AREVA Resources Canada, this mineralized trend consist of 4 ore bodies (Kiggavik, Bong, End & Andrew) hosting 50 000t U of historical resources. Mineralization is closely associated with a clay alteration halo. The alteration paragenesis is very similar to that found in the so called unconformity related uranium deposits. It is composed of illite $\pm$ sudoite $\pm$ hematite $\pm$ aluminum phosphate sulphates minerals (APS). In addition crystalchemistry of alteration minerals (phyllosilicates and APS) is similar to the one described in the Athabasca and Kombolgie Basins, (Beaufort et al. 2005; Laverret 2002) (Gaboreau et al. 2007; Gaboreau et al. 2005)
Alteration, petrography, clays, APS, uranium

1 Introduction

Unconformity related uranium deposits are world class uranium deposits and by far the richest in term of ore grades (Jefferson et al. 2007). Another distinctive feature of these kind of deposits is the occurrence of a clay alteration halo around the ore bodies (Hoeve and Quirt 1984). The basement hosted Kiggavik uranium mineralizations by their location along the erosional contact of the Paleoproterozoic Thelon Basin sandstones (figure 1) raise the question of their potential relationship with the Basin history (Fuchs et al. 1986; Miller and LeCheminant 1985).

At Kiggavik the mineralization is hosted in late Archean metagraywackes retromorphosed to greenschist facies, part of the Woodburn Lake Group. The structural frame of the area is complex. It consists in multiple generations of ductile folds in relation with Archean and Paleoproterozoic deformation stages followed by a strong brittle fracturation which is highlighted by N070 regional faults marked by quartz breccias and hematization of wall rocks.

The mineralization, mainly uraninite subsequently altered in coffinite, is closely associated with broad clay alteration halos and is distributed along the foliation plans and often remobilized in redox fronts at the walls of fractured corridors. The average ore grade is around 0.5% U.

The goal of this study is (1) to characterize the Kiggavik hydrothermal alteration system and its relationship with the uranium mineralization and a comparison of the alteration signature in the Kiggavik area with that of unconformity related uranium mineralization form worldwide Paleoproterozoic Basins (e.g. Athabasca or Kombolgie).
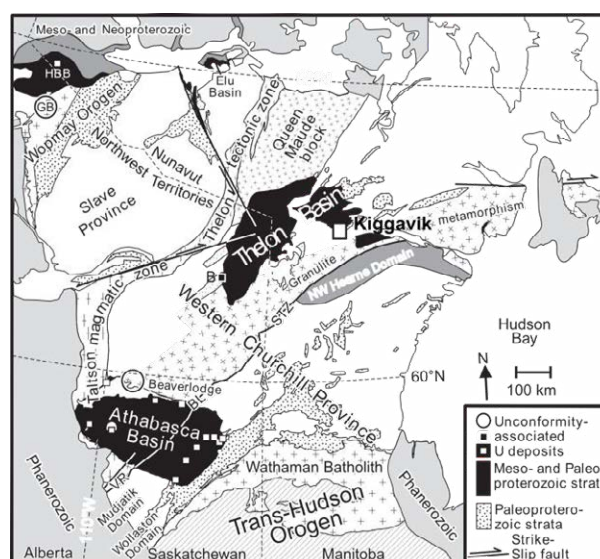
Figure 1, Unconformity associated U occurrences in Western Churchill & Kiggavik project location, modified from Jefferson, 2006.

2 Material and methods

A total of 17 drillholes and more than 200 samples have been studied for clay mineralogy in unaltered host rock, in the altered but barren zones and within the altered and mineralized envelopes. X-ray diffraction on oriented mounts have been systematically performed on the <4µm fraction size for each sample, for clay minerals identification. Randomly oriented mounts were done on altered rock to identify the crystallographic properties of illite which can be used to map of the alteration zones. A JEOL 5600 SEM equipped with EDS was used for alteration petrography and crystal chemistry of clay minerals and associated mineral phases. In addition electron microprobe analyses for Si, Al, Fe, F, P, S, Ca, Ba, Sr, La, Ce, Pr, Nd, Th and U were performed on the APS minerals and primary REE bearing minerals using a CAMECA SX100 (Camparis facility, Paris 6 University, France). Whole rock analyses (ICP-MS) were acquired (SARM Nancy, France) and an additional set of (ICP OES) analysis were obtained courtesy of AREVA Resources Canada.

2 Results

2.1 Alteration petrography & crystal-chemical properties of clay minerals

The hydrothermal alteration takes place as a replacement or dissolution of primary silicates (feldspars, white micas and biotite which were more or less retromorphosed by metamorphic chlorite) or the filling of the neoformed porosity with clay minerals with a mixing of illite and sudoite (a di-trioctahedral variety of Al-Mg chlorite). Alteration processes are contemporaneous with uraninite precipitation at the edge of partly dissolved metamorphic chlorite or primary sulphide, usually pyrite, forming boxwork textures. The general alteration paragenesis is composed of illite ± sudoite ± hematite ± aluminum phosphate sulphates minerals (APS) ±apatite.

Detailed studies of clay minerals crystal chemistry lead to the identification of two illite polytypes 1M transvacant ($1M_{tv}$) and 1M cis-vacant ($1M_{cv}$) by their specific hk. XRD peaks (Drits and Tchoubar 1990). The relative abundance of each shows an increase of the 1Mt polytype in the ore zone. In addition the full width at half maximum intensity (FWHM) of the 001 XRD reflection of potassic dioctahedral phyllosilicates was used to discriminate the illite from the relicts of metamorphic white micas. Then interpolated data of such a "crystallinity parameter" give a broad view of the alteration extent around ore bodies.

Also, the crystal chemistry of both primary and secondary phyllosilicates outlines the geochemical signature of the hydrothermal mineral assemblage (Figure 2). This indicates that hydrothermal alteration proceeded in oxidizing conditions and consisted in the replacement of Fe,Mg-rich phyllosilicates (phengites an Fe-rich chlorite) + pyrite by Al-Mg rich phyllosilicates (illite ±sudoite) + hematite. Most of the iron (essentially ferrous iron) released by the dissolution of minerals of the metamorphic basement was not incorporated in the newly formed phyllosilicates illite and sudoite which coexist with hematite.
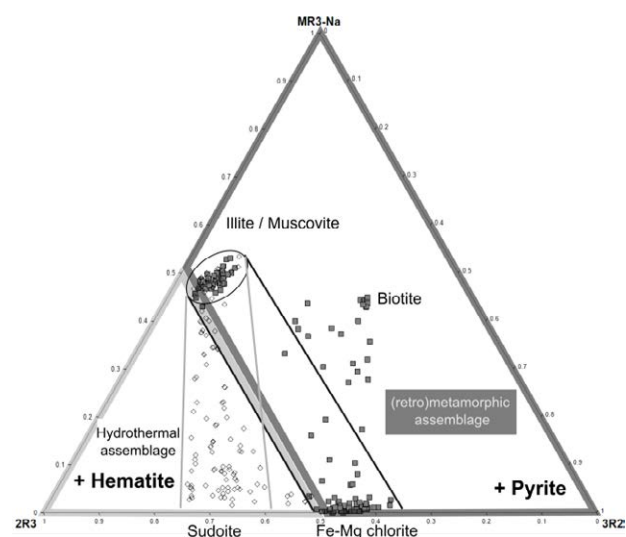
Figure 2, Plot of the structural formulas of phyllosilicates of the metasediments hosting uranium mineralization in a MR^3-$2R^3$-$3R^2$ diagram (Velde 1985). Phyllosilicate

assemblages formed during the hydrothermal (◊) stage strongly differs from those of the retrograde metamorphic stage (■) by their content in divalent elements (3R2) and more particularly in ferrous iron.

2.2 APS minerals as geochemical markers

All along the Kiggavik trend, aluminum phosphate sulphates (APS) minerals occur as very small pseudocubic crystals in two different geological environments. In the basement rocks, APS minerals are closely associated with the hydrothermal alteration processes which controlled the uranium ore genesis. Diagenetic APS minerals are also disseminated in pore cements of the overlying sandstones of the Thelon formation which are preserved of the hydrothermal alteration (sampled near the unconformity contact.

The chemical composition of all the APS minerals observed along the Kiggavik trend can be interpreted in terms of solid solutions between several chemical end-members (figure 3) in response to coupled substitution of Sr by LREE for the A site and P, S for the X site: i.e. svanbergite Sr(Al3)(PO4,SO4)(OH)6, goyazite SrAl3(PO3[(0.5(OH)0.5]2(OH)6 and florencite LREE(Al3)(PO4)2(OH)6.

The chemical composition of the diagenetic APS is dominated by the svanbergite end-member in association with minor goyazite and florencite end-members whereas the chemistry of hydrothermal APS of the basement rocks is dominated by florencite and svanbergite end-members. In the altered basement rocks, the increase of the florencite solid solution in the APS minerals is a general trend with the decreasing distance to the uranium ore bodies.
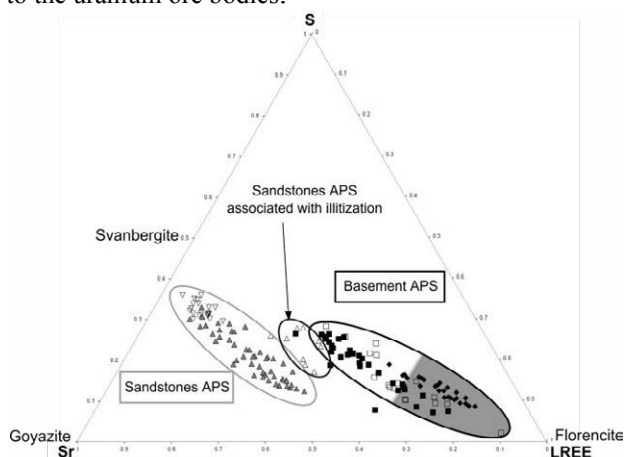
Figure 3, Ternary plot using Sr, LREE & S composition of APS minerals. Grey shaded area represents compositions of APS within the ore zones.

3 Discussion and concluding remarks

From the aforementioned data it results that the alteration pattern associated with the uranium deposits of the Kiggavik-Andrew Lake presents most of the characteristics of those associated with basement hosted unconformity-related uranium deposits wordwide:
They can be summarized as follows:

(1) Similar alteration halos related to fracture controlled uranium mineralization consisting in strong argilization associated with dissolution of silicates and quartz in basement rocks having suffered previously high grade and then retrograde metamorphic conditions.

(2) Similar nature of the secondary mineral phases dominated by illite and di-trioctahedral Al-Mg chlorite (sudoite) and with lesser amounts of phosphate minerals (APS, apatite) and hematite. It would be noted that, if we except the alteration halos of the unconformity type deposits, sudoite is a seldom clay mineral in all other geological geological environments worldwide.

(3) Similar structural and crystal chemical characteristics for clay minerals (illite and sudoite) involved in the hydrothermal alteration process.

This suggests a close link between the genesis of these ore deposits and the tectonic evolution of the Thelon basin which is presently prospected for unconformity related uranium deposits.

Such an interpretation is conforted by the compositional variation of APS minerals around the uranium orebodies which is very similar to that already reported in the unconformity related uranium deposits of the Kombolgie basin in Autralia (Beaufort et al., 2005; Gaboreau et al., 2005) as well as of the Athabasca (Gaboreau et al. 2007). According to these authors, the increase in LREE content of APS with a decreasing distance to the uranium mineralization is a good indicator in change of both redox and pH paleo-conditions which are well known to be major controlling factors on the uranium deposition (Gaboreau et al., 2005, 2007).

The chemical composition, in addition to petrography, of the APS minerals in Thelon sandstones, hightlights an early diagenetic stage, pre-mineralization, as already observed elsewhere in the Thelon basin (Gall and Donaldson 2006).

Finally, when compared to basement-hosted uranium deposits of the Athabasca basin such as Shea Creek (Laverret et al. 2006) or Millenium (Cloutier et al. 2009) the alteration pattern associated with the uranium deposits of the Kiggavik-Andrew Lake only differs by the two following points: (1) the absence of significant amount of graphite in the fault system and (2) absence of dravite in the alteration paragenetic sequence.

Acknowledgements

References

Beaufort D, Patrier P, Laverret E, Bruneton P, Mondy J (2005) Clay Alteration Associated with Proterozoic Unconformity-Type Uranium Deposits in the East Alligator Rivers Uranium Field, Northern Territory, Australia. Economic Geology v. 100:pp. 515–536.

Cloutier J, Kyser K, Olivo GR, Alexandre P, Halaburda J (2009) The Millennium Uranium Deposit, Athabasca Basin, Saskatchewan, Canada: An Atypical Basement-Hosted Unconformity-Related Uranium Deposit. Economic Geology 104:815-840. doi: 10.2113/gsecongeo.104.6.815.

Drits VA, Tchoubar C (1990) X-ray diffraction by disordered lamellar structure. Theory and application to microdivided silicates and carbons. Springer-Verlag, Berlin.

Fuchs HD, Hilger W, Prosser E (eds) (1986) Geology and exploration history of the Lone Gull property. CIM.

Fuchs HD, Hilger W (1989) Kiggavik (Lone Gull): an unconformity related uranium deposit in the Thelon basin, Northwest Territories, Canada In: Agency IAE (ed) Uranium Resources and Geology of North America. International Atomic Energy Agency, Vienna, pp 429-454.

Gaboreau S, Beaufort D, Vieillard P, Patrier P, Bruneton P (2005) Aluminium phosphate sulfate minerals associated with proterozoic unconformity-type uranium deposits in the East Alligator river uranium field, Northern Territories, Australia.Can Mineral 43:813-827. doi: 10.2113/gscanmin.43.2.813.

Gaboreau S, Cuney M, Quirt D, Beaufort D, Patrier P, Mathieu R (2007) Significance of aluium phosphate-sulfate minerals associeted with U unconformity-type deposits: The Athabasca basin, Canada. American Mineralogist 92:267-280.

Gall Q, Donaldson JA (2006) Diagenetic fluorapatite and aluminum phosphate-sulphate in the pPelaoproterozoic Thelon Formation and Hornby Bay Groupe, northwestern Canadian Shield. Canadian Journal of Earth Sciences 43:617-629.

Hoeve J, Quirt D (1984) Mineralization and host rock alteration in relation to clay mineral diagenesis and evolution of the Middle-Proterozoic Athabasca basin, Northern Saskatchewan, Canada Saskatchewan Research Concil Technical report. Saskatchewan Reasearch Council, pp 197.

Jefferson CW, Thomas DJ, Gandhi SS, Ramaekers P, Delaney G, Brisbin D, Cutts C, Portella P, Olson RA (2007) Unconformity-associeted uranium deposits of the Athabasca Basin, Saskatchewan and Alberta EXTECH IV. pp 23-67..

Laverret E, Patrier P, Beaufort D, Kister P, Quirt D, Bruneton P, Clauer N (2006) Mineralogy and geochemistry of the host-rock alterations associated with the Shea Creek unconformity-type uranium deposits (Athabasca basin, Saskatchewan, Canada) Part1. Spatial variation of illite properties. Clays and Clay Minerals 54:275-294.

Miller AR, LeCheminant AN (1985) Geology and uranium metallogeny of Proterozoic supracrustal successions, central District of Keewatin, N.W.T with comparisons to northern Saskatchewan Geology of uranium deposits. Canadian Institute of Mining and Metalurgy, pp 167-185.

Velde B (ed) (1985) Clay minerals: A physico-chemical explanation of their occurence. Elsevier.

Kvanefjeld – a large uranium deposit in Greenland

Kristine Thrane & Per Kalvig
Department of Petrology and Economic Geology, Geological Survey of Denmark and Greenland, Copenhagen, Denmark

Henrik Stendal
Bureau of Minerals and Petroleum, Ministry of Industry and Mineral Resources, Nuuk, Greenland

Abstract. The uranium potential in Greenland is considered good with several uranium occurrences already known. The largest occurrence is the Kvanefjeld deposit in South Greenland. Kvanefjeld is part of the Mesoproterozoic Ilímaussaq complex in the Gardar Province. It is a very rare type of uranium deposit where uranium is hosted by the complex silico-phosphate mineral steenstrupine. While the potential for uranium exploration is good, the current Greenland policy does not allow uranium mining or exploration for radioactive minerals.

Greenland, uranium, Kvanefjeld

1 Greenland policy on uranium

The current Greenland policy does not allow for exploration or mining of radioactive minerals, a policy that has been in place since 1985 – the so called "zero-tolerance" policy. However, in 2007 the Bureau of Minerals and Petroleum approved a continued REE-exploration program for a group working on Kvanefjeld, exploring for the REE-U-Th-bearing mineral steenstrupine. The "zero-tolerance" policy is currently being debated in the Greenland Parliament with the following themes as the focus of discussion: 1) should the "zero-tolerance" policy be maintained, 2) should mining where uranium is a by-product be allowed, and 3) should uranium exploitation be accepted without limitations.

2 Uranium deposits in Greenland

The uranium potential in Greenland is considered good with several uranium occurrences already known. In West Greenland, anomalous amounts of uranium have been discovered in pegmatite veins at Attu and Nassuttooq and are also related to the carbonatite intrusions at Sarfartoq and Qaqqaarsuk (Fig. 1). In the Caledonian fold belt of East Greenland, several uranium anomalies occur in pegmatites, granites and gneisses. One mineralised zone has been discovered in the Stauning Alper, located in a fault zone between late kinematic granites and Permian arkoses (Harpøth et al., 1986). Uranium has also been found as replacement mineralisation in rhyolites at Randbøldal, and in monazite-bearing heavy mineral layers at Milne Land, East Greenland. South Greenland is known as the largest uranium province in Greenland. Except for uraninite at Illorsuit, the occurrences in South Greenland are related to the Mesoproterozoic Gardar Province, and especially

to the Ilímaussaq complex that is described in detail below.

Given the very limited uranium exploration carried out in Greenland to date, a greater potential is presumed based on spot observations and the knowledge of existing favourable geological environments (e.g. the Thule region).
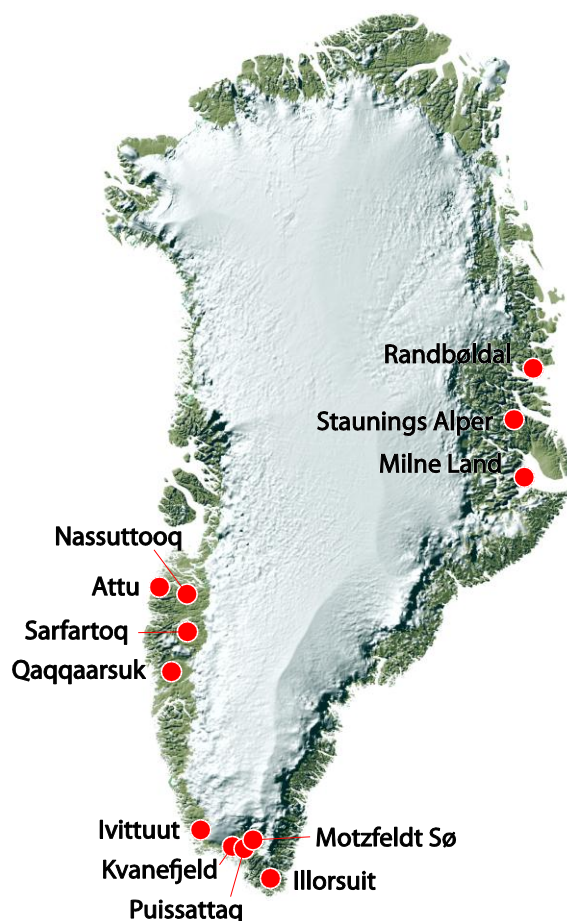
Figure 1. Uranium occurrences in Greenland

3 Geology of Kvanefjeld (Ilímaussaq complex)

The Ilímaussaq alkaline complex of South Greenland hosts the REE-U-Th-Zn-F deposit referred to as Kvanefjeld. The complex intruded into Proterozoic basement granitiods and unconformably overlying

sandstones and basalts belonging to the Eriksfjord Formation. The complex is composed of successive intrusions of augite syenitic, alkali granitic and nepheline syenitic rocks. The nepheline syenites make up the majority of the complex and are divided into a roof series, an intermediate series and a floor series. The floor series consists of cumulates encompassing the kakortokite, the roof series consists of floating cumulates and lujavrite occurs as the middle layer. Several generations of lujavrites were formed from the evolved melts and are now located between the roof series and the kakortokite. The lujavrite is composed of the main minerals microcline, albite, nepheline, sodalite, analcime, naujakasite, aegerine, arfvedsonite, eudialyte, and minor minerals including monazite, britholite, villiaumite, sphalerite, pectolite, steenstrupine, lovozerite, vitusite and usingite. More than 220 minerals occur in the Gardar Provinces, of which nine have not been identified elsewhere.

Steenstrupine is the main radioactive mineral in Kvanefjeld. Steenstrupine is a rare, complex silico-phosphate mineral composed of more than 20 elements and has the chemical formula: $Na_{14}Ce_6Mn_2Fe_2(Zr,Th,U)(Si_6O_{18})_2(PO_4)_73H_2O$. Uranium contents of steenstrupine in Kvanefjeld range from 1000 to 1500 ppm, and thorium from 2000 to 60000 ppm (Wollenberg 1971). In the hyper-agpaitic lujavrites, steenstrupine takes the place of eudialyte, the main rare earth element mineral in the agpaitic part of the complex to the south. Steenstrupine is also common in the hyper-agpaitic pegmatites and hydrothermal mineralisation in the fenitised volcanic roof of the Kvanefjeld plateau. The enrichment of the uranium (and thorium) is thought to have occurred during crystallization and differentiation of the agpaitic rocks (Bohse et al. 1974; Steenfelt & Bohse 1975). The Kvanefjeld uranium deposit was formed where a gas-rich lujavrite magma was trapped in a zone beneath the roof of the magma chamber, and crystallized at high water pressure and temperature (Sørensen 1962).

Table 1. Simple statistics for uranium in the central part of the Kvanefjeld ("Mine area"), based on Clausen 1982.

Rock type	Ns	Mean ppm U	Std. dev. ppm U	Coeff. of var.
Total sample set	3107	287	176	0.61
MC-lujavrite	944	269	156	0.58
Naujakasite lujavrite	340	371	123	0.33
Arfvedsonite lujavrite	644	370	163	0.44

3.1 The potential uranium reserve Kvanefjeld

Mineral resource assessments of the uranium content at Kvanefjeld have been undertaken by both research organisations and private exploration companies since exploration commenced in 1955. Early calculations in 1967 were based on 36 drill-holes located in a relatively

small area of the Kvanefjeld, and mainly concentrated on the most coarse-grained part (MC lujavrite). Subsequent drilling campaigns were executed in 1966, 1977 and since 2002 by private REE exploration companies. To date, more than 11.000 m of drill cores are available as a result of the recent years of REE-exploration. Two arfvedsonite-lujavrite bodies enriched in steenstrupine have been delineated south of the Kvanefjeld deposit e.g. Zone Sørensen and Zone 3. Table 2 shows the historic development of these figures. The aegerine lujavrite is the most uranium enriched of the lujavrites.

Table 2. Historic development in grade.

Area	U_3O_8 – grade	Mt ore	Reference
Kvanefjeld 1958-67	Indicated: 300 ppm	19	Sørensen (1967)
Kvanefjeld 1984	Mineable: 365 ppm	72	Kalvig (1984)
Kvanefjeld 2011	Indicated: 324 ppm	41	GME
Zone Sørensen 2011	Inferred: 375 ppm	148	GME
Zone 3 2011	Inferred: 330 ppm	71	GME

4 Exploration history of the REE-U-Th-Zn-F Kvanefjeld deposit

A large number of exploration programs have investigated the economic potential of the minerals rich in uranium, zirconium, niobium, tantalum, beryllium, and fluorine in the Ilímaussaq Complex, and in particular of the uranium potential of Kvanefjeld in the northern part of the complex.

In 1955, the Danish government on the recommendation of Professor Niels Bohr, the President of the Danish Atomic Energy Commission (AEK), initiated prospecting for uranium deposits in Greenland. The Greenland Geological Survey (GGU) recommended that prospecting for uranium should begin in the Ilímaussaq Complex, the only known occurrence of radioactive minerals in Greenland at that time, apart from allanite in pegmatites. A primitive Geiger counter survey was carried out by military personnel. The southern half of the complex was covered in 1955, the northern half in 1956, in which year the Kvanefjeld deposit was discovered (Nielsen 1981; Sørensen 1981; Bondam 1995). In 1957, detailed studies of the Kvanefjeld deposit were made with chemical assays of the uranium ore and the first attempts were made at developing a method to extract the uranium from the ore. The ore was found to be refractory and impossible to treat with conventional acid or carbonate leaching methods.

The first drilling program was carried out in 1958 resulting in 36 holes and a total core length of 3728 m. In 1962, two of the Kvanefjeld drill holes were deepened
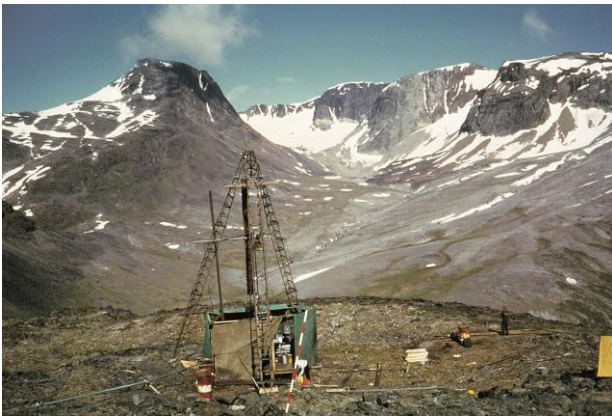
Figure 2. Drill-rig at Kvanefjeld.

with an additional core length of 270 m and another seven holes with a total core length of 1400 m were drilled. In 1977, a drilling program in the northern part of the Kvanefjeld plateau (Fig. 2) and to the east of Kvanefjeld was carried out, comprising 27 holes with a total core length of 5103 m (Nyegaard et al. 1977).

The Kvanefjeld Uranium Project, managed by Risø National Laboratory in the period from 1978 to 1984, was a pre-feasibility study on the Kvanefjeld uranium resource, undertaking mineable ore-reserve estimates and mine planning (Kalvig, 1984), ore beneficiation and processing test-studies on bulk-samples (Sørensen et al. 1983), an assessment of the facilities and energy supply, as well as studies of radiation exposure and the environmental impact of the mining activity (Pilegaard 1990). In about the same period, the Syduran Project carried out a regional prospecting program for uranium in South Greenland by means of airborne radiometric surveying and stream sediment geochemistry programs. This work confirmed the anomalous districts: (i) A 2000 km^2 district surrounding Ilímaussaq complex in which there are small high grade pitchblende occurrences in faults and fractures of the granite; (ii) the eastern area of the Motzfeldt Centre where large parts of the centre is mineralised and may contain large tonnage, low-grade uranium ore with Nb and REE; and (iii) uraniferous-rich districts associated with the migmatitic supracrustal units in the area between Kap Farvel and Lindenow Fjord (Armour-Brown et. al. 1983, 1984).

However, in the early 1980's a resistance against nuclear power rose among the citizens and politicians in both Greenland and Denmark and in 1985, a resolution in the Danish Parliament formally excluded nuclear energy from the national grid and three years later, the Joint Committee on Mining in Greenland made a decision not to issue licenses for exploration or mining for radioactive materials (Vestergard 2013). Thereafter, all exploration or investigation of uranium and thorium occurrences in Greenland was terminated.

References

Armour-Brown, A., Steenfelt, A. & Kunzendorf, H. 1983: Uranium districts defined by reconnaissance geochemistry in South Greenland. Journal of Geochemical Exploration 19, 127-145.

Armour-Brown, A., Tukiainen, T., Nyegaard, P. & Wallin, B. 1984: The South Greenland regional uranium exploration programme. Final report of progress 1980-1983, 110 pp. + appendices. Unpublished report, Geological Survey of Denmark and Greenland.

Bohse, H, Rose-Hansen, J., Sørensen, H.,Steenfelt, A., Løvborg, L. & Kunzendorf, H. 1974: On the behavior of uranium during crystallization of magmas – with special emphasis on alkaline magmas. In: Formation of uranium ore deposits, 49-60. Vienna: International Atomic Energy Agency.

Bondam, J. 1995: The Ilímaussaq nepheline syenite complex in South Greenland. A general overview of exploratory activities and environmental studies. Open File Series Grønlands Geologiske Undersøgelse 95/2, 121 pp.

Clausen, F.L. 1982: A geostatistical study of the uranium deposit at Kvanefjeld, the Ilímaussaq intrusion, South Greenland. Risø-R-468, 289 pp. Risø National Laboratory, Roskilde, Denmark.

Hansen, J.K.G. 1977: Sulphatising roasting of a Greenlandic uranium ore, reactivity of minerals and recovery. Risø Report 355, 125 pp. Roskilde, Denmark: Risø National Laboratory.

Harpøth, O., Pedersen, J.L., Schønwandt, H.K. & Thomassen, B. 1986: Mineral occurrences of central East Greenland. Meddelselser om Grønland, Geoscience 17.

Kalvig, P. 1983: Preliminary mining assessment of the uranium resource at Kvanefjeld, the Ilímaussaq intrusion, South Greenland, 109pp + appendices. Unpublished report, Risø National Laboratory, Roskilde, Denmark

Nielsen, B.L. 1981: Exploration history of the Kvanefjeld uranium deposit, Ilímaussaq intrusion, South Greenland. In: Uranium exploration case histories, 353-388. Vienna: International Atomic Energy Agency.

Nyegaard, P., Nielsen, B.L., Løvborg, L. & Sørensen, P. 1977: Kvanefjeld Uranium Project. Unpublished report, Geological Survey of Greenland, Copenhagen.

Pilegaard, K. 1990: Preliminary environmental impact statement for the Kvanefjeld Uranium Mine. Risø-M-2875, 130 pp. Roskilde, Denmark: Risø National Laboratory.

Steenfelt, A. & Bohse, H. 1975:Mineral efterforskning i en digital verden. Årsberetning 1999, 51-65. København: Danmarks og Grønlands Geologiske Undersøgelse, Miljø- og Energiministeriet.

Sørensen, H. 1962: On the occurrence of steenstrupine in the Ilímaussaq massif, Southwest Greenland. Bulletin Grønland Geologiske Undersøgelse 32, 251 pp.

Sørensen, H. 1967: On the history of exploration of the Ilímaussaq intrusion, South Greenland. Bulletin Grønlands Geologiske Undersøgelse 68, 33 pp.

Sørensen, E., Koefoed, S. & Lundgaard, T. 1983: Uranudvinding ved udludning med natriumkarbonat under højt tryk og høj temperatur. Risø Report. 86pp. Roskilde, Denmark: Risø National Laboratory.

Sørensen, H. 1981: Uraneftersøgning i Grønland indtil 1970. In Uranefterforskning i Grønland, 15-30. Lyngby, Danmark: Akademiet for de Tekniske Videnskaber.

Sørensen, H. & Larsen, L.M. 2001: The hyper-agpaitic stage in the evolution of the Ilímaussaq alkaline complex, South Greenland. In: Sørensen, H. (ed.): The Ilímaussaq alkaline complex, South Greenland: status of mineralogical research with new results. Geology of Greenland: status of mineralogical research with new results. Geology of Greenland Survey Bulletin 190, 83-94.

Vestergaard, C. 2013: The European Union, its overseas territories and non-proliferation: the case of arctic yellowcake. Non-Proliferation papers 25.

Wollenberg, H. 1971: Fission-track radiography of uranium and thorium in radioactive minerals. Risø Report 228, 40 pp. Danish Atomic Energy Commission Research Establishment Risø, Roskilde, Denmark

The atypical Au-(U)-calc-silicate hosted mineralization of Rompas (Northern Finland): fluid-rock interactions and ore genesis

Michel Cathelineau, Jean-Yves Talbot, Marie-Christine Boiron, Nicolas Gaillard, Michel Cuney
CREGU and UMR CNRS-UL Georessources, 54506, Vandoeuvre les Nancy, France

Erkki Vanhanen, Terry Lees, Michael Hudson, Nick Cook
Mawson Resources Ltd, Teknologiantie 1, 90590 Oulu, Finland

Etienne Deloule
CRPG, UMR 7358 CNRS-UL, 15 rue Notre Dame des Pauvres, 54500 Vandoeuvre les Nancy, France

Marc Brouand, Claude Caillat
Areva, Tour AREVA, 1 place Jean Millier, Paris La Défense, France

Abstract. The Rompas prospect located in NW Finland, a few kilometres south of the Arctic Circle, is unique by its specific association of gold with uranium, gold being mostly hosted in uraninite cracks and present at very high concentrations (up to 33 kg/t Au). Both U and Au are hosted by discontinuities in which infillings have undergone a series of mineral changes as a function of physical-chemical conditions during a clock-wise prograde and then retrograde metamorphism. The host rocks are highly metamorphosed basalt units intercalated with micaschists and quartzites interpreted as a former marine platform sedimentary sequence. The present mineral assemblages are therefore the result of a complex succession of fluid-rock reactions up to amphibolite metamorphic grade: an earlier diopside-biotite assemblage was followed by a tremolite-calcite-quartz-(gold) assemblage, particularly in mafic rocks, which acted as chemical traps. This integrated study of the textural and geochemical features of the high grade Au and its relationship with earlier U veins has been undertaken by systematic study of U-Au associations and their relative chronologies, as well as the geochemical characterization of the host rocks and ore fluids.

Keywords : gold, uranium, Svecofennian orogeny, metabasalts

1 Geological context and scientific objectives

The Rompas prospect is located in NW Finland, a few kilometres south of the Arctic Circle and 50 kilometres from Ylitornio to the west and Rovaniemi to the east (Fig. 1). This prospect was discovered by AREVA in 2008 and is now the property of Mawson Resources. More than 150 separate occurrences of high uranium concentrations (up to 43.6%) and extremely high Bonanza-type gold contents (maximum at 33 kg per tonne) were located in the bedrock over an area 6 kilometres long and 200 metres wide (Mawson Resources,
(http://www.mawsonresources.com/s/Rompas.asp)).
Rompas is situated in the Lapland domain, in the northern part of the Paleoproterozoic Peräpohja schist

Figure 1. Location of the Rompas prospect

This area of Finland is a part of the Fennoscandian shield which contains many ore deposits due to a distinctive geological setting during Archean and Paleoproterozoic times (Weihed et al. 2005). Beginning at 2.5 Ga, the Archean Karelian continent was subject to episodic extension, with the development of several intracratonic rift basins. Sedimentation mainly occurred in lacustrine basins until the opening of the Svecofennian Sea and the Kola Ocean at roughly 2.1 Ga (Lahtinen et al. 2008). The development of a passive margin is associated with tholeitic magmatism and led to the formation of oceanic crust (Outokumpu, Jormua and Nuttio 'ophiolites' at 1.97-1.95 Ga, Nironen 1997; Lahtinen 1994). After this phase of spreading, convergence initiated at 1.96 Ga followed by the first collision at 1.92 Ga (Lahtinen et al. 2008), and by continent-continent collisions between 1.87 and 1.79 Ga (Korja et al. 2006). Between 1.89 and 1.84 Ga, progressive oblique accretion of the Svecofennian island arc complex formed regional scale refolding, thrusting and shear zones (Kärki and Laajoki 1995; Sorjonen-Ward 1997).

At Rompas, the very high Au grade and its specific relationship with earlier U veins led to a detailed and integrated study of the textural and geochemical features of these exceptional ores. The aim of this study was to investigate the mineralization of the Rompas Au-U

prospect through a multidisciplinary approach:

- petrography and mineral chemistry of the host rocks and of the mineralization to characterize the U-Au associations, their relative chronologies and textural relationships,

- major and trace element geochemistry of host rocks,

- crystal chemistry of uraninites and U-Pb dating,

- characterization of the mineralizing fluids and reconstruction of their pressure-temperature evolution from fluid inclusion study in quartz (microthermometry, Raman micro-spectroscopy).

Three zones were studied: the so-called North and South Rompas, as well as the Rumavuoma area to the south of the Rompas area.

2 Mineralogy and geochemistry of the host rocks

The Rompas area is dominated by metasedimentary rocks (micaschists, black shales, quartzite) with metavolcanic and metasubvolcanic rock intercalations (metabasalts and metadolerites). Quartzites, dolomites and mafic effusive rocks belong to the Kivalo group whereas micaschists are part of the Paakkola group. Black shales are mainly encountered between these two groups. A regional albitisation event could be related to fluids derived from evaporites to the south of the prospect.

The mineralogical assemblages in the main host rock of the ore bodies consist mainly of amphiboles ± biotite ± plagioclases (An0 to An40) ± quartz (± calcite). Amphiboles are calcic (green hornblendes ranging from hastingsitic to pargasitic compositions) and ferro-magnesian (gedrite to anthophyllite). Twenty samples of the host rock coming from different trenches from North Rompas and South Rompas areas were analysed for major (ICP-AES) and trace (ACP-MS) elements. The results are quite similar in both areas. SiO_2 ranges from 44 to 59 wt.%, with a majority of samples between 47 and 53 wt.%. Al_2O_3 contents vary from 11 to 17.1% whereas MgO ranges from 4 to 8.2 wt.%. TiO_2 and P_2O_5 display similar values for all samples between 1.3 to 2.3 wt% and 0.16 to 0.29 wt.%, respectively. Conversely, CaO contents are variable, from 0.6 to 11.4 wt.%, probably resulting from its strong mobility during fluid-rock interactions, whilst Na_2O and K_2O are nearly constant. Almost all samples have low U (<6 ppm) and Pb (<8 ppm) contents whereas Th values are similar between 3 and 6 ppm.

In an R1-R2 La Roche diagram (Fig. 2), samples of Rompas host rocks mostly fall into fields of basic to intermediate magmatic rocks (basalt to andesibasalt and latiandesite), features similar to those for amphibolite resulting from the metamorphism of basaltic lava flows. The samples outside these domains correspond to those characterized by low Ca content, due to alteration.
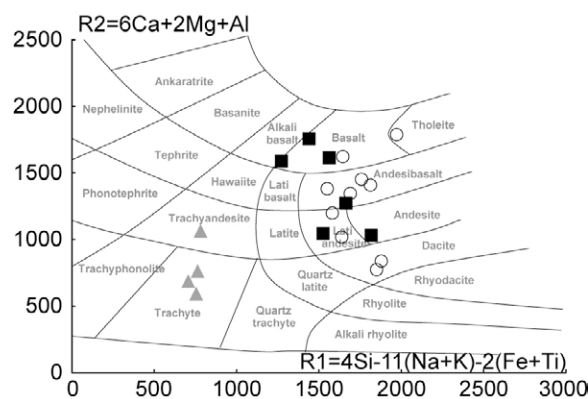
Figure 2. Geochemical features of the host rocks in a R1-R2 diagram from De La Roche (1980). Black squares: North Rompas, open circles: South Rompas, triangles: altered samples

REE spectra normalized to chondrite (Sun and McDonough 1989) are very similar for all samples and show a weak negative slope for LREE, no or weak Eu anomalies, almost flat spectra from Gd to Er and often a very weak positive slope for the heaviest REE. These data confirm that basic rocks correspond to a predominant rock type close to basalts or andesites.

3 U-Ore stage

Rompas is characterized by the spatial association of gold and copper with uranium. Uraninite occurs together with gold in pods of rather limited size (a few cm to dm) within veins of carbonate and diopside, largely replaced by tremolite. Veins crosscut the bedding of the host rock. On the borders of veins, an alteration zone comprised of biotite and amphiboles may be observed. The mineralogical assemblage is quite similar between the three studied zones (North and South Rompas as well as the Rumavuoma area).
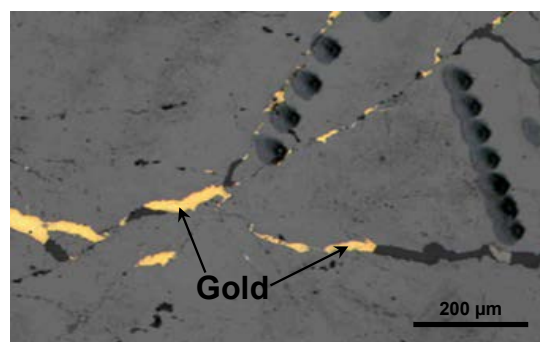
Figure 3. Gold in fractures within the uraninite

Veins contain uranium as centimetre-sized cubes of uraninite. Uraninite is characterized by nearly constant and high Pb contents, but contains only traces of Ca (CaO around 0.25 wt.%). Gold occurs as microfracture infillings mostly within the uraninite (Fig. 3), associated with quartz (Fig. 4), and sometimes as large grains associated with tremolite veinlets.
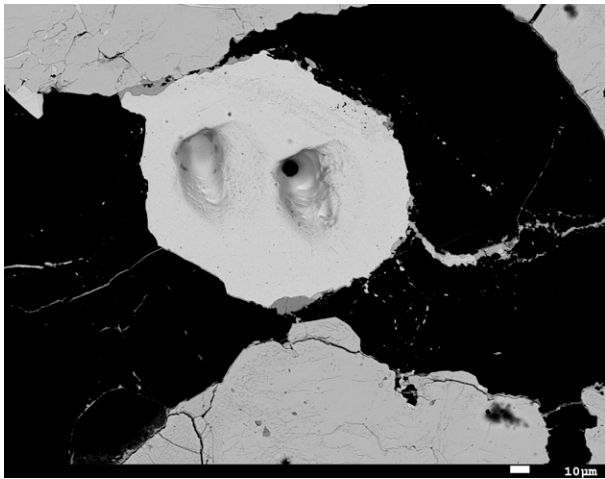
Figure 4. Gold grain in quartz, filling a cavity with euhedral uraninite.

4 Gold stage

Gold is a late phase in the paragenesis and results from a different mineralizing event than the main uranium stage. At Rompas, gold occurs mostly in microfissures within the uraninite and is commonly associated with quartz and tremolite within these microfractures
, but is very rare outside the uraninite. Relationships between gold and uraninite are ambiguous, as uraninite exhibits, in some instances, euhedral shapes along microfractures filled by gold.
Gold is also quite pure with a maximum of 2.5 wt.% of Ag and sometimes 3.5 wt.% of Cu. In the surrounding host rocks, the presence of Ni-Co-As-S assemblages is typical of redistribution of trace elements from the basalts. The rare occurrence of the association Cu-Bi-Te (Fig. 5) is however indicative of gold assemblages found in most late orogenic vein type deposits (Boiron et al. 1996; 2003).
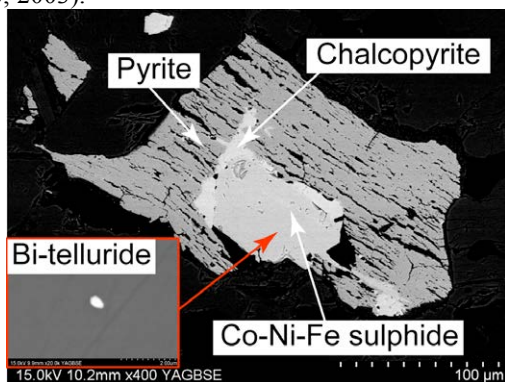
Figure 5. Association of pyrite and chalcopyrite, and Co-Ni sulphide and bismuth telluride

5 Ore fluids

Most inclusions amenable to study were found in undeformed clear quartz which is thought to be related to the gold stage. A few brine inclusions may be possibly related to earlier stage in host rocks, but it is difficult, on the available material, to identify the fluids related to the U-stage, due to the intensity of deformation. In the clear quartz, predominant CO_2-rich fluids are found as carbonic and aqueous-carbonic inclusions in quartz (Fig. 6). The predominant carbonic inclusions show Tm CO_2 (melting temperature of CO_2) ranging from -56.6 to -64.1°C. Tm CO_2 are therefore slightly lower than Tm of pure CO_2 (-56.6°C) indicating the presence of other volatile compounds in addition to CO_2, e.g. N_2 and CH_4, as confirmed by Raman microspectrometry, and in accordance with the occurrence of metamorphosed black shales in the host rocks. Homogenization temperatures of CO_2 are quite widespread from -6.6 to 33.3°C, mostly in the liquid phase.
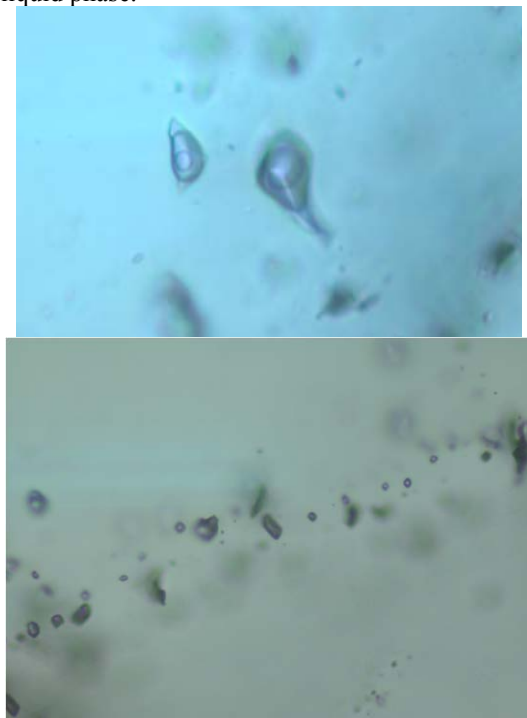
Figure 6. CO_2-H_2O fluid inclusions as isolated inclusions in clear quartz (top), and monophase CO_2-rich inclusions in fluid inclusion plane crosscutting the clear quartz (bottom)

The presence of CO_2-rich fluids may explain the gold–tremolite association, which could result from the interaction between CO_2-rich fluids and diopside following the reaction:
$$5\ CaMgSi_2O_6 + 3\ CO_2 + 1\ H_2O$$
  diopside
$$\Rightarrow 1\ Ca_2Mg_5(Si_8O_{22})(OH)_2 + 3\ CaCO_3 + 2\ SiO_2$$
        tremolite   calcite   quartz
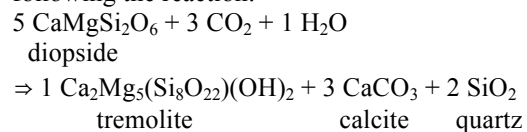
Two main fluid density ranges may correspond to distinct pressure conditions, tentatively attributed to lithostatic to infra-lithostatic pressures, indicating a potential link between gold mineralization and pressure changes, as well as temperature decrease during the retrograde path.

6 Discussion and conclusion

The carbonate-uraninite veins are interpreted as old fracture infillings related to a group of brittle faults cross-cutting the stratigraphy (D1 event). A later tectonic event results in the formation of a high strain zone (D2

event) followed by a D3 deformation (folding) related to a migmatisation episode to the north (Eilu et al. 2003). The carbonate-uraninite veins have been deformed and metamorphosed in the amphibolite facies (diopside crystallization). The veins were then affected by retrograde metamorphic processes with fluid ingress under brittle conditions. This resulted in the quartz-tremolite-gold veinlet association. The formation of the gold mineralization seems thus related to a rather late event in the P-T path.

From the point of view of the localization of the ores and guides to exploration, the boundaries between the amphibolites and their host metasediments are certainly the key factor for the U-Au association. The basic series could have acted as a redox and chemical trap, first for the uranium mineralization event and then for the gold mineralization event, as already observed in Archean gold deposits when shear zones crosscut basic intrusives. The occurrence of black shales could have also favoured local reducing conditions. The U-carbonate veins display many similarities with other occurrences such as the veins from Otish and Mistamisk (Canada, Kish and Cuney 1981). If all gold is introduced at a rather late stage, it will be necessary to better determine the tectonic regime that favoured the reopening of the early fracture systems. This stage seems to be characterized by a seismic fault-valve system since fluid densities have fluctuated from those characteristic of both lithostatic and near-hydrostatic regimes. Such a dynamic system needs to be related to a major stage of (ductile (?))-brittle deformation during the exhumation and the retrograde P-T path.

Acknowledgements

References

Boiron MC, Cathelineau M, Banks DA, Fourcade S, Vallance J, (2003) Mixing of metamorphic and surficial fluids during the uplift of the Hercynian upper crust: consequences for gold deposition. Chem Geol 194:119-141

Boiron MC, Cathelineau M, Banks D, Yardley B, Noronha F, Miller M (1996) P-T-X conditions of late Hercynian fluid penetration at the origin of granite-hosted Au-quartz veins in northwestern Iberia: A multidisciplinary study of fluid inclusion and their chemistry. Geochim. Cosmochim. Acta 60:43-57

De la Roche H, Leterrier J, Grandclaude P, Marchal M (1980) A classification of volcanic and plutonic rocks using R1, R2 diagrams and major element analysis - its relationships with current nomenclature. Chem Geol 29:183-210

Eilu P, Sorjonen-Ward P, Nurmi P, Niiranen T (2003) A Review of Gold Mineralization Styles in Finland. Econ Geol 98:1329-1353

Kärki A, Laajoki K (1995) An interlinked system of folds and ductile shear zones-late stage Svecokarelian deformation in the central Fennoscandian Shield, Finland. J Struct Geol 17:1233-1247

Kish L, Cuney M (1981) Uraninite-albite veins from the Mistamisk Valley of the Labrador Through, Quebec. Mineralogical Magazine 44:471-83

Korja A, Lahtinen R, Nironen M (2006) The Svecofennian orogen: a collage of microcontinents and island arcs. Geol Soc London, Memoirs 32:561-578

Lahtinen R (1994) Crustal evolution of the Svecofennian and Karelian domains during 2.1-1.79 Ga, with special emphasis on the geochemistry and origin of 1.93-1.91 Ga gneissic tonalites and associated supractustal rocks in the Rautalampi area, central Finland. Geol Surv Finl Bull 378

Lahtinen R, Garde AA, Melezhik VA (2008) Paleoproterozoic evolution of Fennoscandia and Greenland. Episodes 31:20-28

Nironen M (1997) The Svecofennian Orogen: a tectonic model. Precambrian Res 86:21-44

Sorjonen-Ward P (1997) An overview of the geological and tectonic evolution of eastern Finland. In: Ruskeeniemi K, Sorjonen-Ward P (eds) Ore deposits in eastern Finland (4th biennial SGA Meeting, August 11–13, 1997, Turku, Finland, Excursion Guidebook A4). Geol Surv Finl, Guide 42

Sun SS, McDonough WF (1989) Chemical and isotopic systematics of oceanic basalts: implications for mantle composition and processes. In: Saunders AD, Norry MJ (eds) Magmatism in Ocean Basins, Geol Soc London, Spec Publ, pp 313-345

Weihed P, Arndt N, Billström K, Duchesne JC, Eilu P, Martinsson O, Papunen H, Lahtinen R (2005) Precambrian geodynamics and ore formation: the Fennoscandian Shield. Ore Geol Rev 27:273-322

S 4:
Metallogeny of Fennoscandia

Convenors:
Raimo Lahtinen & Krister Sundblad

Fennoscandian metallogeny and supercontinent cycles

Pasi Eilu & Raimo Lahtinen
Geological Survey of Finland, PO Box 96, 02151 Espoo, Finland

Abstract. The majority of the dated metallogenic stages and events in Fennoscandia (Norway, Sweden, Finland, Karelia and Kola) show a distinct correlation with the main stages of global supercontinent evolution. VMS, porphyry, epithermal, most of the skarn deposits and, possibly, vein Mo are essentially related to active subduction and arc accretion stages predating the main continent-continent collision stages. Some of the polymetallic vein, orogenic Ni-Cu, iron-apatite, and even IOCG may also relate to arc accretion. Deposits characterising the supercontinent amalgamation (continent collision) include: IOCG, orogenic Ni-Cu, orogenic Au, polymetallic vein, rare metal pegmatite, and eclogitic rutile. Mineralisation styles possibly only occurring in continent break up settings are: rifting-related mafic-ultramafic intrusion-hosted Ni-Cu-PGE and Cr, red bed Cu, clastic-hosted U-V, black shale Ni-Zn-Cu-Co, MVT Pb-Zn and, perhaps, komatiitic Ni. Deposit types detected in several settings are: BIF, skarn Fe, mafic intrusion-hosted V-Ti-Fe, clastic-hosted Zn-Pb and Cu±Co±Au, SEDEX, and carbonatite to peralkaline intrusion-hosted apatite-rare metal. Age determination of certain deposits within Fennoscandia, such as epigenetic Co±Au±Cu±U, and vein and unconformity U, is not precise enough to relate them to the supercontinent evolution stages.

Keywords. Metallogeny, Supercontinents, Fennoscandia

1 Supercontinents and metallogeny

Global supercontinent evolution stages can be seen as the first-order control for the metallogenic evolution of a region (e.g. Groves and Bierlein 2007). Certain deposit types only form during arc formation, accretion and crustal growth, others during continent collision and supercontinent amalgamation, and some during the break up, whereas others are not confined to one stage. This relationship suggests diagnostic mineralisation systems for specific plate-tectonic settings. Hence, a known tectonic setting can be used in defining whether a region is potential for a certain deposit type and, conversely, the known deposit types can be used in broadly defining the tectonic setting of a large area. We give an overview of the possible relationship between supercontinent evolution and metallogeny of the Fennoscandian crust (Norway, Sweden, Finland, Karelia and Kola). The ages given for supercontinent stages are adjusted with plate-tectonic events detected in Northern Europe (Table 1). Hence, not all the ages shown are exactly the same as those published previously for global supercontinent assembly and break up stages.

2 Kenorland

The core of the Fennoscandia comprises the Meso to Neoarchaean TTG–greenstone provinces of Karelia, Belomorides, Kola, Murmansk and Norrbotten (Hölttä et al. 2008) all showing pre-Kenorland evolution with earliest rock ages at 3.6 Ga. No conclusive palaeomagnetic information indicates if any cratons or supercratons were close to the pre-2.75 Ga provinces of Fennoscandia. The 3.2–2.75 Ga greenstones contain extensive BIFs but only minor komatiitic Ni(±Cu,PGE), VMS, and epithermal Ag-Zn deposits. A few Mo deposits of assumed porphyry type have been detected within the 2.9–2.8 Ga granitoids. Especially, the komatiitic Ni and BIF deposits reflect the differences between the early-earth plume-derived and modern subduction-derived plate tectonics (Condie 2000; Groves et al. 2005).

The Neoarchaean supercontinent *Kenorland* was assembled during 2.75–2.60 Ga (Mertanen and Pesonen 2012). That is, it was formed during one of the major continental growth episodes of the Earth's history (Condie 2000). The major metallogenic trends of the time in Fennoscandia are similar to greenstone terrains elsewhere: orogenic gold deposits are abundant, and there are a few other deposit types characteristic for accretionary orogens and supercontinent assembly, such as porphyry Mo and rare metal granitic pegmatites (Eilu et al. 2013). However, the large orogenic gold and VMS deposits detected in many other cratons are missing (cf. Huston et al. 2012). For the Russian part of the region (Korsakova et al. 2012), not much exploration has taken place and most of the deposit age data is inconclusive. This means that we do not know how much there actually are mineral deposits of Kenorland and Columbia ages in the eastern part of the Fennoscandia.

Compared to its assembly in the Neoarchaean, the episodic disintegration of the Kenorland, with main intrusive peaks at 2.45, 2.1, 2.06 and 1.98 Ga, delivered major mineral deposits across the Fennoscandia. The 2.50–2.44 Ga rifting event, possibly related to a major mantle plume, produced reef-type PGE and Cr, contact-type PGE-Ni-Cu, and massive Cr and V-Ti-Fe deposits in layered intrusions. A shallow intracontinental basin stage followed at 2.44–2.1 Ga with, possibly, development towards clastic sediment-hosted Cu and U occurrences. However, it probably was during ca. 2.10–1.95 Ga when most of the sediment-hosted deposits were formed, including the unique Ni-Zn-Cu-Co deposits of Talvivaara type, SEDEX(?) Cu, red bed Cu, and clastic sediment-hosted Cu and U-V. At ca. 2.06 Ga, alkaline intrusion V-Ti-Fe deposits at Otanmäki and the Kevitsa ultramafic intrusion-hosted Ni-Cu-PGE deposit were formed, and the unusual mafic intrusion-hosted Ni-Cu±PGE at Pechenga were deposited at 1.98 Ga. The Outokumpu Cu-Co-Zn proto-ores were produced during the latest stages of Kenorland rifting, probably at 1.95 Ga. (Lahtinen et al. 2008; Peltonen et al. 2008; Hallberg et al. 2012; Kontinen 2012; Korsakova et al. 2012)

Table 1. Supercontinent stages and main mineral deposit types in Fennoscandia.

Age (Ga)	Supercontinent stage	Mineralisation style
3.6–2.75	**Pre-Kenorland**	Komatiitic Ni; Mafic-ultramafic intrusion Cr; BIF; Porphyry Mo
2.7–2.6	**Kenorland** assembly	Orogenic gold; Mafic intrusion Ti-Fe-V; Peralkaline intrusion Nb-REE-Zr; Rare metal pegmatite
2.50–2.44	Kenorland initial break up	Layered-intrusion Cr, V-Ti-Fe, PGE±Ni-Cu
2.1–1.95	Kenorland main break up	BIF; Ultramafic-mafic intrusion Ni-Cu±PGE; Alkaline intrusion V-Ti-Fe; Black shale Ni-Zn-Cu-Co; SEDEX Cu; Red-bed Cu; Clastic sediment Cu, U-V; Outokumpu Cu-Co-Zn
1.93–1.86	**Columbia** first stage assembly (arc magmatism and accretion)	BIF; VMS; Porphyry Cu±Au, Mo; Epithermal gold; Kiruna Fe-apatite; IOCG; Orogenic Ni-Cu; Mafic intrusion Ti-V-Fe; Orogenic gold?; Skarn Fe±REE, W±Mo; Epigenetic Mo?
1.84–1.77	Columbia second stage assembly	Orogenic gold; IOCG; Rare metal pegmatite; Mafic intrusion Ti-V-Fe; Carbonatite REE-Pb; Epigenetic Mo?; Skarn Fe-Mn, W?
1.68–1.48	Columbia final assembly	VMS; Orogenic Ni-Cu; Mafic intrusion Ti-V-Fe; Skarn Zn-Fe, Fe-W, Orogenic gold
1.25–1.18	Columbia break up	Mafic intrusion Ni-Cu, Ti-V-Fe; Rare metal pegmatite
1.10–0.92	**Rodinia** assembly	Stratabound clastic Cu; Carbonatite Nb-Fe-P-REE; Orogenic gold; Epigenetic Mo; Skarn Fe; Anorthositic intrusion Ti-V-Fe; Orogenic Ni-Cu; Epigenetic Mo; Rare-metal pegmatite
0.82–0.60	Rodinia break up	SEDEX Zn-Pb±Cu; VMS; Mafic intrusion Ni-Cu
0.60–0.43	Passive margins + Caledonian rifting → **Laurasia** accretion	Stratiform Fe; Stratabound clastic Cu, Pb±Zn; VMS; MVT Zn-Pb; Black shale–Alum shale U-Mo-V-Ni; Phosphorite U → Orogenic Ni-Cu Skarn Mo, W, Pb-Zn; Orogenic gold?
0.43–0.39	Caledonian collision	SEDEX Zn-Pb?; Orogenic gold; Base-metal vein; Eclogitic rutile; Sandstone Pb-Zn
0.38–0.36	Intracontinental rifting (Kola)	Peralkaline and carbonatite intrusion Apatite±REE±Nb-Ta±Fe±Ti±Zr
0.30–0.24	Intracontinental rifting (Oslo)	Ag-Co-As veins; Porphyry Mo

3 Columbia

Breakup of the Kenorland was followed by extensive arc magmatism (2.0–1.9 Ga) and arc accretion at 1.93–1.86 Ga (Table 1). This stage can also be regarded, in a wide sense, as the first or preliminary stage for the assembly of *Columbia* ('Early Columbia' stage of Pesonen et al. 2003). This magmatic arc and microcontinent accretion-related subduction stage produced numerous VMS, BIF, skarn Fe±Mn±REE, skarn W±Mo deposits, and a few major porphyry Cu-Au, and the Kiruna-type Fe-P deposits (e.g. Hallberg et al. 2012). Arc and microcontinent collision, and incipient amalgamation of Fennoscandia and Laurentia, are regarded the reasons for orogenic gold, orogenic mafic-ultramafic intrusion-hosted Ni-Cu (1.88 Ga), and mafic intrusion-hosted Ti-V-Fe±P (1.88–1.87 Ga) deposits. A major continent-continent collision stage followed, at 1.84–1.77 Ga, when perhaps most of the orogenic gold, rare metal pegmatite, and IOCG deposits of Fennoscandia were formed.

The Gothian (1.68–1.52 Ga) and Telemarkian (1.52–1.48 Ga) stages apparently included magmatic arc accretion plus, possibly, another stage of Fennoscandia–Amazonia collision in the SW of Fennoscandia (Mertanen and Pesonen 2012). This was the final amalgamation of Columbia, and brought numerous small Ni-Cu and Ti-V-Fe deposits and a few orogenic Au, VMS, skarn Fe±W and skarn Zn-Sn occurrences. Columbia broke up at 1.25–1.18 Ga (Mertanen and Pesonen 2012). Within Fennoscandia, there appears to only be mafic intrusion-hosted Ni-Cu and Ti-V-Fe occurrences of that age, in the SW part of the shield (Sandstad et al. 2012).

4 Rodinia

The break up of Columbia was quickly followed by the formation of the *Rodinia* by assembly of nearly all of the then present continents (Huston et al. 2012; Mertanen and Pesonen 2012). Besides the large anorthositic ilmenite deposits in SW Norway, other mineral deposits related to the 1.10–0.92 Ga Grenvillian–Sveconorwegian orogeny (Table 1) are small and have only been detected in the SW part of Fennoscandia. Many deposit types, such as VMS, characterising back-arc and arc magmatism and accretion predating the amalgamation of other supercontinents, were not formed. This is also the case elsewhere within the Rodinia (Huston et al. 2012).

The break up of Rodinia took place at 820–500 Ma. At 820–600 Ma, major SEDEX Zn-Pb±Cu, VMS, and numerous but small mafic intrusion-hosted Ni-Cu deposits were formed in dominantly intracratonic to passive margin settings. The stage from 600 to 500 Ma caused the final break up of Rodinia and the opening of the Iapetus Ocean. This can also be seen as the first stage of the Caledonian evolution described below. (Pesonen et al. 2003; Bingen et al. 2008; Sandstad et al. 2012)

5 Caledonian evolution

Stratiform Fe, stratabound clastic-hosted Cu and Pb±Zn, MVT, polymetallic alum shale–black shale and phosphorite U mineralisation took place at the passive margins of the Iapetus Ocean from 600 to perhaps 500 Ma. Within back-arc settings(?), VMS deposits were formed in ophiolitic environments. SEDEX Cu-Zn deposits were formed either at this stage or slightly earlier, during the Rodinia break up (Grenne et al. 1999; Pesonen et al. 2003; Sandstad et al. 2012).

Between Laurentia and Fennoscandia, the extension changed towards collision at about 500 Ma. With subduction and arc accretion, VMS Cu-Zn, orogenic Ni-Cu, and polymetallic skarn deposits were formed by ca. 430 Ma. Laurentia–Baltica full collision, the Scandian orogeny, took place at 430–390 Ma producing the *Laurasia*. In this stage, orogenic gold and polymetallic vein, metamorphic rutile deposits in eclogites, SEDEX Zn-Pb and, importantly, sandstone-hosted Pb±Zn mineralisation took place (Grenne et al. 1999; Sandstad et al. 2012).

The latest significant stages of metallic mineralisation in Fennoscandia took place in intracontinental rift environments in the Kola Peninsula and in the Oslo graben (Table 1). Very large carbonatite and peralkaline intrusion-hosted rare metal-apatite deposits were formed in the former and porphyry Mo and Ag vein deposits in the latter area (Korsakova et al. 2012; Sandstad et al. 2012).

6 Conclusions

In detail and in terrain scale, the Fennoscandian mineral deposit types and metallogenic events can be directly related to plate-tectonic settings and events. In a wider scale, nearly all events from Neoproterozoic to Permian, from the formation of an individual deposit to an orogenic stage, may be connected to three settings: 1) arc magmatism and accretion, 2) supercontinent assembly, and 3) supercontinent break up. The most productive stages for metallic mineral deposits were the Kenorland break up (2.45–1.98 Ga; Ni, PGE, Cr) and the arc magmatism (2.0–1.9 Ga) and accretion at 1.93–1.86 Ga (Cu, Zn). Final stages of supercontinent assembly have been the least productive. These metallogenic events and their relationship to arc accretion and supercontinent cycles are similar to those recorded elsewhere, in other Precambrian and Palaeozoic terrains (e.g., Groves et al. 2005, Groves & Bierlein 2007; Huston et al. 2012). The setting between continents or supercontinents before ca. 2.70 Ga remains unclear.

References

Bingen B, Andersson J, Söderlund U, Möller, C (2012) The Mesoproterozoic in the Nordic countries. Episodes 31:29–34

Condie, KC (2000) Episodic continental growth models: afterthoughts and extensions. Tectonophysics 322:153–162

Eilu P, Hallberg A, Bergman T, Bjerkgård T, Feoktistov V, Korsakova M, Krasotkin S, Lampio E, Litvinenko V, Philippov N, Sandstad JS, Stromov V (2013) Fennoscandian Ore Deposit Database. Annual update. Geological Survey of Finland, Geological Survey of Norway, Geological Survey of Sweden, The Federal Agency of Use of Mineral Resources of the Ministry of Natural Resources and Ecology of the Russian Federation. Online at http://en.gtk.fi/informationservices/databases/fodd/index.html

Grenne T, Ihlen PM, Vokes FM (1999) Scandinavian Caledonide Metallogeny in a plate tectonic perspective. Miner Dep 34:422–471

Hallberg A, Bergman T, Gonzalez J, Larsson D, Morris G, Perdahl JA, Ripa M, Niiranen T, Eilu P (2012) Metallogenic areas in Sweden. Geol Surv Finland, Spec Paper 53:140–205

Hölttä P, Balagansky V, Gaarde AA, Mertanen S, Peltonen P, Slabunov A, Sorjonen-Ward P, Whitehouse M (2008) Archean of Greenland and Fennoscandia. Episodes 31:13–19

Groves DI, Bierlein FP (2007) Geodynamic settings of mineral deposits. J Geol Soc London 164:19–30

Groves DI, Condie KC, Goldfarb RJ, Hronsky JMA, Vielreicher RM (2005) Secular changes in global tectonic processes and their influence on the temporal distribution of gold-bearing mineral deposits. Econ Geol 100:203–224

Huston D, Blewett RS, Champion DC (2012) Australia through time: a summary of its tectonic and metallogenic evolution. Episodes 35:23–43

Kontinen A (2012) F029 Talvivaara Ni-Zn-Cu. Geol Surv Finland, Spec Paper 53:276–280

Korsakova M, Krasotkin S, Stromov V, Iljina M, Lauri L, Nilsson LP (2012) Metallogenic areas in Russian part of the Fennoscandian shield. Geol Surv Finland, Spec Paper 53:343–395

Lahtinen R, Garde AA, Melezhik VA (2008) Palaeoproterozoic evolution of Fennoscandia and Greenland. Episodes, 31:20–28

Mertanen S, Pesonen LJ (2012) Paleo-Mesoproterozoic assemblages of continents: paleomagnetic evidence for near Equatorial supercontinents. Lecture notes in Earth system sciences 137. Springer, Berlin, pp 11–35

Peltonen P, Kontinen A, Huhma H, Kuronen U (2008) Outokumpu revisited: New mineral deposit model for the mantle peridotite-associated Cu–Co–Zn–Ni–Ag–Au sulphide deposits. Ore Geol Rev 33:559–617

Pesonen LJ, Elming SÅ, Mertanen S, Pisarevsky S, D'Arella-Filho MS, Meert JG, Schmidt PW, Abrahamsen N, Bylund G (2003) Paleomagnetic configuration of continent during the Proterozoic. Tectonophysics 375:289–324

Sandstad JS, Bjerkgård T, Boyd R, Ihlen P, Korneliussen A, Nilsson LP, Often M, Eilu P, Hallberg A (2012) Metallogenic areas in Norway. Geol Surv Finland, Spec Paper 53:35–138

Coeval iron oxide and silicate magmas; structural evidence for immiscibility and mingling at Kiirunavaara and Luossavaara, Sweden

Ulf B. Andersson

LKAB, Research & Development, TFG, FK9, SE-981 86 Kiruna, Sweden

Abstract. The apatite-iron oxide ores at Kiruna formed by liquid immiscibility in Fe-rich syenitic magmas in a subvolcanic-volcanic system. Penecontemporaneous felsic magmas penetrated the package, picked up pieces of yet unsolidified ore and footwall magmas and flowed on top of the footwall-ore sequence.

Keywords. Luossavaara-Kiirunavaara apatite-iron oxide ores, liquid immiscibility, magma-mingling, emplacement.

1 Background

The Kiirunavaara and Luossavaara apatite-iron oxide (AIO) ores are emplaced within a sequence of porphyritic silicate rocks, referred to as the Kiruna porphyries (e.g. Bergman et 2001). The massive AIO bodies are elongated along the border zone of the lower trachytes-trachyandesites (traditionally referred to as syenite porphyries), and the upper dacites-rhyodacites (quartz-bearing porphyries). The emplacement mechanism and origin of Kiruna-type ores have been the focus of a long-standing and still unresolved debate. A deposition from fluid-rich iron oxide magmas, differentiated from precursor iron-rich silicate magmas was proposed early (Geijer 1910). In contrast, Parák (1975) suggested a marine volcanic-exhalative sedimentary deposition of the AIO ores. A deposition entirely from hydrothermal fluids was proposed early (Bäckström 1904), but has gained in popularity recently (e.g. Hitzman et al. 1992, Smith et al. 2009). However, an emplacement as P-rich iron oxide magma continues to find proponents (e.g. Frietsch 1978, Nyström 1985; Nyström et al. 2008; Nordstrand & Andersson 2013).

The present contribution aims at highlighting structural features between the ore and the country rocks to argue for coeval magmatism and emplacement.

2 Ore-country rock relations

2.1 Footwall

The footwall rocks to the ore bodies consist of a c. 700 meters thick succession of intermediate, alkaline igneous rocks (Geijer 1960). There is a transition from lower, medium-grained syenites to upper fine-grained syenite porphyries (Geijer 1910). The latter are subvolcanic to volcanic equivalents of the syenites and are in general lightly feldspar-phyric. The syenite porphyries are irregularly rich in fine-grained magnetite (Fig. 1; e.g. Geijer 1910; Parák 1975; Ekström and Ekström 1997). Locally, they are strongly enriched in FeO and have been termed magnetite syenite porphyry (Geijer 1910). Among the textural varieties the 'nodular syenite porphyry' (Geijer 1910) is the most conspicuous, and

will be in focus here (Figs. 2-5). This rock, which typically occurs close to ore, contains a multitude of rounded nodules consisting mainly of amphibole, titanite, magnetite, apatite, and mica.
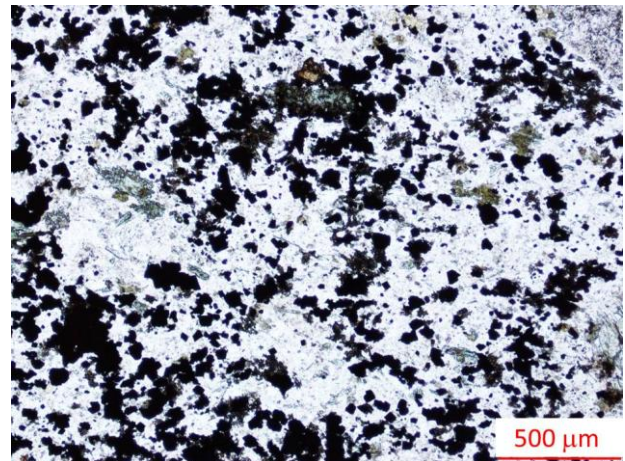
Figure 1. Magnetite-sprinkled matrix of syenite porphyry. Additional minerals in view: feldspar, amphibole, biotite and titanite. Kiirunavaara footwall.

Figure 2. Magnetite-dominated nodules in Kiirunavaara footwall porphyry. The nodules are always rounded, but show variable forms, sizes and length-breadth ratios. Core diameter in all figures = 28 mm.

Figure 3. Commonly, the nodules are oriented in a flow-like or compaction pattern, and associated with a vein network. Kiirunavaara footwall.

The nodule minerals typically have a larger grain size than that of the surrounding matrix. In many areas the nodules are dominated by amphibole and titanite, but magnetite-rich nodules are also common and their importance is highlighted here.

Figure 4. The nodules assemble into larger blobs of magnetite joining up into a network of ore veins. Kiirunavaara footwall.

Figure 5. In places, the nodules are more or less completely engulfed in a chaotic mix of ore veins and remaining pieces of the nodular porphyry. Kiirunavaara footwall.

The small magnetite veins can be seen to assemble into coarser veins and larger network of ore veins. This is particularly well illustrated at Luossavaara.

Figure 6. Magnetite-rich veins assembled in the nodule-rich footwall at Luossavaara. Diameter of coin = 25 mm.

Figure 7. The ore veins grew in size and penetrated the porphyry. Luossavaara. Diameter of pen = 15 mm.

Figure 8. Small veins collected into large magnetite dikes. Luossavaara.

Figure 9. A large number of magnetite dykes joins the lower part of the Luossavaara ore body. Northern part of open pit.

2.2 Hanging wall

The successions in the hanging wall to the ores consist of quartz-bearing porphyries of rhyodacitic-rhyolitic composition up to >1200 m in thickness (Geijer 1960). These are in general relatively densely porphyritic, with <1 cm microperthitic feldspars, while quartz only occurs in the groundmass.

Within this unit a large number of foreign rock enclaves are present (e.g. Geijer 1968). These comprise pieces of variable footwall and hanging wall porphyries, and ore. Close to the ore contacts, irregular sets of magnetite dykes are common. Ore-hanging wall rock relations are often structurally very variable and complex. The small magnetite dykes typically show irregular bulbous contacts to the surrounding porphyry (Fig. 10). Irregular veins of magnetite, or ore enclaves, have typically rounded outlines and carry, in turn, fragments of porphyry with more or less rounded outline (Figs. 11-14).

Figure 10. Typical example of small magnetite vein with irregular, bulbous contacts in the Kiirunavaara hanging wall porphyry. Calcite-filled, radial contraction fractures as seen here are typical for all magnetite veins and dykes. Kiirunavaara hanging wall.

Figure 11. Two examples of irregular and rounded magnetite enclaves, carrying numerous smaller, more or less rounded inclusions of porphyry. Kiirunavaara hanging wall.

Figure 12. Irregular network of magnetite veins, intermingled with porphyry, showing rounded outlines. Kiirunavaara hanging wall.

Figure 13. Variations in structural relation between ore veins and hanging wall porphyry; from intricate network of thin magnetite veins and rounded pieces of porphyry, and thicker vein with irregular contact, to relatively sharply cutting vein. Kiirunavaara hanging wall.

3   Discussion and conclusions

The apparent similarity in the ore-country rock relations in the footwall and hanging wall is deceiving. The nodules and the nodular porphyry exist only in the syenitic footwall porphyries. The footwall rocks appear to represent a succession from more deep-seated syenites, of identical composition but without nodules, to subvolcanic-volcanic porphyries (e.g. Geijer 1910).

These magmas were strongly enriched in volatiles; P, F, CO_2, Cl and S, as evidenced by the associated gangue minerals (see Harlov et al. 2002; Nordstrand and Andersson, 2013). They were also irregularly enriched in FeO.

Figure 14. Rounded enclave of magnetite ore in the hanging wall porphyries at Luossavaara. Width of finger = 20 mm.

When, due to volcanic instability, they reached levels closer to the surface, the original magma separated into silicate-rich and Fe-P-rich magmas, i.e. the magnetite-rich nodules of the nodular porphyry represent magma droplets separated from the surrounding silicate melt by liquid immiscibility, a possibility suggested already by Högbom (1898), and vividly advocated by Lundberg & Smellie (1979). Silicate liquid immiscibility in Fe-rich systems has been experimentally observed (e.g. Gibbon and Tuttle 1967; Philpotts 1967; Naslund 1983); in P-rich systems the miscibility gap is wider (Visser and Koster van Groos 1979), and a Fe-P-rich melt can remain liquid down to c. 600°C (Lledo 2005). Natural examples have been reported by e.g. Hurai et al. (1998) and Clark and Kontak (2004). Continued volcanic unrest and an expected lower viscosity of the ore magma facilitated the formation of an interconnected network of Fe-P-magma.

However, the distribution of numerous, often rounded, enclaves of ore in the hanging wall indicate comingling of magmas (albeit not cogenetic) in a similar way to that well-known from coeval granitic and basaltic magmas (cf. e.g. Frost and Mahood 1987; Didier and Barbarin 1991). This suggests that the footwall, ore and hanging wall magmatism was more or less synchronous. This may be understood if the hanging wall magmas intruded during crystallisation of the footwall package. In the footwall numerous irregular dyke porphyries, texturally inseparable from hanging wall porphyries, are present. These partly pass through the ore, and partly not, forming slivers within ore (e.g. Geijer 1960) (Fig. 15). The dyke porphyries may in fact represent feeders for the hanging wall volcanism, and explain the widespread occurrence of ore and footwall enclaves in the hanging wall. The ore enclaves thus represent magma blobs entrained by pulses of the more viscous felsic hanging wall magma passing through the evolving footwall-ore system. Moreover, this magma replenishment may in fact have acted instrumental for

the separation of the ore magma from its silicate host magma, squeezing it out into low-viscous lubricant layers, interfingered and overlain by more viscous felsic porphyry masses during eruption. The presence of magnetite veins and dykes in the hanging wall rocks in this scenario merely shows that the ore magma was liquid longer and able to penetrate the overlying porphyry upon cooling.
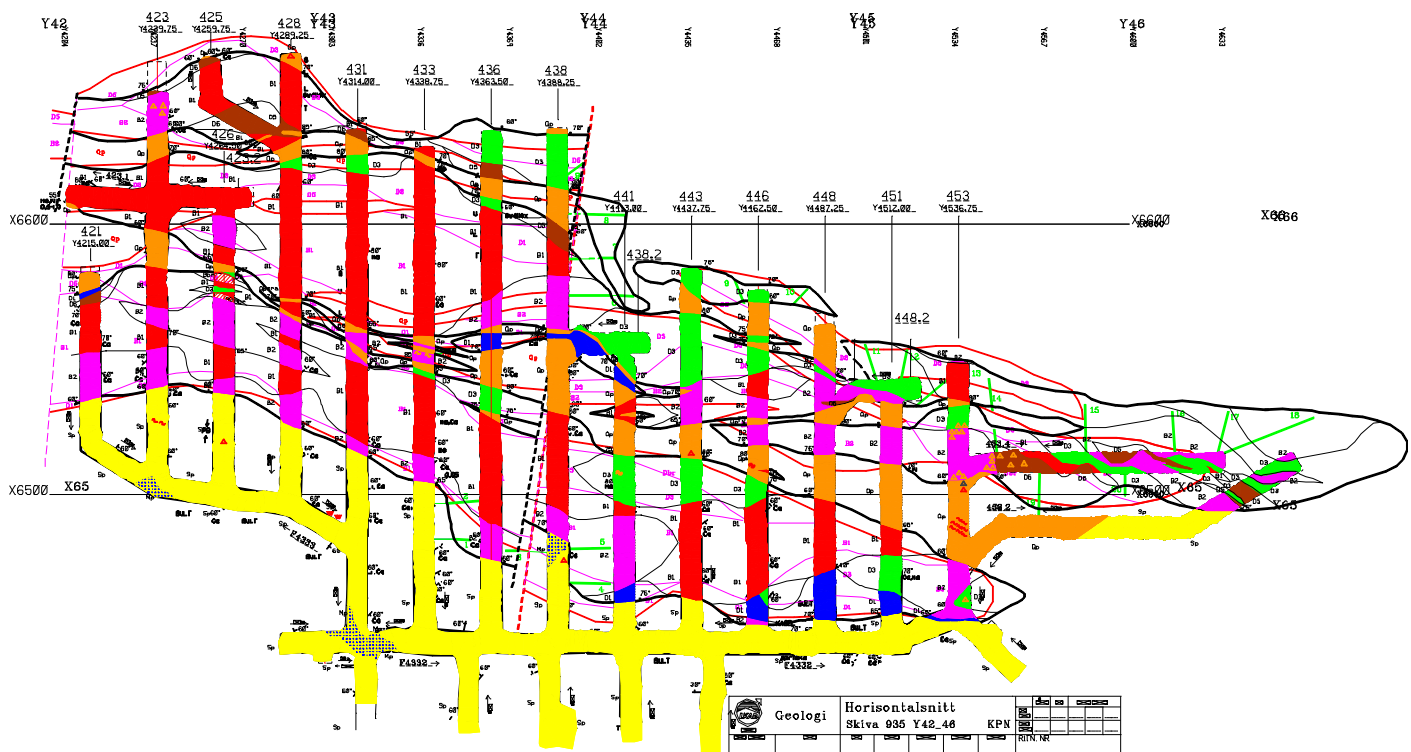
Figure 15. Excerpt from the mine geology database. Horizontal section at level 964 m from the southernmost tip of the ore. Blue, brown and green = various P-rich ore, red = P-poor ore, pink = silicate-enriched ore, yellow = footwall, and orange = dyke and hanging wall porphyries. Note the slivers of dyke porphyries interleaved with the ore tongues and connected to the hanging wall.

References

Bäckström H (1904) Ekströmsbergs och Mertainens järnmalmfälts geologi. GFF 26: 180-183.

Bergman S, Kübler L, Martinsson O (2001) Description of regional geological and geophysical maps of northern Norrbotten County (east of the Caledonian orogeny). SGU Ba 56, 110 pp.

Clark AH, Kontak DJ (2004) Fe-Ti-P oxide melts generated through magma mixing in the Antauta subvolcanic crater, Peru: implications for the origin of nelsonite and iron oxide-dominated hydrothermal deposits. Econ Geol 99: 377-395.

Didier J, Barbarin B (Eds) (1991) Enclaves and granite petrology. Dev Petrol 13, Elsevier, Amsterdam, 625 pp.

Ekström M, Ekström T (1997) Petrografisk beskrivning av sidoberget i Kiirunavaara. Ekström Mineral AB, 21 pp.

Frietsch R (1978) On the Magmatic Origin of Iron Ores of the Kiruna Type. Econ Geol 73: 478-485.

Frost TP, Mahood GA (1987) Field, chemical, and physical constraints om mafic-felsic magma interaction in the Lamarck granodiorite, Sierra Nevada, California. GSA Bull 99: 272-291.

Geijer P (1910) Igneous rocks and iron ores of Kiirunavaara, Luossavaara and Tuollavaara. Scientific and Practical Researches in Lapland arranged by the Luossavaara-Kiirunavaara Aktiebolag, Geology of the Kiruna district 2, Stockholm, 278 pp.

Geijer P (1960) The Kiruna iron ores. In: Sulphide and iron ores of Västerbotten and Lappland, northern Sweden. Int Geol Cong. XX1 session, Guide to excrusions No. A 27 and No. C 22, pp. 24-38.

Geijer P (1968) Problemen kring malmbrottstycken i Kirunas hängväggsporfyr, *Sver Geol Unders C 629, 34 pp.*

Gibbon DL, Tuttle OF (1967) A note on the system FeO-Fe_2O_3-SiO_2-H_2O. Am Mineral 52: 886-889.

Harlov DE, Andersson UB, Förster H-J, Nyström JO, Dulski P, Broman C (2002) Apatite-monazite relations in the Kiirunavaara magnetite-apatite iron ore, northern Sweden. Chem Geol 191: 47-72.

Hitzman MW, Oreskes N, Einaudi MT (1992) Geological characteristics and tectonic setting of Proterozoic iron oxide (Cu-U-Au-REE) deposits. Prec Res 58: 241-287.

Högbom AG (1898) Om de vid syenitbergarter bundna jernmalmerna i östra Ural. GFF 20: 115-134.

Hurai V, Simon K, Wiechert U, Hoefs J, Konecny P, Huraiová M, Pironon J, Lipka J (1998) Immiscible separation of metalliferous Fe/Ti-oxide melts from fractionating alkali basalt: P-T-f_{O2} conditions and two-liquid elemental partitioning. Contr Mineral Petrol 133: 12-29.

Lledo HL (2005) Experimental studies on the origin of iron deposits; and mineralization of Sierra La Banderra, Chile. Doctoral Thesis, Bingham University, New York. 271 pp.

Lundberg B, Smellie JAT (1979) Painorova and Mertainen iron ores: two deposits of the Kiruna iron ore type in northern Sweden. Econ Geol 74: 1131-1152.

Naslund HR (1883) The effect of oxygen fugacity on liquid immiscibility in iron-bearing silicate melts. Am J Sci 283: 1034-1059.

Nordstrand J, Andersson UB (2013) Mineral chemistry of gangue minerals of the Kiirunavaara iron ore, recording a transition from magmatic to hydrothermal conditions. this volume

Nyström J-O (1985) Apatite iron ores of the Kiruna field, northern Sweden: magmatic textures and carbonatitic affinity. GFF 107: 133-141.

Nyström J-O, Billström K, Henríquez F, Fallick AE, Naslund HR (2008) Oxygen isotope composition of magnetite in iron ores of the Kiruna type in Chile and Sweden. GFF 130: 177-188.

Parák T (1975a) The origin of the Kiruna iron ores. Sver Geol Unders C 709, 209 pp.

Philpotts AR (1967) Origin of certain iron-titanium oxide and apatite rocks. Econ Geol 62. 303-315.

Smith MP, Storey CD, Jeffries TE, Ryan C (2009) In situ U-Pb and trace element analysis of accessory minerals in the Kiruna District, Norrbotten, Sweden: New constraints on the timing and origin of mineralization. J. Petrol. 50: 2063-2091.

Visser W, Koster van Groos AF (1979) Effects of P_2O_5 and TiO_2 on the liquid-liquid equilibration in the system K_2O-FeO-Al_2O_3-SiO_2. Am J Sci 279: 970-988.

Additional data on the age and origin of the Bastnäs-type REE deposits, Sweden

Ulf B. Andersson
Dept. of Earth Sciences, Uppsala Univ., Villavägen 16, SE-72 36 Uppsala, Sweden (now at LKAB, R&D, TFG, FK9, SE- 981 86 Kiruna, Sweden)
ulf _b_a@hotmail.com

Dan Holtstam
Swedish Research Council, Research Policy Analysis, Box 1035, SE-101 38 Stockholm, Sweden (formerly at the Swedish Museum of Natural History, Box 50007, SE-104 05 Stockholm, Sweden)

Curt Broman
Department of Geological Sciences, Stockholm University, SE-106 91 Stockholm, Sweden

Abstract. Isotopic, geochemical, mineralogical, and fluid inclusion data are in accordance with the deposition of REE minerals from fluids rich in Cl, F, S, CO_2, Si, REE, and other metal cations, beginning at temperatures >400˚C. Deposition occurred over a time frame of c. 60 Ma (1905-1845 Ma). The fluids had a dominantly igneous origin, possibly related to extensive fluid-rock interaction in an active and evolving volcano-plutonic complex.

Keywords.
REE mineralization, Bastnäs, geochemistry, isotopes, fluid inclusions.

1 Background

The Bastnäs REE deposit have earned a place in the history of science since the discovery of the elements Ce (Hisinger and Berzelius 1804) and La in minerals recovered from there (see Langhof 2004; Öhman et al. 2004). The Bastnäs deposit is one among a group of REE deposits (the Bastnäs-type; Geijer 1961) that are associated with skarn assemblages, Fe-ores, and carbonate lenses along a c. 80 km long zone in strongly altered volcanic and plutonic rocks in central southern Sweden (Fig. 1; Ambros 1983; Holtstam 2004). The deposits consist of complex assemblages of Fe oxide ores, Ca-Mg silicate skarns, REE silicates, REE flurocarbonates, sulphides and sulfosalts of Cu, Mo, Bi, Co, and very minor Au-Ag alloys (Holtstam 2004). About 20 REE minerals have been reported from these deposits, and a few still await full characterization (Geijer 1921; 1927; Holtstam et al. 2003a; 2003b; 2005; 2006; Holtstam and Andersson 2007).

Holtstam and Andersson (2007) divided the deposits into two subtypes: 1) the Bastnäs and Rödbergsgruvan deposits that are enriched in La, Ce and Fe relative to the second type, and 2) the deposits in the Norberg area that are enriched in Y, Mg, Ca and F relative to subtype 1 deposits. The REE-mineralogy in subtype 1 is dominated by cerite-(Ce), ferriallanite-(Ce), törnebohmite-(Ce) and bastnäsite-(Ce), while subtype 2 typically contains fluorbritholite-(Ce), västmanlandite-(Ce), dollaseite-(Ce) and gadolinite-(Ce) – gadolinite-(Y).

2 Results

2.1 Fluid inclusions

In summary, data from bastnäsite from both subtype 1 and subtype 2 deposits show primary fluid inclusions with a mixed H_2O-CO_2 composition and moderate to high salinities (6−29 eq. wt % $CaCl_2$). Homogenization temperatures suggest bastnäsite crystallization between 300 and 400˚C (see also Holtstam and Broman 2002; Holtstam et al. 2006). Late-stage fluorite (subtype 2) show H_2O-dominated inclusions with low to medium salinities (0−16 eq. wt % NaCl), and homogenization temperatures in the range 100−150˚C.
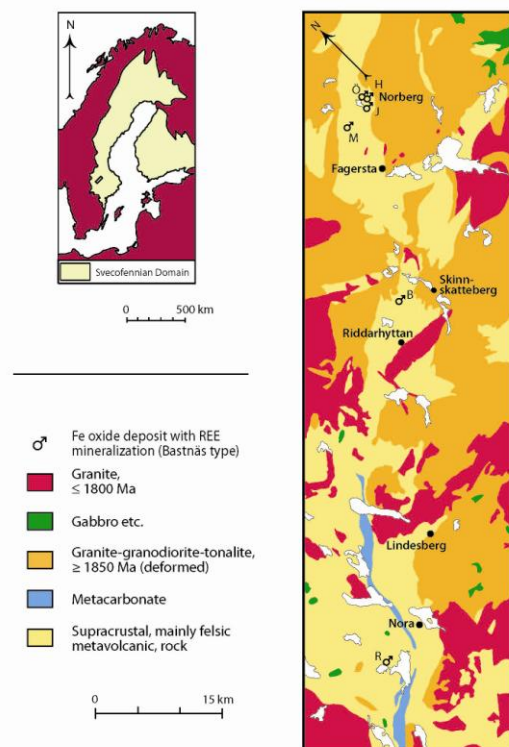
Figure 1. Geological map covering the area with Bastnäs-type deposits, based on maps published by the Geological Survey of Sweden. R = Rödbergsgruvan, B = Bastnäs field. Malmkärra, Johannagruvan, S. Hackspikgruvan and Östanmossa are situated around the town of Norberg.

2.2 Stable isotopes

O and C isotopic data were determined from dolomite and calcite separates from host marbles, 'ophicalcite', and skarns from the Norberg deposits. The 'ophicalcite' is defined as a recrystallized carbonate rock of coarser grain size compared to the host marble (Geijer 1927), with silicate inclusions and often associated with some REE mineralization.

All samples show an overlapping range of $\delta^{18}O_{SMOW}$ values from +6 to +9 ‰ (Fig. 2). In contrast, the $\delta^{13}C_{V-PDB}$ values of the host marbles are higher (-3 to -2 ‰) than that of the skarns and ophicalcite (-7 to -4 ‰).

The O and C isotopic composition of carbonates from the skarn and ophicalcite assemblages essentially overlap the fields for the mantle and primary igneous carbonatites, as well as the compositions of granite-related skarn deposits in Bergslagen (Fig. 2). This is in stark contrast to Precambrian (and Svecofennian) sedimentary carbonates that mostly show distinctly higher $\delta^{18}O$ and $\delta^{13}C$ values. This thus suggests a major magmatic fluid component for these carbonates. Slight excursions to heavier C and O compositions may indicate minor fluid components from decarbonated sedimentary carbonates (cf. De Groot and Sheppard 1988).

Stratabound carbonates associated with Fe-Mn deposits in Bergslagen more or less overlap in isotopic composition with that of sedimentary carbonates unrelated to mineral deposits, while carbonates in Fe-skarns typically are shifted to lighter carbon isotope values (Fig. 2); a feature probably related to decarbonation during metamorphism and skarn formation, probably supplemented by some magmatic fluid input (e.g. Billström et al. 1985; Valley 1986).
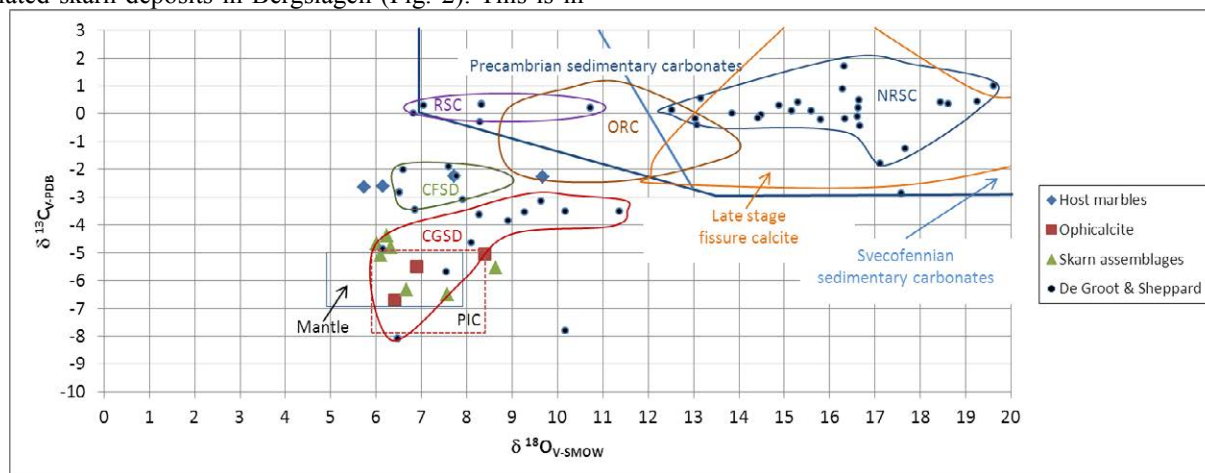
Figure 2. $\delta^{18}O$ vs. $\delta^{13}C$ diagram for the present samples, divided into: host marbles, ophicalcite, and REE-skarn-hosted carbonates. For comparison, fields for carbonates precipitated in different environments have been plotted. PIC=primary igneous carbonatites (Taylor et al. 1967). Mantle field, compiled by Keller and Hoefs (1995). Worldwide Precambrian sedimentary carbonate field (after Veizer et al. 1992; Antonini et al. 2003). Svecofennian sedimentary carbonate field after Karhu (1993). RSC=stratabound carbonates of the Bergslagen region related to stratiform iron-oxide deposits (after De Groot and Sheppard 1988, incl. data of Holtstam and Mansfeld 2001). NRSC=stratabound carbonates of the Bergslagen region not related to iron oxide deposits (after De Groot and Sheppard 1988, including data from Schidlowski et al. 1975; Ehlin and Koark 1980). CFSD=carbonates in Fe-oxide skarn deposits in Bergslagen (data from De Groot and Sheppard 1988; Holtstam and Mansfeld 2001). CSDG=carbonates from granite-related W-Mo skarn deposits (from De Groot and Sheppard 1988). ORC=oxide-related carbonates from the Långban Fe-Mn deposit (after Jonsson and Boyce 2004). Late stage calcite in fissures of Långban type deposits (after Jonsson and Boyce 2004; Holtstam and Mansfeld 2001). The ophicalcite and REE-related skarn carbonates plot within or close to the primary magmatic fields. The associated host marbles show somewhat higher $\delta^{13}C$ values, overlapping with carbonates from skarn-altered Fe-oxide deposits.

S isotopic data were obtained on 13 samples of molybdenite, pyrite, chalcopyrite, and bismuthinite from five deposits. $\delta^{34}S_{CDT}$ values range from -11 to ±0, with small variations within each deposit. The S isotopic signature of the Malmkärra (Norberg area) and Rödbergsgruvan deposits fall within the range of pure magmatic sources ($\delta^{34}S = ±0 ± 2‰$; Ohmoto 1986), while the two other Norberg deposits show distinctly lower values and the Bastnäs deposit is the most depleted in ^{34}S.

The S isotopic composition of ore sulphides (including massive, vein-hosted, and disseminated types) in the Bergslagen region and adjacent areas are mostly within the $\delta^{34}S$ range -5 to + 5‰ (with an average preponderance for slightly positive values) and interpreted as representing an essentially original magmatic signature related to volcanic-hydrothermal formation processes, with limited metamorphic remobilization effects (e.g. Hellingwerf and van Raaphorst 1988; Billström 1991; Wagner et al. 2005). The enrichment in light sulfur for the Bastnäs samples indicates some fractionation during exchange with fluids of a different origin, e.g. cold sea water (Hellingwerf et al. 1987).

2.3 Nd isotopes

Nd isotopic data (see also Holtstam et al. 2006) were collected for a number of REE minerals from Bastnäs, including bastnäsite, cerite, ferriallanite, törnebohmite, and percleveite, and plot on a poorly constrained isochron yielding 1.88±0.11 Ga, and initial ϵ_{Nd}=+0.7. Recal-culating the individual measurements to a 1.88 Ga formation age yields a tight group of initial ϵ_{Nd} values of

+0.2 to +1.6 (Fig. 3).
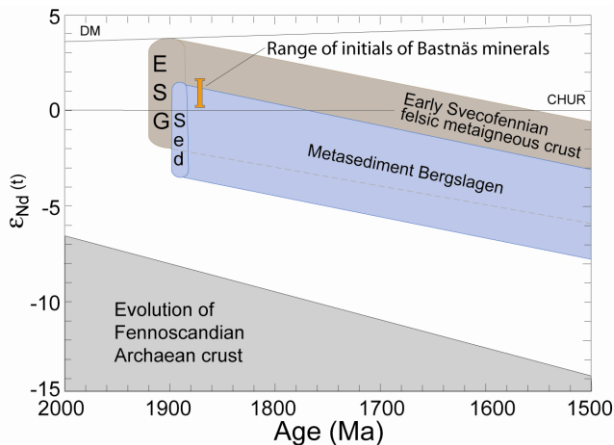
Figure 3. Range of initial ε_{Nd} values for the Bastnäs REE minerals, Background data as compiled in Andersson and Wikström (2004).

2.4 Re-Os geochronology

Molybdenite occurs together with the REE minerals in several deposits, and appears from textures mostly to have crystallized late in relation to the REE minerals (cf. Geijer 1921). Three samples of molybdenite were analysed to obtain Re-Os ages: 1) S. Hackspikgruvan (Norberg area), 2) Bastnäs, and 3) Rödbergsgruvan. Two separates were analysed from each, yielding weighted averages of: 1) 1842±4 Ma, 2) 1863±4 Ma, and 3) 1904±6 Ma.

2.5 Whole rock geochemistry

Whole rock geochemistry was analysed from 21 samples of the REE mineralized zones and various associated country rocks. The total REE contents of the mineralized samples range from 30 to >50 %. Among the country rocks one group appear to be little affected by metasomatism, while the other group suffered strong metasomatic changes of their original magmatic compositions (Fig. 4).
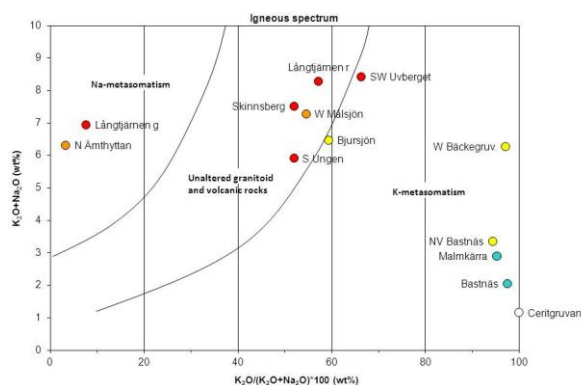
Figure 4. Whole rock alkali diagram ('igneous spectrum'; Hughes 1973) for rocks associated with the Bastnäs-type deposits. Red = metagranitoids, yellow = metavolcanics, orange = granitod gneisses, blue = 'ore quartzites', and Ceritgruvan (Bastnäs) host rock.

The latter fall in two categories: 1) strong metasomatic increase in K and decrease in Na, and 2) the opposite. The former are spatially more closely associated with the Bastnäs-type deposits (e.g. Geijer 1923; 1936).

3 Discussion

The molybdenite Re-Os ages show that sulphides associated with the REE mineralization in the Bastnäs-type deposits crystallized over a 60 Ma time period (1.90−1.84 Ga) with the oldest in the SW (Röd-bergsgruvan) and the youngest in the NE (Norberg area). Textural data indicate that the sulphide minerals precipitated coeval with or later than the REE minerals. These data should thus represent minimum ages for the REE mineralizations, suggesting these deposits to be dominantly early Svecofennian.

The fluid inclusion data from bastnäsite indicate deposition from CO_2-bearing brines, moderately to highly saline, at temperatures of c. 400˚C for the REE mineralization. Fluid inclusions in fluorite record fluid evolution to lower temperatures (100−150˚C) and a concomitant drop in salinity and CO_2 content.

Holtstam and Andersson (2007) suggested that REE deposition took place from fluids enriched in F, Si, and Cl, during interaction with carbonate horizons.

C and O isotopic data for the skarns and 'ophicalcite' essentially fall within the field of CO_2 from magmatic or mantle sources (Fig. 2). The host marbles to the REE deposits overlap in isotopic composition with carbonates from Fe skarn deposits, indicating a mixed magmatic/ sedimentary origin and/or decarbonation of sedimentary carbonates. Similarly, the S isotopes on the associated sulphides indicate magmatic sources, in certain cases mixed with fluids of a different origin.

The Nd isotopic data lend no support for fluid sources in the Archaean crust, but indicate dominating juvenile igneous Svecofennian sources, possibly with a minor sedimentary component.

The REE mineralizations are spatially associated with strongly altered early Svecofennain volcanic and plutonic rocks, typically K-altered in the proximity of the ores. There is no obvious spatial relation with younger, unaltered granites. This fact argues for a relation between the regional metasomatism and REE deposition.

4 Conclusions

The combined evidence suggests REE mineralization from high temperature (400˚C or slightly more) acidic fluids carrying REE, Si, F, Cl, S, CO_2 and other metal cations. The origin of the fluids was mainly magmatic and related to strong regional metasomatic alteration. This may be accomplished by circulating fluids through an extensive, active and evolving volcano-plutonic complex, possibly near brine-rich basins in an extending mature arc system over a protracted time of c. 60 Ma.

Acknowledgements

comments on the present text.

References

Ambros M (1983) Beskrivning till berggrundskartan Lindesberg NO. Sver Geol Unders Af 141: 1-75. (in Swedish).

Andersson, UB, Wikström A (2004): The Småland-Värmland Belt. Overview. *In,* The Transscancinavian Belt in Sweden: a review of its character and evolution (Högdahl, K, Andersson UB, Eklund O, Eds). Geol Surv Finland 37: 15-20.

Antonini P, Comion-Chiaramonti P, Gomes CB, Censi P, Riffel BF, Yamamoto E (2003): The Early Proterozoic carbonatite complex Angico dos Dias, Bahia State, Brazil: geochemical and Sr-Nd isotopic evidence for an enriched mantel origin. Mineral Mag 67: 1039-1057.

Billström K (1991): Sulphur isotope compositions in the Åmmeberg Zn-Pb ore deposit, south-central Sweden: Genetic implications. Geol Runds 80: 717-727.

Billström K, Åberg G, Nord AG (1985): Stable istope data of Bergslagen carbonates and their potential use for sulphide ore prospecting. GFF 107: 169-173.

De Groot PA, Sheppard SMF (1988): Carbonate rocks from W. Bergslagen, Central Sweden: isotopic (C, O, H) evidence for marine deposition and alteration by hydrothermal processes. Geol Mijnb 67: 177-188.

Ehlin P-O, Koark HJ (1980): Svecofennian paradiagenetic concretions. N Jahrb Geol Pal Monatsh 3: 145-154.

Geijer P (1921): The cerium minerals of Bastnäs at Riddarhyttan. Sver Geol Unders C304: 1-24.

Geijer P (1923): Geologisk beskrivning. In Riddarhytte malmfält i Skinnskattebergs socken i Västmanlands län. Kungl. Kommerskollegium and Sveriges Geologiska Undersökning. Victor Pettersson, Stockholm, Sweden (in Swedish).

Geijer P (1927): Some mineral associations from the Norberg district. Sver Geol Unders C343: 1-32.

Geijer P (1936): Norbergs berggrund och malmfyndigheter. Sver Geol Unders Ca 24, 162 pp.

Geijer P (1961): The geological significance of the cerium mineral occurrences of the Bastnäs type in Central Sweden. Ark Min Geol 3: 99-105.

Hellingwerf RH, Baker JH, van Raaphorst JG (1987): Sulphur isotope data of Proterozoic molybdenites of western Bergslagen, Sweden. Geol För Stockh Förh 109: 33-38.

Hellingwerf RH, van Raaphorst JG (1988): Sulphur isotopes from the Gruvåsen sulphide skarn deposit, Bergslagen, Sweden. Mineral Petrol 38: 161-170.

Hisinger W, Berzelius JJ (1804): Cerium, en ny Metall, funnen i Bastnäs Tungsten från Riddarhyttan i Westmanland. Henrik A. Nordström, Stockholm Sweden, 24 pp (in Swedish).

Holtstam D, Mansfield J (2001): Origin of a carbonate-hosted Fe-Mn-(Ba-As-Pb-Sb-W) deposit of Långban-type in central Sweden. Mineral Depos 36: 641-657.

Holtstam D, Broman C (2002): Lanthanide mineralizations of Bastnäs type: overview and new data. GFF 124: 230-231.

Holtstam D (2004): The Bastnäs-type REE deposits. In: The Bastnäs-type REE-mineralizations in north-western Bergslagen, Sweden – a summary with geological background and excursion guide (UB Andersson, Ed). Sver Geol Unders, Rapp Medd 119: 13-22.

Holtstam D, Andersson UB (2007): The REE minerals of the Bastnäs-type deposits, south-central Sweden. Can Mineral 45: 1073-1114.

Holtstam D, Andersson UB, Mansfeld J (2003a): Ferriallanite-(Ce) from the Bastnäs deposit, Västmanland, Sweden. Can Mineral 41: 1233-1240.

Holtstam D, Norrestam R, Andersson UB (2003b): Percleveite-(Ce), a new lanthanide disilicate mineral from Bastnäs, Skinnskatteberg, Sweden. Eur J Mineral 15: 725-731.

Holtstam D, Kolitsch U, Andersson UB (2005): Västmanlandite-(Ce) – a new lanthanide- and F-bearing sorosilicate mineral from Västmanland, Sweden: description, crystal structure, and relation to gatelite-(Ce). Eur J Mineral 17: 129-141.

Holtstam D, Broman C, Mansfeld J, Andersson UB (2006): Tracking ore-forming fluids in Bastnäs-type REE deposits. 27th Nordic Geological Winter meeting, Oulu. Bull Geol Soc Finl, Spec Issue 1, (s. 53) suppl p 2.

Hughes CJ (1973): Spilites, keratophyres, and the igneous spectrum. Geol Mag 109: 513-52.

Jonsson E, Boyce AJ (2004): Stable isotope (C, O, S) study of the Långban Fe-Mn-(Ba-As-Pb-Sb) deposit, Bergslagen, Sweden: implications for processes and paragenesis. In: Jonsson, E. Fissure-hosted mineral formation and metallogensis in the Långban Fe-Mn-(Ba-As-Pb-Sb…) deposit, Bergslagen, Sweden. Medd Stockh univ inst Geol Geok No. 318. (Ph.D. thesis).

Karhu J (1993): Paleoproterozoic evolution of the carbon isotope ratios of sedimentary carbonates in the Fennoscandian Shield. Geol Surv Finl, Bull 371: 1-87.

Keller J, Hoefs J (1995): Stable isotope characteristics of recent natrocarbonatites from Oldoinyo Lengai. In: Bell K, Keller J (Eds), Carbonate volcanism. Oldoinyo Lengai and the petrogenesis of natrocarbonatites. IAVCEI Proceedings in Volcanology 4. Springer-Verlag, Berlin, pp 113-123.

Langhof J (2004): History of the mineral and element discoveries at Bastnäs. In: The Bastnäs-type REE-mineralizations in north-western Bergslagen, Sweden – a summary with geological background and excursion guide (UB Andersson, Ed). Sver Geol Unders, Rapp Medd 119: 22-25.

Öhman L, Nysten P, Langhof J (2004): The Bastnäs mines. Mineral Rec 35: 187-200.

Ohmoto H (1986): Stable isotope geochemistry of ore deposits. Mineral Soc America, Rev Mineral 16: 491-559.

Schidlowski M, Eichmann R, Junge ChE (1975): Precambrian sedimentary carbonates: carbon and oxygen isotope geochemistry and applications fort the terrestrial oxygen budget. Prec Res 2: 1-69.

Taylor HP, Frechen J, Degens ET (1967): Oxygen and carbon isotopic studies of carbonatites from the Laacher See district, West Germany and the Alnö district, Sweden. Geochim Cosmochim Acta 31: 407-430.

Valley JW (1986): Stable isotope geochemistry of metamorphic rocks. Mineral Soc America, Rev Mineral 16: 445-489.

Veizer J, Plumb KA, Clayton RN, Hinton RW, Grotzinger JP (1992): Geochemistry of Precambrian carbonates: V. Late Paleoproterozoic seawater. Geochim Cosmochim Acta 56: 2487-2501.

Wagner T, Jonsson E, Boyce AJ (2005): Metamorphic ore remobilization in the Hällefors district, Bergslagen, Sweden: constraints from mineralogical and small-scale sulphur isotope studies. Mineral Dep 40: 100-114.

Successive uranium enrichment steps in the continental crust through polycyclic orogeny: the example of the Litsa district, Russia

Anne-Sylvie André-Mayer, Michel Cuney, Julien Mercadier
Université de Lorraine, CNRS, GEORESSOURCES - CREGU, Vandœuvre-lès-Nancy, France

Léonid Sérov, Elena Afanasyeva, Alexandre Lipner, Vladimir Fuchs, Yuri Mironov
VSEGEI, Saint-Petersburg, RUSSIA

Philippe Kister, Patrick Ledru, Marc Brouand
AREVA, Paris, FRANCE

Isabelle Duhamel-Achin
Actual address: ERAMET, Paris, FRANCE

Abstract. The Litsa district, located on the Kola Peninsula, Russia, represents one of the best areas in the world for the preservation of a succession of uranium enrichment stages through time, from Archaean to Caledonian. Most of the Litsa area uranium occurrences result from the partial melting of country rocks and subsequent uranium enrichment in the magmas. At least three episodes of partial melting occurred, during the Archaean, Early and Late Palaeoproterozoic. Then, epigenetic processes lead to local higher-grade uranium deposition consisting of pitchblende veins associated with several types of middle and low temperature hydrothermal alterations. The migmatized U-rich metasediments of the Tundra (Archaean) and Kola (Proterozoic) suites are locally uranium enriched in the most deformed and migmatized zones, but such enriched zones represent quite discontinuous and small-sized lenses. The immature and reduced Mesoproterozoic sediments, as observed in the Sredny and Ribachy Peninsulas, are not favorable to generate extensive diagenetic circulation of oxidized acidic brines able to leach and transport large quantities of uranium similar to unconformity related uranium deposits. The most abundant and probably prospective for the economic-grade uranium mineralization is Palaeozoic pitchblende vein type, located around the Litsa-Araguba granitoid complex, where favorable protoliths, structures and epigenetic processes are encountered.

Keywords: uranium, partial melting, polycyclic orogeny, Kola Peninsula, Fennoscandian shield

1 Introduction

The Fennoscandian Shield constitutes one of the largest Archaean outcropping areas on earth (Bleeker 2003, Slabunov et al. 2006, Hölttä et al. 2008). In its northern part, the Kola Province is a result of several stages of crustal accretion from Archaean to Caledonian times and has been intensively explored for mineral resources, including uranium (Eilu and Weihed 2005, Weihed et al. 2005, Weihed et al. 2008).

The metallogenic potential of the Kola Peninsula is well expressed by the world-class Pechenga Ni deposit and the two giant peralkaline nepheline syenite Devonian complexes Lovozero (Nb-Ta) and Khibini (apatite). A recent discovery of diamonds has led to renewed exploration. Moreover, uranium exploration by Soviet geologists, in the sixties and seventies, led to the discovery of several districts with an uraniferous potential, namely, from the oldest to the youngest: Litsa (including the Litsevskoe, Beregovoe, Skalnoe, Polyarnoe, Koskjavr, Dikoe occurrences), Imandra-Varzuga (Solenoye occurences), Elozero, Tersk (Kitsa and Julitsa occurrences), and Khibini-Lovozero.

The Litsa uranium district, located in the north-western part of the Kola Peninsula, represents one of the best areas in the world for the preservation of a succession of uranium enrichment stages through time. The ability of uranium to fractionate into the silicate melt during partial melting and crystal fractionation, its mobility in oxidizing conditions (Cuney and Friedrich 1987, Dahlkamp 1993, Peiffert et al. 1996, Kyser and Cuney 2008, Cuney 2009) and its natural radioactive decay give exceptional tracer properties to this element that can be used to reconstruct and date orogenic processes.

The aim of this paper is to present a review of the Litsa district uranium occurrences. In this review, the Litsa district uranium occurrences will be described through time from Archaean to Caledonian. The description of the different uranium occurrences (field relations, petrology, mineralogy and geochemistry), combined with a determination of the relative contribution of magmatic, metamorphic and hydrothermal processes, together with U/Pb geochronological constraints, will be used (i) to discuss about the fractionation of uranium during the build up and reworking of the continental crust and (ii) to relate them both in space and time with the main geodynamics events affecting the Fennoscandian shield through Archaean to Caledonian times.

2 General characteristics of the Litsa district uranium occurrences

The oldest uranium occurrences in the Litsa district occur in quartz-feldspar-biotite granitoid vein-like bodies injected into mica gneisses of the 2750-2650 Ma Tundra suite (Fig 1) (Anderson et al. 1990). These granitoid and pegmatitic bodies are associated with

migmatization processes of the hosting gneiss. The most representative objects of this type are the Dikoe and Skalnoe uranium occurrences; more targets of the same type also exist within the Voron'ya-Kolmozero tectonic zone beyond the Litsa district.

Figure 1. Archaean occurrences. A boudinated and sub-concordant pegmatoid body within the host gneiss of the Tundra suite.

Early Palaeoproterozoic uranium occurrences occur in pegmatoid vein-like bodies (Fig 2), which display very similar features as the preceding Archaean ones in outcrop i.e.: lenticular, concordant to subconcordant with the host rock gneisses, sharp boundaries, variable amounts of quartz, feldspars and biotite. The host rock gneisses consist of aluminous migmatized biotite ± garnet ± amphibole gneisses of the Kola series.

Figure 2. Proterozoic occurrences. An oxidized pegmatoid body, boudinated and subconcordant with the enclosing biotite-rich gneiss.

The REE-P-U mineralization is located in Mezo-proterozoic - Neoproterozoic (Riphean - Vendian) terri-genous sediments (Fig 3) on the Sredny-Rybachy peninsulas. They are associated with phosphate-bearing arkose sandstones and siltstones of the Kil'din series and conglomerate-breccias of the Volokovaya series.
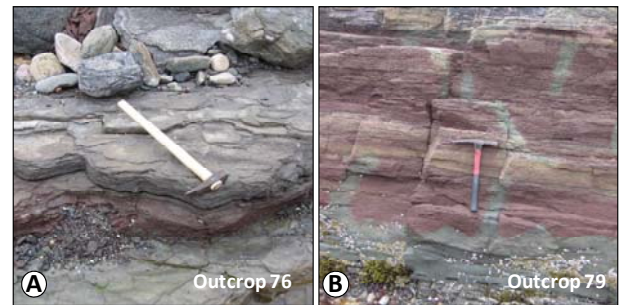
Figre 3. Mesoproterozoic sediments of the Sredny-Rybachy Peninsulas. A. Karujarvi suit siltstone B. Partly reduced oxidized horizon.

The Litsevskoe occurrence (Fig 4) is the most significant of the Palaeozoic age. It is considered to be a small deposit with prognostic reserves of 2,869 tons. Besides Litsevskoe, there are several occurrences (Beregovoe ore-showing and others) of this type in the district. The uranium mineralization is controlled by the zones of intense fracturing and brecciation, expressing albite-hydromica-chlorite alterations (Savitskii et al. 1995).
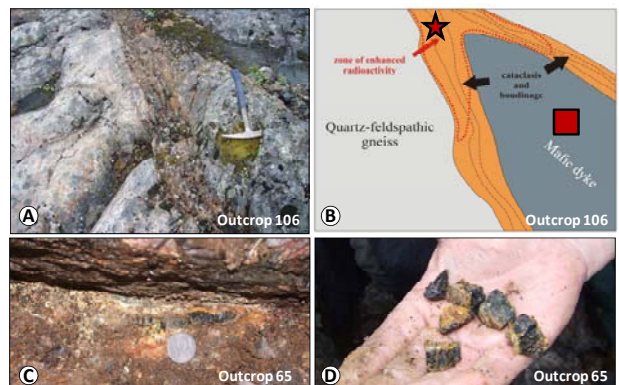
Figure 4. The Palaeozoic Litsevskoe occurrence. A. Photograph and B. scheme showing a NS-striking mafic dyke crosscutting NE-striking quartz-feldspar gneisses. The dyke is characterized by fish-like structures, suggesting a syntectonic emplacement, and by cataclased-oxidized boundaries. C. A pitchblende vein within quartz-muscovite vein; and D. A pitchblende with hexavalent uranium minerals.

3 Geochemical, petrographical and mineralogical characteristics of the ore showing host rocks and related metallogenic processes

The host rock geochemistry expresses strong differences through time which is shown both by chemical-geochemical diagrams (Fig. 5 to 7) and expressed in the mineralogy of the rocks.

The AB chimico-mineralogical diagram (Fig. 5) is

used to discriminate the different granitoid types according to their source (A parameter) and differentiation or color index (B parameter), (Debon and Lefort 1988). The A parameter (in millications) gives the excess of alumina not bound to the feldspars (similar to normative corundum, and A/CNK index). The majority of the Litsa host rocks is weakly peraluminous and is located close to the origin, which corresponds to the granitic eutectic: quartz ± K-feldspar ± plagioclase. Two main trends can be observed (Figure 5):

- The increase of the A parameter is linked to an increase of the aluminous mineral content, i.e. muscovite, thus involving a decrease of the Al content linked to feldspars. Sample 59 from the Archaean Dikoe occurrence is the most peraluminous (A=220). The negative values of the A parameter, leading to a metaluminous character, relate to diabases (sample 91.2) and sulphide-bearing carbonate veins (sample 91.3), in a drill core in the Palaeoproterozoic Polyarnoe occurrence and to the mafic dykes of the Litsveskoe occurrence.

- The B parameter is related to the content of mafic minerals (mainly biotite). The biotite enrichment trend, observed for all host rocks whatever their ages, may be explained either by magmatic or hydrothermal process and will be discussed later.
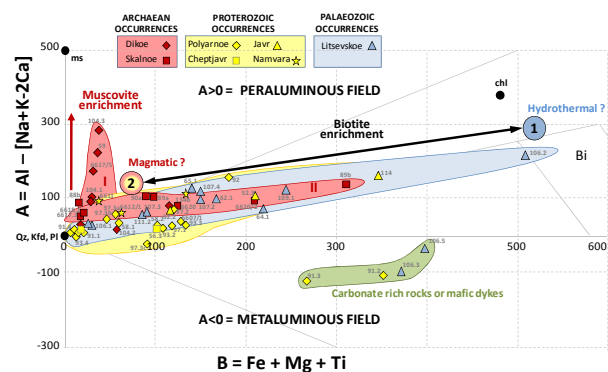
Figure 5. Variation of the peraluminous index A compared to the fractionation parameter B (coloration index) for each individual sample of the Litsa uranium occurrences (diagram from Debon and Lefort 1988). The A and B parameters were calculated in thousands of cations. Mineralogical pole have been indicated: ms=muscovite, chl= chlorite, Bi= Biotite, Qz=Quartz, Kfd=Potassic feldspar, Pl=Plagioclase.

***The Q=Si/3-[Na+K+2Ca/3) vs P=K-[Na+Ca]
diagram (Fig. 6)*** is used to determine the main igneous rock types (Debon and Lefort 1983). A reference grid with the average composition of the major rock types is used to determine the rock typology. The Q parameter estimates the quartz content of a rock by substracting silica bound to the feldspar to the total silica content of the rock. The P parameter discriminates between K-feldspar and/or biotite (high P values) and plagioclase (low P values). The two trends observed within this diagram discriminate the main geological processes which involve biotite enrichment as expressed in the AB diagram: (i) An increase of both the P and Q values may express a magmatic differentiation process for Archaean and Proterozoic occurrences, (ii) A horizontal trend, with only the variation in the P values, may express a hydrothermal process, for the Paleozoic ore-showing.

Samples depleted in the P and Q parameters are linked via albitization processes to carbonate veins.
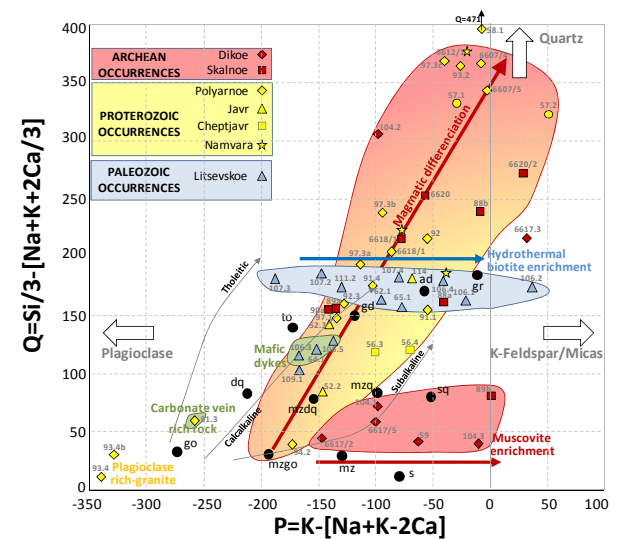
Figure 6. Variation of P versus Q parameters for each individual sample of the Litsa uranium occurrences (diagram from Debon and Lefort 1988). The Q and P values are calculated in thousands of cations. mz = monzonite; mzq = quartz-monzonite; mzdq = quartz monzodiorite; dq = quartz diorite; s = syenite; sq = quartz syenite; to = tonalite; gd = granodiorite; ad = adamellite; gr = granite.

The U/Th ratio (Fig. 7) is below 1 in most of the samples, in such way that the altered and mineralized samples are more enriched in both elements. Archaean and Palaeoproterozoic occurrences express a magmatic trend. Paleozoic samples are characterized by low thorium contents indicating low temperature processes while uranium contents can reach 62900 ppm. The Th/U ratio is << 0.1 as the observed horizontal trend indicates that the uranium enrichment has to be related to a hydrothermal process.
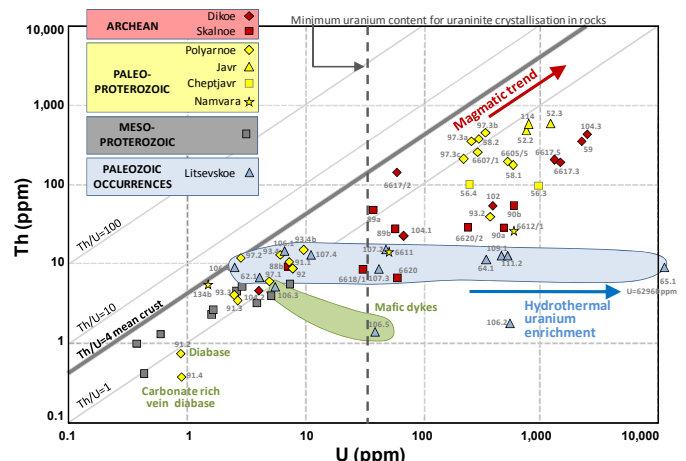
Figure 7. U versus Th contents (ppm) for each individual samples from the Litsa uranium occurrences.

4 Metallogenic processes

The Litsa area experienced a succession of metallogenic processes during which the uranium grades increased:
Magmatic-metamorphic processes: Most of the Litsa area uranium occurrences result from partial melting of

country rocks and subsequent uranium enrichment in the melt (= migmatization process, which corresponds to what Soviet geologists generally call "K-feldspar metasomatism"). Three episodes of partial melting probably occurred, during the Late Archaean, Early and Late Paleoproterozoic.

Hydrothermal processes: These comprise several types of middle and low temperature hydrothermal alteration, often accompanied by uranium deposition in pitchblende veins. Besides, the local uranium enrichment is connected with muscovite-bearing shearing and fluid-rock interaction along mafic dykes. The age of the processes is not constrained, except for pitchblende vein deposition, dated by the U-Pb method.

5. Reworking of uranium during polycyclic orogen

Most of previous uranium metallogenic studies through geological times pointed out that a large proportion of the uranium deposits are hosted in Archaean-Palaeoproterozoic rocks, even if Cuney (2010) underlined the fact that the richest uranium province (Mongolia – Khazakstan) is hosted in Cenozoic sedimentary rocks with Phanerozoic sedimentary uranium source rocks.

The Litsa district witnesses a major uranium input into the continental crust during Archaean and Proterozoic times, with a Phanaerozoic remobilization of the previous uranium stock. The enrichment processes observed in this continental crust segment correspond to three of the five distinct uranium generations through the Earth history previously described by Dahlkamp (1993): (i) generation one (2.8 to 2.2 Ga) with quartz pebble conglomerates assumed to be of detrital origin because of the low oxygen level of the atmosphere, here submitted to migmatization processes (Skalnoe and Dikoe occurrences), (ii) generation two (2.2 to 1.91 Ga) which corresponds to the increase of the oxygen level leading to the U enrichment of Palaeoproterozoic epicontinental platform sediments here also submitted to migmatization processes during worldwide Paleoproterozoic orogenesis (Polyarnoe, Namvara, Cheptjavr, Javr). (iii) Generation five (0.5-0.4 to 0 Ga), with most of vein-related uranium deposits included here, witnesses by the Litsevskoe occurrence.

Generation three (1.5 to 0.9 Ga), comprising mainly the unconformity-related deposits) is not developed in the Litsa area. Indeed Mesoproterozoic basins are observed in the Sredny-Rybachy Peninsula, the reduced and immature character of the Riphean sediments constitutes unfavorable conditions to generate oxidized acid brines able to leach and transport uranium. Generation four (0.7 to 0.5 Ga), restricting for Dahlkamp (1993) to mainly synorogenic magmatic uranium deposits of the Damara-Katanga orogen (Rössing and Shaba province), has not been observed in the Kola district.

Conclusion

The Litsa district is one of the most interesting areas of the Kola Peninsula, Russia, with respect to uranium metallogeny. Presenting all the features of uraniferous province, it endured a protracted geological history with several successive uranium enrichments. The uranium content in the geological formations gradually increased during the geological evolution of the Litsa district from Archaean to Palaeozoic.

References

Anderson EB, Nikitin SA, Zaslavsky VG, Lobickov AF, Markova TA, Drozdov PA (1990) Isotopic dating of uranium occurrences of eastern part of the Baltic Shield. In: Isotopic dating of endogen ore formations, Kiev 174-176

Cuney M (2009) The extreme diversity of uranium deposits, Mineralium Deposita 44:3-9

Cuney M (2010) Evolution of Uranium Fractionation Processes through Time: Driving the Secular Variation of Uranium Deposit Types. Economic Geology 105:553-569

Cuney M, Friedrich M (1987) Physicochemical and crystal chemical controls on accessory mineral paragenesis in granitoids. Implications for uranium metallogenesis. Bull Minéral 110:235–247

Dahlkamp FJ (1993) Uranium ore deposits. Springler-Verlag Berlin Heidelberg

Debon F and Le Fort P (1988) A cationic classification of common plutonic rocks and their magmatic associations: principles, method, applications, Bulletin de Minéralogie 111:493-510

Eilu P and Weihed P (2005) Fennoscandian Shield - orogenic gold deposits. Ore Geology Reviews 27:326–327

Hölttä P, Balagansky V, Garde AA, Mertanen S, Peltonen P et al (2008) Archaean of Greenland and Fennoscandia, Episodes 31:13-19

Kyser TK and Cuney M (2008) Recent and Not-So-Recent Developments in Uranium Deposits and Implications for Exploration. Mineral. Assoc. Can. Short Course Ser. 39

Peiffert C, Nguyen Trung C, Cuney M (1996) Uranium in granitic magmas. Part II: experimental determination of uranium solubility and fluid–melt partition coefficients in the UO2–haplogranite–H2O–halides system at 720–770°C, 200 MPa. Geochim Cosmochim Acta 60:1515–1529

Savitskii AV, Gromov AY, Mel'nikov EK et al (1995) Uranium mineralization of the Litsa district of the Kola Peninsula, Russia. Geology of ore deposits 37:403-416

Slabunov AI, Lobach-Zhuchenko SB, Bibikova EV, Sorjonen-Ward P, Balagansky VV, Volodichev OI, et al (2006) The Archaean nucleus of the Fennoscandian Shield. In: Gee DG and Stephenson RA (eds) European Lithosphere Dynamics, Geological Society of London, Memoirs 32:s627–644

Weihed P, Arndt N, Billström K, Duchesne JC, Eilu P, Martinsson O et al (2005) Precambrian geodynamics and ore formation: the Fennoscandian Shield. Ore Geology Reviews 27:273–322

Weihed P, Eilu P, Larsen RB, Stendal H, Tontti M (2008) Metallic mineral deposits in the Nordic countries. Episodes 31:1

The age of the Kleva intrusion, southeast Sweden

Karolina Bjärnborg, Anders Scherstén & Ulf Söderlund
Department of Geology, Lund University, Sölvegatan 12, Lund SE-22362, Sweden

Wolfgang Maier
Department of Geology, University of Oulu, P.O.Box 3000, Oulu FIN-90014, Finland

Abstract. The Kleva nickel-copper mineralization is situated within a gabbro-diorite intrusion on the border between the late Svecofennian rocks of the Oskarshamn-Jönköping belt and rocks of the slightly younger Transscandinavian Igneous Belt (TIB). The sulphides present in the mafic intrusion are pyrrhotite, chalcopyrite, pentlandite and pyrite, occurring as massive mineralization, disseminations and thin, predominantly chalcopyrite-bearing veins. Age determinations of the gabbro-diorite were conducted to determine the age of the mineralization and its regional context. U-Pb analyses of baddeleyite (TIMS) and zircon (SIMS) from the gabbro-diorite and related rocks indicate an age of c. 1.79 Ga for the Kleva intrusion, broadly coeval with the TIB-rocks in the area, but younger than the late Svecofennian rocks. Further studies will help to constrain whether the sulphide mineralization was modified during later alteration, regional tectonism and metamorphism.

Keywords. Kleva, sulphide, gabbro-diorite

1 Introduction

Kleva is a historical Ni-Cu sulphide mine situated within a gabbro-diorite intrusion to the east of Vetlanda in southeast Sweden. The deposit was first discovered in 1697 and copper was mined from the chalcopyrite-bearing rocks. Production was intermittent throughout the lifetime of the mine, but peaked in the 19th century when it was realized that the ore has relatively high nickel contents. The mine closed at the beginning of the 20th century and is today open for tourists.

The sulphide association (pentlandite, chalcopyrite, pyrrhotite and pyrite) at Kleva is typical of magmatic sulphides in mafic and ultramafic igneous rocks (e.g. Naldrett 1989; Arndt et al. 2005) and is thus considered to be of primary magmatic origin.

There are around 30 Proterozoic Ni-Cu deposits associated with mafic rocks in Sweden (Nilsson 1985). These occur in three main areas; the Skellefte field, the Norrbotten region and the Bergslagen region. The deposits are usually small, and are hosted mainly by mafic sills, dykes, stocks and minor plutons. Some are hosted by layered intrusions and a few occur in tectonized mafic lenses within paragneiss. In southeast Sweden two deposits of this kind are known; Kleva and the layered intrusion in Virserum, southeast of Kleva.

The present project concentrates on two main aspects; (i) characterization of the composition of the mineralization and its host rocks, and (ii) Determination of the age of the intrusion and the sulphides, in order to be able to place the mineralization into the regional geological framework. Here we present the geochronological results that have been produced so far.

1.1 Regional geology

The Kleva intrusion (Fig. 1) is located near the boundary between the late Svecofennian southeast-trending Oskarshamn-Jönköping belt (OJB; Mansfeld et al., 2005) and slightly younger rocks of the Transscandinavian Igneous Belt (TIB). The OJB rocks commonly show foliation in ENE-WSW to E-W orientation, and are metamorphosed at low to intermediate grade. The TIB- as well as the OJB rocks show traces of the WNW-ESE to E-W shear zones that have affected the area (e.g. Persson 1989; Mansfeld et al. 2005).

The Oskarshamn-Jönköping belt consists of intrusive (commonly calc-alkaline), volcanic and sedimentary rocks of maximum ages of c. 1.83-1.82 Ga (Wik et al. 2003; Mansfeld et al. 2005) and the area is thus referred to as late Svecofennian. The belt is considered to have formed during subduction along the southwestern margin of a Svecofennian continent (Mansfeld et al. 2005). South of Kleva the supracrustal rocks are interlayered and intruded by magmatic rocks of various ages (Persson 1989). Numerous base metal mineralizations are known within this area. Apart from the Kleva and Virserum deposits there are e.g. the Fredriksberg Cu-Zn-Pb sulphide mineralization hosted by metavolcanic rocks (Sundblad et al. 1997), the Sunnerskog Cu-Wo-Mo skarn hosted by metagreywacke (Persson 1989), and the Ädelfors tectonically related gold-bearing quartz veins hosted by mafic metavolcanics (Gaál and Sundblad 1990; Sundblad 2003).
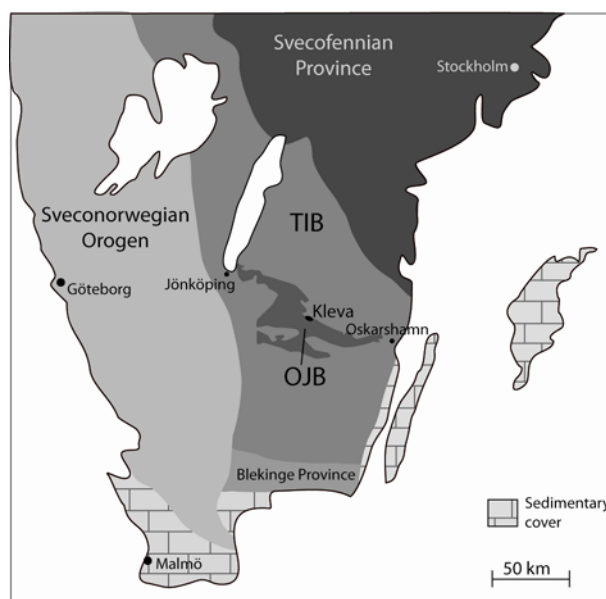
Figure 1. Rough sketch of the main geologic units in southern Sweden, after e.g. Högdahl et al. (eds) 2004 and Mansfeld et al. 2005, with the location of Kleva indicated.

Figure 2. The gabbro-diorite in Kleva is commonly medium grained but varies both in texture and mineral composition.

Figure 3. Outcrop showing fine-grained inclusions within the medium grained gabbro-diorite.

Felsic intrusive and extrusive rocks dominate the Transscandinavian Igneous Belt, although subordinate mafic units do occur. The TIB stretches from northern Norway to southeastern Sweden and, although varying in characteristics, these rocks are commonly alkali rich and porphyritic (e.g. Gorbatschev 2004). These rocks crystallised between 1.85 and 1.67 Ga in two or three magmatic episodes (Gorbatschev 2004), with younger rocks predominantly occurring in the south. To the north of the Kleva intrusion the TIB-related rocks are 1.81-1.79 Ga (Vimmerby batholith; Mansfeld 2004).

1.2 The Kleva intrusion

The intrusion is slightly elongate along a northwest direction, corresponding well to the general structural trend of the area. The rocks are mostly medium grained, but there is considerable heterogeneity with respect to texture and mineral composition (Fig. 2). The main minerals are amphibole, plagioclase and mica with minor amounts of Fe-Ti-oxides, sulphides, apatite, and quartz. The amphibole might be both of magmatic and metamorphic origin (Eichstädt 1887). In the central parts of the intrusion more unaltered rocks can be found, with inclusions of orthopyroxene and clinopyroxene preserved within amphibole. The petrologic variations within the intrusion have been discussed by previous authors. For example, Tegengren (1924) distinguishes a central pyroxene-bearing gabbro from amphibole-bearing gabbro-dioritic rocks.

Plagioclase is predominantly of andesine composition (An c. 30-50%). In the central parts of the intrusion, plagioclase contains abundant oxide needles giving it a dark grey colour; otherwise it is commonly light grey and altered with microscopic inclusions that most probably consist of saussurite.

The intrusion hosts numerous fine grained greenish to grey inclusions of probable supracrustal derivation. The inclusions are commonly angular and with sharp boundaries ranging in size from a few cm to 50 m (Fig. 3). Numerous granite dykes cut the intrusion and associated rocks. These dykes are sometimes pegmatitic and are found within the main gabbro in the mine.

1.3 The sulphide mineralization

While in production, massive sulphide and disseminated sulphide mineralization were mined from the central parts of the Kleva hill. According to historic sources (e.g. Tegengren 1924) the massive pyrrhotite dominated ore bodies occurred as irregular, steeply dipping lenses. The massive ore consists of pyrrhotite, granular pentlandite, chalcopyrite, rounded grains of magnetite and minor pyrite. There are numerous rounded silicate inclusions within the matrix of the massive sulphide samples.

There are also massive chalcopyrite-rich parts, up to a few centimetres thick. These contain chalcopyrite, pyrrhotite with granular pentlandite, coarse pyrite and rounded grains of magnetite. The gabbro-diorite (Fig. 4) contains disseminated chalcopyrite, pyrrhotite with flames and granules of pentlandite, minor pyrite and magnetite with ilmenite intergrowths (lamellae and interconnected granules). The pentlandite is commonly altered into violarite. The amount of sulphides varies across the intrusion. However, the rich disseminated type of mineralization within the gabbro-diorite, and the vein-style mineralization, is more or less restricted to the mined part of the intrusion.

Minor sulphide mineralizations have been observed in the fine-grained varieties elsewhere in the intrusion. In
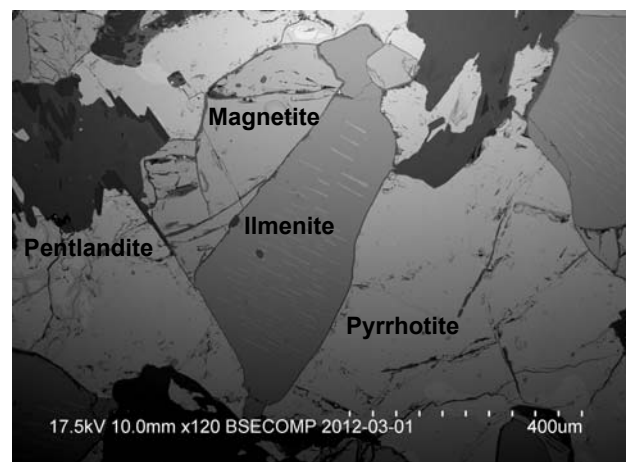
Figure 4. SEM-BSE image of the opaque phases within a disseminated type mineralized sample.

current outcrops of the intrusion very few sulphides are visible to the naked eye.

Tegengren (1924) and other authors have discussed a possible connection between the mineralized parts of the intrusion, especially the massive ore, and hydrothermally related structures that are present within the mine.

2 Age determinations

Previous age estimates of the Kleva gabbro-diorite have been made by Magnusson (1970), and recalculations of the K-Ar age (Wilson and Sundin 1979) yielded an age of 1.585 Ga. Given the geologic setting of the intrusion, it should be much older, and the date by Wilson and Sundin (1979) may represent some level of metamorphic disturbance of the K-Ar system.

Baddeleyite was separated from a well-preserved gabbro-diorite sample from the central part of the intrusion. The baddeleyite crystals are rare, but two 25 μm grains were chosen for analysis. U-Pb TIMS analyses at the Museum of Natural History, Stockholm, of the grains yielded a minimum age of c. 1.79 Ga for the crystallization of the baddeleyite.

In addition, zircon was separated from a gabbro-diorite outcrop in the outer part of the Kleva intrusion and from a granite vein cutting the mafic fine-grained units considered to be related to the intrusion. The zircon samples were dated at the NORDSIM ion-microprobe facility at the Museum of Natural History, Stockholm, and both the granitic zircon and the gabbro-dioritic zircon yield an age of c. 1.79 Ga.

3 What is the age of the mineralization?

All age determinations made in this study show that the age of the gabbro-diorite is c. 1.79 Ga, which corresponds to the TIB-related magmatism within the area, rather than the ages of the OJB-related rocks. However, whether the OJB is an early phase of the TIB-magmatism in the area, or these two groups constitute separate magmatic episodes is not fully understood (c.f. Mansfeld et al. 2005, Wik et al. 2003, Andersson et al. 2004).

The disseminated type mineralization is assumed to be magmatic, and can thus be regarded as coeval with the crystallization age of the baddeleyite and zircon, i.e. 1.79 Ga. However, it remains debatable whether the massive type Ni- and Cu-ore is purely magmatic or if it formed by post-magmatic remobilisation. To fully understand the processes within the intrusion leading to the sulphide mineralization, further studies are in progress.

Acknowledgements

References

Andersson UB, Sjöström H, Högdahl K, Eklund O (2004) The Transscandinavian Igneous Belt, evolutionary models. In: Högdahl K, Andersson UB, Eklund O (eds) The Transscandinavian Igneous Belt (TIB) in Sweden: a review of its character and evolution. Geological Survey of Finland, Special Paper 37:9-15

Arndt NT, Lesher CM, Czmanske GK (2005) Mantle-derived magmas and magmatic Ni-Cu-(PGE) deposits. Economic Geology 100th Anniversary Volume. pp. 5-23

Eichstädt FR (1887) Pyroxen och amfibolförande bergarter från mellersta och östra Småland. I. Systematisk-petrografisk undersökning. Bihang till Kungliga Svenska Vetenskaps-akademiens handlingar band 11, no. 14: 1-123

Gaál G, Sundblad K (1990) Metallogeny of gold in the Svecofennian Shield. Mineralium Deposita 25: S104-S114

Gorbatschev R (2004) The Transscandinavian Igneous Belt – Introduction and Background. In: Högdahl K, Andersson UB, Eklund O (eds) The Transscandinavian Igneous Belt (TIB) in Sweden: a review of its character and evolution. Geological Survey of Finland, Special Paper 37:9-15

Magnusson NH (1970) Atlas över Sverige 5-6. AB Kartografiska institutet, Stockholm

Mansfeld J (2004) The Småland-Värmland Belt in southeastern Sweden. In: Högdahl K, Andersson UB, Eklund O (eds). The Transscandinavian Igneous Belt (TIB) in Sweden: a review of its character and evolution. Geological Survey of Finland, Special Paper 37:20-21

Mansfeld J, Beunk FF, Barling J (2005) 1.83-1.82 Ga formation of a juvenile volcanic arc – implications from U-Pb and Sm-Nd analyses of the Oskarshamn-Jönköping Belt, southeastern Sweden. GFF 127:149-157

Naldrett AJ (1989) Magmatic Sulfide Deposits. Oxford University Press Inc., Oxford

Nilsson G (1985) Nickel-copper deposits in Sweden. In: Papunen H, Gorbunov GI (eds) Nickel-copper deposits of the Baltic Shield and Scandinavian Caledonides. Geological Survey of Finland, Bulletin 33:313-362

Persson L (1989) Beskrivning till berggrundskartorna Vetlanda SV och SO. Sveriges Geologiska Undersökning Af 170 och 171.

Sundblad K, Mansfeld J, Särkinen (1997) Palaeoproterozoic rifting and formation of sulphide deposits along the southwestern margin of the Svecofennian Domain, southern Sweden. Precambrian Research 82:1-12

Sundblad K (2003) Metallogeny of Gold in the Precambrian of Northern Europe. Economic Geology 98:1271–1290

Tegengren FR 1924. Sveriges ädlare malmer och bergverk. Sveriges Geologiska Undersökning (SGU) Ca 17: 349-353

Wik NG, Bergström U, Claeson D, Juhojuntti N, Kero L, Lundqvist L, Petersson, J, Sukotjo S, Wedmark M, Wikman H (2003) Projekt Småland regionalt berg. In: Delin H (ed) Berggrundsgeologisk undersökning. Sammanfattning av pågående verksamhet 2002. SGU Rapporter och meddelanden 112:96-116

Wilson MR, Sundin NO (1979) Isotopic age determinations on rocks and minerals from Sweden 1960-78. SGU Rapporter och meddelanden 16

Structural evolution of the apatite-iron oxide deposit at Grängesberg, Bergslagen, Sweden

Karin Högdahl, Valentin Troll
Dept. Earth Sciences, CEMPEG, Uppsala University, Uppsala, Sweden

Katarina Persson Nilsson, Erik Jonsson
Geological Survey of Sweden, Uppsala, Sweden

Abstract. The apatite-iron oxide deposits in the Grängesberg area are the largest iron mineralisation in central and southern Sweden. These deposits are the only known of this type in the Palaeoproterozoic Bergslagen province. The mineralisations occur along a c 40 km long zone and at Grängesberg they appear as narrow, elongated lenses dipping 50-70° to the SE and reach a depth of at least 1700 m. Competence contrasts between different rock types, including the mineralisation, have been a controlling factor for the structural evolution (D_1-D_3) throughout the orogeny. This is particularly valid for D_2, which is related to oblique top-to-NW dip-slip reverse shear. A large part of the strain has been accommodated by less competent phyllosilicate-altered rocks. Strain partitioning explains the elongated lens-shape of the mineralisation, and is further emphasized by the structures around the lenses. Towards the edges of these lenses, asymmetric F_2-folds with opposite vergence have formed and S>L fabric prevails at the lens crests. At the necks, the fabric is characterised by a strong stretching lineation. The mineralisation has also acted as a competent indenter during D_2 reverse shear and controlled the localisation of shear zones emplacing an 1895±3 Ga coarse-grained granitoid tectono-stratigraphically on top of the mineralisation.

Keywords. Apatite-iron oxide deposit, Grängesberg, strain partitioning, lens-tectonics, Bergslagen, Sweden

1 Introduction

The Palaeoproterozoic Kiruna-type apatite-iron oxide deposit in Grängesberg (Jonsson *et al.,* 2010) is the largest iron mineralisation in the classic Bergslagen ore province, south central Sweden. Bergslagen hosts thousands of variably sized banded iron formation and skarn-type magnetite deposits, but the only known apatite-iron oxide mineralisations occur in the western part of the province. They are located along a 40 km, NE-SW trending zone from Grängesberg through Blötberget to Idkerberget in the NE (Fig. 1). The metavolcanic host rocks are also anomalous to the prevailing felsic metavolcanic rocks in the Bergslagen province by being dacitic to andesitic in composition. It has been argued that these rocks, and thus possibly also the apatite-iron oxide deposits, represent a lower stratigraphic unit in this vast volcanic-sedimentary succession (Geijer & Magnusson 1944).

The origin of apatite-iron oxide deposits has long been debated, including the deposit at Grängesberg and the famous apatite-iron ores at Kiruna-Malmberget in northern Sweden. Recent oxygen (Jonsson *et al.* 2011) and iron isotope studies (Weis *et al.* 2013) suggest that at least the Grängesberg deposit was formed in a high-temperature magmatic system.

The mines at Grängesberg produced 152 Mt ore with an average of 58% Fe and 0.81% P, from the beginning of the 20th century until they closed in 1989. The deposit is now targeted for re-opening, hence a structural analysis of the ore is timely.
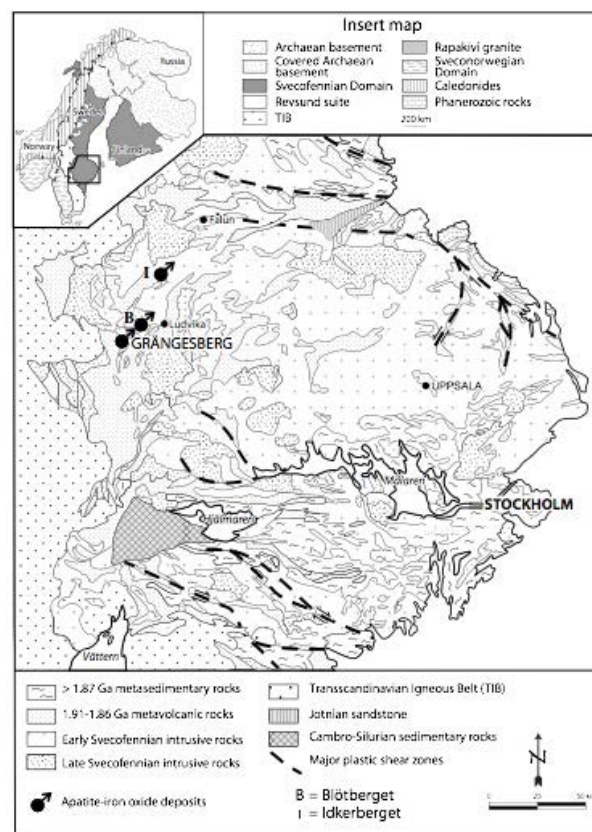
Figure 1. Simplified geological map of the Bergslagen province, showing the location of the apatite-iron oxide deposits (modified after Stephens *et al.* 2009).

2 Geological setting

The Bergslagen province belongs to southern part of the 1.9-1.8 Ga Svecokarelian (Svecofennian) orogen. The oldest rocks in this part of the orogen comprise a volcanic-sedimentary succession and coeval intrusive

rocks, interpreted to have formed in a back-arc caldera setting inboard an active continental margin (Allen *et al.* 1996). The lowest stratigraphic units are exposed in the eastern part of the province, and consist of metagreywackes and 1.90 Ga felsic metavolcanic rocks. The upper part of the succession is found in the west with c. 1.88 Ga volcanic rocks that are overlain by metasedimentary rocks deposited during the waning stage of the volcanic activity (Allen *et al.* 1996).

Overall, metavolcanic rocks with rhyolitic to rhyodacitic compositions dominate, locally intercalated with marble horizons and associated skarns. Mafic and intermediate metavolcanic rocks are subordinate. The majority of the mineralisations, including Zn-Pb-Ag-(Cu-Ag) sulphides and iron oxide deposits, are hosted in the volcanic-sedimentary succession.

The older, metamorphosed intrusive rocks range from granite to gabbro, and younger granites and associated pegmatites were emplaced at the later stages of the orogenic evolution. During the orogeny the rocks were subjected to polyphase deformation and upper greenschist to amphibolite facies metamorphism at 1.85-1.82 Ga (e.g. Stephens *et al.* 2009). On a regional scale, there are two generations of folds. The first generation are tight to isoclinal, upright folds refolded by plunging fold with steep axial surfaces (e.g. Beunk & Kuipers 2012). In general, all foliations including bedding are sub-parallel with a steep to moderate dip. At a later stage, deformation is localised to high-strain belts and ductile deformation zones, mainly with NW-SE dextral, oblique strike-slip kinematics (Stephens *et al.* 2009).

2.1 The geology of the Grängesberg area

The dominating rocks in the Grängesberg area are rhyolitic to dacitic metavolcanic rocks and comprise pyroclastic as well as subvolcanic units (Fig. 2).
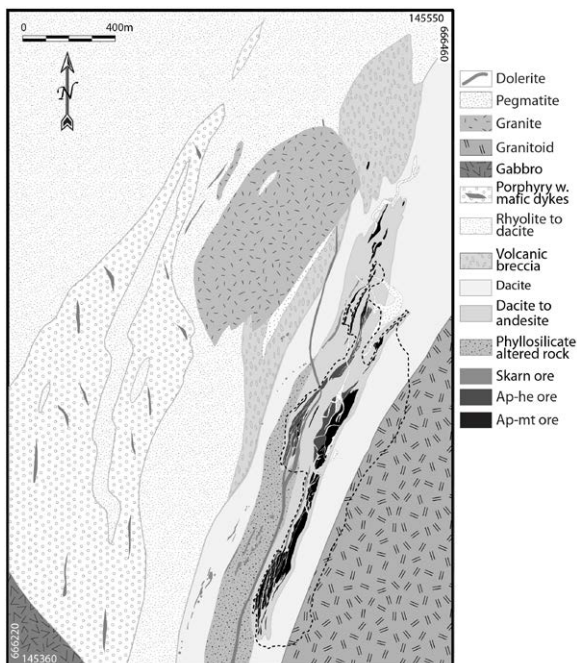
Figure 2. Geological map of the Grängesberg area. The stippled line outlines the Export field open pit. Based on recent fieldwork and Geijer & Magnusson (1944).

The pyroclastic rocks are locally banded or laminated with occasional skarn horizons. Massive beds and feldspar porphyric rocks are common in addition to various types of volcanic breccias. A competent feldspar porphyric dacite, interpreted to be subvolcanic, has had a major effect on the local structural evolution.

There are two different types of granitoids in the area. A fluorite-bearing leucogranite occurs in the footwall to the northwest of the ore. In the hanging-wall to the SE there is a coarse-grained gneissic granitoid hosting mafic enclaves.

The host rocks to the apatite-iron oxide ore are andesitic to dacitic in compositions. At the contact to the ore the host rock is severely altered and contains phyllosilicate-rich assemblages (*sköl*) with variable amounts of amphiboles, iron oxides and fluorapatite. Phyllosilicate-rich zones are also found within the ore that are separated into closely spaced, elongated lens-shaped bodies. The ore is also transected by rhyolitic dykes and sills that are interpreted to be related to the more felsic metavolcanic rocks outside the ore zone.

3 Structural evolution

Three ductile deformation episodes, D_{1b}-D_3, have been recognised in the Grängesberg area. The very first deformation phase in Bergslagen, D_{1a}, is related to early synmagmatic extension (Allen *et al.* 1996; Beunk & Kuipers 2012) that might have caused ductile deformation in the Grängesberg area. As ductile structures that can be correlated to this episode have not been identified here D_{1a} is not discussed further.

The most apparent structural elements are different generations of foliation (S_0-S_2), intersection lineations, and locally a steep L_2 stretching lineation. In general, the angles between the S_0, S_1 and S_2 foliations are small and their intersection lineations are steep.

3.1 Ductile deformation D_{1b}

The structures associated with the first deformation phase (D_{1b}) appear often as a vague, steep, crenulated foliation and as an intersection lineation mainly in phyllosilicate-rich rocks.

F_1 folds have not been found in the Grängesberg area but exist in the overlying metasedimentary unit that are exposed as a disrupted belt further to the east. These folds are tight to isoclinal with a shallow plunging fold axis and steep axial plane (Fig. 3A). The F_1 folds here are overprinted by S_2 foliation at high angle to S_1.

3.2 Ductile deformation D_2

The most obvious structure in the Grängesberg area is an S_2 foliation found in all rock types. Intersection lineation between S_2 and S_0-S_1 is often well developed and occasionally cause a pencil-like cleavage that is parallel to the L_2 stretching lineation. Competence contrasts between the various rocks have had a strong influence on the structural evolution during D_2. The granitoids, the subvolcanic porphyry and the ore itself have acted as

of F_2 folds in the footwall indicate that they are controlled by the development of tectonic lenses.

The coarse-grained granitoid in the hanging-wall has a steep to moderately plunging L>S fabric with occasional kinematic indicators showing top-to-NW movements. This is in accordance with localised shear zones in the hanging-wall metavolcanic rock located further to the west. These zones show oblique, sinistral dip-slip shear with a top-to-NW vertical component emplacing the granitoid on top of the ore.

3.3 Ductile deformation D_3

D_3 structures were formed at post-peak metamorphic conditions by roughly N-S convergence at a late stage of the Svecokarelian orogeny. On a large scale (tens of km´s), the open F_3 folds are clearly visible on aeromagnetic anomaly maps where narrow zones of particularly magnetite-rich mineralisations appear as undulating NE-SW-trending anomalies. On a local scale, open folds with amplitudes of about 100 m can be observed in the walls of the Export field open pit at Grängesberg (Fig. 2) on the footwall side of the ore. However, no other structures (i.e. foliation or lineation) related to D_3 have been formed. Therefore, it cannot be excluded that open folds at Grängesberg are related to the lens tectonics of D_2 rather than to D_3.

4 Geochronology

The coarse-grained gneissic granitoid to the east of the apatite-iron oxide mineralisations (Fig. 2) is tectonically emplaced, i.e. thrust, on top of the ore. U-Pb zircon SIMS analysis of this rock yields a concordant age at 1895±3 Ma (Fig. 4), showing that it was formed at an early stage of the Svecokarelian orogeny and that it is coeval with the 1.90-1.88 Ga volcanic activity in Bergslagen.

Figure 3. A) An F_1-synform with shallow plunging fold axis (arrow; 5-10° to the S) in a metasedimentary unit located to the SE of Grängesberg. **B)** Strong L_2 stretching lineation in an ore breccia at the tapering edge of an iron oxide lens in the footwall. **C)** Asymmetric, F_2 fold at the thinning part of the same ore lens as in A. Photograph viewed from above down.

competent bodies, while the *sköl*-zones have accommodated a large part of the strain.

The lens-shape appearance of the ore, and e.g. the leucogranite, is most likely an effect of D_2. Prolate strain is focused at the tapering edges of the competent bodies, where stretching lineation is strong (Fig. 3B). Oblate strain prevails at the lens crests, and at the narrowing parts there are tight, asymmetric domical folds with opposite vergence (Fig. 3C). These are only found in the footwall as the immediate hanging-wall host-rock at the surface has been mined away. The location and attitude

Figure 4. Tera-Wasserburg concordia diagram showing a concordant U-Pb zircon SIMS age at 1895±3 Ma for the coarse-grained gneissic granitoid.

5 Discussion and conclusions

Throughout the three ductile deformation episodes, the structural development was strongly influenced by the competence contrasts between the various rock types. The foliations are sub-parallel (S_0-S_2) and have a general strike in NE-SW and a dip of 50-70° to the SE. The apatite-iron oxide ore reaches a depth of at least 1700 meter and appears as a number of narrow (20-100 m wide) semi-coherent lenses separated by frequent *sköl*-zones. Due to the competent behaviour of the ore, strain was partitioned to these zones and along the outer margins of the ore lenses.

Structures associated with D_{1b} (and F_1) are discrete and recognised by steep S_0 surfaces in felsic metavolcanic rocks and by a crenulated foliation in phyllosilicate bearing layers. The continuation of the ore along dip to great depths implies that it was resistant to folding, and that it is present at one limb of a large-scale F_1 fold only. Continuous convergence, transitioning into D_2, rotated and flattened regional F_1 folds in the host-rock, which became tight to isoclinal. The D_2 structures in Grängesberg are all related to reverse oblique shear emplacing the 1895±3 Ma coarse-grained granitoid with L>S D_2-fabric on top of the ore zone (Fig. 5). During this reverse movement the competent ore acted as a ramp and thus controlled the localisation of the thrust zones.
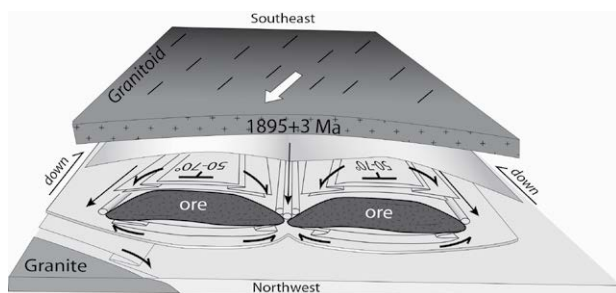
Figure 5. Tectonic model of the apatite-iron oxide deposit at Grängesberg. The model shows the lens-shaped geometry of the ore, the location of strong stretching lineation and opposite verging F_2 folds. The view is down dip from northwest.

Below the coarse-grained granitoid, at lower tectonostratigraphic levels competent rocks were affected by boudinage and became lens-shaped, while asymmetric, occasionally domical F_2 folds have developed in less competent rocks towards the narrowing parts of these lenses. Along strike of individual ore lenses, these folds have opposite vergence on either side, and similar fold geometries are found at the eastern margin of the leucogranite (Fig. 5). In pinch areas, between the lenses, stretching lineation is strong, and parallel to both F_2 fold axis and to the stretching lineation in the coarse-grained granitoid. At the lens crests S>>L fabric prevails that suggests a large pure shear component at these sites.

Even though the ore bodies have withstood most of the ductile deformation their width is most likely modified owing to the abundant *sköl*-zones within the

deposits. Inevitably these must have accommodated part of the oblique D_2 shear strain thus explaining the small width-depth (and length) ratio of the mineralisation.

The locations of prolate and oblate strain emphasize the role of competence contrast for the structural evolution particularly during D_2 in the Grängesberg area. The competence contrast is central for strain partitioning and the development of the lens-shape geometry of not least the ore bodies, and controls the shape and attitude of F_2 folds, sites of shear and stretching. In addition, the localisation of the apatite-iron oxide deposits within a thrust supports the suggestion that the andesitic-dacitic host rock belongs to the lower part of the volcano-sedimentary succession and that the contact to the more common felsic metavolcanic rocks is tectonic.

D_3 has a minor impact on the structural style, but during this deformation the undulating, lens-shape geometry in the area became accentuated.

Acknowledgements

References

Allen RL, Lundström I, Ripa M, Simenov A, Christofferson H (1996) Facies analysis of a 1.9 Ga, continental margin, back-arc, felsic caldera province with diverse Zn-Pb-Ag-(Cu-Au) sulfide and Fe oxide deposits, Bergslagen region, Sweden. Econ Geol 91: 979-1008

Beunk F, Kuipers G (2012) The Bergslagen ore province, Sweden: Review and update of an accreted orocline, 1.9-1.8 Ga BP. Precam Res 216-219: 95-119

Geijer P, Magnusson NH (1944) De mellansvenska järn-malmernas geologi. Sver Geol Unders Ca 35: 1-654

Jonsson E, Nilsson KP, Hallberg A, Högdahl K, Troll VR, Weis F, Harris C (2011) Oxygen isotopes and geochemistry of Palaeoproterozoic Kiruna-type deposits in the Bergslagen province, central Sweden. Abstract volume, SGA biennial meeting 2011, Antofagasta, Chile: 494-496

Jonsson E, Nilsson KP, Hallberg A, Högdahl K (2010) Palaeopreoterozoic apatite-iron oxide deposits of the Grängesberg area: Kiruna-type deposits in central Sweden: In: Nakre HA, Harstad AO, Haukdal G (eds), NGF abstracts and proceedings, 1. 29th Nordic Geological Winter Meeting, 11-13/1-2010, Oslo, Norway: 88-89

Stephens MB, Ripa M, Lundström I, Persson L, Bergman T, Ahl M, Wahlgren C-H, Persson P-O, Wickström L (2009) Synthesis of the bedrock geology in the Bergslagen region, Fennoscadian Shield, south-central Sweden. Sver Geol Unders Ba 58: 1-259

Weis F, Troll VR, Jonsson E, Högdahl K, Barker A, Harris C, Nilsson KP (2013) Oxygen and iron isotope characteristcis of apatite-iron-oxide ores from central Sweden. This volume

Uranium mineralization in the Alum Shale Formation (Sweden)

Andreï Lecomte, Michel Cathelineau, Raymond Michels
GeoRessources, Université de Lorraine, CNRS, CREGU, Boulevard des Aiguillettes B.P. 239 F-54506 Vandoeuvre lès Nancy, France

Marc Brouand
AREVA, 1 place Jean Millier F-92084 Paris La Défense Cedex, France

Abstract. The Alum Shale Formation is a metalliferous black shale, deposited on the Baltoscandian platform between middle Cambrian and early Ordovician. These black shales are of particular economic interest. Indeed, with their relatively high uranium content (200-300 ppm) and their wide distribution from Norway to Estonia, Scandinavian alum shales constitute a great potential resource of uranium for the next decades. In northern Sweden, the Alum Shale Formation was duplicated and affected by metamorphism and hydrothermal activity during Caledonian orogeny. On the contrary, in Southern Sweden the sedimentary sequence remained almost unmodified. The influence of the Caledonian orogeny is recorded in sulphide paragenesis, with plastic deformation in the shale, fracturing and cataclasis of synsedimentary/diagenetic pyrites, followed by chalcopyrite and sphalerite precipitation. In Scandinavian alum shales, uranium mineralization mainly occurs as a complex assemblage of phosphate-silicates U-Si-Ca-P (±Ti ±Zr ±Y). Although similar U concentrations are found in all alum shales occurrences, it is difficult to determine the mineralogical expression of uranium in southern Sweden samples.

Keywords. Uranium, Alum shales, Organic matter, Sweden

1 Introduction

Lower Palaeozoic black shales extend over most of northern Europe, from Norway to Estonia. These sediments were deposited on the Baltoscandian platform during an interval of great tectonic stability (Andersson et al., 1985).

In particular, the Alum Shale Formation is an organic-rich marine sequence deposited over present Scandinavia between middle Cambrian and early Ordovician. The term alum shale refers to the alum salt $KAl(SO_4)_2 \cdot 12H_2O$ that was extracted from this black shale over 300 years ago.

As many other black shales deposited in marine environments, alum shales contain high metal concentration compared to ordinary shales, especially Ni, Mo, Co, Cu, Zn, U, V, As, Se, Ag, Au and PGE (Vine & Tourtelot, 1970; Holland, 1979; Wignall, 1994). Nevertheless, Scandinavian alum shales are of particular interest because of their relatively high uranium content (200-300 ppm) and their wide extension. Therefore, they constitute a great potential resource for the next decades.

The work presented here is part of a comprehensive study on uranium mineralization throughout Sweden, to assess the influence of organic content, oil migration, metamorphism and hydrothermal activity on uranium mineralogical expression.

2 Geological setting

In Sweden, the Alum Shale Formation can be split in three geographical and structural provinces (Fig. 1): (a) parallochthonous alum shales along the Caledonian Front duplicated and affected by metamorphism and hydrothermal activity during Caledonian orogeny (420-400 Ma); (b) allochthonous units in Sweden and Norway metamorphosed to greenschist facies grades (Sundblad & Gee, 1984); (c) autochthonous platform cover units (southern Sweden) lying on the Proterozoic basement, unaffected by Caledonian orogeny.

Scandinavian alum shales are dominated by organic-rich (up to 20%) marine black shales, with variable proportions of grey shales and silts beds, limestones and carbonate concretions. The latter generally trapped large amounts of hydrocarbons (Andersson, 1985; Thickpenny, 1984). In the upper Cambrian, small lenses of organic matter (kolm) occur and are often highly uraniferous (up to 5000 ppm).

This marine sequence was deposited between middle Cambrian and early Ordovician (Tremadoc) on a crystalline Palaeoproterozoic basement. The sedimentation took place in a shallow-water epicontinental basin bordered by the Tornquist Sea to the South and the Iapetus Ocean to the North and West (Scotese & McKerrow, 1990).

The Alum Shale Formation is generally 15-35 meters thick but extremely variable, from 2 meters on Öland to 95 meters in Skåne. In the Caledonides, where the formation is duplicated by thrust sheets, the thickness reaches up to 180 meters (Andersson et al., 1985).

3 Mineralization

3.1 Sulphide paragenesis

In Swedish alum shales, there is significant sulphide mineralization (Fig. 2), sometimes associated with uranium. Five types of sulphides are present: pyrite, pyrrhotite, chalcopyrite, sphalerite and galena. Several generations of pyrite have been identified. The first generation corresponds to framboidal pyrites (scattered in the shale or gathered in clusters), and small euhedral or subhedral crystals generally forming beds

emphasizing the stratification of the shale. This generation is related to the precipitation of pyrite during sedimentation or early diagenesis, probably associated with bacterial reduction of sulfates.
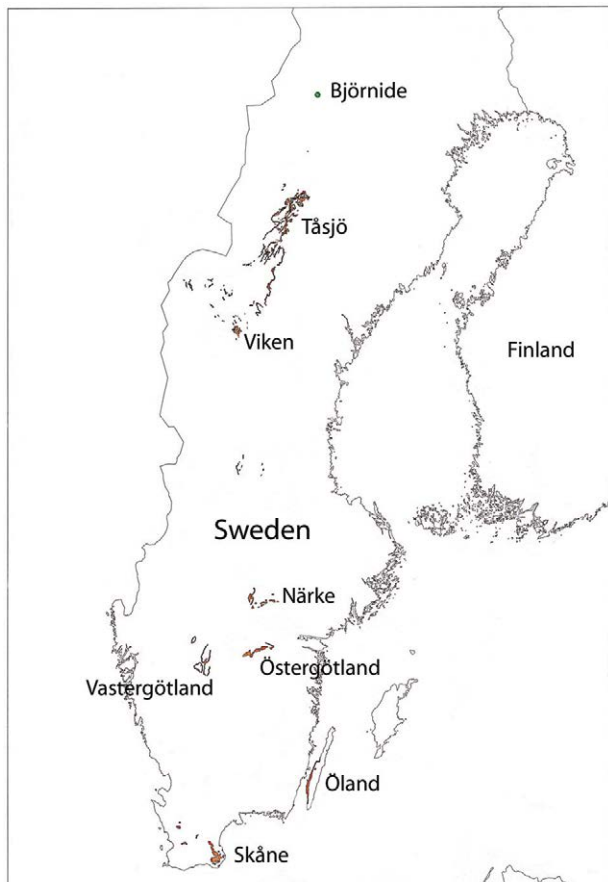
Figure 1. Alum shale occurrences in Sweden

The second generation occurs as beds or nodules of massive pyrite. When looked in detail, they often correspond to recrystallized clusters of subhedral crystals and framboids. The third generation corresponds to the development of large crystals dispersed in the shale or growing on beds or nodules (second generation). In some cases, the shale laminae are deformed around the crystal. Therefore, this pyritization stage probably occurred at the end of sedimentation or early diagenesis, before important compaction of the sediment. Finally, the fourth generation is late and corresponds to the pyrite filling of nodules.

In alum shales along the Caledonian Front, the first four generations are the same as those in southern Sweden, but were strongly affected and modified by metamorphism during the Caledonian orogeny. It is thus possible to observe the evidences of: (a) an episode of intense fracturing that affected the whole black shale. Fractures are filled with pyritic cement and overgrowths, and calcite. These overgrowths do not grow only in fractures but also on previous generations of pyrite affected by cataclastic deformation; (b) plastic deformation of pyrite beds, which were initially parallel to lamination; (c) pressure-dissolution figures, with interpenetration of edges on small euhedral pyrite crystals; (d) precipitation of chalcopyrite and sphalerite after the fracturing stage.

According to previous work in the Norwegian Caledonides (Barrie et al., 2010), plastic deformation would start when the metamorphism reached its highest level (greenschist facies, temperatures around 400 °C), with pressure-dissolution mechanisms and deformation of pyrite beds. Then during retrograde metamorphism, changes in pressure and temperature led to intense fracturing of the largest pyrites (cataclasis). Finally, in the last stages of metamorphism, chalcopyrite and sphalerite crystallized within fractures. The latest generation of pyrite (euhedral overgrowths) is synchronous with chalcopyrite and sphalerite.

Trace elements analysis in sulphides indicates that very few pyrites are enriched in trace elements. No significant differences in the trace elements content were observed. Therefore, the first four generations of pyrite seem to have crystallized in a similar geochemical environment, which is consistent with precipitation during sedimentation and diagenesis. However, framboids are generally enriched in copper and arsenic unlike euhedral cogenetic pyrites. This feature could be explained by a different crystallization of framboids, more favorable to trap some trace elements. In alum shales from the Caledonian front, pyrites are richer in Ni, As, Se and Cd. However, these enrichments are localized and correspond either to overgrowth zones, or areas of possible reconcentration in early pyrites.
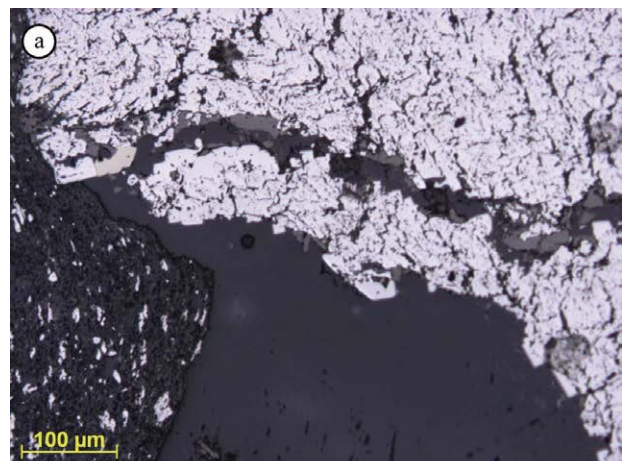
Figure 2. (a) Fractures in pyrite filled with chalcopyrite, bitumen and calcite; (b) framboidal pyrites in shale

It is noteworthy that it is possible to detect small areas enriched in Cu and As within massive pyrites. These zones may be inherited from framboids during recrystallization of primary pyrite.

3.2 Uranium mineralization

In Scandinavian alum shales, uranium mineralization mainly occurs as complex uraniferous phases, associated with organic matter, sulphides or crystals/nodules of hydroxyl(fluor)apatite (Fig. 3). These uraniferous minerals contain U-Si-Ca-P (±Ti ±Zr ±Y) and are interpreted as complex assemblages of uranium phospho-silicates (phospho-coffinite) and hydrated phosphates of Y and Zr. A few uraninites have been found in pyrites. These rare crystals are less than 1 micron large.

Although uranium concentrations remain similar between Northern Sweden and Southern Sweden (around 200 ppm), uranium minerals are hard to detect in unmetamorphosed samples. In the latter, a small part of uranium mineralization consists of an U-Si-Ca-P assemblage surrounded by organic matter and associated with hydroxylapatite nodules.
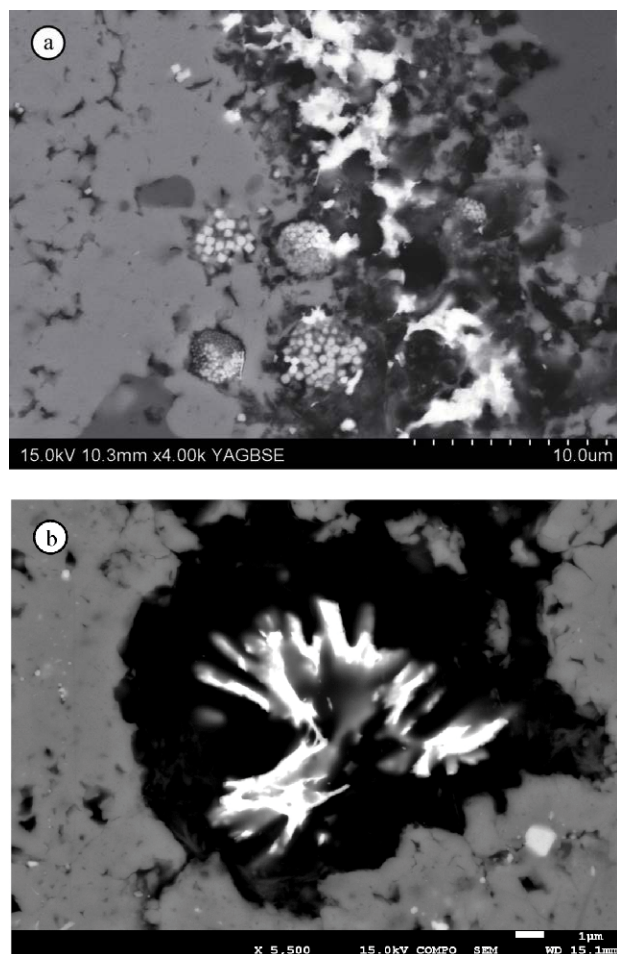
Figure 3. (a) Uranium mineralization as U-Si-Ca-P phases in alum shales along the Caledonian front; (b) rare uranium mineralization in organic matter (southern Sweden)

4 Conclusion

The Alum Shale Formation of Sweden is a metalliferous black shale with a particularly high concentration in uranium. Moreover, it provides an almost continuous sequence from immature/slightly mature to metamorphosed black shale. This temperature/pressure evolution is recorded by sulphide mineralization. Besides, uranium seems to be remobilized by metamorphism/hydrothermal activity from a hardly detectable dispersed U-mineralization (nano-UO_2 or metallic complexes associated with organic matter or calcium phosphates) to a complex assemblage of U-Si-Ca-P (±Ti ±Zr ±Y) phosphate-silicates.

Acknowledgements

References

Andersson A, Dahlman B, Gee DG, Snäll S (1985) The Scandinavian Alum Shales, Sveriges Geologiska Undersökning, Uppsala.

Barrie CD, Boyle AP, Cook NJ, Prior DJ (2010) Pyrite deformation textures in the massive sulphide ore deposits of the Norwegian Caledonides. Tectonophysics 483: 269-286.

Holland HD (1979) Metals in black shales; a reassessment. Economic Geology 74: 1676-1680.

Scotese CR, McKerrow WS (1990) Revised World maps and introduction. Geological Society, London, Memoirs 12: 1-21.

Sundblad K, Gee DG (1984) Occurrence of a uraniferous – vanadiniferous graphitic phyllite in the Köli nappes of the Stekenjokk area, central Swedish Caledonides. Geol. Fören. Stockholm Förh. 106: 269-274.

Thickpenny A (1984) The sedimentology of the Swedish Alum Shales. Geological Society, London, Special Publications 15: 511-525.

Vine JD, Tourtelot EB (1970) Geochemistry of black shale deposits - a summary report. Economic Geology 65: 253-272.

Wignall PB (1994) Black shales. Clarendon Press-Oxford University Press, Oxford-New York.

The mantle-crustal ore-forming systems of the Pechenga ore district (Fennoscandian shield)

K.V. Lobanov, V.I. Kazansky, M.V. Chicherov
The Organization of Russian Academy of Sciences Institute of Geology of Ore Deposits, Petrography, Mineralogy, and Geochemistry (IGEM RAS)

Abstract. The mantle-crustal ore-forming systems of the Pechenga ore district is known for large Cu-Ni ores and smaller occurrences of Pt, U, Au, Pb and Zn. It comprises four superposed systems: plutonic PGE deposits, volcano-plutonic Cu-Ni deposits and hydrothermal U and Au deposits which were formed at different geotectonic conditions in the Karelian and Svecofennian (2.4–1.6 Ga) cycles.

The continental crust in the Pechenga ore district can be divided into an upper heterogeneous and a lower homogeneous zone which differ by the acoustic velocity parameters. The structure and location of Moho was determined from seismic tomography data. Its upper surface is located at the depth of 34-41 km. A minimum depth of 34-36 km was registered below the northern limb of the Pechenga structure which encloses the Cu-Ni deposits. They correspond to the anomaly of seismic tomography data 35-45 km in diameter which is isometric in horizontal plane and can be interpreted as a relic mantle plume. Anomalies with the maximum values of Vp/Vs are revealed above the plume at the boundary between the upper and lower crust at the depth of 20 km. These anomalies indicate previous existing intermediate magma chambers with mafic and ultramafic melts.

Keywords. mantle-crustal ore-forming systems, 3D model, ore deposits and mineralizations

1 Introduction

Correlation of geological, geophysical, and metallogenic data for the border regions between Russia, Norway, and Finland has made it possible to suggest that the Pechenga ore district is an isolated segment of the Pechenga-Imandra-Varzuga metallogenic zone (Fig. 1a, b). In the northeast, the district is bound by the Voron'ya-Kolmosersk fault, in the southeast by the Litsk-Aragubsk fault, in the northwest by the Inari-Kirkenes fault system, and in the southwest by a system of poorly known northwest-trending faults. It should be emphasized that the main tectonic elements of the Pechenga ore district are clearly reflected in the regional gravity field (Fig 1, c).

The Pechenga structure corresponds to a positive gravity anomaly, which embraces both the northern and southern limbs and the adjacent area of the Inari block. Negative gravity anomalies coincide with the Litsk-Aragubsk and Vainospaa granitoid massifs and are symmetric around the positive anomaly. Smaller gravity anomalies are associated with the rheomorphic granitoid domes (Kazansky et al. 1994).

Several ore types can be distinguished within the Pechenga ore district, including the Pechenga and Allarechka Cu-Ni ore fields, the Archaean BIF iron ores of Sydvaranger, the Early Proterozoic PGE-Ni occurrences of Gora Generalskaya and Karikjavr, a variety of Late Archaean to Early Proterozoic U mineralization at Litsevsk, hydrothermal Pb-Zn veins of probable Riphean age, and enigmatic Au-Ag mineralization at deep levels of the SG-3 borehole and at the surface in the South Pechenga structural zone (Gjeddevannet, Poroyarvi, and others).

2 3D Integration model of the Pechenga ore district

The investigation of the Kola Superdeep Borehole was not restricted to the study of the drill core. Its general geological position was also taken into consideration, derived from long-term comprehensive research aimed at the create a 3D model of the Pechenga district. This work was based on specialized documentation of the borehole section and included structural-petrological and petrophysical studies of core samples supplemented by studies of adequate parts of the bedrock surface for correlations with the borehole section and the surface reference profile (Lobanov et al. 2010).

The studies aimed at identifying the relationships between deformation and metamorphism as well as petrophysical properties of rocks and ore deposits. The database consists of 1600 SG-3 core and 2400 samples, collected from the ground surface. Rock density and their Vp anisotropy were used as the main parameters for comparison of the borehole SG-3 section and the reference profile on the surface. The first parameter reflects the rocks' lithology, the second accounts for the intensity of synmetamorphic tectonic deformations. In addition, new age data and morphology of the gravity field of the Pechenga district were considered. Special computer-based programs were used for the parameter calculations. Data for individual samples were compiled for rock types and processed by the weighted average method for the reference borehole section and the surface collected rocks selected for comparison.

The Cu-Ni-bearing Pechenga structure is best studied in the Pechenga ore district. A series of 3D models were proposed in the mid 1980s based on the same geological map of the Pechenga ore field and the SG-3 borehole section. These models consider the Pechenga structure as a graben-syncline, asymmetrical syncline, explosive volcanic center, and continent-continent collision suture zone.
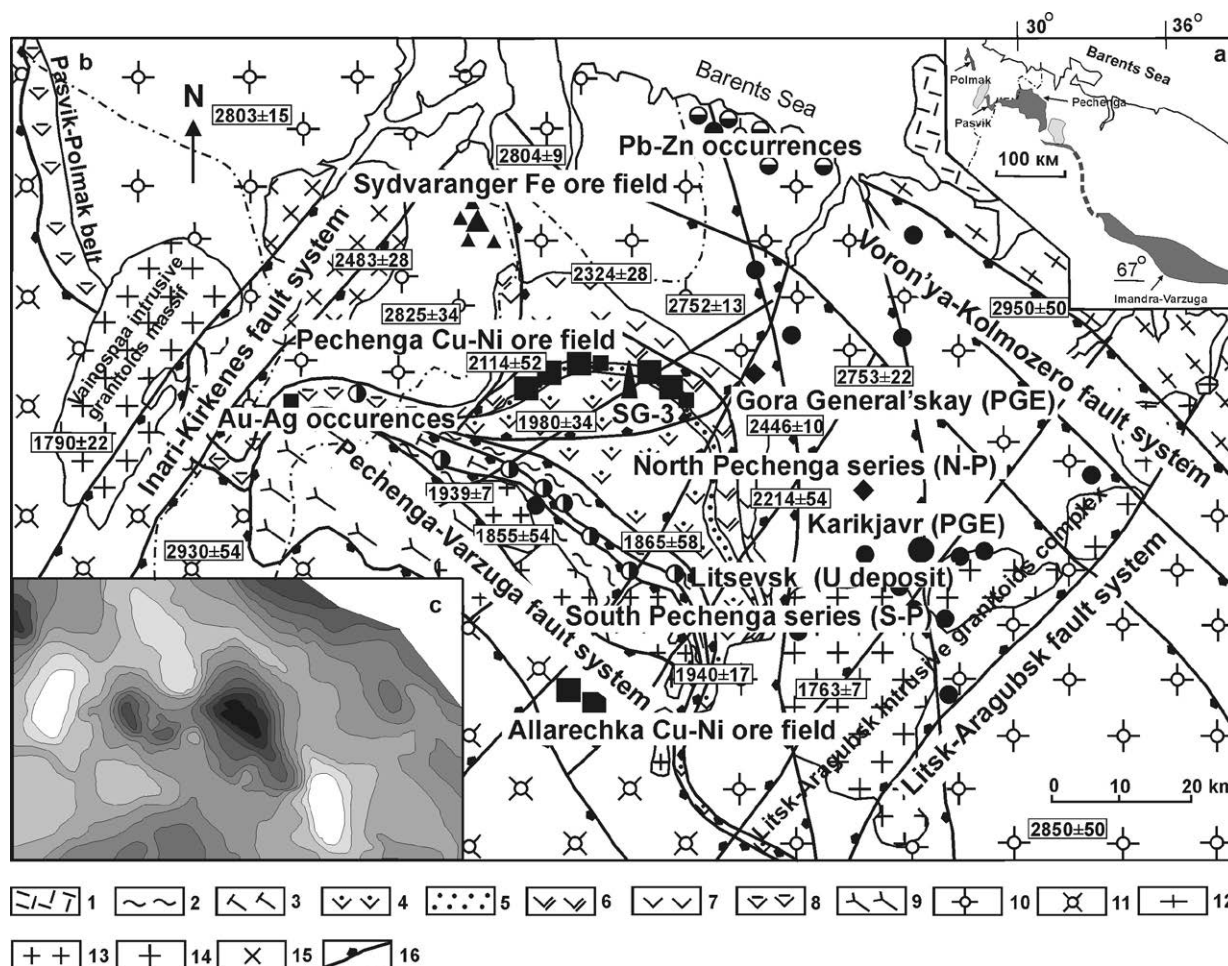
Figure 1. Geographic position (a) and schematic geological map (b) and regional gravity field (c) of the Pechenga ore district (Lobanov et al. 2010).
1 - Late Proterozoic sedimentary rocks; 2-8 - Early Proterozoic. 2-3 – South Pechenga series: 2 - metavolcanic and metasedimentary rocks, 3 - metavolcanic rocks; 4-6 – North Pechenga series: 4 - metabasalts and metapicrites, Pilgujarvi suite, 5 - sedimentary Productive member hosting Ni-bearing gabbro-wherlite intrusions, 6 – metabasalts and metasedimentary rocks (Kolasjoki suite); 7 - metabasalts and metandesites, metasedimentary rocks (Kuetsjarvi and Ahmalahti suites), 8 – South Pechenga and North Pechenga series undivided; 9 - crystalline schists (Tal'ya suite), 10-12 – Archaean: 10 - gneisses, migmatites, granites, amphibolites Kola-Norwegian block, 11 - gneisses, crystalline schists (Inari block), 12 - strongly granitized gneisses (Murmansk block); 13-15 Early Proterozoic granitoids: 13 - rhemorphic granitoids, 14 - intrusive granitoids, 15 - Early granitoid intrusives; 16 – faults.

The computer-based technology allowed revising these alternative models by comparing the observed and calculated gravity profiles passing through the SG-3 site.

Geological constraints of the 3D model, density data and AVp values in the borehole section and on the surface were first used for the reappraisal of the integrated 3D geodynamic model to a depth of 15 km. The reappraisal of the geodynamic model was mainly based on the comparison of observed and calculated gravity profiles along the section going through the SG-3 borehole. The computer-based technology allowed calculation of gravity profiles for various models from the morphology and size of tectonic units and the corresponding average rock densities. In other words, a reverse problem of simulation and fitting of a field caused by an object with known parameters was investigated. In the integrated 3D model, the calculated and observed gravity profiles are in the best agreement with each other.

An important result from elaboration of the integral

3D model of the Pechenga ore district is the conclusion about a relatively shallow depth of its northern limb (i.e. of the North Pechenga series), which in the vertical extent do not exceed 10-12 km (fig. 2). The same is characteristic of the southern limb (or the South Pechenga series). According to the computerized analysis of the gravity data, there are no thick basic and ultrabasic feeder dykes under the central part of the Pechenga structure. Variations of the elastic anisotropy coefficient in the cross-section of the Pechenga structure indicate a more intense deformation of the southern limb compared to the southern limb. In the northern limb, synmetamorphic shearing and faulting mainly influenced the ore-bearing Productive member and the lower suites of the North Pechenga series. Judging from the distribution of rock densities, the maximal depth of the lower contact of the Productive member is less than 5-6 km. In the south, the distribution of the Productive member is limited by the Por'itash fault.

The integrated 3D model regards the Pechenga ore

district as a horizontal section of a mantle-derived volcano-plutonic ore-forming system of a centrally symmetric type. The model defines the northern limb of the Pechenga structure as an imbricated fragment of a volcanic caldera and describes its Southern limb as a sheeted monocline in a juxtaposition with rheomorphic granitoid domes. Development of the system was preceded by rifting of the consolidated sialic crust. The model implies a co-genetic relationship between the Early Proterozoic volcanism and the nickel-bearing basic-ultrabasic plutonism. The basic and younger intermediate volcanic rocks filled two volcano-tectonic depressions traced by a thick zone of northwestern faults. Later on, the volcano-tectonic depressions experienced intense compression and metamorphism, which also affected the basement rocks. Finally, steep-dipping zones of cataclasis and retrograde metamorphism were caused by an extension environment.

There is no evidence of a continuos extension of the Cu-Ni ore-forming system below the Pechenga structure. Along with this, two signatures of the Cu-Ni ore-forming system may be deduced at deeper levels from seismic and petrological data (Kazansky et al. 2008), namely: a Vp/Vs anomaly at 20-25 km depth, similar to that under the Norilsk ore district and assumed to be intermediate magmatic chamber, and a Moho boundary uplift, reaching the maximal height of 34 km under the Pechenga structure, which may be interpreted as a relict mantle plume.

The central part of the Pechenga ore district has been selected for more detailed seismotomographic studies using some geological, geophysical, petrological and additional seismic data. It was established that under the Pechenga structure, the upper boundary of the Moho surface is located at a minimum depth of 34-41 km. Based on recent metallogenic information, we regard this Moho uplift as a relict mantle plume which dominated Paleoproterozoic geological events.

The analysis of the available seismic, geological, and petrophysical data provides the basis for distinguishing three types of first-order seismogeological boundaries: the base of the Earth's ancient continental crust, interface between the lower homogeneous and upper hetero-geneous layers of the crust. All these boundaries affect the metallogenic zoning of the Pechenga ore district of which seismogeological boundaries are most important. Ore deposits of the Karelian cycle correlates with this boundary.

There are sufficient proofs that Paleoproterozoic rocks of the Pechenga ore district experienced tectonic deformations accompanied by zonal metamorphism. An impact of low-temperature metamorphism on gabbro-wherlite intrusions and associated Cu-Ni deposits is a characteristic feature (Gorbunov et al. 1999). If the suggested interpretation of the Pechenga structure as a deformed fault-bound volcanic center is sound. The Pechenga Cu-Ni deposit may be related to the volcano-plutonic type and the corresponding ore-forming system to the mantle-crustal type (Kazansky et al. 2008).
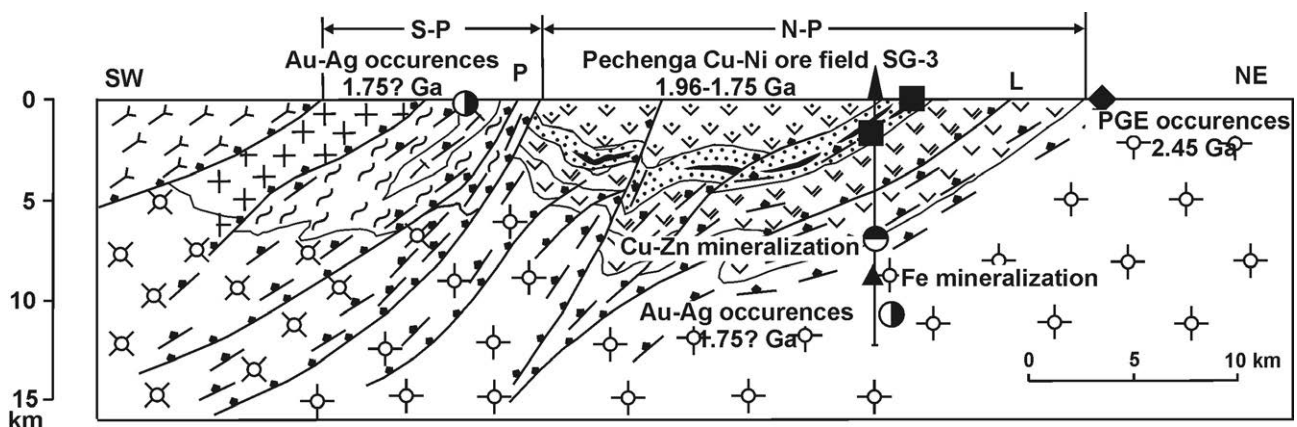
Figure 2. Schematic section of the integrated 3D geodynamic model of the Pechenga ore district in section through Kola Superdeep Borehole and correlation of ore-forming systems (Lobanov et al. 2010).

3 Ore deposits and mineralizations of the Pechenga ore district

The Early Proterozoic Ni- and PGE-bearing Gora General'skaya massif consists of gabbronorites and a small portion of olivine-plagioclase cumulates. Sulfo-arsenides are characteristic of it's low-sulfide PGE mineralization. The enrichment of poikilitic and taxitic host rocks in volatile-containing minerals, abundance of nonequilibrium assemblages, rather complete PGE fractionation, and prevalence of heavy and rare PGE testify to the existence of a spreading center which was probably associated with a hot spot or a mantle plume.

In the frames of the 3D model, the northern limb of the Pechenga structure (where Cu-Ni ores are concentrated), was presumed to be a sheared fragment of a volcanic caldera and its southern limb – a combination of a steeply dipping imbricated monocline with oversthrusted granitoid domes. The vertical extent of the Pechenga structure was estimated to be about 10 km. It was also assumed that the present erosion level of the Pechenga ore district may be considered as a horizontal section of a mantle-derived ore-forming system of central type (Fig. 2).

The Cu-Ni deposits not only occupy a regular position in the Paleoproterozoic volcano-sedimentary complex. The Ni-bearing gabbro-wherlite intrusions are

genetically linked to ferropicrites of the Pilgujarvi formation overlying the Productive member. Within the northern limb, three quarters of Ni-bearing intrusions and Cu-Ni deposits are concentrated within the so-called "structural trench" oriented across the general strike of the Pechenga structure (Gorbunov et al. 1999). The Productive member also reaches maximum thickness in the structural trench. There were several attempts to discover Cu-Ni ores along the extension of the Pechenga structure in the Pasvik belt. The exploration boreholes penetrated several gabbro-wherlite bodies at the bottom of the Productive member. The bodies have the same petrological characteristics as in the Pilgujarvi intrusions but only traces of Ni and Cu.

This inference allows to relate the Pechenga Cu-Ni deposits, overprinted by metamorphism, to the volcano-plutonic types and provides a new insight into their setting, environment and origin. A summary of structural, petrological, mineralogical and geochemical data suggests that at the upper levels the Cu-Ni ore-forming system developed in two stages: 1) emplacement of mantle-derived gabbro-wherlite sills into heterogenous Productive formation, their differentiation and generation of magmatic Cu-Ni ores; 2) dislocation and metamorphism of gabbro-wherlite sills and deposition of remobilized Cu-Ni ores in synmetamorphic shear zones.

Formation of epigenetic Cu-Ni ore zones, related to synmetamorphic secondary shearing, occurred in Svecofennian tectonomagmatic resulting in redeposition of primary magmatic sulfides at 1750 Ma (Lobanov and Kazansky 2009). Productive member on textural and structural features, mineral composition and genesis of ores are similar to those which fall to the surface, which proves the consistency of Cu-Ni mineralization down dip for at least 2.5 km.

A uranium mineralization was discovered in the Pechenga district in the 1970-s (Kazansky et al. 1994). It established that the prolonged and multistage attack of metamorphic and magmatic processes on the Archaean basement resulted in the successive migration and concentration of uranium. Kazansky et al. (1994) subdivided uranium deposits and occurrences into four genetic types: (1) REE-Th-U mineralization in pegmatoid granites, quartz--plagioclase metasomatites, and oligo-clasites (2.75 - 2.65 Ga); (2) Th-U mineralization in quartz-albite-microcline and quartz-microcline meta-somatites (1.85 - 1.75 Ga); (3) U mineralization in chlorite-albite metasomatites and albitites (2.20 - 1.70 Ga); and (4) U mineralization in albite-hydromica-chlorite metasomatites (2.20 - 1.65 Ga). The uranium minerali-zations are spatially associated with the Litsk-Aragubsk chain of granitoid massifs and with meridional faults of the Ladoga-Barents Sea tectonic zone. However, they are mostly hosted by metamorphic rocks of the Kola series. Brannerite ores of the Litsevsk deposits have an age of 1.75 - 1.65 Ga.

The Au-Ag mineralization in the context established by the SG-3 on the surface of the rocks South Pechenga series. The genetic association with gold mineralization and magmatic metasomatic processes was established by (Lobanov and Kazansky 2009). The discovery of gold mineralization at the depth of 9.5-11 km has become an important result of the SG-3. Within this intervale, gneisses and amphibolites of Archean age are crossed by fracture and retrograde zones. Small particles of native gold are dissimininated in biotite, hornblendites and plagyoclase. In this zone were observed the dyke-like body porphyritic granite Litsk-Aragubsk complex (1.76 Ga). The origin of gold mineralization remains obscure: the redistribution of primary concentration in the metamorphic rocks; the deposition from reducing subcrustal fluids.

4 Conclusion

The setting of one of the largest ore field in Europe in an isolated segment of the Karelian Pechenga-Imandra-Varzuga belt and its association with a relict mantle plume should be taken into account at the prognosis of analogues Cu-Ni deposits in another regions.

According to the integrated 3D geodynamic model of the Pechenga ore district, the nickel-bearing gabbro-wherlite intrusions primarily were formed as sills and occupied a subhorizontal position like to the ore-bearing intrusives of the Norilsk district. Ores of the Pechenga ore district formed at the collision development stage of the Svecofennian cycle and are controlled by shear zones in the Productive member.

Epigenetic Cu-Ni ore in secondary shear zones, hydrothermal U and Au ores occurred in Svecofennian tectonomagmatic activation of the Fennoscandian Shield.

Acknowledgements

References

Gorbunov G.I., (1999). Copper-Nikel Deposits of the Pechenga, Moscow. GEOS, 236 p.

Kazansky V.I., Kuznetsov O.L., Kuznetsov A.V., Lobanov K.V., Cheremisina E.N. (1994). Deep Structure and Geodynamics of the Pechenga Ore District: an Experience of the Kola Superdeep Borehole Studies // Geology of Ore Deposits, vol. 36, N 6, pp. 500-519.

Kazansky V.I., Lobanov K.V., Isanina E.V., Sharov N.V. (2008). The Paleoproterozoic Pechenga Cu-Ni ore field (Fennoscandian Shield): a fault-bound volcanic center // Izvestiya Earth Sciences section Russian academy of Natural Sciences 33 International Geological Congress. Oslo, Norway, Moscow, Special Issue, N 17, pp. 43-46.

Lobanov K.V., Kazansky V.I., Kuznetsov A.V., Zharikov A.V. (2010). Integrated geodynamic model of the Pechenga ore district based on the correlation of geological, petrological, and petrophysical data from the Kola super-deep borehole and the reference profile at the surface // Modern Problems of Ore Geology, Petrology, Mineralogy and Geochemistry. IGEM RAS, Moscow, pp. 258-300.

Lobanov K.V., Kazansky V.I. (2009) The mantle-crustal ore-forming Cu-Ni system of the Pechenga ore district (Fennoscandian shield) // Proceedings of 6 Europeann Congress on Regional Geoscientific Cartography and Information Systems EUREGEO, Munich, Germany, V. II, pp. 201-205.

Preliminary results on polymetallic mineralizations in a granitoid-dominated environment near Jyväskylä, Central Finland

Perttu Mikkola & Aimo Hartikainen
Geological Survey of Finland, P.O. Box 1237, 70211 Kuopio, Finland

Abstract. The Paleoproterozoic Central Finland granitoid complex has traditionally been considered as uninteresting with respect to ore potential. Yet several small high grade mineralizations and glacially transported boulders are known from the vicinity of Jyväskylä. The mineralized samples are variably enriched in Pb, Cu, Zn, Mo, Ag and Au. Mineralogically and compositionally they form three groups: porphyric granites, argillized granites and amphibolites. The samples are variably tectonized and the mineralizations are at least affected by fluid activity in shear zones and faults, if not solely formed by such activity. Certain characteristics observed in studies done in the 1980s suggest however that the samples might represent variably mobilized porphyry-type mineralizations.

Keywords. Finland, Silver, Lead, Copper, Granitoids

1 Introduction

The areas surrounding Jyväskylä in Central Finland belong geologically to the Paleoproterozoic Svecofennian domain of the Fennoscandian shield. Geological knowledge of the area is indisputably outdated as basic bedrock mapping in the area was carried out more than a century ago in scale 1:400 000. Thus the Geological Survey of Finland (GTK)

Figure 1. Geological map of the study area (modified from DigiKP). Also shown the location of mineralized samples plotted in figure 2.

initiated a project in 2012 to improve the geological comprehension of this area, which so far has been considered uninteresting with respect to ore potential. However, several high grade ore boulders and outcrops are known in the area from brief initial work carried out in the 1980s (e.g. Ikävalko 1981; Nurmi et al. 1984). Also several layman samples from the area have been sent to GTK over the years.

The majority of the bedrock in the area consists of granitoid intrusions of the Central Finland granitoid complex (Fig. 1). Granitoids are either synkinematic (1890−1870 Ma) or postkinematic (1880−1860 Ma) with respect to the Svecofennian orogeny (Nironen 2005). Supracrustal rocks, both volcanic and sedimentary, presumed to be coeval or older than the plutonic rocks, are present as small segments and enclaves. Several late SE-striking dextral faults can be observed in aeromagnetic maps and as elongated valleys in topographic maps. Dextral NE striking faults are less prominent.

2 Characteristics of the mineralized samples

Altogether 21 mineralized samples, collected by amateur prospectors, were selected from the material archived at GTK and reanalysed using XRF and ICP-MS. Three main mineralogical groups were identified in the thin section studies: porphyric granites, argillized medium-grained granites and amphibolites. Most of the samples were variably tectonized and showed signs of sericitization and saussuritization. According to petrophysical studies, most of the mineralized samples are not substantially magnetic or conductive, but generally somewhat heavier than their barren counterparts.

Three groups can be distinguished based on the mineralogical and chemical differences in the mineralized samples (Table 1 and Fig. 2). The scatter displayed by amphibolites is caused by variable depletion in Ca and Mg and enrichment in K during alteration. The very low Ca and Mg concentrations of the argillized granites and some of the porphyric granite samples are also likely to be secondary. Economically interesting enriched elements include Pb (<7.9 %), Cu (<2.85 %), Zn (<5.5 %), Mo (<0.26 %), Ag (<537 ppm) and Au (<523 ppb). The composition of the host rocks does not correlate with the enriched metals and neither do the enriched metals between each other. Both Au and As display high concentrations in the samples from the area, the latter up to 19.6 %, but the two elements do not
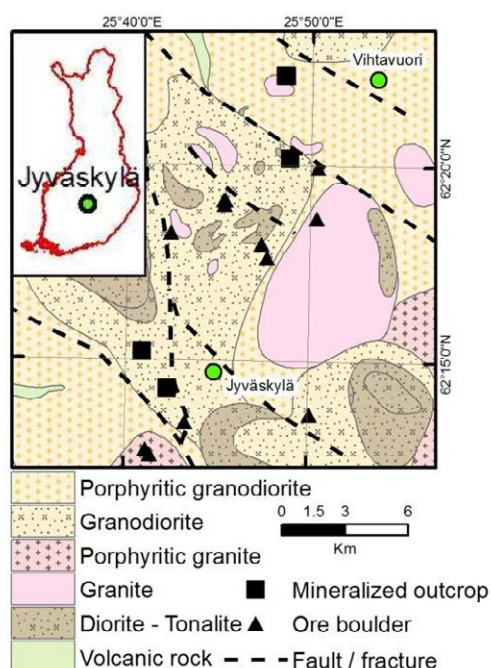
correlate at all in the area, as high Au levels are found in samples with low As and vice versa.

Group	Argillized granite	Porphyric granite	Amphibolite
SiO_2 wt. %	76.6	65.6	45.7
TiO_2	0.01	0.12	0.39
Al_2O_3	7.33	16.60	7.97
Fe_2O_3t	5.35	2.36	19.20
MnO	0.07	0.06	0.47
MgO	0.35	0.19	6.42
CaO	0.02	0.21	15.76
Na_2O	0.20	3.00	0.81
K_2O	3.38	6.58	0.96
P_2O_5	<0.014	<0.01375	0.18
Cu ppm	3494	9650	4130
Pb	43760	15200	8
Zn	5265	7070	161
Sn	61	91	52
Mo	<10	2376	1.37
As	1278	374	<20
Ag	537	75	28
Au ppb	<10	<10	523

Table 1. Chemical compositions of representative samples of different groups.
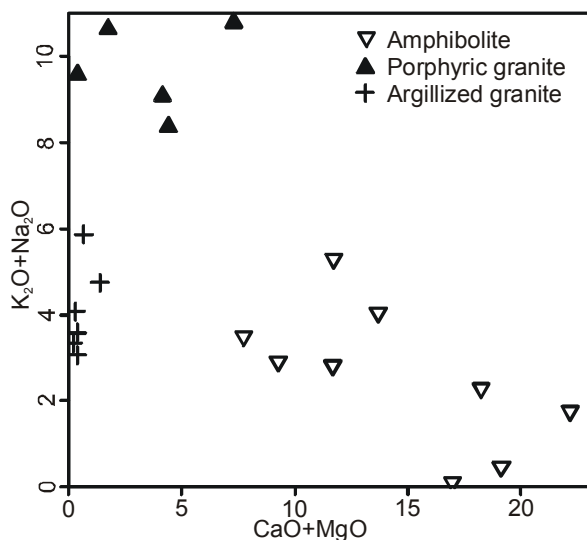
Figure 2. MgO+CaO versus K_2O+Na_2O plot of the whole rock compositions showing the three compositionally different groups.

3 Discussion

The mineralizations known so far from outcrops are high-grade, but low volume (Hangala 1982). The sheared character of the mineralized samples suggests that the mineralizations are related to fluid activity in shear zones or faults (Ikävalko 1981, Hangala 1982). There are also indications that the mineralizations might originally be of porphyry-type because they are often found in contact zones between different granitoid phases (Nurmi et al. 1984). One of the porphyric granite samples is enriched in Mo (0.26 %) and Rb and depleted in Sr. Such an alteration is typical for the innermost parts of porphyry-type mineralizations (Boyle 1982). Low Mo and Sb together with high Cu and Ag contents in most of the analysed samples, especially in amphibolites, indicate extensive fluid transport and that the enrichment occurred further away, up to 10 km, from the centre of porphyry intrusion (John 2010). The current data is however too scattered to be used for locating different alteration zones or even intrusive phases which would be the first step in selecting the targets for more detailed prospecting. The combination of fault related processes and possible younger granitoids overprinting an older porphyry-type mineralization could well explain the heterogeneity observed in the whole-rock compositions as well as in the enriched metals.

4 Planned work

The initiated project will update the basic knowledge about the bedrock and its ore potential in areas surrounding Jyväskylä using bedrock mapping, geophysics, geochemistry and isotope methods. In respect to known ore indications NE of Jyväskylä the aim of the work is to properly characterize the known mineralized samples using whole rock compositions, mineral chemistry and isotope methods in order to evaluate the possible sources of the elements and the factors controlling their later enrichment in the bedrock. The results can then be applied to estimate the ore potential over a wide area in Central Finland displaying similar rock associations and structural framework.

References

Boyle RW (1982). Geochemical methods for the discovery of blind mineral deposits. Part 1. Can. Inst. Min. Metall., Bull 75 (844) 123-142.
DigiKP. Bedrock of Finland - DigiKP. Digital map database [Electronic resource]. Espoo: Geological Survey of Finland [referred 13.01.2013]. Version 1.0. Available at: http://www.geo.fi/en/bedrock.html
Hangala SK (1982). The plutonic rocks and the associated ore mineralizations at Palokka, Jyväskylä, central Finland. Master's thesis, University of Helsinki, the Department of geology and mineralogy, 58 p.
Ikävalko O (1981) Malmitutkimukset Jyväskylän alueella kesällä 1981, 25 s. 26 l. Geologian tutkimuskeskus, archive report, M 19/321206/-81/10. (in Finnish) http://arkisto.gtk.fi/m19/3212/M19_3212_06_81_1_10.pdf
John A. D. (editor) 2010. Porphyry Copper Deposit Model. Scientific Investigations, report 2010-5070-B. U.S. Department of the Interior, U.S. Geol. Surv. 169 p.
Nironen M (2005). Proterozoic orogenic granitoid rocks. In: Precambrian geology of Finland: key to the evolution of the Fennoscandian Shield. Developments in Precambrian geology 14. Amsterdam: Elsevier, 443-479.
Nurmi PA, Front K, Lampio E, Nironen M (1984) Etelä-Suomen svekokarjalaiset porfyyrityyppiset molybdeeni- ja kupariesiintymät, niiden granitoidi-isäntäkivet ja litogeokemiallinen etsintä. Summary: Svecokarelian porphyry-type molybdenum and copper occurences in southern Finland: their granitoid host rocks and lithogeochemical exploration. Geologian tutkimuskeskus. Tutkimusraportti - Report of investigation 67. 88 p. http://arkisto.gtk.fi/tr/tr_067.pdf

Mineral chemistry of gangue minerals of the Kiirunavaara iron ore, evidence for a transition from magmatic to hydrothermal conditions

Joakim Nordstrand
LKAB, Research & Development, TX, MH-Vi, SE-983 81 Kiruna, Sweden

Ulf B. Andersson
LKAB, Research & Development, TFG, FK9, SE-981 86 Kiruna, Sweden

Abstract. Mineral chemical data on gangue minerals in the Kiirunavaara ore suggest an evolution from magmatic conditions at >800˚C, to a hydrothermal, CO_2, S, and Cl-rich system below c. 600˚C.

1 Background

The Kiirunavaara apatite-iron oxide (AIO) ore was emplaced within a thick package of intermediate-silicic volcanic, or partly subvolcanic, rocks, at c. 1.89-1.88 Ga (e.g. Cliff et al. 1990; Romer et al. 1994). This rock sequence occurs in a former rift basin at the edge of the presently exposed Archaean craton (Martinsson 1997; Bergman et al. 2001). In addition to magnetite (and minor hematite) and apatite, parts of the ore contain small amounts of silicates, carbonates, sulphates, and sulphides, as discussed below.

The origin of the Kiruna-type AIO deposits has been on the agenda since the early days of exploitation (e.g. Lundbohm 1910). The earliest theory, based on field mapping of the uncovered ore before the start of mining, suggested the ore to represent an effusive volcanic flow, magmatically differentiated from the associated syenitic magmas, and emplaced among the other volcanic products (Geijer, 1910). Later, he revised his view suggesting that the ore represented a dyke intrusion (Geijer 1919). The magmatic view was challenged by Parák (1975a, 1975b), who suggested a volcanic-exhalative sedimentary origin. Others have maintained a magmatic oxide deposition (e.g. Frietsch 1978; Nyström & Henriques 1994; Nyström et al. 2008). An origin by deposition from hydrothermal fluids was proposed early on (Bäckström 1904), and has gained momentum recently (Hitzman et al. 1992; Smith et al. 2009; 2013).

We present new data on the mineral chemistry of gangue minerals (amphibole, mica, chlorite, talc, titanite, allanite, carbonates and sulphates) in the Kiirunavaara ore (see also Nordstrand 2012), and its bearing on the emplacement of the ore. Apatite was studied by Andersson et al. (2002) and Harlov et al. (2002), and references therein.

2 Mineralogy and mineral chemistry

2.1 Amphibole

Amphibole is the most common silicate mineral in the ore, and elongated crystals are often arranged in a flow-like texture (Fig. 1). These are calcic amphiboles of dominantly actinolitic composition, ranging in Mg/(Mg+Fe^{2+}) (Mg#) from 0.75 to 0.95. Some grains show zoning from Al-, Fe-, alkali-richer cores to Si-, Mg-, and Ca-richer margins. They contain low amounts of TiO_2 (<0.27 wt%, < = up to), MnO (<0.67 %), V_2O_3 (<0.07 %). F is also present in some (<0.50 %), and a low, but ubiquitous level of P_2O_5 (0.07-0.22 %).
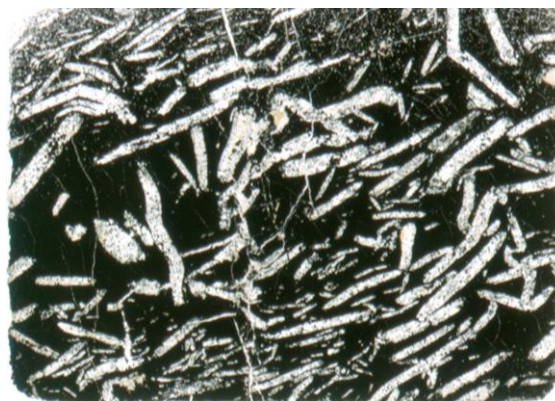
Figure 1. Actinolite crystals, flow-aligned within magnetite-apatite ore, Kiirunavaara. Length of crystals, c. 2-6 mm.

Important substitutions in the amphiboles (Fig. 2, below) are: $^{[M]}Mg = {}^{[M]}Fe^{2+}$,

as seen in the variation in the Mg#, and:

$^{[M1,2,3]}(Mg,Fe,Mn)^{2+} + {}^{[T]}Si^{4+} = {}^{[M1,2,3]}Al^{3+} + {}^{[T]}Al^{3+}$,

the so called tschermak substitution ([M], [M1,2,3] refer to octahedral and [T] to tetrahedral sites). However, these substitutions do not explain the whole chemical variation and the following mechanisms can be shown to be operative on a minor scale:

$^{[T]}Si^{4+} = {}^{[M4,A]}(Na,K)^+ + {}^{[T]}Al^{3+}$
$^{[M4]}Ca^{2+} = {}^{[M4]}(Na)^+ + {}^{[A]}(Na,K)^+$, and
$^{[M4]}Ca^{2+} = {}^{[M4]}(Mg,Fe,Mn)^{2+}$.
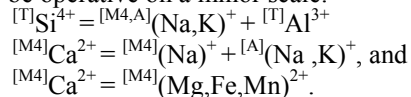
2.2 Mica

Mica is the second most abundant silicate in the ore, and ranges in colour from dark brown to colourless. Due to low, or non-existing, octahedral Al, and high to very high Mg#, the mica classifies as phlogopite, and can be subdivided into three groups. Group 1 is characterized by relatively high Fe, Al, Ti, Mn, K and Cl contents, while group 2 is lower in these elements, but higher in Si, Mg, and F. Group 3 is even higher in latter elements. Both groups 2 and 3 lack octahedral Al.

There is a significant variation in F and Cl contents in the mica; F shows a strong positive, and Cl negative, correlation with Mg# (Fig. 3).
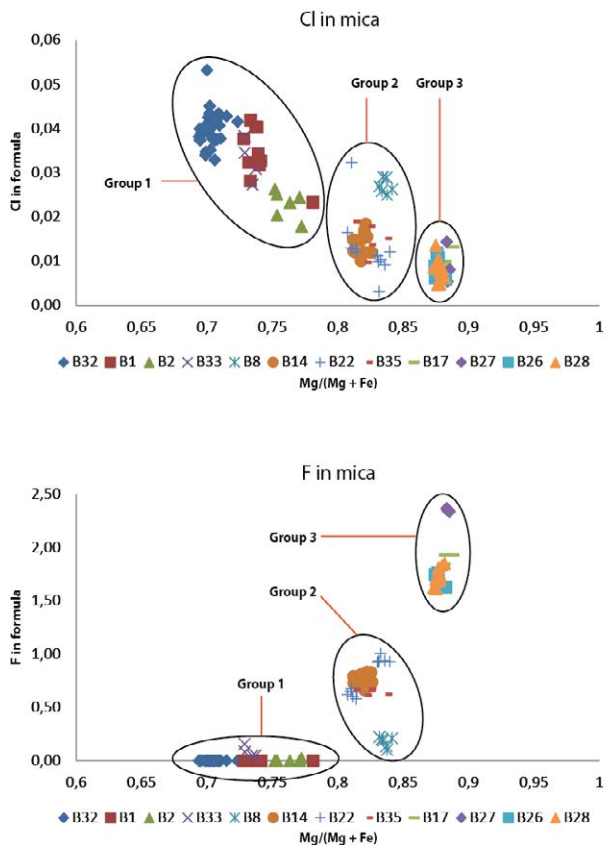
Figure 3. F and Cl contents in the Kiirunavaara mica.

The Fe-rich group is commonly associated with actinolite and carbonates, while the Mg-rich micas tend to be associated with apatite and magnetite.

Also in the phlogopites

$^{[6]}Mg = {}^{[6]}Fe^{2+}$ is the dominant substitution. However, Si/Al < 3/1 suggests that:

$^{[6]}(Mg,Fe)^{2+} + {}^{[4]}Si^{4+} = {}^{[6]}Al^{3+} + {}^{[4]}Al^{3+}$ also operates (Fig. 4) ([6] and [4] refer to coordination numbers). In contrast, the F-rich micas have Si/Al > 3/1. This may be related to vacancies in the octahedral or inter-layer positions. Minor Ti is substituted into the octahedral position.
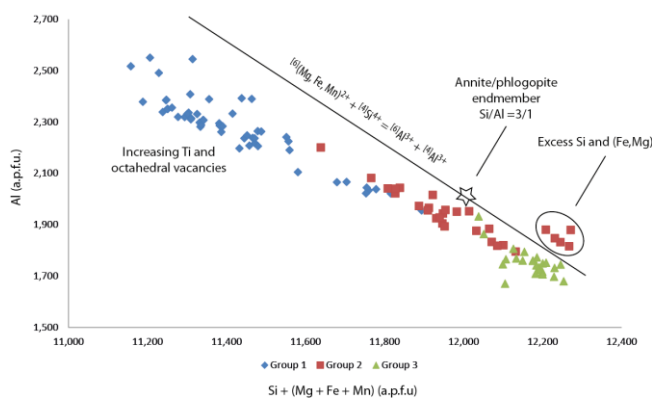
Figure 4. Plot of Si+(Mg+Fe+Mn) vs. Al illustrating substitutional mechanisms in the Kiirunavaara mica.

2.3 Chlorite

Chlorite is common in the ore, often as an alteration product of phlogopite. It shows large variations in the Fe, Mg, and Al contents, but tends to be enriched in Fe. They also carry minor amounts of TiO_2 (<1.05 %) and MnO (<1.23 %) that co-varies with Fe. Small amounts of Cl are present (<0.11 %). The composition is homogeneous within each thin section and tends to mimic that of the associated phlogopite with respect to Mg#.

2.4 Talc

Talc is relatively common in the ore, and is associated with either actinolite or dolomite and phlogopite; in both cases also with magnetite. The chemical variation is small and mainly related to Fe-Mg exchange, ferroan, with FeO in the range 3.65-5.22 %, and carry small amounts of Al_2O_3 (<0.67 %), MnO (<0.07 %), and CaO (<0.25 %). The talc contains F, up to 2.19 %.

2.5 Titanite

Titanite is common in small quantities. It is found, (1) as small grains (some tens of μm) at the edges of magnetite, or (2) as large (>100 μm) crystals in the magnetite-apatite mass. It shows significant abundances of FeO (up to 3.61 %), V_2O_3 (<1.77 %), LREE (Ce_2O_3 <2.28 %), F (up to 1.01 %), and P_2O_5 (<0.40 %). Al_2O_3 is always low (<0.95 %). Trace amounts of Hf, Zr, Nb, K, and Y occur.

Our data extend the compositional range of Kiirunavaara titanites reported by Smith et al. (2009). The small grains at the margins of magnetite are lowest in Fe. There is a rough negative correlation of Fe+Al+V and Ti, and rough positive correlation with the sum of REE (Fig. 5, below). This suggests the operation of:

$^{[7]}Ca^{2+} + {}^{[6]}Ti^{4+} = {}^{[7]}(Y,REE)^{3+} + {}^{[6]}(Fe,Al,V)^{3+}$.

However, this cannot account for all the Fe+Al+V in the titanites. The following substitution mechanism roughly seems to account for the remaining trivalent cations:

$^{[6]}Ti^{4+} + O^{2-} = {}^{[6]}(Fe,Al,V)^{3+} + F^-$,
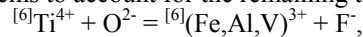
based on the co-increasing F contents.

2.6 Allanite

The allanites in the ore are enriched in Fe^{3+} relative to Al, and range to higher Mg#. Formula recalculations after Ercit (2002) show that they are intermediate between allanite and ferriallanite, but not as Fe^{3+}-rich as those from Bastnäs (Holtstam et al. 2003). The compositions also spread out towards dissakisite (Fig. 6).
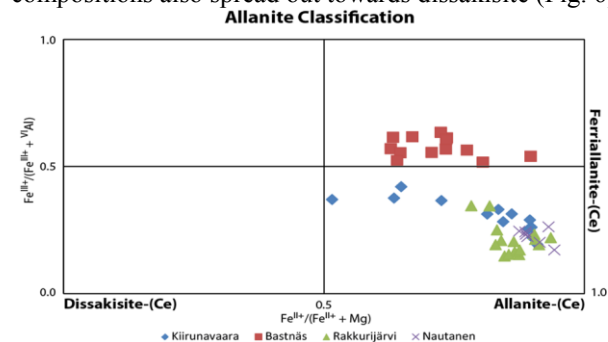
Figure 6. Compositional spread of the Kiirunavaara allanites/ferriallanites. Additional data from Holtstam et al. (2003) and Smith et al. (2009).

The Kiirunavaara (ferri-)allanites contain minor amounts of TiO_2 (<0.75 %), V_2O_5 (<0.29 %), MnO (<1.10 %), P_2O_5 (<0.18 %), ThO_2 (<0.24 %; no detectable U), and F (<0.46 %). Total $LREE_2O_{3tot}$ = 21.81-26.22 %.

2.7 Zircon and thorite

Small amounts of zircon and thorite have been encountered in the ore. Zircons are typically prismatic and display concentric zoning. The zircons contain small quantities of Al, Fe, Mn, Ca and Hf.

The thorites contain, in addition to Th, Si and O, significant amounts of U and LREE; 3–4 wt% of UO_2 and 7-11 % $LREE_2O_{3tot}$. Other elements in minor and trace quantities are FeO (0.42–1.45 %), CaO (0.70–1.56 %), BaO (<0.34 %), and Y_2O_3 (0.09–0.53 %).

2.8 Carbonates

Three different carbonates were found: calcite, dolomite and ankerite. Calcite is typically found in late veins cross-cutting all types of ore. Dolomite and ankerite occur more intimately associated with the ore, in breccias or intergrown with silicates (cf. Harlov et al. 2002). Calcite contains 0.88–1.4 wt% MnO, 0.08–1.41 wt% MgO and 0.06–1.13 wt% FeO. The dolomites contain up to 2.96 % MnO. Trace amounts of Sr and Cl are present.

2.9 Sulphates

Anhydrite and gypsum are common constituents within the ores, typically present in late stage veins cutting through the rock sequence. Their chemical variation appears to be relatively small. Anhydrite carry small amounts of FeO (<0.15 %), SrO (<0.39 %), and P_2O_5 (<0.43 %). In gypsum, some crystals have a significant substitution of Fe for Ca (FeO up to 6.28 %). It also carries minor amounts of Al_2O_3 (<0.64 %), MgO (<0.08 %), SrO (<0.11 %), P_2O_5 (<0.46 %), and Cl (<0.19 %), with trace amounts of alkalies, Ni, and Zn.

3 Discussion and conclusions

Actinolite is the dominant silicate within the AIO ore in Kiirunavaara. Elongated crystals often show trachyoidal flow-like textures within the ore (Fig. 1). According to Lledo and Jenkins (2008) calcic amphiboles of similar compositions to those of the Kiirunavaara actinolites are stable up to 830°C at 1 kbar and 900°C at 4 kbar, in the presence of pyroxene. Pyroxene was not detected in the present study, but reported by Geijer (1910). In the absence of pyroxene these values should be regarded as upper limits (D. Jenkins pers com). Furthermore, Lledo (2005) has shown that P-Fe-rich magmas can exist down to 600°C and coexist with actinolite at low pressure.

The compositional variation in mica is substantial in Kiirunavaara. The most Mg- and F-rich phlogopites are typically associated with apatite and magnetite. F stabilizes phlogopite to higher temperatures, certainly above 600°C (summarized in Fleet 2003).

Titanite and allanite mostly show textural indications of secondary formation after magnetite and apatite, with other components added by fluids (cf. Harlov et al. 2002). Both show extensive substitutions involving F, suggesting that they formed secondary but early in the magmato-fluid evolution.

Talc typically occurs in the presence of carbonates in relatively late schlierens, or veins, and should be stable in such assemblages to >500°C (Tromsdorff & Connolly 1990). However, the high contents of F stabilizes talc to higher temperature (e.g. Abercrombie et al. 1987), suggesting that this assemblage may represent a transition to post-magmatic conditions.

Late stage veins are dominated by calcite, anhydrite, and gypsum, often carrying pyrite and chalcopyrite. Gypsum typically forms central portions of late veins or late fracture fillings. Fe-rich, carbonate-associated phlogopites and chlorites are carrying Cl, as is also gypsum.

The combined evidence suggests magmatic crystallization of magnetite, apatite, actinolite, Mg-F-rich phlogopite at temperatures below 900°C from a magma enriched in volatiles (in addition to P and F) of CO_2, SO_x, and Cl. Following cooling and crystallization of the early phases, titanate, allanite, Fe-Cl-rich phlogopite, talc and dolomite-ankerite precipitates during a transition to a fluid regime that takes place below 600°C. Late stage fluids are expelled and strongly enriched in CO_2, SO_x, and Cl (partly Cu).

References

Abercrombie HJ, Skippen GB, Marshall DD (1987) F-OH substitution in natural tremolite, talc, and phlogopite. Contr Mineral Petrol 97: 305-312.

Andersson UB, Harlov DE, Förster H-J, Nyström J-O, Dulski P, Broman C (2002) On the origin of monazite inclusions from the Kiruna iron ores. GFF 124: 232-233.

Bäckström H (1904) Ekströmsberg och Mertainens järnmalmsfält. Geol För Stockh Förh 26: 180-183.

Bergman S, Kübler L, Martinsson O (2001) Description of regional geological and geophysical maps of northern Norrbotten County (east of the Caledonian orogeny). SGU Ba 56, 110 pp.

Cliff RA, Rickard D, Blake K (1990) Isotope systematics of the Kiruna magnetite ores, Sweden: Part 1. Age of the ore. Econ Geol 85: 1770-1776.

Ercit TS (2002) The mess that is "Allanite". Can Miner 40: 1411-1419.

Fleet ME (2003) Rock-forming minerals. Micas. 2nd ed. Geological Society, 758 pp

Frietsch R (1978) On the magmatic origin of iron ores of the Kiruna type. Econ Geol 73: 478-485.

Geijer P (1910) Igneous rocks and iron ores of Kiirunavaara, Luossavaara and Tuollavaara. Scientific and Practical Researches in Lapland arranged by the Luossavaara-Kiirunavaara Aktiebolag, Geology of the Kiruna district 2, Stockholm, 278 pp.

Geijer P (1919) Recent developments at Kiruna. Sver Geol Unders C 288, 23 pp.

Harlov DE, Andersson UB, Förster H-J, Nyström JO, Dulski P, Broman C (2002) Apatite-monazite relations in the Kiirunavaara magnetite-apatite iron ore, northern Sweden. Chem Geol 191: 47-72.

Hitzman MW, Oreskes N, Einaudi MT (1992) Geological characteristics and tectonic setting of Proterozoic iron oxide (Cu-U-Au-REE) deposits. Prec Res 58: 241-287.

Holtstam D, Andersson UB, Mansfeld J (2003) Ferriallanite-(Ce) from the Bastnäs deposit, Västmanland, Sweden. Can Mineral 41: 1233-1240.

Lledo HL (2005) Experimental studies on the origin of iron

deposits; and mineralization of Sierra La Banderra, Chile. Doctoral Thesis, Bingham University, New York. 271 p.

Lledo HL, Jenkins DM (2008) Experimental investigation of the upper thermal stability of Mg-rich actinolite; implications for Kiruna-type iron deposits. J Petrol 49: 225-238.

Lundbohm H (1910) Sketch of the geology of the Kiruna district. GFF 32: 751-788.

Martinsson O (1997) Tectonic setting and metallogeny of the Kiruna greenstones. Ph.D. thesis, Luleå Univ. of Technology, 1997:19.

Nordstrand J (2012) Mineral chemistry of gangue minerals in the Kiirunavaara iron ore. Master´s thesis. Luleå Univ Technology.

Nyström J-O, Henriquez F (1994) Magmatic features of iron ores of the Kiruna type in Chile and Sweden: ore textures and magnetite geochemistry. Econ Geol 89: 820-839.

Nyström J-O, Billström K, Henríquez F, Fallick AE, Naslund HR (2008) Oxygen isotope composition of magnetite in iron ores of the Kiruna type in Chile and Sweden. GFF 130: 177-188.

Parák T (1975a) The origin of the Kiruna iron ores. Sver Geol Unders C 709, 209 pp.

Parák T (1975b) Kiruna iron ores are not "intrusive-magmatic ores of the Kiruna type". Econ Geol 70: 1242-1258.

Romer RL, Martinsson O, Perdahl J-A (1994) Geochronology of the Kiruna iron ores and hydrothermal alterations. Econ Geol 89: 1249-1261.

Smith MP, Storey CD, Jeffries TE, Ryan C (2009) In situ U-Pb and trace element analysis of accessory minerals in the Kiruna District, Norrbotten, Sweden: New constraints on the timing and origin of mineralization. J. Petrol. 50: 2063-2091.

Smith MP, Gleeson SA, Yardley BWD (2013) Hydrothermal fluid evolution and metal transport in the Kiruna District, Sweden: contrasting metal behavior in aqueous and aqueous-carbonic brines. Geochim Cosmochim Acta 102: 89-112.

Tromsdorff V, Connolly JAD (1990) Constraints on phase diagram topology for the system $CaO-MgO-SiO_2-CO_2-H_2O$. Contr Mineral Petrol 104: 1-7.
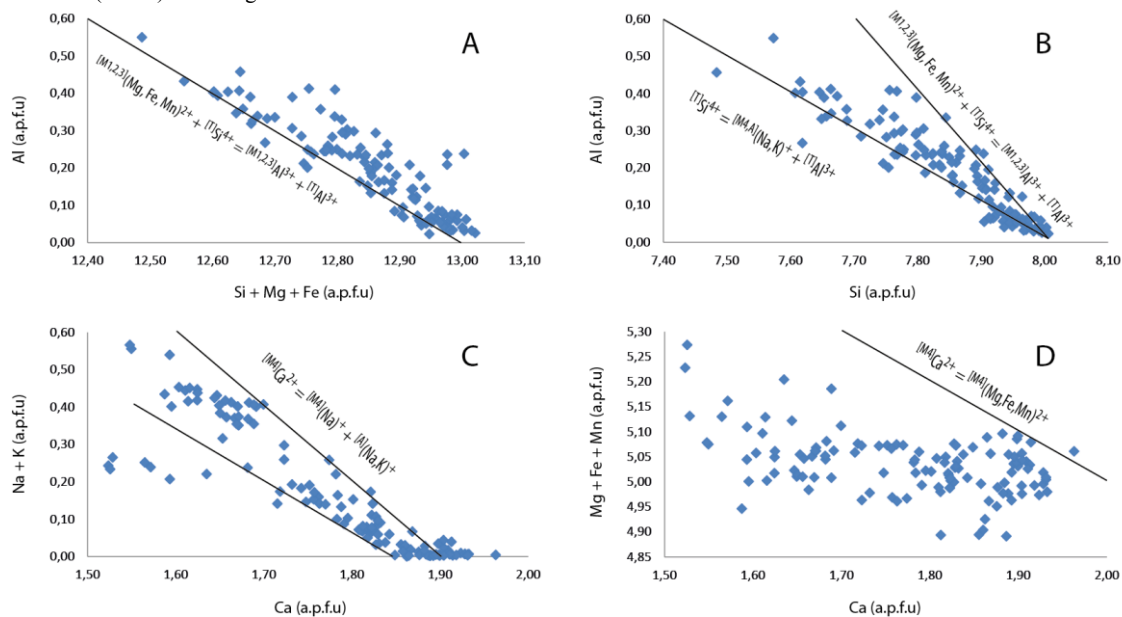
Figure 2. Plots illustrating substitution mechanisms operating in the Kiirunavaara actinolites. A. Si+Mg+Fe (incl. Mn) vs. Al. B. Si vs. Al. C. Ca vs. Na+K. D. Ca vs. Mg+Fe+Mn.
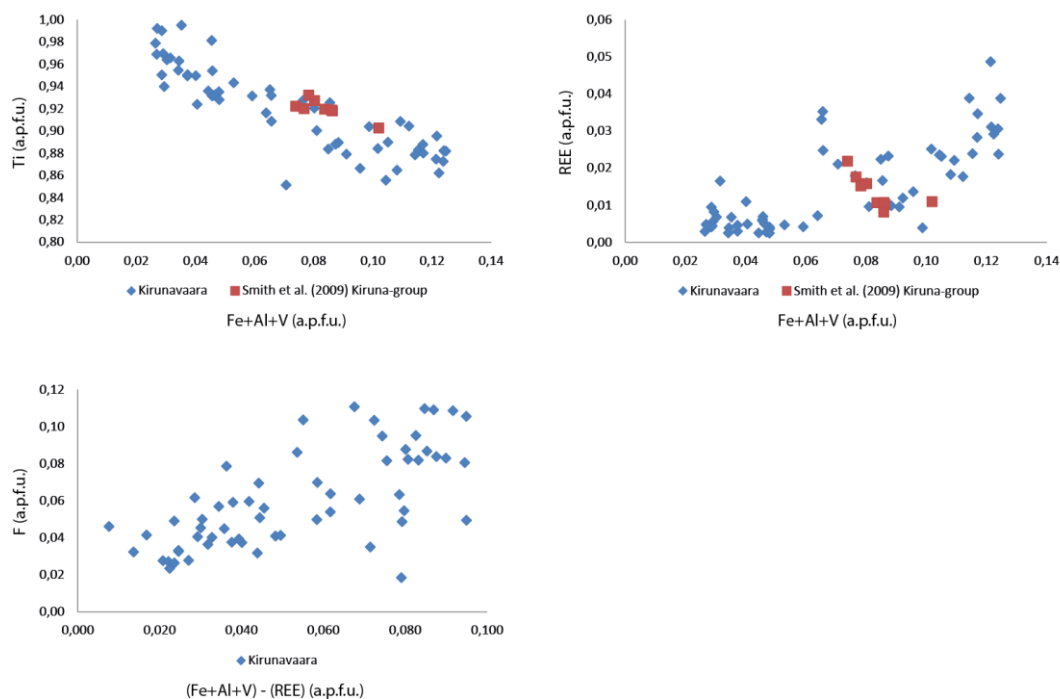
Figure 6. Compositional diagrams of Kiirunavaara titanites, compared to Kiruna-group titanites from Smith et al. (2009).

Reactivated basement structures and their control on sandstone-hosted Pb-Zn deposits along the eastern front of the Scandinavian Caledonides

Nicolas J.D. Saintilan, Lluís Fontboté
University of Geneva, Department of Earth Sciences, Rue des Maraîchers 13, 1205 Geneva, Switzerland

Michael B. Stephens
Geological Survey of Sweden, Box 670, SE-751 28 Uppsala, Sweden

Erik Lundstam
Boliden Mineral AB, S-776 98 Garpenberg, Sweden

Abstract. The Laisvall stratabound Pb-Zn deposit is hosted in Ediacaran–Cambrian sandstone along the eastern front of the Scandinavian Caledonides. Magnetic lineaments identified using airborne geophysical data correspond to geological features in the Palaeoproterozoic crystalline basement beneath this deposit. Geological modelling of the deposit in 3D space shows a correlation between some of the lineaments defined by magnetic minima and faults in the Ediacaran–Cambrian siliciclastic rocks, which are inferred to be spatially coupled to reactivated faults in the basement. Basement fault reactivation caused syn-sedimentary block faulting and also post-sedimentary and post-mineralisation fault movement. The reactivated faults define two major sets, which are inferred to have conditioned basin architecture and deposition of sediment during Ediacaran–Cambrian time, as N–S to NE–SW basin-parallel and WNW–ESE to NW–SE transfer faults. Lead and zinc grade modelling in 3D space revealed plume-like features that are spatially linked to NE–SW faults, suggesting these were conduits to the mineralizing fluids. These conduits and the location of the Laisvall ore bodies are spatially linked to inflection areas along magnetic minima. The geometry of the ore bodies is consistent with the presence of sour gas traps in the sandstone aquifers that may provide reduced sulphur for the formation of economic Pb-Zn deposits.

Keywords. Reactivated basement faults, Ediacaran to Cambrian, sandstone, Pb-Zn

1 Introduction

Stratabound, non-stratiform, sandstone-hosted Pb-Zn deposits and minor occurrences are known in Sweden and Norway, along the eastern front of the Scandinavian Caledonides over a distance of more than 1000 km, and include the Laisvall and Vassbo deposits (Stephens, 1986). Mineralisation is hosted by Ediacaran–Cambrian siliciclastic rocks, both in autochthonous sequences beneath the Caledonian thrust nappes resting unconformably on top of Paleoproterozoic crystalline basement (Fennoscandian Shield), and in the lowermost allochthonous units.

The present study is part of a broader project aiming to re-evaluate the role of the basement, the migration flow path, the driving force, the precipitation mechanism, and the age of sandstone-hosted Pb-Zn mineralisation in a tectonically constrained geological framework. It focuses attention on the structural and broader tectonic controls on the spatial occurrence of the Laisvall stratabound Pb-Zn deposit, hosted in autochthonous sandstone. The Laisvall deposit was an underground mine operated by Boliden Mineral AB until it closed down in 2001. Mineralisation was discovered in 1939 and mining operation started in 1941 (Grip, 1954). As a result of 70 years of mining activity, 64.3 Mt of ore at 0.6 % Zn, 4.0 % Pb and 9 g/t Ag were extracted (Willdén, 2004).

2 Regional geology

The tectonostratigraphic architecture of the Scandinavian Caledonides resulted from a series of tectonic events in Ordovician–Devonian time that involved convergence of the two plates with continental lithosphere referred to as Baltica and Laurentia. This convergence culminated with collision of these two continents during subduction of the margin of Baltica beneath Laurentia. Several allochthonous thrust nappes, comprising Baltica rift-related, platformal and foreland basinal sequences, oceanic arc and exotic continental terranes were thrust eastward onto Precambrian rocks of the Fennoscandian Shield (Gee 1975; Roberts & Gee, 1985; Stephens 1988; Roberts, 2003).

At Laisvall, the autochthonous stratigraphy is well developed and preserved underneath a main decollement overlain by allochthonous thrust sheets. The Palaeoproterozoic basement is composed of granite which formed at 1.8 Ga. The basement is overlain by the Ediacaran–Cambrian Laisberg Formation (Nielsen & Schovsbo, 2011) passing upward into the Grammajukku and Middle Cambrian Alum Shale Formations (Rickard et al., 1979; Willdén, 1980). The Laisberg Formation represents a transgressive, sandstone-dominated sequence. Mineralisation is hosted in the Lower and Upper Sandstone horizons in the upper part of the Laisberg Formation. The Grammajukku Formation comprises various shale and siltstone with subordinate sandstone intercalations. The Alum Shale Formation is composed of black pyritic shale (Ljungner, 1950). It is commonly strongly tectonized and provided the main decollement overlain by the allochthonous thrust sheets.

3 Structural and tectonic controls on stratabound, sandstone-hosted Pb-Zn deposits

3.1 Methodology and workflow

Airborne magnetic field data acquired in 2009 by the Geological Survey of Sweden (SGU) for the Laisvall area have been processed as a basis for a detailed lineament interpretation. The geophysical survey was carried out in a west–east direction at the altitude of 60 m. Line and point spacings were 200 m and 7 m, respectively. Scintrex CS2 sensor and radar techniques for magnetic field measurement and a Global Positioning System (GPS) were used. Magnetic field data were acquired at the resolution of 0.1 nT. Data were processed as Geosoft XYZ files and bi-directional gridding was used with a grid cell size equal to point spacing in each area (point spacing gives grid resolution). Linear magnetic anomalies were systematically identified using Total Magnetic Intensity (TMI), First Vertical Derivative (FVD), Analytical Signal (AS), and Tilt Derivative (TDR) maps but always referring back to TMI maps.

The Laisvall deposit was extensively drilled by Boliden Mineral AB for brown-field and subsequent near-field exploration from the 1930´s to the 2000´s. About 1200 boreholes were drilled. Geology and both Pb and Zn grade data in the autochthonous sedimentary rocks are available for 1120 boreholes, 90 % of which are vertical. Information on the location and dynamics of major faults in the mine and in the field were obtained from these legacy data and from the published literature (Lilljequist in Boliden Mineral AB internal reports, unpub. 1965, 1968; Carlson in Boliden Mineral AB internal reports unpub., 1970; Lilljequist, 1973; Rickard et al., 1979; Lucks, 2004). Key profiles were drawn based on new core logging from boreholes carefully selected at the Malå core storage facilities at SGU. This work identified breaks in the stratigraphy and, in combination with the character of the rocks in the drillcore (i.e. core loss, crushed core, probable fault gouge, intensity of fractures, etc), provided a basis for the location of major faults. Delineation of lithological units and of mineralisation grade in 3D space was made using the Leapfrog Mining 3D software after having modelled fault surfaces in the autochthonous sedimentary sequence.
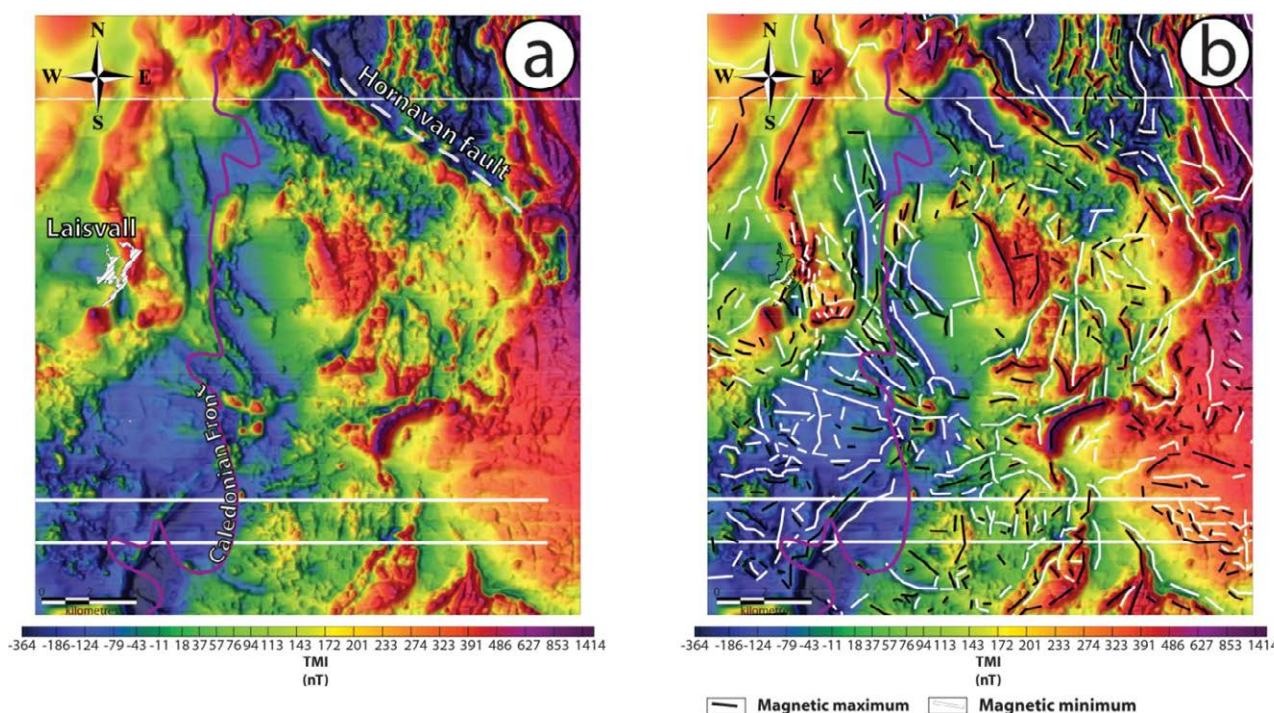
Fig. 1 a) Total Magnetic Intensity (TMI) airborne magnetic map of the Laisvall area. The eastern front of the Scandinavian Caledonides (purple line), the location of the Laisvall deposit and the trace of the fault at the ground surface along Lake Hornavan are shown for reference; b) Linear magnetic anomalies (magnetic minima and maxima) inferred from TMI data. The fault along Lake Hornavan appears as a series of magnetic minima. In the area of the Laisvall deposit, magnetic lineaments show inflection areas where their trend changes from approximately NE–SW to NW–SE. The stratabound Pb-Zn Laisvall deposit is aligned predominantly along magnetic lineaments with a NE–SW trend. The three horizontal white lines are artefacts related to gridding. These do not relate to any magnetic minima.

3.2 Results and discussion

West of the eastern front of the Scandinavian Caledonides (Fig.1a), the Palaeoproterozoic crystalline basement is covered by Ediacaran–Cambrian autochthonous sedimentary rocks and then by allochthonous Caledonian thrust sheets. The trends in magnetic lineaments are the same on both sides of the front and match the regional geological trends to the east in the Fennoscandian Shield, implying that magnetic lineaments correspond to geological features in the basement (Figs. 1a & 1b). Magnetic minima have been

classified into two main sets; N–S to NE–SW and WNW–ESE to NW–SE (Fig. 1b).

Magnetic minima correlate with major faults in the Palaeoproterozoic basement. The NW–SE-striking fault that is related to the 200 m deep Lake Hornavan is identified in geophysical data as a series of magnetic minima. Magnetic lineaments show inflection areas where their trend radically changes direction. The autochthonous stratabound Pb-Zn Laisvall deposit is spatially associated with such an inflection area in the basement and mainly follows a NE–SW trend (Fig. 1b).

Faults mapped in the Laisvall area using aerial photographs and field studies have two main orientations, NNE–SSW and NW–SE (Lilljequist, 1973). Some faults cut through both the allochthonous thrust nappes and the autochthonous Ediacaran–Cambrian rocks. Lilljequist (1973) characterized these faults as being related to orogenic collapse. The present work shows that magnetic minima in the Palaeoproterozoic basement correlate with faults in the Ediacaran–Cambrian sedimentary rocks. For this reason, it has been inferred that the faults affecting the cover rocks (and locally the allochthonous thrust sheets) continue downwards into the Palaeoproterozoic basement and represent reactivated basement structures.
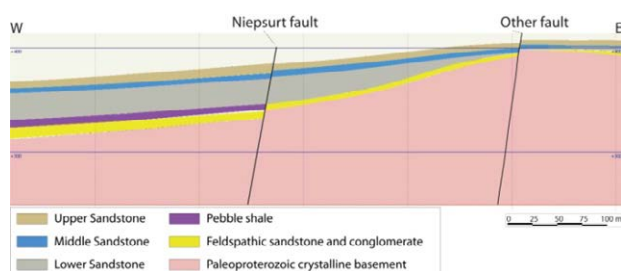
Fig. 2 West-east cross-section through the Niepsurt fault in the Laisvall deposit showing evidence for syn-sedimentary faulting after deposition of the feldspathic sandstone and conglomerate.

Major faults have been recognized in the Laisvall mine (Figs. 2–4; Kautsky & Nadok faults in Lilljequist, 1973; Rickard et al., 1979; Lucks, 2004; Kramaviken & Niepsurt faults, this study). They trend NNE–SSW to NE–SW, NNW–SSE or N–S. The detailed 3D modelling carried out in the present study displays facies changes and thickness variations at the meter scale of several sandstone horizons on either side of several faults (e.g. the Niepsurt fault, Fig. 2). The facies distribution indicates syn-sedimentary block movement after deposition of the feldspathic sandstone and conglomerate that represents the erosion surface of the Palaeoproterozoic basement. These findings are consistent with the interpretation that Baltica was intensively peneplained during the Neoproterozoic and completely flat at the dawn of the Cambrian (Nielsen and Schovsbo, 2011).

The main elongation of the Pb-Zn ore bodies is NE–SW, locally changing to NW–SE. In addition, the highest Pb grades are closely centred on the Nadok fault (Figs. 3–4). Ore grades depict plume-like features as recognized in a NW–SE section across the Nadok fault (Fig. 3): i) Pb grades are the highest closer to the fault and diminish away from it, ii) in contrast to the Pb

grades, the highest Zn grades are more distal away from the Nadok fault, iii) Pb and Zn grades accumulated preferentially towards the top of the host sandstone aquifers in a similar manner as the variation in grades recognized in several MVT Pb-Zn deposits (e.g., Topla-Mežica deposits in Slovenia; Spangenberg & Herlec, 2006). As in other deposits, this morphology and the available stable isotope data (Rickard et al., 1979 & ongoing work) are best interpreted to correspond to sour gas that formed by heating of kerogen and accumulated by density at the top of host permeable horizons. The gas provided H_2S by thermogenic sulphate reduction to the metal-bearing fluids and triggered subsequent precipitation of Pb-Zn sulphides (Anderson and references therein, 2008).
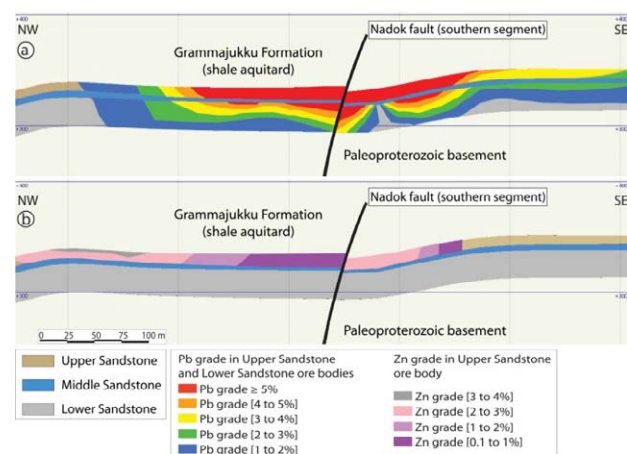
Fig. 3 NW-SE cross-sections through the Nadok fault in the Laisvall deposit; a) distribution of Pb grades in the Upper Sandstone and Lower Sandstone ore horizons of the Laisberg Formation, b) distribution of Zn grades in the Upper Sandstone ore horizon.

4 Conclusions

This multidisciplinary approach has identified the primary role of structures and broader tectonic features in localizing and constraining not only the sedimentary facies distribution but also the origin of the sandstone-hosted Pb-Zn mineralisation at the Laisvall deposit. Magnetic lineaments match geological features in the Palaeoproterozoic basement. Magnetic minima, trending either N–S to NE–SW or WNW–ESE to NW–SE, can be correlated with faults in the autochthonous Ediacaran–Cambrian sedimentary cover rocks. Faults affecting the host sedimentary rocks at Laisvall are interpreted to extend downwards into faults in the underlying Palaeoproterozoic crystalline basement and the latter are inferred to have been reactivated.

The two fault sets (N–S to NE–SW and WNW–ESE to NW–SE) are inferred to have conditioned basin architecture and deposition of sediment during Ediacaran–Cambrian time (syn-sedimentary block faulting) as basin-parallel and transfer faults, respectively. These faults also localized deformation during post-sedimentary and post-mineralisation tectonic regimes.

Stratabound Pb-Zn deposits are spatially associated with inflection areas along magnetic lineaments in the

basement. In these areas, magnetic lineaments abruptly change trend from NE–SW to NW–SE. The former corresponds to the main trend of mineralisation in the stratabound Pb-Zn deposit at Laisvall.

Modelling work in 3D space shows plume-like features for Pb and Zn grades demonstrating that the faults with N–S to NE–SW orientation acted as feeders for at least the metal-bearing mineralizing fluids. In addition, mineralisation tends to accumulate towards the roof of sandstone aquifers in a similar manner as described in MVT deposits in other parts of the world.
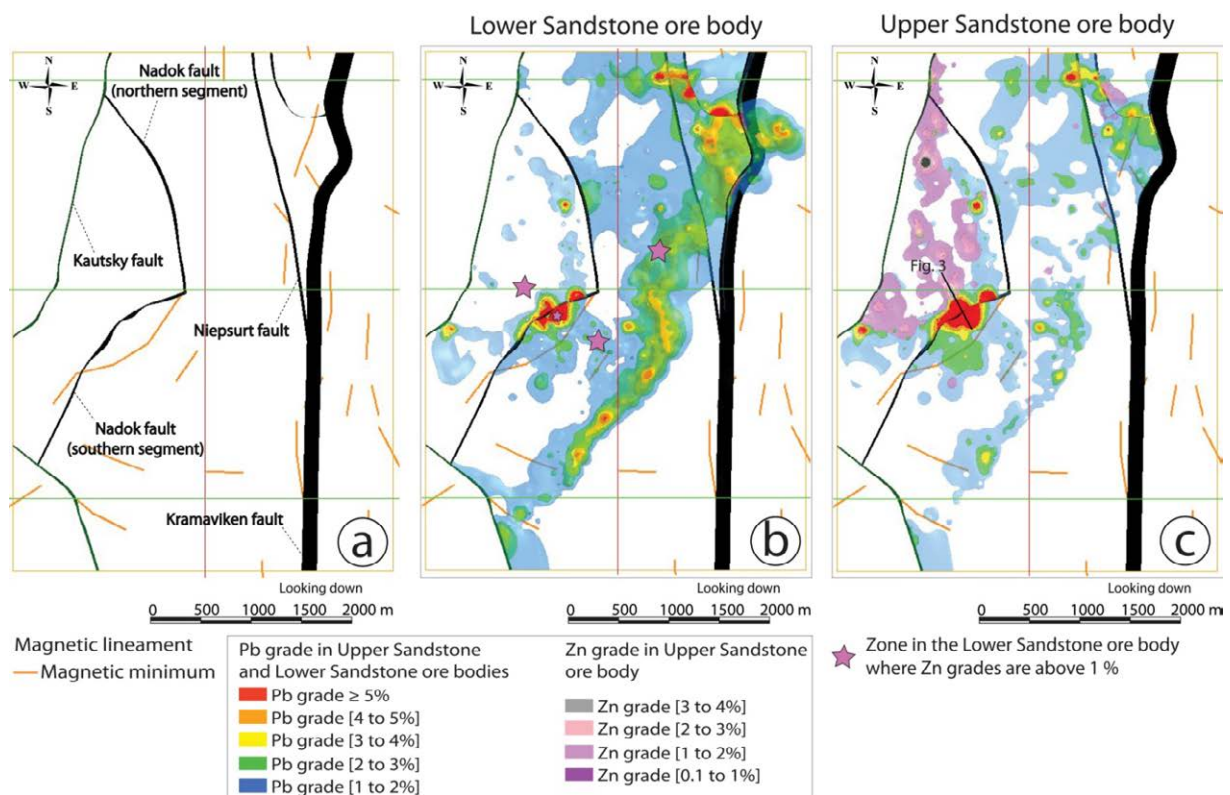
Fig. 4 a) Map showing magnetic minima (brown lines) and faults (black lines) in the Ediacaran–Cambrian siliciclastic cover rocks in the Laisvall mine; b) Pb grade distribution in the Lower Sandstone ore body in the Laisvall mine. Areas with Zn grades above 1% are identified by purple stars; c) Pb & Zn grades in the Upper Sandstone ore body.

Acknowledgements

References

Anderson GM (2008) The mixing hypothesis and the origin of Mississippi Valley-Type ore deposits. Economic Geology 103:1683-1690

Gee DG (1975) A tectonic model for the central part of the Scandinavian Caledonides. American Journal of Science 275A:468-515

Grip E (1954) Blymalmen vid Laisvall, dess geologi och jämförelse med några utländska förekomster. Geologiska Föreningens i Stockholm Förhandlingar 76:357-380 (in Swedish)

Lilljequist R (1973) Caledonian geology of the Laisvall area, Southern Norbotten, Swedish Lappland. Geological Survey of Sweden C 691, 43 p

Ljungner E (1950) Urbergsytans form vid Fjällranden. Geologiska Föreningens i Stockholm Förhandlingar 72-3 (in Swedish)

Lucks, T.J. (2004) Controls on the ore distribution of the Laisvall deposit, Sweden. Unpublished doctoral thesis, University of Cardiff.

Nielsen AT & Schovsbo NH (2011) The Lower Cambrian of Scandinavia: Depositional environment, sequence stratigraphy and paleogeography. Earth-Science Reviews 107:207-310

Rickard DT, Willdén MY, Marinder NE & Donnelly TH (1979) Studies on the genesis of the Laisvall sandstone lead-zinc deposit, Sweden. Economic Geology 74:1255-1285

Roberts D (2003) The Scandinavian Caledonides: event geochronology, paleogeographic settings and likely modern analogues. Tectonophysics 365:283-299

Roberts D & Gee D.G. (1985) An introduction to the structure of the Scandinavian Caledonides. In: Gee, D.G., Sturt, B.A. (eds) The Caledonide Orogen - Scandinavia and related areas, Chichester, Wiley, pp 55-68

Spangenberg JE & Herlec U (2006) Hydrocarbon biomarkers in the Topla-Mežica Zn-Pb deposits, Northern Karavanke/Drau Range, Slovenia: Paleoenvironment at the site of ore formation. Economic Geology 101:997-1021.

Stephens MB (1986) Stratabound sulphide deposits in the Central Scandinavian Caledonides. 7th IAGOD Symposium and Nordkallot project meeting, Excursion Guide n°2, Geological Survey of Sweden Ca 60, 68 p

Stephens MB (1988) The Scandinavian Caledonides: a complexity of collisions. Geology Today 4:20-26

Willdén MY (1980) Paleoenvironment of the autochthonous sedimentary rocks sequence at Laisvall, Swedish Caledonides: PhD thesis, Stockholm, Sweden, Stockholms Universitets Geologiska Institutionen, 100 p

Willdén MY (2004) The Laisvall sandstone-hosted Pb-Zn deposit: Geological overview. Society of Economic Geologists, Guidebook series 33:115-127

Timing and sulphide crystallization sequence of the Håkansboda Cu-Co deposit in Bergslagen, Sweden

Mikael Tillberg, Andreas Inerfeldt, Johan Hogmalm
Earth Sciences Centre, University of Gothenburg, Box 460, S-405 30, Göteborg, Sweden

Marianne Richter
Institut für Geowissenschaften, Johannes Gutenberg – Universität Mainz, J.-J.-Becher-Weg 21, D-55099 Mainz, Germany

Abstract. The Håkansboda Cu-Co sulphide deposit in the Bergslagen ore district, south-central Sweden, is located in a metacarbonate unit within a folded sequence of metavolcanic and metasedimentary rocks in the Guldsmedshytte syncline. The chalcopyrite and pyrrhotite-dominated mineralization is hosted by quartz-rich volcano-sedimentary, calc-silicate and carbonate host-rocks. Solid-solution element exchange between cobalt-bearing sulpharsenides in the NiAsS-CoAsS-FeAsS system suggests that glaucodote formed at temperatures of at least 650°C. Cobaltite crystallized at temperatures below 450°C in equilibrium with the bulk of low-temperature chalcopyrite-pyrrhotite mineralization. The first findings of gersdorffite crystals at Håkansboda are located in a small metabasite dyke, implying that leaching of mafic rocks may have provided Co and Ni to the ore-forming fluids. In-situ U-Pb dating of hydrothermal monazites with LA-ICPMS yield a concordia age of 1786 ± 23 Ma, overlapping late Svecofennian granite intrusions and regional metamorphism in Bergslagen. $\delta^{34}S_{V\text{-}CDT}$ values of ten mineralized samples in varying host-rocks range between -2.95 and -4.66, indicating a predominant magmatic sulphur source. Hot fluid infiltration, probably driven by granitic intrusions or related regional metamorphism, formed the present outline of Cu-Co ore bodies. The main mineralization appears to be structurally controlled and preferentially replaces folded quartz-rich layers associated with dissolution of feldspar and micas.

Keywords: Håkansboda Cu-Co deposit, cobalt sulpharsenides, in-situ monazite dating, sulphur isotopes

1 Introduction

Mining has occurred periodically in the Håkansboda Cu-Co deposit since the first activity in the 15th century. Exploration is currently performed by Kopparberg Mineral AB, the latest in the long list of companies that have owned the exploration rights at Håkansboda. Detailed investigations and extensive drilling during the 1980's led to an understanding of the geometry of the mineralization and structural features of host-rocks (e.g. Carlon 1986 (unpublished)). The origin of the mineralization is however still ambiguous, especially in a larger scale since numerous smaller Cu- and Fe deposits occur at different levels in the folded stratigraphy.

In this study, geochemical patterns in and around the deposit, textural relationships between mineralization and host-rock, in-situ U-Pb monazite dating with LA-ICPMS and sulphur isotope distributions are all presented in order to constrain the timing of sulphide crystallization and decipher ore-forming processes.

2 Geological setting

The mineralizations in the Bergslagen ore district belong to metavolcanic and metasedimentary rocks formed at about 1.9 Ga in the southwestern parts of the Fennoscandian shield. The Guldsmedshytte syncline is a folded volcanic succession with metasedimentary rocks in the upper parts of the stratigraphy (Stephens et al. 2009). The first of the two dominating folding events that affected the stratigraphy produced the major syncline structure with a NE-SW trending fold axis, which later was folded by a second event with NW-SE trending fold axis (Carlon and Bleeker 1988). The deformation events preceded granitoid intrusions with associated regional metamorphism at about 1.88-1.86 Ga and 1.83-1.78 Ga (Stephens et al. 2009).

Håkansboda Cu-Co sulphide deposit consists of elongated ore bodies in a metacarbonate horizon on the eastern limb of the Guldsmedhytte syncline. Iron oxide deposits and occasionally associated Cu-Fe sulphides occur within the stratigraphically underlying metavolcanics, overlying metapelites and also within the major carbonate horizon. Pb-Zn-mineralizations also exist within the stratigraphy, with the currently mined Lovisa Pb-Zn mine located approximately one km southwest of Håkansboda being the most prominent.

The rocks in the upper parts of the stratigraphy have experienced potassic and magnesium alteration on a regional scale related to synvolcanic fluid circulation. The main carbonate is mainly dolomitic and has a spotty appearance because of large amounts of magnesium-iron silicate crystals, now mainly serpentine pseudomorphs or diopside. Calc-silicate reaction skarns were formed at the contacts between carbonates and intercalations of quartz-rich volcano-sedimentary layers due to high-temperature metamorphism.

3 Mineralization characteristics and relationships to host-rocks

The main ore zone in Håkansboda has a strike-length of 900 meter proven from the surface to 600 meters depth along the dip of strata and a thickness rarely exceeding 80 meters (Carlon 1986 (unpublished)). A large number of ore-related minerals have been identified in the ore bodies (Table 1).

The mineralization mainly consists of chalcopyrite and pyrrhotite with minor amounts of cobalt-bearing sulpharsenides, pyrite and magnetite. Textural relation-

ships clearly show that mineralization replaces and crosscuts three types of host-rocks. Volcano-sedimentary layers host the most massive mineralization where the sulphide matrix encloses rounded quartz-dominated aggregates in a vein-type or durchbewegung (ball ore) texture. The calc-silicate host-rocks are mainly composed of diopside with vein-type or disseminated mineralization. The carbonate-hosted mineralization occurs in veins along sub-grain boundaries and in dolomite fractures that was caused by brittle deformation.

The differences in ore grades and mineralization styles between the host rocks may be explained by a combination of pH and Eh conditions and dissolution of host-rock minerals. Silicate-rich host-rocks show evidence of feldspar and mica dissolution providing space for transport of massive mineralization.

Table 1. Ore-related minerals identified at Håkansboda. Cobalt-bearing sulpharsenides are highlighted. Data is partly from Koark (1983).

Major minerals	Chemical formula	Rare minerals	Chemical formula
Chalcopyrite	$CuFeS_2$	Molybdenite	MoS_2
Pyrrhotite	$Fe_{1-x}S$	Galena	PbS
		Sphalerite	ZnS
		Gersdorffite	**(Ni,Co,Fe)AsS**
Minor minerals	**Chemical formula**	Breithauptite	NiSb
		Löllingite	$FeAs_2$
Arsenopyrite	**FeAsS**	Tennantite	$(Cu,Fe)_{12}As_4S_{13}$
Cobaltite	**CoAsS**	Tetrahedrite	$(Cu,Fe)_{12}Sb_4S_{13}$
Glaucodot	**(Co,Fe)AsS**	Cubanite	$CuFeS_3$
Magnetite	Fe_3O_4	Bismuth	Bi
Pyrite	FeS_2	Kallilite	Ni(Sb, Bi)S
		Uranite	UO_2
		Electrum	Au/Ag
		Native Silver	Ag
		Native gold	Au
		Argentite	AgS
		Bournonite	$CuPbSbS_3$
		Gudmundite	FeSbS
		Tetradymite	Bi_2Te_2S
		Chalcocite	Cu_2S
		Allargentum	(Ag,Sb)

4 Sulphide crystallization sequence

Major element analysis of cobalt-bearing sulpharsenides were performed at the University of Gothenburg by a Hitachi S-3400N scanning electron microscope (SEM) equipped with an Oxford systems energy-dispersive spectrometer (EDS). Analyses were performed using a 20 keV accelerating voltage, 3.5 nA beam current with a working distance of 9.9 mm, calibrated with Co, and evaluated with Smithsonian mineral standards. Backscattered electron (BSE) imaging was used to distinguish the high-density minerals on carbon-coated thin sections.

Solid solution exchange of Co, Fe and Ni in the sulpharsenides was used to estimate the crystallization temperature of these sulphides by plotting the relative element proportions in a ternary NiAsS-CoAsS-FeAsS diagram (Fig. 1), with isotherms after Klemm (1965). Cobalt-bearing sulpharsenides associated with massive sulphide mineralization have low Ni contents and plot along the CoAsS-FeAsS solid solution line. The

glaucodote crystallized from a high-temperature fluid, with the subsequent crystallization of cobaltite and Co-rich arsenopyrite accompanied by extensive chalco-pyrite-pyrrhotite mineralization during decreasing fluid temperature. The results agree with previous studies by Koark (1983), textural relationships and the association of chalcopyrite-pyrrhotite with undeformed actinolite, calcite and chlorite.

The only occurrence of Ni-rich sulpharsenides is located within a thin metabasite dyke, where gersdorffite now has been identified for the first time at Håkansboda. The gersdorffite crystals are Co-Fe-rich (Fig. 1) and have no association to other sulphides, but are instead related to fluid flow structures demonstrated by Cr- and Cl-rich biotite. This may imply that leaching of mafic rocks could be sources for at least Co and Ni.
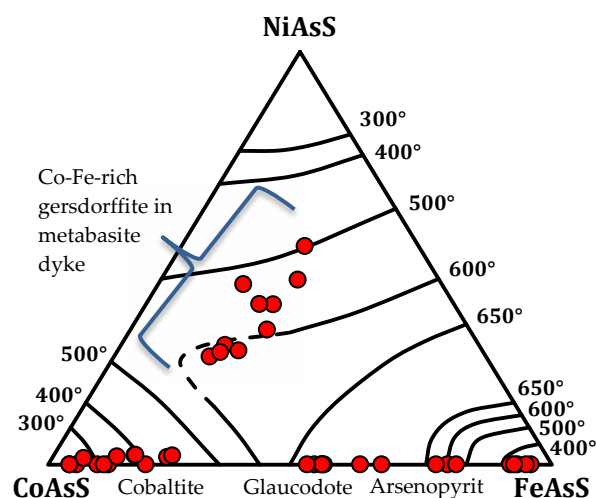
Figure 1. NiAsS-CoAsS-FeAsS diagram with data from cobalt-bearing sulpharsenides in the Håkansboda deposit.

5 Monazite dating

In-situ U-Pb dating of monazites in a massive calc-silicate-hosted sulphide sample was performed by LA-ICPMS, using a Agilent 7500a series NWR 213 with 10 μm spot size, an energy of 5.0 J/cm², 15 sec. dwell time and 10 Hz repetition rate. Data was standardized with the monazite standard 44069 from Wissahickon Formation in the Wilmington Complex, USA, which has an age of 424.86 Ma (Aleinikoff et al. 2006).

The U-Pb concordia diagram (n=17) yields an age of 1786 ± 23 Ma (Fig. 2), which overlaps ages of the late Svecofennian Granite-Pegmatite intrusive suite occur-ring in the area (Stevens et al. 2009), as well as U-Pb monazite ages of associated granulite-facies regional metamorphism in the Bergslagen region (Andersson et al. 2006). Contrary to previous considerations of peak metamorphic temperatures in the Håkansboda area around 550°C (Lundström 1983), several lines of evidence suggest higher temperatures, at least locally. In addition to glaucodote crystallization temperatures, peak metamorphic temperatures of around 650°C are also implied by the occurrence of sillimanite in low-pressure mineral assemblages and local low degrees of migmatitization in metapelites belonging to the upper parts of stratigraphy.

A majority of the investigated monazites display low Th/U ratios (between 0.1 and 0.7), but four concordant analytical spots have Th/U ratios between 2.5 to 6.4. Monazites with anomalously high ratios were most likely subject to exchange of REE out and Th+Si into the crystals caused by the Cu-Fe sulphide-precipitating fluid after monazite crystallization. Monazites with low Th/U ratios often have rims of apatite, suggesting non-equilibrium with lower temperature fluids. The element exchange is not likely to affect the U or Pb isotopic ratios, as ages are concordant despite the discrepant Th/U ratios. The prevalent homogeneity in BSE imaging and generally low Th/U ratios are in line with monazite crystallizing from a hydrothermal fluid rather than surviving peak metamorphism. Chalcopyrite inclusions in a concordant monazite crystal within a partially resorbed glaucodote suggest that a Cu-Fe sulphide-bearing fluid was present during monazite crystallization occurring at temperatures higher or equal to glaucodote crystallization.
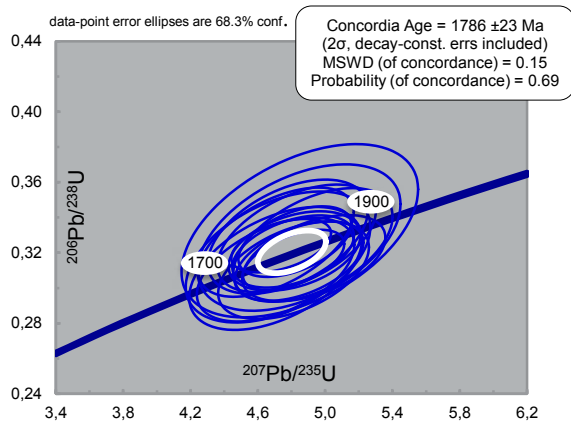
Figure 2. U-Pb concordia diagram of in-situ monazite dating in a massive calc-silicate-hosted sulphide sample from Håkansboda deposit.

6 Sulphur isotopes

A sulphur isotope study was performed on ten samples of ore-related minerals in varying host-rocks. Tin capsules containing reference or sample material plus vanadium pentoxide catalyst were loaded into an automatic sampler for preparation, and analysis was performed using Elemental Analysis - Isotope Ratio Mass Spectrometry (EA-IRMS). Preparation and analysis were executed at Iso-Analytical Ltd, UK. The results were compared to V-CDT (troilite of the Canyon Diablo meteorite), revealing $\delta^{34}S_{V-CDT}$ values between -2.95 and -4.66 (Table 2). The values are slightly too negative for a sole magmatic sulphur source. The sulphur isotopes may have been overprinted by metamorphism, although not supported by literature even at such high metamorphic temperatures indicated in the area. No contributions from seawater or meteoric water are supported.

Table 2. Sulphur isotope data from ten ore-related mineral samples in varying host-rocks. No isotopic fractionation factors exist for the analysed cobalt-bearing minerals.

Cobalt-bearing minerals		$\delta^{34}S_{V-CDT}$
Calc-silicate-hosted	Cobaltite	-2.98 ‰
Carbonate-hosted	Co-rich arsenopyrite	-4.66 ‰
Chalcopyrite-pyrrhotite mineralization	Cpy/(Cpy+Po)	$\delta^{34}S_{V-CDT}$
Quartz-hosted	Pyrrhotite-dominated	0.1	-4.23 ‰
	Chalcopyrite-dominated	0.9	-3.84 ‰
Carbonate-hosted	Pyrrhotite-dominated	0.05	-3.73 ‰
	Pyrrhotite-dominated	0.2	-4.65 ‰
	Pyrrhotite-dominated	0.05	-2.95 ‰
Calc-silicate-hosted	Chalcopyrite-dominated	0.75	-3.39 ‰
	Pyrrhotite-dominated	0.05	-3.32 ‰
	Pyrrhotite mineralization	0	-4.09 ‰

7 Preliminary conclusions

Geochemistry and textures of cobalt-bearing sulphides with different relationships to chalcopyrite-pyrrhotite mineralization indicate protracted sulphide crystallization from high-temperature to major precipitation at lower, post-metamorphic grades. This is supported by crosscutting features of mineralization to all host-rocks and the association of low temperature minerals with massive and vein-type mineralization. The monazite ages suggest that the indicated temperatures were reached during regional metamorphism that could be related to the late Svecofennian granites intruding at 1.83-1.78 Ga. Complete remobilization of sulphides cannot be precluded, but the geometry of the Håkansboda ore zone and the spatial and geochemical distributions of surrounding copper mines suggest that the layers was folded during ore-precipitating fluid infiltration. Metabasites and possibly other metal source rocks were leached at depth by fluids that may have been derived or driven by heat from granitoid intrusions. Fluid flow was possibly channelized upwards through the carbonate horizon with preferential replacement of quartz-feldspar layers.

References

Aleinikoff JN, Schenck WS, Plank MO, Srogi LA, Fanning CM, Kamo SL, Bosbyshell H (2006) Deciphering igneous and metamorphic events in high-grade rocks of the Wilmington Complex, Delaware: Morphology, cathodoluminescence and backscattered electron zoning, and SHRIMP U-Pb geochronology of zircon and monazite. Geological Society of America Bulletin 118:39-64

Andersson UB, Högdahl, K, Sjöström H, and Bergman S (2006) Multistage growth and reworking of the Palaeoproterozoic crust in the Bergslagen area, southern Sweden: evidence from U-Pb geochronology. Geological Magazine 143:679-697

Carlon CJ, Bleeker W (1988) The geology and structural setting of the Håkansboda Cu-Co-As-Sb-Bi-Au deposit and associated Pb-Zn-Cu-Ag-Sb mineralisation, Bergslagen, central Sweden. Geologie en Mijnbouw 67:279-292

Klemm DD (1965) Synthesen und Analysen in den Dreiecks-diagrammen FeAsS-CoAsS-NiAsS und FeS 2-CoS 2-NiS 2. Neues Jahrbuch für Mineralogie 103:205-255

Koark HJ (1983) Håkansboda, *in* Grip E, (ed.) Malmstyrande strukturer i Bergslagen. Svenska Gruvföreningen, pp 42-45.

Lundström I (1983) Beskrivning till Berggrundskartan Lindesberg SV. Sveriges Geologiska Undersökning, v. Af 126. pp 1-140

Stephens MB, Ripa M, Lundström I, Persson L, Bergman T, Ahl M, Wahlgren C-H, Persson P-O, Wickström L (2009) Synthesis of the bedrock geology in the Bergslagen region, Fennoscandian Shield, south-central Sweden. Sveriges geologiska undersökning, Ba 58, pp 259

Iron and oxygen isotope systematics of apatite-iron oxide ores in central Sweden

Franz Weis, Valentin R. Troll, Erik Jonsson*, Karin Högdahl, Abigail Barker
Department of Earth Sciences, CEMPEG, Uppsala University, Villavägen 16, SE-75236 Uppsala, Sweden

Chris Harris
Department of Geological Sciences, Library Rd, University of Cape Town, Rondebosch 7701, Republic of South Africa

Marc-Alban Millet
Department of the Geophysical Sciences, University of Chicago and Enrico Fermi Institute, 5734 South Ellis Avenue, Chicago, IL 60637, United States of America

Katarina P. Nilsson
*Geological Survey of Sweden, Villavägen 18, Box 670, SE-75128 Uppsala, Sweden

Abstract Sweden is the most important iron producer in Europe, yet the genesis of the main iron source, the Kiruna-type apatite-iron-oxide deposits, remains enigmatic. We report oxygen and iron isotope data from the Grängesberg Mining District (GMD), which is the largest Kiruna-type deposit in central Sweden. The data show that massive magnetite ores exhibit $\delta^{18}O$ between +0.1 and +2.8 ‰ and $\delta^{56}Fe$ from +0.26 to +0.9 ‰, whereas vein, disseminated and carbonate-hosted GMD magnetite exhibits $\delta^{18}O$ of -1.1 to -0.8 ‰ and $\delta^{56}Fe$ of -0.02 to +0.24 ‰. In addition, oxygen and iron isotopes of magnetites from other iron oxide deposits, as well as from recent volcanic rocks, were analysed. These include both ortho-magmatic and hydrothermal magnetites and thus provide a reference base to be compared with the GMD samples. About 87 % of magnetites from apatite-iron-oxides at the GMD reflect ortho-magmatic processes (crystallisation from magma or magmatic fluids at high temperatures). The remaining 13 % of the GMD magnetites are of vein, disseminated and carbonate-hosted types, which appear to have been in equilibrium with a high-$\delta^{18}O$ and low-$\delta^{56}Fe$ fluid at temperatures below 400 °C, indicating formation through hydrothermal processes.

Keywords. Kiruna-type apatite-iron-oxide ore, Grängesberg Mining District, Bergslagen, Sweden, oxygen isotopes, iron isotopes.

1 Introduction

The apatite-iron-oxide mineralisations in the Grängesberg Mining District (GMD) are situated in the northwestern part of the Palaeoproterozoic Bergslagen ore province in central Sweden. The Grängesberg mine has a past production of 152 Mt of iron ore with a grade of 58 % Fe and 0.81 % P. The mine closed in 1989, but is currently targeted for reopening. The Kiruna-type GMD deposits are traditionally compared to the iconic Kiruna deposit in northern Sweden (cf. Looström 1929), and all major features suggest a similar origin (Jonsson et al. 2010), although the genetic processes leading to formation of apatite-iron-oxide mineralisations are still not fully understood. Over the last 100 years, a range of

hypotheses has been put forward, and opinions revolve around a direct magmatic origin versus a hydrothermal one. A direct magmatic, or ortho-magmatic origin is normally understood to be either formation by direct magmatic crystallisation or from high-temperature magmatic fluids (e.g. ≥ 800 °C), or as in the case of the Kiruna-type deposits, by the potential segregation of an iron oxide melt, that may subsequently crystallise as a separate body. Hydrothermal processes include hydrothermal replacement, as well as hydrothermal precipitation at more moderate temperatures (≤ 400 °C). Both hypotheses are supported in part by field observation, textural relationships and the geochemical character of key localities like El Laco, Kiruna and to some extent Grängesberg, but a consensus has not been reached (compare Rhodes & Oreskes 1999, Nyström et al. 2008, Corona-Esquivel et al. 2010, Jonsson et al. 2011).

Building on the oxygen isotope dataset of Jonsson et al. (2011), we have analysed iron isotopes on the same samples to further test the ore forming conditions for the apatite-iron-oxide deposits at the GMD. The stable isotope compositions are compared to isotope signatures of other iron oxide deposits that have undisputedly been formed by hydrothermal or magmatic processes. Furthermore, the temperature dependence of stable isotope fractionation allows ore forming temperatures to be calculated, thus providing a crosscheck for the primary isotope results.

2 The Grängesberg deposit

The apatite-iron-oxide deposit at Grängesberg is dominated by magnetite with subordinate hematite, and both oxides occur as associated veins and disseminations in the immediate host rocks. In the massive ores, bands of fine-grained fluorapatite, with variable amounts of silicate minerals, are characteristic. The main deposit, the so called "Export Field", consists of iron oxides in the ratio of approximately 80 % magnetite and 20 % hematite. Hematite-dominated parts occur mostly in the footwall and in the vicinity of crosscutting pegmatite dykes. Alteration zones in the host rocks right next to the

mineralisation comprise disseminated and discrete phyllosilicate (biotite, chlorite) and amphibole-rich assemblages (so-called *sköl*) with variable amounts of iron oxides and fluorapatite (Jonsson et al. 2011). The mineralisation is stratiform and dips between 70° and 80° towards the south-east and could be followed for more than 900 m at the surface where its width ranges between 50 and 100 m (Johansson 1910). The ore is hosted by metavolcanic rocks of andesite to dacite composition belonging to the 1.91-1.87 Ga volcano-sedimentary succession of Bergslagen.

3 Samples for iron and oxygen isotope analyses

Mineralised samples from Grängesberg were collected from three drillcores (DC), DC 690 (n=7), DC 717 (n=3) and DC 575 (n=3), that transect the deposit with a shallow plunge (< 20 °) and were drilled at 650 m (n=2) and 570 m below the surface, respectively. In addition to massive apatite-iron-oxide samples, two samples were selected from magnetite veins and disseminations in the host rocks. One sample was collected from the smaller Blötberget apatite-iron-oxide deposit within the GMD and another from the contrasting limestone-hosted iron oxide deposit at Björnberget. Besides magnetite, quartz fragments were separated from the massive mineralisations (n=3). To obtain a meaningful and widely applicable comparison of the GMD samples with hydrothermal and magmatic reference samples, oxygen and iron isotope values were also determined on massive apatite-iron-oxide ores from El Laco, Chile (n=6), and Kiruna, Sweden (n=1), the iron oxide-polymetallic skarn deposit at Dannemora, Sweden (n=4), the layered igneous intrusion of Panzhihua in China (n=2), the Bushveld igneous complex in South Africa (n=1), the Swedish layered igneous intrusions of Taberg (n=1), Ulvön (n=1), and Ruoutevare (n=1) and from a banded iron formation at Striberg, Sweden (n=1). Samples representative of recent igneous magnetites were chosen from basaltic andesites from Indonesia (n=6), basalts and dolerite from the Canary Islands (n=3) and Iceland (n=1), dacites from New Zealand (n=2), and gabbro from Cyprus (n=1).

4 Isotope Geochemistry

4.1 Oxygen Isotopes

Magnetites from massive GMD ores show oxygen isotope values between +0.2 and +2.8 ‰, while the additional magnetite samples from the GMD (vein and disseminated material, Blötberget and Björnberget magnetite) has much lower values, in the range of -1.1 to +0.1 ‰ (Fig. 1). Quartz fragments from the massive part of the deposit have high $\delta^{18}O$-values of +7.6 to +8.7 ‰. The apatite-iron-oxide ores from Kiruna and El Laco show a much larger range in $\delta^{18}O$ values than the GMD samples, between -4.3 and +4.4 ‰. Magnetite from selected layered igneous intrusions (Taberg, Ulvön,

Ruoutevare, Bushveld, Panzhihua) and volcanic reference samples, in turn, shows positive $\delta^{18}O$-values between +1.78 and +4.84 ‰ and +3.6 to +4.6 ‰ respectively, which is in or near Taylors (1967) range of igneous magnetites ($\delta^{18}O$ = +1.0 to +4.0 ‰). The hydrothermal/low-temperature ore reference materials (e.g. Dannemora and Striberg), show with only one exception very low values for oxygen ($\delta^{18}O$ = -1.2 to +2.1 ‰).
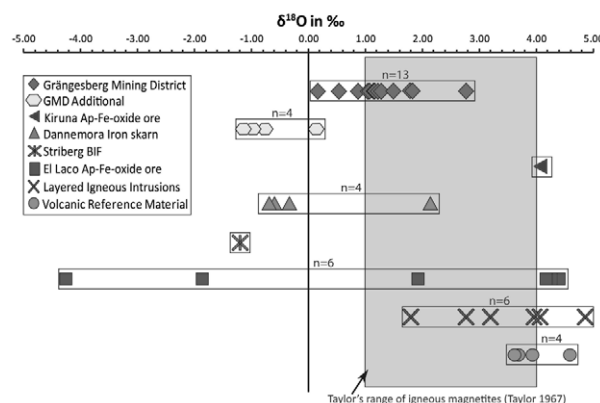
Figure 1. Oxygen isotope signatures of magmatic and hydrothermal magnetites from GMD and selected reference samples.

4.2 Iron Isotopes

Iron isotopes of massive GMD magnetite show a relatively small range with $\delta^{56}Fe$-values of +0.26 to +0.9 ‰ (Fig. 2). The additional GMD samples show $\delta^{56}Fe$-values between -0.02 and +0.33 ‰. Apatite-iron-oxide ores from Kiruna and El Laco yield values similar to the GMD of between +0.19 and +0.36 ‰.
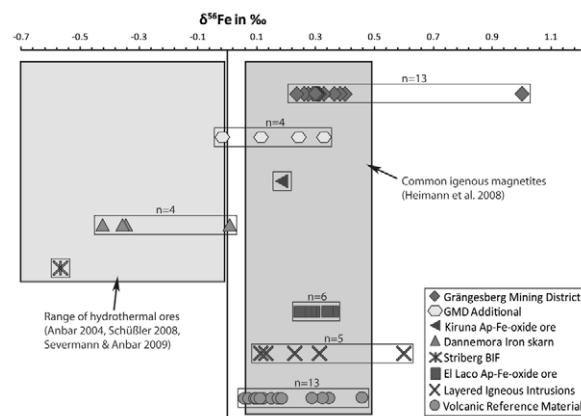
Figure 2. Iron isotope distribution of magnetites from GMD, Kiruna, El Laco and a range of magmatic and hydrothermal reference samples (see text for details).

The Dannemora iron oxide skarn and the Striberg BIF samples are depleted in the heavy isotope and show $\delta^{56}Fe$-values from -0.57 to +0.01 ‰. Magnetites from the layered igneous intrusions and the volcanic reference samples show enrichment in ^{56}Fe with $\delta^{56}Fe$-values from

+0.11 to +0.61 ‰ and from +0.06 to +0.46 ‰ respectively. Notably, most δ^{56}Fe-values of the analysed magnetites in this study lie within the confirmed range of igneous magnetites reported by Heimann et al. (2008, +0.06 to +0.49 ‰).

5 Discussion

The oxygen and iron isotope data from the GMD magnetites (n=14) overlap with the available data from ortho-magmatic magnetites, implying a dominantly magmatic derivation for this mineral. GMD magnetite values are similar to those from layered igneous intrusions and volcanic reference magnetites, and they are distinctly different from hydrothermal magnetites such as those from Striberg or Dannemora (Figs. 1 & 2). Only three samples from the GMD, consisting of vein, disseminated and carbonate-hosted magnetite, overlap with hydrothermal magnetites.

Possible sources calculated for both oxygen and iron isotopes (cf. Zhao & Zheng 2003, Heimann et al. 2008) show that the massive magnetite mineralisation at the GMD with δ^{18}O $\geq$ +0.1 ‰ were in equilibrium with dacite to andesite parent magmas with δ^{18}O between +5.7 and +7.2 ‰ or with magmatic waters of δ^{18}O +6.1 to +8.0 ‰, typical for intermediate arc magmas and their magmatic waters (Fig. 3, cf. Bindemann 2008, Nyström et al. 2008). Iron isotopes reveal that the sources (magma or magmatic water) at the GMD were enriched in the heavy iron isotope (^{56}Fe) compared to common intermediate magmas and magmatic waters, which, in turn, supports an iron oxide enriched melt as the main source for the mineralisation. The source calculations also put the ore formation temperatures in the magmatic window, with derived temperatures between 600 and 900°C. Calculated temperatures from three quartz-magnetite pairs (cf. Chiba et al. 1989) give similar

values of between 600 and 800 °C, which supports the oxygen and iron isotope equilibrium source calculation. Vein, disseminated and carbonate-hosted magnetites from the GMD (δ^{18}O < 0 ‰) can only be explained by high δ^{18}O-fluids at temperatures below 400 °C. These magnetites were in equilibrium with a fluid of δ^{56}Fe = -0.26 to -0.52 ‰, which lies within the spectrum of iron isotopes reported for hydrothermal systems (-0.2 to -0.6 ‰, cf. Severmann & Anbar 2009).

6 Conclusions

On the basis of the presented data, the ore forming processes at the GMD comprised both, an ortho-magmatic and a hydrothermal component, as suggested by Jonsson et al. (2011). The bulk of the ore was formed within a larger volcanic edifice where an oxide enriched melt separated from an andesite to dacite parent magma. Heat-driven hydrothermal activity upon cooling also caused low-temperature (< 400 °C) precipitation of magnetite in form of veins and disseminations. Hydrothermal fluids locally also reacted with limestone to form carbonate-hosted mineralisations.

The isotope data and modelling results are therefore in agreement with a predominantly magmatic origin for the deposits at Grängesberg. Similar apatite-iron-oxide deposits, like those of Kiruna, El Laco, and Blötberget seem also to be of ortho-magmatic origin. The obtained results and interpretations are, moreover, consistent with magmatic magnetite values from various layered intrusions and recent volcanic rocks world-wide, thus lending support to the magmatic hypothesis as the main explanation for the origin of Kiruna-type deposits in Sweden and elsewhere.
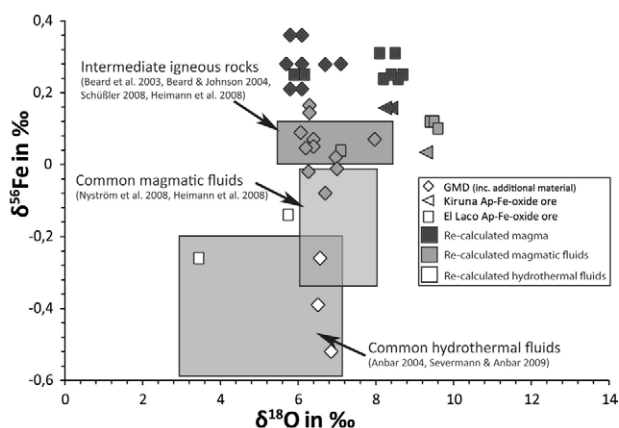
Figure 3. The oxygen and iron isotope relationship of ore forming magmas and fluids with data from Grängesberg, Kiruna and El Laco. Ore forming magmas and fluids were enriched in ^{56}Fe and plot above the reference fields for intermediate magmas and magmatic fluids, suggesting the possible existence of oxide-rich melts in these systems.

References

Anbar AD (2004) Iron stable isotopes: beyond biosignatures. Earth Planet Sci Lett 217: 223-236

Beard BL, Johnson CM, Skulan JL, Nealson KH, Cox L, Sun H (2003) Application of Fe isotopesto tracing the geochemical and biological cycling of Fe. Chem Geol 195: 87-117

Beard BL, Johnson CM (2004) Fe Isotope Variations in the Modern and Ancient Earth and OtherPlanetary Bodies. Rev Mineral Geochem 55: 319-357

Bindeman I (2008) Oxygen Isotopes in Mantle and Crustal Magmas as revealed by Single Crystal Analysis. Rev Mineral Geochem 69: 445-478

Chiba H, Chacko T, Clayton, RN, Goldsmith JR (1989) Oxygen isotope fractionations involving diopside, forsterite, magnetite and calcite: Application to geothermometry. Geochim Cosmochim Acta 53: 2985-2995

Corona-Esquivel R, Martínez-Hernández E, Henríquez F, Nyström JO, Tritlla J (2010) Palynologic evidence for iron-oxide ash fall at La Perla, an Oligocene Kiruna-type iron ore deposit in northern Mexico. GFF 132: 173-181

Heimann A, Beard B, Johnson C (2008) The role of volatile exsolution and sub-solidus fluid/rock interactions in producing high $^{56}Fe/^{54}Fe$ ratios in siliceous igneous rocks. Geochim Cosmochim Acta 72: 4379–4396

Johansson H (1910) Die eisenerzführende Formation in der Gegend von Grängesberg. Geol Fören Förhand l32: 239-410

Jonsson E, Nilsson KP, Hallberg A, Högdahl K (2010) Palaeopreoterozoic apatite-iron oxide deposits of the Grängesberg area: Kiruna-type deposits in central Sweden: In: Nakre HA, Harstad AO, Haukdal G (eds.) NGF abstracts and proceedings Vol 1. 29th Nordic Geological Winter Meeting, 11-13/1-2010, Oslo, Norway, 88-89

Jonsson E, Nilsson KP, Hallberg A, Högdahl K, Troll VR, Weis F, Harris C (2011) Oxygen isotopes and geochemistry of Palaeoproterozoic Kiruna-type deposits in the Bergslagen province, central Sweden. Abstract volume, SGA biennial meeting 2011, Antofagasta, Chile, 494-496

Looström R (1929) Likheter mellan Lapplands- och Grängesbergsmalmerna. GFF 51:303-308

Nyström JO, Billström K, Henríquez F, Fallick AE, Naslund HR (2008) Oxygen isotope composition of magnetite in iron ores of the Kiruna type in Chile and Sweden. GFF 130: 177-88

Rhodes AL, Oreskes N (1999) Oxygen isotope composition of magnetite deposits at El Laco. Chile: Evidence of formation from isotopically heavy fluids. Econ Geol Spec Publ Nr.7: 333-351

Schüßler J (2008) Controls on stable iron isotope variations in magmatic systems - Significance of mineral-melt isotopic fractionation in experiments and nature. PhD-Thesis, Faculty of Natural Science, Gottfried Wilhelm Leibniz Universität Hannover, Germany, 178 p

Severmann S, Anbar AD (2009) Reconstructing Palaeoredox Conditions through a Multitracer Approach: The Key to the past is the Present. Elements 5: 359-364

Taylor HP (1967) Oxygen isotope studies of hydrothermal mineral deposits. In: Barnes HL (ed.): Geochemistry of Hydrothermal Ore Deposits: 109-142, Holt, Rinehart and Winston Inc., New York

Zhao ZF, Zheng YF (2003) Calculation of Oxygen Isotope Fractionation in Magmatic Rocks. Chem Geol 193: 59-80

S 5:
High-tech elements – deposits and processes

Convenors:
Yasushi Watanabe & Laura Lauri

The role of geoscientists in securing the future supply of high technology minerals and metals

Jens Gutzmer, Sandra Birtel, Max Frenzel
Helmholtz-Institute Freiberg for Resource Technology, Halsbruecker Str. 34, 09599 Freiberg, Germany

Abstract. The availability of minerals and metals required for high technology applications has in recent years been widely recognized as being of strategic importance for future development - especially for highly industrialized economies. Because the absolute tonnage of such high technology minerals and metals in industrial products is typically small, inventories in the technosphere will remain limited and widely disseminated. This will significantly hamper recycling efforts. As a direct consequence, primary resources will need to be utilized to secure supply into the foreseeable future. Tapping primary resources appears as a reasonable approach, as these are readily available for most high technology metals. Geoscientists will have to make an important contribution – not only towards exploration and discovery, but also to the implementation of technological concepts for comprehensive resource utilization, i.e., mining operations that are not only economic, but also resource-efficient and environmentally benign.

Keywords. High technology metals, criticality, exploration, mineral systems analysis, geometallurgy

1 Introduction

Price volatility and the danger of supply shortages of the last decade have given rise to the widespread acceptance in industry and politics that the availability of mineral and metalliferous resources (for brevity referred to as minerals and metals from here) is a fundamental ingredient to economic success. There is broad international consensus that metals need to be available in adequate quantities and at economically acceptable prices. Within this context a particular focus has been placed on identifying those resources of which the supply may become "critical". Many of these are essential ingredients for advanced technologies (aka high technologies) in fields such as mobility, renewable energies or communication. In many technology examples, these high technology minerals and metals fulfil nevertheless an essential functional role, but are needed in only very minor quantity. As a result, inventories of such minerals and metals in the technosphere will remain small and disseminated, thus impeding recycling efforts. The demand for such minerals and metals will thus have to be met by exploiting primary resources.

2 Critical vs. High Technology Metals

A number of studies at regional, national and international level have illustrated the difficulty to identify minerals and metals that should be categorized as critical (i.e., NRC 2008; Angerer et al. 2009; Pfleger et al 2009; EC 2010). These studies have taken different approaches to determine the degree of criticality (see Erdmann and Graedel 2011), with supply risk, environmental implications and vulnerability of supply restrictions as common dimensions (Graedel et al. 2012). Given different frames of reference or organizational level (i.e., national, regional, corporate) different suites of minerals and metals are awarded critical status. There is nevertheless a surprising overlap between all studies regarding the choice of critical minerals and metals. This typically includes select industrial minerals (i.e., fluorspar, graphite) and metalliferous resources with small (< 0,5 Mio t/a) to minute (< 1 kt/a) annual production volumes. A further commonality for the selected critical minerals and metals is the expectation that demand will increase due to their use in advanced technologies.

From a geoscientist's perspective the suite of such critical minerals and metals can be subdivided into three groups -based on the single most prominent factor that may limit future supply: (1) geological limitation, (2) geographical limitation, and (3) technological limitation. The first group includes cobalt and the platinum group metals (PGM). In this case, regionally-focused production is justified by geological endowment. Known PGM resources, for example, are focused in only few deposit districts (Bushveld Complex, Norilsk, Great Dyke). The same is true for known cobalt resources that are uniquely concentrated in the Central African Copperbelt.

The second group includes the rare earth elements (REE), antimony, tungsten, graphite, but also niobium and tantalum. In this case, production is currently limited to very few countries, despite the fact that geographic diversification of production appears possible, based on resources and reserves that are known but that remain unutilized.

The third group includes, for example, bismuth, gallium, germanium and indium. These are usually recovered not at the mine site, but as a by-product during metallurgical beneficiation of major commodities such as aluminium (Ga), copper (Ge, Bi, In) or zinc (Ge, In). Furthermore, these metals are produced in only very small tonnages (< 10 kt/a). Their supply appears currently not limited by the amount extracted during mining operations, but by the lack of production capacity and efficient technologies for beneficiation.

3 The role of geosciences

The challenge to secure the future supply of critical high

technology minerals and metals provides unique opportunities for geoscientists. Affiliated with this challenge are many exciting research questions along the entire value chain of raw materials. These range from generating fundamental knowledge for exploration of as yet poorly understood/unknown deposit types, to the development of innovative technological concepts aimed at comprehensive resource utilization, e.g., use of mineral resources that is both economically viable and efficient, as well as environmentally benign. For the purpose of this contribution, only a select few important research questions will be highlighted.

3.1 Exploration

Whilst the mineral systems for major commodities such as gold, copper, zinc or nickel (incl. PGM) are rather well understood, such knowledge remains rudimentary for many high technology minerals and metals. This applies both to those high technology metals that are exploited as major products (i.e., Nb and Ta, REE) as well as to those that are usually recovered as by-products (i.e., Bi, Co, Ga, Ge, In and others). Using REE resources as an example, it is evident that there is currently a unique opportunity to study and compare REE deposits. Exploration projects around the globe cover a large number of geological frameworks and mineralization styles. Using case studies, fundamental advances will be attained towards the understanding of relevant REE mineral systems, such as those associated with alkaline complexes, carbonatites or hydrothermal vein/breccia deposits. Such advances will not only be of academic interest, but are a prerequisite for the development of tangible vectors for exploration. Such advance holds the potential to redress current geographical or geological supply limitations for various high technology metals.

In the case of by-product metals geological processes for their occurrence and concentration in some – but not other – deposits of the same genetic type need to be understood. An excellent example is the apparent enrichment of high technology metals, such as In, in only very few select volcanic-hosted massive sulphide deposits, or the unique enrichment of Ge (and Ga) in Tsumeb-type hydrothermal breccia deposits (Hoell et al. 2007).

Furthermore, the processes controlling the spatial and temporal distribution of by-product metals within the architecture of individual ore deposits need to be better understood. This will be required to guide not only exploration, but also the development of exploitation and processing strategies for by-products in current mining operations.

A particularly attractive challenge in the exploration realm will be the development of novel concepts that may lead to the discovery of previously unknown deposit types in which by-product metals may occur in sufficiently high concentrations to justify exploitation as major product. Although scarce, there are at least some known examples, such as the Apex Ga-Ge deposit in Utah, USA (Bernstein 1986; Dutrizac et al. 1986) or the Dashuigou and Majiagou Bi-Te deposits in Chengdu, China (Mao et al. 1995).

3.2 Comprehensive Resource Utilization

The increasing demand for an ever more complex suite of minerals and metals requires strategies and technologies to exploit primary resources more efficiently and more comprehensively. The decision to develop a particular resource should not only focus on the dominant commodity (major product) – possibly complemented by select by-products (commonly expressed only as "major-product equivalent"). Instead, the entire portfolio of metals and mineral products that are contained in a deposit should be considered during exploration and project development. Excellent examples for the success of such comprehensive resource utilization concepts – though not common – are readily available, such as the Palabora mining operation in South Africa (Verwoerd 1986).

Geoscientists readily appreciate the complexity of natural materials. They are thus uniquely positioned to contribute towards the development and implementation of comprehensive resource utilization concepts. Geometallurgical models considering geological, geochemical, mineralogical, microfabric, as well as geotechnical data (Keeney and Walters, 2011; Birtel et al. 2010) already provide a suitable platform on which such comprehensive resource utilization concepts could be based. For high technology metals occurring only in minor concentrations as substitution within the structure of different minerals this data base will have to be expanded to include information on mineral chemistry/metal deportment. It is proposed that for any future resource development such a comprehensive resource utilization concept should be a technical prerequisite.

4 Conclusion

Natural resources of high technology minerals and metals regarded as critical by politics and industry define a rapidly expanding and important domain for geoscientific research. Geoscientists in academia, in particular, should utilize the opportunity to create the knowledge base needed in the search for such new resources. With an integral understanding of the complexity of natural materials geoscientists are also poised to contribute profoundly to new strategies for comprehensive and efficient resource utilization. Last but not least, there is an urgent need to educate a new generation of graduates in the resource sector that will harness the challenges and opportunities of this field.

References

Angerer G, Marscheider-Weidemann F, Lüllmann A, Erdmann L, Scharp M, Handke V, Marwede M (2009) Rohstoffe für Zukunftstechnologien. Stuttgart: Fraunhofer IRB Verlag.

Bernstein, LR (1986) Geology and mineralogy of the Apex germanium-gallium mine, Washington County, Utah. Utah Geological Association, Utah: 119-127.

Birtel S, Sandmann D, Gutzmer J (2010) Geometallurgy: From ore

to concentrate – a pilot study on the hydrothermal Au deposit at Cavanacaw, Northern Ireland. 11th SGA Conference, Antofagasta, Proceedings.

Dutrizac JE, Jambor JL, Chen TT (1986) Host minerals for the gallium-germanium ores of the Apex Mine, Utah. Econ. Geol. 81: 946-950.

Erdmann L, Graedel TE (2011) Criticality of Non-Fuel Minerals: A Review of Major Approaches and Analyses. Environ. Sci. Technol., 45: 7620−7630.

European Commission (EC) (2010) Critical Raw Materials for the EU. Report of the Ad-Hoc Working Group on Defining Critical Raw Materials. EC, Brussels.

Graedel TE, Barr R, Chandler C, Chase T, Choi J, Christoffersen L, Friedlander E, Henly C, Jun C, Nassar NT, Schechner D, Warren S, Yang M, Zhu C (2012) Methodology of Metal Criticality Determination. Environ. Sci. Technol. 46: 1063–1070.

Hoell R, Kling M, Schroll E (2007) Metallogenesis of germanium—A review. Ore Geol. Reviews 30: 145-180.

Keeney L, Walters SG (2011) A methodology for geometallurgical mapping and orebody modeling. First AusIMM International Geometallurgy Conference, Proceedings: 217-225.

Mao Jingwen, Chen Yuchuan, Zhou Jianxiong, Yang Baichuan (1995) Geology, Mineralogy, and Geochemistry of the Dashuigou Tellurium Deposit inShimian County, Sichuan. Acta Geoscientica Sinica: 1995-03.

National Research Council (NRC), Committee on Critical Mineral Impacts on the US Economy (2008) Minerals, Critical Minerals, and the U.S. Economy; The National Academies Press, Washington.

Pfleger P, Lichtblau K, Bardt H, Reller A (2009) Rohstoffsituation Bayern: Keine Zukunft ohne Rohstoffe. Strategien und Handlungsoptionen. Vereinigung der Bayerischen Wirtschaft, Munich.

Verwoerd, WJ (1986) Mineral deposits associated with carbonatites and alkaline rocks. In: Anhaeusser, CR and Maske, S (eds.) Mineral deposits of Southern Africa. Geol. Soc. S. Africa: 2173-2191.

Rare earth elements and scandium in different types of Ni-laterite profiles from the northern Caribbean: a geochemical comparison

T. Aiglsperger, J.A. Proenza
Departament de Cristal.lografia, Mineralogia i Dipòsits Minerals. Facultat de Geologia Universitat de Barcelona, C/ Martí i Franquès s/n, E-08028 Barcelona, Spain
thomas.aiglsperger@ub.edu; japroenza@ub.edu

J. F. Lewis
Department of Earth and Environmental Sciences, The George Washington University, 20052 Washington D.C., USA
jfkdlewis@aol.com

F. Zaccarini, G. Garuti
Department of Applied Geological Sciences and Geophysics,The University of Leoben, P. Tunner Str, 5, A-8700 Leoben, Austria
Federica.Zaccarini@unileoben.ac.at

A. Rojas-Purón
Departamento de Geología del ISMM, Moa, Holguín, Cuba
arojaspurnh@gmail.com

F. Longo
Falcondo Xstrata Nickel, Box 1343, Santo Domingo, Dominican Republic
flongo@xstratanickel.com.do

A. Chang
Empresa Geominera Camagüey, Carretera Central Este, KM 5.5 Camagüey, Cuba
alfonsochr@gmcmg.gms.minbas.cu

Abstract. The current situation on the global REE market obliges western industries and governments to find alternatives to China for the steady supply of these elements. To be competitive these deposits should be large in scale, easily accessible (open pit mining), readily recoverable material with an extractable ore mineralogy. Among several promising exploration targets Ni-laterites developed on ultramafic rocks have the potential to comply with these requirements.

Three Ni-laterite types (Hydrous Mg-silicate, Fe oxide and Clay silicate) from Cuba and the Dominican Republic have been studied and their geochemistry compared with respect to their potential as REE and Sc deposits. Preliminary results show enrichment within the limonitic horizon, including present ferricrust, for possible economic extraction in all the investigated types.

Keywords. Ni-laterite, REE, Scandium, Dominican Republic, Cuba

1 Introduction

In 2010 the EU Commission defined 14 critical materials on the basis of their high relative economic importance and their high relative supply risk (EC 2010). The entire Rare Earth Elements (REE) are ranked as top priority, as they are needed in various high-end technical applications such as green technologies associated with renewable energy, reduction of greenhouse gases and energy efficiency. The current tense situation on the REE market is mainly explained by the unexpected Chinese export policy which revealed the vulnerability of western

industries. During the last decade cheap REE from China squeezed almost all competitors, creating a monopoly that makes it easy for China to drive prices. As a consequence of western dependency on Chinese REE new exploration projects have been initiated worldwide. Laterites are considered worthy targets as REE can be concentrated during weathering as a result of their limited mobility in surface waters. Intense chemical weathering of REE bearing rocks in tropical regions (e.g. Madagascar, Hampel 2012) can form ion-adsorption clays with elevated contents of valuable heavy REE (HREE). Scandium, often considered a REE as it has similar physical and chemical properties, has been reported in concentrations of up to 390 ppm Sc_2O_3 together with other REE from Jamaican bauxite waste (Wagh and Pinnock 1987). Little is known about the potential of REE enrichment in lateritic profiles developed on ultramafic rocks. Ahmad and Morris (1978) reported elevated Sc values within nickel laterite ores from Guatemala, New Caledonia and Indonesia. Audet (2009) investigated the Ni laterites overlying the Koniambo ultramafic massif in New Caledonia and discovered significant Sc contents up to 70 ppm within the limonite. These discoveries are relevant as both Sc and REE could be readily produced as a by-product during Ni production. A recently published review on metallurgical processes for Sc recovery proposes nickel laterite ores as "the most promising scandium resources for its production" (Wang et al. 2011).

In this work we compare geochemical data from three different nickel laterite types from Cuba and the

Dominican Republic with focus on their potential as future REE and Scandium deposits.

2 The investigated nickel laterite types

Based on their main mineralogical features three important nickel laterite types can be defined: (I) Hydrous Mg-silicate, (II) Fe oxide and (III) clay silicate (Freyssinet et al. 2005). Pure end-member types are rare and mixing of all three types in most laterites is common. However, the dominant features of the laterite profiles in the northern Caribbean examined here are similar allowing a ready comparison of the profiles to be made.

2.1 Hydrous Mg-silicate type

The Falcondo Ni-laterite deposit is situated in the central part of the Dominican Republic. Parent rock is the Loma Caribe serpentinized peridotite, which mainly consists of lherzolite, clinopyroxene-rich harzburgite and harzburgite containing small masses of dunite (Proenza et al., 2007 a). The main ore minerals serpentine (Ni bearing-lizardites) and "garnierites" are found within the saprolitic horizon, which is overlain by limonite. Two lateritic profiles, Loma Peguera and Loma Caribe, have been studied to verify local variations.

2.2 Fe oxide type

Located in northeastern Cuba, the Moa Bay district developed from lateritization of serpentinized peridotites (harzburgite and dunite) from the Mayari-Baracoa ophiolite belt (Proenza et al. 1999). Ni and Co enrichment within the profile is bound to goethite (0.3-4.5 wt%; 0.1-1.7 wt%), maghemite (0.5-8 wt%) and lithophorite (up to 12 wt%; 6 wt%) (Proenza et al. 2007 b; Roqué-Rosell et al. 2010). The investigated profile can be divided, from bottom to top, into protolith, saprolite (usually <10 m), limonite (up to 50 m) and ferricrust.

2.2 Clay silicate type

The little studied laterite profile San Felipe in central Cuba consists of serpentinized lherzolite, serpentinized harzburgite and dunite (protoliths), which are intruded by gabbros. They are overlain by a major horizon of smectite rich saprolite (~19 m) and minor limonite (~1 m) with a thin layer of ferricrust (Gallardo et al. 2010). These authors reported Ni contents up to 2.4 % within the saprolite. Nontronite (an Fe-Mg smectite) was found to be the main ore mineral.

3 REE geochemistry

Chondrite normalized patterns show a general enrichment of REE towards the surface for all investigated types of laterite profiles and that the main enrichment occurs in the the limonite zone (fig. 1 and fig. 2). Parent rocks are consistently enriched in HREE

compared to LREE, whereas the patterns of their weathering products are rather flat shaped with a slight enrichment in LREE over HREE. Unfortunately no data was available for the parent rock of San Felipe.

The laterites from Loma Peguera and Loma Caribe are significantly enriched in REE in the limonitic horizon (with up to 159 ppm and 375 ppm, respectively). Higher HREE contents within the parent rock from Loma Caribe than within that from Loma Peguera can be explained by higher clinopyroxene proportions. However, HREE contents in the parent rock and saprolite are quite similar within the lateritic profile of Loma Caribe.

The oxide type laterite from Moa is characterized by high REE contents within the limonite horizon (up to 127 ppm) with relatively moderate enrichment in its ferrricrust (up to 36 ppm). Chondrite normalized pattern of three samples from the saprolite (0.8 – 8.4 ppm REE) show rather irregular shapes with either Eu positive or negative trends. The lower REE concentrations in the Moa saprolites compared to those from the Falcondo mine areas might be related to the more highly serpentinized nature of the Moa saprolites.

Saprolite and limonite from San Felipe are similarly enriched in REE (up to 68 ppm and 50 ppm, respectively) whereas the duricrust (75 – 98 ppm) show a pronounced Ce positive trend.
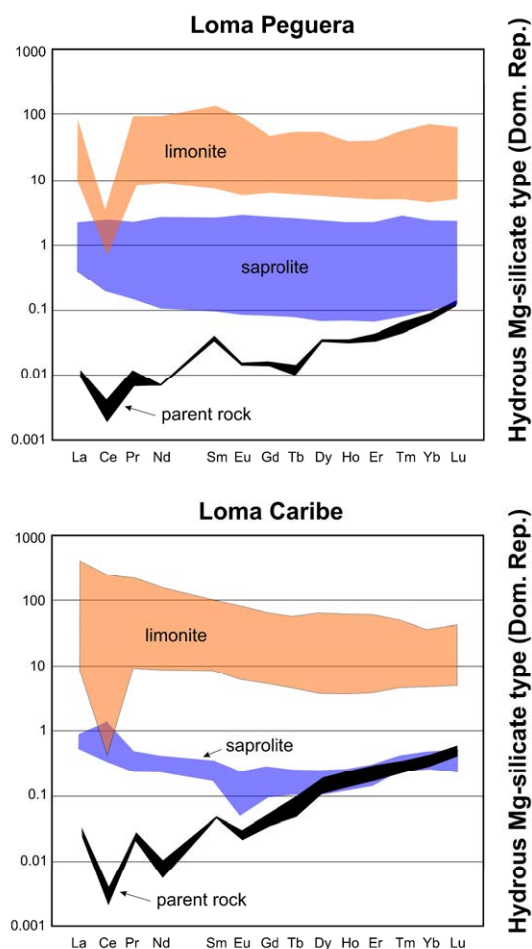
Figure 1. Chondrite normalized REE pattern of parent rocks and their weathering products from investigated Ni-laterites from Dominican Republic. Normalization was performed using chondrite values from Anders and Grevesse (1989).
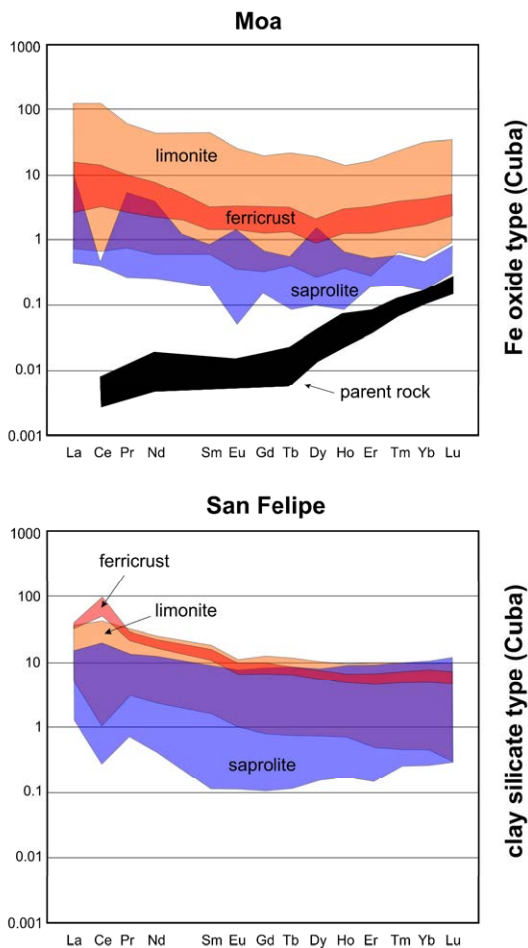
Figure 2. Chondrite normalized REE pattern of parent rocks and their weathering products from investigated Ni-laterites from Cuba. Normalization was performed using chondrite values from Anders and Grevesse (1989).

Figure 3. Geochemical coherence between scandium and Fe_2O_3 in the investigated Ni-laterite profiles

4 Scandium contents

In previous studies ores with Sc values between 20 and 50 ppm have been considered as worthy of exploitation (Xu and Li 1996). Wang et al. (2011) reported important scandium resources within nickel and cobalt deposits from New South Wales with average grades varying from 76 ppm up to 370 ppm. Maximum contents within investigated Ni-laterites are 122 ppm (Loma Caribe), 101 ppm (Moa), 73 ppm (Loma Peguera) and 61 ppm (San Felipe), whereas a general strong correlation can be observed between Sc and Fe_2O_3 (fig. 3). However, three limonite samples from Loma Caribe with highest Sc values do not fallow this trend. A general enrichment from saprolite to limonite and ferricrust can be observed in all Ni-laterite types (fig. 4).

Figure 4. Scandium distribution within the investigated Ni-laterite profiles. sp. = saprolite; li = limonite; fc. = ferricrust

5 Discussion

The investigated ultramafic protholits are strongly enriched in HREE over LREE. However, chondrite normalized patterns reveal a significant enrichment of LREE during lateritization, resulting in a slight overbalance of LREE compared to HREE within the

saprolite and limonite. Previous studies reported leaching and fractionation of REE during advanced weathering causing increasing enrichment of LREE relative to HREE (Brown et al. 2003 and reference therein). Ce is depleted in the parent rocks of the hydrous Mg-silicate type Ni-laterites but shows certain enrichment within its saprolites. Pronounced Ce depletion within the limonite can be observed at Loma Peguera, whereas Ce is generally enriched in limonite samples from Loma Caribe. The oxide type Ni-laterite profile from Moa is characterized by highest REE enrichment within the limonite but shows only moderate enrichment within its ferricrust. Remobilization of REE during the formation of the ferricrust due participation of meteoric waters could explain this observation in this Ni-laterite type. In contrast, ferricrusts from the clay type Ni-laterite San Felipe show significantly higher enrichment in REE with well defined Ce positive trends. Ce(III) could have been oxidized in these soils to highly immobile Ce(IV) as observed by Banfield and Eggleton (1989). Overlapping of chondrite normalized patterns for HREE of several samples from saprolite, limonite and ferricrust indicate a rather moderate enrichment of HREE during lateritization in this Ni-laterite type.

The strong correlation between Sc and Fe_2O_3 for most samples indicates a certain degree of mobility of Sc during lateritization with subsequent incorporation of this element in secondary Fe-oxyhydroxides.

6 Concluding remarks

All three investigated types of Ni-laterite profiles from Cuba and the Dominican Republic show significant REE and Sc enrichment towards the surface. Our preliminary results suggest that Ni-laterites of all types have a promising potential as REE and Sc exploration targets, especially due to the fact that these elements could be produced as by-products during Ni production.

Acknowledgements

References

Ahmad S and Morris DFC (1978) Geochemistry of some lateritic nickel-ores with particular reference to the distribution of noble metals: Mineralogical Magazine 42: p. 143: M 4-8

Anders E, Grevesse N (1989) Abundances of the elements: Meteoritic and solar: Geochimica et Cosmochimica Acta 53: 197-214

Audet MA (2009) Le massif du Koniambo, Nouvelle-Calédonie Formation et obduction d'un complexe ophiolitique du type SSZ. Enrichissement en nickel, cobalt et scandium dans les profils résiduels: PhD thesis (in french), 327 p

Bandfield JF, Eggleton RA (1989) Apatite replacement and rare earth mobilization, fractionation, and fixation during weathering: Clays and Clay Minerals 37: 2: 113-127

Brown DJ, Helmke PA, Clayton MK (2003): Robust geochemical indices for redox and weathering on a granitic laterite landscape in Central Uganda: Geochimica et Cosmochimica Acta 67: 15: 2711-2723

EC (European Commission) (2010) Critical raw materials for the EU. Report of the ad-hocWorking Group in defining critical raw materials: Brussels, Belgium. Available at http://ec.europa.eu/enterprise/policies/raw-materials/files/docs/report-b_en.pdf. Accessed 29 January 2013

Freyssinet P, Butt CRM, Morris RC, Piantone P (2005) Ore-forming processes related to lateritic weathering: Economic Geology 100th Anniversary Volume: 681–722.

Gallardo T, Chang A, Tauler E, Proenza JA (2010) El Yacimiento de San Felipe (Camagüey, Cuba): un Ejemplo de Lateritas Niquelíferas Tipo Arcilla: Macla 13: 87-88

Hampel W (2012) Discovery of a major unconventional heavy rare earths deposit in Madagascar: Africa Business Week: 24 May 2012, Frankfurt am Main: Available at http://www.malekigroup.com/images/AFW2012/Hampel_Wolfgang.pdf. Accessed 21 February 2013

Proenza J, Gervilla F, Melgarejo JC, Bodinier JL (1999) Al- and Cr-rich chromitites from the Mayarí´-Baracoa Ophiolitic Belt (Eastern Cuba): consequence of interaction between volatile-rich melts and peridotite in suprasubduction mantle: Economic Geology 94: 547–566

Proenza JA, Zaccarini F, Lewis JF, Longo F, Garuti G (2007 a) Chromian spinel composition and the Platinum Group Minerals of the PGE-rich Loma Peguera chromitites, Loma Caribe peridotite, Dominican Republic: Canadian Mineralologist 45: 631-648

Proenza JA, Tauler E, Melgarejo JC, Gali S, Labrador M, Marrero N, Perez-Nelo N, Rojas-Puron AL, Blanco-Moreno JA (2007 b) Mineralogy of oxide and hydrous silicate Ni-laterite profiles in Moa Bay area, northeast Cuba: Mineral Exploration and Research: Digging Deeper, 2. Irish Association of Economic Geology: Andrew CJ, et al. (Ed.): 1389–1392

Roqué-Rosell J, Mosselmans JFW, Proenza, JA, Labrador M, Galí S, Atkinson KD, Quinn PD (2010) Sorption of Ni by "lithiophorite-asbolane" intermediates in Moa Bay lateritic deposits, Eastern Cuba: Chemical Geology 275: 9-18

Wagh AS, Pinnock WR (1987) Occurrence of scandium and rare earth elements in Jamaican bauxite waste: Economic Geology 82: 757–761

Wang W, Pranolo Y, Cheng CY (2011) Metallurgical processes for scandium recovery from various resources: A review: Hydrometallurgy 108: 100-108

Xu S, Li S (1996) Review of the extractive metallurgy of scandium in China (1978–1991): Hydrometallurgy 42: 337–343

Granite-related indium mineralisation in SW England

Jens C.Ø. Andersen, Ross J. Stickland, Gavyn K. Rollinson & Robin K. Shail
Camborne School of Mines, University of Exeter, United Kingdom (J.C.Andersen@exeter.ac.uk)

Abstract. Indium occurs widespread in granite-related sulphide deposits across SW England. The metal is found in skarns, greisen-bordered vein systems, and polymetallic lodes throughout the region. It is predominantly hosted by sphalerite and chalcopyrite, locally with significant concentrations in stannite-group minerals and possibly with some in cassiterite. Apart from cassiterite, indium appears to be exclusively chalcophile and was not detected in tourmaline, rutile, garnet or other of the major silicate and oxide minerals. Although indium is unlikely to become a primary commodity in the region, it has potential to add value to projects that focus on W, Sn, Zn and Cu.

Keywords. Indium, granite, magmatic-hydrothermal, QEMSCAN

1 Introduction

SW England is a polymetallic mining district that is well known for the historic production of W, Sn and Cu. Mining peaked through the 18th and 19th centuries with the production of a much wider range of metals including Ag, As, Pb, Sb, and Zn (Dines 1956; Burt 1998). The last metal mine, South Crofty (Sn), closed in 1998, before the recent interest in rare and speciality metals, and these have consequently not been a primary focus for research. However, high metal prices have resulted in renewed regional exploration for W/Sn/Cu/Zn and Hemerdon Tungsten Mine will commence production by 2015.

Indium is a widespread constituent in magmatic-hydrothermal mineral deposits across SW England (Andersen 2008; Andersen et al. 2009). Although the metal has never been commercially extracted, the recent economic focus has led to interest in the development of a marketable indium or rare-metal by-product from W-Sn-Cu mining prospects across the area.

This presentation documents the concentrations and mineralogical distributions of indium in ore specimens from the region.

2 Geological setting

2.1 Regional geology

The geology of SW England is dominated by Devonian-Carboniferous mudstones, sandstones and basic volcanic rocks (Figure 1). These record the development of the Rhenohercynian passive margin, from early Devonian rifting with oceanic spreading represented by the Lizard ophiolite, to late Devonian Variscan convergence and Carboniferous collisional deformation (Leveridge and Hartley 2006; Shail and Leveridge 2009). The successions underwent low-grade regional deformation and were subsequently intruded by granites of the Early Permian Cornubian Batholith. Contemporaneous Early Permian mafic magmatism is expressed by lamprophyre dykes across the region, and lamprophyre and high-K basalt lavas of the Exeter Volcanic Rocks that occur close to the base of the post-Variscan Permian red-bed succession in the Crediton Graben to the NE.

2.2 Mineralisation

Some mineralisation styles pre-date the intrusion of the granites. Sedimentary exhalative occurrences of Pb, Zn and Mn occur in the metasedimentary succession north of Bodmin Moor and Dartmoor, while orogenic quartz veins locally carry Au, Ba, Cu, Fe, Sb and Zn (Scrivener 2006).

Magmatic-hydrothermal and hydrothermal activity developed during and immediately after granite emplacement (Early- to Mid-Permian) and resulted in a variety of mineralisation styles in the upper parts of the granites and their roof rocks. Skarn deposits formed locally where the granite intrusions came into contact with calcareous metasedimentary rocks and altered basic volcanic rocks; greisen-bordered sheeted vein complexes are particularly well-developed in small granite cupolas; steeply inclined faults in both host rocks and granites controlled the development of tourmaline-breccia pipes / lodes and polymetallic sulphide lodes (Jackson et al. 1989; Willis-Richards and Jackson 1989).

The granite-related mineralisation styles record progressive mineral deposition during cooling of the magmatic fluids and their increased mixing with meteoric and metamorphic fluids.

A major episode of post-granite mineralisation occurred during the Mid-Late Triassic. Migration of basinal brines from Permo-Triassic sedimentary basins into the adjacent and underlying basement resulted in the formation of extensive N-S trending Pb-Ag-Zn (Cu-Ba) cross-course veins (Scrivener et al. 1994). Gold and Pd is found in unconformities in Permo-Triassic red-bed sediments (Shepherd et al. 2005).
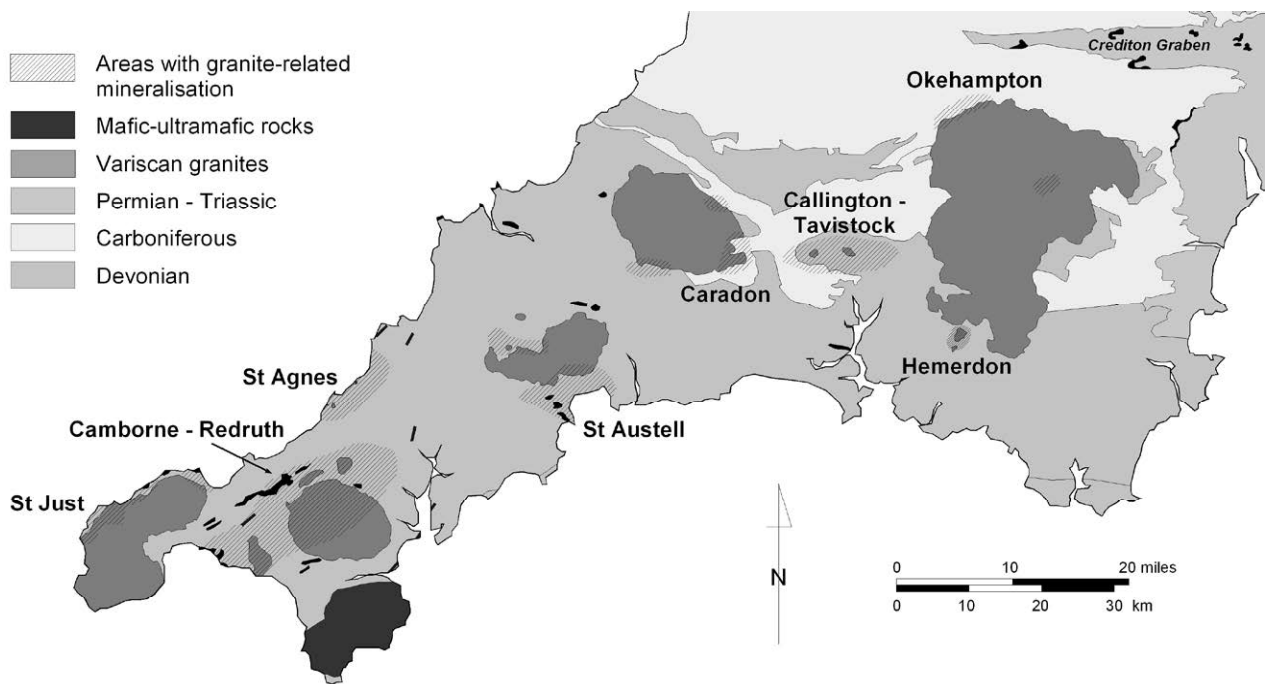
Figure 1. Geological map of SW England showing the principal areas affected by granite-related mineralisation.

3 Sampling and analysis

More than 100 samples were collected from historic collections and mine waste dumps across SW England to represent the major mineral deposit types. Minerals were analysed by electron-probe microanalysis (EPMA; JEOL JXA-8200). Analyses were performed at 15 kV with an electron beam intensity of 180-200 nA and with reference to metal, oxide and sulphide standards. Indium was measured on the Lα-line and corrected for Sn-Lβ interference (0.3 wt% excess indium in 100 wt% Sn). The detection limit for In was calculated to <30 ppm, but due to the Sn interference, concentrations in cassiterite are considered to be indicative only. Matrix reduction followed the CITZAF method.

Mineral abundances were determined by fieldscans using the QEMSCAN 4300 system (Gottlieb et al. 2000; Pirrie et al. 2004). Between 4 and 7 million energy-dispersive X-ray spectra were collected at 10 μm spacing on each sample surface. The spectra were classified by a customised Species Identification Protocol into compositionally distinct mineralogical groups.

Bulk concentrations were estimated by combination of the mineral abundances (determined by QEMSCAN) and average mineral compositions (analysed by EPMA).

4 Results

Results are presented in Figure 2. Significant indium is found in sulphide-bearing skarns from the northern margin of Dartmoor (Red-a-Ven Mine), the greisen-bordered sheeted vein systems at Redmoor and Cligga Head, and more than 20 polymetallic sulphide vein systems across the region. Apart from cassiterite, indium

appears to be strictly chalcophile, and no indium was detected in silicate-oxide skarns or tourmaline breccia pipes or veins.

Within the sulphide mineralisation styles, indium is distributed between sphalerite (<1.2 wt%), chalcopyrite (<2200 ppm), stannite (<6700 ppm) and cassiterite (<1800 ppm). Rare, minute (<2 μm) grains of roquesite ($CuInS_2$), the only discrete indium-mineral identified, are spatially associated with bornite and chalcocite. No indium was detected in tourmaline, rutile, garnet or magnetite. While the mineralogical distribution of indium is variable, there is commonly a broad correlation between the concentrations within coexisting host minerals. Whole-rock concentrations locally reach 420 ppm In (equivalent to 800 ppm in 100% sulphide + oxide) but are very variable within and between individual mineral deposits.

5 Discussion

Indium appears to be confined to the sulphide-bearing mineralisation styles. The richest samples investigated are from Red-a-Ven (Okehampton), Dolcoath, Wheal Concord and Nangiles (Camborne-Redruth), Blue Hills and Wheal Charlotte (St Agnes).

Indium concentrations are highest in sphalerite and stannite, but chalcopyrite is also a significant mineral host throughout the region. In particular, the Caradon and Callington – Tavistock districts have only traces of sphalerite, and here chalcopyrite is the dominant host.

Most economic operations recover indium from sphalerite during smelting by acid leaching and precipitation, so the economic focus is likely to be strongly controlled by the mineralogical distribution of indium.
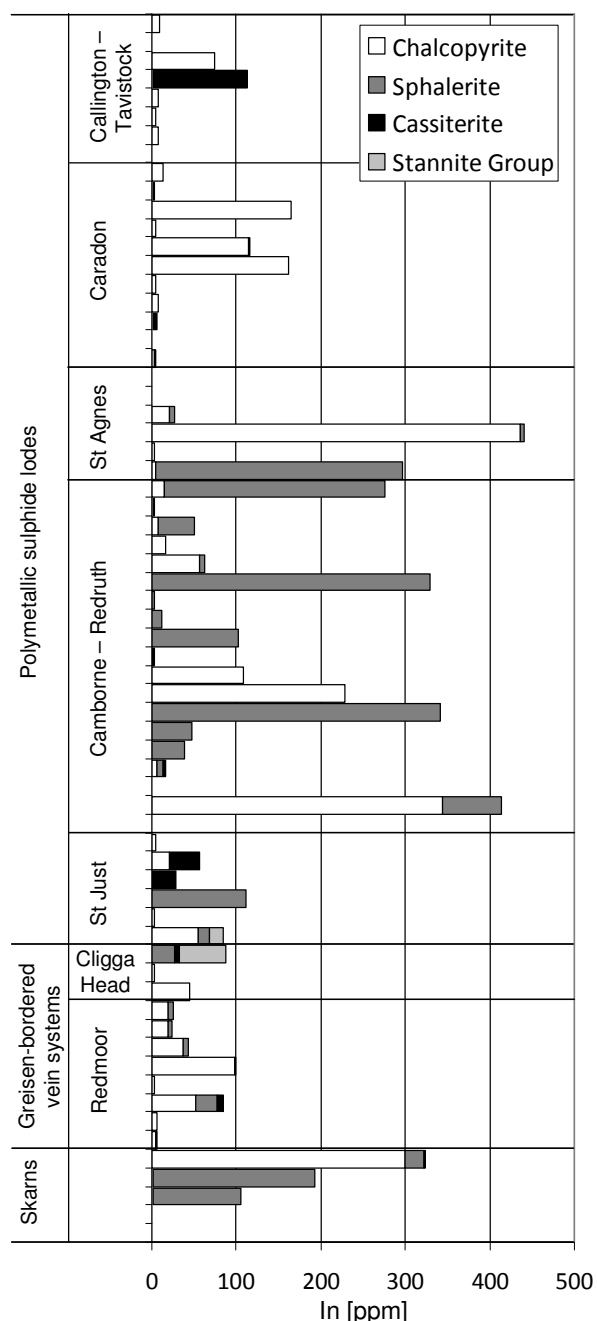
Figure 2. Concentrations and mineralogical distributions of indium within the samples investigated

6 Conclusions

Indium is closely associated with the sulphide-bearing mineralisation styles in SW England. No indium was detected in silicate-oxide skarn or tourmaline breccia pipes or veins. Chalcopyrite and sphalerite are the dominant mineral hosts; locally with significant indium in cassiterite, stannite and roquesite. The highest concentrations are found in the Red-a-Ven skarn and Sn-Cu-As (W-Zn) veins in the Camborne – Redruth and St Agnes districts.

While indium may never become a main commodity for targeted exploration and extraction, the metal has significant potential to add value to the extraction of tungsten, tin, copper and zinc in the region. Although the metal is considered as a potential by-product by Western United Mines (South Crofty / Dolcoath), much more detailed investigations are required to fully understand the timing and nature of indium mineralisation within individual mineral vein systems.

References

Andersen JCØ (2008) Indium in Cornwall In: Benham AJ (ed) 31st Annual Mineral Deposits Studies Group meeting. British Geological Survey, Keyworth.

Andersen JCØ, Dendle JE, Stickland RJ (2009) Indium in main stage polymetallic mineralisation in West Cornwall. Applied Earth Science 118: 24-25.

Burt R (1998) History of Metalliferous Mining In: Selwood EB, Durrance EM, Bristow CM (eds) The Geology of Cornwall. University of Exeter Press, Exeter, pp 211-225.

Dines HG (1956) The Metalliferous Mining Region of South-West England (1994 reprint). British Geological Survey, London.

Gottlieb P, Wilkie G, Sutherland D, Ho-Tun E, Suthers S, Perera K, Jenkins B, Spencer S, Butcher A, Rayner J (2000) Using quantitative electron microscopy for process mineralogy applications. JOM April 2000: 24-25.

Jackson NJ, Willis-Richards J, Manning DAC, Sams MS (1989) Evolution of the Cornubian ore field, Southwest England; Part II, Mineral deposits and ore-forming processes. Economic Geology 84: 1101-1133.

Leveridge BE, Hartley AJ (2006) The Variscan Orogeny: the development and deformation of Devonian/Carboniferous basins in SW England and South Wales In: Brenchley PJ, Rawson PF (eds) The Geology of England and Wales. The Geological Society, London, pp 225-255.

Pirrie D, Butcher AR, Power MR, Gottlieb P, Miller GL (2004) Rapid quantitative mineral and phase analysis using automated scanning electron microscopy (QemSCAN); potential applications in forensic geoscience In: Pye K, Croft DJ (eds) Forensic Geoscience, Principles, Techniques and Applications. Geological Society Special Publication, London, pp 123-136.

Scrivener RC (2006) Cornubian granites and mineralization of SW England In: Brenchley PJ, Rawson PF (eds) The Geology of England and Wales. The Geological Society, London, pp 257-267.

Scrivener RC, Darbyshire DPF, Shepherd TJ (1994) Timing and significance of crosscourse mineralization in SW England. Journal of the Geological Society 151: 587-590.

Shail RK, Leveridge BE (2009) The Rhenohercynian passive margin of SW England : development, inversion and extensional reactivation. Comptes Rendus Geoscience 341: 140-155.

Shepherd TJ, Bouch JE, Gunn AG, McKervey JA, Naden J, Scrivener RC, Styles MT, Large DE (2005) Permo–Triassic unconformity-related Au-Pd mineralisation, South Devon, UK: new insights and the European perspective. Mineralium

Deposita 40: 24-44.

Willis-Richards J, Jackson NJ (1989) Evolution of the Cornubian ore field, Southwest England; Part I, Batholith modeling and ore distribution. Economic Geology 84: 1078-1100.

Ga, Ge and Cd distribution in sphalerite: MVT deposits in Tennessee USA

Julien Bonnet
Laboratoire GeoRessources, UMR 7359, Université de Lorraine

Abstract. The East and Middle Tennessee MVT deposits (ETM and MTM respectively) are very similar in terms of geology, mineralogy, and geometry but sphalerites enriched in Ge and Ga are only present in the MTM. Both districts have Fe- and Cd-enriched sphalerite. Optical microscopy, combined with SEM and EPMA analysis, were performed on sphalerite-rich samples from both districts in order to characterize the distribution of trace elements, mainly Ge and Ga. This present study provides the first geochemical analyses of sphalerites from MTM and ETM highlighting the different distributions and correlations of trace elements in these two zinc districts in Tennessee.

Keywords: Zinc deposits, MVT, Sphalerite, Germanium, Gallium, Cadmium.

1 Introduction

Germanium and Gallium are "strategic metals" for the high-tech industry in the European Union. They are present in sphalerites as traces elements and their distribution at the scale of a deposit as well as at the scale of their host sphalerite is poorly understood. Thus, this paper investigates trace element concentration in sphalerite from zinc deposits in MVT (Mississippi Valley Type) deposits in Tennessee, USA.

MVT deposits in Tennessee have a high grade of Ge and Ga. These deposits are divided in two mining districts: the Middle Tennessee Mines (MTM), with Cumberland, Elmwood and Gordonsville mines, and the East Tennessee Mines (ETM) with Coy, Young and Immel mines. The MTM district produces zinc concentrate with 300 ppm of Ge, 500 ppm of Ga and 2500 ppm of Cd (**Erreur ! Source du renvoi introuvable.**). By contrast, zinc concentrate from the ETM district produces with only Cd at 3500 ppm (and minor Ga ≈ 100 ppm).

This study shows the distributions of Ge, Ga, Cd, Cu and Fe in the sphalerites from these two mining districts and discusses their difference.

Table 1. Composition of zinc Concentrate from MTM and ETM

Sample	S (%)	Zn (%)	Fe (%)	Cd (ppm)	Ga (ppm)	Ge (ppm)
MTM	32,7	62,	0,3	2505,9	536,4	307,8
ETM	33,9	62,	0,2	3683,8	105,4	11,4

2 Geological setting

Deposits from MTM and ETM have many common characteristics in terms of geological environment of ore deposition and paragenetic sequence:

- The mineralization is hosted in a paleokarst formed between the dolomitic Mascot Formation (Lower Ordovician) and the limestone of the Kingsport Formation (Lower Ordovician) (Kyle, 1976). The ore is mainly observed as cement of breccias;
- Presence of low iron sphalerite with traces of galena, pyrite, late fluorine and barite (Kyle, 1976);
- Presence of organic matter (liquid hydrocarbon and bituminous residue) (Kesler et al., 1994).

The main differences between both districts concern:

- Their contrasted Ge and Ga content in sphalerite;
- The color of sphalerite ranging between dark-brown in MTM and pale-yellow in ETM; The gangue minerals dominated by calcite in MTM and dolomite in ETM;
- The coarse-grained and well-crystallized character of the ore in MTM (e.g. Kyle, 1976) compare to the crustiform and colloform texture of the ore in ETM (e.g. Hoagland et al, 1968);
- The ETM belongs to the Appalachian basin whereas the MTM belongs to the Illinois basin.

3 Analyses of Sphalerite

3.1 Material and methods

Polished sections of massive sphalerites from different mines in MTM (4 samples) and ETM (3 samples) were first examined by SEM (Scanning Electron Microscopy) then by Electronic Microprobe following experimental conditions describe by Benedetto et al. (2005).
Profiles were made through sphalerite growth or color zonations as shown in Figure 1.

3.2 Results and discussion

In thin sections, sphalerite from MTM deposits is yellow in color and show discontinuous dark-black and orange bands. Directions of crystal growth are hardly visible.

Sphalerite from ETM deposits appears pale grey in color, and shows successive bands of colloform crystals.

No zonation was observed with SEM owning to the low content of trace elements in sphalerite from both districts. Apart from their different Ga and Ge content, sphalerite from both districts reveals, on average, similar Fe and Cd content. As already noticed by Roedder and Dwornick (1968), the color of sphalerite is clearly not related to their iron content.

In ETM, the yellow sphalerite shows a concentric growth zonation. A compositional profile (A-B) was measured across the zonation in banded sphalerite from Coy Mine (Figure 1). Ge and Ga are under limits of detection.
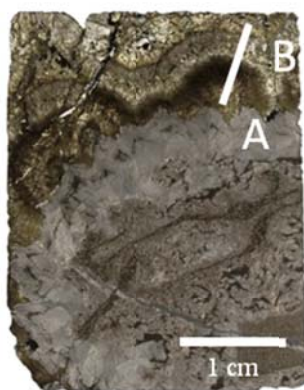
Figure 1. Polished section of yellow Sphalerite (CY3065A) with a zonation of growth in ETM.

Cd and Fe distributions in atomic % are plotted (Figure 2).
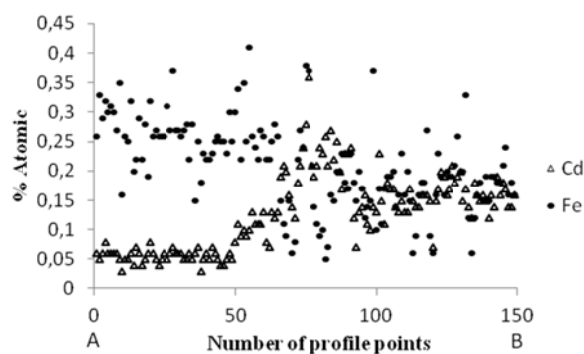
Figure 2. Profiles of Cd and Fe concentrations along A-B in sample CY3065A.

The profile shows an evolution of the sphalerite composition along A-B. Along this profile, early sphalerite is enriched in Fe whereas Cd content is low (Fe/Cd $\approx$ 5). Its composition evolves towards higher Cd and lower Fe content (Fe/Cd $\approx$ 1). This evolution may be explained by two hypotheses: i) a change in fluid composition with an enrichment in Cd or an impoverishment of Fe ii) a change of redox potential inducing the oxidation state of Fe^{2+} to Fe^{3+} which is more difficult to incorporate in sphalerite lattice. A study of oxidation state of Fe is currently in progress.

In MTM, sphalerite is more massive and does not show visible zonation of growth. Under Scanning Electron Microscopy analysis, sphalerite seems to be homogenous.

EPMA profiles on sphalerite from Cumberland mine (MTM) show Fe-Cd rich bands alternating with Cu-Ga-Ge-rich bands (Figure 3 and 4). Ge content up to 1 000 ppm and Ga content of 1 700 ppm are punctually detected.

A strong positive correlation is observed between (Ge+Ga) and Cu that cannot be explained by substitution rules described by Johan (1988).

To date, it is still hardly difficult to interpret the distribution of trace elements in sphalerite from MTM. It may result from variations in chemical and physical conditions (Eh, pH, P, T,…) but a link with the crystallography of ZnS (sphalerite versus wurtzite-like structure) cannot be ruled out.
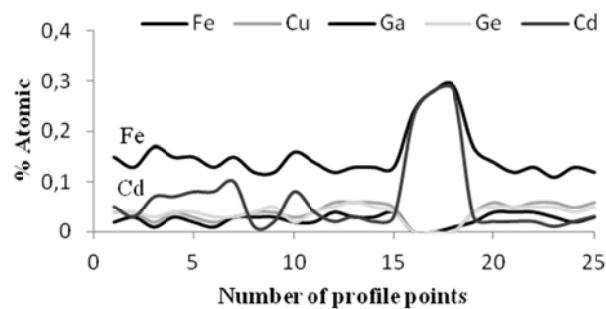
Figure 3. Profiles of Ge, Ga, Cu, Cd and Fe concentrations in MTM sphalerite (CU45S#10-1)
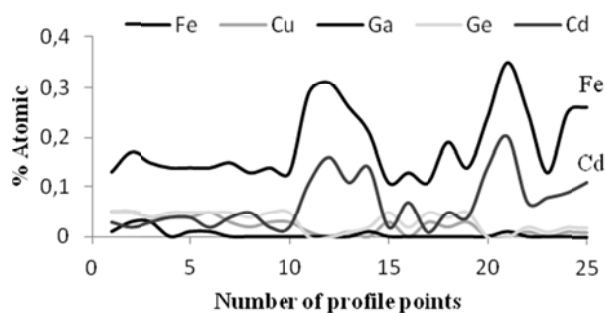
Figure 4. Profiles of Ge, Ga, Cu, Cd, and Fe concentrations in MTM sphalerite (CU45S#10-4).

Even hazardous at this stage of this study, different hypothesis may be proposed to explain the contrasted trace element signature observed between sphalerite from MTM and ETM like, among others, different mineralizing fluid composition implying different fluid source, different physico-chemical conditions of ore deposition. Microthermometric measurements, isotope characterization, etc… will certainly lead to more definitive conclusions.

4 Conclusion

This study is focused on MVT zinc deposits from Central and East Tennessee. Deposits from both districts share many characteristics in terms of geological environment and paragenetic sequence. However, they strongly differ in terms of valuable and high-tech metals, leading to the successful extraction of Ge from zinc concentrates coming from the MTM district. The accurate and exhaustive characterization of deposits from both districts is a quite unique chance to identify the parameters involved in the Ga and Ge enrichment in MVT deposits.

Acknowledgements

References

Benedetto FD, Bernardini GP, Costagliola P, Plant D, Vaughan DJ (2005) Compositional zoning in sphalerite crystals. American Mineralogist 90:1384–1392. doi: 10.2138/am.2005.1754.

Hoagland AD, Hill WT, Fulweiler RE (1968) Genesis of the ordovician zinc deposits in East Tennessee. Economic Geology. 60: 693-714.

Johan Z (1988) Indium and germanium in the structure of sphalerite: an example of coupled substitution with copper, Mineralogy and Petrology, 39: 211-229.

Kesler S, Jones H, Furman F, Sassen R, Anderson W, Kyle J (1994) Role of Crude-Oil in the Genesis of Mississippi Valley-Type Deposits - Evidence from the Cincinnati Arch: Geology. 22:609–612. doi:10.1130/0091-7613(1994)022<0609:ROCOIT>2.3.CO;2.

Kyle JR (1976) Brecciation, alteration and mineralization in the Central Tennessee zinc district: Economic Geology. 71:892–903, doi: 10.2113/gsecongeo. 71.5.892.

Roedder E, Dwornick EJ (1968) Sphalerite color banding: lack of correlation with iron content, Pine Point Northwest territories, Canada. American Mineralogist. 53:1523-1529.

Carbonatite-hosted, late-stage apatite as a potential source of heavy rare earth elements?

S. Broom-Fendley & F. Wall
Camborne School of Mines, University of Exeter, Penryn, Cornwall, UK

A.E. Brady
Mkango Resources Ltd., Suite 1400, 700 - 2nd Street SW, Calgary, Alberta, T2P 4V5, Canada

A.G. Gunn & S.R. Chenery
British Geological Survey, Keyworth, Nottingham, UK

W. Dawes
Leo Mining and Exploration (Leominex), St James' Church, 2, Sheriff Road, London

Abstract. The heavy rare earth elements (HREE) are generally considered to be the most 'critical' of the REE, indispensable for many high-tech applications such as smart-phones and electric vehicles. Currently carbonatites are the main source of REE, but their HREE contents are low. Accordingly, given the predicted high demand for HREE in the future, it is important to find new sources now. New occurrences of HREE-rich carbonatites, have been documented (e.g. Lofdal, Namibia), where late-stage, post-magmatic hydrothermal processes are thought to be the cause of HREE enrichment.

The Songwe Hill carbonatite deposit in Southern Malawi is used here as a case study of a 'typical' carbonatite intrusion. It is a multi-stage intrusion, ranging from calcite-carbonatite to Fe-rich carbonatite. There is textural evidence for late-stage remobilisation of apatite throughout the intrusions at Songwe Hill. New LA-ICP-MS mineral data shows that the late-stage apatite has an unusually high concentration of the HREE, peaking between Eu and Dy on chondrite-normalised plots.

Potential mechanisms for this HREE enrichment include: partitioning of the LREE into REE-fluorocarbonates, such as synchysite-(Ce); preferential mobilisation and crystallisation of the HREE in cool hydrothermal fluids; and preferential stripping of the LREE from the apatite by hot hydrothermal fluids.

Keywords. Carbonatite, apatite, HREE, Songwe, Malawi

1 Introduction

Rare earth elements (REE) are a geochemically similar group of elements composed of the lanthanides (scandium which is not considered here) and yttrium. They are considered by many to be 'critical metals' (e.g. European commission, 2010; Chakmouradian and Wall, 2012; Wall, 2013). These are metals which are of growing economic importance but for which there is a risk of supply disruption. The production of critical metals is generally restricted to a few countries and they are not readily substituted in many of their applications. Furthermore global recycling rates for many are low. The high level of production concentration is a key factor contributing to supply risk. More than 90% of the world's rare earth production is from China (Lusty & Walters, 2011; Humphries, 2012). In recent years China has reduced export quotas and the long-term future of supplies to the West is uncertain. As a result there has been a surge in exploration for new deposits and a move to re-open old REE mines.

1.1 Carbonatites as a REE source

Most REE mines and many exploration projects exploit carbonatites or carbonatite-related deposits. In general carbonatites are very high grade and high tonnage REE sources, but most are typically LREE-rich and relatively HREE-poor (Wall, 2013). Most analyses of future REE availability suggest that there will be no problem in meeting future demands for LREE, whereas shortages of HREE are possible in the short- and medium-term (Bauer et al., 2011; Hatch, 2012).

Some REE deposits in carbonatites meet the grade and tonnage requirements for mining and also have low U and Th contents such that radioactivity does not constitute a significant problem for extraction. HREE-enrichment is rare but currently of particular interest. Such carbonatites include Lofdal, Namibia (Wall et al, 2008), Mount Weld, Duncan Deposit, Western Australia (Lottermoser, 1990) and Khibina, Kola Peninsula, Russia (Zaitsev et al., 1998). All of these are characterised by post-intrusion fluid flow, either hydrothermal, in the case of Lofdal and Khibina, or a weathering effect, as is the case at the Mount Weld, Duncan Deposit.

1.2 Study location and rationale

To investigate if HREE-enrichment in carbonatites is a more common geological process than previously considered, the Songwe Hill carbonatite, south-east Malawi, has been chosen as a case study. Songwe Hill is located in the Chilwa Alkaline Province (CAP), which extends over a roughly circular area about 300–400 km in diameter, encompassing a suite of Early Cretaceous intrusive alkaline rocks (Woolley, 2001). The Songwe Hill carbonatite possesses many of the features typical of 'classic' carbonatites, including an association with alkaline rocks, a systematic variation in composition from calcite-carbonatite to Fe-rich carbonatite, and an apparent increase in REE concentration with increasing Fe concentration.

2 Songwe Hill carbonatite

The Songwe Hill carbonatite is the fourth largest in the CAP. It was mapped in the 1960s and 1980s by the British Overseas Geological Survey and the Metal Mining Agency of Japan, respectively. Recent exploration work by Mkango Resources Ltd. has established an (NI 43-101 compliant) mineral resource estimate for the Songwe Hill deposit, comprising an in-situ indicated and inferred component of 13.2 million tonnes (grading 1.62% total rare earth oxides (TREO)) and 18.6 million tonnes (grading 1.38% TREO) respectively, using a cut off grade of 1% TREO (Swinden and Hall, 2012).

2.1 Petrography

Songwe Hill is essentially composed of two main carbonatite types: early, multi-phase calcite-carbonatite; and later ankerite-bearing ferroan calcite-carbonatite, referred to here as Fe-rich carbonatite. Fe-rich carbonatite is classified on the basis of geochemical data as the fine grain-size makes field classification prohibitive. Increased Fe-concentration in these carbonatites is due to incorporation of Fe into ferroan-calcite and minor ankerite. While pyrite is a minor phase at Songwe Hill it is not the main phase contributing to increased Fe concentration. Comparison of total FeO concentration with 100% − Total (as a proxy for CO_2) shows that the Fe-rich carbonatite does not plot on a mixing curve between FeS_2 and pure calcite-carbonatite. Carbonatite at Songwe Hill is cross-cut by subordinate, narrow (mm–m scale), Fe-Mn-veins, composed of a mixture of Fe-oxides, -hydroxides and wad.

Rare earth minerals at Songwe Hill are dominantly synchysite-(Ce), and minor florencite-(Ce). These are more abundant in later Fe-rich carbonatite, which is typical of late-stage carbonatites, and often associated with sub-solidus hydrothermal alteration.

All apatite at Songwe Hill is fluorapatite. In both Songwe Hill carbonatite lithologies apatite is recrystallised, occurring as stringers and groundmass anhedral crystals (Fig. 1), or as large (up to 10 cm) bands and veins that frequently contain entrained groundmass material, typically carbonate. In samples from the Fe-rich carbonatite, apatite invariably forms large bands and veins and is inter-grown with Fe-carbonate.

2.2 Whole rock data

Whole-rock major and trace element data have been acquired by ICP-MS analysis from diamond drill core samples recently drilled by Mkango Resources Ltd. Later-stage Fe-carbonatites have a higher concentration of REE than the earlier stage calcite carbonatites. The increase in the REE correlates with increasing concentration of SrO due to the association of the REE-fluorocarbonates with strontianite. Yttrium concentrations are used here as a proxy for total HREE contents as Y has a similar cation size to Dy and Ho. In all samples, Y shows a strong correlation with P_2O_5 (Fig. 2). The spread in the data varies depending on the rock type: carbonatite samples cluster together in a tight

group, with Fe-carbonatite having slightly higher P_2O_5 concentrations, typically between 200 to 1,200 ppm Y depending on the P_2O_5 concentrations. In contrast the Fe-Mn veins have more variable Y contents, —up to 4,000 ppm. SrO and Th also weakly correlate with increasing Y, most likely due to substitution into apatite.
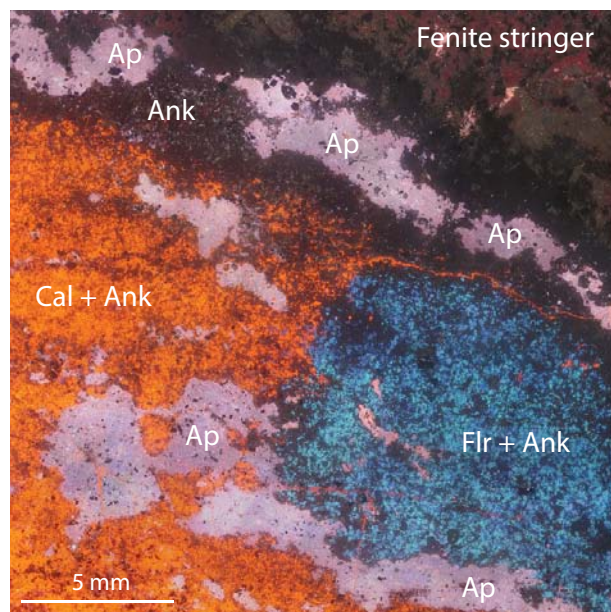
Figure 1. Cold-cathodoluminesce montage of an apatite-bearing calcite-carbonatite from Songwe Hill, showing the anhedral, stringer like crystallisation of the apatite. Ap = apatite, Ank = ankerite, Cal = calcite, Flr = fluorite.
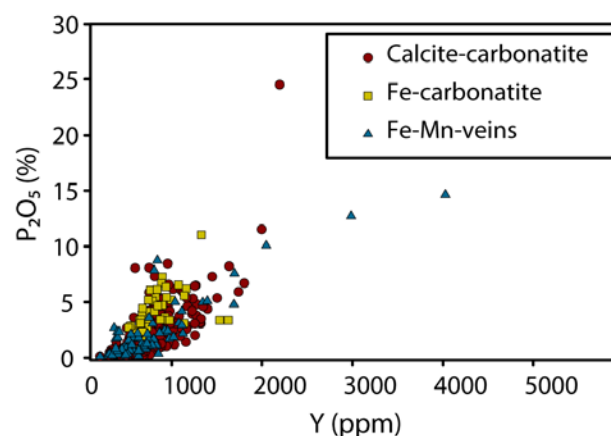
Figure 2. Whole-rock assay data of Songwe Hill carbonatites and Fe-Mn-veins. Data from Mkango Resources Ltd. stage 1 core samples, separated into carbonatite types.

3 Characteristics of 'late-stage' apatite

Although apatite is ubiquitous in the various carbonatite types at Songwe Hill, including early stage calcite-carbonatite, the crystallisation habit of the apatite suggests it formed under sub-solidus hydrothermal/post-magmatic conditions. Further evidence for this comes from the association of the apatite with some late-stage Fe-Mn-veins and in apatite-fluorite boulders found by Garson (1965) associated with the carbonatite, although these have not yet been found in-situ at Songwe Hill.

3.1 REE distribution in Songwe Hill apatite

In order to investigate the correlation of HREE with P_2O_5, apatite from seven carbonatite samples has been analysed for trace-element data by SEM-EDX, EPMA and laser-ablation (LA-ICP-MS). This work was carried out at Aberystwyth University in Wales, the Natural History Museum (NHM) and at the British Geological Survey (BGS) using a NWR 193 nm excimer laser connected to a Agilent-7500 quadrupole mass spectrometer. The data were corrected to internal EDX analyses using a Cameca SX100 electron microprobe at the NHM and FEI Quanta 600 ESEM with an Oxford Instruments INCA 450 EDXA at BGS.

The samples studied included: calcite-carbonatite (5 samples), the Fe-carbonatite (2) and the Fe-Mn-veins (1). Multiple analyses were made from different apatites in each sample. The results show that apatite has average $\sum$REE of 1.4%, but can reach up to 6%. In all lithologies at Songwe Hill the apatite is enriched in Y and HREE compared to other carbonatites worldwide. The HREE enrichment factor of Songwe Hill apatite, defined here as the sum of the concentration of all the HREE from Eu–Lu + Y$\sum$REE, ranges from 40% to 85%, compared to 2% to 11% in apatite from other carbonatites (Hornig-Kjarsgaard, 1998).

Chondrite-normalised REE patterns for the apatite (Fig. 3) illustrate the enrichment of HREE. The position of the HREE peak varies slightly between samples, between Eu and Dy, but no systematic variation with lithology is evident in this preliminary data.
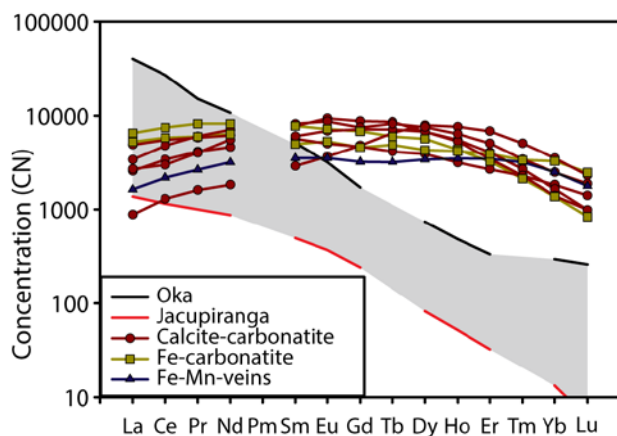
Figure 3. Representative REE distributions of apatite from calcite-carbonatite, Fe-carbonatite and Fe-Mn-veins at Songwe Hill normalised to chondrite (McDonough and Sun, 1995). Data from Oka and Jacupiranga are shown for comparison (Hornig-Kjarsgaard, 1998); other carbonatite analyses fall within the range of these two values (shaded area).

4 Discussion

Apatite is a characteristic phase in carbonatites and usually comprises 2–5% of the rock. Indeed, apatite is known to occur throughout all the stages of carbonatite emplacement (Hogarth, 1989). Typically, in carbonatite emplacement, calcite-carbonatite is intruded first, with apatite often as lozenge-shaped and LREE-enriched crystals. In the later stages of carbonatite intrusions apatite is still a common phase, and is often more enriched in the REE, especially the LREE (Hogarth, 1989). The apatite at Songwe Hill, however, does not follow this pattern. In all the carbonatite types at Songwe Hill the apatite is anhedral in form and often occurs as stringers. It is also relatively enriched in HREE. Such REE patterns are not unknown in silicate rocks (e.g. Nagasawa, 1970), but this is a little-documented phenomenon in carbonatites. The lack of primary apatite at Songwe Hill is not understood but possible reasons include: 1) primary igneous apatite has completely fractionated into cryptic-cumulates; or 2) primary apatite has been completely broken down by a later-stage fluid and replaced by hydrothermal apatite. Of these two possibilities the second is more likely as it provides a mechanism for the formation of the secondary apatite.

The HREE enrichment of the Songwe Hill apatite differs from apatite in other carbonatites worldwide, which typically crystallise as a liquidus phase. In contrast, the apatite at Songwe Hill is most likely to have formed late, under hydrothermal conditions, leading to different behaviour when incorporating REE. Apatite can accommodate the REE in its structure with little bias towards either the HREE or the LREE, as it can accommodate the REE in two different Ca sites (Roeder et al., 1987; Pan and Fleet, 2002). It is, therefore, likely that the REE distribution observed in the apatite is derived from the mineralising fluid from which it precipitated. Three possible mechanisms which might lead to apatite HREE enrichment are suggested: 1) preferential removal of the HREE from an unknown source by a hydrothermal fluid, crystallising HREE-rich apatite in the upper levels of the carbonatite; 2) breakdown of primary apatite by a hot F-, Cl- bearing brine, preferentially removing the LREE and leaving HREE-enriched residual apatite; 3) substitution of the HREE into apatites following removal of the LREE by partitioning into LREE-fluorocarbonates, (e.g. Ngwenya, 1994).

5 Other carbonatites with possible HREE-bearing apatite

As previously shown, most apatite from carbonatite is LREE-rich. However, two carbonatites with possible late-stage, HREE-rich apatite have been reported.

Secondary apatite is described by Walter et al. (1995) at the Juquiá carbonatite, Brazil. Here, late-stage 'type 2' mineralisation rims partially broken-down primary, 'type 1' apatite. REE analyses were carried out on unseparated apatite-concentrate, and samples with a higher proportion of 'type 2' apatite showed HREE enrichment in chondrite-normalised plots.

Evidence for late-stage hydrothermal overprinting is also present at the Tundulu carbonatite, Malawi (Ngwenya, 1994). Apatite in silicified-apatite-carbonatite shows similar characteristics to the 'type 2' apatite at Juquiá, with spongy, broken-down ovoid primary cores and fresh overprints of Na-rich secondary apatite. Preliminary LA-ICP-MS data suggest these rims are also HREE-rich, and form a coupled substitution with the Na in the apatite.

6 Conclusions

The Songwe Hill carbonatite deposit in southern Malawi was produced by multiple stages of intrusion, ranging from calcite-carbonatite to REE-rich Fe-carbonatite. All of the carbonatite types in the deposit contain apatite; however, the apatite differs in crystallisation style from typical primary-carbonatite apatite because it is anhedral and is often found in stringers. New LA-ICP-MS mineral analyses of the Songwe Hill carbonatite apatite reveal that it is HREE-enriched relative to apatite in other carbonatites, and typically peaks between Eu and Dy on chondrite-normalised plots. The data suggest that the apatite crystallised under hydrothermal conditions at a late stage in the carbonatite emplacement.

Acknowledgements

References

Bauer D, Diamond D, Li J, Sandalow D, Telleen P, Wanner B (2011) US Department of Energy critical metals strategy. http://energy.gov/articles/department-energy-releases-its-2011-critical-materials-strategy. Accessed 01 February 2013

Chakmouradian AR, Wall F (2012) Rare earth elements: minerals, mines, magnets (and more). Elements 8:333–340

European Commision (2010) Critical raw materials for the EU. Report of the Ad-hoc Working Group on Defining Critical Raw Materials, Brussels

Garson MS (1965) Carbonatites of Southern Malawi. Government printer, Zomba

Hatch GP (2012) Dynamics in the global market for rare earths. Elements, 8:341–346

Hogarth DD (1989) Pyrochlore, apatite and amphibole: distinctive minerals in carbonatite. In: Bell K (ed) Carbonatites: genesis and evolution, Unwin Hyman, London, pp 105–148

Hornig-Kjarsgaard I (1998) Rare earth elements in sovitic carbonatites and their mineral phases. J Pet 39:2105–2121

Humphries M (2012) Rare earth elements: The global supply chain. CRS Report for congress, R41347

Lottermoser BG (1990) Rare earth elements mineralisation within the Mt Weld carbonatite laterite, Western Australia. Lithos 23:151–167

Lusty P, Walters A (2011) Rare earth elements. British Geological Survey, Nottingham, UK. 45 pp (Minerals Profile).

Nagasawa H (1970) Rare earth concentrations in zircons and apatites and their host dacites and granites. EPSL 9:359–364

Ngwenya BT (1994) Hydrothermal rare earth mineralisation in carbonatites of the Tundulu complex, Malawi: processes at the fluid/rock interface. GCA 58:2061–2072

McDonough WF, Sun SS (1995) The composition of the Earth. Chem Geol 120:223–253

Pan W, Fleet ME (2002) Compositions of the apatite-group minerals: substitution mechanisms and controlling factors. Rev Mineral Geochem 48:13–49

Roeder PL, MacArthur D, Ma XP, Palmer GR, Mariano AN (1987) Cathodoluminescence and microprobe study of rare-earth elements in apatite. Am Min 72:801–811

Swinden S, Hall M (2012) NI 43-101 Technical report and mineral resource estimate for the Songwe Hill rare earth element (REE) project, Phalombe District, Republic of Malawi. MSA group, South Africa

Wall F, Niku-Paavola VN, Storey C, Muller A, Jeffries T (2008) Xenotime-(Y) from carbonatite dykes at Lofdal, Namibia: unusually low LREE:HREE ratio in carbonatite, and the first dating of xenotime overgrowths on zircon. Can Min 46:861–877

Wall F (2013) Rare earth elements. In Gunn AG (ed) Critical metals handbook. Wiley-Blackwell (in press)

Walter AV, Flicoteaux R, Parron C, Loubet M, Nahon D (1995) Rare earth elements and isotopes (Sr, Nd, O, C) in minerals from the Juquiá carbonatite (Brazil): tracers of a multistage evolution. Chem Geol 120:27–44

Woolley AR (2001) Alkaline rocks and carbonatites of the World: Africa. Geological Society Publishing House, London.

Zaitsev AN, Wall F, Le Bas MJ (1998) REE-Sr-Ba minerals from the Khibina carbonatites, Kola Peninsula, Russia: their mineralogy, paragenesis and evolution. Mineral Mag 62:225–250

Rare earth elements in Europe and Greenland: a geological potential? An overview

Nicolas Charles, Johann Tuduri, Dominique Guyonnet, Jérémie Melleton
BRGM (French Geological Survey), 45060 Orléans, France

Olivier Pourret
Institut Polytechnique LaSalle Beauvais - 60026 Beauvais, France

Abstract. Recently, rare earth elements (REE) have occupied a centre-stage owing to the large volatility of prices and stress occasioned on global markets by limitations of Chinese export quotas. Thus, numerous industries which depend on secured and diversified rare earths sources, now consider REE as critical for new technologies. In response, countries are developing and diversifying their supply sources, with new mining projects located outside China and efforts in the REE recycling domain.

Based on a global geological and metallogenic synthesis, a first review map representing more than 270 REE occurrences and deposits classified by typology in Europe and Greenland is proposed. At first glance, the Baltic Shield and South Greenland constitute the main areas with a strong potential. Indeed, northern Europe is characterised by numerous occurrences linked to alkaline intrusions, carbonatites and pegmatites. In southern Greenland, the Ilímaussaq alkaline complex contains the future world-class Kvanefjeld U-REE-Zn deposit.

While REE are relatively ubiquitous in Europe and Greenland and occur in a variety of geological settings, only the two previously mentioned regions appear to have economic potential. However, progress in the understanding of the REE ore forming processes is required to help better guide exploration and make new discoveries. While recycling technologies should be developed, reliance on extracted sources will continue to be indispensable, especially considering annual growth rates for REE demand, which are around 5%.

Keywords: REE, occurrence, deposit, Europe, Greenland, potential.

1 Rare earths: strategic and critical

Recent years have seen unprecedented volatility concerning prices and the dynamics in the global market of the rare earth elements (REE). Nowadays, numerous industries depend on secured and diversified rare earth sources, which are increasingly considered as critical to a wide range of new technologies (i.e. permanent magnets, energy storage, phosphors *etc.*) and as strategic by numerous states, including among the EU-27. As China is practically a monopoly producer, its recent limitations on export quotas have had a severe economic impact. To overcome this, REE consuming countries are developing and diversifying their supply sources, based on both extracted and recycled sources. With respect to the former, new mining projects in the USA and Australia (e.g. Mountain Pass, Mount Weld) provide welcome alternatives to import from China. Regarding Europe and taking into account Greenland, several new projects are currently being developed in Scandinavia and Greenland (e.g. Norra Kärr, Kvanefjeld). A reliable assessment of current European REE resources and reserves and of future potentials should rely on a better understanding of REE ore-forming processes, taking into account the considerable diversity of deposits and associated geological settings within continental Europe. Relying on a global geological and metallogenic synthesis, notably from the European ProMine Project database, a first review map representing over 270 REE occurrences and deposits, classified by typology in Europe and Greenland, is proposed. Such a synthesis provides a basis for identifying preferential areas for future REE exploration (Figure 1).

2 Typology of rare earths deposits

The term REE is often considered as a misnomer since these elements are quite common in the Earth's crust. The REE can occur in a broad range of geological settings and their concentration and distribution in minerals depend on rock forming, hydrothermal, weathering and other surface processes. REE deposits are broadly divided into two main categories: primary deposits associated with magmatic and hydrothermal processes and secondary deposits concentrated by sedimentary processes and weathering (Kanazawa and Kamitani 2006; Walters et al. 2011; Chakhmouradian and Wall 2012).

2.1 Primary deposits

Primary REE deposits - which represent the bulk of REE production since 1960s - are broadly associated with alkaline-peralkaline igneous rocks and carbonatites. However, REE minerals may be also associated with pegmatites, skarns, Fe oxide-phosphates and quartz-fluorine-bearing veins.

In carbonatites, REE are mainly represented by light-group rare earth elements (LREE, from ^{57}La to ^{64}Gd) occurring in minerals such as bastnäsite, allanite, apatite and monazite (Gupta and Krishnamurthy, 2005). REE deposits associated with alkaline-peralkaline rocks are relatively low-grade (<5 % rare earth oxides REO) although they are commonly enriched in heavy-group rare earth elements (HREE, from ^{65}Tb to ^{71}Lu and also ^{39}Y; Chakhmouradian and Zaitsev 2012). Typical minerals are apatite, bastnäsite, eudialyte, gadolinite and loparite, which are often associated with "exotic" rock names such as ijolite, lujavrite, urtite or melteigite.
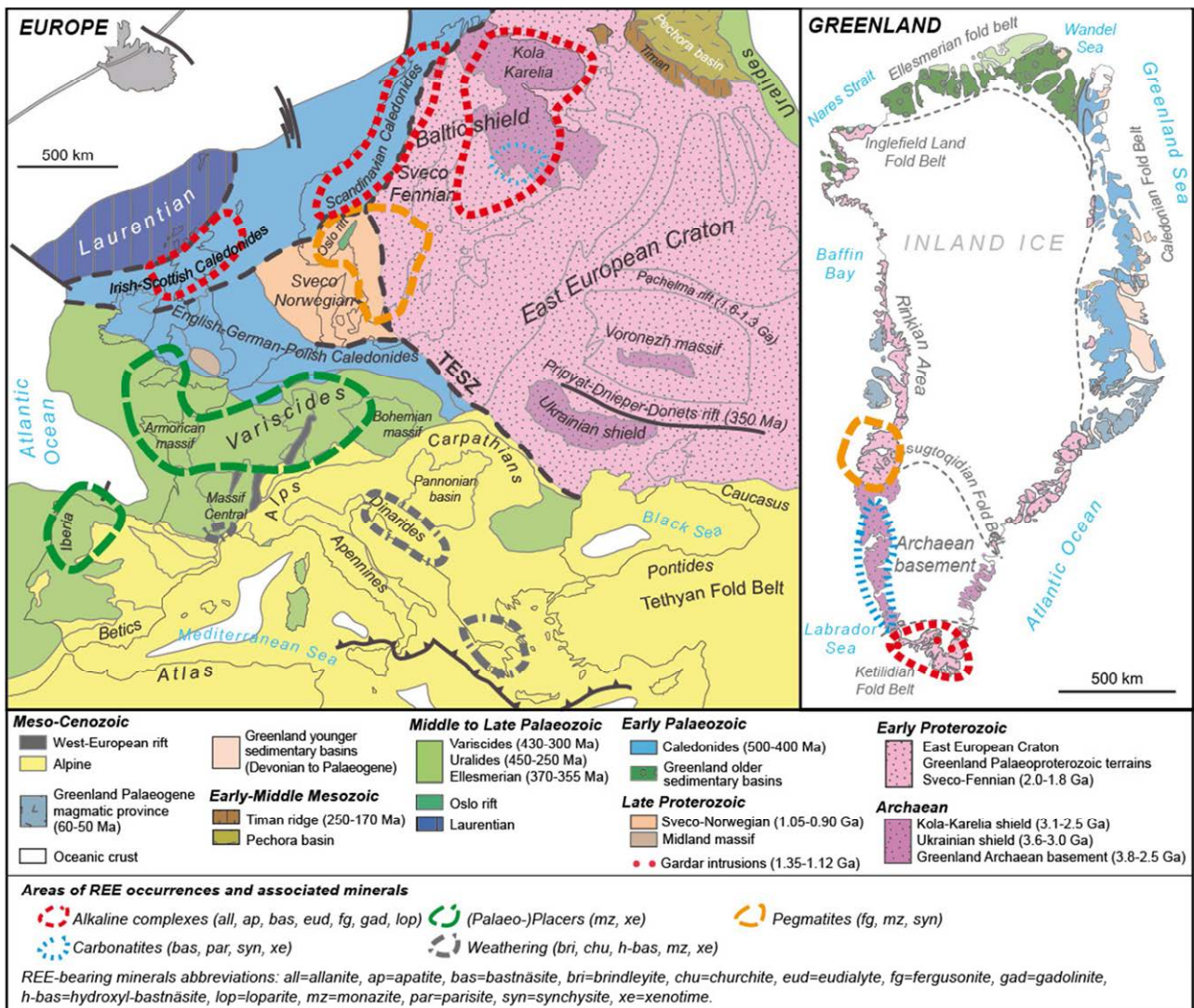
Figure 1. Simplified geotectonic map of Europe and Greenland (modified after Artemieva et al. 2006; Gee and Stephenson 2006; Henriksen 2008) and their potential areas for REE occurrences and deposits. Also indicated are REE-bearing minerals associated with each deposit type.

In addition to alkaline-peralkaline igneous rock deposits, pegmatites containing significant amounts of LREE (allanite, monazite) or HREE (gadolinite) mineralisation can occur.

Moreover, notable REE concentrations are observed within a few iron-oxide-copper-gold (IOCG) deposits or in the magnetite-apatite deposit of the Kiruna district in northern Sweden (Harlov et al. 2002). Such deposits are hosted by a variety of rocks ranging from intrusive igneous to volcanic and sedimentary rocks, with REE-bearing minerals such as apatite or allanite.

It is worth to mention some other REE deposits associated with sedimentary rocks, e.g. fluorite-baryte mineralisations (disseminated in veins and breccia, with synchysite and parisite) or U-deposits.

2.2 Secondary deposits

Secondary deposits represented the bulk of REE production prior to the 1950s (100 kt), especially from monazite-bearing placers (Orris and Grauch 2002).

Secondary deposits are mainly the result of sedimentary remobilization and weathering processes: placers, REE-bearing clays and laterites including ion-adsorption type REE deposits. The latter are currently only mined in southern China for HREE.

Placer deposits are accumulations of heavy minerals in sands and gravels by gravity separation during sedimentary processes. Placers are generally Tertiary and Quaternary in age, although a few are dated as Precambrian. Main REE-bearing minerals are monazite (with or without xenotime), fergusonite, euxenite, allanite and loparite (Donnot et al. 1973; Morteani 1991; Mohanty et al. 2003; Elsner 2007).

Weathering processes lead to the breakdown of many rock-forming minerals, the leaching of certain elements (Mg, Ca) and the residual enrichment of less mobile elements (Fe, Al). Thus weathering of initially REE-enriched rocks (e.g. carbonatite) can provide residual weathering REE deposits (e.g. laterites, bauxite; Lottermoser 1990) with new supergene minerals (e.g. phosphates such as monazite) and high-grades (10-25% REO).

Another type of residual REE deposit has been described: REE-bearing clays, termed ion-adsorption clays (Chi and Tian 2008). These low-grade deposits

(0.03-0.35% REO) are HREE-rich and often associated with weathered REE-enriched granites, where REE are adsorbed by clay minerals such as kaolin or halloysite.

3 Geological potential: an overview

3.1 Rare Earths in Europe

In Europe, primary deposits or occurrences are mainly represented by alkaline complexes and carbonatites, located in northern Europe. Indeed, at first glance, the Baltic shield and Kola Peninsula constitute the main areas with strong geologic potentials. Alkaline intrusions such as Norra Kärr (Sweden) can constitute new projects for REE mining in Europe. This intrusion, represented by a nepheline syenite, contains an inferred REE mineral resource of 60.5 Mt @ 0.54% REO (Tasman Metals, 2013). Other potential deposits linked to alkaline intrusions are Tasjö (Sweden), Katajakangas and Otänmaki (Finland), Kodal and Saeterasen (Norway). Moreover, the Kola Peninsula exhibits the both well-known Khibina and Lovozero alkaline complexes (Sørensen 1997; Arzamastsev et al. 2006) with reserves estimated at 1,000 Mt @ 0.8-1.5% REO (Kogarko 1995 *in* Orris and Grauch 2002). In the north-west of Scotland, several occurrences associated with British Caledonian alkaline intrusions are mentioned close to Loch Borralan, Loch Ailsh and Ben Loyal (Shaw and Gunn 1993; Young et al. 1994). To the latter can be added occurrences related to British Tertiary igneous rocks, such as Skye and St-Kilda. With respect to carbonatites, examples are the Fen Nb-Ta deposit (Norway), with several REE-bearing minerals (monazite, bastnäsite, synchysite), and also the Sokli carbonatite in Finland. Close to the Permian Oslo rift, the Larvik-Langesundfjord region exhibits numerous pegmatites with REE-bearing minerals. Note that anecdotic concentrations of REE-bearing minerals have been reported in pegmatites in the Italian Alps. In northern Sweden, the Kiruna apatite-iron ore deposit has REE resources roughly estimated to ~5.6 Mt @ 0.5% REO (Parák 1973). It is also worth noting the occurrence of REE observed within Zn-Pb-F-Ba deposits in the North Pennine ore field (England; Bau et al. 2003).

Secondary deposits or occurrences in Europe are mainly represented by grey monazite palaeoplacers, associated with Ordovician sediments of Palaeozoic basins (i.e. western France, Wales, Belgium, Czech Republic) and linked to the Variscan orogeny. Current to recent placers that might constitute interesting targets are found in Denmark (Hanstholm), Germany (Cuxhaven) or Poland (Slupsk), and would deserve to be better explored and qualified. Potential occurrences related to weathering processes should not be overlooked, e.g. REEs related to bauxite deposits in the Balkans and Greece (Grebnik, Vlasenica, Marmara; i.e. hydroxyl-bastnäsite, brindleyite, goyazite), or in the south of France. Investigations could be carried out on clays from Permian-Triassic terrains, phosphorous levels within certain Palaeozoic sediments (e.g. southern France) and on F-Ba deposits of the French Massif Central.

3.2 Rare Earths in Greenland

In view of current proposed projects, it has been suggested that Greenland may represent a REE potential capable of meeting 25% of global demand.

Primary deposits or occurrences mainly consist of the Gardar alkaline complexes. Located in South Greenland, the Gardar Province (1.35-1.12 Ga) contains alkaline complexes that exhibit main occurrences with potentially future world-class REE deposits, such as Kvanefjeld in the Ilímaussaq intrusion (6.6 Mt total REO (TREO) coupled with U resources), and the Kringlerne (20 Mt TREO) or Motzfeldt intrusions (Sørensen et al. 2011; Steenfelt 2012). The Gardar Province contains other alkaline intrusions that can be interesting for REE potential, such as Grønnedal-Ika, Igaliko, Nunarssuit or Tugtutôg. Those alkaline complexes mainly consist of nepheline syenite, locally associated with carbonatite, and are intruded into the Julianehab batholith in relation with the Ketilidian fold belt. Alkaline intrusions also occur to the eastern part of Greenland: the Gardiner complex (50 Ma) and Kap Simpson. In the western part of Greenland, in the Archaean craton and Rinkian Palaeoproterozoic mobile belt, many promising occurrences of carbonatites and pegmatites are described. For example the Sarfartoq carbonatite, dated at 565 Ma, contains ~14 Mt @ 1.51% REO (Secher and Larsen 1980). Besides, the Jurassic Qaqqarsuk (156 Ma) and Tikiusaaq (158 Ma) carbonatites show REO contents of 2.4 and 9.6%, respectively. South of the Rinkian Palaeoproterozoic mobile belt, pegmatites dated at 1.8 Ga, largely occur in the Nassuttutata Tasia area. Main REE-bearing minerals are monazite, allanite and apatite.

There are currently few descriptions of secondary deposits or occurrences in Greenland. One occurrence is Milne Land, located in eastern Greenland, which is a Cretaceous monazite-bearing palaeoplacer.

4 Economic considerations

Parallel to current efforts to find alternative extracted sources of REEs, a significant effort is devoted developing technologies for recycling REEs in products. Binnemans et al. (2013) provide a review of current technologies for the three market sectors that appear to provide the most potential in terms of recycling: permanent magnets, NiMH batteries and phosphors. A global perspective of REE flows and stocks in the world economy is provided by Du and Graedel (2011a), using material flow analysis. The diagrams for several REEs illustrate the orders of magnitude of flows between various compartments of the economy (manufacture, use, etc.) but also stocks accumulated in the use compartment (Du and Graedel 2011b). These data suggest accumulated (and hence potentially recyclable) stocks in the economy on the order of 440,000 t REE in 2007. According to Lynas (2010), world rare earth demand in 2010 was on the order of 136,100 t (i.e. approx. 115,000 t REE). Even assuming significant progress in REE recycling technologies, given the annual rate of growth of REE demand (on the order of 5%; Alonso et al. 2012), recycling of accumulated

stocks in the economy cannot be expected to satisfy demand. In a growth based economy, there is a gap between demand and the "offer" provided by the waste stream, due to the lifetime of products in the economy (see e.g. Grosse 2010). Therefore, REEs will need to be extracted in the future, in order to satisfy in particular the demand for clean technologies. Recycling, however, especially of certain HREEs (Dy, Tb, etc.) but also Nd, is essential to reduce the so-called "balance problem" (Binnemans et al. 2013), which generates an excess of the more abundant elements (La, Ce) as a result of mineral extraction. The potential from recycling can be compared to that of mining projects cited previously. For three European projects alone (Kringlerne, Kvanefjeld and Norra Kärr) the potential (resources + reserves) is on the order of 30 Mt REO.

5 Perspectives for exploration?

The review of rare earth occurrences in Europe and Greenland illustrates the relative ubiquity of REEs in various geological settings. Currently, however, the most promising potential is only concentrated in southern Greenland and in the Baltic shield, with a few very large deposits. Further work on REE ore-forming processes applied to specific European geological settings could help guide exploration and allow new discoveries (e.g. Permian-Triassic clays in western Europe, F-Ba deposits in the French Massif Central, phosphorous levels of Palaeozoic sedimentary series, alkaline intrusions of the Gardar complex in Greenland, etc.).

Acknowledgements

References

Alonso E, Sherman A, Wallington TJ, Everson MP, Field FR, Roth R, Kirchain RE (2012) Evaluating rare earth element availability: A case with revolutionary demand from clean technologies. Environmental Science & Technology, 46:3406-3414.

Artemieva IM, Thybo H, Kaban MK (2006) Deep Europe today: geophysical synthesis of the upper mantle structure and lithospheric processes over 3.5 Ga. Memoirs of the Geological Soiciety of London, 32:11-41.

Arzamastsev A, Yakovenchuk V, Pakhomovsky Y, Ivanyuk G (2006) The Khibina and Lovozero alkaline massifs: Geology and unique mineralisation. 33th IGC excursion No 47.

Bau M, Romer RL, Lüders V, Dulski P (2003) Tracing element sources of hydrothermal mineral deposits: REE and Y distribution and Sr-Nd-Pb isotopes in fluorite from MVT deposits in the Pennine Orefield, England. Mineralium Deposita, 38:992-1008.

Binnemans K, Jones PT, Blanpain B, Van Gerven T, Yang Y, Walton A, Buchert M (2013) Recycling of rare earths : a critical review. Journal of Cleaner Production, doi: 10.1016/j.jclepro.2012.12.037.

Chakhmouradian R, Wall F (2012) Rare earth elements: Minerals, mines, magnets (and more). Elements 8:333-340.

Chakhmouradian R, Zaitsev N (2012) Rare Earth mineralization in igneous rocks: Sources and processes. Elements 8:347-353.

Chi R, Tian T (2008) Weathered crust elution-deposited rare earth ores. Nova Science Publishers, Inc., New York, 286 p.

Du X, Graedel TE (2011a) Uncovering the global life cycles of the rare earth elements. Scientific Reports, 1(145):1-4.

Du X, Graedel TE (2011b) Global rare earth in-use stocks in NdFeB permanent magnets. Journal of Industrial Ecology, 15(6):836-843.

Elsner H (2007) Heavy Minerals of Economic Importance. Bundesanstalt für Geowissenschaften und Rohstoffe (BGR) 222 p.

Donnot M, Guigues J, Lulzac Y, Magnien A, Parfenoff A, Picot P, (1973) Un nouveau type de gisement d'europium: la monazite grise à europium en nodules dans les schistes paléozoïques de Bretagne. Mineralium Deposita, 8:7-18.

Gee DG, Stephenson RA (2006) The European lithosphere: an introduction. Memoirs of the Geological Society of London, 32:1-9.

Grosse F (2010) Is recycling "part of the solution"? The role of recycling in an expanding society and a world of finite resources. S.A.P.I.E.N.S. 3(1):1-17.

Gupta CK, Krishnamurthy N (2005) Extractive Metallurgy of Rare Earths. CRC Press 508 p.

Harlov DE, Andersson UB, Förster HJ, Nyström JO, Dulski P, Broman C (2002) Apatite-monazite relations in the Kirunavaara magnetite-apatite ore, northern Sweden. Chemical Geology 191:47-72.

Henriksen N (2008) Geological history of Greenland – Four billions years of Earth Evolution. GEUS, 272p.

Kanazawa Y, Kamitani M (2006) Rare earth minerals and resources in the world. Journal of Alloys and Compounds 408-412:1339-1343.

Lynas (2010) Will there be sufficient rare earths to meet demand from clean energy technology? Presentation at International Minor Metals Conference, London, April 2010.

Lottermoser RBG (1990) Rare-earth element mineralisation within Mt Weld carbonatite laterite Western Australia. Lithos 24:151-167.

Mohanty AK, Das SK, Vijayan V, Sengupta D, Saha SK (2003) Geochemical studies of monazite sands of Chhatrapur beach placer deposit of Orissa, India by PIXE and EDXRF method. Nuclear Instruments and Methods in Physics Research, Section B: Beam Interactions with Materials and Atoms, 211:145-154.

Morteani G (1991) The rare earths: their minerals, production and technical use. European Journal of Mineralogy, 3:641-650.

Orris GJ, Grauch RI (2002) Rare earth element mines, deposits and occurrences. USGS Open-File Report 02-189.

Parák T (1973) Rare Earths in the apatite iron ores of Lappland together with some data about the Sr, Th and U content of these ores. Economic Geology 68:210-221.

ProMine Project database (2013) http://promine.gtk.fi.

Secher K, Larsen LM (1980) Geology and mineralogy of the Sarfartôq carbonatite complex, southern West Greenland. Lithos 13:199-212.

Shaw MH, Gunn AG (1993) Rare earth elements in alkaline intrusions, North-West Scotland. BGS open file report 11, 66p.

Sørensen H (1997) The agpaitic rocks - An overview. Mineralogical Magazine, 61:485-498.

Sørensen H, Bailey JC, Rose-Hansen J (2011) The emplacement and crystallization of the U-Th-REE rich agpaitic and hyperagpaitic lujavrites at Kvanefjeld, Ilímaussaq alkaline complex, South Greenland. Bulletin of the Geological Society of Denmark 59:69-92.

Steenfelt A (2012) Rare earth elements in Greenland: known and new targets identified and characterised by regional stream sediment data. Geochemistry: Exploration, Environment, Analysis 12:313-326.

Walters A, Lusty P, Hill A (2011) Rare Earth Elements profile. British Geological Survey.

Young BN, Parsons I, Threadgould R (1994) Carbonatite near the Loch Borralan intrusion, Assynt. Journal of the Geological Society, 151:945-954.

Geochemical and mineralogical characteristics of the Yonghwa phoscorite-carbonatite complex, Korea

Seon-Gyu Choi, Jung Min Cho, Dong Woo Kim, Jieun Seo
Department of Earth and Environmental Sciences, Korea University, Korea

Jung-Woo Park
Research School of Earth Sciences, Australian National University, Australia

Nam Won Kim
Korea Resources Corporation, Korea

Abstract. A recently discovered Yonghwa phoscorite-carbonatite complex in Korea, is dated at 193.4±4.9 Ma by K-Ar method. The phoscorite mainly consists of olivine, apatite, magnetite, carbonates, amphibole and phlogopite. The carbonatite is predominantly composed of calcite and dolomite with ankerite or siderite as secondary phases. Intensive fenitization occurred along the boundary between the complex and wall rocks of leucocratic banded gneiss and garnet metabasite. Fe contents (20.4–57.8 weight % $Fe_2O_3^T$) of carbonatite are higher compared to typical ferro-carbonatites due to its high magnetite content. REE trends of the phoscorite and carbonatite are highly fractionated with enrichment of LREE and Nb. Apatite also reflects the fractionated trends of LREE relative to HREE. Apatite from phoscorite is enriched in Sr and shows substitution trends between Ca and Sr. Fe and Mg chemistry of mica may reflect the evolutionary trend of a carbonatite melt without Al substitution. The stable isotope compositions of calcite and dolomite from carbonatites and veins suggest magmatic origin of the melt: ca. -8.2 to -3.4‰ $^{13}C_{V-PDB}$ and 6.6 to 11‰ $^{18}O_{V-SMOW}$.

Keywords. Phoscorite, carbonatite, Nb mineralization, stable isotope, Yonghwa, Korea

1 Introduction

Tectonostratigraphic units in Korea include the Proterozoic Gyenggi Massif, the Neoproteozoic Ogcheon, the Paleozoic Taebaek Belt, the Proterozoic Yeongnam Massif, and the Mesozoic Gyeongsang Basin. Recently, the south of the Gyeonggi massif is interpreted to be the extension of the Permo-Triassic Dabie-Sulu orogenic belt between the North China and Yangtze blocks.

The Yonghwa phoscorite-carbonatite complex (YPCC) was discovered recently in the Gyeonggi massif which is composed of the Precambrian metamorphic basement with suprcrustal sequences. This massif mainly consists of banded biotite gneiss, quartzite, mica schist, marble, leucocratic gneiss and amphibolite. The YPCC intruded into the leucocratic banded gneiss and garnet-bearing metabasite. K-Ar age dating of phlogopite from the Yonghwa fenite suggests that the fenitization occurred at 193.4±4.9 Ma.

This study reports the first occurrence of the early Jurassic phoscorite-carbonatite complex in Korea. In this study, we present petrological, mineralogical and geochemical features of the YPCC in order to constrain the integrated genetic environment of the phoscorite-carbonatite complex and its potentiality to host an ore deposit.

2 Petrology

The YPCC consists of phoscorite, carbonatite and fenite. Phoscorite and carbonatite occur as an inclined elliptical pipe and show gradual change between the rock types. The fenites occur along the boundary between carbonatite/phoscorite and country rocks. Carbonate veins are observed in phoscorite, carbonatite, fenite and country rocks. Some veins consist of siderite and ankerite.

Phosocorites are mainly composed of olivine, apatite, magnetite, phlogopite, dolomite and clinohumite, with accessory columbite, pyrochlore and pyrrhotite. Carbonatites consist of calcite, dolomite, ankerite, siderite, phlogopite and magnetite, with accessory pyrrhotite and pyrite. Spherulitic graphite also occurs in phoscorites and carbonatites. The modal compositions of the Yonghwa phoscorites mostly plot on the definitional phoscorite field (Yegorov, 1993), and are similar to the Kovdor phoscorites, Russia (Krasnova et al., 2004) (Fig. 1). The fenites are composed of phlogopite, amphibole, albite and pyrite. Phosphorus, iron and niobium mineralization occurs in the YPCC, represented by apatite, columbite, pyrochlore and magnetite.
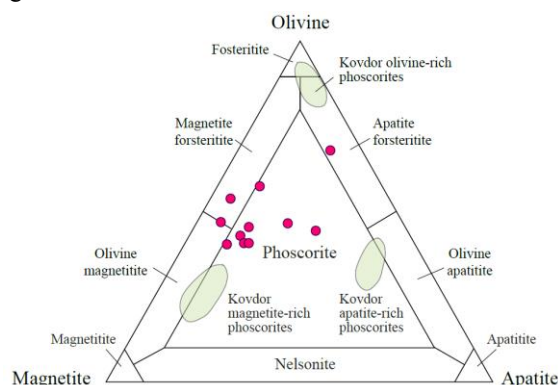
Figure 1. The classification diagram for phoscorite (Yegorov, 1993). The filled circles represent Yonghwa phoscorites. The modal compositons of Kovdor phoscorites are shown by grey fields.

3 Mineralogical characteristics

Yonghwa apatite occurs as anhedral rounded crystals in phoscorite, carbonatite and fenite, and is enriched in Sr and REE, reflecting Sr and REE-rich features of the carbonatite magma. The composition of apatite shows clear trends of substitutions between Ca^{2+} and Sr^{2+} with the various Sr/Ca ratios ranging from 1:2 to 1:1 (Fig. 2). Increasing Sr contents in apatite may suggest the evolution of the carbonatite magma (Cordeiro et al., 2010). The apatites from phoscorites are characterized by their high Mn contents (average 1766 ppm), compared with those from other areas (Drüppel et al., 2005), although their Sr contents are similar (average 2.5 wt. % Sr).
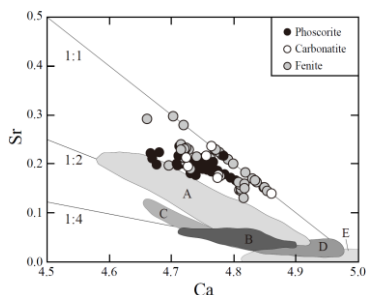
Figure 2. Compositional variation of apatites by substitutions compared with composition fields of apatites in phoscorites and carbonatites from other areas (A-Catalão nelsontie; B-Catalão phoscorite; C-Sokli phoscorite; D-Vuoriyarvi phocorite; E-Kovdor phoscorite) (Cordeiro et al., 2010).

Phlogopite occurs in phoscorite and fenite. However, because of the fenitization of the wall rocks, phlogopite is concentrated in fenite. The textural features of phlogopites from the YPCC vary greatly between rocks of different evolutionary stages. In phoscorite, phlogopite can be divided into two types by its color and shape. The first type (Type 1) is characterized by blue tint, anhedral shape and relatively undeveloped cleavage and the second type (Type 2) is greenish subhedral phlogopite. Type 1 phlogopite usually occurs within apatite or olivine, whereas Type 2 phlogopite is accompanied with carbonates, which infers that the latter is the relatively late stage mineral compared to the former. Phlogopite from fenite is reddish brown, coarse-grained and subhedral. The phlogopites show large compositional variation from Mg-rich Type 1 to Fe-rich Type 2 phlogopites from fenites (Fig. 3) Substitution between Fe and Mg without significant change in Al contents may indicate the evolutionary trend of carbonatite magma.

4 Whole rock and isotope geochemistry

The Yonghwa carbonatite is Fe- and Mg-rich ferrocarbonatite, which contains high proportions of magnetite. The Fe contents (20.4–57.8 wt. % $Fe_2O_3^T$) are 2 to 4 times higher than that of average ferrocarbonatite (13.3 wt. % $Fe_2O_3^T$; Wooley and Kempe, 1989). The Si content is also higher than average ferrocarbonatite whereas Ti and REE are lower. Some carbonatite samples are enriched in Si (up to 14.0 wt. % SiO_2), due to the presence of phlogopite and olivine. Niobium content varies from 138 to 23272 ppm.
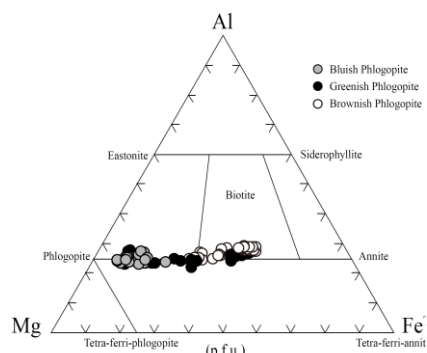
Figure 3. Composition of Yonghwa phlogopite in terms of Al, Mg and Fe^T. Fe^T, total iron calculated as Fe^{2+}.

The Yonghwa phoscorite contains 6.5–36.2 wt. % of SiO_2, 23.1–49.5 wt. % of $Fe_2O_3^T$, and 7.7–18.6 wt. % of CaO. Compared with Sokli phoscorite, Finland, Yonghwa phoscorites are more enriched in P_2O_5 (2.0–9.0 wt. %) and MnO (0.7–3.0 wt. %), since they contain more apatites and Mn-rich olivine (up to 42.5 wt. % MnO). However, TiO_2 contents (0.01–0.12 wt. %) are lower in the Yonghwa phoscorite, because of the rarity of ilmenite-series minerals.

Primitive mantle and C1 chondrite normalized trace element patterns of phoscorite and carbonatite show significant depletion of Rb, Ba, Th and Zr and relative enrichment of Nb and LREE (Fig. 4). C1 chondrite normalized REE pattern shows a similar trend to whole rock compositions, although LREE is slightly more enriched.
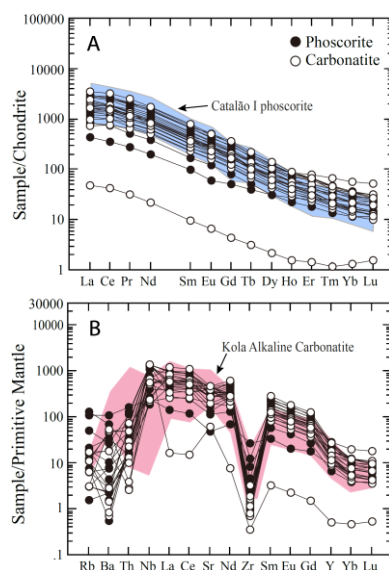
Figure 4. (A) The REE patterns of the Yonghwa carbonatite and phoscorite were normalized by Chondrite values (Sun and McDonough, 1989). (B) The trace element patterns of the Yonghwa carbonatite and phoscorite were normalized Primitive mantle values (Sun and McDonough, 1989). One sample depleted in REE and trace elements in both diagrams is collected from outcrops.

Extreme enrichment of Nb and extreme depletion of Ta (0.10-5.34 ppm) are characteristics of the YPCC. All studied rocks have highly fractionated REE patterns with the LREE enriched two to three orders of magnitude relative to the HREE without Eu anomaly, which are very similar to the patterns of phoscorites from Catalão I complex (Cordeiro et al., 2010).

The $\delta^{13}C_{PDB}$ values of dolomite and calcite from carbonatites and veins vary from -8.2 to -3.4‰. The $\delta^{18}O_{VSMOW}$ values vary from 6.6 to 11‰. $\delta^{13}C$ and $\delta^{18}O$ values generally fall in the field of the primary, mantle-derived carbonatites on a $\delta^{18}O$ *vs.* $\delta^{13}C$ diagram (Fig. 5) and are similar to those of many carbonatites (Deines, 1989). The carbon and oxygen isotope ratios of the igneous carbonatites are believed to represent mantle source (Taylor et al., 1967).
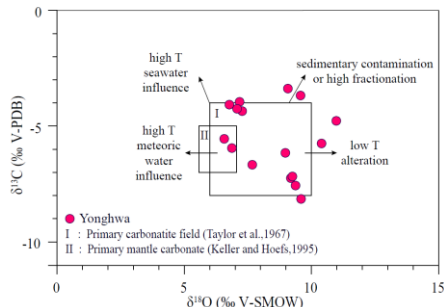
Figure 5. Stable carbon and oxygen isotopic compositions of the Yonghwa carbonatite-phoscorite complex.

5 Discussion and conclusions

The Yonghwa phoscorite and carbonatite are closely related in terms of mineralogy and geochemistry, and their contacts are gradual, which suggests a strong genetic link between the two rock types. Carbon and oxygen isotopic composition of carbonates from the carbonatites supports a magmatic origin for the complex. Chondrite normalized REE patterns of the YPCC are similar or less fractionated relative to that of primitive phlogopite picrite, indicating that the Yonghwa carbonatite magma did not experience significant evolution and is an early phase of the mantle carbonatite magma.
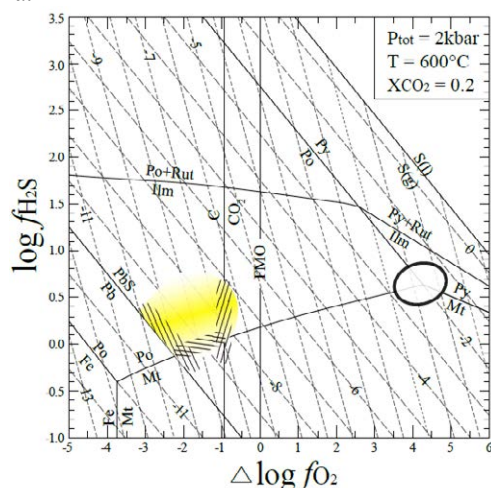
Figure 6. Phase diagram of the system Fe-Cu-Pb-C-O-H-S calculated for the P-T-X conditions. Hatched field represents the conditions for the phoscorite and carbonatite, considered with graphite; white circle field represents conditions for the veins. FMQ = fayalite-magnetite-quartz buffer, Ilm = ilmenite, Mt = magnetite, Po = pyrrhotite, Py = pyrite, Rut = rutile.

Thermodynamic analysis of the early magnetite-pyrrhotite-graphite-carbonate assemblages indicates that the Yonghwa phoscorite and carbonatite crystallized in a X_{CO2}=0.2 environment at a temperature of 600℃ and

estimated total pressure of 2 kbars. As shown in Figure 6, graphite-carbonate minerals reaction intersects with the magnetite-pyrrhotite reaction at log f_{H2S} = 0.1 within the stability fields of PbS (Gieré, 1996).

The compositional variations of apatite and phlogopite show the evolution history of the magma. The increasing Sr and decreasing Ca from early to late apatites indicate that Sr was enriched during magma differentiation (Karchevsky and Moutte, 2004). The variation from the Mg-rich Type 1 phlogopite to Fe-rich Type 2 phlogophite from the fenites suggests iron enrichment in the more differentiated magma.

Acknowledgements

References

Cordeiro, P.F.O., Brod, J.A., Dantas, E.L., Barbosa, E.S.R. (2010) Mineral chemistry, isotope geochemistry and petrogenesis of niobium-rich rocks form the Catalão carbonatite-phoscorite complex, Central Brazil. Lithos 118, 223–237.

Deines, P. (1989) Stable isotope variations in carbonatites. In: Bell, K. (ed) Carbonatites: genesis and evolution. Unwin Hyman, London, pp 301–359.

Drüppel, K., Hoefs, J., Okrusch, M. (2005) Fenitizing Processes Induced by ferrocarbonatite magmatism at Swartbooisdrif, NW Namibia. Journal of Petrology 46, 377–406.

Gieré, R. (1996) Formation of rare earth minerals in hydrothermal systems. In: Jones, A.P., Wall, F., Williams, C.T. (ed) Rare Earth Minerals: Chemistry, origin and ore deposits. Chapman and Hole, pp. 105–150.

Karchevsky, P.I. and Moutte, J. (2004) The phoscorite-carbonatite complex of Vuoriyarvi, northern Karelia. In: Wall, F., Zaitsev, A.N. (ed) Phoscorites and carbonatites from mantle to mine: the key example of the Kola alkaline province. Mineralogical Society Series, London, pp. 163–169.

Keller, J. and Hoefs, J. (1995) Stable isotope characteristics of recent natrocarbonatites from Oldoinyo Lengai. In: Bell, K. & Keller, J. (eds) Carbonatite Volcanism: Oldoinyo Lengai and the Petrogenesis of Natrocarbonatites. Berlin: Springer, pp. 113–123.

Krasnova, N.I., Petrov, T.G., Balaganskaya, E.G., Garcia, D., Moutte, D., Zaitsev, A.N., Wall, F. (2004) Introduction to phoscorites: occurrence, composition, nomenclature and petrogenesis. In: Wall, F., Zaitsev, A.N. (ed) Phoscorites and carbonatites from mantle to mine: the key example of the Kola alkaline province. Mineralogical Society Series, London, pp. 45–79.

Sun, S.S. and McDonough, W.F. (1989) Chemical and isotopic systematic of oceanic basalt: implications for mantle composition and process. In: Saunders, A.D., Norry, M.J. (ed) Magmatism in the Ocean Basins: Geological Society of London, Special Publication 42, pp. 528–548.

Taylor, H.P., Frechen, J., Degens, E.T. (1967) Oxygen and carbon isotope studies of carbonatites from the Laacher See District, West Germany and the Alnö District, Sweden. Geochimica et Cosmochimica Acta 31, 407–430.

Woolley, A.R. and Kempe, D.R.C. (1989) Carbonatites: nomenclature, average chemical compositions, and element distribution. In: Bell, K. (ed) Carbonatites: genesis and evolution. Unwin Hyman, London, pp 1–14.

Yegorov, L.S. (1993) Phoscorites of the Maymecha–Kotuy ijolite–carbonatite association. International Geology Review 35, 346–358.

Geochemistry of Y+REE in stratiform tourmalinites and their tourmalines: implications for their genesis

Renata Čopjaková, Radek Škoda, Milan Novák
1 Department of Geological Sciences, Masaryk University, Kotlářská 2, 611 37 Brno, Czech Republic; copjakova@sci.muni.cz

Michaela Vašinová Galiová
2 Department of Chemistry, Masaryk University, Kotlářská 2, 611 37 Brno, Czech Republic
3 Central European Institute of Technology (CEITEC), Masaryk University, Kamenice 5, 625 00 Brno, Czech Republic

Abstract. Yttrium+REE contents in stratiform tourmalinites and their tourmaline from two different geological units, Svratka Unit and Krkonoše-Jizera Unit (Bohemian Massif, Czech Republic) are reported to reveal tourmalinite genesis and tourmaline growth history. Premetamorphic tourmaline grains rimmed by younger metamorphic schorl-dravite were distinguished in both regions. The wing-shaped Y+REE patterns with minimum close to Eu in premetamorphic oxy-dravite from the Krkonoše-Jizera Unit, and the Y+REE whole rock signature indicate important contribution of seawater in the oxy-dravite forming fluids. On the contrary, Y+REE patterns in premetamorphic schorl cores from the Svratka Unit correspond well to presumable exhalative origin of B-bearing fluids. Metamorphic rims of schorl-dravite at both regions show typically LREE-enriched patterns with pronounced positive Eu anomalies reflecting composition of metamorphic fluids.

Keywords. Y+REE, tourmaline, stratiform tourmalinites, Bohemian Massif

1 Introduction and analytical methods

Tourmalinites are defined as rocks with more than 15 vol. % tourmaline and the most plausible tourmalinite forming-processes include: 1) syngenetic exhalative, 2) premetamorphic replacement, 3) evaporitic, 4) contact metasomatism near granitoid intrusions, and 5) regional metasomatism (Slack 1996). Tourmalinites can occur in association with a variety of metallic mineral deposits (accumulations of Ag, W, Sn, Co, U, and base-metal sulfides; mainly SEDEX and VMS; Slack 1996).

Trace elements, including REE, are particularly usefull for petrogenetic studies. We report Y+REE contents in tourmaline and in stratiform tourmalinites from two different geological units, Svratka Unit (SU), Moldanubian Zone, and Krkonoše-Jizera Unit (KJU), Saxothuringian Zone, Bohemian Massif, Czech Republic, and use Y+REE patterns in tourmaline and tourmalinites to study genesis of tourmalinites and growth history of tourmaline grains.

Whole-rock chemical analyses of tourmalinites were performed on crushed and pulverized sample rocks at Acme Analytical Laboratories (Vancouver, Canada), where the trace elements were analyzed using ICP-MS. Yttrium and REE in tourmaline were obtained using LA-ICP-MS equipment (Agilent 7500ce quadrupole ICP-MS with an attached UP 213 laser ablation system) at the Department of Chemistry, Masaryk University. Tourmaline grains were ablated at frequency of 10 Hz.

Each spot was ablated 60 s by laser beam diameter in range 55-80 μm and fluence 5-8 J.cm^{-2}. The concentrations of trace elements were determined using SRM NIST 610 and 612 and Si as internal reference element. The calculation was performed via peak area.

2 Stratiform tourmalinites

Tourmalinites from the KJU form stratiform layers (<30 cm) hosted in mica schists (Ms + Qtz + Grt + Chl ± Tu ± Bt) and show simple mineral assemblage with major tourmaline (30-60%) and quartz and minor Ms + Chl ± Grt (Fig. 1a,b). The calculated P-T conditions for Variscan metamorphic event from mica schist hosted tourmalinite layer yielded 553 ± 30 °C and 13 ± 2.5 kbar. Tourmalinites show commonly very low ΣY+REE (11-52 ppm), flat REE patterns (La/Yb=1.2-3.8) with negative Ce (0.33-0.75) and Eu (0.53-0.75) anomalies. Rarely they are enriched in LREE (ΣY+REE 110-150 ppm; La/Yb~8) without negative Ce anomaly (Fig. 2a).

The SU tourmalinites form stratiform layers of variable thickness (1 cm - 1 m) hosted in mica schists (Qtz + Ms ± Bt + Grt ± Tu ± Ky ± Sill ± Pl ± St). Tourmalinites consist of tourmaline (15-95%) and quartz with minor Ms ± Grt ± Bt ± Ky ± Sil ± Pl ± Kfs (Fig. 1c,d). The P-T conditions calculated for host mica schist 600–640 °C and 5–6 kbar are interpreted as Variscan retrograde metamorphic event resulted in decompression breakdown of staurolite (Čopjaková et al. 2009). Yttrium + REE range from 35 to 526 ppm and the La/Yb ratios change from 0.6 to 20. The Eu concentrations are usually low with negative Eu anomaly 0.43-0.56 although sample with a slight positive Eu anomaly was observed (Fig. 2a).

3 Tourmaline

Tourmaline in tourmalinites shows multiphase evolution (Čopjaková et al. 2009, 2012; Fig. 1). Premetamorphic oxy-dravite (Mg/(Mg+Fe) = 0.81-0.99; 6.14-7.09 apfu Al; 0.59-0.85 apfu Na; 0.04-0.39 pfu ^{x}vac) volumetrically predominates in the KJU tourmalinites. Grains of oxy-dravite are usually replaced along rims, or locally completely replaced by metamorphic schorl-dravite to foitite-magnesio-foitite (Mg/(Mg+Fe) = 0.42-0.69; 5.90-6.64 apfu Al; 0.00-0.43 pfu ^{x}vac; ~0.06 apfu Ca). Tourmaline from the SU tourmalinites exhibits
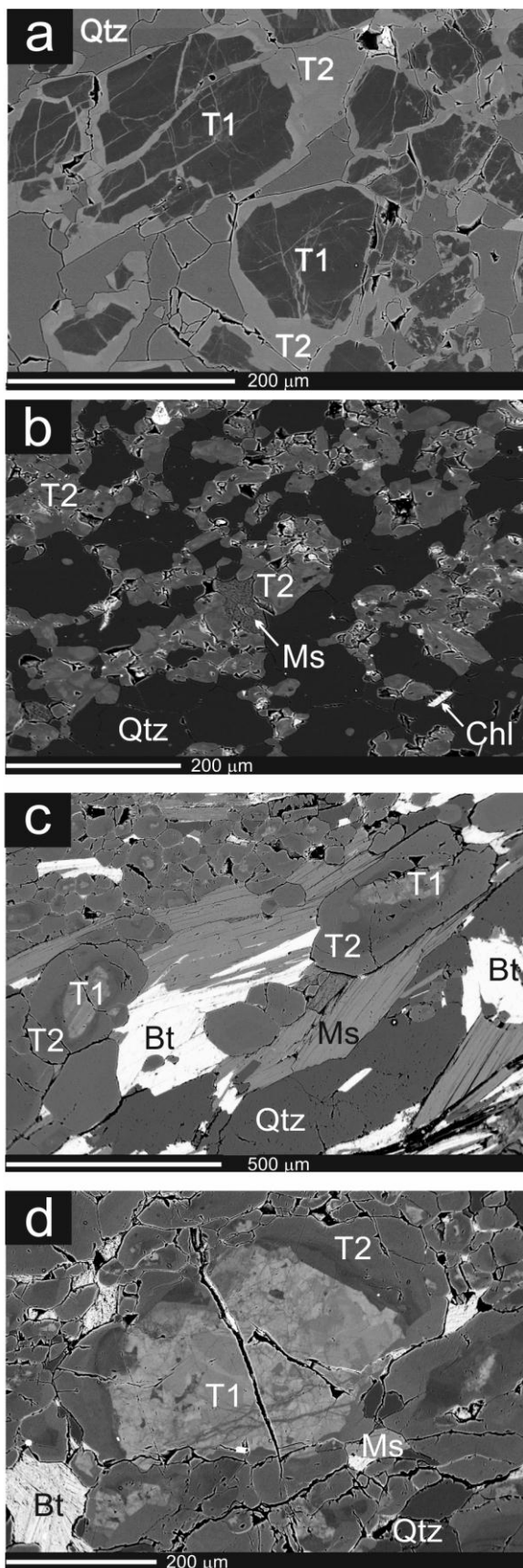
Figure 1. BSE images of tourmaline from the KJU tourmalinites (a,b) and SU tourmalinites (c,d). a) Oxy-dravite (dark in BSE image) replaced from rim and along cracks by metamorphic schorl-dravite (brighter in BSE image); c,d) tourmalinites with schorl cores (brighter) overgrown by metamorphic schorl-dravite with decreasing Mg/(Mg+Fe) ratio to the rim. Premetamorphic schorl- or oxy-dravite cores are labelled as T1, metamorphic schorl-dravite as T2. The symbols for other rock-forming minerals are after Kretz (1983).

chemically heterogeneous premetamorphic schorl cores (Mg/(Mg+Fe) = 0.03-0.53; 6.19-6.66 apfu Al; 0.17-0.46 pfu ^{x}vac; ~0.1 apfu Ca) overgrown by metamorphic schorl–dravite (Mg/(Mg+Fe) = 0.30-0.78; Al 6.00-6.45 apfu; 0.10-0.39 pfu ^{x}vac; <0.13 apfu Ca).

Total Y+REE contents in tourmaline are rather low to moderate 1-66 ppm. Schorl cores from the SU tourmalinites, with ΣY+REE 6-52 ppm, show LREE-enrichment with La/Gd ratio ~14 and positive Eu anomalies ~5. On the contrary, oxy-dravite cores from the KJU tourmalinites with ΣY+REE 16-66 ppm are characterized by wing-shaped Y+REE patterns with minimum close to Eu (Eu/Eu*~0.5) and La/Yb~0.8 (Fig. 2b). Metamorphic schorl-dravite at both regions show lower ΣY+REE 1-31 ppm with LREE enrichment (La/Gd~6) and more pronounced positive Eu/Eu*~10 (Fig. 2c).

4 Discussion

4.1 Y+REE in tourmalinites

Tourmalinites from the KJU with very low ΣY+REE, flat REE patterns with negative Ce and Eu anomalies reflect seawater composition (Fig. 2a), which testify against its siliciclastic precursor. Tourmalinites enriched in LREE without negative Ce anomaly show LREE contents close to the associated mica schists and garnetites (Fig. 2a). Tourmalinites enriched in LREE contain common monazite and early oxy-dravite is completely replaced by metamorphic schorl-dravite (Fig. 1b) indicating intensive metamorphic overprint with high activity of metamorphic fluids and mobilization of LREE from surrounding rocks.

The SU tourmalinites and the surrounding mica schists have similar chemical compositions, the SiO_2 and Al_2O_3 contents in the tourmalinites vary significantly, in accord to modal amounts of quartz and tourmaline. The total Y+REE contents and patterns in tourmalinites reflect the variation in the modal content of the rock-forming minerals (quartz+monazite vs tourmaline, apatite and garnet) and variable mixing of detrital and exhalative component.

4.2 Y+REE in tourmaline

Tourmaline does not selectively incorporate specific REE into its structure and is unable to significantly fractionate trace elements consequently the trace elements in tourmaline can directly record the compositional signature of its genetic environment (van Hinsberg 2011). The main factor affecting REE patterns in tourmaline from sampled tourmalinites seems to be composition of hydrothermal/metamorphic fluids.

Chemical composition (major and minor elements) of schorl cores from the SU tourmalinites seems to be similar to that from other quartz–tourmaline rocks, where the tourmaline precipitated from Fe-rich exhalative fluids, which react with pelitic sediments (Slack 1996). The REE patterns of schorl cores resemble to black smoker fluid REE patterns (Fig. 2d) rather than REE patterns of pelitic sediments and confirm the
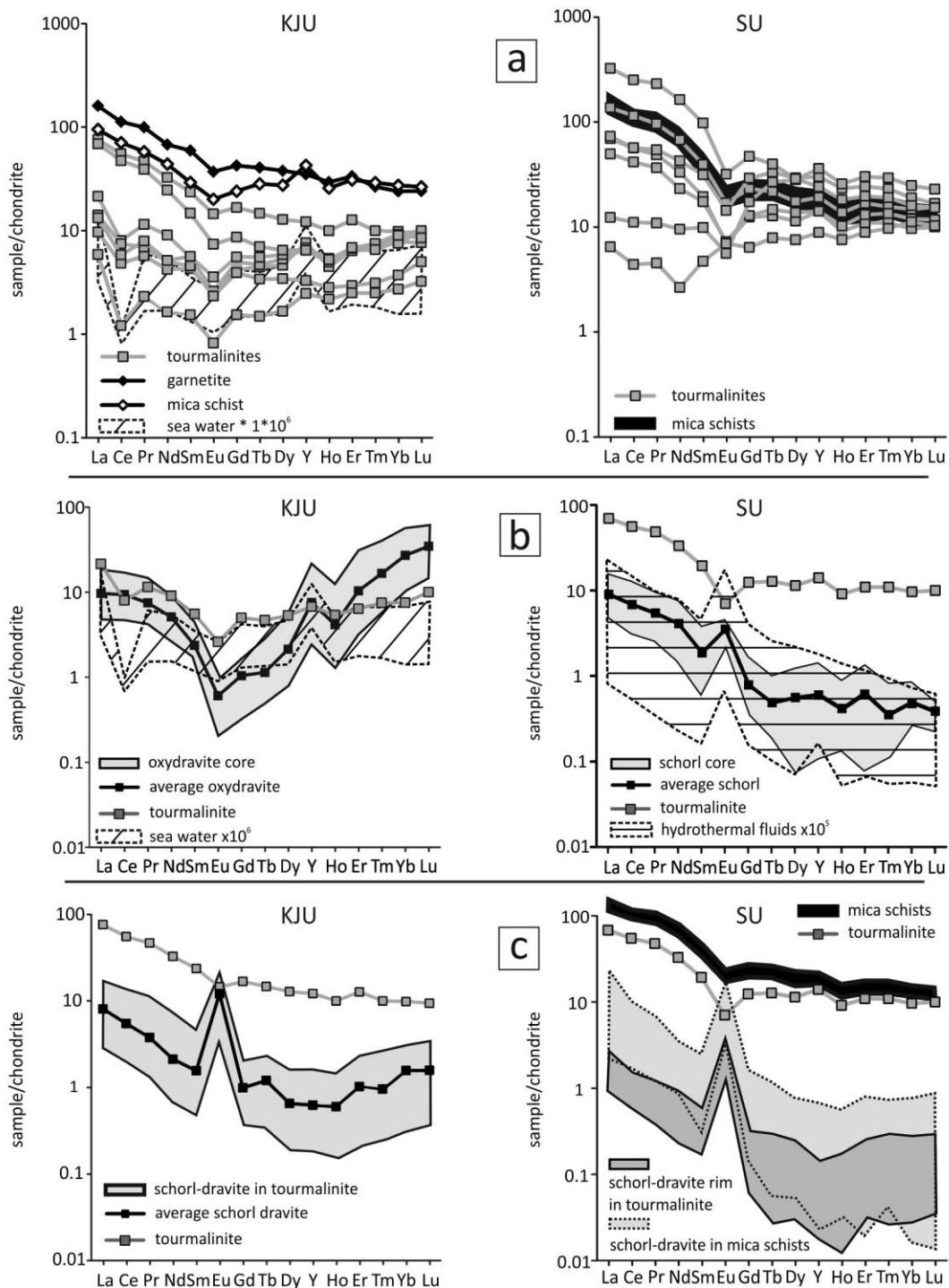
Figure 2. Chondrite (Taylor and McLennan 1985) normalized Y+REE patterns. a) Whole-rock Y+REE patterns in tourmalinites and host rocks; b) Y+REE patterns in hydrothermal premetamorphic tourmaline from tourmalinites compared with whole-rock Y+REE pattern in tourmalinite; c) Y+REE patterns in metamorphic schorl-dravite from tourmalinites compared with whole-rock Y+REE pattern in tourmalinite. Y+REE patterns in metamorphic tourmaline from tourmalinite hosted mica schist from the SU are plotted as well. The seawater patterns are from Alibo and Nozaki (1999); the Y+REE patterns of hydrothermal fluids in mid-ocean ridges are from Bao et al. (2008).

exhalative origin of fluids. Moreover, detrital-exhalative origin is proposed for skarn bodies (Pertoldová et al. 2009) common in the Svratka Unit. On the contrary, tourmaline-rich rocks formed as a result of the replacement of clastic sediments, show high ΣREE, high LREE/HREE and negative Eu anomalies similar to the whole-rock samples and PAAS (Raith et al. 2004). High ΣREE in tourmalinites in the Sierra Nevada comparable to whole-rock samples, however without negative Eu anomalies or with slight positive ones, reflect relatively

high fluid/rock conditions and contribution of Eu from the hydrothermal fluids during tourmalinization and replacement of psammopelitic rocks (Torres-Ruiz et al. 2003).

Flat whole-rock Y+REE patterns with negative Ce and Eu anomalies in the KJU tourmalinites with high modal volume of premetamorphic oxy-dravite along with high Mg/(Mg+Fe) in oxy-dravite indicate a significant portion of Mg-rich seawater in the tourmaline-forming fluids. Yttrium+REE pattern in oxy-

dravite differs slightly from that of seawater by absence of Ce anomaly and steeper pattern from Eu to Lu. Slight enrichment in HREE with increasing atomic number in tourmaline compared with the whole-rock patterns is evident from all studied tourmaline generations and can relate to increasing distribution coefficient for HREE in tourmaline with increasing atomic number (van Hinsberg 2011). Tourmalinite chemistry and association with mica schists, garnetites, magnetite and polymetallic skarns and rift-related volcanic rocks (all rock types enriched in Cr, V, Sr, Sn, Zn, Pb, As) indicate tourmalinite formation distally from the exhalative deposits, from rather low temperature and oxidative fluids with high portion of seawater near the seafloor. Enrichment of oxy-dravite in Cr, V, Ti, Sc, Ni (compared to oxy-dravite from Bačík et al. 2012) as well as the rock association do not support its purely metaevaporitic origin.

Based on the chemical composition and textural relationship to other rock-forming minerals, schorl-dravite overgrowing or replacing premetamorphic core in tourmalinites from both geological units probably corresponds to crystallization of tourmaline during regional metamorphism, mainly during its retrograde stage (Čopjaková et al. 2009, 2012). Yttrium and REE patterns in metamorphic schorl-dravite from both geological units with high La/Yb ratios and positive Eu anomalies (Fig. 2c) reflect the presumable Y+REE patterns of metamorphic fluid. The REE can be mobilized during regional metamorphism and fluids derived from the metasediments show similar La/Yb ratios compared with their source rocks (Tang and Liu 2002). In fluids at T>250 °C the Eu^{2+} is the predominant Eu species and its solubility is higher than trivalent REE (Sverjenski 1984); it indicates presence of Eu^{2+} and positive Eu anomalies in metamorphic fluids under most metamorphic conditions. The differences in REE contents in metamorphic schorl-dravite from the SU tourmalinites and from host mica schists reflect differences in the whole-rock Y+REE contents, which imply derivation of Y+REE from a local source (tourmalinite vs. mica schist). On the contrary, Y+REE patterns in metamorphic schorl-dravite from the KJU tourmalinites suggest proposed metamorphic mobilization of Y+REE from surrounding mica schists or garnetites.

Acknowledgements

References

Alibo DS, Nozaki Y (1999) Rare earth elements in seawater, particle association, shale-normalization, and Ce oxidation. Geochim. Cosmochim. Acta 63:363-372.doi: 10.1016/S0016-7037(98)00279-8

Bačík P, Uher P, Cempírek J, Vaculovič T (2012) Magnesian tourmalines from plagioclase-muscovite-scapolite metaevaporite layers in dolomite marble near Prosetín (Olešnice Unit, Moravicum, Czech Republic). J. Geosciences 57:143-153. doi: 10.3190/jgeosci.120

Bao SX, Zhou HY, Peng XT, Ji FW, Yao HQ (2008) Geochemistry of REE and yttrium in hydrothermal fluids from the Endeavour segment, Juan de Fuca Ridge, Geochem. J. 42:359-370. doi: 10.2343/geochemj.42.359

Čopjaková R, Buriánek D, Škoda R, Houzar S (2009) Tourmalinites in the metamorphic complex of the Svratka Unit (Bohemian Massif): a study of compositional growth of tourmaline and genetic relations. J.Geosciences 54:221–243. doi: 10.3190/jgeosci.048

Čopjaková R, Škoda R,Vašinová Galiová M (2012) „Oxy-dravite" from tourmalinites of the Krkonoše-Jizera Crystalline Massif. Bull. mineral.-petrolog. Odd. Nár. Muz. (Praha) 20:37-46 (in Czech).

van Hinsberg VJ (2011) Preliminary experimental data on trace-element partitioning between tourmaline and silicate melt. Canad Mineral 49:153–163. doi: 10.3749/canmin.49.1.153

Kretz R (1983) Symbols for rock-forming minerals. Amer. Mineral. 68:277-279.

Pertoldová J, Týcová P, Verner K, Košuličová M, Pertold, Z, Košler J, Konopásek J, Pudilová M (2009) Metamorphic history of skarns, origin of their protolith and implication for genetic interpretation; an example from three units of the Bohemian Massif. J. Geosciences 54:101-134. doi: 10.3190/jgeosci.044

Raith JG, Riemer N, Schöner N, Meisel T (2004) Boron metasomatism and behavior of rare earth elements during formation of tourmaline rocks in the eastern Arunta Inlier, central Australia. Contrib Mineral Petrol 147:91–109. doi: 10.1007/s00410-003-0548-9

Slack JF (1996) Tourmaline associations with hydrothermal ore deposits. Rev. Mineral. Geochem. 33:559–644.

Sverjensky DA (1984) Europium redox equilibria in aqueous solutions. Earth Planet. Sci. Lett. 67:70-79. doi: 10.1016/0012-821X(84)90039-6

Tang HF, Liu CQ (2002) Trace element geochemistry during metamorphic dehydration: A case study from the Xingzi Group of Lushan, southeast China. Geochem. J. 36:545-561.

Taylor SR, McLennan SM (1985) The Continental Crust: Its Composition and Evolution. Blackwell Scientific Publications, Oxford, p. 321.

Torres-Ruiz J, Pesquera A, Gil-Crespo PP, Velilla N (2003) Origin and petrogenetic implications of tourmaline-rich rocks in the Sierra Nevada (Betic Cordillera, southeastern Spain). Chem Geol 197: 55-86. doi: 10.1016/S0009-2541(02)00357-1

Timing and geological setting of the world-class Sn, Nb-Ta and Li mineralization of Manono-Kitotolo (Katanga, Democratic Republic of Congo): current state of knowledge

Dewaele, S.
Department of Geology and Mineralogy, Royal Museum for Central Africa, Leuvensesteenweg 13, B-3080 Tervuren, Belgium

Cryns, Y., Muchez, Ph.
Department of Geology and Mineralogy, Royal Museum for Central Africa, Leuvensesteenweg 13, B-3080 Tervuren, Belgium

Henjes-Kunst, F., Goldman, S., Melcher, F.
Bundesanstalt für Geowissenschaften und Rohstoffe, Stilleweg 2, D-30655 Hannover, Germany

Burgess, R.
University of Manchester, School of Earth, Atmospheric and Environmental Sciences, Oxford Road, Manchester M13 9PL, UK

Abstract. The Central African Mesoproterozoic Kibara belt forms a metallogenic province that hosts a variety of granite-related mineralization rich in cassiterite, columbite-tantalite, wolframite/ ferberite, spodumene and beryl. Between 997 ± 8 Ma and 966 ± 21 Ma, granites intruded, associated with pegmatites and quartz veins, locally carrying Sn-Nb-Ta mineralization.
Different highly evolved pegmatites intruded in the Manono-Kitotolo area. The emplacement of the pegmatite veins resulted in an intense alteration of the doleritic and metasedimentary host-rocks. After emplacement, the pegmatites developed a regular zonation during cooling that is affected by later metasomatic/hydrothermal alteration. Nb-Ta mineralization formed prior to metasomatic alteration and has been dated at 940 ± 5.1 Ma, which is significantly younger than the age of pegmatites that have been dated at 973 ± 13 Ma in Katanga. This is interpreted as resetting during (metasomatic) post-crystallization processes. The major part of cassiterite mineralization formed during metasomatic alteration, i.e. during the muscovitization. Muscovite associated with the cassiterite mineralization, in so-called "poches de greisen" has been dated at 923 ± 8.3 Ma. This age is too young to reflect crystallisation during cooling of the granites and is interpreted as resetting during a Late Neoproterozoic event.

Keywords. Kibara belt – Manono-Kitotolo – columbite-tantalite – cassiterite

1 Introduction

The Central African "Kibara" belt extends from the southwestern part of Uganda to the southern part of Katanga in the Democratic Republic of Congo (DRC) (Figure 1) and is situated between the Congo Craton to the west and the Tanzania Craton and Bangweulu Block to the east. In fact, this Mesoproterozoic "Kibara" belt can be divided into two belts, which are separated by a "Rusizian" basement rise that represents the NW extension across Lake Tanganyika of the Palaeoproterozoic Ubende belt (SW Tanzania). The northeastern part, which comprises Rwanda, Burundi,

SW Uganda, northwestern Tanzania and the Kivu – Maniema region in the DRC, is termed the Karagwe – Ankole belt (KAB). The Kibara belt (KIB) occurs in the Katanga province in the southwest of the DRC (Tack et al. 2010; Fernandez et al. 2012).
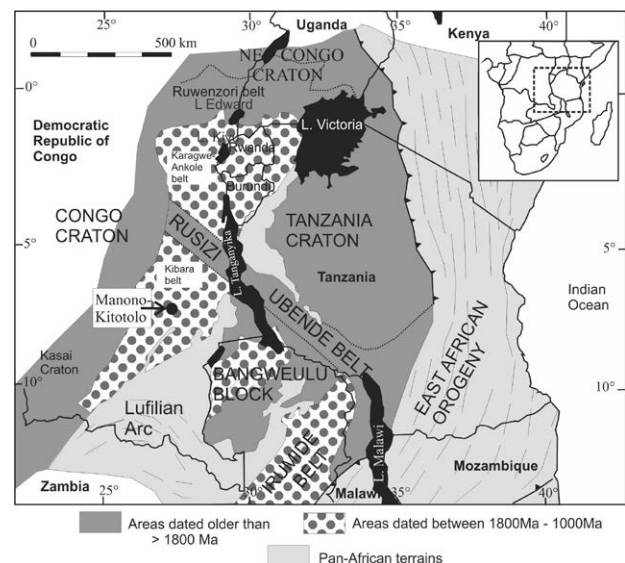
Figure 1. Regional geological setting of the Central African area (modified after Brinckmann et al. 2001). Location of Manono-Kitotolo deposit is indicated by circle.

A metallogenic province that hosts different types of granite-related mineralization, which contain minerals like cassiterite, columbite-tantalite, wolframite/ferberite, gold, amblygonite, beryl, etc. overlaps to a large extent with the KIB and KAB. The minerals occur as primary mineralization in quartz veins and pegmatites, but also as secondary mineralization in alluvial or eluvial deposits.

In this study, we focus on the geology and the timing of the formation of the primary Sn, Nb-Ta and Li mineralization of Manono-Kitotolo, located in the KIB in Katanga, at ~ 500 km NW of Lubumbashi (DRC). From the start of the exploitation in 1919, Manono-Kitotolo has produced about 140,000 tonnes of

cassiterite concentrate and 4,500 tonnes of columbite-tantalite concentrate. Non-altered pegmatite could yield a resource potential of 200,000 tonnes of cassiterite and 10,000 tonnes of columbite-tantalite concentrate (archives Géomines, RMCA), which makes it a world-class deposit. A first attempt to evaluate the Li potential has started in the beginning of the '80ies.

This study of the Manono-Kitotolo deposit is largely based on unpublished geological information available in the mining archives of the Royal Museum for Central Africa (RMCA) and on the study of hundreds of rock and mineral concentrate samples present in the rock and mineral collection of the RMCA.

2 The Kibara belt

The Kibara belt consists dominantly of Palaeo-and Mesoproterozoic metasediments, covered by younger Phanerozoic sedimentary rocks. The Palaeoproterozoic Rusizian rocks are characterized by gneisses, micaschists, amphibolites, migmatites with large quartzite lenses and smaller lenses of marble (Cahen and Lepersonne, 1967). The Mesoproterozoic Kibaran rocks are composed of series of quartzites, quartzophyllites and phyllites, with local intercalations of volcanic and dolomitic rocks and conglomerate.

The main granite generation (type A-D) is ~1381 ± 8 Ma (U-Pb shrimp data, Kokonyangi et al. 2004). These granites form the majority of the granitic bodies on the geological map. The second granite generation is ~977 ± 18 Ma (Rb-Sr, Mwanza Massif) and 966 +/-21Ma (Rb-Sr, Mount Bia Massif), the so-called "E-granites" (Cahen & Ledent 1979). This generation has been interpreted as the parental granite for abundant pegmatites and quartz veins that ore often associated with Sn-W-Nb-Ta mineralization. The pegmatites in Katanga have been dated at 973 ± 13 Ma (Rb-Sr, Cahen & Ledent 1979), while an age of ~1030 Ma (Rb-Sr, Cahen & Snelling, 1966) has been obtained for the quartz veins.

3 The Manono-Kitotolo deposit

The Manono-Kitotolo deposit consists of two sectors: Kitotolo in the southwest and Manono-Kahungwe in the northeast (Figure 2). The two areas with exploited pegmatites are located at a distance of 2-3 km, separated by the Lac Lukushi, which was formed by damming the Lukushi river. Between both sectors, granite and spodumene bearing pegmatite are exposed. The general orientation of the Manono and Kitotolo sectors is NE-SW, forming a zone that is 700m wide and over ~5km long. The average thickness of the eluvial cover is ~8 m. It consists either of lateritic sands, crumbly laterites or laterites, which are mineralized.

The Manono and Kitotolo sectors contain different individual pegmatite veins that intruded along cleavage planes. In the Kitotolo sector, the pegmatite lenses occur in metasedimentary rocks, while the lenses of the northeastern sector crosscut doleritic rocks. The contact with host-rock is undulating and varies between 50° S to subvertical.
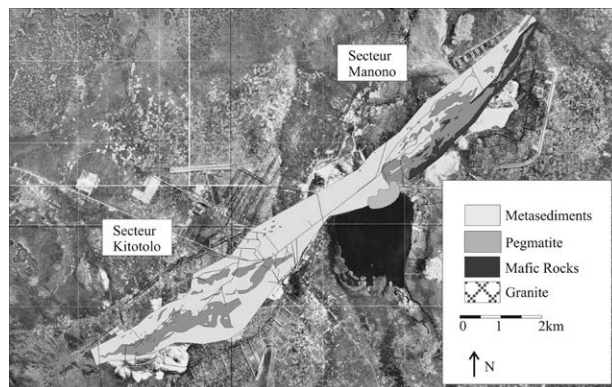
Figure 2. Map of the Manono-Kitotolo mine

The individual pegmatite veins have been affected by important – post-emplacement – folding and fracturing, which often resulted in complex displacements between blocks. Superficial weathering resulted in the alteration of the pegmatite to a brownish sandy or clayey-sandy material in the upper part of the pegmatite. This weathering can extend to a depth of 80m in the Manono sector and obscures the identification of the mineralogy, structure and zonation of the primary pegmatites.

4 Zonation and paragenesis

The intrusion of the pegmatites resulted in an intense alteration of the host-rocks. Tourmalinization, muscovitization, silicification and local formation of staurolite and andalusite are identified in the metasedimentary rocks that host the pegmatites. The doleritic host-rocks show tourmalinization, muscovitisation, silicification and biotitization, with the formation of staurolite, biotite, muscovite, tourmaline and quartz.

The pegmatite lenses show important metasomatic/hydrothermal overprinting, but zoning is largely obscured. The zonal development is largely obscured by intense weathering, lack of coloured minerals and the dimension and orientation of pegmatite veins. A "border zone" consists of fine-grained quartz, microcline, albite and micas, which has historically been called "aplite albitique". The next zone, "the wall zone", consists of coarser grained quartz, microcline, albite and micas. The "intermediate zone" is formed by quartz, spodumene, microcline, albite and micas. The latter zone is historically called the zone of "pegmatites à colonnes", due to the large spodumene crystals. It should be noted that samples of quartz cores have neither been found in the rock collection or have they been described in the literature. The metasomatic/hydrothermal overprinting is mainly albitization, with the neoformation of albite replacing K-feldspar, and muscovitization with the formation of greisenized zones ("poches de greisen").

Li-mineralization is mainly present as spodumene crystals in the "intermediate zone", while Nb-Ta minerals can be found in the "border zone" and "intermediate zone". The spodumene and columbite-tantalite clearly formed prior to the metasomatic alteration. Nb-Ta minerals present in general 5-10% of the cassiterite concentrates. Cassiterite is rare in rocks

that have not been affected by the metasomatic alteration. It is more common in albitized rocks, but not clear if it resulted from neoformation or remnants of pre-existing mineralization. Cassiterite is very abundant in zones of muscovitization ("poches de greisen"), zones that are mainly composed of quartz, muscovite and cassiterite.

Columbite-tantalite is the major carrier of Nb and Ta, with minor wodginite and tapiolite present. The mineralization is almost unaffected by later alteration to microlite. Mn-rich columbite and tantalite follow a fractionation trend typical for Li-rich pegmatites, with an early Mn-for-Fe substitution associated with minor Ta-for-Nb substitution that is progressively followed by extreme Ta-Nb fractionation at constantly high Mn/Fe ratios (Melcher et al., submitted to Ore Geology Reviews). Cassiterite shows element enrichments characteristic for rare-element pegmatites, including Ta (median 1.1 wt%), Nb (0.5 wt%), Fe (0.15 wt%), Zr (700 ppm), Ti (600 ppm), Hf (100 ppm) and Mn (100 ppm).

5 Dating Nb-Ta and Sn mineralization

5.1 U-Pb dating of columbite-tantalite

U-Pb dating of columbite-tantalite grains was performed on crystal fragments from a concentrate from Manono-Kitotolo by conventional thermal ion mass spectrometry (TIMS) at the University of Toronto. The chemical procedure to separate U and Pb was adapted from Romer and Wright (1992) and Romer and Smeds (1994). U and Pb were measured in multi-collector mode on a MM354 TIMS. Individual fragments (<100 µm; <<1 mg) from one grain were analyzed separately ("single-grain method"). This allows very careful inspection of the quality of the fragments to be dated. Isoplot (Ludwig 2003) was used for graphical presentation of all U-Pb isotope data and for age calculation.

Columbite-tantalite grains from two concentrate samples were investigated. A discordia calculation for five individual grains within one concentrate gave an upper intercept age of 940.2 ± 5.1 Ma (Figure 3); three data points plot within error on the concordia while two others plot above the concordia (reverse discordance). In the second sample, four splits analyzed from one grain gave 947 ± 2.8 Ma. Thus, an approximate age of 945 Ma may be considered as the formation age of the Nb-Ta (and associated Li) mineralization and based on the petrographic observation as the timing of the pegmatite crystallization.

5.2 ^{40}Ar-^{39}Ar dating of cassiterite mineralization

Large crystals of muscovite up to several cm in size have been selected from a massive "greisen" sample that consists of large cassiterite crystals in a matrix of quartz and muscovite. Feldspar is completely altered in this sample. To avoid influence of alteration on the muscovite, large crystals were crushed to a smaller size (< 5mm) and clean transparent sheets of muscovite were selected for dating by hand-picking under a binocular microscope.
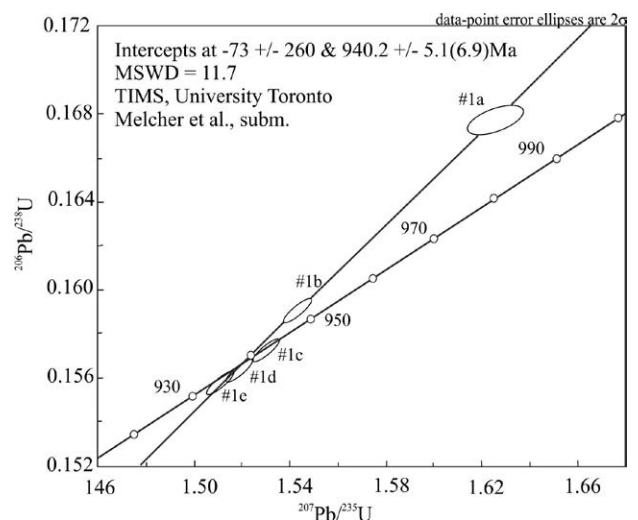
Figure 3. U-Pb Concordia diagram for 5 columbite-tantalite grains from Manono

Experimental details on ^{40}Ar-^{39}Ar dating are given by Burgess et al. (2004). Ar–Ar ages were determined from age spectra, using the ISOPLOT/Ex 3.23 software (Ludwig, 2003), and all data are reported at the 2 σ level of uncertainty.

The muscovite sample shows a well-defined age plateau at 923.3 ± 8.Ma for the intermediate to high temperature degassing steps (51.6 % of the released ^{39}Ar, MSWD 0.60; Figure 4). This age is younger than the Nb-Ta mineralization.
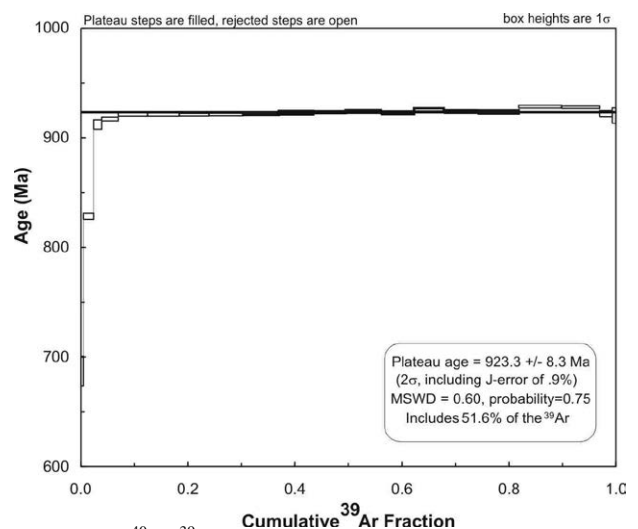
Figure 4. ^{40}Ar-^{39}Ar spectra muscovite associated with main cassiterite mineralization.

6 Proposed model for the formation of the Nb-Ta and Sn mineralization in the Kibara belt

In the Kibara belt, the main granite generation (type A-D) intruded the Palaeo- and Mesoproterozoic rocks at 1381 ± 8 Ma (Kokonyangi et al. 2004). These granites are not associated with an economically significant concentration of rare metals. Some 400 Ma later, the so-called "E-type granites" were emplaced (Cahen and Ledent 1979). These small granite intrusions dated at 977 ± 18 Ma and 966 ± 21 Ma, contain no mineralisation, but show geochemical enrichment trends

typical for parental granites for rare metal mineralization (Dewaele et al. 2008). Associated with these granites, pegmatites emplaced at 973 ± 13 Ma (Cahen & Ledent 1979). Highly evolved pegmatites intruded in the Manono-Kitololo area are mineralised with cassiterite, columbite-tantalite and spodumene. Fractional crystallization resulted in the development of an internal zonation in pegmatitic bodies that is affected by later metasomatic/hydrothermal alteration. Nb-Ta minerals formed prior to the metasomatic alteration, while cassiterite could have formed prior and during the metasomatic alteration. The columbite-tantalite mineralization has been dated at ~945 Ma, which is significantly younger than the Rb-Sr age reported for the pegmatites in Katanga. The younger age of the columbite-tantalite could be related to variable degrees of resetting by (metasomatic) post-crystallisation processes. The resetting could either be due to recrystallisation of early Nb-Ta minerals or due to the disturbance of the U-Pb isotopic signature of the Nb-Ta minerals. This has also been described for Nb-Ta mineralization in the KAB (Dewaele et al. 2011). Muscovite associated with the cassiterite mineralization in the so-called "poches de greisen" has been dated at 923 ± 8. Ma. This age is, however, too young to be directly related to crystallization from magma, so resetting during a Late Neoproterozoic tectonothermal events is also suggested for this age.

Acknowledgements

References

Brinckmann, J., Lehmann, B., Hein, U., Höhndorf, A., Mussallam, K., Weiser, Th. & Timm, F., 2001. La géologie et la minéralisation primaire de l'or de la chaîne Kibarienne, Nord-Ouest du Burundi, Afrique orientale. Geologisches Jahrbuch Reihe D, 101: 195 pp.

Burgess, R., Kiviets, G.B., Harris, J.W., 2004. ^{40}Ar/^{39}Ar age determinations of eclogitic clinopyroxene and garnet inclusions in diamonds from the Venetia and Orapa kimberlites. Lithos 77, 113–124.

Cahen, L., Snelling, N.J., 1966. The geochronology of Equatorial Africa. North-Holland Publishing Company, Amsterdam

Cahen, L., Lepersonne, J. 1967. The Precambrian of the Congo, Rwanda and Burundi. In Rankama, K. (Ed.): The Precambrian, volume 3. Interscience Publishers. 143 – 290.

Cahen, L. & Ledent, D. 1979. Précisions sur l'age, la pétrogénèse et la position stratigraphique des «granites à étain» de l'est de l'Afrique Centrale. Bulletin de la Société Belge de Géologie, 88, 33-49.

Dewaele, S., Tack, L., Fernandez-Alonso, M., Boyce, A., Muchez, Ph., Schneider, J., Cooper, G., Wheeler, K.,

2008. Geology and mineralisation of the Gatumba area, Rwanda: Present state of knowledge. Etudes Rwandaises 16, 6-24.

Dewaele, S., Henjes-Kunst, F., Melcher, F., Sitnikova, M., Burgess, R., Gerdes, A., Fernandez-Alonso, M., De Clercq, F., Muchez, P., Lehmann, B., 2011. Late Neoproterozoic overprinting of the cassiterite and columbite-tantalite bearing pegmatites of the Gatumba area, Rwanda (Central Africa). Journal of African Earth Sciences 61, 10-26.

Fernandez-Alonso, M., Cutten, H., De Waele, B, Tack, Tahon, L.A., Baudet, D., Barritt, S.D. 2012. The Mesoproterozoic Karagwe-Ankole Belt (former NE Kibaran belt): the result of prolonged extensional intracratonic basin development punctuated by 2 short-lived far-field compressional events. Precambrian Research, 216-219, 63-86.

Kokonyangi, J., Armstrong, R.,Kampunzu, A.B, Yoshida, M., Okudaira, T. 2004. U-Pb geochronology and petrology of granitoids from Mitwaba (Katanga, Congo): implications for the evolution of the Mesoproterozoic Kibaran belt. Recambrian Research, 132, 79-106.

Ludwig, K., 2003. Isoplot/Ex, version 3: A Geochronological Toolkit for Microsoft Excel. Geochronology Center, Berkeley, USA..

Romer, R.L., Wright, J.E., 1992. U-Pb dating of columbites: a geochronological tool to date magmatism and ore deposits. Geochimica et Cosmochimica Acta 56, 2137-2142.

Romer, R.L., Smeds, S.A., 1994. Implications of U-Pb ages of columbite-tantalites from granitic pegmatites for the Palaeoproterozoic accretion of 1.90-1.85 Ga magmatic arcsto the Baltic Shield. Precambrian Research 67, 141-158.

Tack, L., Wingate, M., De Waele, B., Meert, J., Belousova, E.A., Griffin, B., Tahon, A., Fernandez-Alonso, 2010. The 1375Ma "Kibaran event" in Central Africa: Prominent emplacement of bimodal magmatism under extensional regime. Precambrian Research 180, 63-84.

Mineralogy of the Kvanefjeld multi-element deposit

Henrik Friis
Natural History Museum, University of Oslo, PO 1172, Blindern, 0318 Oslo, Norway
MDRU, Department of Earth and Ocean Sciences, University of British Columbia, 6339 Stores Road, Vancouver B.C., V6T 1Z4, Canada

Abstract.
The Kvanefjeld deposit is placed in the northern part of the Ilímaussaq alkaline complex, which is situated in South Greenland and is one of several alkaline complexes related to Mesoproterozoic NE-SW continental rifting. The complex forms a layered, ellipsoid body measuring 17 by 8 km and covering an area of 85 km^2, and represents an enormous resource of rare elements, particularly REEs, Y, Zr, U, Nb, Th, Li and Be.

The Kvanefjeld deposit is hosted in lujavrite, a nepheline syenite, and the main ore mineral is the complex REE-phosphosilicate steenstrupine-(Ce). It is a primary mineral, only found in a few places in the world, and its alteration leads to a fractionation of the REEs into separate LREE and HREE bearing minerals. Furthermore, one of the gangue minerals is unique to Ilímaussaq, illustrating the need for a detailed mineralogical study to evaluate the deposit and prepare metallurgical work.

This paper will give an introduction to the geology and mineralogy of the Kvanefjeld deposit and how mineralogy may be inferred based on assays, even in this complex system with >220 known minerals of which 34 are REE-minerals.

Keywords.
REE, Ilímaussaq alkaline complex, mineralogy, Kvanefjeld, steenstrupine-(Ce)

1 Introduction

The Kvanefjeld deposit is situated in the northern part of the Ilímaussaq alkaline complex, in South Greenland. The Ilímaussaq complex was first mapped by the Danish geologist N. V. Ussing, who also introduced the term 'agpaitic' for extreme alkaline peralkaline complexes (Ussing 1912). Although, Ussing was the first to map the area and describe the geology, exploration of the area started already in 1806 by K. L. Giesecke. However, the first 100 years of research in the area were mostly focused on the unique mineralogy of the complex. Ilímaussaq is well exposed in an elliptical area measuring approximately 8 x 17 km.

The mineralogy of Ilímaussaq is complex and the alkaline nature of the complex has given rise to more than 220 different minerals. Thirty four of these are described from Ilímaussaq for the first time in the world and 34 are REE-minerals *sensu stricto*. The uniqueness of the complex is further stressed by the fact that 16 minerals are only found here, and one of these is actually a major rock-forming mineral.

The complex mineralogy of Ilímaussaq makes it a challenge for exploration and exploitation. Compared to normal exploration projects it is even more important to have a good understanding and control of the mineralogy of the deposit. This is not just the case for Ilímaussaq but for most other deposits in highly alkaline systems.

2 Exploration History

In the wake of the Second World War the demand on uranium lead to a uranium-focused survey of Greenland. In the mid 1950s, the Kvanefjeld deposit was discovered after a radiometric survey of the area. Material was collected from the area with the highest radioactivity to explore extraction via conventional acid and carbon leach methods. However, the ore was refractory (Sørensen 2001).

Following the discovery a drilling program was started in 1958, which was followed by extraction of 180 t of ore from a 20 m adit in 1962. The ore was used to test sulphatising roasting for extracting uranium and thorium. The ore processing tests were carried out at the Danish National laboratories (RISØ), which opened in 1955 with the aim to explore peaceful applications of radiation. One of the main persons behind RISØ was Professor Niels Bohr.

Drilling campaigns and field mapping continued in the area every summer from 1964 to 1977. In 1978 the 'Kvanefjeld Uranium Project' was initiated to examine the economic potential of a uranium mine at Kvanefjeld. The project involved further drilling and in 1980-81 a 1 km adit was made into Kvanefjeld. Each blast was checked with a scintillometer and high grade ore was shipped to RISØ where a 1:10 scale pilot plant had been constructed. A total of 4700 metric tons of ore was processed and by pressurized carbonate leaching gave recoveries of up to 80% (Sørensen 2001).

The Kvanefjeld project was terminated in 1983 as a political decision was made that Denmark should maintain its status as a nuclear free zone. At the end of the project a total of 69 drill holes had been made with a total core length of more than 10 km and 20000 metric ton of ore had been mined.

In 2007 Kvanefjeld received renewed interest as a multi-element deposit. Greenland Minerals and Energy Ltd. set up renewed drilling program and metallurgical studies. Previous work on Kvanefjeld was focused solely on U and Th but its potential as a REE deposit has now been explored. In addition to U, Th and REE

the deposit contains significant Zn in the form of sphalerite. The new drilling program at Kvanefjeld consists of 146 holes with a total of 35.5 km core. The prefeasibility report gave a resource of 619 Mt containing 350 Mlbs U_3O_8, 6.6 Mt TREO, 1.4 Mt zinc with a 150 ppm U_3O_8 cut-off (http://www.ggg.gl/docs/ASX-announcements/Kvanefjeld-Prefeasibility-Study-4-May-2012.pdf).

3 Geology

3.1 Geological setting

The Ilímaussaq alkaline complex belongs to the Gardar province, which comprises several alkaline intrusions related to continental rifting at 1.16 Ga (Waight et al. 2001). It intruded into a series of lavas and sandstones in the northern part and granite in the southern part.

The complex was formed via four successive magma influxes, creating a layered complex with distinct rock types. The first pulse produced an augite syenite, which now forms a marginal shell. This was followed by intrusion of a sheet of peralkaline granite that is mostly preserved in the roof of the complex. The third batch of magma differentiated to produce pulaskite, foyaite and naujaite that form the roof series. Stage four produced the agpaitic lujavrites and kakortokites. These rock types formed from volatile-rich alkaline magmas that were extremely enriched in incompatible elements, e.g. REE, Li, Be, U and Nb. It is interpreted that the roof series had crystallized prior to the injection of the fourth batch of magma, which was emplaced across the complex and integrated with the overlying roof series via a process of piecemeal stoping. The result is that the lujavrite body is a heterogeneous unit entwined with naujaite, and is generally sandwiched between the naujaite and kakortokite.

3.2 Major rock units

The three main rock types found in Ilímaussaq, in terms volume and from a resource point of view, are:

Lujavrite: Aegirine or arfvedsonite dominated rock, with nepheline and alkali feldspar. If dominated by aegirine it is often called green lujavrite and black lujavrite if arfvedsonite is the dominating mafic mineral. The average grain size is a few mm, but it can increase to a pegmatoidal type often referred to as m-c lujavrite.

Naujaite: The main minerals are sodalite, nepheline, aegirine, alkali feldspar, arfvedsonite and sometimes eudialyte, where the latter three can be found enclosing the sodalites giving a characteristic poikilitic texture. The poikilitic texture results in some grains being up to decimeter in size.

Karkortokite: A layered part of the intrusion consisting of successive black (arfvedsonite), red (eudialyte) and dominated by a white (feldspar) layer. Karkortokite is restricted to the southern part of the complex. Each succession is on average 10 m thick, and may contain all or just some of the layers.

At Kvanefjeld, both naujaite and lujavrite are present,

but the ore rock is the lujavrite. Lujavrite comes in four different subtypes: *Black lujavrite* - a fine grained, arfvedsonite, nepheline, albite, microcline, sodalite syenite; *Green lujavrite* - as above but dominated by aegirine rather than arfvedsonite; *Naujakasite lujavrite* - a naujakasite, arfvedsonite, microcline syenite with only little nepheline; *M-C-lujavrite*, which is coarse grained, approaching pegmatitic, arfvedsonite/aegirine, nepheline feldspar syenite. Sodalite is found in all types of lujavrite.

3.3 Ore mineralogy

The main ore mineral at Kvanefjeld is a complex phoshosilicate named steenstrupine-(Ce) $(Na_{14}Mn^{2+}_2(Fe^{3+},Mn^{3+})_2REE_6(Zr,Th)(Si_6O_{18})_2(PO_4)_6(HPO_4)(OH)_2*2H_2O)$. As seen from the formula, steenstrupine-(Ce) is the host for both REE and uranium/thorium. It forms up to 0.5 mm euhedral or larger poikilitic grains, suggesting that it can both be an early primary phase or slightly later when some of the gangue minerals have already formed. In pegmatites, steenstrupine-(Ce) can form up to 5 cm euhedral crystals (Fig. 1).
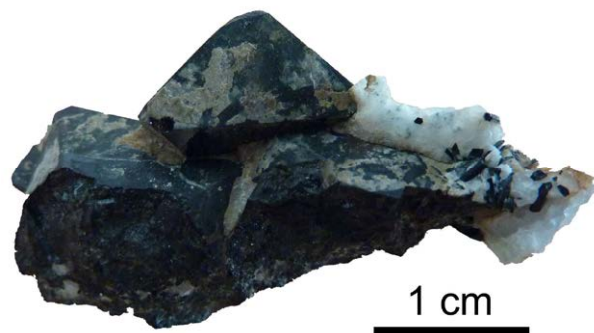
Figure 1. Steenstrupine-(Ce) crystals from a pegmatite

Steenstrupine-(Ce) was the main mineral targeted in the early exploration of Kvanefjeld. However, recoveries of U never got beyond 80%, but new mineralogical studies may explain this as members of the lovozerite group have been found to be present in most lujavrite rocks. Lovozerite *sensu stricto* $(Na_3CaZrSi_6O_{15}(OH)_3)$ has been shown to carry a significant amount of U in the deposit. Furthermore, lovozerites will incorporate REE, and preferentially HREE, therefore making them an important ore mineral. Lovozerite group minerals were not found in the historical work on Kvanefjeld but they may account for several volume percent of the target lujavrites.

Other primary REE minerals of importance include vitusite-(Ce) $(Na_3REE(PO_4)_2)$ and different members of the apatite group, e.g. britholites and belovite-like phases.

The gangue mineralogy is mostly as explained in section 3.2. However, one thing to bear in mind is that although the ore minerals may be exotic so are some of the gangue minerals. The mineral naujakasite $((Na,K)_6(Fe,Mn,Ca)(Al,Fe)_4Si_8O_{26})$ does not have a particularly rare composition, but it only exists in

extreme agpaitic environment and as such it only occurs in Ilímaussaq. Despite it being a one-locality mineral it is rock-forming, *naujakasite lujavrite*, and may constitute up to 75 vol.% of the rock (Sørensen and Larsen 2001).

Villiaumite (NaF) is another gangue mineral that is found especially at depth in the deposit. It is water soluble, which may explain why it is not abundant close to the surface of the deposit. Villiaumite occurs as up to cm large area and its red color, and often efflorescence on cores, makes it a good indicator mineral for highly alkaline rock units during core logging.

3.4 Alteration

As with all ore deposits it is important to understand the alteration and how it influences both grade and mineralogy of the deposit. Because of the high alkalinity of this deposit both gangue and ore minerals are prone to alteration at minor changes in the environment. The replacement of feldspathoids by zeolites has been known from many alkaline complexes and it is a known cause for remobilization of immobile elements (Brögger 1890).

From an exploration point of view it is important to understand the alteration as it may concentrate elements in a certain area, leach elements from a certain area or change the mineralogy to generate refractory phases.

4 Methodology

The company supplied approximately 10 cm sections of metallurgical core, where the opposite half had been assayed with the normal procedure applied for the ores. Thin sections were made in order to make a direct comparison between mineralogy and assay data.

Initially, the cores were described before the thin sections were checked under a petrographic microscope and then qualitative EDS analyses were applied for mineral identification. This information was compiled to create an understanding of the different types of parageneses in the deposit. EPMA analyses were carried out on selected minerals to better understand their chemistry and finally LA-ICPMS was conducted on individual minerals within a selection of samples.

Finally, the mineralogy and chemistry was compared to the whole rock assay data to show what minerals controlled the assays.

5 Results

Initially, a simple database was compiled with the main minerals present in each sample. Using the ioGAS software the different minerals were compared with the assays. However, this technique did not show what minerals controlled the chemistry of the assays. This is exemplified with steenstrupine-(Ce) in Figure 2. However, the initial work did reveal some correlations, e.g. all samples containing villiaumite also contained steenstrupine and lovozerite group minerals.

It became apparent that no single chemical parameter

could be used to tie mineralogy and whole rock data together. Consequently, different parameters were
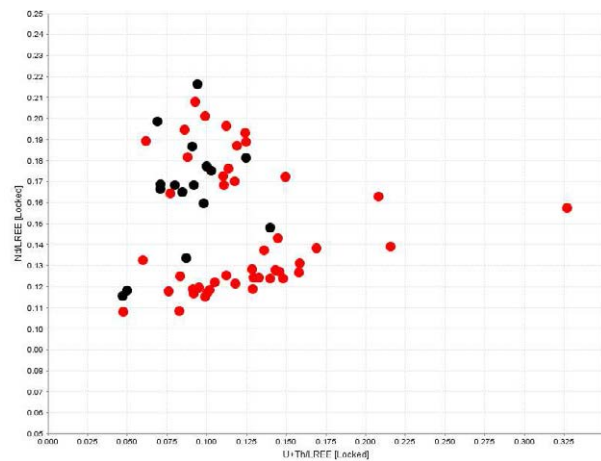
Figure 2. Plot of Nd/LREE *vs.* (U+Th)/LREE used by GME to define ore groups. The red and black represent steenstrupine-(Ce) bearing and steenstrupine-(Ce) free ore samples, respectively

investigated to explore, which would be able to separate what minerals and not others. A total of three subsequently plots enabled the separation of 98% of the steenstrupine-(Ce) bearing ore samples. After each chemical selection the samples were removed from the dataset and the next step is only applied to the remaining samples.

The selection method developed resulted in some samples not containing steenstrupine also being selected. However, these are also REE-ore and account for just 6% of the selected samples.

The alteration of the rocks does not result in a lowering of grade; hence all valuable elements are maintained but the mineralogy changes. However, metallurgical tests have shown that the extraction method works for both primary and secondary REE-minerals.

6 Conclusions

The combination of mineral chemistry and assay data made it possible to explore which minerals controlled the assays. Furthermore, the project showed which phases were formed during alteration and whether or not they were refractory.

The detailed mineralogical study enabled us to build the framework of a geometallurgical model for the deposit. In addition, a method was developed to predict the presence of some of the primary ore minerals directly from assays.

References

Brögger WC (1890) Die Mineralien der Syenitpegmatitgänge der südnorwegischen Augit- und Nephelinsyenite. Z Krystallogr Minera 16:1-663 (in German)

Sørensen H (2001) Brief introduction to the geology of the Ilímaussaq alkaline complex, South Greenland, and its exploration history. Geology of Greenland Survey Bulletin 190:7-23

Sørensen H, Larsen LM (2001) The hyper-agpaitic stage in the evolution of the Ilímaussaq alkaline complex, South Greenland. Geology of Greenland Survey Bulletin 190:83-94

Ussing NV (1912) Geology of the country around Julianehaab, Greenland. Medd Grøn 38:1-376

Waight T, Baker J, Willigers B (2002) Rb isotope dilution analyses by MC-ICPMS using Zr to correct for mass fractionation: towards improved Rb–Sr geochronology? Chem Geol 186:99-116

A new type of magmatic Sc-Zr occurrence located in the Kiviniemi area, Rautalampi, Central Finland

Tapio Halkoaho
Geological Survey of Finland. P.O. Box 1237, FI-70211 Kuopio, Finland

Marjaana Ahven & O. Tapani Rämö
Department of Geosciences and Geography, Division of Geology. P.O. Box 64, FI-00014 University of Helsinki, Finland

Abstract. The Kiviniemi intrusion with a new type of Sc-Zr occurrence is located in Rautalampi, in the northeastern margin of the Paleoproterozoic Central Finland Granitoid Complex. The intrusion consists of a heterogeneous ferrogabbro, leucogabbro, diorite and a garnet-bearing fayalite ferrogabbro with abnormally high Sc and Zr contents, and it is surrounded by a porphyritic granite. The main rock-forming minerals of the Sc and Zr-rich fayalite ferrogabbro are fayalite, almandine, ferrohedenbergite, ferrohastingsite and plagioclase. The accessory minerals include potassium feldspar, quartz, ilmenite, fluorapatite, zircon, pyroxferroite, ferrostilpnomelane and pyrite. The crystallization ages of the Kiviniemi ferrogabbro and granite are both about 1.86 Ga and this magmatic activity thus belongs to the post-kinematic stage of the Svecofennian orogeny. Because of the differences of the initial ε_{Nd}, the source areas of the fayalite ferrogabbro (+0.1) and the surrounding porphyritic granite (-2.4) were different. These rocks are cogenetic but they were not comagmatic.

Keywords: scandium, zirconium, fayalite, ferrogabbro, Fennoscandian shield, Paleoproterozoic, Finland

1 Introduction, location and geology

A new type of Sc-Zr occurrence has been recently found at Kiviniemi, some 22 km north of the town of Rautalampi, in central Finland (Fig. 1). The initial reason for investigating the Kiviniemi area was to assess the Ni-Cu potential of a gabbroic intrusion. However, instead of the anticipated Ni-Cu mineralization, the study resulted in a discovery of an interesting Sc-Zr occurrence (Halkoaho et al. 2013).

During the years 2008-2010, nine (9) diamond drill holes were drilled in the Kiviniemi area, totalling 1251.80 m. The main rock type in the Kiviniemi prospect area is a reddish granite with tabular megacrysts of potassium feldspar (Fig. 2A). The granite encloses a body of dark, fine- to medium-grained gabbroic rock (Fig. 2B). The northern-most corner of this gabbroic body consists mainly of coarse-grained to pegmatitic garnet-bearing fayalite ferrogabbro (Fig. 2C). The outcrop area of the pegmatitic occurrence is about 2.5 hectares, and there is also a small (about 100 long and 20 m wide) satellite occurrence of similar rock type some 50 m to the NE of the main body. In addition to gabbro these two bodies also include leucocratic ferrogabbro and diorite. The U-Pb TIMS zircon age of the pegmatitic garnet-bearing fayalite ferrogabbro is 1857±2 Ma (Halkoaho et al. 2013) and that of the porphyritic granite 1859±9 Ma (LA-MC-ICPMS). The

initial $\varepsilon_{Nd(1857)}$ of the garnet-bearing fayalite ferrogabbro is +0.1 and $\varepsilon_{Nd(1859)}$ of the porphyritic granite is -2.4 (Ahven 2012).

Figure 1. Geological map of the Vihtalahti area, Rautalampi, showing the location of the Kiviniemi Sc-Zr occurrence. Modified after Pääjärvi (1991, 2000).

2 Mineralogy and mineral chemistry

The main silicate minerals in the pegmatitic garnet-bearing fayalite ferrogabbro are plagioclase ($An_{26.7-45.9}$), ferrohedenbergite (Fig. 3), ferrohastingsite, fayalite ($Fo_{0.9-3.9}$) and almandine garnet. Potassium feldspar, quartz, ilmenite, fluorapatite, zircon, pyroxferroite, ferrostilpnomelane, and pyrite occur as accessory minerals (Ahven 2012, Halkoaho et al. 2013).
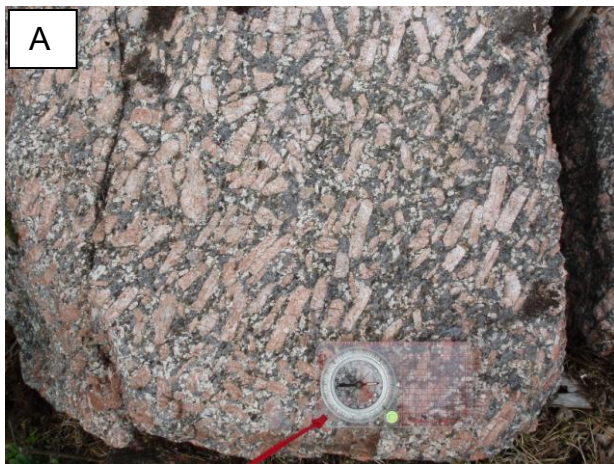
Figure 2. Photographs of the main rock types of the Kiviniemi area. A) the porphyritic granite, B) the fine- to medium-grained ferrogabbro and C) the garnet-bearing fayalite ferrogabbro. Photos Tapio Halkoaho.

All of the above mentioned rock types, apart from porphyritic granite, are characterized by outstandingly high zirconium contents (mostly > 1000 ppm Zr). Analyzed porphyritic granite samples (n=3) contain 355 ppm zirconium. It is noteworthy that only zircon grains in the pegmatitic garnet-bearing fayalite ferrogabbro show golden fluorescence under ultraviolet light (Fig. 4) (Ahven 2012, Halkoaho et al. 2013).
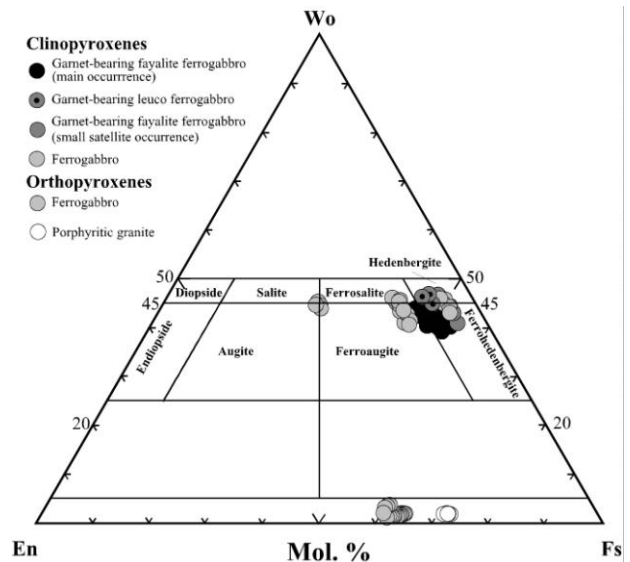
Figure 3. Clinopyroxenes and orthopyroxenes from the Kiviniemi area plotted on a pyroxene quadrilateral. Nomenclature of clinopyroxenes after Poldervaart and Hess (1951).

The main carriers of scandium are ferrohedenbergite and ferrohastingsite with average scandium contents of 863 ppm (n=27, max. 1361 ppm) and 751 ppm (n=34, max. 1174 ppm), respectively. In the small satellite occurrence average scandium content of ferrohedenbergite is 530 ppm (n=8) and ferrohastingsite 522 ppm (n=10). In addition, in the main occurrence zircon contains in average 187 ppm scandium as well as 357 ppm yttrium and 0.92 % hafnium (n=12). Apatite contains, in average, 717 ppm scandium (n=4) and 540 ppm yttrium (n=3) (Ahven 2012, Halkoaho et al. 2013).
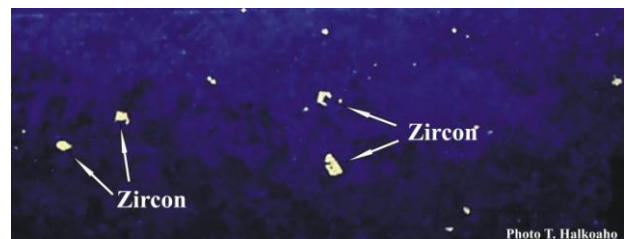
Figure 4. Photographs of drill core sample in ultraviolet light from the garnet-bearing fayalite ferrogabbro typical of the Kiviniemi Sc-Zr occurrence. In the image the white spots mark zircon grains. The width of the drill core is 4 cm. Photo T. Halkoaho.

3 Whole rock chemistry

The highest analyzed contents of scandium (drill core sample length 1.1 m), zirconium (sample length 0.85 m) and yttrium (sample length 1.3 m) are 293 ppm, 6760 ppm and 255 ppm, respectively; these values were determined by ICP-OES from solutions after sodium peroxide fusion of 0.2 g samples in a Ni crucible (Labtium Oy, analytical method 724P) (Halkoaho et al. 2013).

The main feature of the garnet-bearing fayalite ferrogabbro is its extremely iron-rich composition and very low MgO, Ni and Cr contents. The FeO content (not recalculated volatile-free) varies between 17.5–29.9 wt. % (pyroxenitic sample 37.7 wt. %), MgO between 0.57–1.39 wt. % (pyroxenitic sample 1.8 wt. %), Ni < 20–40 ppm and Cr < 20 ppm. Locally, the concentrations of titanium and phosphorus can be high (max. TiO_2 3.06 % and P_2O_3 1.53 %).

Even though the garnet-bearing fayalite ferrogabbro has high Sc, Zr, Y and Hf contents, the REEs are not abnormally high in abundance (Fig. 5). The overall normalized REE pattern of the porphyritic granite is similar to that of the garnet-bearing fayalite ferrogabbro (Fig. 5), but is less enriched in the HREEs (Ahven 2012).

4 Discussion and Conclusions

The garnet-bearing fayalite ferrogabbro and associated fine- to medium-grained ferrogabbro and porphyritic granite belong to the post-kinematic magmatic phase of Svekofennian orogeny. The initial ε_{Nd} of fayalite ferrogabbro (+0.1) and the surrounding porphyritic granite (-2.4) differ from each other, which means that they bear Nd from different sources. The available U-Pb zircon data set the age of the Kiviniemi fayalite ferrogabbro and granite at ~1857 Ma. These rocks are thus cogenetic but not comagmatic (cf. Nironen et al. 2000).

The abundance of the water-bearing minerals, high Zr, Y, Hf, alkali metals and Sc contents in the fayalite ferrogabbro are probably the result of hydrothermal alteration or contamination. On the basis of the mineralogy and petrography the garnet seems to be magmatic. The source of scandium is still unknown and the genesis of the garnet-bearing fayalite ferrogabbro at Rautalampi remains open for discussion.

References

Ahven M (2012) Rautalammin Kiviniemen granaattipitoinen fayaliittiferrogabro (Petrology and geochronology of the Kiviniemi garnet-bearing fayalite ferrogabbro, Rautalampi). Masters thesis. Manuscript at the Department of Geosciences and Geography, University of Helsinki, pp 62 (in Finnish)

Boynton WV (1984) Cosmochemistry of the rare earth elements: meteorite studies. In: Henderson P (ed) Rare earth element geochemistry. Elsevier, Amsterdam, pp 63–114

Halkoaho T, Johanson B, Niskanen M (2013) A new type of Sc-Zr occurrence located in the Kiviniemi Area, Rautalampi, central Finland. In: Höltta P (ed) Current Research – GTK Mineral Potential Workshop, Rauhalahti/Kuopio, May 2012. Geol Surv Finland, Report of Investigation 198: 33-35

Nironen M, Elliott BA, Rämö OT (2000) 1.88–1.87 Ga post-kinematic intrusions of the Central Finland Granitoid Complex: a shift from C-type to A-type magmatism during lithospheric convergence. Lithos 53: 37–58

Poldervaart A, Hess HH (1951) Pyroxenes in the crystallization of basaltic magmas. J Geol 59: 472–489

Pääjärvi A (1991) Karttula. Geological map of Finland 1:100 000, pre-Quaternary Rocks, Sheet 3224. Geol Surv Finland.

Pääjärvi A (2000) Rautalammin ja Karttulan kartta-alueiden kallioperä. Summary: Pre-Quaternary rocks of the Rautalampi and Karttula map-sheet area. Geological Map of Finland 1:100 000, Explanation to the Maps of Pre-Quaternary Rocks, Sheets 3223 and 3224. Geol Surv Finland, pp 81 (in Finnish)

Figure 5. Average chondrite-normalized REE patterns of the porphyritic granite (n=3) and the garnet-bearing fayalite ferrogabbro (n=16) of the Kiviniemi area. Chondrite values are from Boynton (1984).

Trace element evolution, REE patterns and crystal/melt modelling of the Nb-Ta-Sn mineralised Gatumba pegmatite field (Rwanda)

Niels Hulsbosch, Jan Hertogen, Philippe Muchez
Geodynamics and Geofluids Research Group, KU Leuven, Celestijnenlaan 200E, B-3001 Leuven, Belgium.

Luc André, Stijn Dewaele
Department of Earth Sciences, Royal Museum for Central Africa, Leuvensesteenweg 13, B-3080 Tervuren, Belgium

Abstract. Alkali metals and rare earth elements (REE) have been analysed in feldspar, biotite and muscovite mineral separates taken throughout the regional pegmatite zonation sequence in Gatumba (Rwanda). The observed alkali metal fractionation trends and REE pattern evolution have been successfully modelled by a single continuous fractionation trend starting from a parental G4 granite initial composition. The zonation sequence from common to rare-element pegmatite zones developed by extreme fractional crystallisation. Namely, biotite pegmatites crystallise during fractionation from $F = 0$ to 0.70, two-mica pegmatites from $F = 0.70$ to 0.90 and muscovite pegmatites are high fractionation products with $F = 0.9$. The extreme Rb- and Cs-enrichment in the rare-element pegmatites originates from fractionation of at least $F = 0.98$. The importance of accessory monazite as REE-fractionating mineral has been demonstrated. This mineral phase is decisive for the development of LREE-depleted REE patterns for the minerals from the two-mica and late-stage pegmatites.

Keywords. LCT pegmatites, regional zonation, alkali metals, REE, fractional crystallisation

1   Introduction

The Gatumba pegmatite field (969 ± 8 Ma, Rb–Sr on muscovite and whole-rock; Brinckmann and Lehmann 1983) is situated in the Rwandan part of the Mesoproterozoic Karagwe-Ankole belt (KAB). The KAB hosts a large metallogenic province which is characterised by the presence of either numerous Nb-Ta-Sn mineralised pegmatites or hydrothermal Sn–W mineralised quartz veins (Pohl 1994; Dewaele et al. 2010). Both types of mineralisation are related to barren S-type granites that formed at 986 ± 10 Ma, i.e. the G4 granites in Rwanda (U–Pb on zircon; Tack et al. 2010).

The Gatumba field ($\pm$ 150 km^2) is a representative district for the study of the pegmatite mineralisation in the KAB (Dewaele et al. 2007). The area is located between two granitic batholiths: the Gitarama pluton to the east and the Kabaya pluton to the west. The granites have been emplaced in a regional series of Mesoproterozoic shallow-water metasediments and dolerites/amphibolites (Gérards 1965). More than 130 individual pegmatite bodies of the lithium-caesium-tantalum (LCT) family have been indentified; some of them are partially affected by metasomatic albitisation and greisenisation (Dewaele et al. 2011).

2   Regional zonation

The regional zonation sequence of the Gatumba

pegmatite field has been recently redefined on the basis of chemical differentiation trends (Hulsbosch et al. 2013). The zonation comprises four distinct zones which seem to develop along the northwestern margins of the Gitarama pluton. Common pegmatites rich in schorl occur proximal in the zonation sequence (Varlamoff 1954). Outwardly they grade into (1) biotite, (2) two-mica and (3) muscovite pegmatites. Most distal in the zonation partially metasomatised, (4) rare-element, Nb-Ta-Sn mineralised pegmatites are developed.

The mineralogy of the biotite and two-mica pegmatites mainly consists of quartz, microcline, minor plagioclase, biotite and schorl. The two-mica pegmatites are furthermore characterised by centimetre-sized sheets of greyish muscovite. Monazite appears as an accessory mineral enclosed in microcline, orthoclase and muscovite starting from the two-mica pegmatite zone. Muscovite pegmatites show the typical mineralogy of the previous zones, but they contain additional grey-coloured muscovite, pink K-feldspar and minor beryl. Monazite is also observed in this zone as inclusions in microcline or in rare apatite. Primary assemblages in the rare-element pegmatites are made up of pink K-feldspar, microcline, albite-oligoclase (An_{7-17}), quartz, Li-rich muscovite, beryl, minor apatite, spodumene, elbaite, columbite-tantalite, rare phosphates, minor cassiterite and secondary lepidolite (Varlamoff 1961, 1963; Hulsbosch et al. 2013). Secondary albite occurs as grains with saccharoidal and cleavelandite morphologies ($An_{0.2-6.4}$). Its composition differs markedly from that of the primary magmatic plagioclase (Hulsbosch et al. 2013).

3   REE systematics

In order to constrain the G4 granite origin and the evolution of the Gatumba pegmatite system, mineral separates of K-feldspar, plagioclase, biotite and muscovite have been analysed by ICP-OES and ICP-QMS for alkali metals (K, Rb and Cs) and rare earth elements (REE). The samples represent the whole range of the regional pegmatite zonation.

K-feldspar and primary plagioclase from biotite pegmatites have fractionated, chondrite normalised REE patterns, with selective HREE-depletion ($La_N/Yb_N = 140\text{-}200$ for K-feldspar and $La_N/Yb_N = \pm 215$ for primary plagioclase) (Fig. 1A&C). The REE patterns shift to less fractionated, more horizontal shapes ($La_N/Yb_N = 6\text{-}130$ for K-feldspar and $La_N/Yb_N = \pm 1$ of primary plagioclase) starting from the two-mica pegmatites. This transition to the two-mica pegmatites is marked by the

occurrence of fractionated (La_N/Yb_N = 130), as well as horizontal patterns for K-feldspar (La_N/Yb_N = 6). K-feldspar and primary plagioclase of muscovite and rare-element pegmatites contain flat, less-fractionated patterns (La_N/Yb_N = ± 1.35) (Fig. 1B&C). Secondary albite generally shows low La_N/Yb_N ratios. The evolution from HREE-depleted, fractionated patterns to more flat, less fractionated patterns with the two-mica pegmatites as the transition point is also expressed by a general decline in $\sum REE_N$ from 15 in biotite pegmatites to 8 and 2.5 in two-mica and rare-element pegmatites respectively. $\sum REE_N$ in plagioclase decline from 2 in primary plagioclase in two-mica pegmatites to 0.4 in secondary albite from rare-element pegmatites. K-feldspar in biotite pegmatites has a strong positive Eu/Eu*-anomaly (Eu/Eu* = 2.5-21). Plagioclase has analogous positive anomalies with a ratio between 3.5 and 6.2. K-feldspar and plagioclase of more evolved pegmatites (two-mica, muscovite and rare-element pegmatites) show weakly developed negative/positive to absent Eu-anomalies (Eu/Eu* = 0.7-1.5 for K-feldspar and 0.7-1 for plagioclase).
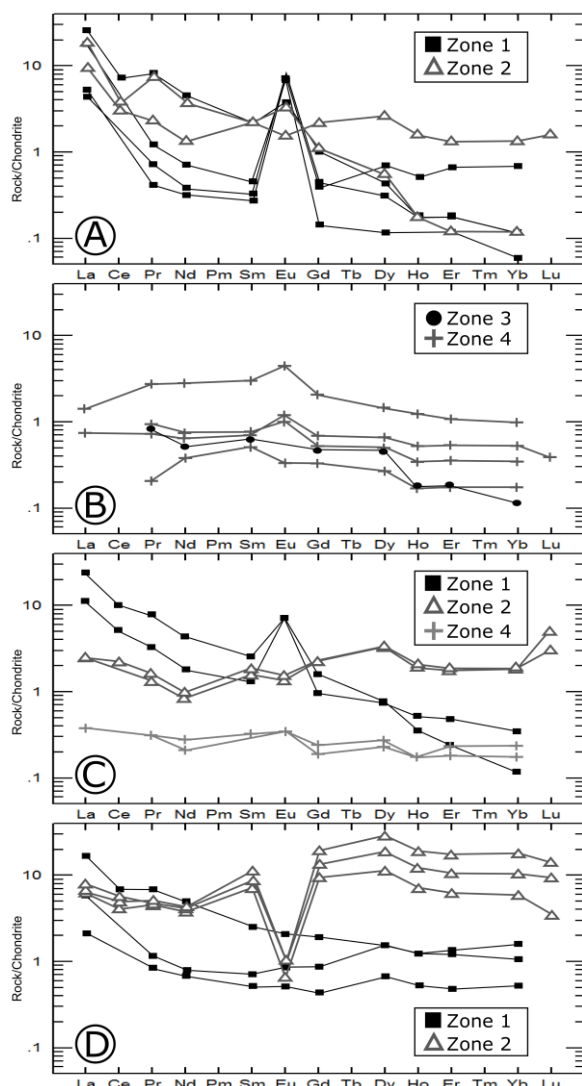
Figure 1. Measured chondrite normalised REE patterns of (**A**) K-feldspar in biotite (zone 1) and two-mica (zone 2) pegmatites, (**B**) K-feldspar in muscovite (zone 3) and rare-element (zone 4) pegmatites, (**C**) plagioclase and (**D**) biotite sampled along the zonation. (Normalisation values from Sun and McDonough 1989)

Biotite, which is only present in biotite and two-mica pegmatites, shows a more distinct REE pattern evolution along the zonation sequence (Fig. 1D). Biotite from biotite pegmatites is characterised by fractionated, HREE-depleted patterns (La_N/Yb_N = 4-15 and $\sum REE_N$ = 4-15) and no Eu-anomaly (Eu/Eu* = 0.92-0.99). Biotite from two-mica pegmatites has a more flattened pattern. As for the feldspars, biotite from two-mica pegmatites shows the transition from fractionated, HREE-depleted to horizontal patterns (La_N/Yb_N = 0.34-0.98 and $\sum REE_N$ 14-27). Moreover, LREE-segments are lower than the HREE-segments due to La_N/Yb_N ratios below unity. The LREE (La-Nd) and even MREE-segments (to Gd) of biotite from two-mica pegmatites demonstrate depletion compared to the same segments from biotite pegmatites, which cause weakly developed convex-up patterns. The Eu-anomaly in biotite evolves from absent in biotite pegmatites (Eu/Eu* = ± 0.95) to distinctly negative (Eu/Eu* = 0.07) in two-mica pegmatites.

Muscovite becomes stable from the two-mica pegmatites onwards. The La-, Ce- and Eu-content of muscovite is often below the limit of quantification (respectively 0.3, 1.4 and 0.02 ppm). Muscovite from the two-mica pegmatites shows similar patterns as for biotite: convex-upwards REE patterns with a maximum at Dy. Muscovite from muscovite pegmatites and rare-element pegmatites show depleted, flat patterns.

In general, minerals from biotite pegmatites commonly display moderately to highly HREE-depleted patterns. The overall incompatibility of the sampled minerals and early crystallising mineral phases (quartz) for the trivalent REE causes the initial, bulk pegmatitic melt to become enriched in REE which in turns causes the parallelism in the REE patterns of the biotite pegmatite zone. From the two-mica pegmatites onwards, the mineral patterns flatten or become somewhat MREE-enriched (convex-up) due to the preferential depletion of the LREE-segments. Monazite is petrographically observed starting from the two-mica pegmatite zone. The precipitation of this accessory mineral is interpreted to be responsible for the progressive LREE-depletion of the differentiating melts due to extremely high REE crystal/melt partition coefficients and its LREE-preference (Yurimoto et al. 1990). For example, progressively enrichment and pattern parallelism is observed in biotite from biotite pegmatites. LREE-depletion is evident starting from the two-mica pegmatites. Progressive enrichment and pattern parallelism is still observed in the continuing zone but only for the HREE-segments. Eu-anomalies develop along the zonation from positive in Eu^{2+}-compatible phases (plagioclase and K-feldspar) and absent in Eu^{2+}-incompatible phases (biotite and muscovite) in the biotite pegmatites, to absent in the Eu^{2+}-compatible phases and negative in Eu^{2+}-incompatible phases of two-mica, muscovite and rare-element pegmatites.

4   Fractionation model

4.1   Specifications

The geochemical fractionation model has three objectives: (1) confirm the G4 granite generation as the

parental magma for the Gatumba pegmatite field; (2) quantitatively evaluate Rayleigh fractional crystallisation as the differentiation process giving rise to the pegmatite zonation sequence; (3) model the observed evolution from fractionated to flat REE patterns, starting from the two-mica pegmatites, related to the fractional crystallisation of monazite. The model is implemented in a spreadsheet, and based on the Nernst crystal/melt partition coefficient (K_D) and bulk distribution coefficient (D). Both coefficients are used as input in the equation of Rayleigh for fractional crystallisation together with the concentration of the trace element in the parental melt before any crystallisation has occurred (C_p). The degree of fractionation (F), expressed as the fraction of crystallised phases, is modelled as a variable. The intended trace element concentration in the mineral of interest is recalculated from the concentration in the fractionated melt by use of the partition coefficient.
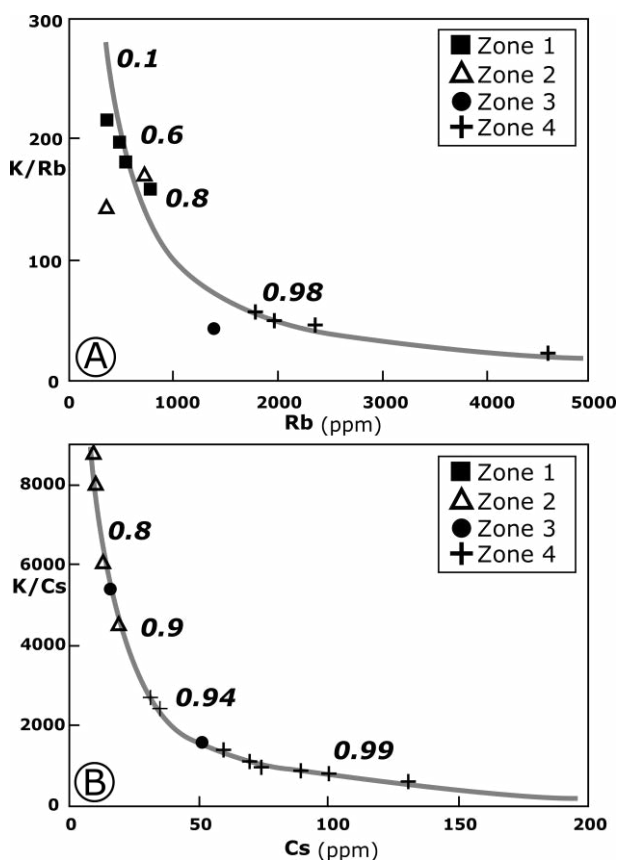
Figure 2. Measured data and modelled fractionation trend (in grey) with indication of degree of fractionation of (**A**) Rb in K-feldspar and (**B**) Cs in muscovite along the zonation (Zone 1 = squares, zone 2 = triangles, zone 3 = circles and zone 4 = crosses).

The model structure is twofold. Firstly, the alkali metal variations (Rb-Cs) in K-feldspar and muscovite along the zonation sequence (Fig. 2) are used to constrain the total degree of fractionation of the entire pegmatite system, as well as the degree of fractionation between the different pegmatite zones. A forward modelling approach is in this case preferred because of the mineralogical evolution in the zonation sequence (variations in D per pegmatite zone). The mass fractions of the mineral phases per pegmatite zone, C_p of K-Rb-Cs in the parental G4 granite generation (unpublished data

Royal Museum for Central Africa, RMCA) and the K-Rb-Cs partition coefficients (Philpotts and Schnetzler 1970; Mahood and Hildreth 1983; Nash and Crecraft 1985; Yurimoto et al. 1990; Bea et al. 1994; Adam and Green 2006; London 2008) are used as input.

Secondly, the modelled degrees of fractionation derived from the forward approach and the bulk pegmatite zone compositions are used as constraints in a second, reverse approach. Petrographic observation indicated monazite stability starting from the two-mica pegmatite zone and subsequent forward modelling previously constrained the specific degree of fractionation corresponding to this pegmatite zone. This reverse approach requires as input the C_p of the REE in the parental G4 granite generation (unpublished data RMCA) and REE partition coefficients (Schnetzler and Philpotts 1970; Nash and Crecraft 1985; Bacon and Druitt 1988; Yurimoto et al. 1990; Bea et al 1994; Adam and Green 2006). Moreover, since feldspars prefer Eu^{2+} and the Eu^{2+}/Eu^{3+} ratio is dependent on oxygen fugacity (Drake 1975); the behaviour of Eu is ignored in the further modelling and discussion of the REE patterns.
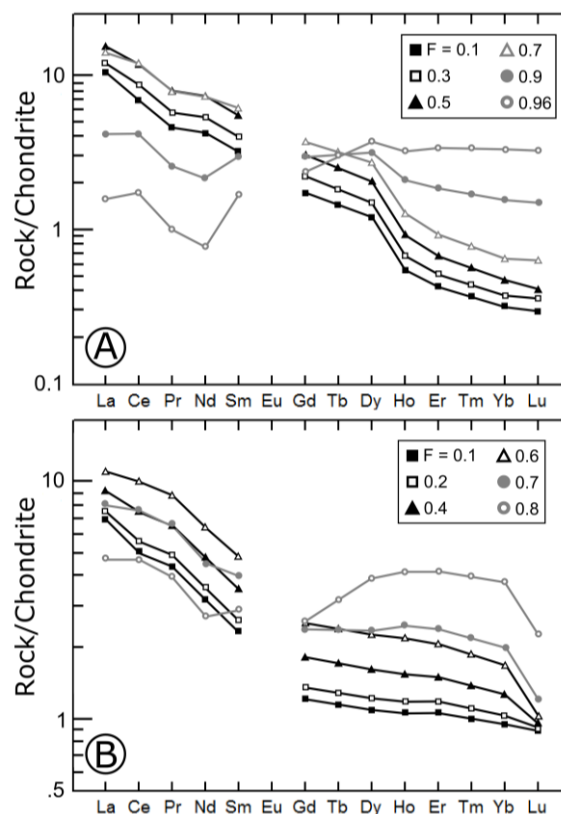
Figure 3. Modelled REE patterns of (**A**) plagioclase and (**B**) biotite with monazite stability starting from F = 0.7.

4.2 Results

Modelled degrees of fractionation for the system are 0.70 for the transition from the biotite to two-mica, 0.90 for two-mica to muscovite and 0.98 for muscovite to rare-element pegmatite zones (Fig. 2). REE pattern changes are modelled with monazite saturation starting from F = 0.70 (plagioclase and biotite examples in Fig. 3). LREE-segments show first signs of depletion, however HREE-segments continue to rise until F = 0.98 at which the rare element pegmatites start to crystallise.

5 Discussion and conclusion

Accurate assessments of the REE pattern changes can be obtained up to F = 0.98. Restrictions occur at higher degrees of fractionation due to the complex mineralogy of the rare-element pegmatite zone. Chemical complexity at F ≥ 0.98 is caused by the precipitation of REE–compatible phases such as apatite, elbaite, columbite-tantalite and rare phosphates (e.g. amblygonite, lithiophilite, gatumbaite etc.), which resulted from the progressive fractionation and subsequent REE-depletion of the differentiating melt. Uncertainties occur as such between the measured and modelled REE patterns for the last 1-1.5% of fractionation, as can observed in the discontinue REE patterns of muscovite, K-feldspar and secondary albite of rare-element pegmatites.

Nevertheless, alkali metal and REE fractionation modelling demonstrate that the origin of the regional pegmatite zonation in Gatumba can be explained by a single path of extreme fractional crystallisation, starting from a G4 granite melt composition. The regional zonation sequence reflects the increasingly more fractionated melt composition, caused by the systematic enrichment of incompatible trace elements (e.g. Rb, Cs and REE). Modelled REE patterns of biotite, muscovite and feldspar show the transition of a fractionated, HREE-depleted pattern in biotite pegmatites to a more flat or slightly convex-up pattern starting from the two-mica pegmatites. These first order pattern changes can be explained by processes of fractional crystallisation and progressive REE-depletion of the differentiating melt by precipitation of monazite.

A pegmatite model for the Gatumba field is proposed as a final point by combining the field observations of the granite-pegmatite system (Dewaele et al. 2011; Hulsbosch et al. 2013) with the demonstrated extreme fractional crystallisation trends and genetic relationship between the G4 granite generation and the different pegmatites zones. The Gatumba rare-element pegmatites represent the last small portion of melt remaining after fractionation of geochemically specialised G4-granites.

Acknowledgements

References

Adam J, Green T (2006) Trace element partitioning between mica- and amphibole-bearing garnet lherzolite and hydrous basanitic melt: 1 Experimental results and the investigation of controls on partitioning behavior. Contrib Mineral Petr 152: 1-17

Bacon CR, Druitt TH (1988) Compositional Evolution of the Zoned Calcalkaline Magma Chamber of Mount-Mazama Crater Lake Oregon. Contrib Mineral Petr 9: 224-256

Bea F, Pereira MD, Stroh A (1994) Mineral/leucosome trace-element partitioning in a peraluminous migmatite (a laser ablation-ICP-MS study). Chem Geol 117: 291-312

Brinckmann J, Lehmann B (1983) Exploration de la bastnaésite monacite dans la région de Gakara, Burundi. Rapport sur la phase 1. Unpublished Report,Bujumbura/Hannover.

Dewaele S, Tack L, Fernandez M, Boyce A, Muchez Ph (2007) Cassiterite and columbite-tantalite mineralisation in pegmatites of the northern part of the Kibara orogen (Central Africa): the Rutongo area (Rwanda). Proceedings of the 9th Biennal SGA Meeting Mineral Exploration and Research: Digging Deeper: 1489-1492

Dewaele S, De Clercq F, Muchez P, Schneider J, Burgess R, Boyce A, Fernandez Alonso M (2010) Geology of the cassiterite mineralisation in the Rutongo Area,Rwanda (Central Africa): current state of knowledge. Geol Belg 13: 91–112

Dewaele S, Henjes-Kunst S, Mecher F, Sitnikova M, Burgess R, Gerdes A, Fernandez Alonso M, De Clercq F, Muchez Ph, Lehmann B (2011) Late Neoproterozoic overprinting of the cassiterite and columbite-tantalite bearing pegmatites of the Gatumba area Rwanda (Central Africa). J Afr Earth Sciences 61: 10-26

Drake MJ (1975) The oxidation state of europium as an indicator of oxygen fugacity. Geochim Cosmochim Ac 39: 55-64

Gérards J (1965) Géologie de la région de Gatumba. Bull. Serv. Géol Rwandaise 2: 31–42

Hulsbosch N, Hertogen J, Dewaele S, André L, Muchez Ph (2013) Petrographic and mineralogical characterisation of fractionated pegmatites culminating in the Nb-Ta-Sn pegmatites of the Gatumba area (western Rwanda). Geol Belg 16: 105-117

London D (2008) Pegmatites. The Canadian Mineralogist, Special Publication 10, Mineralogical Association of Canada

Mahood GA, Hildreth EW (1983) Large partition coefficients for trace elements in high-silica rhyolites. Geochim Cosmochim Ac 47: 11-30

Nash WP, Crecraft HR (1985) Partition coefficients for trace elements in silicic magmas. Geochim Cosmochim Ac 49: 2309-2322

Philpotts JA, Schnetzler CC (1970) Phenocryst-matrix partition coefficients for K, Rb, Sr, and Ba with applications to anorthosite and basalt genesis. Geochim Cosmochim Ac 3: 307-322

Pohl W (1994) Metallogeny of the northeastern Kibara belt Central Africa – recent perspectives. Ore Geol Rev 9: 105–130

Schnetzler CC, Philpotts JA (1970) Partition coefficients of rare-earth elements between igneous matrix material and rock-forming mineral phenocrysts; II. Geochim Cosmochim Ac 34: 331-340

Sun SS, McDonough WF (1989) Chemical and isotopic systematics of oceanic basalts: implications for mantle composition and processes In: Saunders AD, Norry MJ (eds) Magmatism in the Ocean Basins. Geological Society London Special Publications 42: 313-345

Tack L, Wingate MTD, De Waele B, Meert J, Belousova E, Griffin B, Tahon A, Fernandez-Alonso M (2010) The 1375 Ma 'Kibaran event' in Central Africa: Prominent emplacement of bimodal magmatism under extensional regime. Precambrian Res 180: 63-84

Varlamoff N (1954) Répartition des types de pegmatites autour de la partie nordouest du grand massif granitique de Nyanza. Ann. Soc. geol. Belgique 78: 1-21

Varlamoff N (1961) Pegmatites à amblygonite et à spodumène et pegmatites fortement albitisées à spodumène et à cassitérite de la région de Katumba (Ruanda). Annales de la Société Géologique de Belgique 84: 257-278

Varlamoff N (1963) Les phénomènes de greisenification d'albitisation et de lépidolitisation et leurs relations spatiales avec les granites et les pegmatites granitiques d'Afrique. Ann. Soc. geol. Belgique 86: 285-322

Yurimoto H, Duke EF, Papike JJ, Shearer CK (1990) Are discontinuous chondrite-normalized REE patterns in pegmatitic granite systems the result of monazite fractionation? Geochim Cosmochim Ac 54: 2141-2145

New evidence for the timing of formation of Bastnäs-type REE mineralisation in Bergslagen, Sweden

Erik Jonsson
Geological Survey of Sweden, Box 670, SE-75128 Uppsala, Sweden;
Department of Earth Sciences, CEMPEG, Uppsala University, Villavägen 16, SE-75236 Uppsala, Sweden

Karin Högdahl
Department of Earth Sciences, CEMPEG, Uppsala University, Villavägen 16, SE-75236 Uppsala, Sweden

Abstract. The REE-Cu-Fe-(Au) deposits of Bastnäs-type in the Bergslagen ore province in central Sweden have a long history of mining as well as scientific study and discovery. Yet, relatively little information on their timing of formation has been available, and their overall genesis remains unclear. Here we present data and observations on an uncommon style of Bastnäs-type REE silicate mineralisation, from the Högfors deposit. It represents the only direct observation of this type of mineralisation that is apparently stratabound, inter-layered in a banded iron formation (BIF). The deposit is located in the northern part of the Riddarhyttan district. Here, cerite and västmanlandite-dominated, banded REE silicate mineralisation occurs within a hematite-dominated, quartz-banded iron formation together with modest amounts of associated, amphibole-dominated Fe-Mg-Ca skarn assemblages. The REE minerals, as well as the associated iron oxides, are extensively recrystallised to a granoblastic texture. Furthermore, these banded assemblages are extensively folded, and we conclude that REE mineralisation formed prior to the polyphase deformation and regional metamorphism associated with the c. 1.90-1.80 Ga Svecokarelian orogeny. These observations contradict post-orogenic processes as responsible for the Bastnäs-type REE deposits, and support a model involving syn-volcanic (Svecofennian), magmatic activity.

Keywords. Bastnäs-type deposit, BIF, Högfors, REE line, Bergslagen, Sweden

1 Introduction and background

The recent World-wide scramble for rare earth elements (REE), primarily a result of China´s dominance in mine production during the past decades, combined with their new limitations on export quotas, has led to renewed interest in REE deposits old and new.

The first mining activity focused on REE in the Fennoscandian shield took place during the late 1800s in the Bastnäs mines in the central part of the Bergslagen ore province, significantly also the place of the original discovery of the element cerium (Hisinger and Berzelius 1804). Overall, the Bastnäs-type deposits (Geijer 1961) are arranged along a more than 100 km long, narrow belt that we collectively call "the REE line". It represents both a geological anomaly and a zone of significant concentration of mostly light REE, but to some extent also yttrium and heavy REE. Over time, the Bastnäs-type deposits have been debated both as to their process of formation and their temporal relations to surrounding host rocks and mineralisation types.

Their formation, together with that of associated skarn iron ores, was originally interpreted to be related to large-scale, so-called magnesia metasomatic processes, generated by granitoid intrusives, essentially synchronous with the waning stage of regional metamorphism (Geijer 1961; Magnusson 1970). Later studies have rendered this theory obsolete, and accumulating observations tend to favour a more or less syn-volcanic magmatic-hydrothermal scenario (cf. Holtstam and Andersson 2007, and references therein). Yet, no conclusive theory has been presented for these deposits.

2 Geology and mineralisation

2.1 The Bergslagen ore province

The ancient Bergslagen ore province in south central Sweden is well-known for its abundance of mineral deposits, mainly in the form of base metals (Cu, Pb, Zn) and iron oxides (e.g. Tegengren 1924; Magnusson 1970). The primary ore-bearing rock sequence in Bergslagen is dominated by rhyolitic to rhyodacitic, alkali-rich metavolcanic rocks, together with smaller volumes of metabasic rocks, clastic metasedimentary rock units and marbles.

These rocks formed at c. 1.90-1.87 Ga during an early stage of the Svecokarelian (Svecofennian) orogeny. The predominantly felsic volcanic rocks and related penecontemporaneous intrusives were formed in a shallow marine, caldera environment, in a back-arc region inboard an active continental margin (Allen et al. 1996; Lundström et al. 1998; Stephens et al. 2009). During the orogenic evolution these rocks were subsequenly metamorphosed under mainly greenschist and amphibolite facies conditions and subjected to polyphase deformation. Younger granites and associated pegmatites, post-dating the c. 1.85-1.80 Ga regional metamorphism, are ubiquitous in the province.

Mineralisation occurs both in the felsic metavolcanic rocks and the commonly occurring, interlayered carbonate rocks and associated skarns (variably Fe, Mg and/or Mn-bearing calc-silicate assemblages formed both as a variably isochemical consequence of regional metamorphism of impure carbonate rocks, as well as through metasomatic reactions between granite-derived fluids rich in silica and other components and carbonate rocks).
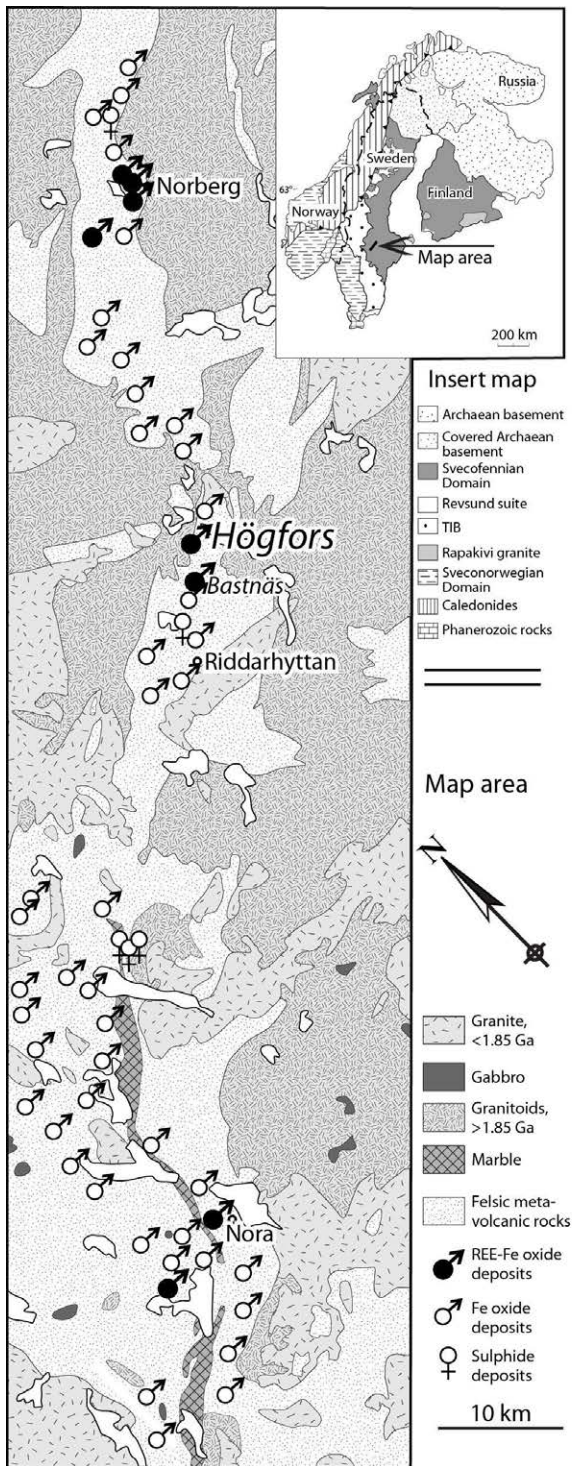
Figure 1. Geological overview map of the main part of the REE line in Bergslagen. Inset map of the geological outline of Fennoscandia with rectangle showing the position of the detailed map. Major REE-iron oxide (± Cu, Au, Co, Bi...) deposits are highlighted as filled iron ore symbols. Modified after Andersson (2004) and SGU datasets.

Figure 2. Chevron-style folding in hematite-quartz-dominated c. 1.90-1.88 Ga banded iron (BIF) ore at Högfors, central Bergslagen ore province. Estwing hammer for scale.

2.2 The "REE line" and the Högfors mines

The distribution of skarn iron ore-associated REE silicate mineralisation in Bergslagen is concentrated to a discontinuous belt or "corridor" of deposits within a sequence of mostly extensively altered felsic metavolcanic rocks (Fig. 1; cf. Geijer 1961). This belt is very narrow, yet the linear extent of REE mineralisation is, based on all available information, likely to be over 100 kilometers, and hence we suggest the term "REE line". The deposits of the northern part of the line are centered around Norberg, whereas in the central and southern parts, they cluster around Riddarhyttan and Nora, respectively (Fig. 1). Based on mineralogy and REE geochemistry, Holtstam and Andersson (2007, and references therein) subdivided the Bastnäs-type deposits in two main classes; subtype one with predominant LREE enrichment (mainly the southern and central deposits, including Bastnäs itself), and subtype two, featuring both enrichment in LREE and Y+HREE (the latter typified by the Norberg area deposits).

The Högfors deposits are situated to the north of the well-known Bastnäs field, in the Riddarhyttan district (Fig. 1). The Högfors field is, in turn, subdivided into two smaller fields, the Lilla Högforsgruvan and Stora Högforsgruvan (Högbom and Lundqvist 1930). The presently studied material comes from the Stora Högfors mine. Although magnetite-dominated skarn ores comprise parts of these fields, the major ore type mined at Högfors was a hematite-dominated, modestly skarn-bearing banded iron formation (Fig. 2).

3 Mineralogy, textures and structures

An initial study of the REE silicate assemblages was performed utilising limited optical microscopy, powder X-ray diffraction and scanning electron microscopy with energy-dispersive microprobe analysis (EDS). Based on this, the predominating REE mineral in the studied samples is a fluorine-enriched cerite-(Ce), that occurs as a major component of folded REE silicate bands within the BIF (Figs. 3, 4), together with an iron-rich and fluorine-poor västmanlandite-like mineral (possibly identical to the close to end-member composition of the suggested Fe-analogue to västmanlandite-(Ce); cf. Holtstam et al. 2005; Fig. 4A, Tab. 1). A second assemblage type within the banded mineralisation comprises a similar västmanlandite-type mineral as the major component, with abundant anhedral inclusions of gadolinite-(Ce), minor fluorocarbonates and sparse euhedral to subhedral crystals of ferriallanite-(Ce) (Fig. 4B).

Table 1. General chemical formulae of REE minerals.

Mineral:	General formula:
Bastnäsite-(Ce)	$(Ce,LREE)(CO_3)F$
Cerite-(Ce)	$(Ce,LREE,Ca)_9(Mg,Fe)(SiO_4)_6(SiO_3OH)(OH)_3$
Ferriallanite-(Ce)	$Ca(Ce,LREE)Fe^{3+}AlFe^{2+}(SiO_4)(Si_2O_7)O(OH)$
Gadolinite-(Ce)	$(Ce,LREE,Y)_2FeBe_2Si_2O_{10}$
Monazite-(Ce)	$(Ce,LREE)(PO_4)$
Synchysite-(Ce)	$Ca(Ce,LREE)(CO_3)_2F$
Västmanlandite-(Ce)	$(Ce,LREE)_3Ca(Mg,Fe)_2Al_2Si_5O_{19}(OH)_2(F,OH)$

REE fluorocarbonates (and possibly fluoride(s)) occur throughout the studied assemblages in relatively sparse amounts, often exhibiting heterogeneous compositions and textures, indicating incipient alteration and breakdown to secondary phases. Based on SEM-EDS data, the predominating minerals comprise bastnäsite-(Ce) together with phases with compositions between synchysite-(Ce) and röntgenite-(Ce). Of these, bastnäsite seems to be the earliest-formed phase.

Figure 3. Hand-specimen scale folding of REE silicate bands in metamorphosed banded iron (BIF) ore at Högfors. Lighter cerite-(Ce)-dominated band is faulted and offset by a quartz vein (lower left). These veins carry additional allanite-type minerals. Scale bar equals 1 cm.

Additionally, sparse anhedral, rounded crystals of a partly sulphur and silicon-substituted monazite-(Ce) (Ce>La>Nd) occur within the REE silicate bands.

The folded, banded REE silicate assemblages exhibit a re-crystallised texture, with internal grain fabric being mostly granoblastic. All phases except sparse inclusions of ferriallanite are anhedral. The overall interpretation is of an extensively metamorphosed (and deformed) assemblage. A second generation of REE silicate(s), predominantly an allanite mineral, occur as more coarse-grained and distinctly euhedral crystals in thin quartz veins. These cross-cut and displace banded assemblages (including the BIF) at high angles (Fig. 3). We presently interpret these quartz vein-hosted assemblages as more likely to represent remobilisation of pre-existing REE, rather than a second mineralising event.
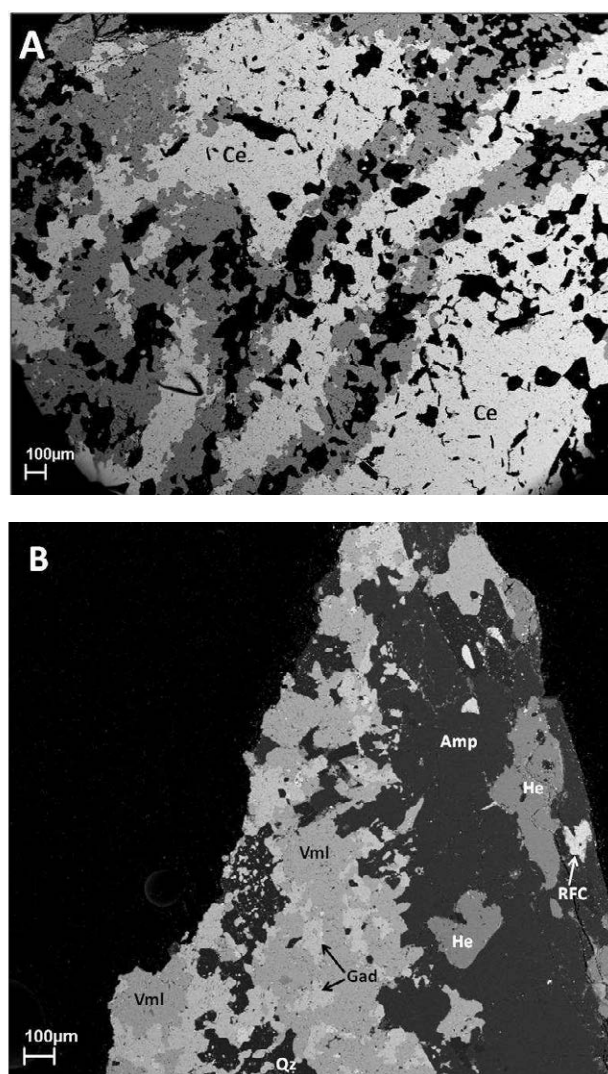
Figure 4. Field emission SEM back-scattered electron (BSE) images of representative textures of REE silicate assemblages in a metamorphosed banded iron formation at Högfors.
A. Complexly folded bands of cerite-(Ce) (Ce in figure) and a västmanlandite-type mineral (grey) and other silicates and quartz (black). Scale bar equals 100 micrometers. B. Irregular bands of a västmanlandite-type mineral (Vml) with inclusions of gadolinite-(Ce) (Gad), minor REE-fluoro-carbonates (RFC), hematite (He) and associated silicates including amphibole (Amp) and quartz (Qz). Scale bar equals 100 micrometers.

4   Discussion

The overall mineralogy and chemistry of the REE silicate assemblages at Högfors shows similarities with both subtypes of deposits in the classification by Holtstam and Andersson (2007). The two most abundant REE minerals here are cerite-(Ce), similar to Bastnäs (subtype 1), and a Ce-dominated västmanlandite-like mineral, typical of deposits in the Norberg area (subtype 2). Several of the minerals show enrichment in iron, which is not unexpected considering the BIF environment. The local, but relatively high abundance of the beryllium mineral gadolinite-(Ce) is an additional similarity with the deposits of subtype 2. Cerite-(Ce) is relatively enriched in fluorine, but other than the sparsely distributed fluorocarbonates, minerals with essential fluorine seem to be lacking. This is in accordance with the relatively low amounts of Y+HREE encountered at Högfors, considering the higher degree of complexing and transport possible for HREE in fluoride-rich fluids (cf. discussion in Holtstam and Andersson 2007).

The textural and structural interpretations of the Högfors assemblages are relatively unambiguous, and clearly suggest that REE mineralisation formed during an early stage of the Svecokarelian orogeny.

Based on the present observations, we cannot say whether the REE rich bands formed as a primary, interlayered component, syngenetic in relation to the banded iron formation, or if REE mineralisation was introduced later, as an epigenetic replacement of selected bands (e.g. carbonate-dominated). What is clear is that the formation of the REE silicate assemblages predates peak regional metamorphism and associated folding of the ores and its host rocks. This can be compared with the Bastnäs molybdenite Re-Os data of Holtstam (2004), yielding ages between c. 1.86-1.85 Ga, albeit with rather large errors. These ages seem too low for Svecofennian volcanic-associated processes. In order to clarify this contradicting evidence, tests will be made to attempt chemical dating of the monazites in the Högfors sample material.

It has been suggested that in the Norberg region, the banded iron formations belong to a higher "etage", or stratigraphic level, than the neighbouring skarn iron ores including Bastnäs-type deposits (e.g. Magnusson 1970). Thus, speculatively, in the comparable setting of the nearby Riddarhyttan area, the Högfors field with its REE-mineralised BIF´s could represent an originally seafloor or shallow sub-seafloor expression of the process responsible for deeper situated, coarse, skarn-hosted REE silicate mineralisation represented by the Bastnäs deposits proper. An alternative, and perhaps more realistic, interpretation is that both the Bastnäs and Högfors mineralisations could have formed similarly through carbonate-replacement, the only major difference being the primary availability of carbonate: abundant at Bastnäs, while sparse within the Högfors banded iron formation.

Acknowledgements

References

Allen RL, Lundström I, Ripa M, Simeonov A, Christofferson H (1996) Facies analysis of a 1.9 Ga, continental margin, back-arc, felsic caldera province with diverse Zn-Pb-Ag-(Cu-Au) sulfide and Fe oxide deposits, Bergslagen region, Sweden. Econ Geol 91: 979-1008

Andersson UB (ed) (2004) The Bastnäs-type REE mineralisations in north-western Bergslagen, Sweden**.** SGU Rapporter and Meddelanden 119

Geijer P (1961) The geological significance of the cerium mineral occurrences of the Bastnäs type in central Sweden. Arkiv för Mineralogi Geologi 3: 99-105

Hisinger W, Berzelius JJ (1804) Cerium, en ny metall, funnen i Bastnäs Tungsten, från Riddarhyttan i Westmanland. Henrik A. Nordström förlag, Stockholm

Högbom A. Lundqvist G, (1930) Beskrivning till kartbladet Malingsbo. SGU ser Aa 168

Holtstam D (2004) Isotopic constraints on the origin of Bastnäs type REE deposits in Bergslagen, Sweden. GFF 126: 149

Holtstam D, Andersson UB (2007) The REE minerals of the Bastnäs-type deposits, south-central Sweden. Can Mineral 45: 1073-1114

Holtstam D, Kolitsch U, Andersson UB (2005) Västmanlandite-(Ce) – a new lanthanide- and F-bearing sorosilicate mineral from Västmanland, Sweden: description, crystal structure, and relation to gatelite-(Ce). European J Mineral 17: 129-141

Lundström I, Allen RL, Persson P-O, Ripa M (1998) Stratigraphies and depositional ages of Svecofennian, Palaeoproterozoic metavolcanic rocks in E. Svealand and Bergslagen, south central Sweden. GFF 120: 315-320

Magnusson NH (1970) The origin of the iron ores in central Sweden and the history of their alterations, SGU ser C 643

Stephens MB, Ripa M, Lundström I, Persson L, Bergman T, Ahl M, Wahlgren C-H, Persson P-O Wickström L (2009) Synthesis of the bedrock geology in the Bergslagen region, Fennoscadian Shield, south-central Sweden. SGU ser Ba 58

Tegengren FR (1924) Sveriges ädlare malmer och bergverk. SGU ser Ca 17

Textural relations and mineral chemistry of REE in the Grängesberg apatite-iron oxide deposit, Sweden: the role of fluids

Jarosław Majka, Erik Jonsson*, Karin Högdahl, Valentin R. Troll
CEMPEG, Department of Earth Sciences, Uppsala University, Villavägen 16, SE-75236 Uppsala, Sweden

Daniel E. Harlov
GeoForschungsZentrum Potsdam, Telegrafenberg, D-14473, Potsdam, Germany

Katarina P. Nilsson
*Geological Survey of Sweden, Box 670, SE-75128 Uppsala, Sweden

Abstract. The metamorphosed and deformed Kiruna-type deposits of the Bergslagen province in south central Sweden not only represent the biggest iron ore resource in central and southern Sweden, but also a significant occurrence of REE's as well as phosphorous. Here we present data from comprehensive mineralogical, textural and mineral chemistry studies of the major REE-bearing assemblages in the Grängesberg deposit, primarily comprising REE-substituted fluorapatite, allanite-(Ce), monazite-(Ce) and xenotime-(Y).

It is evident that relatively intense fluid-mediated overprinting has led to alteration of the more reactive phases, such as apatite. This likely occurred in two stages, where the first introduced acidic fluids along apatite grain boundaries during the later stages of crystallization of the apatite-iron oxide deposit. This resulted in the formation of monazite and xenotime inclusions in the apatite. The second stage may have occurred in association with fluid mobility related to the amphibolite-facies metamorphism of the ores and host rocks. This resulted in mass transfer of (Y+REE+P) (due to leaching from the apatite grain rims) and elements from the surrounding groundmass, which in turn led to the formation of allanite along with minor monazite and xenotime in the metavolcanic host rocks.

Keywords. Kiruna-type deposit, apatite, monazite, xenotime, allanite, REE, Bergslagen, Sweden

1 Introduction

Apatite-iron oxide ores of the so-called Kiruna-type occur worldwide and are generally associated with volcanic rocks of variable ages. One major current theory suggests that they represent highly evolved, late stage, igneous bodies, most likely directly related to volcanism with a concurrent or perhaps slightly later metasomatic component. Examples of Kiruna-type apatite-iron oxide ores include the eponymous Kiirunavaara as well as the Malmberget mines (northern Sweden), the Grängesberg (Bergslagen, central Sweden), Mineville, (Adirondacks, New York, USA), and Pea Ridge deposits (Arkansas, USA), the mineralisations of the Bafq region (central Iran) and a series of larger and smaller deposits occurring within the Chilean High Andes and the Coastal Andean Cordillera. These mostly magnetite-dominated iron ores carry variable, but often substantial amounts of apatite, primarily as fluorapatite. Characteristically, the apatite as well as several associated phosphates and silicates harbour significant amounts of rare earth elements (REE; particularly the lanthanides and yttrium). In view of the present rush for REE resources, understanding the specific REE mineralogy and chemistry of these deposits where REE´s and phosphorous may become by-products, becomes increasingly relevant.

In most apatites in this deposit type, monazite-(Ce) ± xenotime-(Y) inclusions occur frequently. This phenomenon is explained by a complex process of fluid-aided coupled dissolution-reprecipitation of apatite (e.g. Harlov et al. 2005). This results in depletion of Y+REE in primary apatite and causes both, reprecipitation of (Y,REE)-poor apatite and nucleation of new (Y,REE)-phosphates, such as monazite and xenotime (e.g. Harlov et al. 2005).

Here, we focus on the textural and mineral chemical relations of REE-bearing phases, and hypothesize about the fluid-aided alterations in the Grängesberg apatite-iron oxide deposit in central Sweden.

2 Geological setting

The apatite-iron-oxide deposits in the Grängesberg District (GD) belong to the Palaeoproterozoic Bergslagen ore province in central Sweden. This classic and ancient region hosts a large variety of mineralisations including Ag-(Cu-Ag) sulphide and iron oxide deposits. e.g. skarn, banded iron formations and apatite-iron oxide mineralisations. The latter have only been found the (north-) western part of the province along a 40 km long zone. The majority of the mineralisations are hosted by a volcanosedimentary succession formed in a back-arc region inboard an active continental margin during the 1.9-1.8 Ga Svecokarelian orogeny (Allen el al. 1996). The rocks have been subjected to polyphase deformation and metamorphism under mainly greenschist to amphibolite facies conditions.

The GD deposits were compared to those of the Kiruna district, northern Sweden at an early stage (Looström 1929), and similarly debated as to their actual mode of formation (Johansson 1910; Magnusson 1970; Hitzman et al. 1992).
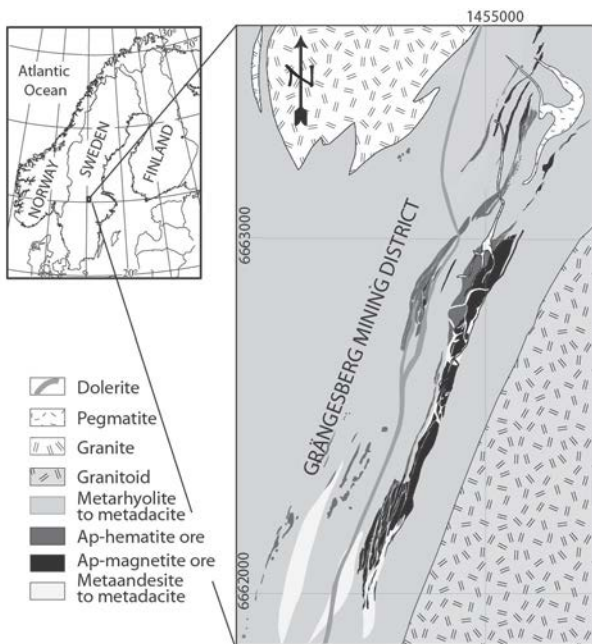
Figure 1. Simplified geological map of the main ore zone in Grängesberg (source: Geological Survey of Sweden).

Based on the mineralogy, deposit geometry, relations to host rocks and overall geochemical character, the GD apatite-iron oxide ores clearly represent deformed amphibolite-facies metamorphosed Kiruna-type deposits (Jonsson et al. 2010). Evidence from geochemistry, oxygen (Jonsson et al. 2011) and iron isotope systematics (Weis et al. 2013) suggest an orthomagmatic origin for the Fe oxide formation with related, localised hydrothermal alteration of the host rocks (Jonsson et al. 2011). The ores and host rocks where regionally metamorphosed, and also affected by at least two generations of later intrusives, including older granitoids as well as abundant, c. 1.8 Ga granitic pegmatites. Even later brittle deformation overprints all other structures.

3 Sampling and methodology

Apatite-rich samples investigated in this study were collected from existing outcrops and drill-core profiles transecting the main ore zone in the central part of the GD (Fig 1).

Electron microprobe analyses of the REE-minerals were carried out using a Cameca SX100 electron microprobe at the Deutsches GeoForschungsZentrum Potsdam (see e.g. Harlov et al. 2002 for details).

4 Results

The samples in this study represent different lithologies, including magnetite-apatite and hematite-magnetite-apatite mineralisation types, apatite breccias and apatite ± iron oxide-bearing host rocks. All rock types may carry apatite and iron oxides, whereas the abundances of monazite-(Ce), xenotime-(Y) and allanite-(Ce) vary between the different samples. A total of twenty-one samples were investigated.

The magnetite ores are fine to medium-grained and massive with a quite distinct "grainy" appearance. Hematite-dominated ores generally consist of massive, fine to medium-grained, often platy hematite, often with magnetite blasts. Almost all ore types show a variable degree of banding. Apatite and accessory silicates mostly dominate the bands, occurring as fine-grained aggregates.

High-resolution BSE imaging revealed that apatite in both types of ores occurs in two main varieties. One variety exhibits visible concentric zoning (Fig 2).
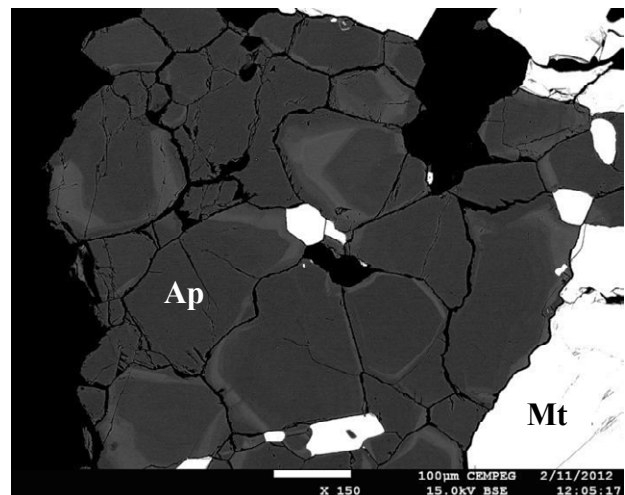
Figure 2. BSE photomicrograph of zoned apatite (Ap) in the magnetite-apatite ore.

Usually, such apatite is darker in the cores of crystals and increasingly lighter towards the rims, but darker again in the outermost rims. This trend is rarely reversed. Light zones are highly enriched in Y+REE (up to 2.5 wt.% of $(Y+REE)_2O_3$) and Si. Rare tiny (< 5 μm) and scattered monazite (± xenotime) inclusions are present in the dark zones. In some cases, the monazite (± xenotime) inclusions are epitaxially oriented, and grow parallel to the apatite c-axis (Fig 3).
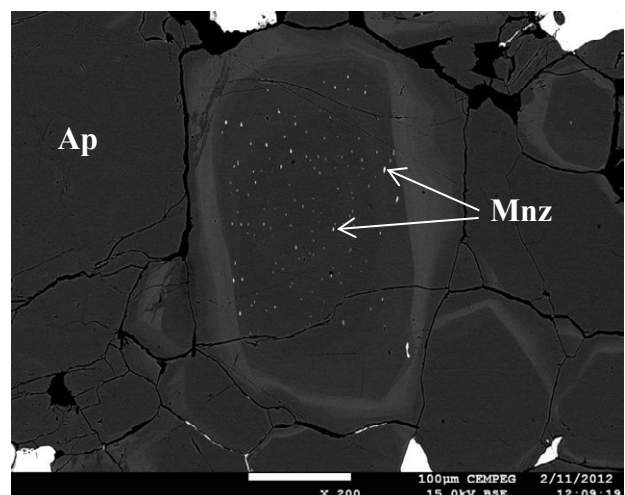
Figure 3. BSE photomicrograph of zoned apatite (Ap) from the magnetite-apatite ore. The apatite contains aligned inclusions of monazite (Mnz).

The other variety of apatite is unzoned and contains variable amount of monazite (± xenotime) inclusions (Fig 4). Monazite (± xenotime) inclusions can also differ in size and in some cases exceed several tens of micrometers. Such relatively large monazite grains can also be found outside of the apatite. The other (Y,REE)-bearing phase present is allanite, which forms along apatite grain boundaries or as large composite crystals outside the apatite.
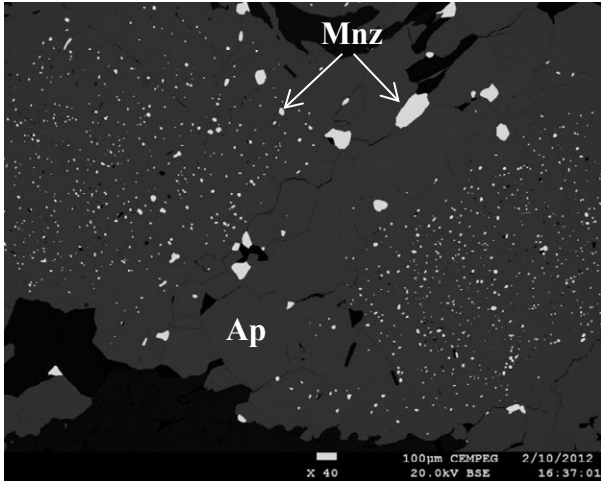
Figure 4. BSE photomicrograph of unzoned apatite from the hematite-magnetite-apatite ore. Apatite contains abundant inclusions of monazite (Mnz) of variable size.

The apatite breccia consists of dominant apatite and minor silicates. Apatite is unzoned and generally (Y+REE)-poor. It contains numerous inclusions of monazite (± xenotime) of variable size. These are concentrated in the cores of the apatite crystals, whereas the rims commonly lack inclusions (Fig 5). Allanite is common and occurs either as veins within the apatite interior, as overgrowths on the rims of apatite grains (Fig 5), as discrete grains along grain boundaries or as individual larger crystals.
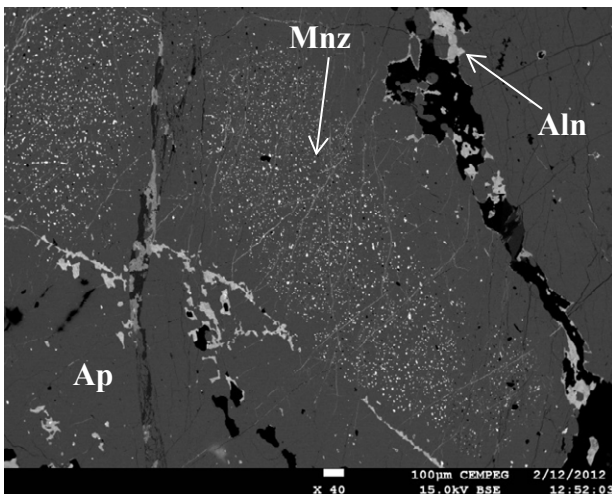
Figure 5. BSE photomicrograph of apatite containing inclusions of monazite in the apatite breccia. Allanite forms infill of veins within apatite as well as larger composite crystals outside apatite.

The host-rocks to the GD deposits consist of often schistose, variably altered metavolcanics where the apatite and iron oxides (magnetite and/or hematite) occur as bands, veins or disseminations. In these, the apatite is (Y+REE)-poor and inclusion-free. Allanite commonly occurs as interstitial grains in the iron oxide-apatite bands (Fig 6).
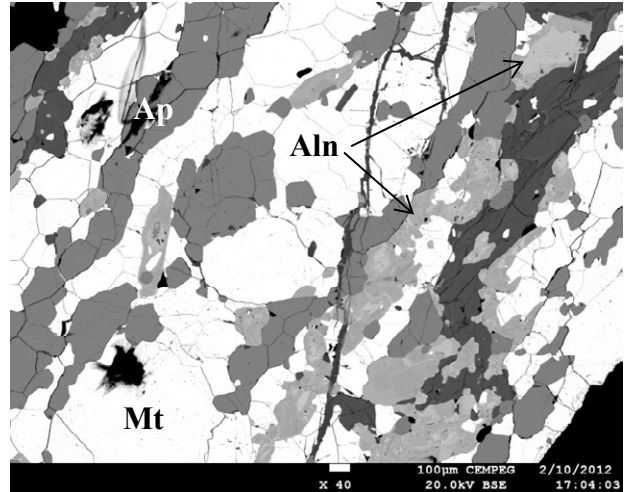
Figure 6. BSE photomicrograph of the magnetite-apatite-allanite band in the metavolcanic rock.

5 Discussion

Apatite intergrown with Fe oxides is enriched in Y+REE to varying degrees, which can be expressed in the form of two coupled substitution reactions: (1) $Na^+ + (Y+REE)^{3+} = 2Ca^{2+}$, and (2) $Si^{4+} + (Y+REE)^{3+} = P^{5+} + Ca^{2+}$. Of these reaction (2) is the dominant one (Fig 7).
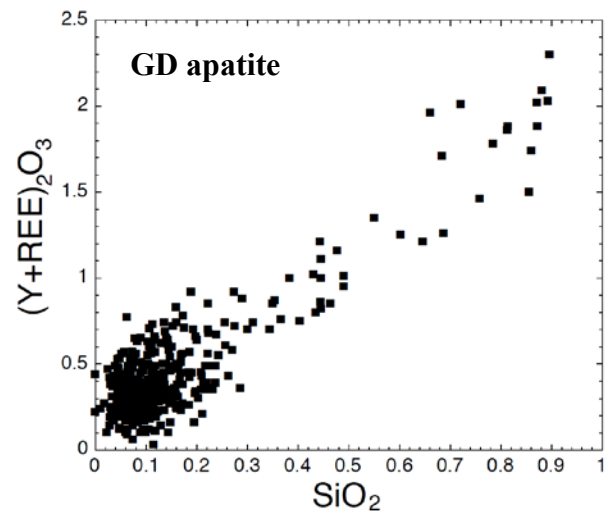
Figure 7. $(Y+REE)_2O_3$ versus SiO_2 in apatite from all studied samples.

Nucleation of monazite (± xenotime) in apatite was most probably caused by a metasomatizing fluid during the early stages of formation of the deposit. Assuming that the ore deposit is of an orthomagmatic origin, this

fluid could have been generated from the residual melt allowing for fluid-ore interaction to occur during crystallization of the residual melt. Studies of other apatite-iron oxide ore deposits suggest that such fluids were most likely acidic (e.g. Harlov et al. 2002). Experimental studies have shown that acidic fluids such as HCl and H_2SO_4 react with the apatite, which leads to the formation of a micro/nano porosity and chemical alteration during the coupled dissolution-repreciptitation process (Harlov et al. 2005). Fluid infiltration via this porosity promotes mass transfer of (Y+REE), Si, Na, Ca, and P and the subsequent formation of monazite (± xenotime) inclusions with the micro-pores serving as nucleation sites for the inclusions.

Examination of the apatite reveals sharp boundaries between the (Y+REE)-enriched outer zones and (Y+REE)-depleted interiors, which are commonly full of monazite inclusions. Along apatite grain rims, the (Y+REE) distribution is more diffusive, suggesting that these rims were the source of (Y+REE) for monazite xenotime, and allanite formation in the surrounding mineral matrix. Whether this was the result of the same fluid responsible for the formation of the monazite and xenotime inclusions is not clear. It cannot be excluded that a second, later, fluid infiltration occurred during the amphibolite-facies overprint of the deposit. Such a fluid enriched in elements from the host rock, could have induced leaching of the apatite along the grain boundaries and promoted the crystallization of secondary REE-phases (predominantly allanite) in the surrounding mineral matrix.

In summary, the Grängesberg apatite-iron oxide ore deposit has been subjected to a relatively intense fluid-mediated overprinting, leading to alteration of the more reactive phases, such as apatite. The most likely scenario is that it occurred in two steps. The first led to the presence of acidic fluids along apatite grain boundaries during the later stages of crystallization of the apatite-iron oxide deposit. This resulted in the formation of monazite and xenotime inclusions in the apatite. The second step most likely occurred during fluid mobility related to the late stage magmatic cooling or amphibolite-facies overprint of these rocks. This resulted in mass transfer of both, (Y+REE+P) (due to leaching from the apatite grain rims) and elements from the surrounding mineral matrix which in turn led to the formation of allanite along with minor monazite and xenotime in the iron oxide-bearing assemblages associated with the host metavolcanic rocks.

Acknowledgements

References

Allen RL, Lundström I, Ripa M, Simenov A, Christofferson H (1996) Facies analysis of a 1.9 Ga continental margin, back-arc, felsic caldera province with diverse Zn-Pb-Ag-(Cu-Au) sulfide and Fe oxide deposits, Bergslagen region, Sweden. Econ Geol 91: 979-1008

Harlov HE, Wirth R, Förster H-J (2005) An experimental study of dissolution-repreciptitation in fluorapatite; fluid infiltration and the formation of monazite. Contr Min Petrol 150: 268-286

Harlov HE, Andersson UB, Förster H-J, Nyström J-O, Dulski P, Broman C (2002) Apatite-monazite relations in the Kiirunavaara magnetite-apatite ore, Northern Sweden. Chem Geol 191: 47-72

Hitzman MW, Oreskes N, Einaudi MT (1992) Geological characteristics and tectonic setting of Proterozoic iron oxide (Cu-U-Au-REE) deposits. Precam Res 58: 241-287

Johansson H (1910) Die eisenerzführende Formation in der Gegend von Grängesberg. Geol Fören Stockholm Förhandl 32: 239-410

Jonsson E, Nilsson KP, Hallberg A, Högdahl K, Troll VR, Weis F, Harris, C (2011) Oxygen isotopes and geochemistry of Palaeoproterozoic Kiruna-type deposits in the Bergslagen province, central Sweden. Abstract volume, SGA biennial meeting 2011, Antofagasta, Chile: 494-496

Jonsson E, Nilsson KP, Hallberg A, Högdahl K (2010) Palaeopreoterozoic apatite-iron oxide deposits of the Grängesberg area: Kiruna-type deposits in central Sweden: In: Nakrem HA, Harstad, AO, Haukdal G (eds.), NGF abstracts and proceedings 1: 88-89

Looström R (1929) Likheter mellan Lapplands- och Grängesbergsmalmerna. Geol Fören Stockholm Förhandl 51: 303-308

Magnusson NH (1970) The origin of the iron ores in central Sweden and the history of their alterations. Sver Geol Unders C 643: 1-232

Weis F, Troll VR, Jonsson E, Högdahl K, Barker A, Harris C, Nilsson KP (2013) Oxygen and iron isotope characteristcis of apatite-iron-oxide ores from central Sweden. This volume

Preliminary characterization of the REE mineralization of the St-Honoré ferro-carbonatite (Québec, Canada)

Néron A., Bédard L.P., Gaboury D.
Sciences de la Terre, Université du Québec à Chicoutimi, Chicoutimi, Québec, Canada G7H 2B1 neron.alex@gmail.com

Thivierge, S.
Niobec inc,, 3400 route du Columbium, Saint-Honoré (Qc) Canada, G0V 1L0

Abstract. Exploration for rare earth elements (REE) has gained tremendous interest lately. Understanding economic REE deposits is prerequisite to generate new exploration targets. The St-Honoré carbonatite is a world-class deposit. The mineralization is hosted in a brecciated Fe-carbonatite composed of carbonate (calcite, dolomite, siderite), barite, REE-minerals (bastnaesite with minor monazite), quartz, halide (halite and sylvite) and chlorite. The Fe-carbonatite divides at depths in upper and lower zones characterised by presence or absence of halide, quartz and/or barite associated with the mineralization. The relationship of halide and REE minerals and the abundance of barite suggest a rich magmatic source with a late hydrothermal remobilization.

Keywords. REE deposit, Carbonatite, St-Honoré.

1 Introduction

The market of rare earth elements (REE) is in expansion with the rapid development of green technologies and the recent limitation of Chinese exportations. The exploration for these elements is stimulated because they are becoming an important resources for the future (Hatch 2012).

Carbonatites are known to have a high natural concentration of REE, but in many cases, that is not enough to make an economical deposit. An additional magmatic or hydrothermal concentration process has to be present to develop economic REE grades (Chakhmouradian and Wall 2012). To our knowledge, no single ore-forming model is widely accepted. Although ore descriptions are the basis to generate valuable models, few are available. Furthermore, exotic mineralogy of REE mineralization renders descriptions more complex.

The St-Honoré alkaline complex is a niobium mine which host substantial unexploited REE mineralisation. The carbonatite would classify as a world-class deposit with its 466.8 Mt at 1.65 % wt TREO (Total Rare Earth Oxide) (Lafleur and Ayad 2012). Mainly, the mineralization is constituted by LREE (light rare earth elements) minerals. Some previous descriptions are available (Fournier 1993, Gauthier 1979) but they are limited to the thin upper part of the complex that has been altered to laterite during Ordovician time. The general geology of the St-Honoré REE deposit, as well as the description of the REE ores are presented here for the first time.

2 Geological setting

The Saguenay region (Fig. 1) is composed by four petrographic domains (Dimroth, et al. 1981). The first one is a gneiss complex deformed during the Hudsonian Orogeny (1,735 ma). The second unit comprises anorthosite and granitoid batholiths dated from pre- to post-Grenvillian orogeny (935 ma). The third unit corresponds to calc-alkaline intrusions related to St-Lawrence River rift and associated Saguenay Graben (Kumarapeli and Saul 1966). This extensional event provided anisotropies for channelling alkaline magmas that includes the St-Honoré carbonatite at 650 ma (Vallee and Dubuc 1970). The last unit is the Ordovician limestone overlying the St-Honoré alkaline complex (Fig. 1).
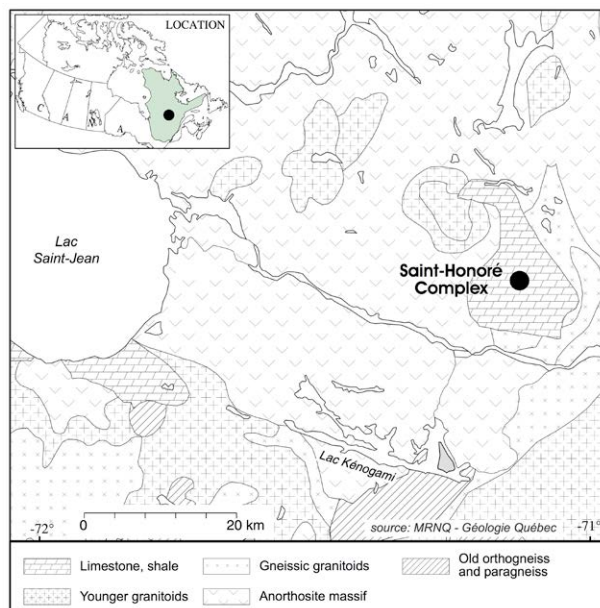
Figure 1. Regional geology of the St-Honoré alkaline complex in Québec, Canada.

The St-Honoré alkaline complex (Fig. 2) is a vertical chimney-like intrusion composed of a carbonatite core, surrounded by alkaline silicate rocks. The carbonatitic unit has an elliptical shape orientated NE-SW. From the periphery to the center of the carbonatitic complex, there is a concentric pattern from an older calcitic carbonatite to a younger Fe-carbonatite in the center. The REE mineralization is hosted in the youngest and most evolved unit: the Fe-carbonatite (Belanger 1977). The alkaline complex is covered by Ordovician Trenton limestone and the 60-120 first metres of the Fe-carbonatite were heavily weathered to an orange to red laterite prior to deposition of the Trenton limestone.

According to previous studies (Fournier 1993;

Gauthier 1979), the principal economic REE minerals are fluoro-carbonates (bastnaesite, parasite and synchisite) occuring as minute needles.
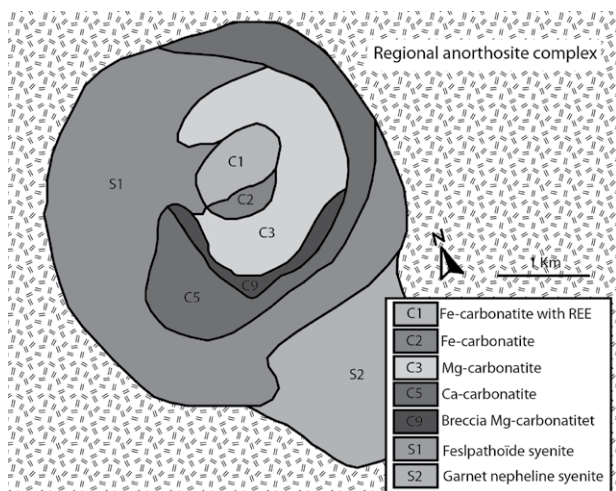
Figure 3. Geological map and section of the St-Honoré carbonatite. The mineralization is hosted in the central Fe-carbonatite unit.

3 Ferro-carbonatite description

Two main petrographic units characterize the Fe-carbonatite: massive and brecciated. T̄   ive Fe-carbonatite is composed of coarse-grained carbonates (80-90 % dolomite, ankerite, and siderite) and barite (5%-10 %) with minor fine-grained pyrite. Centimeter-size purple minerals clusters, hosting REE minerals, represent 5-10 % of the mineral assemblage in the massive unit. The mineralogy of these clusters is not constant through the unit. The following minerals have been observed in these purple clusters: REE minerals, hematite, quartz, halite, barite and carbonate but not all these minerals are present in all clusters. The clusters are interstitial to carbonates and in some cases they show some brecciation suggesting they are a late feature.

The second petrographic unit, the brecciated carbonatite, is composed of sub-angular mm-size clasts of carbonates and barites in similar proportions as in the massive Fe-carbonatite. The mineralogy of the matrix between the brecciated fragments is similar to the mineralogy of the purple clusters of the massive Fe-carbonatite. The contact between massive and brecciated units is, in some area, transitional with an increasingly brecciation over a few metres whereas in other areas the contact is sharp.

The REE mineralization, despite looking homogeneous in hand specimen, is highly heterogeneous at the microscopic scale. The purple mineral clusters, hosting mineralization, have been divided in two groups based on halite and barite content. Those with halite and barite are at depth whereas those without occur closer to the surface. The matrix between breccia fragments can also be divided on the basis of halite and barite abundance and show similar field relationships. REE fluoro-carbonates minerals are concentrated mainly in the matrix of the brecciated Fe-carbonatite and in bastnaesite clusters within the massive carbonatite. Bastnaesite clusters are made of needles of a few μm in diameter and up to 20 μm in length (Fig. 3).
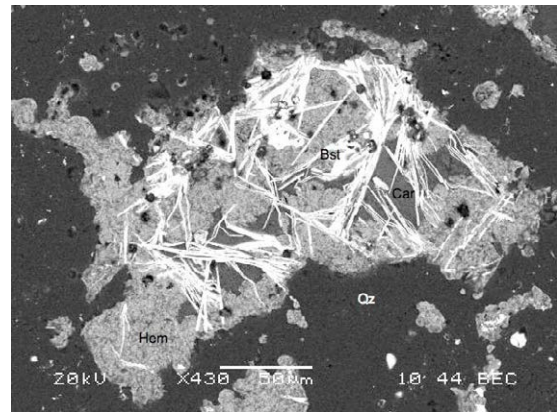
Figure 3. SEM image of a REE-mineralized cluster localized in the upper part of the deposit. Qz=quartz, Bst = bastnaesite, Hem = hematite, Car = carbonate.

4 Discussion

The current status of observations suggests that the REE ore of St-Honoré carbonatite are formed by magmatic and hydrothermal processes. Haxel (2005), in his study of the Mountain Pass deposit and in a compilation of Ba in Fe-carbonatites, demonstrated that abundant barite in Fe-carbonatite suggest a REE-rich magmatic source. Haxel (2005) has found an average concentration of 3.12 % Ba in Fe-carbonatite. The Fe-carbonatite of the REE zone of St-Honoré has 5.15% Ba in addition to abundant barite, hence arguing for a magmatic component. Alternatively, halite composes nearly 20% of the minerals present in clusters observed in deeper part. Such Cl-rich minerals could be an indication that some REE were concentrated by hydrothermal fluids as chloride-rich solutions which are known to effectively transport REE (Williams-Jones et al. 2012).

References

Belanger MF (1977) Le complexe annulaire à carbonatites de St-Honoré (PQ, Canada) et sa minéralisation a niobium: étude pétrographique et géochimique. Dissertation, Université Claude Bernard.

Chakhmouradian AR, Wall F (2012) Rare earth elements: Minerals, mines, magnets (and more). Elements 8:333-340.

Dimroth E, Woussen G, Roy DW (1981) Geologic history of the Saguenay region, Quebec (Central Granulite Terrain of the Grenville Province): a working hypothesis. Can Jour Earth Sci 18:1506-1522.

Fournier A (1993) Magmatic and hydrothermal controls of LREE mineralization of the St.-Honoré carbonatite, Québec. Dissertation, McGill University.

Gauthier A (1979) Étude minéralogique, pétrographique et géochimique de la zone à terres rares de la carbonatite de St-Honore. Dissertation, Université du Québec à Chicoutimi.

Hatch GP (2012) Dynamics in the Global Market for Rare Earths. Elements 8:341-346.

Haxel G (2005) Ultrapotassic Mafic Dikes and Rare Earth Elements-and Barium-rich Carbonatite at Mountain Pass, Mojave Desert, Southern California: Summary and Field Trip Localities. US Geological Survey.

Kumarapeli PS, Saul VA (1966) The St. Lawrence valley system: A North American equivalent of the East African rift valley system. Can Jour Earth Sci 3:639-658.

Lafleur PJ Ayad AB (2012) Technical Report to present the Mineral Resources of the Rare Earth Elements Zone Niobec Mine-IAMGOLD. NI 43-101 Technical report.

Vallee M, Dubuc F (1970) The St-Honoré carbonatite complex, Quebec. Can Min Metall Bull 63:1384-1389.

Williams-Jones AE, Migdisov AA, Samson IM (2012) Hydrothermal Mobilisation of the Rare Earth Elements–a Tale of "Ceria" and "Yttria". Elements 8:355-360.

Geology and exploration of the Li-Sn-W-Rb-Cs deposit Zinnwald, eastern Erzgebirge, Germany

Jörg Neßler[1], Thomas Seifert[1], Jens Gutzmer[2], Armin Müller[3], Silvio Stute[3], Kersten Kühn[4]
[1] TU Bergakademie Freiberg, Brennhausgasse 14, D-09596 Freiberg, joerg.nessler@mineral.tu-freiberg.de
[2] Helmholtz Institute Freiberg for Resource Technology, Halsbrücker Str. 34, D-09599 Freiberg
[3] SolarWorld Solicium GmbH, Berthelsdorfer Str. 111, D-09599 Freiberg
[4] G.E.O.S. Ingenieurgesellschaft mbH, Gewerbepark „Schwarze Kiefern", D-09633 Halsbrücke

Abstract. The polymetallic Zinnwald deposit is represented by greisen-type mineralisation hosted in the apical portion of a small pipe-shaped granitic intrusion. Since the 14th century the deposit has been mined predominantly for tin, later also for its tungsten content. The deposit straddles the border between Germany and the Czech Republic (where it is called Cínovec deposit). It is known to contain elevated concentrations of a range of other metals that have recently gained economic interest. These include Li, Cs and Sc. In March 2011, the SolarWorld Solicium GmbH started to reinvestigate and explore the German part of the deposit. In addition to the examination of historic information from previous exploration campaigns two drill holes and systematic channel samples from historic underground galleries were studied to critically assess and amend historic data on mineralogy and geochemistry. In comparison to historic data first results indicate an excess of Li concentrations obtained by recent analysis.

Keywords: Lithium · Greisen · Zinnwald · Erzgebirge

1 Geology and Mineralogy

The greisen-type Zinnwald ore deposit is located in the eastern part of the Erzgebirge region, Saxony, Germany. The deposit extends into the Cinovec deposit in the Czech Republic. The Zinnwald granite constitutes one of several typical small, highly evolved granitic intrusions of the Erzgebirge region. These intrusions are marked by prominent enrichment of incompatible elements (F, Li, Rb, Cs, Sn, Nb, Ta, Th) and the depletion of P_2O_5 (cf. Seifert and Kempe, 1994). Similar to other small granitic stocks known to host Sn(-W-Mo) mineralisation in the Erzgebirge, the Zinnwald granite intruded during the post-collisional stage of the late-Variscan (Permo-Carboniferous) magmatic evolution, ascending along deep-reaching fault zones into high metamorphic and igneous basement rocks and into the volcanic complex of the Altenberg-Teplice caldera (ATVC) (cf. Seifert and Kempe, 1994). The post-collisional small intrusions of "Sn granites" in the Erzgebirge/-Krušné hory are probably associated with Permo-Carboniferous, post-collisional lamprophyric intrusions (Seifert, 2008; Štemprok and Seifert, 2011). The granite stock at Zinnwald is ovoid in shape with dimensions of 3 x 1 km. It is regarded as highly altered albite granite which intruded the volcanic pile of the Teplice rhyolite. The deposit itself is characterised by flat dipping, sheet-like greisen ore bodies and veins in the apical part and along the steep dipping edges of the Zinnwald granite stock. Flat-dipping veins with pegmatitic appearance are accompanied by steeply dipping faults, so called "Morgengänge", striking NE-SW. The greisen bodies predominantly consist of quartz, Li-Rb-Cs-bearing mica (named zinnwaldite), topaz, fluorite and accessory cassiterite and wolframite. Grain sizes of quartz and zinnwaldite greisen mineralisation range from 3 to 10 mm. Associated topaz and cassiterite is generally more fine grained with grain sizes of 1 and 0.1 mm, respectively.

Zinnwaldite, named after its type locality, is considered as a series of trioctahedral micas on the siderophyllite-polylithionite join (Rieder et al., 1998). It represents one of the most common mica species along this join and is reported from various types of granitic rocks all around the world (Cundy et al., 1960; Uhlig, 1992; Haynes et al., 1993; Novak et al., 1999; Lowell et al., 2000; Roda Robles et al., 2012). Lithium content of the zinnwaldite mica is in the range of 0.8 to 1.9 wt%. Additionally, it contains high contents of iron (8.1 to 11.0 wt%) and fluorine (3.5 to 7.2 wt%) (Gottesmann, 1962; Rieder et al., 1970; Uhlig, 1992; Govindaraju et al., 1994; Tischendorf et al., 1997; Johan et al., 2012).

With lithium resources of all categories of about 42,000 t for the German part of the Zinnwald deposit (Bolduan and Lächelt, 1960) and 112,775 t for the Czech portion (Starý et al., 2011) Zinnwald is regarded as one of the largest Li deposits in Europe.

2 Historic and recent exploration

The German part of the Zinnwald granite body was exploited from the 15th century to the end of WW II. On the Czech side, exploitation continued until 1991. Several exploration campaigns were carried out on the German portion of the deposit following closure until 1989. Noticeable are exploration campaigns from 1954 to 1960 with a focus on lithium carried out by the governmental Geological Commission of the former GDR (Bolduan and Lächelt, 1960). A total of 27 surface and underground drill holes were used to reconstruct the overall geometry and position of the greisen ore bodies. In 1977/78 two drill cores and a total of 1305 underground samples were gathered in a second exploration campaign (Grunewald, 1978). In 1988, finally, the Zinnwald deposit was once more explored, this time with the sole focus on Sn and W mineralisation (Kühne and Besser, 1989). In the latter campaign, 9 drill holes were added to the existing data base.

With the expected increasing demand in highly efficient decentralised energy storage systems, lithium-based batteries have gained considerable interest in the past decade. This, in turn, has increased the demand for

lithium. Therefore, the SolarWorld Solicium GmbH, member of the SolarWorld AG, took the decision to explore the Zinnwald for its potential as a possible source of lithium.

Exploration is carried out by a team of SolarWorld Solicium GmbH, Technical University Bergakademie Freiberg and G.E.O.S. Ingenieurgesellschaft mbH. A first 3D geological model was created based on existing geological data from mine workings and drill logs. The approach then has been: (1) to gain new and representative samples of greisen material in order to determine mineralogical and geochemical data of the ore and host rock lithologies by contemporary analytical technology (especially ICP mass spectrometry) and (2) to assess the validity of the historic data. Bulk samples were taken from historic mine workings for mineral processing and metallurgical test work (Seifert and Gutzmer, 2010). A series of underground channel samples and two inclined twinned drill cores 280 m (DH1) and 262 m (DH2) long were gathered in 2012.

This paper aims to present the results from DH1, DH2 and channel samples including lithological information and data from whole rock geochemistry. Basic statistics and description of element-dependency provide information on the distribution of lithium within different lithologies, particular greisen, greisenised albite granite and albite granite

Figure 1: Lithological and geochemical log of DH1 and DH2.

3 Methodology/analytical approach

Sampling of quarter core was performed in intervals of one meter. Shorter intervals were chosen when transgressing lithological boundaries. Duplicates of quarter core were used to assess the adequacy of sampling technique. The crushed and milled material from drill cores and underground samples was sent for multi-element chemical assay by ICP-MS, ICP-AES and XRF at an accredited commercial laboratory. The total data set currently comprises 192 samples from DH1 and 214 samples from DH2 as well as 88 samples from underground trenches.

4 Results

Within the study area medium to strongly altered Teplice-type rhyolite immediately overlies the granite stock. The rhyolite is commonly impregnated by dark mica locally associated with cassiterite. In DH2, a greisen body of nearly 40 m thickness was intersected in the granite stock directly below the contact to the rhyolite. In contrast, DH1 passes into albite granite and greisenised granite. With increasing depth, both DH1 and DH2 encountered albite granite and greisenised granite with only minor intercalations of greisen mineralisation. The cumulative intersected thickness of greisen mineralisation is about 7 m and 67 m for DH1 and DH2, respectively. Fine grained, schlieren-like aplitic veins and microgranites of little thickness occur below drilled depths of 150 m. In addition, DH 1 intersected a porphyritic albite granite at drilled depths from 245 to 270 m (Fig. 1).

Petrographic analysis of lithotypes recognized in DH1 and DH2 reveal close similarity to lithology from previous exploration campaigns and confirm the geometric character of greisen mineralisation with most intense greisen formation in the apical part of the stock and decreasing intensity to the flanks. However, mineralogical and textural variations on small scale are very common. It is these variations – and their interpretation – that hamper detailed correlation between sections constructed during different exploration campaigns.

Lithological and geochemical profiles of DH1 and DH2 are displayed in figure 1. The assumed correlation of elevated Li values with the occurrence of intense greisen mineralisation is easily recognized. Li concentration in greisen mineralisation ranges from 600 to 8,200 ppm. The distribution of values is close to normal, with a mean at 3,600 ppm. Li contents at 25th (Q1) and 75th (Q3) percentile are about 3,000 and 4,300 ppm and variation coefficient of Li is remarkably low (0.36), indicating an evenly and constant dissemination of Li-bearing mica on the scale of sample intervals. Transitional greisenised granites and "unmineralised" albite granites are characterised by a mean Li concentration of 1,800 ppm and 380 ppm, respectively (Fig. 2). The latter values are in good agreement with results obtained by previous authors (Štemprok and Šulcek, 1969; Tischendorf et al., 1988; Breiter et al., 1991; Sala, 1999, Seifert and Gutzmer, 2010). In
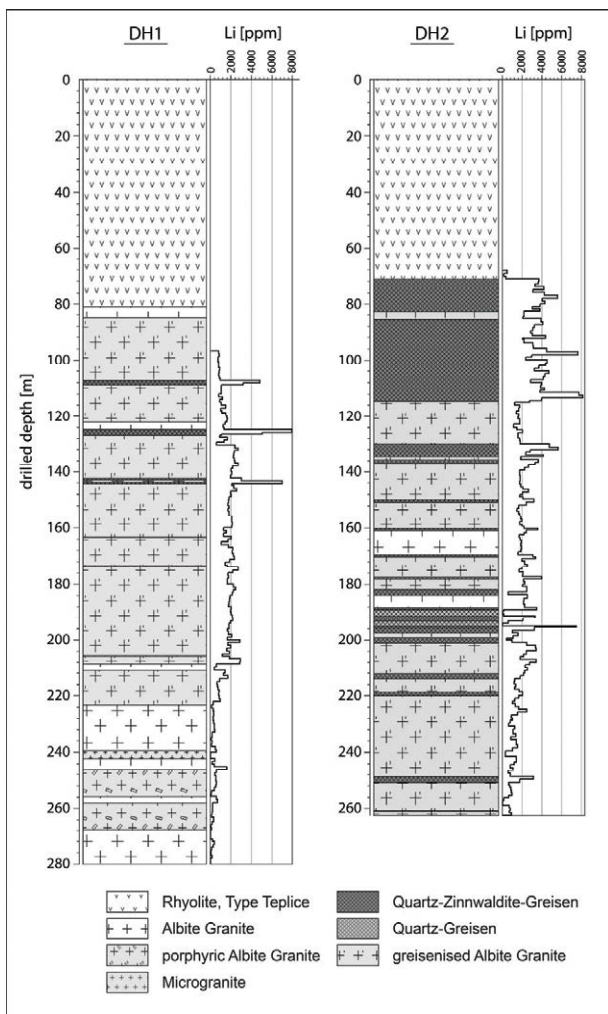
addition to other elevated incompatible elements (F, Rb, Sn, Ta), this indicates the highly specialised character of the intrusion. Underground channel samples revealed element contents which are comparable to drill core, both in magnitude and distribution characteristics.

The distribution of Sn and W within greisen mineralisation is more heterogeneous. Values range from 10 to 3,700 ppm for Sn and 20 to 320 ppm for W, respectively. No mean was calculated for these two elements, because of the considerably screwed distribution. Other elements of possible commercial interest that show elevated contents within the greisen mineralisation comprise Nb, Ta, Sc, Zn and F. Whereas Zn is thought to be completely hosted in Zinnwaldite, numerous possible by-products are tentatively associated with other minerals. This applies in particular to Rb and Nb/Ta that are thought to be hosted by alkali feldspar and Sn and W oxides, respectively.
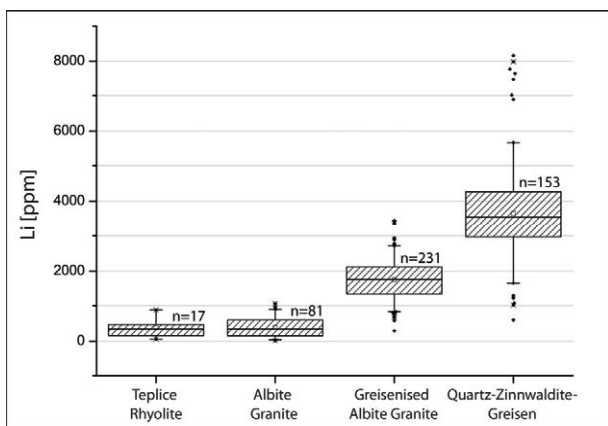
Figure 2: Box Plot of Li concentrations from different lithologies.

Even more complex is the situation for F that is contained as a structural component in zinnwaldite, fluorite and topaz. Scandium can be incorporated in numerous minerals as well, reported by Kempe and Wolf (2006). However, correlation data from whole rock geochemistry indicate a strong dependency of Sc with Li and Rb and hence no significant incorporation into minerals other than zinnwaldite.

The overall lithogeochemical character of the mineralisation shows the maximum enrichment of valuable elements in the apical part of the intrusion and decreasing contents of all mentioned elements with increasing depth.

5 Conclusions

Exploratory work confirms the overall character of the Zinnwald deposit in terms of lithology, mode of occurrence, mineralogy and geochemistry as documented in previous exploration reports.

Measured concentrations of lithium within the greisen ore of Zinnwald at least confirm values from past investigations. Moreover, results for Li contents obtained in the present exploration campaign consistently exceed values obtained during previous exploration campaigns. Statistic characteristics indicate an evenly distributed Li-concentration and therefore an uniform nature of Li-mica mineralisation within greisen ore lithologies. Analysis of Sn and W revealed, however, heterogenic character of their distribution and thus difficulties for the utilisation of historic data.

Acknowledgements

References

Bolduan H, Lächelt A (1960) Bericht der Staatlichen Geologischen Kommision der DDR über die Ergebnisse der Erkundungsarbeiten 1954/55 und 1958/60 mit Bohrungen auf Lithium in Zinnwald (Erzgeb.). Geologischer Dienst Freiberg (unpubl.); Geologisches Archiv LfULG - EB 0498

Breiter K, Sokolová M, Sokol A (1991) Geochemical specialization of the tin-bearing granitoid massifs of NW Bohemia. Miner Deposita 26:298-306

Cundy EK, Windle W, Warren IH (1960) The occurrence of zinnwaldite in Cornwall. Clay Miner Bull 4 (23):151-156

Grunewald, V (1978) Neueinschätzung Rohstofführung Erzgebirge, Gebiet Osterzgebirge, Metallogenie und Prognose Zinnwald. Ergebnisbericht, Berlin, 1975-1978, (unpubl.), Geologisches Archiv LfULG - EB 1391

Gottesmann B (1962) Über einige Lithium-Glimmer aus Zinnwald und Altenberg in Sachsen. Geol 11:1164-1176

Govindaraju K, Rubesska I, Paukert T (1994) 1994 report of zinnwaldite ZW-C analysed by ninety-two GIT-IWG member-laboratories. Geostand Newsl 18(1):1-42

Haynes L, Webb PC, Tindle AG, Ixer RA (1993) W-Sn-Mo-Bi-Ag mineralization associated with zinnwaldite-bearing granite from Glen Gairn, Scotland. Transactions - Institution of Mining and Metallurgy.Section B: Appl Earth Sci 102:211-214

Johan Z, Strnad L, Johan V (2012) Evolution of the Cinovec (Zinnwald) granite cupola, Czech Republic; composition of feldspars and micas, a clue to the origin of W, Sn mineralization. Can Mineral 50(4):1131-1148

Kempe U, Wolf D (2006) Anomalously high Sc contents in ore minerals from Sn–W deposits: Possible economic significance and genetic implications. Ore Geol Rev 28(1): 103-122.

Kühne R, Besser M (1989) Zwischenbericht Zinn Altenberg Suche 2, TG Zinnwald. VEB Geologische Forschung und Erkundung Freiberg (unpubl.), Geologisches Archiv LfULG - EB 2241

Lowell GR, Ahl M, Jones AP (2000) Chemistry of dark zinnwaldite from Bom Futuro tin mine, Rondonia, Brazil. Mineral Mag, 64(4), pp. 699-709

Novak M, Cern P, Selway JB (1999) The zinnwaldite-masutomilite-elbaite granitic pegmatite from the Trebic Durbachite Massif at Kracovice; a complex pegmatite related to the NYF family. Can Mineral 37(3):815-816

Rieder M, Huka M, Kučerová D, Minařík L, Obermajer J, Povondra P (1970) Chemical composition and physical properties of lithium-iron micas from the Krusné hory Mts. (Erzgebirge). Part A: Chemical composition. Contrib Mineral Petr 27:131-158

Rieder M, Cavazzini G; D'yakonov Yu S, Frank-Kamenetskii VA, Gottardi G (1998) Nomenclature of the Micas. Can Mineral 36: 905-912

Roda Robles E, Pesquera A, Gil-Crespo P, Torres-Ruiz J (2012) From granite to highly evolved pegmatite; a case study of the

Pinilla de Fermoselle granite-pegmatite system, Zamora, Spain. Lithos 153:192-207

Sala M (1999) Geochemische und mineralogische Untersuchungen an alterierten Gesteinen aus dem Kuppelbereich der Lagerstätte Zinnwald (Osterzgebirge). Diss. (unpubl.), Bergakademie Freiberg, pp. 103

Seifert Th (2008) Metallogeny and Petrogenesis of Lamprophyres in the Mid-European Variscides – Post-Collisional Magmatism and Its Relationship to Late-Variscan Ore Forming Processes (Bohemian Massif). IOS Press BV, Amsterdam

Seifert Th, Kempe U (1994) Zinn-Wolfram-Lagerstätten und spätvariszische Magmatite des Erzgebirges. Beih. z. Eur J Mineral 6:125-172. (in German)

Seifert Th, Gutzmer J (2010) Li-reiche Sn(-W-Polymetall)-Greisenlagerstätten im Freistaat Sachsen / Li-rich Sn(-W-polymetallic) deposits in Saxony. In: Voigt W (ed), Freiberger Forschungsforum: 61. Berg- und Hüttenmännischer Tag, 9. - 11. 06. 2010, TU Bergakademie Freiberg, FK 3: „Lithium for Li-Ion Batteries - Resources and Recovery", abstracts volume Fachkolloquium 3.

Starý J, Sitenský I, Hodková T (2011) Mineral Commodity Summaries of the Czech Republic – Ministry of Environment, Czech Geological Survey, Geofond:208

Štemprok M, Šulcek Z (1969) Geochemical Profile through an Ore-Bearing Lithium Granite. Econ. Geol. 64, 392-404.

Štemprok M, Seifert Th (2011) An overview of the association between lamprophyric intrusions and rare-metal mineralization. Mineralogica 42(2-3):121-162

Tischendorf G, Just G, Gottesmann B (1988) Distribution of elements at a contact albite granite/rhyolite, Zinnwald, Erzgebirge (G. D. R.). Chem Erde 48(2):155-162

Tischendorf G, Gottesmann B, Förster HJ, Trumbull RB (1997) On Li-bearing micas: estimating Li from electron microprobe analyses and an improved diagram for graphical representation. Mineral Mag 61:809-834

Uhlig J (1992) Zur Mineralogie und Geochemie der Granitoid- und Greisenglimmer aus Zinnlagerstätten des Sächsischen Erzgebirges und der Mongolei. Diss. (unpubl.), Bergakademie Freiberg, pp 129

Indium fractionation in the granites of SW England

B. Simons*, J.C.Ø. Andersen & R.K. Shail
Camborne School of Mines, University of Exeter, Tremough Campus, Penryn, TR10 9EZ.
*corresponding author: bjs207@exeter.ac.uk

Abstract. Biotite granites in SW England are enriched in Ge, In, and Sn whereas the topaz granites are enriched in Li, Ga, Nb, Ta, Sb and W. Within biotite granites the micas (biotite and muscovite) are the primary carriers of critical metals.

Analysis of metasediment samples from the Porthscatho formation, an analogue for the source of the granites, and subsequent trace element modelling indicates that a mantle contribution to the biotite granites is not required for the critical metals. A model with 30% partial melting of metasedimentary rocks and 10 to 50% subsequent fractional crystallisation is sufficient for the biotite granites to reach the observed indium concentrations. Topaz granites require a more complex model.

Keywords: Granite. Trace element modelling. Indium.

1 Introduction

1.1 Project rationale

The polymetallic mining district of SW England has been exploited for a variety of metals including tin (Sn), copper (Cu), zinc (Zn) and lead (Pb) since the Bronze Age with the last mine closing in 1998. Now, with the increasing need for speciality metals for new technological developments (in the following called critical metals) and increases in the price of traditional commodities such as Sn and Cu, the area is once again prospective. A combination of the traditional commodities (Sn, Cu) alongside critical metals (In, W) are key for current development at Hemerdon (Wolf Minerals) and exploration at South Crofty (Western United Mines), St. Columb (Treliver Minerals Ltd.) and Redmoor (New Age Exploration Ltd.). Despite the rich history of geological research in the region and current activities, there has been little research into the distribution of critical metals in the region.

There have been limited studies on the partitioning of the critical metals into the common silicate minerals. Sb, In and W in particular are elements that are poorly represented in partitioning studies, and there is very little information in the literature on how they become concentrated in the crust. This paper presents data for the abundance of critical metals in biotite and topaz granites of SW England and the major minerals in biotite granite and discusses a possible source of indium for the biotite granites.

1.2 Methods

A total of 70 samples have been collected to encompass the various granite types and other significant rock types present in SW England (e.g. lamprophyres, metasedimentary rocks). These samples have had the weathered edges removed, been crushed and ground using an agate barrel. For whole rock analysis, samples were analysed by an Agilent 7700 ICP-MS using the 4-acid digestion technique of Garbe-Schönberg (1993). Sample duplicates and standards were analysed with each sample batch. For metal distribution studies, individual minerals were handpicked from crushed material, washed and powdered using a mortar and pestle before 4-acid digestion and analysis by ICP-MS.

2 Study Area

2.1 Location and regional geology

The polymetallic mining district of SW England extends through the county of Cornwall into West Devon (Figure 1). The Early Permian Cornubian Batholith is exposed as a series of major plutons including, from west to east, the Isles of Scilly, Land's End, Tregonning-Godolphin, Carnmenellis, St. Austell, Bodmin Moor and Dartmoor granites. The batholith was emplaced into Devonian and Lower Carboniferous sedimentary and volcanic rocks that underwent low-grade regional metamorphism and deformation during the Variscan Orogeny. Magmatic activity spanned approximately 25 Ma with the earliest granite pluton dated at ~293 Ma and the youngest at 268 Ma (e.g., Chen et al. 1993; Chesley et al. 1993). Coeval basaltic magmatism is represented by basaltic lavas and lamprophyre dykes.

The region had several stages of mineralisation but the most widespread synbatholith polymetallic "lode" systems formed during variable mixing of S-bearing magmatic, meteoric and metamorphic fluids (Jackson et al. 1989). Establishing the distribution of critical metals in the granites themselves will aid understanding of where these metals are likely to be concentrated within the mineralisation systems.
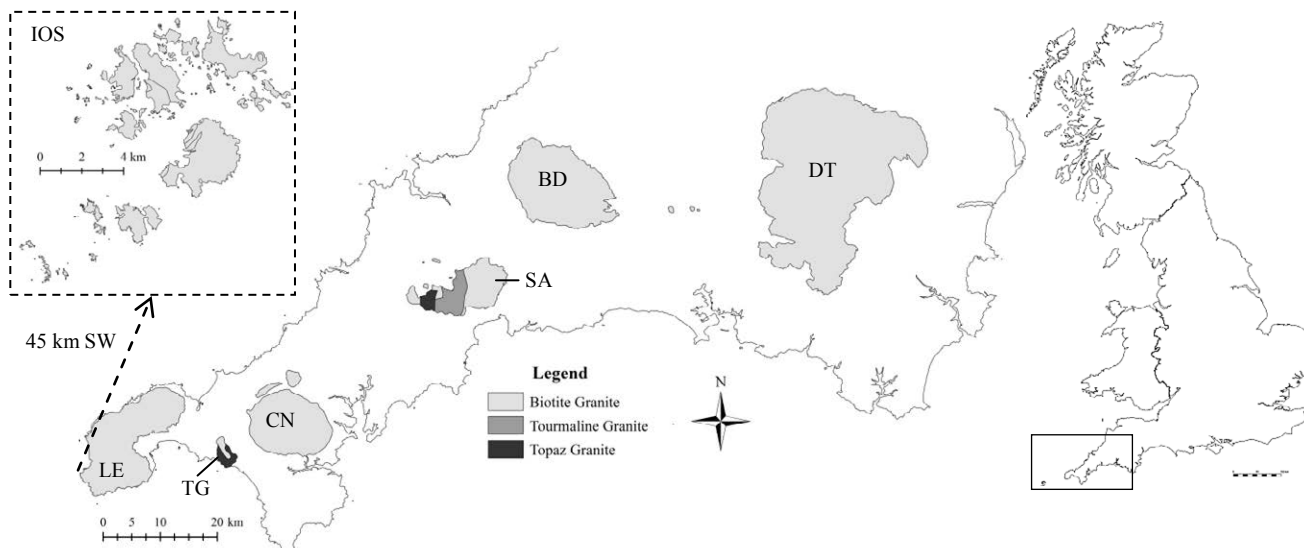
Figure 1. Map showing the study area summarising different granite types. Major plutons are marked: DT – Dartmoor, BD – Bodmin, SA – St. Austell, CN – Carnmenellis, TG – Tregonning-Godolphin, LE – Land's End and IOS – Isles of Scilly. Map modified after Manning et al. (1996) and Dangerfield & Hawkes (1981).

2.2 Granite characteristics

The granites are peraluminous with A/CNK values of >1.1, relatively low Na_2O (<3.2%) and restricted range of SiO_2 compositions. The batholith is enriched in As, B, F, Li, P, Sn and Zn amongst other elements, and contains ilmenite as the main ferrous phase (Chappell & Hine, 2006). Major element data from this study are in agreement with previous studies.

The granites can be subdivided by mineralogy into biotite, topaz and tourmaline granites with biotite granites accounting for over 90% of the upper parts of the batholith. These mineralogical classifications can be further refined texturally by variations in groundmass grain-size and varying abundance / size of alkali feldspar phenocrysts. The main granite types are accompanied by later stage aplites, quartz porphyry dykes and quartz-tourmaline rocks.
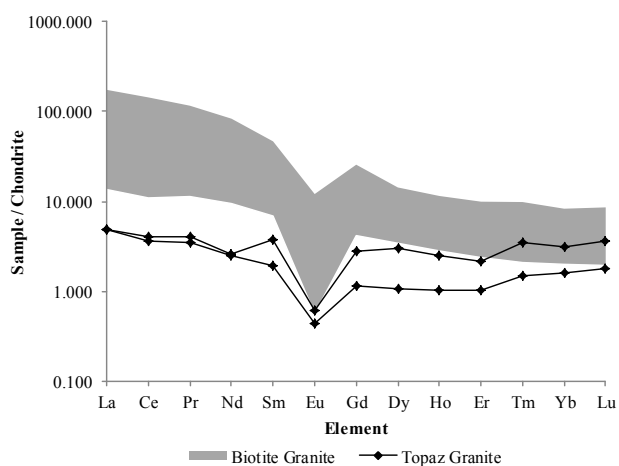
Figure 2. Chondrite normalised REE diagram showing the differences between the biotite and topaz granites. Chondrite values are from McDonough & Sun (1995).

The source of the granites has long been a subject of debate with various authors arguing for and against a mantle contribution. REE plots for biotite granite are consistent with a crustal source, showing strongly enriched LREE whereas the plots for topaz granites are largely flat with lower total REE. A negative Eu anomaly occurs in both granite types (Figure 2).

3. Critical metal distribution and source

3.1 Whole rock geochemistry

Whole rock samples were analysed by ICP-MS for Li, Be, Ga, Ge, Nb, In, Sn, Sb, Ta, W and Bi. The results (Table 1) define two distinct mineral groups that are significant for different granite types. Overall Be, Ge, In and Sn are more strongly enriched within the biotite granites, while Li, Ga, Nb, Sb, Ta, W and Bi are more enriched in the topaz granites.

Table 1. Table summarising the average abundances (ppm) of critical metals in SW England biotite and topaz granites compared to the average continental crustal abundances (Taylor & McLennan, 1985).

Element	Biotite granite	Topaz granite	Average crust
Li	268	1509	13
Be	7.14	4.83	1.50
Ga	20.01	24.52	18.00
Ge	2.59	1.29	1.60
Nb	13.63	61.14	11.00
In	0.11	0.06	0.05
Sn	11.51	6.35	2.50
Sb	0.24	0.67	0.20
Ta	2.75	16.49	1.00
W	4.17	30.69	1.00
Bi	0.45	1.04	0.06

3.2 Indium fractionation and source

Trace element modelling can aid in the determination of the possible source for critical metals within the biotite granites. Four samples of the Porthscatho Formation (Darbyshire & Shepherd, 1994), a metasedimentary rock into which the granites intruded, have also been analysed for a selection of metals using ICP-MS. These samples have been used as a bulk compositional analogue for a lower crustal granite source. Although derived from the upper plate during the final stages of Variscan convergence, their peri-Gondwanan Mid-Proterozoic basement source is likely to be similar to SW England lower crust and both these samples and granites have similar T_{DM} model ages (Shail & Leveridge, 2009).

Trace element modelling followed the method by Williamson et al. (2010) with equations for batch melting and Rayleigh fractionation. For the purpose of this exercise, all metals have been assumed to be completely incompatible with partition coefficients of 0. Consistent with Williamson et al. (2010), 30% and 50% partial melting with 10% and 50% fractionation have been modelled for each metal.

For In, combining 30% partial melting of Portscatho Formation sandstones with 10% and 50% crystal fractionation is sufficient to produce a range of In concentrations that account for the majority of concentrations of In in the granites (Figure 3).
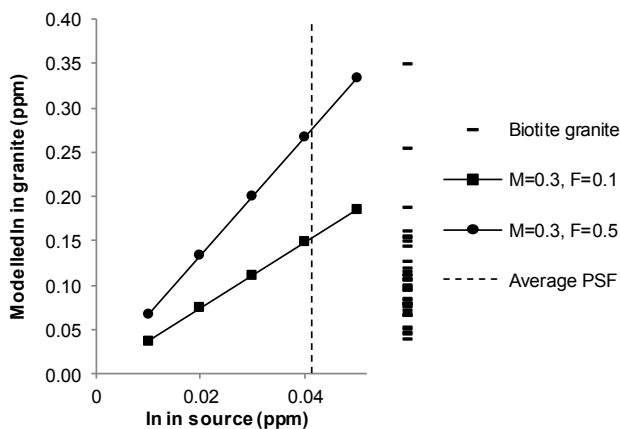
Figure 3. Modelled In concentrations expected in granites for different degrees of partial melting (M) and crystal fractionation (F). In contents of all biotite granites in this study (n=43) are also shown along with the average Portscatho Formation (PSF) In content (n=4).

Using a source value of 0.41 ppm In, the average value obtained in the analysis of the Portscatho Formation, partial melting of 30% and fractionation of <10% up to 50% is sufficient to obtain the range of In values observed in the granites. This implies that there is no need for a mantle contribution of material, at least in the biotite granites, as the source can provide enough material to account for the granite values. The same model also accounts for the range of Be, Ga, Ge, Nb, Sn, Sb, Ta and Bi within the biotite granites.

The topaz granites cannot be modelled using the above method and it is believed that there are different controls on the enrichment of these metals in the granites. With the flat REE profile for these granites, as shown above, it may be possible there is a mantle component process in these granites or there could be another fractionation process that is not yet understood.

3.3 Metal concentrations in silicate minerals

The major minerals found in biotite granite have been analysed for their critical metal content. Abundances are summarised in Table 2.

Table 2. Table summarising metal abundances (ppm) in major minerals of biotite granite. Qtz = Quartz; Kfs = Alkali Feldspar; Pl = Plagioclase; Bt = Biotite; Ms = Muscovite.

Element	Qtz	Kfs	Pl	Bt	Ms
Li	63.12	20.16	3.41	721.43	658.56
Be	0.54	0.43	0.10	13.04	40.74
Ga	2.83	9.78	1.38	80.20	80.24
Ge	1.05	0.85	0.12	10.13	3.63
Nb	1.04	1.00	0.09	101.51	49.81
In	0.01	0.02	0.00	0.05	0.07
Sn	1.12	3.46	0.05	48.74	77.65
Sb	0.12	0.29	0.02	3.45	0.53
Ta	0.46	0.40	0.03	37.08	22.11
W	0.67	1.25	0.12	21.69	67.51
Bi	0.33	0.21	0.02	0.61	0.13

The micas appear to be the major carriers of critical metals. This can be explained by their similar ionic charge and radius to other elements that are major constituents in micas. For example, the ionic radius of Mg^{2+} (0.86Å) is closely matched by Ge^{2+} (0.87Å), while In^{3+} (0.94Å) is only moderately larger. Substitution of the critical metals into the mica lattice appears to be a likely mineralogical control on the metal fractionation within the biotite granites.

4. Conclusions

Several critical metals are enriched relative to average continental crust, in the biotite and topaz granites of SW England. The metals can be broadly subdivided into two groups that help to outline the potentially fertile granite stocks that would be prospective for particular metals. Indium deposits would be expected (along with Ge and Sn) to be preferentially associated with the biotite granites, while Li, Ga, Nb, Sb, Ta and W would be expected to be associated with the topaz granites.

The source of the indium enrichment in biotite granites can be explained by partial melting of a metasedimentary host rock (similar to the Portscatho Formation) without any mantle involvement. The limited mantle contribution to the biotite granites is supported by isotope data (Darbyshire & Shepherd, 1985) as well as REE patterns. There are other controls on concentration of metals in the topaz granites.

The micas (biotite and muscovite) are the likely major hosts for many of the critical metals. This is in agreement with their ionic radii and charges, which make them compatible with other metals usually contained within these minerals.

Acknowledgements

References

Chappell BW, Hine R (2006) The Cornubian Batholith: an example of magmatic fractionation on a crustal scale. Res Geol 56:203-244

Chen Y, Clark AH, Farrar E, Wasteneys HAP, Hodgson MJ, Bromley AV (1993) Dichronous and independent histories of plutonism and mineralisation in the Cornubian batholith, southwest England. J Geol Soc London 150:1183-1191

Chesley JT, Halliday AN, Snee LW, Mezger K, Shepherd TJ, Scrivener RC (1993) Thermochronology of the Cornubian Batholith in southwest England: implications for pluton emplacement and protracted hydrothermal mineralisation. Geochim Cosmochim Acta 57:1817-1835

Dangerfield J, Hawkes, JR (1981) The Variscan Granites of southwest England: additional information. Proc Ussher Soc 5:116-120

Darbyshire DPF, Shepherd TJ (1994) Nr and Sr isotope constraints on the origin of the Cornubian batholith, SW England. J Geol Soc London 151:795-802

Garbe-Schönberg C (1993) Simultaneous determination of thirty-seven trace elements in twenty-eight international rock standards by ICP-MS. Geostand News 17:81-97

Jackson NJ, Willis-Richards J, Manning DAC, Sams MS (1989) Evolution of the Cornubian ore field, southwest England: Part II. Mineral deposits and ore-forming processes. Econ Geol 84:1101-1133

Manning DAC, Hill PI, Howe JH (1996) Primary lithological variation in the kaolinised St. Austell Granite, Cornwall, England. J Geol Soc London 153:827-838

McDonough WF, Sun, S (1995) The composition of the Earth. Chem Geol 120:223-253

Shail RK, Leveridge BE (2009) The Rhenohercynian margin of SW England: Development, inversion and extensional reactivation. C R Geoscience 341:140-155

Taylor SR, McLennan SM (1985) The continental crust: its composition and evolution. Blackwell Scientific Publications, Oxford

Williamson BJ, Müller A, Shail RK (2010) Source and partitioning of B and Sn in the Cornubian batholith of southwest England. Ore Geol Rev 38:1-8

The carbonatites of Mt. Vulture as a (re)source of rare earth elements

Giovanni Mongelli, Michele Paternoster, Giovanna Rizzo, Maria T. Cristi Sansone
Department of Sciences, University of Basilicata, Italy

Rosa Sinisi
Department of Nature and Earth Sciences, University of Sassari, Italy

Abstract. Mt. Vulture volcano is situated at the easternmost border of the Italian Apennine compressive front. It is a composite volcano whose activity was both explosive and effusive from middle to upper Pleistocene. The final volcanic products have carbonatitic composition and represent the object of this study. In particular, two lava flows (upper and lower) and a dyke were sampled and analyzed. The mineralogical assemblage is similar in all samples: calcite, clino- and/or orthopyroxene, melilite, phlogopite, amphibole and ± plagioclase are the primary minerals, while apatite, opaque minerals, ± rutile and ± zircon are the accessory phases. The main difference between analyzed rocks are the amounts of primary calcite and plagioclase, the Ba contents and the $(La/Yb)_{ch}$ values, larger in the lower lava flow. In all samples, rare earth elements have very high concentrations and show high LREE/HREE fractionation that, through the R-mode factor analysis and PCA extraction method, has been attributed at different mineral phases.

Keywords. Rare earth elements, alvikites, Pleistocene, Italy

1 Introduction

Rare earth elements are an interesting group of metals that have recently become quite useful in high-tech applications due to their unique catalyst, magnetic, and optical properties (for example, cell phones and laptops contain rare earth elements). Today they are strategic materials in the world economy and therefore the rapid rise in world demand for the rare-earth elements (REEs) has expanded the search for new REE resources (Tucker et al. 2012). In addition, the rare earth elements are a major research tool in studying igneous rock petrogenesis and the processes underlying the genesis of chemical sediments.

Different types of deposits concentrate different amounts of the rare earth elements depending on many factors, such as geochemical behavior of REEs within a selected geological system and the physico-chemical features of mineralizing fluids.

The most common REE deposits are associated with alkaline magmatic rocks, carbonatites, pegmatites, laterites and sulphide accumulations occurring in widespread areas of the Earth (mainly China, United States, Brazil, India, Russia and Australia). Among these, carbonatites and alkaline intrusive complexes, as well as their weathering products, are the primary sources of REEs (Long et al. 2010).

Carbonatites are igneous rocks composed of more than 50 modal per cent magmatic carbonate and containing less than 20 wt.% SiO_2 (Le Maitre 2002). They are usually associated with alkaline igneous rocks and the study of carbonatites-alkaline rocks association provide important clues to reconstructing mantle and crustal processes as well as the secular evolution of the mantle (e.g. Ray et al. 2000, and references therein). However, the increasing interest in carbonatites is led mainly by their high REE contents that are the highest in any igneous rocks. In addition, ores of Cu, Nb, Mo, fluorite, phosphate, and vermiculite are also associated with carbonatites (Xu et al. 2010) and increase their importance within the industrial minerals framework.

In southern Italy carbonatites occur at the Mt. Vulture volcanic area only. Literature related to these carbonatites is focused on the petrologic and geodynamic aspects of their genesis, which is still a matter of debate (e. g. Stoppa and Principe 1997; D'Orazio et al. 2007; Rosatelli et al. 2007; Stoppa et al. 2008). These studies, however, mainly concern the mineral chemistry and isotopic records, and data on REE concentration (D'Orazio et al. 2007; Rosatelli et al. 2007) are few.

The aim of this study, therefore, is to provide new chemical data for a set of carbonatitic rocks from the Mt. Vulture volcano, and to evaluate their potential of exploitable REE (re)source.

2 Geological setting

The southern Apennines are a roughly NW–SE oriented segment of a fold-and-thrust belt that belongs to the complex geodynamic setting characterizing the central Mediterranean. Since the Tortonian, the thrust front has migrated to the southeast due to the convergence of Africa and Europa plates (Gueguen et al. 1998), the rollback of a west dipping slab and the following back-arc basin opening to west (Malinverno and Ryan 1986).

Mt. Vulture is located at the outer edge of the Italian Apennine belt (Fig. 1) and represents the most striking example of an asthenospheric upwelling along slab wrench faults (Caracausi et al. 2012, and references therein). It is a relatively small stratovolcano composed both of pyroclastic deposits and lava flows. Its volcanic activity started at 742±11 kyr and continued until 142±11 kyr, interrupted by several long inter-eruptive periods (Büttner et al. 2006, and references therein). The volcanism is strongly silica undersaturated, from alkaline potassic to ultrapotassic affinities (De Fino et al. 1982, 1986). Giannandrea et al. (2006) have grouped the volcanic units in two distinct supersynthems: 1) Mt.

Vulture and 2) Monticchio units. The Mt. Vulture units are the oldest volcanic products and are represented by lavas and pyroclastic deposits that range in composition from basanite–foidite to phonolite. The Monticchio units are products of the most recent eruptions. They produced some maar-type vents with tuff aprons and have a carbonatitic–melilititic composition (Stoppa and Principe 1997).

According to D'Orazio et al. (2007), the studied rocks belong to a volcanic sequence erupted from a small volcanic center occurring at the north-western slope of the Mt. Vulture, in the Vallone Toppo Lupo site (Fig. 1). In particular, the samples comes to: (1) two distinct massive alvikite Ca-carbonatite lava flows, hereafter named upper (ULF) and lower (LLF) lava flow, that are divided by a 5-10 meters-thick pyroclastic level; (2) a 70 centimeter-thick, carbonatitic dyke (DY) cross-cutting both the lavas.
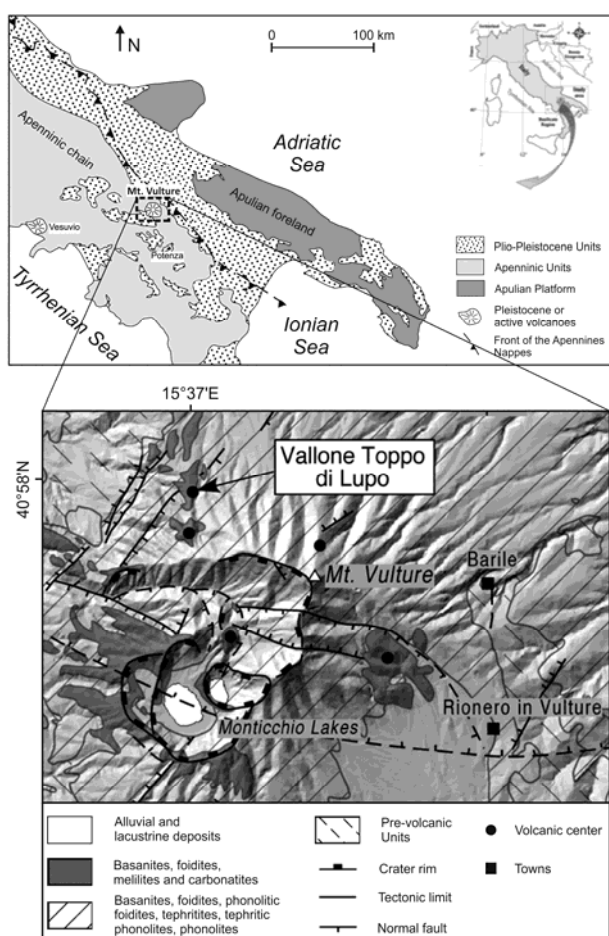
Figure 1. Geological sketch map of Southern Apennines and zoom of the Mt. Vulture volcano area (after Bentivenga et al. 2004 and D'Orazio et al. 2007, modified). The sampling site (Vallone Toppo di Lupo) is shown.

3 Analyses and results

All carbonatite samples were subjected to petrographic and chemical analyses. Thin sections were observed both with an optical polarizing microscope and an environmental scanning electron microscope (ESEM) XL30 Philips LaB6, equipped with an energy dispersion spectrometer (EDS). The abundances of major, trace, and RE elements were determined by inductively coupled plasma–mass spectrometer (ICP-MS), instrumental neutron-activation analysis (INAA), and thermal desorption mass spectrometry (TD-MS). Average errors are less than ±5%, except for elements occurring at concentrations of 10 ppm or less, for which the error is ±5–10%.

3.1 Petrography

The lavas and dyke show porphyritic texture. Large calcite and/ or pyroxene phenocrysts and wide calcite aggregates are widespread in a glass-bearing hypidiomorphic matrix. The optical microscope observations revealed the same mineralogical composition for the three volcanic rocks. The paragenesis consist of calcite, (clino- and/or ortho-) pyroxene, melilite, phlogopite, amphibole and ± plagioclase as primary minerals, and apatite, opaque minerals, ± rutile and ± zircon as accessory phases. Calcite, zeolite and rarely saussurite (as alteration phase of plagioclase in LLF only) are secondary phases.

Crystals of primary calcite show polysynthetic twinning and have prismatic to granular habit. Fine-grained crystals of secondary calcite instead are observed in amygdales where show various optical orientations. These amygdales, permeating the rocks, are often infilled also by zeolite and plagioclase.

The composition of amphibole is variable. It is richterite in the lavas and hastingsite in the dyke. The amphibole shows prismatic habit and often forms aggregates that rim the pyroxene.

In the analyzed rocks melilite, amphibole, and the accessory phases (mainly zircon, apatite and opaque minerals) are commonly pseudomorphs after, or enclosed by, pyroxene and/or phlogopite. Occasionally, phlogopite and amphibole form aggregates with pyroxene.

Some significant compositional differences among studied volcanic rocks were observed: the abundance of primary carbonate (calcite) in LLF is higher than those of both ULF and DY; in LLF the clinopyroxene contents are lower than those of the other analyzed rocks; large, mantle-derived xenoliths of clinopyroxene xenocrysts have been also found within lower lava samples only.

3.2 Chemistry

As for the chemical composition, CaO is the dominant oxide followed by SiO_2, Al_2O_3, and $Fe_2O_3(T)$ which, as expected for alvikites, show very low concentrations just like those of the remaining major element oxides.

The greater abundance of primary calcite of the lower lava samples, in respect to those of upper lava and dyke, determine for LLF a larger CaO content (ranging from 40.96 to 45.10 wt.%), a highest CaO/(CaO+MgO+FeO(T)+MnO) ratio (fluctuating in the 0.88-0.90 range) and lower amounts of the other principal oxides (SiO_2, Al_2O_3 and $Fe_2O_3(T)$) due to dilution effect. Among the major element oxides, only

P_2O_5 shows contents generally higher than 1.79 wt.% in keeping with the large amount of apatite observed.

Regarding trace elements, the transition metals (Sc, Cr, Co and Cu) and alkaline elements (Rb and Cs) have low contents. The actinides (Th and U) and Pb have generally low concentrations, except for LLF sample where these are appreciably higher. The amount of Sr and Ba is large in all samples. However the highest Ba concentrations are detected in the lower lava flow samples resulting in lower values of Sr/Ba ratio for this rock (from 0.68 to 0.98 for LLF and from 1.03 to 1.83 for ULF and DY).

The total amount of REE is high in all analysed rocks and ΣREE ranges between 1956 and 2404 ppm. The REE chondrite-normalized distribution patterns (Fig. 2, chondrite data are form Evensen et al. 1978) are characterized by a remarkable LREE/HREE fractionation and negative Eu anomalies (in the 0.80-0.86 range).
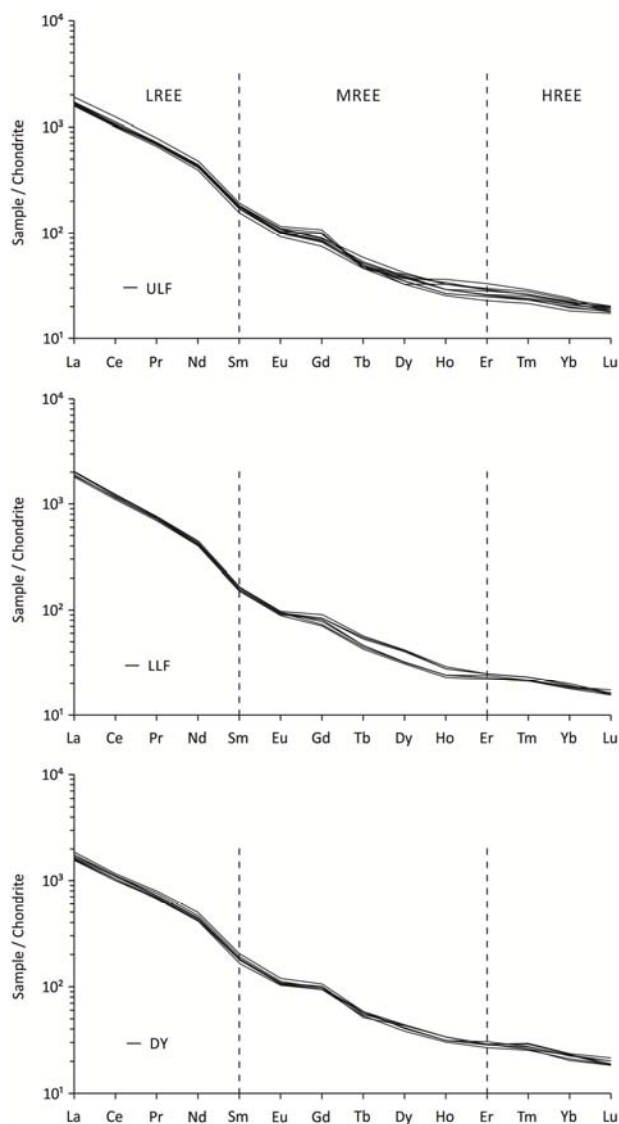
Figure 2. REE chondrite-normalized distribution patterns for upper lava (ULF), lower lava (LLF), and dyke (DY) samples.

The $(La/Yb)_{ch}$ index values, as well as the LREE/MREE fractionation (expressed as $(La/Sm)_{ch}$), is larger in LLF samples and in particular is from 100.0 to 110.2 for lower lava and between 71.7 and 88.8 for upper lava flow and dyke. On the contrary, the values of MREE/HREE fractionation, expressed as $(Gd/Yb)_{ch}$, are very similar in all samples (from 3.86 to 4.63).

4 Discussion and conclusions

Although the composition of most magmas can be represented by the basalt-andesite-rhyolite spectrum, some deviate from this trend and are compositionally unusual. These magmas give rise to volcanic rocks that are rare as well as economically significant due to their content of a wide range of ore-forming metals such as mainly Cu, P, Zr, U, Th and all rare earth elements.

To identify the mineral phases determining the REE enrichments in the Mt. Vulture carbonatites, the R-mode factor analysis were performed on ULF, LLF and DY samples using the StatGraphic® Centurion XVI.I software. To extract factors from the data sets, the Principal Components Analysis method was applied. This operation was performed on the standardized correlation matrix, thus weighting all the variables equally, and allowing us to convert the principal component vectors into factors. Subsequently, the factor loadings, which represent the correlation coefficients between the variables and the factors, were considered. The factor loadings forming the factor matrix are shown in Table 1.

	Factor 1	Factor 2	Factor 3
SiO_2	0.92		
CaO	-0.69	0.66	
P_2O_5		0.67	
Sc	0.89		
Ba	-0.83		
Sr			0.86
Zr	0.91		
Cr	0.68		
Co	0.84		
Cu	0.81		
La		0.85	
Yb	0.91		
ΣREE		0.93	
Pb		0.72	
Th	0.82		
U			0.55

Table 1. Factor matrix for the Mt. Vulture carbonatitic rocks resulting after Varimax rotation. Numbers are weights of the variables in the extracted factors. Variables having weight less than 0.55 are omitted.

Three factor were detected for carbonatites. The first factor includes most of the selected variables. Among these, CaO and Ba only show negative weights suggesting their independence from the other variables of this factor. The presence of both primary and secondary calcite in studied rocks justifies the weights of CaO in this factor. The association of Ba and CaO, instead, is due clearly to the previously stated presence of secondary Ba-bearing zeolite and calcite within amygdules widespread in the rock samples. The first

factor is also characterized by significant weights of SiO_2, as major element oxide, of all transition metals, Zr, Th and Yb, suggesting a clear relationship between silicate phases and all selected elements. It is a well known fact that pyroxene, phlogopite, and amphibole are able to host transition metals (Stoppa et al. 2005; Reguir et al. 2009). It is worthy of note, that in the Factor 1 the HREE only, represented by Yb, are included. The fractionation of heavy rare earths from the other REE may be likely ascribed to the presence of zircons, that commonly concentrate heavy REE (Harley and Kelly 2007) and Th in their crystal structure likely as inclusions (e.g. Seifert et al. 2012). In fact, besides Yb, also Zr and Th are contained within the first factor.

The Factor 2 comprises CaO and P_2O_5, as major element oxides, and Pb, La and total REE amount. It is obvious that the large content of apatite in the carbonatites determines the link between CaO and P_2O_5. However, also the presence of La enclose in this factor may be related to presence of apatite crystals suggesting the inclusion of LREE in this phase. In addition, it is no surprising that ΣREE contents are comprise in this factor. As previously noted, the Mt. Vulture carbonatites are characterized by very high values of LREE/HREE fractionation index suggesting the higher concentrations of light RE elements than those of heavy RE elements in these rocks. The Pb and CaO relationships, instead, likely involves that most of the lead in the Mt. Vulture carbonatite is housed in calcite, according to the fact that Pb contents detected in calcite from carbonatite are not negligible (Chen and Simonetti 2012).

The third factor includes only Sr and U, proving that these two elements are not related to the main mineral phases of carbonatites but likely to accessory phases enclosed in their glassy matrix.

Acknowledgements

References

Bentivenga M, Coltorti M, Prosser G, Tavarnelli E (2004) A new interpretation of terraces in the Taranto Gulf: the role of extensional faulting. Geomorphology 60:383–402

Büttner A, Principe C, Villa IM, Bocchini D (2006) $^{39}Ar-^{40}Ar$ geochronology of Monte Vulture. In: Principe C (Ed.), La Geologia del Monte Vulture. Grafiche Finiguerra, Lavello (Italy), pp. 73–86

Caracausi A, Martelli M, Nuccio PM, Paternoster M, Stuart FM (2012) Active degassing of mantle-derived fluid: A geochemical study along the Vulture line, southern Apennines (Italy). JVol Geo Res doi.org/10.1016/j.jvolgeores.2012.12.005

Chen W, Simonetti A (2012) In-situ determination of major and trace elements in calcite and apatite, and U–Pb ages of apatite from the Oka carbonatite complex: Insights into a complex crystallization history. Chem Geol, doi: 10.1016/j.chemgeo.2012.04.022

De Fino M, La Volpe L, Piccarreta G (1982) Magma evolution at the Mount Vulture (Southern Italy). Bulletin of Volcanology 45:115–126

De Fino M, La Volpe L, Peccerillo A, Piccarreta G (1986) Petrogenesis of Mount Vulture volcano (Italy): inferences from mineral chemistry, major and trace elements data. Contributions to Mineralogy and Petrology 17:135–145

D'Orazio M, Innocenti F, Tonarini S, Doglioni C (2007) Carbonatites in a subduction system: The Pleistocene alvikites from Mt. Vulture (southern Italy). Lithos 98:313–334

Evensen NM, Hamilton PJ, O'Nions RK (1978) Rare earth abundances in chondritic meteorites. Geochim Cosmochim Acta 42:1199–1212

Giannandrea P, La Volpe L, Principe C, Schiattarella M (2006) Unità stratigrafiche a limiti inconformi e storia evolutiva del vulcano medio-pleistocenico di Monte Vulture (Appennino meridionale, Italia). Boll Soc Geol It 125:67–92

Gueguen E, Doglioni C, Fernandez M (1998) On the post-25 Ma geodynamic evolution of the western Mediterranean. Tectonophysics 298:259–269

Harley SL, Kelly NM (2007) The impact of zircon–garnet REE distribution data on the interpretation of zircon U–Pb ages in complex high-grade terrains: An example from the Rauer Islands, East Antarctica. Chem Geol 241:62–87

Le Maitre RW (2002) Igneous Rocks: A Classification and Glossary of Terms. Cambridge University Press, Cambridge, UK

Long KR, Van Gosen BS, Foley NK, Cordier D (2010) The principal rare earth elements deposits of the United States - A summary of domestic deposits and a global perspective: U.S. Geological Survey Scientific Investigations Report 2010–5220, 96 pp., available at http://pubs.usgs.gov/sir/2010/5220

Malinverno A, Ryan WBF (1986) Extension in the Tyrrhenian sea and shortening in the Apennines as a result of arc migration driven by sinking of the lithosphere. Tectonics 5:227–245

Ray JS, Ramesh R, Pande RK, Trivedi J, Shukla P, Patel PP (2000) Isotope and rare earth element chemistry of carbonatite±alkaline complexes of Deccan volcanic province: implications to magmatic and alteration processes. Journal of Asian Earth Sciences 18:177–194

Reguir EP, Chakhmouradian AR, Halden NM, Malkovets VG, Yang P (2009) Major- and trace-element compositional variation of phlogopite from kimberlites and carbonatites as a petrogenetic indicator. Lithos 112S:372–384

Rosatelli G, Wall F, Stoppa F (2007) Calcio-carbonatite melts and metasomatism in the mantle beneath Mt. Vulture (southern Italy). Lithos 99:229–248

Seifert W, Förster HJ, Rhede D, Tietz O, Ulrych J (2012) Mineral inclusions in placer zircon from the Ohře (Eger) Graben: new data on "strontiopyrochlore". Mineralogy and Petrology 106:39–53

Stoppa F, Principe C (1997) Eruption style and petrology of a new carbonatitic suite from the Mt. Vulture, southern Italy: the Monticchio lakes Formation. J Volc Geotherm Res 78:251–265

Stoppa F, Rosatelli G, Wall F, Jeffries T (2005) Geochemistry of carbonatite-silicate pairs in nature: A case history from Central Italy. Lithos 85:26–47

Stoppa F, Principe C, Giannandrea P (2008) Comments on: Carbonatites in a subduction system: The Pleistocene alvikites from Mt. Vulture (southern Italy) by d'Orazio et al., (2007). Lithos 103:550–556

Tucker RD, Belkin HE, Schulz KJ, Peters SG, Horton F, Buttleman K, Scott ER (2012) A major light rare-earth element (LREE) resource in the Khanneshin carbonatite complex, southern Afghanistan. Econ Geol 207:197–205

Xu C, Wang L, Song W, Vuet M (2010) Carbonatites in China: A review for genesis and mineralization. Geoscience Frontiers 1:105–114

Stable isotope and trace element constraints to the origin of carbonate rocks in the Korsnäs Pb-REE deposit, Western Finland

Akseli Torppa
Geological Survey of Finland, P.O. Box 1237, FI-70211, Kuopio, Finland

Juha A. Karhu
Department of Geosciences and Geography, P.O. Box 64, FI-00014, University of Helsinki, Finland

Abstract. We have examined archived drill-cores of intrusive carbonate rocks from the Korsnäs Pb-REE deposit in western Finland. The samples were studied for their major and trace element compositions, and isotope ratios of C and O. The deposit was operated in the 1960's and 70's, yielding a total 36 000 tons of Lanthanide concentrate as a by-product of Pb beneficiation. The origin of the dike swarm that hosts the mineralization, whether related to hydrothermal, late-stage igneous, or carbonatitic processes, has remained controversial, however. Our new results set geochemical constraints to the origin of these rocks, and will be used as a basis for further studies on the deposit that represents a mile stone in the Finnish mining history, and one of the first large-scale rare earth element (REE) mines in Europe.

Keywords. Finland, Pb-REE Deposit, Rare Earth Element, Stable Isotope

1 Introduction

The Korsnäs Pb-REE deposit is located on the westernmost flank of the mainland Finland ca. 25 km south of the town of Vaasa (Fig. 1). It comprises a network of several hundred carbonate dikes and veins, ranging in width from centimetres to meters, and one larger mass, the Svartören dike, that hosts the main ore body. The Svartören dike is a 1.5 km long and 5-30 m wide intrusion of carbonate rock in an N-S trending bedrock fracture that extends down to a depth of at least 350 m (Isokangas 1975). The ore body was mined by the Outokumpu Oy in 1961-1972 yielding a total of 45 000 tons of Pb and 36 000 tons of lanthanide concentrate (Himmi 1975). The average ore grade was 3.6% Pb and 0.9% RE_2O_3, with galena, apatite, and monazite as the principal ore minerals (Papunen and Lindsjö 1972).

Geologically, the Korsnäs deposit is contained within the Paleoproterozoic metasedimentary rocks of the South Ostrobothnian Schist Belt (SOSB) belonging to the Svecofennian accretionary arc complex of the central Fennoscandian Shield. In the western parts of SOSB, the bedrock consists predominantly of migmatized, ca. 1.9 Ga mica schist and gneiss, with intercalations of pyroxene-amphibole schist and gneiss, meta-chert, and graphite-bearing layers of sulphide schist. Plutonic rocks are relatively sparse, mainly represented by Svecofennian ca. 1.89-1.87 Ga granitoids and minor mafic to ultra-mafic intrusions (Nykänen 1960 Lehtonen *et al* 2005). The Korsnäs deposit was emplaced
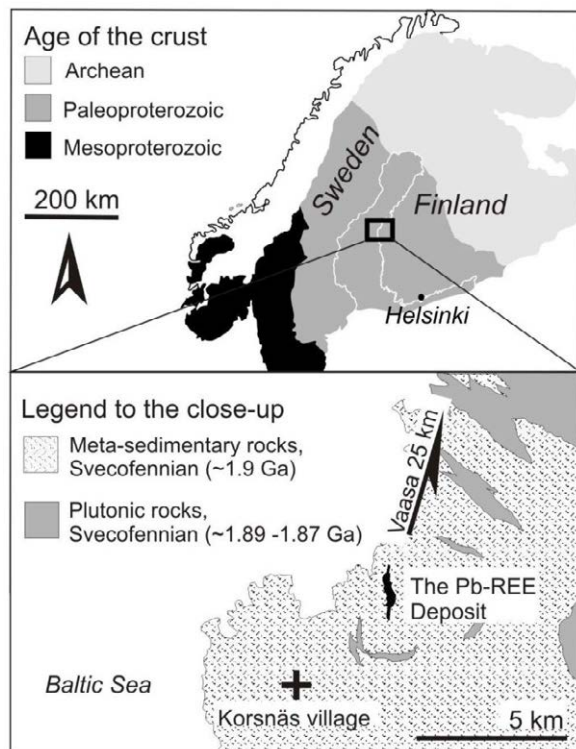
Figure 1. Study area on a simplified geological map of the Fennoscandian Shield. The close-up shows the location of the Korsnäs Pb-REE deposit

within the SOSB rocks around 1.8 Ga (Papunen 1986), forming an assemblage of carbonate dikes, calc-silicate-barite-sulphide vein-dikes, skarn rocks, and granite pegmatites, in a strongly sheared fracture zone. The emplacement of the dike swarm caused a hydrothermal imprint on the country rocks, displayed by chloritization and intense weathering on the hanging wall side of the main ore body (Eskola *et al.* 1961, Björklund, 1966, Papunen & Lindsjö 1972, Isokangas 1975).

The carbonate and calc-silicate dikes and veins form a mineralogically heterogeneous group, with calcite as the major constituent, along with variable amounts of diopside, apatite, barite, amphibole, sphene, scapolite, and a number of accessory minerals including exceptionally well-developed varieties of harmotome and apophyllite in crystal cavities. Near the contacts to the granite pegmatites, megacrysts of feldspar have occasionally formed. The distribution of ore minerals in the deposit is sporadic; galena occurs both dispersed in

the groundmass, and as crosscutting veinlets and clusters in the dikes and skarns, often together with pyrite, pyrrhotite, and other sulphides. Apatite, which is the main REE carrier, with up to 6% RE_2O_3, occurs as phenocrysts in the dikes and veins, and also in the skarn rocks, apparently followed by monazite and sometimes allanite (Eskola 1961, Björklund 1966, Papunen & Lindsjö 1972).

There are a number of reports and layman's articles about the Korsnäs Pb-REE deposit and mine, but the scientific papers are few and mainly concern crystallographic and mineralogical topics (Sahama 1965, Sahama and Lehtinen 1967, Papunen and Lindsjö 1972, Rehtijärvi and Kinnunen 1979, Akagi *et al.* 1997). In the lack of published geochemical and isotopic data, the origin of the Korsnäs dike swarm has remained controversial; whether hydrothermal, late-stage igneous, or carbonatitic. Here we report the first results of our research project in which the Korsnäs deposit is studied by geochemical and isotope geochemical methods. In this paper, we focus on the C and O isotope ratios and the whole-rock geochemical characteristics of the intrusive carbonate rocks.

2 Sampling and analyses

Samples for this study were collected from the national drill core archive of the Geological Survey of Finland (GTK). The Korsnäs deposit itself does not have any known outcrops, as it is situated in the lowlands of the Finnish west coast, and the old mine tunnels have collapsed and filled with water. A total of 5 km of drill core has been studied in this first part of the study, of which seven representative whole-rock samples of carbonate and calc-silicate rocks were selected for analyses. In addition, the isotope ratios of C and O were measured from the groundmass calcite in a total of 22 dikes and veins, and from six samples of idiomorphic calcite crystals collected from crystal cavities.

The whole-rock geochemical XRF and ICP-MS analyses were carried out in the Labtium Oy, Espoo, Finland. The C and O isotopic IRMS analyses were carried out in the Department of Geosciences and Geography of the University of Helsinki, Finland. The isotopic results are expressed as conventional δ-notations relative to the VPDB and VSMOW standards for $\delta^{13}C$ and $\delta^{18}O$, respectively.

3 Geochemical and Isotopic Data

3.1 Major, Trace and Rare Earth Elements

The Korsnäs data are divided in two groups: the Svartören samples of the main ore body and the calc-silicate dikes and veins in the surroundings of the ore body. Major and trace element data for representative samples from the both groups are presented in Table 1.

Korsnäs #1 represents a fine-grained, massive to slightly sheared calcite rock from the main ore body at Svartören, with some barite, apatite, and galena as accessory minerals.

Korsnäs #2 represents a 20-25 cm wide calc-silicate dike (or *carbonate-silicate-barite-sulphide dike*) from

Sample	Korsnäs #1	Korsnäs #2	Average Carbonatite
SiO_2 (wt. %)	0.06	19.90	2.72
TiO_2	n.d.	0.01	0.15
Al_2O_3	n.d.	6.80	1.06
Fe_2O_3t	0.18	15.10	2.25
MnO	0.24	0.11	0.52
MgO	0.15	0.70	1.80
CaO	52.50	26.15	49.12
Na_2O	n.d.	0.86	0.29
K_2O	n.d.	1.90	0.26
P_2O_5	0.05	0.04	2.10
CO_2	43.27	20.68	36.64
S	0.15	6.11	0.41
Cl	0.01	0.01	0.08
Ba (ppm)	3850	16000	3045
Rb	n.d.	50	14
Sr	6360	19900	7272
Th	n.d.	4	52
U	<1	4	9
Y	109	16	119
Zr	60	133	189
Nb	n.d.	1	1204
Ta	n.a.	n.d.	5
Pb	1220	13500	56
Cr	n.d.	14	13
Ni	30	231	18
La (ppm)	903	133	608
Ce	1790	257	1687
Pr	228	31	219
Nd	925	121	883
Sm	128	17	130
Eu	30	10	39
Gd	86	14	105
Tb	8	1	9
Dy	25	4	34
Ho	4	1	6
Er	8	2	1
Tm	1	0.1	1
Yb	5	1	5
ΣYREE	4250	607	3846

Table 1. Chemical compositions of two representative samples of the Korsnäs carbonate rocks. Composition of an average calcite carbonatite by Woolley and Kempe (1989) is given as a reference.

the surroundings of the ore body, composed of coarse grained calcite, diopside, and barite, with abundant galena, pyrite, and pyrrhotite, and accessory fluorite.

In general, the Svartören sample does not differ significantly from an average carbonatite given as reference from Woolley and Kempe (1989), in regard to the data for major elements, LILE, and REE, with an exception of the very high concentration of Pb. The sample shows, however, notably low contents of HSFE, especially Nb that characterizes typical carbonatites. The calc-silicate dike sample, on the contrary, differs from both Svartören and the reference data with clearly higher contents of SiO_2, Fe_2O_3, Al_2O_3, and S, and also with very high contents of LILE, especially Ba and Sr, but rather low contents of HSFE (yet higher than the Svartören sample), and with significantly lower concentrations of REE. The LREE to HREE ratios show variable enrichments towards LREE for both samples.

With respect to the geochemical characteristics, the samples in our dataset that are not represented in numbers mostly resemble those given as examples in Table 1. However, there are also some variations, especially in the group of calc-silicate dikes. One of the samples in that sub-group shows distinctly lower Ba

content than the others, while another sample differs with clearly higher contents of REE (as seen in Fig. 2). In this sense, the group of samples from the Svartören ore body is much more homogeneous, with the only exception presented by one sample that is notably lower in REE than the others (Fig. 2.). Clearly more data are needed, however, to precisely bracket the studied rocks in distinct geochemical groups
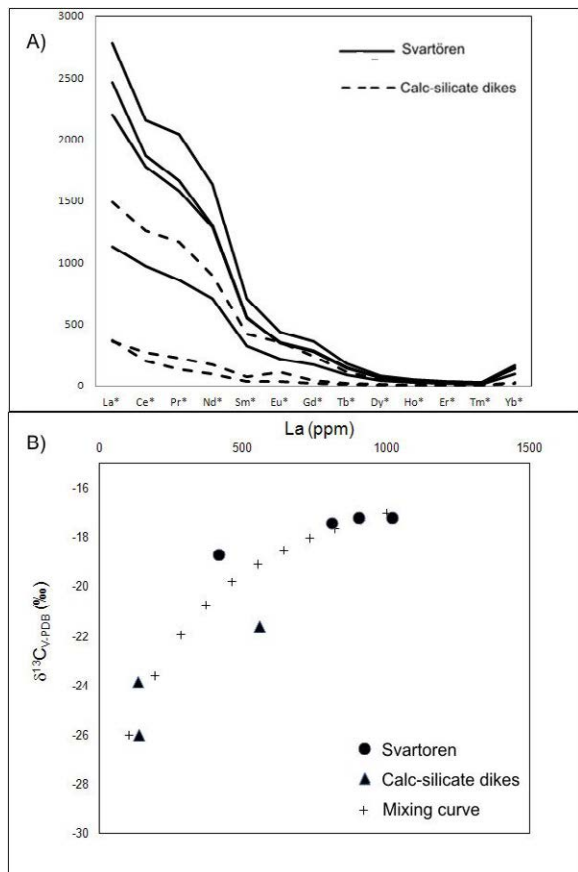
Figure 2. A) Chondrite-normalized (Taylor and McLennan 1985) REE patterms for the Korsnäs samples **B)** Lanthanum vs. $\delta^{13}C$ for the same dataset. Mixing curve describes a simple binary mixture between samples with the highest and lowest lanthanum concentration

3.2 C and O isotopes

Data for the C and O isotopic compositions of calcite in the studied rocks are shown in Figure 3. The open circles include data for both the Svartören ore body and smaller dikes and veins. Around 70% of the values range from -17 to -19 ‰ for $\delta^{13}C$ and +10 to +12 ‰ for $\delta^{18}O$; including the studied Svartören samples (black circles). These data are bracketed in Figure 3. and labelled as "Korsnäs bulk values". A smaller set of samples display a range of $\delta^{13}C$ values from -20 to -26 ‰, with a fairly constant $\delta^{18}O$ at around +11 ‰. These data include the studied calc-silicate dikes and veins (black triangles).

The crystal cavity calcites (open diamonds) form a distinct group of their own, characterized by large variations for both $\delta^{13}C$ and $\delta^{18}O$, with the $\delta^{18}O$ values exclusively falling above +15 ‰.
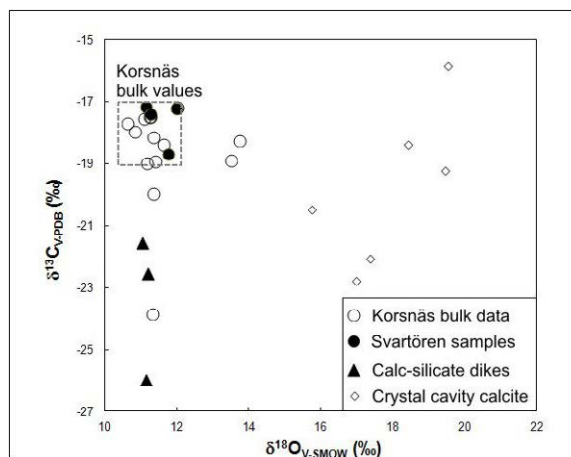
Figure 3. Carbon and oxygen isotopic data for calcite in the Korsnäs samples.

4 Discussion and conclusions

REE, Y, Ba, and Sr contents of the carbonate rocks from the Svartören ore body are identical to those of an average carbonatite, supporting the idea presented already in the 1960's that the occurrence could be carbonatitic in origin (Isokangas 1975). However, the idea is not consistent with our isotope data, since the $\delta^{13}C$ values measured from the Korsnäs rocks fall clearly out of the typical range of mantle-derived carbonatites, which extends from -3 to -7 ‰, (Deines 1989). More precisely, our data display that the bulk volume of the intrusive carbonate material that forms the Pb-REE deposit yields $\delta^{13}C$ values ranging from -17 to -19 ‰, and those of $\delta^{18}O$ from +10 to +12. This large negative $\delta^{13}C$ values are usually associated with fractionation processes in the Earth's surface environments and, thus, suggest a crustal source for carbon in the studied rocks. A mantle-derived origin for the dike swarm cannot be ruled out, but would require extensive modification of the carbon isotope composition of the source material.

Björklund (1966) suggests an igneous-hydrothermal origin for the Korsnäs intrusion, related to granitic magmatism. He also proposes that diopside and scapolite, which always occur together with pyrite and pyrrhotite in the intrusion, formed through an interaction between the hydrothermal fluid and host rocks. This could be a feasible explanation for some characteristics in our data as well, given that the studied calc-silicate dikes, which are rich in these minerals, also show a wide range of distinctly low $\delta^{13}C$ values and are relatively depleted in REE (Fig. 2). Following this hypothesis, the minor dikes and veins could be late-stage aqueous-hydrothermal emanations from an originally carbonate-dominated fluid or melt, which were capable of oxidizing graphite from the host rocks, and as a consequence precipitate metal sulphides, but not carrying large concentrations of REE. A simple binary mixture between the end members of our rock data, illustrated in Figure 2B, can possibly demonstrate some of these interactions. In any case, it seems likely that hydrothermal processes have played a key role in the formation of the Korsnäs Pb-REE deposit.

The exceptionally well-developed varieties of calcite, harmotome, apophyllite, and a plethora of other cavity minerals from the Korsnäs deposit are well-known among mineral collectors worldwide and also gained lots of scientific interest at one time. Rehtijärvi and Kinnunen (1979) report a substantially young K/Ar age of 88 Ma for apophyllite in one crystal cavity. Also, our C and O isotope data for the cavity calcites (Fig. 3.) are in line with the post-depositional crystal growth. The $\delta^{13}C$ values are possibly adopted from the intrusive carbonate rocks, but the range of large positive $\delta^{18}O$ values suggests calcite growth in equilibrium with low-temperature waters, probably of meteoric origin.

Acknowledgements

References

Akagi T, Nakai S, Masuda A (1997). In-pattern tetrad effect like variation, so far overlooked, but obviously observed in REE abundances of REE minerals. Geochemical Journal 32: 135-141

Björklund A (1966). Om Korsnäs blyglansförekomst och dess geologi. Unpublished Master's Thesis, University of Helsinki

Deines P (1989). Stable isotope variations in carbonatites. In: Bell K (ed) Carbonatites Genesis and Evolution, Unwin Hyman, London: 301-359

Eskola K, Tuominen H, Palviainen M, Autio M (1961). Geologia, Outokumpu Oy:n Korsnäsin kaivos. Vuoriteollisuus - Bergshanteringen 19: 23-33

Himmi R (1975). Outokumpu Oy:n Korsnäsin ja Petolahden kaivosten vaiheita. Summary in English: the history of Korsnäs and Petolahti mines. Vuoriteollisuus Bergshanteringen 33: 35–38

Isokangas P (1975). The Mineral Deposits of Finland. Unpublished licenciate thesis, University of Helsinki, Finland

Lehtonen MI, Kujala H, Kärkkäinen N, Lehtonen A, Mäkitie H, Mänttäri I, Virransalo P, Vuokko J (2005). Etelä-Pohjanmaan alueen kallioperä. Summary in English: Pre Quaternary rocksof the South Osthrobothnian Schist Belt. Geological Survey of Finland, Report of Investigation 158, 155 p.

Nykänen O (1960). Suomen geologinen kartta, kallioperäkartan selitys 1:100 000, lehti 1242, Korsnäs. Summary in English: The geological map of Finland, explanation to the map of rocks, 1:100 000, sheet 1242, Korsnäs, Geologinen Tutkimuslaitos, Helsinki, 34 p.

Papunen H, Lindsjö O (1972). Apatite, monazite, and allanite, three rare earth mineral from Korsnäs, Finland. Bulletin of Geological Society of Finland 44: 75-79

Papunen H (1986). Korsnäs In: Papunen H, Haapala I, Rouhunkoski P (eds.) Suomen Malmigeologia Metalliset Malmiesiintymät, Suomen Geologia Seura r.y. 317 p.

Rehtijärvi P, Kinnunen KA (1979). Fluid and mineral inclusions and inclusion zones of cavity calcite from Korsnäs mine, western Finland. Bulletin of the Geological Society of Finland 51 (1-4): 75-79

Sahama ThG (1965). Yellow apophyllite from Korsnäs Finland. Mineralogical Magazine 34: 406-415

Sahama ThG, Lehtinen M (1967). Harmotome from Korsnäs Finland. Mineralogical Magazine 36: 444-448

Taylor S.R., McLennan S.M. (1985). The continental crust: Its composition and evolution. Blackwell, Oxford. 312 p.

Woolley AR, Kempe DRC (1989). Carbonatites: Nomenclature, average chemical compositions, and element distribution. In: Bell K (ed) Carbonatites, Genesis and Evolution, Unwin Hyman, London: 1-14

Emerging Li-potential in Kaustinen

Wik Henrik & Laxström Heidi
Geological Survey of Finland, Western Finland Office, P.O. Box 97, FI-67101, Kokkola, Finland

Ahtola Timo & Kuusela Janne
Geological Survey of Finland, Southern Finland Office, P.O. Box 96, FI-02151, Espoo, Finland

Abstract. The Kaustinen region of Central Ostrobotnia in Western Finland, situated in the Pohjanmaa schist belt between the Central Finland Granite complex and the Vaasa Migmatite complex, has long been known for its potential for high-tech metals and lithium in particular. The area has been subject to exploration work by several private companies during the past decades. Today there are some 20 known Lithium pegmatite occurrences in the area with a combined geological resource exceeding 11 Mt. The Geological Survey of Finland (GTK) has been exploring the area during the past 10 years. Three hard rock lithium deposits have been reported to the Ministry of Employment and the Economy (TEM), Leviäkangas and Syväjärvi in 2010 and Rapasaaret in 2012. The exploration work, by the GTK, in the area comprises mainly of boulder mapping, diamond drilling, geophysical ground surveys and re-assaying of old till sample material which had been kept in storage for almost 40 years. The assay result have revealed several sub-areas in the region with the potential for future discoveries.

Keywords. Lithium, Spodumene, Pegmatite, Sodium-peroxide fusion

1   Regional geology

The Kaustinen Li-province is located in the Fennoscandian shield within the 350 km long Pohjanmaa schist belt, a 70 km wide arc shaped belt between the Central Finland Granite complex in the east and the Vaasa Migmatite complex in the west (Figure 1). The schist belt comprises of Svecofennian 1.95-1.88 Ga greywackes and mica schists with intercalations of sulphide bearing black schists and volcanic metasediments. Lithium pegmatites in the Kaustinen area belong to the albite-spodumene subgroup of LCT (Li, Cs, Ta) pegmatite family of Černý & Ercit (2005). These paleoproterozoic, 1.79 Ga old (Alviola et al. 2001), pegmatites crosscuts the Svecofennian supracrustal rocks post dating the 1.89-1.88 Ga peak of regional low to high amphibolite facies metamorphism (Mäkitie et al., 2001).

2   Exploration history

The first indication of spodumene bearing pegmatites in the Kaustinen was found by the farmer Mr. Arvo Puumala in 1959. Subsequently the area has been subject to exploration work by Suomen Mineraali Oy in the 1960's, Paraisten Kalkki Oy in the 80's and Keliber Oy since 1999.

3   GTK Exploration work

GTK's exploration work in the Kaustinen area begun in 2003 marked by the launch of the "Industrial mineral mapping"- project. The initial work focused on re-logging and assaying of historical drill cores. Field work commenced a year later in 2004.
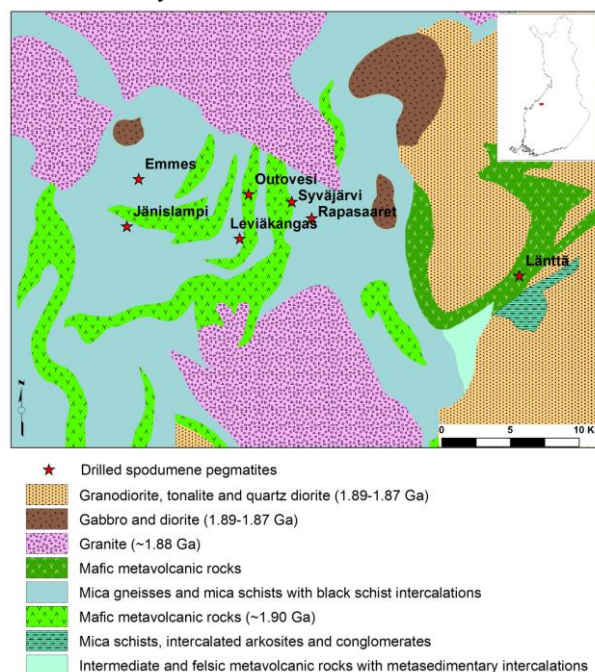
Figure 1. Regional geological map of the Kaustinen Li area, after Korsman et al. (1997), and the locations of the drilled spodumene pegmatites.

The Kaustinen area is poorly exposed and geological fieldwork was mainly done through boulder mapping and digging of 27 excavation pits to study the glacial transportation of the Li-pegmatite boulders.

The results indicated a transport distance of less than 2 km from, approximately, a 330-340° direction.

Geological maps of the reported deposits were drawn based on drill core information and geophysical data.

GTK conducted a low altitude high resolution airborne magnetic and radiation survey over the Kaustinen area in 2004 as a part of an exploration program for ilmenite deposits. The data was also utilized in the exploration work for Li-pegmatites. Ground magnetic-, gravimetric and electromagnetic surveys were carried out over selected targets in 2006-2011.

During the period 2003-2012 GTK has drilled 155 diamond drill holes (total 17 km) in eight study areas of the Kaustinen Li-province (Ahtola et al. 2010).

4 The known Li resources of the Kaustinen area

As of today there are 7 deposits in the Kaustinen area, with a combined calculated mineral resource of 11 Mt with an average grade of approximately 1.0 % Li_2O. The deposits are listed in table 1.

Table 1. Known lithium resources of the Kaustinen area. *JORC compliant mineral resource (Measured + Indicated) @ 0.5 % cut-off (Lovén and Meriläinen 2011).

Deposit	Tonnage	Li_2O wt%
Leviäkangas	2.10	0.70
Syväjärvi	2.60	0.98
Rapasaaret	3.70	1.02
Länttä*	1.30	1.08
Outovesi*	0.29	1.49
Emmes	1.1	1.30
Jänislampi	0.06	0.50

4.1 Leviäkangas

The Leviäkangas spodumene pegmatite was discovered by Suomen Mineraali Oy in the 1960's. Two decades later Paraisten kalkki Oy continued the exploration work by drilling 12 diamond drill holes into the deposit.

Drilling done by the GTK in 2006 to 2008 (2032 m/22 DDH) resulted in a definition of a 500 m long and 1-20 meter wide spodumene pegmatite dyke with an indicated resource of 2.1 Mt grading 0.7 wt% Li_2O (Ahtola et al. 2010). The results were reported to the TEM in 2010. As a result of international tender in 2011, the claim of Leviäkangas was transferred to Keliber Oy in 2012.

4.2 Syväjärvi

The Syväjärvi lithium deposit was also discovered by Suomen Mineraali Oy and later explored by Paraisten Kalkki Oy. The 2006-2010 drilling (2547 m /24 DDH) conducted by the GTK delineated a dyke along a distance of 500 with spodumene pegmatite bodies varying in with between 1-22 m. On the basis of solid modeling the Syväjärvi deposit contains a 2.6 Mt indicated mineral resource with 0.98 wt% Li_2O (Ahtola et al. 2010). The Syväjärvi claim was transferred to Keliber Oy at the same time with Leviäkangas.

4.3 Rapasaaret

The Rapasaaret spodumene pegmatites were discovered by GTK in 2009. The two separate dyke swarms have a length of 700 and 275 meters (figure 2). Thickness of the dykes varies from 1 m to 24 m. On the basis of solid modelling, the Rapasaaret deposit contains a 3.7 Mt indicated mineral resource at 1.02 wt% Li_2O.The estimation is based on 26 diamond drill holes (3653 m)

drilled in 2009-2011 of which 8 were done during the KaLi-project (Lithium resources of the Kaustinen region) which was partly financed by the European Regional Development Fund (ERDF) and coordinated by the GTK. The Rapasaaret Li deposit was reported to the TEM in 2012. The Ministry will open a tender for the deposit in the near future.
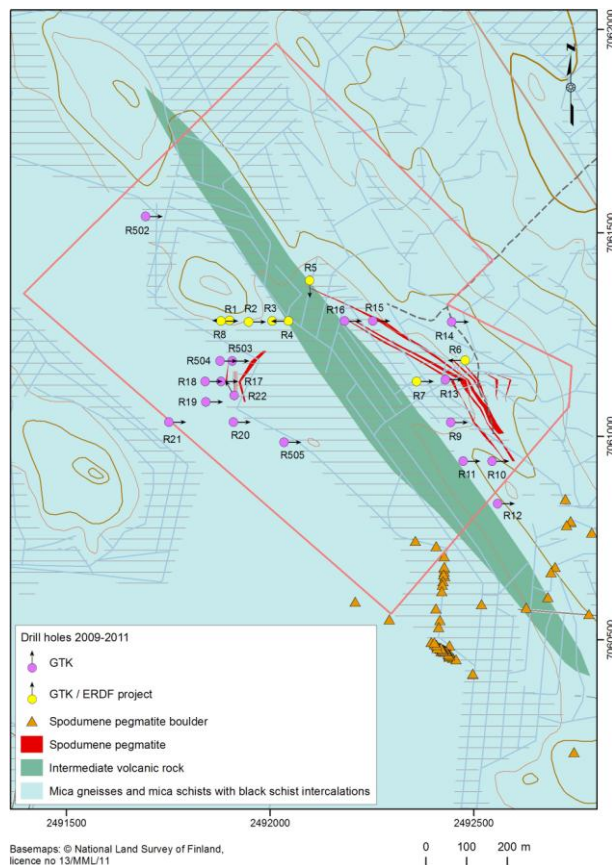
Figure 2. Geological map of the Rapasaaret lithium pegmatite deposit (Kuusela et al. 2011).

4.4 Länttä and Outovesi

The Länttä and Outovesi deposits are owned by the private company Keliber Oy. The JORC compliant mineral resource (Measured + indicated) of the two deposits are 1.3 Mt grading 1.08 wt% Li_2O for Länttä and 0.29 Mt at 1.49 wt% Li_2O for Outovesi respectively (Lovén P and Meriläinen M, 2011). The Länttä project is fully permitted and production is estimated to begin in 2014.

5 KaLi-project

The KaLi-project (Kaustisen seudun Li-potentiaali) was launched in mid 2010 to intensify the Li-exploration work in the area. The project was partly financed by the ERDF. Apart from the 8 diamond drill holes drilled at Rapasaaret, exploration work was also conducted on a regional scale, consisting of boulder mapping and till geochemistry, including re-assaying of old till sample material. The field work was mainly conducted during 2010 to 2011. The project ended in December 2012.
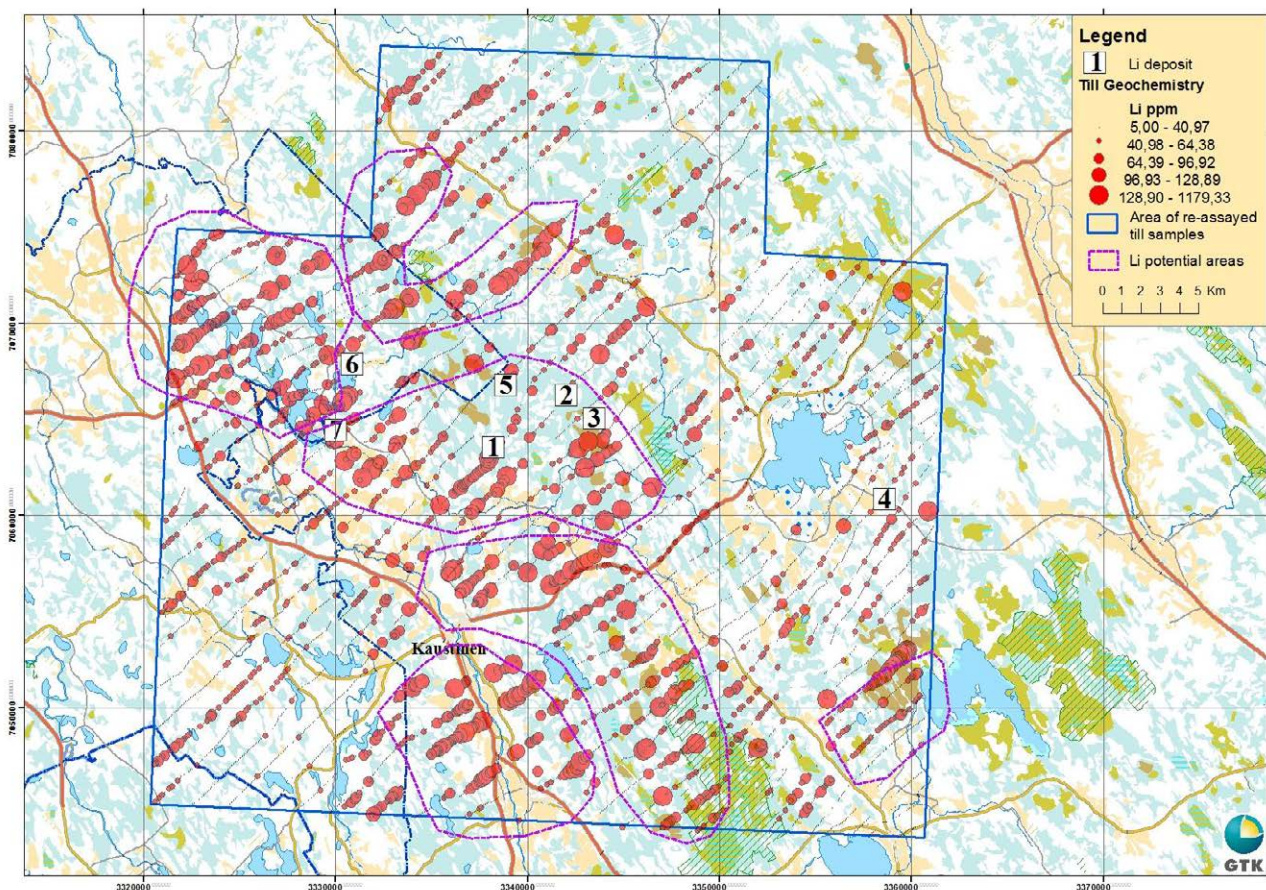
Figure 3. Li content in till. Values below detection limit (10 ppm) have been assigned to 5 ppm. Lithium deposits in the area Leviäkangas (1), Syväjärvi (2), Rapasaaret (3), Länttä (4), Outovesi (5), Emmes (6) and Jänislampi (7). Base map: © National Land Survey of Finland, License no 13/MML/12

5.1 Re-assaying of old till samples

A regional till sampling program was conducted by the GTK from the early 1970's through to the mid 1980's over selected areas in Finland. Samples were collected along lines preferably designed perpendicular to the direction of the ice movement and ideally also perpendicular to lithological units. Sample line separation varied between 500 to 2000 meters and with 100-400 meters between sampling sites. Average sample depth was 2.4 m but with large variations within the data set. The samples were semi-quantitatively assayed for base metals and major elements (17 elements). No assays for Li were done.

Utilizing this material for re-assaying, as part of the regional work, was one of the main outcomes of the KaLi-project. The sample material had been kept in storage in GTK's facility in Kuopio. A test batch consisting of 542 samples was submitted to Labtium Oy's laboratory for assaying.

5.2 Analytical methods

For the test batch the 0.06-0.5 mm fraction was selected because the idea was that there would be more Spodumene in relation to micas in this fraction. The samples were milled (Ring mill) in a carbon steel bowl (Method 40/Labtium). A Sodium peroxide fusion was made on a 0.2 g sub sample, since spodumene is hardly

digested in Aqua Regia. Analyses on the fusion were done using ordinary ICP-AES technique (720P) for 22 elements. This technique was used on all the samples and in addition a multi element analyse package was made on most of the samples for 41 elements using ICP-MS and ICP- OES on Aqua Regia digestion (method 515PM) (Kontoniemi 2012).

6 Results

The results from the test batch were extremely encouraging and a decision was made to have samples from the entire area re-assayed using the methods described above. In all 7120 samples were re-assayed.

Some of the Li anomalies in the till, depicted in figure 3, can be explained by known occurrences of spodumene pegmatites like the Leviäkangas, Syväjärvi and Rapasaaret deposits in the central part of the area. The Emmes and Jänislampi areas also show a strong Li anomaly in the till down ice of the deposits. Worth noticing, however, is the relatively poor expression of Li in the till over the Länttä deposit in the east.

Apart from the anomalies around the known occurrences there are several subareas within the Kaustinen region which show elevated Li contents in the till. For example there are strong till anomalies to the northwest and northeast of Emmes and Jänislampi deposits and to the south of Kaustinen municipality. Another area standing out as a fairly well defined Li anomaly is the Venetjoki lake area in the southeast.

Further exploration work will be required to locate the source of these till anomalies and for the full potential of the Kaustinen lithium province to be revealed.

References

Ahtola T, Kuusela J, Koistinen E, Seppänen H, Hatakka T, Lohva J (2010) Report of investigation on the Leviäkangas lithium pegmatite deposit in Kaustinen, Western Finland. 30 p. Geological Survey of Finland. Mineral deposit report. M19/2323/2010/32

Ahtola T, Kuusela J, Koistinen E, Seppänen H, Hatakka T, Lohva J (2010) Report of investigation on the Syväjärvi lithium pegmatite deposit in Kaustinen, Western Finland. 30 p. Geological Survey of Finland. Mineral deposit report. M19/2323/2010/44

Alviola R, Mänttäri I, Mäkitie H, Vaasjoki M (2001) Svecofennian rare-element granitic pegmatites of the Ostrobothnia region, western Finland; their metamorphic environment and time of intrusion. Geological Survey of Finland, special paper 30:9-29.

Černý P, Ercit TS (2005) The classification of granitic pegmatites revisited. The Canadian mineralogist 43:2005-2026.

Kontoniemi O (2012) Kaustisen alueen Li-potentiaali - vanhojen moreeninäytteiden uudelleenanalysointi, 12 p. Archival report. 69/2012

Korsman K, Koistinen T, Kohonen J, Wennerström M, Ekdahl, E, Honkamo M, Idman H, Pekkala Y (1997). Bedrock map of Finland 1:1 000 000

Kuusela J, Ahtola T, Koistinen E, Seppänen H, Hatakka J, Lohva J (2011) Report of investigations on the Rapasaaret lithium pegmatite deposit in Kaustinen-Kokkola, Western Finland. 42/2011. Currently confidential mineral deposit report.

Lovén P and Meriläinen M (2011) Mineral resource and ore reserve estimation of the Länttä and Outovesi lithium deposits. Outotec OY. http://www.keliber.no/getfile.php/Keliber-/Keliber%20Mineral%20Resource%20Reserve%20Statements%20Final.pdf

Mäkitie H, Kärkkäinen N, Lahti SI, Alviola R (2001) Compositional variation of granitic pegmatites in relation to regional metamorphism in the Seinäjoki region, Western Finland, Geological Survey of Finland: Special paper 30: 31-59.

The Ngualla rare earth element deposit, Tanzania

W.K. Witt[1], D.P. Hammond[2] & R. Townend[3]

[1.] The Walter Witt Experience, 122 Edward Street, Bedford WA 6052, Australia
[2.] Peak Resources Limited, 2/46 Ord Street, West Perth, WA 6005, Australia
[3.] Roger Townend and Associates, 4/40 Irvine Drive, Malaga, WA 6090, Australia

Abstract. The Ngualla carbonatite complex in southwest Tanzania comprises a central plug of "ferrocarbonatite" (actually magnesiocarbonatite) within an annular calcite carbonatite. Apatite and monazite are present in the calcite carbonatite and apatite is locally enriched where the carbonatite magma mingled and mixed with mica-rich (glimmerites) magmas. Weathering of calcite carbonatite has further concentrated apatite as a residual mineral following dissolution of $CaCO_3$. Rare earth elements (REE) are concentrated in the "ferrocarbonatite" as synchesite and bastnaesite where it occurs in miarolitic domains interstitial to ferroan dolomite. Weathering of the "ferrocarbonatite" in structurally-controlled zones has upgraded the REE concentration by dissolution of $MgCO_3$ and $CaCO_3$, leaving a porous goethite- and barite-rich rock without significant modification of the REE mineralogy. The Southern Rare Earth and Southwest Alluvials Zones contain a Mineral Resource of 40 Million tonnes at 4.07% TREO with low Th and U that are amenable to further concentration through acid leaching and solvent extraction processes.

Keywords. Carbonatite, rare earths, phosphate, igneous, regolith, Tanzania

1 Introduction

The Ngualla Project in southwest Tanzania contains a JORC compliant total Mineral Resource of 40 million tonnes at 4.07% total rare earth element oxides (TREO) at a 3% TREO cut-off grade (Peak Resources, 2013). The resource is contained within the Southern Rare Earth and Southwest Alluvials Zones and, at the time of the maiden resource in February 2012, was the fifth largest rare earth deposit outside China and the highest grade of the world's seven largest deposits. The carbonatite complex also contains concentrations of apatite and niobium that are being assessed for their economic viability.

This report describes the geology and mineralisation of the Ngualla carbonatite complex. The rare earth and apatite mineralisation developed in two stages: a magmatic stage followed by further concentration as a result of weathering.

2 Geology of the Ngualla carbonatite complex

2.1 Igneous geology

The Ngualla carbonatite complex has a circular outline with a diameter of approximately 4 km by 3.5 km and is probably pipe-like in form. It was intruded into Precambrian gneisses, quartzites and rhyodacitic volcanic. The age of the intrusive complex is uncertain but a K-Ar age of 1,040 (±40) Ma for igneous biotite was determined by Cahen and Snelling (1966). Country rocks surrounding the carbonatite complex have been hydrothermally altered to alkali feldspar, biotite and riebeckite by K- and Na-rich fluids expelled by the crystallizing carbonatite magmas. The resulting "fenite" alteration zone produced by this process is up to 1km wide, is relatively resistant to erosion and therefore forms a ring of hills surrounding the carbonatite intrusion.
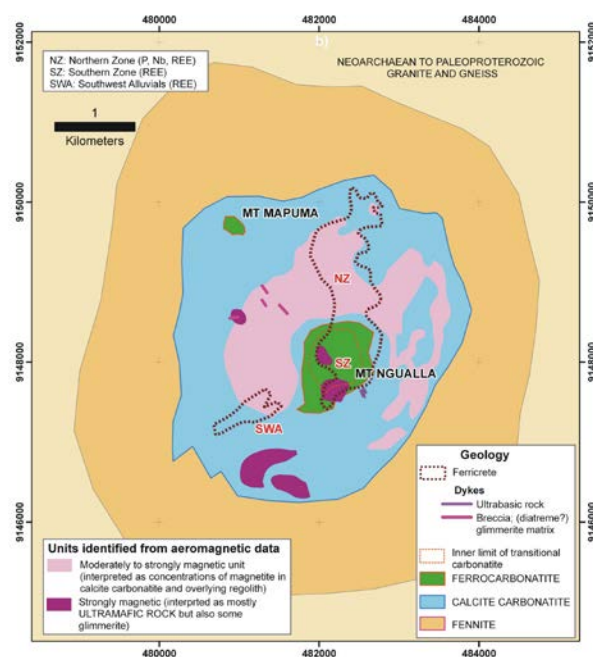
Figure 1. Interpreted geology of the Ngualla carbonatite complex.

The predominant components of the complex are an annular calcite carbonatite and a central plug of "ferrocarbonatite" (Figure 1). Whole-rock geochemical data indicate that the latter is actually magnesiocarbonatite but the term "ferrocarbonatite" is used locally to distinguish the central plug from barren magnesiocarbonatite dykes with a similar bulk composition (Figure 2a). Magnesiocarbonatite dykes cut the calcite carbonatite but these are cut by "ferrocarbonatite" dykes emanating from the central plug. The contact between the central plug and the annulus is a 200 metre wide zone of "ferrocarbonatite" dykes and calcite carbonatite xenoliths known locally as

the transitional carbonatite. A second "ferrocarbonatite" plug is exposed at Mt Mapuma in the northwest part of the complex (Figure 1). The calcite carbonatite and "ferrocarbonatite" are distinguished by their Ba/P ratio (Ba/P >77 in "ferrocarbonatite").

Calcite is the dominant component of calcite carbonatite, and is accompanied by variable phlogopite, richteritic amphibole, magnetite apatite and minor to trace ilmenite, monazite and sulphides (mainly pyrrhotite). "Ferrocarbonatite" is predominantly ferroan dolomite with interstitial (miarolitic cavities) quartz, calcite, barite, fluorite and rare earth fluorocarbonate minerals (synchesite, bastnaesite). The abundance of these minerals appears to increase inwards from the margins of the "ferrocarbonatite" plug. Segregations of hematite – barite form ovoid to irregular bodies up to several metres within the central part of the "ferrocarbonatite" plug. Sulphides, where present, are minor and pyrite is dominant.

In addition to the carbonatite phases, several silicate-rich phases have been distinguished within the complex (Figure 1). These are generally poorly exposed but can be recognised as strong magnetic anomalies. Silicate-rich phases are olivine-bearing ultramafic rock and mica-rich glimmerite. Exploration drilling and outcrops present extensive structural and textural evidence for mingling between carbonatite and silicate-rich magmas.

2.2 Weathering processes

Different modes of weathering highlights compositional differences between calcite carbonatite and "ferrocarbonatite". Outcrops of calcite carbonatite are relatively fresh since weathering proceeds mainly by dissolution of calcite. Calcite carbonatite is recessive in outcrops of mixed calcite carbonatite and "ferrocarbonatite". The central "ferrocarbonatite" plug is partly obscured by ferricrete, which now forms a ridge as a result of topographic inversion. Where exposed, "ferrocarbonatite" weathers through oxidation of $FeCO_3$ and dissolution of $MgCO_3$ and $CaCO_3$ components of ferroan dolomite. This process results in significant mass reduction and a porous goethite-rich regolith unit with very low S.G. (1.84). Quartz, barite and rare earth minerals are unaffected by weathering and are residually enriched in the goethite-rich regolith. Further oxidation of goethite to hematite involves a volume reduction of 27% and a more compact, higher density rock (S.G. ~2.28) but does not seem to result in further upgrading of rare earths. Weathering of the Ngualla "ferrocarbonatite" is concentrated in several north- to northeast-trending zones that probably reflect structurally weak fracture or fault zones, and is also apparently concentrated along some contacts between carbonatite and ultramafic units.

3 Rare earth and other mineralisation

3.1 Igneous processes

Rare earth elements are enriched in the central "ferrocarbonatite" relative to the calcite carbonatite and magnesiocarbonatite, but the calcite carbonatite is the main source of phosphate. Total rare earth oxide (REO) concentrations in the calcite carbonatite are generally <0.25% and are concentrated in monazite. Within the "ferrocarbonatite", %TREO increases inwards from about 0.5% or less in the transitional carbonatite to 1 to 2% in the centre of the intrusion. The central "ferrocarbonatite" contains rare earth elements in fluorocarbonate minerals (bastnaesite, synchesite), which are found associated with quartz, calcite, fluorite and barite in miarolitic cavities that are interstitial to ferroan dolomite crystals. Rare earth elements, along with other chemical components rejected by ferroan dolomite (Si, Ba, F), were enriched by *in situ* fractional crystallization of the "ferrocarbonatite" magma. Local, very high primary %TREO grades (3 to 5%) are found in proximity to some ultramafic units; however, this rare earth element enrichment is not present in proximity to all ultramafic units. The "ferrocarbonatite" mineralisation is characterised by lower HREE/LREE compared to the calcite carbonatite.

Phosphate occurs as apatite, mainly in the calcite carbonatite, where concentrations as high as 6% P_2O_5 are found, commonly as intervals of mixed calcite carbonatite and glimmerite where water clear, colourless to pale yellow crystals form aggregates at the contact zones between the two rocks types. Phosphate concentrations in the central "ferrocarbonatite" plug are characteristically <0.5% although there is minor enrichment (to about 1%) where the carbonatite contains inclusions of the same ultramafic unit associated with TREO enrichment (see above).

Percent Nb_2O_5 is generally <0.15% and Ta_2O_5 <20 ppm in all Ngualla rock types, below the weathering interface. Although some higher grades have been intersected, no clear relationship to rock types has been recognized. The Ta_2O_5 and Nb_2O_5 concentrations are well correlated.

3.2 Weathering processes

Economic mineralisation at Ngualla is closely related to weathering, for all commodities. *The Southern Rare Earth Zone* is centred on Mount Ngualla where rare earth mineralisation is hosted by *in situ* iron oxide and barite-rich weathered "ferrocarbonatite" and underlying fresh "ferrocarbonatite". The depth of weathering is extremely variable and appears to be partly structurally controlled. Grades of >3% total REO are common within the iron oxide-rich material, which extends from surface to depths of up to 140 metres. Petrographic studies of the iron oxide-rich saprolite indicate that rare earths are present as bastnaesite and synchesite and that *in situ* weathering of the "ferrocarbonatite" has not significantly modified the rare earth mineralogy relative to the primary source. Upgrading of the rare earth grades in the regolith by up to 300% is caused by residual concentration of rare earth minerals (bastnaesite, synchesite) resulting from the mass reduction following dissolution of $CaCO_3$ and $MgCO_3$ and conversion of
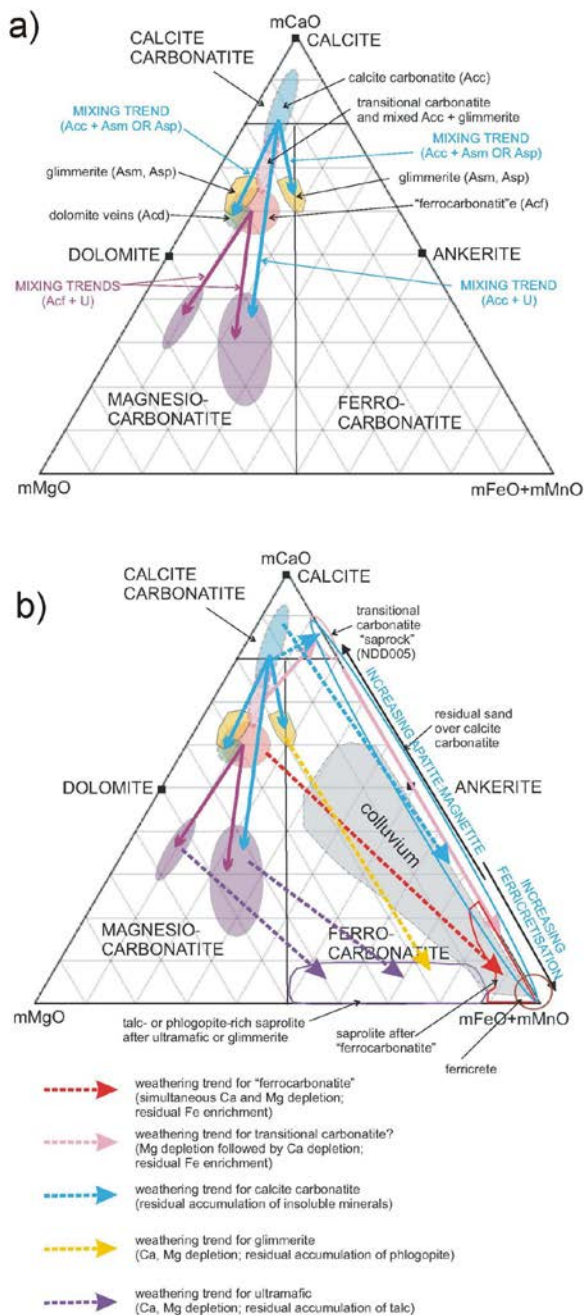
Figure 2. Triangular mCaO-mMgO-mFeO diagrams a) showing fields of rock types belonging to the Ngualla carbonatite complex, and some interpreted magma mixing trends also defined by whole rock (drill sample) data; b) showing fields of primary rock types and interpreted weathering trends; also shown are fields of ferricrete and colluvium.

FeCO$_3$ to goethite (hydrated iron oxide). RC drill chips in the saprolite ore zone typically comprise residual goethite dust and insoluble barite with characteristic negative crystal shapes produced by dissolution of ferroan dolomite. A minor component of the Southern Zone Rare Earth Zone resource is hosted by colluvium deposited in an erosional channel incised into the barren transitional carbonatite. In contrast to the mineralogy in the central "ferrocarbonatite" plug and its overlying regolith, rare earths in the colluvium are hosted by monazite and lesser cerianite, as well as bastnaesite. This colluvium was probably formed partly by erosion of

adjacent calcite carbonatite.

Rare earths are also concentrated in the *Southwest Alluvial*s. a Recent alluvial deposit derived from the central "ferrocarbonatite" plug and adjacent areas of calcite carbonatite. Consequently, rare earths are hosted by variable proportions of bastnaesite, monazite and cerianite.

No phosphate resource has yet been estimated by Peak but primary apatite in calcite carbonatite has been upgraded by weathering in the *Northern Zone*. Dissolution of calcite resulted in upgrading of primary apatite concentrations from about 6% P$_2$O$_5$ to produce residual phosphate concentrations of >20% P$_2$O$_5$.

Apatite is accompanied by fine-grained goethite and variable amounts of other insoluble minerals (phlogopite, amphibole, magnetite) but coarse, idioblastic magnetite (commonly pseudomorphed by hematite) is the most consistent additional mineral. Triangular (mCaO – mMgO – mFeO+mMnO) plots (Figure 2) support field and petrographic observations that many drill intervals within this residual apatite mineralisation consist of essentially apatite and magnetite and the P$_2$O$_5$ grade can be directly related to %CaO. Two generations of apatite can be recognised: residual primary apatite and secondary apatite infill. Secondary apatite, re-deposited from downwardly percolating groundwater, is tentatively identified as stafflerite, the low-temperature form of the mineral. The residual apatite – magnetite unit is partly overprinted by near surface ferricrete resulting in the introduction of secondary goethite and hematite from groundwater and an increase in the concentration of iron at the expense of the P$_2$O$_5$ grade (Figure 2).

Rare earth grades in the residual apatite – magnetite unit are generally in the range 0.5 to 3% REO. Residual primary apatite contains approximately 0.5% rare earth oxides and is probably the main source of rare earths but grades additionally reflect the presence of monazite (residual from calcite carbonatite), minor synchesite (derived from nearby "ferrocarbonatite"?), and secondary rare earth-bearing minerals, including cerianite and florencite. These secondary rare earth-bearing minerals may have been introduced during the ferricretisation process.

The *Northern Zone* residual apatite – magnetite regolith unit is enriched in niobium and tantalum, in addition to rare earths and phosphate. Background values of generally <0.25% Nb$_2$O$_5$ in fresh calcite carbonatite are upgraded to >0.75% in the residual apatite – magnetite regolith unit. Niobium in fresh calcite carbonatite is present as trace amounts of pyrochlore. By comparison, the residual apatite – magnetite unit in the Northern Zone contains accessory to trace ferrocolumbite and pyrochlore as the main source of niobium. These minerals are probably also the source of tantalum, which however does not achieve economic levels over significant widths. In detail, the three commodities are slightly offset vertically from one another. These displacements suggest variations in the relative roles of residual enrichment and supergene enrichment for each commodity.

4. Conclusions

The Ngualla carbonatite complex contains a Mineral Resource of 40 million tonnes at 4.07% total rare earth element oxides (TREO) with low U, Th, and has potential for economic phosphate (apatite) mineralisation. Rare earths were concentrated in two stages. In-situ fractionation concentrated rare earths as bastnaesite and synchesite in miarolitic cavities achieving grades of 1 to 2% TREO. Further upgrading to >3% TREO resulted from weathering during which $CaCO_3$ and $MgCO_3$ were leached from the host rock leaving a porous rare earth-enriched mass of goethite and barite. Mixing between carbonatite and mica-rich (glimmerite) magmas may have resulted in crystallisation of apatite and an initial igneous stage of concentration. The apatite was further concentrated during weathering by residual accumulation following dissolution of calcite.

Acknowledgements

References

Cahen, L. and Snelling, NJ. 1966. The geochronology of Equatorial Africa. Elsevier (North-Holland Publishing), Amsterdam.

Peak Resources Limited, 2013, Quarterly Report to ASX, December, 2012.

S 6.1:
Industrial minerals

Convenors:
Axel Müller & Håvard Gautneb

Titanium deposits in Norway

Are Korneliussen
Geological Survey of Norway, P.O.Box 6315 Sluppen, NO-7491Trondheim, Norway
are.korneliussen@ngu.no

Abstract. Norwegian Ti and Fe-Ti mineral resources are very large, comprising magmatic ilmenite ± vanadiferous magnetite ± apatite deposits, as well as metamorphic deposits with predominant rutile.

The Neoproterozoic Rogaland Anorthosite Province in southwest Norway is by far the most important in terms of volume of Ti deposits and Ti-enriched igneous rocks. This province includes two major mineral resources: The Tellnes ilmenite deposit which is operated in a Ti-rich norite intrusion within anorthosite, and the nearby Bjerkreim-Sokndal Layered Intrusion with specific units in the sequence enriched in vanadiferous magnetite, ilmenite and apatite.

Metamorphic processes have affected the magmatic Ti deposits to various extents. A rather extreme example is the formation of eclogite from a mafic igneous protolith during Caledonian high-pressure metamorphic phase, during which Fe from ilmenite entered garnet, and the remaining Ti formed rutile. Thus, large volumes of ilmenite-bearing rocks were transformed into rutile-bearing eclogite.

A number of rutile-eclogite deposits of potential economic interest have been identified, of which the Engebøfjellet deposit in the Sunnfjord region of W Norway is presently under development by Nordic Mining ASA.

Keywords. Magmatic, metamorphic, titanium, ilmenite, rutile.

1 On the significance of titanium mineral resources

Titanium is a major element in the Earth's crust, and the Ti-oxide content commonly varies from 0.1 wt% TiO_2 in acid rocks to more than 2-3 wt% TiO_2 in certain intermediate and basic rocks.

Titanium is present in many minerals as a common minor constituent, but only ilmenite ($FeTiO_3$) and rutile (TiO_2) are of economic importance. TiO_2 mining from sand deposits makes up 75 wt% of the global Ti mineral supply, the remaining comes from magmatic (hard-rock) deposits, according to recent data (Gambogi 2012; Bedinger 2013). Norway and Ukraine are the only European countries producing Ti-minerals, contributing 5 wt% and 4 wt% of total world supply, respectively.

The dominant industrial use of Ti minerals is production of white pigment for use in paints, plastics, etc.; only a minor portion is refined to Ti metal.

Force (1991) presents a general overview of the geology of Ti mineral deposits.

2 Titanium ore-forming mechanisms

Norwegian Ti/Fe-Ti deposits classify as 'hardrock types' of magmatic or metamorphic origin (Korneliussen et al. 2000a); sedimentary Ti deposits of any significance are not known. Most hardrock Ti-deposits occur within distinct geological provinces in the coastal regions in the southernmost part of the country, along the western coast and in the north. The geographic distribution is shown in Fig. 1A while age relationships are indicated in Fig. 1B and C.

Metamorphic processes have affected magmatic Fe-Ti deposits in various degrees, commonly as retrograde alteration of the host rock also affecting the Fe-Ti oxides. In extreme cases, the character of Fe-Ti oxide-rich rocks has been completely transformed.

One such metamorphic transformation is the alteration of mafic igneous rocks to eclogite during Caledonian high-pressure metamorphism in west Norway, associated with the ca. 400 Ma continent-continent collision at the western margin of the Baltic continent. In this transformation, ilmenite in the protolith broke down, the Fe entering newly formed garnet and the residing Ti into rutile. This mechanism, as roughly indicated in Fig. 1C with respect to age-relations, transferred large volumes of ilmenite-bearing rocks belonging to a variety of Proterozoic magmatic suites, into rutile-bearing eclogite rocks. The most important rutile/eclogite deposits are found in the Sunnfjord province of west Norway (Korneliussen et al. 2000b).

Another extreme metamorphic transformation took place in the Bamble region in south-east Norway, in which metasomatism transformed gabbros and amphibolites into scapolite-amphibole rocks and albitites. During the scapolitisation process Cl-rich fluids selectively leached Fe from ilmenite, while Ti, which is fairly immobile, was incorporated into rutile; this mechanism was firstly pointed out by Brögger (1934). In addition, Na-metasomatism formed albitites, occasionally distinctly rutile-bearing. Thus, both eclogitisation and metasomatism are rutile ore-forming processes.
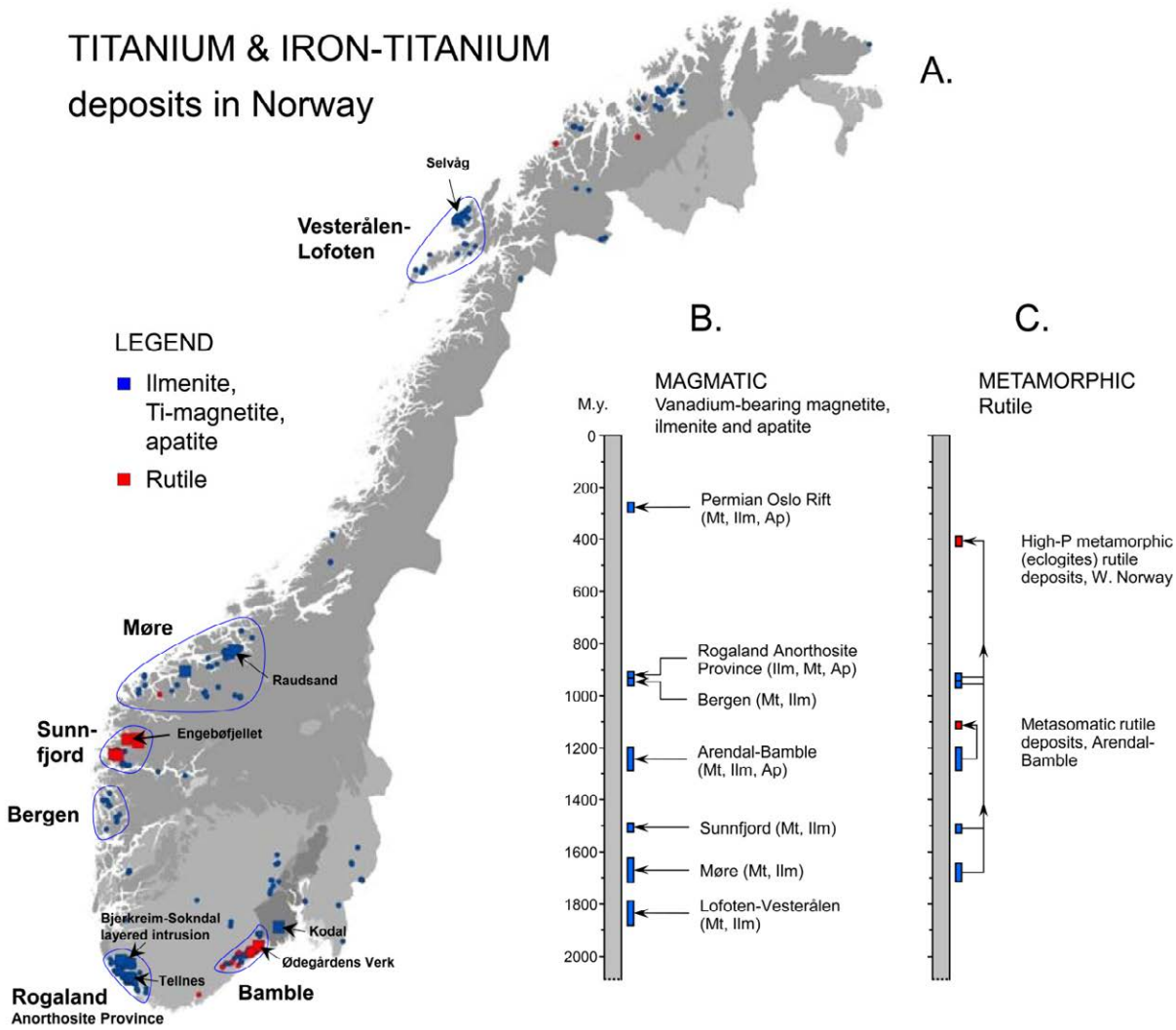
Figure 1. Overview map of Ti and Fe-Ti deposits in Norway (A) and age-relations for magmatic (B) and metamorphic (C) Ti ore provinces. Arrows in Fig. C indicate that rutile deposits have formed by metamorphic transformation of older ilmenite-enriched magmatic rocks.

3 Titanium and iron-titanium deposits and provinces

The Rogaland Anorthosite Province (922-932 Ma) near the southwestern tip of the country (Fig. 1A) is by far the most important in terms of the identified volume of Ti-enriched igneous rocks and deposits. The main deposit is Tellnes, an ilmenite-rich norite intrusion within anorthosite (see Charlier et al. 2006, 2007, and references therein). Tellnes is being mined by Titania AS, producing 0.9 Mt/year of ilmenite concentrate (Neeb et al. 2012) which is approximately 5 wt% of global Ti mineral production in contained TiO_2 (Gambiogi 2012; Bedinger 2013). The Tellnes proven reserve is 180 Mt ilmenite ore averaging 18 % TiO_2 (S. Molund, personal communication.)

The neighbouring Bjerkreim-Sokndal Layered

Intrusion is not in production today but represents a potential future resource, comprising a 'probable resource' of more than 500 Mt ore with 30 wt% combined ilmenite, V-bearing Ti-magnetite and apatite (see summary in Korneliussen 2012, based on data from Meyer et al. 2002, Schiellerup et al. 2001, 2003).

The second major Ti mineral resource situation is the Sunnfjord eclogite province in West Norway (Fig. 1A), containing several deposits of rutile-bearing eclogite (Korneliussen 2000b). The main deposit known in the region is Engebøfjellet, which is being developed by Nordic Mining ASA; the proven reserve is 154 Mt of 3.8 wt% TiO_2. The potential for additional Ti-resources at Engebøfjellet and elsewhere in the region is considerable.

Other significant deposits shown in Fig. 1A include the Kodal apatite-titanomagnetite deposit in the Permian

Oslo Rift (Lindberg 1985), Paleoproterozoic V-bearing Ti-magnetite deposits in the Rødsand area in the Møre region (Sanetra 1985), and the Selvåg V-bearing titanomagnetite deposit in the Paleoproterozoic Vesterålen-Lofoten region (Priesemann & Krause 1985).

Acknowledgements

References

Bedinger, GM (2013) USGS Mineral Commodity Summaries, Titanium. 2 p.

Brögger WC (1934) On several Archaean rocks from the south coast of Norway. II. The South Norwegian hyperites and their metamorphism. Skrifter Norsk Videnskaps-Akademi, Matematisk-naturvidenskapelig klasse 1, 421 p.

Charlier B, Duchesne J-C, Vander Auwera J (2006) Magma chamber processes in the Tellnes ilmenite deposit (Rogaland Anorthosite Province, SW Norway) and the formation of Fe-Ti ores in massif-type anorthosites. Chemical Geology 234: 264-290.

Charlier B, Skår Ø, Korneliussen A, Duchesne J-C, Vander Auwera J (2007) Ilmenite composition in the Tellnes Fe-Ti deposit, SW Norway: fractional crystallization, postcumulus evolution and ilmenite-zircon relation. Contributions to Mineralogy and Petrology 154: 119-134

Force E (1991) Geology of titanium mineral deposits. Geological Society of America Special Paper 259, 112 p.

Gambogi J (2012) USGS 2010 Mineral Yearbook, Titanium. 18 p.

Korneliussen A (2012) N001 Rogaland Fe-Ti-V. In Pasi P (ed.) Mineral deposits and metallogeny of Fennoscandia. Geological Survey of Finland, Special Paper 53, 37-43.

Korneliussen A, McEnroe SA, Nilsson LP, Schiellerup H, Gautneb H, Meyer GB, Størseth LR (2000a) An overview of titanium deposits in Norway. Norges geologiske undersøkelse Bulletin 436, 27-38.

Korneliussen A, McLimans R, Braathen A, Erambert M, Lutro O, Ragnhildstveit J (2000b) Rutile in eclogites as a mineral resource in the Sunnfjord region, Western Norway. Norges geologiske undersøkelse Bulletin 436, 39-47.

Lindberg PA (1985) Fe-Ti-P mineralizations in the larvikite-lardalite complex, Oslo Rift. Norges geologiske undersøkelse Bulletin 402, 93-98.

Meyer GB, Schiellerup H, Tegner C (2002) Chemical characterization of ilmenite, magnetite and apatite in the Bjerkreim-Sokndal Layered Intrusion, Rogaland, South Norway. Norges geologiske undersøkelse, report 2002.042, 25 p.

Neeb PR, Sandvik G, Boyd R, Brugmans PJ, Erichsen E, Kaasbøll B, Løseth L, Strand G, Tangstad R, Wennberg H (2012) Mineralressurser i Norge 2011. Mineralstatistikk og Bergindustriberetning. Norges geologiske undersøkelse og Direktoratet for mineralforvaltning. 52 p.

Priesemann F, Krause H (1985) The Selvåg deposit: A Proterozoic magmatic Fe-Ti-V occurrence on Vesterålen, Northern Norway. Norges geologiske undersøkelse Bulletin 402, 51-64.

Sanetra S (1985) The Rødsand Fe-Ti-V deposit, Møre, Western Norway. Norges geologiske undersøkelse Bulletin 402, 39-49.

Schiellerup H, Meyer GB, Tegner C, Robins B, Korneliussen A (2001) Resources of apatite, ilmenite and magnetite in the Bjerkreim-Sokndal Layered Intrusion, Rogaland, South Norway. Norges geologiske undersøkelse, report 2001.092, 33 p.

Schiellerup H, Korneliussen A, Heldal T, Marker M, Bjerkgård T, Nilsson LP (2003) Mineral resources in the Rogaland Anorthosite Province, South Norway: origins, history and recent developments. Norges geologiske undersøkelse, Special Publications 9, 117-135.

Correlation between test-methods for alkalisilica-reactivity of Swedish aggregates for concrete

Karin Appelquist, Magnus Döse, Jan Trägårdh
The Swedish Cement and Concrete Research Institute, c/o SP, Box 857, 501 15 Borås

Mattias Göransson
Geological Survey of Sweden, Box 670, 751 28 Uppsala

Abstract. Three methods detecting alkali-reactivity of different aggregate-types from Sweden are assessed in this study. 21 rock samples considered either unlikely to be alkali-reactive (Class 1), uncertain/potentially alkali-reactive (Class 2) or likely to be alkali-reactive (Class 3) have been analyzed with regard to its alkalisilica-reactivity in mortar/concrete. A modified Rilem AAR 1, petrographical method is compared with the Rilem AAR 1 method (extended petrographic examination based on microscopic point-counting) as well as the Rilem AAR 2 method (ultra-accelerated mortar-bar test, in which mortar-bars containing the potentially reactive aggregates are stored in a 1.0 M NaOH-solution at 80°C for 28 days).

Whereas the petrographic examinations detect potentially reactive aggregates, an expansion of the mortar-bars gives a dimension of the potential alkalisilica-reactivity of the aggregates.

Preliminary results show that alkalisilica-reactive aggregates, with expansion ≥0.25%, include metavolcanic rocks, deformed granitoids, mylonites, and sandstones. Non-reactive rocks, with expansion ≤0.15%, are mainly 'undeformed' or weakly foliated granitoids, whereas potentially reactive aggregates with an expansion between 0.19-0.25% include recrystallized porphyritic rhyolite/dacite; and deformed granitoids with moderate degrees of deformed or microcrystalline quartz.

Keywords. Aggregate, concrete, alkali-silica reactions (ASR).

1 Introduction

This paper presents results from an ongoing comparative study of test-methods for alkalisilica-reactivity of Swedish aggregates for concrete. 21 of 23 samples have so far been analysed and are presented in this paper.

Alkali-Silica Reactions (ASR) in concrete occur when silica from aggregates reacts with hydroxyl ions from the cement. However, this reaction requires reactive aggregates, cement with sufficiently high alkali content, as well as excessive water to be able to occur. When all three of these criteria are met, ASR gel may develop. The ASR gel increases in volume when absorbing excessive water and thus may cause expansion in the concrete pore fluid, which in turn can lead to cracking and essential degradation of constructions.

The Swedish Standard SS-EN 12620 (Aggregates for concrete) states the relevance of alkalisilica-reactivity in aggregates in conjunction with cement. In the Swedish standard SS137003 (Concrete-Application of EN 206-1 in Sweden) a specific note is made giving guidance for acceptable contents of potentially alkali-reactive particles within the aggregates. According to the Rilem AAR 1 method, the content of potentially alkali-reactive particles should be less than 15vol% for an aggregate to be defined as low-reactive. For the Rilem AAR 2 method, the recommendation is a maximum expansion of 0.25%. This condition is valid for mortar bars with dimensions 40x40x160mm under testing for 28 days.

In 1995-2011 the Geological Survey of Sweden carried out aggregate quality mapping near or around the conurbations in Sweden. As a part of this survey, the Swedish Cement and Concrete Research Institute studied more than 1700 thin-sections from bedrock samples. Alkalisilica-reactive aggregates in Sweden include deformed rocks such as cataclasite and mylonite, gneissic metagranitoids, fine-grained metavolcanic rocks, as well as sedimentary rocks such as metagreywacke, quartzite, sandstone etc. To establish whether varieties of these rocks are alkali-reactive, a number of Class 2 (uncertain/potentially alkali-reactive rocks) along with Class 1 (unlikely to be alkali-reactive) and Class 3 (likely to be alkali-reactive) rocks have been analyzed with three different methods. The methods were also evaluated to see how or if they correlate.

2 Samples

21 rock samples are studied with regard to its potential alkalisilica-reactivity in mortar/concrete. These include two metavolcanic rocks, two recrystallized metavolcanic rocks, one recrystallized meta-/subvolcanic rock, two sandstones and 14 metagranitoids of varying structure. Metagranitoids vary from massive, foliated, gneissic to mylonitic in order to describe the great variety of rocks represented in Sweden (Table 1).

3 Methods

3.1 Rilem AAR 1

The Rilem AAR 1 petrographic method is described in RILEM 2003. In this study, the point counting technique is used and the amount of potentially alkalisilica-reactive material refers to the quantity of

crypto-, microcrystalline or highly strained quartz. Hence, cross-points falling onto crypto-, microcrystalline or highly strained quartz-grains are recorded as potentially reactive mineralgrains (as opposed to counting reactive aggregate grains).

3.2 Modified Rilem AAR 1, petrographical method

The modified Rilem AAR 1, petrographical method is an evaluation method, based on an estimation of the content of potentially alkali-reactive material (crypto-, microcrystalline or highly strained quartz) in thin-section. No point-counting is carried out; instead an estimated value of the potentially reactive material is used to classify the aggregate. The material is classified into the three groups (1) *unlikely to be alkali-reactive*, with a low (<10vol%) estimated value for potentially reactive material; (2) *potentially reactive*, with an estimated value of potentially reactive material between approximately 10 and 20vol% and (3) *very likely to be alkali-reactive*, with a high estimated value (>20vol%) of potentially alkalireactive material. Hence, the potential alkali-reactivity of the material is classified on the basis of its petrographic composition (cf. RILEM 2003, Lindgård 2010).

3.3 Rilem AAR 2

The Rilem AAR 2 accelerated mortar bar test is described in RILEM 2000. Mortar bars made with a 1.0 Na_2O-eq. cement are stored in 1.0 M NaOH at 80ºC and their expansion is measured over a 28 days period.

4 Results

4.1 Rilem AAR 1

Eight samples were classified as non-reactive aggregates (potentially reactive components <15vol%) according to Swedish Standard SS 137003. These include 'undeformed' to gneissic granitoids and one sandstone with quartz-grains >120µm. Two samples are classified as potentially alkali-reactive if the uncertainty (±3) of the measurement is considered (sample 14, gneissic to mylonitic granitoid and sample 20, sandstone with major quartz-grains >120µm). The remaining 11 samples have potentially reactive component contents above 15vol% and are considered likely to be alkali-reactive. These include metavolcanic rocks (including a recrystallized variety), one heterogeneous gneissic granitoid, gneissic to mylonitic granitoids and sandstone with major quartz-grains <120µm. The results are summarized in Table 1.

4.2 Modified Rilem AAR 1, petrographical method

Four samples were classified as Class 1 (unlikely to be alkali-reactive) aggregates. These include three 'undeformed' granitoids and one sandstone with quartz-grains mainly >120µm. 12 samples are classified as Class 2 (unknown/potentially reactive aggregates) and include recrystallized metavolcanic rocks, 'undeformed' to gneissic granitoids (some with mylonitic components) and sandstone with quartz-grains <120µm. Five samples are classified as Class 3 (likely to be alkali-reactive) aggregates and include metavolcanic rocks and mylonites. The results are summarized in Table 1.

Table 1. Sample description and results

Sample	Sample description	Class[1]	ASR, vol%[2]	Expansion, %[3]
10	Granitoid	1	1	0.06
11	Granitoid	1	2	0.10
17	Granite	1	4	0,15
20	Sandstone (quartz mainly >120µm)	1	12	0.25
22	Foliated granitoid	2	4	0.10
23	Foliated granitoid	2	6	0.11
8	Heterogeneous granitoid, partly deformed	2	8	0.12
5	Heterogeneous gneissic granitoid	2	10	0.20
6	Heterogeneous granitoid, partly foliated	2	10	0.24
14	Heterogeneous gneissic to mylonitic granitoid	2	13	0.23
2	Recrystallized metavolcanic rock	2	17	0.19
15	Heterogeneous gneissic to mylonitic granitoid	2	19	0.28
18	Recrystallized meta-/subvolcanic rock	2	22	0.14
7	Heterogeneous gneissic granitoid, partly mylonitic	2	29	0.30
21	Recrystallized metavolcanic rock	2	39	0.32
19	Sandstone (quartz mainly <120µm)	2	41	0.43
12	Gneissic to mylonitic granitoid	3	15	0.23
13	Mylonite	3	43	0.35
16	Mylonite	3	50	0.34
4	Metavolcanic rock (porphyritic)	3	61	0.55
3	Metavolcanic rock (porphyritic)	3	69	0.44

[1] Results from modified Rilem AAR 1, petrographical method. 1: unlikely to be alkali-reactive, 2: potentially reactice/uncertain, 3: very likely to be alkali-reactive

[2] Results from Rilem AAR 1, ASR: potentially alkalisilica-reactive components

[3] Results from Rilem AAR 2, prisms 40x40x160mm, measurement after 28 days in 1.0 M NaOH

4.3 Rilem AAR 2

Non-reactive aggregates, with expansion ≤0.15%, are mainly 'undeformed' granitoids. One recrystallized meta-/subvolcanic rock also fall into this category. Potentially reactive aggregates with an expansion between 0.19-0.25% include one recrystallized metavolcanic rock; and deformed granitoids with moderate degrees of deformed or microcrystalline quartz. Alkalisilica-reactive aggregates, with expansion ≥0.25%, include metavolcanic rocks (including one recrystallized variety), gneissic to mylonitic granitoids and sandstones. The results are summarized in Table 1.

5 Discussion

5.1 Reactivity of aggregates

Almost all (4 of 5) metavolcanic rocks are classified as alkalisilica-reactive, as expected, regardless of being rhyolitic or dacitic in composition. Thus, volcanic rocks in Sweden should be handled carefully for use as aggregates in concrete, especially in outdoor structures.

Most samples regarded non-reactive or likely to be reactive in the modified Rilem AAR 1, petrographical method follow the expected trends in the Rilem 1 and 2 methods. However, a sandstone, with quartz-grains mainly larger than 120μm, which is classified as non-reactive in the petrographic evaluation (modified Rilem AAR 1) and potentially reactive in the Rilem AAR 1 point-counting method (13±3vol%), shows an expansion of 0.25% in the Rilem AAR 2 accelerated mortar bar test method. If the sandstone is indeed alkalisilica-reactive, the mineral grain size for reactive quartz in sandstone must be reconsidered if counting the whole grain. However, it should be further tested for its potential alkalisilica-reactivity with Rilem AAR 3 concrete prism method before any conclusions can be made. Further, after mortar-bar testing, microscopic investigations including crack-pattern studies of the mortar-bars is needed to determine whether a supposed expansion is actually caused by alkalisilica-reactions (cf. RILEM 2000).

Samples regarded uncertain/potentially alkali-reactive in the modified Rilem AAR 1 method show a wide spectrum in the Rilem 1-2 diagram (Fig. 1). Some granitoids are classified as Class 2 rocks due to its heterogeneity, with gneissic features. Also foliated granitoids were classified in this category. However, these can easily be redefined as non-reactive after point-counting. The potentially reactive (Class 2) rock types with ASR-contents 10-20vol% are more ambiguous. Their potential alkalisilica-reactivity must be investigated further with Rilem AAR 3 or 4 (RILEM 2000, in progress) in order to assess its true nature.

If all methods are considered, only medium- to coarse-grained massive to foliated granitoids are considered non-reactive. Potentially reactive aggregates include recrystallized metavolcanic rocks and deformed granitoids with moderate degrees of deformed or microcrystalline quartz. Alkali-reactive aggregates, include porphyritic metavolcanic rocks, high-grade

gneisses, mylonites and sandstones.
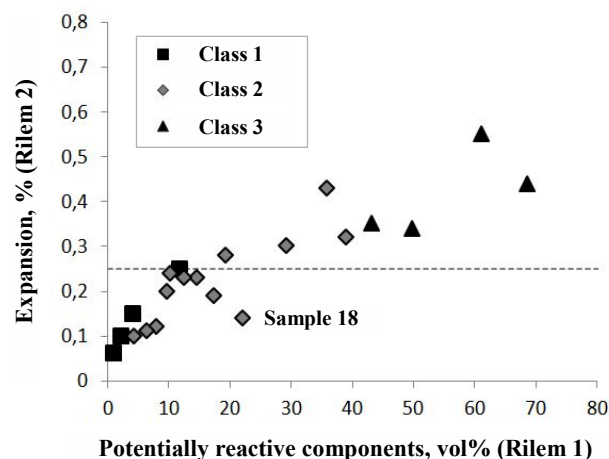
Figure 1. The amount of potentially alkali-silica reactive components in different aggregates plotted against the expansion (in percent) of mortar bars molded from the same aggregate. Aggregates classified regarding its potential alkali-reactivity in concrete, on the basis of its petrographic composition (Modified Rilem AAR 1, petrographical method). Class 1: unlikely to be alkali-reactive, Class 2: potentially reactive, Class 3: likely to be alkali-reactive.

5.2 Correlation between methods

The correlation between Rilem AAR 1 and Rilem AAR 2 has previously been accentuated (e.g. Lindgård et al. 2010) and is well established in this study (Fig. 1). Sample 18 however, deviates from this trend, which probably is explained by its ambiguous character.

However, the modified Rilem AAR 1, petrographical method does not have as good correlation. The more detailed microscopic point-counting is required to get an adequate comprehension of the potential alkali-reactivity of an aggregate.

6 Conclusions

The Rilem 1 and 2 methods correlate rather well with each other, whereas the modified Rilem AAR 1 method should be treated with care. However, with ASR-contents between 10-20 vol%, the Rilem 1 and 2 methods need to be evaluated more carefully.

From the investigated rock types only 'undeformed' massive to weakly foliated granitoids can be considered non-reactive. Potentially reactive aggregates include recrystallized metavolcanic rocks and deformed granitoids with moderate degrees of deformed or microcrystalline quartz. Porphyritic metavolcanic rocks, high-grade gneisses, mylonites and sandstones are considered very likely to form alkalisilica-reactive aggregates in concrete.

References

RILEM (2003) AAR-1 – Detection of potential alkali-reactivity of aggregates – Petrographic method. Materials and Structures 36: 480-496

RILEM (2000) AAR-2 – Detection of potential alkali-reactivity of aggregates – the ultra-accelerated mortar bar test. Materials and Structures 33: 283-289

Lindgård J, Nixon PJ, Borchers I, Schouenborg B, Wigum BJ, Haugen M, Åkesson U (2010) The EU "PARTNER" Project – European standard tests to prevent alkali reactions in aggregates: Final results and recommendations. Cement and Concrete Research 40: 611-635

Swedish Standard SS-EN 12620+A1:2008 (2010) Ballast för betong (Aggregates for concrete)

Swedish Standard SS 137003:2008 (2008) Betong – Användning av EN 206-1 I Sverige (Concrete – Application of EN 206-1 in Sweden)

Industrial minerals deposits map of the Fennoscandian shield

Gautneb H.
Geological Survey of Norway, Trondheim, Norway

Ahtola T.
Geological Survey of Finland, Rovaniemi, Finland

Bergman T., Gonzalez J., Hallberg A.
Geological Survey of Sweden, Uppsala, Sweden

Litvinenko V.
SC Mineral, St. Petersburg, Russia

Shchiptsov V.
Karelian Geological Institute, Petrozavodsk, Russia

Voytekhovsky Y.
Kola Science Centre, Apatity, Russia

Abstract. A new map product, Industrial Minerals Deposits of the Fennoscandian Shield is presented. The map is a result of cooperation between the Geological Surveys of Finland, Norway and Sweden, SC Mineral, Saint Petersburg, Karelian Geological Institute, Petrozavodsk, Russia and the Kola Science Center, Apatity, Russia. The purpose of the map is to show the most significant industrial mineral deposits of the Fennoscandian Shield and includes active mines and quarries, past producers, potential deposits and showings. About 10-20 %, with some variation between countries, of all registered industrial mineral deposits in each country`s national database is plotted on the map. In total 576 deposits, 119 in Norway, 225 in Sweden, 119 in Finland and 115 in Russia, are shown on the map. These deposits illustrates the variation in type and distribution of industrial minerals deposits in the Fennoscandian Shield, and their location in different geological provinces. In total 35 different commodities are plotted. The most common group of commodities comprise carbonates, feldspar, quartz, olivine, talc and magnesite, which together make up 65% of the total. The map will in due course be accompanied by an online database where the deposits and their most important information will be presented on an interactive map.

Keywords.
Industrial minerals, Fennoscandia, Mineral deposit, Mining, Finland, Norway, Russia, Sweden.

1 Introduction

The industrial minerals map of the Fennoscandian Shield (Fig. 1) is a continuation of the FODD prosject (Fennoscandian Ore Deposit Database) it covers the same area and has the same geological base map as the Fennoscandian ore deposit map of the (Eilu et al 2013). The deposits are grouped into 5 size classes according to our best knowledge of size and tonnage.

2 Finland

In 2011 there were 33 active industrial mineral and industrial rock mines and quarries in Finland. Raw material of Palaeoproterozoic calcitic marble deposits of southern Finland are used for cement, fillers and paper pigments. Dolomitic marbles are mined for agricultural use. Proterozoic soapstone hosted talc is mined from four open pit mines in eastern Finland. Finland has been the largest talc producer in Europe for decades. Finnish talc concentrate is used mainly in paper and pulp as well as paint and coating industries. Finland is the only European producer of wollastonite, a by-product from crystalline limestone deposit of Ihalainen at Lappeenranta. Industrial rocks are mined for rock wool and cement production, from six deposits. The Archean carbonatite hosted apatite deposit Siilinjärvi in eastern Finland is the biggest active industrial mineral mine in Finland and the only active phosphate mine in western Europe. Apatite concentrate is used in fertilizer plant nearby. Quartz is produced from three deposits of which one in south western Finland is also producing feldspar. In addition, there are industrial mineral deposits, which are not currently in production like diamondiferous kimberlites and kaolin deposits in eastern Finland, hard rock lithium deposits in western and southern Finland and world class phosphate deposit Sokli in northern Finland.

2 Norway

The most important industrial minerals in Norway are olivine, limestone and quartz. Norway is the world's leading producer of olivine and produces about 50% of the worlds annual production. Until recently there were 3 olivine producing mines, however presently (Feb. 2013) only one is active. The map contains several olivine occurrences with indicated resources in excess of 50 Mt. The Norwegian limestones occur essentially in two geological settings, one as part of the Cambro-Silurian succession of the Oslo rift and one as the part different tectonic units in the Norwegian Caledonides. The limestones of the Oslo rift are all low metamorphic marble that is used for cement production and agricultural use. The occurrences comprise several tens of deposits of high grade marble that is raw material for GCC (ground calcium carbonate) and some that burned for PCC (Participated calcium carbonate) production. The Norwegian quartz deposits occur as rock forming quartzites, hydrothermal quartz and as part of pegmatites all with a very variable purity. In Norway there are several potentially large deposits of apatite. They occur in various geological settings, alkaline intrusions within the Caledonian orogenic belt, as part of layered intrusions of the Bjerkreim-Sogndal intrusion, and as part of alkaline intrusions of the Oslo rift.

3 Russia

The Kola Peninsula comprises the following important industrial minerals provinces. On the central eastern Kola, the 1.9 Ga Keivy terrain contains some of the world's largest kyanite/staurolite deposits. The Devonian alkaline Khnibiny complex hosts some of the largest apatite deposits and is perhaps one of the most important industrial mineral provinces within the Fennoscandian shield. The Northern part of Karelia comprises a number of feldspar, muscovite, quartz, kyanite and large garnet deposits. The south eastern Karelia is the only place in the world where shungite rock is mined. Reserves of shungite in the order of several hundred million tons are found along the northern part of the Lake Onega. Easth of the lake Ladogathe graphite deposit Ihala was discovered. The probable reserves of the ore field includes about 200 Mt graphite ore and 6.4 mt tons of graphite. A thick trending quartz vein zone (Melomais prospect) was discovered in the eastern Karelia. It is large enough to be considered as an unique potential quartz occurrence in the Fennoscandian Shield.

4 Sweden

The largest industrial mineral deposits of Sweden are carbonate rock deposits, comprising Paleozoic limestone deposits and Early Proterozoic crystalline carbonate rock deposits. Currently, there are approximately 20 carbonate deposits in operation. Quartz and feldspar have been produced from several hundreds of minor deposits known from all over the country. Only the largest deposits are shown on the map.

Large talc, olivine and magnesite deposits associated with ultramafic rocks are found within the Caledonian thrust nappes of Sweden. Current production of soapstone and talc occurs at Handöl. Fluorite-mining is planned at the Storuman sandstone-hosted fluorite deposit. Several small fluorite occurrences are known but not exploited. Graphite is also known from several small occurrences but only a few has been, or are, of economic size. The most promising prospect is currently at Nunasvaara, in the Kiruna area, and several deposits around Kringeltjärn, central Sweden. Apatite is present in large quantities in the apatite-iron-ores in the Bergslagen and Norrbotten areas but apatite extraction has been minor. In addition, minor occurrences of high alumina silicates, mica, anthophyllite, nepheline, wollastonite, garnet, beryll and clay minerals are also presented in the map (Fig 1).

5 References

Eilu P., Bergman T., Bjerkgård T., Feoktistov, V., Koraskova, M., Kraskotin, S., Litvinenko, V., Nurmi P.A.,Phillipov, N., and Sandstad,J.S., (comp.) (2013) Metallic Mineral Deposit Map of the Fennoscandian Shield 1:2000.000 Revised edition. Geologcal Survey of Finland, Geoloical Survey of Norway, Geological Survey of Sweden, the Federal Agency of Use of Mineral recources of the Ministry of Natural Recources of the Russian Federation.
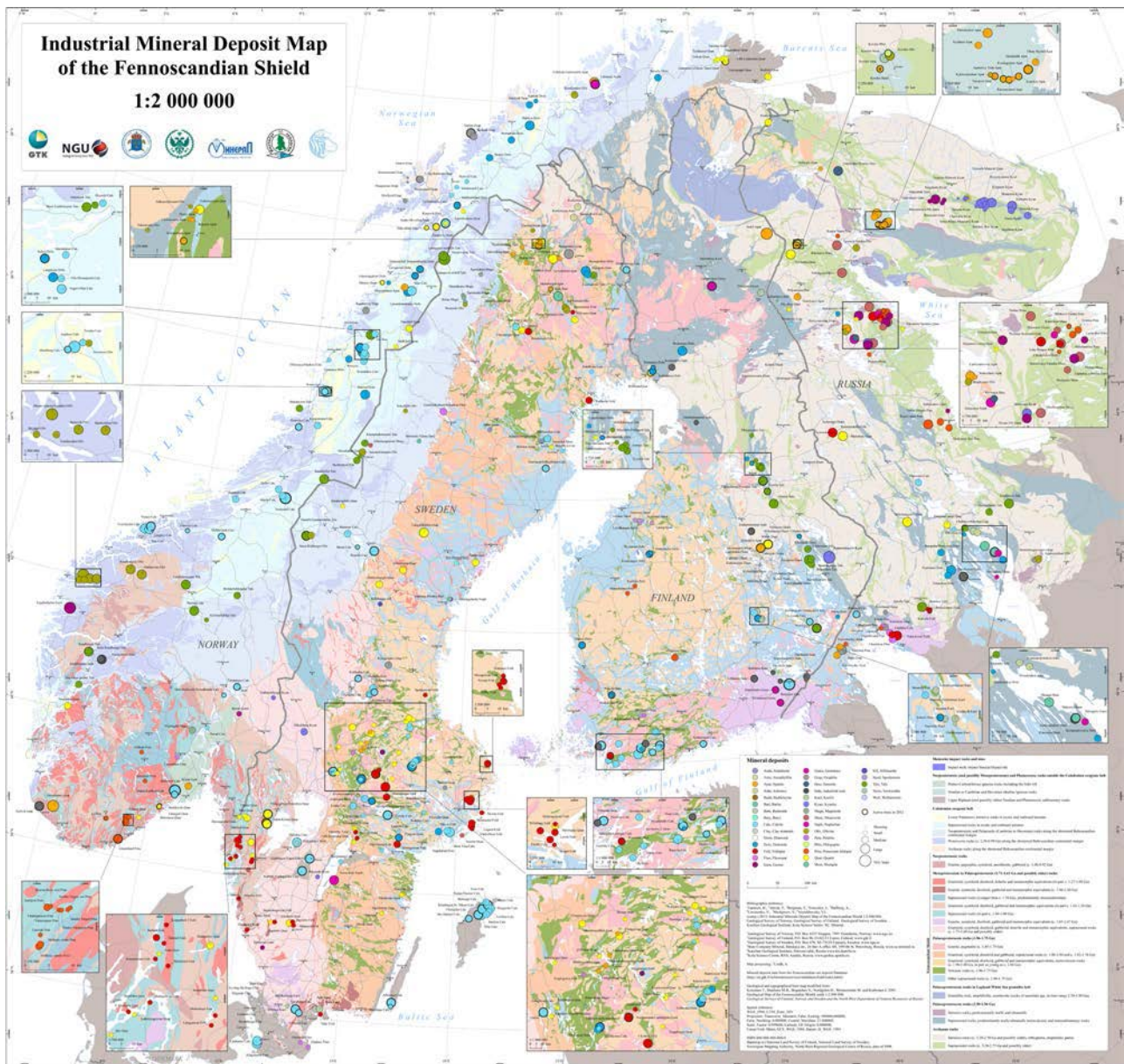
Fig 1 Industrial Minerals Map of the Fennoscandian Shield

Genesis of pencil clay deposits in Germany

H. Albert Gilg & Martin Schwangler
Lehrstuhl für Ingenieurgeologie, Technische Universität München, 80333 Munich, Germany

Abstract. We present geological, mineralogical (XRD) and geochemical data on two German special clays from Klingenberg (Southern Spessart) and Kärlich (Neuwied basin, East Eifel) that were or are used in pencil lead production. The Mid to Late Oligocene clays occur both in a lacustrine terrestrial sedimentary environment. The extremely fine grain size is related efficient particle size sorting. Both clays consist of disordered kaolinite and an expandable 2:1 clay mineral as main constituents with trace amounts of anatase, illite and quartz. Unusually high Ti, Cr, V, Nb and Zr and steep chondrite-normalized REE patterns with no Eu anomaly suggest that the Kärlich clays had a distinct alkaline mafic protolith in the source region. In contrast, the trace element geochemical characteristics of the Klingenberg clays show near average upper crustal compositions and thus no specific volcanic rocks in the catchment of the lake.

Keywords. Pencil clays, geochemistry, REE

1 Introduction

Germany is a leading producer of natural clays used with graphite in the manufacture of pencil leads. The clay content controls the hardness of the lead.

The Klingenberg deposit near Aschaffenburg in northwestern Bavaria had a 270 year-old mining history and was the World's most important pencil clay deposit before its closure in December 2011. The valuable clay was mined underground (Fig.1).

The Kärlich blue clay from the Neuwied basin in Rhineland-Palatinate is the present-day successor and is mined in an open pit. Both clays were mainly used in diverse ceramic products (crucibles, floor tiles, isolators) or as additives to special ceramic masses with only a small portion going into pencil lead production.

Here, we present a comparison of geological settings, mineral compositions and geochemical characteristics of the two deposits to better understand the genesis of natural pencil clays. Combined mineralogical and geochemical studies of sedimentary kaolinitic clays have shown to be extremely useful in deciphering control by source rocks, paleoclimate and post-depositional alteration (e.g., Baioumy and Gilg 2011; Baioumy et al. 2012).

2 Geological setting

The Klingenberg deposit is located in a small isolated Tertiary half-graben filled with lacustrine fine-grained sediments within the red sandstones of the Bunter (Early Triassic) in the southern Spessart area (Dobner 1987). The economic clay bed has a maximum thickness of about 30 m. New palynological data (M. Hottenrott, pers. comm.) infer a Mid to Late Oligocene age of the clay, as opposed to previous views of a Late Pliocene age (e.g., Dobner 1987).

The Kärlich blue clay is hosted within the Late Oligocene lacustrine Kärlich Formation of the Neuwied basin, Eastern Eifel, in the Variscan Rhenish Massif (Hofmann et al. 2003, 2005; Schäfer and Kadolsky 2011). The bluish black refractory clay with a thickness of about 6 m shows a gradual transition to the underlying sedimentary Fe-rich bentonite (Kärlich Grünton) which overlies a thick sequence of brackish Fe-rich clays of the Maifeld Formation (Schäfer and Kadolsky 2011). In the hanging wall of the blue clay, a trachyte tuff and tuffite horizon ("Knubb") cap the Tertiary sediments.

Figure 1. Top: Underground mining of pencil clay in the Klingenberg deposit, bottom: open pit mining of the Kärlich blue clay.

2 Mineral composition

Both pencil clays are highly plastic and extremely fine-grained bluish black clays with more than 80 to 98% of the <2μm fraction.
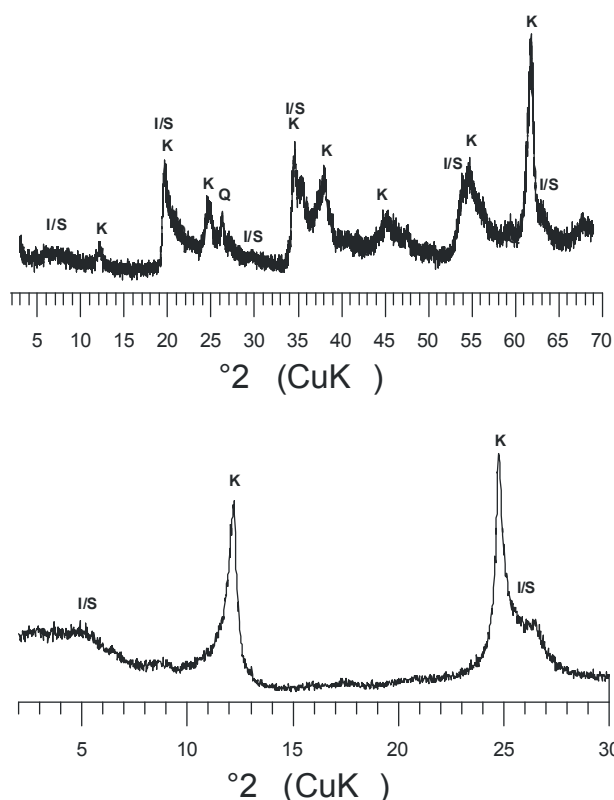
Figure 2. XRD patterns of bulk powder (top) and oriented <2μm fraction of the Klingenberg pencil clay (I/S: illite-rich illite-smectite, K: kaolinite, Q: quartz).
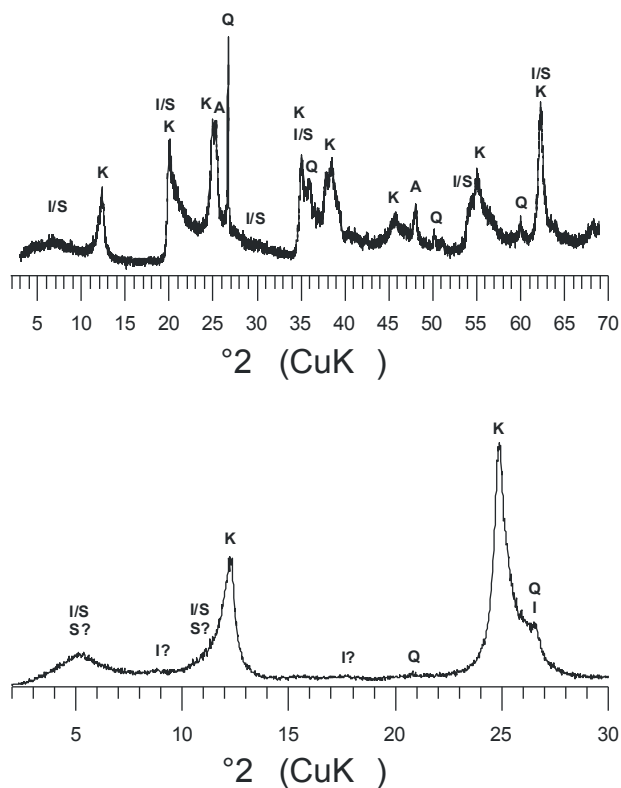
Figure 3. XRD patterns of bulk powder (top) and oriented <2μm fraction of the Kärlich blue clay (I/S: smectite-rich illite-smectite, S: smectite, I: illite, K: kaolinite, Q: quartz, A: anatase).

The XRD analyses of bulk samples and clay fractions (Fig. 2, 3) indicate that the mineral composition of the two pencil clays is quite similar with disordered kaolinite and smectite-rich R0 illite-smectite as the main two components. Traces of discrete illite, quartz and anatase are noted. The Kärlich blue clay, however, contains significantly more quartz and anatase than the Klingenberg clay.

3 Geochemical Analyses

The major and trace element compositions of the different layers in the pencil clay beds of the two deposits have been determined using X-ray fluorescence analysis on glass disks and powders, as well as solution ICP-MS analysis following Na_2O_2 dissolution.

The major element compositions of the clays are remarkably similar (Table 1). However, the Klingenberg clays have slightly higher potassium and magnesium content, while the Kärlich blue clays show much higher titanium values. Also other compatible trace elements such as Cr, V, Ni and Co, as well as Nb, REE, Li and S are enriched in the Kärlich clays, whereas the other trace element contents are the same.

The chondrite-normalized REY patterns of the Klingenberg clays are comparable to average shale (PAAS) with slightly lower HREE. We note that most other trace element contents of the Klingenberg clays are similar to average shale (Taylor and McLennan 1985).

Table 1. Major and selected trace element compositional ranges of natural German pencil clays in comparison with average shale (PAAS; Taylor and McLennan 1985).

	Klingenberg		PAAS	Kärlich	
SiO₂	49.44 -	54.52	62.8	47.24 -	51.72
TiO₂	0.96 -	1.55	1.0	3.38 -	3.79
Al₂O₃	28.27 -	32.05	18.9	27.65 -	32.53
Fe₂O₃	2.72 -	3.62	7.2	2.51 -	3.37
CaO	0.51 -	0.76	1.3	0.51 -	0.60
MgO	1.10 -	1.22	2.9	0.74 -	0.88
K₂O	1.06 -	1.54	3.7	0.61 -	0.81
Na₂O	0.27 -	0.37	1.2	0.25 -	0.43
P₂O₅	0.07 -	0.09	0.2	0.09 -	0.10
LOI	8.54 -	10.38		9.91 -	10.52
Cr	143 -	146	110	268 -	284
V	198 -	226	160	326 -	356
Ni	51 -	84	55	95 -	114
Co	3 -	5	23	12 -	14
Rb	98 -	132	160	45 -	83
Cs	14 -	17	15	14 -	18
Zr	140 -	197	210	273 -	298
Nb	20 -	32	19	98 -	110
B	140 -	150	100	140 -	160
S	328 -	567		965 -	1234
Ba	260 -	343	650	284 -	310
Li	97 -	145	75	179 -	218
Mn	25 -	35	142	32 -	55
Sr	255 -	350	200	205 -	209

In contrast, the Kärlich blue clays have higher REE contents, no Eu anomalies and steep chondrite-normalized REY patterns. All these geochemical features indicate that the Kärlich blue clays have a distinct alkalibasaltic geochemical "flavor". Geochemical and mineralogical data show that this mafic component is not derived from the underlying Kärlich bentonite (Thüns and Gilg 2012).
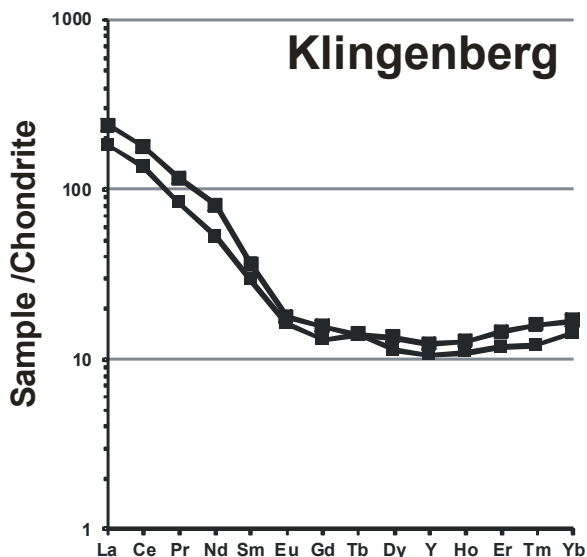
Figure 4. Chondrite-normalized REY (REE +Y) patterns of the Klingenberg pencil clay.
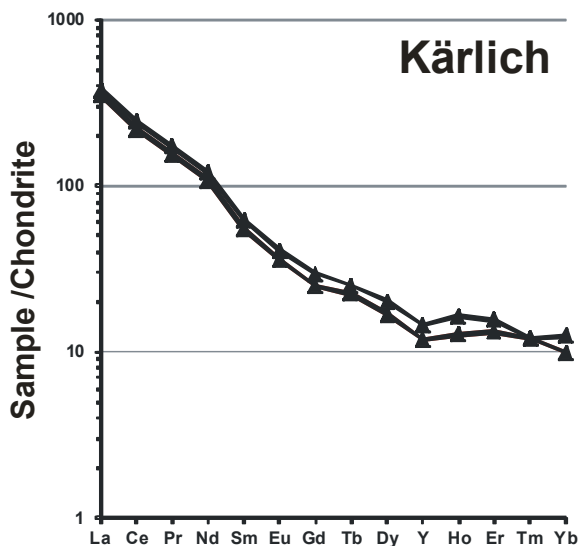
Figure 5. Chondrite-normalized REY patterns of the Kärlich blue clay.

4 Discussion

The mineral composition of both clays is surprising considering their local geological environment.

The Neuwied basin is located within the Rhenish Massif that consists of very low-grade metamorphic clastic sediments, predominately slates. Most Tertiary sedimentary clays that formed from weathering crust within or adjacent to the Massif, such as the famous Westerwald ball clays, are dominated by kaolinite, illite and silt-sized quartz with only minor contents of expandable clay minerals (e.g., Kromer 1980; Petrick et al. 2011). The very low content of illite in the Kärlich clays clearly indicates that weathered slates are not major lithotypes in the source region despite being the predominant rock type in the surroundings of the Neuwied basin.

Our geochemical and mineralogical data suggest that weathered alkali-basaltic protoliths represent a dominant rock type in the catchment of the Late Oligocene lake Neuwied. The volcanic activity in the neighbouring Westerwald and Siebengebirge area with basanites, alkaline basalts and more fractionated alkaline volcanic rocks including trachytes started in the Mid-Oligocene (Lippolt and Todt 1978; Todt and Lippolt 1980; Mertz et al. 2006; Linthout et al. 2009). A resedimented trachyte tuff and tuffite ("Knubb") overlying the Kärlich blue clay is dated at 25.48 ± 0.04 Ma by ^{40}Ar-^{39}Ar on sanidine (Mertz et al. 2006). We therefore consider the Westerwald and Siebengebirge volcanic fields to the NE and N of the Neuwied basin with their dominant alkaline basaltic rocks as the most probably source region for the Kärlich blue clay.

The small Tertiary Klingenberg deposit is surrounded by reddish sandstones of the Lower Triassic Bunter. The feldspar component of the locally arkosic sandstones is often kaolinized, but has never been reported to contain major amounts of expandable 2:1 clay minerals. The nearest outcrops of volcanic rocks are the predominately basaltic units of the Vogelsberg area (~2500 km²) that erupted in the Miocene (Bogaard et al. 2001) after the deposition of the clays. Additionally, our trace element geochemical data preclude weathered mafic protoliths as a dominant component in the source area. The origin of the expandable clay minerals in the Klingenberg clays remains unclear. A possible source could be smectite-rich Early Oligocene marine Rupel clays of the Hessian depression. Further geochemical and mineralogical studies are warranted.

The high kaolinite content of both clays is related to tropical weathering in the region and is characteristic for Mesozoic to Tertiary weathering zones in the Rhenish Massif (e.g. Felix-Henningsen 1990). The expandable clay minerals most probably derive from weathering crusts in less well drained areas and/or specific source lithotypes.

5 Conclusions

The German natural pencil clays are characterized by high contents of disordered kaolinite and expandable 2:1 clay minerals and an extremely fine grain size.

The latter parameter is related to an unusually efficient sedimentary grain size sorting process and a very quiet lacustrine depositional environment.

Specific protoliths in the source region (mafic alkaline rocks) are indicated by our new trace element geochemical data for the Kärlich blue clay, but not for the Klingenberg pencil clays.

We note here that an American patent (Murray and

Johnson 1961) describes the production of pencil clay using a mixtures of the <2μm fraction of a Georgia kaolin and a natural Na-Ca-bentonite. They argue for an optimal behaviour of the clay mixture if the expandable smectite-to-kaolinite ratio is about 2:3. These values are comparable to those in the German natural pencil clays.

Acknowledgements

References

Baioumy HM, Gilg HA (2011) Pisolitic flint kaolin from Kalabsha, Egypt: A laterite-derived facies. Sed Geol 236:141-152.

Baioumy HM, Gilg HA, Taubald H (2012) Mineralogy and geochemistry of the sedimentary kaolin deposits from Sinai, Egypt. Implications for control by the source rocks. Clays Clay Min 80:633-654

Bogaard PJF, Wörner G, Henjes-Kunst F (2001) Chemical stratigraphy and origin of volcanic rocks from the drill core "Forschunsgbohrung Vogelsberg 1996". Geol Abh Hessen 107:69-99

Dobner A (1987) Spezialton. Geol Bavarica 91: 121-134

Felix-Henningsen P (1990) Die mesozoisch-tertiäre Verwitterungs-decke (MTV) im Rheinischen Schiefergebirge. Relief, Boden, Paläoklima 6:1-192

Hofmann P, Urbat M, Hensel A, Schäfer P (2003) Age model for the Late Oligocene Kärlich Blauton of the Neuwied Basin, Germany. N Jb Geol Paläont Mh 2003: 283-296

Hofmann P, Urbat M, Hensel A (2005) Geochemical cycles recorded in Late Oligocene lake sediments of the Kärlicher Blauton (Neuwied Basin, Germany): a response to climate? N Jb Geol Paläont Abh 235:265-287

Kromer H (1980) Tertiary clays in the Westerwald area. Geol Jb D39:69-84

Linthout K, Paulick H, Wijbrans JR (2009) Provenance of basalt blocks from Roman sites in Vleuten-De Meern (The Netherlands) traced to the Tertiary Siebengebirge (Germany): A geoarcheological quest using petrological and geochemical methods. Geol Mijnbouw 88:78-99

Lippolt HJ, Todt W (1978) Isotopische Alterbestimmungen an Vulkaniten des Westerwaldes. N Jb Geol Paläont Mh 6:332-352

Mertz D, Renne PR, Wuttke M, Mödden C (2006) A numerically calibrated reference level (MP28) for the terrestrial mammal-based biozonation of the European Upper Oligocene. Intl J Earth Sci 96:353-361

Murray HH, Johnson HM (1961) Pencil Clays. US Patent 2,986,472

Petrick K, Diedel R, Peuker M, Dieterle M, Kuch P, Kaden R, Krolla-Siedenstein P, Schuhmann R, Emmerich K (2011) Character and amount of I-S mixed-layer minerals and physical-chemical parameters of two ceramic clays from Westerwald, Germany: implications for processing properties. Clays Clay Min 59:58-74

Schäfer P, Kadolsky D (2011) Neuwieder Becken, In: Deutsche Stratigraphische Kommision (ed.) Stratigraphie von Deutsch-land IX, Tertiär, Teil 1. Schriftenr Dtsch Ges Geowiss 75, Hannover, pp 210-224

Taylor SR, McLennan SR (1985) The Continental Crust: its composition and evolution. Blackwell, Boston

Thüns N, Gilg, HA (2012) Bentonites in the Neuwied basin and the adjacent Westerwald. 6th MECC, Prague, Book of Abstracts, pp 107

Todt W, Lippolt HJ (1980) K-Ar- Age Determinations on Tertiary Volcanic Rocks: V. Siebengebirge und Siebengebirgs-Graben. J Geophys 48:8-23

Diversity of the quartz chemistry of NYF- and LCT-type pegmatites and its economic implications

Axel Müller
Geological Survey of Norway, Trondheim and Natural History Museum of London, UK, e-mail: Axel.Muller@ngu.no

Ben Snook
Camborne School of Mines, University of Exeter, UK and Geological Survey of Norway, Trondheim

Peter M. Ihlen
Geological Survey of Norway, Trondheim

Hartmut Beurlen
Federal University of Pernambuco, Department of Geology, Recife, Brazil

Karel Breiter
Institute of Geology of the Academy of Sciences, Praha, Czech Republic

Abstract. Contents of Al, Ti, Li and Ge in quartz from 215 pegmatites in Froland, Evje-Iveland and Tysfjord in Norway, Borborema in Brazil, western Erzgebirge in Germany, and northern Portugal were determined by laser ablation inductively coupled plasma mass spectrometry (LA-ICP-MS). Quartz of Lithium-Caesium-Tantalum (LCT)-type pegmatites has significantly higher Al and Li concentrations than quartz of Niobium-Yttrium-Fluorine (NYF)-type pegmatites. There are no distinct differences in the Ti and Ge contents between these types. Quartz from Froland and Tysfjord does not show chemical zoning within the individual pegmatites, whereas the content of Al, Li, and Ge in quartz increase and Ti decreases from the border zone to the core of the other pegmatites. The results imply that the chemistry of pegmatite quartz is predominantly controlled by the initial source composition of the pegmatite melts and, thus, by the geodynamic setting rather than by intermediate magmatic fractionation processes. In summary, NYF-type pegmatites provide quartz of better chemical quality and can, as in the case of the Tysfjord pegmatites, even reach high purity quality with less than 50 ppm total trace element contents.

Keywords.
Quartz, pegmatite, LA-ICP-MS, industrial mineral

1 Introduction

Numerous pegmatite mines worldwide provide quartz of different qualities for the glass, ceramic, semiconductor, telecommunication and photovoltaic industries. However, a better knowledge of pegmatite origin and genesis is needed to meet the increasing raw material quality demands of the high-tech industry. This requires systematic geochemical investigations for the development of exploration tools which will allow for the efficient identification of new deposits containing quartz of high chemical quality.

In this study we analyzed the Al, Ti, Li and Ge contents of quartz from six pegmatite fields worldwide. The fields include Froland, Evje-Iveland and Tysfjord in Norway, Borborema in Brazil, western Erzgebirge in Germany, and northern Portugal. General features of the pegmatites are given in Table 1. Data from Borborema, Erzgebirge and Froland have been published previously and are included here to consider a large data set (Müller et al. 2008; Breiter and Müller 2009; Beurlen et al. 2011).

The Norwegian pegmatites are classified as NYF-type pegmatites whereas those from Portugal, Germany and Brazil are LCT-type pegmatites according the classification given in Černý (1990; 1991). The pegmatites show commonly structural zoning comprising border zone, wall zone, intermediate zone and core zone. The study is in the initial stage and, therefore, unequal numbers of pegmatites have been sampled and investigated in the different areas. The total number of investigated pegmatites so far is 215. Sampling traverses were taken across some representative pegmatites in order to test the chemical variability of quartz within pegmatites. Additional aims of the study are to reveal possible differences and variation in quartz chemistry between different genetic pegmatite types to facilitate the identification of high purity quartz deposits.

2 Method

Analyses of the trace elements Al, Ti, Li and Ge in quartz were performed on the double-focusing sector field mass spectrometer model ELEMENT XR from Thermo Instruments which is combined with the New Wave 193-nm excimer laser probe. Laser raster ablation was applied in the centre of quartz crystals on an area of approximately 400×150 μm using a spot size of 75 μm. External calibration was performed using six silicate glass reference materials. The isotope ^{30}Si was used as internal standard. Ten sequential measurements on a synthetic quartz crystal were used to estimate the limits of detection (LOD) which were based on 3 x standard deviation (3σ). LOD's are 5 ppm for Al, 1 ppm for Ti, 0.5 ppm for Li and 0.2 ppm for Ge. More details of the measurement procedure are described in Flem et al. (2002) and Flem and Müller (2012).

3 Results

3.1 Quartz chemistry in relation to pegmatite types and their setting

Average concentrations of Al, Ti, Li and Ge in quartz from the six investigated pegmatite fields are listed in Table 1. Concentrations of these elements are variable both within and between the pegmatite fields as illustrated for the case of the Al and Ti contents in Figure 1. Quartz of the Tysfjord pegmatites has the lowest total content followed by quartz from Froland and Evje-Iveland. High Ti is characteristically for the Evje-Iveland quartz. The LCT-type pegmatites from Portugal and Brazil have significantly higher Al and Li, and pegmatitic quartz from the Erzgebirge shows the highest levels of Al and Li. The most essential results are that (1) quartz of the LCT–type pegmatites contains much higher Al and Li compared to NYF-type pegmatites and (2) quartz of the Tysfjord pegmatites has trace element concentrations below the upper limits of the high purity quartz definition according to Müller et al. (2012) (Figure 1).

3.2 Intra-pegmatite zoning of quartz chemistry

Up to 10 quartz samples were taken along profiles across representative pegmatites in order to test the chemical homogeneity of quartz within pegmatites. Pegmatites in Froland and Tysfjord contain quartz with consistent chemistry, whereas all other pegmatites contain quartz with variable chemistry. In these pegmatites the quartz chemistry changes from the border zone to the core, whereby Al, Li, and Ge generally increase and Ti decreases. The chemical zoning is reflected by the wide spread of the data in Figure 1. For example, Al in quartz of the Steli pegmatite from Evje-Iveland increases from 18 ppm in the border zone to 44 ppm in the intermediate and core zone. Ge increases from 0.9 to 2.4 ppm, Ti decreases from 13 to 5 ppm and Li is constant. The contrasts of quartz chemistry between pegmatite margin and core are much more distinct in the LCT-type pegmatites. In the quartz of the Quintos pegmatite from Borborema Al increases from 278 to 545 ppm, Li from 46 to 100 ppm, and Ge from 2.0 to 20.0 ppm. Titanium decreases from 15 to <1 ppm.

4 Conclusions

The investigation of 215 pegmatites in six pegmatite fields worldwide revealed that quartz of LCT-type pegmatites has significantly higher Al and Li concentrations than quartz of NYF-type pegmatites. There are no distinct differences in the Ti and Ge content. Consequently, NYF-type pegmatites provide quartz of better chemical quality; in the case of the Tysfjord pegmatites it can even reach high purity quality with less than 50 ppm of total trace element content. The zoning of quartz chemistry detected in pegmatites of most of the investigated fields makes the production of a homogeneous quartz product challenging. The contrast of quartz chemistry between pegmatite margin (border and wall zone) and core increases with the increasing differentiation of the pegmatites melts. The results imply that the chemistry of pegmatite quartz is mainly controlled by the origin of pegmatite melts and, thus, by the geodynamic setting of the pegmatite fields. However, more pegmatite fields have to be studied to confirm these initial results.

References

Beurlen H, Müller A, Silva D, Da Silva MRR (2011) Petrogenetic significance of trace-element data analyzed with LA-ICP-MS in quartz from the Borborema pegmatite province, northeastern Brazil. Miner Mag 75:2703–2719

Breiter K, Müller A (2009) Evolution of rare-metal granitic magmas documented by quartz chemistry. European J Miner 21:335-346.

Černý P (1990) Distribution, affiliation and derivation of rare-element granitic pegmatites in the Canadian Shield. Geol Rundschau 79:183-226

Černý P (1991) Fertile granites of Precambrian rare-element pegmatite fields: is geochemistry controlled by tectonic setting or source lithologies? Precamb Res 51:429-468

Flem B, Müller A (2012) In situ analysis of trace elements in quartz using laser ablation inductively coupled plasma mass spectrometry. In: Götze J, Möckel R (eds) Quartz: Deposits, mineralogy and analytics. Springer Geology, Berlin, Heidelberg, pp 219-236

Flem B, Larsen RB, Grimstvedt A, Mansfeld J (2002) In situ analysis of trace elements in quartz by using laser ablation inductively coupled plasma mass spectrometry. Chem Geol 182: 237-247

Müller A, Ihlen PM, Wanvik JE, Flem B (2007) High-purity quartz mineralisation in kyanite quartzites, Norway. Mineral Dep 42:523-535

Müller A, Ihlen PM, Kronz A (2008) Quartz chemistry in polygeneration Sveconorwegian pegmatites, Froland, Norway. Europ J Mineral 20:447-463

Müller A, Wanvik JE, Ihlen PM (2012) Petrological and chemical characterisation of high-purity quartz deposits with examples from Norway. In: Götze J, Möckel R (eds) Quartz: Deposits, mineralogy and analytics. Springer Geology, Berlin, Heidelberg, pp 71-118

Table 1. General features of the investigated pegmatite fields and average concentrations of Al, Li, Ti, and Ge in quartz. Numbers in parentheses are the upper concentration limits of the high purity quartz definition (Müller et al. 2012). The approximate emplacement age is according to different sources.

	Froland	Evje-Iveland	Tysfjord	North Portugal	Borborema	Podlesi
	Norway	Norway	Norway	Portugal	Brazil	Czech Republic
pegmatite type	NYF	NYF	NYF	LCT	LCT	LCT
appr. emplacement age (Ma)	1030	910	1710	300	510	320
average pegmatite size (m^3)	550,000	15,000	50,000	25,000	250,000	1,000
number of investigated pegmatites	100	100	5	3	5	2
number of quartz analyses	300	300	13	6	72	24
Al (30)	45±23	94±58	21±7	281±256	265±180	766±198
Li (5)	12±7	7±5	6±4	78±69	56±46	98±21
Ti (10)	8±3	20±13	2±2	5±3	10±6	10±4
Ge (2)	2±1	3±3	2±1	3±1	5±5	2±1
sum (50)	**66±34**	**134±79**	**37±14**	**376±329**	**342±237**	**919±224**
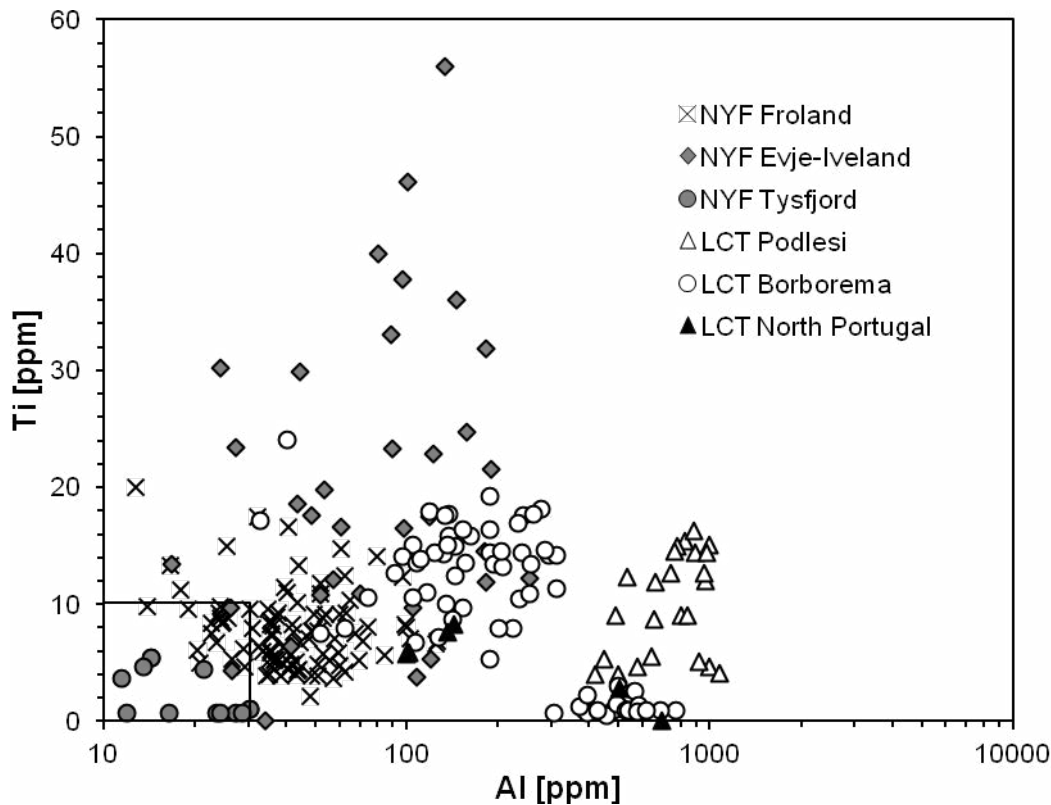
Figure 1. Plot of the Al versus Ti concentrations in pegmatite quartz. Each data point represents the average of three analyses carried out on one quartz sample. The square framing Al <30 ppm and Ti <10 ppm indicates the field of high purity quality (Müller et al. 2007, 2012)

Contributions to pegmatite exploration within granitic plutons in central and northern Portugal

B. Pereira, J. Azevedo, J. Oliveira, P.A. Dias
Sinergeo, Ltd, Vila Verde, PT

C. Leal Gomes
Departamento de Ciências da Terra, University of Minho, Braga, PT

J. Carvalho
Geologia e Geotecnia Consultores, Ltd, Porto, PT

Abstract. Exploration programs for granitic pegmatites face the lack of detectable contrasts, either geophysical or geochemical, between pegmatites and their granitic host-rocks. The known productive sectors bearing pegmatites located inside granitic plutons, with economic interest for quartz and feldspar provide adequate field testing for alternative research, dealing with the peculiarities of lithological diversity and the arrangement of structural elements, around pegmatite swarms at suitable granite cupolas. The most efficient assessment for pegmatite positioning in tactical stages of exploration is the use of geological factors analyzed through raw or specifically treated remote imagery, enhancing the favorable lineaments and the most productive granite-host matrixes. The identification of targets using this approach led to a reasonable success tested by experimental drilling in some selected sites.

Keywords. Remote sensing, pegmatite, quartz, feldspar, granite, Portugal.

1 Introduction

Irregularly shaped pegmatites are the main source of industrial quartz and feldspar in Central and Northern Portugal. They may occur as clusters of small sized bodies individually reaching up to 150000 tons of industrial quartz and feldspar. However, no specific exploration methodology has been applied for locating such pegmatitic deposits.

2 Orogenic constraints for pegmatite emplacement

In Central and Northern Portugal the pegmatite distribution is related to the emplacement of Variscan granites and follows its main structural trends, as shown in Figure 1.
Their spatial location and structural trend led to the definition of the Central Iberian Pegmatite Belt (CIPB) (Leal Gomes and Nunes, 2003)
This belt was conceived on the basis of a regional unit – the pegmatite field – allowing the structural discrimination of the pegmatitic bodies having distinguishable shape, size, internal structure, paragenesis and granite affiliation (Leal Gomes and Nunes, 2003).
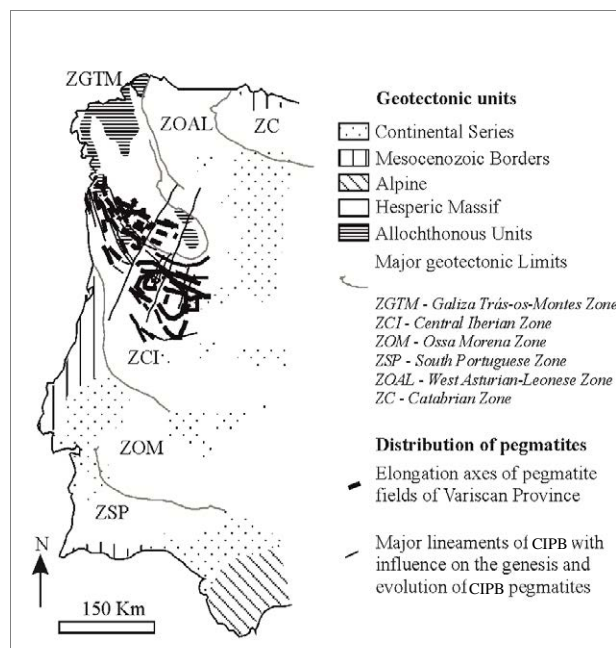
Figure 1 – Location and trends of pegmatite fields in the Central Iberian Pegmatite Belt according to Leal Gomes and Nunes (2003).

3 Regional structure of pegmatite fields in North and Central Portugal

Prior structural analysis of inner-granite swarms of irregular (non-tabular) pegmatite bodies in CIPB – Variscan Province (fig. 2) – yielded the assumption of four major patterns of 3D organization at the top of the assumed, parental magma chambers (Leal Gomes, 1995, 2010):

1 – pegmatite swarms are genetically and spatially related to mingling corridors expressed as aligned outcrops of xenolith clusters, granular enclaves and roof-pendants;
2 – individual volumes with variable modal compositions concentrate in the apical sectors of plutons; these volumes evolve by fractionation
3 – occasionally, the magma flowing under sub-newtonian conditions allows the formation of irregular pods of pegmatite drawing curvilinear trends that can be field-mapped; convoluted-flow lineaments and helicoidal shapes have been recorded;

4 – metric to decametric pegmatitic bodies occur in the vicinity of the host-granite's contacts; the pegmatites are aligned with the feldspar phenocryst and their trend is related to the magma flow.
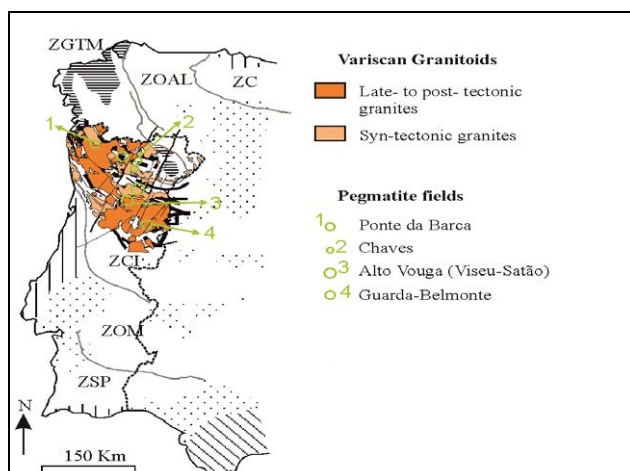
Figure 2. Location of the studied pegmatite fields according to the geographical distribution of syn and late to post-tectonic granites (divisions for Iberian Massif as in fig.1).

The upper-mentioned patterns of distribution, supported the present investigation concerning the adequacy and liability of existent exploration methods for the detection of sub-surface, buried or hidden, pegmatite pods.

The lack of detectable indirect contrasts due to weak geophysical and geochemical boundaries between pegmatite, granitic lithologies and soils as well as the dimensions of the expected and observed pegmatites, strongly suggested the choice of an alternative exploration method.

In this study, the applied approach combines remote sensing and 3D modeling of the pegmatite distribution.

Remote assessment and analysis included straight or specifically treated imagery, establishing the enhancement of favorable lineaments and remote rock matrix adjustments, trough Maximum Likelihood Estimation (MLE), searching for the combining factors that make the presence of pegmatite bodies most probable (Pereira et al, 2011).

4 Case study

In the example of Alto Vouga pegmatite field (fig. 3), overlapping of geological, geomorphological and structural factors, allowed the identification of "Salgueiro" as the area of potential economic interesting fig. 3.

As shown, the first step of the approach consisted on the generation of a geometrical intersection, inside a GIS environment, for the expression of the chosen criteria.

The overlapped areas (shown in red in the same fig. 3) were selected and targeted for subsequent remote sensing and fieldwork
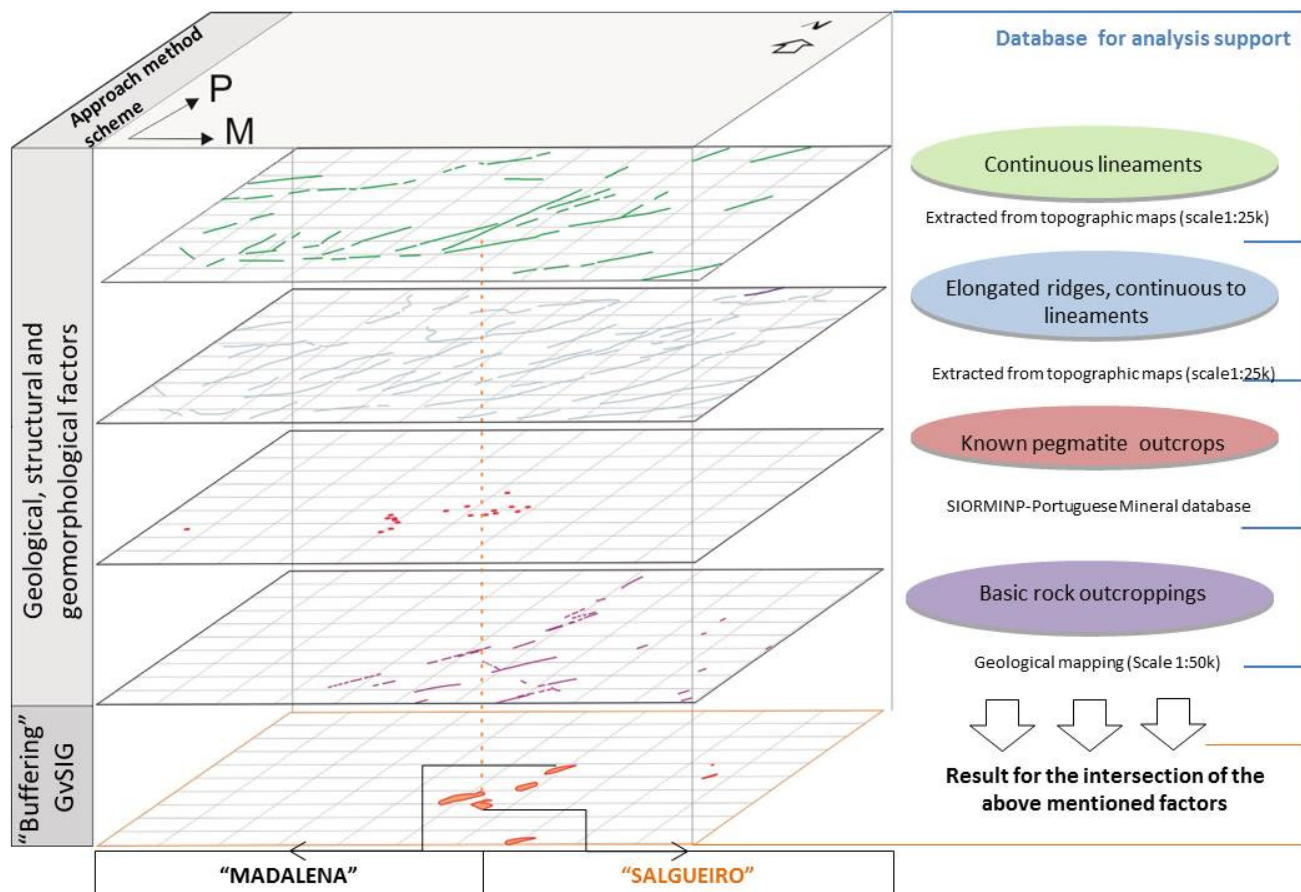
Figure 3. Example of map layering, applied to different selection factors within the Alto Vouga pegmatite field.

Afterwards, a conjunction of SPOT and Google Earth PRO imagery with detailed geological mapping, allowed the construction of the geological map shown in fig. 4.
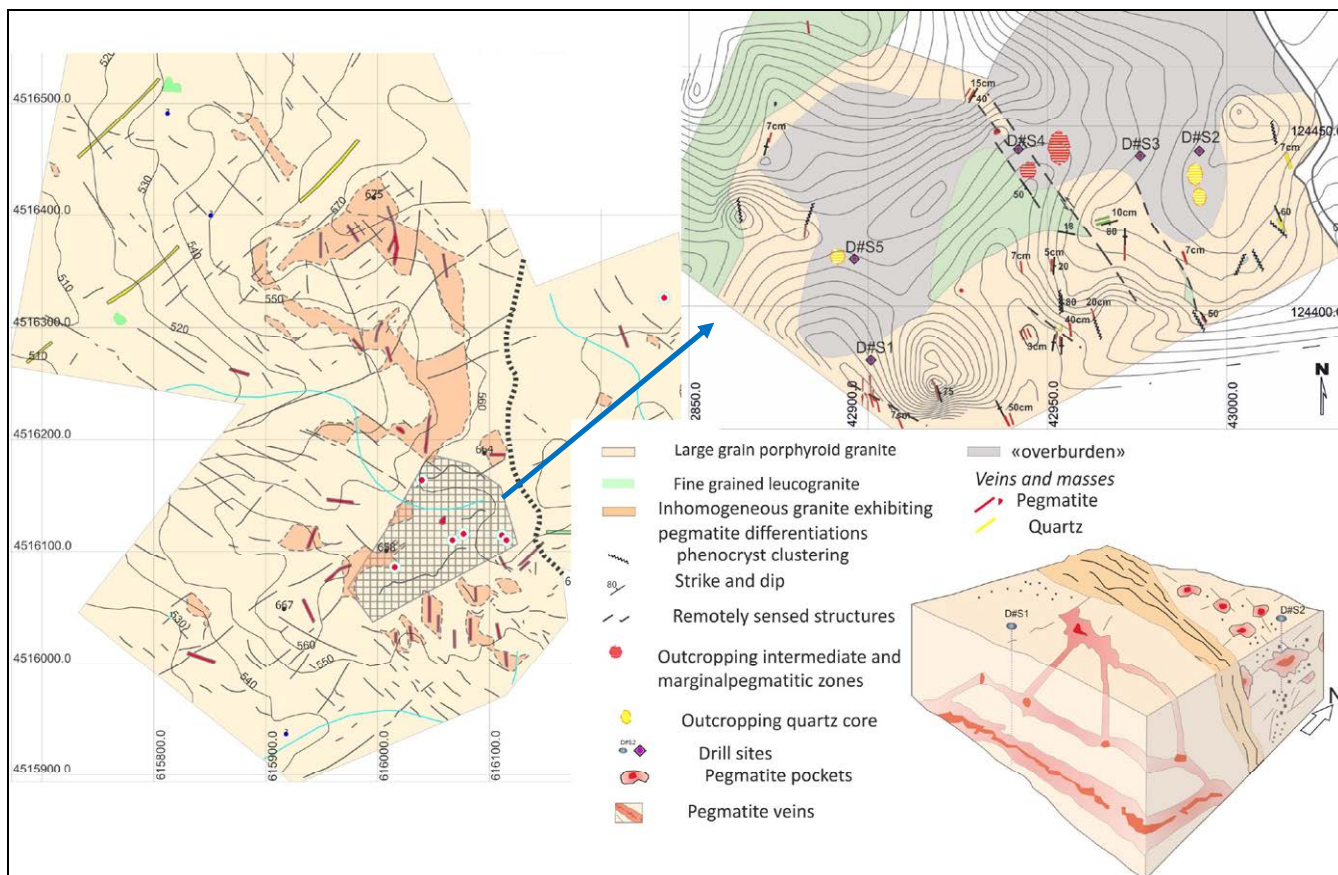
Figure 4. Detailed mapping and 3D conceptual model for the distribution of pegmatites in "Salgueiro" site, within the Alto Vouga pegmatite field.

A conceptual, 3D model, was generated from the structural and lithological data (fig.4), and supported the implementation of a drilling program – drill holes D#S1 to D#S5.

The most encouraging results of this preliminary program are shown in fig. 5. The drillhole intersections of some non-outcropping, medium sized, pegmatite pods, suggest the development of a subsequent drilling program. Furthermore, the preliminary results support the adequacy of the chosen 3D model.

5 Conclusions

When the signature of an individual pegmatite is considered, scale inadequacy is the major obstacle concerning the resolution-detection level of selected satellite imagery.

But, some encouraging results were obtained at the identification of bigger areas with potential for holding clusters of economic pegmatite bodies.

The results of the drilling campaign revealed that the used combination of methods is useful as a medium scale and tactical tool. In favorable structural and image-solvable situations the proposed method allowed the direct drilling intersections obtained in the case of drill holes S1 e S2 (fig. 5).
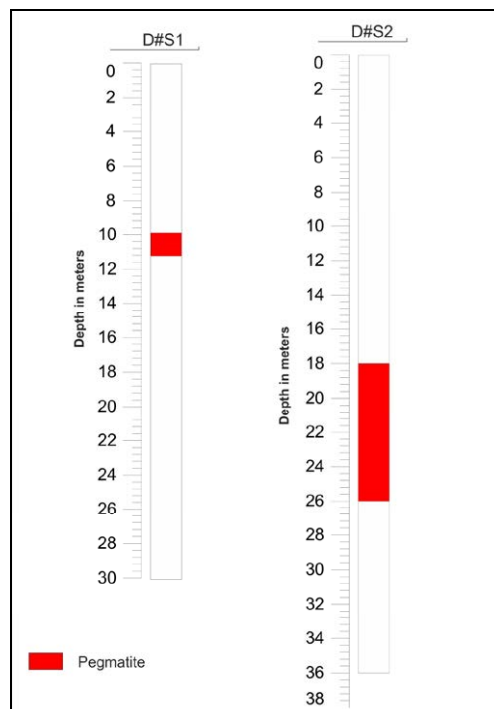
Figure 5. Pegmatite intersections in D#S1 and D#S2 sites – site location shown in fig. 4.

Acknowledgements

References

Leal Gomes, C. (1995) - Anatomia e classificação de pegmatitos cerâmicos intra-graníticos do Norte de Portugal. Memórias nº4, publ. mus. lab. mineral geol., Univ. Porto, pp. 725-729.

Leal Gomes, C. (2010) - Distribuição espacial dos recursos de materiais cerâmicos pegmatíticos no noroeste de Portugal – matriz orogénica e metalogénese relacionada - "Ciências Geológicas – Ensino e Investigação e Sua História" - Volume II - Capítulo I - Geologia e Recursos Geológicos, pp. 25 – 36.

Leal Gomes C, Nunes J E L (2003) Análise paragenética e classificação dos pegmatitos graníticos da Cintura Hercínica Centro-Ibérica. A Geologia de Engenharia e os Recursos Geológicos, Coimbra – Imprensa da Universidade II:85-109.

Pereira, B, Oliveira, J, Azevedo, J, Dias, P, Leal Gomes, C, Carvalho, J, Marques, A (2011) – PROSPEG Projecto de Prospecção, Análise distanciada e Detecção Remota de Pegmatitos, "Valorização de pegmatitos litiníferos", Eds Luis M P Martins, Daniel P S de Oliveira, Rita Silva, Helena M C Viegas, Roberto C Vilas Boas, Lisboa, Portugal, DGEG/LNEG/ADI/CYTED, pp.71–73.

Industrial minerals of the Tiksheozero-Eletozero alkaline ultramafic-carbonatitic and alkaline gabbroic complexes in Karelia, Russia

Vladimir V. Shchiptsov
Institute of Geology, Karelian Research Centre of the Russian Academy of Sciences, Petrozavodsk, 185910, Republic of Karelia

Abstract. The Tiksheozero ultramafic-alkaline rock and carbonatite intrusion and the Eletozero pyroxene-gabbro-alkaline intrusion in northern Russian Karelia are a Paleoproterozoic component of the continental crust of the Fennoscandian Shield. U-Pb ID-TIMS age of the Tiksheozero carbonatite: expression of 2.0 Ga alkaline magmatism. The age also emphasizes the fact that not all members of the Kola alkaline province are of Paleozoic age. Those complexes are shown to host industrial minerals such as apatite, calcite, olivine, ilmenite, titanomagnetite as well as alkaline and nepheline syenites as the sources of feldspar. Geological-technological and economic assessment of the integrated use of carbonatites from the Tiksheozero complex were tested. The Suurivaara ilmenitic ore occurrences is very attractive. Another essential industrial mineral occurrence is the Eletozero central part of nepheline syenite massif. Based on the geological and technological data obtained on ilmenitic and titanomagnetitic ores and law-iron feldspatic concentrates from nepheline syenites. These occurrences can be evaluated. And the mineral reserves are assumed to be accessible from modern geological, technological, economic and environmental points of view.

Keywords. alkaline magmatism, carbonatite, ilmenite, nepheline syenite, Paleoproterozoic

1 Introduction

Alkalic complexes are a widespread and ubiquitous component of the continental crust in the northern regions of the Fennoscandian Shield. The majority, including the economically most important ones, formed in the Paleozoic but there are also several older generations reaching into the Paleoproterozoic and the Neoarchean. The Tiksheozero ultramafic-alkaline rock and carbonatite intrusion and the Eletozero pyroxene-gabbro-alkaline intrusion in northern Russian Karelia are the Paleoproterozoic age (Fig.1).

2 The Tiksheozero intrusion

The Tiksheozero intrusion is located in northern Russian Karelia and belongs to the Karelian-Kola alkaline ultramafic and carbonatitic province, being, in terms of silicate rock composition, referred to as the transitional type between the alkaline ultramafic - carbonatitic and alkaline gabbroid rock assemblages.

At different levels, the Tiksheozero intrusion displays
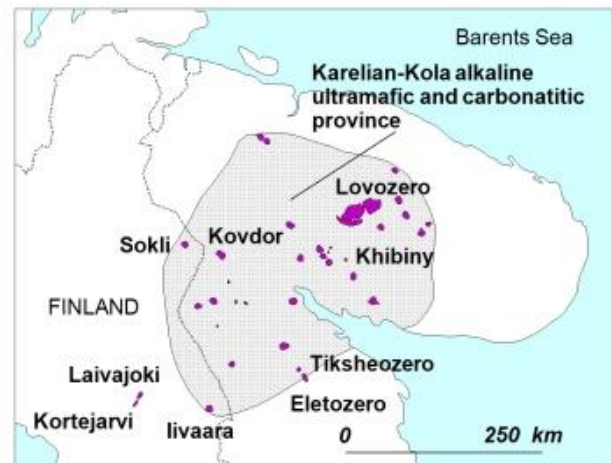
Figure 1. Alkaline complexes and carbonatites in Kola peninsula, northern Russian Karelia and northeastern Finland,

weaker differentiation than the Paleozoic ultramafic-alkaline rocks and carbonatites of the Kola Peninsula. The Tiksheozero intrusion (Fig. 2) presents a north-south trending, bowlshaped body over an area of ca. 20 km2, and is split up into three large blocks: the Tiksheozero, Central, and Shapkozero blocks. They are composed dominantly of pyroxenite (80%), together with olivinite, ijolite, teralite, alkalingabbro, gabbronorite, and nepheline syenite. The core of the Central block consists of carbonatite occurring as a large body of ca. 2 km2 and numerous carbonatite veins. The carbonatite cuts gabbronorite.

The large, tabular carbonatitic body is gently dipping with an uneven upper contact complicated by bulges and apophyses, and by strike-slip faults. Carbonatite can be detected by local negative gravimetric anomalies.

The carbonatites cut the stratigraphy of the intrusion and are variously expressed in the local topography. The spatial arrangement of the carbonatitic bodies is accounted for by local N-trending fractures. They are in turn intersected by oblique northeastern and northwestern faults.

The carbonatitic body is dominated by fine-to-mediumgrained, grey and light grey, banded, occasionally massive and spotted varieties connected by gradual transitions with coarser-grained, leucocratic, pink and pinkish-white carbonatites. The pink carbonatite forms veinlets that cut the grey carbonatite. The contact between the carbonatite and the host rock is

sharp with pronounced exocontact aureoles represented by pyroxenite metasomatically altered into katophorite-carbonate rock, zeolite aggregates with sodalite, albite, prehnite and aegirine after alkaline rocks, and with albite and aegirine after granitoid rocks. The host rock is often brecciated and cemented with carbonate substance. Mylonite developed in the exocontact of the carbonatite points to a tectonically active setting during the formation of the carbonatite. It is usually represented by dark green, fine-grained amphibole-Mg-carbonate or biotite-amphibole-Mg-carbonate schists with richterite. alcitic carbonatites predominate, while dolomite-(ankerite)-calcitic and dolomitic carbonatites are subordinate. Coarse-grained to pegmatitic varieties of the calcitic carbonatite (sevite) bond shatter zones in the pyroxenites, form tiny veins escaping into the gabbronorite, and appear in the central part of the carbonatitic body

Figure 2. Geological map of the Eletozero pyroxene-gabbro-alkaline intrusion, compiled by V. Shchiptsov and N.Shchiptsova

Massive carbonatite has widespread taxitic structures associated with uneven distribution of magnetite and silicate minerals that produce spotty patterns or dark speckles in the light background of the carbonatitic rock. Geochemically it is characterized by relatively low concentrations of rare-earth elements, Sr and radioactivity. Main ore components are iron, concentrated in magnetite, and phosphorus in apatite.

Table 1. Average mineral composition of the carbonatite (%)

Cal	Do	Ap	Mt	Phl	Amf	Prcl
70	9	9	5	ca 3	ca 4	ca 1

Cal –calcite, Do – dolomite, Ap – apatite, Mt – magnetite, Phl – phlogopite, Amf – amphibole, Prc – pyroclore

Apatite formed in two stages: magmatically and metasomatically (or autometasomatically (Shchiptsov et al, 2007).

U-Pb ID-TIMS age of the Tiksheozero carbonatite: expression of 2.0 Ga alkaline magmatism in Karelia,

Russia (Corfu et al)].

Geological-technological and economic assessment of the integrated use of carbonatites from the Tiksheozero ultramafic-alkaline rock and carbonatite massif is made. Their dressability is estimated on the basis of the technological study of apatite-bearing carbonatites. Several schemes for the production of apatite and calcite concentrates have been tested. The conclusion has been drawn that the production of high-quality apatite and calcite concentrates is ensured by an integrated approach to dressing schemes using the flotation and magnetic dressing methods. Gross technological and economic calculations of the integrated waste-free use of carbonatites from the Tiksheozero deposit have been made (Shchiptsov et al, 2007).

3. The Eletozero intrusion

In plan view, the Eletozero massif, which extends approximately N-S, is an concentrically-zoned ellipsoid body with a flexure-shaped axial line. It covers an area of about 100 km^2, and extends for 18-20 km along the long axis and for 6-8 km along the short axis. Most of the peripheral part of the massif consists of gabbroic rocks and its central part is composed of alkaline and nepheline syenites. Explosion breccia supported by carbonated matrix has been identified in the northern portion of the massif (Shchiptsov et al? 2009).

The conditions of its formation suggest that the massif is a complex multi-phase long-evolving pluton. Based on petrographic composition and the sequence of formation, the following rock classes and rock groups are distinguished: sideronitic clinopyroxenites, gabbroic rocks (a fine-grained marginal gabbro series with a transitional subseries of alternating fine-grained and coarse-grained gabbro and a gabbroic rock series proper represented by coarse-grained gabbro, medium-grained gabbro, plagioclasite-ore peridotite, leucocratic orthoclase gabbro, mica gabbro and mica peridotite), spessartine dykes, miaskite-type alkaline and nepheline syenites with their veined and dyke derivatives, and rocks associated with a carbonatite stage in the formation of the rock complex (Fig.3). It's supposed the age of alkaline and nepheline syenites generated at the final stage is similar to the age of the Tiksheozero carbonatite.

Mineralogenically, the attention is drawn by industrial mineral prospects identified as part of the massif formed, such as ilmenite and titanomagnetite occurrences as well as alkaline and nepheline syenites of the sources of feldspar.

Alkaline and nepheline syenites are common in the central part of the Eletozero massif, where they make up a body which covers an area of about 10 km^2. The chemical and mineralogical compositions of the alkaline ahd nepheline syenites are corresponding to miascite (miascite type).

The Suurivaara ore prospect of the Eletozero massif (East Ore Body) is most promising. Here, several bodies with various mineralizations represented by titaniferous magnetite and ilmenite have been located. Five bodies, namely Severnaya, Zapadnaya, Tsentralnaya, Parallelnaya and Glavnaya, are distinguished. Based on TiO_2 content , titanomagnetite and ilmenite ores fall into three grades: grade I = over 12%/ grade II = 8-12%, grade III = 5-8%.
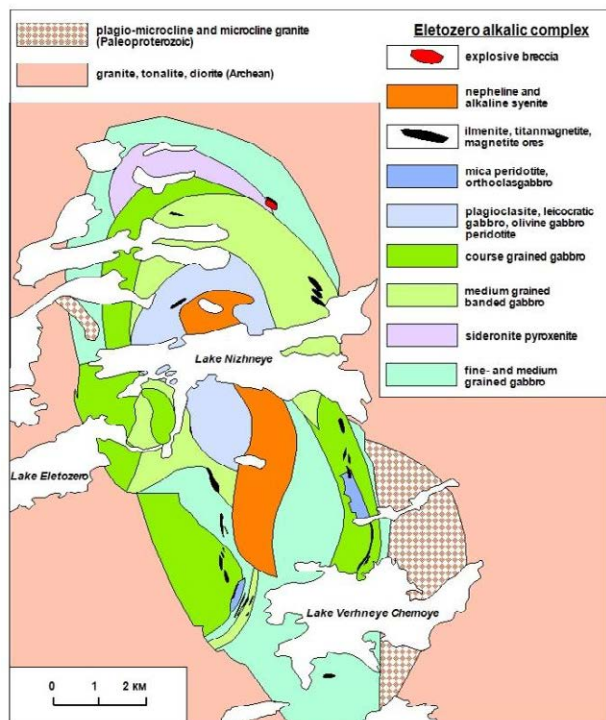
Figure 3. Geological map of the Tiksheozero alkalic complex displaying the geometry of the carbonatite body, compiled by V. Shchiptsov and N.Shchiptsova

The study of the prospects which contain such valuable minerals as ilmenite, titanomagnetite and syenite has shown their industrial significance. The updating of technological methods makes it possible to assess the accessibility of mineral resources from the modern understanding of geology, technology, economy and ecology.

4.   Summary

Those complexes are shown to host industrial minerals such as apatite, calcite, olivine, ilmenite, titanomagnetite as well as alkaline and nepheline syenites as the sources of feldspar.

Geological-technological and economic assessment of the integrated use of carbonatites from the Tiksheozero carbonatite were tested.

The Suurivaara ilmenitic ore occurrences is very attractive.

Another essential industrial mineral occurrence is the Eletozero central part of nepheline syenite massif.

Based on the geological and technological data obtained on ilmenitic and titanomagnetitic ores and low-iron feldspatic concentrates from nepheline syenites. These occurrences can be evaluated. And the mineral reserves are assumed to be accessible from modern geological, technological, and environmental points of view.

References

Corfu F, Bayanova T., Shchiptsov V, Frantz N. 2011. U-Pb ID-TIMS age of the Tiksheozero carbonatite: expression of the 2.0 Ga alkaline magmatism in Karelia, Russia // Cent. Eur.J.Geosci. 3(3),. 302−308.

Shchiptsov V.V., Bubnova T.P., Garanzha A.V., Skamnitskaya L.S., Shchiptsova N.I. 2007, Geological, technological and economic assessment of the carbonatitic resource potential of the Tiksheozero intrusion (ultramafic alkaline and carbonatitic rock association) // *Geology and Deposits of Karelia*, 10, 159-170 (in Russian)

Shchiptsov V.V., Skamnitskaya L.S., Bubnova T.P.   2008 Industrial mineralsof the Eletozero massifand their analogues on the Fennoscandian Shield // *Geology and Deposits of Karelia*, 11, 159-170 (in Russian)

Mullite synthetization at low temperature

Ariana Zeballos[1,2], Pär Weihed[1], Mario Blanco[2] & Vladimir Machaca[2]
[1] *Luleå University of Technology (LTU)-Sweden*
[2] *Instituto de Investigaciones Geológicas y del Medio Ambiente (IGEMA)-Bolivia*

Abstract. The mineral mullite ($3Al_2O_3 2SiO_2$) is frequently used by the industry in the preparation of refractory ceramics. However, it is uncommon in nature and, therefore, synthetically manufactured. The commercial mullite is synthetized from kaolinite + Al_2O_3 (gibbsite, bauxite), making the synthetization expensive. For that reason, naturally occurring deposits that can be utilized for the process are sought for. The Micaya deposit, located outside La Paz, Bolivia, is composed of a layer of kaolinitic shale hosted within the Vila Vila Formation composed of Devonian coarse-grained sandstones and siltstones. The shale is composed of quartz, kaolinite, muscovite and feldspar. The kaolinite can be separated from the shale by gravity separation, thus decreasing the SiO2 content and obtaining a new product with a higher Al_2O_3 content. The two major components (quartz and alumina) are then subjected to a calcination process at high temperatures in a suitable ceramic firing programme and results in the formation of mullite without adding extra Al_2O_3.

Keywords. Kaolinite, Mullite, Synthetization

1 Introduction

The objective of this research project is to open a possibility to commercialize kaolinitic material from a residual kaolinitic deposit by producing a higher value product such as mullite. The Target deposit Micaya, is located 60 km south of La Paz, Bolivia and is composed of quartz (56%), kaolinite (18%), muscovite (21%) and feldspar (5%). The deposit is a residual deposit formed by local weathering of siltstones from the Vila Vila Formation (Zeballos, 2009).

The mineral mullite has the nominal chemical composition $3Al_2O_3 2SiO_2$ and its name is derived from the Isle of Mull outside Scotland. It it crystallizes in the orthorhombic system, has a very high melting point (1840° C) and it is very scarce in the nature. Mullite is widely used in the production of refractory materials and therefore it is necessary to optimize the synthetization process to produce marketable mullite at a low cost. The general formula for the production of mullite from pure kaolinite is as follows: Kaolinite – metakaolinite – spinel phase – primary mullite – mullite.

Mullite displays excellent thermal properties in ceramic bodies, improves the thermal shock in ceramic bodies, has low thermal expansion and improves the resistance of the material. Its main uses include porcelain refractory, refractory bricks, electrical insulators and pipe protectors. The triaxial porcelains acquire significant hardness and strength through mullite formation during calcination as a result of vitrification (Hong-Yang et. al., 2004).

2 Geological setting

The deposit is located in the town of Micaya, La Paz - Bolivia (Fig. 1). The deposit consists of whitish kaolinitic shale intercalated with sandstones from the Devonian Vila Vila Formation. The shale is composed of quartz (56%), kaolinite (18%), muscovite (21%) and feldspar (5%) (Zeballos, 2009).

The rock units in the Micaya region are Devonian to Permian in age, where the oldest unit, sandstones of Vila Vila Formation occur in the west, followed by rocks of the Belen, Sica Sica and Collpacucho Formations, and the youngest unit, limestones of the Copacabana Formation of Permian age outcropping in the east (Zeballos, 2009). Towards the east several dacitic subvolcanic intrusions occur, related to extrusive magmatic events of Cenozoic age (Soria, 1980).
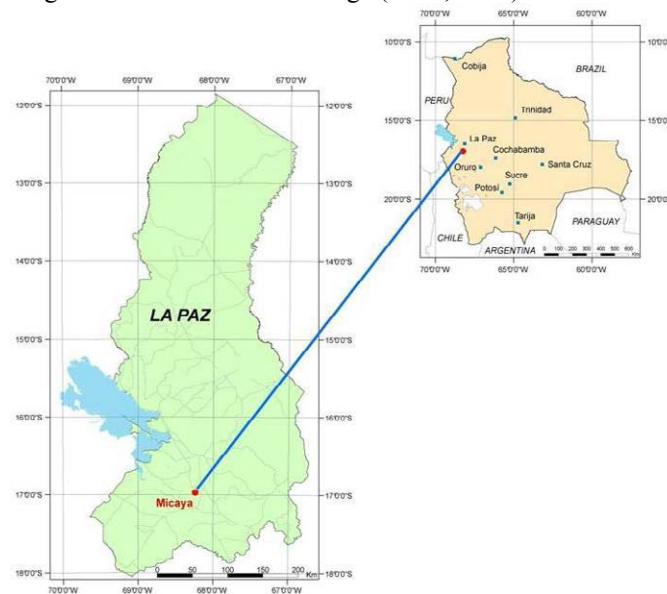
Figure 1. Location map of the study area. Micaya (S 16° 58' 07,4''; W 68° 14' 22,9''), Aroma Province in La Paz state from Bolivia.

3 Methodology

The chemical, mineralogical and structural studies were carried out at the ALS-in Sweden, the laboratory of the Geological Research Institute in La Paz and at Luleå University of Technology in Sweden. The chemical characterization was carried out by ICP-AES, using 0.1 g of dehydrated sample, which was dissolved with 15 ml HF, 2 ml HCl, 2 ml HNO_3 and 2 ml H_2O homogenised to temperatures above 1000° C. Mineralogical phase identification of the raw material and the synthesized products were performed with X-Ray diffraction on a Rigaku Geigerflex equipment, with Cu tube and Ni filter, under operating conditions of 35kV and 15 mA,

speed goniometer registration of 2°/min., slits of 1° - 0.15 mm. For phase identification a mineralogical specialized software X'Pert PanAnalitical High Score was applied. The microstructure of the synthesized material was evaluated in a scanning electron microscope (SEM, Magellan UHR) and Energy Dispersive X-Ray Spectroscopy (EDX, X-MAX 80 mm2, Oxford Instruments, Oxford, United Kingdom).

The mullite synthesis was done in two stages: gravity concentration and firing. The procedure starts by concentrating the clay phase (grain sizes < 2 µm) by gravity concentration in an aqueous medium for 2 hours, after which concentration by a firing program was conducted with the ramp/hold firing method which creates a programmed differential burning by raising the temperature from 0° C to 1250° C following a segmented curve with clearly defined times of burning. This means that each segment of temperature in turn consists of a "ramp of burning" and a "hold time of temperature", which are themselves defined by the starting temperature, rate of temperature increase, the final temperature to be reached and the time that must be maintained under the final condition.

The number of segments is set according to the expected final product specification having in mind all mineralogical phase changes that occur in the material while calcination. In this case, we applied a burning program consisting of five segments (Table 1); each segment was based on the phase shifts that occur in ceramic material during burning, as suggested by Machaca (2010), and the possibility of phase changes that occur from kaolinite to mullite, described below.

	RANGE OF T°	MINERALOGICAL PHASES	PHASES OF MULLITE
1st segment	0°C a 570°C	Qz α – Qz β	Kaolinite
2nd segment	570°C – 800°C	Triclinic Ab – monoclinic Ab	Metakaolinite
3th segment	800°C – 1100°C	orthoclase - sanidine,	Spinel phase
4th segment	1100°C – 1150°C	Sol. phases – liq. phases	Primary Mullite
5th segment	1150°C - 1250°C	Ceramic products	Acicular Mullite

Table 1. Ramp/Hold firing program, five segments based on crystallization changes of the mineralogical phases (Machaca, 2010) and their possible relationship with kaolinite phases.

4 Preliminary Results

The chemical composition of the concentrated sample compared to the studied raw material shows an enrichment of Al_2O_3 and some others major oxides and a decrease in silica (SiO_2). This means that the process of gravimetric concentration in aqueous medium could effectively separate detrital components (> 2 µm), represented by quartz and feldspar, and, thus, favouring the concentration of kaolinite in the finer fraction. This, however, does not imply the total elimination of quartz

as this component is also found in abundance in the finer fractions. Table 2 summarizes the results of the chemical analysis of major oxides described above.

	Raw material	Concentrated material
SiO_2	72,7	57.3
Al_2O_3	17,6	32.8
CaO	0,13	0,294
Fe_2O_3	1,29	1,69
K_2O	3,87	5.27
MgO	0,68	1.07
MnO	0,02	0,0458
Na_2O	0,09	0.115
P_2O_5	0,07	0,129
TiO_2	0.96	0.975
TOTAL	**97.04**	**99.45**

Table 2. General chemical composition of the raw material compared to the concentrated material, expressed as major oxides (wt.%).

SEM images and the X-Ray diffraction curve, both methods applied after calcination, confirm a positive mullite synthetization. Figure 2 shows a micrograph of the sintered material, where crystals of acicular mullite can be observed dispersed in the sample.
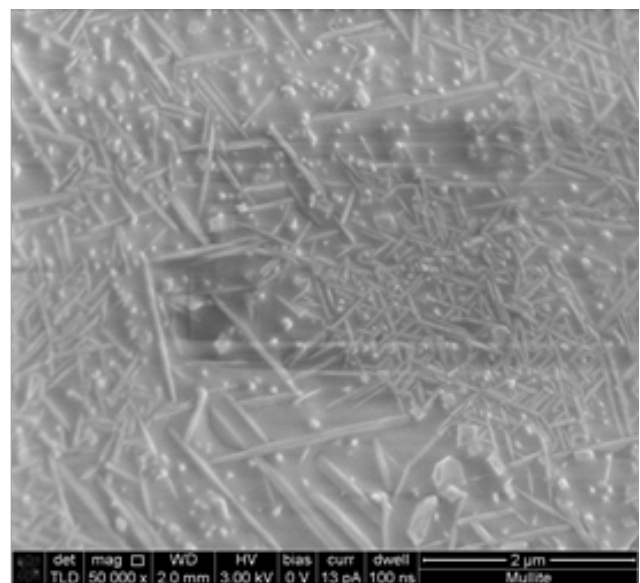
Figure 2. Acicular mullite observed in a SEM micrograph.

Two X-ray diffractograms, shown in figure 3, corroborate the electron microscopic study. The upper diffractogram shows the raw material, a sample without calcination where four mineralogical phases are observed: quartz, kaolinite, muscovite and feldspar. The second diffractogram shows a calcinated material where only two mineralogical phases, quartz and mullite are present, indicating a transformation from kaolinite to mullite. The raw material was calcinated into five segments up to 1250° C.
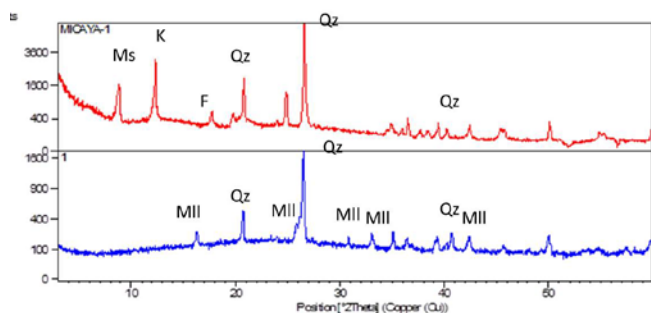
Figure 3. Upper curve shows the XRD pattern of the Micaya raw material and the lower curve the XRD pattern of calcinated material.

5 Conclusions

The studied raw material, kaolinite of a residual origin from the Micaya deposit in La Paz-Bolivia, is suitable for synthesizing mullite, a mineral widely used as a component in refractory ceramics. The properties of the material during firing during which recrystallization processes occur should thus be studied in more detail.

Acknowledgements

References

Hong-Yang Lu,Wei-Lin Wang, Wei-Hsing Tuan and Ming-Hong Lin (2004) Acicular Mullite Crystals in Vitrified Kaolin. Journal of the American Ceramic Society, 87. pp. 1843-1847.

Machaca V (2010) Aplicación de los recursos no-metálicos de la mina Fabulosa y Choquetanga grande en el Departamento de La Paz. Tesis de Grado, Universidad Mayor de San Andrés, La Paz-Bolivia.

Soria Flores A (1980) Estudio Hidrogeológico Del Área Viacha, Surusaya Y Villa Remedios. Tesis de Grado, Universidad Mayor de San Andrés, La Paz – Bolivia.

Zeballos A (2009). Aplicación de los recursos no-metálicos de la localidad Micaya, Provincia Aroma, Departamento de La Paz. Tesis de Grado, Universidad Mayor de San Andrés, La Paz-Bolivia.

S 6.2:
Construction materials

Convenors:
Richard Přikryl & Karel Miskovsky

Characterization of "Xisto de Foz Côa" a typical natural stone from northern Portugal

S. Aires, H. Sant'Ovaia, F. Noronha
Centro de Geologia da Universidade do Porto — FCUP - DGAOT, Rua do Campo Alegre 687, 4169-007 Porto, Portugal

C. Carvalho
Laboratório Nacional de Energia e Geologia — R. da Amieira, Apartado 1089, 4466-901 S. Mamede de Infesta, Portugal

M. Búrcio
SOLICEL (Sociedade do Centro Industrial de Esteios de Lousa, Lda.-http://www.solicel.pt/web/eng_index.php) Vila Nova de Foz Côa; Laboratório de Investigação de Rochas Industriais e Ornamentais da Escola de Ciências e Tecnologia da Universidade Évora, Portugal

Abstract. The main purpose of this work is to contribute to the characterization of a very important geological resource of Trás-os-Montes and Alto Douro (TMAD) region the "Xisto de Foz Côa" (Portuguese word for "Foz Côa slate"), considering its economic and social impact.
The most important outcome of this work is to improve the knowledge about mineralogy, fabric, chemistry and technology of the "Xisto de Foz Côa", in order to promote its use as a natural stone.

Keywords. Slate, natural stone, Foz Côa, Portugal

1 Introduction

The Trás-os-Montes and Alto Douro (TMAD) region is located in Northern Portugal. Its lithology consists essentially of metassedimentary rocks mainly formed from pre-existing sediments, Precambrian to Devonian in age, that were deformed and affected by regional Variscan orogenic metamorphism.

Although slate and schist are very common in TMAD region, only a small part of them are being used as natural stone. The geological structure, the deformation intensity, the metamorphism degree and the rock mass fracturing state are important to determine mining capability and profitability of an exploitation of this material.

With this study we carried out a characterization of "Foz Côa slate", occurring in Northern Portugal on the south margin of the Douro River, where Oporto Wine vines are grown, in order to promote its use as natural stone in Europe.

2 Geology

2.1 Regional geology

The Iberian Massif is a structural unit divided into several geotectonic zones with different geological, petrological and structural characteristics and separated by important tectonic structures (Julivert et al., 1972).

Foz Côa area is geologically located in the Central Iberian Zone (CIZ) that corresponds to an Autochthonous terrain (Ribeiro et al. 1990; Pereira &

Ribeiro, 2006) (Fig.1).

The dominant rocks from CIZ are metassediments. They usually exhibit a well-marked foliation, generally parallel to the stratification and a low grade metamorphism.

2.2 Tectonics

In TMAD metassediments were structured by a succession of three phases of Variscan deformation: D1, D2 and D3 (Ribeiro, 1974; Noronha et al. 1979). D1 is upper Devonian; D2 has an age ranging between Upper Devonian to Namurian; D3 is intra-Westefalian. D2 is mainly represented in the allochthonous and sometimes in the upper parautochthonous domains. D3 affected the autochthonous, allochthonous and parauthochtonous, generating folds of low-amplitude and vertical axial planes. In, CIZ, only D1 and D3 phases are represented.
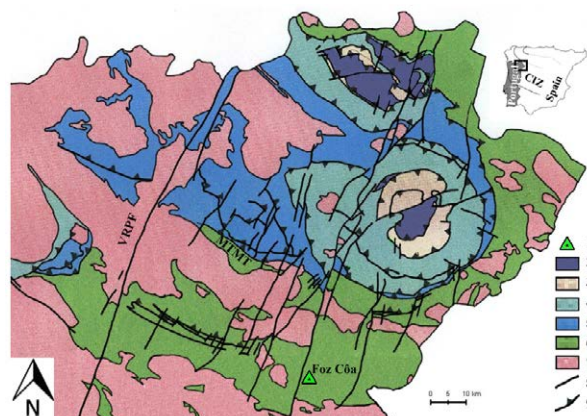
Figure 1. Structural domains of the TMAD region. Caption: 1- Foz Côa location; 2-upper allochthonous; 3- middle allochthonous; 4- lower allochothonous; 5- parauchthonous; 6- autochthonous and sub-autochthonous; 7- granites; 8- fault; 9- thrust. VRPF- Verín-Régua-Penacova fault. MTMT- Main Trás-os-Montes Thrust. After maps 1:500,000 sheet North and 1:200,000 sheet 2 from IGM (simplified).

2.3 Metamorphism

The metamorphic evolution is characterized by a regional orogenic metamorphism of Barrovian type, which changed to high temperature and low pressure between D2 and D3 phases (Arenas & Catalán, 2003).

The geology of TMAD region was strongly affected by the occurrence of NNE-SSW faults that conditioned the existence of distinct crustal levels.

3 Methods

Geological survey of the metamorphic formations was carried out based upon the published and available geological mapping (1:50 000).

In the laboratory petrographic, chemical and technological studies were performed on samples of two different varieties.

The petrographic and mineralogic characterization was based on the macroscopic description and petrographic observations of thin sections using polarized light microscopy. Chemical analysis of major and minor elements was performed by X-Ray Fluorescence to complement the petrographic studies and improve the classification of the different lithologies.

It is necessary to know the natural stones properties and also to understand its behavior when subjected to stress, action of atmospheric agents and human activity, in order to give them the most appropriate use. The selection of tests, to be run on a particular natural stone, should always take into account: (i) the type of natural stone; (ii) the type of application; (iii) the environmental conditions of the site where the natural stone is going to be applied (Carvalho et al. 2013) European Standards (EN) of natural stone test methods were used to determine a set of properties on the studied slates. The properties determined (and the respective EN's) were: 1) water absorption at atmospheric pressure (EN 13755); 2) apparent density and open porosity (EN 1936); 3) compressive strength (EN 1926); 4) flexural strength under concentrated load (EN 12372); 5) abrasion resistance (EN 14157); 6) resistance to ageing by thermal shock (EN 14066). 1) and 2) are physical properties. The properties 3) and 4) are of mechanical nature. Finally, 5) and 6) are technological properties.

Anisotropy of Magnetic Susceptibility (AMS) studies were also carried out. At each sampling site in-situ several oriented cores were collected with a portable drill machine. In the laboratory those cores were sawed perpendicularly to their axis, to obtain individual specimens with dimensions of 22 mm height and 25 mm diameter. AMS measurements were performed on a Kappabridge KLY-4S equipment, AGICO model (Czech Republic), from the Center of Geology (Oporto University).

4 Results and Discussion

In this work we considered of particular importance to determine the relationship between deformation and metamorphism, including, respectively, its intensity and grade.

4.1 Geology

The studied area corresponds to an example where the the metamorphism is of low grade, on greenschist facies, and the deformation of the metasediments caused a slaty cleavage because is located in a shallower level at East of important NNE-SSW faults (Noronha et al. 2013).

Foz Côa sequence correspond to a multilayer stratigraphic sequence (S0) belonging to Desejosa Formation included in the Douro Group of Lower Cambrian age (Sousa, 1982). The deformation of the "Douro Group" which is a very important feature to consider, is generally characterized by the action of a single phase of progressive deformation, common in the CIZ. Regarding the intensity of deformation, D1 has a very heterogeneous distribution. This heterogeneity leads to sectors with tight folds and others with large folds (Dias et al. 2006). D1 generated an axial plane cleavage (S1) subvertical with WNW-ESE direction.

The existence of slightly deformed bands alternating with bands where deformation is more intense is extremely important at a regional level. D1 deformation phase induced the formation of zones gently folded (sinforms) and others with strong deformation (antiforms).

The site of "Foz Côa slate" quarry (Fig.2) is located in the center of a sinform, where the structural relationship between stratification (S0) and a slaty cleavage is 90^0 (Moreira et al. 2010).

Figure 2. Foz Côa quarry.

4.2 Petrography

Macroscopically the rocks show a dark grey color (XNFC-"Xisto negro Foz Côa"- "Black slate"), sometimes yellowish (XOFC-"Xisto oxidado Foz Côa"- "Oxidized slate"). They show a fine grain size.

The alternation between layers richer in argillaceous components with others richer in silt gives to the rocks a striped aspect.

Microscopically a granoblastic to lepidoblastic texture formed by quartz, white mica, chlorite, opaque and clay minerals can be observed. In XOFC, the layering is characterized by the alternance of layers with organic matter with others, more abundant, rich

on quartz and oxides which contribute to the rock's brownish color. XNFC is characterized by more abundant organic matter impregnating the layered minerals.

4.3 Magnetic anisotropy

The magnetic anisotropy degree expressed by the parameter P', which corresponds to the ratio between higher and lower magnetic susceptibility, is 1.222. Parameter T (Jelinek, 1981), which shows the AMS ellipsoid shape, is -0.664. The obtained values are similar with those found by Hrouda (1982) in slates. Parameter T indicates a prolate AMS ellipsoid which reflects regional structures.

AMS studies show magnetic susceptibility mean value of 282×10^{-6} SI. "Foz Côa slates" samples are characterised by a paramagnetic behaviour, due to the presence of iron silicates. Magnetite is not present as accessory mineral.

4.4 Geochemistry

The geochemical studies are an important tool in the classification of the studied rocks because they are usually very fine grained.

The major elements content (Table 1), particularly SiO_2 and Al_2O_3 and trace elements (Table 2) such as V and Zr can discriminate the relative abundance of argillaceous and silt components. Higher values of Al_2O_3 and V and lower values of SiO_2 and Zr denote a more important involvement of argillaceous component.

Table 1. Chemical analysis – major elements (Wt%)

		XNFC	XOFC
SiO_2	[wt%]	66.38	69.29
Al_2O_3	[wt%]	15.49	13.81
Fe_2O_3*	[wt%]	5.70	3.94
MnO	[wt%]	0.05	0.06
CaO	[wt%]	0.89	1.55
MgO	[wt%]	2.09	1.41
Na_2O	[wt%]	2.19	2.99
K_2O	[wt%]	3.67	2.87
TiO_2	[wt%]	0.74	0.79
P_2O_5	[wt%]	0.13	0.14
L.O.I.**	[wt%]	2.60	3.05
Total	[wt%]	99.93	99.90

* Total Fe as Fe_2O_3; ** Loss On Ignition

We can differentiate the XOFC from XNFC, with 69.29 and 63.38% of SiO_2 respectively. XNFC shows higher content on Al_2O_3 (15.49%) and V (70 ppm) in opposition to XOFC, which is more siliceous and richer on Zr (362 ppm) and therefore exhibits a lower content on Al_2O_3 (13.81%) and V (58 ppm).

The XNFC is also richer on Fe_2O_3 , MgO and K_2O.

Table 2. Chemical analysis – minor elements (ppm)

		XNFC	XOFC
Rb	ppm	149	118
Sr	ppm	184	250
Y	ppm	34	27
Zr	ppm	215	362
Nb	ppm	16	14
Ba	ppm	814	627
Sn	ppm	6	6
W	ppm	<6	<6
Th	ppm	16	18
U	ppm	<6	<6
La	ppm	57	36
Ce	ppm	105	90
Nd	ppm	45	40
Ni	ppm	29	20
Cu	ppm	18	14
Zn	ppm	85	60
Pb	ppm	25	22
Sc	ppm	13	11
V	ppm	70	58
Cr	ppm	59	53
Co	ppm	11	7
Ga	ppm	19	16

4.5 Physical, Mechanical and Technological Characterization

Tests results are shown in **Table 3**.

Table 3. Test results (mean values).

	XNFC	XOFC
Water absorption	0.2 %	0.5 %
Apparent density	2760 kg/m^3	2700 kg/m^3
Open porosity	0.4 %	1.1 %
Compressive strength	114 MPa	136 MPa
Flexural strength under concentrated load	61.0 MPa	45.5 MPa
Abrasion resistance (Method A - Wide Wheel)	22.0 mm	20.0 mm
Resistance to ageing by thermal shock	0.02 %[1] (weight loss)	0.03 %[2] (weight loss)

[1] Besides the weight loss which is insignificant, during cycling, the iron oxide spots and stains that existed in all specimens before cycling became larger and more intense; also new iron oxide spots developed on the surface of all tested specimens (see **Figure 3**).

[2] XOFC did not experience significant changes in its visual appearance during cycling (see **Figure 4**).

Figure 3. Resistance to ageing by thermal shock of XNFC. Surface detail of 3 tested specimens. Notice that the spots of iron oxide appeared mainly on the lighter colour levels. The specimen with coin on his top face is the reference specimen which was not submitted to testing.

Figure 4. Resistance to ageing by thermal shock of XOFC. Surface detail of 3 tested specimens. Notice that the visual appearance of the tested specimens is similar to the reference specimen — specimen with coin on his top face — which was not submitted to testing.

5 Conclusions

The future of the mining industry both in TMAD region and in Portugal goes through the exploitation of natural stones.

With this work we gathered a much better knowledge about the structural, mineralogical, petrographic, chemical and technological characteristics of "Foz Coa slates", that can help to promote its application as natural stone in Europe.

Since ancient times "Foz Côa slates" are being applied as vine support and also as rustic masonry units, in the vicinity where they occur. However, for other applications, which demand technical specifications, the evaluation of the test results allowed us to set out a list of recommended applications for each slate. Thus, we conclude that both slates are suitable to be applied as: cladding, lintels, bearing masonry units and columns. Regarding paving, both slates can be applied in sites with moderate traffic, but only XOFC slate should be applied in sites with high traffic. This slate is also the only one suitable to be applied as roofing, as slabs of various thicknesses. The changes in visual appearance that XNFC suffered in the resistance to ageing by thermal shock test, led us to conclude that this variety is more suitable to be used indoors.

Acknowledgements

References

Arenas, R. and. Catalán, J.R.M. (2003). Low-P metamorphism following a Barrovian-type evolution. Complex tectonic controls for a common transition, as deduced in the Mondoñedo thrust sheet (NW Iberian Massif). Tectonophysics, 365: 143-164.

Carta Geológica de Portugal 1:200 000, Folha 2, Instituto Geológico e Mineiro, Portugal E. Pereira (Coord) (2000).

Carvalho, C., Noronha, F., Aires, S., Casal-Moura, A. and Ramos, F. (2013). "Schist" from Trás-os-Montes and Alto Douro (NE of Portugal) — Potential use as Natural Stone, Key Engineering Materials Vol. 548, pp 205-211, Trans Tech Publications, Switzerland.

Dias, R., Coke, C. e Ribeiro, A. (2006). Da deformação na Serra do Marão ao zonamento do autóctone da Zona Centro Ibérica. Edited by: Dias, R., Araújo, A., Terrinha, P. e Kulberg, J., in: Geologia de Portugal no contexto da Ibéria (pp.35-61). Évora: Univ. Évora. ISBN: 972-778-094-6.

Hrouda, F. (1982). Magnetic anisotropy of rocks and its application in geology and geophysics. Geophys. Surv. 5: 37-82.

Jelinek, V. (1981). Characterization of the magnetic fabric of rocks. Tectonophysics 79, 63-67.

Julivert, M.. Fontbote, J. M Ribeiro A. and Nabais Conde L. E. (1972). Mapa Tectonico de la Peninsula Iberica y Baleares E. 1: 1.000.000. Inst. Geol. Min. Esp. Madrid.

Moreira, N., Búrcio, M., Dias, R., Coke, R. (2010). Partição da deformação Varisca nos sectores de Peso da Régua e Vila Nova de Foz Côa (autóctone da Zona Centro Ibérica). Comunicações Geológicas, t 97, pp. 147-162.

Noronha, F., Ramos, J. M. F. Rebelo, J. A Ribeiro A.and Ribeiro M. L.: (1979). Essai de corrélation des phases de déformation hercynienne dans le Nord-Ouest Péninsulaire. Bol. Soc. Geol. Portug., 21, 2/3: 227-237

Noronha, F., Carvalho, C., Aires, S., Casal-Moura, A. and Ramos, F. (2013). Characterization of "Xisto" as a Way to Promote its Use as Natural Stone, Key Engineering Materials Vol. 548 pp 197-204, Trans Tech Publications, Switzerland.

Pereira, E., Ribeiro, A. (2006). In: E. Pereira, coord. Carta Geológica de Portugal. Notícia Explicativa da Folha 2.

Ribeiro, A. (1974). Contribution à l'ètude tectonique de Trás-os-Montes oriental, Mem. Serv. Geol. Portugal, N. S. 24, 168.

Ribeiro, A., Pereira, E. & Dias, R. (1990). Structure in the Northwest of the Iberian Peninsul. Edited by R.D. Dallmeyer & E. Martinez-Garcia, in: Pre-Mesozoic Geology of Iberia, (pp. 220-236). Berlin Heidelberg: Springer-Verlag.

Sousa, M. B. (1982). Litoestratigrafia e estrutura do Complexo Xisto-Grauváquico ante-Ordovícico – Grupo do Douro (NE Portugal). PhD Thesis. Universidade de Coimbra, 222 p.

Provenance study of limestones used for historical mortar production in the Great Moravian archaeological site Břeclav-Pohansko, Czech republic

Miroslava Gregerová, Dalibor Všianský, Ludmila Kurdíková
Institute of Geological Sciences, Faculty of Science, Masaryk University, Brno, Czech Republic; dalibor@sci.muni.cz

Abstract. The paper gives an overview of identification possibilities of source limestones used for lime burning in the Břeclav-Pohansko archaeological site. Limestones from four sites were examined: Skalica, Holíč, Hlohovec, and the Pálava Hill. The chemical compositions of limestones were compared to compositions of mortars and underburned limestones extracted from mortars. Hlohovec was excluded as a source site based on the results.

Keywords. Limestone, historical mortars, chemical composition

1 Introduction

Historical mortars have been in the focus of material scientists and petrographers for decades. The examination of historical mortars provides the information on technological knowledge of our ancestors and may be important for conservators. First relatively detailed written information on lime and mortar production may be found in antique (Vitruvius). Technology of historical mortars' production was studied e.g. by Moropoulou el. al. (2000), Miriello et al. (2010). Technology of production of lime mortars and plasters and their application in historic constructions was described by Rovnaníková (2009). From petrographic point of view, historical mortars have been examined for instance by Elsen (2006), Blauer and Kueng (2007), Adriano et al. (2009). X-ray diffraction investigation was carried out by Mertens et al. (2007). Deterioration of historic mortars was studied e. g. by Sabbioni et al. (2001).

Identification of historic mortars hydraulicity is a complicated problem. If there are any hydraulic phases present in a mortar sample, they usually occur in low amounts. Hydraulic phases may be identified by diffraction methods, however it is complicated due to low contents and peak overlaps.

Historic mortars contain limestone fragments partly decomposed by burning. These fragments may be used for limestone provenance identification by the means of petrographic analysis, i.e. mineral composition, microstructure, identification of fossils, or by chemical analysis.

2 Material and Methods

Early mediaeval Great Moravian mortars, mechanically separated relics of underburned limestones from the mortars, and limestones used as building rocks from the archaeological site Břeclav – Pohansko were analysed. Chemical composition of these samples was compared to those of limestones from Holíč and Skalica assumed as raw materials for mortars' production by Přichystal et al. (2008). Other limestones from nearby sites Hlohovec and from historical quarry in the Pálava Hill were also analysed.

List and description of analysed samples – see Table 1.

Table 1. List and description of analysed samples

Sample no.	Sort of sample	Specification	Origin
1	mortar	fire burial site, grey	Pohansko
2	mortar	light ochre	Pohansko
3	underburned limestone	greyish	Pohansko
4	underburned limestone	greyish	Pohansko
5	mortar, underburned limestone	smoothed mortar	Pohansko
6	mortar	smoothed mortar	Pohansko
7	mortar	northern settlement, gray	Pohansko
8	underburned limestone	northern settlement	Pohansko
9	mortar	church, light brown to pinkish	Pohansko
10	plaster	church, light brown to pinkish	Pohansko
11	underburned limestne	grave	Pohansko
12	underburned limestone	greyish	Pohansko
13	limestone	limestone from outcrops	Holíč
14	limestone	limestone from outcrops	Hlohovec
15	limestone	limestone from outcrops	Skalica
16	limestone	limestone from historical quarry	Pálava

All the samples were subjected to chemical analysis of main and trace elements in the Acme Labs (Vancouver, Canada). The results were processed using the MS Excel software. Normative minerals' calculations were done using the MINLITH software and statistic values, spider-and ternary diagrams were obtained using GCDkit 2.3. Cluster analysis was done by the Ward method.

Optical microscopy examination was done using

Olympus BX-51 polarizing microscope.

Samples of underburned limestone clasts no. 3 and 5 were also analysed by X-ray diffraction. The analysis was conducted on Bruker D8 Advance diffractometer equipped with position sensitive detector (PSD) Lynx Eye, Cu anode ($\lambda_{K\alpha} = 0.15418$ nm), and programmable slits. The analyses were conducted at conventional Bragg-Brentano para focusing $\Theta - \Theta$ reflexion geometry. Step size – $0.02°2\Theta$, time per step – 376 s. The results were processed using Diffrac plus and Topas 3 software.

3 Results

3.1 Micropetrographic characterization

Microstructural properties of examined mortars and plaster and results of micropetragraphic study are summarized in Tables 2 and 3. Limestones used for lime burning probably contained variable amounts of Fe oxyhydroxides. These variations, variable portion of slaked lime, different exposition to climatic conditions, and subsequent deposition in soil caused variable shades of the mortars. Relics of underburned limestones occur in all the mortar samples. Fragments of ceramics are sporadically present in the mortars. Samples of photomicrographs of examined mortars – see Figures 1 and 2.
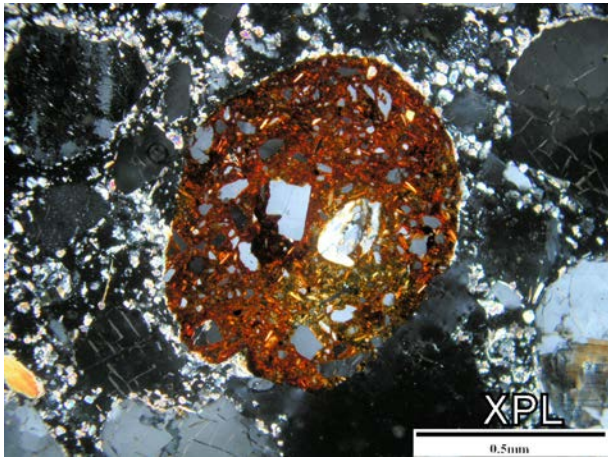
Figure 1. Fragment of ceramics in the mortar no. 1.

Figure 2. Preserved fossil in the mortar no. 2.

Table 2. Microstructural properties of examined mortars and plaster.

Sample no.	Granulometry	Microstru-cture	Underburned limestone fragments
1	>10mm:12% 5-10mm:15% 0.5-1mm: 33% <0.5mm: 42%	sparite	white > 1cm
2	>10mm:9% 5-10mm:12% 0.5-1mm: 42% <0.5mm: 35%	micrite, recrystallized	white > 1cm
5	>10mm:9% 5-10mm:17% 0.5-1mm: 41% <1mm: 33%	micrite, recrystallized	white > 1cm
6	>10mm:2% 5-10mm:3% 0.5-1mm: 81% <0,5mm: 14%	micrite, recrystallized	cracked, recrystallizatio n of CaCO$_3$ along cracks
7	>10mm:14% 5-10mm:9% 0.5-1mm: 46% <1mm: 31%	sparite, recrystallized	small white < 1cm
9	>10mm:7% >5mm:3% 0.5-1mm: 52% <1mm: 38%	micrite, recrystallized	white > 1cm
10	>10mm:5% 5-10mm: 10% 0.5-1mm: 36% <0.5mm :49%	micrite, recrystallized	white > 1cm

Table 3. List of mineral and rock fragments identified in the mortars and plaster and their relative abundance.

Sample no.		1	2	5	6	7	9	10
Mineral fragments	**Quartz**	++	++	++	+	++	+	+
	Feldspars	+	+	+	+	+	+	+
	Amphibole	+	+	+	+	+	+	+
	Pyroxen						+	+
	Epidote	+			+		+	+
	Kyanite						+	+
	Sillimanite	+	+	+	+			
	Chlorite	+				+		
	Glauconite					+		
	Garnet		+	+	+	+	+	
	Staurolite			+	+			
	Calcite	+	+	+	+	+	+	+
	Zircon	+	+	+	+	+	+	+
Rock fragments	**Quartzite**	+	+	+	+	+	+	+
	Aplite	+	+	+	+	+	+	+
	Gneiss				+	+	+	+
	Mica-schist, fylite	+		+	+	+	+	+
	Marble		+		+	+	+	++
	Sendstone	+		+		+		
Comment	Fragments of ceramics were identified in all the examined mortars.							

3.2 Chemical analyses

The results of chemical analyses were used for provenance determination of limestones used for lime burning in Břeclav-Phansko site.

The correlation of chemical composition of the Great Moravian mortars, underburned limestones and limestones from nearby sites was done by the Ward method of cluster analysis (Fig. 3).
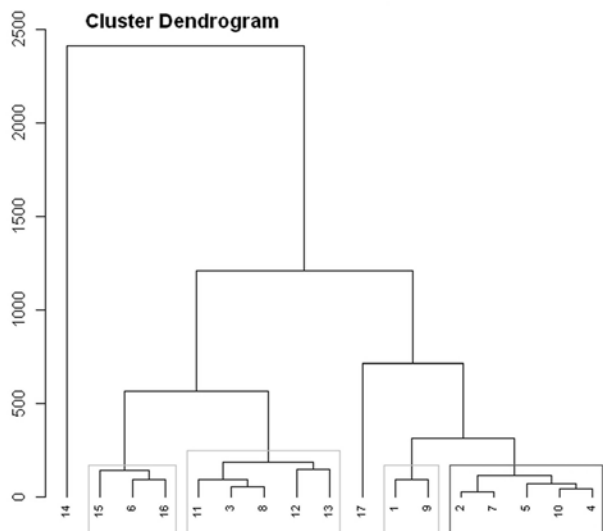
Figure 3. Cluster analysis results.

Based on the cluster analysis results, it may be stated that limestone from Hlohovec (no. 14) was not used for lime burning in the site. The sample no. 14 displays extremely higher Sr content (1578 ppm) than the rest of the samples (limestones 181 – 370, underburned limestones 115 – 234 ppm). Underburned limestones (no. 3, 8, 11, 12) and limestone from Holíč (no. 13) have similar compositions. Compostition of mortar no.6 is close to those of limestones from the Pálava Hill and Skalica.

Normative mineral compositions of the samples were estimated based on the recalculation of elemental compositions. There is a logical difference between normative composition of the mortars and limestones. There are significantly higher contents of normative feldspars in the mortars than in the limestones. The analysed limestones have low contents of clay and sand fraction. The projection of normative minerals in PelFsp-Q-Cc ternary diagram (Fig. 4) shows that the mortars no 1 and 9 have the highest contents of normative quartz, feldspars and clay minerals. Relatively high content of normative feldspars and clay minerals is present in the plaster no. 10. Mortar samples no. 2, 5, and 7 and underburned limestone no. 4 project closer to carbonate vertex. In contrast to cluster analysis, the mortar no. 6 and limestone from Holíč (no. 13) project in this field also. The normative composition of underburned limestones (no. 3, 8, 12, and 11) and limestones from Hlohovec, Skalica, and Pálava (no. 14, 15, 16) project to close distance of the carbonate vertex (Fig. 4.).
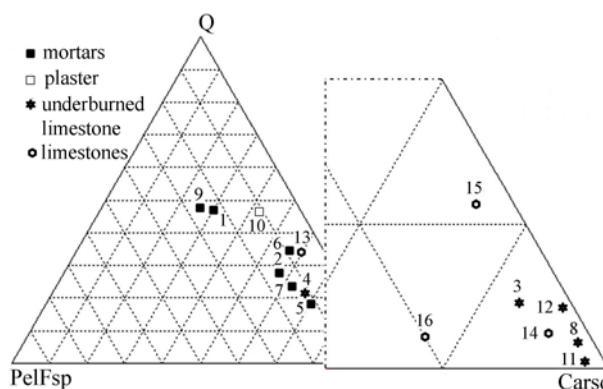
Figure 4. Normative mineral compostion of examined samples.

Because of the provenance study, analyses of trace elements (LREE and HREE) were normalised by chondrite (Boynton, 1984). The contents of LREE (Fig. 5) are similar in all the samples. In spite of the differences in REE enrichment, there are significant similarities.
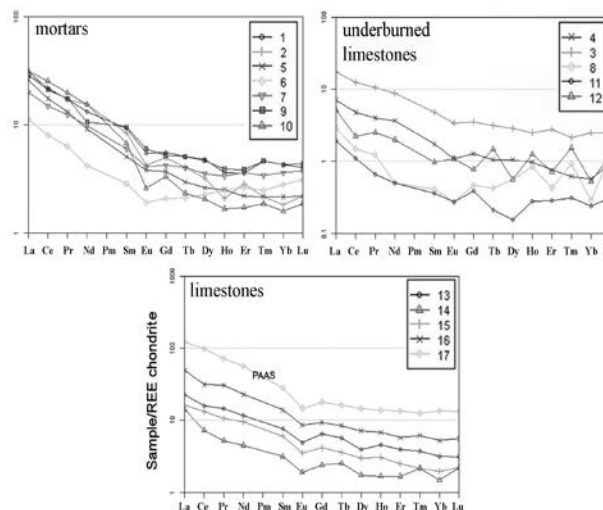
Figure 5. REE contents normalised by chondrite.

In comparison to the PAAS standard (Taylor, and McLennan, 1985), the results of REE analyses are not surprising (Fig. 6). All the curves display horizontal course. The mortar no. 6 and underburned limestone no. 8 display relatively higher contents of HREE.
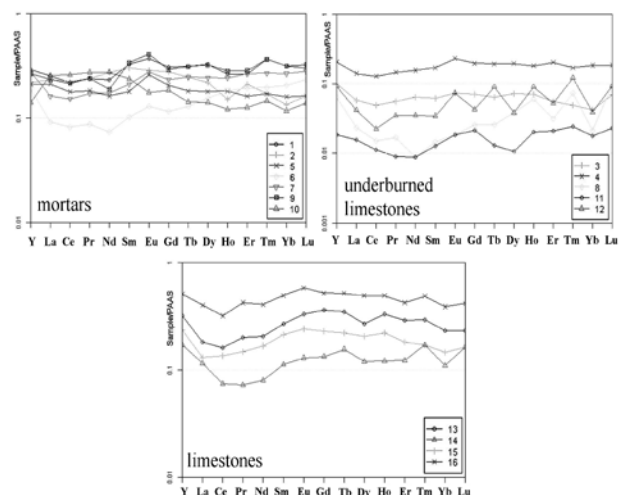
Figure 6. REE contents normalised by PAAS.

3.3 X-ray diffraction analyses of underburned limestones

Samples of underburned limestones no. 3 and 5 were subject to XRD analysis. Mineral composition of both the samples is similar. The semiquantitative analysis results are given – see Table 4.

Table 4. Semiquantitative results of XRD analysis of underburned limestones

sample no/mineral	3	5
calcite	+++	+++
hydromagnesite	++	++
quartz	+	++
dolomite	?	?

4 Discussion and conclusion

The conducted analyses proved correspondence between mortars no. 1 and 9. Underburned limestones (no. 3, 8, 11, 12) and limestone from Holíč (no.13) display similar composition. Chemical composition of the mortar no.6 is close to both limestone from Pálava Hill (no. 16) and limestone from Skalica (no. 15). Mortars no. 2, 7, and 5, plaster (no. 10) and underburned limestone no. 4 do not have any equivalent among the examined limestones. It is very probable that limestones from Holíč, Skalica, and Pálava Hill, or at least some of them, were used for lime burning and mortar production in Břeclav-Pohansko Great Moravian site. Chemical composition of these limestones is very close. Some of parameters of the mortars and limestone from Hlohovec are similar. Despite this fact, the limestone from Hlohovec may be excluded as a potential source. The reason is extremely high Sr content (1578 ppm) in the sample.

Acknowledgements

References

Adriano P, Silva AS, Veiga R, Mirão J, Candeias AE (2009) Microscopic characterisation of old mortars from the Santa Maria Church in Évora. Mater Charact 60:610-620.

Blaeuer C, Kueng A. (2007): Examples of microscopic analysis of historic mortars by means of polarising light microscopy of dispersions and thin sections. Mater Charact 58:1199-1207.

Boynton WV (1984) Cosmochemistry of the rare earth elements: meteoritic studies. In: Henderson, P. (ed.) Rare Earth Elements Geochemistry, Elsevier, Amsterdam. pp. 63–114.

Elsen J (2006): Microscopy of historic mortars - a review. Cement Concrete Res 36:1416-1424.

Mertens G, Madau P, Durinck D, Blanpain B, Elsen J (2007) Quantitative mineralogical analysis of hydraulic limes by X-ray diffraction. Cement Concrete Res 37: 1524-1530.

Miriello D, Barca D, Bloise A, Ciarallo A, Crisci GM, De Rose T, Gattuso C, Gazineo F, La Russa MF (2010): Caracterisation of archaeological mortars from Pompei (Campania, Ilaty) and identification of construction phases by compositional data analyses. J Archeol Sci 37:2207-2223.

Moropoulou A, Bakolas A, Bisbikou K (2000) Investigation of the technology of historic mortars. J Cult Herit 1:45-58.

Přichystal A, Doláková N, Hladilová Š (2008): Kamenné suroviny opevnění na raně středověkém centru Pohansko u Břeclavi (Česká republika) a jejich provenience. In: Petroarchaeology in the Czech Republic and Poland at the beginning of the 21st Century. UGV MU, MZM, Brno, pp 121–131. (in Czech)

Rovnaníková P (2009) Vápno - historie, výroba, vlastnosti. Proceedings of the Tradiční vápenné technologie conference. Národní památkový ústav. Ostrava. (In Czech).

Sabbioni C, Zappia G, Riontino C, Blanco-Varela MT, Aguilera J, Puertas F, Van Balen K, Toumbakari EE (2001) Atmospheric deterioration of ancient and modern hydraulic mortars. Atmos Environ 35: 539-548.

Taylor SR, McLennan SM (1985) The Continental Crust: Its Composition and Evolution. Blackwell Scientific, Oxford, London, Edinburgh, Boston, Palo Alto, Melbourne.

Vitruvius MP (1914) The ten books on architecture. Harvard University Pres, Cambridge.

The use of airborne geophysics in exploration for natural stone

Paavo Härmä, Meri-Liisa Airo
Geological Survey of Finland, Espoo, Finland

Olavi Selonen
Åbo Akademi University, department of natural sciences, geology and mineralogy

Abstract. The study comprises natural stone explorations carried out in the Wiborg rapakivi granite batholith in southeastern and Tampere region in southern Finland. The Wiborg rapakivi granite batholith intruded the SE Fennoscandian shield 1.67-1.62 Ma ago with multiple intrusions. The batholith consists of the number of types of rapakivi granites: wiborgite, pyterlite, even-grained rapakivi granite and porphyritic rapakivi granite. The southern parts of Tampere region consist of the Tampere and Pirkanmaa Schist Belts, and the northern parts of Central Finland Granitoid Complex.

The aim of this study was to evaluate the usefulness of low-altitude airborne geophysical material in exploration for natural stone. The potentiality of the rocks for natural stone in the study areas was evaluated. The available geophysical material was processed and analyzed, and used as help in the potentiality mapping. The geophysical data could be used mainly for identifying lithologies and individual intrusions, and in revealing unknown intrusions.

Keywords. natural stone; dimension stone; ornamental stone; geophysics, exploration; rapakivi; granite; Finland

1 Introduction

According to the European standard EN 12670 natural stone is defined as a piece of naturally occurring rock. A natural stone product is a worked piece of naturally occurring rock used in buildings and for monuments. Dimension stone and ornamental stone are other terms used synonymously for natural stone for architectural purposes.

The aim of the study was to evaluate the usefulness of low-altitude airborne geophysical material in exploration for natural stone. The potentiality of the rocks for natural stone in the study areas was evaluated (Härmä et al. 2006, Härmä & Selonen 2008). The available geophysical material was processed and analyzed (e.g., Karell 2006, Nyman 2007, Arponen et al. 2009), and used in locating natural stone prospects through potentiality mapping. The airborne geophysical data sets have been utilized also to predict the prevalent fracture directions in bedrock using the trend analysis of aeromagnetic high-resolution data (e.g., Airo & Wennerström 2010).

2 Exploration process for natural stone

The exploration process for natural stone includes a desk study, regional scale prospecting, detailed site investigation, and sampling (Luodes et al. 2000, Selonen et al. 2000, Ashmole & Motloung 2008). During the desk study, all background material for the target area is gathered and analyzed, including airborne geophysical material. During the regional stage, the appearance and soundness is observed on the outcrop surface by visually defining the outlook of the stone and mapping the spacing of the fractures. During the detailed investigation, the outlook and the fracturing are defined in detail, samples for aesthetical evaluation and for laboratory tests are taken. Ground penetrating radar and core drilling are used for further assessment.

3 Study area

The study area is located in southern Finland covering the Wiborg rapakivi granite batholith and Tampere region (Fig. 1). The Wiborg rapakivi granite batholith intruded the SE Fennoscandian shield 1.67-1.62 Ma ago with multiple intrusions. The batholith consists of the number of types of rapakivi granites: wiborgite, pyterlite, even-grained rapakivi granite, and porphyritic rapakivi granite (Simonen, 1987, Härmä & Selonen 2008).

On the large scale, Tampere region consists of Tampere and Pirkanmaa Schist Belts, and the southern parts of the Central Finland Granitoid Complex (CFGC).
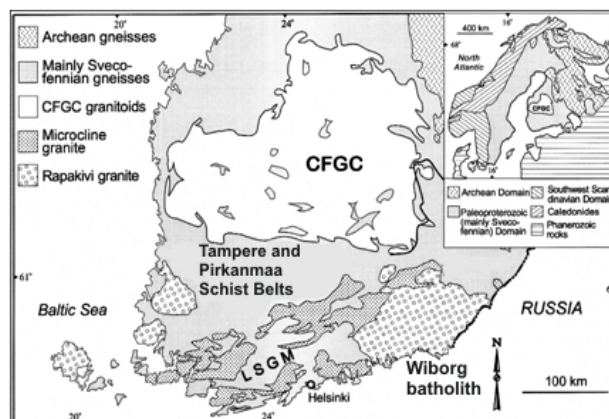

Figure 1. A simplified geological map of southern Finland showing the areas of the Central Finland Granitoid Complex (CFGC), Tampere and Pirkanmaa Schist Belts and Wiborg batholith. LSGM is Late Svecofennian granite-migmatite zone. Modified after Korsman et al. (1997) and Nironen et al. (2000).

4 Airborne geophysical data

The airborne low-altitude geophysical material used in this study comprises aeromagnetic data and derivates of it. Also airborne radiometric data sets were used when visually outlining and characterizing geological units and defining lithological boundaries.

5 Geological outline and natural stone qualities

The Finnish Proterozoic rapakivi granites occur as four major batholiths and several smaller batholiths and stocks in southern Finland (Rämö & Haapala 2005). The large Wiborg rapakivi granite batholith in southeastern Finland consists of five granite types: wiborgite, pyterlite, even-grained granite, porphyry aplite, and porphyritic granite, of which the wiborgite is the most common type (Simonen 1987, Härmä & Selonen 2008). "Carmen Red" and "Eagle Red" are red rapakivi granites, and "Baltic Brown" a brown variety extracted in the Wiborg batholith (Härmä & Selonen 2008). These stones are coarse-grained rocks with a typical rapakivi texture of large round K-feldspar ovoids, with or without a plagioclase rim. The rapakivi granites from the Wiborg batholith are produced in the large scale, and often globally used in projects demanding large amounts of homogeneous material. The Wiborg batholith still has high natural stone potential for the future (Härmä & Selonen 2008).

The northern part of the Tampere region is characterized by the igneous rocks of the CFGC. The most abundant rock types are the synkinematic intrusions (1890-1880 Ma), but also undeformed or weakly foliated post-kinematic intrusions (1885-1870 Ma) occur (Selonen & Ehlers 1996, Nironen et al. 2000, Nironen 2005). The southern part of the area is characterized mainly by sedimentary and volcanic rocks of the Tampere and Pirkanmaa schist belts (Kähkönen 2005). The Tampere belt comprises graywackes and mudstone with 1905-1890 Ma old volcanic and sedimentary rocks (Kähkönen 2005). The Pirkanmaa belt consists of high-grade migmatites and gneisses (Kähkönen 2005). Well-known grey granite, "Kuru Grey" is extracted from several quarries in the southern part of the CFGC (Selonen et al. 2012). Future prospects include granitic rocks as well as schists (Härmä et al. 2006).

5 Results

The positive magnetic anomalies in airborne geophysical maps are commonly coupled to mafic rocks, whereas granites generally show only weak magnetism.

In Wiborg batholith, rapakivi granites have usually low magnetic anomalies. Some large positive anomalies coincide with anortosite or gabbronorite intrusions; however some gabbronorites show even negative magnetic anomalies. With the help of the magnetic data some previously unknown intrusions or intrusion phases could be identified in the batholith (Fig. 2).
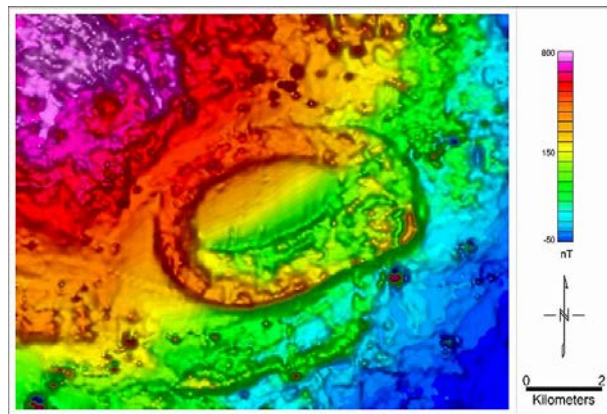
Figure 2. Detail of Wiborg rapakivi granite batholith. The magnetic low altitude map reveals outlines and form of an individual intrusion inside the rapakivi granite batholith. New intrusion phases and their distributions into covered areas can be identified more precisely than in an ordinary geological map. Interesting areas for the natural stone prospects increase. The magnetic map is the property of Geological Survey of Finland ©

In Tampere region there is a distinct change of magnetic patterns between Schist Belts in the south and the CFGC in the north and there is also change in magnetic trends in the individual granite batholiths inside the CFGC. Generally, the magnetic anomalies were connected to gabbros, whereas granites were weakly magnetic. However, postkinematic granite intrusions can show either strong magnetic anomalies or even weak anomaly. For example, the Orivesi granite batholith has a weak anomaly, but to the east of it occur the Juupajoki granite with a strong magnetic anomaly (Fig. 3). In the Orivesi batholith, the qualified natural stone reserves are found in the western parts of the batholith, usually on even areas.

The usefulness of airborne radiometric data was limited to outlining and characterizing geological units and defining lithological boundaries.

It seems that geophysical data is best suited for identification of lithological contacts and geological units, as used often in conventional geological mapping. Combing all available geophysical material, including ground geophysical data, with geological and topographical data, more accurate definition of the areas having a potential for natural stone prospects can be made.

6 Summary

The usage of low-altitude airborne geophysical and radiometric data in exploration for natural stone was studied in this work. The study area consisted of Wiborg rapakivi granite batholith in southeastern and Tampere region in southern Finland. The natural stone potential of the rocks in these areas was also evaluated. The available geophysical material was processed and analyzed, and used as a tool in the exploration process.

The main use of the airborne geophysical data could be contributed to the identification of lithologies and individual intrusions, and revealing "new" intrusions.

The combined lineament analysis could be used in interpreting the regional scale fracturing of the target areas.
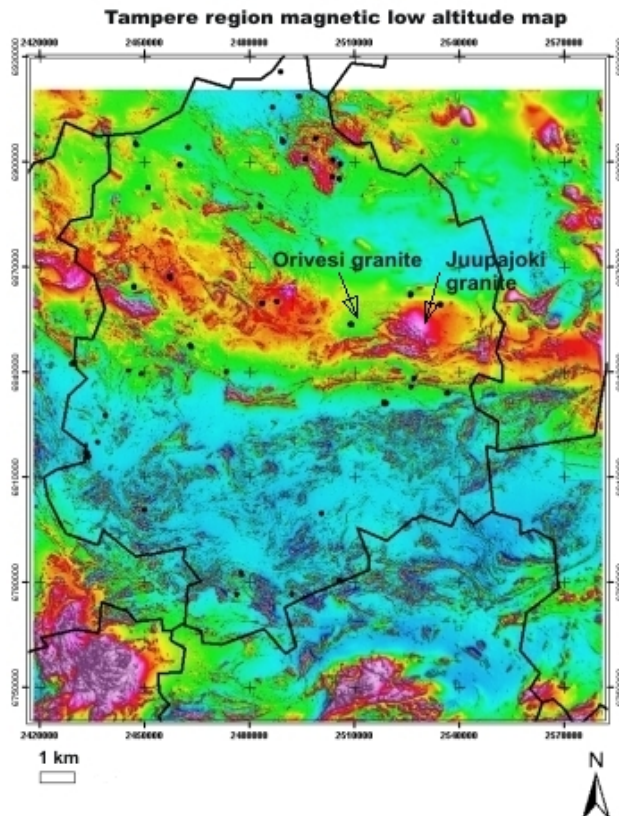
Figure 3. The magnetic low altitude map of the Tampere region shows a distinct change of magnetic patterns between Schist Belts in the south and the CFGC in the north. The granite intrusions can show either strong magnetic anomalies (Juupajoki) or even weak anomaly (Orivesi). The black sports on the map are observations of the natural stone prospects, found during the inventory mapping. The magnetic map is the property of Geological Survey of Finland ©

Acknowledgements

References

Airo, M-L. & Wennerström, M. 2010. Application of regional aeromagnetic data in targeting detailed fracture zones. Journal of Applied Geophysics 71 (2-3), 62-70.

Arponen, E., Härmä, P., Selonen, O. Luodes, H. & Pokki J. 2009. Anorthosite and spectrolite in the Wiborg rapakivi granite batholith and the lithological control of spectrolite deposits. Geological Survey of Finland, Report of Investigation 178. Espoo, Finland. (In Finnish with English summary).

Ashmole, I. & Motloung, M., 2008. Dimension stone: the latest trends in exploration and production technology. In: The International Conference on Surface Mining 2008 - Challenges, technology, systems and solutions - Papers. The Southern African Institute of Mining and Metallurgy, Johannesburg, Republic of South Africa, 35-70.

Härmä P. & Selonen, O. 2008. Surface weathering of rapakivi granite outcrops – implications for natural stone exploration and quality evaluation. Estonian Journal of Earth Sciences 57, 3. 135-148.

Härmä, P., Karttunen, K., Nurmi, H., Nyholm, T., Sipilä, P. & Vuokko, J., 2006. Natural stone exploration project in the Tampere region 2001-2005. Geological Survey of Finland, Report KA 33/2006/1. 24 pp. + 8 app. (in Finnish with English summary).

Kähkönen, Y., 2005. Svecofennian supracrustal rocks. In: Lehtinen, M., Nurmi, P.A. & Rämö, O.T. (eds.) Precambrian Geology of Finland – Key to the Evolution of the Fennoscandian Shield. Elsevier B.V. Amsterdam, Netherlands, 343-406.

Karell, F. 2006. Magnetic fabric investigations on rapakivi granites in Finland. In Kukkonen, I.T., Eklund, O., Korja, T., Pesonen, L.J., and Poutanen, M. (Eds.), 2006. Lithosphere 2006 – Fourth Symposium on the Structure, Composition and Evolution of the Lithosphere in Finland. Programme and extended Abstracts, Espoo, Finland, November 9-10, 2006. Institute of Seismology, University of Helsinki, Report S-46, pp. 51-56.

Korsman, K., Koistinen, T., Kohonen, J., Wennerström, M., Ekdahl, E., Honkamo, M., Idman, H., Pekkala, Y. (eds.) 1997. Suomen kallioperäkartta = Bedrock map of Finland 1:1 000 000. Espoo: Geologian tutkimuskeskus.

Luodes, H., Selonen, O. & Pääkkönen, K. 2000. Evaluation of dimension stone in gneissic rocks — a case history from southern Finland. Engineering Geology 58, 209-223.

Nironen, M., 2005. Proterozoic orogenic granitoid rocks. In: Lehtinen, M., Nurmi, P.A. & Rämö, O.T. (eds.) Precambrian Geology of Finland – Key to the Evolution of the Fennoscandian Shield. Elsevier B.V. Amsterdam, Netherlands, 443-480.

Nironen, M., Elliott, B. A. & Rämö, O. T. 2000. 1.88-1.87 Ga postkinematic intrusions of the Central Finland Granitoid Complex: a shift from C-type to A-type magmatism during lithospheric convergence. Lithos 53, 37-58.

Nyman, R. 2007. Geological, geophysical, and structural features of the Kuru batholith. MSc thesis, Åbo Akademi University, Department of geology and mineralogy, Turku, Finland.

Rämö, O.T. & Haapala, I., 2005. Rapakivi granites. In: Lehtinen, M., Nurmi, P.A. & Rämö, O.T. (eds.) Precambrian Geology of Finland – Key to the Evolution of the Fennoscandian Shield. Elsevier B.V. Amsterdam, Netherlands, 533–562.

Selonen, O. & Ehlers, C., 1996. The Orivesi granite batholith, southern central Finland — characteristics and emplacement. Bull. Geol. Soc. Finland 68, Part 1. 11-24.

Selonen, O., Luodes, H. & Ehlers, C. 2000. Exploration for dimensional stone — implications and examples from the Precambrian of southern Finland. Engineering Geology 56, 275-291.

Selonen, O., Ehlers, C., Härmä, P. & Nyman, R. 2012. Natural stone deposits in an assemblage of subhorizontal intrusions - The Kuru granite batholith. Bulletin of the Geological Society of Finland 84, 167-174.

Simonen, A., 1987. Pre-Quaternary rocks of the map sheet areas of the rapakivi massif in SE Finland. Explanation to the Geological map of Finland 1:100000. Geological Survey of Finland, 49 p. (In Finnish with English summary).

ASROCKS project: Evaluation of arsenic concentrations in aggregate resources and construction sites in the Tampere-Häme region of Finland

Paavo Härmä, Tarja Hatakka, Birgitta Backman, Timo Tarvainen, Kirsti Loukola-Ruskeeniemi
Geological Survey of Finland, Espoo, Finland

Pirjo Kuula-Väisänen
Tampere University of Technology, Tampere, Finland

Outi Pyy
Finnish Environment Institute, Helsinki, Finland

Abstract. The ASROCKS project is co-funded by the EU Life+ Environment Policy and Governance programme. The main objective of the project is to provide guidelines and risk management tools for the exploitation of natural aggregate resources, i.e. crushed bedrock, sand and gravel, in areas with naturally elevated arsenic concentrations in bedrock and soil in the Tampere-Häme region, southern Finland. In addition, guidelines are also being developed for the re-use of aggregates in construction areas with higher than average arsenic concentrations. In the first phase of the project, ten production sites for crushed bedrock aggregates, seven sand and gravel excavation sites and four construction sites were selected for the sampling of rock, soil, aggregate products, groundwater and surface water. The variation in As concentrations was higher in crushed bedrock aggregates than in sand and gravel products. Arsenic concentrations in groundwater were with one exception lower than the guide value of 10 µg/l designated for household water. In surface water, the arsenic concentrations were typical for the Tampere region, but higher than in stream waters for the whole Finland on average. The guidelines generated in the ASROCKS project will be available to both aggregate producers and local and environmental authorities.

Keywords. Aggregate, arsenic, crushed bedrock, environment, gravel, groundwater, sand, surface water, Tampere, Häme, Finland

1 Introduction

The ASROCKS project, co-funded by the EU Life+ Environment Policy and Governance programme, started in September 2011. The main objective is to provide guidelines and risk management tools for the exploitation of natural aggregate resources (crushed bedrock, sand and gravel) in areas with naturally elevated arsenic concentrations in bedrock and soil. The focus is on the Tampere-Häme region in southern Finland (Fig. 1). In addition, guidelines are also being developed for the re-use of aggregates in construction areas with elevated arsenic concentrations. The guidelines and tools produced during the project will be of use to both aggregate producers and environmental authorities.
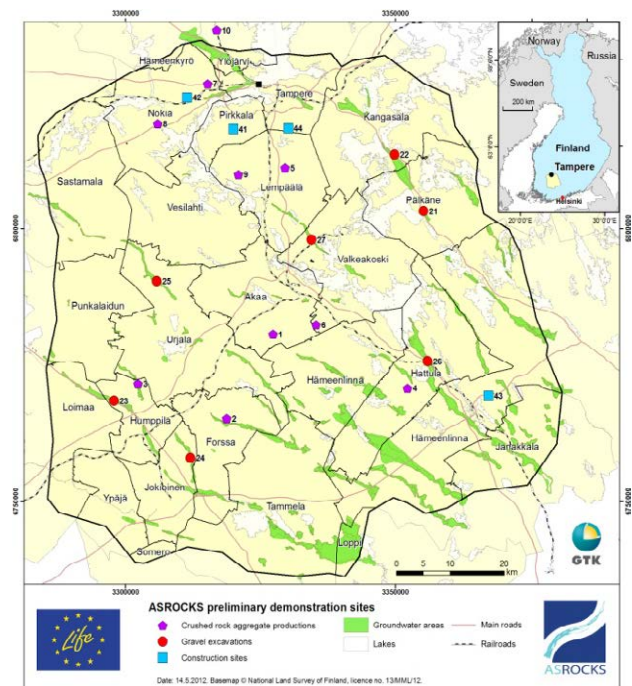
Figure 1. The area of naturally elevated arsenic concentrations in bedrock and soil in the Tampere-Häme region, with 21 preliminary demonstration sites.

Arsenic (As) occurs naturally in soil and bedrock. The long-term use of drinking water with a high As concentration is a risk to human health. One of the findings of a previous EU project, RAMAS (Risk assessment and risk management of arsenic in the Tampere region), was that arsenic can dissolve and be naturally transported to the groundwater in areas with high As in bedrock (Loukola-Ruskeeniemi et al. 2007, Loukola-Ruskeeniemi et al. 2008). In areas with naturally elevated arsenic concentrations, such as the Tampere region, arsenic typically resides in the soil, near the surface of the underlying bedrock.

The Geological Survey of Finland (GTK), Tampere University of Technology (TTY) and the Finnish Environmental Institute (SYKE) are participating in the ASROCKS project. The project is being carried out in co-operation with aggregate producers, municipalities and authorities.

2 Study setting

The project is divided into separate actions. In the first action, ten production sites for crushed bedrock aggregates, seven sand and gravel excavation sites and four construction sites were selected for the sampling of rock, soil, aggregate products, groundwater and surface water. Concentrations of arsenic and several other potentially harmful elements were analysed, and the risk to human health and the environment will later be evaluated. Based on the results of the first action, two construction sites and two aggregate production sites were selected for a detailed investigation, which will be completed in 2013.

3 Sampling strategy

The basic sampling strategy was to collect samples of bedrock, soil, aggregate product piles, ground water and surface water at each production site. In bedrock quarries, about five samples were collected from points expected to contain arsenopyrite, e.g. sulphide-bearing rusted rock, the contacts of different rock types, adjacent to veins and dykes, shear zones and from the rusted surface on various fracture types. From aggregate product piles, six samples were collected from different points of which only one sample of each pile with the maximum As concentration measured by the portable XRF was sent to the laboratory for analysis. The same method was applied to the sampling of excavated, disturbed natural soil. Only one random sample was taken from undisturbed soil, and this method was essentially also applied to the surface and groundwater samples. The principal objective in the preliminary demonstration phase of the project was to find the areas with the maximum As concentrations in the bedrock, soil and aggregate products and where the arsenic was easily leachable.

4 Preliminary results and discussion

The variation in As concentrations was higher in the crushed bedrock aggregates than in sand and gravel products. Elevated As concentrations were measured from some sulphide-bearing veins and from the surfaces of cracks in the bedrock. The highest As concentrations in bedrock (up to 916 mg/kg) were measured from a planned construction site. Only a small proportion of the total As concentration was easily leachable. Only eight groundwater samples were taken in the first action, and the arsenic concentrations in them were with one exception lower than the guide value of 10 µg/l designated for household water. Arsenic concentrations in surface water were typical for the Tampere region, but higher than in stream water for the whole of Finland on average (Lahermo et al. 1996, Backman et al. 2007, Tenhola & Tarvainen 2008 and Backman et al. 2010). The highest arsenic concentrations in surface water were found at the production sites of crushed bedrock aggregates (Fig. 2). The project is ongoing and more detailed results will be available in 2014.

High arsenic concentrations also occur globally due to anthropogenic activities, caused for example by mining, metal refinement or the combustion of fossil fuels. In areas with naturally elevated arsenic concentrations in bedrock and glacial till, such as the Tampere-Häme region, arsenic does not typically cause risks unless the soils are disturbed, for example by earthworks. Therefore, it is important to ensure that arsenic is not transported to groundwater or surface waters during large-scale groundwork or excavation of rock aggregate products. The long-term use of drinking water containing high concentrations of arsenic may cause health risks.

In Finland, guidelines for assessing and managing the risks caused by naturally high arsenic concentrations are lacking, causing challenges in the process of granting environmental and construction licences. Based on the investigation carried out during the ASROCKS project, the transport of arsenic to groundwater and surface waters is being assessed and guidelines are being generated to assist in granting environmental licences for aggregate production. The guidelines will be available to both industry and to local and environmental authorities.
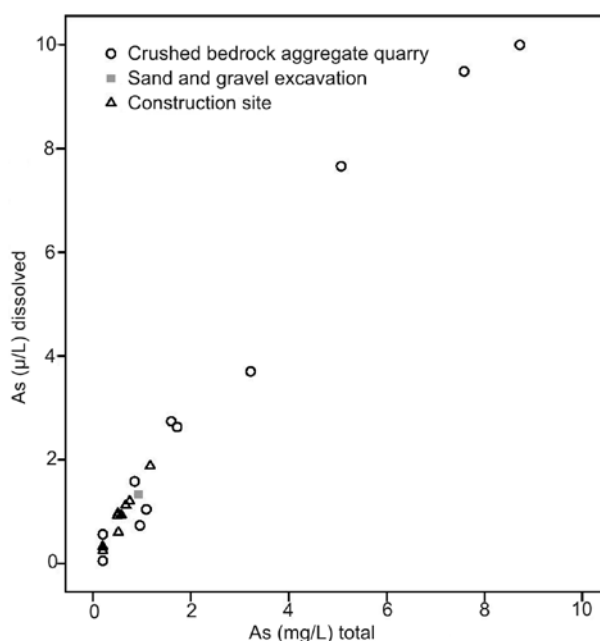
Figure 2. Scatter diagram of the dissolved (y-axis) and total (x-axis) As concentrations in surface water at ASROCKS demonstration sites in the Tampere-Häme region in 2012.

5 Summary

The main objective of the ASROCKS project is to provide guidelines and risk management tools for the exploitation of natural aggregate resources, i.e. crushed bedrock, sand and gravel, in areas with naturally elevated arsenic concentrations in bedrock and soil in the Tampere-Häme region, southern Finland. In the first phase of the project, ten production sites for crushed bedrock aggregates, seven sand and gravel excavation

sites and four construction sites were selected for the sampling of rock, soil, aggregate products, groundwater and surface water. The results of the first phase studies can be summarized as follows: the variation in As concentrations was higher in the crushed bedrock aggregates than in sand and gravel products due to the variation in the As concentration between bedrock types and bedrock heterogeneity. The arsenic concentrations in groundwater were with one exception lower than the guide value of 10 µg/l designated for household water. The arsenic concentrations in surface water were typical for the Tampere region. The project is ongoing and more detailed results will be available in 2014.

Acknowledgements

References

Backman, Birgitta; Eklund, Mikael; Luoma, Samrit; Pullinen, Arto; Karttunen, Virpi 2007. Luontaisia ja ihmisen aiheuttamia arseenipitoisuuksia Pirkanmaan alueella: arseenipitoisuustietoa maaperän eri kerroksista, kaivoksen rikastehiekasta ja sen pölystä, vedestä louhoksilla, kyllästämöalueilla ja kaatopaikkojen lähellä sekä marjoista, sienistä ja koivumahlasta [Electronic resource]. Abstract: Natural and anthropogenic arsenic contents in the Pirkanmaa region : arsenic contents in different soil horizons, in tailing sand and dust, in water at quarries, at CCA wood preservative plants, and at landfills and in natural berries, mushrooms and birch sap. Espoo: Geological Survey of Finland. 33 p. Electronic publication.

Backman, Birgitta; Reinikainen, Juha; Jarva, Jaana; Luoma, Samrit 2010. Pirkkalan ja Nokian alueen maaperän sekä pinta- ja pohjaveden arseeni- ja raskasmetallipitoisuudet rakennushankealueilla - esiselvitys. 35 s. Geological Survey of Finland, Archive report, S41/2123/2010/8.

Lahermo, P.; Väänänen, P.; Tarvainen, T.; Salminen, R. 1996. Suomen geokemian atlas. Osa 3 : Ympäristögeokemia - purovedet ja -sedimentit = Geochemical atlas of Finland. Part 3: Environmental geochemistry - stream waters and sediments. Espoo. Geologian tutkimuskeskus. 149 p.

Loukola-Ruskeeniemi, K., Ruskeeniemi, T., Backman, B., Rossi,E. Lehtinen, H., Schultz, E., Sorvari, J., Makela-Kurtto, R., Parviainen, A.,Vaajasaari, K., Bilaltdin, A., 2008. Arsenic in the Tampere region in Finland: occurrence in the environment, risk assessment and risk management - final results of the RAMAS project. 28th Nordic Geological Winter Meeting, Aalborg – Denmark January 7-10, 2008.

Loukola-Ruskeeniemi, K., Ruskeeniemi, T., Parviainen, A. & Backman, B. (eds.) 2007. Arsenic in the Pirkanmaa region in Finland - Occurrence in the Environment, Risk Assessment and Risk Management. Helsinki University of Technology. Geoenvironmental Technology. Special Publications, 156 pp.

Tenhola, Markku; Tarvainen, Timo 2008. Purovesien ja orgaanisten purosedimenttien alkuainepitoisuudet Suomessa vuosina 1990, 1995, 2000 ja 2006. Summary: Element concentrations in stream water and organic stream sediment in Finland in 1990, 1995, 2000 and 2006. Geological Survey of Finland. Report of Investigation, 172. Espoo. 60 p.

Re-evaluation of Lower Palaeozoic limestones from the Prague Basin (Barrandian area, Czech Republic) as a raw material for production of natural hydraulic lime and/or natural cement

Petr Kozlovcev & Richard Přikryl
Institute of Geochemistry, Mineralogy and Mineral Resources, Faculty of Science, Charles University in Prague, Prague, Czech Republic

Abstract
Lower Palaeozoic limestones from the Prague Basin, making up part of the Barrandian area (Bohemian Massif, Czech Republic), have been employed for the firing of construction binders since early Medieval times. Several lithostratigraphic members exhibit variable compositions - from pure limestone to clay/silica-rich members that exhibit a considerable degree of hydraulicity when fired. Despite extensive explorations for large limestone deposits suitable for various industrial uses in the Prague Basin after WW2, the potential of these rocks for the firing of hydraulic binders, which can be an alternative to Portland cement (hydraulic lime and/or natural cement) remained absolutely unexplored in modern times, despite the fact that multiple sources of evidence of their production and use can be found throughout history. In this study, we have employed several thousand chemical analyses from exploration reports performed since the 1950s, and recalculated them by using traditional indexes used for the evaluation of raw materials suitable for the production of hydraulic lime. From 12 examined stratigraphic members, 2 have been designated as a raw material eminently suitable for hydraulic lime (or even natural cement); 6 others for moderately hydraulic lime. Based on these results, the most promising sites have been selected as sources of raw materials for experimental firings.

Keywords: Palaeozoic limestones, Prague Basin, Barrandian area, natural hydraulic lime, natural cement

1 Introduction

Despite the dominant role of Ordinary Portland Cement (OPC)-based inorganic binders in the modern construction industry, the long-term development of binders in constructional practice is marked by the use of quick (air) lime (QL) and/or various types of natural hydraulic lime (NHL) (Blezard 1998). In contrast to OPC, which must be fired at temperatures above 1250°C (commonly 1400-1500°C) in order to obtain cement clinker, NHL and/or natural cement (NC) are produced at much lower temperatures, not exceeding 1250°C (Hughes et al. 2009). The increased interest for these, recently called "alternative" binders (Juenger et al. 2011) is not only due to their need in restoration practices (Elert et al. 2002; Gulotta et al. 2013), but also due to the fact that their production and use is less energetically demanding than OPC (Cahn et al. 1997). Their environmental friendliness is further supported by lower emissions of CO_2 (Worrell et al. 2001) and the presence of free-lime (CaO) in the product, which undergoes recarbonation (i.e. the binder reincorporates atmospheric CO_2) during setting and hardening (Cultrone et al. 2005).

Bohemia and Moravia, two major historical lands of the Czech Republic, are well known for the production and use of different types of inorganic binders throughout their history (Lánik and Cikrt 2001). Along with the most widespread firing of QL, limestones from some areas were also suitable for the production of NHL. From numerous limestone-bearing areas (both sedimentary basins and metamorphic terranes in the Bohemian Massif, the largest geological unit found within the territory of the Czech Republic), the Prague Basin is probably the best known and the most exploited unit due to the presence of several lithostratigraphic members of Lower Palaeozoic age (Chlupáč et al. 1998) that have found broad industrial use. Favoured by its location close to Prague, capital of the Czech Republic, the locally produced binders have been employed during Prague's construction since Medieval times (Lánik and Cikrt 2001), as analytically proven from several monuments, including the Gothic Charles Bridge in Prague (Přikryl and Šťastná 2010). Many types of historically produced inorganic binders in the Prague Basin were replaced by only two products - QL and OPC during the 20th century. Extensive exploration and related analytical work conducted after WW2 only focused on the use of local limestones in these industries, without paying any attention towards alternative products (NHL/NC). For this reason, we have focused in a re-examination of the potential of the principal lithostratigraphic members for their use as raw materials for the firing of these binders.

2 Overview of geology of the Prague Basin

2.1 Geological setting and development

Prague Basin is a rift-like depression (Havlíček 1981) elongated in SW-NE direction (i.e. from Plzeň / Starý Plzenec in SW to Prague in NE) filled with Lower Palaeozoic unmetamorphosed marine deposits (Chlupáč et al. 1998). The complete sedimentary record from the Silurian up into the Middle Devonian is extraordinarily fossiliferous, and thus makes the Barrandian area one of the world famous palaeontological regions (Chlupáč 1988; Chlupáč et al. 1998). The sedimentary fill of the Prague Basin shows a remarkably diverse tectonic development, ranging from germanotype to alpinotype features, which can be partly explained by the segmented

heterogeneous Upper Proterozoic basement (Röhlich 2007) composed of metamorphic rocks of the Teplá-Barrandian Unit (Cháb 1993). Extensive sedimentary activity in a passive-margin setting has occasionally been accompanied with volcanism and synsedimentary deformation of the basin fill (Chlupáč et al. 1998).

The lithology of the Prague Basin is characterised by the presence of various sedimentary rocks (shales, siltstones, sandstones, limestones, silicites). In contrast to dominant shale deposition in the Lower Silurian, eustatic movements caused basin shallowing during the Upper Silurian (Kříž 1991) and specifically in the Lower/Middle Devonian (Chlupáč and Kukal 1986), which favoured the deposition of various types of limestone; most of them of industrial importance. Sedimentation in an offshore environment is marked by the presence of dominant bioclastic (shallower parts of the basin representing a high energy environment) and micritic (deeper parts of the basin, with pelagic conditions) facies.

2.2 Late Silurian to Middle Devonian sedimentation in the Prague Basin

The late Silurian (Ludlov and Přídolí series) sedimentation was characterised by facial diversity of two major formations - Kopanina and Požáry in which various biomicritic and biodetritic limestones deposited.

The first stage of the Early Devonian - Lochkovian was characterised by sedimentation of medium- to coarse-grained packstones (Kotýs limestone) in a shallow subtidal environment (Chlupáč et al. 1998). Kotýs limestone ranges to relatively $CaCO_3$-rich limestones, although intercalations of shales contribute to a feebly-moderate hydraulic character of this rock type at some localities. At the same stage, the deeper parts of the Prague Basin are characterised by the presence of dark-coloured (grey to black) Radotín and Kosoř limestones, which petrographically belong to mudstone and/or wackestone.

Similarly to the Lochkovian, the following Pragian stage was also dominated by deposition of coarse-grained packstones (Koněprusy limestone) at shallower portions (reef complexes) of the Prague Basin. Basinwards, these gradually transform into bedded wackestones and packstones (Slivenec limestone) and to deep-water basinal facies of micritic limestones (mudstones and/or wackestones, locally named as Dvorce-Prokop limestone).

During the last stage of Early Devonian - Emsian, the Prague Basin faced uniform facial development that is represented by the presence of mudstones/wackestones (Zlíchov limestone). The uniform character of early Emsian sedimentation was altered with bioclastic materials accumulations in shallower portions (crinoidal grainstones and packstones, locally named as Suchomasty limestone) and pelagic limestones (nodular mudstone and wackestone, locally named as Třebotov limestone) during the Upper Emsian.

The Middle Devonian sedimentation started with the deposition of the prevalent deep facies Choteč limestone (fine-grained packstone and wackestone, intercalated with shales). The shallower parts were marked by the evolution of coarse-grained crinoidal packstones and grainstones (Acantopyge limestone in the Koněprusy area).

3 Approaches to the evaluation of limestone suitability for firing of hydraulic binders

The suitability of a limestone for the production of specific type of constructional binder is evaluated based primarily on its chemistry (Eckel 1922; Cowper 2000), but knowledge of the mineralogical composition is also advantageous (Varas et al. 2005). When employing chemical composition, specific oxides from bulk silicate analysis (specifically CaO, Al_2O_3, SiO_2, Fe_2O_3, MgO) are employed. Hydraulicity potential (i.e. ability to form hydraulic phases, to set and to harden in humid conditions or under water) of a raw material for NHL/NC can then be expressed by three basic formulae: the hydraulic index (HI), cementation index (CI), and hydraulic module (MH).

The hydraulic index (HI) discriminates binders into three groups: feebly hydraulic lime (HI = 0.1 - 0.2), moderately hydraulic lime (HI = 0.2 - 0.4), and eminently hydraulic lime (HI = 0.4 - 1.5). Raw materials used for the production of natural cement exhibit even higher HI values (Cowper 2000).

The cementation index (CI) provides more complex information (Eq. 2). Apart from the contents of SiO_2 and Al_2O_3 it also considers the content of Fe_2O_3 and MgO (Weber et al. 2007). The value of CI is from 0.3 to 0.5 for the feebly hydraulic lime, 0.5 - 0.7 for moderately hydraulic lime, and 0.7 - 1.1 for eminently hydraulic lime. CI values higher than 1.1 indicate raw materials suitable for the production of natural cement (Eckel 1922).

The hydraulic (lime) module (M_H) is usually set around 1.7 to 2.4 in hydraulic limes and normal cements (Cowper 2000). Higher values of M_H leads to an increase of firing temperature, sensitivity to dilation, and chemical changes, as well as to a higher hydrating temperature.

When focusing on the mineralogical composition, the percentage of carbonates (specifically calcite) vs. non-carbonate minerals (silica, clay minerals) must be specified. In general, a raw material suitable for hydraulic lime production must contain more than 6.5% (but usually 10 to 20%) of SiO_2, Al_2O_3, MgO, and Fe_2O_3 (Lanas et al. 2004). Limestones containing 30 - 40% of non-carbonate component can be employed for the production of natural cement (Varas et al. 2005).

4 Re-evaluation of limestones from the Prague Basin

4.1 Chemistry

Several thousands of chemical analyses from 67 limestone localities in the Prague Basin, explored during the past decades, have been evaluated by the approach

described in a previous chapter. The analytical data were taken from unpublished exploratory reports, and were statistically treated for each lithostratigraphhic member and each locality (Kozlovcev 2012). Other lithostratigraphic members (Třebotov, Choteč, Suchomasty, and Vinařice limestones) are not dealt with in detail in this paper, as they both are no longer mined, and recent analytical data on them are missing.

The limestones studied significantly differ in the content of carbonates and show considerable variation in the content of SiO_2 and Al_2O_3, and in their ratio (Tab. 1). Whilst carbonate content can be used as a direct measure of the suitability of raw materials for firing either quick lime (over 95 wt.%) or for various types of hydraulic binders, the SiO_2/Al_2O_3 ratio can serve as an indirect measure of the proportion between the silica and clay minerals. Based on the later approach, Chýnice and Zlíchov limestones seems to be rich in silica,; Řeporyje, Slivenec, Lochkov, and Kosoř limestones are rich in clay minerals; whilst the remaining contain both silica and clay minerals.

Table 1. Carbonate content and SiO_2/Al_2O_3 ratio in the examined Lower limestones from Prague Basin (Czech Republic). Numbers in brackets indicate number of localities and number of analyses for each lithostratigraphic member. Explanation to abbreviations of lithostratigraphic members: ChLs = Chýnice limestone, ZlLs = Zlíchov limestone, DPLs = Dvorce-Prokop limestone, ŘeLs = Řeporyje limestone, LoLs = Loděnice limestone, SlLs = Slivenec limestone, KoLs = Koněprusy limestone, KsLs = Kosoř limestone, RaLs = Radotín limestone, KtLs = Kotýs Limestone, PřLs = Přídolí limestone, and KpLs = Kopanina limestone.

Limestone	CaCO₃	SiO₂/Al₂O₃
Devonian		
ChLs (1; 22)	99.52	14.33
ZlLs (6; 418)	76.16 – 83.55	7.10 – 12.63
DPLs (7; 1211)	74.05 – 90.36	3.25 – 6.79
ŘeLs (8; 176)	77.02 – 90.30	2.15 – 4.94
LoLs (6; 329)	77.02 – 92.66	1.92 – 3.14
SlLs (8; 260)	84.61 – 95.86	1.90 – 4.85
KoLs (10; 2751)	87.50 – 98.48	1.17 – 6.36
KsLs (3; 102)	74.07 – 89.64	3.68 – 4.23
RaLs (4; 122)	69.64 – 83.57	3.80 – 8.79
KtLs (6; 847)	77.32 – 90.46	4.10 – 7.72
Silurian		
PřLs (5; 347)	47.71 – 72.86	3.54 – 6.45
KpLs (3; 308)	34.38 – 76.61	3.40 – 5.53

4.2 Hydraulic potential

The examined Lower Palaeozoic limestones from the Prague Basin exhibit considerable differences in the degree of hydraulicity, as confirmed after the computation of all three relevant indices (Tab. 2). From the 12 examined lithostratigraphic members, 2 are of high $CaCO_3$ content and low $MgCO_3$ admixture (below 2%). From the examined limestones, specifically the Chýnice and Koněprusy limestone belong to this group. They are only suitable for quick lime production, although some specimens from the later show the presence of some non-carbonate admixtures. Koněprusy

limestone has recently been used as a source of relatively pure limestone for the firing of industrial quick lime (used e.g., for desulphurization, steel industry, etc.).

Eight lithostratigraphic members examined show chemical compositions suitable for the firing of hydraulic lime of variable degrees of hydraulicity, due to a $CaCO_3$ content below 90%, but generally above 80%, as well as a higher content of silica and/or clay minerals. Slivenec and Kosoř limestones can only be used for feebly hydraulic lime. Řeporyje, Lochkov, and Kotýs limestone contain higher amounts of silica and clay minerals and thus can produce feebly to moderately hydraulic lime when being fired. Most of the Radotín, Dvorce-Prokop and Zlíchov limestones are suitable for the production of moderately hydraulic lime (Tab. 2). However, an increasing content of silica and clay minerals at some localities makes all three of these limestones suitable raw materials for the production of eminently hydraulic lime. This has been experimentally confirmed for Dvorce-Prokop limestone taken from the abandoned Bráník (Prague) quarry (Kozlovcev 2012).

Two remaining limestones - Přídolí and Kopanina, of Silurian age (Tab. 2), are potentially suitable for the firing of natural cement. Variable, but generally low $CaCO_3$ (generally below 75%, very often around 60% or even lower), and the presence of silica/chert nodules decreases their quality and suitability for the firing of hydraulic binders.

Table 2. HI, CI, and M_H values for examined limestones from the Prague Basin (Czech Republic) and their suitability for production of specific types of constructional binders (QL = quick lime, FHL = feebly hydraulic lime, MHL = moderately hydraulic lime, EHL = eminently hydraulic lime, NC = natural cement). For explanation of limestone (Ls) type see Table 1.

Ls	HI	CI	M_H	Binder
Devonian				
ChLs	0.05	0.15	14.6	QL
ZlLs	0.24–0.44	0.62–1.12	2.21–3.53	M-EHL
DPLs	0.14–0.47	0.33–1.15	2.44–5.86	F-EHL
ŘeLs	0.11–0.26	0.27–0.60	3.41–7.56	F-MHL
LoLs	0.06–0.21	0.15–0.44	4.26–12.80	F-MHL
SlLs	0.01–0.15	0.03–0.36	6.12–23.20	FHL
KoLs	0.01–0.11	0.02–0.25	9.12–90.40	QL/FHL
KsLs	0.12–0.15	0.26–0.37	5.96–7.19	FHL
RaLs	0.15–0.48	0.29–1.16	1.95–6.05	F-EHL
KtLs	0.11–0.20	0.27–0.52	4.45–8.98	F-MHL
Silurian				
PřLs	0.39–1.52	0.93–3.81	0.61–2.23	EHL/NC
KpLs	0.39–2.56	1.09–5.58	0.36–2.21	EHL/NC

5 Summary

Re-examination of 12 lithostratigraphic members of Lower Palaeozoic limestones from the Prague Basin (Bohemian Massif, Czech Republic) confirmed their broad potential for the firing of various types of inorganic binders. From the rocks examined, two are only suitable for the production of quick lime. Eight others proved their potential for production from feebly

to eminently hydraulic lime. From the lithostratigraphic members examined, Dvorce-Prokop and Zlíchov limestones present the most promising materials for the production of hydraulic lime in the entire Prague Basin (Barrandian) area, due specifically to their material homogeneity.

Acknowledgements

References

Blezard RG (1998) The history of calcareous cements. In: Hewlett PC (ed) Lea's Chemistry of Cement and Concrete, 4th edn. Elsevier, Oxford, pp 1–23

Cahn D, Greer W, Moir R (1997) Atmospheric CO_2 and the U.S. Cement Industry. World Cem 28:64–68

Cháb J (1993) General problems of the TB (Teplá-Barrandian) Precambrian, Bohemian Massif, the Czech Republic. Věst ČGÚ 68:1–6

Chlupáč I (1988) The Devonian of Czechoslovakia and its stratigraphic significance. In: McMillian NJ, Embry AF, Glass DJ (eds) Devonian of the World, Canadian Society for Petroleum Geologists, Memoirs, 14, pp 481–497

Chlupáč I, Kukal Z (1986) Reflexion of possible global Devonian events in the Barrandian area, C.S.S.R. Lect Notes Earth Sci 8:171–179

Chlupáč I, Havlíček V, Kříž J, Kukal Z, Štorch P (1998) Palaeozoic of the Barrandian (Cambrian to Devonian). Czech Geological Survey, Prague

Cowper AD (2000) Lime and Lime Mortars. Donhead Publishing, Shaftesbury

Cultrone G, Sebastián E, Ortega Huertas M (2005) Forced and natural carbonation of lime-based mortars with and without additives: Mineralogical and textural changes. Cem Concr Res 35:2278–2289

Eckel EC (1922) Cements, Limes and Plasters: Their Materials, Manufacture, and Properties. John Wiley & Sons, New York

Elert K, Rodriguez-Navarro C, Sebastian Pardo E, Hansen E, Cazalla O (2002) Lime mortars for the conservation of historic buildings. Studies Cons 47:62–75

Gulotta D, Goidanich S, Tedeschi C, Nijland TG, Toniolo L (2013) Commercial NHL-containing mortars for the preservation of historical architecture. Part 1: Compositional and mechanical characterisation. Constr Build Mat 38:31–42

Havlíček V (1981) Development of a linear sedimentary depression exemplified by the Prague Basin (Ordovician - Middle Devonian, Barrandian, Central Bohemia). Sbor geol Věd G:7–48

Hughes DC, Jaglin D, Kozłowski R, Mucha D (2009) Roman cements — Belite cements calcined at low temperature. Cem Concr Res 39:77–89

Juenger MCG, Winnefeld F, Provis JL, Ideker JH (2011) Advances in alternative cementitious binders. Cem Concr Res 41:1232–1243

Kozlovcev P (2012) Experimental study of Palaeozoic limestones of the Barrandian and their possible use for burning of hydraulic limes and natural cement. Unpubl. manuscr. MSc thesis, Charles University in Prague (In Czech with English summary)

Kříž J (1991) The Silurian of Prague Basin (Bohemia) – tectonic, eustatic and volcanic controls on facies and faunal development. In: Basset MG, Lane PD, Edwards D (eds.) The Murchinson Symposium. Proceedings of and International Conference on the Silurian System. Special Papers in Palaeontology 44, pp 179–203

Lanas J, Pérez Bernal JL, Bello MA, Alvarez Galindo JI (2004) Mechanical properties of natural hydraulic lime-based mortars. Cem Concr Res 34:2191–2201

Láník J, Cikrt M (2001) Two thousand years of the Czech lime and cement industries. Svaz výrobců cementu a vápna Čech, Moravy a Slezska, Výzkumný ústav maltovin Praha spol. s r. o., Praha (In Czech)

Přikryl R, Šťastná A (2010) Contribution of clayey-calcareous silicite to the mechanical properties of structural mortared rubble masonry of medieval Charles Bridge in Prague (Czech Republic). Eng Geol 115:257–267

Röhlich P (2007) Structure of the Prague Basin: The deformation diversity and its causes (the Czech Republic). Bull Geosci 82:175–182

Varas MJ, Alvarez de Buergo M, Fort R (2005) Natural cement as the precursor of Portland cement. Methodology for its identification. Cem Concr Res 35:2055–2065

Weber J, Gadermayr N, Kozłowski R, Mucha D, Hughes D, Jaglin D, Schwarz W (2007) Microstructure and mineral composition of Roman cements produced at defined calcination conditions. Mater Character 58:1217–1228

Worrell E, Price L, Martin N, Hendriks C, Ozawa Meida L (2001) Carbon dioxide emissions from the global cement industry. An Rev Ener Environ 26:303–329

Thermal properties of volcanic ash and pumice

Elena Kuznetsova
SINTEF Building and Infrastructure, Trondheim, Norway

Rimma Motenko
Lomonosov Moscow State University, Moscow, Russia

Svein Willy Danielsen
SINTEF Building and Infrastructure, Trondheim, Norway

Abstract. This paper presents the results on thermal conductivity of volcanic ash and pumice collected from Kamchatka, Far East of Russia, and from Iceland, in dependence on different humidity and density. The research shows that the humidity of the samples is the key factor for thermal conductivity, both in the frozen and thawed state. And this in turn depends on porosity/density and chemical composition.

Keywords: thermal conductivity, volcanic ash and pumice

1 Introduction

People started to use volcanic materials for construction and industrial purpose already many centuries ago, and still do. Uses range from cut slabs of tuff for construction to very fine ash for polishing automobiles.

According to Heiken G. (2005) volcanic materials can be grouped as (1) pumice and ash, (2) pozzolan (fine-grained or zeolitized ash), (3) quarried tuff, (4) perlite, (5) basaltic scoria and lava, and (6) volcanic clays and zeolites.

Pumice is a natural material of volcanic origin produced by the release of gases during the solidification of lava (Neville 1995). Volcanic pumice has been used as aggregate in the production of lightweight concrete in many countries of the world. So far, the use of volcanic materials was dependent on the availability and limited to the countries where it is locally available or easily imported. Satisfactory light weight concrete having good insulating characteristics, but also with high absorption and shrinkage can be manufactured using volcanic pumice (Neville 1995, Hossain 2004)

Volcanic activities are common phenomena in various part of the world, especially like Iceland, Kamchatka on Far East of Russia, Papua New Guinea and others.

In this paper we are going to present some results on thermal conductivity of volcanic ash and pumice from Kamchatka area in Russia and from south of Iceland.

2 Methods

Scanning electron microscope (SEM) images of the samples and chemical composition of the volcanic glass and some minerals were obtained at the petrology department of Moscow State University by EPMA using "Jeol JSM-6480LV" with inversions spectrometer «INCA-Energy 350».

Transmission Electron Microscopy (TEM) analysis was performed in the NTNU/SINTEF Gemini Centre using a JEOL 2010F instrument equipped with an Oxford Instruments SDD x-ray detector for composition analysis.

Thermal conductivity (Λ, (W/(mK))) was calculated as: $\Lambda = C \cdot p \cdot a$, where C – specific heat capacity (J/(kgK)), p – rock density (g/cm^3), a – temperature conductivity (m^2/sec).

The temperature conductivity (a) was determined by using I type regular mode method (α-calorimeter) (Ershov, 2004). We realize detecting of temperature conductivity (a) by heating and cooling of ground in environment with constant temperature (outside of area with intensive phase changes). The temperature range was $0...+20$ and $-22...-12$ °C. All measurements were done two times. Precision of measurements is about 10%.

Specific heat capacity (C) was calculated as sum of ground components (rock matrix, water, ice). Thermal capacity was set to 4200 J/(kgK) for water and 2100 J/(kgK) for ice. Thermal capacities for rock matrix were measured on ITS-400 by monotonous heating. Precision of measurements is about 10% (Platunov, 1972).

The content of unfrozen water in frozen ground was determined by a combination of cryoscopic and contact methods (over the range from 0 to –15°C). The contact method is based on the principle of equilibrium in the ice, water and steam. The total moisture content was obtained by this method in the initially dry plates corresponding to the equilibrium content of unfrozen water at a given temperature. Cryoscopic method is based on the assumption that amount of the unfrozen water at the temperature t is equal to moisture content of the soils at the freezing (thawing) temperature (Ershov, 1979).

3 Volcanic pumice and ash

Samples for laboratory study were collected in Kamchatka peninsula, Far East of Russia, and in the south of Iceland.

For Kamchatka's samples natural humidity and density are ranging from 10 to 65% and from 0.9 to 1.5 g/cm^3 respectively. Hygroscopic water and particle density are ranging from 0 to 4% and from 2.1 to 2.8

g/cm^3. The chemical composition of volcanic glass in ash samples are rhyolitic and andesitic, in volcanic pumice – basaltic composition. The age of volcanic material is ranging from 35 to 9000 years.

For Iceland's samples humidity and density are up to 40% and 2.75 g/cm^3 accordingly. The chemical composition of the volcanic glass – basaltic. The age of material is approximately 100,000 years.

4 Alteration processes

Pyroclastic ash is the least stable solid phase of sediments that is predisposed to different mineral transformation in all lithogenetic stages. Volcanic ashes mainly consist of volcanic glass as the major component. They also include plagioclase, feldspar, quartz and pyroxene (Dahlgren et al. 1993). As a result of volcanic activity, volcanic glass is transported to a great distance and is then weathered forming secondary minerals. Among the alteration products caused by weathering and diagenesis are smectites, halloysite, kaolinite, allophane, palagonite and others.

For samples from Kamchatka IR-absorption spectra allowed diagnosing the composition of ashes with mafic (basaltic and andesitic) glass as allophane, and the composition of ashes with acidic (rhyolitic) glass - as opal; for samples from Iceland IR-spectra showed appearance of palagonite (Kuznetsova et al. 2010).

4.1 Allophane

Allophanes (from Greek allophanes – "turning out to be different") are amorphous minerals of variable chemical composition. Wada (1989) gives the approximate chemical formula of allophanes as $Al_2Si_2O_5 \cdot nH_2O$. They belong to sheet silicates because they have similar chemical composition and some common structural peculiarities with them, but differ from them through the lack of crystalline texture. Allophane is fully amorphous and was found for the first time as a product of volcanic ash transformation. Allophane consists of hollow spheres with the outer diameter of about 4-5 nm (Henmi & Wada 1976).

On the Figure 1 there is presented the glass particle from Kamchatka's samples, where neoformation of allophane is taking place from the borders of the vitric material towards the inside.

4.2 Opal

Opal (from Sanskrit *upalah* – stone) is amorphous silica, silicon dioxide hydrate, the chemical formula of which is $SiO_2 \cdot nH_2O$, where n usually varies from 0.5 to 2.

Two types of opal silicon are the most common for volcanic ashes: pedogenic (more known as laminar opal silicon) and biogenic (diatoms). Laminar opal silicon emerges at the early weathering stages and is characterized by the existence of spheric bunches of reticulate-like spheres of hydrated silicon. Opal silicon is formed in silicon-rich environment from over-saturated solutions which appear due to surface evaporation and, probably, water freezing in soils (Shoji et al. 1993;

Nanzyo 2002). Its quantity falls with the increase of the volcanic soil age as a result of particles weathering.

During our research it was assumed that the unit particle of opaline silica is roughly spherical in form and that these spheres are closely packed in microaggregates (Figure 2), as described by Shoji and Masui (1971). The opaline silica particles are extremely thin; the size of each peculiar sphere can be up to 10-20 nm. An eroded edge of the opaline silica can be seen which suggests that dissolution occurs during weathering. Most of the cells in the completely altered soft zone are filled with spherical bodies.
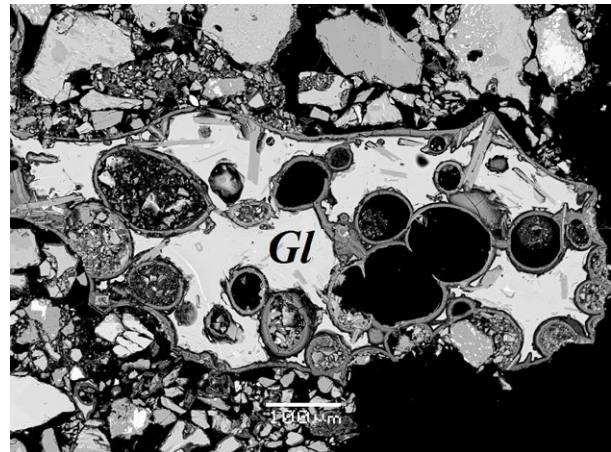
Figure 1. Allophane crust around glass particle; *Gl* – volcanic glass
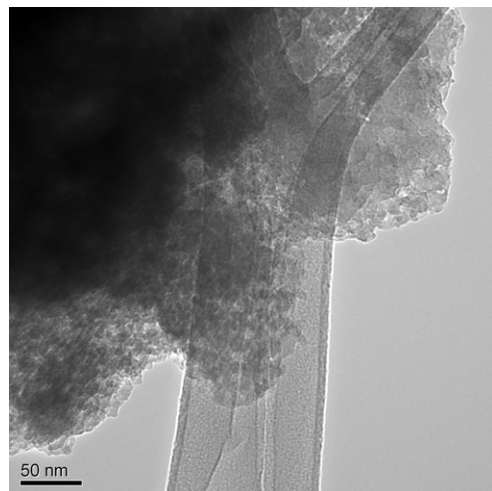
Figure 2. Transmission electron micrographs glass particle with opaline silica around; the boundary between altered and unaltered zones is visually distinguishable

4.3 Palagonite

"Palagonite" (gel to fibro palagonite depending on the degree of crystallinity) is a mixing of phases resulting from the process of palagonitisation which is an alteration of the glass by sea-water or by unsalted-water, submitted to different temperature or pressure conditions. The highly hydrated gel palagonite, related to low temperature alteration, is optically similar to the allophanic material: a clear yellowish to brownish isotropic and commonly concentrically banded material, in which the primary vitric morphology is preserved.

Palagonite was described as the first stable product resulting from the alteration of glass below water, forming a ring of insoluble material at the glass-fluid interface. In gel-palagonite spherical structures of 20 to 60 nm were observed by high resolution electron microscopy and interpreted as precursors of smectites. Amorphous "gel", palagonite is related to Si, Al, Mg, Ca, Na, K losses, H_2O gain and immobile Ti, Fe behavior (Gerard & Stoops, 2005).

On figure 3 there is presented volcanic glass particles from Iceland's samples. Palagonite borders are surrounding the glass material and the process is very similar with allophane formation.
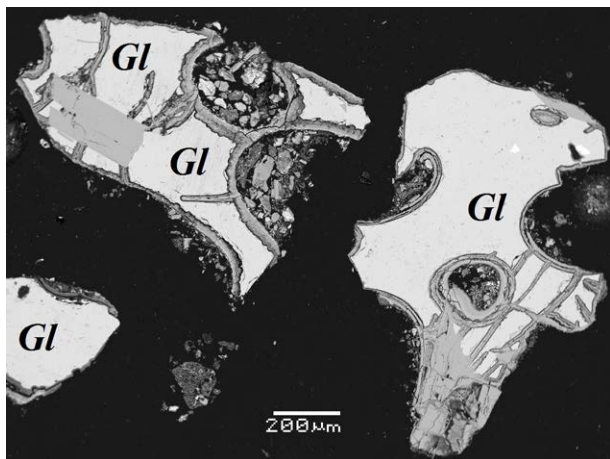
Figure 3. Palagonite crusts around glass particles in the samples from Iceland; *Gl* – volcanic glass

5 Thermal conductivity

Figure 4 presents the dependences of thermal conductivity versus humidity for both volcanic ashes and pumices in the thawed and frozen states. Samples nos. 1-21 – volcanic ash and nos. 1'-4' – volcanic cinder, collected from Kacmhatka, nos. 1^*-3^* - volcanic ash and no. 4^* - volcanic pumice, collected from Iceland.

Evidently, increasing of humidity and density resulted in increasing thermal conductivity coefficients. It is because low-conductivity air is replaced by more high-conductivity liquid or ice. The highest increasing of conductivity for samples with highest density values is explained by greater part of soil skeleton.

To compare data for thermal conductivity is possible only for samples with the same dry density ρ_d. Lines are summarizing the values for the same dry density. With increasing humidity W (from 0 to 80%) and dry density ρ_d (from 0.7 to 1.7 g/cm^3) thermal conductivity λ is increasing from 0.13 to 1.0 W/mK in thawed and from 0.14 to 1.27 W/mK in frozen states. For dry samples the values of thermal conductivity are close – 0.13-0.17 W/mK.

The dry density has a bigger influence on thermal conductivity in the thawed than in the frozen state. We also can see it on this example: the values for samples with dry density 1.0 and 1.1-1.2 g/cm^3 are summarized by two lines in the thawed state and by one line in frozen state.

It is very important to mention the fact that the values for both ash and cinder are summarized by the same line

despite the fact that cinder has bigger grain size than the ash. The reason for this is the cinder particles having a very high porosity and these two factors, particle size and porosity, are compensating each other; the major influence on thermal conductivity is due to the soil dry density.
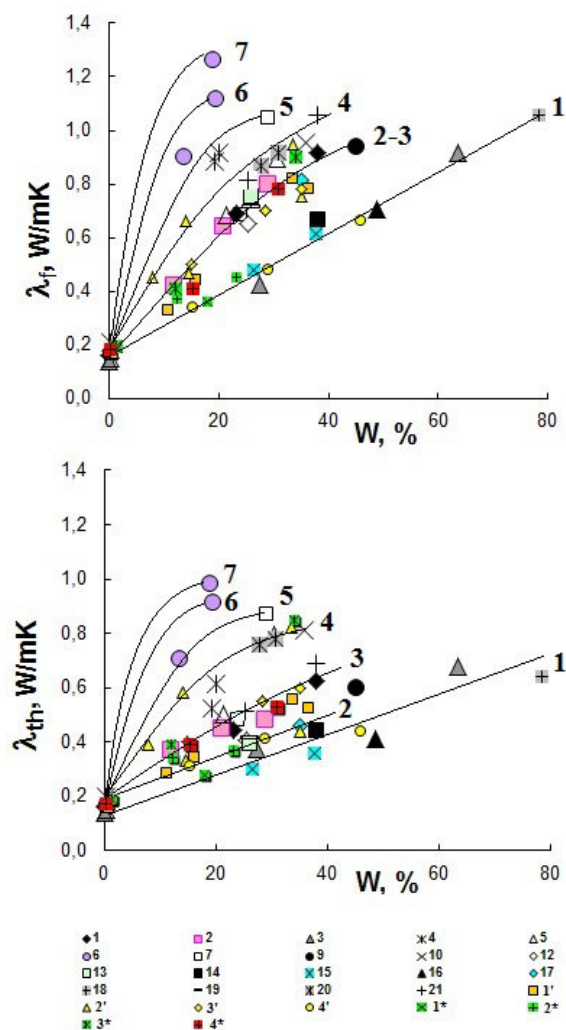
Figure 4. The dependence of thermal conductivity (λ) versus humidity (W) for volcanic deposits studied in the frozen (λ_f) and thawed (λ_{th}) states: nos. 1-21 – volcanic ash from Kamchatka, nos. 1'-4' – volcanic pumice from Kamchatka, nos. 1^*-3^* – volcanic ash and no. 4^* - pumice from Iceland. Lines summarize the values for the same dry density ρ_d: 1 – 0.8–0.9 g/cm^3, 2 – 1 g/cm^3, 3 – 1.1-1.2 g/cm^3, 4 – 1.3 g/cm^3, 5 – 1.5 g/cm^3, 6 – 1.6 g/cm^3, 7 – 1.7 g/cm^3

6 Unfrozen water content

The unfrozen water content in the frozen volcanic materials has been reported in a previous investigation (Kuznetsova et al. 2011). Figure 5 is a crossplot showing the unfrozen water content W_w and negative temperature for samples from Kamchatka containing either allophane or opal. For temperature below -3°C the content W_w changes from 2 to 13% for ashes containing allophane (area 1) and from 0 to 3% for ashes containing opal (area 2). For samples from Iceland, containing palagonite, the content W_w for temperature below -3°C is 2%.
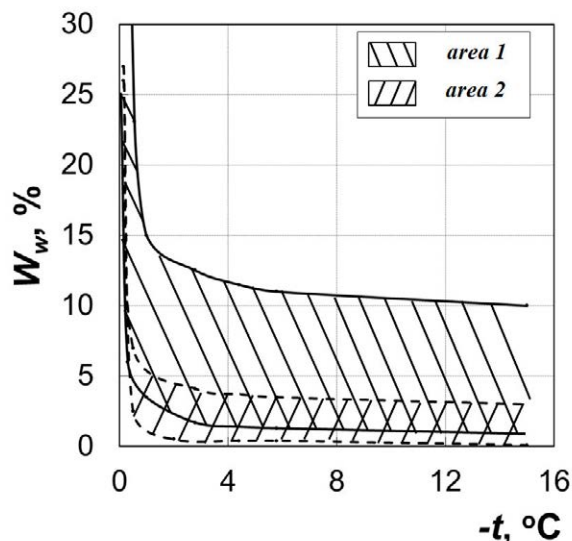
Figure 5. The dependence of unfrozen water content on temperature for studied samples from Kamchatka. Area 1 - ash samples containing allophane, area 2 –ash samples containing opal

According to many investigations (e.g. Theng et al. 1982, Henmi & Wada, 1976), allophane consists of hollow spheres with the outer diameter of about 4-5 nm, with defects in the wall texture which consequently form micro-pores 0.3-2.0 nm and with active surface area estimated is 800 m^2/g. The moisture retention capacity of allophanes is related to the presence of these very small pores and high active surface areas.

Palagonite is a proto-smectite, that's why it also has high active surface area and good absorption properties (Gerard & Stoops, 2005).

7 Conclusions

The main results obtained by the study are summarized below.
• The mineralogical analysis showed that for Kamchatka's samples: allophane was found in samples with andesitic and basaltic glass, opal - in samples with rhyolitic glass; for Iceland's samples: palagonite was found in samples with basaltic glass.
• In dry state, thermal conductivities for all volcanic deposits are very close and equal to 0.15-0.18 W/mK.
• On condition that the density (ρ_d) and humidity (W) are changing from 0.7 to 1.65 g/cm^3 and from 10 to 80 % respectively the thermal conductivity (λ) increases from 0.37 to 1.0 W/(mK) in a thawed state and from 0.41 to 1.27 W/(mK) in a frozen state.
• Thermal conductivity values under fixed humidity and density are close for pumice and ash in both thawed and frozen states, which related to two competing effects: grain size and particle porosity. Pumice particles have enclosed porosity which decrease their thermal conductivity and compensate the fact that cinder particles are bigger than ash particles.
• Volcanic deposits have very good thermo insulation properties.
• The content of unfrozen water is higher in volcanic ashes containing allophane than in those containing opal.

Thereby, the ash and pumice is found to be suitable as a thermal insulating material and has the potential to be utilized in manufacturing heat-insulating concrete and building blocks, especially where weather is cold and wet.

References

Dahlgren, R., S. Shoji, & M. Nanzyo (1993) Mineralogical characteristics of volcanic ash soils. In: S. Shoji, M. Nanzyo & R. Dahlgren: Volcanic ash soils - genesis, properties and utilization. Developments in Soil Science 21, Elsevier, Amsterdam, pp 101–143.

Ershov , E.D (editor) (1979) Fazovyi sostav vlagi v merzlykh porodakh (Phase Composition of Water in Frozen Rocks). MSU, Moscow (in Russian).

Ershov, E.D (editor) (2004) Geocryological research methods MGU, Moscow (in Russian)

Gerard, M. & Stoops, G. (2005) Allophane and palagonite similar neoformation at low temperature. EGU letters: №09053

Henmi T. & Wada K. (1976) Morphology and composition of allophane. American Mineralogist, 61, 379-390.

Kuznetsova E.P., Motenko R.G., Vigasina M.F. & Melchakova L.V. (2011) Unfrozen water research in Kamchatka volcanic ash. Vestnik MGU. Geology, **1**, 62-67.

Kuznetsova E.P., Motenko R.G., Vigasina L.V., Melchakova L.V. (2010) Allophane and palagonite as the product of volcanic glass alteration of different ages // Geochimica et Cosmochimica Acta, volume 74, issue 11, supplement 1, Knoxville, Tennessee, pp 551.

Heiken G. (2005) Industrial uses of volcanic materials. Chapter 13 in Volcanoes and the Environment, edited by J. Marti and G.G. Ernst. Cambridge University Press, pp 387-403.

Hossain K.M.A. (2004) Potential use of volcanic pumice as a construction material. Journal of materials in civil engineering, pp 573-577.

Nanzyo M. (2002) Unique properties of volcanic ash soils / Global environmental research. Vol. 6, issue 2, pp 99-112.

Neville A.M. (1995) Properties of concrete, 4th Ed., Longman Group Limited, Esses, England.

Platunov E.S. (1972) Thermo Physical measurements at monotonous regime. Energy, Moscow. (in Russian)

Paterson, E. (1977) Specific surface area and pore structure of allophone soil clays. Clay minerals, 12: 1–9.

Shoji S., Masui J. (1971) Opaline silica of recent volcanic ash soils in Japan // J. Soil Sci. **22**, pp 101-108.

Shoji S., Nanzyo M., Dahlgren R. (1993) Volcanic ash soils: genesis, properties, and utilization. Elsevier.

Theng B.K.G, Russell M., Churchman G.J. & Parfitt R.L. (1982) Surface properties of allophone, halloysite and imogolite. Clay and Clay minerals, **30** (2), pp 143–149.

Wada S-I. & Wada K. (1977) Density and structure of allophone. Clay Minerals, **12**, pp 289-298.

Wada K. (1989) Allophane and imogolite. Pp: 1051–1087 in: Minerals in Soil Environments (Dixon J.B. & Weed S.B., editors), **21**.

Assessment of the use of natural stone in St. Petersburg, the Leningrad region, and south-east Finland

Hannu Luodes, Heikki Pirinen, Paavo Härmä
Geological Survey of Finland (GTK)

Elena Panova
Saint-Petersburg State University, Russian Federation

Olavi Selonen
Palin Granit Oy, Finland

Abstract. A three-year project, started in 2012, "Efficient use of natural stone in the Leningrad region and South-East Finland", studies the use and durability of natural stone in urban environments along the Eastern Baltic Sea coast between Helsinki and St. Petersburg. Granitic rocks from that area, especially rapakivi granite, have been utilized in construction since the 18th century and the area still holds potential for future economic growth.
The project will document the use of natural stone in larger cities and the future needs of natural stone products, long term durability properties of local stones, natural stone reserves in the project region as well as the best natural stone evaluation methods from Finland and Russia. Preparation of guidelines for stone selection in construction and renovation will be carried out. The use of left-over material from the natural stone production will be promoted and suggestions for making the natural stone trade between the EU and Russia easier will be generated. According to preliminary results the local stone have performed well in the city environments. The main stresses for the stone are various human activities like modifications of structures and renovation together with mechanical and biological weathering.

Keywords, Natural stone, Durability, Weathering, Left-over

1 Introduction

Due to favourable geological reasons the border zone between South-East Finland and the Leningrad region in Russian Federation has great potential as a source of natural stone for the construction industry. This area contains e.g. the Vyborg rapakivi granite that has been utilized in a number of historically important buildings worldwide since the 18th century. The success of this stone is based on its visual appearance and favourable properties, with high durability and long life cycle. The use and durability of natural stone from this region is being studied in a three-year project "Efficient use of natural stone in the Leningrad region and South-East Finland", which started in 2012. The project focuses on the area along the Baltic Sea coast between Helsinki and St. Petersburg (Fig. 1), in which the Nordic climatic conditions demand special requirements for natural stones used outdoors.

The main objective of the project is to provide background information and justification for the long term development of natural stone resources in the project area. To achieve this goal it is essential to study and document the main characteristics of the stone materials of the area. The aim of the project is also to give a comprehensive view of future potential as well as available natural stone reserves both in Finland and Russia, and to study the effects of weathering and long term durability properties under Nordic climatic conditions.

The natural stone companies operating in the region fall into the category of Small and Medium Sized Enterprises (SME) with limited resources. Therefore, enhancing knowledge of the material reserves in the area gives them a better basis for long term economic development. This knowledge is also important for the permitting and supervising authorities in planning more sustainable future production together with industry. There is also a need to increase networking and the development of new products especially for the left-over stone that is currently quarried but not used in primary production. Innovative developments in the use of left-over stone could also generate new entrepreneurship and to reduce the environmental impacts of quarrying.
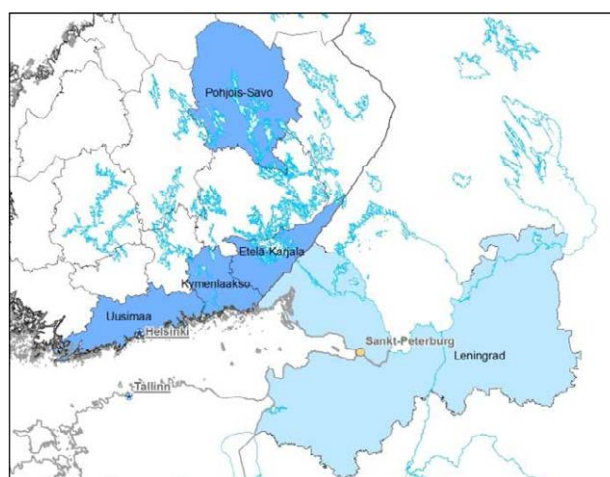
Figure 1. Project area.

The project is led by the Geological Survey of Finland (GTK) and the partners in the project are the Saimaa University of Applied Sciences from Finland, Federal State Unitary Enterprise "Petersburg Complex Geological Expedition" and Saint-Petersburg State University from the Russian Federation. Associates in

the project include natural stone companies from Finland, Ylämaa Group Oy and Palin Granit Oy. The project is co-funded by the European Union, the Russian Federation and the Republic of Finland through the European Neighbourhood and Partnership Instrument (ENPI).

2 Objectives of the project

Figure 2. Natural stone in the embankment of the River Neva in St. Petersburg. Photo Elena Panova.

The project consists of several themes. The use of natural stone in larger cities from the 18th century until today including the towns St. Petersburg, Vyborg, Helsinki, Kuopio and Kotka will be documented (Fig. 2). The use of natural stone in St. Petersburg has been previously described e.g. by Bulakh (2010). Natural stone in construction of Helsinki has been presented by Lehtinen (2008). An analysis of the need for natural stone (qualities and quantities) in the near future in reconstruction and construction in the southern Finland and St. Petersburg regions will also be carried out, based on consultations with planning authorities, architects, designers and constructors.

The project will provide detailed data about the long term durability of stone structures that are subject to mechanical, chemical and biological weathering in the cities along the Baltic Sea coast (St. Petersburg, Helsinki). Mechanical weathering caused by several annual freeze-thaw cycles is especially typical in these

coastal climate conditions. For comparison the Pohjois-Savo region, representing drier climatic conditions will also be considered. The use of salt in maintenance of raod and pavements in the winter may also have additional effects. The data gathered will be used in characterization of the durability and weathering mechanisms of different stone types and will be used in preparation of guidelines for stone selection in construction and renovation.

The data from existing quarries and natural stone reserves in the project area will be evaluated and compiled into a database. This will also assists in detecting old quarries where the stones of historical buildings have original been taken from. The best natural stone evaluation methods from both Finland and Russia will be assessed to produce guidelines for application of best practices in prospecting and evaluation of natural stone occurrences.

In the natural stone industry the utilization level of the total quarried stone is increasing but still quite low and the need for improvement has also been considered important by the industry itself. One of the aims in this project is to generate ideas for new products and applications for left-over stone (Fig. 3). Increasing the use of left-over stone and promoting the use of local natural stone as a sustainable, long life-cycle product in future construction projects requires knowledge that will be useful also for the permitting and supervising authorities who plan and decide the future conditions of natural stone quarrying.

Figure 3. An example of the use of left-over stone in the Katariina Seaside Park in Kotka, Finland. Photo Heikki Pirinen.

The project will also provide suggestions for making the natural stone trade between the EU and Russia easier. The need for making the use of stone more efficient and to increase its competitiveness is common to both Finland and Russia.

3 Methodology

Several historical and modern buildings and stone constructions have been photographed and documented using the gigapixel techniques, in which a large number of photos are combined to form a mosaic picture that can be viewed at different magnifications and zoomed into very small details (Fig. 4 and 5).

Figure 4. A photo done with the gigapixel technique of the house of Nylands Nation in Helsinki. Photo Heikki Pirinen.

Figure 5. A close-up of the facade of Nylands Nation house from the same photo as in Figure 5. Photo Heikki Pirinen.

The purpose is to document the use of natural stone with high quality pictures and to use these pictures in evaluation of the durability of constructions and especially stone facades. In stone constructions the effect of the climate conditions as well as the interaction between sealing mortar and stone are reported and evaluated. The evaluation of the condition of stone facades is based on systematic methodologies, such as the classification of weathering forms presented by Fitzner, Heinrichs and Kownatzki (1995).

Stone weathering and decay is evaluated from small drill core samples or hand samples taken from stone structures. The major methods will be thin section studies with optical microscopy together with SEM and MLA (Mineral Liberation Analysis) as well as chemical analyses to detect possible depletion effects on the stone surfaces. With SEM it is especially possible to study the effects of stone surface decay and biological weathering.

In research of the weathering of stone buildings and constructions, ground penetrating radar (GPR) with high frequency antennae will also be used together with ultrasound (UPV) apparatus.

To find the best available techniques for natural stone deposit evaluation it will be necessary to use detailed field mapping, diamond core drilling, GPR as well as various geophysical methods. The aim is to compare the techniques used both in Finland and in Russia to see the advantages and limitations of each method.

Figure 6. Sampling from a stone basement covered with moss. Photo Hannu Luodes.

All the results from stone characterization as well as evaluation of durability will be used to define new ideas for the use of left-over material of the natural stone quarrying.

4 Preliminary results

The historical usage of natural stone in construction in the cities in southern Finland and Leningrad region differ from each other to some degree. The stones used e.g. in Helsinki have usually been quarried quite close to the city and the quarries are actually nowadays within the city itself. As a result, the quarries themselves have practically disappeared already making room for buildings and roads. The rocks represent the Late Svecofennian Granite–Migmatite zone, described e.g. by Ehlers et al. (1993), having a migmatitic structure. Rapakivi granite from the Vyborg massive situated on the border between southeastern Finland and the Leningrad region has been utilized extensively in the construction of St. Petersburg since the beginning of the 18th century. This is due to lack of hard silicate rocks in the immediate vicinity of St. Petersburg, the good quarrying and working properties of rapakivi granite, as well as easy transport by sea from the main quarrying areas that were located by the coast in Virolahti, Finland. The rapakivi granite massif in southeastern Finland has been described e.g. by Simonen (1987) and Rämö and Haapala (1995).

Study of the condition of stone facades shows that they have performed well in urban conditions and that the main stress is due to various human activities, such as modifications in the structures and renovation.

Based on the study of samples taken from stone buildings and stone structures, the weathering effects are caused mainly by mechanical and biological processes. According to unpublished data of The Finnish Meteorological Institute covering the years 2003-2012 there can be annually from 10 to 20 freezing/thawing cycles on the southern coast of Finland. Continuous freezing and thawing of the stone surface leads to disaggregation of mineral grains increasing the porosity and allowing penetration of more water and biological growth. The weathering effect of salt used in winter maintenance of the cities will also be studied.

Processes of destruction of a natural stone in the city environment are caused by complex interaction of closely connected physical, chemical and biological factors. Studies have shown that abiotic stone damage precedes the development of biofilms, which prepare the stone surface for its subsequent biological colonization. This is connected with change in surface structure, emergence of cracks, cavities and irregularities on a surface where micro organisms can accumulate and develop. Biofilms also bind mineral grains on the stone surface.
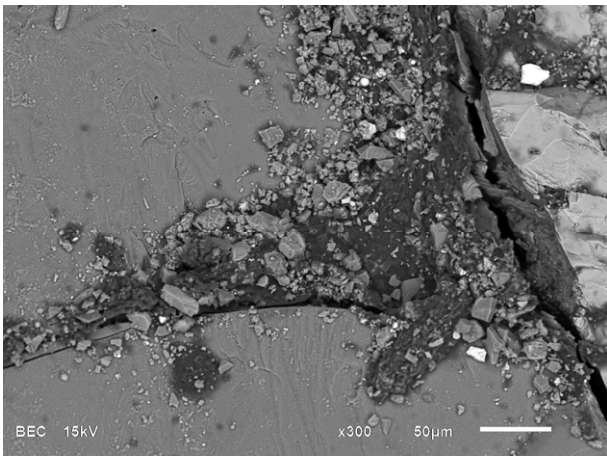
Figure 7. Biological growth (dark grey) concentrated in the fractures holds mineral grains on the stone surface. Rapakivi granite from St. Petersburg. BSE image by Elena Panova.

The role of chemical weathering in stones of the project area is not so evident and it will be studied further in the project using samples from stone structures and buildings.

5 Summary

Construction of the historical cities along the coast of the Baltic Sea between Helsinki and St. Petersburg have mostly made use of local stones. Weathering processes and man-maid stresses affect the stones and slowly change their properties and visual appearance even if

they are usually durable silicate rocks like granites. The project "Efficient use of natural stone in the Leningrad region and South-East Finland" aims, during 2012-2014, to determine the geological and technical characteristics of the local stones and the weathering processes affecting the region. The aim is to document the regional stone reserves and to provide background for sustainable utilization of the stone reserves also in the future.

The weathering of stone surfaces is mainly caused by mechanical freezing/thawing cycles and biological growth. The weathering process itself is slow and affecting mainly the visual appearance of the stone. Biological growth is found to be diverse and complex and will be examined more later on in the project.

References

Bulakh AG (2010) St.Petersburg; a History in Stone. St. Petersburg: St Petersburg: University Press House. (In collaboration with N.B.Abakumova and J.V.Romanovsky)

Ehlers C, Lindroos A, Selonen O (1993) The late Svecofennian granite-migmatite zone of southern Finland—a belt of transpressive deformation and granite emplacement. Precambrian Research, Volume 64, Issues 1-4, 295-309

Fitzner B, Heinrichs K and Kownatzki R (1995) Weathering forms – classification and mapping. Denkmalpflege und Naturwissenschaft, Natursteinkonservierung I: 41-88, Berlin: Verlag Ernst & Sohn.

Lehtinen M, Lehtinen I (2008) Helsingin kaupunkikiviopas. Karttakeskus

Rämö OT and Haapala I (1995). One hundred years of Rapakivi Granite. Mineralogy and Petrology, 52, 129-185.

Simonen A (1987) Pre-Quaternary Rocks of the Map Sheet Areas of the Rapakivi Massif in SE Finland. Explanation to the geological map of Finland 1 : 100 000, pre-Quaternary rocks, sheets 3023 + 3014, 3024, 3041, 3042, 3044, 3113, 3131, 3133. Geological Survey of Finland, Espoo, 49 pp. [in Finnish, with English summary].

Neogene pure limestones in eastern Austria for multiple applications

Beatrix Moshammer
Department of Mineral Raw Materials, Geological Survey, Neulinggasse 38, A-1030 Wien, Austria
e-mail: beatrix.moshammer@geologie.ac.at

Abstract
This article describes deposits and uses of Leitha Limestone (Middle Miocene, Badenian) in Austria. Notes of their geological setting from the margins of the Vienna Basin and western Pannonian Basin System are given. Numerous smaller and a few large quarries, many of them exploited or abandoned, provide insight into the local variations and different sequences of these strata. Selected quarry areas from the Leitha Mountains, from the Ruster Hills and from the Middle Styrian Swell are presented. From the few presently active quarries, dimension stone (Römersteinbruch St. Margarethen, Römerbruch Aflenz), cement raw material (Mannersdorf, Weissenegg, Retznei), high grade calcium carbonate filler from an exceptional chalky variety (Müllendorf), and sand and plaster (St. Margarethen) are produced. Quality parameters of chemical purity and whiteness are discussed. Leitha Limestone reveals its outstanding cultural value as building and sculpture stone in Medieval, Baroque and Historicism epochs, visible in Vienna, Graz, Bratislava, etc. Microfacies analysis and laboratory tests of geotechnical parameters on the various Leitha Limestone types from sampled quarries provide fundamental data recorded in a data base. In addition to describing the litho- and biostratigraphy of these Neogene limestones, the presented data serve in the determination of provenance, availability and durability behaviour for restauration and conservation purposes.

Keywords Dimension stone, historical quarries, mineral raw material, Leitha Limestone, Middle Miocene

1 Geological overview

Compact and sandy algal limestones developed in the Central Paratethys Sea during the Middle Miocene - Langhian and Serravallian, corresponding to the Badenian and Sarmatian of the regional stages (Piller et al. 2007a). The strata under focus (Leitha Limestones in the southern Vienna Basin and its transitions to the Pannonian Basin System, and Weissenegg Formation in the Styrian Basin) are the sedimentary biogenic limestones of shorelines and shallow marine realms around land, peninsulas and islands in the western part of the Central Paratethys (Harzhauser and Piller 2005). They developed on top of the terrigenic clastic sediments of the Karpatium when, during a new transgression, coralline algae took over as the main sediment producers in the shallow marine Badenian. Algae crusts and maërl sediments developed wherever terrestric influence did not interfere. Especially at the onset, repeated intercalations with coarse clastic sediments occur. Later, marly layers are intercalated as well, corals however show limited distributions. The maximum thicknesses lie in the range of decameters, exceeding 50 meters in special tectonic settings. Local and regional differences in the component spectra and diagenetic histories of the sandy or solid limestones result in different rock behaviour and usage, ranging from natural stone over cement use and sand products for the building industry to high grade fillers (Rohatsch 2005, Piller et al. 2007b). For completeness, historical uses of these limestones for the production of lime and the tanning of leather are mentioned. A section across the southern Vienna Basin in Piller and Harzhauser (2000) shows the time equivalent basinal and terrigenic rim sediments and the deep listric faults of the basin flanks that explain the lack of facies transitions on a wider scale.

The stratigraphy of the Leitha Limestone strata in the southern Vienna Basin and connected parts of the Pannonian Basin was published for selected outcrops or quarries. Among these are the Upper Badenian stratotype north of Großhöflein, the Fenk quarry, which was operated for lime burning in the past (Steininger and Papp 1987, Riegl and Piller 2000) and the Mannersdorf quarry which was earlier quarried for dimension stone use and is nowadays utilized for cement production (Wiedl et al. 2012). Due to synsedimentary tectonics the different sections show hiatuses and different faunal developments. Attempts to identify characteristic horizons and to combine different sections from the Vienna Basin, the Leitha Mountains, but also in its northeastern continuation in Slovakia are highly important, last but not least for the petroleum geology (Kovac et al. 2004, Piller et al. 2007a). The upper part of the limestone sequence, which continues after a distinct transgression, is of Sarmatian age. Here the strata often consist of redeposited Badenian sediment, of mollusc dominated limestones and oolithic rock types.

Comparable Middle Miocene corallinacean limestones are widespread in the Paratethys and Mediterranean Sea, e.g. in northern Croatia (Medvednica Mountains), Slovakia, (eastern rim of the Vienna Basin), Hungary (e.g. Fertörakos to the south of St. Margarethen), as well as in northern Moravia of Czech Republic and in Poland (Holy Cross Mountains).

2 Uses of Leitha Limestone

Quarries of Badenian-Sarmatian limestones are shown in Fig. 1. Rocks extracted from these quarries are used in different ways.

2.1 Building and statuary stone

The softness of Leitha Limestone and the resistance

against weathering processes led to the impressive and widespread use as building stones. The here mentioned selection of quarry areas are famous for this purpose. Limestone can be regarded as the most characteristic building stone in Vienna (Kieslinger 1972). Knowing the antique and historical town-building periods, it is possible to distinguish different types and sources of the Neogene Limestones. In the large quarry of St. Margarethen in the Ruster Hills, colloquially namend Römersteinbruch (Fig. 1: A, Fig. 2), an old quarry face called St. Stephan's wall was the source for the material of the cathedral in Vienna. A part of the quarry is nowadays used as open-air theatre. The active part of the quarry is the most prominent site, where Leitha Limestone is still mined both for restauration purposes and new building sites, with an annual production of up to 500 m^3. The Leitha Limestone from St. Margarethen displays a very porous, light brown, detrital algae facies, occasionally containing characteristic strands of rhodoliths.
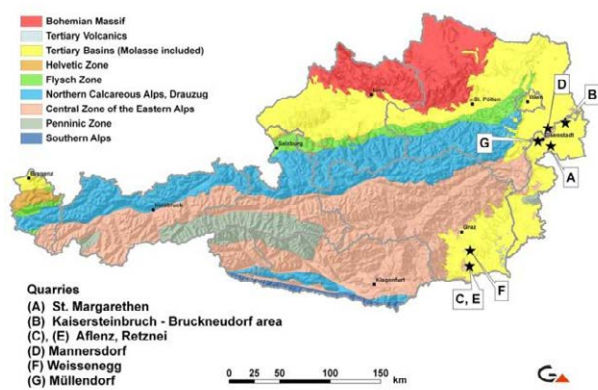

Figure 1. Neogene Badenian-Sarmatian Leitha Limestone quarry locations: (A) quarry district St. Margarethen providing dimension stone and in recent times also plaster sands; (B) historical quarries in the Kaisersteinbruch-Bruckneudorf area were mined for dimension stone; (C) subsurface Roman quarry Aflenz near Leibnitz mined for dimension stone; (D) quarries Mannersdorf am Leithagebirge, (E) Retznei and (F) Weissenegg providing material for cement production; (G) "chalk-quarry" in Müllendorf, where slightly consolidated limestone is grinded for filler material.

Figure 2. St. Margarethen quarry ("Römersteinbruch") in the Ruster Hills, historical photo by Forstner (before 1897?) from Heinrich (2000).

Numerous small and some larger quarries are situated in the area of Kaisersteinbruch-Bruckneudorf (Fig. 1: B). Most of them are nowadays located within the military training ground. They show a high variability of Leitha Limestone lithofacies, expressed in varying grades of cementation, degrees of sorting and composition of the components. The hard, thick-bedded limestones from Kaisersteinbruch typically contain sparse quartz-pebbles and a high proportion of reworked Leitha Limestone clasts. Quarrying was intensive since the 15th century, providing ashlars for heavy loads, like steps, balconies or columns. Well bedded detrital algae limestones of fine grained homogenous facies were quarried 6 km to the east at Teufelsjoch, an area of overgrown, large, irregular quarries, which were probably already used for famous antique settlements, like Carnuntum at the Danube.

For masterpieces of statuaries and stone carvings, like the pulpit in St. Stephen's cathedral in Vienna, a special type of Sarmatian limestone was preferred to Leitha Limestone. This type is very homogeneous and mainly made up of small foraminifers and ooliths. It was quarried approximately 4 km SSE of Kaisersteinbruch near Breitenbrunn.

Rohatsch (2005) and Häusler (2010) describe additional limestone quarries in the Leitha Mountains and other areas, which in some cases were used already in ancient times, as e.g. Sommerein. Comprehensive information and worked objects are exhibited in the Kaisersteinbruch and Mannersdorf museums.

A distinct variety of white Leitha Limestone, typically with bivalve molds, was produced from several quarries in Mannersdorf (Fig. 1: D). Since 1430 the stones were used for the cathedral in Vienna (Häusler 2010). Moreover, this limestone type was widely used for load bearing parts, e.g. pedestals and floorings. The deposit is nowadays quarried for cement raw material, but a small amout of natural stones is still obtained.

In the Styrian Basin Leitha Limestone occurs between north of Wildon and Retznei. According to comprehensive studies by Friebe (1991) it comprises several types of carbonates and siliciclastic rocks. The carbonates are built up by coralline algae, corals and bioclasts and together with interfingering siliciclastics (conglomerates, sandstones, marls and clays) are defined as the Weissenegg Formation of Badenian age. Numerous abandoned smaller quarries exist in this region, but the underground quarry at Aflenz a.d. Sulm (Fig. 1: C) stands out among these and is very famous for its stone. Parts of it were already quarried in Roman times. Later the "Aflenz stone" was intensely used as building stone of widespread reputation, e.g. in Graz and in Vienna. The quarry, with approximately 150 x 100 m spacing and 8 m height, shows a regular grid of chambers and pillars. It displays a very porous, whitish, detrital, bioclastic limestone. During Word War II the quarry functioned as a weapon factory. As a consequence, the stone was partly polluted. In the restoration period after WW II it was used all over Austria (Christian 1999). Nowadays quarrying is carried out every few years, yealding an annual average of about 100 m^3. The quarry area for the Retznei cement plant is situated 1 km to the southeast (Gross et al. 2007).

The described quarries were sampled for microfacies

investigations coupled with laboratory tests of geotechnical parameters. The study establishes types of Leitha Limestone according to their geophysical and geomechanical values in comparison with lithofacies. The results, which are an essential tool for provenance studies of ancient stone objects and for restauration purposes, will soon be published by Bednarik et al.

2.2 Sand production

In a sand pit, 200 m south of the "Römerquarry" St. Margarethen, weakly consolidated sandy limestones with minor marly layers crop out and, compared with that one, reveal lateral facies changes within the Leitha Limestone sequence (Schmid et al. 2001). They are excavated with a mechanical digger and hydraulic rock breaker to produce sand used for plaster as well as for engineered stones for the construction industry.

2.3 Cement raw material

High calcium limestone is quarried at Mannersdorf (Fig. 1: D) as well as at Retznei and Weissenegg (Fig. 1: E, F) for cement production. In these exceptionally large deposits Leitha Limestone shows the necessary continuity and homogeneity. Using drilling and blasting techniques, around 1 mio t of limestone are quarried annually at Mannersdorf, and about 700.000 t in both Retznei and Weissenegg. Ongoing quarrying and recultivation offer only limited time to access the long and high quarry walls. Nevertheless excellent insight into the depositional histories of the strata was gained in recent times by Wiedl et al. (2012) in Mannersdorf and by Erhard (2004) and Hohenegger et al. (2009) in Retznei.

2.4 Ground calcium carbonate filler

A quarry on the southern flanks of the Leitha Mountains is operated for its white and soft variety of Leitha Limestone (Fig. 1: G). The facies is similar to the adjacent and stratigraphically famous Fenk quarries in the east (chapter 1). In rarely consolidated beds rhodoliths, corals and algal detritus are preserved. Moreover, oysters are found frequently, accompagnied by other bivalves and sea urchins (Piller et al. 2007b). The chalky, very soft quality distinguishes this deposit from the others. According to Dullo (1983) the deposit lay in the phreatic meteoric realm under vadose influence. Fresh water passed through the unaltered limestone at varying flow rates. Under conditions of fast flowing undersaturated fresh water, the unstable components of the limestone, especially the aragonitic parts, were dissolved without simultaneous calcite-precipitation, whereas at low flow rates, caused by changed sediment porosities, a fast cementation could take place. Now the boundaries between cemented layers and chalky limestone run oblique to the stratification.

The soft and pure limestone is excavated by rippers. The production rate slightly exceeds 50.000 t per year.

After dry processing and grinding, the finest product has an average particle size of 1,8 micron, a carbonate content of 98,5 % and a whiteness of 87 (Ry C 2°). A range of products is used for plastics, adhesives, rubber and paints, and they show high covering capacities. Residual products are used for fertilizers, polishing agents and ceramics.

3 Chemical composition and degree of whiteness

The use as industrial filler affirms that some varieties of Leitha Limestone show high chemical purity and, in micron sized fractions, potentially remarkable whiteness compared to chalks or other limestones in Austria. A study on carbonate mineral raw materials carried out by the Geological Survey across Austria in the 1990's provided geochemical and whiteness properties of Leitha Limestone deposits. Table 1 shows average chemical properties of rock samples mainly taken from active quarries of Leitha Limestone in eastern Austria (Moshammer 1999). It can be concluded that white varieties like the one from Müllendorf quarry reach the highest possible whiteness.

Table 1. Geochemical and whiteness parameters of Leitha Limestone (Moshammer 1999)

Data source: 14 sampled quarries, 13 chemical analyses, 20 whiteness measures						
chemistry wt% whiteness	CaCO₃	MgCO₃	insol. residue	SiO₂	Y	Yellow Index
median	**96,79**	**1,28**	**1,61**	**0,93**	**80,70**	**13,26**
minimum	94,56	0,50	0,30	0,04	70,76	7,36
maximum	99,15	2,70	3,11	2,04	89,55	24,91
standard dev.	1,42	0,67	0,85	0,61	5,21	5,03
analysis methods: XRF, as well as combination of wet chemistry with AAS						

$CaCO_3 = CaO*1,7848; MgCO_3 = MgO*2,0919$
insoluble residue = total of all major elements except CaO, MgO and LOI
Y: standard colour value CIE 1964 (D65/10°); Yellowness Index DIN 6167

The hydrological reservoir capacity of Leitha Limestone sequences is well known (Häusler 2010). A study for drinking water supply provided samples from a well drilling. This 90,2 m deep drillhole at Oggau, 5 km NNE from Römersteinbruch St. Margarethen, was drilled with an in-hole hammer and encountered 61 m thick Leitha Limestones, underlain by gravels of metamorphic rocks.

Table 2. Leitha Limestone geochemistry and whiteness indices of samples from the borehole Oggau

drilling depth	wt%					
	CaCO₃	MgCO₃	insol. res.	SiO₂	Al₂O₃	FeO
23,5m	87,45	5,23	7,82	5,3	1,6	0,47
30,5m	92,99	4,18	2,91	1,9	0,6	0,20
abbreviations explained in Table 1, analysis method: XRF						

drilling depth	wt%	ppm		whiteness	
	K₂O	Ba	Sr	Y	Yellown. I.
23,5m	0,3	50	412	77,72	18,39
30,5m	0,08	20	415	83,73	11,65

Table 2 shows geochemical and whiteness parameters of two macroscopically different samples, a more yellowish one from 23,5 m depth and a lighter and more crumbled one from 30,5 m depth (reproduced from Kollmann et al. 2010).

The two samples show different degrees of impurities, interpreted as quartz and silicates. The relatively high values of calculated $MgCO_3$ contents are interpreted as high-Mg calcite, which is the skeletal material of corallinacean red algae and echinoderms. It remains unexplained why the magnesium content exceeds the range of $MgCO_3$ given in Table 1. Mineral chemistry and further petrographical analyses are needed to solve this problem.

4 Summary

The mineral raw material potential of the Leitha Limestones and the Weissenegg Formation, both Badenian-Sarmatian limestones from eastern Austria, is outlined. Due to their good workability and durability properties, the Leitha Limestones are a very important building material today and have been so in former times. In the Vienna Basin, around the Neusiedler See and in southwest Styria they were used overwhelmingly as building- and sculpture stones in history. Nowadays the limestones serve as prominent raw material for cement and, to a limited extent, even as high grade filler material. Their chemical purity and whiteness grades were pointed out in a raw material study. Recent studies on samples from quarries describe the microfacies characteristics of various Leitha Limestone types thus complementing litho- and biofacies studies and providing information on the sedimentary history and the mechanical behaviour of these stones.

Acknowledgements

References

Bednarik M, Moshammer B, Heinrich M, Holzer R, Laho M, Rabeder J, Uhlir C, Unterwurzacher M (in press) Typology of Engineering Geological Properties of Leitha Limestone from Historic Quarries in Burgenland and Styria

Christian G (1999) Die Muschelkalk-Sandsteinbrüche in Aflenz bei Leibnitz (Marktgemeinde Wagna, Steiermark). Mitteilungsblatt der Korrespondenten der Historischen Landeskommission für Steiermark 6, 22-32

Dullo WC (1983) Diagenesis of Fossils of the Miocene Leitha Limestone of the Paratethys, Austria: An Example for Faunal Modifications Due to Changing Diagenetic Environments. Facies 8, 1-112

Erhard CW (2004) Fazies und Geometrie von Leithakalken am Beispiel Retznei/Rosenberg. Diploma thesis, Karl-Franzens-University Graz

Friebe G (1991) Carbonate sedimentation within a siliclastic environment: the Leithakalk of the Weißenegg Formation (Middle Miocene, Styrian Basin, Austria). Zbl Geol Paläont Teil 1 1990 H 11, 1671-1687

Gross M, Fritz I, Piller WE, Soliman A, Harzhauser M, Hubmann B, Moser B, Scholger R, Suttner TJ, Bojar HP (2007) The Neogene of the Styrian Basin - Guide to Excursions. Joannea Geol Paläont 9, 117-193

Harzhauser M, Piller WE (2005) Neogen des Wiener Beckens. 75. Jahrestagung Paläontolog. Ges., Exkursionen, Graz, pp 1-42

Häusler H (2010) Erläuterungen zur Geologischen Karte 78 Rust. Geologische Bundesanstalt, Wien

Heinrich M (2000) Baurohstoffe. In Schönlaub H P (ed) Erläuterungen zur Geologischen Karte des Burgenlandes 1:200.000. Geologische Bundesanstalt Wien, pp 56-58

Hohenegger J, Rögl F, Ćorić S, Pervesler P, Lirer F, Roetzel R, Scholger R, Stingl K (2009) The Styrian Basin: a Key to the Middle Miocene (Badenian/Langhian) Central Paratethys Transgressions. Austrian Journal Earth Sciences 102, 102-132

Kieslinger A (1972) Die Steine der Wiener Ringstrasse. Franz Steiner Verlag, Wiesbaden

Kollmann W, Bieber G, Ćorić S, Hadfi J, Hobiger G, Moshammer B, Rabeder J, Römer A (2010) Geologische Auswertung von hydrogeologischen Erkundungsbohrungen als Grundlage für eine erfolgreiche Tiefengrundwassererschließung im Neogen des nördlichen Burgenlandes. Jb Geol B-A 150, 351-387

Kovac M, Barath I, Harzhauser M, Hlavaty I, Hudackova N (2004) Miocene depositional systems and sequence stratigraphy of the Vienna Basin. Cour Forsch-Inst Senckenberg 246, 187-212

Moshammer B (1999) Vorkommen von hochreinen und weißen Karbonatgesteinen in Österreich. Zusammenfassender Bericht Projekt Ü-LG-038/94-98. Ber. Geol Bundesanst 48, 1-33

Piller WE, Harzhauser M (2000) Badenian (Middle Miocene) Ecosystems. In: Piller et al. Palaeontological Highlights of Austria. Mitt Österr Geol Ges 92 (1999), 220-224

Piller WE, Harzhauser M, Mandic O (2007a) Miocene Central Paratethys stratigraphy - current status and future directions. Stratigraphy 4, 2/3, 151-168

Piller WE, Kroh A, Mandic O (2007b) Müllendorf: Der "diagenetische" Kreidesteinbruch. In: Hofmann T (ed) Wandern in die Erdgeschichte (22) Wien Niederösterreich Burgenland. Dr. Friedrich Pfeil, München, pp. 164-165

Riegl B, Piller WE (2000) Biostromal Coral Facies - A Miocene Example from the Leitha Limestone (Austria) and its Actualistic Interpretation. Palaios 15, 399-413

Rohatsch A (2005) Neogene Bau- und Dekorgesteine Niederösterreichs und des Burgenlandes. In: Schwaighofer B, Eppensteiner W (eds.) „Junge" Kalke, Sandsteine und Konglomerate - Neogen. Mitteilungen IAG BOKU, 9-56

Schmid HP, Harzhauser M, Kroh A (2001) Hypoxic Events on a Middle Miocene Carbonate Platform of the Central Paratethys (Austria, Badenian, 14 Ma). Ann Naturhist Mus Wien 102 A, 1-50

Steininger F, Papp A (1987) Faziostratotypus: Gross Höflein NNW, Steinbruch „FENK", Burgenland, Österreich. In: Papp A et al. (eds.) M4-Badenien (Moravien, Wielicien, Kosovien) Chronostratigraphie und Neostratotypen. Miozän der Zentralen Paratethys 6, Slovak Akad Wiss, Bratislava, pp 194-203

Wiedl T, Harzhauser M, Piller WE (2012) Facies and synsedimentary tectonics on a Badenian carbonate platform in the southern Vienna Basin (Austria, Central Paratethys). Facies. doi 10.1007/s10347-011-0290-0

Experimental testing of ASR potential of volcanic rocks

Zuzana Nekvasilová, Šárka Šachlová, Richard Přikryl
Charles University in Prague, Faculty of Science, Institute of Geochemistry, Mineralogy and Mineral Resources, Czech Republic,
zuza.nekvasilova@centrum.cz

Volcanic rocks are widely used in the Czech Republic as crushed aggregate (34% of the total crushed stone production). This study aims to experimentally quantify the alkali-silica reaction (ASR) potential of eight different volcanic rocks sampled in quarries producing crushed aggregates. The accelerated mortar bar test (following the ASTM C1260 standard) and chemical test (following the ASTM C289 standard) were employed and combined with microscopic methods. The accelerated mortar bar test simulated the influences of cement, high alkaline solution and increasing temperature. Duration of the accelerated mortar bar test was prolonged to 42 days. Chemical tests simulated the ASR by combining a highly alkaline solution and high temperature. The amount of Si and reductions of alkalinity of the solution were measured after the 24 hour testing period. Particles leached in alkaline solution were subjected to microscopic analysis with the aim to find those mineral phases contributing to the development of ASR. The ASR potential of volcanic rocks was found to be highly variable, and connected to their mineral composition. Basic volcanic rocks exhibit almost no ASR potential. High ASR potential was found in rocks containing significant amounts of SiO_2 (quartz or SiO_2-rich glass).

Keywords: Alkali-silica reaction, alkaline leaching, accelerated mortar bar test, volcanic rocks.

1. Introduction

In the last few decades, several methods have been proposed to assess whether the components of aggregates and concrete mixtures are prone to the formation of ASR. The most effective approach seems to be an expansion test (mortar-bar test) combined with microscopic techniques (e.g. Korkanc & Tugrul, 2005; Min et al., 2008). Chemical testing represents another possibility of how to quantify the ASR potential of aggregates under laboratory conditions (e.g. Wakizaka, 2000).

Volcanic rocks are widely used in the Czech Republic as crushed aggregate (34% of total crushed stone production). The extent of their use in concrete constructions has been documented in previous studies (e.g. Lukschová et al., 2009; Šťastná et al., 2012). Various volcanic rocks were investigated, with an aim to experimentally quantify their ASR potential (Seidlová et al., 2011). The ASR potential of aggregates was tested, based on experimental methods that consisted of a prolonged accelerated mortar bar test and the leaching of aggregates in alkaline solution. Alkali reactive phases were identified employing microscopic techniques (polarizing microscopy, scanning electron microscopy).

2. Experimental methods

2.1 Samples

Experimental material was selected for current study by using following criteria: (1) volcanic rocks come from active quarries; (2) rocks differ according to their mineralogy and chemistry; (3) variable ASR potential was indicated by previous studies and tests. Each of the samples consisted of 15-30 kg of crushed material of the 0/5 mm fraction.

2.2 Chemical test (ASTM C289)

Aggregate leaching in high alkaline solutions is the main principle of the chemical test (following the ASTM C289 standard). The 0.125/0.250 fraction (each sample of 25 grams) was used, and put into Teflon bottles. A solution of 1 M NaOH (25 ml) was added to the bottles and mixed with the aggregates. The mixture was tempered at 80°C for 24 hours. After rapid cooling, the mixture was filtered, and 20 ml of the solution was kept apart. The solution was diluted with distilled water at the ratio of 1:20. Part of the diluted solution was analysed using ICP OES (Charles University in Prague, Laboratories of the Geological Institutes, operator O. Šebek), with the aim to detect Si content. Another solution was titrated using 0.05 N HCl and phenolphthalein, and the reduction of alkalinity was measured.

2.3 Accelerated mortar bar test (ASTM C1260)

ASR potential of aggregates was quantified based on the expansion values of mortar bars (tested following the ASTM C1260 standard). The samples were crushed and sieved into the 0/5 mm fraction. Three different mortar bar specimens were prepared from each sample using the 0.125/5 mm fraction and stored in 1M NaOH solution at 80°C. Standard expansion of mortar bar specimens was measured during the 14 day testing period. Measurement of two mortar bar specimens was prolonged up to 42 days. The test was performed in cooperation with ZKK Hořice v Podkrkonoší, Ltd.

2.4 Microscopic techniques

Polarising microscopy was performed on LEICA DMLP optical microscope (Laboratory of Optical Microscopy, Charles University in Prague) using polished uncoated thin sections prepared from rock samples and/or crushed

aggregates (2 thin sections for each specimen).

Scanning electron microscopy combined with energy dispersive spectrometer (SEM-EDS) was conducted at the Laboratory of Electron Microscopy and Microanalysis (Charles University in Prague). The thin sections were coated in a carbon atmosphere. The measurements were performed on a Tescan Vega instrument, with an energy-dispersive analytical system (Oxford Instruments LINK ISIS 300) under the following conditions: 0.8 nA; 180 s counting time; and a 20 - 30 kV accelerating voltage. A 53 Minerals Standard Set #02753-AB (SPI Supplies) was used for the standard quantitative calibration.

3. Results

3.1 Chemical method

Two different values were measured according to the chemical test: Si dissolved into solution (S_C) and reduction of alkalinity (R_C). S_C values varied between 9.7 and 41.10 mmol/l. R_C values varied between 118 - 305 mmol/l (Table 1). Both values, plotted into the diagram (Figure 1) indicate no potential for ASR, according to the ASTM C289 classification.

Table 1. Expansion values of mortar bars, reduction of alkalinity (R_C) and Si dissolved into the solution (S_C), measured according to the chemical test.

Sample No.	Expansion 14 days (%)	Expansion 42 days (%)	Sc (mmol/l)	Rc (mmol/l)
CZ 12	0.034	0.088	9.9	198
CZ 17	0.115	0.166	13.7	257
CZ 31	0.015	0.028	10.5	258
CZ 33	0.015	0.022	14.5	212
CZ 35	0.073	0.260	9.7	305
CZ 21	0.130	0.280	54.5	118
CZ 45	0.223	0.372	31.1	248
CZ 46	0.220	0.380	41.1	165

Two different groups of samples could be distinguished based on alkaline leaching: Group I (sample Nos. CZ12, CZ17, CZ31, CZ33, and CZ35) indicating very low S_C values (9.7 - 13.7 mmol/l); and Group II (sample Nos. CZ21, CZ45, and CZ46) indicating higher S_C values (31.1 - 54.5 mmol/l). No difference could be seen in R_C values of investigated samples.

3.2 Accelerated mortar bar test

The investigated samples indicated expansion of the mortar bars ranging from 0.015 to 0.223% for the 14 day testing period, and from 0.022 to 0.380%, for the 42 day testing period (Table 1, Figure 2). The classification of the samples (following the ASTM C1260 standard)

classifies aggregates as: reactive (expansion < 0.100% after 14 days); and non reactive (expansion > 0.100% after 14 days).

Group I could be classified as non reactive, indicating low expansion values (0.015 - 0.073%). Only sample No. CZ17 indicate higher expansion (0.115%), exceeding the limit of reactive samples. All samples of Group II can be classified as reactive, indicating expansion values from 0.130 - 0.220%.
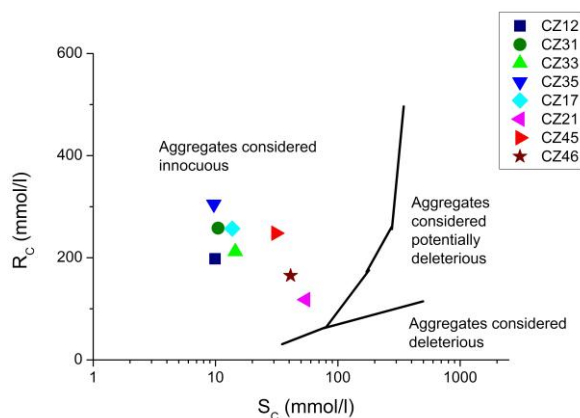
Figure 1. Diagram of reduction of alkalinity (R_C) vs. Si dissolved into the solution (S_C). Limits between areas of aggregates considered deleterious, potentially deleterious, and innocuous to ASR (based on ASTM C 289).
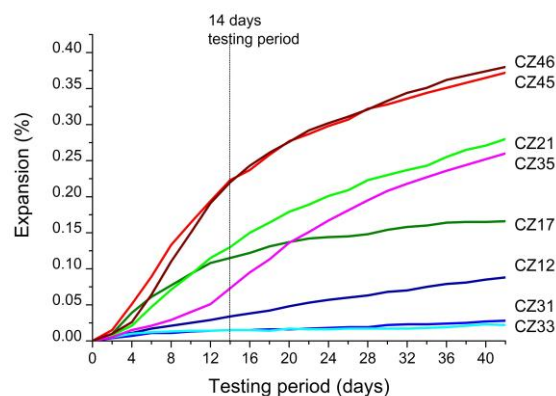
Figure 2. Expansion values of accelerated mortar bars. On the horizontal axis is the 42 day test period; the green line the 14 day test period.

4. Discussion

4.1 Correlation of chemical method with accelerated mortar bar test

Significant misunderstandings could be found when a standard classification of the chemical method is used. According to ASTM C289, all investigated samples should be classified as non reactive (Figure 1).

A more detailed view showed differences between the samples investigated. The five samples indicating very low S_C values could be considered as non reactive. This conclusion correlates well with the expansion values of the mortar bars (Figure 3). The other three samples (Nos. CZ21, CZ45, CZ46), indicating higher S_C values, show higher expansion of the mortar bars. These three samples should be classified as reactive.
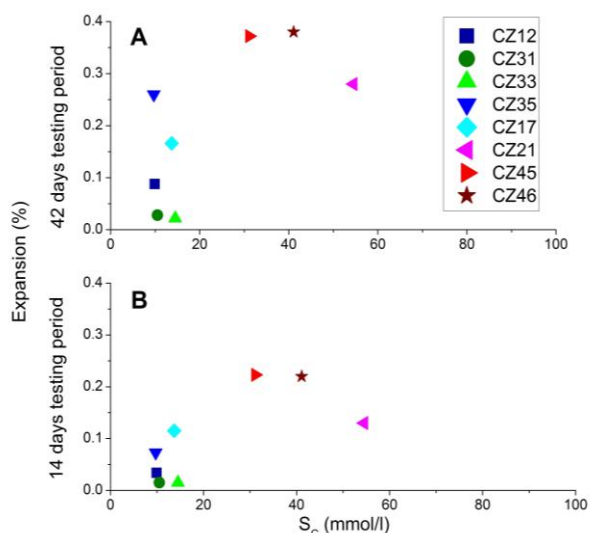
Figure 3. Comparison of expansion values and dissolved silica (S_C).

4.2 Phases causing ASR of investigated samples

Significant differences were found in the mineral compositions of the samples of Group I compared to Group II (Figures 4 and 5). The samples of Group I are mainly of basalt composition (classification of the rock types were based on the scheme suggested by Le Maitre et al., 1989; and on Gillespie & Styles 1999) containing a prevailing content of Ca-rich plagioclase (andesine-bytownite) together with amphibole, pyroxene, and chlorite. Minerals such as apatite, titanite, ilmenite, and pyrite were found in accessory amounts.

Samples of Group II belong to acid and/or intermediate volcanic rocks, which contain the Na-rich as well as Ca-rich plagioclase (albite-labradorite) and K-feldspar accompanied by significant content of SiO_2-rich glass and quartz. Pyroxene, white mica, chlorite, and clay minerals (smectite) are less common. The high ASR potential of SiO_2-rich phases is well known (e.g. Wakizaka, 2000, Çopuroğlu et al., 2009). The influence of K-feldspar and albite is more complicated. Bérubé et al. (2002) documented the possible leaching of alkalis from alkali feldspars, and their contribution to ASR.

4.3 Standard vs. delayed expansion of mortar bars

A different shape of the expansion curve was found in the case of sample No. CZ 35 indicating a very low
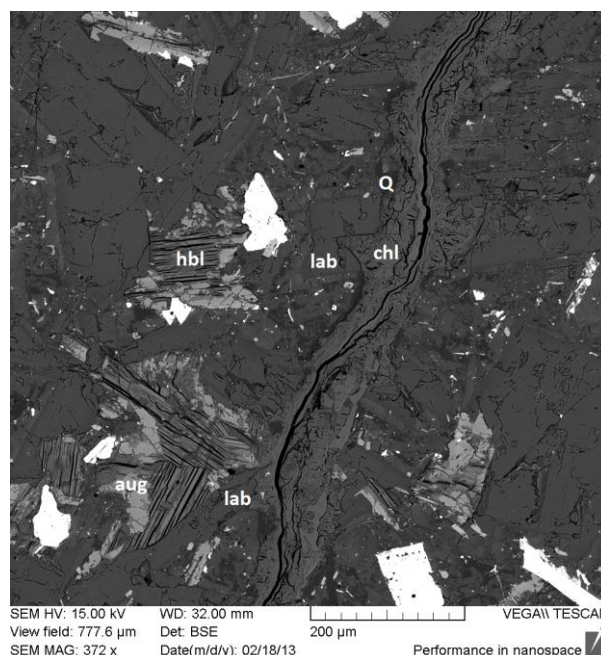
Figure 4. Overview of the microscopic image (from SEM-BSE) of Sample No. 35 (Group I). Mineral phases: chl - chlorite, lab - labradorite; aug - augite; Q - quartz; hbl - hornblende.
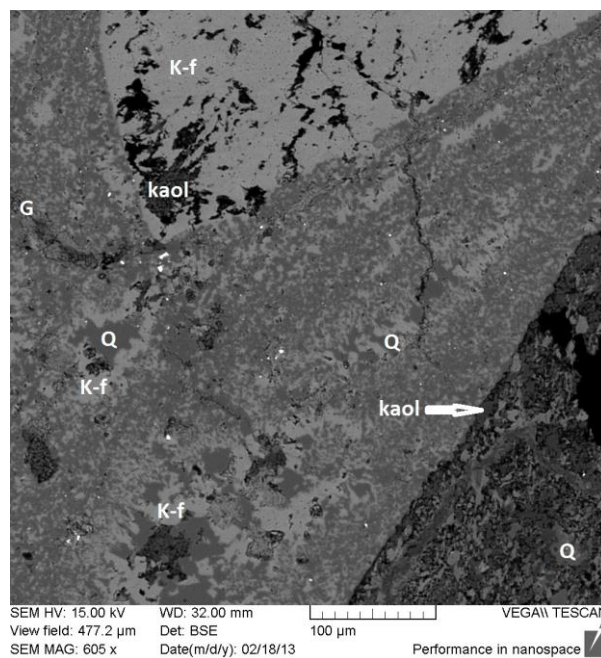
Figure 5. Overview of the microscopic image (from SEM-BSE) of Sample No. CZ 45 (Group II). Mineral phases: K-f - K-feldspar; Q - quartz; kaol - kaolinite; G - glass.

expansion value within the first 12 days of the testing period. The expansion curve indicates rapid increase after 12 days testing period (from 0.051% up to 0.26% after 42 days testing period). After 42 days testing period the expansion is comparable with reactive samples (0.26% compared to 0.28% of the sample No. CZ21). This is in

contradiction with standard classification indicating the sample as non reactive after 14 days testing period.

5. Conclusions

Rocks of basaltic composition preferentially containing plagioclase and mafic minerals exhibit almost no ASR potential. ASR potential increases with increasing content of SiO_2-rich phases (SiO_2-rich glass and microcrystalline quartz). The sample No. CZ35 exhibits delayed expansion leading to different classification after 14 days testing period (sample classified as non reactive) compared to prolonged 42 day testing period, when the expansion of the sample approaches the values of reactive samples.

Acknowledgements

References

ASTM C1260-07 (2011) Test method for potential alkali reactivity of aggregates (Mortar-bar method). ASTM, West Conshohocken, 04.02

ASTM C289-07 (2011) Potential Alkali - Silica Reactivity of Aggregates (Chemical Method). ASTM, West Conshohocken, 04.02

Bérubé MA, Duchesne J, Dorion JF, Rivest M (2002) Laboratory assessment of alkali contribution by aggregates to concrete and application to concrete structures affected by alkali–silica reactivity. Cem Concr Res 32:1215-1227

Çopuroğlu O, Andiç-Çakir Ö, Broekmans MATM, Kühnel R (2009) Mineralogy, geochemistry and expansion testing of an alkali-reactive basalt from western Anatolia, Turkey. Mat Char 60:756-766

Gillespie MR, Styles MT (1999) BGS Rock Classification Scheme. Classification of igneous rocks. British Geological Survey Report 1: 54

Korkanc M, Turgul A (2005) Evaluation of selected basalts from the point of alkali-silica reactivity. Cem Concr Res 35: 505-512

Le Maitre RW, Bateman P, Dudek A, Keller J, Le Bas MJ, Sabine PA, Schmid R, Sorensen H, Streckeisen A, Woolley AR, Zanettin B (1989) A classification of igneous rocks and glossary of terms. Blackwell, Oxford

Lukschová Š, Přikryl R, Perold Z (2009) Evaluation of the alkali-silica reactivity potential of sands. Mag Concr Res 61: 645-654

Min D, Lingling X, Xianghui L, Mingshu T (2008) Microstructures and alkali-reactivity of Permian Emeishan group basaltic rocks. In: Broekmans M.A.T.M., and Wigum B.J. (Eds.) Proceedings 13th ICAAR, pp 50-59

Seidlová Z, Přikryl R, Šachlová Š (2011) Improvement of microscopic method for the assessment of alkali-silica reaction in mortar specimens. A. Mauko, T. Kosec, T. Kopar, N. Gartner (Eds.), e-proceedings of 13th EMABM Conference, Ljubljana, Slovenia, June 14 - 18 2011, pp 7, ISBN 978-961-90366-7-9

Šťastná A, Šachlová Š, Pertold Z, Přikryl R, Leichmann J (2012) Cathodoluminescence microscopy and petrographic image analysis of aggregates in concrete pavements affected by alkali-silica reaction. Mat Char 65:115-125

Wakizaka Y (2000) Alkali–silica reactivity of Japanese rocks. Eng Geol 56:211-221

Automated evaluation of renewable aggregate resources

Pfleiderer, S., Heinrich, M., Rabeder, J., Reitner, H. & Untersweg, T.
Geological Survey of Austria, Neulinggasse 38, 1030 Vienna, Austria, spfleiderer@geologie.ac.at

Hofer, V.
Dept. of Statistics and Operations Research, Univ. of Graz, Universitätsstr. 15/E3, 8010 Graz, Austria

Bach, H.
Inst. for Railway Engineering and Transport Economy, Graz Univ. of Technology, Rechbauerstr. 12/2, 8010 Graz, Austria

Abstract. In alpine regions, alluvial fans, debris cones and alluvial valley fill are important sand and gravel resources which are constantly renewed due to high sedimentation rates. Their resource quality is usually described by parameters such as grain size, sorting, particle shape and lithological composition. These parameters are largely controlled by morphological and geological properties of the provenance area and by the mode of sediment transport and deposition.

A GIS routine was developed to derive and quantify these properties automatically by means of geological maps and elevation models. The results are translated into material properties and resource quality of the sediment using simple trend analysis.

The geoprocessing method was verified by classical petrographic analysis of field samples taken in Austria. In addition to manual measurements, a PetroScope® was used to derive grain size and form optically. This machine quantifies 3D shape parameters of each particle automatically through laser triangulation. The results provide a good approximation of the quality of aggregate resources and compare well to the actual usage of mined gravel deposits.

Keywords. Renewable aggregates, resource quality, alluvial fans, geoprocessing, PetroScope®

1 Introduction

Alluvial fans and debris cones represent important sand and gravel resources in the Austrian Alps. They are all mapped on geological maps at the scales of 1:50.000 or 1:200.000, however these maps do not systematically provide a description of lithological or petrographic properties. Yet, these properties are of utmost importance for the assessment of resource quality of sand and gravel deposits.

An automated evaluation method was developed to give a first approximation of aggregate quality. The method makes use of the fact that the petrographic characteristics of a gravel deposit depend on the morphology and geology of the provenance area. Since the latter can easily be derived by GIS routines the former can be estimated in principle. For the verification of the results, petrographic analysis of field samples can again be automated by using a PetroScope® which derives the size and form of gravel particles optically.

This paper presents the resource quality estimates obtained by GIS routines and the results of petrographic analyses obtained manually and automatically by the PetroScope® for selected aggregate resources in Austria.

2 Materials and Methods

2.1 Description of provenance area using GIS

A geoprocessing tool was developed to delimit the provenance area of a gravel deposit automatically by means of a digital elevation model (DEM) using standard GIS functionality and further programming with ModelBuilder. The tool quantifies morphological parameters of the area such as surface, altitude range, travel distance and slope angle (Reitner et al. 2013).

The tool then superimposes the geological map onto the area and calculates the area percentage of each geological unit occurring in the provenance area as well as the travel distance of any erosion products down to the deposit. Figure 1 shows an example of the results of the GIS routine.
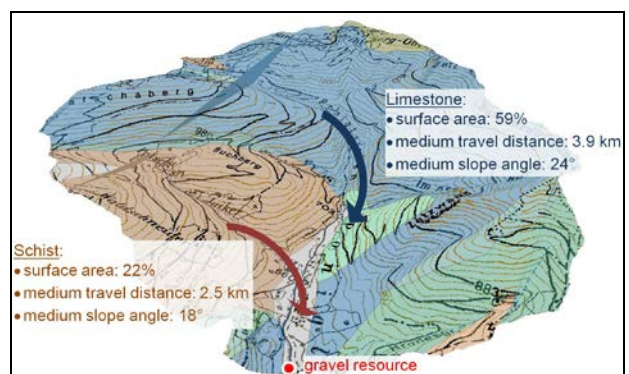
Figure 1. Quantification of morphological and geological properties of the provenance area of sand and gravel resources

Simple trend analysis was used to translate GIS results into material properties and resource quality of the sediment. This regards the forecast of litho-spectra by GIS-derived area percentages of geological units, the estimation of grain size distribution based on transport mode and distance, the prediction of grain shape depending on the weathering style of original rock types and the degree of sphericity as a function of the hardness of rocks and minerals.

2.2 Derivation of petrographic properties using the PetroScope®

To calibrate the translation of GIS results, 13 representative field samples of selected gravel resources were taken in all major tectonic units of Austria. Petrographic analysis was performed manually on the grain size fraction > 2 mm to determine lithological composition as well as grain size and shape parameters.

The grain size distribution and 3D shape measurements were complemented by an automated analysis technique using the PetroScope®. For grains larger than 4 mm this machine determines rock type by means of reflectance spectra (Hofer 2011) and geometric properties such as size, elongation, flatness, angularity and sphericity by means of laser triangulation (Lee et al. 2005). The sample is loaded into a feeder system which separates the grains and drops them on a conveyor belt where each grain is scanned individually (Figure 2). The data allow for the analysis of grain geometry as function of rock type or grain size.

Figure 2. PetroScope® conveyor belt with optical cameras scanning individual grains

3 Results

Table 1 summarizes the GIS derived parameters of the 13 field sites. These include 3 debris cones with small areas of provenance (maximum travel distance 0.4 – 1.7 km), 3 alluvial valley fills with medium sized provenance areas (5 – 6 km travel distance) and 7 alluvial fans with provenance areas of medium to large extent (2 – 16 km travel distance). They represent accumulations of the erosional products of various rock types ranging from carbonate rocks, schists, phyllites and quartzites to gneiss and granites.

Figure 3 illustrates a screenshot of an ongoing PetroScope® analysis. As an example it shows individual measurements of particle no. 33 such as sieve size, lengths of long, medium and short axes, volume, shape, angularity, as well as cumulative results of all analysed particles such as particles size distribution and frequency histograms of particle shape and angularity.

Table 1. GIS derived parameters of the provenance area of gravel resources

type of deposit	maximum distance of travel [km]	altitude range [m]	dominating rock type
debris cone	1.65	840	limestone
debris cone	1.19	360	gneiss, mica-schist
debris cone	0.44	200	phyllite, limestone
alluvial fan	8.97	2170	granite, ortho-gneiss, mica-schist
alluvial fan	16.03	850	phyllite, gneiss
alluvial fan	5.09	1422	limestone, quarzite, schist
alluvial fan	3.20	1616	limestone, marl, dolostone
alluvial fan	15.89	2071	mica-schist, gneiss
alluvial fan	3.18	1277	limestone, dolostone
alluvial fan	2.07	1320	granitic gneiss, phyllite
alluvial valley fill	4.72	704	mica-schist
alluvial valley fill	5.85	644	limestone, schist
alluvial valley fill	5.58	560	schist, dolostone

The geoprocessing tool yields reliable results concerning the delineation of provenance areas provided the morphology of the terrain is sufficiently accentuated. For very flat alluvial fans the GIS routine reaches its limit of applicability. The quality of the elevation model determines the rate of success for provenance area delineation and controls the accuracy of derived morphological parameters.

As a first approximation the GIS-derived area percentages of geological units correspond to the litho-spectra found in field samples. Deviations occur where schists, phyllites and marls make up a small portion of the provenance area yet dominate the litho-spectrum of the fine grain size fraction of the sediment.

Medium grain sizes are found to be larger for sediments resulting from carbonate rocks (pebble size) or granites (granule to pebble size) compared to deposits which represent weathering products of paragneis and schists (coarse sand to granule size). Sorting is observed to be low altogether but comparatively higher in valley fills (medium value of $D_{60}/D_{10} = 22$) than in alluvial fans ($D_{60}/D_{10} = 38$) and debris cones ($D_{60}/D_{10} = 53$). Sphericity is found to be highest for sandstone and mica schist particles, less high for limestones and dolostones and lowest for quartz and quartzite. Phyllites, paragneis and schists yield platy particles whereas granites and especially carbonate rocks and amphibolites provide for cuboid or elongated grains.
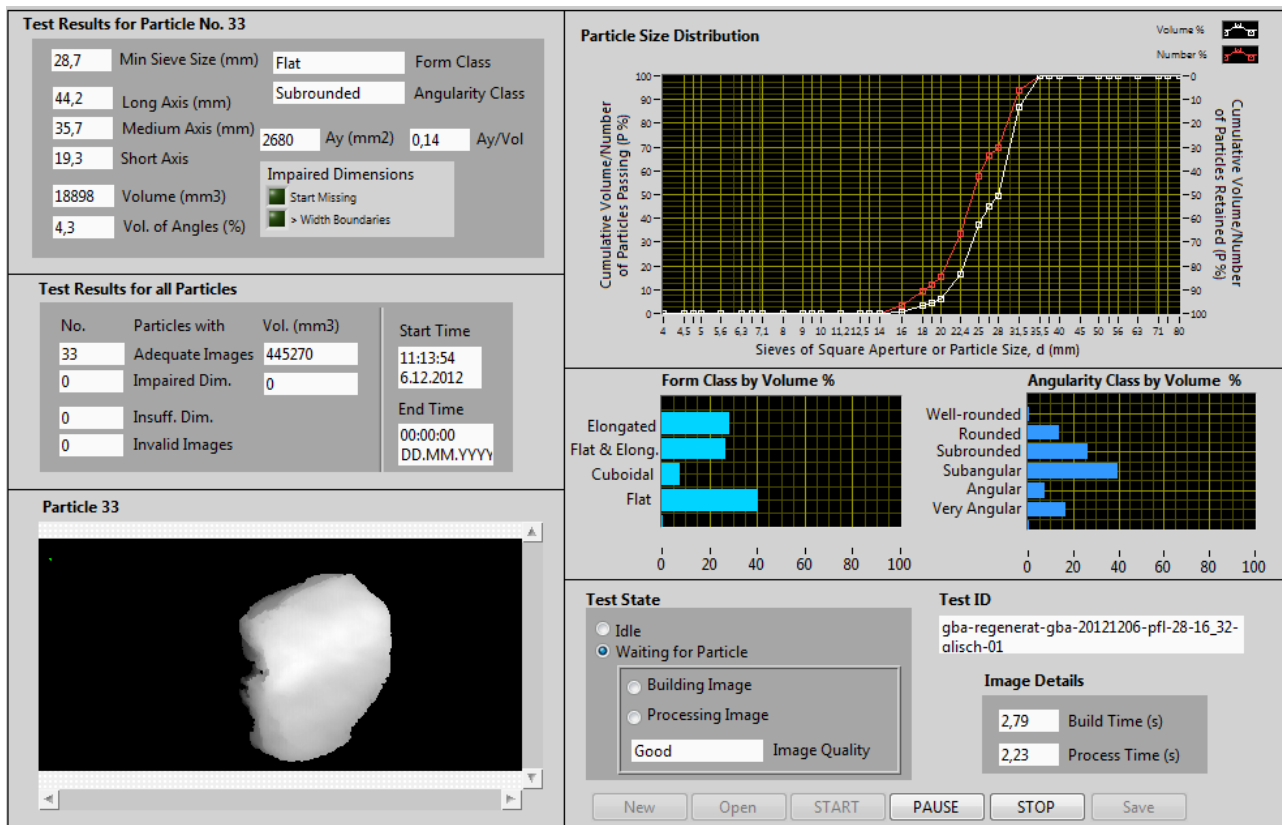
Figure 3. Screenshot of ongoing PetroScope® analysis

4 Discussion and conclusion

Mistakes and inaccuracies in the geological maps result in false predictions of material properties and resource quality estimates. If a high resolution DEM and correct geologic data are available, results provide a good approximation of the quality of aggregate resources and compare well to the actual usage of mined gravel deposits.

However, these conclusions are based on a limited number of routine runs and sample-based verifications. Both the GIS routine and the automated petrographic analysis will be applied further to gain more experience. A systematic study of aggregate resource quality across Austria is planned to substantiate the preliminary results presented here.

Acknowledgements

References

Hofer V (2011) Functional methods for classification of different petrographic varieties by means of reflectance spectra. Math. Geosci. 43(2):165-181.

Lee JRJ, Smith ML, Smith LN, Midha PS (2005) A mathematical morphology approach to image based 3D particle shape analysis. Mach. Vis. Appl. 16(5):282-288.

Reitner H, Pfleiderer S, Untersweg T, Heinrich M, Lipiarska I, Lipiarski P, Rabeder J, Wimmer-Frey I (2013) Geoprocessing tool Regenerat – Characterization of mineral resource quality of renewable sediment deposits. Abstr. IAMG Conf. Proc.

Comparison of standardized thermal shock tests used to measure expansion-contraction in soapstone

Heikki Pirinen, Seppo Leinonen & Ilona Romu
Geological Survey of Finland, P.O. Box 1237, FI-70211 Kuopio, Finland

Abstract. In this abstract we compare two standardized thermal shock tests, developed originally for synthetic ceramic refractory materials.
Comparison of the two different standardized thermal shock tests used for soapstone shows that the test with water cooling (DIN 51 068) may not be suitable with this material. Presently, the standard methods for technical testing of soapstone are based on the properties of artificially homogeneous ceramic materials (DIN 51 068 and EN 993-11). Soapstone, however, represents a natural material composed mainly of talc and magnesium carbonate together with variable amounts of other minerals such as dolomite, chlorite and magnetite. The two thermal shock tests differ in the size and form of the test sample as well as the method of cooling. Both thermal shock tests stress the tested material by heating to 950°C followed by rapid cooling either with flowing water (DIN 51 068) or blowing air (EN 993-11). Carbonate minerals decompose to oxides and carbon dioxide when soapstone is heated to high temperatures. Newly formed oxides, 5-40 w% react strongly with water, forming magnesium and calcium hydroxides. Expansive hydroxides cause excess stress in samples disrupting the actual purpose of expansion-contraction resistance measurements.

Keywords. Soapstone, magnesium carbonate, talc, thermal shock test, eastern Finland

1 Introduction

Soapstone is a dimension stone which is widely used in fireplaces because it can cope with the high temperature existing in the interior of the furnace. Granitic dimension stone varieties are not suitable for such high temperature applications, because of the existence of quartz, which shows a significantly higher coefficient of heat expansion relative to the other minerals in granites. Soapstone has usually been used for cladding the smaller stoves, for the frames and surfaces of bigger heat retaining fireplaces and in many cases also used for inner parts of the big heat retaining fireplaces and baking ovens.

The standard for slow heat release appliances fired by solid fuel (EN 15 250) does not require thermal shock testing. However soapstone fireplace producers have commonly used thermal shock tests with water cooling (DIN 51 068) for ensuring that the stone type intended for use as furnace lining and exhaust channel material is suitable for that purpose. The temperature of the furnace, 950°C, used in both tests, is considerably higher than the temperature achieved in the fireplaces and ovens. As observed in experiments (Tulikivi Oyj, personal communication), the surface stones of large heat retaining fireplaces are not exposed to temperatures

exceeding 100°C. The cladding stones of smaller stoves and framework of big fireplaces can heat up to 200°C. The furnace linings and the exhaust channel, however, may heat up to 800°C, but temperatures >630°C are restricted to the outermost 10 mm layer of the lining in direct contact with the fire.

The Geological survey of Finland, Tulikivi Oyj and Vuoleri Oy implemented a project to study the material properties of soapstone in the years 2010-2012, Soapstone; a parallel in Utility Properties and Classification project (VUOLU). The project was co-funded by Finnish Funding Agency for Technology and Innovation (TEKES). In this abstract we present our preliminary results of the tests concerning the suitability of the standardized thermal shock tests for natural, production-quality soapstone. The studies of petrography, whole-rock chemical composition, mineral reactions in the heated soapstone, and the thermal shock tests constitute a part of the VUOLU project.

2 Materials and Methods

Samples represent the production-quality soapstone from six quarries in eastern Finland. Eleven soapstone types were tested. The starting material mineralogy was studied with standard petrographic procedure and Mineral Liberation Analyzer (MLA) at GTK and geochemistry with XRF at the laboratory of Labtium Ltd. The Standard thermal shock tests DIN 51 068 and EN 993-11 were carried out in the StonePole Oy testing laboratory in Juuka, Finland. The mineralogy of heated samples was analysed with x-ray diffraction analysis (XRD) at GTK Outokumpu and Espoo laboratories. The mineral reactions of the heated soapstone were studied using thermo gravimetric analysis (TGA) and differential scanning calorimetry (DSC). XRD mineral content was determined within 5% accuracy using the PANalytical Highscore program. TGA /DSC analyses were made using a heating rate of 10° C per minute from room temperature to 1480°C.

2.1 DIN 51 068

The specimen used in this test is cylindrical in shape, 50 mm in diameter and height. Briefly, the DIN 51 068 "Testing of ceramic raw and basic materials - Determination of resistance to thermal shock - Water quenching method for refractory bricks" method includes the following steps: prior to testing, the specimen will be dried in an oven at temperature of 110°C. Preheated specimen will be kept in the furnace at

950°C for 15 min. After heating, the specimen will be cooled for 3 minutes under flowing 10°C - 20°C water (Fig. 3). The heating-cooling cycle will be repeated until the specimen is shattered in two or more pieces, but not more than 30 cycles (DIN 51 068).

2.2 EN 993-11

The specimen used in this test is the size of a quarter-standard brick (114 mm x 64 mm x 64 mm). Briefly, EN 993-11 "Dense shaped refractory products – Part 11: Determination of resistance to thermal shock" method includes the following steps: prior to the testing, the specimen will be dried to a constant mass in an oven at a temperature of 110°C. After the drying, the specimen will be put in the pre-heating oven (250 - 300°C) for at least four hours. Preheated specimen will be kept in the furnace at 950°C for 45 min. After heating the specimen will be placed on a metal plate and cooled with compressed air (pressure of 0.1 MPa) for 5 minutes (Fig. 3). After quenching, the specimen is submitted to a bending strength of 0.3 MPa, gradually and without shock. The heating-cooling-bending cycle will be repeated until the specimen is broken in two or more pieces, but not more than 30 cycles (EN 993-11).

In addition to the standard 950°C temperature we also applied the DIN 51 068 (water cooling) at temperatures of 1000°C and 700°C. These temperatures were selected on the basis of calorimetric measurements pointing to the exothermic mineral reactions taking place during heating of the soapstone (Fig. 4).

3. Soapstone

The term "soapstone" is used for talc-bearing metamorphic rocks soft enough to be carved. The most common type of soapstone is comprised of talc and carbonate minerals. The talc-carbonate association occurs in equilibrium with a wide set of chemical compositions of ultramafic rocks from low to high grade metamorphic conditions. Hence talc and carbonate minerals are quite common equilibrium phases, soapstone may have more diverse mineral associations, including Fe-Cr oxides, olivine, amphiboles, chlorite, serpentine, biotite, and quartz.

The "Sustainable use of Soapstone" (VUKE) – project in 2010-2012 was carried out in cooperation with the Geological Survey of Finland (GTK) and the University of Oulu Department of Geoscience. VUKE proposed a more precise definition of the term "soapstone" to European standardization committee CEN TC 264, standard EN 12670 Natural stone, terminology. Scientifically, soapstone is a metamorphic rock composed of 30-70% talc. In addition, soapstone may include carbonate minerals and/or chlorite up to 70% and less than 50% of hard silicates. Commercially, soapstone is a rock consisting of 30-70% talc, carbonate, chlorite and serpentine. Soapstone is soft enough to be carved with a knife, 2-3 on the Mohs scale and characterized by a soapy feel caused by the talc. In the future the VUKE project will also formulate a procedure of detailed naming according to standard metamorphic rock terminology (Kärki et al. 2008).

3.1 Mineralogy and Geochemistry

During the VUOLU-project modal mineralogical and whole-rock chemical compositions of 11 types of soapstone were determined. The average modal content of the most common major minerals was as follows: talc ~51%, carbonate minerals 34%, chlorite and serpentine, when present, 7% and up to 17%, respectively. The minor minerals include oxides and sulphides. Oxides, most commonly magnetite, occur as the main accessory mineral (< 5%) but in the most iron rich soapstones it may occur as a major mineral, up to 20%. Ferrichromite, chromian magnetite, and ilmenite are found only in very low amounts (< 0.1%). Sulphides, usually pyrrhotite and pentlandite occur also only in sparse amounts (< 0.2%). Typically, magnesite is the only carbonate, but some soapstone types contain also dolomite, comprising as much as 45% of the total carbonate content. Calcite was not observed in the studied samples. The whole-rock composition of the studied soapstone types shows variable contents of silica and iron from 32.5 to 49.1wt% SiO_2 (avg. 40.1wt%); 6.5 to 22.0wt% $Fe_2O_3^{tot}$ (avg. 10.6wt%), and high contents of magnesium, 32.4-36.2wt% MgO (avg. 34.6wt%). The contents of calcium and aluminium are low, in the range of 0.06-3.0wt% CaO and 0.6-3.3wt% Al_2O_3, respectively. TiO_2 has very low values (< 0.1wt%, avg. 0.18wt%) as well as K_2O (avg. 0.01wt%), which was usually below the detection limit. There was minor amount of sulphur in each sample (avg. 0.12wt%).

3.2 Texture and structure

The soapstone types studied in the VUKE project show nine major types of texture and structure. The main textural types include fine grained massive, slightly banded or highly deformed schistose and striped with chlorite and re-crystallized flaky talc (Fig. 1). The main structural types show gradation between massive to schistose and even grained to coarse porphyroblastic structures (Fig. 2).
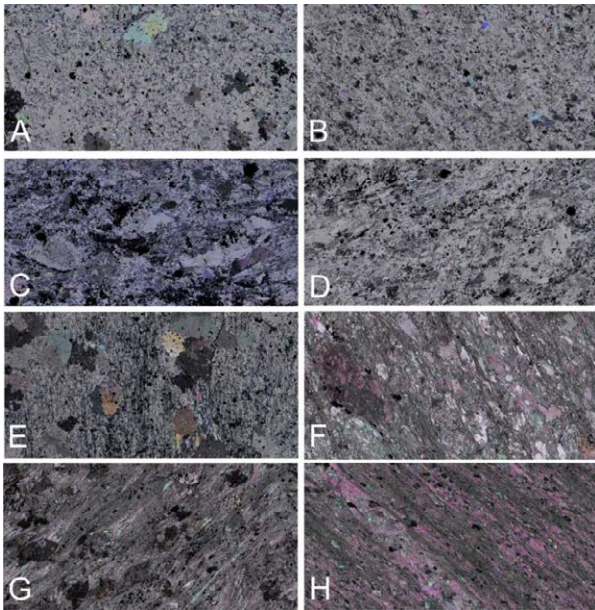
Figure 1. The texture of soapstones, scanned thin sections. A) Massive, B) Sparsely oriented, C) Oriented, D) Slightly banded, E) Banded, F) Striped, G) Schistose H) Striped and schistose. The long side of the section is 47 mm.
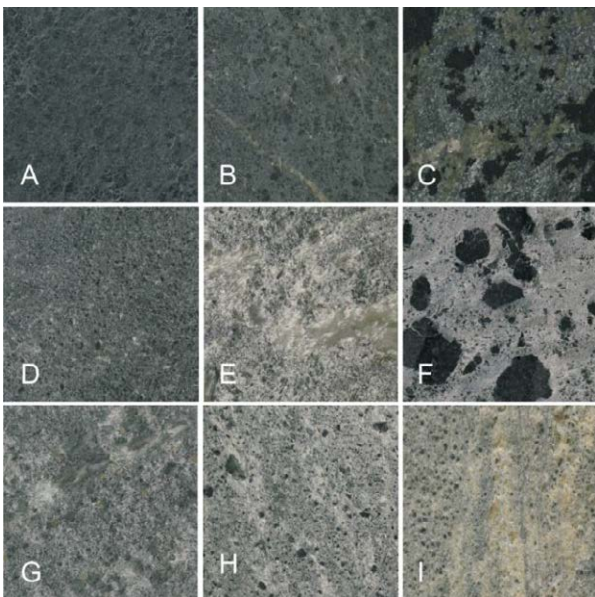
Figure 2. The structures of soapstone. A) Massive, B) Massive with thin cutting veins, C) Massive and porphyroblastic, D) Sparsely or hiddenly oriented, E) Oriented, F) Oriented and porphyroblastic, G) Slightly banded, H) Banded and I) Striped and schistose**.** The sides of the macroscopic photographs represent 60 mm.
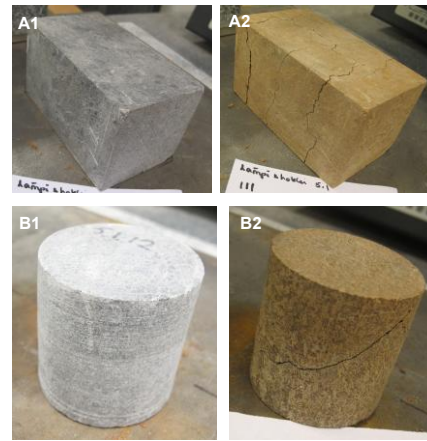
Figure 3. Photographs of samples used in thermal shock tests. A1,A2 test samples with air cooling (EN 993-11). B1,B2 test samples with water cooling (DIN 51 068). Same soapstone types were used in the both tests.

4 Mineral reactions in heated soapstone

Figure 4 shows the heat producing (exothermic) and heat consuming (endothermic) reactions in 2 types of soapstone during progressive heating. Accordingly, the first exothermic mineral reaction begins at 620-640°C and ends at 680-690°C, when magnesium carbonate with some amount of Fe, $(FeMgCO_3)$ decomposes to periclase (MgO), breunnerite $(FeCO_3)$ and carbon dioxide (CO_2). The second exothermic reaction begins at 706-718°C and ends at 730°C, when breunnerite decomposes to wustite (FeO) and carbon dioxide. The third exothermic reaction begins at 740-750°C and ends at 775-785°C when dolomite $(CaMg(CO_3)_2)$, if present, decomposes to calcium carbonate $(CaCO_3)$, periclase and carbon dioxide. The fourth exothermic reaction begins at 790-820°C and ends at 830-835°C when calcium carbonate decomposes to calcium oxide (CaO) and carbon dioxide. The final exothermic reaction in the range of the temperature of the thermal shock tests, takes place when talc $(Mg_3SiO_4O_{10}(OH)_2)$ dehydrates and water is released. This reaction begins at 900-925°C and ends at 975-980°C when talc has decomposed to enstatite $(MgSiO_3)$, forsterite (Mg_2SiO_4) and periclase (Fig 4.).
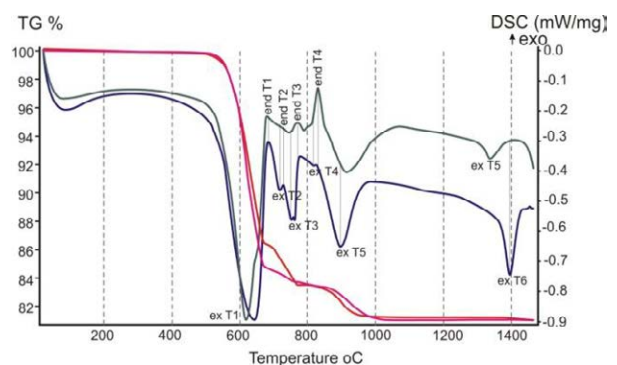
Figure 4. The results of thermo-gravimetric analysis (TGA) and differential scanning calorimetry (DSC) of two different types of soapstone from eastern Finland. TGA: red and DSC: blue and green.

5 Results of thermal shock tests

Thermal shock tests measure expansion-contraction induced decomposition of test materials. Figure 5 shows that the character of the heat stress caused by the standard tests is more aggressive and acute relative to the stress caused by normal use in heat retaining fireplaces.
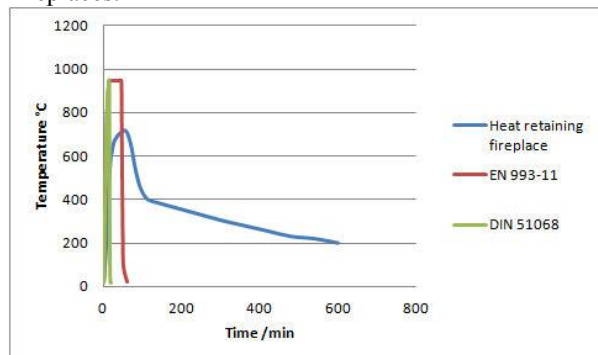
Figure 5. Comparison of heat stress in soapstone during normal use in heat retaining fireplaces, and during the standard tests DIN 51 068 and EN 993-11.

Figure 6 shows how many cycles were required to shatter samples 1-11 at least in two pieces during a standardized test (T=950°C).
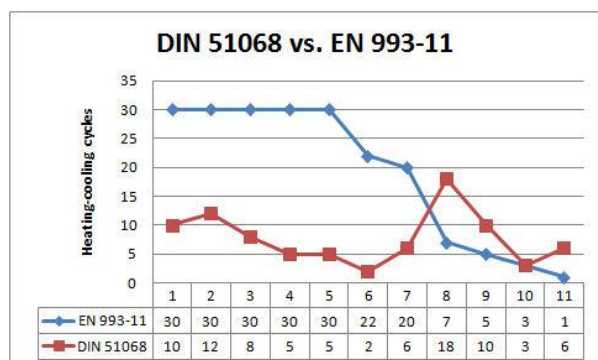
Figure 6. The number of heating-cooling cycles needed to break a soapstone test samples 1-11; thermal shock test with water cooling (DIN 51 068) and with air cooling (EN 993-11).
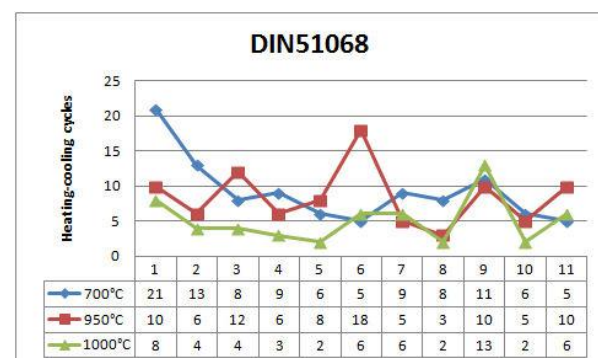
Figure 7. Results of the thermal shock test with water cooling (DIN 51 068) at three temperatures 700°C, 950°C and 1000°C.

The durability of 7 soapstone types was higher in the air cooling (EN 993-11) relative to the water cooling test (DIN 51 068). For 4 soapstone types the durability in water cooling was slightly higher or equal to the air cooling test. Figure 7 shows considerable scatter in the results of the water cooling test, when temperatures 700°C, 950°C and 1000°C were applied. The results correlate with the hypothesis that the testing temperature (expansion-contraction) is not the only parameter affecting the rate of disintegration of natural soapstone.

6 Conclusions

The thermal shock test with water cooling (DIN 51 068) is not showing as clear differences between durable and non durable soapstone types as the test with air cooling (EN 993-11) does. The results of the modified thermal shock test with water cooling with two different temperatures of 700°C and 1000°C suggests that DIN 51 068 test is extremely sensitive to the different textures and structures of the soapstone samples. Reason for this sensitiveness is most likely that the magnesite and dolomite carbonates in soapstone decompose to periclase and calcium oxide at 620-680°C and around 800°C the oxide phases react readily with water forming magnesium and calcium hydroxides. The volume increase associated with the hydroxide formation considerably weakens the structure of the tested soapstone. The test with air cooling (EN 933-11) suites better for thermal shock testing of the soapstone, but neither of the examined testing methods stress the test samples in a similar manner than lining stones experience in furnace interiors and exhaust channel (Fig 4). In summary, as the standardized tests were developed to measure microfracturing phenomena in artificial ceramics, the hydration reactions associated with the water-cooling of the natural soapstone minerals causes erratic results and cannot be reliably applied to the testing of natural soapstone.

References

Slow heat release appliances fired by solid fuel. Requrements and test methods. EN 15 250.
Testing of ceramic raw and basic materials; Determination of resistance to thermal shock; Water quenching method for refractory bricks. DIN 51 068.
Methods of test for dense shaped refractory products. Part 11: Determination of resistance to thermal shock. EN 933-11.
A. Kärki, S.Leinonen, J.U.S. Jokinen and J. Uusitalo: Soapstones - how should they be defined. IGC 33 webpage (2008). http://www.cprm.gov.br/33IGC/1344364.html. Accessed 22 February 2012.

Suitability of natural stone for restoration of monuments: a rock mechanical approach to durability assessment

Richard Přikryl
Institute of Geochemistry, Mineralogy and Mineral Resources, Faculty of Science, Charles University in Prague, Prague, Czech Republic

Abstract
The suitability of a natural stone for use in monuments covers both technical and aesthetic aspects. Among the technical aspects, durability plays an important role. The durability of natural stone is commonly evaluated by different types of indirect laboratory tests that simulate its resistance to certain forces involved in the weathering process (e.g., freeze-thaw cycles, salt crystallization, hygric or thermal dilation). Evaluation of test results by non-destructive methods (e.g., weight loss, porosity change, ultrasonic wave velocity, etc.) is generally insufficient for an understanding of the complexity of material responses to major weathering agents. In the recent study, five different porous natural stones (quartz sandstones) were studied for their rock mechanical behaviours. The results of these tests were compared to the decay patterns obtained during accelerated laboratory durability tests (freeze/thaw cycling, salt crystallization resistance).

Keywords: natural stone, sandstone, rock mechanics, stress-strain behaviour, durability

1 Introduction

Natural stone is the oldest of employed construction materials (Shadmon 1996). Many structures built of natural stone suffer from weathering/decay due to a multitude of reasons (Smith et al. 2008). Large quantities of natural stone are intermittently required for their restoration. The replacement stone must match the original one in both technical aspects (physical and mechanical properties, durability) and in appearance.

Durability can be considered as a measure of resistance of a natural stone against the weathering / decay processes, which develop by multiple interactions between the material and the surrounding environment (Soronis 1992). Durability assessment presents one of the most difficult tasks because durability is not a fundamentally intrinsic property of a material; therefore, it cannot be measured by any single test method.

Durability is commonly evaluated under laboratory conditions by a series of indirect 'durability' tests (Ross and Butlin 1989) that simulate one (or some) of the governing deterioration processes such as freeze-thaw action, hygric expansion, salt crystallization, etc. The results of these accelerated tests on the material's cohesion are then evaluated by measurement of some physical properties including weight loss, velocity of elastic waves, and/or porosity (Goudie 1999; Benavente et al. 2001; Thomachot and Jeannette 2002). The durability of porous natural stone is also explained by complex porosity models based on data from quantitative porosimetric studies, specifically from mercury porosimetry (Rübner and Hoffmann 2006). Other durability assessment techniques include complex environmental testing in test cabinets and/or exposure site testing (Matsukura and Hirose 1999; Taylor-Firth and Laycock 1999). Both of these approaches bring more reliable results, but are less accessible for common testing due both to the experiments' duration and operational costs.

The durability of natural stone can be viewed as its ability to preserve its original shape and worked surface; it must represent the resistance against development of brittle damage phenomena and material retreat due to the formation of microcracks or granular disintegration. Based on this basic assumption, arguably, there must be a link between the durability and mechanical properties. However, this link has not been seriously discussed before, partly due to the lack of appropriate techniques for the evaluation of standard rock mechanical data (specifically, stress-strain behaviour) from the durability point of view. In this recent study, rock mechanical and physical data obtained from standard laboratory tests have been employed for a set of sandstones used as historical natural stone, and which have been designated as potential replacement stones for the repair of decayed ashlars in the stone masonry of the Gothic Charles Bridge in Prague (Czech Republic).

2 Basic concepts of rock mechanical testing

Rock mechanical testing focuses on the problems related to the response of rocks to the applied load including the peak load, at which point the material collapses (Goodman 1989). Rock mechanical properties can be evaluated by different types of loading set-ups (Fig. 1).
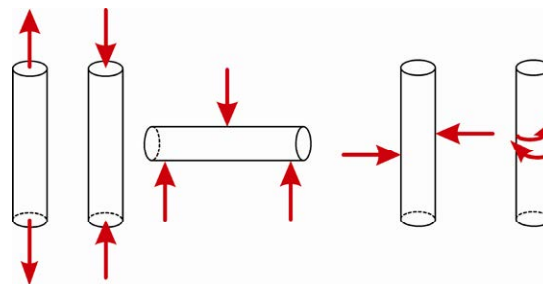

Figure 1. The different loading set-ups employed during laboratory rock mechanical tests (from the left: direct tension, uniaxial compression, bending, shearing, and torsion).

Rocks are heterogeneous solids containing some free space (pores and/or microcracks). These voids can be of a syngenetic nature, but they can also arise from later brittle deformation, weathering/decay, and/or technological process connected with the extraction of the stone. Voids, together with grain boundaries, act as fracture nuclei when being stressed by any external load (including stresses generated by weathering processes). There exists an inverse relationship between the length of a microcrack and the stress damage threshold, as has been both theoretically and experimentally proven.

Common testing of rock mechanical properties (e.g. uniaxial compressive strength) relies upon the gradual increase of a load applied on standard specimens, and on recording the respective stress-strain behaviours, expressed by a stress-strain curve. Four basic stages visible on these curves (Fig. 2) include: (1) non-elastic (non-linear) deformation at low stress (connected with closure of pre-existing microcracks); (2) elastic deformation (linear relationship between stress and strain according to Hooke's law), the slope of this part of stress-strain curve designates the material's stiffness; (3) moderately inelastic deformation at the stable crack growth stage (formation of new microcracks generally formed parallel to the applied load); and (4) apparently plastic deformation during the unstable crack growth stage (marked by dilation of the specimen due to coalescence of previously formed microcracks), which is terminated by the macroscopically visible failure of the specimen. Load at this point is recorded and referred to as the ultimate strength of the material.
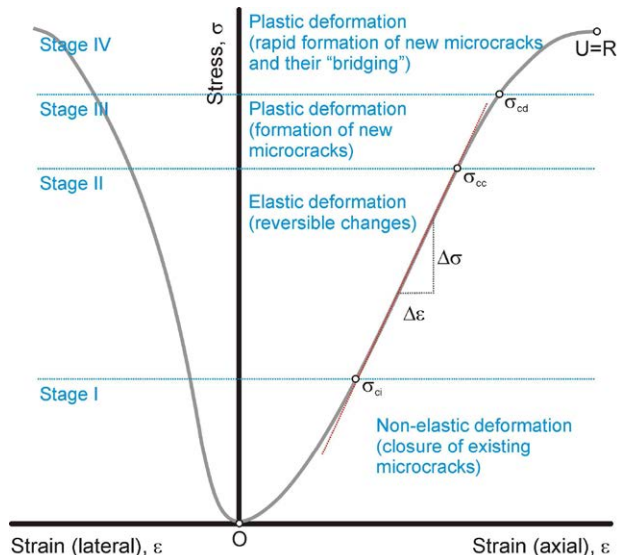
Figure 2. Generalized stress-strain curve for axial and lateral deformation, with four major stages of the material's response to the compressive load applied (for details see text).

Despite the fact that ultimate strength is commonly taken as an arbitrary value in safety considerations, it is highly dependent on other non-intrinsic characteristics of the tested material (load conditions, shape of the specimen, etc.). However, it has been proven experimentally that the turning point between stage III and IV, the so called crack-damage threshold (σ_{cd}), is independent of scale, humidity, and loading rate (Martin 1993). Thus, the stress level at which the cracks begin to spontaneously develop can be taken as a damage initiation criterion.

3 Experimental approach

3.1 Experimental materials

The experimental study was conducted on five types of Upper Cretaceous quartz sandstones sampled in the Bohemian Cretaceous Basin (Czech Republic). The stone types were: Hořice sandstone from the Podhorní Újezd quarry (fine-grained quartz sandstone with a significant amount of clay matrix), Božanov arkosic sandstone (medium-grained sandstone with I/M type clay minerals in the matrix), Kocbeře quartz sandstone (fine- to medium-grained quartz sandstone with two colour varieties – white with a SiO_2-rich cement, and yellow with some clay minerals in the matrix), and Libná glauconite-rich quartz sandstone (fine-grained quartz sandstone with a significant admixture of glauconite and clay minerals in the matrix). The compositional variation among the samples studied can also be seen from their chemical analyses (Tab. 1).

Table 1. Chemical composition of the studied sandstones (adopted from Procházka 1984); (n.d. = not determined, b.d.l. = below detection limit).

	Božanov	Libná	Podhorní Újezd	Kocbeře
SiO_2	94.62	90.78	94.64	97.89
TiO_2	0.05	0.34	0.18	0.03
Al_2O_3	2.84	3.10	2.64	0.75
Fe_2O_3	0.31	2.20	0.71	0.21
FeO	n.d.	0.14	n.d.	n.d.
CaO	0.03	0.24	0.19	0.01
MgO	0.08	0.46	0.15	0.03
MnO	0.004	0.038	n.d.	b.d.l.
Na_2O	0.07	n.d.	0.06	b.d.l.
K_2O	1.44	n.d.	0.24	0.04
P_2O_5	0.03	n.d.	n.d.	b.d.l.
SO_3	b.d.l.	0.02	n.d.	n.d.
CO_2	0.03	0.06	n.d.	b.d.l.
LOI	0.55	1.44	1.08	0.18

For all of the rocks studied, their significant usage in historical monuments is well documented. All of the rocks studied also have recently been exploited and along with others are used in various restoration projects. However, these rocks show a considerable variation of physical and mechanical properties. The same can be stated about their durability, although this aspect is not reflected during selection of an appropriate replacement stone.

3.2 Test program

In the recent study, the results of accelerated durability tests (freeze/thaw cycling, salt crystallization) have been compared to the rock mechanical behaviours (stress-strain curves for uniaxial compression). The accelerated durability tests consisted of the testing of resistance of the studied sandstones against the influence of freezing water and/or of crystallizing salts. For each

rock type, 100 specimens (height of 100 mm, width of 50 mm) were prepared. For each rock type, the specimen batch was split into three sub-sets: for freeze/thaw cycling, for salt crystallization, and for combined freeze/thaw cycling and salt crystallization. For the freeze/thaw test, a portion of the specimens were taken out after the 6th, 12th, 24th, 48th, 72nd, 96th, 120th, and 144th cycle, in order to evaluate changes of certain physical properties (porosity, P-wave velocity, weight, and compressive strength). For salt crystallization, the specimens were subjected to 5, 10, 15, 20, and/or 25 cycles of crystallization of a solution of Na_2SO_4. For the combined action of freeze/thaw and salt crystallization, the number of cycles was 6, 12, 24, and 48 for freeze/thaw, and 5, 10, 15, 20; and/or 25 cycles of salt crystallization.

Prior to the durability tests, the non-destructive testing focused on the determination of basic index (physical) properties such as apparent density, open porosity, water uptake, and P-wave velocity (Tab. 2). For each rock type, a set of 10 specimens were tested for their uniaxial compressive strength.

Table 2. Basic physical properties of the studied sandstones.

	Min	Mean	Max
Božanov sandstone			
apparent density [g/cm³]	2.124	2.177	2.233
open porosity [vol. %]	8.18	10.00	11.33
water uptake [wt. %]	3.66	4.60	5.32
P-wave velocity [m/s]	1551	1998	2383
uniaxial compressive strength [MPa]	50.0	52.3	55.2
Hořice sandstone			
apparent density [g/cm³]	1.921	1.974	2.047
open porosity [vol. %]	12.27	15.31	16.85
water uptake [wt. %]	5.98	7.75	8.73
P-wave velocity [m/s]	2032	2241	2444
uniaxial compressive strength [MPa]	34.6	36.7	39.2
Libná sandstone			
apparent density [g/cm³]	2.199	2.230	2.256
open porosity [vol. %]	8.42	9.12	10.06
water uptake [wt. %]	3.73	4.08	4.55
P-wave velocity [m/s]	1312	2060	2391
uniaxial compressive strength [MPa]	68.5	71.6	74.6
Kocbeře sandstone (white variety)			
apparent density [g/cm³]	2.181	2.222	2.279
open porosity [vol. %]	6.13	7.66	9.97
water uptake [wt. %]	2.69	3.43	3.89
P-wave velocity [m/s]	1875	2251	2772
uniaxial compressive strength [MPa]	83.1	89.0	96.3
Kocbeře sandstone (yellow variety)			
apparent density [g/cm³]	2.169	2.207	2.243
open porosity [vol. %]	7.48	8.48	9.44
water uptake [wt. %]	3.35	3.84	4.34
P-wave velocity [m/s]	1617	2133	2739
uniaxial compressive strength [MPa]	71.9	76.7	80.4

The rock mechanical tests were conducted on intact materials by using another set of cylindrical specimens (height of 100 mm, diameter of 50 mm), loaded at a constant stress rate (0.05 MPa/s), using a common "soft" press. The axial and lateral strains were measured by coupled wire resistance tensometers. The stress-strain curves were plotted, and the corresponding parameters (Young modulus, Poisson ratio) were computed.

4 Results and discussion

4.1 Damage due to the accelerated durability tests

The accelerated durability tests were effective, in terms of evaluating the different responses of the sandstones studied to the principal decay processes. In the case of testing freeze/thaw resistance, three of the studied materials showed the presence of fractures cross-cutting the specimens (Fig. 3). For one specimen (Hořice sandstone) showing the lowest strength, the brittle damage was accompanied with significant material loss.

Figure 3. Studied sandstones after 120 freeze/thaw cycles. Rock types from the left: Hořice sandstone (P), Božanov sandstone (B), white variety of Kocbeře sandstone (K), yellow variety of Kocbeře sandstone (Z), Libná sandstone (L).

By using the combined action of freeze/thaw and salt crystallization, only one rock type (a white variety of Kocbeře sandstone) seems to be durable (Fig. 4), i.e. no obvious decay patterns were observed for this rock type. For the remaining rock varieties, significant material loss was observed due to granular disintegration, spalling, and/or fracturing.

Figure 4. Studied sandstones after 48 freeze/thaw cycles and 20 salt crystallization cycles (same order of specimens as in the previous figure).

4.2 Stress-strain behaviour

There were remarkable differences in the stress-strain behaviours of the studied sandstones (Fig. 5). Both varieties of Kocbeře sandstone showed similar stiffness, the only difference being in the ultimate strength. Libná

sandstone shows a similar slope of the stress-strain curve in the elastic portion (Fig. 5); however, its initial deformation is extremely non-elastic due to its increased porosity and high content of clay minerals. For Božanov, and especially for Hořice sandstone, the stiffness is much lower than for the previously mentioned sandstones. This, together with a lower ultimate strength, contributes to their lower resistance in durability tests.
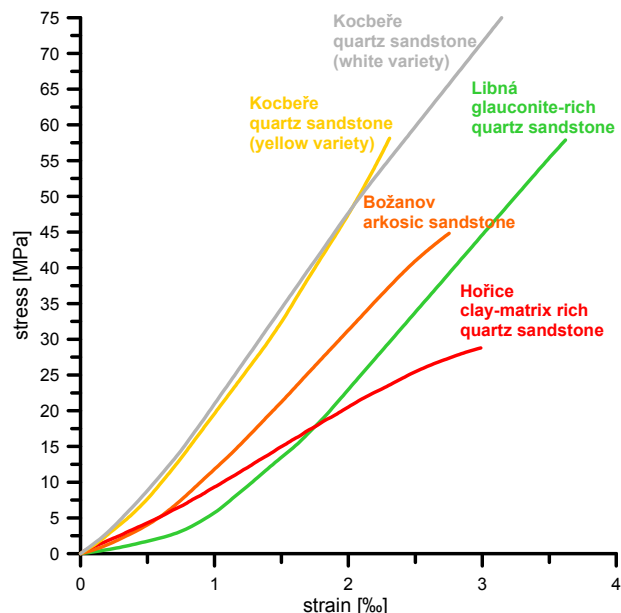

Figure 5. Stress-strain behaviours of the studied sandstones (only axial strain is shown).

4.3 Indirect indicators of durability

The degree of wetting softening (ratio of strength of water-saturated and dry specimens) and the degree of saturation (ratio of water accessible portions of porosity under atmospheric and increased-pressure conditions) seem to be alternative indirect indicators of the durability of porous natural stones. For the studied sandstones, fit into the IA and I classes (Fig. 6) means a satisfactory durability, while I-II (and lower categories) indicates an increasing susceptibility to be damaged by weathering/decay processes.
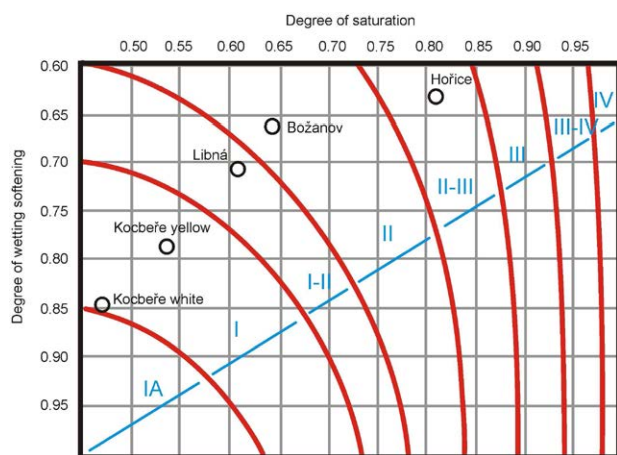
Figure 6. The coefficients of water saturation, and the coefficients of wetting softening of studied sandstones (plot modified after Hirschwald 1908).

4 Conclusions

The analysis of rock mechanical data (stress-strain behaviour) obtained from conventional laboratory tests contributed to an understanding of brittle damage initiation of the tested porous sandstones designated for restoration of monuments. Selected parameters of stress-strain curves combined with indirect indicators (degree of hydraulic weakening, degree of saturation) seem to be effective predictors of durability.

Acknowledgements

References

Benavente D, García del Cura MA, Bernabéu A, Ordóñez S (2001) Quantification of salt weathering in porous stones using an experimental continuous partial immersion method. Eng Geol 59:313–325

Goodman RE (1989) Introduction to rock mechanics. John Wiley & Sons, New York

Goudie A (1999) Experimental salt weathering of limestones in relation to rock properties. Earth Surf Proc Landf 24:715–724

Hirschwald J (1908) Die Prüfung der Natürlichen Bausteine auf ihre Wetterbeständigkeit. Verlag von Wilhelm Ernst & Sohn, Berlin

Martin CD (1993) The strength of massive Lac du Bonnet granite around ground openings. PhD. thesis, University of Manitoba, Winnipeg, Canada

Matsukura Y, Hirose T (1999) Five year measurements of rock tablet weathering on a forested hillslope in a humid environment. Eng Geol 55:69–76

Procházka J (1984) Chemical composition of building sandstones from north-east Bohemia. Výběr prací 12, Geoindustria, Praha, pp 45–60 (In Czech)

Ross KD, Butlin RN (1989) Durability tests for building stone. Building Research Establishment (BRE), Watford

Rübner K, Hoffmann D (2006) Characterization of mineral building materials by mercury-intrusion porosimetry. Part Part Sys Char 23:20–28

Shadmon A (1996) Stone – an introduction. 2nd ed., Intermediate Technology Publications, London

Smith BJ, Gomez-Heras M, McCabe S (2008). Understanding the decay of stone-built cultural heritage. Progr Phys Geogr 32:439–461

Soronis G (1992) The problem of durability in building design. Constr Build Mat 6:205–211

Taylor-Firth A, Laycock EA (1999) Weathering simulation for durability assessment of the in-service performance of construction materials. Q J Eng Geol 32:291–302

Thomachot C, Jeannette D (2002) Evolution of the petrophysical properties of two types of Alsatian sandstone subjected to simulated freeze-thaw conditions. In: Siegesmund S, Weiss T, Vollbrecht A (eds) Natural stone, weathering phenomena, conservation strategies and case studies. Geological Society, London, Special Publications, 205, pp 19–32

Factors affecting ASR potential of quartzite from a single quarry (Bohemian Massif, Czech Republic)

Šárka Šachlová, Aneta Šťastná, Richard Přikryl, Zdeněk Pertold & Zuzana Nekvasilová
Charles University in Prague, Faculty of Science, Albertov 6, 128 43, Prague 2, Czech Republic

Abstract. The alkali-silica reaction (ASR) originates under highly alkaline conditions in concrete, where reactive forms of SiO_2 react with hydroxyl ions and alkalis, forming alkali-silica gels. Alkali-silica gels tend to absorb water molecules and expand causing deterioration of the concrete. Quartz, a dominant component of aggregates used in concrete, exhibits variable potentials to cause ASR. This paper aims to quantify the ASR potential of quartzite aggregate sampled from the Těchobuz quarry (Moldanubian Zone, Bohemian Massif, Czech Republic). Various macroscopic and microscopic techniques (image analysis, polarising and electron microscopy, cathodoluminescence) were employed and combined with the accelerated mortar bar test. Slight variations were found in the ASR potentials of aggregates crushed by different laboratory crushers. Parameters such as particle shape and specific surface were suggested to be responsible for these variations in the ASR potential. A higher ASR potential was measured in the case of sample Nos. A2 and B2, crushed employing a Retsch BB3A jaw crusher (1970). In contrast, sample Nos. A1 and B1, crushed with a MEZ Mohelnice AP100L/4S/1 jaw crusher (1968), showed a lower ASR potential. Particle shape analysis did not indicate any differences when comparing aggregates crushed by different crushers. The same conclusions were found when comparing the specific surface values. Some explanation could be seen in the different mineral compositions and microstructures of the samples investigated (quartz content, quartz deformation).

Keywords. Particle shape, quartzite, alkali-silica reaction, accelerated mortar bar test, microscopy

1 Introduction

High alkaline conditions, sufficient humidity, and the presence of reactive SiO_2-rich phases are the main factors causing the alkali-silica reaction (ASR). Formation of alkali-silica gels and their expandability lead to the formation of cracks and decrease the durability of concrete constructions (e.g. St John et al. 1998). Many methods have been proposed in the last few decades in order to assess how the components of aggregates and concrete mixtures are prone to the formation of ASR. A combination of microscopic methods (polarising and electron microscopy) and expansion tests seem to be the most effective (mortar-bar test, e.g. Haha et al. 2007; Çopuroğlu et al. 2008).

Quartzite is well known due to its variable ASR potential. Recent studies indicated various factors to be responsible, e.g. quartz deformation (Locati et al. 2010), for quartz grain size (del Amo and Perez; 2001) or the presence of a quartz-feldspar-mica interface (Hagelia and Fernandes, 2012). In the Czech Republic, quartzite aggregates were found forming minor components of coarse and fine aggregates in concrete (Lukschová et al. 2009; Šachlová et al. 2011). Quartzite from Těchobuz quarry was investigated with the aim to quantify its ASR potential, employing the accelerated mortar bar test. The influence of particle size and particle shape parameters on ASR was verified employing image analysis and microscopic techniques (polarising, cathodoluminescence, and electron microscopy).

2 Experimental

2.1 Samples

A recent experimental study was performed by using quartzite samples coming from the Těchobuz quarry (Moldanubian Zone, Bohemian Massif, Czech Republic). The sampling consisted of two blocks of quartzite (A and B) indicating similar macroscopic characteristics: grey colour, massif structure, small grain size, low amounts of mafic minerals. Both samples were crushed employing the following laboratory equipment: Retsch BB3A jaw crusher (1970) and MEZ Mohelnice AP100L/4S/1 jaw crusher (1968), both with a drive power of 3 kW.

2.2 Accelerated mortar bar test

The accelerated mortar bar test (following the standard ASTM C1260) was used with the aim to quantify the ASR potential of aggregates. The 0.125/5 mm fraction was used. Four different mortar bar specimens were prepared from each sample and tested in 1M NaOH solution at 80°C. Expansion of mortar bar specimens was measured for the fourteen day test period.

2.3 Particle shape analysis

Particle shape analysis was based on image analysis of macroimages of aggregate particles (2/4 mm fraction). The system of image analysis employed in this study consisted of manual particle preparation and image pre-processing, computer assisted image analysis, and data evaluation. Manual particle preparation involves the fixation of particles on the solid plate (orientation of particles according to *a*-major, *b*-minor, resp. *c* axis must be kept). Two macroimages are taken for each particle: macroimage of *a/b* axis and *a/c* axis. Image pre-processing involves: capturing of the image by means of digital photography, and image modification using graphic software with a final image resolution of 300 dpi (Corel Draw v. 12.0). The image modification is a crucial point in the image pre-processing, because the software used (SigmaScan®Pro, v. 5.0.0 by SPSS Inc.) requires a binary image in which the object is differentiated from the background based on the

intensity along a grey scale. This means that the object must either be "lighter" or "darker" than the background. The analysis of multiphase materials requires measurement of an appropriate number of objects, which ranges from 80 to 100 per sample. Using SIGMASCAN Pro software, the image measurement is performed by a feature-specific approach (i.e. fill measurement). In practice, the objects are measured separately. After the measurement, each object is filled with a contrasting colour, in order to avoid multiple analyses of a grain already measured. Finally, the data obtained are analysed using any type of statistical software. The following parameters were determined: equivalent diameter; length of principal axes; area; perimeter; compactness; shape factor; aspect ratio; and specific surface (see Table 1). More details concerning image preparation and analysis can be found elsewhere (e.g. Přikryl 2006).

Table 1. Definitions of fabric parameters measured using image analysis.

Fabric parameter	Units	Definition and references
Equivalent diameter	mm	diameter of circle, which has the same area as measured object; Equivalent diameter = $(4 \times area/\pi)^{1/2}$ (Petruk 1986)
Area	mm^2	area reports the area for the selected object (Systat Software Inc. 2010)
Perimeter	mm	the length of object boundary (Systat Software Inc. 2010)
Major (minor) axis length	mm	length between the two most distant points on the object (major) or between two most distant points on the object that creates a line perpendicular to the major axis (minor) (Přikryl 2006)
Compactness	-	shape of the object cross-section; Compactness = perimeter^2/area (Přikryl 2006)
Shape factor	-	shape factor indicates circularity of investigated object; Shape factor = $4 \times \pi \times area / perimeter^2$ (Howarth and Rowlands 1987)
Aspect ratio	-	calculated as ratio of major and minor axis lengths (Přikryl 2006)
Specific surface	mm^{-1}	calculated from perimeter divided by area (del Amo and Perez 2001)

2.4 Microscopic techniques

Microscopic investigation of the samples consisted of polarising microscopy (PM), cathodoluminescence (CL), and scanning electron microscopy with an energy dispersive spectrometer (SEM-EDS). Uncovered polished thin sections prepared from rock samples were used. PM and CL microscopy were performed in the Laboratory of microscopic techniques (Charles University in Prague). For CL studies, CCl 8200 Mk4 cold cathodoluminescence equipment, coupled with a LEICA DMLP optical microscope, was employed. The electron energy applied to the thin sections was 15 - 18 kV, and the beam current was operated at 300 μA.

The luminescence colours of each lithotype were photographed with a Canon digital camera. SEM-EDS was conducted at the Laboratory of Electron Microscopy and Microanalysis (Charles University in Prague). The thin sections were coated in a carbon atmosphere. The measurements were performed on a Tescan Vega instrument, with an energy-dispersive analytical system (Oxford Instruments LINK ISIS 300) under the following conditions: 0.8 nA; 180 s counting time; and a 20 - 30 kV accelerating voltage. A 53 Minerals Standard Set #02753-AB (SPI Supplies) was used for the standard quantitative calibration.

3 Results

3.1 ASR potential

A higher ASR potential, indicated expansion of the mortar bars ranging from 0.19% to 0.22%, was measured in the case of sample Nos. B2 and A2, respectively (both crushed employing Retsch BB3A jaw crusher) (Fig. 1). In contrast, sample Nos. B1 and A1 displayed a lower ASR potential, with expansion around 0.13% (both crushed by MEZ Mohelnice AP100L/4S/1 jaw crusher) (Fig. 1). The studied samples exhibited an expansion above 0.1%, and thus are classified as reactive. Sample Nos. A1 and A2 showed slightly increased expansion values in comparison to sample Nos. B1 and B2 (Fig. 1).
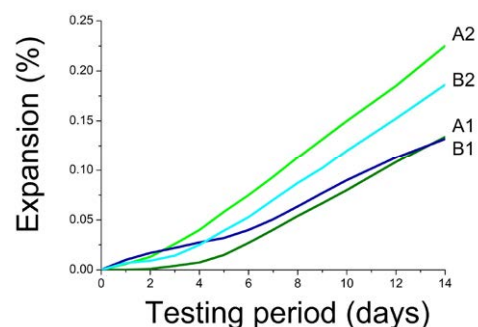
Figure 1. Expansion curves of mortar bars.

3.2 Particle shape parameters

Image analysis provided the required quantification of various fabric parameters (Table 1) of aggregate particles to allow a juxtaposition of shape characteristics with different jaw crushers, as well as with two quartzite blocks (A and B) (Table 2).

The mean aggregate size, represented by the equivalent diameter (Petruk 1986), was revealed not to be a discriminating fabric parameter, with regard to the different jaw crushers. Considering the aggregate particle shape and size (parameters as equivalent diameter, area, perimeter, and specific surface), there is an evident similarity of sample Nos. A1 and B2, as well as Nos. A2 and B1 (Table 2). Moreover, the compactness, the shape factor, and the aspect ratio which describes circularity and ellipticity of an aggregate particle cross-section also gave similar results for different jaw crushers. A slightly higher value of the compactness and the aspect ratio, as

well as a lower value of the shape factor was displayed by sample No. B1 (see Table 2). The distinguishing effect of the specific surface related to the perimeter and area data was also not completely confirmed (Table 2). Samples that exhibit different expansion curves (Fig. 1) displayed similar lengths of the major (a), minor (b) and c axis, in different jaw crushers from one quartzite quarry (Fig. 2).

Table 2. Image analysis of studied aggregate particles. The fabric parameters are shown as mean values.

		A1	**A2**	**B1**	**B2**
Equivalent diameter (mm)	a/b	4.64	4.39	4.43	4.71
	a/c	4.03	3.76	3.55	3.96
Area (mm²)	a/b	17.29	15.49	15.83	17.89
	a/c	13.05	11.45	10.31	12.69
Perimeter (mm)	a/b	16.71	15.60	16.07	16.74
	a/c	15.22	14.19	14.05	14.79
Compactness	a/b	16.52	16.11	16.72	16.03
	a/c	18.26	18.25	20.75	17.83
Shape factor	a/b	0.77	0.78	0.76	0.79
	a/c	0.70	0.70	0.65	0.72
Aspect ratio	a/b	1.46	1.45	1.53	1.37
	a/c	1.95	2.07	2.45	1.89
Specific surface (mm⁻¹)	a/b	1.01	1.06	1.07	0.98
	a/c	1.22	1.32	1.52	1.23

Figure 2. Statistical evaluation of the major (a), minor (b) and c axis length of aggregate particles with different jaw crushers (A1, B1 vs. A2, B2). The colour-framed box bars show 25% (bottom) and 75% (top). The ends of the lower and upper whistlers represent the minimum and maximum values, respectively.
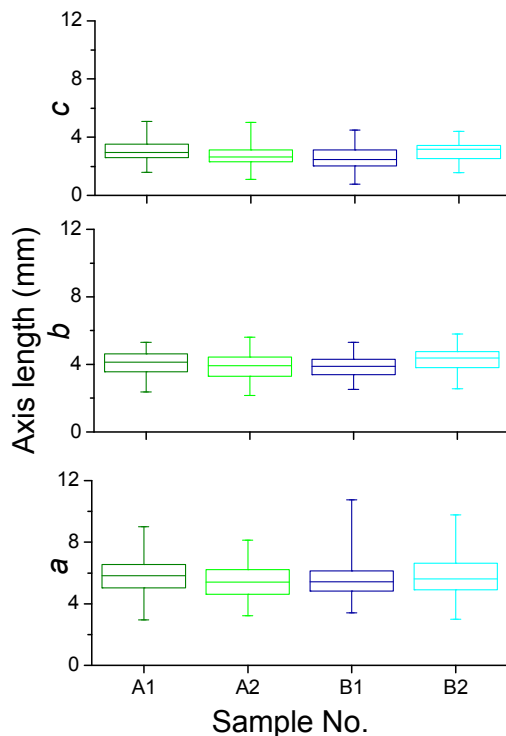
4 Discussion

4.1 Influence of particle shape parameters on ASR potential

No correlation was found comparing expansion values with particle shape parameters. Sample Nos. A2 and B2 exhibit higher expansion values compared to sample Nos. A1 and B1. In contrast, particle size and particle shape parameters of sample No. A2 are comparable to sample No. B1; and the particle size and particle shape parameters of sample No. B2 are comparable to sample No. A1.

4.2 Other parameters responsible for ASR

The investigated samples were subjected to microscopic analysis with the aim to find other parameters responsible for variable ASR potential. All investigated samples were classified as medium-grained plagioclase quartzite. They are typical of quartz + Ca-plagioclase (andesine, labradorite, and anortite) + K-feldspar + biotite + chlorite + diopside + pyrite + apatite + titanite ± calcite. All samples show more than 80 vol% of quartz and 10 vol% of feldspars. The mean quartz grain size was measured as 0.1 - 0.2 mm.

Differences were found to be connected to: (1) quartz deformation and recrystallization, (2) feldspar alteration, and (3) mica microstructure. Sample No. A2 is typical of quartz with undulose and patchy extinction, formation of quartz subgrains, strong alteration of plagioclase, and the presence of flaky-like mica grains. Plagioclase alteration (sericitization) is quite visible on the grain boundaries or the whole grains (Fig. 3). All features mentioned above are less common in sample No. B2, and relatively rare in sample Nos. A1 and B1.

Undulose extinction, patchy extinction, and formation of quartz subgrains are deformation characteristics, increasing dislocation density of quartz and increasing quartz ASR potential (e.g. Locati et al. 2010).

Presence of feldspars and their alteration are factors frequently discussed in connection to ASR due to the release of alkalis (e.g. Bérubé et al. 2002; Constantiner and Diamond 2003). High alkaline conditions and relative humidity can facilitate the solubility of feldspars, release of alkalis from feldspars into pore solution in mortar bars, and increase the ASR potential of aggregates. Alteration products (sericite) and mica minerals can increase the porosity and specific surface of aggregates. Mica particles also act as pathways of pore solution, as well as weak planes through which the internal stress caused by gel expansion can dissipate. The planes can propagate into microcracks and cracks (Ponce and Batic 2006).

5 Conclusions

The ASR potential of medium grained plagioclase quartzite, quantified employing the accelerated mortar bar test, indicated slight differences, comparing the investigated samples. Application of different jaw
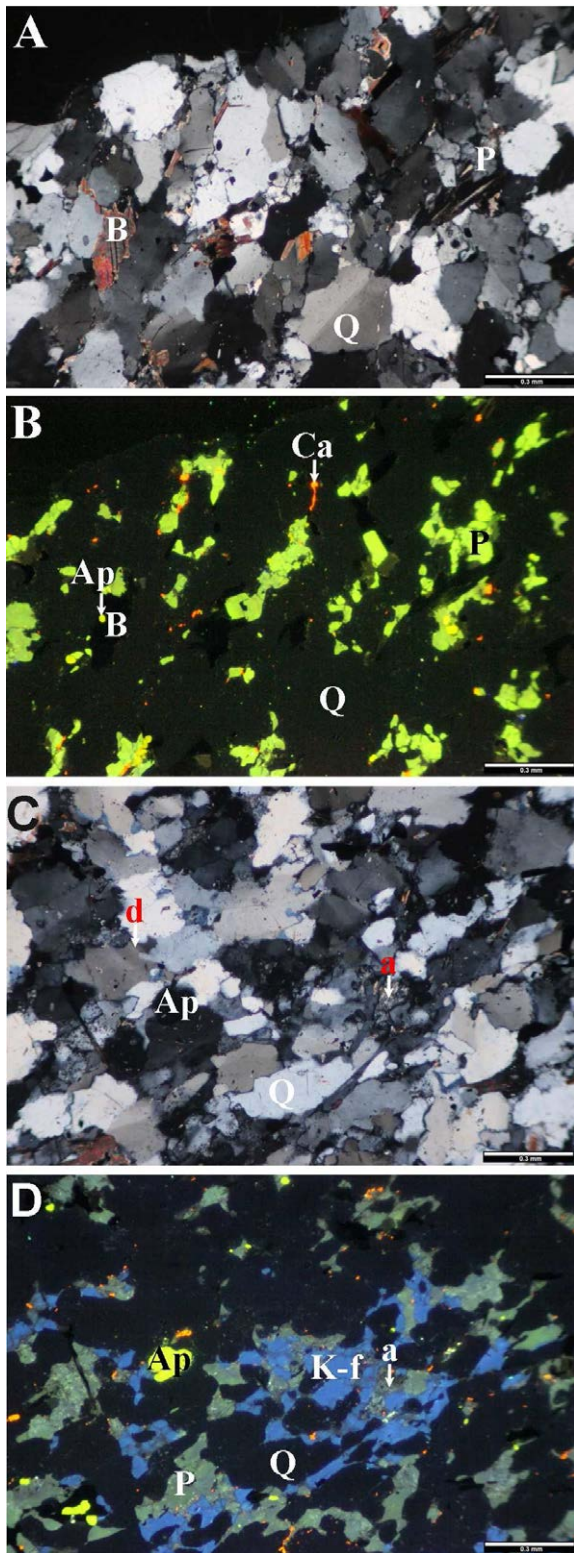
Figure 3. Microscopic images (in cross-polarized light: A, C and under CL: B, D) of sample Nos. A1 (A, B) and A2 (C, D) which were crushed with different jaw crushers. Mineral phases and changes: a - alteration of feldspars; Ap - apatite; B - biotite; Ca - calcite; D - quartz deformation (undulose and patchy extinction); K-f - K-feldspar; P - plagioclase (labradorite An_{63}); Q - quartz.

crushers was suggested to be responsible for these differences. This suggestion was not confirmed due to the almost identical particle size and particle shape parameters of the investigated samples. Differences were found in the mineral composition and microstructure.

Quartz deformation, plagioclase alteration, and presence of flaky-like mica particles are characteristics typical to those samples indicating the highest ASR potentials; they are less common in the samples with a low ASR potential. All of these characteristics can increase the ASR potential of plagioclase quartzite.

Acknowledgements

References

ASTM C1260-07 (2011) Test method for potential alkali reactivity of aggregates (Mortar-bar method). ASTM, West Conshohocken, 04.02.

del Amo DG, Perez BC (2001) Diagnosis of the alkali-silica reactivity potential by means of digital image analysis of aggregate thin sections. Cem Concr Res 31(10):1449-1454

Bérubé M-A, Duchesne J, Dorion JF, Rivest M (2002) Laboratory assessment of alkali contribution by aggregates to concrete and application to concrete structures affected by alkali–silica reactivity. Cem Concr Res 32:1215-1227

Constantiner D, Diamond S (2003) Alkali release from feldspars into pore solutions. Cem Concr Res 33:549-554

Çopuroğlu O, Schlangen E, Andiç-Çakır Ö, Garcia-Diaz E (2008) Effect of silica dissolution on mechanical properties of alkali-reactive basalt. In: Broekmans MATM, Vigum BJ (eds) Proceedings of 13th ICAAR, Trondheim, Norway, pp 574-583

Haha MB, Gallucci E, Guidoum A, Scrivener KL (2007) Relation of expansion due to alkali silica reaction to the degree of reaction measured by SEM image analysis. Cem Concr Res 37:1206-1214

Hagelia P, Fernandes I (2012) On the AAR susceptibility of granitic and quartzitic aggregates. Proceedings of 14th ICAAR, Austin, Texas, 030811-HAGE

Howarth DF, Rowlands JC (1987) Quantitative assessment of rock texture and correlation with drillability and strength properties. Rock Mech Rock Eng 20:57-85

Locati F, Marfil S, Baldo E (2010) Effect of ductile deformation of quartz-bearing rocks on the alkali-silica reaction. Eng Geol 116:117-128

Lukschová Š, Přikryl R, Pertold Z (2009) Petrographic identification of alkali-silica reactive aggregates in concrete from 20th century bridges. Constr Build Mater 23(2):734-741

Petruk W (1986) Image analysis: an overview of developments, CANMET Report 86-4E, pp 1-5

Ponce JM, Batic OR (2006) Different manifestations of the alkali-silica reaction in concrete according to the reaction kinetics of the reactive aggregate. Cem Concr Res 36:1148-1156

Přikryl R (2006) Assessment of rock geomechanical quality by quantitative rock fabric coefficients: Limitation and possible source of misinterpretations. Eng Geol 87:149-162

Ramyar K, Topal A, Andic Ö (2005) Effects of aggregate size and angularity on alkali–silica reaction. Cem Concr Res 35:2165-2169

SPSS Inc. (2010) SigmaScan®Pro 5.0.0. http://www.sigmaplot.com/index.php. Accessed 22 February 2013

St John DA, Poole AB, Sims I (1998) Concrete petrography. A handbook of investigative techniques. Arnold, London

Šachlová Š, Burdová A, Pertold Z, Přikryl R (2011) Macro- and micro-indicators of ASR in concrete pavement. Mag Concr Res 63(8):553-571

The relationship between dry rheology and particle shape of natural and manufactured sand

Rebecka Stomvall, Johannes Quist, Magnus Evertsson
Chalmers University of Technology

Ramin Lindqvist
Gammadata Finland Oy

Abstract

Understanding the effect of particle shape on dry rheology is considered to be an important aspect in order to replace natural sand used in concrete with man-made manufactured sand. There is a significant difference in particle shape and surface texture between crushed rock material (aggregates) and natural sand. The crushed aggregates are normally less rounded and have less equally shaped dimensions compared to natural sand. Thus, the flow ability of the concrete will be different. The main difference is explained by a difference in the wet rheology of the cement paste which in turn is affected by the smallest particles in the size range from microns to a few millimetres. In previous research, it has been demonstrated how different crushing techniques affects the shape of the produced particles. In many cases it is believed that Vertical Shaft Impact (VSI) -technology is the way forward to replace natural sand.

The aim of this paper is to investigate the relationship between dry rheology measured with the so called flow cone and particle shape parameters measured with an optical image analyser technique.

Keywords: Dry rheology, Optical image analysis, Particle shape, Manufactured sand, Natural sand.

1 Introduction

Natural sand has traditionally been used in concrete and for many other applications. In the Swedish environmental goals it is stated that the use of natural gravel should be reduced due to protection of the groundwater resources. To replace natural sand with manmade sand in concrete the shape of the individual particles in the aggregates is very critical. It has previously been proven that Vertical Shaft Impact crushing significantly improves the shape of aggregates compared to crushed materials from compressive crushers (Bengtsson, 2009), see Figure 1. The shape of the larger particles (i.e. 5-16mm) is in general considered to be sufficient for concrete production whilst the smaller fractions (i.e. 63-500 micron) still need attention as these particles have an direct impact on the properties of the cement past and in turn the flow ability of concrete in the wet state.
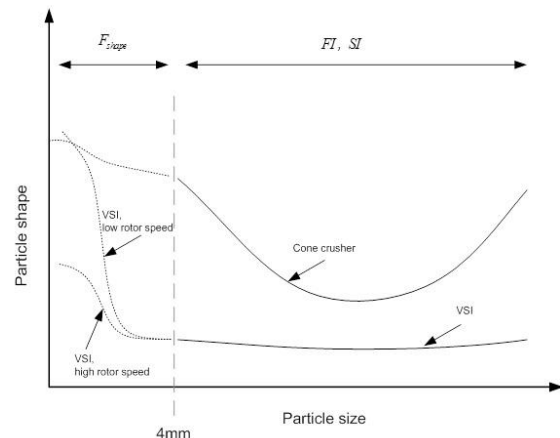
Figure 1 The effect of cone and VSI crushing on particle shape at different particle size. (Bengtsson, 2009)

Further studies are needed to determine how impact (VSI) crushing affects the particle shape of aggregates below 4 mm. In such studies it is important to have sufficient methods to analyze and understand particle shape. The so called "flow cone" is a method from New Zealand which determines the dry rheology properties of sands by monitoring the mass flow through a defined nozzle. The dependence between particle shape and the mass flow rate in the flow cone has been proven in an earlier investigation (Bengtsson et al., 2006). To be able to fully understand the impact that different crushing techniques have on the particle shape a more advanced method is needed in addition to the flow cone. Optical tools to analyze the aggregates would make it possible to study a large amount of particles at small fractions. The determination of particle shape of aggregates is challenging since the shape is highly irregular and the size span of particles are very large. Camsizer is one of the latest developed optical tools for digital imaging determination of shape and size distribution.

2 Methods

In this study flow cone tests and particle shape measurements with Camsizer XT are performed with natural sands and VSI crushed material to investigate how well the two methods correlate.

2.1 Flow Cone

The flow cone was originally proposed by Cleland (1968) as a test method for determining the flow ability of sand materials in concrete. An example of a flow cone can be seen in figure 2. The conceptual idea behind the flow cone is that the dry rheological behaviour can be related to the particle size, shape and surface characteristics of a sand material. Further on, if the dry rheological behaviour is decent the material is probably a suitable material for concrete. In the test the sand material is placed in the flow cone while keeping the discharge closed. The mass flow rate through the funnel can then be recorded by measuring the sample mass and flow time. The European standard EN 933-6 describes this procedure in detail. In the standard it is stated that the 63-2000 µm fraction should be tested. If the 0-63 µm is still present in the sample the flow behaviour is unpredictable and difficult to measure.

Figure 2
The Flow cone

In the European standards it is only proposed to measure the mass flow rate for the full 63-2000 µm fraction. However, by analysing individual size fractions the dry rheological behaviour can be captured for each size class (Beverloo et. al, 1961). It was discovered by Quist and Evertsson (2010) that the manual measurement technique used for measuring the flow time is not statistically adequate when measuring individual fractions since the sample mass is less than in the standard test for the full fraction test. In the standard test the sample mass is 1000 grams which is not a practical amount to produce in each size class by conventional laboratory sieving techniques.

In figure 3 and 4 the results from a further developed method for the flow cone can be seen.

$$y = 28{,}011x - 35{,}652$$
$$R^2 = 0{,}9941$$
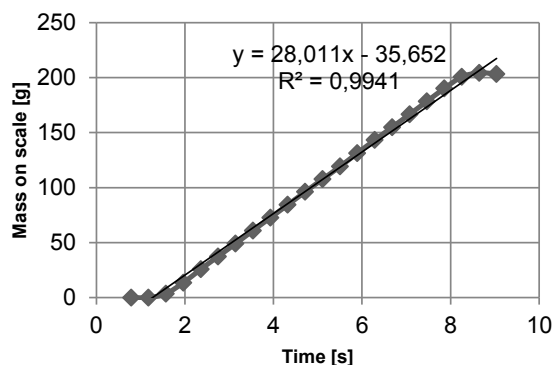
Figure 3: Linearization before removing the boundary effects.

$$y = 29{,}853x - 44{,}773$$
$$R^2 = 1$$
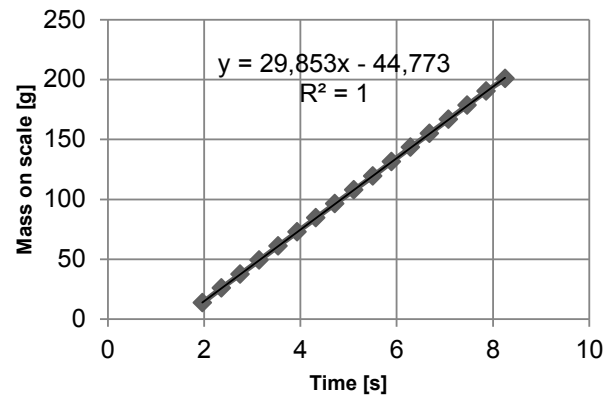
Figure 4: Linearization after removing the boundary effects.

By using a digital laboratory scale coupled to PC interface the mass flow rate can be determined as the derivative of the cumulative mass on the scale over time (Quist and Evertsson, 2010). This approach eliminates both the variation due to manual error as well as the boundary effects in the beginning and end of the test. In figure 3 and 4 the results of the linearization before and after removing the boundary effects can be seen.

2.2 Optical Tool

Retsch Technology manufactures two different products for dynamic imaging analyses; Camsizer with the size range 30µm-30mm and Camsizer XT with the size range 1µm-3mm. Both models have a two camera system, the basic and the zoom camera, see figure 5. The basic camera takes pictures of a large amount of particles and the shape of the larger particles are determined from these pictures. The zoom camera takes pictures with higher resolution, but the frame includes a smaller amount of particles. The pictures from the zoom camera are used to determine the shape of the small particles.

Aspect Ratio
$$b/l = \frac{x_{c\,min}}{x_{Fe\,max}}$$

Sphericity
$$SPHT = \frac{4\pi A}{p^2}$$

Symmetry
$$Symm = \frac{1}{2}\left(1 + \min\left(\frac{r_1}{r_2}\right)\right)$$

Figure 5 Principle of Camsizer and Camsizer XT. The basic camera (red) takes a larger picture on a large amount of particles. At the same time the zoom camera (blue) takes a smaller picture with higher resolution. The definitions are of the parameters used in the study. (Westermann, 2013)

The particles pass the cameras in free fall. In the Camsizer XT it is also possible to use pressurized air for fine and agglomerated particles. In this study a Camsizer XT has been used, see figure 6.

The software uses image analysis to determine size and particle shape, a number of different definitions for shape is available. In this study, three different shape parameters has been used for the Camsizer XT; *b/l*, *SPHT* and *Symm*. The definitions of these parameters can be seen in figure 5. The parameter *b/l* is commonly known as aspect ratio or F-shape. The parameter denotation *SPHT* stands for sphericity, a perfect sphere has the value 1. The denotation *Symm* stands for symmetry, an asymmetric particle has a value below 1.

Figure 6 The Camsizer XT

3   Results

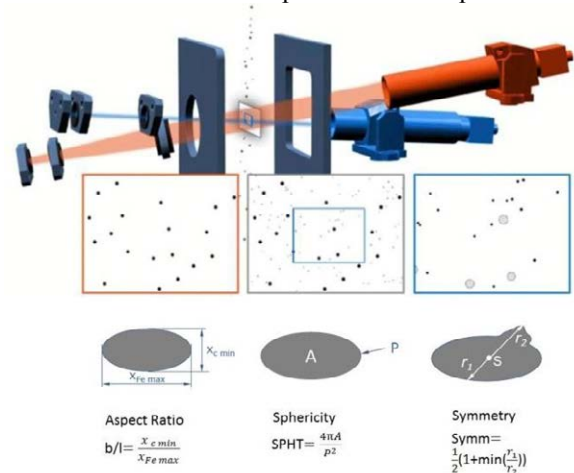In figure 7-9 the dependency between the dry rheology and the Camsizer parameters can be seen. The dry rheology is expressed in mass flow rate and was tested with the flow cone. The natural and manmade sands have been screened into three different fractions, 125-250 µm, 250-500 µm and 500-1000 µm. For each fraction a linear relationship between the Camsizer parameters and the results from the flow cone test is indicated.
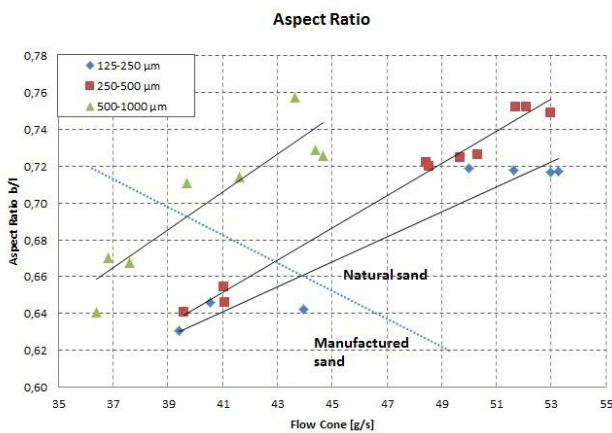
Figure 7 The relationship between dry rheology and aspect ratio
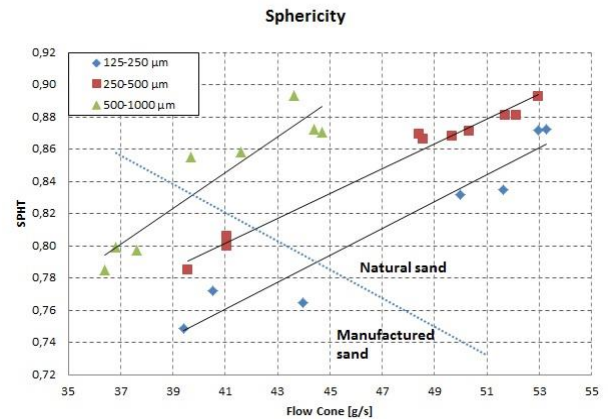
Figure 8 The relationship between dry rheology and sphericity.
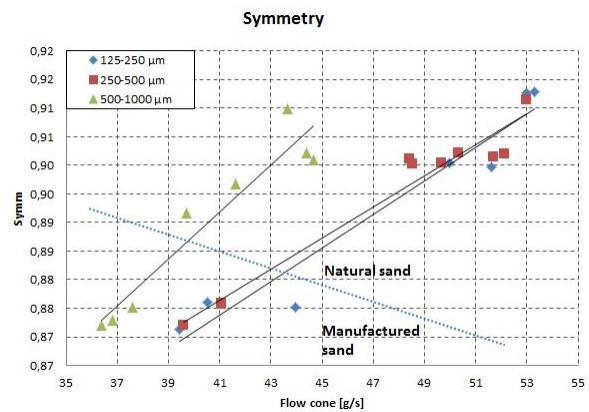
Figure 9 The relationship between dry rheology and symmetry.

4 Conclusions

The study has proven a good correlation between the results of the flow cone and the Camsizer parameters. The flow cone is a widely used method within the aggregate industry, the correlation between the results shows that the two methods can be used to complement each other. The flow cone is a fast method that can be easily used in the production sites to get a first indication of the particle shape. The optical analyser can then be used to get further knowledge about the material with more parameters. More studies are needed to determine the optimal way to use Camsizer to analyse different aggregates and fractions. Though, the good correlation with the results of the flow cone shows very good potential.

From the graphs showing the relationship between the optically retrieved parameters and the mass flow it is obvious that the correlation is good, but there is still a noticeable gap between the manufactured and the natural sand. The potential of further improving the particle shape and the dry rheology is currently explored in a Swedish VINNOVA project.

References

Bengtsson, M. (2009). Quality-Driven Production of Aggregates in Crushing Plants. Dep. Product and production Development. PhD Gothenburg, Sweden, Chalmers University of Technology.

Bengtsson, M., Evertsson, C. Magnus (2006). "Measuring characteristics of aggregate material from vertical shaft impact crushers." Minerals Engineering 19: 1479-1486.

Beverloo, W.A., Leniger, H.A., van de Velde, J., 1961, "The flow of granular solids through orifices", Chemical Engineering Science 15 (3-4), 260-269.

Cleland, J. (1968) Sand for Concrete – a new test method, New Zealand Standards Bulletin, 14, October

EN 933-6 (2001) Tests for geometrical properties of aggregates – Part 6: Assessment of surface characteristics – Flow coefficient of aggregates

Quist, J. Evertsson, M. (2010) Slutrapport – 1.4.1 Krossteknik för produktion av fina ballastfraktioner till betong, Chalmers Tekniska Högskola, MinBas, MinFo

Westermann, J., 2013, "Building Materials- Size and shape analysis for improved product performance", Haan, Application Note Retsch Technology

Possible green building materials using bioenzymatic calcite precipitation

Piero Tiano, Oana Adriana Cuzman, Emma Cantisani, Silvia Rescic, Irene Malesci
CNR – ICVBC, (Florence IT)

Abstract. Microbial induced carbonate precipitation is a promising biotechnological application for producing new environmentally friendly building materials. The system uses the capacity of urease production by ureolytic bacterial microorganisms *Sporosarcina pasteurii* and the waste from cement and building industry in order to obtain a new compound that can be used to create new artificial bricks, or to consolidate soils and earth made constructions (adobe).

The objective is to develop a suitable economical and ecological way for large-scale production of these kind of new construction material. The best rate of bacterial carbonatogenesis performance in the presence of different types of solid wastes was investigated. The quality of these preliminary end-user products are evaluated as a function of the type and nature of the original solid waste, such as the Cement Kiln Dust (CKD).

Keywords.
Microbial Calcite Precipitation, *Sporosarcina pasteurii*, Biocementation, Urease Activity, CKD waste.

1 Introduction

Approximately 5 % of global carbon emissions originate from the manufacturing of cement. According to the International Energy Agency's (IEA) Greenhouse Gas R&D Programme cement production generates an average world carbon emission of 0.81 kg CO_2 per kg cement produced. Despite significant improvements in efficiency, cement related emissions are expected to increase by 260 % throughout the 1990-2050 period. Moreover, the continued growth of key world economies results in an increasing demand for construction materials and, specifically, for cement.

As a consequence, the global production of cement in 2030 is projected to grow to a level roughly five times higher than its level in 1990, with close to 5 billion tonnes worldwide. Taking into account the carbon emission per kg cement produced, the emissions of the global cement sector alone are very likely to surpass the total amount of CO_2 emissions of the EU before 2030.

Industrial wastes, causing environmental and economic harm, are now a global concern. Industries are rapidly trying to find a solution, searching for optimal ways to manage waste and to change the most common practices as landfill or incineration. Industrial waste is very heavy burden for the environment, where a significant proportion of this industrial waste is attributable to construction and demolition waste.

In order to mitigate the threats mentioned above (greenhouse gas emissions and waste management) an European co-funded project (ECO-CEMENT) will allow recovering valuable resources from industry and transforming these into ecological cement that can be use in construction or novel environmental applications.

The idea is based on the nature's way of creating natural formations through bacterial contribution to carbonate precipitation (Tiano et al. 2006). The controlled biological formation of $CaCO_3$ is based on the decomposition of urea to carbonate and ammonium ions by the catalytic action of the urease enzyme produced in situ by a bacterium with urease activity. As source of calcium ions is foreseen to use a waste product of the cement industry, the Cement Kiln Dust (CKD).

2 Material and Methods

2.1 Microbial growth conditions

The bacterial strain *Sporosarcina pasteurii* has been selected as the most suitable microbial source for the cementation trials, it has demonstrated a high level of enzyme activity and to be tolerant to high concentrations of calcium and ammonium. It has been cultivated in an organic medium enriched with urea[1]. The culture medium was therefore inoculated with *S. pasteurii* inoculum (1.3 x 10^9 CFU/ml) and let to grow overnight at 30°C under continuously and horizontally shaking (130 rpm). The bacteria growth was checked using the following methods: optical density at 600nm (OD_{600}), plate counts and dry weight, while the bacterial urease activity was checked by Nessler assay method.

The bio-chemical process involved is :

i) $CO(NH_2)_2 \text{ (Urea)} + 2H_2O \xrightarrow{\text{Urease}} 2NH_4^+ + CO_3^{2-}$

ii) $Ca^{2+} + CO_3^{2-} \longrightarrow CaCO_3 \downarrow$
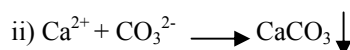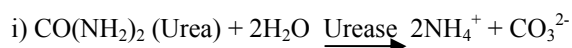
In order to optimize the process in field conditions the urease positive organism must be able to growth and maintain its activity also in not sterile environments.

The bacterial calcite precipitation was checked using the calcein (10 mg/L), a fluorescent dye able to binding the calcite of new formation.

2.2 Waste and biocalcite characterization

Powder of different types of wastes and biocalcite were analysed with a PANalytical diffractometer X'Pert PRO

---

with radiation CuK $_{\alpha 1}$= 1,545Å, operating at 40 KV, 30 mA, investigated range 2 Θ 3-90°, equipped with X' Celerator multirevelatory and High Score data acquisition and interpretation software.

The chemical composition of the waste samples and the precipitated biocalcite were analysed using a Philips PW 1480 XRF spectrometer.

3 Results and discussions

3.1 Bacterial activity and calcite production

The OD_{600}, dry weight and CFU/ml of the bacterial broth progressively increase for almost 16 h from inoculation.

Good correlation in time between cells concentration and urease activity, was determined with Nessler assay (Fig 1).
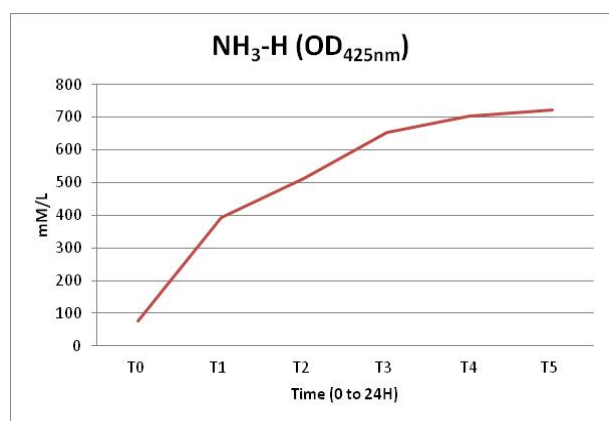
Figure 1. Graphical representation of the mean values of ammonium generated by S. pasteu*rii* cultures at 330 mM concentration of urea.

The rate of bacterial induced calcite precipitation, by adding solutions of $CaCl_2$, was estimated about 100 %. This is related to the concentration of Ca free ions in the bacterial broth solution maintaing constant the total number of bacterial cells.

3.2 Waste characterization and Ecocement trial test

A sample of CKD (solid cement waste) coming from a cement plant was analysed and its main mineralogical and chemical composition is reported in Table 1. With respect to the literature data *alite* and *belite* (clinker) are absent such as calcium oxide (quick lime) and calcium hydroxide (slaked lime). The amount of calcite in this CKD sample has been determined used a gasometric technique (Dietrich Fruling calcimeter). The percentage of calcite is 75%, significantly higher than literature data (Khanna 2009; Maslehuddin et al. 2009).

Table 1 Mineralogical composition of CKD obtained with X ray diffraction. Chemical composition obtained with XRF.

Mineralogical composition	Calcite	Quartz	Others
	XXX	XX	muscovite

Chemical composition	%
L.O.I.	35.80
SiO_2	11.79
Al_2O_3	2.64
Fe_{TOT}	1.91
MgO	1.31
CaO	45.58
Na_2O	0.18
K_2O	0.44
Ti O_2	0.12
P_2O_5	0.06
MnO	0.16
SO_3	Tr.
Total alkali (Na_2O + 0.658 K_2O)	0.47

A preliminary cementation tests has been made using this sample of CKD (10g/100 ml). It was mixed with CASO-urea bacterial culture in the exponential phase (OD600 0.3900 for the 10-1 dilution) and the mixture was continuously stirred for 10 minutes, and then placed in a silicone molds and left to dry for 2 days. The block obtained (see Fig 2) is consolidated but with low strength due to the lack of calcium oxide and hydroxide, calcium silicate compounds and the low amount of alkali in the CKD sample. In order to improve the strenght of the final product such type of CKD should be processed, before to mix with the ureolytic bacterial suspension.

One way to improve the *qualities* of this CKD could be the activation of the hydraulic reactivity via the mechanical process called mechano-chemical grinding (Ryou 2004). This treatment could leads to materials with increased surface free energy, which makes it more reactive.

Another way would be to add to the CKD the waste of the manufacturing process of lime, namely Lime Kiln Dust (LKD), and other materials with pozzolanic properties such as rice husk ash, ceramic waste, activated clay minerals (Zerbino et al. 2012; Fernandez et al., 2011; Mucsi et al., 2011; Rattanasak et al., 2010; Mertens et al., 2009).

The LKD waste would provide the oxide and calcium hydroxide lacking and the addition of these materials with pozzolanic properties allows to the formation of a hydraulic binder.

Figure 2. Sample of the Ecocement Block obtained mixing the CASO-urea bacterial culture with CKD.

4 Conclusions

Concrete is a composite material which is made up of a aggregate and a hydraulic binder. The binder (cement paste or natural hydraulic lime) "glues" the aggregates together to form a synthetic conglomerate. The constituents used for a cementitiuos composite material are binder, water, aggregates (generally sand) and any eventual additive useful to improve the properties of the concrete. The final product has specific physical and mechanical characteristics that enable this material to different applications.

In the case of Eco-cement the process will mix the bio enzymatic active component with the integrated CKD waste.

Preliminary tests with one samples of CKD have shown that this sample needs to be pre-processed before to obtain a more efficient construction material.

Acknowledgements

References

Fernandez R, Martirena R,. Scrivener KL (2011) The origin of the pozzolanic activity of calcined clay minerals: A comparison between kaolinite, illite and montmorillonite. Cement Concrete Res 41:113–122

Khanna OS (2009) Characterization and Utilization of Cement Kiln Dusts (CKDs) as Partial Replacements of Portland Cement. PhD thesis, Department of Civil Engineering University of Toronto.

Maslehuddin M, Al-Amoudi OS, Rahman MK,. Ali MR, Barry MS (2009) Properties of cement kiln dust concrete. Constr Build Mater 23:2357–2361

Mertens G, Snellings R, Van Balen K, Bicer-Simsir B, Verlooy P, Elsen J (2009) Pozzolanic reactions of common natural zeolites with lime and parameters affecting their reactivity. Cement Concrete Res 39:233–240

Mucsi G, Debreczenia A, Madai V, Dudok T, Csoke B (2011) Development of hydraulic binder using industrial wastes. Építőanyag, 63:28-32

Rattanasak U, Chindaprasirt P, Suwanvitaya P (2010) Development of high volume rice husk ash alumino silicate composites. Int J Miner Metallurgy Mater 17:654-659. Doi:10.1007/s12613-010-0370-0

Ryou J (2004) Improvement on reactivity of cementitious waste materials by mechanochemical activation. Mater Lett 58:903–906

Tiano P, Cantisani E, Sutherland I, Paget JM (2006) Biomediated reinforcement of weathered calcareous stones. J Cult Heritage 7:49-55

Whiffin VS (2004) Microbial $CaCO_3$ precipitation for the production of Biocement. PhD Thesis, School of Biological Sciences & Biotechnology, Murdoch University, Western Australia

Zerbino R, Giaccio G, Batic OR, Isaia GC (2012) Alkali–silica reaction in mortars and concretes incorporating natural rice husk ash. Constr Build Mater 36:796–806

Characterization of loess used for building a replica of folk house by traditional technique

Dalibor Všianský[1], Martin Novotný[2]
[1] Institute of Geological Sciences, Faculty of Science, Masaryk University, Brno, Czech Republic, dalibor@sci.muni.cz
[2] National Institute of Folk Culture, Strážnice, Czech Republic, novotny@nulk.cz

Abstract. The paper describes mineralogical and petrographic examination and testing of mechanical properties of loess and experimental adobe bricks. The tested material corresponds to a common loess, which was used in traditional clay building in the region. Due to its composition and mechanical properties it was found to be applicable as rammed earth building material and was later used for building a replica of traditional Moravian folk house in the open-air museum in Strážnice, Czech Republic. The research is a part of a cultural heritage documentation and preservation project.

Keywords. Loess, adobe bricks, mineral composition, mechanical properties

1 Introduction

The research combined material science, geology, and ethnography. It covered the examination and usability of traditional building techniques applied in lowland and flatland regions of Moravia to rehabilitate and safeguard the sustainable condition of clay architecture monuments. Those monuments are the most endangered group of historic rural buildings of regional and supra-regional importance. Therefore, the implementation of the presented research results is very relevant now.

There have been many authors dealing with adobes or rammed earth both in archaeological and technological context. For instance Silveria (2012, 2013), Delgado (2007), Calabria (2009), Ciancio (2013), Bui (2009), Adorni (2013), and others.

The research followed-up previous material studies by Havlíček and Souček (1958), Minke (2006) and Žabičková (2002). A systematic study on traditional historic clay building techniques in Moravia is still missing.

Due to its low cost, thermal insulating properties, and for ecological reasons, clay (soil) becomes relatively popular building material again.

2 Material and Methods

Loess from historic pit in Kunovice, Czech Republic was examined by optical microscopy, thermal analysis and x-ray diffraction. Its binding force and compressive strength and microstructure of experimentally prepared adobes were also tested. Later, a replica of a rammed earth traditional house was built out of the tested material.

Optical microscopy was done using Olympus BX-51 polarizing microscope.

X-ray diffraction analysis was conducted on Bruker D8 Advance diffractometer equipped with 1D position sensitive detector (PSD) Lynx Eye, Cu anode ($\lambda_{K\alpha} = $ 0.15418 nm), and programmable slits. The analyses were conducted at conventional Bragg-Brentano para focusing $\Theta - \Theta$ reflexion geometry. Step size – 0.02°2Θ, time per step – 188s. The results were processed using Diffrac plus software.

Thermal analysis (TG/DTA) was done using Netzsch STA 429 in the temperature range 30 – 1100°C.

Three samples taken from different places of the historic pit were subjected to binding force test, also called the 8 test (DIN 18952). Binding force is considered to be one of the most important characteristics of earth for building (Delgado 2007, Souček 1958). The soil was dried at 60°C and mechanically processed. Six eight-shaped testing samples with the central diameter of 5 cm^2 (22.5 x 22.5 mm) were prepared out of each of three samples of processed soil. The bodies were tested on TESTOMERIC M350 – 20CT instrument (Fig. 1). The speed of load – 5 mm/min.

Figure 1. Binding capacity test

Experimental adobes were prepared according to three formulas (Table 1). Compressive strength tests were carried out on six pieces of each formula according to the ČSN 72 2605 standard, speed of load 5 kN.s^{-1}

Table 1. Composition of experimental adobe bricks

Formula no.	Composition
1	soil + straw (1 m^3 of soil + 20 kg of straw)
2	soil + sand in the 1/1 volume ratio
3	soil + sand + straw (soil/sand=1/2 + 3.5 kg of straw)

3   Results

3.1   Mineralogical and petrographic characterization

The material is formed by heterogeneous loess rich in carbonates. Carbonates form concretions (Fig. 2).

Except of carbonates and clay minerals, quartz, feldspars, muscovite, Fe-oxihydroxides, titanite, and zircon are present there. Organic matter occurs rarely. Microstructure of the material – see Figure 3.

Figure 2. Carbonate concretion in loess from Kunovice.

Figure 3. Microstructure of loess from Kunovice.

The results of XRD examination of three loess samples from Kunovice are summarized in Table 2.

The results show variable contents of carbonates (calcite, dolomite) within the historic pit and relatively high contents of clay minerals.

Table 2. Semiquantitative results of XRD analyses.

sample/mineral	Kunovice 1	Kunovice 2	Kunovice 3
chlorite	+	+	+
montmorillonite	?	?	?
illite/muscovite	++	++	++
kaolinite	++	+++	++
amfibole	++	++	++
quartz	+	+	+
feldspars	+++	+++	+
calcite	++	–	+++
dolomite	–	–	+++
goethite	+	+	+

+++, ++, +, –, ?: relative abundance

The quantitative results of thermal analysis (TA) are presented in Table 3. DTA and TG curves – see Figure 4.
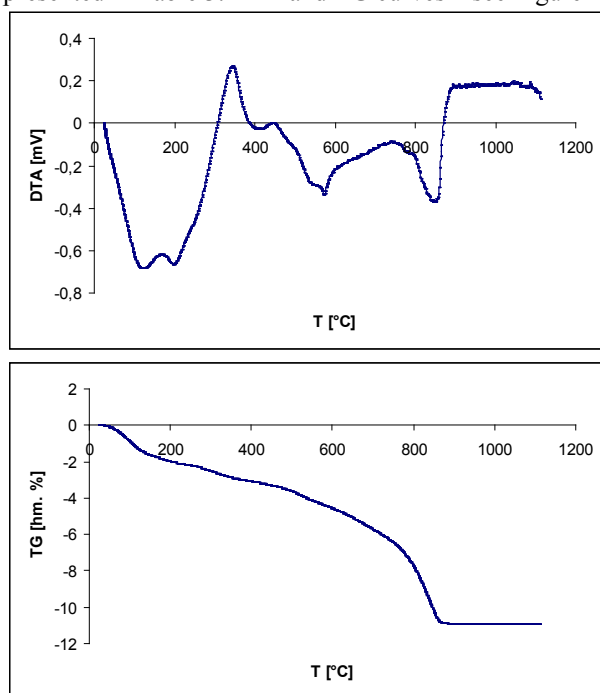
Figure 4. Thermograms of the tested material

Table 3. Quantitative results of thermal analysis in wt.%

sample	loess Kunovice
humidity and H_2O bound in kaolinite	1,8*
H_2O bound in illite	0,5*
organic compounds	1,1
hydroxyl H_2O [kaolinite]	1,3
hydroxyl H_2O [illite]	1,4
dolomite	2,4*
calcite	8,9*
total loss of ignition (30 - 1000°C)	11,0

* the process is affected by another parallel process (processes)

3.2 Binding capacity test of loess

The average results of binding capacity tests of three loess samples are given in Table 3.

Table 3. Binding capacity test results.

Sample	Binding capacity [N]
Kunovice 1	$12,5 \pm 1,1$
Kunovice 2	$7,3 \pm 0,5$
Kunovice 3	$5,1 \pm 0,9$

3.3 Microstructure and compressive strength tests of experimental adobes

Experimental adobes were prepared according to three formulas (see chapter 2) by pressing the mixtures into wooden forms and drying in the sun.

Microphotographs of microstructures of adobe bricks made of mixtrures of loess and straw (formula no. 1) and loess and sand (formula no. 2) – see Figures 4 and 5.
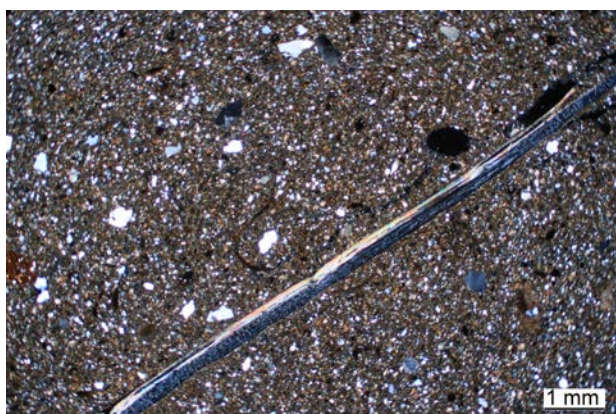
Figure 4. Microstructure of adobe with straw addition (formula 1); XPL.
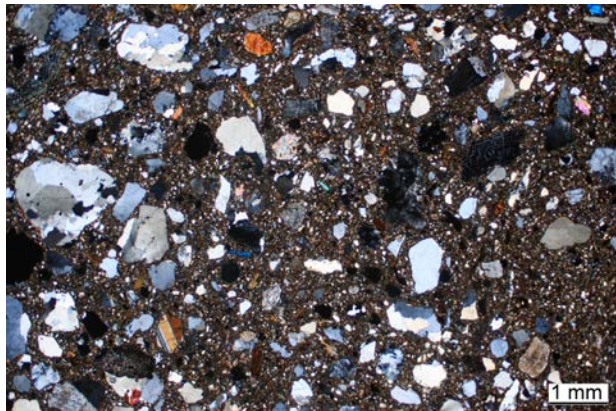
Figure 5. Microstructure of adobe with sand addition (formula 2); XPL.

The average results of compressive strength tests of adobes are given in Table 4.

Table 4. Average compressive strenghts tests results of experimental adobe bricks.

Formula no.	Compressive strength [MPa]
1	$5,2 \pm 0,6$
2	$4,3 \pm 0,3$
3	$4,5 \pm 0,5$

3.4 Building a replica of traditional Moravian house

The tested loess was used as a basic material for building the replica in open-air museum in Strážnice, Czech Republic.

The experimental work has been focused on the rammed earth – a wall construction technique which was used in traditional building mainly in the south-eastern part of the Czech Republic. Rammed earth is built from soil with the natural content of moisture. If the soil is too clayey and shrinks while drying up, it is necessary to add admixtures, in this case the chopped straw. The principle of this technique lies in manual tamping of the homogenized earthen mixture in a formwork. A 10 cm high layer of earth is placed between the boards; it is gradually rammed down to 5 cm. In this way, a compact whole is created and the whole building turns into an earthen monolith. Wooden rammers were used to tamp the earthen mass. An experimental hut with the outside dimensions 4 x 5 m was built. The walls are 2.5 m high and 0.5 m wide. The building has no foundations. There are four openings – three for the windows (0.6 x 0.8 m) and one for the door 1.8 x 0.2 m. The result of the project is a building with compact walls and a provisional roof.

The building was reinforced in the quoins every 40 cm with wattle which was surrounded by a mass of compacted earth. A vertical crack appeared in the middle of every wall during the process of drying. This phenomenon was caused by the small amount of admixtures in the building material and the absence of the horizontal reinforcement (wattle) in the walls, which would prevent the emergence of s continuous shrinking crack. When the masonry dried, the cracks were filled with daub and the whole building seems to be very solid.

The building works begun in 2011 and were finished in 2012.

The building procedure is documented in Figures 6 and 7.

Figure 6. Building procedure of traditional house replica.

Figure 7. Building procedure of traditional house replica.

4 Discussion

Mineral and petrographic composition of loess from Kunovice corresponds to common loess, which was used in traditional clay building.

Binding force of the material is very favourable according to the scale published by Havlíček and Souček (1958) and Delgado (2007). It is caused by relatively high content of clay minerals (see the results of XRD and TA).

The best compressive strength test results were obtained for the mixture of loess and straw (formula no. 1). The results of the other formulas are slightly lower. According to Žabičková (2002), the minimum acceptable value of compressive strength of clay is 1 – 1.5 MPa. Therefore, the obtained results may be considered as very good.

5 Summary

During the research, loess material was examined. Its properties were found favourable for building purposes. Experimental adobe bricks were prepared out of the loess with the additions of straw and sand. The best compressive strength results were obtained for the mixture with straw addition.

A replica of traditional house was built out of the tested material.

Acknowledgements

References

Adorni E, Coïsson E, Ferretti D (2013): In situ characterization of archaeological adobe bricks. Constr Build Mater 40:1-9.

Bui QB, Morel JC, Reddy BVV, Ghayad W (2009) Durability of rammed earth walls exposed for 20 years to natural weathering. Build Environ 44:912-919.

Delgado MCJ, Guerrero IC (2007): The selection of soils for unstabilised earth building: A normative review. Constr Build Mater 21:237-251.

Calabria JA, Wander L, Vasconcelos L, Boccaccini AR (2009): Microstructure and chemical degradation of adobe and clay bricks. Ceram Int 35:665-671.

Ciancio D, Jaquin P, Walker P (2013): Advances on the assessment of soil suitability for rammed earth. Constr Build Mater 42:40-47.

Havlíček V, Souček K (1958) Stavby z nepálené hlíny. Státní zemědělské nakladatelství, Praha. (In Czech)

Minke G (2006) Building with earth. Birkhäuser. Basel.

Silveria D, Varum H, Costa A, Martins T, Pereira, Almeida J (2012) Mechanical properties of adobe bricks in ancient constructions. Constr Build Mater 28:36-44.

Silveria D, Varum H, Costa A (2013) Influence of the testing produres in the mechanical chracterization of adobe bricks. Constr Build Mater 40:719-728.

Žabičková I (2002) Hliněné stavby. ERA. Brno. (In Czech)

S 7:
Open session

Convenors:
Karin Högdahl & George Morris

Non-sulfide Zn deposits in the Moroccan High Atlas

Choulet F., Barbanson L., Branquet Y., Sizaret S.
ISTO, Université d'Orléans/CNRS (UMR7327), Orléans, France

Charles N.
BRGM (French Geological Survey), Orléans, France

Ennaciri A.
Groupe Managem, Casablanca, Morocco

Badra L.
Université Moulay Ismaïl, Meknès, Morocco

Abstract. We have investigated six Zn non-sulfide ore deposits (also called "calamines") from the Moroccan High Atlas, in order to understand processes and timing of their formation. Structural field observations have revealed a genetic link between regional faulting and cavities filled by ores. Based on our mineralogical investigation, we propose the following stages: 1) formation of the protore sulfides, 2) early supergene weathering with formation of Zn-Pb-bearing carbonates and iron oxi-hydroxides and 3) late supergene weathering with deposition of Zn-carbonates and silicates. Direct replacement of primary sulfides is the dominant process. A complementary rock magnetism study shows similar horizontal magnetic fabrics for calamines and internal sediments. Isolated high temperature components are of primary origin and the paleomagnetic directions of calamines and internal sediments are compatible. The calculated poles are consistent with the last 30 Ma of the Apparent Polar Wander Path (APWP) of Africa. These promising results pave the way for an efficient method to constrain the age of Zn supergene deposits.

Keywords. Supergene deposits, Calamines, Moroccan High Atlas, Rock magnetism.

1 Introduction

Non-sulfide zinc ore deposits, also called "calamines" have been reconsidered, as metallurgical techniques have improved. Typical examples are found in Sardinia, in Belgium and in Iran (Hitzman et al. 2003). Hypogene and supergene deposits are distinguished and supergene deposits may be divided into three subtypes: 1) direct-replacement deposits, 2) wall-rock replacement deposits and 3) karst-fill deposits.

Reichert and Borg (2008) have pointed out the features that control the formation of such deposits. These include: 1) the morphology of the protore sulfide body, the structure of the host rocks and the pre-existing faults, 2) the nature of the host rock and its ability to interact with Zn-rich solutions, 3) the open or closed conditions of the karst, 4) the climatic factors and 5) the competition between regional uplift and erosion.

In Morocco, the High Atlas Mountains expose a great number of non-sulfide Zn ore deposits, whose origin is not well constrained by traditional models. This Tertiary intra-continental belt has recorded represents a natural laboratory to understand the link between tectonic, climatic and weathering processes.

This work presents new field and mineralogical observations from six ore deposits, and we propose a scenario for calamines formation. In parallel, rock magnetism studies revealed the rock fabric and allow us to timely constrain ore deposition.

2 Geological setting

2.1 The Moroccan High Atlas

The Moroccan High Atlas is composed of Mesozoic to Cenozoic sedimentary rocks (mainly carbonates) covering a Variscan basement (Fig. 1). A complex evolution with successive episodes of uplift related to intra-plate tectonics has been recorded (Frizon de Lamotte et al., 2000). This ENE-WSW trending fold belt displays narrow faulted anticlines and large synclines.

Mechanisms for belt formation are still debated. Thin-skinned tectonics, with a décollement zone located in the soft Triassic layers is generally opposed to thick-skinned tectonics, which emphasizes the role of Variscan structures and suggests deformation of the crust in depth.

2.2 Zn-Pb ore deposits

Zn-Pb ore deposits are numerous in northern Africa; they often represent stratabound lenses in the Jurassic carbonate series. In Morocco, two metallogenic periods can be distinguished. Lower Jurassic deposits are related to normal faulting associated with the opening of Tethys and Atlantic oceans. Middle Jurassic deposits may be of magmatic and hydrothermal origin, but several deposits seem to present similarities with MVT ore deposits.

3 Sampling and methodology

In this study, we have selected six ore deposits or prospects from the Moroccan High Atlas (Fig. 1): Aït Labbès, Beni Tajite, Bou Arhous, Tadaghast, Tizi n'Firest and Toulal. Samples have been collected from galleries or dumps. At Aït Labbès, Beni Tajite, Tadaghast and Toulal, we have collected 165 cores of limestone, flat lying internal sediments and calamines from 10 sites to perform rock magnetism studies.
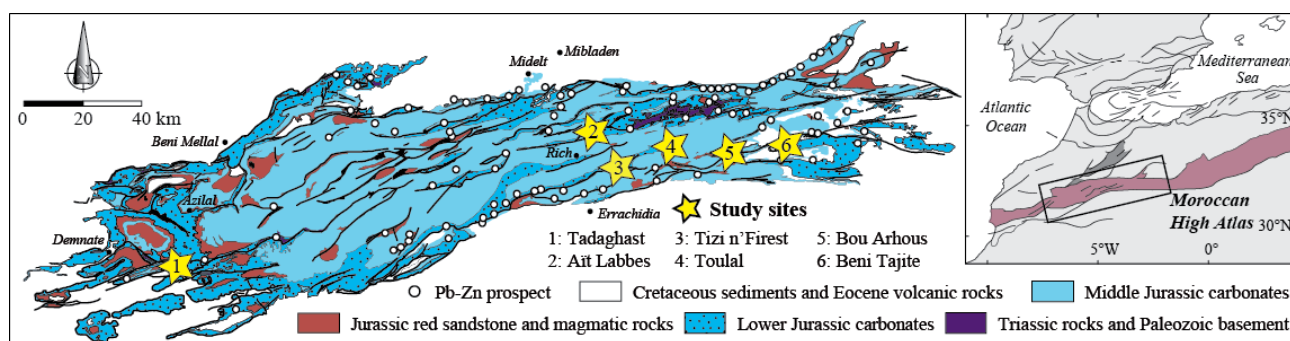
Figure 1. Map of the Moroccan High Atlas and location of the six studied ore deposits.

Mineralogy was investigated by using petrographic microscopy, secondary electron microscopy, Raman spectroscopy and X-ray diffraction at ISTO and CBM, Orléans. To get quantitative compositions, we have used the Cameca SX50 electron microprobe at BRGM.

Thermomagnetic measurements for determining the Curie points and isothermal remanent magnetization (IRM) acquisition have provided constraints for the magnetic mineralogy. The anisotropy of the magnetic susceptibility (AMS) was measured by using an AGICO KLY3S kappabridge susceptometer. Stepwise thermal demagnetizations were performed with a laboratory-built furnace and magnetic remanence was measured with an AGICO JR-5A automatic spinner magnetometer.

4 Results

4.1 Macroscopic observations

The Toulal prospect is located in the periclinal termination of an ENE-WSW trending narrow anticline. The northern and southern limbs display Pliensbachian thin-bedded limestone, while the Upper Sinemurian para-reef massive black limestone forms the fold hinge. White massive calcite (early calcite) occurs in the extrados fractures of the fold. Syn-compressive faults are documented by cataclasite and breccia. Calamine veins are mainly located in the cataclastic zone that cuts the Upper Sinemurian black limestone. Red and grey calamines occur within veins that form N70°E striking steeply dipping boudins and crosscut the extrados fractures. Preserved sulfides (galena and sphalerite) are enclosed in the red calamine. Internal sediments such as marl or calcareous shale are with horizontal bedding.

The Bou Arhous Ore Deposit is a part of an ENE-WSW trending anticline. Folding is associated with faulting along a major top-to-the-south thrust, which exposes crushed Triassic clayey material. The entire mineralization is located in the footwall of this fault and ore, hosted in Sinemurian black limestone, is distributed in E-W trending veins that parallel the anticline axis. The veins form a complex karst network, but often display a vertical zonation related to the oxidation process, with sulfide preserved in the deeper levels. Calamine is red or white (black in case of willemite). Internal sediments with horizontal bedding fill the karstic cavities. These sediments are generally barren but may sometimes have high Zn content and contain fragments of calamine.

The Tadaghast Ore Deposit is situated in the southern shallow-dipping limb of an open anticline. Liassic formations include Pliensbachian beige marl and limestone, and Sinemurian black para-reef limestone with intra-formational breccia and evidence of intense karstification. Internal sediments, with horizontal bedding, fill the grikes. N-S trending fractures are filled by massive white calcite, and these fractures may be reactivated to form a breccia containing fragments of the black limestone cemented by drusy or collomorphic calcite. This calcite is observed in the subsidiary E-W trending fractures. In depth, mineralization seems to be distributed according to three structural directions. N-S trending fractures are filled by calamine but also present breccia and white massive calcite. E-W trending fractures include banded and/or vacuolar red calamine. The horizons are concordant to the bedding of Sinemurian black limestone and display sulfide lenses partly replaced by red and white calamine.

The Beni Tajite Ore Deposit is a part of a WSW-ENE range including preserved Pliensbachian coral reef. The ore body mainly occurs within E-W trending veins or NW-SE trending fractures. Sulfides are frequent at depth, as disseminations within limestone, or in association with rhombohedral white calcite. The latter may represent the original karst hosting the sulfides prior to weathering. In the shallow levels, the banded red calamine is distributed according to a complex vein network, whereas the white calamine includes botryoidal masses of hemimorphite or bands of white hydrozincite, which impregnates the wall of the veins.

The Aït Labbès Ore Deposit is located in a narrow anticline cut by an ENE-WSW trending fault. The bedding of the limestone is steep and the fold hinge has been eroded. The ore body occurs within ENE-WSW vertical veins that parallel the bedding of the Sinemurian black para-reef limestone. The calamine veins show a boudin-like distribution along this fault. Isolated masses of sulfides are preserved within the red calamine composed of smithsonite and clays. Large euhedral crystals of beige calcite, predating the calamine lodes, fill fractures in the host limestone. Conversely, white or translucent banded calcite postdates the Zn-rich veins. Internal sediments with horizontal bedding are barren.

The Tizi n'Firest Ore Deposit is part of an anticlinal ridge, whose axis parallels an E-W trending thrust. Folding has exhumed Triassic marl and basalt, as well as Sinemurian massive limestone hosting the ore. The ore body represents a vast cavity that dips to the north at 70°.

Calamine veins striking parallel to the E-W major thrust form numerous digitations, which are partly filled by clays with horizontal stratification. Clays may contain residual galena associated with euhedral crystals of white calcite and concretions of banded smithsonite.

4.2 Microscopic observations

Based on previous investigation in the six studied ore deposits, we have established the following paragenetic successions: 1) limestone, 2) protore sulfides, 3) red or black calamine and 4) grey or white calamine.

The host rocks always correspond to massive limestone with coral fossils. Dolomite was only identified in Toulal within fractures. Quartz needles often occurred and are preserved during weathering.

A protore composed of primary sulfides and massive white calcite is common to the six deposits. Protore sulfides are galena, sphalerite and pyrite, with relative proportions. Sphalerite shows correlated variations in Cd and Fe content, while the Bi content of galena may reach 7600 ppm. The initial amount of sulfides can be different between ore deposits and relative proportions may vary with supergene oxidation. Massive white calcite cleaving into rhombs is often deformed, identically to galena.

For each ore deposit, pyrite has been pseudomorphed by iron oxi-hydroxides, with hematite surrounded by goethite. Such replacement textures are typical of supergene oxidation in neutralizing carbonates. At Toulal, lepidocrocite was identified (Fig. 2) and may have been formed after maturing of a ferric gel (Kosakevitch, 1983), frequently observed in the pseudomorphs. Galena is frequently replaced by botryoidal cerussite, and anglesite has only been observed close to dissolved pyrite (Fig. 2). Direct replacement of sphalerite by smithsonite is rarely observed. Smithsonite and cerussite are associated with secondary sulfides (covellite, galena and greenockite).
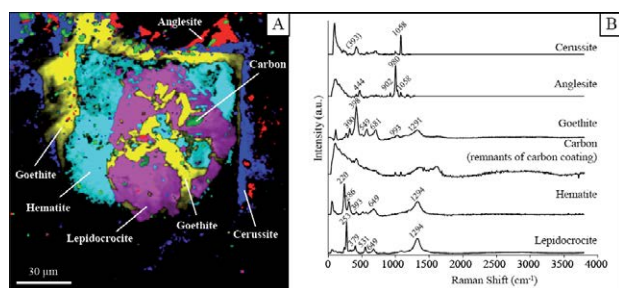

Figure 2. Raman composition map (A) and associated Raman spectra (B) of the iron oxi-hydroxides pseudomorph after pyrite (Toulal ore deposit).

Red calamine often shows high Fe content and is composed of iron oxi-hydroxides and smithsonite concretions therefore. Atypically, black calamine including willemite occurs at Bou Arhous, but never coexists with the red calamine. Several infrequent minerals, such as decloizite or psilomelane form thin encrustations closely associated with iron oxides.

Grey or white calamine develops after the red type, or is precipitated in karst cavities. It is characterized by the absence of iron oxi-hydroxides and includes hemimorphite and translucent smithsonite. The association of hydrozincite with red or grey calamine is not obvious. At Toulal or Bou Arhous, hydrozincite is contemporaneous to the formation of iron oxi-hydroxides, which impregnate the white patches of hydrozincite. Conversely, hydrozincite clearly postdates the red calamine of Beni Tajite ore deposit. However, the simplistic succession smithsonite I-hydrozincite-hemimorphite±smithsonite II remains a constant for each ore deposit. A late generation of drusy translucent calcite cements the calamine breccia or fills the karst cavities.

Internal sedimentation and recycling of calamine is a continuous process during the development of the karst. At Tadaghast, sedimentary reworking of quartz needles in the fractures of the sphalerite lodes predates the concretions of smithsonite. Conversely, in other deposits, internal sediments often fill post-red calamine cavities. The occurrence of clayey materials like sauconite, however, remains a constant.

4.3 Rock magnetism

IRM and X-ray diffraction analyses have revealed magnetite as the main magnetic carrier, and subsidiary high coercive minerals like goethite and hematite. Host limestone, calamines and internal sediments with horizontal bedding present similar mineralogical assemblage, and only the relative proportions may vary.

AMS directions of calamines and internal sediments are often consistent, while AMS data from limestone are too weak to be used. The magnetic foliation is horizontal, even if sedimentary reworking or differences in the supergene evolution may have disturbed the AMS signal (e.g. at Aït Labbès and at Tadaghast). The magnetic lineation is usually horizontal and parallel to the direction of the calamine veins. The attitude of the AMS parameters (P_J and T) suggests that deformation is lacking and supports the formation of magnetic fabric from sedimentary dynamics within the veins.

Directions of the high temperature component (HTC) were isolated for samples collected at Toulal, Aït Labbès and Tadaghast. For the two first localities, the reverse and normal directions of this HTC of both calamines and internal sediments are antipodal and similar within error. We therefore calculated an average paleomagnetic direction for each locality. HTC directions of calamines from Tadaghast are scattered, while the average HTC direction of internal sediments is isolated from others.

5 Formation of non-sulfide ore deposits

We have distinguished three types of ores (protore, red-black calamine, grey-white calamine), corresponding to the successive stages of ore deposition: 1) pre-oxidation stage, 2) supergene stage I and 3) supergene stage II.

5.1 Pre-oxidation stage

For each ore deposit, there is a strong lithological control of the protore deposition, which only occurs within Upper Sinemurian and Pliensbachian limestone formed in a reef environment. Deposition of primary sulfides closely follows the limestone sedimentation. The

concordant sulfides lenses are closely associated with white massive calcite; both experienced post-deposition deformation. Silicification revealed by quartz needles and limited dolomitisation occurred before weathering.

5.2 Supergene stage I

Compression related to the Atlasic events contributes to tilting of the strata. This has facilitated the percolation of mildly acid meteoric water and dissolution of the host limestone giving rise to the karst. O_2 also reacts with pyrite to form iron oxi-hydroxide. In consequence, the pH decreases, although acidity is buffered by the dissolution of the host limestone. Oxidation also affects the other sulfides. Lead and zinc ions are released in the solution and may form smithsonite, cerussite and anglesite of the red calamine. Supergene secondary sulfides are frequent and their precipitation may be explained by short intervals of reducing conditions caused by local variations of the level of the water table due to seasonal or tectonic effects. Willemite occurring at Bou Arhous is traditionally interpreted as being of hydrothermal origin, but may be formed under low water activities, alkaline pH, oxidizing conditions, high silica activities and low P_{CO2} conditions.

5.2 Supergene stage II

This stage is dominated by "grey to white calamine" and occurs after the partial to total consumption of pyrite due to oxidation. Consequently, the pH conditions become neutral to slightly alkaline. Smithsonite continues to precipitate causing a drop of P_{CO2}, which facilitates replacement of smithsonite by hydrozincite. In the case of solutions saturated with silica, hemimorphite is stable under pH below 7-8, but small variations of P_{CO2}, pH or [Zn] may rapidly change the equilibrium of the system, resulting in hemimorphite-hydrozincite assemblages. Much of the internal sediments were deposited lately in cavities of the gangue and of the calamine as well. Sauconite mainly composes the infilling material, although its origin is still unclear. It may be formed by interaction of Zn-rich solutions with barren clays observed in limestone interlayers.

6 Timing of calamines formation

Since paleomagnetic directions of internal sediments and calamines are consistent, an average direction has been calculated for Toulal and Aït Labbès ore deposits. Based on the AMS horizontal fabrics and the occurrence of antipodal polarities, we conclude that magnetization is primary and its acquisition is coeval with ore and sediment deposition. Therefore, the age of calamines may be estimated by comparing the paleopoles from Toulal and Aït Labbès to the apparent pole wander path of Africa (APWP; Besse and Courtillot, 2002; Fig. 3).

For Toulal, the age is statistically bracketed between 30 and 10 Ma. For Aït Labbès, the range of 60-10 Ma may be reduced to 40-10 Ma, since field observations have shown that ore deposits postdate the major tectonic event related to the Atlasic compression. It is worth noting that no orogenic rotation has been recorded by the samples. Statistical constraints could be improved after increasing the number of sample, but the limited absolute motion of Africa during the last 40 m.y. hinder better resolution for characterizing age deposition.
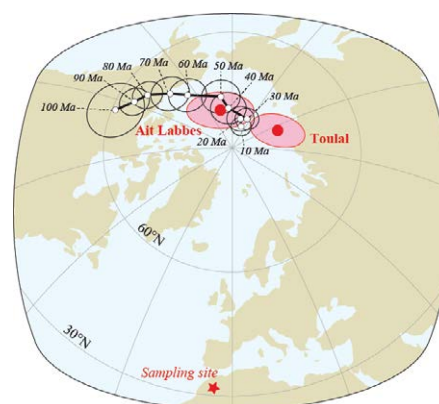
Figure 3. Equal-area projection of Toulal and Aït Labbès paleopoles and of the last 100 m.y. of Africa APWP.

6 Conclusion

Field observation and mineralogical investigation have revealed a two-stage supergene evolution controlled by both climate and tectonics. Calamines have mainly been formed by replacement of sulfide lenses or by minor precipitation and internal sedimentation in karst cavities. The AMS study brings crucial information on the structure of calamines and of the internal sediments, and thus reveals the dynamics within the karst. Age deduced from paleomagnetism is consistent with field interpretation. Dating ore deposition is therefore possible and could be cautiously applied to other targets where no field constraints are available.

Acknowledgements

References

Besse J, Courtillot V (2002) Apparent and true polar wander and the geometry of the geomagnetic field over the last 200 Myr. J Geophys Res. doi:10.1029/2000JB000050.

Frizon de Lamotte D, Saint Bezar B, Bracene E et al. (2000) The two main steps of the Atlas building and geodynamics of the western Mediterranean. Tectonics 19:740-61

Hitzman MW, Reynolds NA, Sangster DF, et al (2003) Classification, Genesis, and Exploration Guides for Nonsulfide Zinc Deposits. Econ Geol 98:685-714

Kosakevitch A (1983) Etude morphogénétique des textures de remplacement et de remplissage dans les chapeaux de fer. BRGM Report No.: 83SGN936MGA.

Reichert J, Borg G (2008) Numerical simulation and a geochemical model of supergene carbonate-hosted non-sulphide zinc deposits. Ore Geol Rev 33:134-51

The role of water diffusion in quartz investigated by experimental fluid inclusion re-equilibration

Gerald Doppler, Ronald J Bakker, Miriam Baumgartner
Chair of Resource Mineralogy, Department of Applied Geological Sciences and Geophysics, University of Leoben, Austria
Correspondence: gerald.doppler@unileoben.ac.at

Abstract. Natural rock samples and fluid phases are used in a widespread field of geological investigations to support reconstructions of pressure-temperature-time interpretations of ore forming processes. Analyses of the fluid phase based on fluid inclusion studies must be taken with care due to possibilities of inclusion modification. Natural fluid inclusions can be affected by diffusion processes, and pore fluid compositions may totally control inclusion compositions at elevated P–T conditions. Experimental fluid inclusion studies are performed to determine diffusion rates of water-related species such as H_2O, D_2O, H_2, O_2, and $NaCl$-H_2O mixtures through quartz crystals. Synthesized and natural fluid inclusions are exposed to different surrounding fluid species during the re-equilibration experiments. Due to the difference in chemical potential of the entrapped and the surrounding fluid, movement of the fluid species can be detected. The magnitude of compositional changes is mainly dependent on (**1**) distance to the crystal surface; (**2**) size of inclusion; (**3**) temperature; and (**4**) re-equilibration time. This experimental study identifies huge compositional changes in fluid inclusions after only 24 hours of re-equilibration at 600 °C and 337 MPa.

Keywords. Fluid inclusions – Quartz – Diffusion – Experimental study – Re-equilibration

1 Introduction

The origin of fluids from which ore-forming minerals have grown is of major interest for the interpretation of mineralization processes (Wilkinson 2001). As most of the nominally anhydrous minerals within the Earth's crust and mantle can incorporate considerable amounts of hydrogen, fluids are used in a widespread field of geological investigations (Keppler and Smyth 2006). One of the major incorporated fluid species is assumed to be H_2O, which is generally concentrated in isolated cavities within individual crystals. These cavities are usually known as fluid inclusions.

Fluid inclusion research is generally based on a closed-system assumption. Several experimental studies that have been published enhance post-entrapment modifications of fluid inclusions under specific conditions (Sterner and Bodnar 1989; Bakker and Jansen 1990, 1994; Doppler et al. 2013). A gradient in volatile fugacities of the entrapped fluid and the surrounding pore-fluid induce diffusion processes of the fluid species.

The aim of the present study is to perform re-equilibration experiments on synthetic and natural fluid inclusions to identify the major parameters that play a significant role in post-entrapment modifications of fluid inclusions. These modifications are of major interest for the interpretation of the origin and the evolution of parental ore-forming fluids. The recent experimental work on diffusion of fluid species in nominally anhydrous minerals is an appropriate tool for discovering the major factors of non-decrepitative changes of fluid inclusion properties; i.e. (**1**) depth below the crystal surface; (**2**) fluid inclusion size; (**3**) temperature; and (**4**) time.

The re-equilibration experiments in this study are performed to detect the mobility of water-related species within nominally anhydrous crystals under hydrothermal conditions by using H_2O–D_2O–$NaCl$ fluids. Two series of experiments are performed: (**1**) re-equilibration at different experimental temperatures (ΔT); and (**2**) re-equilibration with a surrounding fluid that differs to the initially entrapped fluid at constant temperature (Δf). The newly acquired experimental data result in new diffusion models to support reconstructions of pressure–temperature–time (P–T–t) interpretations of ore forming processes.

2 Experimental setup

Both synthesis and re-equilibration experiments are performed in the hydrothermal high pressure / high temperature laboratory at the University of Leoben (Fig. 1). Ten Nimonic IOS/René 41 autoclaves (Ni–Cr alloy) are installed in a vertical position in a cold-seal system (Kerrick 1987). The temperature of the loaded sample is monitored by an internal thermocouple. During the experiment both pressure and temperature are continuously logged.

Carefully selected inclusion-free natural Brazilian quartz crystals are used as starting material. Rods with a diameter of 2.75 mm are drilled from the quartz crystal and are partially cracked by a thermal shock. The synthesis of fluid inclusions is performed by fracture-healing according to the method of Bodnar and Sterner (1987).

The experimental run-time of each synthesis is 19 days. After the synthesis experiment, up to 100 fluid inclusions of each sample are analyzed by petrographical investigations (morphological properties), microthermometry (homogenisation and melting temperatures of the entrapped fluid phases) and Raman spectroscopy (chemical composition of the fluid phases).
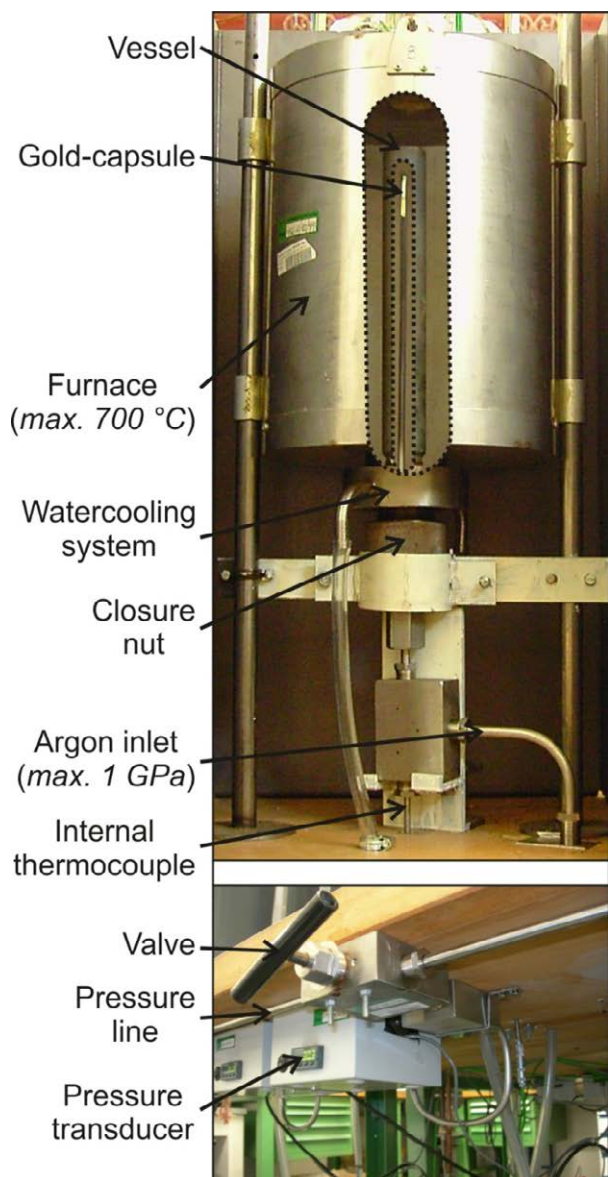
Figure 1. Hydrothermal high pressure / high temperature laboratory setup at the University of Leoben, Austria.

In experiments *GMR002a*, *GMR002b* and *GMR004a* pure H_2O inclusions have been synthesized at 337 MPa and 600 °C. After analysing the entrapped fluid inclusions, these samples have been subsequently re-equilibrated at variable temperatures.

GMR002a and *GMR002b* have been re-equilibrated with the experimentation time of 19 days with pure H_2O as the surrounding fluid species at the same pressure conditions as the initial synthesis and reduced temperatures (ΔT); e.g. 500 °C for *R002a* and 400 °C for *R002b*. Consequently, a pressure and fugacity gradient are active in this experiment.

The sample *GMR004a* has been re-equilibrated with pure D_2O as the surrounding fluid phase at the same *P–T* conditions as the initial synthesis. The run-time of this re-equilibration experiment was also 19 days. A gradient in chemical composition of the fluid species is induced (Δf).

Inclusions are analyzed before and after re-equilibration. To affirm the diffusion behaviour of fluid inclusions we perform equivalent re-equilibration experiments using natural fluid inclusions of well-known properties (Baumgartner et al. 2011).

3 Experimental results

The *P–T* conditions of the performed experiments and detailed fluid inclusion properties are given in Table 1. The properties of H_2O and D_2O fluids are calculated with the appropriate equations of state from Haar et al. (1984) and Hill et al. (1982), respectively, that are available in the software package FLUIDS that is provided by Bakker (2003, and http://fluids.unileoben.ac.at).

Table 1. Experimental conditions and fluid properties

a	b	c	d	e	f
Syntheses					
GMR002a	338.48	600.2	-	176.87	294.2
GMR002b	338.48	600.2	-	176.87	292.9
GMR004a	338.48	600.2	-	176.87	293.1
Re-equilibration					
R002a	336.54	499.5	81.49	121.39	290.0–298.3
R002b	336.71	400.4	29.12	68.88	290.0–297.5
R004a	337.30	599.5	175.75	176.26*	289.3–295.9

* D_2O
(a) Number of experiment
(b) Pressure (MPa)
(c) Temperature (°C)
(d) H_2O fugacity of fluid inclusions (MPa)
(e) H_2O/D_2O fugacity of surrounding fluid (MPa)
(f) T_h-range (homogenization temperature; °C)

3.1 Morphological changes

By measuring the size and the shape of each individual fluid inclusion before and after the re-equilibration experiment considerable morphological modifications can be detected (Fig. 2 and Fig. 3).

The size and shape of the synthesized fluid inclusions are measured by tracing digitally around the outside edge of each individual inclusion according to Bakker and Diamond (2006), shown in Figure 3. Shape properties of re-equilibrated fluid inclusions are compared to the initially synthesized inclusions.

The initially synthesized fluid inclusions of the experiment *GMR002b* show a shape distribution of regular to equant (Fig. 2a and Fig. 3). After the re-equilibration experiment *R002b* at reduced experimental temperature the shape distribution field is shifting to elongated and irregular shapes (Fig. 2b and Fig. 3).

Irregular shaped inclusions of the synthesis *GMR004a* (Fig. 2c) tend to become more regular and more equant shaped after the re-equilibration experiment *R004a* (Fig. 2d).
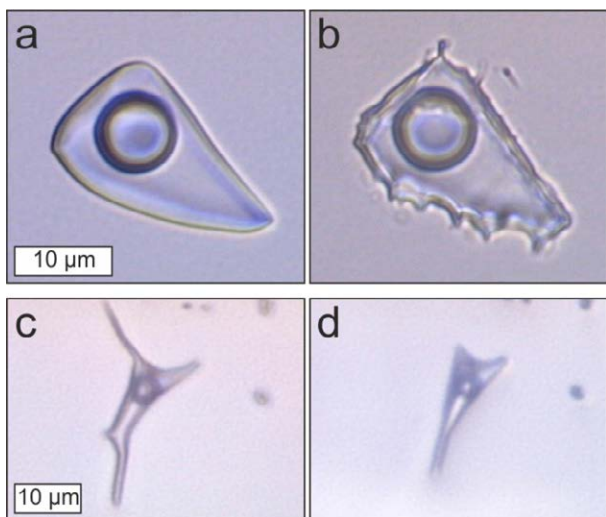
Figure 2. Photomicrograph of a pure H_2O fluid inclusion of the sample *GMR002b* in (**a**). The same inclusion after re-equilibration with pure H_2O at reduced $T_{exp.}$ of the sample *R002b* in (**b**). Fluid inclusion in (**c**) of the synthesis *GMR004a*. The same inclusion after re-equilibration with pure D_2O at the same pressure and temperature conditions as the initial synthesis, sample *R004a* in (**d**).
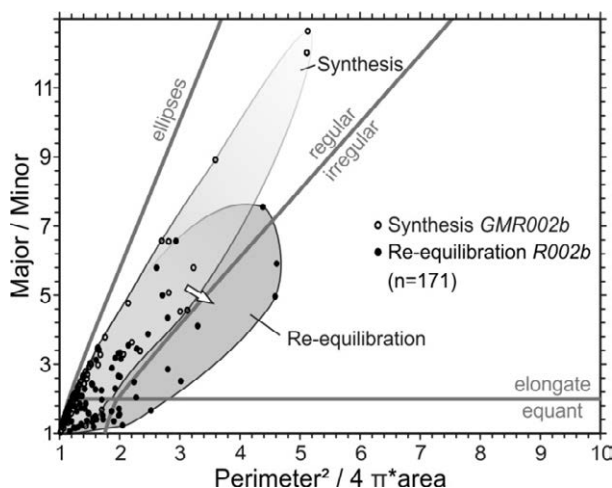

Figure 3. Fluid inclusion shape classification diagram of synthesized fluid inclusions (open circles) that have been formed with pure H_2O at 600 °C and 337 MPa and the same fluid inclusion shapes after the re-equilibration experiment (filled circles) with pure H_2O at 400 °C and 337 MPa. The shape distribution field is clearly shifting to the irregular field.

3.2 Density changes

Noticeable changes in fluid inclusion density are obtained in all re-equilibration experiments. Homogenization temperatures $T_h(LV{\rightarrow}L)$ are directly related to fluid inclusion densities. The changes can be easily detected by measuring the homogenization temperatures of the fluid inclusions.

After the re-equilibration experiments *R002a* (500 °C and 337 MPa) and *R002b* (400 °C and 337 MPa) the T_h-values are shifting to lower temperatures, approaching density values of the surrounding fluid phase (Fig. 4).
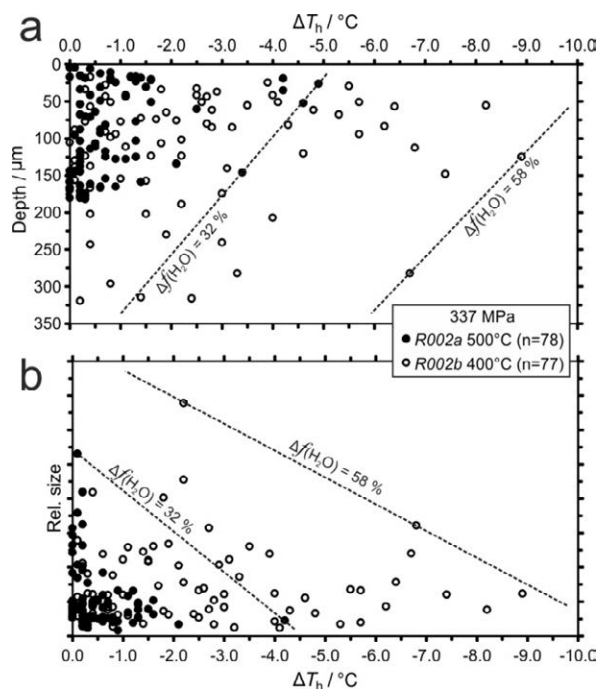
Figure 4. Changes in homogenisation temperatures of initially synthesized pure H_2O fluid inclusions (synthesis at 337 MPa and 600 °C) after re-equilibration (*R002a*) at 500 °C and (*R002b*) 400 °C as a function of distance to the crystal surface in (**a**) and different fluid inclusion size in (**b**). The Δf-values represent the difference of fluid fugacity between the entrapped fluid and the surrounding fluid during re-equilibration.

Potential density changes of fluid inclusions are directly related to the inclusions position within the quartz crystal. The diagram in Figure 4a illustrates that relatively shallow inclusions are more affected by density changes than deep inclusions. Potential changes of the entrapped fluid inclusions during re-equilibration directly correlate with the fluid inclusion size. Small inclusions are more affected than large inclusions (Fig. 4b).

4 Discussion

The present re-equilibration experiments confirm the assumed mobility of H_2O through quartz crystals at 337 MPa and between 600 and 500 °C. The driving force for water diffusion in these experiments is the fugacity gradient of the fluid phases. Due to different fugacities between the entrapped fluid and the external fluid phase during re-equilibration diffusion through the quartz crystal is induced. It is assumed that bulk diffusion is the dominant process in the presented experiments in this temperature range.

The major parameters that play a significant role in diffusion are: (**1**) fugacity gradients between the entrapped fluid inclusions and the surrounding fluid; (**2**) experimental temperature conditions; (**3**) distance between individual fluid inclusion and the crystal surface; (**4**) fluid inclusion size; and (**5**) the experimental run-time.

Shallow inclusions are more affected compared to deep inclusions within the crystal. It is assumed that

large inclusions are less affected compared to small inclusions. The above mentioned unravelled parameters that play a significant role in post-entrapment changes of fluid inclusions support our experiments on natural fluid inclusions.

In the study of Doppler et. al (2013), it is assumed that the threshold temperature of water diffusion through quartz is around 450 °C at 337 MPa. The changes in fluid inclusion density in the **ΔP** experiment at 400 °C are assumed to be controlled by volume changes of each individual fluid inclusion.

Recently performed re-equilibration experiments confirm the expected compositional changes of the inclusions.

5 Conclusion

Synthetic pure H_2O fluid inclusions have been re-equilibrated with pure H_2O and pure D_2O with the surrounding fluid phase at various temperatures; e.g. 600, 500 and 400 °C. Each experiment was performed at 337 MPa in the α-quartz stability field. The experimental setup generates gradients in fugacity between the inclusion and the pore fluid. Due to the fugacity gradient, movement of the water through the quartz crystal is induced. The magnitude of compositional changes of fluid inclusions is directly related to the inclusions depth and their size. During the re-equilibration process initially irregular shaped inclusions tend to become more regular and equant shaped. This study leads to the assumption that pore fluid strongly affects fluid inclusions in natural rock above 400 °C and around 300 MPa.

Acknowledgements

References

Bakker RJ, Jansen JBH (1990) Preferential water leakage from fluid inclusions by means of mobile dislocations. Nature 345:58–60

Bakker RJ, Jansen JBH (1994) Raman Spectra of fluid and crystal mixtures in the systems H_2O, $H_2O–NaCl$ and $H_2O–MgCl_2$ at low temperatures: applications to fluid-inclusion research. Can Miner 42:1283–1314

Bakker RJ (2003) Package FLUIDS 1. Computer programs for analysis of fluid inclusion data and for modelling bulk fluid properties. Chem Geol 194:3–23

Bakker RJ, Diamond LW (2006) Estimation of volume fractions of liquid and vapor phases in fluid inclusions, and definition of inclusion shapes. Am Mineral 91:635–657

Baumgartner M, Doppler G, Bakker RJ (2011) Preliminary results of experimental re-equilibration studies of natural $H_2O–CO_2–NaCl$-bearing fluid inclusions in quartz. ECROFI-XXI, Abstracts, pp 44–45

Bodnar RJ, Sterner SM (1987) Synthetic fluid inclusions. In: Barnes HL, Ulmer GC (eds) Hydrothermal experimental techniques. Wiley, New York, pp 423–457

Doppler G, Bakker JR, Baumgartner M (2013) Fluid inclusion modification by H_2O and D_2O diffusion: the influence of inclusion depth, size, and shape in re-equilibration experiments. Contrib Mineral Petrol (DOI) 10.1007/s00410-013-0857-6

Haar L, Gallagher JS, Kell GS (1984) NBS/NRC steam tables. Hemisphere Publishing Corporation, Washington

Hill PG, MacMillan CRD, Lee V (1982) A fundamental equation of state for heavy water. J Phys Chem Ref Data 11(1):1–14

Keppler H, Smyth JR (2006) Water in nominally anhydrous minerals. Rev Mineral Geochem 62

Kerrick DM (1987) Cold-seal systems. In: Ulmer GC, Barnes HL (eds) Hydrothermal experimental techniques. Wiley, New York, pp 293–323

Sterner SM, Bodnar RJ (1989) Synthetic fluid inclusions. VII. Reequilibration of fluid inclusions in quartz during laboratory simulated metamorphic burial and uplift. J Metamorphic Geol 7:243–260

Wilkinson JJ (2001) Fluid inclusions in hydrothermal ore deposits. Lithos 55:229–272

Structural controls on veins within the Sisson intrusion-related tungsten-molybdenum deposit, New Brunswick, Canada

Rob Duncan
Mineral Deposit Research Group, University of British Columbia, Vancouver, British Columbia, Canada

James Lang
Hunter Dickinson Inc, Vancouver, British Columbia, Canada

Abstract. Sisson is a large, Late Devonian, intrusion-related tungsten-molybdenum deposit. The geometry of the deposit is controlled by the location of the north-northeast striking Sisson Shear which juxtaposes gabbro and granodiorite against a sequence of bi-modal metavolcanic and metasedimentary rocks. Veins within the deposit have a consistent spatial orientation and dip moderately to steeply to the southwest, consistent with mineralization at Sisson being part of a large sheeted vein complex. The nature and geometry of the mineralized vein sets are most compatible with formation during crustal extension with a near-vertical principal stress. The overall arrangement of southeast-striking veins around the Sisson Shear, however, reflects a component of sinistral syn-mineral movement across the fault. There is no major variation in vein orientation throughout the deposit and therefore the shear is the dominant control on the geometry of mineralization. The northwest trend of mineralized veins at Sisson is similar to vein orientations in other tungsten, molybdenum, and tin deposits in the region and suggests that they were all generated under similar tectonic conditions near the end of the Acadian orogeny in the Late Devonian

Keywords. Sisson, porphyry-related, tungsten, molybdenum, oriented core, Acadian orogeny

1 Introduction

The Sisson deposit is a large, Late Devonian, intrusion-related W-Mo deposit and is located 100 km by road from Fredericton, New Brunswick. A positive feasibility study completed in January 2013 reports a NI 43-101 compliant resource for the deposit of 383 Mt grading 0.067% WO_3 and 0.021% Mo (measured and indicated categories) and an additional 178 Mt grading 0.051% WO_3 and 0.021% Mo (inferred category; Northcliff Resources 2013). These resources place Sisson among the largest tungsten deposits in the world. The deposit is covered by a thin (on average 8 m thick) veneer of glacial till. This study uses structural measurements derived from a range of geologic features in oriented drill core within the deposit to develop a structural model for the formation of this important mineralized system.

2 Geological setting

The Sisson deposit is approximately centred on a north-northeast-striking, near-vertical sheared contact (Sisson Shear) between gabbroic and granodioritic intrusive rocks and interbedded metavolcanic and metasedimentary rocks (Fig. 1). From west to east rock types consist of: quartz diorite and gabbro phases of the Howards Peak Granodiorite (age undetermined); interbedded bimodal metatuffs that are interlayered with a series of metawackes assigned to the Turnbull Mountain Formation of the Ordovician Tetagouche Group; and siliceous metasedimentary rocks of the Cambro-Ordovician Miramichi Group (Poole and Neuman 2003). Fine-grained feldspar-quartz-biotite dikes and pegmatites intrude all rock types within the deposit. The Acadian granites of the Nashwaak Batholith crop out ~1.6 km northwest of the deposit.

The deposit can be divided into three contiguous zones based on host rock, the nature of mineralization, and the orientation of the orebody. The majority of the mineralization is located on either side of the Sisson Shear and is elongated parallel to its strike (Zone III). Both the gabbro and metavolcanic and metasedimentary rocks host mineralization at Zone III. The Ellipse Zone is hosted entirely by the gabbro and quartz diorite and forms a distinctive northwest-trending offshoot to Zone III. Zones I and II contain relatively continuous quartz-wolframite-scheelite-chalcopyrite veins within or immediately adjacent to the Sisson Shear at the northern end of Zone III. Zone III and the Ellipse Zone contain all of the currently defined resource. Previous work demonstrated an overall northwest trend to mineralized veins in a trench that was excavated in Zone I at Sisson (Nast and Williams-Jones 1991), which was supported by limited mapping in two (now backfilled) trenches in Zone III and the Ellipse Zone.

The majority of mineralization is hosted in quartz veins, with some additional scheelite disseminated in narrow alteration envelopes to the veins. The earliest mineralizing event formed very minor disseminated and vein-hosted molybdoscheelite associated with actinolite±magnetite veins with albite alteration envelopes that are generally restricted to mafic rock units. The main phase of mineralization is characterized by quartz-(molybdo)scheelite veins with narrow biotite alteration envelopes. These are overprinted by quartz-molybdenite veins without alteration envelopes. The final stage of mineralization is represented by comparatively thick quartz-sulfide±scheelite ±wolframite veins with a polymetallic signature and sericite alteration envelopes. The age of the deposit is constrained by Re-Os molybdenite model ages of ~375 Ma (D. Lentz and W. Zhang, unpub. data).
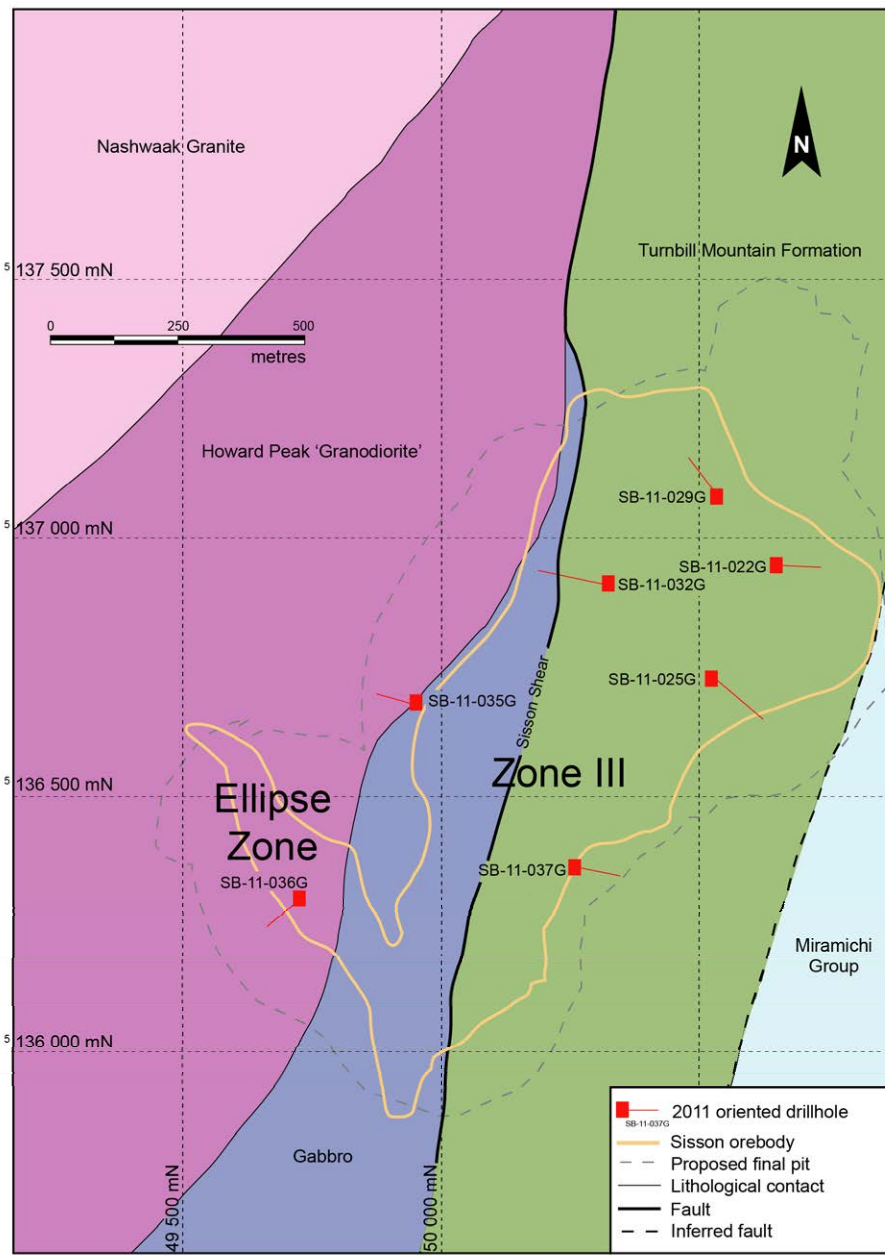
Figure 1. Interpreted simplified geology of the Sisson deposit showing the location of oriented drillholes used in this study.

The Sisson deposit is believed to have a genetic relationship to a felsic, Late Devonian stock, located below the limit of drilling, and presumably associated with granitic and pegmatitic dykes in the deposit area which appear to be syn-mineral in timing (no current age determinations). Early stage molybdoscheelite mineralization has been attributed to the circulation of meteoric or formational waters and low fluid-wallrock ratios (Nast and Williams-Jones 1991), which is consistent with the paucity of strong, pervasive alteration and the low density of quartz veins in the deposit. During the main stage of molybdenum and tungsten precipitation, the fluid signature was dominantly magmatic and subsequent infiltration of meteoric fluids through large open fractures generated the late stage quartz-sulfide veins (Nast and Williams-Jones 1991).

3 Data collection and quality

Alpha and beta measurements (Stanley and Hooper 2003) were taken on whole diamond drill core (seven holes for a total of 1455.2 metres; drilled for geotechnical purposes) using wrap-around linear protractors. Beta measurements were taken using the relative downhole apical measurement. Angles were recorded to the nearest 1° to avoid data clustering. Data quality was maintained by only taking measurements in sections of core where there was good intra- and inter-run continuity of the orientation line (<10° difference in β angle). Measurements were then converted to true dip and dip direction by applying a macro written in Excel that corrected for both the dip and azimuth of the drill hole as measured by downhole surveys and the magnetic declination at the deposit. The data were validated using another conversion program (Stanley and Hooper 2003). The data have been plotted on equal area lower
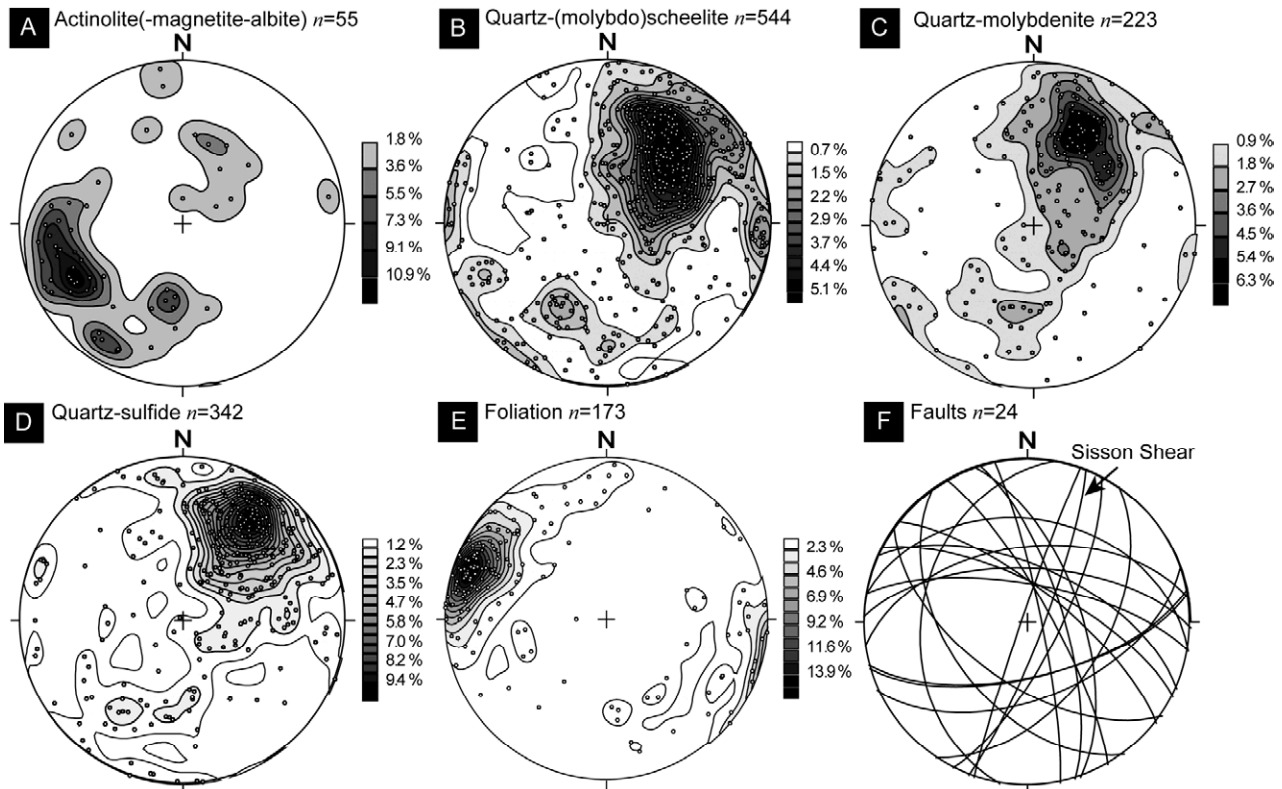
Figure 2. Equal area lower hemispheric stereographic projections for Sisson oriented core data. A-E contoured pole to vein and foliation measurements. F great circles of faults, including the Sisson Shear.

hemispheric stereographic projections and classified according to the vein paragenesis for the deposit (Fig. 2).

4 Vein sets

There is a remarkable consistency in the orientations of each principal vein type at Sisson, with a strong predominance of moderately to steeply southwest-dipping, southeast striking mineralized veins (Fig. 2). This is consistent with previous data (Nast and Williams-Jones 1991). This spatial distribution of veins implies that they formed in response to a constant stress field during a single tectonic event. Veins are discussed below in paragenetic order from early to late.

4.1 Actinolite(-magnetite-albite) veins

Two populations are evident (Fig. 2A), one dips moderately to the north-northeast (40° towards 025°), and the other main population dips moderately to steeply towards the east-northeast (between 50 to 70° towards 070°). The first population appears to be sub-parallel to subordinate groups of overprinting veins, but the main group is sub-parallel to north-northwest striking faults (Fig. 2F).

## 4.2 Quartz-(molybdo)scheelite and quartz-molybdenite veins

One major grouping of quartz-(molybdo)scheelite veins that dips moderately to steeply towards the south-southwest and southwest (50 to 65° towards 210 to 230°; Fig. 2B) is present in all drill holes. The slight variations

in orientation may potentially be associated with distance from shear zones. The influence of faults on the dominant quartz-(molybdo)scheelite vein orientation is demonstrated by the appearance of sub-vertical north-northeast striking veins proximal to the Sisson Shear; this orientation is not seen in drill holes away from the fault. Another set of sub-vertical veins that strike northwest is well developed in the Ellipse Zone and may represent a conjugate set to the overall dominant vein set. This orientation may reflect the presence of north-northwest to northwest striking splays of the Sisson Shear that control the geometry of mineralization in the Ellipse Zone. Data from the southeastern boundary of the deposit are comparatively scattered and this reflects the brecciated nature of rock types encountered during drilling in this area. The main group of these veins in the same area is sub-parallel to the Sisson Shear and therefore a sub-parallel structure may control the location of the orebody boundary.

The overall orientation of quartz-molybdenite veins in the central portion of the deposit is similar to that recorded for quartz-(molybdo)scheelite veins (Fig. 2C). The strongest cluster of quartz-molybdenite veins dips at around 55° towards between 220 and 250°. Adjacent to the Sisson Shear a north-northeast striking vein orientation is also noted, similar to that identified in the quartz-(molybdo)scheelite data. Outside of this central zone groupings of quartz-molybdenite veins are poorly developed; this could reflect simple counting statistics or the fact that molybdenite-bearing veins on the periphery of the deposit are part of a stockwork rather than a sheeted vein system.

4.3 Quartz-sulfide-rich veins

The majority of quartz-sulfide-rich veins dip moderately to steeply to the southwest (Fig. 2D). In the northern
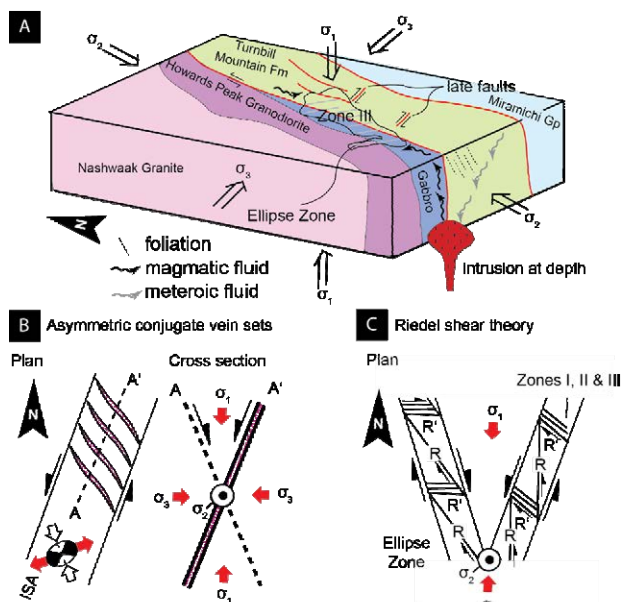
portion of the deposit these veins tend to dip moderately

Figure 3. (a) Summary diagram for the structural setting of mineralization at Sisson where the hydrothermal system was concentrated along the north-south trending Sisson Shear. Internally vein geometry and orientation is best explained by a near vertical maximum principal stress with a sinistral shear component which generated an asymmetric conjugate vein set (summarized in b) rather than a Riedel Shear arrangement (c) that would have meant that veins in the Ellipse Zone and Zone III would not have had the same orientation and that σ_1 would have to be sub-horizontal to explain the arrangement of ore zones.

to the west (080 to 260°). This change in orientation represents proximity to the Sisson Shear and, in the very north part of Zone III, veins of this orientation are laterally persistent and extend north into Zones I and II outside of the orebody.

5 Structural model

The structural data identify three major fault orientations at Sisson. The major orientation dips steeply, and strikes north-northeast parallel to the Sisson Shear (Fig. 3F). The other two groups dip moderately to steeply towards the north-northeast and moderately towards the south-southeast; these fault populations appear to be late, do not correspond with vein orientations and displace the Sisson orebody. Kinematic indicators in faults examined during core logging reveal inconsistent senses of movement which suggests that certain fault segments may have undergone reactivation during post-mineralization tectonic events.

The consistent orientation of the majority of mineralized veins at Sisson demonstrates that they likely formed during one tectonic event. Mineralization in quartz-sulfide veins in Zones I and II had been related to the development of ductile S-C fabrics that were indicative of sinistral shearing (J Oliver, unpub. data).

The mineralization at Sisson formed in a shallow environment in a brittle regime where ductile fabrics would not develop. Therefore, the S-C fabrics record an earlier episode of sinistral movement along north-northeast striking faults sub-parallel to the Sisson Shear. However, the geometry of veins at Sisson and their extensional characteristics are compatible with formation when the principal stress (σ_1) was close to vertical, i.e., crustal extension and normal faulting (Fig. 3). The dominant vein orientations at Sisson are best described as an asymmetric conjugate vein set which developed in a fracture envelope to pre-existing north-south trending shear zones during a period of transtension which generated both normal and sinistral movement across the shears (Fig. 3).

There is no variability between mineralized vein orientation in Zone III and the Ellipse Zone, although the grade block model demonstrates that the overall northwest-trending grade continuity in the Ellipse Zone is controlled by the orientation of the veins themselves and not the geometry of the orebody.

The northwest trend of mineralized veins recognized at Sisson is also present at other deposits and prospects related to Acadian magmatism in the region that are hosted by both intrusive and volcano-sedimentary rock types, including Burnthill, Tin Hill, and Todd Mountain (e.g., Fyffe and Thorne 2008). The predominance of a single vein orientation among these widely-separated deposits implies that fracturing and vein formation were controlled by the same far field stress regime, likely during a single, regionally important metallogenic event.

Acknowledgements

References

Fyffe LR, Thorne KG (2008) Polymetallic deposit of Sisson Brook and Mount Pleasant, New Brunswick, Canada. New Brunswick Lands, Minerals and Petroleum Division, 67p.

Nast HJ, Williams-Jones AE (1991) The role of water-rock interactions and fluid evolution in forming the porphyry-related Sisson Brook W-Cu-Mo deposit, New Brunswick. Econ Geol 86: 302-317.

Northcliff Resources (2013) Northcliff release positive feasibility study. Press release.

Poole WH, Neuman RD (2003) Arenig volcanic and sedimentary strata, central New Brunswick and eastern Maine. Atlantic Geology 38: 109-134.

Stanley CR, Hooper JJ (2003) POND: an Excel spreadsheet to obtain structural attitudes of planes from oriented drillcore. Computers and Geosciences 29: 531-537.

Gold exploration in Iceland

Hjalti Franzson[1], Guðmundur Ómar Friðleifsson[2] & Hallgrímur Jónasson[3]
[1] Iceland GeoSurvey, Grensasvegur 9, 108 Reykjavik, [2] HS Orka hf, Brekkustígur 36, Reykjanesbær, [3] Rannís, Laugavegur 13, 101 Reykjavík

Abstract. Exploration for gold in Iceland commenced in the early twentieth century and then again after 1990. The target areas were exhumed fossil high temperature systems outside the volcanic rift zones. These were explored by using stream sediment, rock and float sampling. Enrichment of gold and pathfinder elements confirmed an association with low-salinity epithermal environments. The most notable anomaly, Thormodsdalur, is a multivein structure of transform character, and is classified as a low sulphidation adularia-sericite epithermal Au-Ag deposit. The Au enrichment in the licence areas varies from less than 0,5 to over 400 ppm. The exploration established the ability of Icelandic low-salinity systems to precipitate gold.

Keywords. Iceland, epithermal, gold

1 Geological Setting

Iceland lies astride the Mid-Atlantic Ridge, and is a basaltic province that is underlain by an anomalous mantle plume. Rifting in the volcanic zones occurs mainly along specific fissure swarms, with a central volcano residing in the centre. Here a wider variety of differentiated rock types occur. Vigorous high temperature hydrothermal systems with temperatures surpassing 300°C and extensive prophylitic alteration are associated with the central volcanoes. These migrate out of the rift zone with time, become extinct and erode due to the repeated glaciations of the last 3 my (Fig. 1). The erosion level of the extinct high temperature systems varies from a few hundred meters to about 2 km. The high-T geothermal systems are dominantly freshwater, but with more saline varieties on the western part of the Reykjanes peninsula (e.g. Harðardóttir 2011). Primary Au concentrations in Icelandic basalts range from 0.5 to about 20 ppb with an average value of 3.6 ppb (Zentilli et al. 1985, Geirsson 1993, Momme et al. 2003). These are higher values than 2 ppb quoted for regular MORB basalts (Peach et al., 2003).

2 History of Gold Exploration in Iceland

Exploration for gold dates back to early 20th century (Kristjánsson 1929, Fridleifsson et al. 1997). The early prospectors were Björn Kristjánsson, a politician and a bank manager, and Einar Benediktsson, a famous poet and entrepreneur who found a number of gold rich locations. The most notable are in Mogilsá north of Reykjavík and in Þormodsdalur (Fig. 1). The latter, a multiple quartz vein was explored by tunnelling and surface excavations. The exploration apparently stopped due to economic recession in Europe during and following the First World War. The gold exploration, however, led to the import of a drillrig that, though unsuccessful in finding gold, initiated the drilling for geothermal water within the limit of Reykjavík (Jónasson, 2006).

A renewed interest in gold exploration started about 1989 when the close connection of thermal activity and gold deposition was realized even in a low salinity environment. This sparked short reconnaissance surveys financed by the Rannis grants and National Energy Authority´s funds, which were then expanded by the companies of Malmis and Sudurvik who made large scale low density reconnaissance surveys in eroded sections of the country. Sudurvík´s licence areas were confined to North and West Iceland. Here we confine ourselves to Malmis which made extensive surveys in many of the exhumed high temperature areas. Figure 2 shows the licence areas that the company held in 2006. Earlier licence areas, which have now been relinquished, include large areas of eastern Iceland (c.f. Fig. 2).
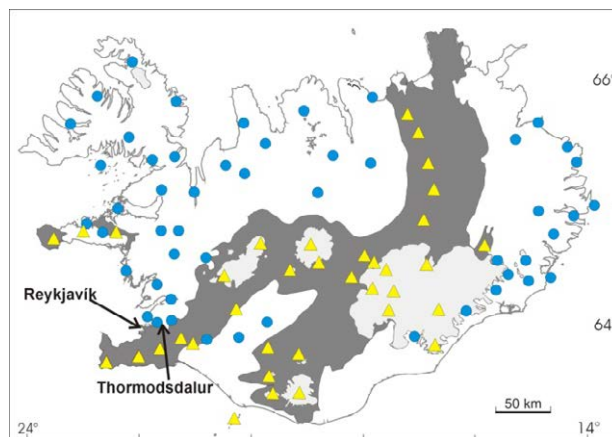
Figure 1. A map of Iceland showing the outline of volcanic zones (dark shade), glaciers (light grey shade), active central volcanoes (yellow triangles) and extinct and exhumed fossil central volcanoes and high temperature systems (blue circles).

3 Malmis/Melmi Exploration

3.1 Regional Surveys

The exploration methods used by the Malmis/Melmi affiliated teams consisted of stream sediment, rock chip and float sampling. The first included low density Bleg and higher density -300 µ sediment fraction analyses for Au, Bi, Sb, Se, and Te. The rock and float samples mostly included hydrothermal veining material within

the prophylitic cores of the geothermal systems. The detection limit was 0.1 ppb Au and above 1 ppb for the pathfinder elements for a large part of the surveys. The laboratories used for analysis included Caleb Brett (UK), aallabs.com and Geol. Surv. Finland. The total number of samples taken for analyses in the main main campaigns surpassed 7000.

The results of the exploration surveys show elevated values of gold and pathfinder elements within the fossil geothermal areas as expected. Rock and float samples show Au values up to 1 ppm in most areas, increasing to approx. 5 and 9 ppm in Hafnarfjall and Mógilsá in the west respectively as indicated in Figure 3. Furthermore a float sample taken in the 2007 field season from the Víðidalur-Vatnsdalur area in the north returned a Au value of 32.6 ppm. The more spectacular Thormodsdalur anomaly is described separately below.

The data presented in this paper is largely taken from unpublished Malmis/Melmi reports (Corbett 2004, Dahl 1997, Fleming et al. 2006, Franzson and Friðleifsson 1992, Franzson and Friðleifsson 1993, Martin and Fleming 2007, Karajas 1998)
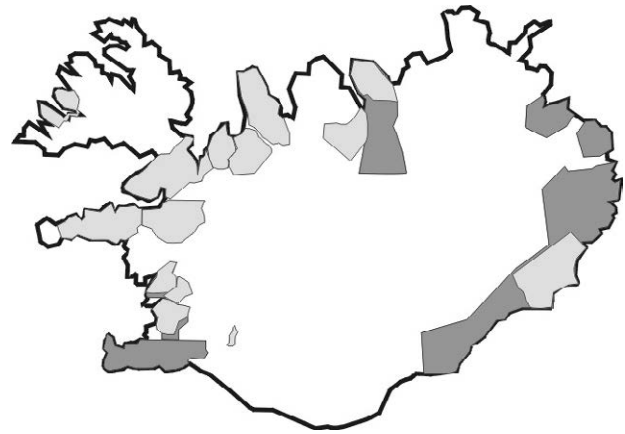

Figure 2. Map of Iceland showing the Malmis/Melmi permits. Early licence areas are dark shaded, and areas retained in 2006 in lighter shade.
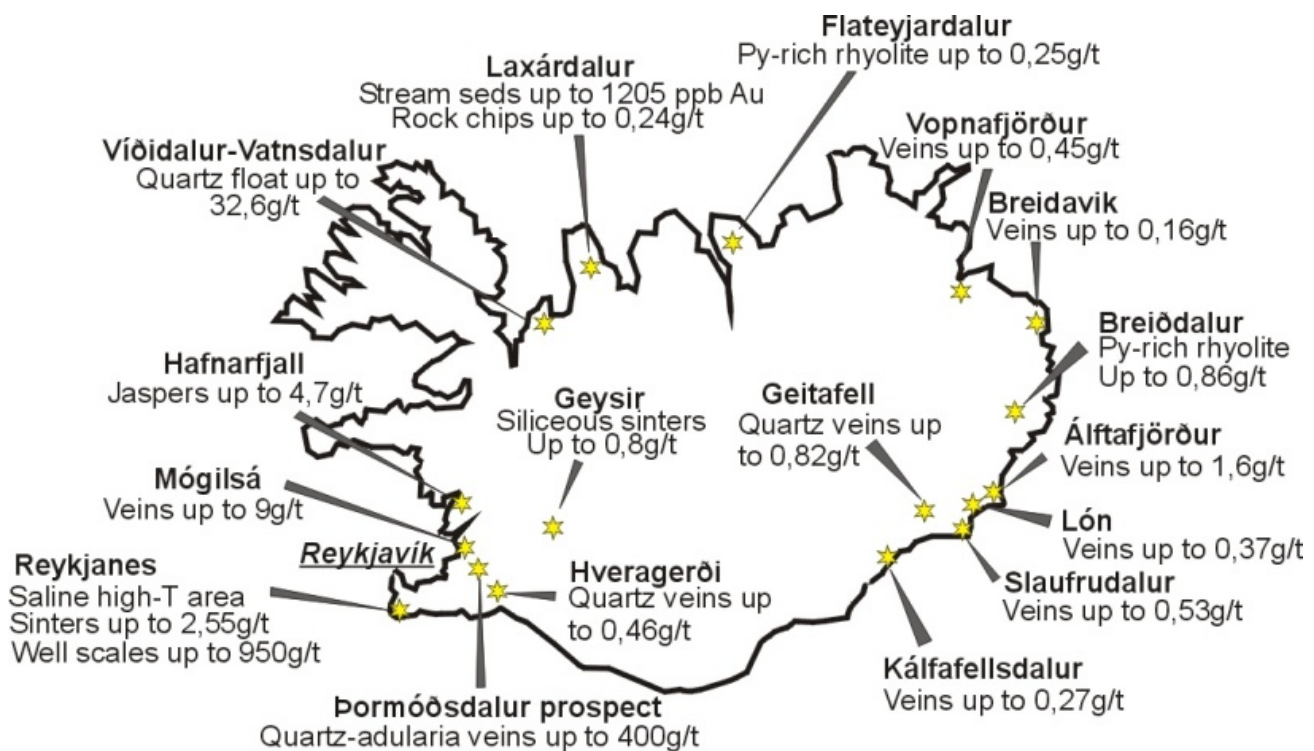

Figure 3. Map of Iceland showing the known gold localities found up to year 2007.

3.2   Thormodsdalur project

The Thormodsdalur project is as yet anomalous in Iceland with respect to gold enrichment. Its location is about 10 km from the outskirts of Reykjavik (Fig. 1). The country rock is dominantly pillow-rich hyaloclastites with subordinate sub-aerial lavas. The strata dips about 12° SE. Volcanically the area may belong to the Stardalur central volcano (1.5-2 m.y.) and is at a 6 km distance from the caldera margin (Friðleifsson 1975). The area is within the chapazite-thomsonite alteration zone indicating a low temperature environment (30-50°C) and a burial depth of 300-500 m. However, borehole data from nearby wells to the north show an underlying prophylitic alteration of a fossil high temperature reservoir, possibly belonging to the late Stardalur central volcano. Presently this is the reservoir to a very productive low-temperature geothermal field.

The area is densely faulted, mostly by NE-SW faults which parallel the rift fractures. More northerly normal faults with a dextral strike slip fault and fracture trends are also evident. Their occurrence may be related to the structural change from normal rift to the hybrid rift-transform environment of the Reykjanes peninsula to the south. The Thormodsdalur structure belongs to the latter northerly trend and is thus of a transform character. The fault has been traced for about 700 m (Fig. 4).

Initial exploration of the locality was made by Einar Benediktsson (see above), with over 300 m of excavations and tunnelling done, and the rock exported to Germany, though reports of the Au content remain speculative (Friðleifsson 1997). The excavations and tunnels were later partly reopened by Malmis/Melmi teams as shown in Figure 4.

Petrographic and XRD studies show an evolution of the vein system from a zeolite assemblage to quartz-adularia and lastly to minor calcite. The Au-enriched zone belongs to the quartz-adularia assemblage. A preliminary SEM study shows Au-grains up to 20 μm. Temperature estimates based on mineral zonation and a minor fluid inclusion study suggests 180-230°C which concurs with a boiling condition of a geothermal system at approx. 300 m depth. A review of the data suggests that the deposit is a low sulphidation adularia-sericite epithermal Au-Ag type (Corbett 2002, 2004). The limited wall rock alteration suggests that this part of the geothermal system may have been short lived but intense.

Thirty two cored wells have been drilled into the vein system totalling 2439 m. These wells extended generally less than 100 m. They indicate significant grades and thicknesses confined to two shoots along the vein structure (Fleming 2006). Further to that a 400 m deep temperature gradient well (HSY-27, see Figure 4) was drilled slightly to the west of the vein system, and intersected Au-enriched veins as deep as 400 m. The Au grade of the veining is variable, which is not surprising considering the mineral evolution discussed above and range from less than 0.5 ppm to a maximum of 415.4 ppm (40 cm core sample in one well).
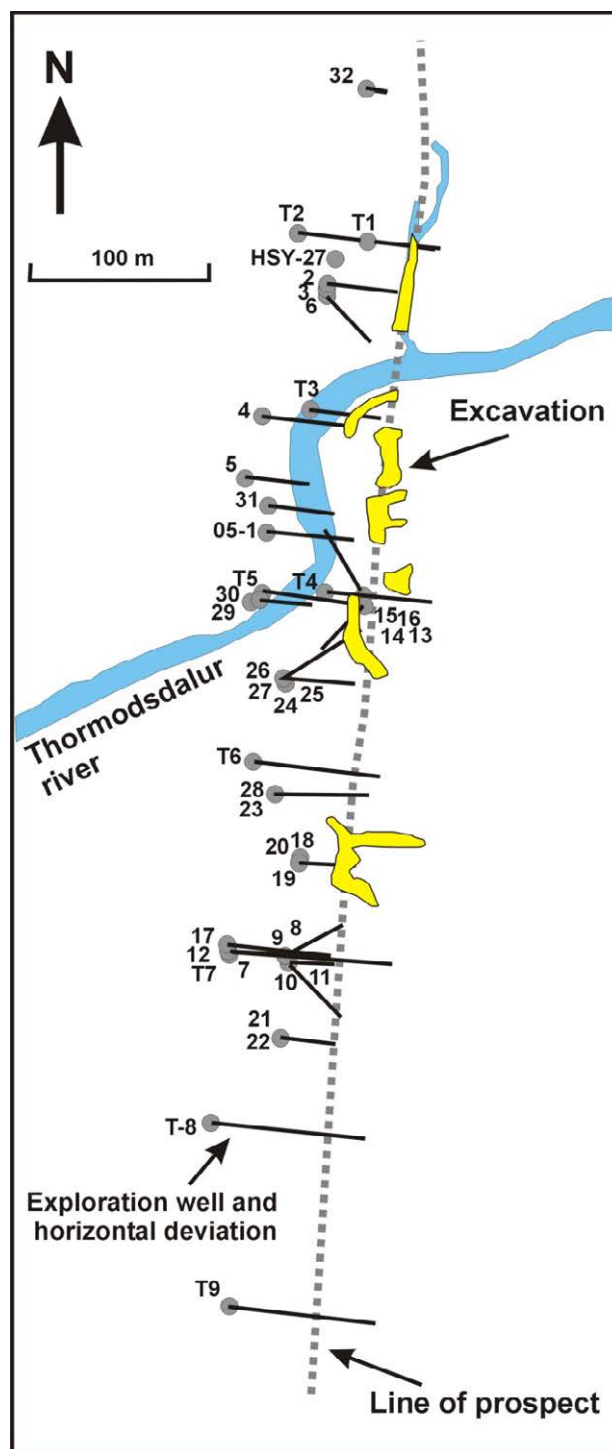

Figure 4. Thormodsdalur prospect. Broken line is the trace of the mineral vein, the yellow patches indicate excavations. The traces of wells shown on the figure are dominantly oblique to the alignment of the mineral vein.

4 Discussion and conclusions

Gold exploration in Iceland during the last two decades has been approached on the grounds of epithermal/ geothermal philosophy and assuming low-salinity systems. This model has been verified. The depth of assumed Au-enrichment in such systems would be found in the upper part of geothermal systems at a temperature range of 200-260°C, particularly where boiling conditions prevail. The erosive levels of the exhumed high-temperature systems outside the volcanic zones in Iceland vary but appropriate alteration levels within such systems were often reached.

Tectonic activity is intense at an oceanic divergent plate boundary such as in Iceland. Assuming a tectonic relation to an epithermal gold rich body, the structure must be assumed to be repeatedly reactivated for an extended time interval within a similar geothermal environment in order to achieve an economical deposit.

Although Malmis/Melmi and Sudurvik have scanned several of the fossil high-temperature areas, these must be considered to be at a reconnaisance level, and would merit further exploration. The results of the gold exploration by Malmis/Melmi can be summarized as follows:

- Regional sampling of stream sediments and rocks have conclusively shown enrichments of gold and associated pathfinder elements in regions of exhumed fossil geothermal systems. Follow up surveys have only partly been done.
- At least three locations have been found where samples of >5 ppm Au occur. By far the most enriched location is Thormodsdalur.
- Thormodsdalur is a 700 m long Au enriched vein system of a transform fault character. The extreme Au enrichment reaching 415 ppm shows the ability of a low-salinity geothermal system to precipitate such deposit.

Acknowledgements

References

Corbett G (2002) Epithermal gold for explorationists: AIG Presidents Lecture, AIG On Line Journal 2002, AIG website www.aig.asn.au

Corbett G (2004) Comments on the prospectivy of the Tyr project, Iceland for epithermal Au-Ag mineralization. Unpublished report for Melmi Ltd. 21 p

Dahl N (1997) Melmi ehf, Reykjanes Permit. Report on Exploration from October 1996 to July 1997. Unpublished Melmi Company Report

Fleming A, Nyman M, Histed R (2006) Technical report on a core drilling program at the Thormodsdalur gold prospect and other exploration by Melmi ltd. 2006. Melmi report 78 p

Franzson H, Fridleifsson GO (1992). Malmis ltd. Exploration for gold and other preious metals. Results of second year of exploration. Unpublished Malmis Company Report

Franzson H, Fridleifsson GO (1993) Malmis ltd. Exploration for gold. Results of third year of exploration. Unpublished Malmis Company Report

Franzson H, Friðleifsson GO, Bjarnason B, Jónasson H (1995) Epithermal gold exploration in Iceland. Water Rock Interaction, ed. Kharaka and Chudaev. Balkema, Rotterdam, 671-674

Franzson H, Friðleifsson GO, Bjarnason B, Jónasson H (1997) Gold exploration in Iceland. Geol. Soc. Iceland, Spring Meeting 26-28 (In Icelandic)

Franzson H, Friðleifsson GO, Jónasson H (2008) Gold exploration in Esja Mountain. Spring Meeting of Geol. Soc. of Iceland. (in Icelandic)

Friðleifsson IB (1975) Petrology and structure of the Esja quaternary volcanic region, Southwest Iceland. PhD thesis from Oxford University, 199 p

Friðleifsson GO, Franzson H, Bjarnason B, Jónasson H, Ros F, Flavelle A, Miller P, Karajas J (1997) Saga gullleitar í Þormóðsdal (history of gold exploration in Thormodsdalur). Geol. Soc. Iceland, Spring Meeting, 23-25 (In Icelandic)

Geirsson K (1993) Pétrologie d´une serie tholéiitique compléte: le volcan central de Fagridalur, nord-est de l´Islande. Unpublished Ph.D thesis, Université Pierre et Marie Curie, Paris, 218 p

Harðardóttir V (2011) Metal-rich scales in the Reykjanes Geothermal System, SW-Iceland: Sulfide minerals in a seawater-dominated hydrothermal environment. PhD thesis Dept. Earth Sciences University of Ottawa. 288 p

Jónasson Þ (2006) Gull og vatn í Reykjavík (Gold and water in Reykjavik). Náttúrufræðingurinn 74:109-117

Kristjánsson B (1929) Um málma á Íslandi (The presence of metals in Iceland). Vaka, 34p (In Icelandic)

Nesbitt BE, St.Luis RM, Muehlenbachs K (1986) Mobility of gold during hydrothermal alteration of basaltic units. Water Rock Interaction, 5:401-404

Peach CL, Mathes EA, Keays RR (1990) Sulfide melt-silicate melt distribution coefficients for noble metals and other chalcophile elements as deduced from MORB: Implications for partial melting: Geochemical et Cosmochimica Acta, 54:3379-3389

Zentilli M, Brooks RB, Helgason J, Ryan DE, Zang H (1985) The dirstribution of gold in volcanic rocks of eastern Iceland. Chem. Geol., 48, 17-48

Proterozoic supercontinents and ore provinces – the Baltica – Amazonia – West Africa link

Åke Johansson
Department of Geosciences, Swedish Museum of Natural History, Box 50 007, SE-104 05 Stockholm, Sweden.

Abstract. According to the SAMBA model, Baltica, Amazonia and West Africa formed one coherent landmass from at least 1.8 Ga to at least 0.8 Ga, and perhaps until 0.6 Ga, as part of the Columbia (Nuna) and Rodinia supercontinents. Geological correlation between these now dispersed cratons could have important implications for exploration of Precambrian ore deposits in these regions of the world. Late Archean BIF deposits in Ukraina, Liberia and Venezuela may have formed in close connection of each other, and early Paleo-proterozoic gold deposits in Guyana and Venezuela would form a continuation of the Ashanti gold belt in Ghana. There may also be connections between the ore-bearing 1.9-1.75 Ga Svecofennian province of Baltica and the Ventauri-Tapajos province of Amazonia. Further west, the Sveconorwegian province of SW Baltica corresponds to the Sunsas and Rondonian provinces in Amazonia with their tin-bearing granites. Although granites of similar age are present in SW Baltica, they are apparently devoid of tin mineralization.

Keywords. SAMBA model, ore deposits, Baltica, Amazonia, West Africa, Archean, Proterozoic, Columbia, Rodinia.

1. Baltica, Amazonia and West Africa correlation in the SAMBA model

Reconstructions of past supercontinents may be of importance when tracing ore provinces from one continent to another, and thus of potential interest for prospectors. Conversely, the continuation of ore trends and ore provinces from one continent to the other may lend additional support to such reconstructions. Recently, a model was suggested, based on geological correlation, where Baltica, Amazonia and West Africa formed a coherent landmass throughout much of the Proterozoic, from at least 1.8 Ga to at least 0.8 Ga, and possibly until 0.6 Ga, with northwest Amazonia attached to the southwest margin of Baltica (along the future Trans-European suture zone), and the present-day west coast of West Africa attached to the southern margin (Black Sea – Caspian Sea margin) of Baltica (The SAMBA configuration; Johansson 2009). In this configuration, West Africa, together with the small Sao Luis craton in NE Brazil, would be shifted "westwards" relative to Amazonia, with the Sao Luis craton adjacent to Surinam. West Africa, eastern Amazonia, and southeastern Baltica (Sarmatia) would have formed a landmass with Archean nuclei welded together by early Paleoproterozoic mobile belts during the Eburnean / Transamazonian orogeny at 2.2 – 2.0 Ga. To the present-day west or southwest, Baltica and Amazonia formed a continuation of the Laurentian active continental margin, with addition of sequentially younger orogenic belts towards the west, ending with the Grenville-age (1.2 – 0.9 Ga) Sunsas and Sveconorwegian orogens in Amazonia and Baltica, respectively (Fig. 1).

Together with Laurentia, the Baltica – Amazonia – West Africa landmass formed part of the Paleo- to Meso-proterozoic supercontinent Columbia (also known as Nuna). After break-up at around 1.25 Ga, Baltica together with Amazonia and West Africa rotated at least 75° clockwise relative to Laurentia (possibly more, depending on the preceeding Laurentia-Baltica configuration), and collided with Laurentia's Grenville margin as part of the Grenvillian – Sunsas – Sveconoregian orogeny, leading to the formation of the Rodinia supercontinent (Fig. 2). This configuration may have persisted until c. 0.6 Ga, when Laurentia, Baltica and Amazonia separated from each other, and West Africa shifted its position relative to Amazonia.

2. Ore deposits within a SAMBA framework

Major Archean iron ore deposits within this region include the Sör-Varanger deposit in northernmost Norway, and the Carajas deposit in the Central Amazonian province of Brazil. However, during the Archean, these regions may have been equally far apart as today, as the Columbia supercontinent was not yet assembled, and the SAMBA configuration did not exist at that time. Even within the SAMBA configuration, they are located c. 4500 km:s apart. However, Archean domains within the Ukrainian shield (Sarmatia, southeast portion of the not yet assembled Baltica), the Archean Kenema-Man domain in West Africa, and the Imataca belt in northern Amazonia, which were located closely together in the SAMBA configuration (Figs. 1-2), may have formed a coherent unit already in late Archean time. This area is also characterized by late Archaean banded iron formation deposits, such as the Nimba deposit on the border between Liberia and Guinea (Berge 1974) and the deposits of the Cerro Bolivar district in the Imataca belt of Venezuela (e.g. San Isidro deposit; Ferencic 1969), as well as the Krivoy Rog ("Kryvyi Rig" in Ukrainian) deposit in Ukraina (Kulish et al. 2002; Stepanyuk et al. 2011), also believed to be late Archean in age (L. Shumlyanskyy, pers. com. 2013). If these areas were united already in late Archean time, the above deposits would have been located only about 1000 km apart during their formation.

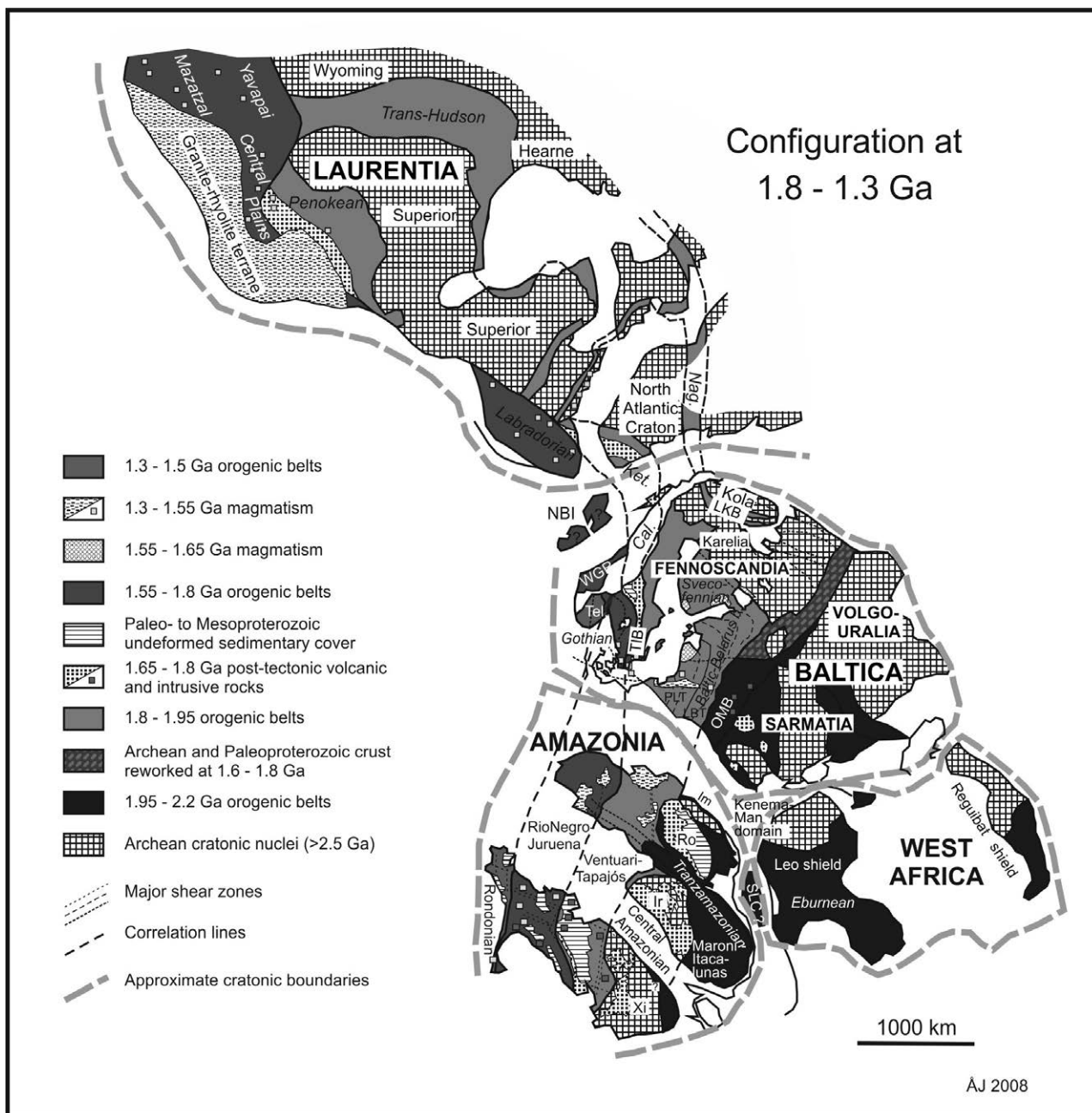Ghana in West Africa is famous for the early

Figure 1. Proposed fit of Laurentia, Baltica, Amazonia and West Africa during the 1.8 to 1.3 Ga time period (Columbia configuration) according to the SAMBA model of Johansson (2009). Names of orogenic belts in italics, names of proto-cratons and other geological provinces in normal letters, names of major cratons and cratonic segments in capitals. Abbreviations: Nag = Nagssugtoqidian belt, Ket = Ketilidian belt, NBI = Northern British Isles, LKB = Lapland-Kola Belt, WGR = Western Gneiss Region, Tel = Telemarkia, TIB = Transscandinavian Igneous Belt, PLT = Polish-Lithuanian Terrane, LBT = Lithuanian-Belarus Terrane, OMB = Osnitsk-Mikashevichi Belt, SLC = São Luis Craton, Ro = Roraima Block, Xi = Xingu block, Ir = Iricoumé Block, Im = Imataca belt.

Paleoproterozoic vein and stockwork gold deposits of the Ashanti gold belt (e.g. Obuasi; Yao and Robb 2000), which may extend via the Sao Luis craton (now located in NE Brazil, but at that time sandwiched between Surinam and the Ivory Coast) with the Caxias gold deposit (Klein et al. 2002a) into Guyana (e.g. Omai; Voicu et al. 2000) and Venezuela (e.g. Las Cristinas) in South America.

In the Fennoscandian part of Baltica, the 1.9 – 1.75 Ga Svecofennian province is rich both in iron deposits (e.g. Kiruna and Malmberget in northern Sweden, Dannemora

in central Sweden), copper (Aitik in northern Sweden), and volcanite-hosted massive sulfide Cu-Zn-Pb (Skellefte and Bergslagen ore districts in Sweden and their counterparts in Finland), as well as orogenic gold in quartz veins (e.g. Björkdal in the Skellefte district). Most of these deposits are related to 1.91 – 1.87 Ga arc-related magmatism in northern and central Sweden and southwest Finland (For an overview of Fennoscandian ore deposits and further references, see Weihed et al. 2005). The similarly aged Ventauri-Tapajos province in central Amazonia, which would be the continuation of
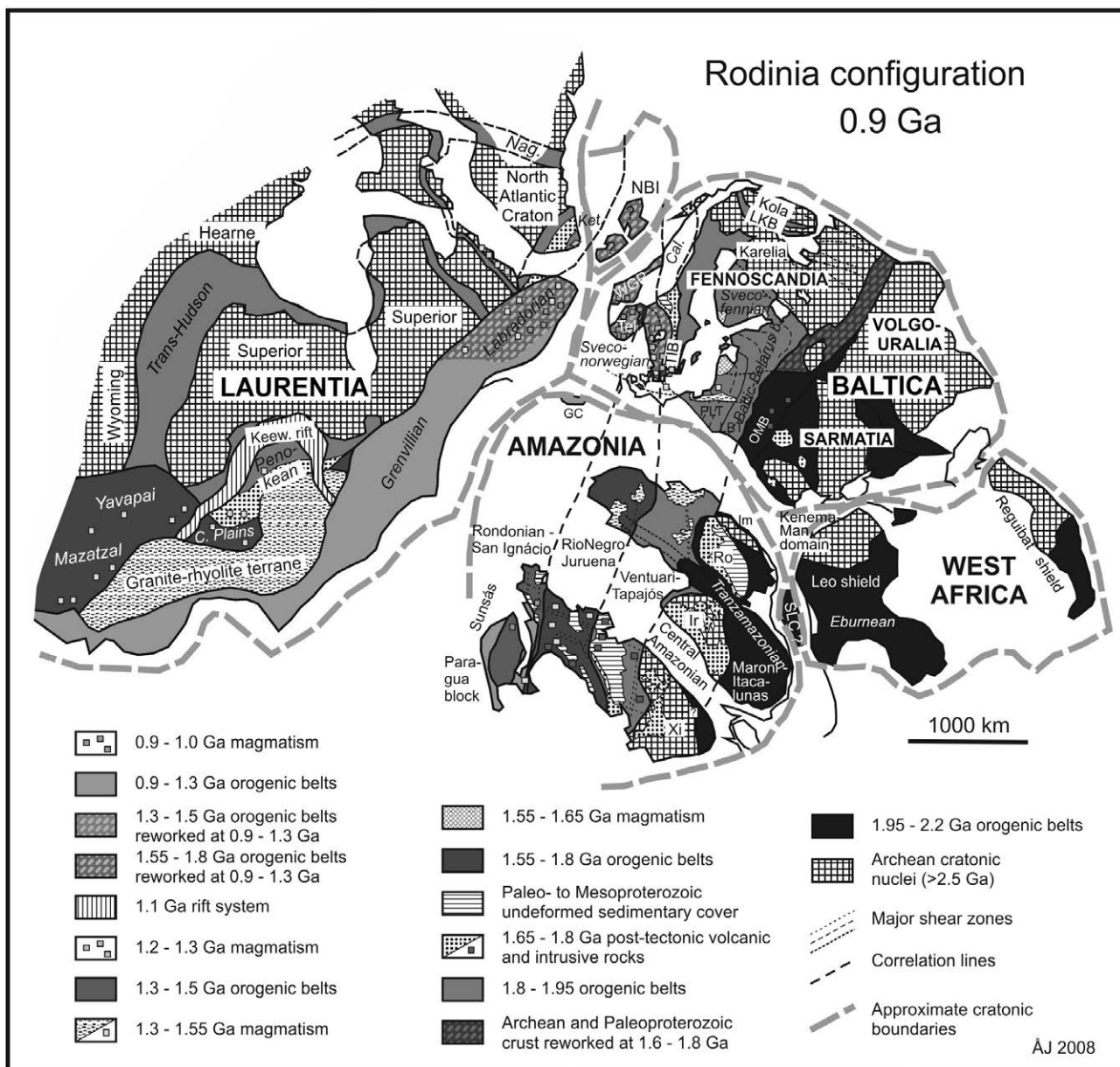
Figure 2. Proposed fit of Laurentia, Baltica, Amazonia and West Africa at 0.9 Ga (Rodinia configuration) from Johansson (2009). Abbreviations as in Figure 1; additional abbreviations: Keew. rift = Keewanawan rift, GC = Garzon Complex.

the Svecofennian province according to the SAMBA reconstruction, would hence be a good target in searching for similar deposit types. At present, the main deposit type encountered there seems to be gold in gold in quartz veins within the Tapajos and Alta Floresta domains (Santos et al. 2001; Klein et al. 2002b). Copper-gold and tungsten mineralization related to c. 1.88 Ga granitoids occur within the Archean bedrock of the Carajas district in central Brazil (Teixeira et al. 2007, who provide an overview of South American ore deposits with further references, but with the Paleoproterozoic deposits put in the somewhat different supercontinent context of "Atlantica").

The Sunsas province of southwest Amazonia is the host of the Grenville-age Rondonian tin granites, with associated vein-type and greisen mineralization of tin (e.g. Priem et al. 1971). However, no similar tin

mineralization is known to be associated with Sveconorwegian granites in SW Sweden and southern Norway, which would be the corresponding province in Baltica. Either tin mineralization never extended this far "north", or it has been removed by subsequent erosion, since a deeper erosional level may be exposed in the Sveconorwegian province of Baltica. Apart from minor Cu mineralization in shales and vein-type base metal and gold mineralization, the Sveconorwegian province hosts the major Tellnes Ti deposit within anorthosite of the 0.92 Ga Rogaland igneous complex in southern Norway (Weihed et al 2005). Older rock units (e.g. 1.70 – 1.55 Ga Gothian, 1.45 – 1.40 Ga Hallandian) within the same province seem generally devoid of associated mineralization.

References

Berge JW (1974) Geology, geochemistry, and origin of the Nimba itabirite and associated rocks, Nimba county, Liberia. Econ Geol 69:80-92.

Ferencic AJ (1969) Geology of the San Isidro iron ore deposit, Venezuela. Miner Deposita 4:283-297.

Johansson Å (2009) Baltica, Amazonia and the SAMBA connection – 1000 million years of neighbourhood during the Proterozoic? Prec Res 175:221-234.

Klein EL, Koppe JC, Moura CAV (2002a) Geology and geochemistry of the Caxias gold deposit, and geochronology of the gold-hosting Caxias microtonalite, Sao Luis Craton, northern Brazil. J S Am Earth Sci 14:837-849.

Klein EL, Vasquez ML, da Rosa-Costa LT, de Azevedo Carvalho JM (2002b) Geology of Paleoproterozoic gneiss- and granitoid-hosted gold mineralization in southern Tapajos gold province, Amazonian Craton, Brazil. Int Geol Rev 44:544-558.

Kulish EO, Voinovsky AS, Komov IL, Lebid MI (2002) Geology and metallogeny of ferrous metal (Fe, V, Cr, Mn) deposits of the Ukrainian Shield's Precambrian. Mineral J (Ukraine) 24:16-25.

Priem HNA, Boelrijk NAIM, Hebeda EH, Verdurmen EATh, Verschure RH, Bon EH (1971) Granitic complexes and associated tin mineralization of 'Grenville' age in Rondonia, western Brazil. Geol Soc Am Bull 82:1095-1102.

Santos JOS, Groves DI, Hartmann LA, Moura MA, McNaughton, NJ (2001) Gold deposits of the Tapajos and Alta Floresta Domains, Tapajos-Parima orogenic belt, Amazon Craton, Brazil. Miner Deposita 36:278-299.

Stepanyuk LM, Bobrov OB, Paranko IS, Ponomarenko OM, Sergeev, SA (2011) Genesis and age of zircon from amphibolite of new Kryvyi Rig suite of the Kryvyi Rig structure. Mineral J (Ukraine) 33:69-76.

Teixeira JBG, Misi A, Silva MG (2007) Supercontinent evolution and the Proterozoic metallogeny of South America. Gondwana Res 11:346-361.

Voicu G, Bardoux M, Stevenson R, Jebrak M (2000) Nd and Sr isotope study of hydrothermal scheelite and host rocks at Omai, Guiana Shield: implications for ore fluid source and flow path during the formation of orogenic gold deposits. Miner Deposita 35:302-314.

Weihed P, Arndt N, Billström K, Duchesne J-C, Eilu P, Martinsson O, Papunen H, Lahtinen R (2005) Precambrian geodynamics and ore formation: The Fennoscandian Shield. Ore Geol Rev 27:273-322.

Yao Y, Robb LJ (2000) Gold mineralization in Palaeoproterozoic granitoids at Obuasi, Ashanti region, Ghana: Ore geology, geochemistry and fluid characteristics. S Afr J Geol 103:255-278.

Principal geologic and tectonic events and mineralization in the northern margin of the North China Craton

Jian-min Liu, Yue Zhao, Shu-wen Dong, Shuan-hong Zhang
Institute of Geodynamics, Chinese Academy of Geological Sciences, Beijing, 100081, China

Guo-hui Hu
Guangzhou Institute of Geochemistry, Chinese Academy of Sciences, Guangzhou, 510640, China

Abstract. The northern margin of the North China craton has abundant supplies of multi-metal resources. The mineralization mainly occurred in four different geological times, which corresponding with the principal geologic and tectonic events. They are as follows: (1) 1800 Ma for the formation of the banded iron, gold, copper-zinc in the greenstone rocks, and lead – zinc mineralization in metasediments; (2) 800 Ma for the lead – zinc - copper and REE (iron) deposits in the submarine volcanic sedimentary rocks, as well as the mafic - ultramafic magmatic vanadium – titanium – magnetite deposits; (3) 280 – 340 Ma for the porphyry gold-copper (molybdenum) deposit, mafic - ultramafic magmatic copper – nickel deposit; gold deposit in ductile shear belt; and (4) 130 – 180 Ma for the skarn copper deposits, lead-zinc deposits; lode gold, silver, lead-zinc and copper deposits by hydrothermal process, porphyry copper – molybdenum deposit, altered and lode gold deposits.

Keywords Geologic and tectonic events, Mineralization, Northern margin, North China craton

1 Introduction

The North China craton (NCC) is one of the old continents in the world with a complex geological history from the Archean era to the present. The northern margin of the NCC has been one of the most important exploration regions in China for the past few decades because of the abundant multi - metal mineralization. It is essential for the exploration and assessment to understand the relationship between the principal geologic and tectonic events and the corresponding mineralization in the northern margin of the NCC.

2 Principal Geologic and Tectonic Events and Mineralization

The northern margin of the NCC is bounded to the north by the Paleozoic Bainiaomiao - Ongniud accretionary belt, a part of the Central Asian Oceanic Belt (CAOB), and it is separated from it by the NEE – SWW – trending Chifeng – Bayan Obo fault zone (Xiao et al. 2003) (Fig 1). The NCC is a Precambrian craton that is believed to have been stabilized at around 1.85 Ga (Zhao et al. 2001; Wilde et al. 2002). The basement of the NCC is composed of highly metamorphosed Neoarchean and Paleoproterozoic rocks that are partly covered by thick marine clastic and carbonate platformal sediments of Meso – Neoproterozoic and Paleozoic age (Cui et al. 2000), especially in the southeast. Traditionally, the NCC has been considered to have been stable from Neoproterozoic through Triassic times (Ren et al. 1990, Song 1999). However, recent geological and geochronological data reveal that a major break-away took place inside the crystalline basement around 1.30 Ga, which was related to the breakup of Columbia supercontinent with the large volumes of 1.35 – 1.30 Ga mafic sill (dyke) swarms in northern NCC (Zhang et al. 2009). Meanwhile, the northern NCC had also been strongly affected by the Paleo – Asian tectonic domain from at least the Late Paleozoic (Davis et al. 2001, Xiao et al. 2003, Zhang et al. 2007b, 2009a), with the emplacement of voluminous intrusions. Xiao et al. (2003) and Zhang et al. (2009a) proposed that the northern margin of the NCC was an Andean-style active continental margin during the Late Carboniferous to Early Permian.

Since late Mesozoic time, the regional tectonic system in east China and the northern NCC has undergone a considerable transformation (Zhao 1990, Zhao et al. 2004). The general trend of the tectonic system changed from dominantly NEE – SWW in the early Mesozoic to dominantly NE – SW and / or NNE - SSW in the late Mesozoic and early Cenozoic. Most mountain ridges in east
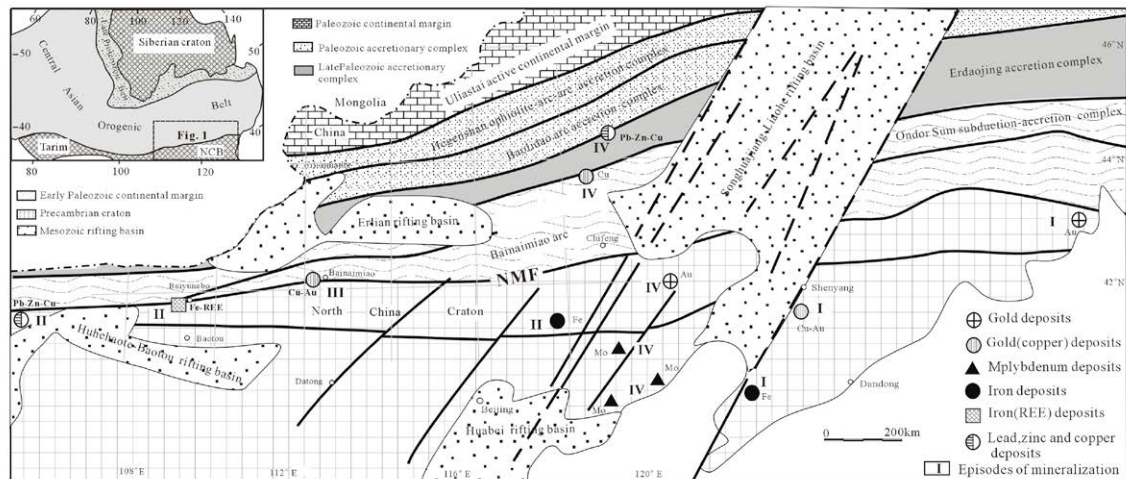
Figure 1. Simplified tectonic framework and distribution of the main large deposits in the northern margin of North China craton

China have NE – SW and / or NNE – SSW trends, as do major fault zones. Although the mechanism for this change is still controversial, most researchers attribute it to major lithospheric thinning and crustal extension during the Jurassic and Early Cretaceous in east China (e.g. Griffin et al. 1998, Webb et al. 1999, Davis et al. 2001, Wu et al. 2002, 2005, Darby et al. 2004). The extensive distribution of Middle-Late Jurassic and Early Cretaceous alkali A-type granite supports this hypothesis.

Based on geological and isotopic data, the principal tectonic evolution in the northern margin of the NCC can be divided into four episodes: (1) 3000-1800 Ma for the formation of cratonic basement with high grade metamorphic and deformation. It is mainly composed of a series of rock assemblage, e.g. the trondhjemite – tonalite – granodiorite (TTG), granite greenstone belt, mafic and ultra - mafic intrusives; (2) 1800-600 Ma for the rifting and development of large aulacogen inside the craton with voluminous diabases. This episode consists of the anorthosite – gabbro – norite, diabase sill, and carbonatite-alkali basalt etc. (3) 600-250 Ma for the formation of trench – arc – basin systems with a series of ENE – WSW – trending thrust – fold and ductile shearing deformation by the southward subduction of the Paleo – Asian Ocean. This episode is composed of an assemblage of ophiolitic suites, mafic – ultramafic intrusives, voluminous granite – granodiorite – diorite – monzonites, and submarine mafic – ultramafic volcanic rocks with the spilite – keratophyre sequence and pillow lava. (4) 250-65 Ma for the formation of various ENE – WSW and NNE – SSW trending folds, thrust-folds, ductile – shearing tectonics, decollement structure by the westward subduction of the Pacific plate and southeastward subduction of the Paleo – Okhotsk ocean, which was characterized by intracontinental compressional orogenese. It has an assemblage of the multiperiodic volcanic eruptions with abundant mafic-intermediate-acidic volcanic rocks and voluminous granite – granodiorite – diorite – monzonite – syenite – alkali series intrusions with minor mafic – ultramafic intrusives and alkali volcanic rocks.

The northern margin of the NCC has been proved to be a large prospective region for the multi-metal mineralization. It hosts a series of major gold, copper, molybdenum, lead – zinc, iron and REE deposits. Four principal mineralization episodes have been established as follows:

(1) 1800 Ma for the formation of the banded iron, gold, copper – zinc in the greenstone rocks, and lead – zinc mineralization in metasediments.

(2) 800 Ma for the lead – zinc – copper and REE (iron) deposits in the submarine volcanic sedimentary rocks, as well as the mafic – ultramafic magmatic vanadium – titanium – magnetite deposits.

(3) 340-280 Ma for the porphyry gold – copper (molybdenum) deposit, mafic – ultramafic magmatic copper – nickel deposit; gold deposit in ductile shear belt.

(4) 180-130 Ma for the skarn copper, lead – zinc deposits; lode gold, silver, lead-zinc and copper deposits by hydrothermal process, porphyry copper-molybdenum deposit, altered and lode gold deposits.

The principal geologic and tectonic events and the corresponding mineralization in the northern margin of the NCC are summarized in Table 1.

TABLE 1 Summary of Principle Geologic Stages and Events in the North Margin of North-China Craton

Age (Ma)	Tectonic events	Rock assemblages	Mineralization assemblages
3000 – 1800	Formation of the cratonic basement with High grade metamorphic and deformation	(1) TTG; (2) Granite greenstone belt; (3) Mafic and ultra – mafic intrusive	(1) Banded iron, Au, Cu – Zn deposits in the Green – stone; (2) Pb – Zn deposits in the meta – volcano - sedimentary rocks
1800 – 600	Rifting and Development of large aulacogen inside the craton with voluminous diabase	(1) Anorthosite – gabbro - norite; (2) Diabase sill; (3) Carbonatite – alkalibasalt	(1) Volcanosedimentary Pb – Zn and REE (Fe) deposits; (2) mafic – ultramafic magmatic V – Ti – Fe deposit
600 – 250	Formation of trench – arc - basin systems and NEE – SWW – trending thrust-fold and ductile shearing deformation by the southward subduction of Paleo – Asian Ocean	(1) Ophiolitic suite; mafic – ultramafic intusives; voluminous; (2) Granite – granodiorite – diorite - monzonite assemblages. Submarine (3) Mafic – ultramafic volcanic rocks with the spilite – keratophyre sequence and pillow lava	(1) Porphyry Au – Cu(Mo) deposit; (2) Mafic – ultramafic magmatic Cu – Ni deposit; (3) Au deposit in ductile shear belt; (4) Cr (Chromite) deposit in the Ophiolitic suite
250 – 65	Intracontinental compressional orogeneses with the various NEE–SWW and NNE – SSW trending folds, thrust – folds, ductile – shearing tectonics, decollement structure folds by the westward subduction of the Pacific plate and southeastward subduction of the Paleo – Ehuocike ocean	(1) Voluminous granite – granodiorite – diorite – monzonite – syenite –alkali series with minor mafic – ultramafic intrusive; (2) Multiperiodic volcanic eruption with abundant mafic – intermediate – acidic volcanic rocks and minor alkali volcanic rocks.	(1) Skarn Cu,Pb – Zn deposits; (2) Vein Au, Ag, Pb, Zn, Cu deposits by hydrothermal process; (3) Porphyry Cu – Mo deposit; (4) Altered and lode gold deposits
0 – 65	Intracontinental extensional orogeneses with the strong NNE – SSW trending rifting and basin-mountain ridges	Local alkaline – calc – alkali flood basalt with minor diabase vein	Alluvial gold deposits

3 Discussion

It is generally accepted that the large scale mineralization is associated with some specific tectonic events. For example, porphyry and hydrothermal replacement deposits generally occur in two main tectonic settings within orogenic belts; in island arcs or near continental margins (McMillan and Panteleyev 1988).

As stated above, the northern NCC had historically undergone several major geologic and tectonic events, especially those at 3000-1800 Ma, 1800-600 Ma, 600-250 Ma and 250-60 Ma, not only did a variety of specific structural deformation and rock assemblages form with each event, but also the unique mineralization. For example, most of the banded iron deposits mainly occurred in the Neoarchean metavolcanic rocks with the characteristic rheomorphic folds. Some of the early large Au, Cu, Pb and Zn deposits mainly developed in the granite – greenstone rocks, especially in the metavolcano – sedimentary rocks. These deposits can be defined as the first episode of mineralization (No.1 in Fig.1). Similarly, the super large scale Fe (Nb) – REE deposit at Bayan Obo and some of large Pb – Zn deposits were mainly formed by rifting and a large scale magmatic intrusion during 1800-600 Ma as the second episode of mineralization.

At the end of Early Paleozoic, the Bainaimiao island arc was accreted to the NCC and brought about a series of alkaline complexes and the Bainaimiao copper – gold deposit (i.e. the third episode of mineralization) (Zhang et al. 2006).

One of the most important mineralizing episodes was during the Late Permian to late Mesozoic (180-80 Ma), with many large scale skarn Cu, Pb – Zn deposits, lode Au, Ag, Pb – Zn deposits formed by hydrothermal processes, and porphyry Cu – Mo deposits. This episode has been referred to as the Mesozoic metallogenic explosion (Mao et al., 1999). Most of those deposits mainly occurred along a series of NNE – SSW fault systems and proved to be genetically related with the occurrence of large voluminous inter mediate – acid - alkaline granite intrusions which formed by major lithospheric thinning and crustal extension during the Jurassic and Early Cretaceous in east China.

To sum up, the major episodes of mineralization in northern NCC was genetically related with the principal tectonic events. However, it must be pointed out that many deposits were generated not by a single tectonic event, but several, as for the Bayan Obo REE deposit (Kynicky et al. 2012) and other deposits (Zhao et al. 2012).

Acknowledgements

References

Cui SQ, Li JR, Sun JS, Wang JP, Wu ZH, Zhu D.G（2000）Sequences of tectonic movement and regional tectonic framework of north margin of the North China Plate. Beijing, Geological Publishing House (in Chinese with English summary)

Darby BJ, Davis GA, Zhang X, Wu F, Wilde S, Yang J（2004）The newly discovered Waziyu metamorphic core complex, Yiwulushan, western Liaoning Province, North China. Earth Science Front 11:145–155

Davis GA, Zheng YD, Wang C, Darby BJ, Zhang CH, Gehrels, GE(2001) Mesozoic tectonic evolution of the Yanshan fold-and-thrust belt with emphasis on Hebei and Liaoning Provinces, northern China. In: M.S. Hendrix and G.A. Davis, Editors, Paleozoic and Mesozoic Tectonic Evolution of Central Asia: From Continental Assembly to Intracontinental Deformation. Geological Society, America Memoir 194:171–198

Griffin WL, Zhang A, O'Reilly SY, Ryan CG (1998) Phanerozoic evolution of the lithosphere beneath the Sino-Korean Craton. In: M.F.J. Flower, S.L. Chung, C.H. Lo and T.Y. Lee, Editors: Mantle Dynamics and Plate Interaction in East Asia. Geodynamics Series 27, American Geophysical Union 107–126

Kynicky J, Smith PM, Xu C (2012) Diversity of rare earth deposits: The key example of China. ELEMENTS 8:361-367

Mao JW, Hua RM, Li XB (1999) A preliminary study on large scale metallogenesis and large clusters of mineral deposits. Mineral Deposits 18:291–299 (in Chinese with English abstract)

McMillan W J and Panteleyev A (1988) Porphyry copper deposits. In: R.G. Roberts and P.A. Sheahan, Editors, Geoscience Canada Reprint Series vol. 3:52–63

Ren J, Chen T, Niu B, Liu Z, Liu F (1990) Tectonic Evolution of the Continental Lithosphere and Metallogeny in Eastern China and Adjacent Area (in Chinese). Beijing, Science Press

Song H (1999) Characteristics of Yanshan type intraplate orogenic belts and a discussion on its dynamics (in Chinese with English abstract). Earth Science Frontier 6:309–316

Webb LE, Graham SA, Johnson CL, Badarch G, Hendrix MS (1999) Occurrence, age, and implications of the Yagan–Onch Hayrhan metamorphic core complex, southern Mongolia. Geology, 27:143–146

Wilde SA, Zhao GC, Sun M (2002) Development of the North China craton during the Late Archaean and its final amalgamation at 1.8 Ga; some speculations on its position within a global Palaeoproterozoic supercontinent. Gondwana Research 5: 85–94

Wu FY, Lin JQ, Wilde S, Zhang XO, Yang JH (2005) Nature and significance of the Early Cretaceous giant igneous event in eastern China. Earth and Planetary Science Letters 233:103–119

Wu FY, Sun D, Li H, Jahn B, Wilde S (2002) A-type granites in northeastern China: age and geochemical constraints on their petrogenesis. Chemical Geology 187:143–173

Xiao W, Windley BF, Hao J, Zhai MG (2003) Accretion leading to collision and the Permian Solonker suture, Inner Mongolia, China. Termination of the central Asian orogenic belt. Tectonics 22, 1069. doi: 10.1029/2002TC001484

Zhang SH, Zhao Y, Song B (2006) Hornblende thermobarometry of the Carboniferous granitoids from the Inner Mongolia Paleo-uplift: Implications for the geotectonic evolution of the northern margin of North China block. Mineralogy and Petrology, 87:123–141

Zhang SH, Zhao Y, Song B, Hu JM, Liu SW, Yang YH, Chen FK, Liu XM, Liu J (2009a) Contrasting Late Carboniferous and Late Permian–Middle Triassic intrusive suites from the northern margin of the North China craton: Geochronology, petrogenesis, and tectonic implications. Geological Society of America Bulletin 121: 181–120

Zhang SH, Zhao Y, Song B, Yang ZY, Hu JM, Wu H (2007b) Carboniferous granitic plutons from the northern margin of the North China block: Implications for a late Paleozoic active continental margin. Journal of the Geological Society, London 164:451–463

Zhang SH, Zhao Y, Yang ZYu, He ZF, Wu H (2009) The 1.35 Ga diabase sills from the northern North China Craton: implications for breakup of the Columbia (Nuna) supercontinent. Earth and Planetary Science Letters. 288(3–4): 588–600

Zhang ZL, Zeng QD, Qu WJ, Liu JM, Sun XG, Zhang RB, Chen WJ, Qin F (2009) The molybdenite Re-Os dating from the Nianzigou Mo deposit, Inner Mongolia and its geological significance. Acta Petrologica Sinica 25:212–218 (in Chinese with English abstract)

Zhao GC, Wilde SA, Cawood PA, Sun M (2001) Archean blocks and their boundaries in the North China craton: Lithological, geochemical, structural and *P-T* path constraints and tectonic evolution. Precambrian Research 107:45–73

Zhao Y (1990) The Mesozoic orogenics and tectonic evolution of the Yanshan Area. Geological Review 36:1–13 (in Chinese with English abstract)

Zhao Y, Zhang SH, Xu G, Yang ZY, Hu JM (2004) The Jurassic major tectonic events of the Yanshanian intraplate deformation belt. Geological Bulletin of China 23, 854–863 (in Chinese with English abstract)

Zhao Y, Liu JM, Dong FM, Zhang SH, Chen BL, Wang ZX (2012) The ore-forming regularity and exploration of the gold (silver) and multi-metal deposits on the middle-eastern parts of the northern North China Block. Beijing, Geological publishing Press (in Chinese）

Mineral composition and trace elements in Balkan bituminous coal, Bulgaria

Mariana G. Yossifova
Geological Institute – Bulgarian Academy of Sciences, Acad. Georgi Bonchev Str., Bl. 24, 1113 Sofia, Bulgaria

Abstract. Raw coal, coal concentrate, coal slime and host rock were studied. The identified minerals and phases are sulphur, gold, pyrite, marcasite, $Fe_{1.24}S_{0.76}$, pyrrhotite, galena, spinels, Ti-bearing minerals, Fe-oxyhydroxides, quartz, clay minerals, mica, feldspars, zircon, calcite, dolomite, ankerite, celestine, gypsum, cosmogenic dust (?), etc. The elements Mo, Cs, W, S, V, Cr, Cd, Te, and U are enriched in the coal concentrate as compared with the average values of the world hard coal. Magnesium, Be, V, Sr, W, Cu, Ge, U, S, Ag, Sc, Yb, Lu, Tm, Ni, Er, and Y (and to a lesser extent Sb, Ho, Co, Dy, Th, Tb, Zn, and Cr) are organically associated, while Al, K, Si, Rb, Li, Ti, P and Se have a distinct inorganic mode of occurrence. Some of the trace elements were found as impurities in different minerals, while La, Ba, Cu, Re, Pb, Gd, Nd, Sr, Sn, Nd, Cr, and others were detected in discrete phases.

Keywords. Coal, Minerals and phases, Geochemistry

1 Introduction

Coal is an alternative source for extraction of some trace metals. Studying of coal mineralogy and geochemistry therefore has fundamental, practical and ecological importance.

This paper presents the mineral and geochemical investigations of the Balkan bituminous coal (Bulgaria).

2 Geological Setting

The Balkan coal basin is located in the South-eastern part of the central Balkan Range and occupies its highest parts (Fig.1). It has a length of 75 km eastward-westward and a width from 5 to 20 km. The basin was formed in a coastal lagoon environment and a further transgression cycle followed when the sea drowned three river valleys The Subhercynian, Laramide, and Pyrenean orogenic phases formed the geological development of the basin.

The age of coal-bearing sediments has not been completely specified, but Early Cenomanian age is accepted. The Balkan coal-bearing sediments are divided to three formations: Basal, Coal-bearing and Marl Formations. The Basal Formation (0-100 m) lies discordantly upon Paleosoic (gneisses, amphibolites, granitoids), Triassic and Jurassic rock materials and includes conglomerates, sandstones and argillites. Coal-bearing Formation (20-100 m) is represented by dark to black argillites including siderite concretions, clay marls, sandstones and eight coal seams. Due to thrusting the coal formation is repeated two or occasionally three times in the exposed tectonic stratigraphic sequence. The Marl Formation includes dark to light-grey clay-siltstone

marls (60-95 m). Natural coke occurs also in the western part of the basin, and is a result heat from Lutetian basalt dykes. The northern and eastern margins of the Balkan basin are in contact with Upper-Triassic evaporate sediments. One of the polymetal deposits in the region is the Sliven industrial U-polymetal deposit (Fig. 1). It is included in the contact zone between Triassic sediments and a Permian quartz-porphyry. The volcanic and magmatic rocks to the south of the basin are part of the magmatic belt that covers the region from Apuseni Mountains to Small Caucasus. The age of these magmatic rocks varies, but for Sredna Gora (Bulgaria) it is between Late Cenomanian up to Early Campanian. Tuffs in a marl suit of Upper Cenomanian in the region of Tranak village (Kanchev, 1966) indicate the start of andesitic volcanism (Fig. 1).

Figure 1. Location of the Balkan coal deposit, Bulgaria

3 Material and Methods

Four types of composite samples were taken from the laboratory and depositories at the Tvarditsa Central Flotation Plant and studied. They include: (1) five different samples of raw coal from Kachulka, Chumerna, Sheshkingrad, Boyan Dol and Paissiy mines. The names of mines are listed according their location in direction from East to West; (2) coal flotation concentrate; (3) coal slime (small-grained waste product ≤ 1 cm); and (4) host rock (coarse-grained waste product > 1 cm). Water from Tvardishka river, kerosene as collector and boric oil as foaming agent are used in the technological process.

The following treatments and methods were applied: (1) Sample preparation included: drying at room temperature; sieving of coal concentrate and coal slime; magnetic separations of coal concentrate and coal slime; handpicking under a binocular microscope to concentrate the minerals present; high-temperature ashes were produced from combustion in an open muffle furnace at

450°C; obtaining of water leachates and dry water-soluble residues; (2) Analysis was carried out using: powder X-ray diffraction; SEM equipped with an EDS; X-ray fluorescence (Al, Si, Na, K, Ca, Mg, Ti, Fe, Mn, P and S); atomic absorption spectroscopy (Li); neutron activation analyses (Ir, Pt, and Au) and LA-ICP-MS.

4 Results and Discussion

4.1 Coal-hosted minerals

The major minerals identified during this study are pyrite, quartz, and kaolinite, while the minor minerals include illite, muscovite, plagioclase, K-feldspar, gypsum, calcite, dolomite, and siderite. Other species found in this coal occur as accessory minerals (gold, sulphur, marcasite, pyrrhotite, the phase $Fe_{1.24}S_{0.76}$, galena, hematite, magnetite, spinels, Ti-bearing minerals, gibbsite, zircon, stilbite, apatite, celestine, anhydrite, chalcanthite, ankerite, etc.). The minerals are listed according the mineral classification of Kostov (1993).

4.1.1 Native elements

Gold contains Cu (1.3 wt.%,) and is present as grains sized 10 and 20 μm. It is most likely of a terrigenous origin according to its occurrence in an association with clay minerals and quartz grains.

Sulfur was observed as: (1) lumps containing impurities of Al, Si, Fe, K and Cl up to 10 wt.% associated with terrigenous quartz grains. The sulfur lumps are most likely of autigenic origin and impurities of clay minerals and chlorides; (2) irregular grains (10-15 μm) associated with euhedral pyrite; powdered aggregates containing chlorine (2-3 wt.%) and associated with cryptocrystalline gypsum concretions on framboidal pyrite; and as transparent monoclinic crystal. An epi-exogenic origin is suggested for the latter as a result of pyrite oxidation.

4.1.2 Sulfides

Syngenetic pyrite forms framboids, euhedral crystals and massive grains. The epigenetic pyrite is present as crypto-crystalline massive crusts or as individual 2D crystals. Epigenetic framboidal pyrite forms lenses fracture fillings in the organic matter. It has probably due to environment changes. Marcasite is closely associated with pyrite. It occurs as tabular, bi-pyramidal crystals and poly-crystalline aggregates.

The phase $Fe_{1.24}S_{0.76}$ was identified as aggregates in coal. This phase has probably a syngenetic origin and was formed in a highly reducing environment. It could have formed a result of a dehydration of hydrotroilite or sulfure replacement in siderite.

Pyrrhotite (10-100 μm) and galena (2x3 and 6x10 μm) were identified as grains in coal slime. Pyrrhotite was also found in the magnetic fraction of coal concentrate. Impurities such as Sb (8.2 wt.%,) in galena and Ni (2-7 wt.%) in pyrrhotite were identified. These phases are assumed to be authigenic and associated with the other sulphides. Grains with a composition close to pyrrhotite were also found in lenses of euhedral pyrite were analyzed.

4.1.3 Oxides and hydroxides

Hematite is present as flakes and as a recovered single plate particle (10x30 μm). Magnetite is present as 10 μm sized octahedral crystals and irregular or semi-rounded grains up to 0.1 mm. Hercynite is present as 5 μm grains containing impurities of P (1.1 wt.%,), Ni (6.8 wt.%), Cu (1.3 wt.%) and As (2.9 wt.%). Cr-spinel is present as 40x50 μm grains associated with clay minerals. Gibbsite occurs as 1x10 μm aggregates of kidney-shaped grains and impurities of Ni, K, Fe, and P.

Ti-bearing minerals include rutile (2x8 μm), anatase/broockite (8x10 μm), and ilmenite (3x4 and 5x10 μm). These minerals are probably of terrigenous origin. Hematite could be also a weathering product resulted from the oxidation of other Fe-bearing minerals. Gibbsite may be of authigenic origin as a result of low-temperature hydrothermal solutions.

4.1.4 Silicates

Quartz is present as terrigenous rounded grains up to 100 μm in size. The clay minerals present are mainly kaolinite, illite and halloysite. Kaolinite and illite contain impurities of S, Cl, Na, and Mg and have both terrigenous and authigenic origin. Halloysite was identified as tubular crystals up to a length of 30 μm and has authigenic origin, probably from weathered volcanic material.

Mica present as muscovite and subordinate biotite and siderophyllite. Feldspars are represented by K-feldspar, mainly sanidine and by calcium-rich plagioclase. Zircon recovered in coal slime was one elongated crystal sized 5x10 μm and rounded grains sized 30x40 μm. Impurities of Hf (1.3 wt.%) and Y (3.2 wt.%) were detected in the elongated crystal. The zircon grains have a dominant detrital origin, while sanidine probably originate from pyroclastic materials.

4.1.5 Sulfates

Gypsum occurs as: (1) cryptocrystalline concretions and as crusts on framboidal pyrite; (2) plate crystals sized up to 30 μm; (3) prismatic crystals with a length up to 0.1 mm; (4) forming lenses and veinlets as well as fine-grained crusts in cracks in the organic matter. Gypsum has either an epigenetic origin or is a weathering product (exogenic) of other minerals (Yossifova, 2007).

Celestine is found as platy crystals forming aggregates, and contains impurities of Ba, K, Ca and Fe. It has an epigenetic origin. Anhydrite is a characteristic mineral of waste products. It is most likely a result from gypsum dehydration. Chalcanthite was identified in dry water-soluble residues. Its origin could either be exogenic or detrital.

4.1.5.1 Neoformed phases by microbial activity

The Balkan coals "whiten" as a result of microbial processes. This mineralization (sulfates of Ca, Fe, Al,

and Na, sulfur and Fe-oxides) has a whitish to lemon-yellowish color and is often associated with pyrite. Microorganism colonies have been shown to be responsible for this mineralization process. The exogenic mineralization is observed: (1) in mined coals that are stored in the open in a hot and dry environment; and (2) and in partially dried samples at room temperature. These samples show that the whitening appears after some time and is most intense in pyrite-rich coal samples.

4.1.6 Carbonates

Calcite has syngenetic and epigenetic origin. Massive syngenetic calcite was observed separately or associated with massive pyrite to fill cell lumens of fossilized plants and to encrust cellular walls. It also occurs as matrix between euhedral pyrite in well-formed veinlets and lenses in organic matter. Prismatic and rhombohedral calcite crystals sized up to 90-100 μm forms within ankerite matrix. Rhombohedral calcite is present as veinlets and lenses and as cover on fine-grained octahedral pyrite. Epigenetic calcite is most probably hydrothermal or precipitated from meteoric fluids. Calcite occurs both as massive bands cementing coal pieces and as fine semitransparent lamella deposited in cracks in organic matter.

Ankerite forms saddle-like prismatic crystals in aggregates and crusts. Epigenetic ankerite was also found as massive bands cementing coal pieces together.

Dolomite, siderite and Mn-calcite were identified by X-ray diffraction. Siderite spherulites (10 μm) were observed in the fine slime fraction. It could be a relict of a syngenetic cryptocrystalline mineralization, which has been replaced by pyrite during the evolution of the basin. Fe-dolomite and pure $CaFe(CO_3)_2$ were identified by SEM. The former mineral was observed as veinlets filling cracks in the organic matter. Both phases have an epigenetic origin.

4.1.7 Other phases

Spherules, spheroids and irregular particles of alumosilicate and iron-oxide composition were found included in coal samples and the magnetic fractions. They may be of cosmogenic origin and had been deposited during coal formation.

4.2 Mineral composition of slime and host rock

The mineralogy of the host rock is quartz, kaolinite > muscovite, illite, calcite > pyrite+marcasite > plagioclase of which quartz and clay and mica minerals constitute about 90%. The dominant minerals in coal slime are also quartz, kaolinite and muscovite, but their concentrations are lower than in the host rock. A large number of accessory minerals were found in coal slime as well as the neomineralised secondary barite and gypsum.

Dry residues of water leachates from host rock, slime, and coal were studied in order to understand the formation of some secondary phases. The identified phases are: thenardite, gypsum, calcite, konyaite, burkeite, blödite, hexahydrite, halite, vanthoffite,

epsomite, sylvite, K-sulfate, chalcanthite, sulfur, trona, barite, cerussite as well as some unusual phases (Table 1 and Fig. 2).

Table 1. Composition of uncommon phases (wt. %) in dry water-soluble residues

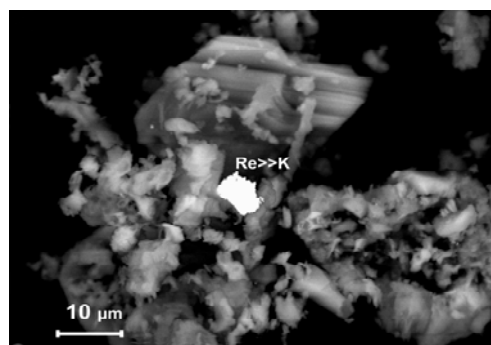| Elements	μm	Elements	μm
Fe>>W>Cr>V>>Mn	5x7	Pb>Re>Cu>K	3x3
Ce>>Fe>La>S	10x10	Re>>S>Ca>K	2x5
La>Ba>Cu	5x6	Re	>1
Sr>Gd	1.5x3	Re>Pb>As>K	10x10
Ba>Nd>Al>>Ca,S,Mg	2x2.5	Re>>Ca,K,S	≥ 1
Ag(57%)>Au(43%)	25x25	Re>>K>Ca	1.5x5
Au=Cu	8x12	Re>>K	6x8
Au>>Cu	2x6.5	Re>K>Cl	1.5x2
Au	4x4	Re>>K>Ca>>S	2x3
Cu>>Sn	5X7	Re>Pb>Cu>K	1.5x2
Cu>>Mg,Ca,S	2x2	Re>Pb>>Cl,Mg	2x3
Ni>Fe>Cr>Cu	1x1	Re>K>Cu>Pb	1.5x1.5
Pb>>S	5x5	Re=Cu=K	1.5x2
Pb>Re>K,Ca,S	3x4	Re=Cu+Pb>K	2x2.5

Figure 2. Re-bearing phase in dry water-soluble residues

4.3 Geochemistry of coal

A total of 64 chemical elements were analysed. The concentration of these elements in the coal samples were compared with their respective Clarke values of world hard coal (Ketris and Yudovich 2009). The term "Clarke" represents average composition of chemical elements in different rocks, coal, soils, plants, etc. world-wide. Historical background and definition of the term "Clarke" is described in Ketris and Yudovich (2009). Concentrations in the coal slimes were compared both with the Clarke values for hard coal and for sedimentary rocks (Ronov et al. 1990). The concentrations of the elements in the host rock are compared with those for the sedimentary rocks.

The major ash-forming elements (>1% by weight) in the coal concentrate (ash yield, 13.7%) are S, Si, and Al. Minor elements are Fe, K, and Mg (1-0.1%). Nine elements exceed the Clarke concentration (Te_{10-50}, $S_{7.0}$, $Cd_{2.0}$, $U_{1.9}$, $Cs_{1.4}$, $V_{1.4}$, $Mo_{1.3}$, $W_{1.3}$, and $Cr_{1.1}$). Variations in major, minor and trace elements in the raw coal and coal slime reflect the influence of the local bedrock, the increase of the terrigenous and authigenic minerals. Host rocks contain some organic matter (ash yield, 20%) and thirty-two elements show concentrations in excess of the Clarke values.

4.3.1 Concentration trends of elements

The ratios between the equivalent elements (ash basis) in low-ash coal to high-ash coal samples or sedimentary rocks show whether a specific element has an organic matter affinity. In respect to the coefficient (Cf) from this ratio the elements are specified in three groups.

The first group (Cf=1) elements of coal concentrate includes Sm, Eu, Gd, P, and Ga; the second group (Cf=1-2): Cr, Zn, Tb, Th, Dy, Co, Ho, Sb, Y, Er, Ni, Tm, Lu, Yb, Sc, Ag; and the third (Cf>2): Mg, V, Be, Sr, W, Cu, $Ge_{3.3}$, $U_{4.3}$, and $S_{10.2}$. The elements of the last group have an affinity to organic matter as well as to syngenetic micromineral inclusions. The same may be valid for Ga in the same sample, because the ratio Ga/Al is the highest than the other samples, which suggests an organic affinity (Eskenazy, 1969).

The coal concentrate does not conspicuously differ from the worldwide bituminous coals in respect to the contents of the studied elements (with the exception of Te and S). Typomorphic elements for the Balkan coals are those with a Cf ≥ 1.5: Mg, Be, V, Sr, W, Cu, Ge, U, S, Y, Er, Ni, Tm, Lu, Yb, Sc, and Ag. Magnesium and S in Boyan Dol raw coal also show organic affinity. In coal samples from the mines Paissiy, Sheshkingrad, Kachulka and Chumerna the mineral mode of occurrence prevails, and with increasing of the quantity of carbonates, silicates and Fe-sulfides the concentrations of Sr, Ca, Zr, Hf, Re, Se and Au also increase.

Magnesium correlates positively to Fe, Ta, Mo, and Sb. Sulfur does not correlate significantly to ash yield and any other element. Zirconium and Hf correlate positively to each other (r=0.97). Their modes of occurrence are both mineral and organic. Neither element correlates with the ash yield, Si, Al, and K. Zirconium correlates with Ge, Ag, Ca, Sr, Mo, and As, while Hf correlates with Ge, Ag, Mo, As, Sr, and Sb. This could be explained as an association of elements and/or their phases which correlate with the organic matter. Re indicates a dominant organic affinity and correlates positively with Be, Ba, Bi, and Ni, and more weakly with Na, Cs, La, Tb, Lu, P, V, and Th. Selenium correlates strongly with ash yield (0.99); Al, K, Rb, Nb, Pr, Si, and Zn (0.98-0.96); Y, Cs, La, Ce, Nd, Sm, Eu, Dy, Ho, Er, Tm, Ta, P, Sc, Ti, Cr, Ga, Sn, Te, Bi, and Th (0.95-0.91); Li, Ba, Gd, Tb, Yb, Lu, V, Co, Ni, Cd, and In(0.90-0.81); and more weakly (0.80-63) with Na, Mo, W, Mn, Fe, As, Sb, Tl, Pb, and Be.

Other elements with a positive and significant correlation to ash yield are: Si (0.98); K (0.97); Al (0.96); Rb, Nb, Ce, P, Zn (0.94); Y, La, Pr, Nd, Sm, Ta (0.93); Ho, Tm, Sc, Tl, Co (0.92); Eu, Dy, Ga, Sn (0.91); Gd, Lu, Th (0.90); Er (0.89); Li, Cs, Ba, Cr, Bi (0.88); Ni, Te (0.87); In (0.86); Yb (0.85); Cu (0.84); Tb, V (0.83); Cd (0.82); Na, Mn (0.81); Fe (0.78); As, Pb (0.73); W (0.72); Mo (0.71); Sb, Tl (0.68); Be (0.61), and U (0.50).

The Th/U ratio is 1.7, based on the Clarke value for hard coal. In the samples studied it increases in the following order: coal concentrate and Kachulka coal → coal slime → Chumerna coal → Sheshkingrad coal and Boyan Dol coal → Paissiy coal → Host rock. This order shows a decrease in U enrichment in the organic matter from East to West. The Sliven U-polymetal deposit is thought to be the source of this element. In the coal wastes, Th/U value increases from the coal concentrate towards the coal slime and the host rock and depends on the quantity of organic matter. Uranium correlates positively with W, Sb, Sc, V, Zn, Cd, and Ag, and more weakly with Rb, Mo, Ta, Ti, Cr, Co, Ni, Ga, Tl, REE, Th, Al, Ba, Fe, Cu, As, ash yield, Li, Be, K, Si, P, Sn, Te, and Bi.

Almost all of the discussed elements have the highest concentrations in the eastern part of the basin. Mg, Cs, Ta, S, Sc, Ti, Fe, V, Ga, Cd, Sb, and Tl concentrations decrease to the west. This suggests that some of Pb is a radioactive decay product of pitchblende from Sliven U-polymetal deposit.

Some elements in the separated minerals have concentrations higher than in the coal concentrate sample: Sr, Ba, P, and Mn in calcite and dolomite; Mo, Mn, As, Pb, Sb, Tl, Li, Ti, Pb and Nb in pyrite;

The concentration of Cs, Tm, Yb, Ni, Cu, Sb, Ge, V, Cr, Be, U, Tl, Re, Bi, Yb, Ba, Mg, Ag, Au, and Ir(?) in coal slime is higher (≥1.5 times) than in the host rock.

5 Conclusion

The preconditions for forming of minerals and the sources or transport of various element are: fresh, mineral and sea waters; host rocks, source province, U-polymetallic ore and evaporate deposits; cosmogenic (?) and volcanic dust; hydrothermal and circulating water solutions; tectonic fault system; and probably radioactive decay of pitchblende from the Sliven U-polymetallic ore deposit.

The coal slime could be used for both fuel and as a resource for a number of elements.

References

Eskenazy G (1969) On the geochemistry of gallium during the coal formation process. Livre 1-Geologie, Annuaire de l'Universite de Sofia 61:321-348

Kanchev I (1966) Mediterranean type Upper Cretaceous in Ludakamchia area of Eastern Stara Planina. Proc Sci Res Geol Inst 3:45-70 (in Bulgarian)

Ketris M, Yudovich Ya.E (2009) Estimation of Clarkes for Carbonaceous biolithes: world averages for trace element contents in black shales and coals. Int J Coal Geol 78:135-148

Kostov I (1993) Mineralogy. Tehnika, Sofia, 734p

Ronov AB, Yaroshevsky AA, Migdisov AA (1990) Chemical Composition of the Earth's Crust and Geochemical Balance of Main Elements. Nauka, Moscow, 192p

Yossifova M (2007) Mineral and inorganic chemical composition of the Pernik coal, Bulgaria. Int J Coal Geol 72:268-292

Concentration trend of trace elements in coal, partings and vegetation from the Maritza East Coal region, Bulgaria

Mariana G. Yossifova, Dimitrina A. Dimitrova
Geological Institute – Bulgarian Academy of Sciences, Acad. Georgi Bonchev Str., Bl. 24, 1113 Sofia, Bulgaria

Abstract. The trace element composition in coal from the Troyanovo-2 and 3 open-pit mines, partings, waste products (fly and bottom ash), soil and vegetation have been analysed. Obtained element concentrations were compared to respective average world concentrations for coal, sedimentary rock, soil and vegetation. Coal is characterized with higher concentrations of S, Ti, P, Mn, Rb, Mo, Cs, Ba, Sc, Cr, As, Th, U and Au. Fly ash concentrates more trace elements than bottom ash (Mo, Cu, Pb, Zn, As, Co, Sb, Ba, etc). Black clay partings have Ag, Se, P, S, Pd, C, Cu, Zn, Te, Cd, Bi, As, Y, Pb, Pt, Ce, La, Th, Mo, Be, Ni, and Ca in higher concentrations compared to bluish-green and yellow clay partings. Concentrations of Cu, Zn, Pb and As in soil are bellow the guideline values and do not point out contamination. The accumulation ability of the studied plants in respect to the number of elements with concentrations over the lower Clarke limit values can be arranged as follows: *Hypericum perforatum* (blossom) > sunflower (heads) > wheat-ear ≥ *Typha* (blossom). Apparent contamination of soil and vegetation resulting of the mining and power-producing activity in the area for the present cannot be established.

Keywords. Lignites, Trace elements, Wastes, Partings, Vegetation

1 Introduction

Coal is a combustible sedimentary rock in which almost all elements of the periodical table can be present (Lebedev et al. 1980). Concentrations of elements in coal can be compared to so called "Clarke" values to find implications on coal genesis. The term "Clarke", used in this work, represents average contents of chemical elements in different rocks, coal, soils, plants, etc. world-wide. Historical background and definition of the term "Clarke" is described in Ketris and Yudovich (2009).

The aim of this study is to characterize in detail the relation and concentration trend of trace elements in coal, coal partings, waste products from coal combustion (fly and bottom ash), agricultural soils and vegetation from the Maritza East coal region and to evaluate the impact of coal mining and power production on the environment. Coal partings are interseam layers of clayey rocks usually found within coal seams.

The mining and power producing enterprise Maritza East (Fig. 1) is the biggest unit for lignite mining and thermo-electric power production in Bulgaria. It includes three large open-pit mines and four thermo-electric power stations (TEPS). The total area of the coal and power-producing enterprise includes more than 200 km².

2 Geological Setting

The Maritza East lignite basin is a part of the Zagore depression of the Upper Thracian tectonic trough and has a complex geological structure (Valćeva et al. 2000). The formations have been divided into three units: basement, coal-bearing and superstructure (Nedyialkov 1979). The basement consists of granites, metamorphic and sedimentary rocks of different age (from Late Cambrian to Late Cretaceous) and variably altered. The Miocene coal-bearing formation is well developed with a sandy–clayey suite at bottom (Nedyialkov 1985) and Marishka (Troynovo) coal level (Panov 1982). The coal-bearing level consists of three lignite seams interbedded by grayish-black thinly layered clays. The second seam with maximum thickness of 24 m bears the main coal reserves. The superstructure - Gledachevska Formation (Nedyialkov and Kojumdgieva 1983) covers the Maritza coal-bearing sediments. It lies in conformity with Marishka Formation and is covered, in turn, by Quaternary sediments. The lithology of Gledachevska Formation consists of clays, sands, and limestones. The clays are the dominant rocks in the sedimentary sequence. They are grey to bluish-green or light green, and rust-yellowish in colour, layered, dense with variable quantity of sand. The sands and sandstones form lenses or pinching out intercalations between the clayey layers, mostly in the uppermost parts of the sediments covering the coal complex (Valćeva et al. 2000).

Volcanic-sedimentary, magmatic and metamorphic rocks outcrop in the surrounding area of the basin: 1) Tuffs and limestones of Oligocene age occur at the S-SW end of the basin; 2) Late Paleozoic granites exist at ~10 km away in NW direction; and 3) Late Paleozoic metamorphosed granites occur at ~20 km SE away of the coal basin.

3 Materials and Methods

Six types of composite samples were studied: 1) fuel for burning in TEPS, taken from the depositories; 2) partings (black, blue-green and yellow coloured clays); 3) coal from the Troyanovo-2 and 3 mines; 4) waste products of coal combustion (fly and bottom ash) from the Maritza East-2 TEPS and Brikel TEPS; 5) cultivated and wild vegetation; and 6) agricultural soil associated with wheat.

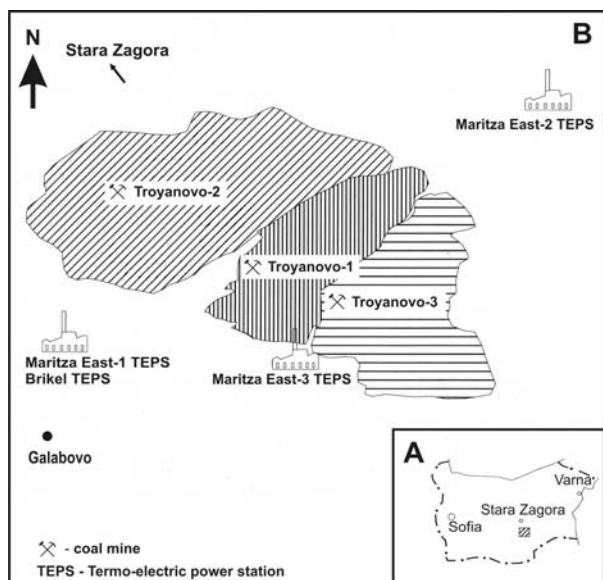The samples were studied by wet chemical analysis, XRF, ICP-MS and INAA.

Figure 1. (A) Location of Maritza East region, Bulgaria; (B) Sketch map of Maritza East lignite thermo-electric power enterprise unit, modified after Ganchev and Bossev (1988).

4 Results and Discussion

4.1 Geochemistry of coal

The concentrations of 43 elements measured in coal samples were compared to the Clarke values for brown coal (Ketris and Yudovich 2009) and shales (Beus and Grigorian 1975) to evaluate the specific geochemical characteristics of the basin compared to other coal basins world-wide. The major ash-forming elements exceeding Clarke concentrations are: S (3.4-5.71 %), Ti (0.1-0.2 %), P (0.03-0.06 %) and Mn (0.01-0.02 %). The ash content of coal is in the range 20-34%. The highest concentrations of trace elements are respectively detected in samples with highest ash content (fuel for burning in the Maritza East 2 TEPS). This can be explained with presence of mineral content and xylite (woody material) in them. Xylite concentrates more sulphur than other coal lithotypes. The following trace elements show equal or relatively higher concentrations than Clarke values in ppm: Rb (16), Mo (9-10), Cs (2), Ba (260-330), Br (4.3-5), Sc (3.4-4.7), Cr (15-25), Co (4-6), As (13-16), Th (2.9-4.7), Au (0.005-0.006).

Vitrain lithotype is characterized by higher concentrations of the following elements in ppm, compared to other lithotypes: Mo (6), Ba (180), As (18), Ir (0.005) and Au (0.018).

4.2 Geochemistry of fly and bottom ash

The waste products are composed of SiO_2 (38.6-46 wt.%), Al_2O_3 (18-23 wt.%), Fe_2O_3 (11.6-13.9 wt.%) and CaO (7.7-11 wt.%). Fly and bottom ash mainly comprises amorphous aluminosilicate glass spheres and angular particles formed during combustion. Ash is enriched in magnetite as a result of thermal transformation of Fe sulphides and carbonates during coal burning (Vassilev 1991). Titanium (4700-5900 ppm), P (800-2000 ppm) and Mn (700-900 ppm) show equal or relatively higher concentrations compared to Clarke values for ash of brown coal, excepting Mn (2500 ppm) in the bottom ash from Maritza East-2 TEPS. The bottom ash from Brikel TEPS has 46.2 % ash yield, which suggests the presence of char (unburned organic matter). Rubidium (59-88 ppm), Mo (20-76 ppm), Cs (5-8), Cr (60-110 ppm), Co (13-61 ppm), Zn (<50-160 ppm) and As (15-86 ppm) exceed the Clarke values for brown coal ashes.

4.3 Geochemistry of partings

The concentrations of 55 elements have been analyzed in parting (interseam) layers. They represent black thin layered clays interbedding the coal seams and bluish-green and yellow clays covering the coal-bearing formation. Major and trace element concentrations in partings were compared to Clarke values for shale (Beus and Grigorian 1975) and sedimentary rocks (Ronov et al. 1990), respectively, excepting for Pt and Pd, which were compared to Clarke values for brown coal. It was found that 22 elements in black clays have concentrations higher than the Clarke values. Their factor of enrichment/depletion (EDF) is as follows: $Ag_{(13.2)} > Se_{(7.8)} > P_{(7.3)} > C_{(6.28)} > S_{(6.1)} > Pd_{(5.2)} > Cu_{(3.3)} > Zn_{(3.2)} > Te_{(3.0)} > Cd, Bi_{(2.9)} > As_{(2.5)} > Y, Pb, Pt_{(2.3)} > Ce_{(2.2)} > La, Th_{(2.1)} > Mo_{(1.9)} > Be_{(1.8)} > Ni_{(1.7)} > Ca_{(1.1)}$. The concentrations of trace elements in black clays are higher than those detected in bluish-green and yellow clays (Fig. 2A). This can be explained with the presence of organic matter (6.41% C_{total}). Mercury, In, Sc have concentrations equal to Clarke values.

Unlike black clays, bluish-green and yellow clays show enrichment in regards to 13-14 elements. Bluish-green clay is characterized by elevated concentrations of U and Pt compared to Clarke values ($Pt_{(27.2)} > Se_{(4.8)} > U_{(4.2)} > Te_{(3.0)} > Bi, Ag_{(2.8)} > Pb_{(2.4)} > Th_{(2.3)} > Cu_{(1.5)} > Zn_{(1.3)} > Be_{(1.2)} > S, Co_{(1.1)}$).

Yellow clays are enriched in Pb, Th and Au in comparison to other partings and Clarke values. Their factor of enrichment/depletion (EDF) is as follows: $Ag_{(9.1)} > Bi_{(3.3)} > Pb_{(3.1)} > Te_{(3.0)} > Th_{(2.7)} > Co_{(2.2)} > Ce_{(2.2)} > S, Cu_{(1.9)} > La_{(1.7)} > Au_{(1.4)} > Be, Y_{(1.3)} > Zn_{(1.2)}$.

4.4 Geochemistry of soil and vegetation

A total of 55 elements were determined in soil from the wheat field. 22 elements have concentrations over Clarke values for chernozem soil (Kabata-Pendias and Pendias 1985). The concentrations of these elements (in ppm) are as follows: Li (11.4), Mg (6145), Sr (80.9), Ba (343), Ce (60.2), Ti (3652), V (44), Cr (26.2), Mn (698), Co (22), Ni (22.5), Cu (23.2), Zn (35.7), As (5.8), In (0.02), Sn (0.9), Pb (23.8), Bi (0.24), Th (8.8), U (0.7) and Ag (0.28).

The coefficient of biological consumption (CBC) (Perelman 1975) of wheat is defined by the element concentration ratio of plant/soil. It shows that P and Pb are enriched in wheat-ears, while K and Au are enriched in wheat stems+leaves. Molybdenum and S are enriched in both wheat-ear and stems+leaves.

The vegetation samples comprise cultivated (wheat

and sunflower) and wild plants (*Hypericum perforatum* and *Typha*), taken from areas in the vicinity of the coal mines and TEPSs. The obtained concentrations for 53 elements were compared to both lower and upper limit of Clarke values for terrestrial vegetation world-wide (Kabata-Pendias and Pendias 1979). Since vegetation samples were taken in the vicinity of mining and power producing region, only EDF compared to the upper limit of Clarke will be taken into consideration (Fig. 2B).

Wheat-ears show concentrations of 13 elements exceeding the lower limit of Clarke values (Al(?), K, Mo, P, Sc, Ti, V(?), Cr, Zn, Te(?), Bi, and Au). Only the following elements have EDF compared to the upper limit of Clarke values: $V_{(<2.9)}$, $Sc_{2.0}$, $Au_{1.3}$, and $Cr_{1.1}$. Aluminum (?), K, Sr, Mo, Ba, S, Sc, Ti, V(?), Cr, Ni, Te(?), Pb, Bi, and Au have concentrations over the lower Clarke limit in wheat stems+leaves, whereas these with values above the upper Clark limit are: $Au_{23.0}$, $Cr_{3.2}$, $V_{<2.9}$(?), $Sc_{2.0}$, $Pb_{1.7}$, $Sr_{1.4}$, $(Mo, Ni)_{1.1}$. Half of the measured elements show trend for concentration in stems+leaves: Pb, Au, Hg, Ag, Ba, Bi, Ca, K, Sr, Li, Y, Cr, Ni, Na, Zr, and La. Only 6 elements tend to accumulate in the wheat-ears: P, Ti, and Zn. The other 17 elements are equally distributed in all parts of the plant.

Sunflower samples were taken from two different areas, near the Maritza East-2 TEPS and Maritza East-3 TEPS. However, the concentrations of detected elements in both samples are similar. Sunflower concentrates Sc, Ti, K, P, Cr, Bi, Ca, Au, Mo, Sr, Mg, B, S, Se, Bi and Cu with EDF ≥ 2 compared to lower Clarke values. Iron, Ce and Y are enriched in stems+leaves, while Re, B, P, Ni, Bi, Co, Cu, Zn, Ge, Se, Hg and Ag are enriched in sunflower heads.

Hypericum perforatum accumulates 29 elements of all measured, having concentrations over the lower Clarke limit. Unlike sunflower and wheat where most of the elements are enriched in stems+leaves, a wide variety of elements is observed in the blossoms of *Hypericum perforatum*. Elements with EDF exceeding the upper limit of Clarke values in blossoms are: $Au_{11.8}$, $La_{6.7}$, $Li_{5.2}$, $(Mo, Se)_{4.0}$, $U_{3.4}$, $V_{<2.9}$(?), $As_{2.5}$, $Sr_{2.2}$, $Sc_{2.0}$, $P_{1.5}$, $Cr_{1.3}$. The stem+leaves samples contain the same group of elements, but with different EDF values such as: $Au_{37.5}$, $Cr_{2.9}$, $V_{<2.9}$(?), $Li_{2.3}$, $La_{2.1}$, $(Sc, Se)_{2.0}$, $U_{1.8}$, $Sr_{1.5}$, and $Mo_{1.4}$.

In both *Typha* samples, namely blossoms and stem+leaves, a total of 14 and 15 elements, respectively, have concentrations over the lower Clarke limit. Elements which have concentrations exceeding the upper limit of Clarke value in blossoms are $Au_{21.0}$, $V_{<2.9}$(?), $Sr_{1.7}$, and $Se_{1.5}$, while these elements for stem+leaves are $Au_{15.8}$, $V_{<2.9}$(?), $Li_{2.7}$, $(Sc, Se)_{2.0}$, $Sr_{1.7}$, and $K_{1.1}$. Almost all elements (23) are equally accumulated in blossoms and stem+leaves.

Elements such as Hg, Ni, Y, Mo, Mg, P, Zn, K, Co, Se, Au, Ba, Ca, and Pt were concentrated in blossoms. On the other hand, elements such as Li, Cd, Hf, Sc, B, Pb, Mn, Ti, Cu, Na, Cr, Sb, Zr, S, and Re were determined in stem+leaves. It should be stated that Li demonstrates a trend of high concentration in stem+leaves (27 times).
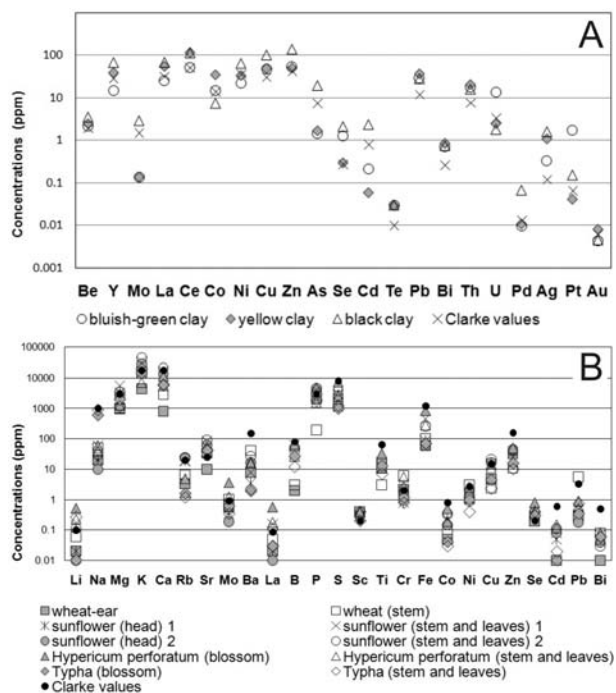

Figure 2. Concentrations of elements exceeding Clarke values: A) partings; B) cultivated and wild vegetation.

4.5 Element concentration trends in different types of samples

The concentration of only 18 elements detected in all samples are considered potentially toxic to the environment, and monitored by the authorities (Cu, Pb, Zn, As) are compared in Fig. 3.

The concentrations of almost all elements in vegetation samples are very low compared to other samples, except Cu, Zn, Mn, Ba, which exceed 10 ppm (Fig. 3). It is well known that Cu, Zn and Mn take part in photosynthesis and normally are intaken by plants. However, these concentrations do not point out pollution. Compared to concentrations in soil, only Mo and Zn show trend to concentrate in cultivated plants (sunflower and wheat). Even the concentrations of the most hazardous elements Cu (23.2 ppm), Zn (35.7 ppm), Pb (23.8 ppm) and As (5.8 ppm) in soils, monitored by the authorities, are below the guideline values. Thus, apparent contamination of agricultural soil is not observed. Only Ba and Mn concentrations reach values above 340 ppm, but normally they are not considered as harmful. These elements are present in soil mainly in carbonates (calcite). Comparison between soil and covering partings (yellow and bluish-green clays) show that only Mo, Mn, As, Cr and Ba are enriched in soil, thus can suggest some relation to them.

The influence of coals and waste products (fly and bottom ash) on the trace element composition of soil is indistinct. Gas emissions could have influence on the soil composition, but such connection is not confirmed in this study. Compared to coals, waste products are generally enriched in all elements. Highest concentrations are detected in fly ash, especially As and Pb.

Comparison between coal and covering partings (yellow and bluish-green clays) show that most of the elements are enriched in clays. However, these contents suggest gradual enrichment related to the influx material in the basin coming from the source province. Concentrations of La, Ce, U and Th are usually relatively high in granitic rocks. In this case their presence in clays can be related to the Late Paleozoic granites outcropping SE and NW from the basin. Since black clay partings are inbedded within coal seems, their composition is very similar. Only few elements tend to concentrate in coal (Mo, U, Sb, Ba and Cs) and are probably incorporated by organic matter.
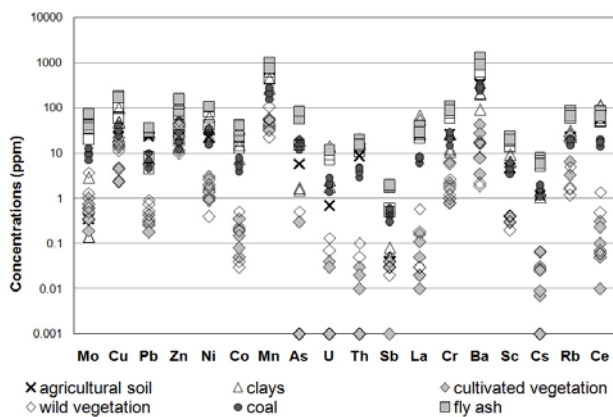

Figure 3. Element distribution in different types of samples.

5 Conclusions

This study shows that coal from the Maritza East coal region is characterized with equal or higher concentrations of S, Ti, P, Mn, Rb, Mo, Cs, Ba, Br, Sc, Cr, As, Th, U and Au compared to Clarke values for brown coal. Vitrain lithotype accumulates Mo, Ba, As, Ir and Au in concentrations higher than those detected in coal and other lithotypes.

Black clay partings have more elements (Ag, Se, P, S, Pd, C, Cu, Zn, Te, Cd, Bi, As, Y, Pb, Pt, Ce, La, Th, Mo, Be, Ni, and Ca) in higher concentrations compared to bluish-green and yellow clay partings. This is caused by the organic matter, which also incorporates certain elements, especially Mo and As.

Fly ash generally concentrates more trace elements than bottom ash (Mo, Cu, Pb, Zn, As, Co, Sb, Ba, etc).

Same geochemical signature is found in vegetation from the Maritza East region. Each plant species, however, have specific affinity to intake certain elements and accumulates them in different parts (stems+leaves, blossoms). The accumulation ability of the studied plants in respect to the number of elements with concentrations over the lower Clarke limit values can be arranged as follows: *Hypericum perforatum* (blossom) > sunflower (heads) > wheat-ear ≥ *Typha* (blossom).

Possible sources for enrichment of these elements in the Maritza East coal region can be: basement host rocks, volcanic-sedimentary rocks (volcanic ash and limestones), granites and granitic gneisses, circulating underground and surface waters, and tectonic fault system. Surface water influx probably has a major role in element mobility from sources (host rocks, granites, volcanics) to coal basin as it carries elements as soluble complex ions, colloids and mineral particles. Within the basin pH and Eh of waters decrease due to organic matter decay, which enhances further biochemical weathering of mineral grains and their incorporation in the organic matter as organic-metallic compounds.

The results give an important information about the concentration trend of some trace elements in the food chain, biofuel and boimass.

The obtained results do not show apparent environmental impact of the mining and power-producing activity in the area.

References

Beus A, Grigorian C (1975) Cheochemical Methods of Prospecting and Exploration of Solid Mineral Resource Deposits. Nedra, Moscow, 279p (in Russian)

Ganchev G, Bossev G (1988) 120 MW new and replacing powers in "Maritza East" until 2010. Minno Delo Geologia 5-6:24-27 (in Bulgarian)

Kabata-Pendias A, Pendias H (1979) Trace Elements in the Biological Environment. Wydawnictwa Geologictwa, Warszawa, 299p (in Polish)

Kabata-Pendias A, Pendias H (1985) Trace elements in soils and plants. CRC Press. Inc Boca Raton, Florida, 315p

Ketris M, Yudovich YaE (2009) Estimation of Clarkes for Carbonaceous biolithes: world averages for trace element contents in black shales and coals. Int J Coal Geol 78:135-148

MOEW (Ministry of Environment and Water) (2008) Regulation № 3 of 1 August 2008 on the maximum permissible concentration values of pollutants in soil. State Gazette 71 (in Bulgarian)

Nedyialkov N (1979) Maritza East lignite basin – mining and geological conditions, qualitative characteristics and features of the deposit. Coal 9:8-12 (in Bulgarian)

Nedyialkov N (1985) Geological structure of the Maritza East basin and landslide phenomenon. Summary of PhD theses, Bulgarian Academy of Science, Sofia 32p (in Bulgarian)

Nedyialkov N, Kojumdgieva E (1983) Stratigraphy of over coal-bearing sediments in Maritza East basin. Rev Bulg Soc 44:239-264 (in Bulgarian)

Panov G (1982) The Tertiary coal-bearing sedimentation in upper Thracian graben. Summary of PhD theses, Bulgarian Academy of Science, 32p (in Bulgarian)

Perelman A (1975) Landscape geochemistry. Vishaya Shkola Press. Moscow, 341p (in Russian)

Ronov AB, Yaroshevsky AA, Migdisov AA (1990) Chemical Composition of the Earth's Crust and Geochemical Balance of Main Elements. Nauka, Moscow, Science Pub. House, 192p

Valćeva S, Djourova E, Stanimirova T, Dimitrova D, Aleksieva L (2000) Mineralo-geochemical features of Gledachevska formation sediments in the Maritza East lignite basin and in the technogeneous soils of the recultivated tettains. Annuare de L'Universite de Sofia, Livre 1-Geologie 92:203-212

Vassilev S (1991) Phase mineralogy studies of solid waste products from coal burning at some Bulgarian thermoelectric power plants. Fuel 71:625-633